NASA

IEEE

THIRD INTERNATIONAL SYMPOSIUM ON SPACE TERAHERTZ TECHNOLOGY

JPL

The University of Michigan

SYMPOSIUM PROCEEDINGS

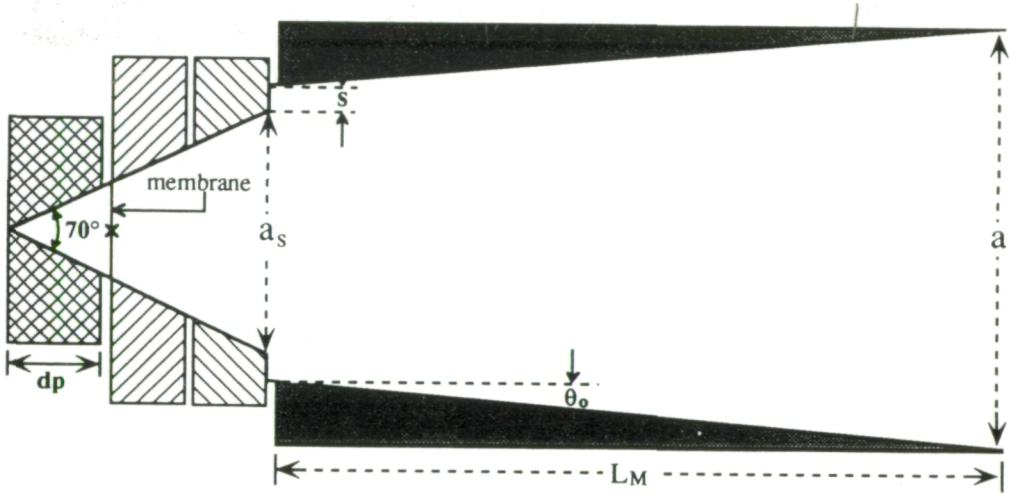

Integrated on Si section

Machined gain and phasing section

March 24-26, 1992

University of Michigan
Ann Arbor, Michigan

Sponsored by:
NASA Office of Aeronautics and Space Technology (OAST), University Space Engineering Research Centers Program, with cooperative sponsorship by the Microwave Theory and Techniques Society of IEEE.

Organized Jointly by:
The University of Michigan's NASA Center for Space Terahertz Technology and JPL's Center for Space Microelectronics Technology.

Proceedings of the
THIRD INTERNATIONAL SYMPOSIUM ON SPACE TERAHERTZ TECHNOLOGY

March 24-26, 1992

University of Michigan
Ann Arbor, Michigan

Organizing Committee

Symposium Co-chairs:	Fawwaz T. Ulaby, University of Michigan Carl A. Kukkonen, Jet Propulsion Laboratory
Technical Co-chairs:	Gabriel M. Rebeiz, University of Michigan Margaret A. Frerking, Jet Propulsion Laboratory
Local Arrangements:	Valerie Kabat, University of Michigan
Symposium Proceedings:	Valerie Kabat, University of Michigan

Group Photo

A group photo of some of the 1992 Symposium participants.

Preface

The Third International Symposium on Space Terahertz Technology was held at the University of Michigan in Ann Arbor, Michigan, on March 24-26, 1992. The Symposium, which was attended by approximately 165 scientists and engineers from the U.S., Europe, and Japan, featured papers relevant to the generation, detection, and use of the terahertz spectral region for space astronomy and remote sensing of the Earth's upper atmosphere. The program included thirteen sessions covering a wide variety of topics including solid-state oscillators, power-combining techniques, mixers, harmonic multipliers, antennas and antenna arrays, submillimeter receivers, and measurement techniques.

The Symposium was sponsored by the University Space Engineering Research Centers Program of NASA's Office of Aeronautics and Space Technology (OAST), and organized jointly by the University of Michigan's NASA Center for Space Terahertz Technology and JPL's Center for Space Microelectronics Technology. The Microwave Theory and Techniques Society of IEEE served as a cooperative sponsor of the Symposium, as well as a medium for publication of some of the papers that were presented at the Symposium in the form of a mini-special issue (April 1993) of the *IEEE-MTT Transactions.*

The Fourth International Symposium on Space Terahertz Technology will be held at the University of California, Los Angeles, on March 30-April 1, 1993.

Fawwaz T. Ulaby
Carl A. Kukkonen

Contents

*Presentation only.

Session 3: Varactors II **Chair: Ray Blundell**

Session 4: SIS Receivers I **Chair: Neville Luhmann**

Session 5: SIS Receivers II **Chair: David Rutledge**

**Abstract only.

Session 9: Sources II **Chair: James Mink**

Session 10: SIS Theory & Fabrication II **Chair: Anthony Kerr**

**Abstract only.

Session 11: Sources III **Chair: George Haddad**

Session 12: Mixers and Detectors I **Chairs: Margaret Frerking**

Session 13: Mixers & Detectors II **Chair: Thomas Crowe**

COHERENT SYSTEMS IN THE TERAHERTZ FREQUENCY RANGE: ELEMENTS OPERATION & EXAMPLES

PAUL F. GOLDSMITH

MILLITECH CORPORATION

South Deerfield MA, 01373

and

FIVE COLLEGE RADIO ASTRONOMY OBSERVATORY

Department of Physics and Astronomy

University of Massachusetts, Amherst MA 01003

TERAHERTZ COHERENT SYSTEMS APPLICATIONS

RADIOMETRY / SPECTROSCOPY

ASTRONOMY
ATMOSPHERIC REMOTE SENSING
ALL–WEATHER SYNTHETIC VISION SYSTEMS
CONTRABAND DETECTION

HIGH POWER

PLASMA HEATING
HIGH ENERGY ACCELERATORS

PLASMA DIAGNOSTICS

THERMAL IMAGING
DENSITY PROBING
BACKSCATTER MEASUREMENTS

COMMUNICATIONS

PERSONAL & VEHICULAR
DIGITAL DATA LINKS
TV REMOTE / STUDIO LINKS

MATERIALS MEASUREMENT AND COMMERCIAL PROCESS CONTROL

PAPER MAKING
HV CABLE MANUFACTURING

RADAR SYSTEMS

MILITARY – SEEKERS, INSTRUMENTATION, AND MODELING
AUTOMOTIVE COLLISION AVOIDANCE
ATMOSPHERE, METEOROLOGY, GROUND, ICE, AND FOLIAGE

COMPONENTS OF COHERENT SYSTEMS AT MILLIMETER & SUBMILLIMETER WAVELENGTHS

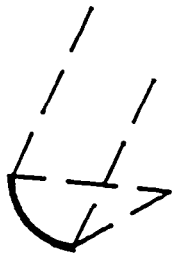

INPUT OPTICS

COLLIMATING MIRRORS AND LENSES

SIGNAL PROCESSING ELEMENTS

POLARIZING GRIDS
WAVEPLATES

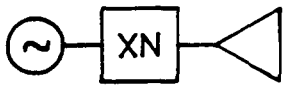

COHERENT SOURCE

LOCAL OSCILLATOR; TRANSMITTER

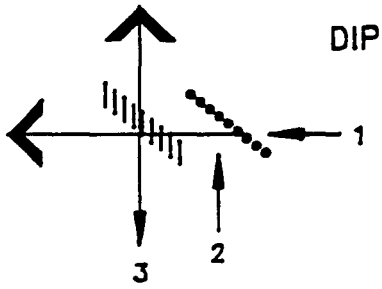

DIPLEXER

COMBINATION OF LOCAL OSCILLATOR AND SIGNAL

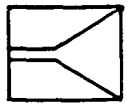

ANTENNA/FEED ELEMENTS

EFFICIENCY, BEAMWIDTH, BANDWIDTH, CONSTRUCTION INTEGRABILITY

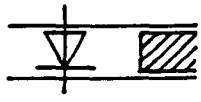

MIXER

CONVERSION LOSS; NOISE; L.O. POWER; BANDWIDTH

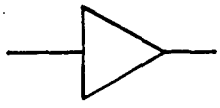

IF SYSTEM

NOISE; BANDWIDTH

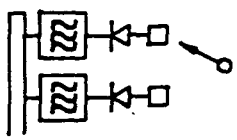

DETECTION/SIGNAL PROCESSING

SPECTROMETERS: FREQUENCY COVERAGE; RESOLUTION; FLEXIBILITY; POWER CONSUMPTION

BRIEF OVERVIEW OF SELECTED COMPONENTS

EMPHASIZE AREAS THAT I FEEL DESERVE MORE ATTENTION THAN THEY ARE RECEIVING AT PRESENT

[1] MATERIALS MEASUREMENT

FUNDAMENTAL FOR MANY ASPECTS OF SYSTEMS DESIGN

NEED MORE DATA, BETTER DATA, AND BETTER ACCESS

REXOLITE DATA FROM G. J. SIMONIS, J. P. SATTLER, T. L. WORCHESKY, AND R. P. LEAVITT, *INT. J. INFRARED AND MILLIMETER WAVES*, VOL. 5, 57 – 72, 1984.

BORON NITRIDE DATA FROM A. J. GATESMAN, R. H. GILES, AND J. WALDMAN *PROC. MATERIALS RESEARCH SOCIETY SYMPOSIUM ON WIDE BANDGAP SEMICONDUCTORS*, 1991 FALL MEETING, BOSTON

INTERCOMPARISON OF TECHNIQUES FOR DETERMINATION OF NEAR MILLIMETER DIELECTRIC PROPERTIES

JAMES BIRCH ET AL. – NATIONAL PHYSICAL LABORATORY
TEDDINGTON, MIDDLESEX
U.K. TW11 OLW

REPORT DES 115, OCTOBER 1991

[2] QUASIOPTICAL COMPONENTS

HOW CAN THEY BE FABRICATED IN SUBMILLIMETER REGION ?

TRADITIONAL MACHINING METHODS BECOME VERY DIFFICULT AND EXPENSIVE–

NEED TO FIND CONSTRUCTIVE COMBINATIONS OF METAL–WORKING AND SEMICONDUCTOR PROCESSING APPROACHES SUCH AS SELECTIVE ETCHING

EXAMPLES:

PROCESSING SILICON TO FABRICATE TWO DIMENSIONAL IMAGING HORN ANTENNA ARRAYS (REBEIZ ET AL. IEEE MTT 38, 1473 (1990))

ETCHING AND PLATING SILICON TO MAKE DICHROIC PLATE HIGH PASS FILTERS IN 1000 GHZ RANGE
(SIEGEL AND LICHTENBERGER 1990 MTT–S SYMP. DIGEST, 1341)

RADIOMETRY AND SPECTROSCOPY : ASTRONOMY

OBSERVING LOCATION DEPENDS PRIMARILY ON FREQUENCY:

GROUND – BASED
AIRPLANE AND BALLOONS: KAO; SOFIA
SPACE: SWAS; SMIM; FIRST

[1] SENSITIVITY

HIGHEST SENSITIVITY ALWAYS REQUIRED

CRYOGENIC COOLING IS ACCEPTABLE

BROADBAND SYSTEMS WILL BE REQUIRED FOR FUTURE SYSTEMS

[2] IMAGING SYSTEMS

FOCAL PLANE ARRAYS DEVELOPED FOR MILLIMETER RANGE:

FCRAO 15 – ELEMENT QUARRY ARRAY 85 – 115 GHZ
NRAO 8–ELEMENT ARRAY IN 230 GHZ RANGE

CANNOT SACRIFICE FEED EFFICIENCY SIGNIFICANTLY JUST TO OBTAIN LARGER NUMBER OF ELEMENTS DUE TO COST AND COMPLEXITY OF ASSOCIATED SIGNAL PROCESSING.

[3] OTHER COMPONENT DEVELOPMENT

RAPID PROGRESS IN FREQUENCY MULTIPLIER SOURCES, BUT FURTHER DEVELOPMENT REQUIRED FOR GREATER BANDWIDTH AND REACHING HIGHER FREQUENCIES

PLANAR HETERODYNE ARRAY USING A DIELECTRIC-FILLED PARABOLA

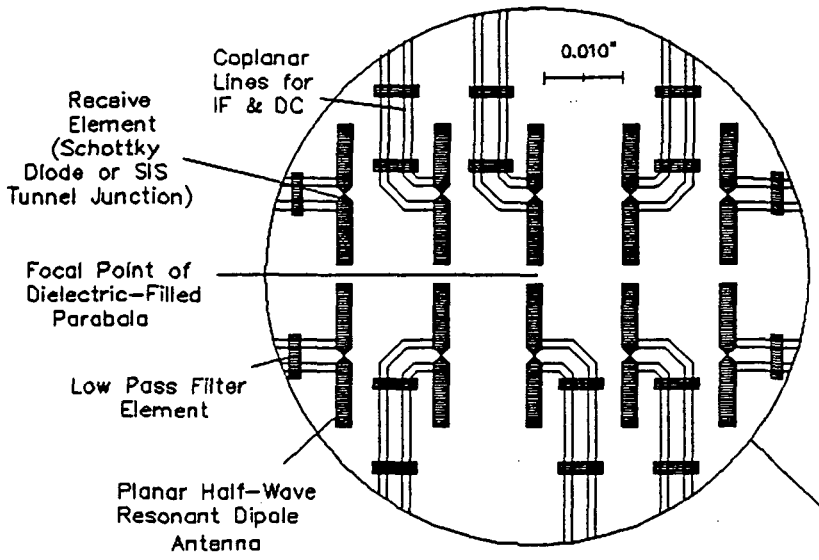

BLOW UP SHOWING ANTENNA ELEMENTS

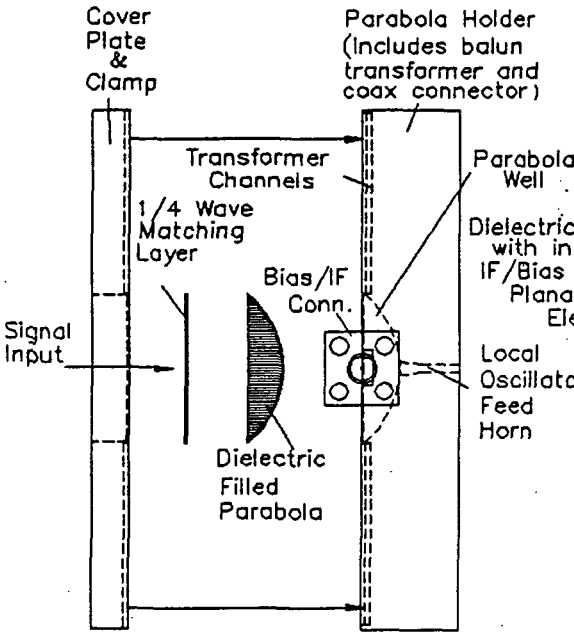

EXPLODED VIEW (SIDE)

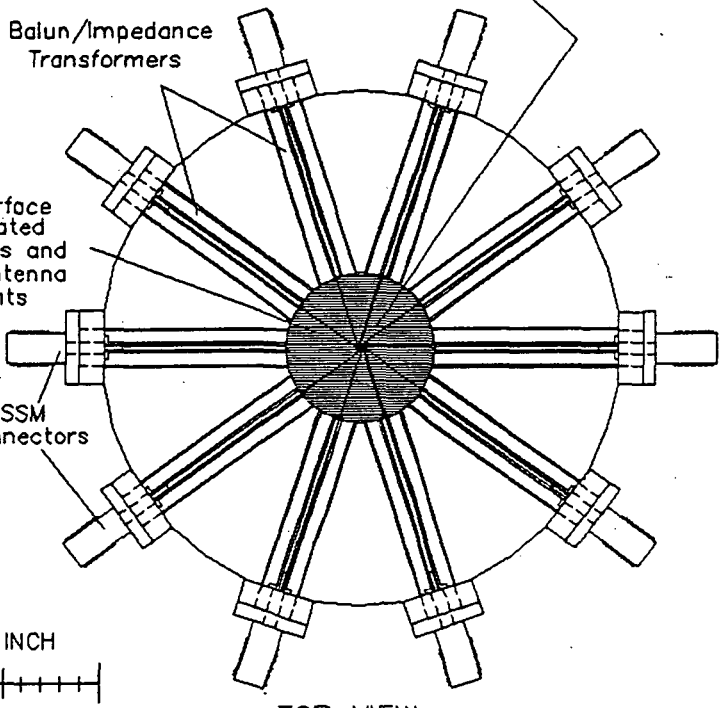

1.0 INCH

TOP VIEW (COVER REMOVED)

P.H. Siegel California Institute of Technology Jet Propulsion Laboratory

RADIOMETRY:

AIRCRAFT ALL WEATHER LANDING SYSTEM

APPROACH

FOCAL PLANE IMAGING SYSTEM AT 94 GHZ TO PROVIDE SYNTHETIC VISION CAPABILITY FOR AIRCRAFT LANDING IN ALMOST ALL WEATHER CONDITIONS

MILLIMETER – WAVE IMAGING ALLOWS GOOD VISIBILITY OF RUNWAY BOUNDARIES AND POSSIBLY DANGEROUS OBSTACLES FROM APPROPRIATE DISTANCE

FOCAL PLANE RADIOMETRIC IMAGING PERMITS REAL – TIME (30 / SECOND) UPDATE RATE

IMAGES READILY INTERPRETABLE WITHOUT EXTENSIVE PROCESSING

HEADS–UP DISPLAY STRAIGHTFORWARD TO IMPLEMENT

TECHNOLOGY:

FOCAL PLANE ARRAY OF 256 (TO DATE) PIXELS UTILIZING CONSTANT – WIDTH SLOT ANTENNAS

SINGLE – ENDED HARMONIC MIXERS WITH QUASIOPTICAL LOCAL OSCILLATOR INJECTION

DICKE –TYPE LOAD COMPARISON ESSENTIAL
MECHANICAL OR ELECTRONIC (QUASIOPTICAL HYBRID OR MONOLITHIC) REALIZATIONS POSSIBLE

COMPACT OPTICS

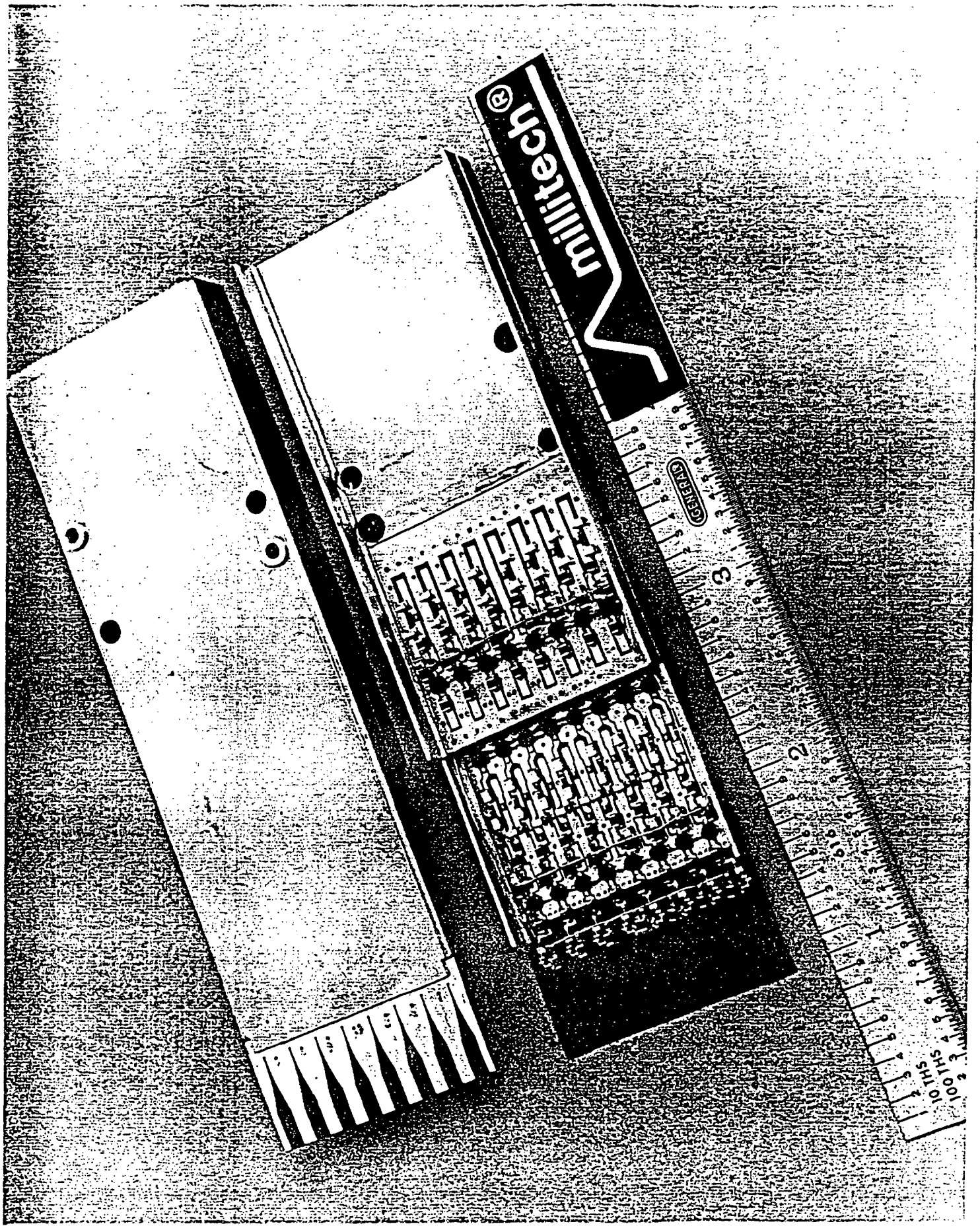
millitech
GENERAL

DETECTION OF CONCEALED WEAPONS AND CONTRABAND MATERIAL

PROBLEM:

- DETECTION OF PLASTIC WEAPONS AND EXPLOSIVES CONCEALED BENEATH CLOTHING OF AIRLINE PASSENGERS.

CONSTRAINTS:

- EFFECTIVE PERFORMANCE
- NON-INVASIVE OPERATION
- RAPID PROCESSING

TECHNICAL APPROACH:

- ACTIVE (REFLECTING) AND PASSIVE (RADIOMETRIC) MILLIMETER-WAVELENGTH IMAGING SYSTEMS

- RADIOMETRIC SYSTEM LEAST INVASIVE AND OFFERS GOOD FIDELITY

- CLOSE FOCUSED OPTICS AND FOCAL PLANE ARRAY

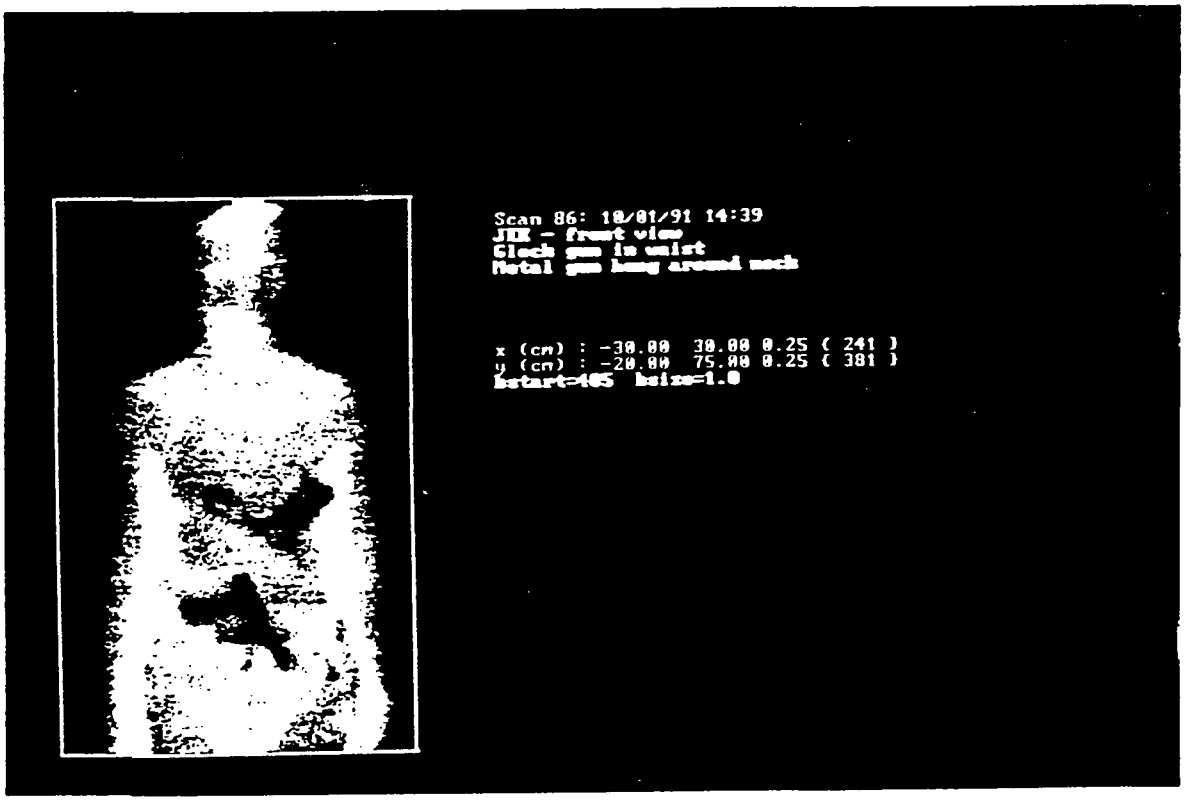

Passive Line Scan 94 GHz Millimeter Wave Image

RADIOMETRY: ATMOSPHERIC REMOTE SENSING

[1] ISSUES:

MEASUREMENT OF TRACE CONSTITUENTS INCLUDING : H_2O
O_3
ClO
N_2O

PHYSICAL CONDITION (TEMPERATURE) PROFILING

DELAY MEASUREMENTS FOR RADAR ALTIMETERS

MESOSPHERIC WIND VELOCITY DETERMINATIONS

TRACE EMISSIONS FROM LOCALIZED SOURCES

[2] OBSERVING LOCATIONS

GROUND – BASED: O_3 AND ClO MONITORING NETWORK

ANTARCTIC AND POLAR REGIONS

AIRPLANE: USEFUL AS TEST PLATFORM AND FOR STUDY OF LOCALIZED PHENOMENA

SPACE : UARS – SUCCESSFULLY OPERATING !

MAS (SHUTTLE LIMB – SOUNDER)

EOS (EARTH OBSERVING SYSTEM)

AMSU – B / METEOSAT

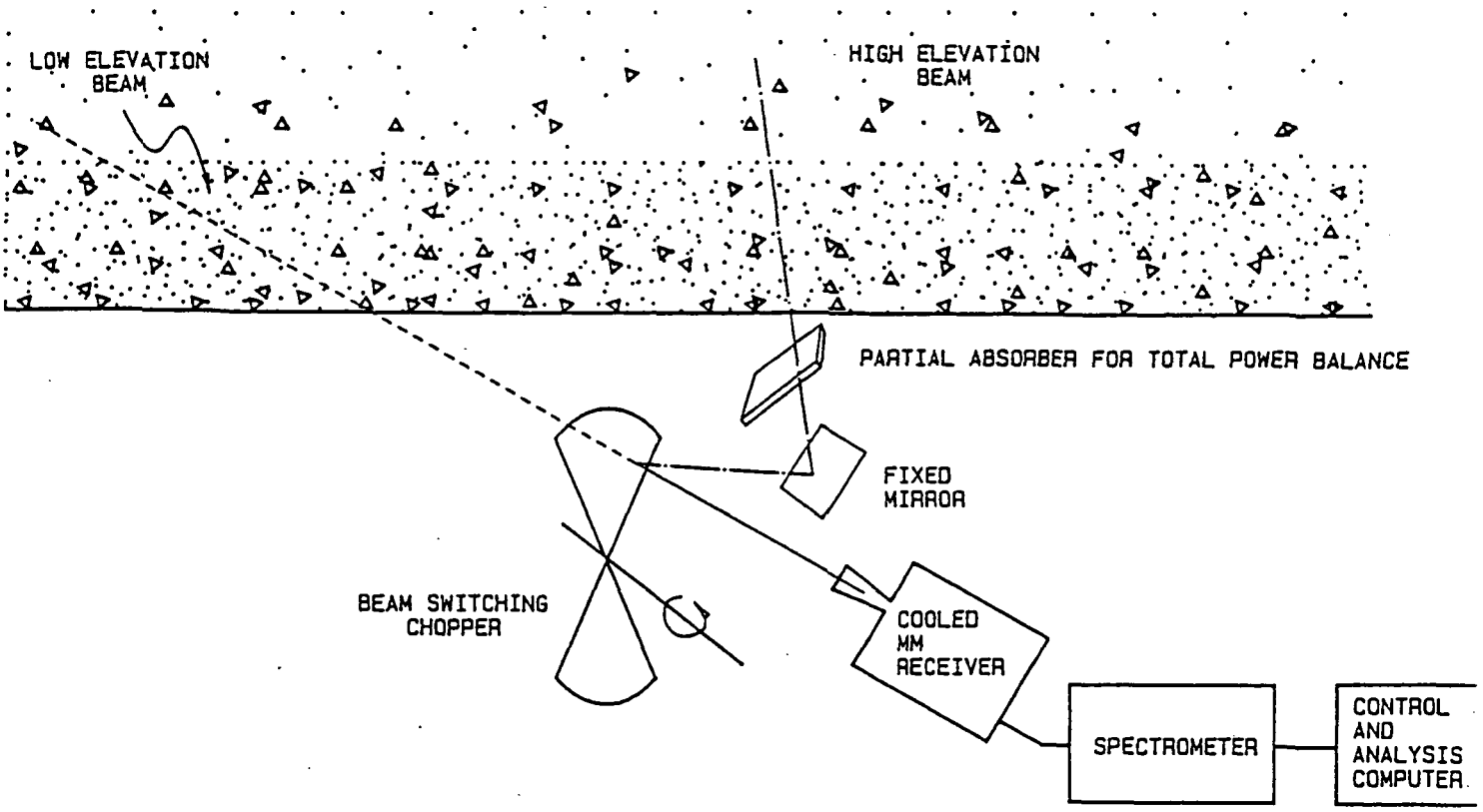

CONFIGURATION FOR GROUND-BASED RADIOMETER TO STUDY ATMOSPHERIC TRACE GASES

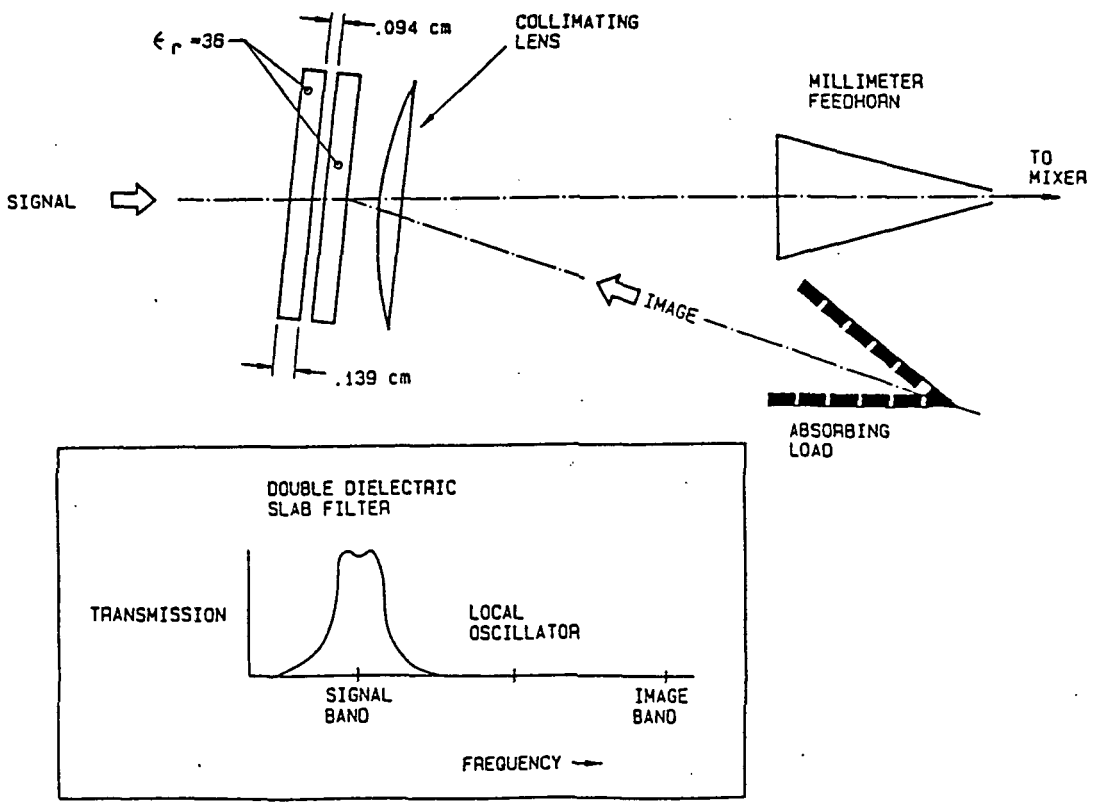

DIELECTRIC SLAB SINGLE-SIDEBAND FILTER FOR 279 GHZ C1O RADIOMETER

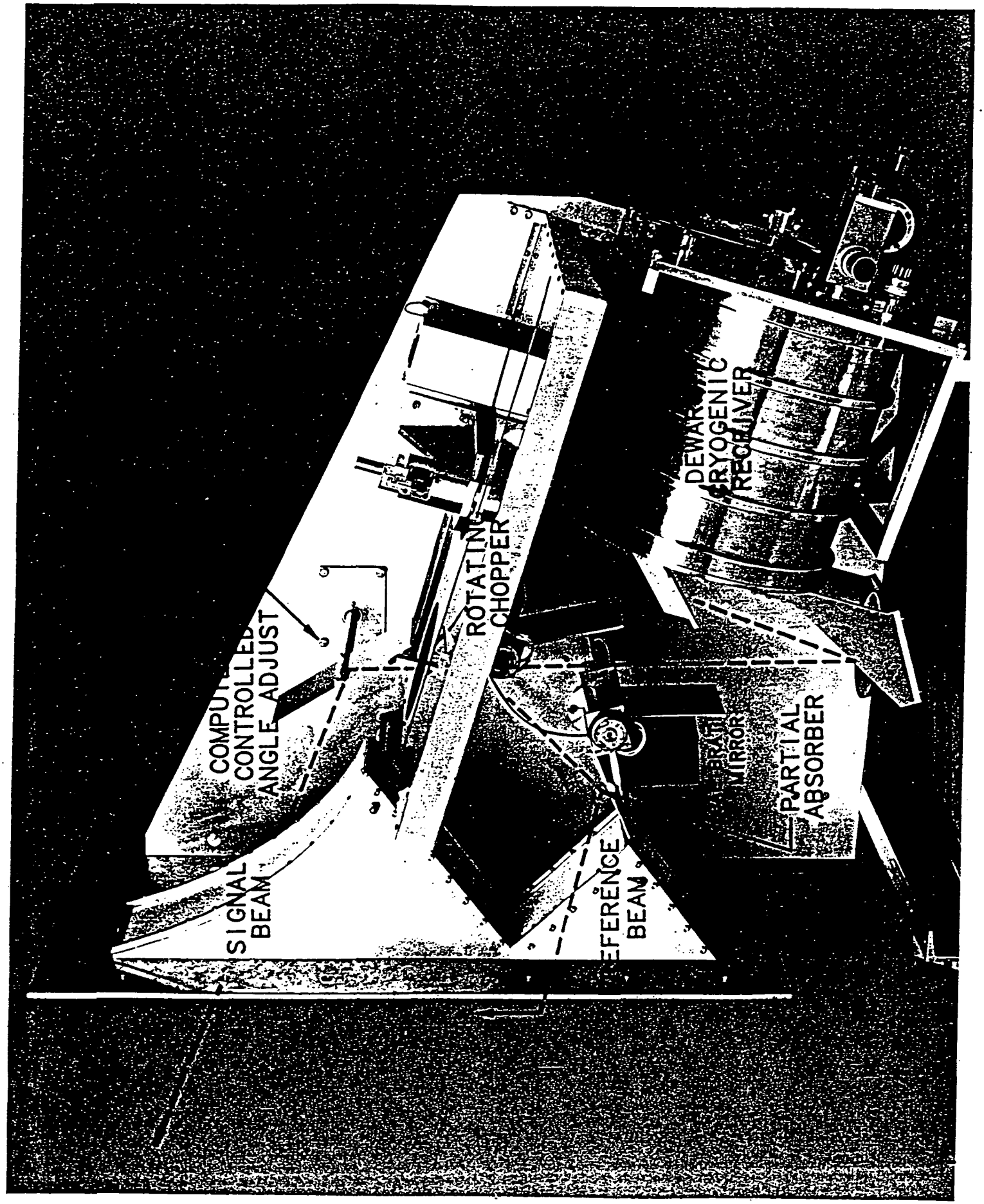
COMPUTER CONTROLLED ANGLE ADJUST
ROTATING CHOPPER
DEWAR CRYOGENIC RECEIVER
SIGNAL BEAM
REFERENCE BEAM
BRASS MIRROR
PARTIAL ABSORBER

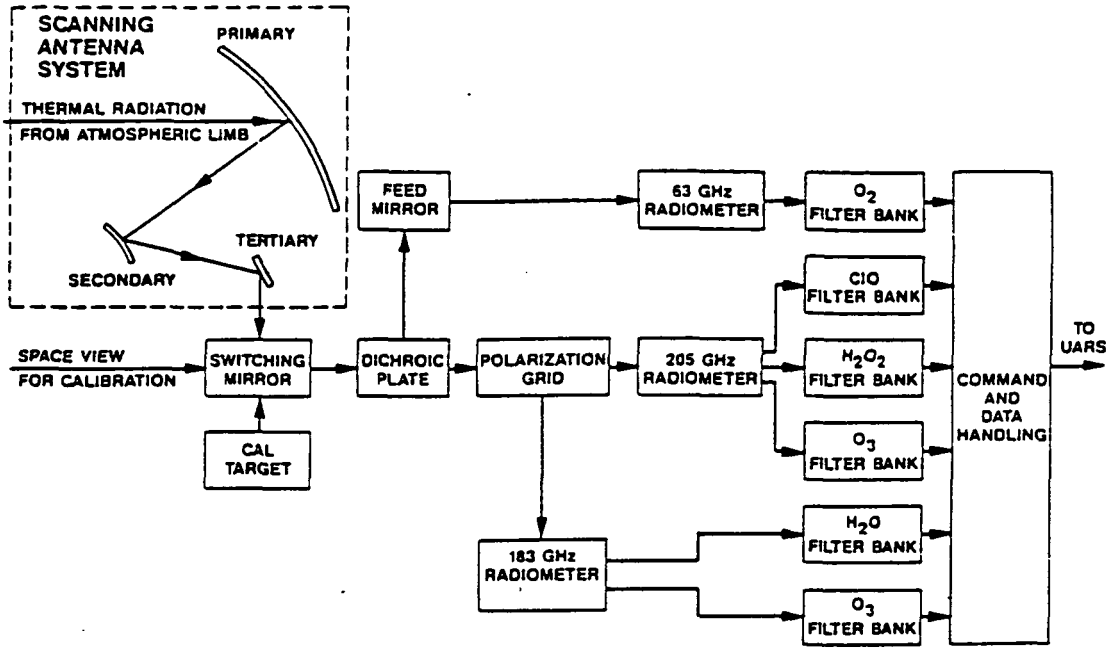

UARS MICROWAVE LIMB SOUNDER INSTRUMENT SIGNAL FLOW PATH

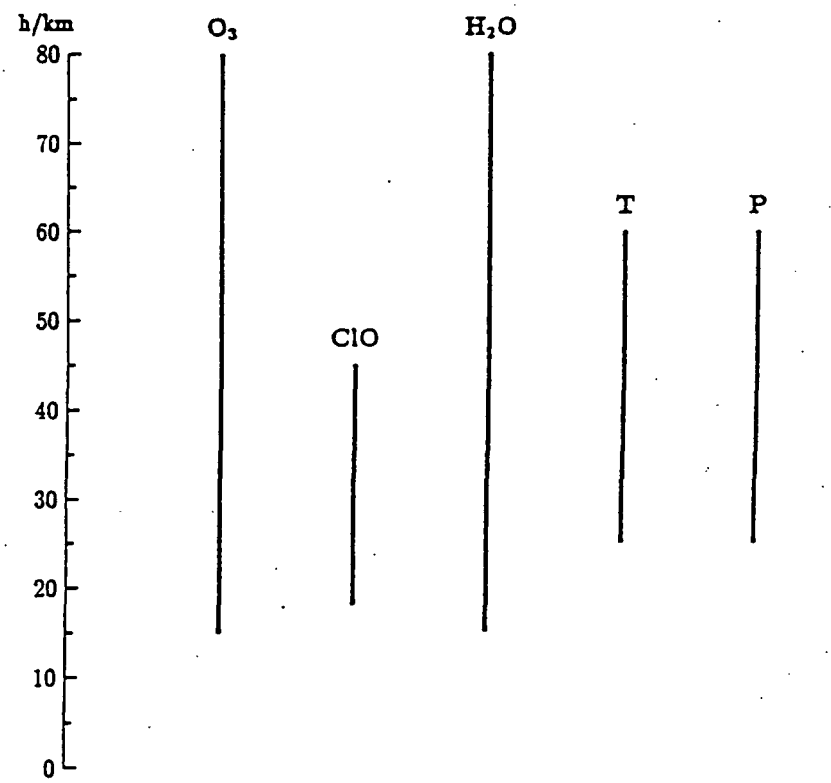

UARS - MLS TARGETS AND ALTITUDE RANGES

PLASMA DIAGNOSTICS

THERMAL IMAGING – RADIOMETRY WITH HIGH TIME RESOLUTION

EXTREMELY BROADBAND AND/OR SWEPT – FREQUENCY

DENSITY PROFILING – MEASUREMENT OF ELECTRON COLUMN DENSITY THROUGH PLASMA

INTERFEROMETERS – EITHER RADIO OR OPTICAL TYPES DEPENDING ON WAVELENGTH

SCATTERING EXPERIMENTS – PROBE TURBULENCE AND SCALE OF FLUCTUATIONS IN PLASMA

EXAMPLE OF PLASMA DIAGNOSTIC SYSTEM

2 – MM WAVELENGTH 180 DEGREE BACKSCATTER IMAGING SYSTEM DEVELOPED BY DR. P. EFTHIMION (PRINCETON PLASMA LABORATORY) AND E.L. MOORE ET. AL. (MILLITECH CORPORATION)

INCLUDES PHASELOCKED TRANSMITTER AND 64 ELEMENT FOCAL PLANE IMAGING ARRAY

COMMUNICATIONS

APPLICATIONS:

- PERSONAL
- VEHICULAR – CAR TRAIN AND PLANE
- DIGITAL DATA LINKS – SATELLITE AND GROUND
- MILITARY COMMUNICATIONS (MILSTAR)
- TV REMOTE – STUDIO LINKS

DEVELOPMENTS IN FIELD HAVE BEEN REVIEWED BY H. MEINEL IN PROC. 18th EUROPEAN MICROWAVE CONFERENCE, STOCKHOLM, pp. 1203 – 1216, 1988

RADAR SYSTEMS

- **MILITARY RADAR SYSTEMS**

  INSTRUMENTATION RADARS

  SEARCH RADARS

  SEEKERS

  HELICOPTER OBSTACLE AVOIDANCE SYSTEMS

- **AUTOMOTIVE RADAR**

  PRESENTLY VERY ACTIVE FIELD

  GOALS ARE COLLISION AVOIDANCE AND ULTIMATELY AUTOMATIC CONTROL OF VEHICLE

- **ATMOSPHERE** CLOUD STRUCTURE (ICE & WATER)
  METEOROLOGY

- **REMOTE SENSING** OCEANS
  VEGETATION
  ICE

- **MODELING**

  MILLIMETER / SUBMILLIMETER MODELING OF LOWER FREQUENCY RADAR SYSTEMS AND TARGETS

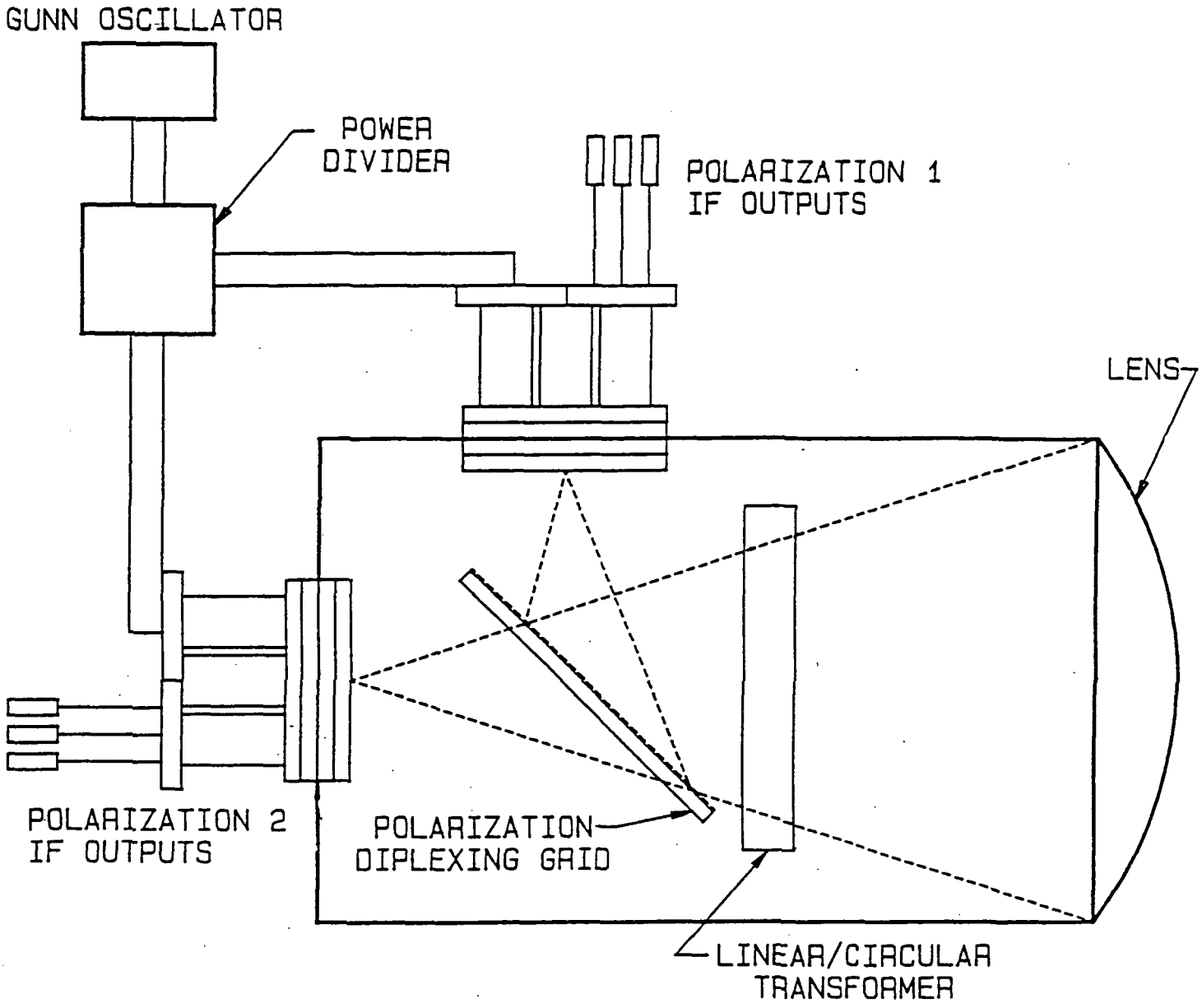

DUAL POLARIZATION MONOPULSE LENS ANTENNA

SPECIFICATIONS SUMMARY

TYPE: PULSE
TRANSMITTER FREQUENCY: 77GHz
PULSE WIDTH: 40ns
RISE/FALL TIME: 4ns
ANTENNA: THREE BEAM SCANNING
BEAM WIDTH: 2° ELEVATION AND AZIMUTH
IF BANDWIDTH: 1KHz TO 200MHz

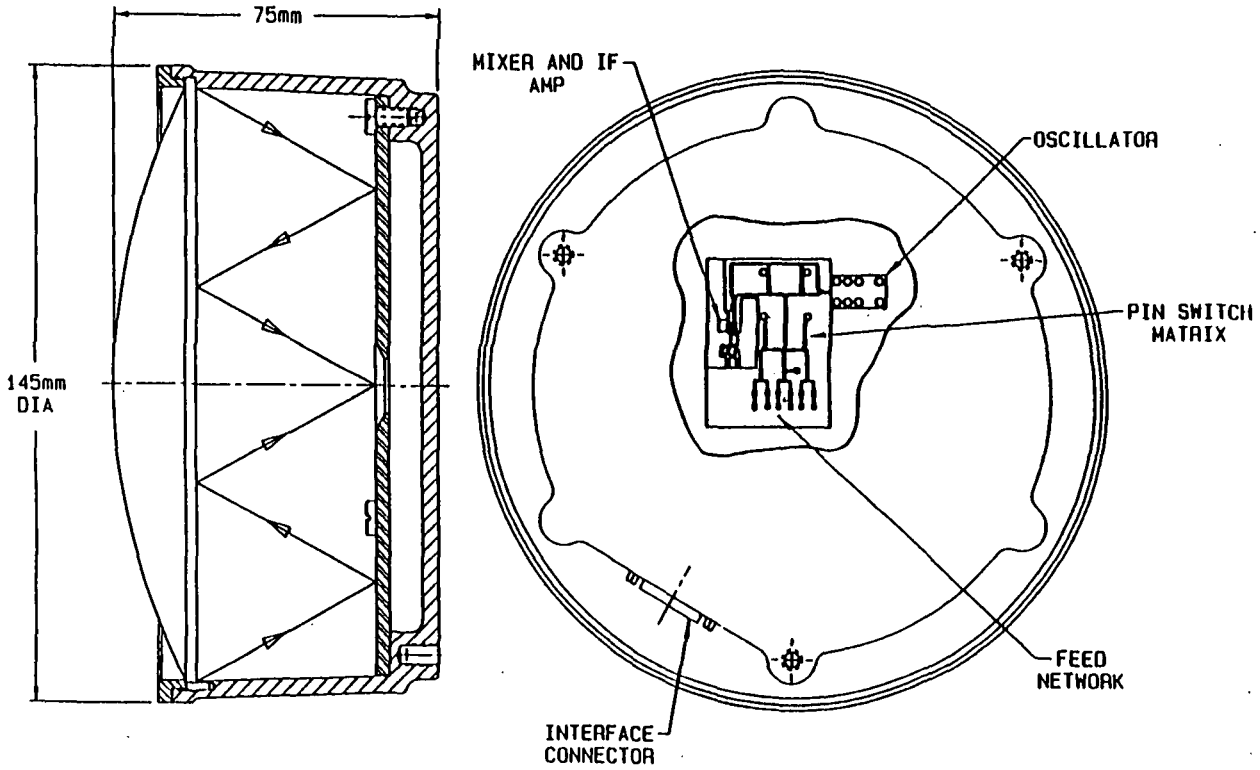

MILLITECH AUTOMOBILE RADAR FRONT END

millitech

MATERIALS MEASUREMENT AND MANUFACTURING PROCESS CONTROL

MAJOR CONSIDERATIONS

- DEMANDS EXTREMELY RUGGED SYSTEMS
- COST IS A CRITICAL FACTOR
- MOST INDUSTRIES ARE CONSERVATIVE AND NEED TO BE CONVINCED OF VALUE OF NEW SYSTEM
- WHAT ARE THE UNIQUE CAPABILITIES OF TERAHERTZ RANGE?

APPLICATIONS:

HIGH VOLTAGE CABLE INSPECTION

PAPER MAKING

PAPER MEASUREMENTS AT SUBMILLIMETER WAVE LENGTHS

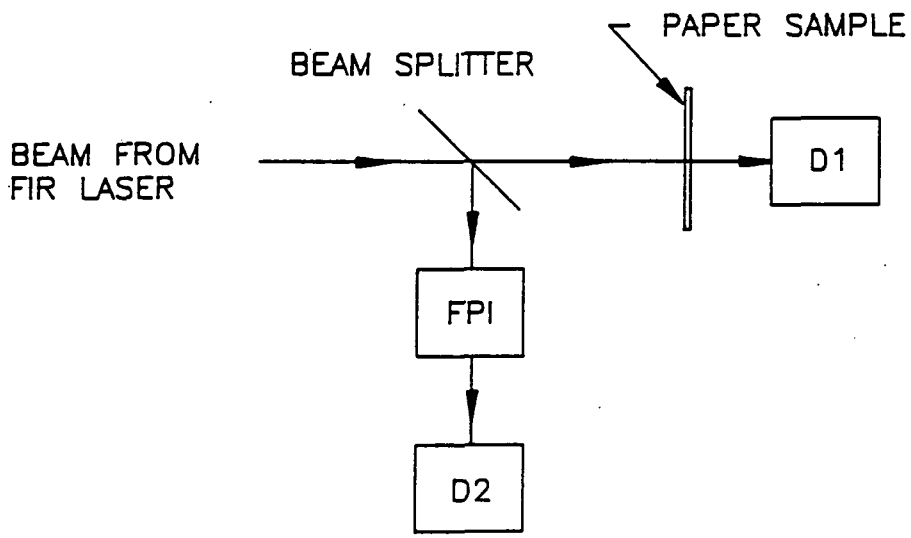

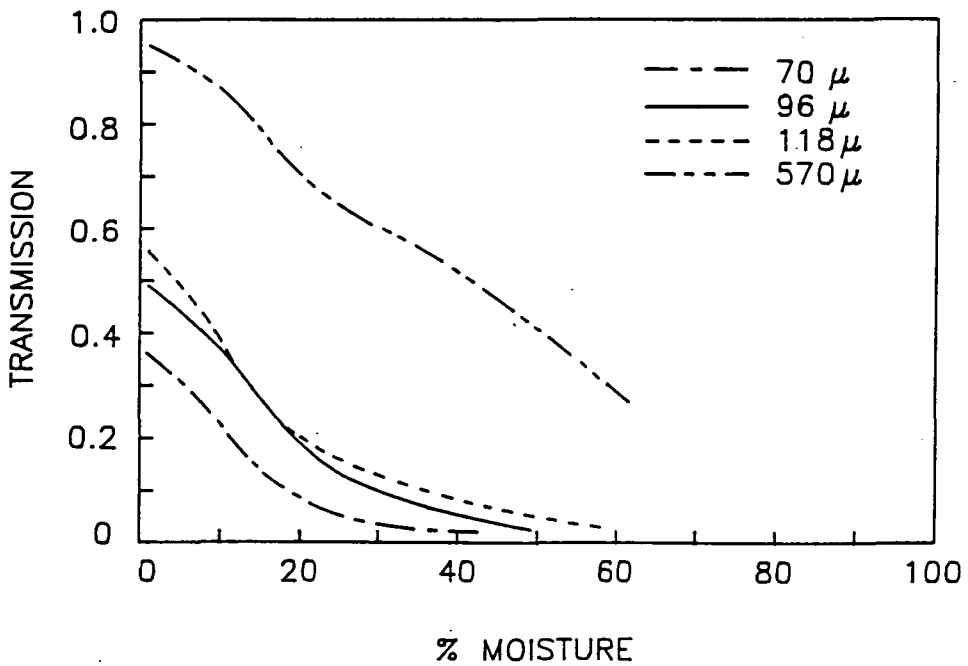

TRANSMITTANCE OF 80 μM NEWSPRINT
AS A FUNCTION OF MOISTURE CONTENT

FROM BOULAY, ET AL., IR & MM WAVES, VOL. 5, PP 1221–1234, 1984

CONCLUSIONS

APPLICATIONS OF COHERENT SYSTEMS IN TERAHERTZ RANGE ARE EXTREMELY DIVERSE AND ARE EXPANDING

RAPID TECHNICAL PROGRESS IS TAKING PLACE ON MANY FRONTS

TRANS – MILLIMETER REGION IS NOW SIMILAR TO MILLIMETER RANGE JUST A FEW YEARS AGO AND $\lambda \leq 3$ MM RANGE IS COMPARABLE TO MICROWAVE REGION IN RECENT PAST

REAL SUBMILLIMETER REGION STILL HAS MANY CHALLENGES INCLUDING BASIC QUASIOPTICAL COMPONENTS, FREQUENCY SOURCES, ANTENNAS (INCLUDING ARRAYS) AND HIGH EFFICIENCY AND RUGGED MIXERS AND DETECTORS

AN IMPORTANT CONSIDERATION: **DIFFERENT APPLICATIONS HAVE ENORMOUSLY DIVERSE REQUIREMENTS**

THE SINGLE GREATEST OBSTACLE TO BROADER COMMERCIAL AND INDUSTRIAL UTILIZATION OF TERAHERTZ REGION IS COST

WE NEED TO MAKE IT CHEAP AS WELL AS GOOD!

I WOULD LIKE TO ACKNOWLEDGE CONSIDERABLE ASSISTANCE FROM J. BIRCH, P. EFTHIMION, R. GILES, D. KEAVENEY, R. MCINTOSH, E. MOORE, A. PARRISH, P. SIEGEL, J. WATERS AND OTHER CO–WORKERS AT MILLITECH AND AT F. C. R. A. O.

Broadband Millimeter-Wave GaAs Transmitters and Receivers Using Planar Bow-Tie Antennas

Y. Konishi*, M. Kamegawa*, M. Case, R. Yu, M. J. W. Rodwell, R. A. York,
and D. B. Rutledge†
Department of Electrical and Computer Engineering.
University of California, Santa Barbara
*On leave from Shimadzu Corp. Kyoto, Japan.
†Division of Engineering and Applied Science. California Institute of Technology

Abstract

We report broadband monolithic transmitters and receivers ICs for mm-wave electromagnetic measurements. The ICs use non-linear transmission lines (NLTL) and sampling circuits as picosecond pulse generators and detectors. The pulses are radiated and received by planar monolithic bow-tie antennas, collimated with silicon substrate lenses and off-axis parabolic reflectors. Through Fourier transformation of the received pulse, 30-250 GHz free space gain-frequency measurements are demonstrated with ≈ 0.17 dB accuracy, RMS.

Introduction

For mm-wave and sub-mm wave gain-frequency measurements, convenient, broadband power sources and detectors have been required for some time. Measurement systems based upon waveguide components (harmonic mixers, frequency multipliers, and horn antennas)[1] have played a dominant role, but each component has narrowband frequency coverage (1.5:1). To measure over a broad bandwidth, many waveguide systems must be used, which is both inconvenient and very expensive. In addition, above 100 GHz it is difficult and expensive to machine the small waveguides and difficult to attain efficient device-waveguide coupling. Broadband monolithic mm-wave ICs address these difficulties.

Several groups have reported superconductor devices such as SIS (Superconductor-Insulator-Superconductor) detectors[2-4] or oscillators[5] for mm-wave measurement or

for radio astronomy. Popular devices based on niobium technology (e.g., $Nb/AlO_X/Nb$ junctions) must be cooled to liquid helium temperature, so a large and expensive cooling system is required. Additionally, due to the very low impedance of superconducting devices ($\approx 0.1\ \Omega$), impedance matching to a 50 Ω system is difficult.

Antenna-coupled picosecond photoconductors have also been used to generate and detect picosecond radiated electromagnetic pulses. Though Fourier analysis of the received signals, several groups have recently demonstrated broadband spectroscopy (≈ 50 GHz-1.5 THz) [6-8]. Such systems require expensive and complex mode-locked lasers (≈ $150,000) to excite the photoconductors, and the radiated power is extremely small.

As with the photoconductive systems, our system for mm-wave measurements radiates and detects picosecond pulses and obtains frequency information through Fourier transformation. Our system uses solid-state monolithic devices, NLTLs and sampling circuits for pulse generation and detection[9-11]. With the NLTLs, we have several advantages. First, the system has fewer components and is very compact without the laser or its optics. Second, there is substantially more radiated power than the photoconductive system. Third, since the NLTL is driven by a microwave synthesizer and the NLTL input frequency can be varied by as much as one octave, the system can easily be tuned to any desired mm-wave harmonic frequency. Finally, the transmitters and receivers are inexpensive components fabricated on GaAs with a 5 mask process at 3 μm device geometries. No cooling system is required for GaAs ICs as with the superconducting devices.

Here we will describe the system, especially the broadband bow-tie antenna and its optics. We have demonstrated the system performance by spectroscopic measurement of a thin alumina substrate with accuracy of 0.17 dB RMS and reproducibility better than 0.3 dB from 30 to 250 GHz.

NLTLs & sampling circuits

The NLTL is a ladder network of high impedance transmission line sections periodically loaded with reversed biased monolithic Schottky diodes serving as voltage-variable capacitors[9]. The resulting voltage-variation in wave propagation velocity results in the compression of negative-going wavefronts and the formation of picosecond shock-waves. The NLTL converts an input 7 - 14 GHz sine wave to a sawtooth waveform. In on-wafer measurements, ≈ 1.5 ps falltime and ≈ 5 V peak to peak voltage swing has been attained. NLTL-gated sampling circuits attained similar risetime. Such devices allow

generation and detection of transient signal with ≈ 250 GHz bandwidth. The transmitter NLTL is typically driven by a 10 GHz + 100 Hz sinusoidal wave from a microwave synthesizer. This NLTL drives an on-wafer bow-tie antenna. The receiver consists of an NLTL-gated sampling circuit integrated with a bow-tie antenna. The NLTL which generates the sampler's strobe pulse is typically driven by a 10 GHz sinusoidal waveform from a second synthesizer. The resulting sampled 100 Hz IF signal is observed on a standard oscilloscope.

Antenna and quasi-optical system

In the case of a planar antenna on a dielectric substrate, most of the power is radiated into the substrate, and is trapped. This causes standing waves and resulting resonances within the GaAs substrate (ε_r= 13). To avoid this, hyper-hemispherical substrate lenses are used with the bow-tie antennas[12,13].

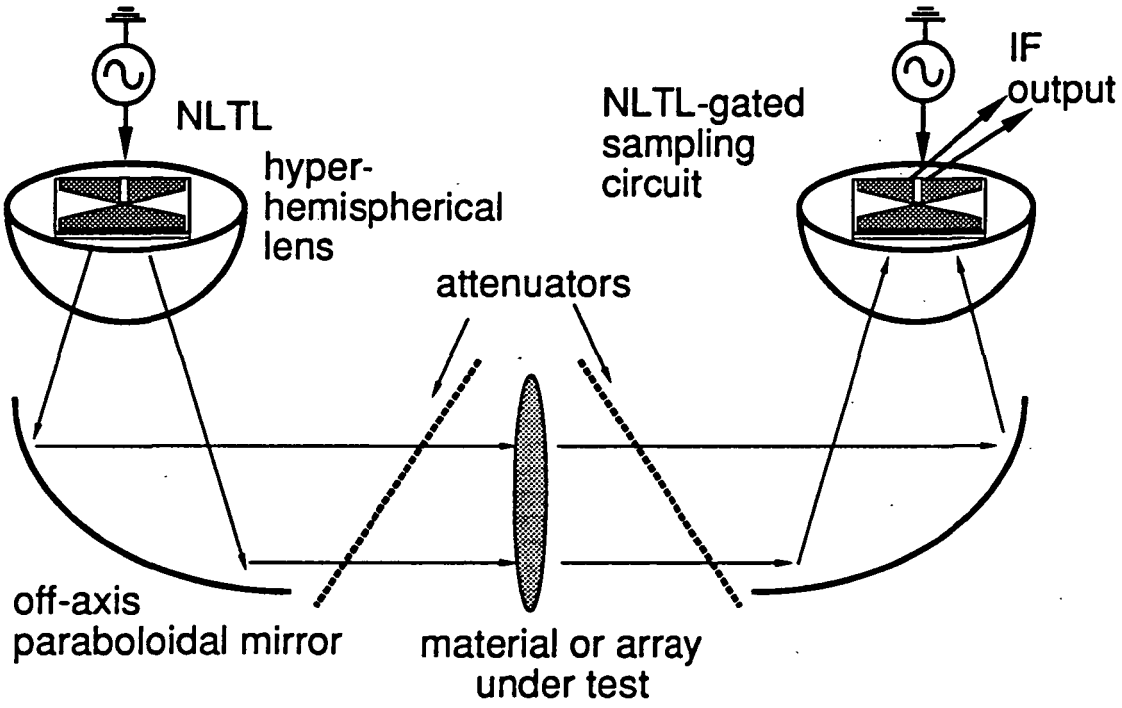

Figure 1: Measurement system schematic diagram (left: transmitter, right: receiver)

The output of the transmitter NLTL is connected by a coplanar waveguide (CPW) feed line to the feedpoint of the bow-tie antenna. This structure also serves as a balun. Sawtooth waves generated by the NLTL are radiated from the antenna. The bow-tie antenna is scale-invariant and has frequency-independent radiation impedance and frequency-independent far-field radiation patterns as long as its linear dimensions are larger

than a free space wavelength. The antenna thus acts as a high pass filter, with the 2 mm length resulting in a ≈ 35 GHz low-frequency cut-off[14]. The 55 μm total width of the CPW feedline defines a ≈ 1.3 THz upper frequency limit for the antenna.

The radiation is extracted through a silicon (ε_r= 11.8, 16 mm diameter) hyper-hemispherical substrate lens on the back side of the IC. Matching of the IC and lens dielectric constants is very important. For example, a sapphire lens (ε_r= 9.9) causes standing waves in GaAs substrate due to the discrepancy in ε_r. This results in substantial resonances at 60 GHz, 120 GHz and 180 GHz. Compared to hemispherical lenses, hyper-hemispherical lenses improve the poor numerical aperture of the bow-tie antennas, and provide defocusing of the parasitic reflections arising at the lens-air interface. In contrast, hemispherical lenses exhibit strong spherical-mode resonances. The radiated beam is collimated with off-axis parabolic mirrors, and is focused on the receiver through similar optics. The antenna system loss, including substrate lenses absorption, coupling loss between the antenna and the lens etc., is ≈ -20 dB as determined by 10 MHz - 40 GHz network analysis[14].

Metal surfaces surrounding the experimental apparatus are covered with microwave absorber (Emerson & Cuming, FGM-40) to suppress reflections. Additionally, imaging the transmitter antenna onto the receiver produces a resonant cavity because of reflections at the air-lens and lens-antenna interfaces. To obtain accurate gain-frequency measurements, these resonances are suppressed by placing ≈ 5 dB thin-film metal attenuators on both sides of the sample under test.

Device Fabrication

The circuits were fabricated on GaAs semi-insulating substrates with a five mask process at 3 μm design rules. Schottky diodes are formed on GaAs with a 425-nm-thick exponentially graded N^- active layer with a $2x10^{17}$ cm^{-3} surface doping and 225 nm exponential grading constant. Beneath the N^- layer, a buried 1 μm-thick N^+ layer ($6x10^{18}$ cm^{-3}) provides the diode cathode connection. Ohmic contacts to the N^+ later (the diode cathode connections) are formed by a 0.5 μm recess etch to the N^+ layer, a self-aligned AuGe/Ni/Au liftoff, and subsequent alloying. Proton implantation (masked by 1.6 μm gold on 1.1 μm polyimide) provides isolation between diodes and defines Schottky contact areas. The transmission line sections are implemented in CPW, formed with a 1.1 μm Ti/Pt/Au liftoff; Schottky contacts result where this liftoff intersects unimplanted regions. With two additional mask steps, air-bridge crossovers are formed.

Results

The received signal (Fig. 2) shows that the sawtooth waveform has changed to a pulse train with initial fast rise and a decay time set by the antenna system's low-frequency cut-off. The peak-peak amplitude is 167 mV, and the pulse risetime is 2.6 ps as limited by the speed of sampling circuits, the NLTL, and the antenna system.

Because the far-field radiation pattern is frequency-independent, the antenna effective aperture size is proportional to λ^2. Consequently, misalignment selectively attenuates high-frequency components and limits the system bandwidth. With poor alignment, the pulse risetime degrades due to the reduced bandwidth.

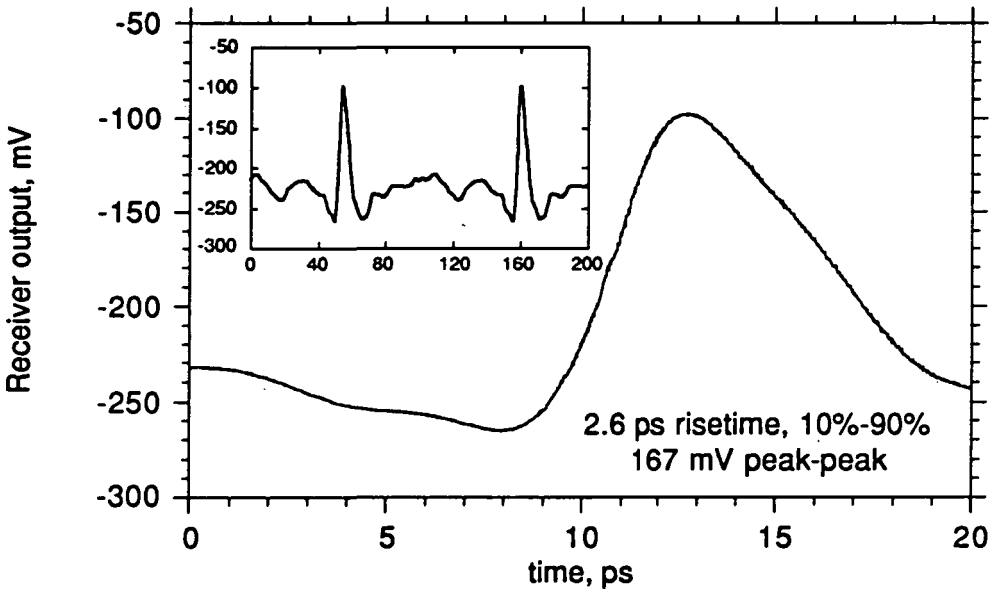

Figure 2: Received waveform.

To demonstrate the system accuracy, we measured the insertion loss of a 254 μm alumina substrate (ε_r= 9.9). From 30 to 250 GHz the measurement values correspond well to theory. (Fig.3) With three subsequent measurements, the accuracy attained was 0.17 dB RMS, and the reproducibility was better than 0.3 dB.

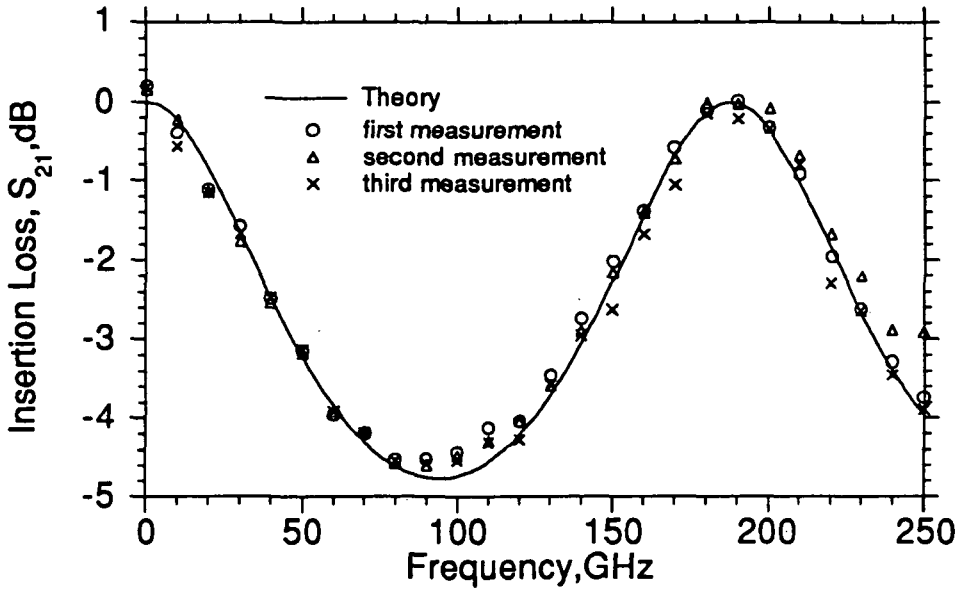

Figure 3: mm-wave measurement of 254 μm-thick alumina test sample.

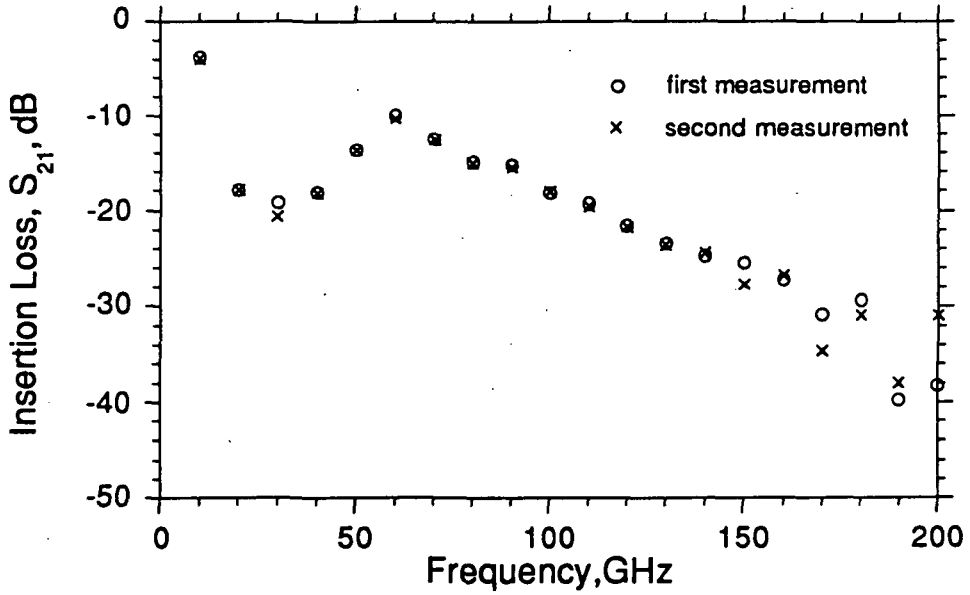

Figure 4: mm-wave measurement of microwave absorber.

We also measured the insertion loss of a microwave absorbing material (Emerson & Cuming FGM-40, 1.0 mm thickness). (Fig.4) A loss minimum is seen at 60 GHz, with the attenuation improving at higher frequencies.

Above 150 GHz, this measurement is limited by the ≈ 35 dB system dynamic range. This dynamic range can be greatly improved by using narrowband signal detection (e.g., a lock-in amplifier).

Conclusion

We have demonstrated a simple and inexpensive system for broadband mm-wave electromagnetic measurements. Reproducible, accurate measurements are possible from 30 to 250 GHz. The combination of the bow-tie antennas and the substrate lenses provides acceptable coupling efficiency over a broad bandwidth, despite the high systems loss (≈ -20 dB between antennas) and the additional (≈ 10 dB) attenuation required to suppress standing waves. The bow-tie antenna is readily integrated with monolithic circuits.

The current system will allow convenient and accurate measurement of materials and emerging mm-wave quasi-optical amplifier arrays. With attainable improvements in the diode cut-off frequency, system bandwidth can potentially be extended to 1 THz.

Acknowledgment

This work was supported by the Air Force Office of Scientific Research under grant number (AFOSR-89-0394)

References

[1] Tektronix, Inc. 1991 Catalog

[2] L. R. D'Addario, "An SIS mixer for 90-120 GHz with gain and wide bandwidth", Int. J. of IR and MM waves, Vol. 5 , No.11, pp. 1419-1433, 1984.

[3] T. H. Büttgenbach, R. E. Miller, M. J. Wengler, D. M. Watson, T. G. Phillips, "A Broadband Low Noise Receiver for Submillimeter Astronomy", IEEE, MTT-S. Digest, pp. 469-472, 1988.

[4] S. Kodaira, J. Inatani, K. Sakai, T. Fukushima, "Phase Locking of SWL Array Junctions in Submillimeter Mixing", Jpn. J. Appl. Phys. Vol. 29, No. 3, pp. L463-L465, March, 1990.

[5] J. Inatani, Y. Konishi, K. Sakai, and S. Kodaira, "Flux-Flow Oscillator connected with a Bow-Tie Antenna", ISEC, Tokyo, June, 12-13, 1989.

[6] D. H. Auston and M. C. Nuss, " Electro-optic generation and detection of femtosecond electrical transients", IEEE, Quantum Electron., Vol. 24, pp.184-197, 1988.

[7] G. Arjavalingam, Y. Pastrol, J. M. Halbut and G. V. Kopcsay, "Broad-band microave measurements with transiet radiation from optelectronically pulsed antenna", IEEE, Trans. MTT., Vol. 38, No.5, pp. 615-621, May, 1990.

[8] N. Katzenellenbogen and D. R. Grischkowsky, "Efficient generation of 380 fs pulses of THz radiation by ultrafast laser pulse excitation of a biased metal-semiconductor interface", Appl. Phys. Lett., Vol.58, No.3, pp. 222-224, January, 1991.

[9] M. J. W. Rodwell, M. Kamegawa, R. Yu, M. Case, E. Carmen, K. S. Giboney, "GaAs Nonlinear Transmission Lines for Picosecond Pulse Generation and Millimeter-Wave Sampling", IEEE, Trans. MTT., Vol. 39, No.7, July, 1991.

[10] R. Yu, M. Case, M. Kamegawa, M. Sandram, M. J. W. Rodwell and A. Gossard, "275 GHz 3mask Integrated Sampling Circuit", Elect. Lett., Vol. 26, No. 13, pp. 949-951, June, 1990.

[11] R.A. Marsland, C. J. Maden, D. W. Van Der Weide, M. S. Shakouri, and D. M. Bloom, "Monolithic Integrated Circuits for MM-Wave Instrumentation", in Technical Digest, GaAs IC Symposium, New Orlens, La. October, 7-10, 1990.

[12] D. B. Rutledge, D. P. Neikirk, and D. P. Kasilingam. "Integrated-Circuit Antenna" in Infrared and Millimeter Waves, K. J. Button, Ed., Vol. 10, pp. 1-90, New York: Academic Press, 1984.

[13] R. C. Compton, R. C. McPhedran, Z. P. Popovic, G. M. Rebeiz, P. P. Tong and D. B. Rutlegde, "Bow-Tie Antennas on a Dielectric Half-Space: Theory and Experiment", IEEE, Trans. Antenna Propag., AP-35, pp. 622-631, June, 1987.

[14] M. Kamegawa, Y. Konishi, M. Case, R. Yu, and M. J. W. Rodwell, "Coherent, Broadband Millimeter-Wave Specroscopy Using Monolithic GaAs Circuits", LEOS Summer Topical Meetings, Newport Beach, July, 24-26, 1991.

ACTIVE CPW-FED SLOT ANTENNAS FOR POWER COMBINING APPLICATIONS

Brian K. Kormanyos and Gabriel M. Rebeiz

NASA/Center for Space Terahertz Technology
Electrical Engineering and Computer Science Department
University of Michigan
Ann Arbor, MI 48109-2122

ABSTRACT

We have combined integrated circuit antenna technology with microwave oscillator design to build an active slot-oscillator. The design is planar, does not require via holes and is compatible with monolithic transistor technology. The CPW-fed antenna impedance is calcualted using a full-wave analysis technique. Slot-oscillators were built at 7, 13, and 22 GHz and the predicted oscillation frequencies agree well with experiments. The design is easily scaled to millimeter-wave frequencies and can be extended to power combining arrays.

INTRODUCTION

Millimeter-wave systems are becoming increasingly important in many military and commercial applications. Millimeter-wave receivers and transmitters have been traditionally waveguide-based systems and these are expensive to build at these frequencies. To solve this problem, several groups researched quasi-optical power combining topologies and active antennas [1-4]. In this paper, we present a novel active transmitter suitable for low-cost millimeter-wave applications. The transmitter consists of a cpw-fed slot antenna (or a dual-slot antenna) on a high-dielectric substrate- lens and a three-terminal device (millimeter-wave HEMT). The novelty in this approach is that we use the antenna impedance, calculated by a full-wave analysis method, as a parameter in the design of the oscillator. This results in a much more compact circuit than the conventional approach which consists of an oscillator with a 50Ω output that is matched to a radiating slot-antenna. In our design, the matching network is eliminated (or minimized), the circuit is much smaller than a wavelength and this

allows the design of a power combining array without trigerring grating lobes. The design can be easily scaled to millimeter wavelengths when HEMT transistor technology is available at these frequencies.

OSCILLATOR DESIGN AND MEASUREMENTS

The oscillator design is based on the S-parameters of the transistor used. An indefinite scattering matrix is employed so that short circuited lengths of CPW may be placed at the gate and source. Computer optimization is then applied to the lengths of CPW to maximize the reflection coefficient at the drain of the device. In this way a reflection magnitude greater than one is obtained without the use of an external feedback network and its associated complications. A slot antenna is connected to the drain through a length of CPW. In order for oscillations to build up, the impedance the slot antenna presents to the drain must have a reflection coefficient magnitude at least as large as the reciprocal of the reflection coefficient at the drain and the phase must be opposite in sign. The impedance of the CPW fed slot-antenna on a substrate must be well known and is calculated by a full wave moment method analysis. The terminals of the FET are DC isolated from eachother to allow bias voltages to be applied. This is done by integrating metal-insulator-metal capacitors and bypassed slits in the ground plane.

Slot-oscillators were designed and built at 13GHz and 22GHz (Fig 1.) using commercially available hetero-junction FETs (NE32100, NE32184). The circuits oscillated near the predicted frequency when placed at the focus of a one inch diameter elliptical silicon substrate lens (Fig. 1). The radiation patterns of the oscillators on the substrate lens were measured (Fig. 2) and are used to estimate the directivity. Total oscillator power is calculated with the radar equation. The total radiated power measured was 5.4mW at 13.01GHz and 3mW at 22.45GHz. The DC to RF efficiency is 5.4% at 13.01GHz and 3.8% at 22.45GHz. These numbers are consistent with the capability of the transistor which is a low noise small signal devices operated at maximum bias. In the future medium power transistors will be used.

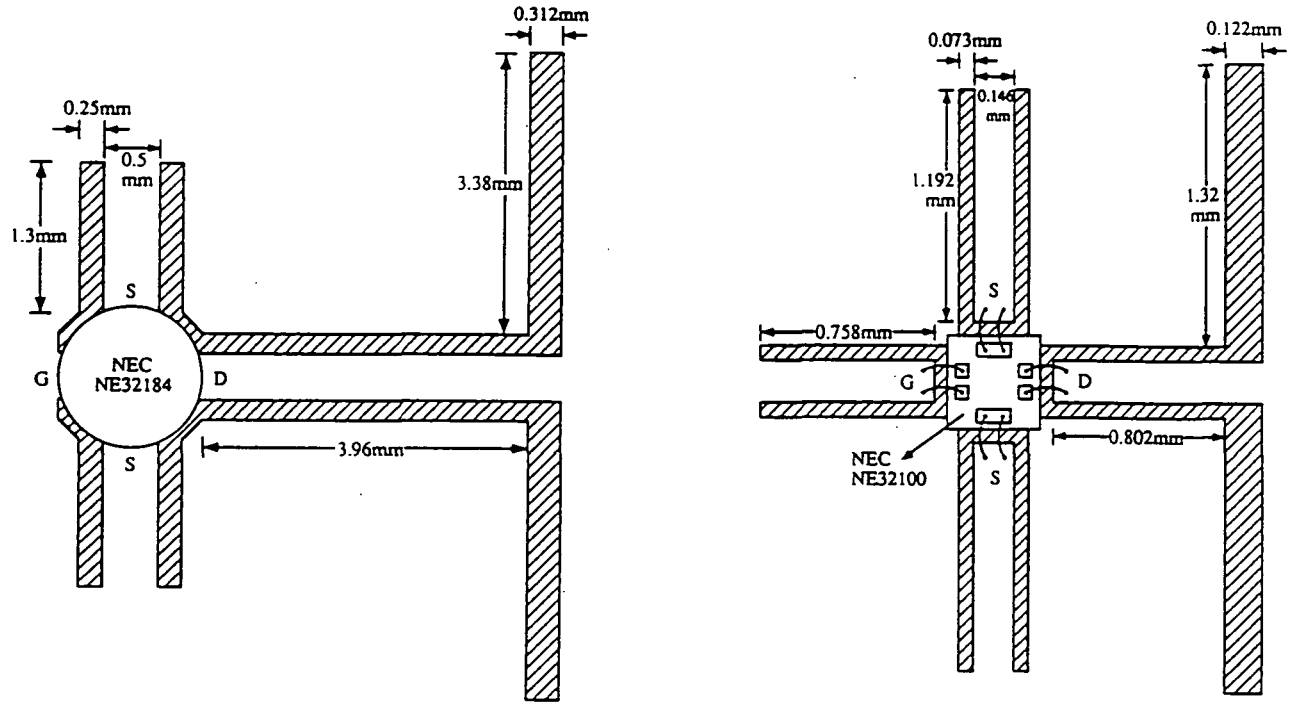

Figure 1: 13GHz and 22GHz slot-oscillator designs.

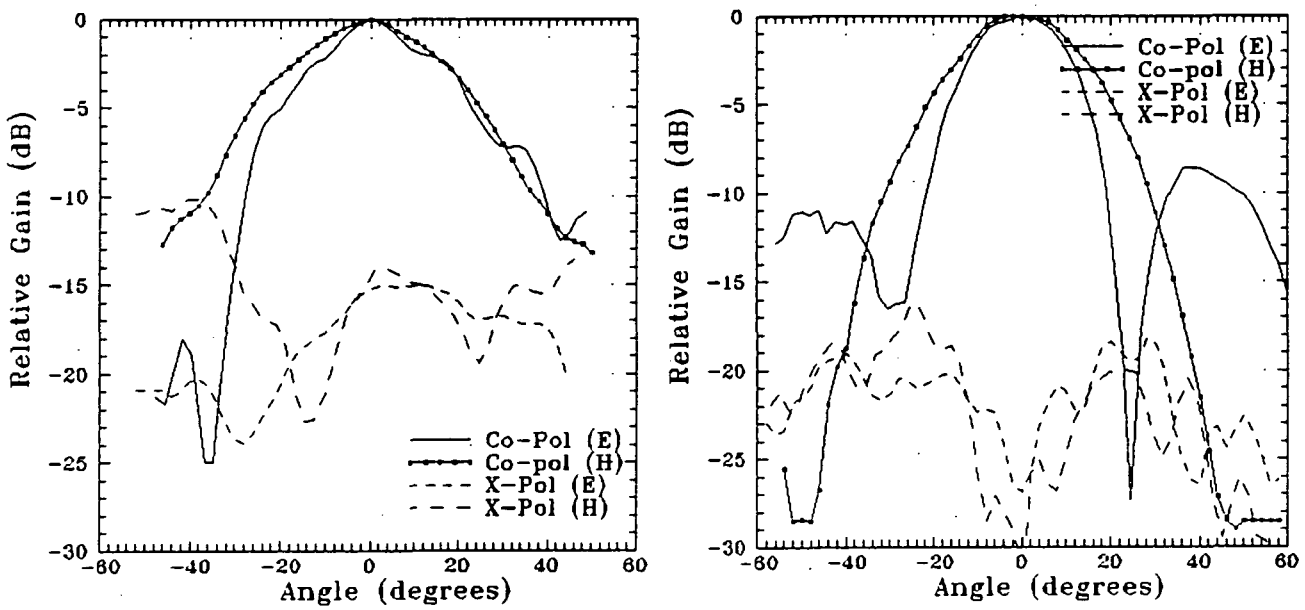

Figure 2: Radiation patterns of 13GHz and 22GHz slot-oscillators on one inch diameter silicon substrate lens.

A 7GHz VCO (Fig 3.) was designed using the above method with the incorporation of varactor diodes (Metelics MSV34-60-E28) at the source terminals of the FET. An oscillator tuning range of 850MHz was achieved from 6.68GHz to 7.35GHz. This shows that electronically tunable slot-oscillators are possible for phase locked loops or other applications.

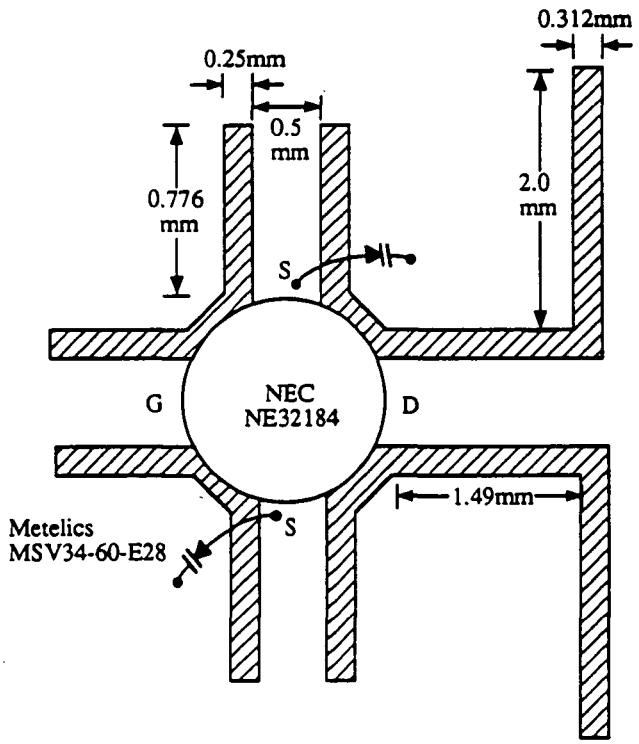

Figure 3: 7 GHz VCO with 850 MHz tuning range

The oscillators are well suited for use in power combining arrays synchronized by the mutual coupling between antennas. One possible array configuration (Fig. 4) is to place a two dimensional array on a dielectric block of quarter wavelength thickness. Most of the power will radiate out the opposite side of the block. A weak substrate mode will exist in the block and may enhance the mutual coupling. If neccessary a reflector may be used on the back side of the block to further enhance mutual coupling and improve phase equalization between elements.

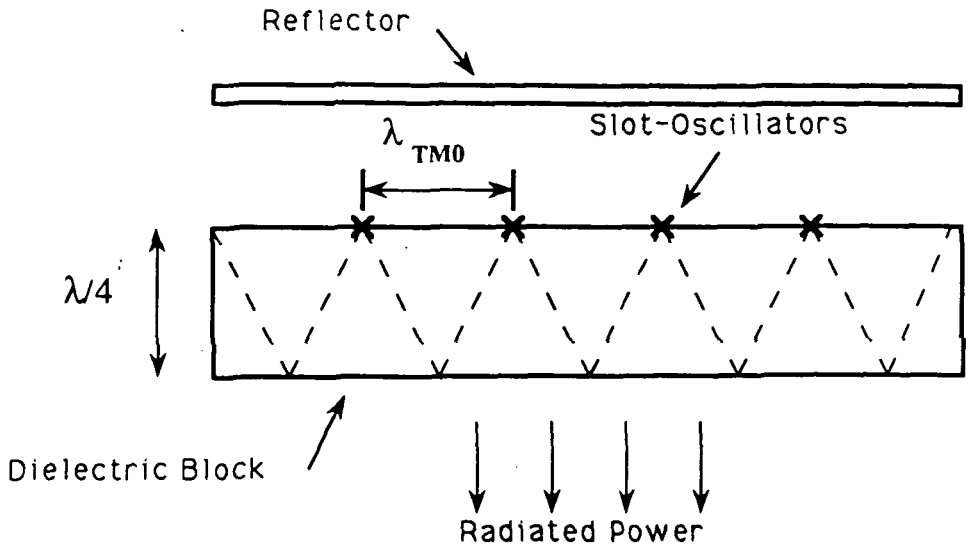

Figure 4: Possible slot-oscillator array configuration

ACKNOWLEDGEMENTS

This work is supported by the AF/ Rome-Air Development Center and by the NASA/Center for Space Terahertz Tehnology at the University of Michigan. We thank Prof. Linda Katehi for providing us with the full-wave solution of a cpw-fed slot antenna on an infinite dielectric substrate.

REFERENCES

[1] J.W. Mink, "Quasi-Opical Power Combining of Solid State Millimeter wave Sources," IEEE Trans. Microwave Theory Tech., vol. 34, pp. 273-279, Feb. 1986

[2] Z.B. Popovic, R.M. Weikle, M. Kim, and D.B. Rutledge, "A 100 MESFET Planar Grid oscillator," IEEE Trans. Microwave Theory Tech., vol. 39, pp. 193-199, Feb. 1991

[3] R.A. York, and R.C. Compton, "Quasi-Optical Power Combining Using Mutually Synchronized Oscillator Arrays," submitted to IEEE Trans. Microwave Theory Tech., Oct. 1990

[4] N. Camilleri and T. Itoh, "A Quasi-Optical Multiplying Slot-Array," IEEE Trans. Microwave Theory Tech., vol. 33, pp.1189-1195, Nov.1985

2x2 QUASI-OPTICAL POWER COMBINER ARRAY AT 20 GHz

Shigeo Kawasaki and Tatsuo Itoh

Department of Electrical Engineering
University of California
Los Angeles, CA 90024

ABSTRACT

Investigation of a power combiner made of two FET oscillators for an active array are reported. As an approach by a quasi-optical method, a two-dimensional planar array of strongly coupled oscillators by direct connection through a microstrip line is used. In-phase condition between the oscillators as well as in-phase condition of each radiation wave was accomplished by regulating length of feed microstrip lines. The radiation elements of 1λ-slot are embedded in a circuit ground plane. At an operation frequency of 20 GHz, in both H- and E-planes, reasonable Σ radiation patterns were obtained which have good agreement with theoretical patterns.

INTRODUCTION

Quasi-optical circuits have been of growing interest for compact and simple microwave and millimeter-wave systems. Among many solid-state devices, FETs are preferred as an active source for applications based on the MMIC technology[1]. However, due to low efficiency, individual FET has limited capability of the power generation at higher operating frequencies. Therefore, a power combining technique is

essential for high power and high frequency systems. Further, the need for such systems has resulted in a variety of power combining configuration using FETs.

As one of such power combiners, the planar grid oscillator using MESFETs has been developed in a distributed fashion[2]. Also, the weakly coupling oscillator array in a periodic fashion supported by a reflector element has been reported[3]. Recently, using external injection locking, the power combiner array with feedback FET oscillators was made[4]. However, due to a multimoding problem, the power combiner array with strong coupling has not made great progress to date. Regarding linear spatial power combiner arrays with strong coupling, we have already reported a few results obtained under the stratified structure[5],[6]. Through these results, in-phase operation for high combining efficiency was facilitated.

In this paper, we describe design and experimental results of a quasi-optical spatial power combiner array made of two negative resistance HEMT oscillators and 4 slots. Radiation patterns from the slots aligned as 2x2 were compared with theoretical patterns in both H-plane and E-plane. Further, through these patterns, it was confirmed that the radiation waves from each slots were in-phase.

DESIGN

In order to demonstrate topology for the MMIC technology, the circuit was made in a layered structure by adopting slot radiators in a circuit ground plane. Fig. 1 shows the configuration of 2x2 spatial power combiner array designed at 20 GHz. The circuit structure made of two negative resistance oscillators and feed lines is etched on the top side of the substrate, while the slot radiators shown by cross-hatched sections in Fig. 1 are embedded in the ground plane of the bottom side of the same substrate. Each oscillator was designed with -50 Ω for an input impedance. Since both sides of the substrate can be effectively used, the slot radiators in the circuit ground plane increase design flexibility.

RF energy generated from one FET oscillator is divided and delivered to two slots aligned in the E-plane. In addition, a part of this energy is used to lock the other oscillator through a direct coupling between the two oscillators. The locked and amplified signal flows into another two slots aligned in the E-plane as well. Each pair of the slots aligned in the E-plane are connected in series. Therefore, this 2x2 array consists of two slots aligned in the E-plane and two slots aligned in the H-plane with 1λ separation between the centers of two slots. The direct connection of two slots in H-plane separated by a thin line enhances high packaging density.

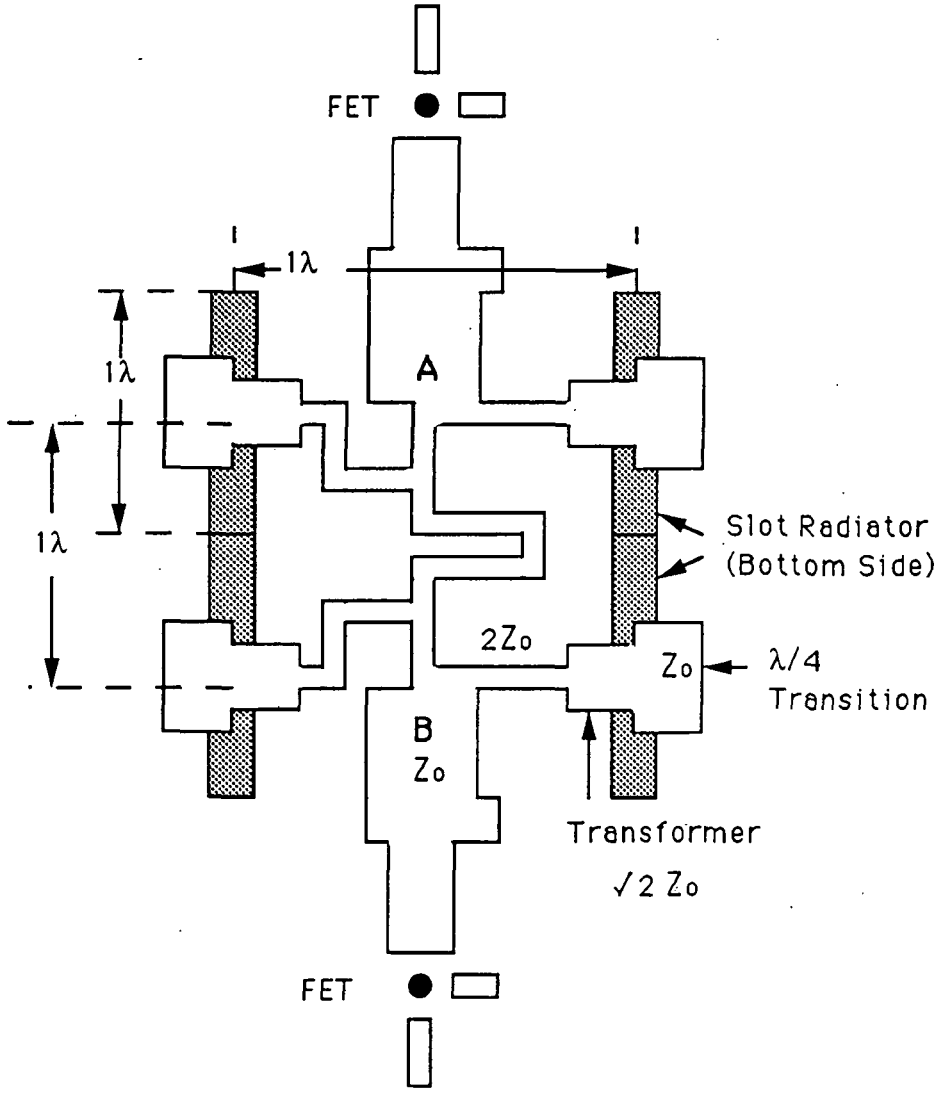

Fig.1 Circuit Configuration

According to the previous results about the direct connection of oscillators[6], when the distance between two branch-points from the oscillators (shown as A and B in Fig. 1) is an odd number of half wavelength, the radiation waves from the two branching points A and B are in-phase. Since the length of a straight line between A and B is 1λ, a microstrip line with $\lambda/2$ should be added. As a result, the radiation waves from the slots in H-plane can have the same phase.

The distance between two centers of slots is 1λ. Thus, the divided energy from one branching point A or B can reach the centers of both slots at the same time. This results in an anti-phase radiation. For the in-phase condition, one of these pass must have additional $\lambda/2$ to invert the phase on one of the slots. By means of this control of pass length between an oscillator and a slot as well as between two oscillators, the in-phase condition was obtained in both H-plane and E-plane.

In addition to the consideration of phase condition, input matching condition needs to be taken into account. A one-stage $\lambda/4$ transformer is inserted from a center of a slot toward a branched feed line connected to the branch-point A or B. In order to electromagnetically couple a feed line with a slot radiator, a $\lambda/4$ microstrip-to-slotline is adopted.

On the other hand, the slot radiators were also designed at 20 GHz with a 1λ slot length and a 0.081λ slot width. Since input impedance of the center feed 1λ slot radiator provides the circuit with 50 Ω load, the slot and the 50 Ω feed line are matched in the steady state oscillation condition.

EXPERIMENTAL RESULTS

The circuit were fabricated on 31 mil thick substrate with ε_r=2.33, using NEC NE32484 package HJFETs. The negative resistance FET oscillator was optimized at 21 GHz with 5 % margin by using small signal S parameters so that the actual circuit can also

be operated at 20 GHz. The maximum operation frequency of 19.5 GHz was observed from the fabricated circuit as shown in Fig. 2.

It is found that, in this two-device power combiner case, a frequency margin of 7.7 % is required under the design condition of -50 Ω for an input impedance. in reference [1], we investigated the frequency margin of a single quasi-optical oscillator with a single slot using the same NE32484. In this case, the frequency margin of 4.4 % was obtained.

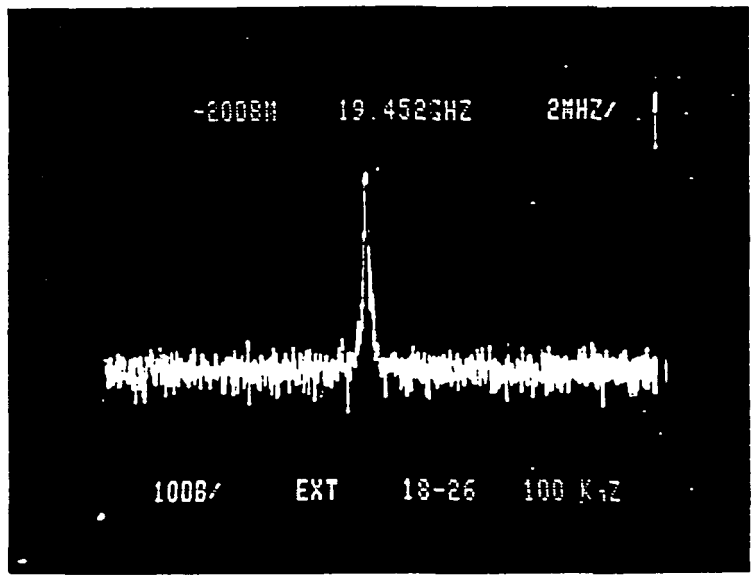

Fig. 2 Operation Spectrum

Compared with this previous results, the difference between the operation frequency and the design frequency is increased. This implies that, in the case of a large number of FET combiners, accumulation of a difference of input impedances due to such frequency difference becomes a cause of load pulling, and, due to this phenomenon, the frequency difference is increasingly enhanced. The tuning range obtained by changing the applied DC voltages, V_{ds} (2.6~5.0 V) and V_{gs} (-1.0~-1.6 V), was 121 MHz.

Radiation patterns in both the H-plane and the E-plane are shown in Fig. 3. In both cases, it is easy to find out null points around ±30° which result from array factor. For comparison, the theoretical analysis was carried out by using the point matching method to obtain numerical data from the Pocklington type integral equation. In the calculation, the voltage ratio of two source generators to excite each slot was set to 1, while the phase difference of these generators was set to 0. Using these data, theoretical radiation patterns

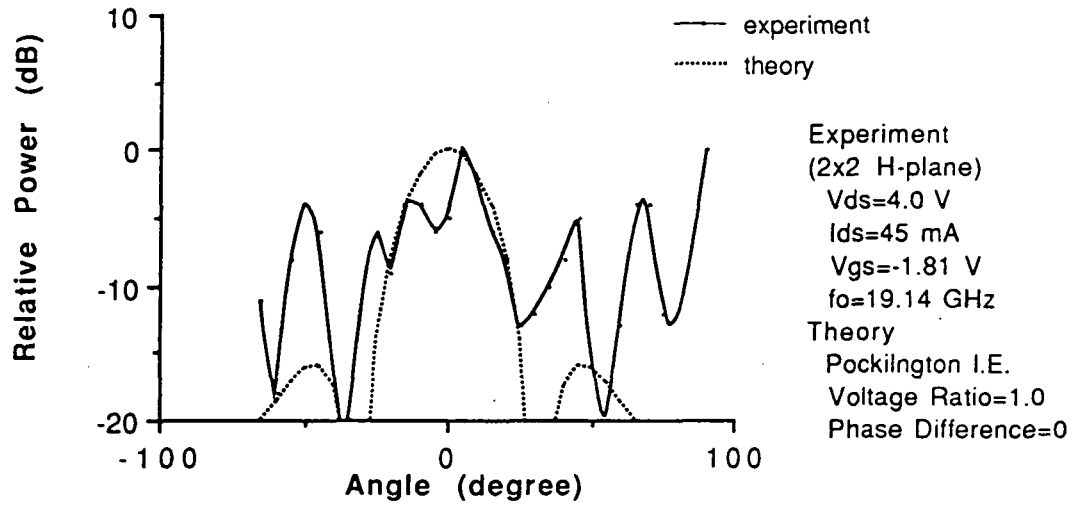

Comparision in Radiation Pattern (H Plane)

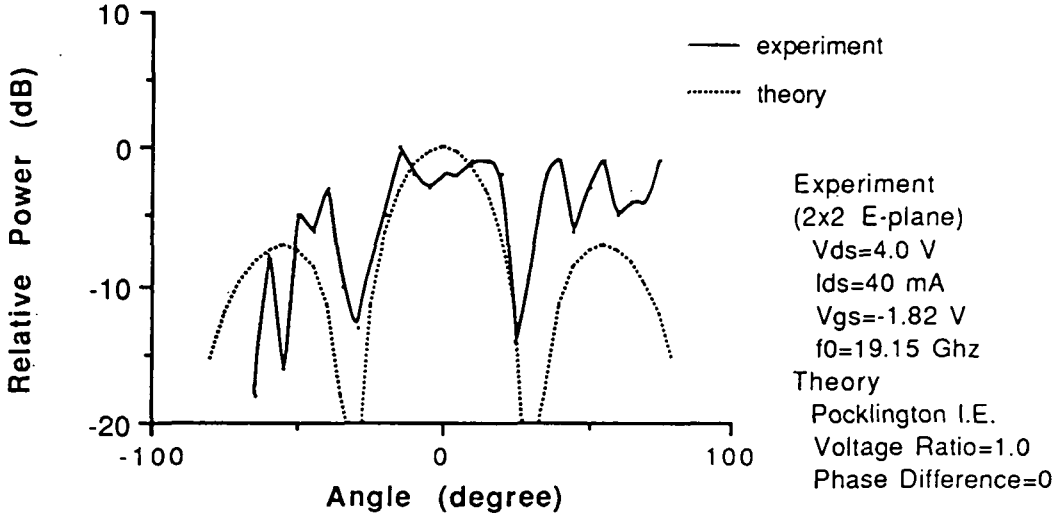

Comparision in Radiation Pattern (E plane)

Fig. 3 Radiation Patterns

are obtained as shown in Fig.3 for both the H-plane and the E-plane. Agreement around the main beams is good.

Sidelobes in the E-plane becomes lager than those in the H-plane because of a single element factor. This fact is shown in the theoretical patterns in Fig. 3. However, the sidelobes obtained from the experiment were still large in both H-plane and E-plane. These discrepancies may result from the inadequate experimental setup.

CONCLUSIONS

Design and experimental results of a 2x2 quasi-optical spatial power combiner was reported as a prototype of two dimensional quasi-optical power combiner array. Although the impedance matching conditions as well as the in-phase condition have been taken into account carefully, the difference of the operation frequency (19.2~19.5 GHz) to the design frequency (20 GHz) has increased. In the case of a large array, more attention should be paid to avoid increase of this frequency difference resulting in phenomena such as load pulling.

In both the H-plane and the E-plane of a 2x2 quasi-optical power combiner array, Σ radiation patterns were obtained by controlling the lengths of feed lines. Good agreement between the experiment and the theory was obtained about mainlobes in both radiation patterns.

It is believed that,through this prototype circuit, the fundamental data for a monolithic quasi-optical power combiner array were obtained.

ACKNOWLEDGEMENT

This work was supported by US Army Research Office under contract DAAL 03-88-K-0005.

REFERENCES

[1] S. Kawasaki and T. Itoh, "24 GHz FET Oscillator with Slot Antenna for Quasi-Optical Transmitter", 16th In't Conf. on IR & MMW, Switzerland, Aug. 1991, pp 286-287

[2] Z.B. Popovic, R.M. Weikle II, M. Kim and D.B. Rutledge, "A 100-MESFET Planar Grid Oscillator", IEEE Trans. Microwave Theory Tech., vol. 39, pp 193-200, Feb. 1991

[3] R.A. York and R.C. Compton, "Quasi-Optical Power Combining Using Mutually Synchronized Oscillator Arrays", IEEE Trans. Microwave Theory Tech., vol. 39, pp 1000-1009, June 1991

[4] J. Birkeland and T. Itoh,"Two-Port FET Oscillators with Applications to Active Arrays", IEEE Microwave and Guided Wave Lett., vol.1, pp112-113, May 1991

[5] S. Kawasaki and T. Itoh, "40 GHz Quasi-Optical Second Harmonic Spatial Power Combiner Using FETs and Slots", to be published in 1992 IEEE MTT-S Int'l Microwave Symposium, Albuquerque, NM.

[6] S. Kawasaki and T. Itoh, "6-Element Periodic and Nonperiodic Linear Arrays for Quasi-Optical Spatial Power Combiner", to be published in URSI Radio Science Meeting, Chicago IL, July 1992

MONOLITHIC MILLIMETER-WAVE DIODE ARRAY BEAM CONTROLLERS: THEORY AND EXPERIMENT

L. B. Sjogren, H-X. L. Liu, F. Wang, T. Liu, W. Wu, X-H. Qin, E. Chung, C.W. Domier, N. C. Luhmann, Jr.
Center for High Frequency Electronics
Department of Electrical Engineering
University of California
Los Angeles, California 90024-1594

J. Maserjian
Jet Propulsion Laboratory
Pasadena, California 91109

M. Kim, J. Hacker, D.B. Rutledge
California Institute of Technology
Pasadena, California 91125

L. Florez, J. Harbison
Bellcore, Inc.
Red Bank, New Jersey 07701-7030

I. Introduction

Power-combining arrays of semiconductor devices offer a promising approach to the realization of compact, reliable, economical systems for watt-level operation at millimeter-wave and submillimeter-wave frequencies. Such ("grid") arrays have demonstrated numerous functions at microwave and millimeter-wave frequencies in recent experimental efforts. Monolithic diode arrays have demonstrated phase shifting at 93 GHz [1], frequency doubling from 33 to 66 GHz [2] and frequency tripling from 33 to 99 GHz [3]. One dimensional monolithic imaging arrays have been demonstrated at 94 GHz [4]. Additional quasi-optical functions have been demonstrated at microwave frequencies by arrays employing hybrid technology. These include the oscillator grid [5-6], mixer grid [7], and amplifier grid [8]. The hybrid grids operate on the same basic quasi-optical principle as the monolithic arrays, so the functions demonstrated to-date in hybrid form should be feasible also in a monolithically integrated form at millimeter-wave frequencies. Additional array design approaches have been suggested for further development of millimeter-wave components [9].

Construction of complete systems based on the millimeter-wave array technology requires not only source and detector arrays, but control components for such functions as amplitude modulation, phase modulation, and beam steering. The first effort

at addressing this need by a semiconductor device array was an experimental demonstration of a phase shifter at 93 GHz [1]. In this work, phase control of a reflected beam over a range of 70 degrees with 6.5 dB loss was achieved by a monolithic array of Schottky diodes. The stacking of more than one array [1] should allow a phase range of greater than 360 degrees to be achieved. Operated in a nonuniform phase (bias) mode, such an array should be capable of (phased array) beam steering and beam focusing.

In the current work, multi-function beam control arrays have been fabricated, and have successfully demonstrated amplitude control of transmitted beams in the W and D bands (75-170 GHz). While these arrays are designed to provide beam control under DC bias operation, new designs for high-speed electronic and optical control are under development. These arrays will fill a need for high-speed watt-level beam switches in pulsed reflectometer systems under development for magnetic fusion plasma diagnostics.

A second experimental accomplishment of the current work is the demonstration in the 110-170 GHz (D band) frequency range of a new technique for the measurement of the transmission phase as well as amplitude [11]. Transmission data can serve as a means to extract ("de-embed") the grid parameters; phase information provides more complete data to assist in this process.

Additional functions of the array beam controller yet to be tested include electronically controlled steering and focusing of a reflected beam. These have application in the areas of millimeter-wave electronic scanning radar and reflectometry, respectively.

II. Theory and Design

The beam control device consists of a monolithic two-dimensional array of varactor diodes embedded in metal strips. Its quasi-optical behavior is represented by a shunt impedance across a transmission-line representation of the beam. The impedance is that of a series RLC circuit. The inductance, some fixed (undesired bias-independent) capacitance, and a small resistance are due to the metalization grid structure; the bulk of the capacitance is due to the diode; the bulk of the (undesired) resistance is a parasitic effect of the diode and its Ohmic contact.

The initial objective of the current effort was the design of the proposed stacked 360 degree reflection phase shifter array [1]. In this approach, an effective load reactance of arbitrary value is obtained by the use of two diode grids, each of which possesses a reactance range of at least $-Z_{GaAs}$ to Z_{GaAs}, where Z_{GaAs} is the plane wave impedance of Gallium Arsenide (approximately 105 Ω), and the grids are separated by an odd multiple of $\lambda/4$.

The capability of the array to control beam transmittance is based on its ability to be switched, under bias control, between a low and high impedance state. When the array is biased at resonance, it appears to the beam as nearly a short circuit, and reflects most of the beam back. When the array is biased far from resonance (i.e. at high impedance), the beam is affected very little by it. In this case, the beam transmittance is large.

The dimensions and doping profile for the monolithic Gallium Arsenide Schottky varactor diode were determined with the assistance of a finite difference solution program for Poisson's equation in one dimension. This provided an estimate of the diode C-V characteristics. Additional routines were employed to estimate tunneling, avalanche, and thermionic emission currents. A hyperabrupt doping profile, similar to that employed by W. Lam [1], was chosen to provide linearity of reflection phase versus DC bias. Different doping levels were simulated to optimize the capacitance range and breakdown voltage. A heterojunction barrier, pioneered at JPL for frequency multiplier diodes, has been incorporated to suppress tunneling current under reverse bias and thermionic emission under forward bias. The experimental results in this paper were obtained with arrays fabricated from MBE wafers with the profile shown in Fig. 1.

Design of the array requires the theoretical prediction of the electromagnetic (grid) behavior as well as the C-V characteristics of the embedded varactor diode. For the passive (electromagnetic) design, a simple method of moments analysis has been employed. This has provided a new model which includes the effect of the discontinuity of the current at the site of the diode ("grid capacitance")[12] (Fig. 2). This model somewhat underestimates the fixed (bias-independent) capacitance at the diode site, since it idealizes the current discontinuity as that for a "gap" at the diode site when the diode is (analytically) open circuited. Even so, the capacitive effect was found to be considerable (5-10 fF for typical array geometries at 100 GHz), and sufficient to reduce the simulated phase range of the stacked phase shifter from well above 360 degrees (with the "grid capacitance" not included) to a value considerably below 360 degrees (with it included). A rigorous simulation of the C-V characteristics of the grid would require a three dimensional simulation which includes the effect of the anode "finger", absence of dielectric beyond the etched walls of the diode, etc. A more precise determination of the grid inductance should be possible with the Hewlett Packard High Frequency Structure Simulator electromagentic analysis program. Such an analysis may provide a more precise estimate of the grid capacitance.

The grid impedance model and diode model programs were combined and incorporated into a quasi-optical (transmission line) circuit analysis program based on the application of Kirchoff's laws at the dielectric (and grid) interfaces. Simulations were performed to determine unit cell and strip dimensions which maximized the grid impedance range. The grid capacitance effect was suppressed by use of a "rectangular unit cell", in which diodes are effectively placed "in series" by spacing them closer along the axis of current flow. Such a configuration has the additional benefits of allowing use of a large (easier to reliably fabricate) diode and providing significantly higher power-handling capability. The one drawback of this design is a somewhat higher loss, since the effective diode resistance is a/b times the actual diode resistance. The increased size of the diode will partially, but not completely, offset this effect. A possible alternative for the reduction of grid capacitance is to employ a narrower metal strip in the vicinity of the diode [13]. This was not feasible for the current design, since the strip was too narrow to taper.

The simulations provided the optimized unit cell dimensions a=300 μm, b=120 μm, and w=7 μm, with diode dimensions of 3 μm x 13 μm. The diode area assumed

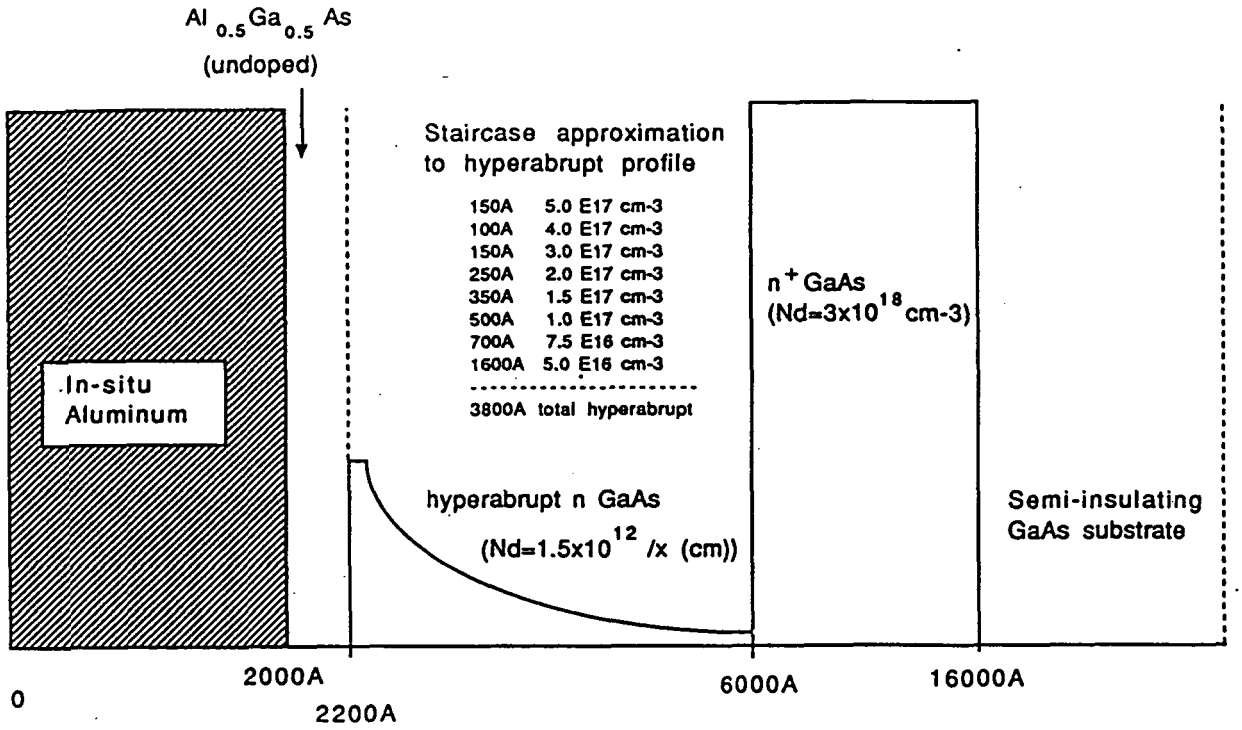

Figure 1: MBE profile of the beam control array.

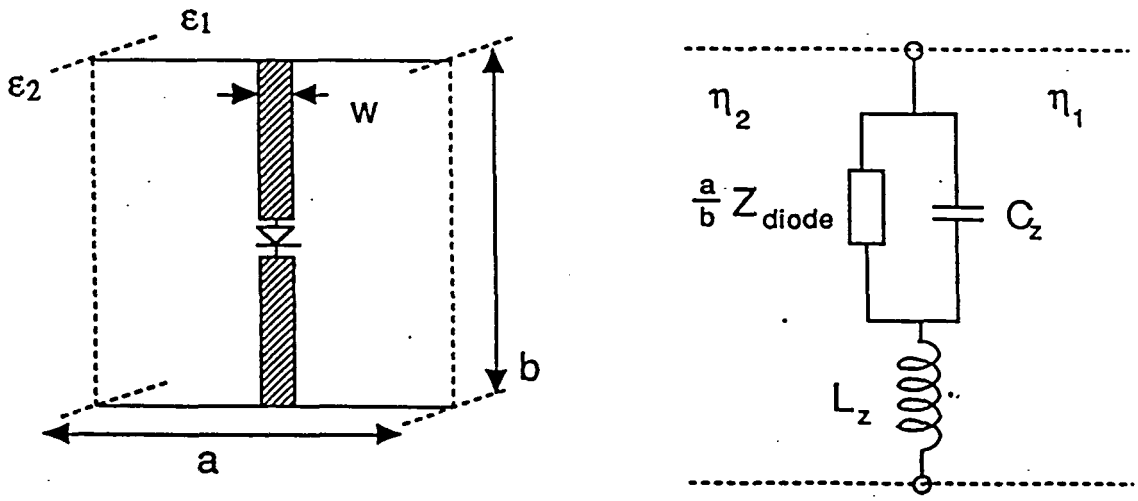

Figure 2: Electromagnetic model of the diode array.

in the simulations is 26 μm^2, since the effective diode width after fabrication should be about 1 μm less than the drawn dimension. Due to the small cell dimensions, the device count per array is very high, about 12,000 for a full sized (2.5 cm x 1.8 cm) array. To allow reasonable spacing between wirebonds, the array was layed out so that each bias line connects to eight contiguous rows of 60 diodes each. Thus, each bias line connects to 480 array diodes.

As previously stated, the array should show some capability for electronic beam steering and focusing. The array model cannot predict the extent of these capabilities, however, since it is applicable only to uniform array operation.

III. Fabrication and Testing

Array fabrication is based (with some modifications) on the self-aligned Aluminum Schottky diode process developed by C. Zah for millimeter-wave imaging diodes [4]. Most of the processing was performed at the JPL Microdevices Laboratory, a facility with state-of-the-art microfabrication capability.

Device isolation was performed, as in [4], by proton implantation, with an implant mask of thick photoresist. A two-step implant of $4x10^{14} cm^{-2}$ at 200 keV and $4x10^{14} cm^{-2}$ at 100 keV provided good isolation. However, photoresist edge bead resulted in the corners of the arrays being unisolated. Several of the arrays were therefore re-implanted to isolate these areas. However, the capacitance range of the diodes was greatly reduced after the second implant. It thus appears that some of the implant penetrates the photoresist mask and into the active device. The arrays which were not re-implanted had some unuseable areas due to the edge bead problem, but have proved sufficient for the experimental proof-of-principle testing.

Due to the parallel connection of array diodes, short circuited devices must be disconnected from the array. An HP4145 Semiconductor Parameter Analyzer, HP9836 controller, and Electroglas 1034 wafer prober were combined into a system which allowed automated testing and storage of I-V characteristics for every array device. Device probing was facilitated by an extra metalization step which creates probe pads connected to each device prior to grid (bias) metalization. With the short-circuited devices identified, a microprobe was used to sever their connection to the array. Following final metalization, very few of the bias lines were short-circuited. Therefore, further identification of short-circuited devices by "hotspot" detection [1] was not neccessary. Photographs of a single array device and a small region of an array are shown in Figs. 3 and 4, respectively. The final steps for completion of the array are the attachment and wirebonding of the array to a printed circuit "bias" board, and the attachment of bias wires to the board. Series resistors of 220 Ω are added to the bias wires to prevent damage if an array device becomes short-circuited.

IV. Results

Millimeter-wave transmission testing was performed with the system shown schematically in Fig. 5. A small array (1.8 cm x 1.0 cm, 4800 diodes) successfully demonstrated transmitted amplitude control throughout the W and D frequency bands

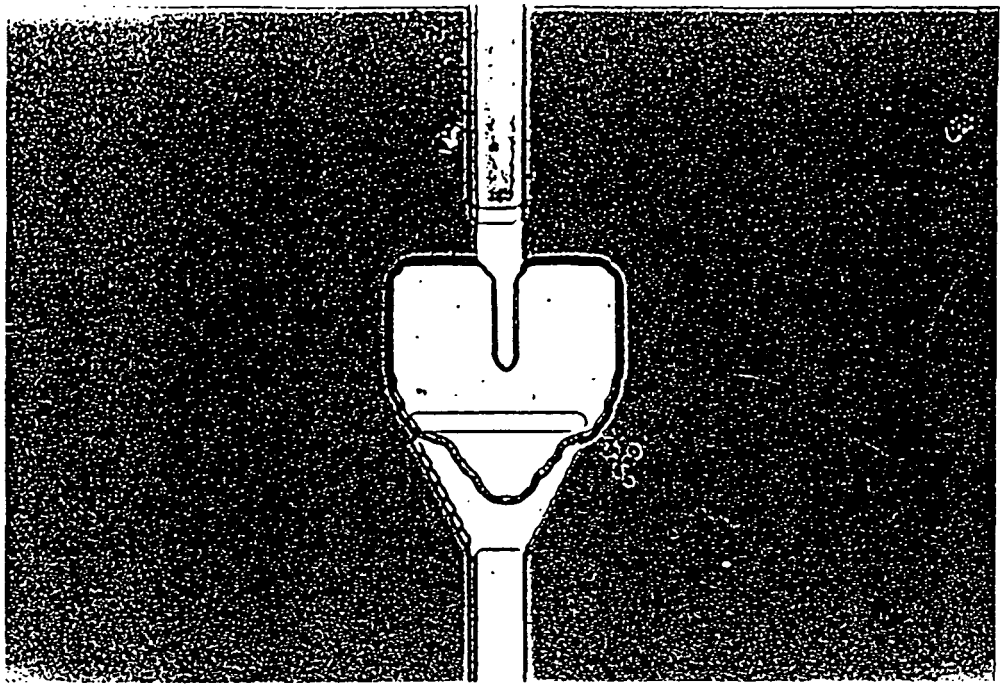

Figure 3: Photograph of a single device in a beam control array.

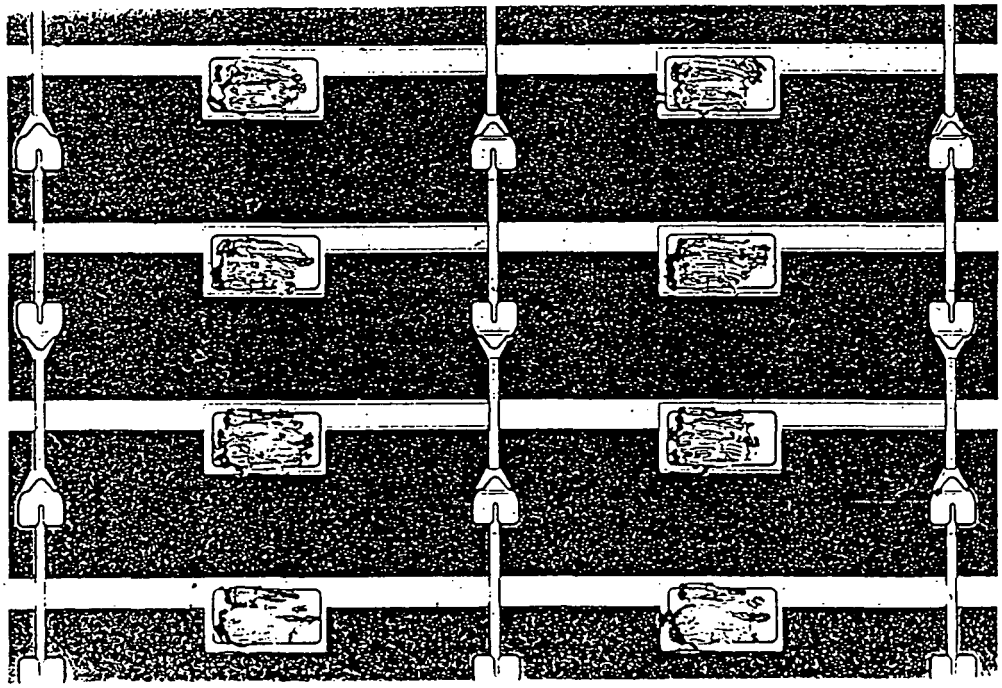

Figure 4: Photograph of a small section of the beam control array. Unit cell dimensions are 300 μm x 120 μm. The vertical strips serve as the "antenna" elements, while the horizontal strips provide bias voltage to the diodes. The marks on the large rectangular test pads are from automated device probing.

(75-170 GHz). Results at 99, 132, and 165 GHz are shown in Fig. 6. Substantial amplitude control was obtained (except near resonance), despite leakage currents on a number of the bias lines preventing most of the bias from showing up their associated sections of the array. In addition to amplitude control under DC bias, the array successfully demonstrated low frequency (200 kHz) modulation of a 165 GHz beam (Fig. 7). The modulation frequency was limited by the bandwidth of the detected beam amplifier. Further testing will be performed to determine the maximum modulation frequency of the array.

To allow further verification of the grid behavior, a technique has been developed to obtain the phase, as well as amplitude, of the transmitted beam [11]. The method involves tilting the incident beam, so that a portion of it is aligned orghogonal to the operational ("active") axis of the grid. The orthogonal beam component is employed as a reference, with the polarization of the transmitted beam providing the relative phase of the beam in the active versus orthogonal ("passive") axis. Since the phase of the passive axis is highly predictable, the absolute phase of the transmitted beam in the operating axis can be determined by this method. The method was verified by application to strip arrays, whose theoretical behavior can be well predicted and compared to the experimental results. The method was then applied to obtain the transmission coefficient of the beam control array as a function of frequency and bias. This was done for an 8600 diode beam control array. Estimates of parameters for the series RLC model of the grid were obtained by varying the parameters until a good match between the theoretical and experimental transmission curves was obtained. This provided a fairly precise estimate of grid resistance and resonant frequency $f_{res} = (2\pi\sqrt{LC})^{-1}$. For the array tested, the grid resistance is approximately 40 Ω over the entire bias range, and the resonant frequency versus bias is shown in Fig. 8. The individual value of L (or C) has some range in which the theoretical and experimental curves agree. This range is centered at an inductance value of L= 160 pH, with the capacitance ranging from 5.2 fF to 13.9 fF as a function of bias for this value of L. The results indicate a cutoff frequency for the beam control array $f_c = (C_{min}^{-1} - C_{max}^{-1})(2\pi R)^{-1}$ of about 400 GHz. It appears that both the grid inductance and capacitance are considerably lower (about 35 %) than predicted. The deviation in the inductance value is probably due to the idealization of the inductive effect as that of a uniform (and narrower than actually fabricated) vertical strip. Simulation by the High Frequency Structure Simulator will provide a more definitive verification of this. The deviation in grid capacitance is with respect to the values expected based on 1 MHz C-V measurements of sample diodes from the same wafer. This discrepancy requires further investigation.

Initial reflection tests have been performed for "calibration" devices (strip grids), with use of a focusing lens [14] and the polarization technique [11]. The phase of the reflection coefficient has been successfully obtained by this method. Since the grid parameters of the currently fabricated arrays are largely now known, the reflection phase shift for a stack of two of these grids can be well-predicted. Predicted results at 128.3 GHz (at which the thickness of the GaAs can be made the desired odd multiple of $\lambda/4$), along with the originally simulated behavior at the design frequency of 99 GHz rescaled to 128.3 GHz, are shown in Fig. 9. The lower than desired C_{max}/C_{min} ratio

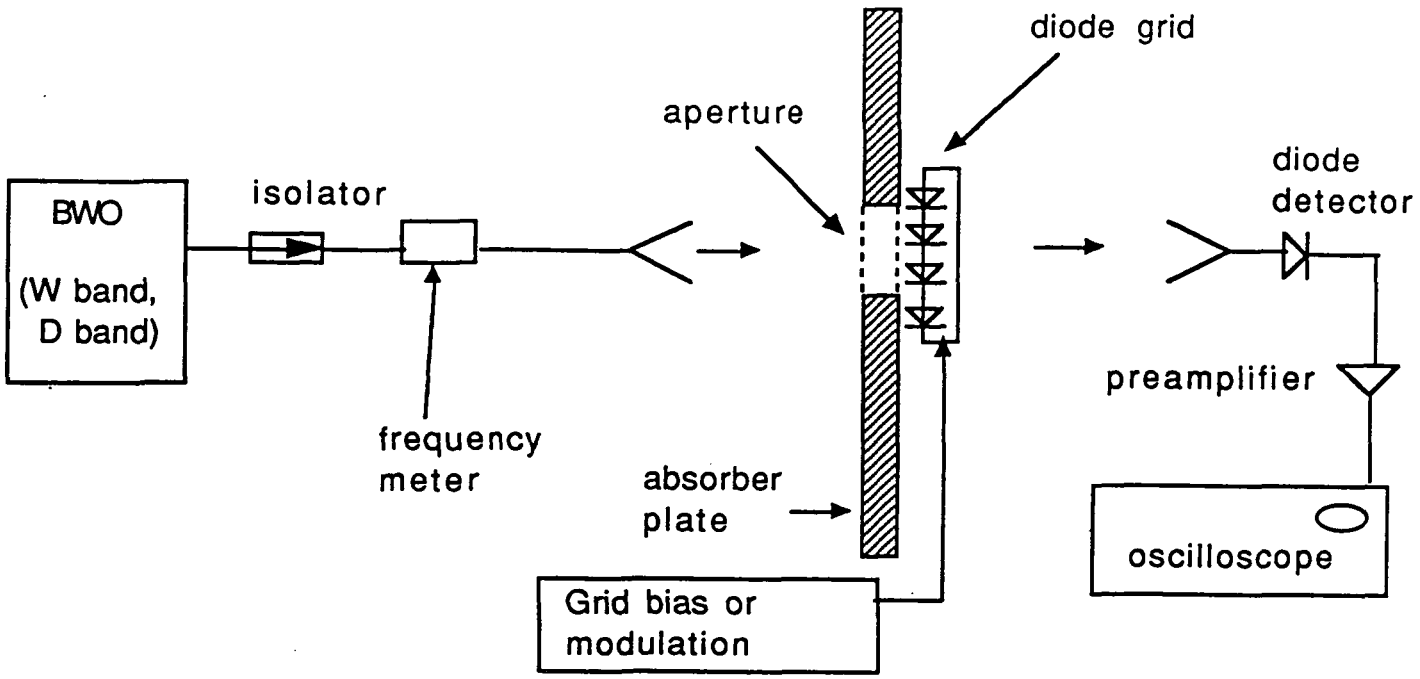

Figure 5: Schematic diagram of the test system for transmitted beam testing.

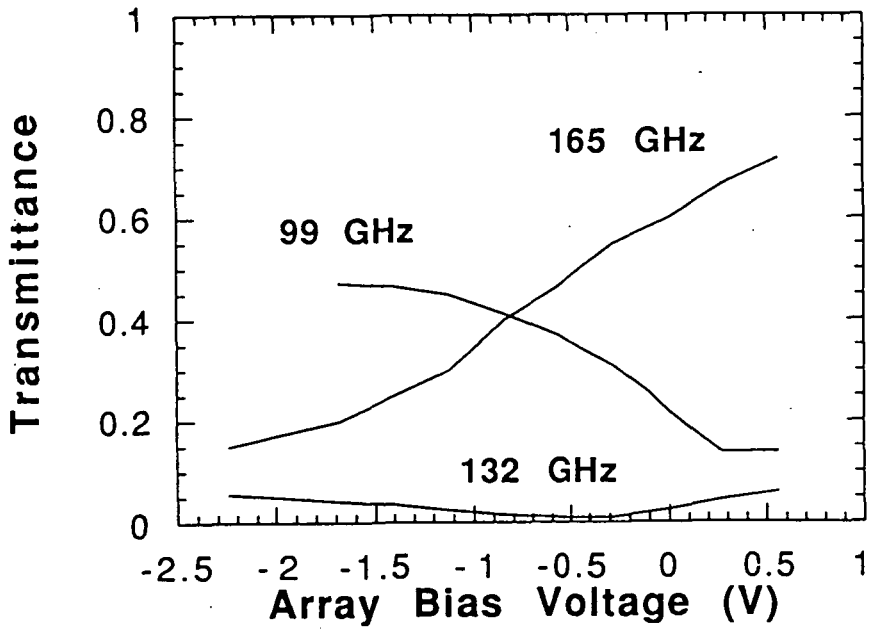

Figure 6: Experimental beam transmittance at 99 GHz, 132 GHz, and 165 GHz as a function of DC bias applied to the array. The basic form of the curves can be understood by the fact that the array is capacitive at 99 GHz, resonant at 132 GHz, and inductive at 165 GHz.

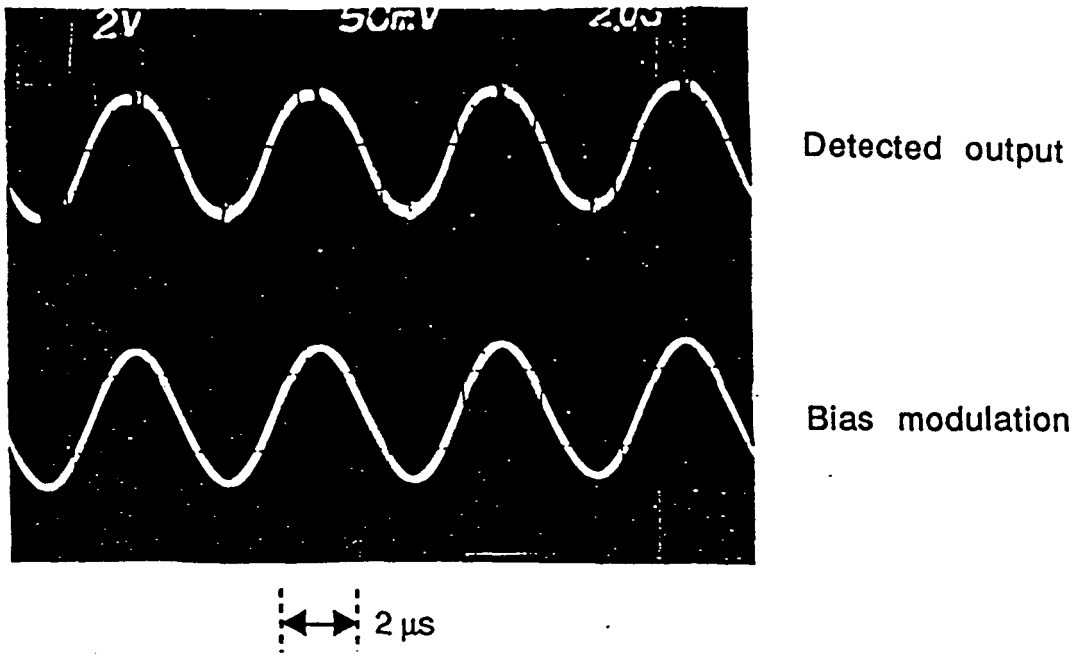

Figure 7: Detected output versus array input voltage for a sinusoidal modulation of the array at 200 kHz. The lower waveform is the array bias modulation voltage, whose range was -3V to +1V. The upper waveform is the detected output from the transmitted beam.

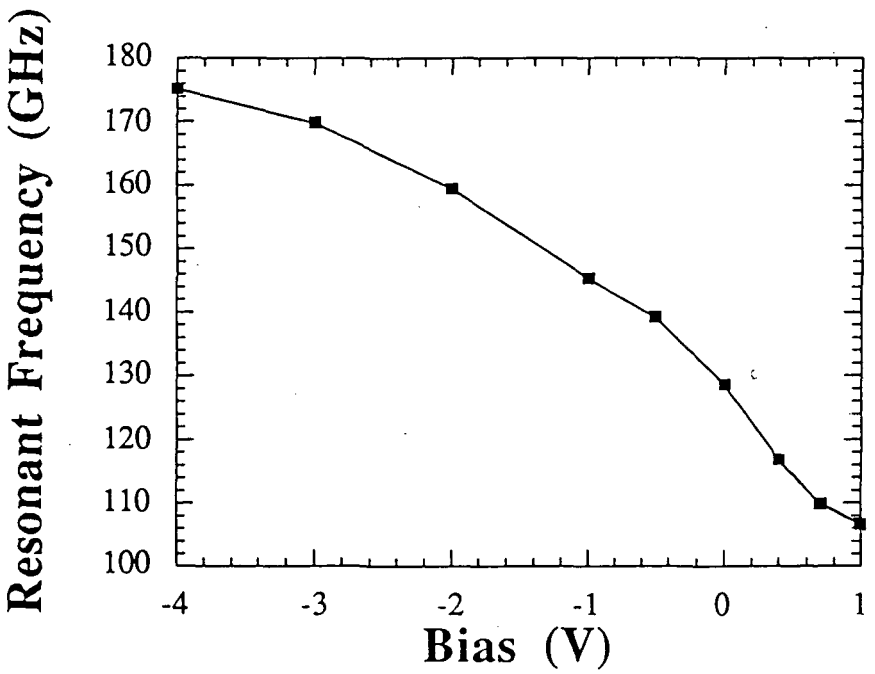

Figure 8: Resonant frequency versus DC bias for the beam control array.

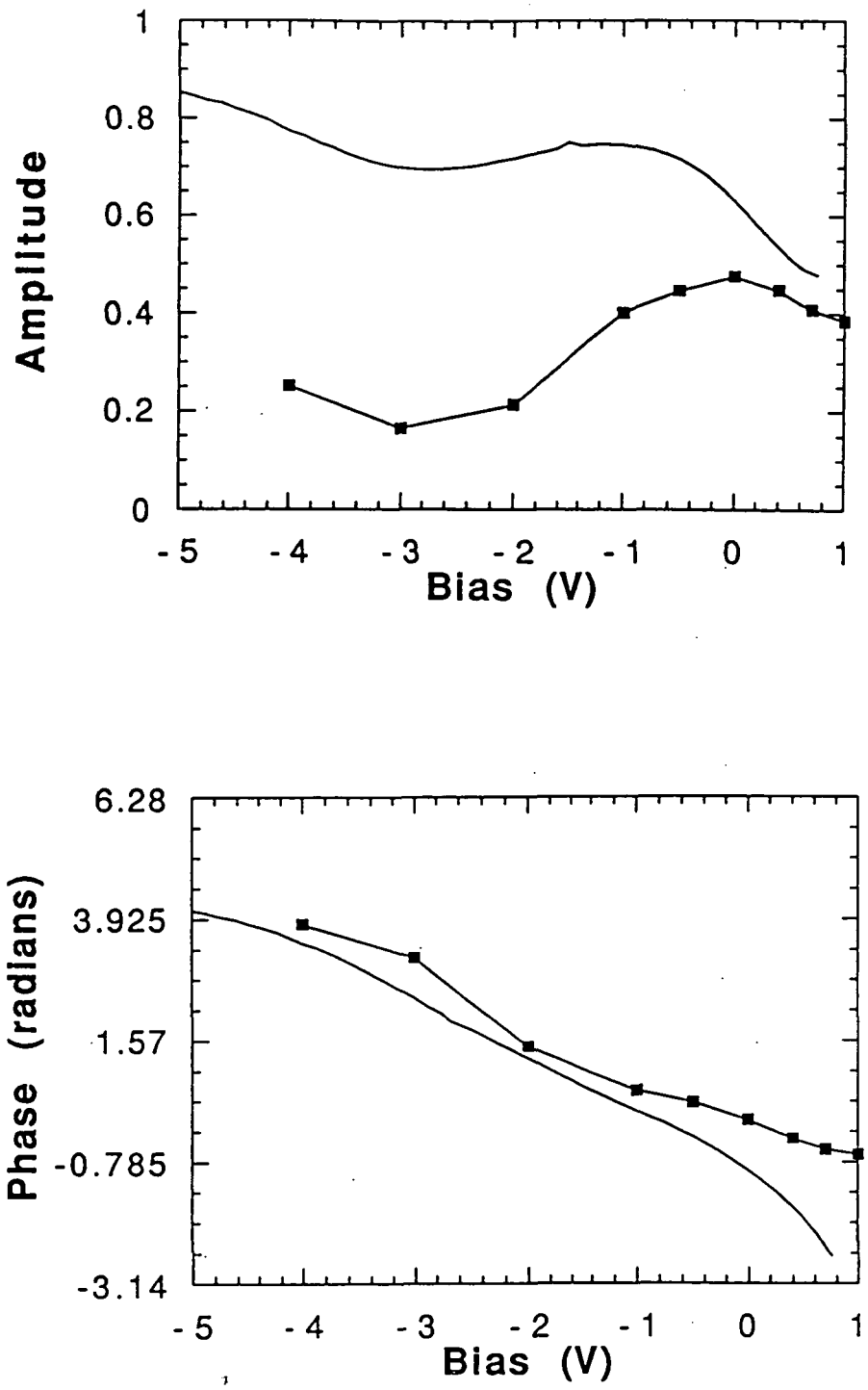

Figure 9: Predicted reflection coefficient for a two layer stacked phase shifter with fused silica "window" at 128.3 GHz. Lines with no markers represent the predictions based on originally simulated grid parameters. Lines with markers represent the predictions based on estimates of the grid parameters based on transmission measurements.

results in a phase range less than 360 degrees, contrary to the original simulation. This, however, does not preclude the possibility of beam steering to small angles. The higher than desired grid resistance results in a reflectance which is lower and is much more variable over the bias (phase) range. A preliminary attempt at steering of a transmitted beam with the current array was unsuccessful. This may be due to an inability of the grid to produce the strong amplitude variation with position associated with the desired phase distribution. Since steering to a fixed angle has been successfully demonstrated by a (low-loss) passive grid [15], the beam control array's ability to steer a reflected beam is likely to be governed largely by the grid loss as well as phase shift range. To obtain higher performance for the beam control functions, new arrays are being fabricated which should possess a larger C_{max}/C_{min} ratio and Ohmic contact resistance. In addition, we are considering the stacking of a large number of arrays of the current design and operating them in the high impedance region to accomplish transmitted beam steering.

V. Conclusions

A "second generation" millimeter-wave beam control array device has been constructed. This array has successfully demonstrated a new function by a millimeter-wave quasi-optical array, that of beam transmittance control. Phase of the transmitted beam has also been measured by a newly-developed technique. Reflection measurements, which will test the arrays as phase shifters, beam steerers, and beam focusers, will be performed soon. In addition, new arrays with a modified doping profile for higher C_{max} and lower resistance are being fabricated. These "higher performance" arrays should provide, for example, a greater "contrast ratio" (maximum to minimum transmittance) when the array is operated as a beam modulator.

New array designs have been initiated for high-speed (under 200 psec) electronic and optical beam control. For electronic control, the bias lines of the beam control array are being designed to function as high-speed guided-wave paths. For optical control, monolithic arrays of photoconductive switch devices are being fabricated. New concepts for barrier varactor photodiodes are under study for application toward optically-controlled modulator and beam steering arrays. High-speed beam switching arrays have immediate application in plasma diagnostic reflectometry, and have potential additional application for such functions as electronic input beam chopping in high-speed imaging systems. Longer term possibilities include exciting possibilities such as amplifying beam steeres with two-axis scan control.

Acknowledgements

Work supported by Northrop Corporation/University of California MICRO program, Department of Energy, and the Army Research Office.

The authors wish to thank the personnel of the JPL Microelectronic Devices Laboratory for their assistance toward the fabrication of the beam control arrays. In particular, we wish to thank R. Peter Smith, Suzanne Martin, Chuck Manning, Rich Muller, Judy Podosek, and Doug Waltman.

Essential to the project has been the availability of high-quality MBE wafers generously provided by Prof. C. Jou (National Chiao Tung University, Taiwan), Prof. M. Spencer (Howard University), John Liu (JPL), as well as Bellcore, Inc. Assistance in this area has also been provided by Larry Kapitan (formerly with Northeast Semiconductor, currently with QED).

The stepping wafer prober, along with technical assistance, was generously provided by Edith Baltram, Jack Hayden, Frank Freeman, Soo Kok Leng, and Gary Castleman (Hewlett-Packard, Northwest Integrated Circuits Division).

We gratefully acknowledge the essential assistance in Ohmic contact alloying by Dr. Marko Sokolich of Hughes.

Indispensible assistance with millimeter-wave measurement systems was provided by Matt Espiau and Misti Christianson of the UCLA Millimeter-Wave Laboratory.

Additional individuals who provided essential assistance for this project include Wayne Lam (TRW), Charles Meng, Prof. D.S. Pan, Prof. H.R. Fetterman (UCLA), Mike DiLisio (Cal Tech), Prof. R.J. Hwu (University of Utah), Clarence Becwar (Becwar Engineering), and Rene Bernescot (Rockwell).

References

(1) W.W. Lam, C.F. Jou, N.C. Luhmann,Jr., and D.B. Rutledge, "Millimeter-wave diode-grid phase shifters," *IEEE Trans. Microwave Theory Tech.*, 36, No. 5, p. 902, 1988.

(2) C.F. Jou, W.W. Lam, H.Z. Chen, K.S. Stolt, N.C. Luhmann,Jr., and D.B. Rutledge, "Millimeter Wave Diode-grid Frequency Doubler," *IEEE Trans. on Microwave Theory and Techniques*, 36, No. 11, 1988.

(3) H-X. King, X-H. Qin, W. Wu, L.B. Sjogren, E. Chung, N.C. Luhmann, Jr., W.A. Peebles, "Monolithic Millimeter-Wave Quasi-Optical Frequency Multiplier Arrays", presented at, *1991 International Semiconductor Device Research Symposium*, pp. 68-72, December, 1991.

(4) C. Zah, D.P. Kasilingam, J.S. Smith, D.B. Rutledge, T. Wang, and S.E. Schwartz, "Millimeter-wave Monolithic Schottky Diode Imaging Arrays", *Intl. J. of Infrared and Millimeter Waves*, 6, pp. 981-997, 1985.

(5) Z.B. Popovic, R.M. Weikle, M. Kim, K.A. Potter, and D.B. Rutledge, "Bar Grid oscillators," *IEEE Trans. Microwave Theory Tech.* , 38, No. 3, p. 225-230, March,1990.

(6) Z.B. Popovic, R.M. Weikle, M. Kim, and D.B. Rutledge, "A 100-MESFET Planar Grid Oscillator," *IEEE Trans. Microwave Theory Tech.*, 39, No. 2 pp. 193-200, February, 1991.

(7) J.B. Hacker, R.M. Weikle III, M. Kim, D.B. Rutledge, "A 100 Element Schottky Diode Grid Mixer", *1991 IEEE AP-S symposium digest.*

(8) M. Kim, J.J. Rosenberg, R. P. Smith, R. M. Weikle III, J.B. Hacker, M.P. DeLisio, D.B. Rutledge, "A Grid Amplifier", *IEEE Microwave and Guided Wave Letters*, 1, No. 11 pp. 322-324, November, 1991.

(9) R.J. Hwu, C.F. Jou, N.C. Luhmann,Jr., M. Kim, W.W. Lam, Z.B. Popovic, and D.B. Rutledge, "Array concepts for solid state and vacuum microelectronics millimeter wave generation," *IEEE Trans. Elec. Dev.*, 36, No. 11, 1989.

(10) L.B. Sjogren, R.J. Hwu, H-X. King, W. Wu, X-H. Qin, N.C. Luhmann, Jr., M. Kim, D.B. Rutledge, "Development of a 94 GHz Monolithic Quasi-Optical 360 Degree Phase Shifter," *Proc. of the 15th Intl. Conf. on Infrared and Millimeter Waves*, pp. 696-698, 1990.

(11) L.B. Sjogren, et. al., "A Technique for the Measurement of Complex Transmission Coefficient of Millimeter-Wave Grid Arrays", to be submitted, *Microwave and Optical Technology Letters*, 1992.

(12) L.B. Sjogren and N.C. Luhmann, Jr., "An Impedance Model for the Quasi-Optical Diode Array", *IEEE Microwave and Guided Wave Letters*, 1, No. 10, pp. 297-299, October, 1991.

(13) H-X. King, L.B. Sjogren, N.C. Luhmann, Jr., D.B. Rutledge, "New Concepts for High Frequency and High Power Frequency Multipliers and Their Impact on Quasi-Optical Monolithic Array Design", *Int. J. of Infrared and Millimeter Waves*, Feb. 1992.

(14) David R. Gagnon," Highly Sensitive Measurements With a Lens-Focused Reflectometer", *IEEE Transactions on Microwave Theory and Techniques*, 39, No. 12, pp. 2237-2240, December, 1991.

(15) Moonil Kim, Robert M. Weikle III, Jonathan B. Hacker, David B. Rutledge, " Beam Diffraction by a Planar Grid Structure at 93 GHz", *1991 IEEE APS Symposium.*

A Study of Subterahertz HEMT Monolithic Oscillators *

Youngwoo Kwon and Dimitris Pavlidis
Center for Space Terahertz Technology
Solid State Electronics Laboratory
Department of Electrical Engineering and Computer Science
The University of Michigan, Ann Arbor, MI 48109-2122, USA

Abstract

A detailed study of monolithic InP-based HEMT oscillators for subterahertz operation is presented. InAlAs/InGaAs HEMT's have been optimized for high frequency operation and showed very high maximum oscillation frequencies (f_{max}) of 310 GHz using offset self-aligned Γ-gate technology. Power characteristics of HEMT oscillators are reported. An oscillation power of more than 10 mW was evaluated by large-signal analysis at 320 GHz using HEMT's with f_{max} = 450 GHz, V_{br} = 10 V and a gate width (W_g) of 8 × 22.5 μm. Oscillator topology studies showed that complex feedback schemes such as dual and active feedback enhance the negative resistance. Push-push oscillator designs based on harmonic signal generation can finally be used to overcome the frequency barrier imposed by f_{max}.

1 Introduction

InAlAs/InGaAs HEMT's have shown excellent high frequency characteristics and operation capability as discrete devices. A current gain cut-off frequency (f_T) of 305 GHz [1] and a maximum oscillation frequency of 455 GHz have been reported using heterostructures of this type [2]. These very encouraging discrete device results indicate that InP-based HEMT's can be used to realize monolithic circuits with operation frequency well into the millimeter-wave region. A number of such monolithic integrated

*Work supported by NASA under contract NAGW-1334

circuits have recently been demonstrated by the authors. These include monolithic HEMT mixers at 94 GHz showing conversion gain of 1 dB [3] and HEMT doublers at 180 GHz with a conversion loss of 6 dB [4]. Monolithic HEMT oscillators also have been realized by the authors up to W-band showing more than 1 mW power with devices having 36 μm gate periphery [5].

Another possibility opened to HEMT technology is its use for space-based remote sensing and radiometry, where fundamental sources are required to operate above 100 GHz. A first detailed study concerning the power characteristics and the upper frequency limit of InAlAs/InGaAs HEMT's when used as oscillators, has recently been presented by the authors [6]. This paper provides further details on related issues of HEMT use for signal generation. It addresses first the ways of further optimization of InP-based HEMT technology in view of obtaining enhanced f_{max} performance (Section 2). Power and frequency characteristics of monolithic oscillators evaluated with the help of a large-signal analysis are presented in Section 3. Finally, specific designs and topologies of 160 GHz fundamental monolithic HEMT oscillators are discussed in Section 4.

2 Device Optimization for High f_{max}

A very high f_{max} of several hundred gigahertz is necessary to guarantee the device operation as oscillator at millimeter-wave frequencies. Optimization for high f_{max} can be achieved by reducing the parasitic resistances and capacitances of the HEMT. The parasitic source resistance (R_s) consists of two parts : one coming from the contact region (R_c) and the other from the ungated region between the gate and source. In an attempt to minimize the ungated region resistance, a self-aligned gate technology has been applied to InAlAs/InGaAs HEMT's [7]. The ungated region between source and gate has been reduced in this case to less than 0.2 μm and the source access resistance was minimized, resulting in a very high extrinsic f_T of 250 GHz. Although f_{max} is directly proportional to

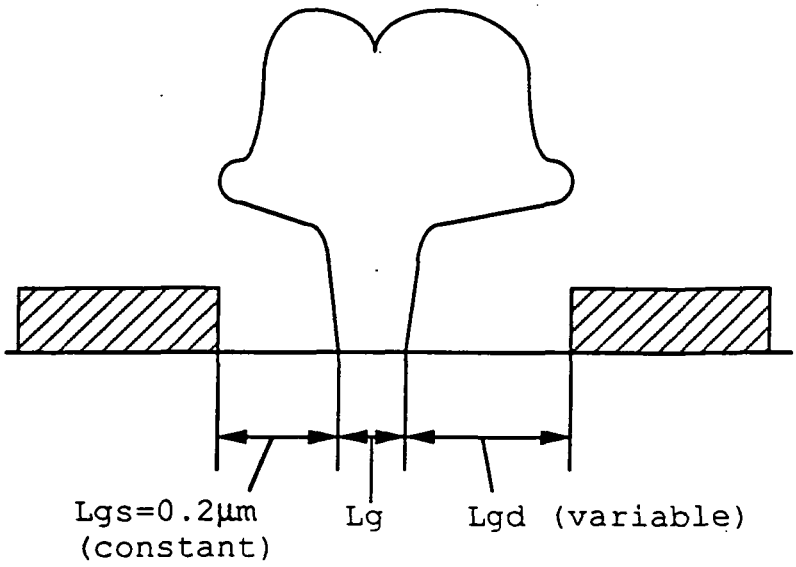

Figure 1: Schematic view of the self-aligned offset Γ gate HEMT

f_T, it was limited in this case due to the high output conductance (G_{ds}) and gate-to-drain capacitance (C_{gd}); this was caused by the proximity of the gate and drain making G_{ds} and C_{gd} higher than in HEMT's fabricated by conventional technology.

A better insight to the problem can be obtained by examining the f_{max} expression which is given by [8]:

$$\frac{f_{max}}{f_T} = \{4\frac{G_{ds}}{G_m}(G_m R_i + \frac{R_s + R_g}{1/G_m + R_s}) + \frac{4}{5}\frac{C_{gd}}{C_{gs}}(1 + 2.5\frac{C_{gd}}{C_{gs}})(1 + G_m R_s)^2\}^{-\frac{1}{2}}$$

It is obvious from Eq. (1) that a high f_{max}/f_T ratio can be achieved by increasing both C_{gs}/C_{gd} and G_m/G_{ds}. These two ratios are related to L_{gd}/L_{gs}, where L_{gs} is the distance between gate and source, and L_{gd} is the distance between gate and drain. L_{gd}/L_{gs} can be increased by offsetting the gate instead of placing it at the center of the source-to-drain region. The novel self-aligned offset Γ-gate developed by the authors [9] and employed in the analysis presented here, allows one to satisfy these requirements. An additional feature of this approach is that L_{gd} and L_{gs} can be controlled much more accurately in this way than in processes where the gate has to be offset aligned between two ohmic contacts. Various L_{gd} values ranging from 0.2 μm to 0.6 μm were employed while L_{gs}

Figure 2: SEM photograph of self-aligned offset Γ-gate (L_{gd} = 0.6 μm)

was fixed at 0.2 μm as shown in Fig. 1.

The devices were fabricated following the self-aligned process described in [9]. The SEM photograph of the completed gate after the ohmic metal deposition is shown in Fig. 2. The highest f_{max} values were obtained with L_{gd} = 0.4 μm and the corresponding microwave results are shown in Fig. 3. f_T is in this case around 150 GHz and f_{max} is greater than 300 GHz. By increasing L_{gd} further, the value of f_{max}/f_T increases due to the higher C_{gs}/C_{gd} and G_m/G_{ds} ratios. However, the magnitude of f_T becomes smaller with L_{gd} due to the increased gate length and source-to-drain spacing. The increase of f_{max}/f_T ratio with L_{gd} is thus compensated by the decrease of f_T and the maximum f_{max} occurs for L_{gd} = 0.4 μm.

Further f_{max} optimization is expected by reducing the gate length of the devices which had large offsets; due to the increased number of line scans for highly offset gates, the gate length becomes larger than in the case of the symmetric/centered realizations. This

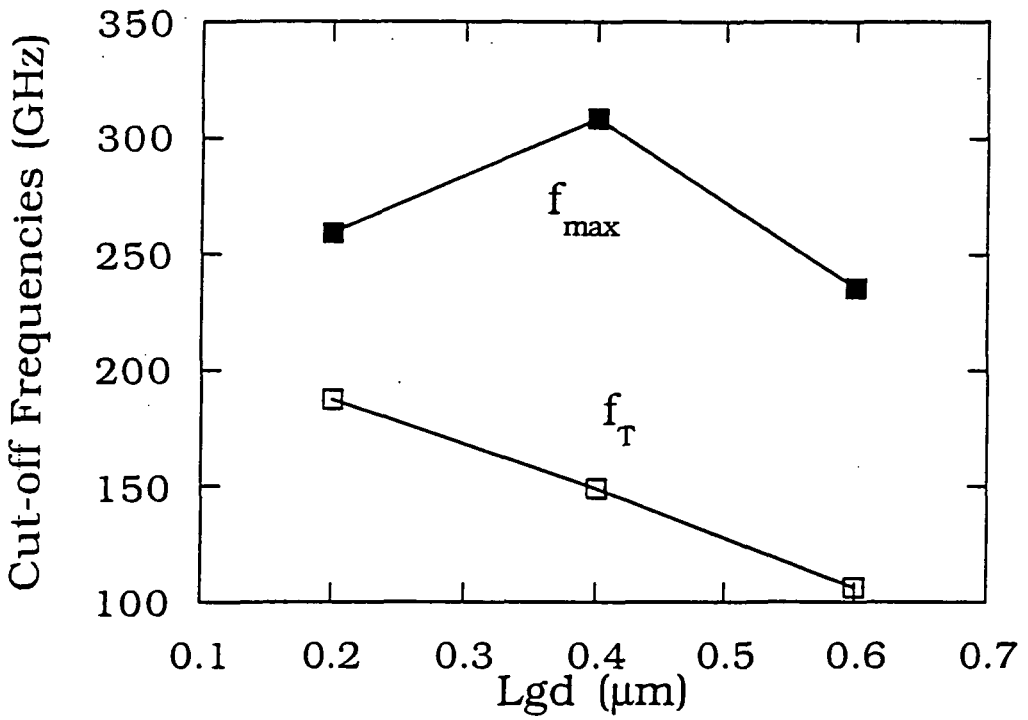

Figure 3: Microwave data of offset self-aligned InAlAs/InGaAs HEMT's ($L_{gd} = 0.4\ \mu m$). The results show an f_T of 150 GHz and an f_{max} of 310 GHz, corresponding to a high f_{max}/f_T ratio of 2.0

drawback can, however, be eliminated by a better optimization of the doses used for the footprint and side lobes of the gate.

3 Evaluation of Oscillator Characteristics Using Large-Signal Analysis

The design of high frequency oscillators is generally based on either small-signal S-parameters or measured large-signal S-parameters. The small signal S-parameters predict the initial conditions necessary for oscillation build up. However, the steady-state oscillation condition can not be accurately predicted from small-signal S-parameters. Designs using measured large-signal S-parameters present also certain difficulties arising from measurement accuracy and differences between measured and simulated conditions.

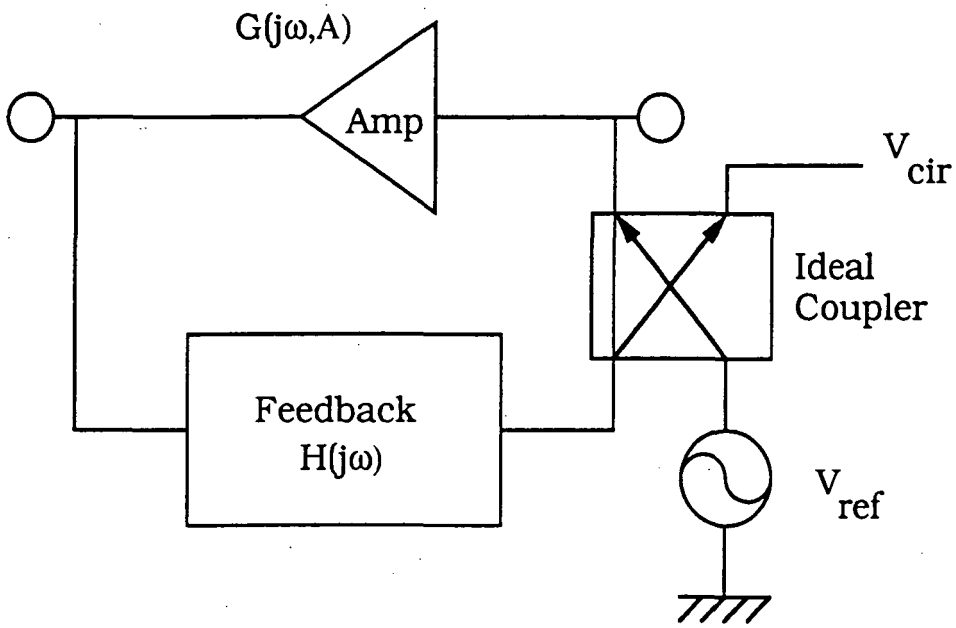

Figure 4: The schematic circuit setup for the large-signal oscillator analysis

An all frequency-domain large signal oscillator analysis method has been developed in view of evaluating the HEMT potential as oscillator. It employs small-signal S-parameters and a harmonic balance routine with 2-D interpolation functions. The method predicts the operation frequency, output power and optimum load termination conditions.

A special circuit set-up is used to perform the large-signal oscillator analysis (Fig. 4). It consists of an amplifying unit and frequency-selective feedback loop together with an excitation signal. The HEMT is used in common source topology and is considered as an amplifying unit with power-dependent gain saturation characteristics. An ideal coupler is placed between the amplifying unit and feedback loop to initiate and monitor the oscillation (V_{cir}). The excitation signal (V_{ref}) is increased from a small signal level until the gain of the HEMT saturates and the steady-state oscillation condition is reached.

The large-signal oscillator analysis method has been applied to study the oscillation power dependence on the termination impedance of common source InAlAs/InGaAs HEMT oscillators. The simulation results are shown in Fig. 5 for a HEMT with 2

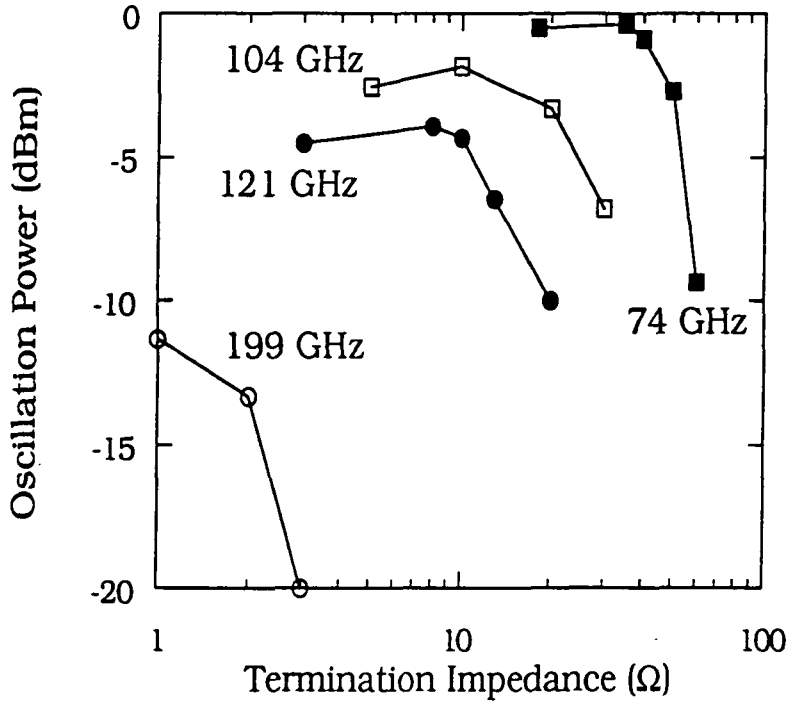

Figure 5: The oscillation power dependence on the termination impedance at various frequencies for a HEMT (L_g = 0.1 μm) with f_{max} = 200 GHz and gate periphery of 2 × 45 μm

× 45 μm gate periphery and f_{max} of 200 GHz. The analysis shows that an optimum output power level is obtained when the load impedance is of the order of 1/2 to 1/4 of the small signal negative resistance at frequencies which are sufficiently away from f_{max}. At very high frequencies, the load impedance determined by the above criteria is reduced to very small values (below 5 Ω) which are difficult to implement in monolithic form. This termination load requirement sets the practical limit of upper frequency at which the oscillator circuit can be implemented. These effects were studied and design criteria were established on the basis of practical realization constraints imposed by load terminations which should exceed 5 Ω.

The available power was evaluated at different frequencies using optimum termination

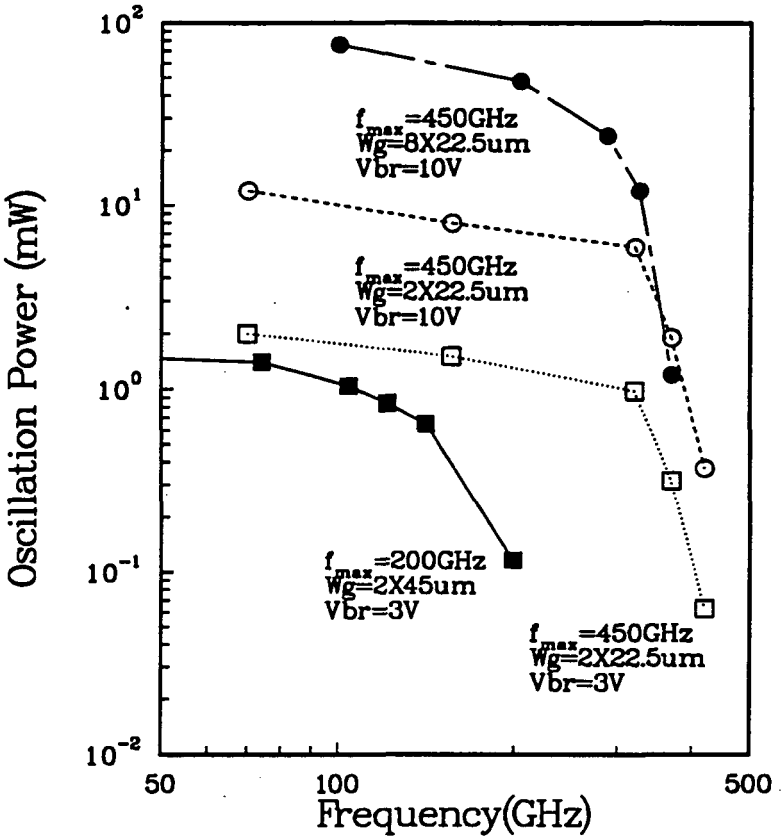

Figure 6: Power delivered by InAlAs/InGaAs HEMT oscillators as a function of frequency, gate periphery (W_g), maximum frequency of oscillation (f_{max}) and breakdown voltage (V_{br})

conditions. Three parameters are used for the simulation: gate periphery (W_g), maximum frequency of oscillation (f_{max}) and breakdown voltage (V_{br}). The results are shown in Fig. 6. The oscillation power decreases first slowly and shows a more dramatic degradation at high frequencies close to f_{max}. This corresponds to the degradation of maximum available gain (G_{max}) and negative resistance (R_{neg}) at high frequencies. The reduced R_{neg} imposes a smaller value of termination load with the result of less power delivered to the load. The overall characteristics suggest that generation of reasonable power levels is feasible up to a frequency of 2/3 of f_{max}. From Fig. 6, it is obvious that a higher f_{max} ensures large oscillation power for a given frequency. More than 15 mW of output power can be expected up to 300 GHz out of 0.1 μm HEMT's with eight 22.5

μm gate fingers assuming an f_{max} of 450 GHz and V_{br} of 10 V. This prediction doesn't include any parasitic effects coming from mismatches, losses of transmission lines and source grounding.

Fig. 6 also shows the characteristics of devices with different gate widths in view of studying the effect of gate periphery on the output power level. Larger devices provide higher oscillation power, but they are harder to implement in oscillator circuits. This is due to their lower induced negative resistance, which implies the need for very small termination impedance. As a result, the oscillation power degrades fast at the high frequency end of operation bandwidth. A compromise has consequently to be made between the oscillation power and ease of realization when choosing the device periphery.

Another important parameter in the oscillator evaluation is the breakdown voltage. A higher breakdown voltage allows one to bias the transistor at larger drain bias and thus to apply higher DC power to the device. The RF power generated from the device is proportional to the DC power and increases consequently with higher V_{br}. Under conditions of optimum biasing for power, the maximum voltage swing is $\sim V_{br}/2$. By increasing the breakdown voltage of the HEMT's from 3 V to 10 V, it was found that the RF power increased by approximately 6 dB. Breakdown improvements in InAlAs/InGaAs HEMT's have recently been reported by Matloubian et al [10] and validate this assumption. Further work is, however, necessary to justify this possibility, especially at millimeter-wave frequencies. Similar improvements can also be made by increasing the current density of the device and may be even easier to achieve in InAlAs/InGaAs HEMT's with the help, for example, of multi-heterojunction designs [11].

It should finally be noted that the simulation results in Fig.6 were obtained using a simple series feedback topology and the evaluated oscillation power values do not therefore necessarily reflect the maximum power capability of the devices.

Overall, the HEMT's can be optimized for generation of adequate power levels at

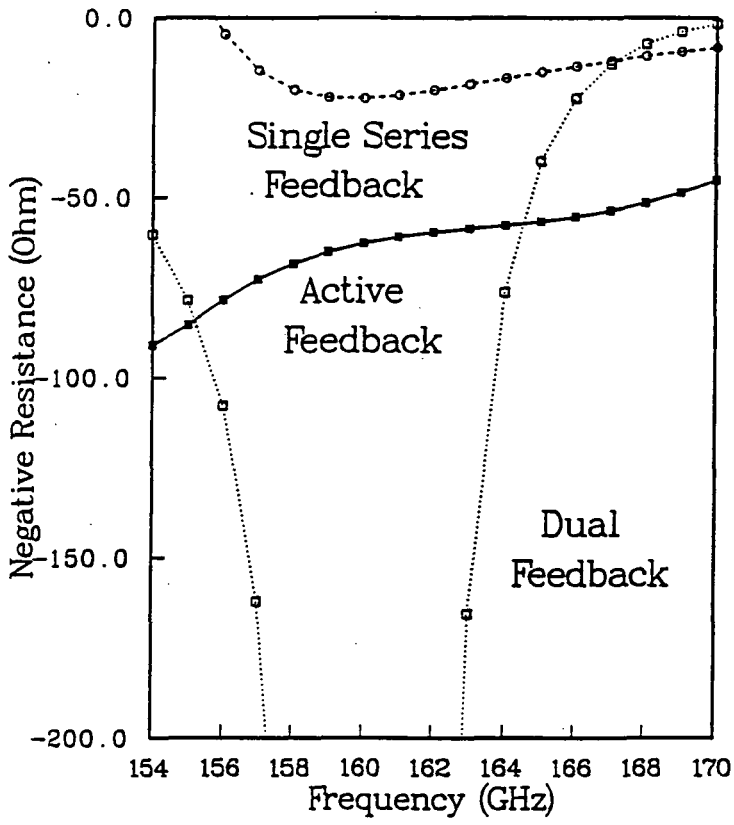

Figure 7: Comparison of negative resistance for three different feedback schemes: 1) single series feedback, 2) dual feedback, 3) active feedback

high frequencies with the help of: i) high f_{max}, ii) high V_{br}, iii) high current density, iv) choice of appropriate gate periphery.

4 Circuit Topologies for Subterahertz Monolithic HEMT Oscillators

As already discussed earlier on, the negative resistance available at subterahertz frequencies is usually rather small. Furthermore, the induced negative resistance is present over a narrow frequency range especially when the oscillation frequency is close to the f_{max} of the device. The availability of small negative resistance values make the design task very difficult. Therefore, appropriate topologies have to be selected such that the negative resistance can be maximized over a wide frequency range.

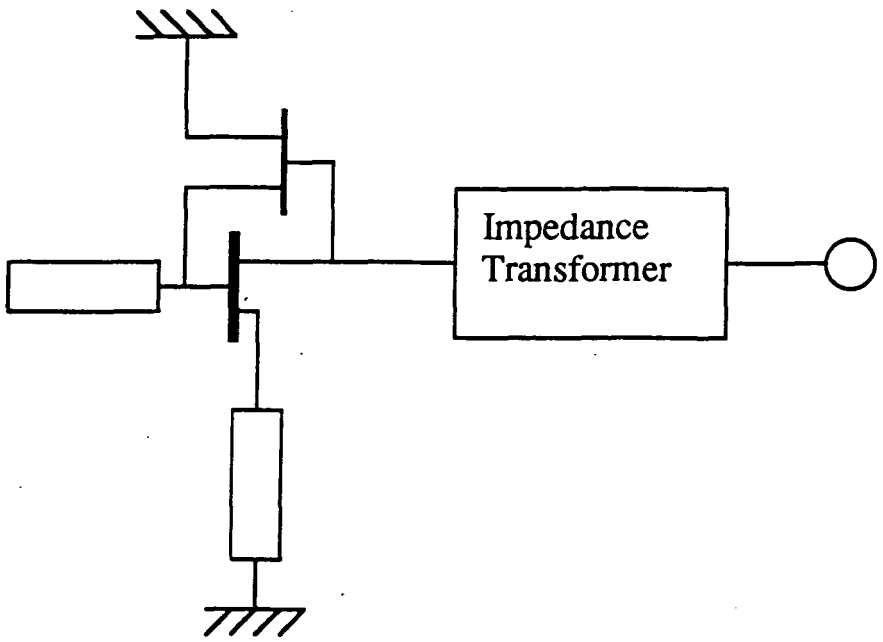

Figure 8: Equivalent circuit schematic of active feedback oscillator for subterahertz application

Dual feedback schemes can be used to improve R_{neg} over a narrow frequency range. In addition to the series feedback element from source to ground, a parallel feedback element can be inserted between the gate and drain. The negative resistance of this topology is compared with that of single series feedback topology in Fig. 7. As shown in this figure, dual feedback circuits provide the possibility of obtaining larger negative resistance. However, the negative resistance is present over a narrower range of frequencies than in the case of single series feedback circuits.

The active feedback approach is another alternative for designing oscillators with devices of small R_{neg}. It uses a small FET as a phase shifting element between the gate and drain (see Fig. 8). Since the feedback loop is provided by active rather than passive elements, the feedback phase shift is fairly independent of frequency and therefore oscillation is guaranteed over a wide range of frequencies. This can be verified from Fig.7. Furthermore, the active feedback approach is less sensitive to the parasitics coming from passive elements and interconnects because it does not strongly depend on passive

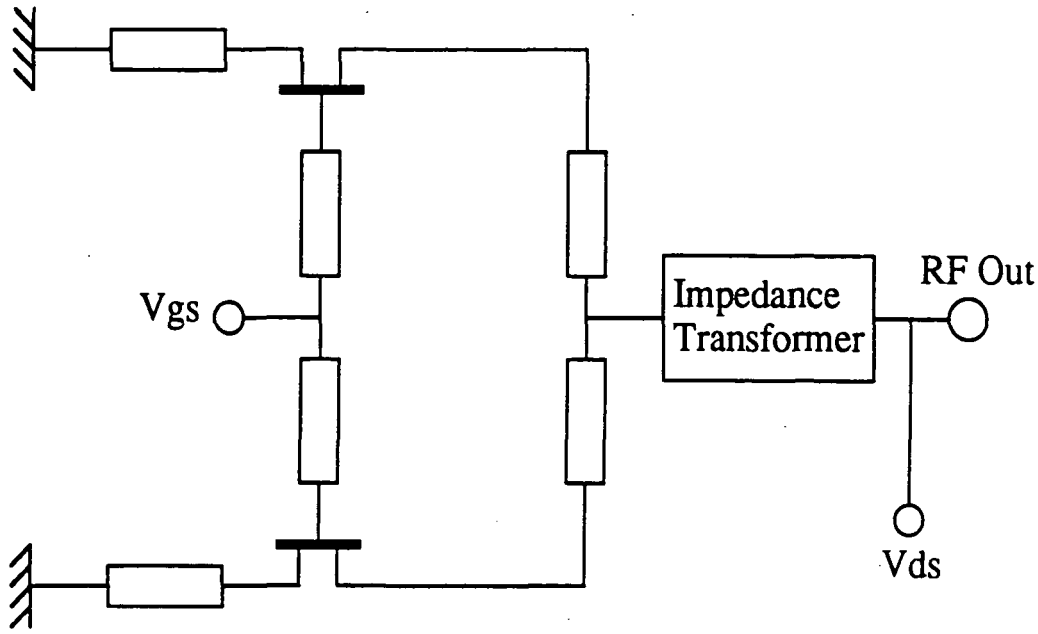

Figure 9: Equivalent circuit schematic of push-push feedback oscillator for subterahertz signal generation

circuitry for inducing the oscillation. It is therefore very suitable for high frequency circuit applications, where accurate modeling of passive circuit elements is not really available.

Another very interesting topology is the push-push configuration. The circuit schematic is shown in Fig. 9. It consists of two subcircuits combined in push-push arrangement. Each circuit oscillates at half the output frequency. The second harmonics are here combined in phase at the output terminal, while the first harmonics cancel each other. This configuration has the advantage of essentially doubling the operation frequency of the discrete devices. Thus, the circuit may operate beyond the frequency limit imposed by f_{max}. This topology also, provides the possibility of lowering the phase noise because all the odd harmonics and associated noise are canceled at the output. Good balance between the two subcircuits has to be maintained for the successful operation of this circuit, but mutual interaction between the two devices is expected to make this requirement less stringent. Monolithic technology provides additional means

of achieving perfect balance. The monolithic push-push HEMT oscillator is therefore a very promising candidate for satisfying the needs for subterahertz signal generation using HEMT's.

5 Conclusions

The use of submicron InAlAs/InGaAs HEMT technology has been discussed in view of the possibility of realizing subterahertz oscillators. InP-based HEMT's have been optimized for this purpose and showed very high f_{max} of 310 GHz using offset self-aligned Γ-gate technology. A gate-to-drain separation of 0.4 μm was used in these devices.

A large signal modeling method has been developed and applied to the evaluation of power characteristics of HEMT oscillators. The optimum termination loads have been found to be 1/4 - 1/2 of the small-signal negative resistance of the devices. Upper frequency limit criteria have been established and indicated the feasibility of signal generation up to $\sim$ 2/3 of the f_{max} of the device. The large signal analysis has also been used to evaluate the oscillation power of HEMT oscillators in the subterahertz region. The use of HEMT's with f_{max} = 450 GHz, V_{br} = 10 V and $W_g = 8 \times 22.5$ μm should allow an oscillation power of 15 mW at 320 GHz.

The topology study of subterahertz oscillation has shown that enhanced negative resistance can be obtained by using complex feedback schemes such as the dual feedback and active feedback scheme. The frequency barrier imposed by f_{max} can be overcome by harmonic oscillation operation as for example in the case of push-push oscillators.

Acknowledgment

The help of T. Brock, G. Munns and G. I. Ng in technology and material growth are greatly appreciated.

References

[1] L. D. Nguyen, A. S. Brown, M. A. Thompson, L. M. Jelloian, L. E. Larson, and M. Matloubian, "650-Å Self-Aligned-Gate Pseudomorphic $Al_{0.48}In_{0.52}As$ / $Ga_{0.20}In_{0.80}As$ High Electron Mobility Transistors," *IEEE Electron Dev. Lett.*, vol. 13, no. 3, pp. 143–145, March 1992.

[2] P. Ho, M. Y. Kao, P. C. Chao, K. H. G. Duh, J. M. Ballingall, S. T. Allen, A. J. Tessmer, and P. M. Smith, "Extremely High Gain 0.15 μm Gate-Length InAlAs/InGaAs/InP HEMTs," *IEE Electron. Lett.*, vol. 27, pp. 325–327, 1990.

[3] Y. Kwon, D. Pavlidis, P. Marsh, G. I. Ng, and T. Brock, "Experimental Characteristics and Performance Analysis of Monolithic InP-Based HEMT Mixers at W-Band," *To appear in IEEE Trans. Microwave Theory Tech.*, 1992.

[4] Y. Kwon, D. Pavlidis, P. Marsh, M. Tutt, G. I. Ng, and T. Brock, "180GHz InAlAs/InGaAs HEMT Monolithic Integrated Frequency Doubler," in *Tech. Digest of 1991 IEEE GaAs IC Symposium*, pp. 165–168, October 1991.

[5] Y. Kwon and D. Pavlidis, "Large Signal Analysis and Experimental Characteristics of Monolithic InP-Based W-Band HEMT Oscillators," in *Proceedings of the 21st European Microwave Conference*, pp. 161–166, September 1991.

[6] Y. Kwon, D. Pavlidis, and M. N. Tutt, "An Evaluation of HEMT Potential for Millimeter-Wave Signal Sources Using Interpolation and Harmonic Balance Techniques," *IEEE Microwave and Guided Wave Letters*, vol. 1, pp. 365–367, December 1991.

[7] U. K. Mishra, A. S. Brown, L. M. Jelloian, M. Thompson, L. D. Nguyen, and S. E. Rosenbaum, "Novel High Performance Self-Aligned 0.15 Micron Long T-Gate," in *Tech. Digest of 1989 International Electron Device Meeting*, pp. 101–104, December 1989.

[8] M. B. Das, "A High Aspect Ratio Design Approach to Millimeter-Wave HEMT Structures," *IEEE Trans. on Electron Devices*, vol. ED-32, no. 1, pp. 11–17, January 1985.

[9] Y. Kwon, T. Brock, G. I. Ng, D. Pavlidis, G. O. Munns, M. E. Sherwin, and G. I. Haddad, "F_{max}-Enhancement in CBE-Grown InAlAs/InGaAs HEMT's Using Novel Self-Aligned Offset-Gate Technology," in *4th Conf. on InP and Rel. Materials*, April 1992.

[10] M. Matloubian, L. D. Nguyen, A. S. Brown, L. E. Larson, M. A. Melendes, and M. A. Thompson, "High Power and High Efficiency AlInAs/GaInAs on InP HEMTs," in *1991 IEEE Int. Microwave Symp. Dig.*, pp. 721–724, June 1991.

[11] G. I. Ng, D. Pavlidis, M. Tutt, J.-E. Oh, and P. K. Bhattacharya, "Improved Strained HEMT Characteristics Using Doouble-Heterojunction $In_{0.65}Ga_{0.35}As$ / $In_{0.52}Al_{0.48}As$ Design," *IEEE Electron Dev. Lett.*, vol. 10, no. 3, pp. 114–116, March 1989.

VARACTOR DIODES FOR MILLIMETER AND SUBMILLIMETER WAVELENGTHS

Brian J. Rizzi, Jeffrey L. Hesler, Hasan Dossal and Thomas W. Crowe
Semiconductor Device Laboratory
Department of Electrical Engineering
Thornton Hall
University of Virginia
Charlottesville, VA 22903-2442

ABSTRACT

Whisker-contacted GaAs Schottky barrier varactor diodes are the most common high-frequency multiplier element in use today. They are inherently simple devices that have very high frequency response and have been used to supply local oscillator power for Schottky heterodyne receivers to frequencies approaching 700 GHz. This paper discusses the development of improved varactor diode technology for space based applications at millimeter and submillimeter wavelengths.

I. INTRODUCTION

Whisker contacted GaAs Schottky varactor diodes are presently in use to supply local oscillator power at frequencies as high as 700 GHz for ground based and airborne applications [1,2,3]. These diodes are also used in the Microwave Limb Sounder on NASA's Upper Atmosphere Research Satellite which is now monitoring global ozone depletion [4]. Although these devices have proven to be quite useful, there is great interest in developing technologies that are more mechanically robust, have higher operating frequency and have the potential to generate greater amounts of power. This paper will review recent work at the University of Virginia on multiplier elements. This includes both the development of planar Schottky varactors and investigation of new devices that have the potential for improved performance.

Section II will review our first attempt to fabricate a planar varactor diode for use at millimeter wavelengths. The preliminary design is presented and the limitations of this structure are considered. A next generation device is then proposed. It is hoped that this new device will become a standard replacement for a very successful and commonly used whisker-contacted varactor diode (U.Va.-6P4). Through development of this device we hope to demonstrate the potential of planar varactor technology and investigate the factors that will most seriously degrade planar varactor performance at high frequency.

We are developing varactor diodes for a multiplier chain to 1 THz. This system will incorporate two doublers (80 to 160 GHz and 160 to 320 GHz) and a tripler (320-960 GHz). The doublers will use multiple diodes integrated on a single chip to enhance power handling ability. These chips are designed to be used in a balanced doubler developed by Erickson [5]. The prototype doubler design and some preliminary results are presented in section III.

The tripler to 1 THz will be extremely challenging. Fortunately there is a great deal of effort being expended world-wide on new varactor structures which may be useful for this work. In section IV we will consider a variety of possible technologies, with special emphasis on an integrated δ–doped varactor diode pair and consideration of the new heterojunction barrier varactors. Section V is a brief summary of this work.

II. DEVELOPMENT OF A PLANAR VARACTOR TECHNOLOGY

As a first step in the development of planar varactor diodes we will fabricate planar devices to replace two commonly used whiskered diodes. These are the 6P4 diode, which is commonly used for doubling in the millimeter wavelength range, and the 2T2, which is used to double and triple at submillimeter wavelengths. The parameters of both of these devices are listed in Table I. The primary electrical benefits of the whiskered diode technology is the

low shunt capacitance of the whisker and the ability of the diode user to tune the whisker inductance to optimize performance.

A scanning electron micrograph of a prototype planar varactor is shown in Fig. 1a. The surface channel fabrication procedure has been described previously [6,7]. The nominal parameters for this diode, designated SC6T1, are also listed in Table I. This diode was designed as a replacement for the 6P4 diode, however, there are two problems. First, series resistance is substantially higher than the 6P4's and second, the planar diode has a parasitic shunt capacitance of 12 fF which is unacceptably high. As might be expected, preliminary RF measurements have been disappointing. The excess series resistance is due to the use of

Table I: Schottky Varactor Diodes

Batch	Type	Anode Diameter (μm)	Epitaxial Layer Thickness (μm)	Epitaxial Layer Doping (cm^{-3})	Series Resistance (Ω)	Zero-bias Junction Capacitance (fF)	Minimum Junction Capacitance (fF)	Breakdown Voltage (V)
6P4	Whiskered	6	1.0	$3x10^{16}$	9.5	20	5.5	20
2T2	Whiskered	2.5	0.59	$1x10^{17}$	12	5.5	1.5-2.0	11
SC6T1	Planar	6.2	1.3	$2x10^{16}$	20	20	4	30

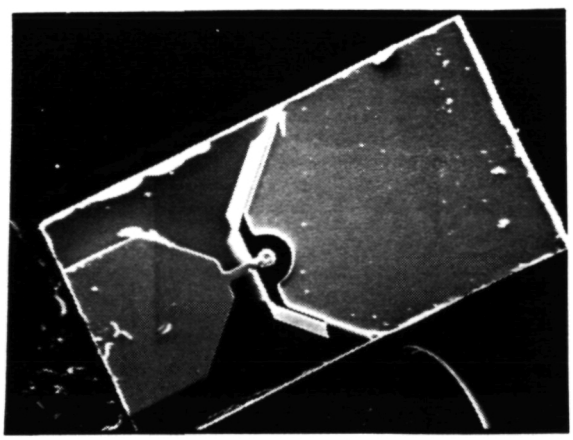

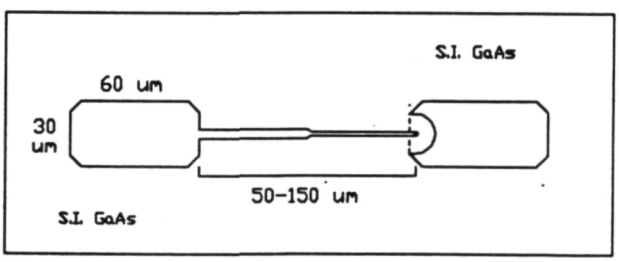

Fig. 1. a) A prototype planar varactor diode. The surface channel technology is used to achieve isolation between the contact pads [6,7]. b) A sketch of the second generation device which has smaller contact pads and variable finger length.

an epitaxial layer that is too thick and too lightly doped. Although this epitaxial layer yields a higher breakdown voltage, the penalty in R_s outweighs this benefit. Since the fabrication of the SC6T1, new material has been obtained and diodes with characteristics closer to those of the 6P4 will be fabricated.

The increased shunt capacitance of the planar diode is a serious problem. This capacitance is due primarily to the fringing field between the contact pads through the high dielectric constant GaAs substrate. To reduce this capacitance there are three options:

1) Reduce the pad dimensions,

2) Increase the pad separation (and therefore the finger length), and/or

3) Use a substrate with a lower dielectric constant.

The first two improvements will be implemented in our next generation device, as shown in Fig. 1b. The primary limitations on pad dimensions are the ohmic contact resistance and the need to make a reliable solder contact. Although the proposed pad width of 30 μm is about the minimum size that most users feel comfortable soldering to, it is clear that if smaller pads will lead to better performance, users will develop more elaborate soldering techniques. However, the minimum pad size is also limited by our ohmic contacts. We use SnNi/Ni/Au plating for our standard ohmic contact and reliably obtain resistivities of $10^{-5}\ \Omega cm^2$ or slightly less. Thus, a 30 μm x 30μm pad should have roughly one ohm of contact resistance. Smaller pads will require a significantly improved ohmic contact technology.

The new mask set will have several finger lengths, from 50 - 150 μm. This will allow evaluation of RF performance as a function of pad-to-pad capacitance and finger inductance. It is expected that one specific finger length will give optimum performance in a given

multiplier mount at a given frequency. Thus, we expect that detailed RF evaluation of these devices will yield important guidelines for future chip designs.

The use of a quartz substrate for planar Schottky diodes has been demonstrated for mixer applications [7]. This has led to significant reductions in shunt capacitance which may be important for multiplier applications. However, the thermal properties of the GaAs Schottky diode on quartz are not well understood, and we have noticed that mixer diodes on quartz substrates are more likely to show signs of heating effects than equivalent diodes on GaAs. Since the removal of heat from the varactor diode is particularly important, it is not clear if quartz substrates will yield an overall performance benefit. Our next batches of planar varactors will have GaAs substrates. However, we also hope to investigate quartz and perhaps sapphire substrates in the near future.

III. INTEGRATED SCHOTTKY VARACTORS FOR BALANCED DOUBLING

The first step in the proposed multiplier chain to 1 THz is a doubler from 80 to 160 GHz. Since there are sources available that can deliver large amounts of power at 80 GHz, our goal is to develop a doubler that is fairly efficient, but, more importantly, can handle large input powers. With this goal in mind, a planar chip was designed based on the balanced doubler configuration of Erickson, which has generated up to 25mW at 160 GHz using two whisker contacted diodes [5].

One benefit of the planar diode technology is the ability to integrate several diodes on a chip to increase power handling ability. For example, when two diodes are placed in series their individual areas can be doubled in order to maintain the same total series resistance and junction capacitance as a single device. However, the series pair will have twice as much reverse breakdown voltage. The increased area and breakdown voltage will yield improved

power handling ability. Two scanning electron micrographs of our prototype are shown in Fig. 2. The chip consists of four varactor diodes, two for each leg of the balanced doubler.

The design parameters and dc characteristics of the prototype balanced doubler chips are shown in Table II. Our goal was to achieve a reverse breakdown voltage of 20V for each anode. Also, the anode diameters of 10 and 12 μm were chosen to achieve zero-bias junction capacitances of 40 and 60 fF per anode. As is seen in the table, the first batch had excessive series resistance and extra breakdown voltage. This is due to the low doping density and thickness of the epitaxial layer. For the second batch this problem was corrected at the cost of reduced breakdown voltage. However, this trade-off is expected to yield significantly improved RF performance.

The capacitance-voltage (C-V) curves for a single diode and a diode series pair are shown in Fig. 3, indicating the increased breakdown voltage of the diode pair.

Preliminary RF tests for the first prototype balanced doubler were performed by Dr. Erickson at the University of Massachusetts and the results are presented in Table II. These initial results are quite encouraging, but not yet competitive with the whiskered-diode

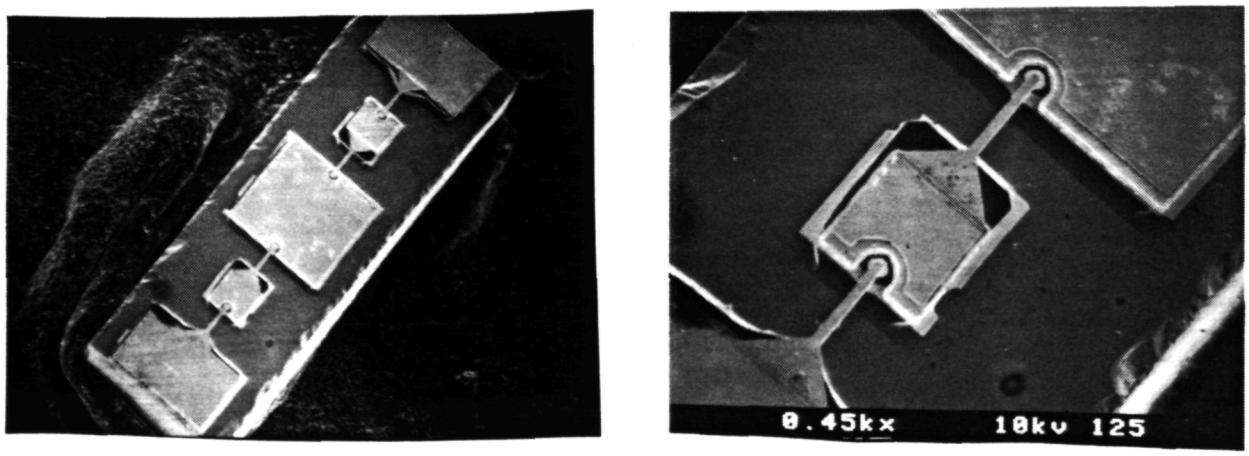

Fig. 2. SEM photographs of the prototype balanced doubler to 160 GHz.

Table II: Prototype Balanced Doubler Chips

DC Characteristics

Batch #	Epitaxial Layer Thickness (μm)	Epitaxial Layer Doping (cm^{-3})	Anode Diameter (μm)	Pair Series Resistance (Ω)	Pair Breakdown Voltage (V)
1	1.3	$1.8x10^{16}$	10	20	45
2	1.2	$2.5x10^{16}$	10	14	35

Preliminary RF Data†

Batch #	Input Freq. (GHz)	Output Freq. (GHz)	Input Power (mW)	Output Power (mW)	Efficiency (%)
1	82	164	55	3	6
1	82	164	100	6	6

† Preliminary RF data supplied by N. Erickson, University of Massachusetts. Measurements have not been performed with batch #2.

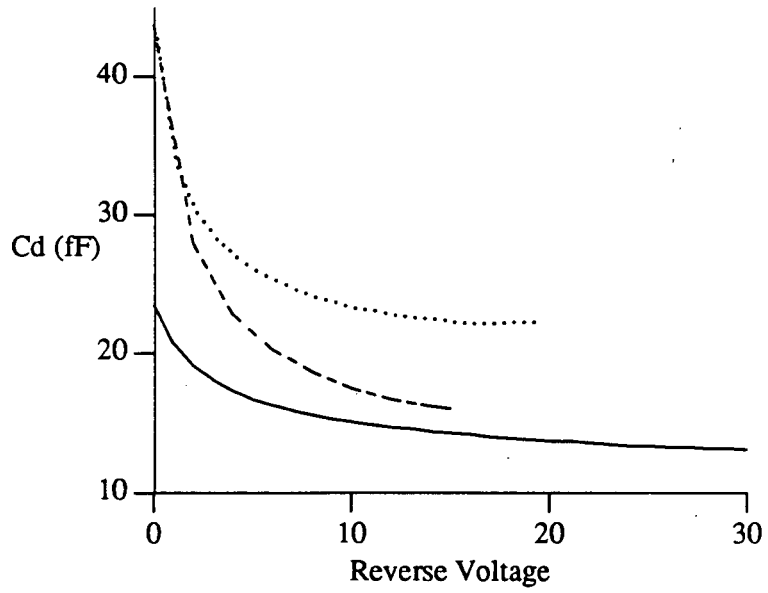

Fig. 3. C-V Characteristics of the prototype balanced doubler chip for a single varactor diode (dotted), a diode series pair (solid) and for a single diode with anode-to-pad connection to eliminate the pad-to-pad shunt capacitance (dashed).

results. Two changes in the chip design are planned to improve performance. The first is the increase in epitaxial layer doping to reduce series resistance, as was achieved with batch #2. The second is the reduction of pad-to-pad capacitance. The importance of this is demonstrated by the third curve (dashed) in Fig. 3. This curve was measured from the anode to ohmic contact pad on a diode that had no finger, and therefore does not include the pad-to-pad capacitance. This curve has much greater modulation and much lower minimum capacitance. This clearly demonstrates that the pad-to-pad capacitance is having a major effect on performance. The shunt capacitance of future chips will be reduced through a redesign of the contact pads and possibly through the use of quartz substrates.

Once the first stage multiplier has been optimized, the next step is to design a chip for the doubler to 320 GHz. Since the second stage will not have to handle as much power as the first, we will be able to trade-off some power handling ability in order to increase cut-off frequency. It is expected that the optimum diodes for this stage will have smaller anodes and higher epitaxial layer doping density.

There is much work to be done on the integrated balanced doublers. However, the prototype devices have yielded encouraging results, and the improvements necessary to increase performance are clearly defined. Thus, we expect to achieve significantly improved output powers at 160 GHz in the near future. Also, the lessons learned on the first stage doubler will be applied to the second stage, so that development of the higher frequency chips should progress more rapidly.

IV. POTENTIAL VARACTORS FOR TRIPLING TO 1 THZ

The development of a tripler to 1 THz is an extremely challenging task. Fortunately there are several device technologies that may yield suitable performance. We have chosen to investigate five of these, each of which is discussed in the following sections. The whiskered Schottky and planar Schottky are considered briefly and the new two-dimensional-electron-gas/Schottky (2-DEG/Schottky), which is considered in detail in a separate paper, is also only briefly overviewed. The other two technologies, the integrated δ–doped varactor pair and the heterojunction barrier varactor, are considered in more detail.

A. Whiskered Schottky Diodes

The most likely candidate for the first successful tripler to 1 THz is simply a standard whisker contacted Schottky varactor. The 2T2 diode has already been successfully used in triplers to 500-700 GHz and can probably be extended to the THz range. However, the efficiency will certainly be decreased and it is not clear how much output power will be achieved. A more optimized diode can probably be developed, perhaps with slightly higher doping density and smaller diameter. Although this technology appears to be reaching fundamental limitations [8], it should continue to be pursued because the probability of some level of success is high.

B. Planar Schottky Varactors

There are two advantages of using a planar Schottky device; the elimination of the fragile whisker contact and the opportunity to use several integrated diodes to increase power handling ability or achieve a more beneficial C-V characteristic. The drawback is the increased shunt capacitance that is inherent in the planar diode. There are several areas that must be researched. As discussed previously, these include the redesign of the contact pads

and anode finger, and the use of low dielectric constant substrates. Also, the potential use of two Schottky varactors in an anti-series combination to achieve a symmetric C-V characteristic may have substantial benefits for tripling applications. It is not yet clear if planar Schottky technology will be useful at 1 THz, however we hope to answer many important questions through our development of planar diodes for lower frequencies.

C. The 2-DEG/Schottky Diode

This device consists of a metal contact to the edge of a two-dimensional-electron-gas (2-DEG) formed at a heterointerface. The capacitance is between the Schottky metal and the undepleted portion of the 2-DEG. The voltage on the Schottky metal modulates the depletion depth in the 2-DEG, thereby varying the capacitance. This device should benefit from increased electron mobility and perhaps higher electron saturation velocities compared to bulk devices. This may lead to significantly improved high frequency performance. Also, this is an inherently planar device. Prototype diodes have demonstrated excellent capacitance modulation and high reverse breakdown voltages. This new device is discussed in greater detail in a separate paper [9].

D. An Integrated δ-Doped Diode Pair

A design for a planar chip with two integrated δ-doped varactor diodes in a back-to-back configuration is shown in Fig. 4. The symmetric C-V characteristic of such a diode pair will yield significant benefits for tripler applications since an idler circuit at the second harmonic is not needed. The δ-doped diodes have been shown to have a sharp C-V characteristic [10,11]; which is a significant advantage at high frequencies since the available input power is quite low.

The planar tripler has been designed to produce a capacitance ratio (C_{max}/C_{min}) of 2.5, with an estimated cut-off frequency of 6 THz. The material structure is described in Table III. The mask set and epitaxial material for this device are now being purchased.

E. Evaluation of the Heterostructure Barrier Varactors

In 1990 Rydberg et al. demonstrated that a thin layer of high band-gap material sandwiched between two thicker layers of low band-gap material could yield a symmetric C-V characteristic that is ideal for tripler applications [12]. This Quantum (or Heterostructure) Barrier Varactor (QBV or HBV) has promise for high frequency multiplier applications, and is now being investigated by several groups. The goal of our investigation

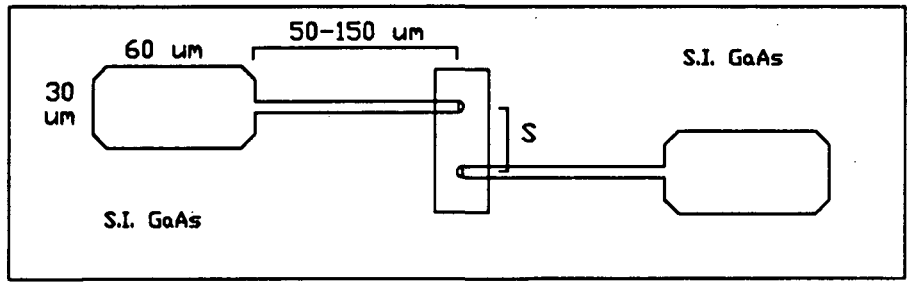

Fig. 4. A sketch of the proposed integrated δ-doped varactor pair. The finger length will be variable on the mask set and the anode spacing has not yet been determined

Table III: Epitaxial Material for the δ-doped Diode Pair

Layer Type	Doping Density	Thickness (μm)
N GaAs	$<1x10^{15}$ cm^{-3}	0.05
Si atomic layer	$3.4x10^{12}$ cm^{-2}	-
N GaAs	$2x10^{17}$ cm^{-3}	0.13
N^+ GaAs	$>3x10^{18}$ cm^{-3}	3.0
$Al_xGa_{1-x}As$ etch stop	undoped ($x \geq 0.5$)	2.0-2.5
GaAs substrate	S.I.	-

is to determine if HBVs offer significant improvement over standard Schottky technologies, and, if so, to demonstrate such improvement. To determine the potential of these devices we will discuss the design of HBVs that have characteristics similar to the state-of-the-art whiskered varactors whose characteristics were presented in Table I.

A schematic band diagram of a zero-biased single barrier GaAs/AlGaAs/GaAs HBV is shown in Fig. 5a. When a voltage is applied to the device a depletion region is created on one side of the barrier which increases in length as the voltage is increased. The capacitance of this device is approximated as

$$C = \frac{A}{X_B/\varepsilon_B + X_{D,total}/\varepsilon_M} \qquad (1)$$

where A is the device area, ε is the permittivity of the barrier (B) and the modulation region (M) materials, X_B is the barrier layer thickness and $X_{D,total}$ is the total depletion layer thickness on both sides of the barrier as a function of voltage. The maximum capacitance can be as high as $\varepsilon_B A/X_B$ if there is negligible depletion in the modulation layers at zero-bias. The series resistance for a single barrier HBV, including spreading, epilayer and ohmic contact resistance, is estimated as

$$R_{1,s} = R_{1,spr} + R_{1,epi} + R_{1,oc} = \frac{1}{2d\sigma_S} + \frac{2X_M}{\sigma_E A} + \frac{R_c}{A} \qquad (2)$$

where d is the anode diameter, σ is the conductivity of the substrate (S) and epilayer (E) materials, X_M is the length of the n-type modulation regions, and R_c is the specific resistivity of the ohmic contact. It is important to note that the device area affects not only the junction capacitance, but also the resistance of the ohmic contact. Therefore, although we can reduce the junction capacitance by shrinking the device area, this is not beneficial unless the ohmic contact resistivity, R_c, is low enough so that the third term in (2) remains negligible. For this

study we will assume a specific contact resistivity of $10^{-7}\,\Omega\,cm^2$, which is consistent with the best contacts reported in the literature.

An important parameter for all varactor diodes is the voltage at which the conduction current becomes significant. For a standard Schottky varactor, impact ionization in the depletion region determines the reverse breakdown voltage and thermionic emission over the Schottky barrier determines the forward conduction current. For the HBV either thermionic emission or avalanche breakdown can play the critical role, depending on the device parameters. Figure 5b shows an HBV band diagram with voltage applied, with a depletion region on one side of the barrier and an accumulation region on the other. As the HBV is biased, the accumulation region grows and therefore the effective barrier height, given by $\Delta E_c - qV_{acc}$, decreases. Simultaneously, the electric field strength in the depletion region grows. Whether avalanche breakdown or thermionic current occurs first depends primarily on the conduction band discontinuity ΔE_c and the band-gap in the modulation region.

We would like to have a method to compare HBV diodes to standard varactors. A simple computer model was developed in order to simulate the operation of the HBV under applied bias. The simulation assumes that little current flows through the device, and

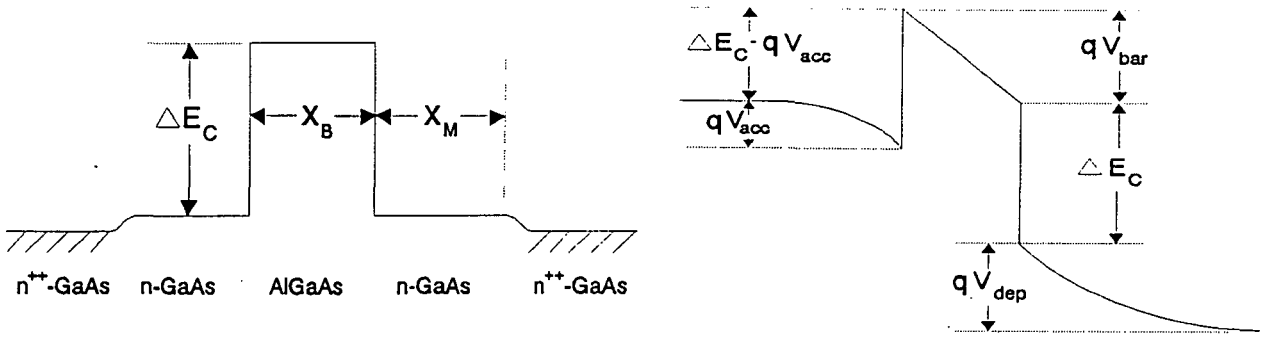

Fig. 5. The band-diagram of a simple Heterostructure Barrier Varactor (HBV), a) zero-bias and b) bias applied.

calculates the quasi-equilibrium band diagram for different bias levels. The approximations developed by Delagebeaudeuf et al. [13] are a relatively standard method to analyze a 2-DEG at a heterostructure interface. For our case, these approximations were extended to include additional energy levels due to the high doping density in the 2-DEG region. The most crucial parameter to estimate is the maximum voltage that can be applied before conduction current begins to degrade the multiplier efficiency. For this discussion we will assume that impact ionization becomes important at the voltage where the electric field strength exceeds a critical value. Since there is no experimental data from which to estimate the critical field of HBVs, we have assumed that the critical field will be similar to that of GaAs pn junctions [14]. For devices dominated by thermionic emission, the maximum voltage was assumed to be that voltage at which

$$\Delta E_c - qV_{acc} = nkT, \tag{3}$$

and we have assumed a value of n=5 for this study.

For GaAs/AlGaAs devices the value of ΔE_c is rather small ($\Delta E_c \approx 0.35$ [15]) and thermionic emission becomes important before impact ionization. Simulations show that for low doping levels (less than about $10^{16}\,cm^{-3}$) these devices can have a maximum voltage comparable to a standard Schottky varactor, however, R_{epi} will be extremely large. Increasing the doping level decreases R_{epi}, but also decreases V_{max}, which indicates that single barrier GaAs/AlGaAs HBVs will have less power handling ability than standard Schottky varactors. There are several possible solutions to this problem, two of which will be considered in this paper; epitaxial stacking of barriers and the use of different material systems. Epitaxial stacking divides the applied voltage among several barriers, thus increasing the maximum device voltage. For an HBV with N barriers, $V_{N,max} = N \cdot V_{1,max}$.

As N is increased, it is best to increase the device area in order to maintain reasonable values of junction capacitance and modulation layer resistance. Assuming that the area is increased proportionally to the number of barriers, the series resistance of an N barrier HBV can be expressed as,

$$R_{N,s}=\frac{1}{\sqrt{N}} R_{1,spr} + \frac{N+1}{2N} R_{1,epi} + \frac{1}{N} R_{1,oc}. \quad (4)$$

This equation shows that the increase in area has the important effect of reducing the spreading and ohmic contact resistances. In fact, without using multiple barriers it would be impossible to fabricate an HBV with reasonable capacitance and series resistance unless the ohmic contact resistivity is exceptionally low.

Other material systems can have significantly higher values of ΔE_c. For example, the InGaAs/InAlAs system can yield barriers of near 0.8 eV, while the GaAs/GaN system allows 0.9 eV barriers. The computer simulation indicates that the maximum voltage in both of these material systems is limited by impact ionization, rather than thermionic emission.

In the following paragraphs, the simulation results for single and multiple barrier HBVs are discussed for the previously mentioned material systems. In order to compare the HBVs with the 2T2 and 6P4 varactors, barriers are added until V_{max} is greater than that of the standard varactor. The area is then chosen so that C_{min} of the HBV is the same as the standard varactor. A common varactor figure-of-merit used in our comparisons and listed in Table IV is the dynamic cut-off frequency, given by [16]

$$f_{co} = \frac{1/C_{min} - 1/C_{max}}{2\pi R_s}, \quad (5)$$

where C_{max} and C_{min} are the maximum and minimum device capacitance.

GaAs/AlGaAs: Figure 6 shows the simulation results for GaAs/AlGaAs HBV's. As the modulation doping density is increased, more barriers are needed to achieve the desired maximum voltage and the series resistance is reduced due to the increase in both σ_E and device area. Table IV gives examples of GaAs/AlGaAs HBV's with V_{max}, C_{min} and R_s similar to the 2T2 and 6P4. However, the HBVs will have the added benefit of a symmetric C-V curve.

InGaAs/InAlAs: With the InGaAs matched to InP (i.e. 53% In), $In_{0.32}Al_{0.68}As$ will give a ΔE_c of about 0.8 eV with a 1% lattice mismatch. However, InGaAs has a narrower band gap than GaAs, and will thus have a smaller critical field for impact ionization. In these simulations, we used the critical field data versus doping for a Ge abrupt p-n junction [14] since Ge and $In_{0.53}Ga_{0.47}As$ have similar bandgaps. Because of the lower critical field, single barrier InGaAs/InAlAs HBV's will not have sufficient V_{max}, and thus multiple

Table IV: Heterostructure Barrier Varactors

Material System	N	X_B (μm)	N_{mod} (cm^{-3})	Diam. (μm)	V_{max} (V)	R_s (Ω)	C_{min} (fF)	C_{max} (fF)	f_{co} (THz)
GaAs/AlGaAs	1	0.02	$5x10^{16}$	2.3	4.0	37	1.5	22	2.6
	1	0.02	$1x10^{17}$	1.7	2.6	21	1.5	12	4.4
	1	0.02	$5x10^{17}$	1.0	1.2	19	1.5	4	3.4
(6P4-like)	5	0.02	$5x10^{16}$	9.0	20	7	4.5	66	4.6
(2T2-like)	5	0.02	$1x10^{17}$	3.8	13.2	11	1.5	12	8.6
InGaAs/InAlAs	1	0.02	$5x10^{16}$	2.6	6.7	25	1.5	32.3	4.0
	1	0.02	$1x10^{17}$	1.9	4.3	16	1.5	17.2	6.0
	1	0.02	$5x10^{17}$	1.2	2.8	16	1.5	6.4	5.1
(6P4-like)	3	0.02	$5x10^{16}$	8.0	20.0	5.5	4.5	97	6.0
(2T2-like)	3	0.02	$1x10^{17}$	3.4	12.9	9.5	1.5	17.2	10.4
GaAs/GaN	1	0.008	$5x10^{16}$	6.0	19.2	13	4.5	367	2.7
	1	0.008	$1x10^{17}$	2.5	11.4	20.5	1.5	63	5.1
(6P4-like)	2	0.008	$1x10^{17}$	6.1	23	5	4.5	190	7
(2T2-like)	2	0.008	$2.3x10^{17}$	2.8	18.2	9.5	1.5	38.6	10.7

barriers must be used. Figure 7 and Table IV show that devices similar to the 2T2 and 6P4 varactors can be achieved with three barriers.

GaAs/GaN: The GaAs/GaN material system has a high ΔE_c and the critical field of GaAs. The major disadvantage is that it is a relatively new material system on which little experimentation has been performed [17]. Our simulations showed that impact ionization will be the limiting factor for these devices. Single barrier GaAs/GaN HBV's have sufficient V_{max}, but tend to have higher R_s than comparable Schottky varactors due to modulation region resistance. Characteristics of single barrier GaAs/GaN HBV's are given in Table IV for several dopings. By using higher N_{mod} and multiple barriers, HBV's with low R_s and very little conduction current should be possible. Figure 8 and Table IV show that only two barriers are required to achieve device characteristics similar to the 2T2 and 6P4.

V. SUMMARY

Whisker-contacted GaAs Schottky barrier varactor diodes are the best multiplier elements available for millimeter and submillimeter wavelength applications. However, the development of planar diode technology and new devices promise to improve both system reliability and performance. Our prototype planar Schottky varactors are not yet competitive at millimeter wavelengths, but several straight-forward improvements in the chip design should alleviate the problems of high series resistance and shunt capacitance. The ability to integrate several varactor diodes onto a chip is being exploited to increase power handling ability, and an integrated balanced doubler for millimeter wavelengths has been described. The prototype devices have shown promising performance at 160 GHz and the second generation chips have greatly improved dc characteristics. Both the single-diode planar Schottky varactor and the balanced doubler will benefit from improved contact-pad/finger

geometries and lower ohmic contact resistances. The use of low dielectric substrates is also being investigated.

Several device technologies may be useful for a proposed tripler to 1 THz. While the whisker-contacted Schottky diode is likely to be the first device to yield reasonable output power at this frequency, planar diodes and other device structures promise improved performance. The 2-DEG Schottky, δ-doped Schottky and the quantum (heterostructure) barrier varactors (QBV or HBV) are being investigated at U.Va. The 2-DEG Schottky research is described elsewhere [9]. An integrated δ-doped varactor pair with symmetric C-V was described and will be fabricated in the near future. The HBV devices are particularly promising. Our simple analysis has shown that HBVs with parameters similar to the state-of-the-art Schottky varactors can be designed if multiple barriers are used and ohmic contact resistances are in the $10^{-7}\,\Omega\,cm^2$ range. These devices will also have the benefit of a symmetric C-V curve. The use of InGaAs/InAlAs or GaAs/GaN for the HBVs promises the best performance if epitaxial layers of the required quality can be obtained.

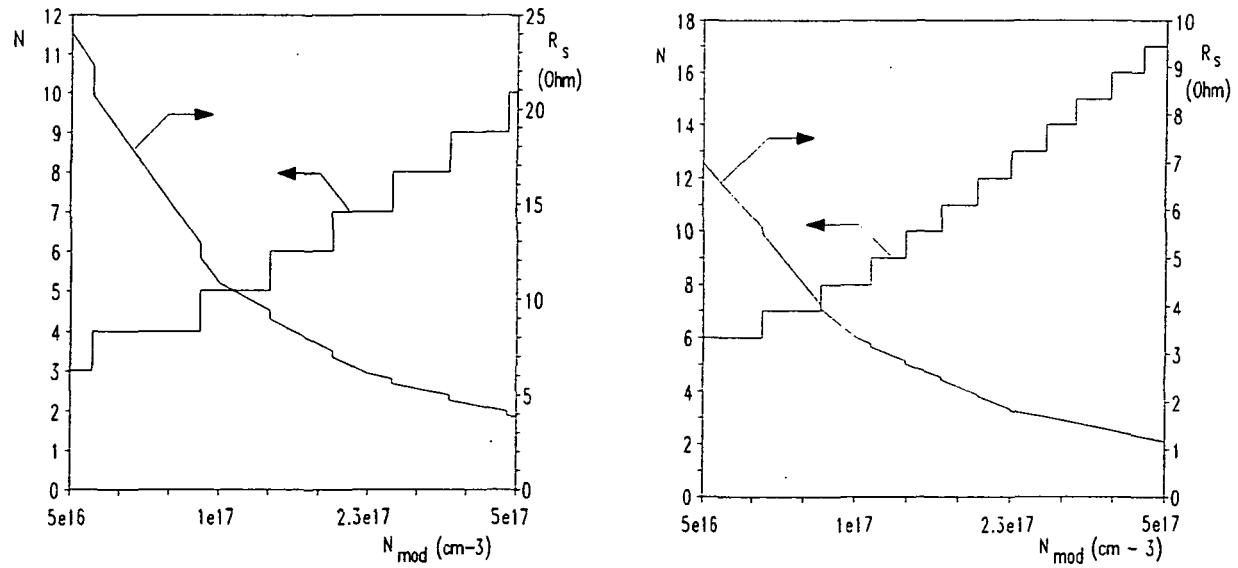

Fig. 6 The number of barriers necessary to achieve a GaAs/AlGaAs HBV with the same maximum voltage as the 2T2 (left) and 6P4 (right) varactors as a function of N_{mod}. *Also, shown is the series resistance when the area is chosen to yield the same minimum device capacitance as the standard varactors. Additional parameters are listed in Table IV.*

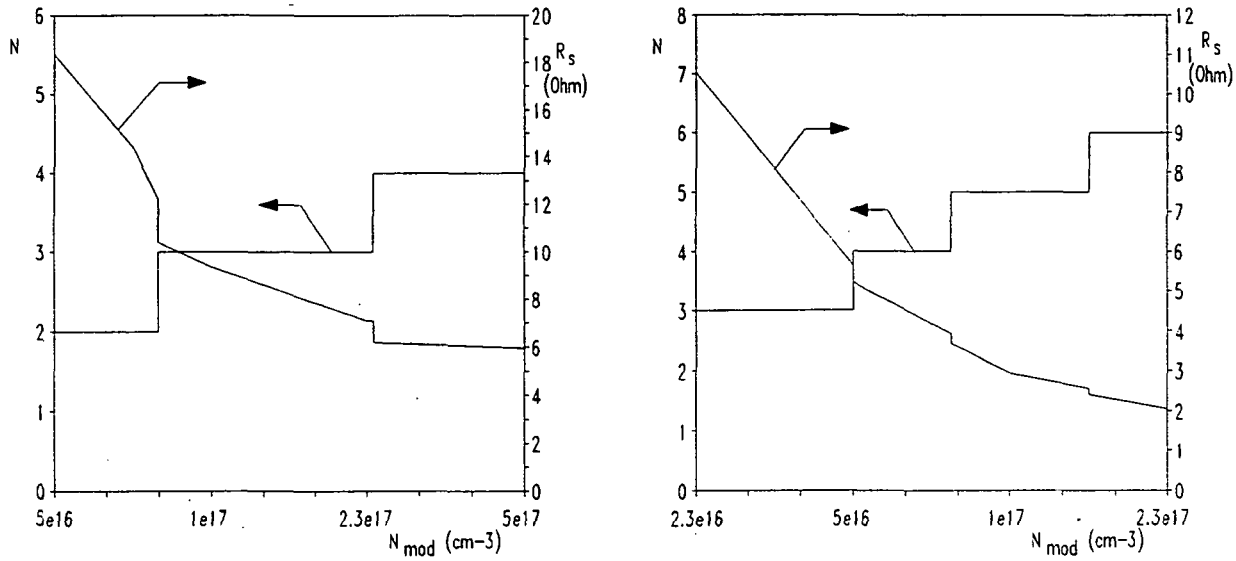

Fig. 7. The same as Fig. 6, but for InGaAs/InAlAs.

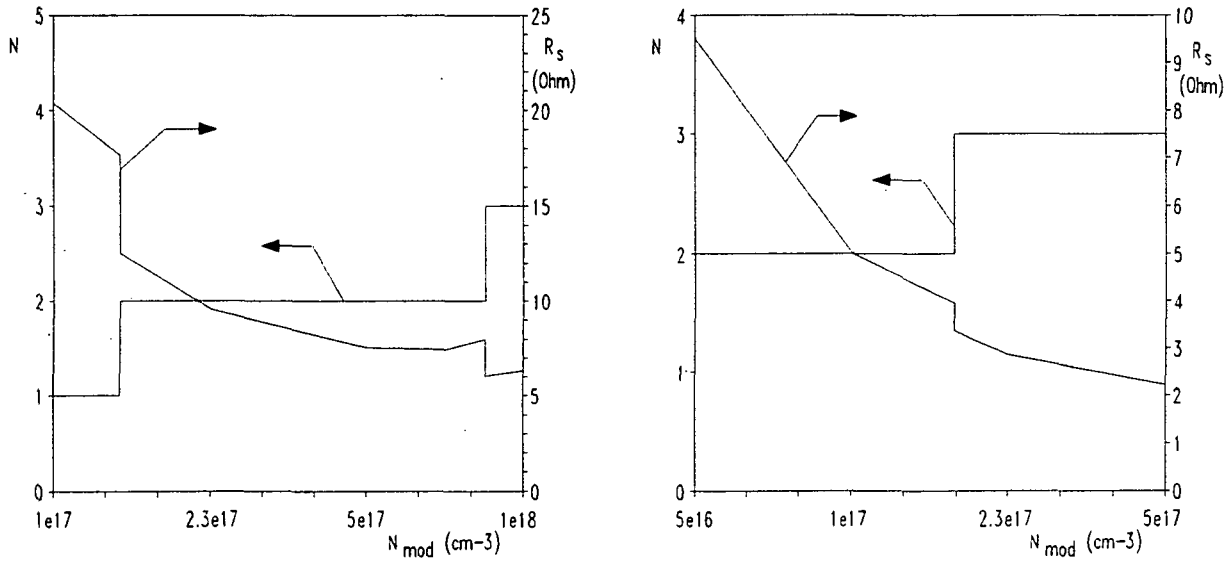

Fig. 8. The same as Fig. 6, but for GaAs/GaN.

ACKNOWLEDGEMENT

The authors would like to thank Dr. Neal Erickson (U. Mass, Amherst) for supplying the initial RF measurements on the prototype balanced doubler and Dr. Peter Siegel (Jet Propulsion Laboratory) for initial evaluation of the SC6T1 planar varactor. This work has been supported by the National Science Foundation under Grant ECS-8720850, NASA and the Jet Propulsion Laboratory.

REFERENCES

[1] R. Zimmermann, R. Zimmermann, and P. Zimmermann, "All Solid-State Radiometers for Environmental Studies to 700 GHz," Third Int'l Symp. Space THz Tech., Ann Arbor, MI, March 1992.

[2] H. Nett, S. Crewell, K. Kunzi, "A 625-650 GHz Heterodyne Receiver for Airborne Operation," 16th Int'l Conf. IR and MM Waves, Lausanne, Switzerland, August 1991.

[3] S. Crewell and H. Nett, "Measurements of the Single Sideband Suppression for a 650 GHz Heterodyne Receiver," Third Int'l Symp. Space THz Tech., Ann Arbor, MI, March 1992.

[4] A.L. Riley, UARS Microwave Limb Sounder Instrument Description, Jet Propulsion Laboratory Document D-1050, 1984.

[5] N.R. Erickson, "High Efficiency Submillimeter Frequency Multipliers," 1990 IEEE MTT-S Int'l. Microwave Symp., Dallas, TX, May 1990.

[6] W.L. Bishop, K. McKinney, R.J. Mattauch, T.W. Crowe, and G. Green, "A Novel Whiskerless Schottky Diode for Millimeter and Submillimeter Wave Applications," Proc. 1987 IEEE MTT-S Int'l. Symp., Las Vegas, NV, pp. 607-610, June 1987.

[7] W.L. Bishop, E.R. Meiberg, R.J. Mattauch and T.W. Crowe, "A Micron Thickness, Planar Schottky Barrier Diode Chip for Terahertz Applications with Theoretical Minimum Parasitic Capacitance," 1990 IEEE MTT-S Int. Microwave Symp., Dallas, TX, May 1990.

[8] T.W. Crowe, W.C.B. Peatman and E.M. Winkler, "GaAs Schottky Barrier Varactor Diodes for Submillimeter Wavelength Power Generation," Microwave and Optical Technology Letters, Special Issue on Space THz Technology, Vol. 3, No. 1, pp. 49-53, Jan. 1991.

[9] W.C.B. Peatman, T.W. Crowe, and M. Shur, "A 2-DEG Varactor Diode for Millimeter and Submillimeter Wave Multiplier Applications," Third Int'l Symp. Space THz Tech., Ann Arbor, MI, March 1992.

[10] T.W. Crowe, W.C.B. Peatman and W.L. Bishop, "GaAs Schottky Barrier Diodes for Space Based Applications at Submillimeter Wavelengths," The First International Symposium Space Terahertz Technology Proceedings, pp. 256-272, Ann Arbor, Michigan, March 1990.

[11] B.J. Rizzi, T.W. Crowe, and W.C.B. Peatman, "A δ-Doped Varactor Diode for Submillimeter Wavelengths," The Digest of the 15th International Conference on Infrared and Millimeter Waves, pp. 478-480, Orlando, Dec. 1990.

[12] A. Rydberg, H. Gronqvist and E. Kollberg, "Millimeter- and Submillimeter- Wave Multipliers Using Quantum-Barrier-Varactor (QBV) Diodes," IEEE Electron Device Letters, Vol. 11, No. 9, pp. 373-375, 1990.

[13] D. Delagebeaudeuf and N.T. Linh, "Metal-(n)AlGaAs-GaAs Two-Dimensional Electron Gas FET," IEEE Trans. Electron Devices, Vol. ED-29, No. 6, pp. 955-960, 1982.

[14] S.M. Sze, *Physics of Semiconductor Devices*, Wiley, New York, p. 103, 1981.

[15] J. Batey and S.L. Wright, "Energy band alignment in GaAs:(Al,Ga)As heterostructures: The dependence on alloy composition," J. Appl Phys., Vol. 59, No. 1, pp. 200-209, 1986.

[16] P. Penfield and R.P Rafuse, *Varactor Applications*, MIT Press, p.86, 1962.

[17] G. Martin, S. Strite, J. Thornton, and H. Morkoc, "Electrical properties of GaAs/GaN/GaAs semiconductor-insulator-semiconductor structures," Appl. Phys. Lett., Vol. 58, pp. 2375-2377, 1991.

A Schottky/2-DEG Varactor Diode for Millimeter and Submillimeter Wave Multiplier Applications

W. C. B. Peatman, T. W. Crowe, M. Shur, and B. Gelmont

Semiconductor Device Laboratory
Department of Electrical Engineering
University of Virginia
Charlottesville, VA 22903

ABSTRACT

A new Schottky diode is investigated for use as a multiplier element in the millimeter and submillimeter wavelength regions. The new diode is based on the Schottky contact at the edge of a 2-dimensional electron gas (2-DEG). As a negative voltage is applied to the Schottky contact, the depletion layer between the Schottky contact and the 2-DEG expands and the junction capacitance decreases, resulting in a non-linear capacitance-voltage characteristic. In this paper, we outline the theory, design, fabrication and evaluation of the new device. Recent results include devices having cutoff frequencies of 1 THz and above. Preliminary multiplier results are also presented.

I. BACKGROUND

Schottky barrier varactor diodes are used as frequency multiplier elements for local oscillator (LO) sources for the millimeter and submillimeter wavelength region. These sources are used in heterodyne receivers for a variety of applications including radio astronomy, atmospheric studies and plasma diagnostics. For space-based receiver systems, the LO source must be compact, lightweight and reliable; and power and cooling requirements must be minimized. While molecular gas lasers have been used as LO sources for airborne radioastronomy measurements at frequencies as high as 2.5 THz [1,2], the stringent requirements for space applications will require the use of a solid-state LO source. Although standard varactor diodes have been used to generate 0.7 mW at 474 GHz [3] and 0.2 mW at 640 GHz [4], these devices will not provide usable amounts of LO power above about 1 THz [5]. Schottky barrier varistor diodes and quantum well oscillators have been proposed as sources of LO power but these technologies will not provide sufficient power to drive the GaAs Schottky barrier mixer diodes used in these receivers [6,7,8]. We report here on a new planar varactor diode in which the Schottky contact is formed at the edge of the 2-dimensional electron gas (2-DEG). This new device, which is essentially the 2-d analog of the standard (3-d) Schottky diode, has unique properties and is a promising candidate for use in millimeter and submillimeter wave multiplier applications [9,10]. In addition, it may be possible to use this device to investigate conduction in a 2-d electron gas at frequencies significantly above 100 GHz.

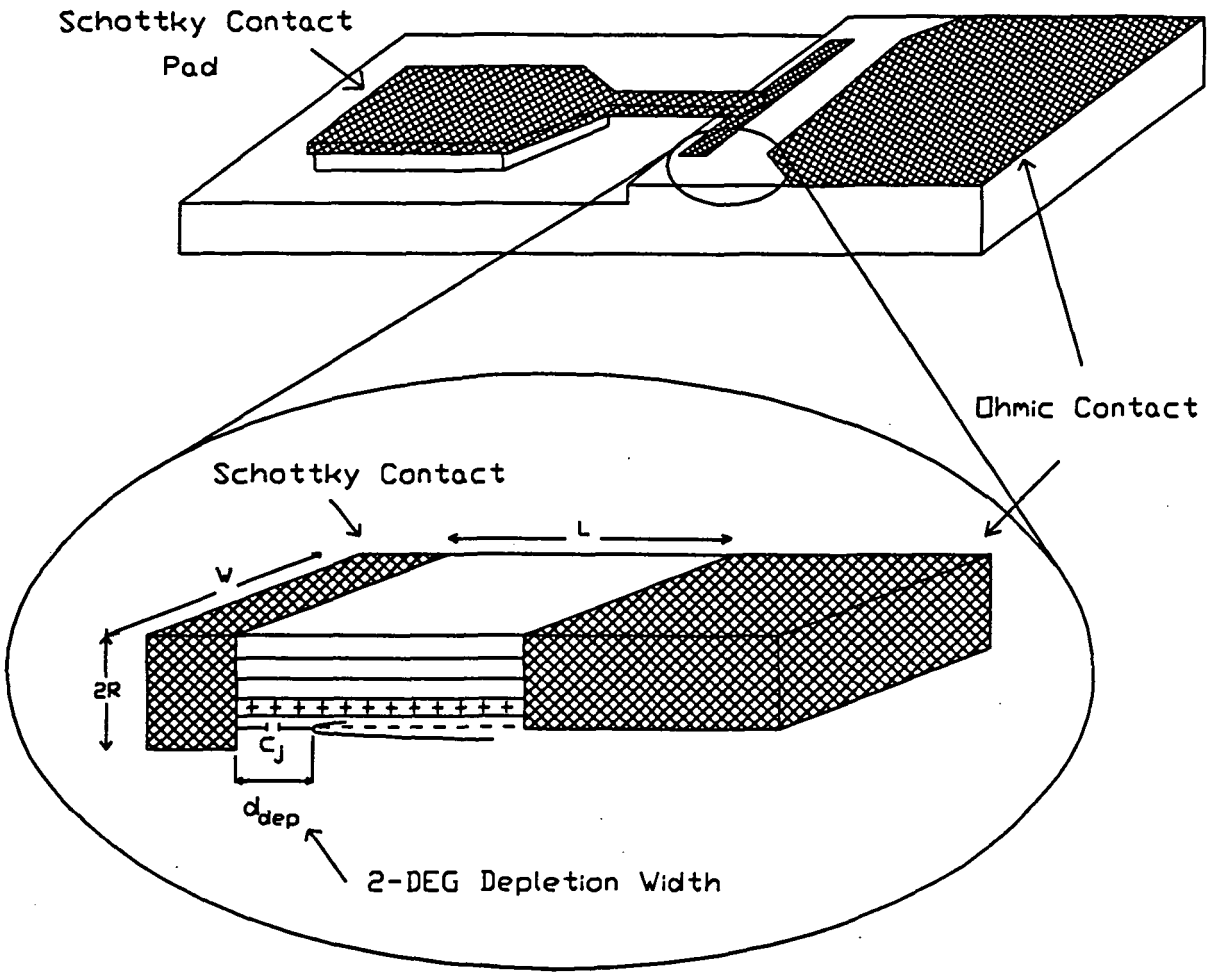

Fig. 1. Schematic of the planar Schottky/2-DEG varactor diode.

In Section II, the theory of the device and the design for multiplier applications is reviewed. In Section III, the fabrication of the devices is briefly described. The low frequency evaluation is presented in Sections IV and V for the interdigital-type and the "refined prototype" devices, respectively. The preliminary multiplier performance of the "refined prototype" devices are presented in Section VI. Finally, a summary of the work and outlook for future research is presented in Section VII.

II. THE SCHOTTKY/2-DEG DIODE

A. Overview

A sketch of the Schottky/2-DEG diode is shown in Fig. 1. Also shown is an expanded view of the Schottky contact region. The chip dimensions are typically 100 μm by 200 μm by about 50 μm thick. Two device configurations are discussed in this paper. These are the interdigitated contact device (also described in [9,10]) and the "refined prototype" device which is similar to that shown in Fig. 1. The interdigitated devices have been realized in both single and dual anode configurations, the latter being intended for symmetric C(V)

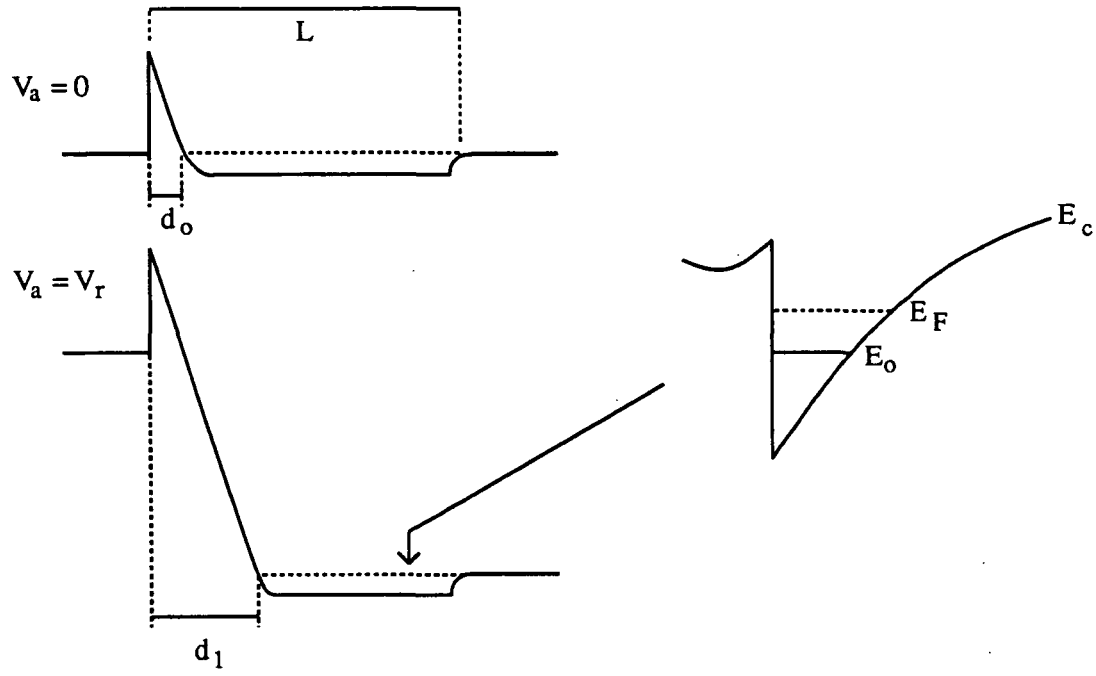

Fig. 2. Conduction band diagram of the Schottky/2-DEG diode. The 2-DEG is bounded on the left by a Schottky contact and on the right by an ohmic contact. The depletion depths for two applied voltages are shown (left). A qualitative sketch of the potential well in the undepleted channel is shown (right) with the Fermi and lowest sub-band energies indicated.

applications. These devices had Schottky contact widths in the range 150-350 μm. The "refined prototype" devices are single anode devices (whose cathode is an ohmic contact) with widths of about 100 μm. The isolation between pads is achieved by etching through to the semi-insulating GaAs substrate everywhere except in the channel region and beneath the pads. Further details of the fabrication process are outlined in Section III.

B. Physics and Equivalent Circuit

The conduction band diagram of the Schottky/2-DEG diode is shown in Fig. 2. The theory of the metal/2-DEG junction was first considered in [11] and more recently extended in [12]. In [12], the junction capacitance was derived using a conformal mapping technique and by making suitable assumptions about the boundary conditions. The capacitance-voltage characteristic was given by the expression

$$C_j(V) = \frac{W\varepsilon}{\pi} \ln\left[\frac{(R^2 + d_{dep}^2)^{1/2} + R}{(R^2 + d_{dep}^2)^{1/2} - R}\right] \qquad (1)$$

where W is the width of the contact (see Fig. 1), ε is the permittivity of GaAs and R is the

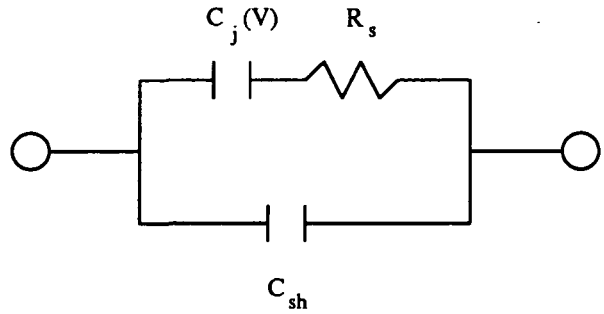

Fig. 3. A simple equivalent circuit model of the Schottky/2-DEG diode.

half-height of the Schottky metalization. The depletion depth d_{dep} of the 2-DEG is given as

$$d_{dep} = \frac{2\varepsilon(V_{bi} - V_a)}{qn_s} \tag{2}$$

where V_{bi} is the built-in voltage (0.7-1.0 V), V_a is the applied voltage (which is negative for reverse-bias), and n_s is the 2-DEG sheet charge density. For a 2-DEG sheet charge density of 10^{12} cm^{-2} (10^{13} cm^{-2}) and assuming ε of GaAs, the 2-DEG depletion depth is 3 μm (0.3 μm) at 20V reverse bias. The total capacitance is equal to the junction capacitance in parallel with the shunt capacitance associated with the pad-to-pad fields and anode-to-ohmic fields.

The equivalent circuit is shown in Fig. 3. For simplicity, the junction conductance is neglected. [The skin effect is probably not important for this device since the length and depth of the 2-DEG are small]. Also, the inductive effect of charge carrier inertia is neglected although this effect may be important at cryogenic temperatures due to the long momentum relaxation time of the 2-DEG. The junction capacitance C_j can be estimated using Eq. 1. The series resistance, R_s, is composed of the resistance of the undepleted channel and the ohmic contact resistance. The former is given by

$$R_s = \frac{(L - d_{dep})}{q\mu_n n_s W} \tag{3}$$

where L is the channel length and μ_n is the electron mobility in the undepleted channel. The ohmic contact resistance is simply $R_{OC} = r_{sc}/W$ where r_{sc} is the specific contact resistivity (normally specified in units Ωmm) of a HEMT-like ohmic contact, and W is the device width (in mm). The shunt capacitance term C_{sh} includes pad-to-pad capacitance and Schottky-to-ohmic capacitance. For high frequency design, C_{sh} and the R_s must be minimized.

The theory of the junction breakdown has not been fully developed. However, V_{br} in long channel devices is assumed to be caused either by impact ionization or by tunneling. Experimental observations of very large breakdown voltages in prototype devices [9] lead to the conclusion that for short channel length devices, the breakdown voltage was limited by punch-through. In this paper, those devices with channel lengths of 1 μm are probably punch-through limited whereas the 2-3 μm length devices may be limited by impact ionization or

tunneling, or both. The breakdown voltage may also be limited by the geometry of the anode metalization (for example, the half-height R) or by processing and material defects. A more detailed discussion of the breakdown in these devices will be presented in a later paper.

C. Frequency and Power Limitations

Several factors limit the frequency response and power performance of the multiplier. The frequency response may be limited by the dynamic cutoff frequency which is usually defined [13] as

$$\nu_{co} = \frac{S_{max} - S_{min}}{2\pi R_s} \tag{4}$$

where S_{max} (S_{min}) is $1/C_{min}$ ($1/C_{max}$), and R_s is the series resistance of the varactor diode. It is desirable for the device to have a ν_{co} value much higher than the operating frequency to ensure that the multiplier efficiency is not degraded. To achieve high ν_{co}, the series resistance should be as small as possible, the minimum capacitance (near breakdown) should be small and the capacitance modulation ratio C_{max}/C_{min} should be large.

Another important quantity which may limit both the frequency response and maximum output power is the finite velocity of the electrons traversing the modulation region (the epilayer in GaAs diodes or the 2-DEG channel in the Schottky/2-DEG diode). Recently, Kollberg et al [14] showed how the finite electron velocity limited the current in the 6P4 diode used by Erickson [3]. Kollberg argued that the ac displacement current could not exceed the saturation current which in turn is limited by the electron drift velocity. Using Monte Carlo analysis, the effective velocity and the saturation current in the 6P4 diode were estimated (in [14]) to be 2.4×10^7 cm/s and 44 mA, respectively. At input powers beyond that which causes the current to saturate, the diode's rf impedance increases (since the current cannot). Kollberg used this analysis to simulate the roll-off in efficiency with input power, which was observed by Erickson.

The velocity saturation current is written here for the 2-d case as

$$I_{vs} = qn_s v_{eff} W \tag{5}$$

where n_s is the 2-dimensional sheet charge density, W is the contact width and v_{eff} is the effective velocity of the electrons in the channel. As will be shown, a Schottky/2-DEG diode with $W = 100\ \mu m$ and $n_s = 1.85 \times 10^{12}\ cm^{-2}$ has roughly the same characteristics as the 6P4 diode. Assuming the same effective velocity as was used for the 6P4, namely $v_{eff} = 2.4 \times 10^7$ cm/s, I_{vs} is about 70 mA.

The finite electron velocity may also limit the frequency response if the transit-time for electrons traversing the modulation region is comparable to the period of the LO frequency. The transit-time corner frequency has been proposed [10] as a useful design parameter for the diode's frequency response, and is defined as

$$\nu_{tt} = \frac{v_{eff}}{2\pi L} \tag{6}$$

where L is the channel length (or the epilayer thickness in the standard diode). Note that the

frequency given by Eq. 6 is a corner frequency since, as the frequency increases beyond this value, the maximum rf modulation length shortens, resulting in a smaller capacitance ratio and thus to a roll-off in the multiplier efficiency. For example, assuming an effective electron velocity of 2.4×10^7 cm/s (as was used in [14]), a varactor diode with input frequency of 80 GHz will have a maximum modulation length of about 0.48 μm. In comparison, the 6P4 diode, which is often used at this frequency, has an epilayer thickness (and maximum dc modulation length) of about 1.0 μm. Thus, both standard and 2-DEG diodes should be designed to achieve a large capacitance modulation ratio within the length given by Eq. 6.

Having outlined the equations for the capacitance, resistance, punch-through voltage (Eq. 2 with $d_{dep} = L$), the dynamic cutoff and the transit-time frequencies and the saturation current, the Schottky/2-DEG diode may be designed for particular applications. This procedure is simplistic but is similar to the design of the state-of-the-art varactors currently in use. This design procedure was used for the "refined prototype" devices whose results are given in Section V. Before presenting the device results, the fabrication will be briefly reviewed.

III. FABRICATION

The prototype Schottky/2-DEG devices discussed here were fabricated on a pseudomorphic $Al_{.25}Ga_{.75}As/In_{.15}Ga_{.85}As/$ GaAs structure shown in Fig. 4. This structure was grown by MBE and analyzed using the Van der Pauw method to determine the mobility and sheet charge density. The electron sheet charge density at both 77 K and 300 K was 1.85×10^{12} cm^{-2} and the electron mobilities were 31,400 $cm^2/V\text{-}s$ and 6640 $cm^2/V\text{-}s$ at 77 K

Layer			
1	GaAs	5×10^{18} cm^{-3}	40 Å
2	$Al_{0.25}Ga_{0.75}As$	5×10^{17} cm^{-3}	300 Å
3	Si Atomic Plane	5×10^{12} cm^{-2}	--
4	$Al_{0.25}Ga_{0.75}As$	--	50 Å
5	$In_{.15}Ga_{.85}As$	--	150 Å
6	GaAs	--	5000 Å
7	SI GaAs Substrate		

Fig. 4. AlGaAs/InGaAs/GaAs heterostructure used for the devices discussed here.

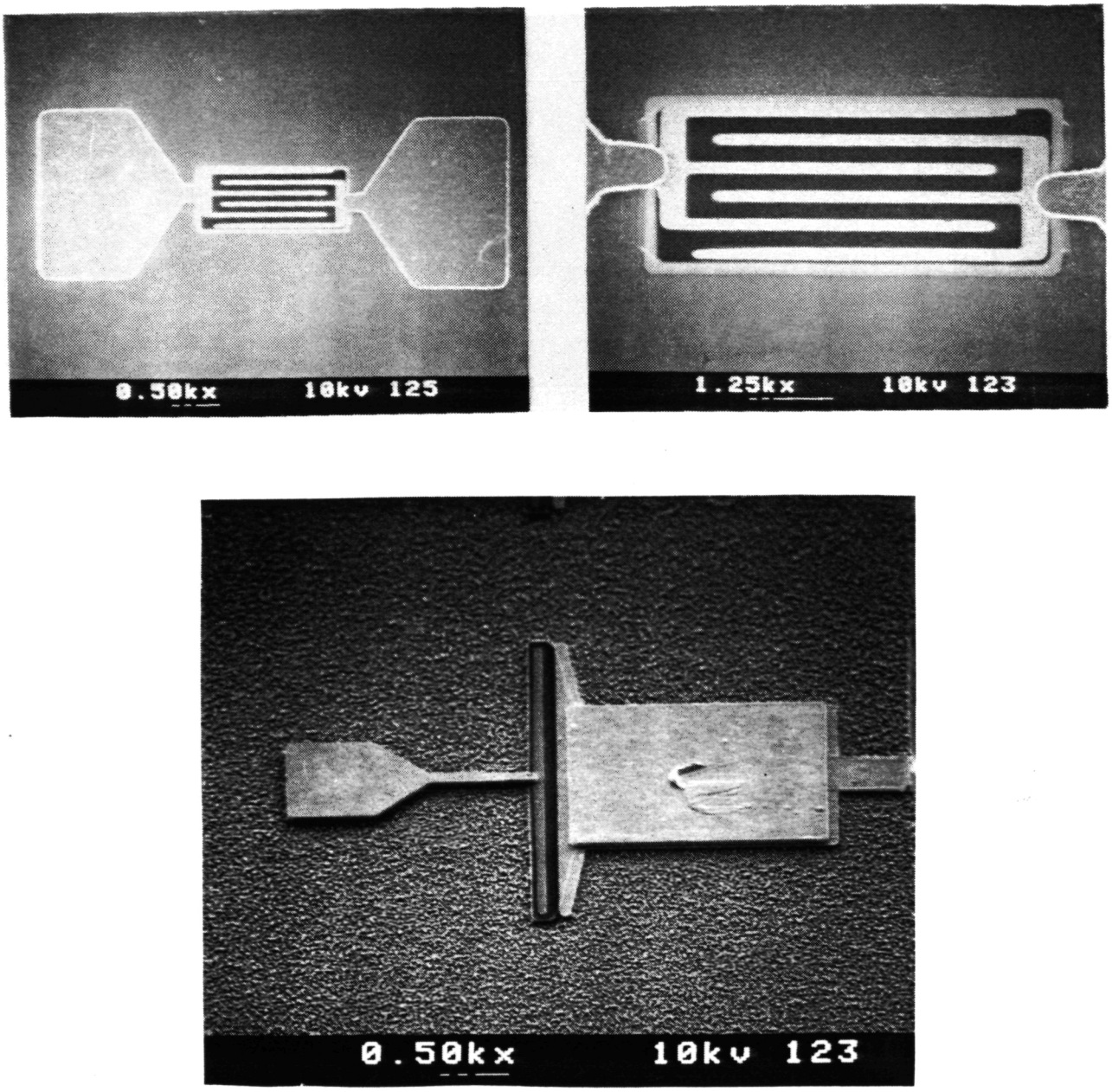

Fig. 5. Scanning electron micrographs of Schottky/2-DEG devices. The interdigitated device (top) has anode width of 250 μm *and channel length of 2* μm. *The "refined prototype" device (bottom) shown here is similar to the devices discussed in Section V. Here, the anode width is 100* μm *and the channel length is 5* μm.

and 300 K, respectively. The supply and cap layers are substantially depleted to the 2-DEG and/or the surface, to minimize parallel conduction. The ohmic contact consists of an electroplated SnNi/Ni/Au trilayer which is alloyed at about 380°C. To form the Schottky contact, a trench is etched through the 2-DEG layer and a Pt/Au contact is electroplated into the trench. Next, the contact pads are plated and finally a 2-3 micron deep $NaOH:H_2O_2$ etch to the SI-GaAs substrate is performed to isolate the two pads. All lithography levels are performed using a Karl Suss MJB-3 (405 nm). An SEM photo of the interdigitated device is shown in Fig. 5 (top). A sketch of a "refined prototype" is also shown (bottom). The rough surface of this device was due to the isolation etch, performed using chlorine reactive ion etching. A subsequent wet chemical etch reduced the surface roughness considerably.

IV. Low Frequency Evaluation Of Interdigitated Devices

The dc evaluation of the Schottky/2-DEG diodes include I(V), C(V) and reverse breakdown voltage measurements. First, the interdigitated device results are presented (these results were also presented in [10]). The forward and reverse I(V) of a single Schottky/2-DEG device is shown in Fig. 6 (top), measured at room temperature. The exponential diode characteristic is seen as the linear portion of this semi-log I(V) plot, in the range 0.35 - 0.7 V. The "knee" voltage (at 1 μA) was 0.512V. The ΔV values for the current intervals 0.1 – 1.0μA, 1.0 – 10.0μA and 10.0 – 100μA are 74mV, 74mV and 81mV, corresponding to inverse slope parameters, V_o, of 32.1mV, 32.1mV and 35.2mV, respectively. This corresponds to a diode ideality factor of 1.26. The series resistance of this device was determined to be 56Ω. The expected 2-DEG channel resistance at room temperature is 6 Ω. Allowing for a pessimistic value of the ohmic contact resistivity, r_{sc} of 2.5 Ωmm, the total series resistance expected for this device was about 16 Ω. The remaining 40 Ω series resistance is most likely due to insufficient plating of the ohmic contacts, as was substantiated by inspection using scanning electron microscopy. The dual anode devices have no ohmic contact resistance. In these devices, the I(V) is dominated by the characteristic of the reverse-biased junction and a series resistance measurement cannot be made. However, using Eq. 3, the L = 2μm, W = 250μm device resistance is about 4 Ω at 295K and about 1.0 Ω at 100 K due to the increase in mobility upon cooling.

The C(V) curves of the single and dual anode interdigitated devices are shown in Fig. 6 (bottom). The channel length (gap between fingers) is 2 μm (3 μm) for the dual (single) Schottky device. The anode widths were 250 μm for both devices. As expected, the dual Schottky device has a nearly symmetric C(V) characteristic and it's zero-bias capacitance is about half that of the single anode device. Subtracting the pad-to-pad capacitance which was measured to be 4 fF, this symmetric C(V) device had a dynamic cutoff frequency of about 1 THz at 295K and about 4 THz at 100 K. The velocity saturation current (Eq. 5 using $v_{eff} = 2.4 \times 10^7$ cm/s) is 178 mA. Also, the transit-time corner frequency of the 2 μm channel length device is about 19 GHz, calculated using Eq. 6. The capacitance levels of the dual anode device is probably too high for most multiplier applications. Nevertheless, multiplier testing of these devices will be performed in the near future.

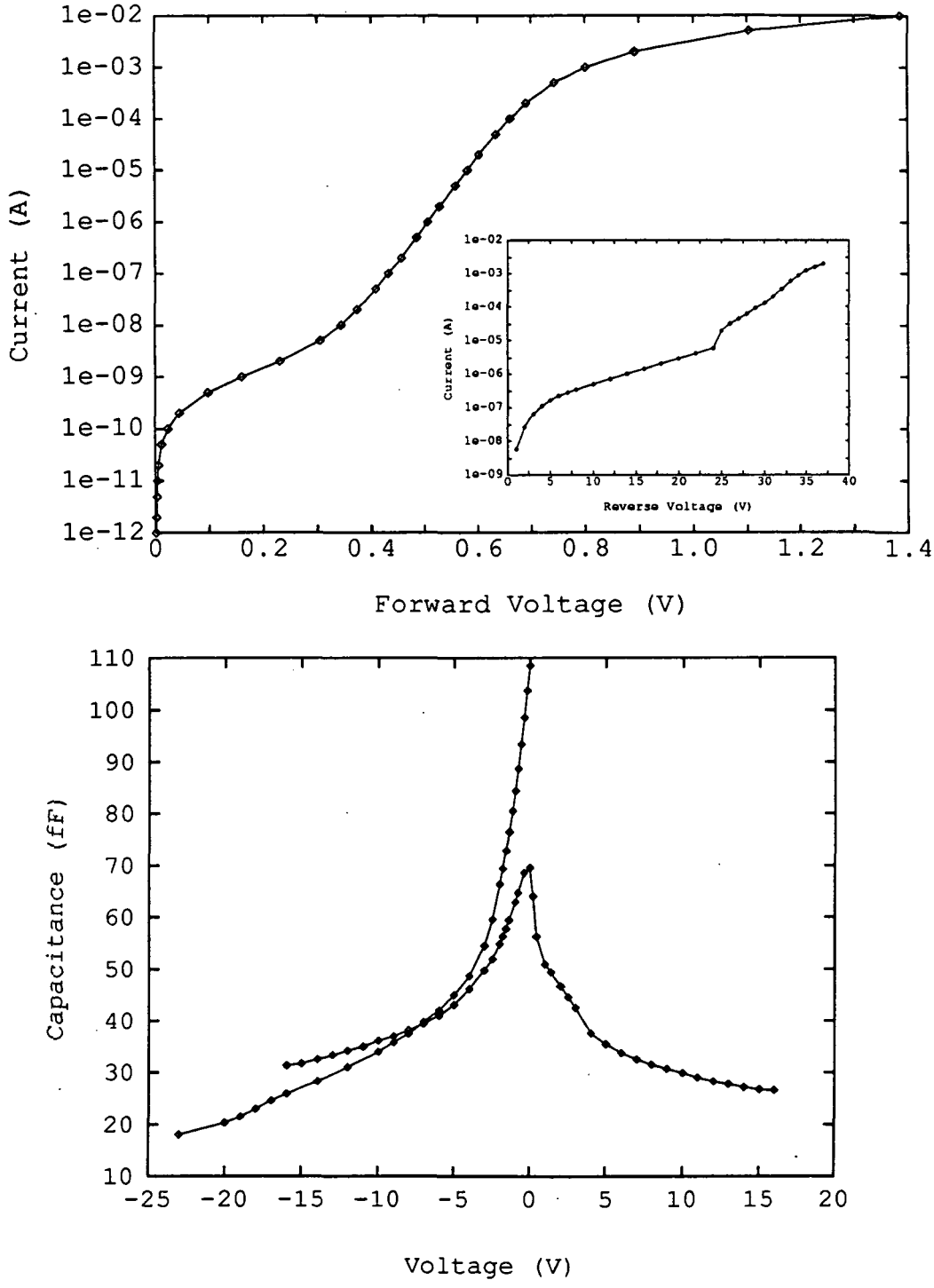

Fig. 6. Forward and reverse I(V) of single anode interdigitated device (top) with W = 250 μm *and* L = 3.0 μm. *C(V) characteristics (bottom) of* L = 3.0 μm *single and* L = 2.0 μm *dual anode interdigitated devices of width 250* μm.

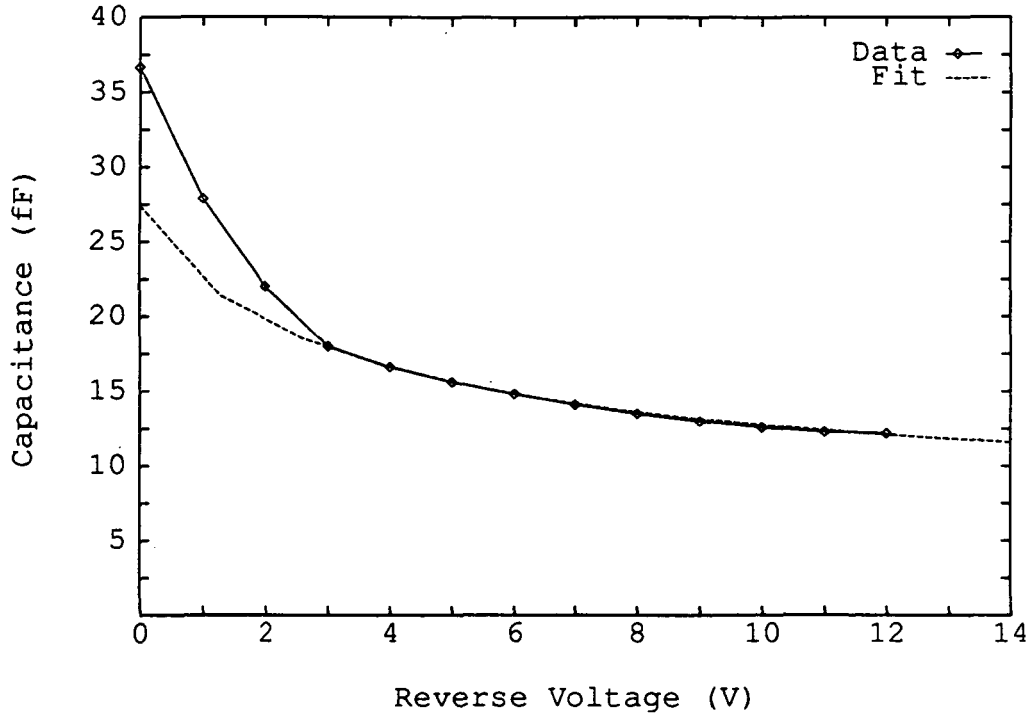

Fig. 7. C(V) of refined prototype device A. Also shown is a fit (Eq. 1) using $R = 0.75\ \mu m$, $C_{sh} = 8.0\ fF$, $V_{bi} = 0.7\ V$ *and* $W = 90\ \mu m$.

V. Low Frequency Evaluation Of Refined Prototype Devices

The refined prototype devices had two anode width/channel length combinations. The "A" devices had anode widths of 90 μm (on average) and channel lengths of 2.5 μm while the "B" devices had anode widths of 80 μm and channel lengths of 3.0 μm. The C(V) characteristic of device A is shown in Fig. 7. The theoretical capacitance, shown fitted to the data, agrees well with the data except near zero-bias where the fit is lower than the data. The fit assumed a reasonable value of the anode metal half-height ($R = 0.75\ \mu m$) and a shunt capacitance of 8.0 fF. This value of C_{sh} is higher than expected since the pad-to-pad capacitance was measured to be about 2 fF. The additional shunt capacitance may be due in part to fields between the anode and ohmic metals. This contribution to the capacitance is not easily determined and is also not substracted for the v_{co} calculations. The difference between the theory and the data near zero-bias is either due to inaccuracy of Eq. 1 for the geometry of this device or to effects related to the leakage current at low bias. We are currently investigating a more general theory of the junction capacitance for devices of various geometries.

The forward I(V) as a function of temperature of device A is shown in Fig. 8. As the temperature decreased, several changes occured. First, the entire I(V) curve shifted to higher voltages, as expected due to the temperature dependence of the saturation current (the theory of the thermionic saturation current of the Schottky/2-DEG junction is being investigated [15]). At lower currents, the "leakage" current which has been routinely observed at room temperature is seen to decrease substantially so that, at 220 K, it is much less than one nanoamp. Finally, the strong temperature dependence of the series resistance is evident at high currents.

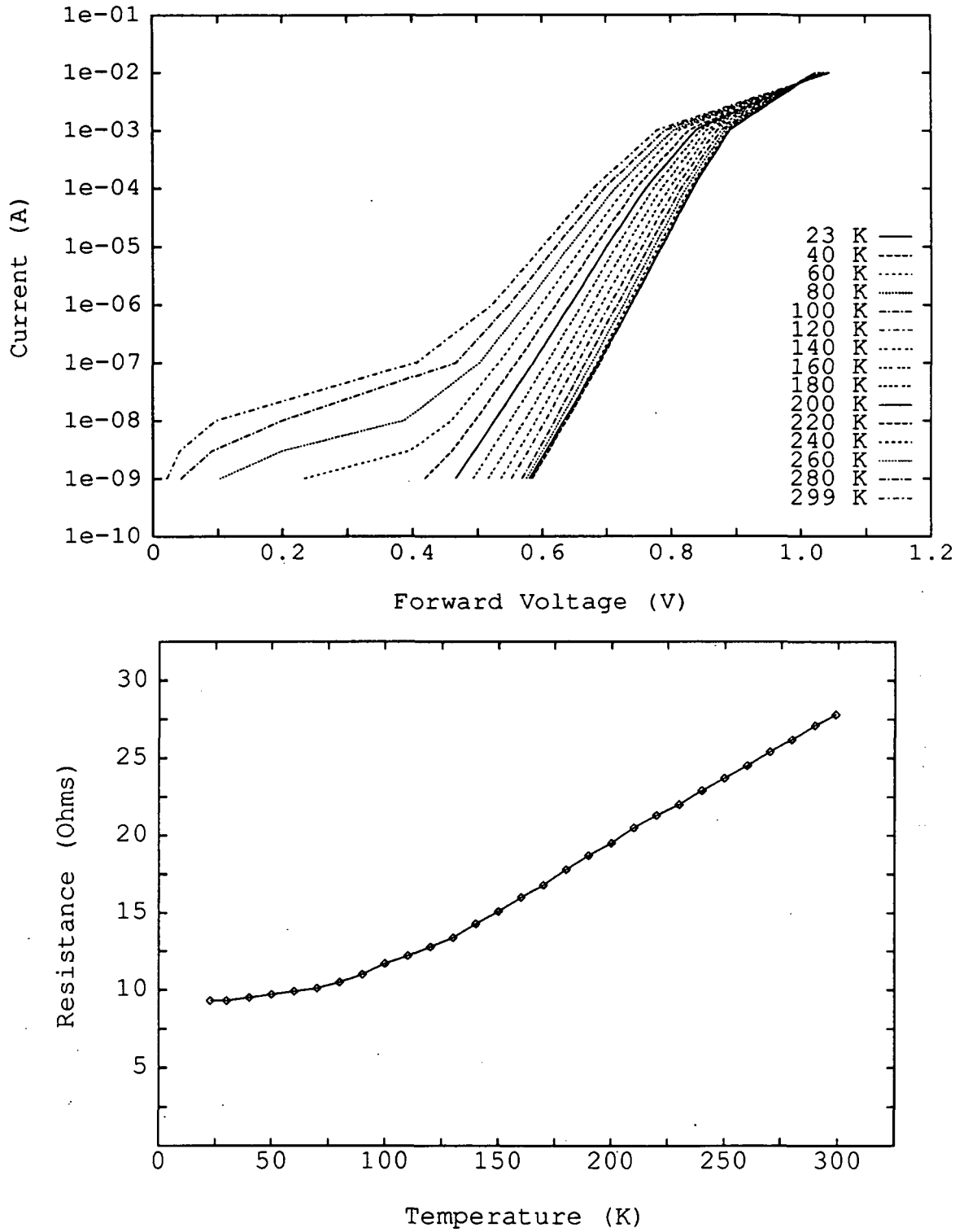

Fig. 8. Forward I(V) (top) and series resistance (bottom) versus temperature of device A.

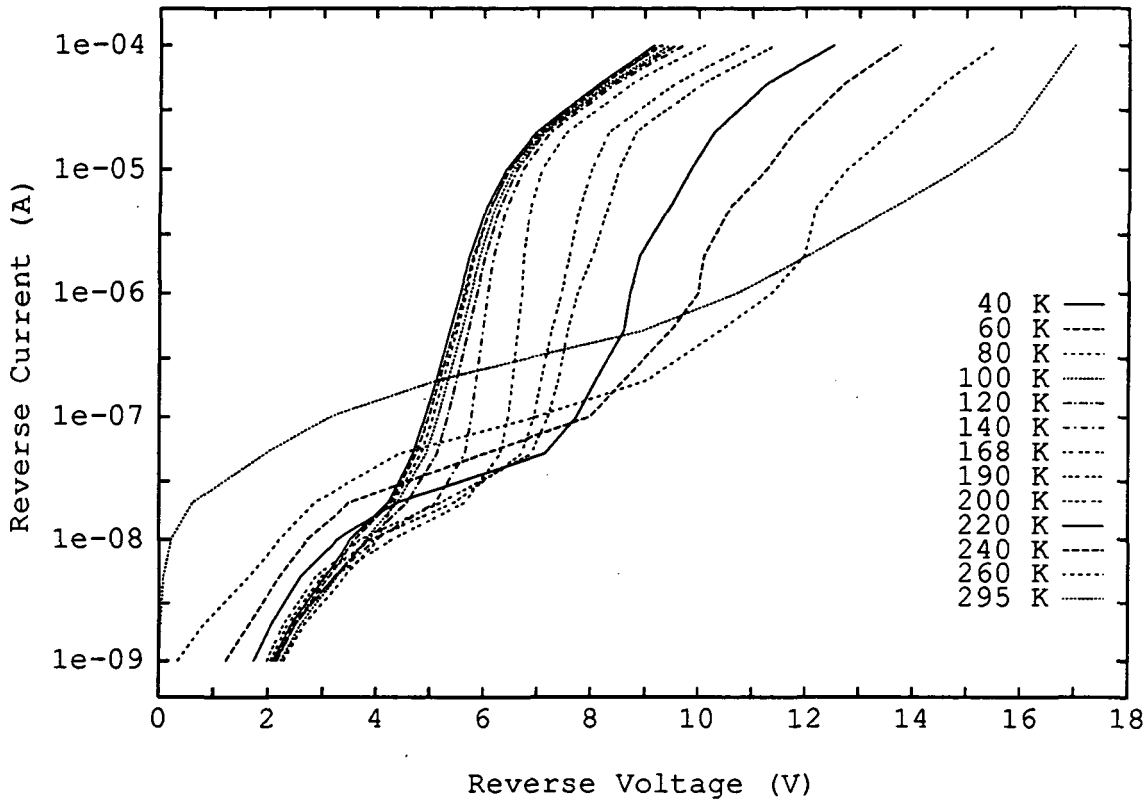

Fig. 9. Reverse I(V) versus temperature of device A.

The measured series resistance of device A is plotted as a function of temperature in Fig. 8 (bottom). The resistance decreased nearly linearly from 19.9 Ω at 300 K to 10.5 Ω at 130 K, and the resistance at 77 K was 8.9 Ω. The 2-DEG resistances calculated using Eq. 3 with the low field mobility values at 300 K and 77 K are 14.1 Ω and 3.0 Ω, respectively. Thus, the ohmic contact resistivity (for the width 90 μm) is estimated to be about 0.6 Ωmm. This value of r_{sc} is much lower than was achieved on the earliest Schottky/2-DEG devices. The improvement is probably a consequence of the higher doping at the heterostructure surface and an improved ohmic plating and alloying procedure. Further reduction of r_{sc} (perhaps to 0.1 Ωmm) should be possible using evaporated Ni/Ge/Au ohmic contacts.

The reverse I(V) of device A was measured as a function of temperature and is shown in Fig. 9. As in the forward I(V), the leakage current is seen to decrease upon cooling. At the highest reverse current (100 μA), the reverse voltages decreased with temperature from 17 V at 300 K to about 9 V at 40 K. This temperature dependence of the breakdown voltage is qualitatively consistent with impact ionization theory. Since the mean free path for electron phonon interactions increases with decreasing temperature, the electrons can achieve higher kinetic energies before phonon scattering occurs. Consequently, as the temperature decreases, electrons reach the impact ionization energy at lower field strengths (lower reverse voltages) and the breakdown voltage decreases.

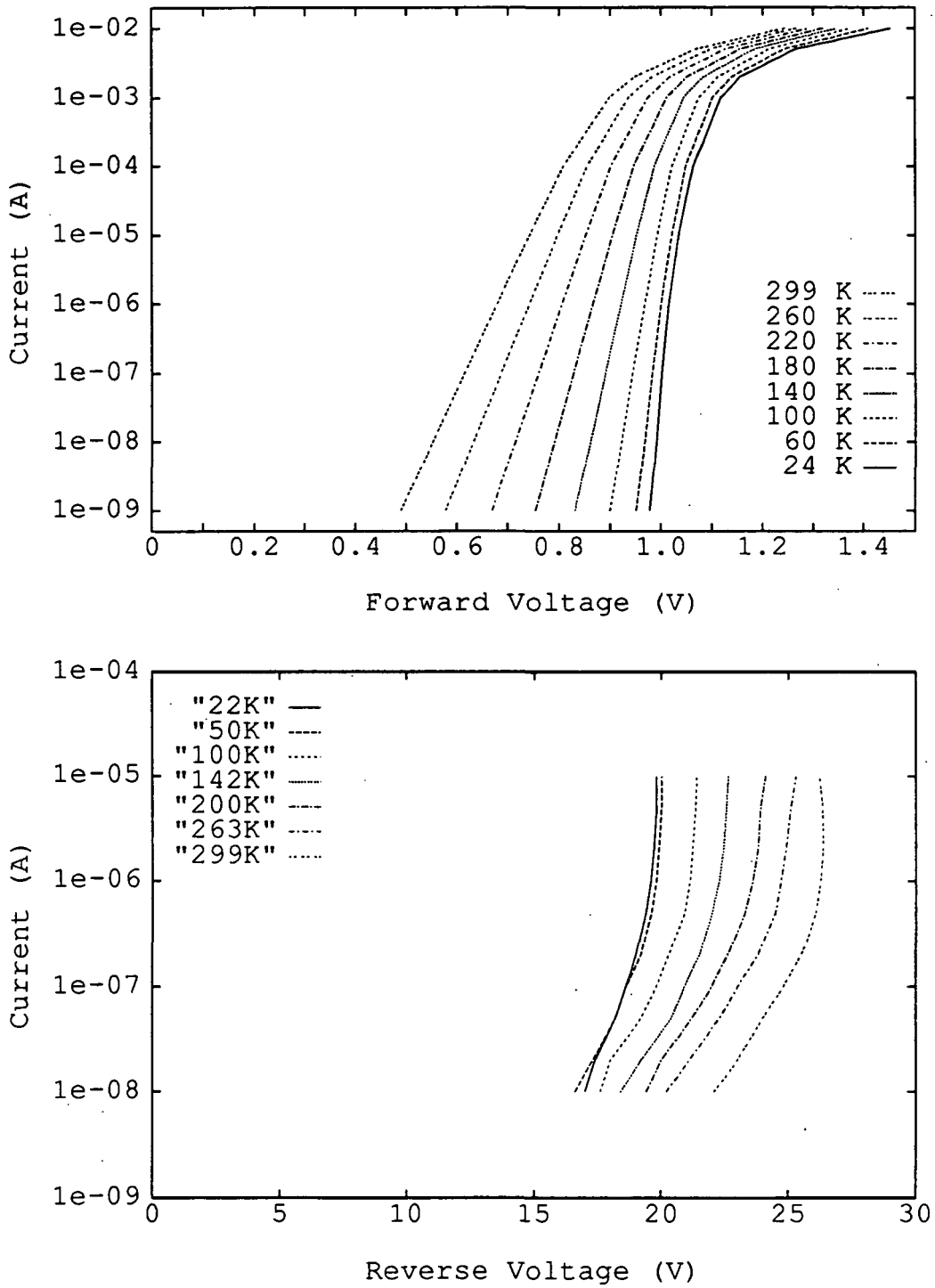

Fig. 10. Forward I(V) (top) and reverse I(V) (bottom) vs. temperature of planar GaAs Schottky diode SC6T1.

The temperature dependence of the breakdown voltage of the Schottky/2-DEG diode raised the question of whether the breakdown voltage in standard GaAs varactors had a similar temperature dependence. To investigate further, the I(V) of several planar GaAs varactor diodes (UVA-SC6T1) were measured as a function of temperature. The doping concentration and anode diameter for this diode were 2×10^{16} cm^{-3} and 6 μm, respectively, compared to the respective values 3×10^{16} cm^{-3} and 6 μm for the whisker-contacted UVA-6P4 diode. The forward and reverse I(V) of one device is shown in Fig. 10. The forward I(V) is typical for a low doped diode. Here, the knee voltage increased from 0.678 V at 299K to 1.015 V at 24K. The inverse slope parameter decreased from 28.7 mV at 299 K to 12.7 mV at 24 K. The series resistance was constant and equal to 30 Ω (± 1 Ω) over the range 24-299 K. The reverse I(V) was measured from 10 nA to 10 μA. The breakdown voltage characteristics are all very sharp. Of the three SC6T1 diodes tested, all had breakdown voltages of 18-19 V at 24K, although the room temperature breakdown voltages were 26 V, 29 V and about 30 V. Thus, the average reduction in V_{br} was about 35 percent upon cooling, compared to a reduction of about 50 percent for the Schottky/2-DEG diode. A decreasing breakdown voltage in these devices upon cooling may impact the low temperature multiplier performance. On the other hand, the large decrease in the series resistance of the 2-DEG upon cooling should result in higher multiplier efficiency.

Finally, the saturation drift current of device A was calculated, using Eq. 5 with $v_{eff} = 2.4 \times 10^7$ cm/s, to be 64 mA. This may be a conservative estimate since higher velocities may be possible in the 2-DEG than in bulk GaAs. In any case, the Schottky/2-DEG diode of roughly equivalent properties as those of the 6P4 diode has a significantly higher saturation current (at least 64 mA) than does the 6P4 diode (44 mA according to [14]).

VI. Preliminary Multiplier Results

The first rf measurements of a Schottky/2-DEG diode were performed at the National Radio Astronomy Observatory using a modified NRAO tripler which was designed [16] for whisker contacted diodes (such as the UVA-6P4). The Schottky/2-DEG diode chip was soldered across the output waveguide. A klystron was used as a source and two power meters were used to measure the power at the input and output ports of the multiplier. Further details of the measurement setup may be found in [17].

The preliminary measurements were of device A having chip width and length dimensions of 100 μm and 180 μm. The chip thickness was about 60 μm. After soldering, the clearance between the back of the chip and the waveguide wall was estimated to be only 2-3 μm, due in part to the thick solder "bump". The I(V) of the device was checked after soldering and found to be the same as before soldering. The room temperature R_s and V_{br} of this device were 20 Ω and 12 V, respectively.

The first multiplier test was to determine the optimum frequency. Using 50 mW input power, the multiplier tuners and dc bias were optimized for maximum output power at several frequencies over the range 70-79 GHz. The result is shown in Fig. 11 where the input power was 50 mW. The best performance was obtained at 75 GHz where P_{out} was 160 μW at 225 GHz. The input return loss was measured at 75 GHz to be about -20 dB so the input tuning was relatively well optimized. Next, the output power at 225 GHz was measured as a function of

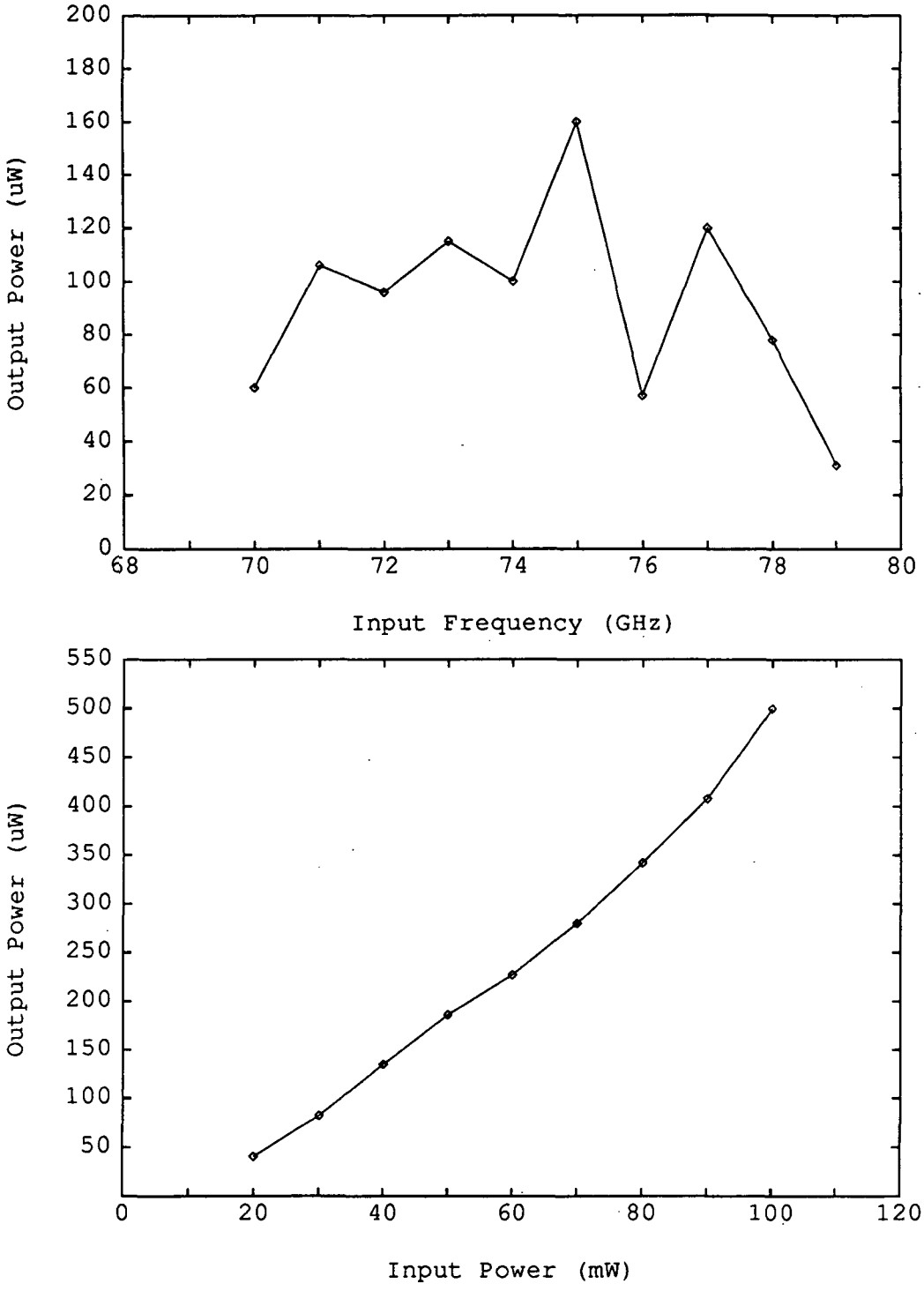

Fig. 11. Tripler output power versus input frequency (top) with $P_{in} = 50$ *mW and output power versus input power (bottom) for tripling to 225 GHz.*

the input power, as shown in Fig. 11 (bottom). P_{in} was varied over the range 20 -100 mW. As the input power increased, the output power increased, reaching a maximum value of 500 μW at 100 mW at the input. This corresponds to an efficiency of 0.5 percent. In comparison, Bradley [17] used this multiplier with a planar GaAs varactor of doping 1.1 x 10^{17} cm^{-3} and diameter 7 μm and obtained 3.7 mW output power and 4.1 percent efficiency at 219 GHz. This first multiplier measurement of the Schottky/2-DEG diode is encouraging but much higher performance should be possible. Even the current devices should yield higher multiplier efficiencies if they are thinned to 25 μm or less and if a thinner solder layer is used to reduce the shunt capacitance between the chip and the waveguide wall.

VII. SUMMARY AND FUTURE RESEARCH

In summary, we have reported on the recent progress in the research of a novel Schottky/2-DEG varactor diode. Observations of reduced breakdown voltages upon cooling in both the standard GaAs and the novel Schottky/2-DEG diodes were in agreement with the theory of impact ionization. The problem of current saturation was discussed and the Schottky/2-DEG diode of width 90 μm was found to have a significantly higher saturation current than the comparable GaAs 6P4 varactor. Recent improvements to the design and fabrication procedures have resulted in devices having lower series resistance and lower capacitance. Both single anode and dual anode (with symmetric C(V)) devices have been investigated. The cutoff frequency of the dual anode device was estimated to be 1 THz (4 THz) at 300 K (100 K), whereas the single anode device had cutoff frequency of about 0.6-1.0 THz, depending on the temperature. Preliminary multiplier measurements of a single anode device were encouraging, resulting in 500 μW output power at 225 GHz with 0.5 percent efficiency. Ongoing research will include more extensive multiplier testing of both the single anode and the symmetric C(V) devices. Also, shorter channel length devices with Ni/Ge/Au ohmic contacts will be fabricated to achieve much higher cutoff and transit-time frequencies. In addition, AlInAs/InGaAs/InP heterostructures will be investigated. Finally, the theories relating to the junction capacitance and breakdown are being developed and the current transport in these devices will be investigated using Monte Carlo simulations.

ACKNOWLEDGEMENTS

This work has been supported by the National Science Foundation under contracts ECS-8720850 and ECS-9113123 (contract monitors Dr. T. Hsiang and Dr. B. Clifton) and by the Office of Naval Research under contract #N00014-90-J-4006 (contract monitor Dr. Y.S. Park). The authors thank R. Bradley and N. Horner of the National Radio Astronomy Observatory for assistance with the multiplier measurements, and T. Hierl of Quantum Epitaxial Designs, Inc. for providing the MBE material and Van der Pauw data.

REFERENCES

[1] H. P. Röser, "Heterodyne Spectroscopy for Submillimeter and Far-Infrared Wavelengths From 100 μm to 500 μm," Infrared Physics, Vol. 32, pp. 385-407, 1991.

[2] J. Zmuidzinas, A.L. Betz, and R.T. Boreiko, "A Corner-Reflector Mixer Mount for Far Infrared Wavelengths," Infrared Phys., Vol. 29, No. 1, 119-131, 1989.

[3] N. Erickson, "High Efficiency Submillimeter Frequency Multipliers," The 1990 IEEE MTT-S Int. Microwave Symposium, Dallas, TX, May 1990.

[4] P. Zimmermann, private communication, March and May 1990.

[5] T. W. Crowe, W.C.B. Peatman, and E. Winkler, "GaAs Schottky Barrier Varactor Diodes for Submillimeter Wavelength Power Generation," Microwave and Optical Tech. Lett., Special Issue: Space Terahertz Tech., Vol. 3, No. 1, January 1991.

[6] K. Benson and M.A. Frerking, "Theoretical Efficiency for Triplers Using Nonideal Varistor Diodes at Submillimeter Wavelengths," IEEE Trans. Microwave Theory Tech., Vol. MTT-33, No. 12, 1367-1374, Dec. 1985.

[7] C. Kidner, I. Medhi, J. East, G. Haddad, "Performance Limitations of Resonant Tunneling Diodes," The First Int'l. Symposium on Space Terahertz Technology, Ann Arbor, MI, March 1990.

[8] H. Rothermel, T.G. Phillips, J. Keene, "A Solid-State Frequency Source for Radio Astronomy in the 100 to 1000 GHz Range," Int. J. Infrared and Millimeter Waves, Vol. 10, No. 1, 83-100, 1989.

[9] W. C. B. Peatman, T. W. Crowe and M. Shur, "Design and Fabrication of Heterostructure Varactor Diodes for Millimeter and Submillimeter Wave Multiplier Applications," Proc. IEEE/Cornell Conf. on Advanced Concepts in High Speed Semic. Dev. and Circuits, Ithaca, NY, 1991.

[10] W.C.B. Peatman, T.W. Crowe and M. Shur, "A Novel Schottky/2-DEG Diode for Millimeter and Submillimeter Wave Multiplier Applications," *IEEE Electron Device Lett.*, Vol. 13, No. 1, pp. 11-13, January 1992.

[11] S.G. Petrosyan and A. Ya Shik, "Contact Phenomena in a two-dimensional electron gas," Soviet Physics Semicond., 23 (6), pp. 696-697, June 1989.

[12] B. Gelmont, M. Shur and C. Moglestue, "Theory of Junction Between Two-Dimensional Electron Gas and P-Type Semiconductor," to be published, IEEE Trans. Electron Devices, Vol. 39, No. 5, May 1992.

[13] P. Penfield and R. Rafuse, Varactor Applications, MIT Press, 1962, p. 86.

[14] E. Kollberg, T. Tolmunen, M. Frerking and J. East, "Current Saturation in Submillimeter Wave Varactors," Proc. Second Int'l. Symp. Space Terahertz Technology, Pasadena, CA, pp. 307-322, 1991.

[15] B. Gelmont, M. Shur (unpublished).

[16] J. Archer, "An Efficient 200-290 GHz Frequency Tripler Incorporating A Novel Stripline Structure," IEEE Trans. Micrwave Theory and Tech., Vol. 32, No. 4, pp. 416-420, 1984.

[17] R. Bradley, Ph.D. Thesis, University of Virginia, pp. 42-65 May, 1992.

THERMIONIC EMISSION CURRENT IN A SINGLE BARRIER VARACTOR

Hans Hjelmgren[a], Jack East[b], and Erik Kollberg[a]
a) Applied Electron Physics, Chalmers University of Technology, S–412 96 Göteborg, Sweden
b) Solid-State Electronics Laboratory, University of Michigan, Ann Arbor, MI 48109–2122

Abstract—From I–V measurements on Single Barrier Varactors (SBV) at different temperatures we concluded that thermionic emission across the barrier of the actual device is mainly due to transport through the X band. The same structure was also modelled with a one-dimensional drift-diffusion model, including a "boundary condition" for thermionic emission across the heterojunction interface. By including thermionic field emission through the top of the triangular barrier of a biased diode and the effect of a non-abrupt interface at the heterojunction, we obtained good agreement between the modelled and measured I–V characteristics.

1. Introduction

SBV diodes have been proposed as an alternative to Schottky barrier diodes for harmonic multiplier applications [1]. However, the device discussed in [1] showed a higher than expected current. We will present experimental data and the results of a numerical model to explain the current vs. voltage characteristics of SBV diodes.

2. Experimental results

The device consists of a 200 Å wide undoped $Al_{0.7}Ga_{0.3}As$ barrier, surrounded by 5300 Å wide GaAs layers, doped to 1×10^{17} cm^{-3}. On both sides of the AlGaAs layer there is a 50 Å wide undoped GaAs spacer layer. If the effect of field emission is neglected the current is mainly limited by thermionic emission across the barrier and can be described by the Richardson law,

$$J = A^* T^2 e^{-\phi_b(V)/kT} \qquad (1)$$

where A^* is the modified Richardson constant and ϕ_b is the bias dependent barrier height. Both can be determined from the experimental data by plotting $\ln(J/T^2)$ against $1000/T$ for different voltages [2]. The intersection with the y-axis gives us the Richardson constant, while the slope is proportional to the barrier height for that specific bias voltage. Since our barrier is comparatively thin, the influence of tunneling is observable even at quite high temperatures, causing a deviation from a straight line in Fig. 1. This makes the determination of the Richardson constant quite cumbersome. It must be chosen in such a way that the barrier heights at low voltages are close to the expected barrier height at zero bias voltage. A Richardson constant of 0.30 $Acm^{-2}K^{-2}$, much lower than the value expected for thermionic emission in GaAs but in fairly good agreement with that measured by Solomon et al. [2], corresponds to a barrier height at low voltages of about 0.29 eV. This low Richardson constant together with the high current indicates that the electrons are transferring to the X valley within the barrier. The assumed offset in Γ conduction band corresponds to 59 % of the difference in bandgap [3].

3. Numerical results

A drift-diffusion model for one-dimensional heterojunction structures was also used to study the device characteristics. It accounts for thermionic emission across the barrier by calculating the current at the heterojunction interfaces from,

$$J = q\eta_2 n_2 v_{r2} - A^* T^2 e^{-\phi_b(V)/kT} \qquad (2)$$

where the first term describes the current from the AlGaAs side [4] while the second term is the current from the GaAs side emitted above the barrier. Without this "bottleneck" for the current, the drift-diffusion model results in a much too high current. Since a theoretical determination of the actual emission constant across the interface is quite complicated, we have used the experimentally determined Richardson constant in Fig. 1. The probability of emission above the barrier depends on several parameters, such as thickness of the barrier, crystal orientation, and roughness of the interfaces. The thermally emitted electrons were assumed to be transferred to the X–valley when they reached the AlGaAs barrier, causing an effective barrier height at zero bias of 0.29 eV. During a simulation the barrier height is determined self consistently from the modelled conduction band, Fig. 2. Even at 300 K the effect of thermally assisted tunneling is considerable, and it has to be included in the model. Since the top of the biased barrier is triangular, the probability of tunneling as a function of electric field and carrier energy can be estimated from the WKB approximation [5],

$$P = \exp\left\{-\frac{4\sqrt{2qm_e}\,\Delta e^{3/2}}{3(h/2\pi)E_{max}}\right\} \qquad (3)$$

where E_{max} is the electric field in the barrier and Δe is the energy distance from the top of the barrier. The effect is included in the model by reducing the barrier height in eqn. (2) with an amount Δe corresponding to a tunnelling probability of e^{-1}. We assumed the tunneling process to be indirect tunneling in the AlGaAs X band [6], and used a transverse electron mass in the X band of $0.20m_0$. Tunneling through the Γ band is less probable due to the much higher barrier, and tunneling from X valleys with the longitudinal mass perpendicular to the interface is less probable due to the higher mass. Apart from band bending due to accumulation of electrons at the interface, and thermionic field emission, the fact that the transition between the two materials is not completely abrupt will also result in a field dependent barrier height [7]. In Fig. 2 we roughly modelled this effect by using a grid distance of 25 Å at the interface. The obtained I–V characteristic in Fig. 3 is very sensitive to the grid distance at the right interface of the barrier, while its value elsewhere is of less importance.

The model has also been used to predict the capacitance vs. voltage. The capacitance is determined from the change of charge concentration in the depletion layer for an incremental change in voltage. As can been seen in Fig. 4, the agreement between modelled and measured C–V characteristics is fairly good. In order to get reasonably good accuracy the grid-distance in the depletion layer and the voltage step should not be too large.

4. Conclusions

The presented expression for the current between the two grid-points adjacent to the heterojunction interface (eqn. 2) includes effects caused by the existence of two interfaces and other effects, which for a theoretical determination require quantum mechanical calculations [8]. It also gives us a possibility to model the effect of a non-abrupt transition between the two materials. Similar expressions, have been used before in drift-diffusion models, but they are restricted to a single interface [3,4]. The drawback with the model used here is that it relies on measured results in order to find a value for the Richardson

emission constant. However, since the actual emission constant may be quite difficult to calculate, we considered it as a device parameter specific for the actual device dimensions and growing conditions, which could be measured instead of calculated. The good agreement with measured results indicates that the current is mainly due to thermionic emission and thermionic field emission across the X–valley of the barrier.

The inaccuracy in the experimental determination of the Richardson constant can be reduced by using slightly thicker barriers and by performing measurements at elevated temperatures and lower bias voltages.

References

1. A. Rydberg, H. Grönqvist, and E. Kollberg, "Millimeter- and submillimeter-wave multipliers using quantum-barrier-varactor (QBV) diodes," *IEEE El. Device Lett.*, vol. 11, pp. 373–375, 1990.
2. P. Solomon, S. Wright, and C. Lanza, "Perpendicular transport across (Al,Ga)As and the Γ to X transition," *Superlattices and Microstructures*, vol. 2, pp. 521–525, 1986.
3. G. B. Tait and C. R. Westgate, "Electron transport in rectifying semiconductor alloy ramp heterostructures," *IEEE Trans. Electron Devices*, vol. 38, pp. 1262–1270, 1991.
4. K. Horio and H. Yanai, "Numerical modeling of heterojunctions including the thermionic emission mechanism at the heterojunction interface," *IEEE Trans. Electron Devices*, vol. 37, pp. 1093–1098, 1990.
5. E. H. Rhoderick and R. H. Williams, "*Metal–Semiconductor Contacts, 2nd edition*," Oxford, England: Claredon, 1988.
6. E. E. Mendez, E. Calleja, and W. L. Wang, "Tunneling through indirect-gap semiconductor barriers," *Physical Rev. B*, vol. 34, pp. 6026–6029, 1986.
7. S. C. Lee and G. L. Pearson, "Rectification in $Al_xGa_{1-x}As$–GaAs N–n heterojunction devices," *Solid-State Electronics*, vol. 24, pp. 561–568, 1981.
8. M. Rossmanith, J. Leo, and K. von Klitzing, "Model of Γ to X transition in thermally activated tunnel currents across $Al_xGa_{1-x}As$ single barriers," *J. Appl. Phys.*, vol. 69, pp. 3641–3645, 1991.

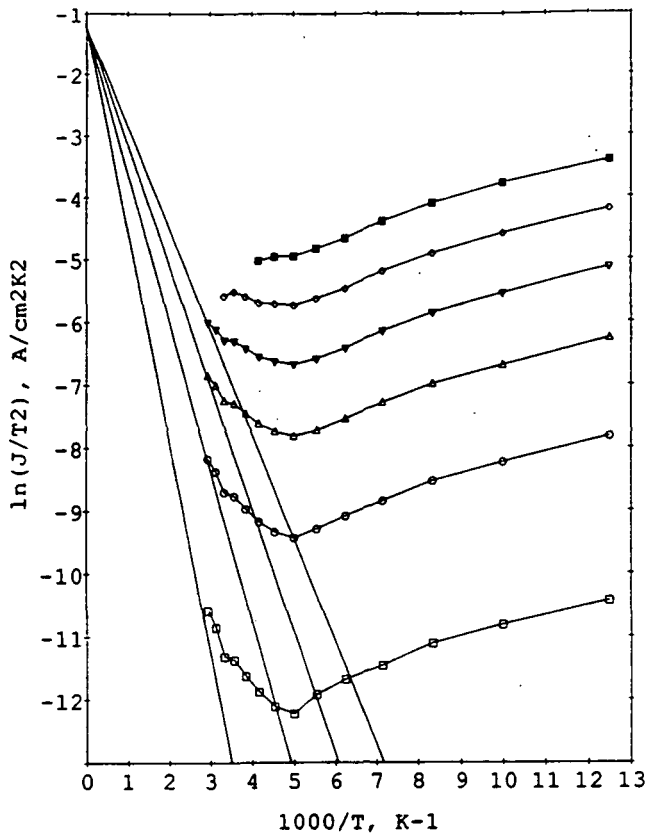

Fig. 1. Plotting of experimental data in a $\ln(J/T^2)$ vs. 1000/T diagram. The applied voltages are 0.1 V, 0.5 V, 1.0 V, 1.5 V, 2.0 V, and 2.5 V (filled squares).

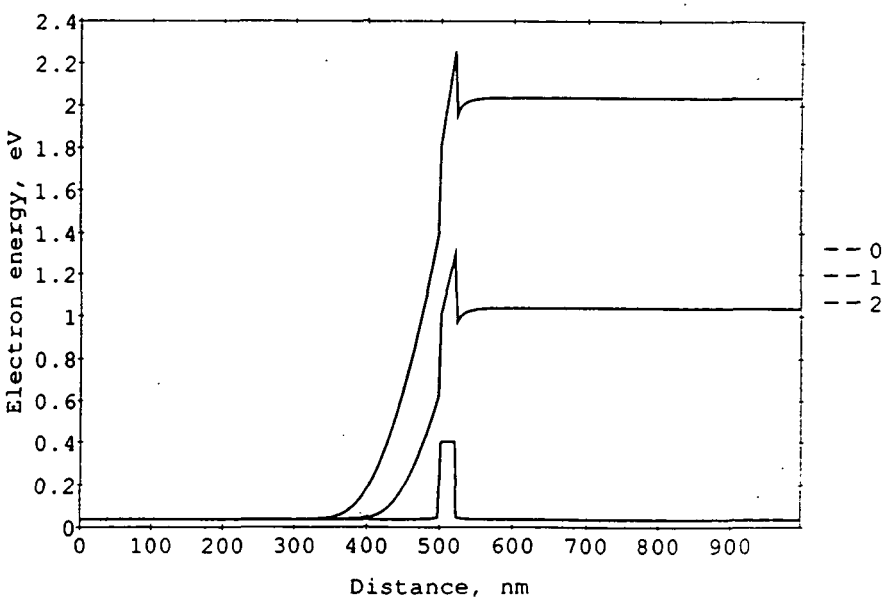

Fig. 2. Simulated conduction bands for different applied voltages (0.0 V, 1.0 V, and 2.0 V).

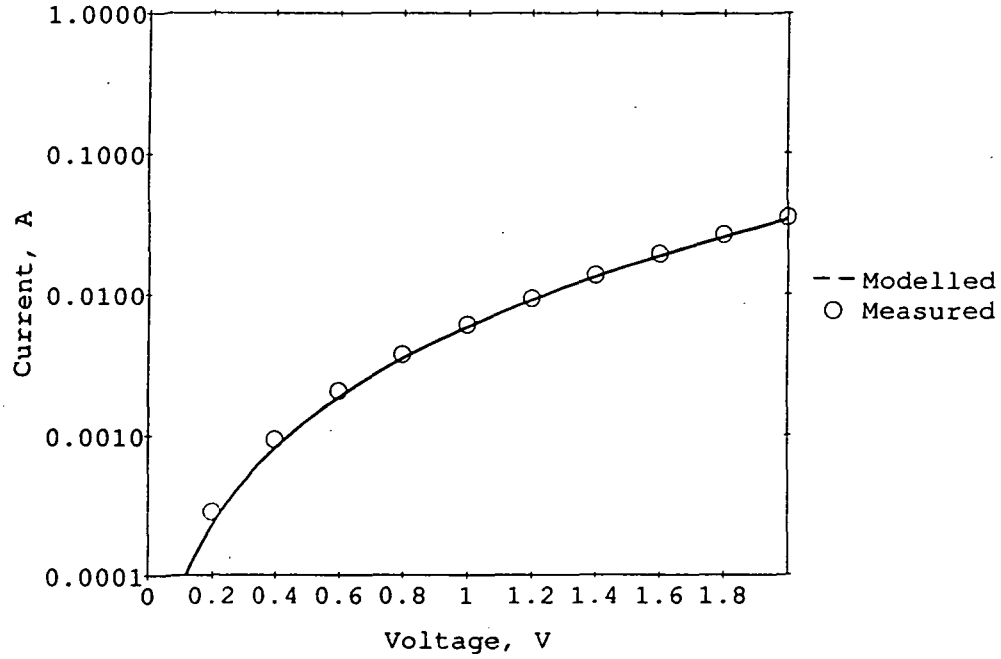

Fig. 3. Comparison between modelled and measured I–V characteristics at 300 K. The effects of thermally assisted tunneling and a nonabrupt heterojunction interface are included in the simulation.

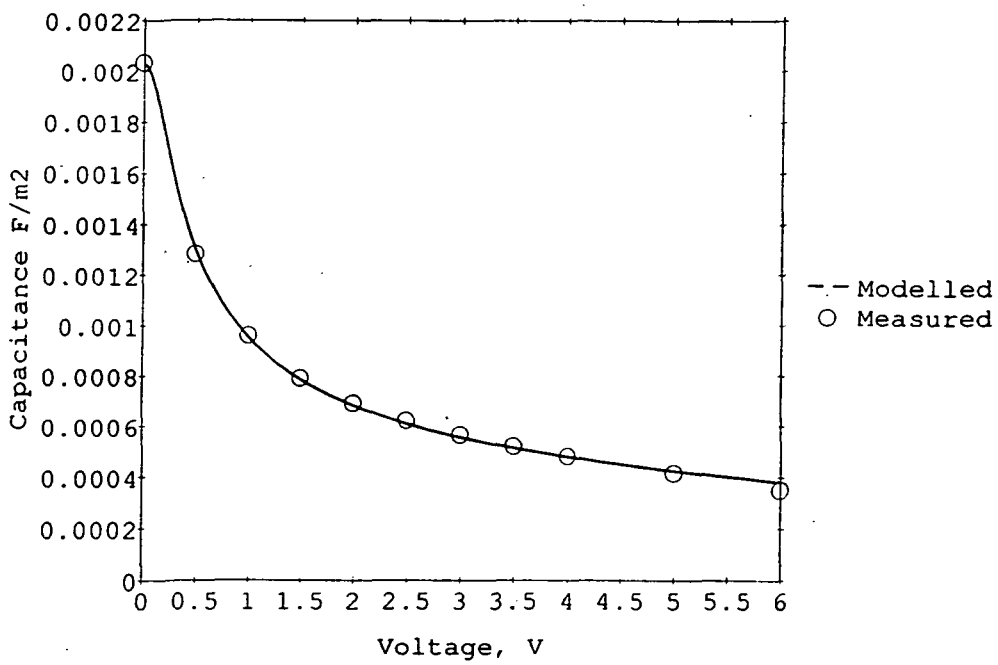

Fig. 4. Comparison between modelled and measured C–V characteristics at 300 K.

PROGRESS ON SINGLE BARRIER VARACTORS FOR SUBMILLIMETER WAVE POWER GENERATION

Svein M. Nilsen, Hans Grönqvist, Hans Hjelmgren, Anders Rydberg, and Erik L. Kollberg

The Millimeter Wave Group

Department of Applied Electron Physics, Chalmers University of Technology, S-412 96 Göteborg, Sweden

ABSTRACT

Theoretical work on Single Barrier Varactor (SBV) diodes, indicate that the efficiency for a multiplier has a maximum for a considerably smaller capacitance variation than previously thought. The theoretical calculations are performed, both with a simple theoretical model and a complete computer simulation using the method of harmonic balance. Modelling of the SBV is carried out in two steps. First, the semiconductor transport equations are solved simultaneously using a finite difference scheme in one dimension. Secondly, the calculated IV-, and CV characteristics are input to a multiplier simulator which calculates the optimum impedances, and output powers at the frequencies of interest. Multiple barrier varactors can also be modelled in this way. Several examples on how to design the semiconductor layers to obtain certain characteristics are given. The calculated conversion efficiencies of the modelled structures, in a multiplier circuit, are also presented. Computer simulations for a case study of a 750 GHz multiplier show that InAs diodes perform favourably compared to GaAs diodes. InAs and InGaAs SBV diodes have been fabricated and their current vs. voltage characteristics are presented. In the InAs diode, was the large bandgap semiconductor AlSb used as barrier. The InGaAs diode was grown lattice matched to an InP substrate with InAlAs as a barrier material. The current density is greatly reduced for these two material combinations, compared to that of GaAs/AlGaAs SBV diodes. GaAs based diodes can be biased to higher voltages than InAs diodes.

1. INTRODUCTION

A SBV device, in its simplest form, consists of a thin layer of a large bandgap material which acts as a barrier, and a thicker layer of a small bandgap material on each side of the barrier. A cross section of a typical SBV diode is shown in Fig. 1. The low bandgap material at both ends of the device is normally highly doped in order to make possible, the formation of low resistance contacts. Provided the layer thicknesses and doping concentrations are symmetrical around the barrier, the current I vs. voltage V and the capacitance C vs. voltage V will be be symmetrical around zero volt. An applied rf-voltage will then generate only odd harmonics. This makes it possible to design higher order multipliers with fewer idler circuits and thus less losses. Also the design procedure and mechanical construction of a higher order multiplier, making use of a SBV device as the non linear element will become much easier compared to that of one using a Schottky diode. It is the purpose of this paper to give an overview of our work on SBV diodes [1][2][15].

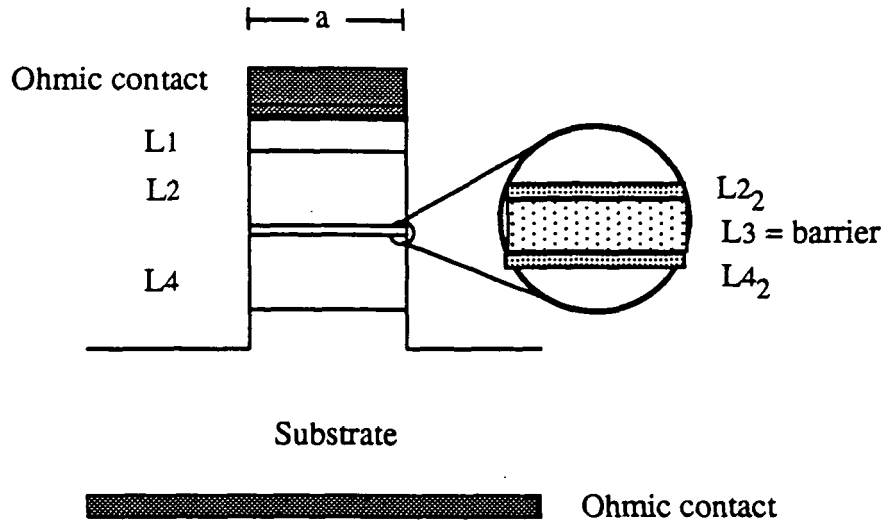

Fig. 1. Schematic cross section of a SBV mesa diode. L1 is the highly doped contact layer, $L2_n$ and $L4_n$ are the depletion regions on either side of the barrier, index n denotes sublayers, $L3_n$ is the barrier and L5 is part of the buffer/substrate layer. In the simulations L1 and L5 are set equal. Mesa diameter = a.

2. DIODES

2.1 Quality factor of SBV's

The cutoff frequency for a varactor, as defined in Eq. 1, is often used as a quality factor, suggesting that C_{max} should be as large as possible for a fixed C_{min}.

$$f_c = \frac{1}{2\pi R_{slo}}\left(\frac{1}{C_{min}} - \frac{1}{C_{max}}\right) \qquad (1)$$

where R_{slo} is the dc series resistance of the device, C_{max} and C_{min} are the calculated device capacitances for accumulated and depleted low doped epilayers, L2 and L4 in Fig.1, respectively.
However, a simple analysis show that an optimum C_{max}/C_{min} ratio exist. Choosing a CV characteristic as shown in Fig. 2 and assuming that all harmonics, except the first and third harmonics are shortcircuited over the variable capacitance, only these two frequency components have to be considered. The bias voltage is of course always zero volts. This makes the analysis quite simple. In Fig. 3 we have plotted the efficiency vs. C_{max}/C_{min} for different values of R_S, assuming $1/\omega C_{min}$ = 180 Ω. The important conclusion from this graph is that there is an optimum value for C_{max}/C_{min} , and that too large C_{max} values will deteriorate the multiplier's efficiency. Table 1 shows input and output impedances. Although this model is much simplified the results show that the input is highly reactive with a fairly low resistance while the output seems to be easier to match. This result will be confirmed below in the harmonic balance simulations employing a modified version of the computer program by P.H. Siegel et.al. [8].

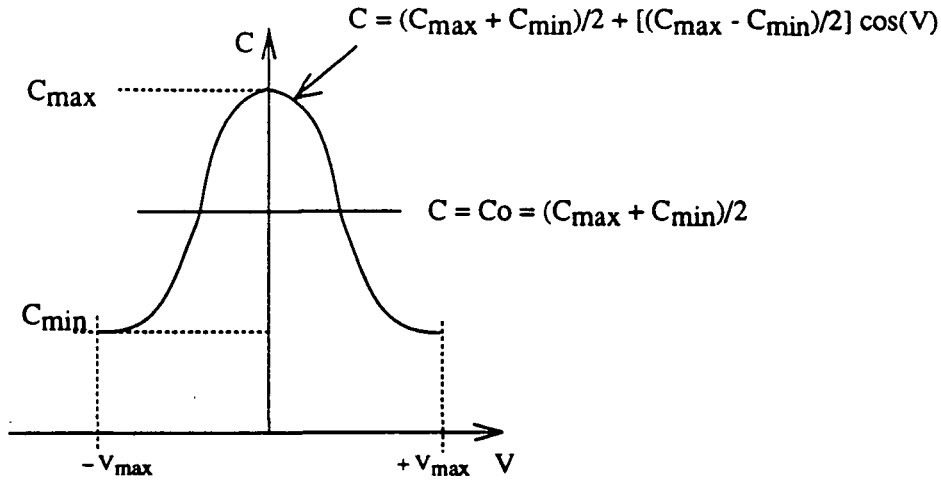

Fig. 2 Approximate CV characteristic of SBV diode used in the simplified analysis. V_{max} is the maximum voltage across the diode.

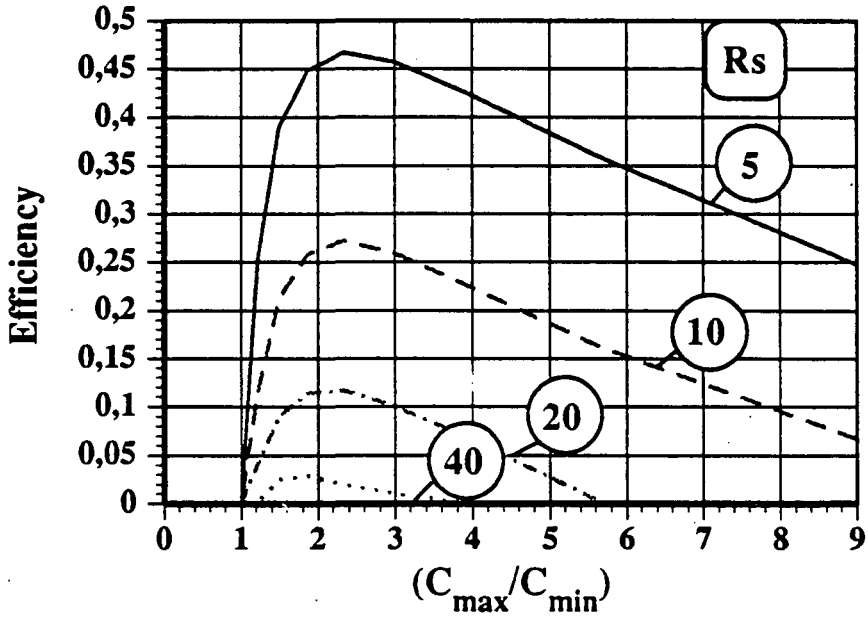

Fig. 3 Efficiency vs. the C_{max}/C_{min} ratio for different values of R_S.

Table 1 Calculated efficiencies, optimum input and output imedances for a SBV diode tripler with the approximate cosine shaped CV characteristic for different series resistances.

		SOURCE IMPEDANCE		LOAD IMPEDANCE	
Rs Ω	η_{max} %	R1 Ω	X1 Ω	R3 Ω	X3 Ω
2.5	65.5	8.6	91.0	29.5	34.0
5	46.7	10.9	90.0	30.4	33.0
10	27.2	15.7	95.0	30.2	36.0
20	11.8	25.0	90.0	23.0	33.0
40	2.9	44.1	106.0	14.0	38.0

2.2 MEASUREMENTS

2.2.1 DC measurements

We have fabricated several diodes based on the materials: GaAs, InGaAs and InAs, see Table 2 for details. Our efforts at modelling these devices are however, more recent. For the GaAs based diode we use a barrier of $Al_xGa_{1-x}As$, in the InGaAs case we use AlInAs as a barrier. The latter diode is grown lattice matched on an InP substrate. For the InAs diodes we use an AlSb barrier which gives a very high barrier, 1.3 eV for indirect transitions. It should therefore be very efficient in blocking the current through the varactor. The InAs device is grown on a GaAs substrate with thick GaAs and InAs buffer layers.

Table 2 Material from which diodes of various sizes have been fabricated.

Wafer #ID & Crystal Grower	Material system	Layer thickness (top/down) and doping concentration
#614 IMEC	GaAs/$Al_xGa_{1-x}As$/GaAs x = 0.70 in L3 Buffer: n^+ GaAs Substrate: n^+ GaAs	L1 = 400 nm, $N_d = 3.4*10^{18}$ [cm^{-3}] $L2_1$ = 533 nm, $N_d = 1.0*10^{17}$ [cm^{-3}] $L2_2$ = 5.3 nm, undoped L3 = 21.3 nm, undoped $L4_2 = L2_2$, $L4_1 = L2_1$ L5 = 1998 nm, $N_d = 3.4*10^{18}$ [cm^{-3}]
#1566 Chalmers	InAs/AlSb/InAs Buffer: n^+ InAs, and n^+ GaAs Substrate: n^+ GaAs Barrier thickness = L3	L1 = 200 nm, $N_d = 5.0*10^{18}$ [cm^{-3}] $L2_1$ = 400 nm, $N_d = 6.0*10^{16}$ [cm^{-3}] $L2_2$ = 5 nm, undoped L3 = 20 nm, undoped $L4_2 = L2_2$, $L4_1 = L2_1$ L5 = 2000 nm, $N_d = 5.0*10^{18}$ [cm^{-3}]
#1567 Chalmers	InAs/AlSb/InAs Buffer: n^+ InAs, and n^+ GaAs Substrate: n^+ GaAs Barrier thickness = L3	L1 = 200 nm, $N_d = 5.0*10^{18}$ [cm^{-3}] $L2_1$ = 320 nm, $N_d = 1.0*10^{17}$ [cm^{-3}] $L2_2$ = 5 nm, undoped L3 = 25 nm, undoped $L4_2 = L2_2$, $L4_1 = L2_1$ L5 = 2000 nm, $N_d = 5.0*10^{18}$ [cm^{-3}]
#ST1 Tampere	Lattice matched InGaAs/AlInAs/InGaAs Buffer: n^+ InGaAs Substrate: n^+ InP Barrier thickness = L3	L1 = 400 nm, $N_d = 4.0*10^{18}$ [cm^{-3}] L2 = 400 nm, $N_d = 6.0*10^{16}$ [cm^{-3}] L3 = 25 nm, $N_d = 6.0*10^{16}$ [cm^{-3}] L4 = L2 L5 = 1000 nm, $N_d = 4.0*10^{18}$ [cm^{-3}]
#1047 IMEC	InAs/AlSb/InAs Buffer: n^+ InAs, and n^+ GaAs Substrate: n^+ GaAs Barrier thickness = L3	L1 = 200 nm, $N_d = 2.6*10^{18}$ [cm^{-3}] L2 = 150 nm, $N_d = 1.0*10^{17}$ [cm^{-3}] L3 = 14 nm, undoped L4 = L2 L5 = 3000 nm, $N_d = 2.6*10^{18}$ [cm^{-3}]

The influence of the epilayer design on the IV-, and CV characteristics has been investigated theoretically in some detail.
The different SBV diodes fabricated by us have been DC characterized with a DC parameter analyzer. Most of the measurements have been done on large area diodes, 100– 2500 μm^2. A limited number of measurements have been made on small area, 7 μm^2, diodes of the #614 type.
Diodes characterized are one GaAs varactor with an AlGaAs barrier, one diode grown on InP with InGaAs and InAlAs epilayers lattice matched to the substrate and two InAs diodes with AlSb barriers grown on GaAs substrates. The material from which we have fabricated devices are listed in Table 2. DC characterization of the different SBV diodes show that the current density is decreased as the barrier height is increased as expected, see Fig. 4. The InAs/AlSb material system has a 1.3 eV barrier for indirect transitions and ≈ 2 eV for direct. The lowest current density is obtained for InAs/AlSb devices. They also show a large variation in their characteristics, a factor of two or more in current density over a distance of a few millimeters on the wafer. Whether this variation is caused by the epilayers being severely lattice mismatched to the substrate or by some growth parameter, is difficult to say. In comparison, diodes of the lattice matched InGaAs/InAlAs materials grown on InP substrate as well as those of GaAs/AlGaAs show current density variations of only a few percent over the same distance. It can also be noted that the breakdown voltage of the InAs and InGaAs diodes is low, about 2 Volt, in comparison with the GaAs diode. For a varactor to be used in practice the breakdown voltage needs to be higher since the pump voltage otherwise could destroy the diode. One method of increasing the total breakdown voltage is to fabricate several varactor diodes in series. Each of n identical diodes would then only need to sustain the total pump voltage divided by n.

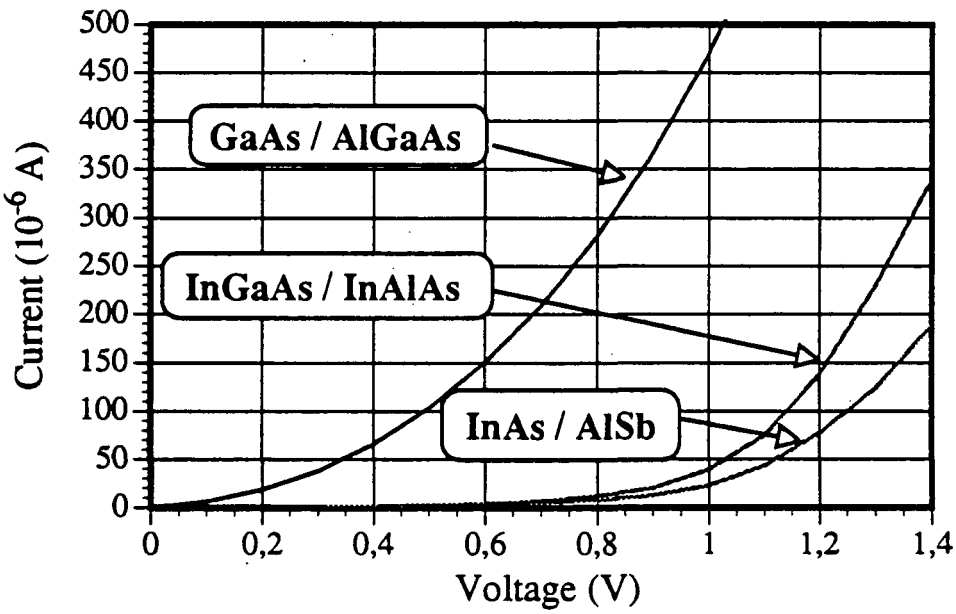

Fig. 4 Measured current vs. voltage for SBV diodes of size 25*25 μm^2 in different material systems.

2.2.2 RF measurements

Two methods have been developed for measuring the capacitance of these diodes, the results will be published elsewhere [14]. One method is similar to the one by Tolmunen et. al. [15], the other method uses a 60 GHz coplanar probe to contact a mesa diode surrounded by a large ring which is contacted by the two ground contacts of the probe.

2.3 MODELLING DEVICES AND MULTIPLIER PERFORMANCE

2.3.1 CV and IV modelling

For calculating the CV-, and IV characteristics, the semiconductor transport equations including the energy balance equations for holes and electrons are solved simultaneously using a finite-difference scheme in a detailed one-dimensional energy transport model for GaAs/$Al_xGa_{1-x}As$ heterojunction structures with $0.0 < x < 1.0$. The computer program is a modified version of the program developed by H. Hjelmgren [3][4]. The program can readily be modified further for other heterostructures. A non-uniform grid-mesh is used to obtain the necessary accuracy and acceptable calculation times. Position dependent barrier parameters were implemented following the procedure of M. S. Lundstrom and R.J, Schuelke [5]. The model used is based on the paper by R. Stratton [6]. The five variables are the electric potential, the quasi-Fermi levels for holes and electrons, and hole and electron temperatures. The equation system has a 19 diagonals band-matrix which is solved by LU decomposition. To improve the convergence properties of the program the energy balance equation for holes is not used, hence the hole temperature is set to the lattice temperature for all applied voltages. Hot electrons and lattice heating are not simulated, hence the five equation model is reduced to a three equation (Poisson's and current continuity equations) model. Recombination is modelled with Shockley Read Hall (SRH) recombination. The relaxation time was set to 3.0 ps, the electron life time to 1.0 ns, and the conduction band-offset to 65 % in most simulations for which $x < 0.45$. The contact resistivity of the two ohmic contacts can be set to a value of choice. They are modelled by modifying the boundary conditions for the potential. The thermoionic emission current, which limits the current through the device, is then calculated from the equation for a reverse biased Schottky diode, using a voltage dependent barrier-height obtained from the shape of the conduction band. Tunneling current is assumed to be sufficiently small and thus neglected altogether.
The diode capacitance, $C = dQ/dV \approx \Delta Q/\Delta V$ is determined numerically from the change ΔQ in the stored electric charge in the semiconductor for an incremental change ΔV in the applied voltage. The integration of charges is carried out to the middle of the barrier for single barrier devices. To obtain the depletion capacitance one must correct for the influence of the series resistance on the voltage across the depletion layer.

2.3.2 CV characteristics and conversion efficiencies of modelled structures.

It is of importance to understand how the CV characteristic can be modified by changes to the design of the epitaxial structure. It is obvious that increasing the width of the barrier will decrease C_{max}, and that a wider L2 region, see Fig. 1, will allow a larger capacitance swing, i.e. make C_{min} smaller. Below we will investigate how the doping profile of the diode affects the efficiency of a 3*60 GHz tripler. The effect of the plasma resonance on the series resistance was not included in the multiplier calculations on structures #100-103B, #112 and #114 at 3*60 GHz.

The following rules are basic to the understanding of the behaviour of the CV characteristic for different choices of doping concentrations, viz.

i. Doping the barrier will increase C_{max} without influencing the capacitance value at large biases, i.e. C_{min} is not much affected. This phenomenon is studied in structures #100-103B. However, too many dopants in the barrier and its blocking capability may be destroyed.

ii. A similiar effect, an increase in C_{max}, can be obtained by introducing thin regions with high doping concentration adjacent to the barrier on each side. One such example is #112. This scheme may be less damaging to the barrier's blocking capability, but it may also affect material quality in a negative way or make symmetrical growth more difficult.

iii. A reduced doping concentration in the L2 layer where the depletion occurs, will cause a more rapid change in the capacitance vs. bias voltage. It will also lead to a larger series resistance. The method cannot therefore be recommended as a stand alone measure.

iv. To avoid an increase in the series resistance according to **iii.**, a tapered doping concentration in the L2 region will improve the situation. A comparison between #112 and #114 illustrates this phenomenon.

Please note that the choice of doping profile will also influence the series resistance. An advantageous CV characteristic may offer an undesireably large series resistance.

The effect of doping the barrier on the CV characteristic is illustrated in Fig. 5 which show the results for structures #100-103B. The increase in C_{max} is as large as 70 % when the doping is increased from $1*10^{15}$ cm^{-3} to $1*10^{18}$ cm^{-3}. To see any effect at all, the doping in the barrier needs to exceed $1*10^{17}$ cm^{-3}. The series resistance remains the same of course, since it is essentially determined by the doping in region L2. In Fig. 6 is shown the conversion efficiency vs. input power (all input power is assumed to be absorbed). It is interesting to note that the efficiency actually decreases as C_{max} increases. This is in agreement with the results presented in paragraph 2.1.
The effect of a high doping concentration near the barrier interface is illustrated by the CV characteristic of #112 in Fig. 7. Notice that the CV is almost identical to the one of #103. Since the series resistances are also very similar, the efficiencies vs. pump power are virtually identical as can be seen in Fig. 6 and Fig. 8.
Structure #114 has a linearly graded doping concentration in the L2 and L4 regions, starting with $1*10^{15}$ cm^{-3} near the barrier and increasing to $2*10^{17}$ cm^{-3} at a distance of 385 nm from the barrier. The ratio C_{max}/C_{min} is increased considerably compared to that of a homogenously doped L2 region, but the series resistance is larger than for #100-103B. The CV resembles mostly that of #103B. The capacitance swings down faster, but have the same C_{min} and a small reduction in efficiency.

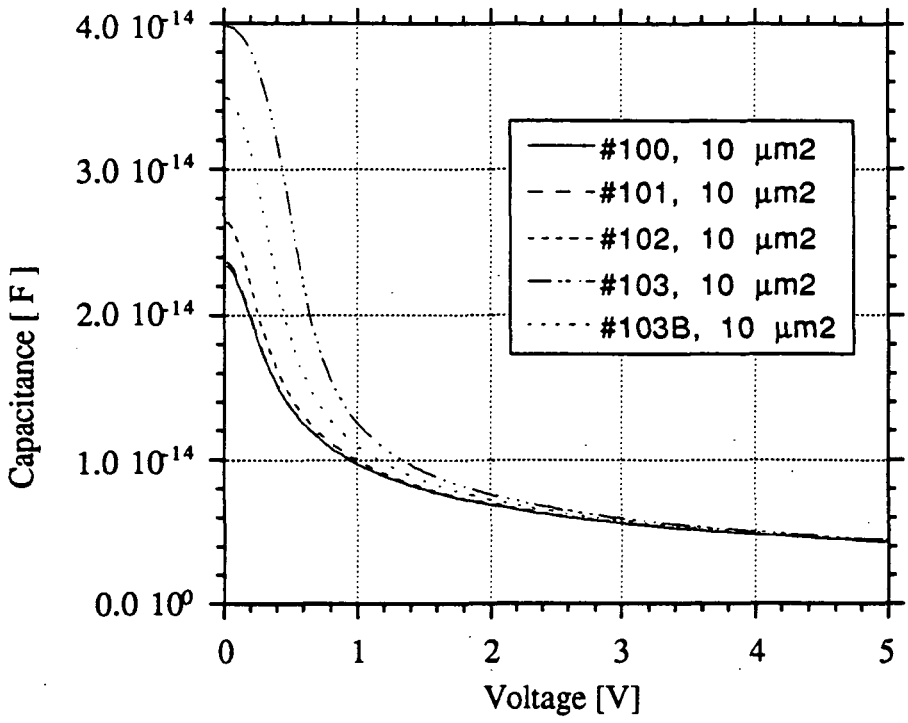

Fig. 5 Calculated CV characteristics for symmetric GaAs/$Al_{0.44}Ga_{0.56}As$ structures #100-103, #103B with different barrier doping. L2 = L4 = 390 nm with $1.0*10^{17}$ cm^{-3}, L3 = 20 nm, for **#100:** $N_d = 1.0*10^{15}$ cm^{-3}, for **#101:** $N_d = 1.0*10^{16}$ cm^{-3}, for **#102:** $N_d = 1.0*10^{17}$ cm^{-3}, for **#103B:** $N_d = 5.0*10^{17}$ cm^{-3}, for **#103:** $N_d = 1.0*10^{18}$ cm^{-3}.
For all structures L1 = L5= 100 nm, $N_d = 3.4*10^{18}$ cm^{-3}

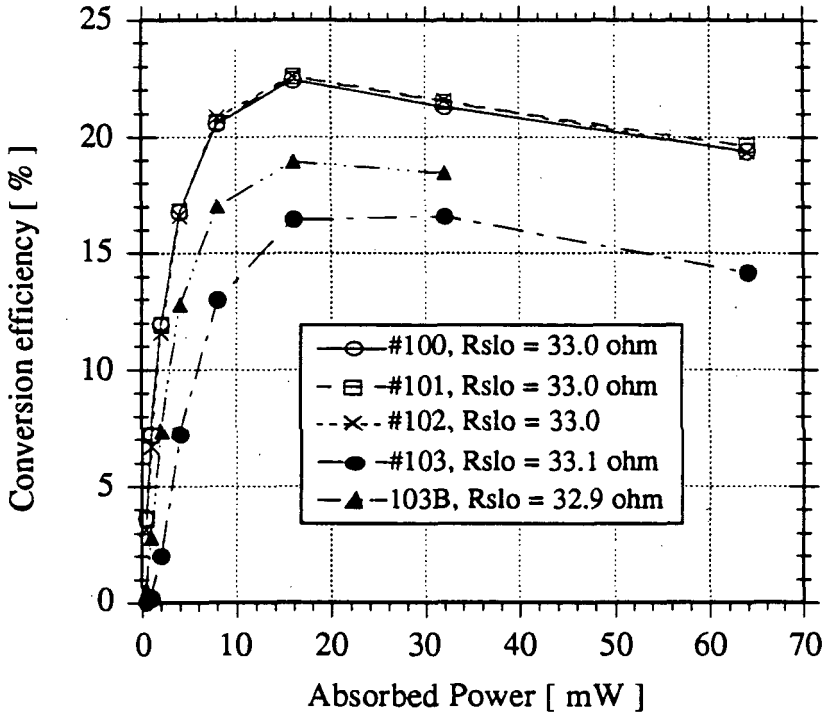

Fig. 6 Calculated conversion efficiency vs. pump power for structures #100-103 and #103B at 3*60 GHz. It is the devices with undoped or low doped barrier which have the highest conversion efficiency. The series resistance R_{slo} used was between 32.9 and 33.1 ohm (calculated by the simulation program) for all five structures.

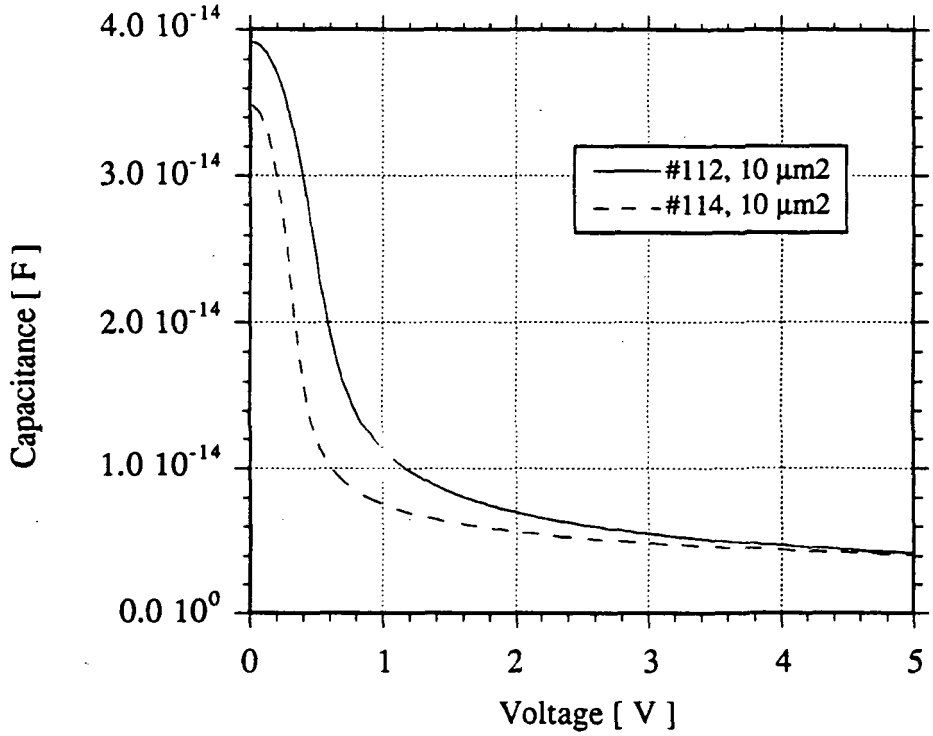

Fig. 7 Calculated CV characteristics for symmetric GaAs/$Al_{0.44}Ga_{0.56}As$ structures for different doping profiles in the L2 region meant to enhance the C_{max}/C_{min} ratio.
#112 has $L2_1 = L4_1 = 386$ nm with N_d going from $1.0*10^{17}$ cm^{-3} to $0.8*10^{17}$ cm^{-3} at the barrier interface, i.e. a weak gradient, $L2_2 = L4_2 =$ 4 nm with $N_d = 1.0*10^{17}$ cm^{-3}, L3 consists of three parts, $L3_1 = L3_3 = 7$ nm $N_d = 1.0*10^{18}$ cm^{-3}, $L3_2 = 6$ nm $N_d = 2.0*10^{17}$ cm^{-3}.
#114 has $L2_1 = L4_1 = 385$ nm with N_d going from $2.0*10^{17}$ cm^{-3} to $1.0*10^{15}$ cm^{-3} at the barrier interface, i.e. a steep gradient, $L2_2 = L4_2 =$ 5 nm with $N_d = 5.0*10^{16}$ cm^{-3}, L3 consists of three parts, $L3_1 = L3_3 = 6$ nm $N_d = 1.0*10^{18}$ cm^{-3}, $L3_2 = 8$ nm $N_d = 5.0*10^{16}$ cm^{-3}.
$L1 = L5 = 100$ nm with $N_d = 3.4*10^{18}$ cm^{-3} for both structures.

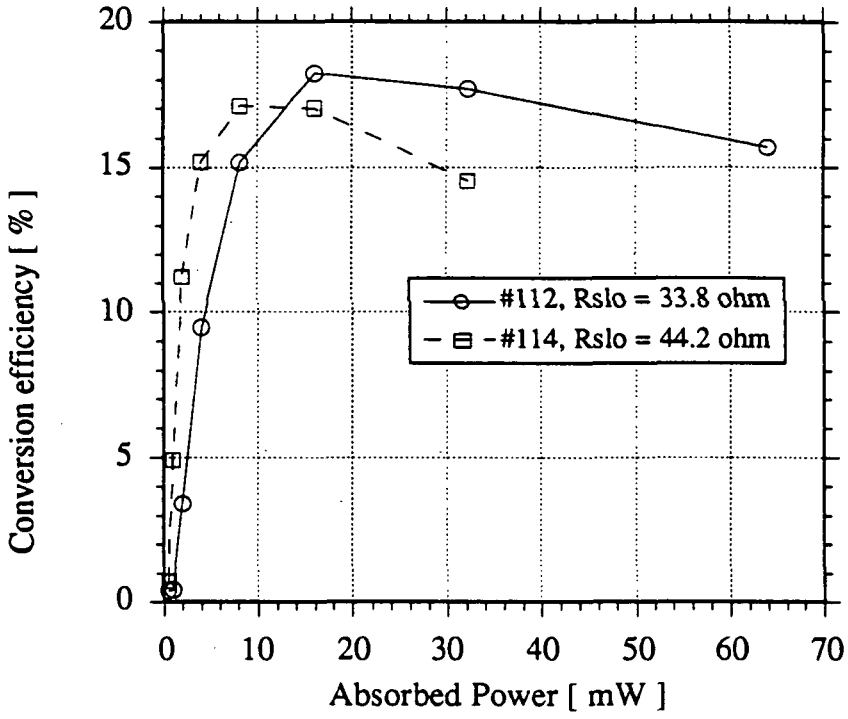

Fig. 8 Calculated conversion efficiency vs. pump power for structures #112 and #114 at 3*60 GHz. The value of R_{slo} was 33.8 ohm for #112 and 44.2 ohm for #114.

3. A 750 GHz MULTIPLIER DESIGN STUDY

A study on different 750 GHz multiplier configurations using GaAs and InAs SBV-diodes was performed. The aim of the study was to evaluate theoretically the optimum frequency multiplier configuration for generating ≥ 50 μW of output power at 750 GHz, assumed to be enough for pumping a 750 GHz SIS mixer, using a Single Barrier Varactor (SBV) diode as the nonlinear element.
Different important diode parameters were investigated, such as the cutoff frequency which is a direct function of the doping level N_d of the low doped epilayers, L2 and L4 in Fig.1, in the device. The cutoff frequency was calculated for GaAs and InAs SBV-diodes of three different sizes, see Fig. 9. In these calculations of C_{max} and cutoff frequencies, it was assumed that the effective barrier width was three times that of L3 because of the distance necessary for a lineup of the fermi levels at the interface between the low doped layer L2 and the undoped barrier L3. It can be seen that the optimum doping concentration is $1*10^{17}cm^{-3}$ and $2*10^{17}cm^{-3}$ for GaAs and InAs devices respectively, both having a diameter of 2 μm.

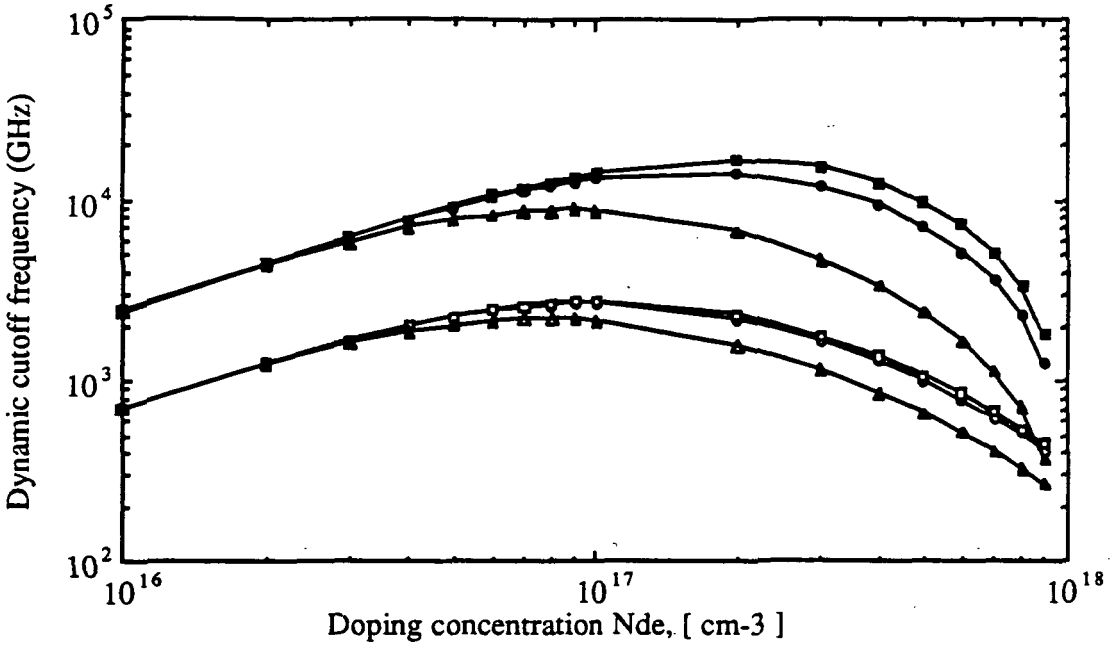

Fig 9 Calculated cutoff frequency vs. doping level N_{de} for GaAs and InAs SBV-diodes of different diameters a. $N_{ds} = 3.4*10^{18}cm^{-3}$ in L1 and L5, $N_{db} = 1*10^{17}cm^{-3}$ in L3, L1 = 100 nm, L5 = 100 nm, L2 varies with N_{de}, the barrier width L3 is 20 nm.
GaAs: (□): a = 2 μm., (○): a = 4 μm., (Δ): a = 20 μm.
InAs: (■): a = 2 μm., (●): a = 4 μm., (▲): a = 20 μm.

Another important parameter to consider is the effect of the plasma resonance frequency on the series resistance of the diodes [7]. This is of great importance to devices intended for THz frequencies. In Fig.10 is plotted the calculated series resistance for InAs SBV-diodes when the plasmaresonance is taken into account . It is found that by using InAs instead of GaAs in the low doped epilayers and in the substrate, the plasma resonance frequencies are shifted to higher frequencies. This is due to the higher electrical conductivity σ of InAs compared to that of GaAs. It can be seen in Fig. 10 that a doping N_d in L2 and L4 of about $1*10^{17}$ cm^{-3} gives sufficient clearence up to a frequency of 2 THz

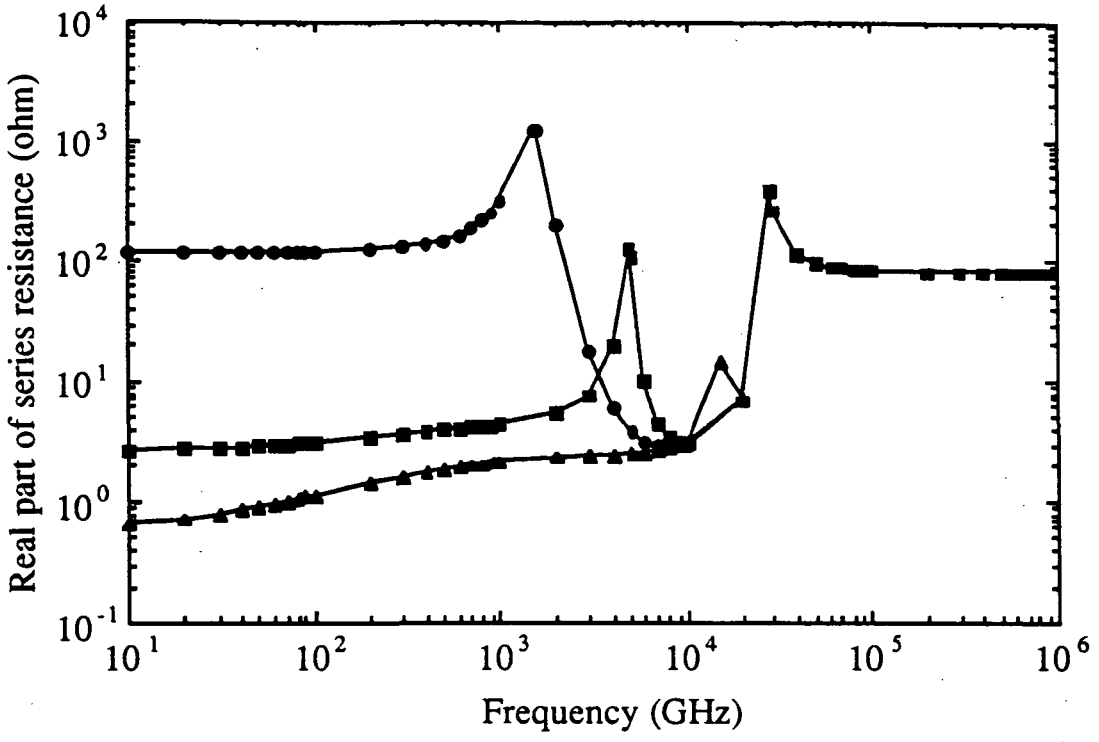

Fig. 10 Calculated series resistance vs. pump frequency for an InAs SBV-diode for different doping levels N_{de} in the low doped epilayers L2 and L4. Doping concentration N_{ds} is $3.4*10^{18}$ cm^{-3} in L1 and L5, N_b is $1*10^{17}$ cm^{-3} in the barrier L3, L1 =100 nm, L5 = 100 nm, L2 = L4 = 533 nm, L3 = 20 nm, diameter a = 3.57 μm.
(●): N_{de} is $1*10^{16}$ cm^{-3}., (■): N_{de} is $1*10^{17}$ cm^{-3}.,
(▲): N_{de} is $1*10^{18}$ cm^{-3}.

The avalanche breakdown voltage for the low doped epilayers limits the maximum pump power that can be used for the device. Using the optimum doping concentration the breakdown voltage was calculated to be 15.7 V for GaAs and 1.2 V for InAs, and having depletion lengths of 480 nm and 100 nm respectively. Due to the very small breakdown voltage for the low doped InAs epilayers, L2 and L4 in Fig. 1, the doping of the epilayers was reduced slightly to a constant value of $1*10^{17}$ cm^{-3} which gives a breakdown voltage of 2 V and a length of 179 nm for the L2 and L4 epilayers.
The structure chosen for further study in the InAs/AlSb/InAs material system was the following: L1 = 100 nm with $N_d = 3.4*10^{18}$ cm^{-3}, L2 = 150 nm with $N_d = 1*10^{17}$ cm^{-3}, L3 = 14 nm with $N_d = 5*10^{15}$ cm^{-3}, L4 = L2, L5 > L1.
Since the barrier length is choosen to be 14 nm thick, the tunneling current may for such a thin barrier not be negligable in reality, especially not at room temperature, why a thicker barrier may be more appropriate. The total current through the SBV-diode consists of (i) the dc-current, mainly thermionic current, and (ii) the displacement current due to the rf-voltage variation over the depletion region. Increasing the dc-current compared to the displacement current makes the tripler work more in a varistor mode with a reduced efficiency, see Fig. 11.

It is assumed in the simulations that the same IV and CV characteristic calculated for a GaAs based SBV-diode can also be used for InAs based diodes, of a similar design. This assumption is due to the fact that the difference in conduction current, see Fig.4, between InAs and GaAs diodes at a fixed bias voltage, has been found to have a negligible influence on the efficiency, see Fig. 11.

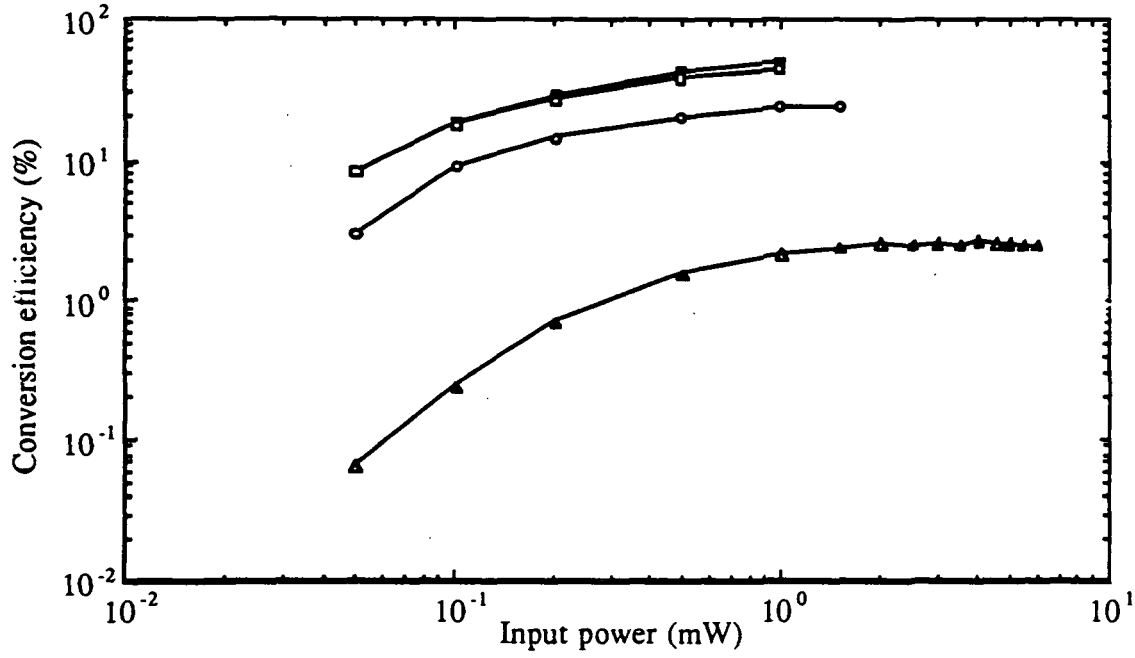

Fig. 11 Calculated conversion efficiency versus input power, when varying the calculated conductance, dI/dV, for the device in steps of $(dI/dV)*10^{y}$, where y is 0, 1, 2 or 3. $N_{ds} = 3.4*10^{18}$ cm^{-3}, $N_{de} = 1*10^{17}$ cm^{-3}, $N_{db} = 5*10^{15}$ cm^{-3}, L1 = 100 nm, L5 = 100 nm, L2 = L4 = 150 nm, L3 = 14 nm, diameter a = 2 μm. (■): y=0.0, (□): y=1.0, (○): y=2.0, (△): y=3.0

Three different multiplier configurations for generating the desired output power of ≥ 50 μW at 750 GHz have been investigated, see Fig. 12. In the calculations was the effect on the series resistance from the plasma resonance included.
Due to the different frequencies for pumping the 750 GHz SBV-diode multipliers, see Fig. 12, the expected maximum available input power differs considerably, as shown in the figure. It should be observed that 11 mW of output power from a 250 GHz Schottky-varactor diode tripler, see Fig. 12, is achieved at operating conditions close to the Schottky diode burnout [9]. Thus a more realistic value of a maximum of 6 mW of output power was used for the 250 GHz tripler. In the calculations the maximum allowed input power was set to such a value that the rf-voltage V_{rf} over the device, minus the rf-voltage over the series resistance, is less than or equal to the breakdown voltage V_{br} of the low doped epilayer L2.

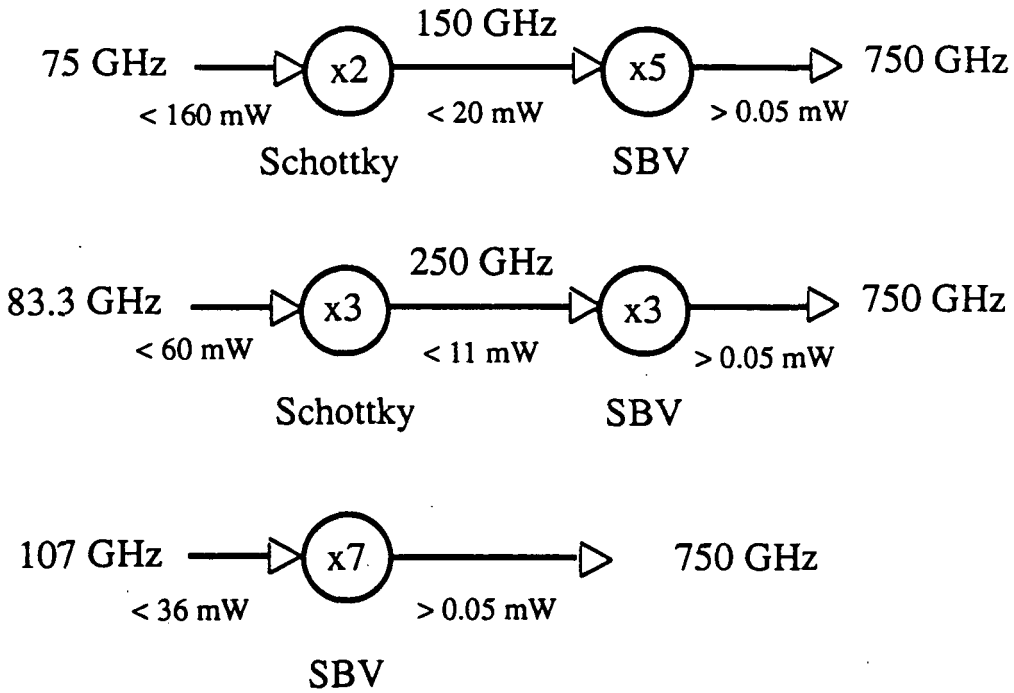

Fig. 12 The different 750 GHz multiplier configurations investigated in this study.

The conversion efficiency for 750 GHz SBV-diode multipliers using SBV-diodes based on InAs and GaAs is shown in Fig. 13. Simulations for two different contact resistances Rc = $8*10^{-7}$ ohmcm^2 and $1*10^{-8}$ ohmcm^2 were used for the GaAs SBV-diodes, in order to evaluate what implications the choice of material has on the efficiency of the device. The higher electron mobility in InAs reduces the series resistance of the diode, thus giving InAs SBV-diodes an advantage in efficiency for low input powers over GaAs SBV-diodes, having the same ohmic contact resistance. This advantage in efficiency is even larger when a more realistic ohmic contact resistance, Rc, of $8*10^{-7}$ ohmcm^2 is used for the GaAs SBV-diodes. The efficiency of the multipliers increases with increasing multiplication rate, see Fig. 13, in principle in the same way for the different SBV-diodes. This is due to the fact that at lower frequencies the impedance (resistance R_V and reactance jX_V) of the variable capacitance increases, i.e. becomes larger as compared to R_S. The efficiency is proportional to $R_V//(R_V + R_S)$, see ref.[10]. The cutoff frequency is defined in Eq. 1.

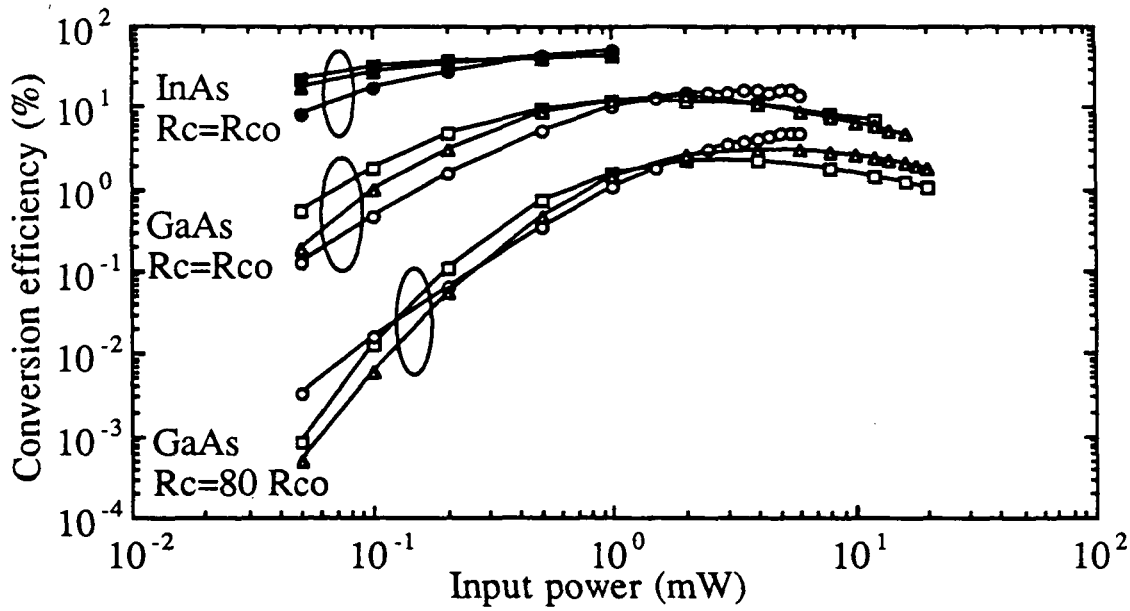

Fig. 13 Calculated conversion efficiency versus input power for various multiplier configurations, see Fig.12, using InAs and GaAs SBV-diodes as the nonlinear element. Two GaAs SBV-diodes having different contact resistances Rc, (=R_{co} in the figure), are shown in the figure where $R_{co} = 1*10^{-8}$ ohmcm^2. $N_{ds} = 3.4*10^{18}$ cm^{-3}, $N_{de} = 1*10^{17}$ cm^{-3}, $N_b = 5*10^{15}$ cm^{-3}, L1 = 100 nm, L5 = 100 nm, L2 = L4 = 150 nm, L3 = 14 nm, diameter a = 2 μm.
(○): GaAs SBV-diode tripler, (△): GaAs SBV-diode quintupler,
(□): GaAs SBV-diode heptupler, (●): InAs SBV-diode tripler,
(▲): InAs SBV-diode quintupler and (■):InAs SBV-diode heptupler.

Using a larger diameter SBV-diode means of course a lower impedance, although it can handle a larger input power before V_{rf} exceeds the breakdown voltage V_{br}. A larger diameter device will also withstand larger thermal heating, caused by the absorbed pump power, before efficiency degradation occurs due to the reduced mobility of the electrons. The mobility μ of the electrons is proportional to the temperature T of the material, where for GaAs: $\mu \sim T^{1/2}$ and for InAs: $\mu \sim T^{3/2}$ [11][12]. Thus InAs is more sensitive to thermal heating. However, since the breakdown voltage for InAs material is small compared to GaAs, the level of the absorbed power is restricted from that point of view. The influence of the thermal characteristics of the SBV-diode on the efficiency is not taken into account in this study.
The calculated output power, using the values for the efficiency shown in Fig. 13, is shown in Fig. 14. The simulated output power for a state of the art 2.8 fF Schottky-varactor diode described in [13], is also shown in Fig. 14 where it can be seen that the maximum output power for the Schottky-varactor diode clearly exceeds the output power for GaAs SBV-diodes having a contact resistance of $8*10^{-7}$ ohmcm^2 ($80R_{co}$), for the same input power. However, it should be noted that output powers comparable to the Schottky-varactor diode tripler are achieved from the InAs SBV-diode multipliers at much lower input power, even though the Schottky-varactor diode is capable of generating at least twice the output power compared to the InAs SBV-diode before the diode voltage exceeds the breakdown voltage for the device.

It should be noted that the calculations for the Schottky-varactor tripler assume optimum match at all frequencies for the tripler, i.e. including the idler. For the SBV-diode tripler is optimum match only considered for the input and output frequencies. Thus the matching conditions are much easier to obtain for the SBV-diode compared to the Schottky-varactor diode, in reality giving the SBV-diode an advantage in efficiency compared to the Schottky-varactor diode. Also the unavoidable resistive losses at the idler frequency in the Schottky-varactor diode tripler gives the SBV-diode tripler an even greater advantage.
The expected losses in the 750 GHz tripler mount is assumed to be less than 10 dB. However it can be seen from Fig. 14 that the only realistic SBV-diodes capable of generate ≥ 500 μW, necessary for ≥ 50 μW of output power at 750 GHz are InAs based diodes, even though this is achieved close to or at the breakdown voltage V_{br} limit for the InAs devices. Although the breakdown voltage V_{br} and thereby also the maximum allowed absorbed input power for the InAs SBV-diodes are much smaller than for the GaAs SBV-diodes, it can be compensated for by connecting several InAs/AlSb junctions in series, creating a multiple barrier InAs SBV-diode.

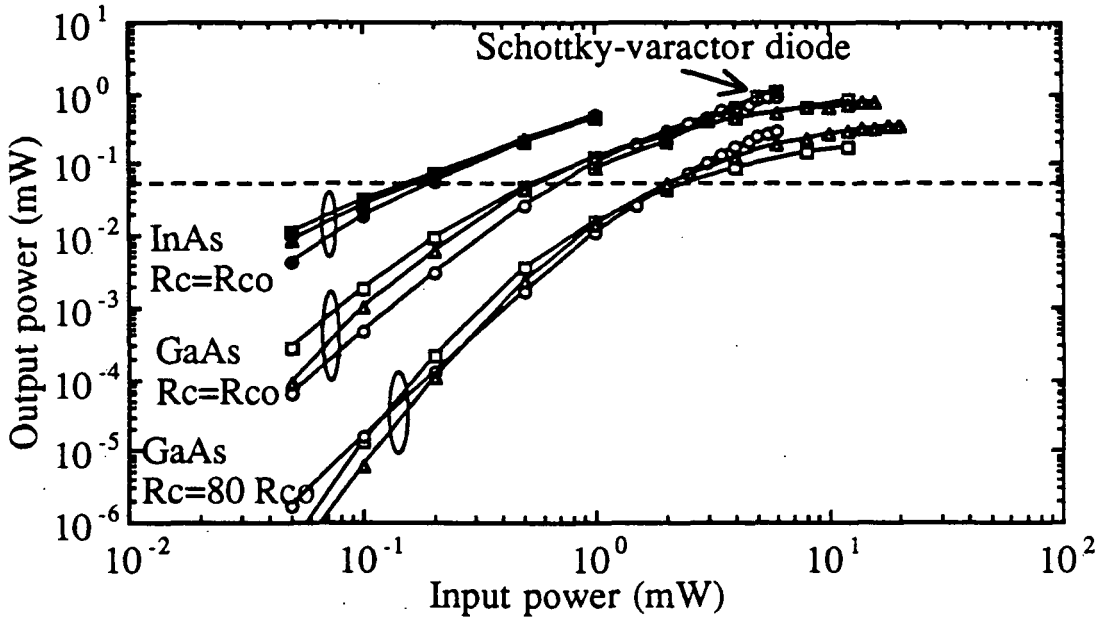

Fig. 14 Calculated output power versus input power for various multiplier configurations, using InAs and GaAs SBV-diodes and a Schottky-varactor diode as the nonlinear element in the multiplier. Two GaAs SBV-diodes having different contact resistances Rc, (=Rco in the figure), are shown in the figure where $R_{co} = 1*10^{-8}$ ohmcm^2. $N_{ds} = 3.4*10^{18}$ cm^{-3}, $N_{de} = 1*10^{17}$ cm^{-3}, $N_b = 5*10^{15}$ cm^{-3}, L1 = 100 nm, L5 = 100 nm, L2 = L4 = 150 nm, L3 = 14 nm and diameter a = 2 μm.
(○): GaAs SBV-diode tripler, (△): GaAs SBV-diode quintupler,
(□): GaAs SBV-diode heptupler, (●): InAs SBV-diode tripler,
(▲): InAs SBV-diode quintupler, (■): InAs SBV-diode heptupler, and
(⊞): Schottky-varactor tripler with $C_0 = 2.8$ fF and $R_S = 20$ ohm [13].

It should also be noted that the GaAs SBV-diode, Rc = $8*10^{-7}$ ohmcm^2, could in principle be pumped by a much larger input power than 6 mW, used in Fig. 14, before the diode voltage exceeds the breakdown voltage V_{br} of the device.
The dotted line in Fig. 14 marks the minimum 50 μW output power limit, which has to be exceeded, assuming no losses in the mount.
As can also be seen in Fig. 14, higher order InAs SBV-diode multipliers can be used for generating the necessary 500 μW of output power. The penalty for using a higher order multiplier is more resistive losses due to a larger number of idler circuits.

4. CONCLUSIONS

Theoretical work on multipliers show a maximum efficiency for a lower Cmax to Cmin ratio than expected. This has been shown both in simplified calculations as well as in full harmonic balance simulations. These findings have several implications. First, there is no need for a thin barrier. Secondly, a wider barrier reduces the current. This also make simulations easier. The C vs. V characteristics have been simulated from epilayer parameters and the impact of different doping structures on both the CV and the efficiency for the multipier has been presented. The examples presented can be used as *design rules*.. In a case study for a 750GHz multiplier an InAs SBV diode outperforms a Schottky diode.

5. ACKNOWLEDGEMENTS

Mikael Ekenstedt, Dept. of Physics, Chalmers University of Technology for growing wafers #1566 and #1567. This work has been supported by ESA/ESTEC under contract 7898/88/NL/PB(SC) and The Swedish National Board for Industrial and Technical Development (NUTEK).

6. REFERENCES

[1] Hans Grönqvist, Erik Kollberg, Anders Rydberg, "Quantum-well and quantum-barrier diodes for generating submillimeter wave power", Microwave and Optical Technology Letters, Vol. 4, No. 1, pp 33-38, 1991.

[2] E. Kollberg, T. Tolmunen, M. Frerking, J. East, "Current saturation in sub-millimeter wave varactors", to be published in IEEE Transactions on.Microwave Theory and Techn., May 1992.

[3] Hans Hjelmgren, "Numerical modelling of hot electrons in n-GaAs Schottky barrier diodes", IEEE Trans. on Electron Devices, vol. ED-37, No. 5, pp 1228-1234, May 1990.

[4] Hans Hjelmgren, Erik Kollberg, and Lennart Lundgren, "Numerical simulations of the capacitance of forward-biased Schottky diodes", Solid-State Electronics Vol. 34, No. 6, pp. 587-590, 1991

[5] M. S. Lundstrom and R.J, Schuelke, "Numerical analysis of heterostructure semiconductor devices," IEEE Trans. Electron Dev., vol. ED-30,p.1151-1159, 1983.

[6] R. Stratton, "Diffusion of hot and cold electrons in semiconductor barriers", Phys. Rev., vol. 126, pp 2002-2014, 1962.

[7] K.S. Champlin and G. Eisenstein, "Cutoff frequency of submillimeter schottky-barrier diodes," IEEE Trans. on Microwave Theory and Tech., vol. MTT-26, pp. 31 - 34, 1978.

[8] P.H. Siegel, A.R.Kerr and W. Hwang, "Topics in the optimization of millimeter-wave mixers," NASA Technical Paper 2287, 1984.

[9] N.R. Erickson, "Very high efficiency frequency tripler for 100-300 GHz," Proc. of the 10th Int. Conf. on Infrared and Millimeter Waves, pp. 54-55, 1985.

[10] P. Penfield Jr. and R.P. Rafuse, " Varactor applications ", Massachusets Institute of Technology, Cambridge, Massachusets, USA, The MIT Press, 1962.

[11] S.M. Sze, "Physics of Semiconductors," John Wiley & Sons, pp. 28-29, 1981.

[12] Landolt-Börnstein, "Numerical data and functional relationships in science and technology, Group III: Crystals and solid state physics," Volume 17 Semiconductors, Springer-Verlag Berlin, pp.577, 1982.'

[13] A. Rydberg, B. N. Lyons and U.S. Lidholm, "On the development of a high efficiency 750 GHz frequency tripler for THz heterodyne systems," To be published in IEEE Trans. on Microwave Theory and Techn., May 1992.

[14] H. Grönqvist, S. Nilsen, A. Rydberg and E. Kollberg,"Characterizing highly efficient millimeter wave Single Barrier Varactor multiplier diodes", to be presented at The European Microwave Conference, Helsinki, Finland, 1992

[15] T. Tolmunen, S. Nilsen, O. Boric, M. Frerking and E. Kollberg, "Accurate characterization of varactors with fF capacitance", Conference Digest, 16th International Conference on Infrared and Millimeter Waves, Lausanne, Switzerland, August 26-30 1991, pp 214-215

Effect of Cooling on the Efficiency of Schottky Varactor Frequency Multipliers at Millimeter Waves

Jyrki Louhi[1], Antti Räisänen[1], Neal Erickson[2]

[1] Helsinki University of Technology, Radio Laboratory, SF-02150 Espoo, Finland
[2] Five College Radio Astronomy Observatory, University of Massachusetts, 619 Lederle Graduate Research Center, Amherst, MA 01003, USA

Abstract

The efficiency of the Schottky diode multiplier can be increased by cooling the diode to 77 K. The main reason for better efficiency is the increased mobility of the free carriers. Because of that the series resistance decreases and a few dB higher efficiency can be expected at low input power levels. At high output frequencies and at high power levels the current saturation decreases the efficiency of the multiplication. When the diode is cooled the maximum current of the diode increases and much more output power can be expected. There are also slight changes in the $I - V$ characteristic and in the diode junction capacitance, but they have a negligible effect on the efficiency of the multiplier.

1 Introduction

It is well known, that cooling a Schottky diode mixer improves its sensitivity, i.e. reduces the mixer noise temperature. This is mainly due to the sharper $I - V$ characteristic at cryogenic temperatures, only partly due to the smaller series resistance and lower metal losses in the mixer mount. In satellite applications the heterodyne receiver is readily cooled passively to temperatures of 110...150 K. Also, a space qualified 80 K cooler is available. This makes it very reasonable to consider the effect of cooling on the frequency multiplier performance. This is especially important at submillimeter waves, where not enough power is available from ordinary all-solid-state frequency multipliers.

2 Diode model and effect of cooling

A simple equivalent circuit of the Schottky diode contains three components: nonlinear junction capacitance, nonlinear junction conductance and series impedance [1].

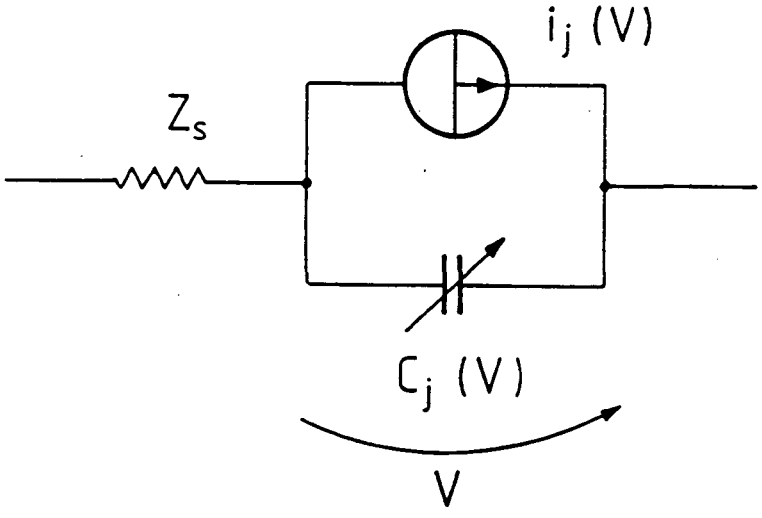

Figure 1: Simple equivalent circuit of the Schottky diode.

Capacitance

The basic model for the junction capacitance of the Schottky diode is

$$C_j(V) = \frac{C_0}{\sqrt{1 - V/\phi_{bi}}}, \tag{1}$$

where ϕ_{bi} is the built-in potential (about 1 V) and C_0 is diode capacitance, when the voltage over the junction is zero. For very small submillimeter wave diodes the edge effect must be included in the diode model as [2]

$$C_j(V) = \frac{A \cdot \epsilon_s}{w(V)} \cdot \left(1 + \frac{3 \cdot w(V)}{2 \cdot r_a}\right) \tag{2}$$

$$w(V) = \sqrt{\frac{2 \cdot \epsilon_s}{q \cdot N_D} \cdot \left(\phi_{bi} - V - \frac{k_0 \cdot T}{q}\right)}, \tag{3}$$

where A is the anode area, ϵ_s is the dielectric constant of the semiconductor, $w(V)$ is the length of the depletion region, r_a is the anode radius, q is the charge of an electron, N_D is the doping density in the semiconductor, k_0 is Boltzmann's constant and T is the temperature. In these models the junction capacitance is very high near the contact potential ϕ_{bi}. Physically this is impossible, and a better model for junction capacitance must be calculated by using the drift-diffusion model [3]. In any of the models, the primary mechanism for the efficiency of the multiplier, the degree of capacitance nonlinearity, is not temperature dependent. Thus, cooling has no effect on the diode's inherent capability to generate harmonics. In the two simple models the only temperature dependent factor is ϕ_{bi}.

When the diode is cooled from 300 K to 77 K, the contact potential ϕ_{bi} increases by about 0.1 V [4]. Because ϕ_{bi} varies only slightly when the diode is cooled, the same operation point can be reached if the bias potential V_{Bias} is also increased as much as ϕ_{bi}. In all, the effect of cooling on the junction capacitance is so small that it has an almost negligible effect on the multiplier efficiency.

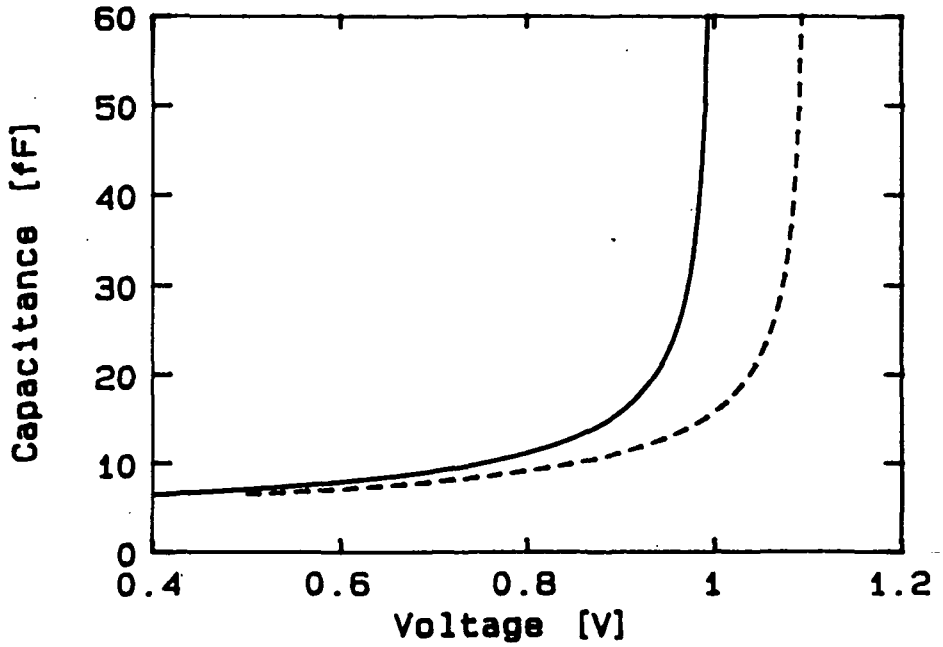

Figure 2: The junction capacitance at temperatures 300 K (solid line) and at 77 K (dashed line).

Series impedance

When the nonlinearity of the epitaxial layer above the plasma resonance is not included, the series impedance of the submillimeter wave Schottky diode is modeled as [5]

$$Z_s(\omega) = Z_{epi}(\omega) + Z_{sub}(\omega) + Z_{skin}(\omega) + R_c \tag{4}$$

$$Z_{epi}(\omega) = \frac{\rho_{epi} \cdot t_{e(eff)}}{A} \cdot \left[\frac{1}{1 + j\omega/\omega_s} + j\frac{\omega}{\omega_d}\right]^{-1} \tag{5}$$

$$Z_{sub}(\omega) = \frac{\rho_{sub}}{4 \cdot r_a} \cdot \left[\frac{1}{1 + j\omega/\omega_s} + j\frac{\omega}{\omega_d}\right]^{-1} \tag{6}$$

$$Z_{skin}(\omega) = \sqrt{2j} \cdot \frac{\rho_{sub}}{2\pi \cdot \delta_s} \cdot \ln\left(\frac{b}{r_a}\right) \Big/ \sqrt{\frac{1}{1 + j\omega/\omega_s} + j\frac{\omega}{\omega_d}}, \tag{7}$$

where R_c is the contact resistance (about 1 Ω), ρ is resistivity, $t_{e(eff)}$ is $t_e - w(V_{bias})$, t_e is the thickness of the epitaxial layer, b is the radius of the chip and δ_s is the skin depth in the substrate given by

$$\delta_s = \sqrt{\frac{2 \cdot \rho_s}{\omega \cdot \mu_0}}, \tag{8}$$

where μ_0 is permeability of GaAs. Scattering frequency ω_s and dielectric relaxation frequency ω_d are

$$\omega_s = \frac{q}{m^* \cdot \mu_s}, \tag{9}$$

$$\omega_d = \frac{1}{\rho_s \cdot \epsilon_s}, \tag{10}$$

where m^* is the effective carrier mass and μ_s is the carrier mobility. The resistivity is

$$\rho = \frac{1}{q \cdot n \cdot \mu_s}, \tag{11}$$

where n is the concentration of the free electrons in the conduction band.

In a semiconductor, the concentration of the free carriers n and the mobility of the carriers μ_s are the most important temperature dependent factors in equations given above. In GaAs the donor binding energy E_D is so small and the concentration of donors N_D is usually so high that the concentration of the free carriers n is equivalent to N_D at all temperatures, where the diode should be used. At a very cold temperature, below 10 K, the concentration drops, because there is not enough thermal energy to ionize electrons to the conduction band, and so the resistivity of GaAs becomes high. At very high temperatures the concentration of the intrinsic carriers is higher than N_D, and thus n is also higher than N_D.

In GaAs the mobility of the free carriers can be calculated from the mobilities of the various scattering processes by using the Matthiessen rule

$$\frac{1}{\mu_s} = \sum \frac{1}{\mu_i}. \tag{12}$$

In GaAs the most important scattering processes are the ionized impurity scattering, acoustic-mode scattering and polar-optical scattering. At room temperature, the polar-optical scattering dominates. When GaAs is cooled, the mobility increases until the mobility of the polar-optical scattering and the mobility of the impurity scattering are equal. At that temperature, mobility μ_s has a maximum, and when the diode is cooled more the mobility decreases. When N_D is rather low ($1 \cdot 10^{16}\text{cm}^{-3}$) the optimum temperature is low ($\sim$ 50 K) and the mobility greatly increases [6]. At very high doping concentration ($2 \cdot 10^{17}\text{cm}^{-3}$) the optimum temperature is higher ($\sim$ 150 K) and the mobility increases only a little when the diode is cooled to 77 K.

When considering the effect of cooling on the series impedance of the Schottky diode, it is simplest to consider first its effect on the DC resistance and then the effect on the series impedance at high frequencies. When the diode is cooled to 77 K, the mobility of electrons increases and thus the resistivity of the epitaxial layer decreases, which also decreases the DC resistance of the diode. When the doping concentration of the epitaxial layer is low, the DC resistance decreases significantly. (For diode UVA 6P2 the measured decrease is about 4.5 Ω, from a

value of 10.5 Ω to 6 Ω; the calculated values agree very well, see Figure 3) When the doping rate is higher the decrease of the resistance is not as large. (For diode UVA 2T2 the calculated decrease is about 3.5 Ω, from a value of 12 Ω to 8.5 Ω) When considering the effect of the decreased series resistance on the efficiency of the multiplication, it must be noticed that the resistance of the epitaxial layer Z_{epi} is a function of the thickness of the layer. In an efficient reactive multiplication, the voltage over the depletion region spends a substantial part of the pump cycle in the low voltage region, where the contribution of Z_{epi} in Z_s is large, but a small part of the pump cycle in the high reverse voltage region, where the contribution of Z_{epi} in Z_s is small. When the diode is now cooled, the decrease of the series resistance is smaller than the decrease of the DC resistance, but still the decrease of resistance has a very strong positive effect on the efficiency of multiplication.

At high frequencies the series impedance of the Schottky diode is no longer purely resistive, because of the plasma resonance and the skin effect. When the diode is cooled, the plasma resonance frequency

$$\omega_p = \sqrt{\omega_s \cdot \omega_d} = \sqrt{\frac{n \cdot q^2}{m^* \cdot \epsilon_s}} \tag{13}$$

does not change, because it is independent of the electron mobility μ_s. Because ω_s and ω_d are temperature dependent, the Q-factor of the resonance is also temperature dependent, and when the diode is cooled to 77 K the Q is increased (Figure 3). Because the mobility in the substrate changes only very little when the diode is cooled, the impedance of the substrate Z_{sub} and the impedance of the skin effect are not changed significantly.

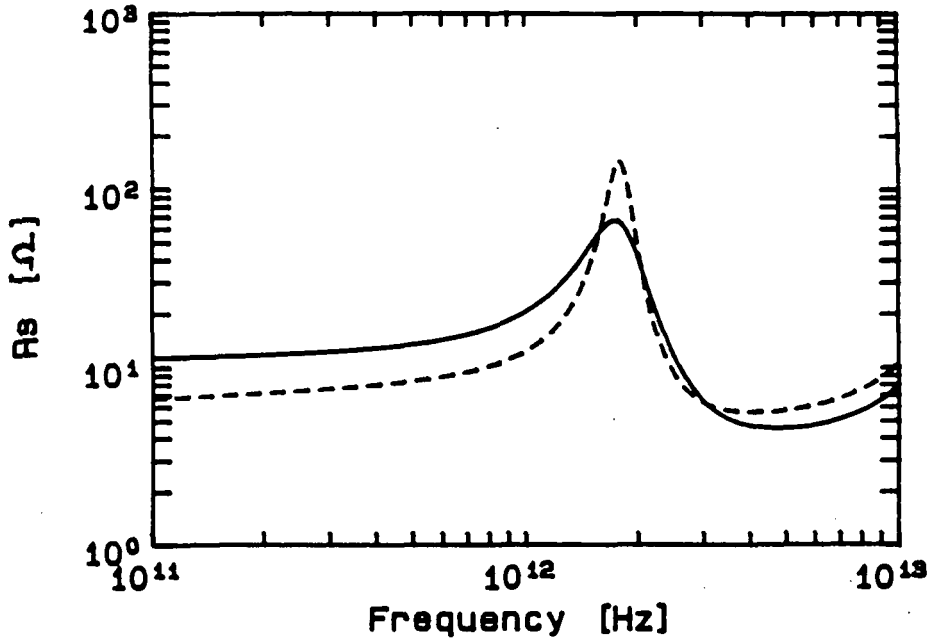

Figure 3: The series resistance of diode UVA 6P2 at temperatures 300 K (solid line) and 77 K (dashed line).

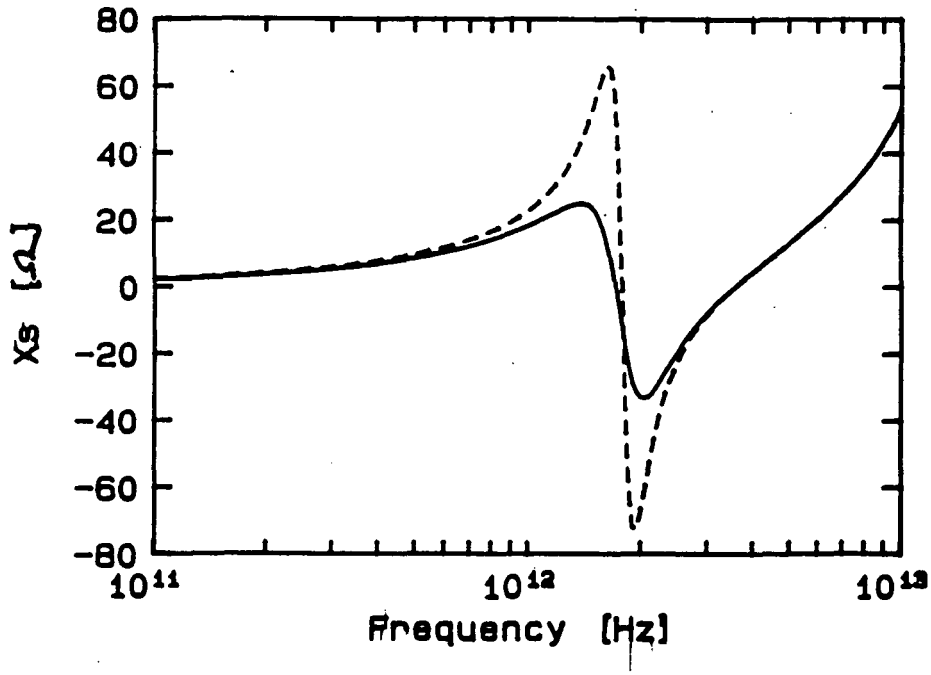

Figure 4: The series reactance of diode UVA 6P2 at temperatures 300 K (solid line) and 77 K (dashed line).

I-V characteristic

For a Schottky diode the $I-V$ characteristic is assumed to be [4]

$$I_j(V) = A \cdot R^{**} \cdot \theta^2 \cdot e^{q\cdot(V-\phi_{bi})/k_0\cdot\theta} \quad (14)$$

$$\theta = \theta_f \cdot \coth\left(\frac{\theta_f}{T}\right) \quad (15)$$

$$\theta_f = \frac{q\cdot\hbar}{k_0}\cdot\sqrt{\frac{N_D}{4\cdot\epsilon_s\cdot m^*}}, \quad (16)$$

where R^{**} is modified Richardson's constant, $\hbar$ is $h/2\pi$ and h is Planck's constant.

There are two important factors of the $I-V$ characteristic for the efficiency of the frequency multiplication: the turn-up point of the $I-V$ curve, and the steepness of the $I-V$ curve beyond that. When the Schottky diode is cooled, the possible voltage range where the multiplication is mainly reactive, increases, and thus the maximum efficiency can also increase. For a cooled diode the shape of the $I-V$ characteristic is also sharper, and therefore the resistive multiplication is slightly more effective.

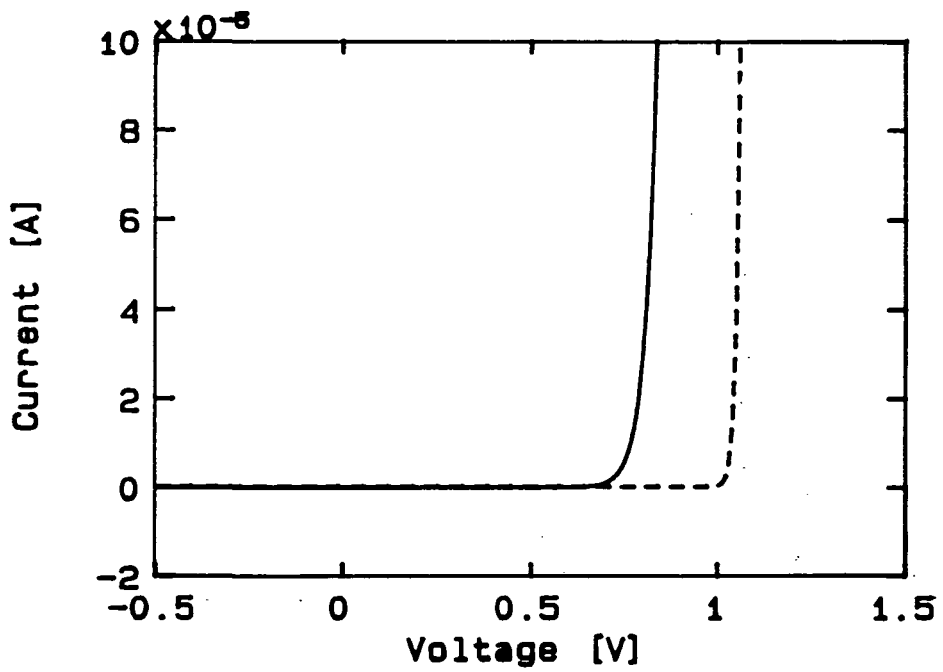

Figure 5: The current-voltage characteristic at temperatures of 300 K (solid line) and 77 K (dashed line).

Current saturation

At a low electric field the electron drift velocity v_d is directly related to the electric field $\mathcal{E}$ as

$$v_d = \mu_s \cdot \mathcal{E}. \tag{17}$$

When the electric field increases the drift velocity also increases until the velocity reaches a maximum value v_{max} ($= 2.2 \cdot 10^5$ m/s at about 3.2 kV/cm in an intrinsic case). In that situation the electron conduction current

$$i_e = A \cdot n \cdot q \cdot \mu_s \cdot \mathcal{E} \tag{18}$$

must be replaced by the maximum current

$$i_{max} = A \cdot n \cdot q \cdot v_{max}. \tag{19}$$

This current saturation causes a very significant decrease in the efficiency of the multiplier at high power levels and also when the output frequency is high, because the junction capacitance cannot be pumped with optimum current. The current saturation seems to be the most important factor for a submillimeter wave frequency multiplier, when the efficiency of the multiplication is considered. When the diode is cooled, the maximum drift velocity increases [6] and because of that the maximum electron current also increases. Therefore, when the diode is cooled the effect of the current saturation is less significant. This increases the efficiency especially at high power levels, at high frequencies, and in the case of a high multiplication factor.

The current saturation may be modelled by strongly current dependent series resistance $R_s(i)$ above the maximum current. Kollberg et al. have presented the following model [7]:

$$R_s(i) = R_s(DC) \cdot a \cdot i^6, \tag{20}$$

where a is a parameter, depending on the maximum current of the diode i_{max}. The meaning of the $R_s(i)$ is to modify the current waveform approximately as required by causing a very strong increase in the series resistance when the current of the diode is higher than the maximum current i_{max}. The parameter a has been fitted empirically to the measured results only in one case and must be estimated for other diodes and frequencies. There seems to be no physical background for this model, but so far no better model has been proposed.

3 Analysis of multipliers

At millimeter waves Schottky varactors are often driven into conduction, which is only nearly optimal. In this case, the usefulness of classical theories [8] is poor and harmonic balance analysis [9] should be used. One form of the harmonic balance analysis is the multiple reflections technique, where the multiplier circuit is divided into linear and nonlinear subcircuits, which are then analyzed in the frequency and time domain.

Doubler for 160 GHz

Let us first consider the effect of cooling on a two diode balanced doubler for 160 GHz, because we have also experimental results for it [10].

Table 1: Parameters used for UVA 6P2.

	C_0	A	t_e	N_D	μ	i_{max}
300 K	21	33	1.0	$3.5 \cdot 10^{16}$	0.61	44
77 K	21	33	1.0	$3.5 \cdot 10^{16}$	1.40	66
	fF	μm^2	μm	cm^{-3}	m/s	mA

The two diode construction has been analyzed both at 300 K and at 77 K. First, the efficiency has been calculated with optimum embedding impedances. These results have been plotted in Figure 6 (solid lines). Here the efficiency has only a very poor correlation with the measurements (O and X) because of the VSWR, which is mainly caused by the fact that the embedding impedances are optimized for high input power. When the doubler is then analyzed by using the optimum embedding impedances for high input power at all input power levels, the correlation is much better, especially when 0.5 dB losses in the input and 0.8 dB losses in the output have been taken into account.

Table 2: Experimental output power versus temperature and input power (two diodes).

		Input power				
		10	33	50	100	mW
Temperature	300 K	1.6	9.0	13.9	22.0	mW
	223 K	1.9	10.4	16.3	26.7	mW
	77 K	2.2	12.8	18.7	30.7	mW

In order to understand better the agreement between the theory and experiment, it is worth separating the effects of the decreased series impedance and the increased current handling capability due to the cooling. First, if the current saturation is omitted in the theoretical analysis, the effect of cooling is as follows. At low input power levels when the multiplication is purely reactive, the decreased series impedance causes a clear increase in the efficiency due to smaller losses in the series impedance. According to simulations, the increase of the efficiency in the above case at low input power levels is about 1.5 dB. However, when the input power per diode is large (i.e. $>$ 10 mW), the multiplication efficiency tends to decrease with the increased input power due to the resistive multiplication. This

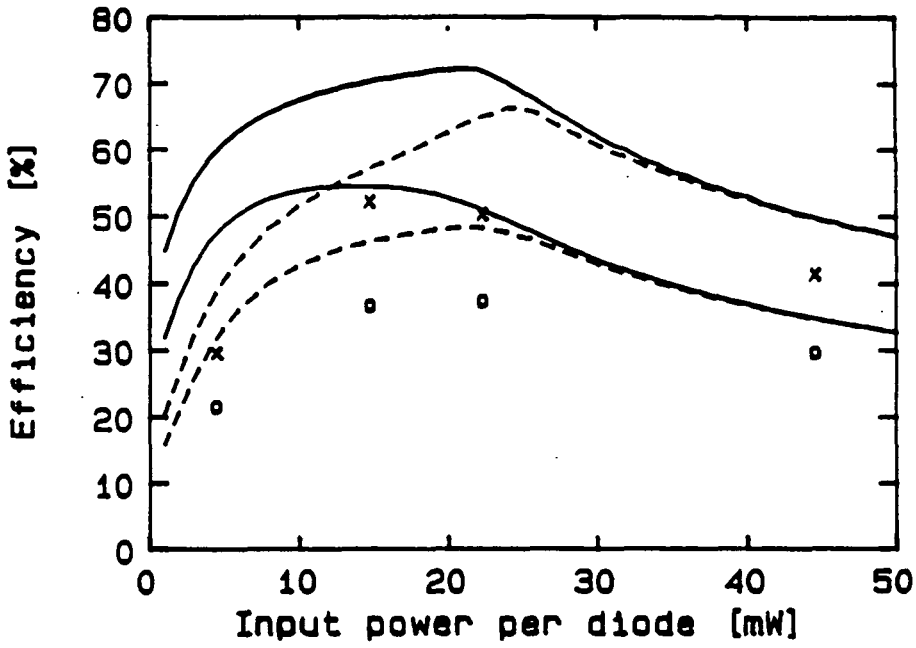

Figure 6: The efficiency of the 160 GHz doubler at 300 K and at 77 K (above), when using optimum impedances (solid line) and impedances optimum for high power (dashed line). Measurement results, when 0.5 dB input losses and 0.8 dB output losses have been taken into account, at 300 K (o) and at 77 K (x) have also been plotted.

is because the voltage swing reaches the conduction region during every cycle. The smaller the series impedance, the lower the input power needed to reach this conduction, and thus, resistive multiplication. Therefore, the gain due to the smaller series impedance is smaller at high input power levels than at low power levels. According to the simulations, the efficiency increase due to the smaller series impedance in the multiplier described above is only 0.5 dB at 50 mW input power per diode.

When the current saturation is taken into account, but not the series resistance, the positive effect of cooling is seen only at high power levels. This is because the junction capacitance can be pumped at 77 K more effectively than at 300 K. At small power levels the saturation, of course, does not play an important role. According to our simulations, the higher current handling capability of the cooled diode 6P2 improves the efficiency by 1 dB at 50 mW input power per diode.

These two effects of cooling together, the decreased series impedance and the increased current handling capability, explain the experimentally verified 1.5 dB increase in the multiplication efficiency of all power levels and therefore give some kind of a proof of the current saturation in the diode at high input power levels. Due to the higher efficiency at high input power levels, the maximum output power is also increased by the same amount, which helps in pumping the following stage in the multiplier chain producing submillimeter wave frequencies.

Multipliers for 1 THz

When constructing multiplier chains for 1 THz, a reasonable choice is first to double the output frequency of a powerful W-band Gunn oscillator and then to follow by a tripler and a doubler or by a doubler and a tripler. The latter choice does not only depend on the varactor diodes but also on the technology to build fine mechanical multiplier mounts.

In order to get some understanding of how much power could be available at 1 THz, the choice of a tripler to 500 GHz and doubler to 1 THz has been made because this allows comparison with experimental results up to 500 GHz [10]. The tripler for 500 GHz and the doubler for 1 THz can be analyzed the same way as the doubler for 160 GHz, but now current saturation plays a very important role. Because the presented model for current saturation has only poor correlation to the physics, the results for high frequency multipliers should be considered only qualitatively.

Some general aspects can still be presented. First, when the diode is cooled, the maximum drift velocity increases, which also increases the maximum current. Second, when the output frequency is high, the changes during the voltage swing are very fast. In that situation, the current needed for optimum multiplication is very high, and then current saturation plays a very important role by greatly decreasing the efficiency. By cooling, the maximum current should increase and the efficiency of the multiplication may increase by a few dB. Third, when the first or second stage multiplier is cooled, the maximum input power for the last stage multiplier increases, and so also the maximum output power for 1 THz increases. Our simulations have indicated an increase of about 7 dB from 100 μW to 500 μW in the optimum situation.

4 Conclusions

Cooling of a Schottky varactor multiplier increases its efficiency by as much as a few dB. Because of the smaller series impedance the efficiency of frequency multiplication increases by 1-2 dB at small input power levels. At large input power levels the efficiency increases by 2-10 dB due to the higher current handling capability of the diode. A cooled multiplier can be readily used in satellite applications, where the receiver is cooled to 50...150 K. The positive effect of the cooling should be utilized especially in submillimeter wave multipliers when the output power necessary cannot be reached in any other way.

Even though the model of a Schottky diode is already rather complex, it should be studied more. The main reason for a poor model is that current saturation is poorly handled. Much more work must be done to model the saturation exactly. Also much more experimental work on cooling multipliers is needed, before all the effects of the cooling can be understood.

References

[1] Räisänen A.V., Sironen M.: Capability of Schottky-diode multipliers as local oscillators at 1 THz. *Microwave and Optical Technology Letters*, vol. 4, no. 1, 1991, p. 29-33.

[2] Copeland J.A.: Diode edge effect on doping-profile measurements. *IEEE Transactions on Electron Devices*, vol. ED-17, no. 5, 1970, p. 401-407.

[3] Hjelmgren H., Kollberg E., Lundgren L.: Numerical simulations of the capacitance of forward-biased Schottky-diodes. *Solid-State Electronics*, vol. 34, no. 6, 1991, p. 587-590.

[4] Kollberg E.L., Zirath H., Jelenski A., Temperature-variable characteristics and noise in metal-semiconductor junctions. *IEEE Transactions on Microwave Theory and Techiques*, vol. MTT-34, no. 9, 1986, p. 913-922.

[5] Crowe T.W.: GaAs Schottky barrier mixer diodes for the frequency range 1-10 THz. *International Journal of Infrared and Millimeter Waves*, vol. 10, no. 7, 1989, p. 765-777.

[6] Ruch J.G., Fawcett W.: Temperature dependence of the transport properties of Gallium Arsenide determined by a Monte Carlo method. *Journal of Applied Physics*, vol. 41, no. 9, 1970, p. 3843-3849.

[7] Kollberg E., Tolmunen T., Frerking M., East J.: Current saturation in submillimeter wave varactors. *Proceedings of the 2nd International Symposium on Space Terahertz Technology*, 1991, p. 306-322.

[8] Penfield P., Rafuse R.P.: *Varactor Applications*, Cambridge, Mass., The MIT Press, 1962.

[9] Siegel P.H., Kerr A.R., Hwang W.: *Topics in the Optimization of Millimeter - Wave Mixers*, NASA Technical Paper 2287, 1984.

[10] Erickson N.: High efficiency submillimeter frequency multipliers. *IEEE MTT-S International Microwave Symposium Digest*, vol III, Dallas, 1990, p. 1301-1304.

Superlattice Barrier Varactors*

C. Raman, J. P. Sun, W. L. Chen, G. Munns,
J. East and G. Haddad
Solid State Electronics Laboratory
University of Michigan, Ann Arbor, Michigan

Abstract

SBV (Single Barrier Varactor) diodes have been proposed as alternatives to Schottky barrier diodes for harmonic multiplier applications. However these show a higher current than expected. The excess current is due to X valley transport in the barrier. We will present experimental results showing that the use of a superlattice barrier and doping spikes in the GaAs depletion regions on either side of the barrier can reduce the excess current and improve the control of the capacitance vs. voltage characteristic.

The experimental results consist of data taken from two types of device structures. The first test structure was used to study the performance of AlAs/GaAs superlattice barriers. The wafer was fabricated into 90 micron diameter mesa diodes and the resulting current vs. voltage characteristics were measured. A 10 period superlattice structure with a total thickness of approximately 400 Å worked well as an electron barrier. The structure had a current density of about one A/cm^2 at one volt at room temperature. The capacitance variation of these structures was small because of the design of the GaAs cladding layers. The second test structure was used to study cladding layer designs. These wafers were InGaAs and InAlAs layers lattice matched to an InP substrate. The layers have n^+ doping spikes near the barrier to increase the zero bias capacitance and control the shape of the capacitance vs. voltage characteristic. These structures have a capacitance ratio of 5:1 and an abrupt change from maximum to minimum capacitance. The measurements were made at 80 K. Based on the information obtained from these two structures, we have designed a structure that combines the low current density barrier with the improved cladding layers. The capacitance and current-voltage characteristics from this structure are presented.

*This work was supported by the Center for Space Terahertz Technology under NASA Contract No. NAGW-1334 and by the URI-ARO Program Contract No. DAAL03-87-K-0007.

Introduction

Varactor diodes are an important component of harmonic multipliers operating above 100 GHz. These multipliers are the primary source of power in the submillimeter wave frequency range, where the diode predominantly used is a Schottky barrier device. However, a multiplier based on Schottky diodes suffers certain disadvantages. The circuit is complex, with higher order conversion requiring matching at all frequencies–the input, the output, as well as idler frequencies. The varactor must also be biased to increase the voltage swing and prevent current flow over the barrier in the forward direction. These problems can be overcome by using heterojunction based varactor structures. Implementation of such novel diode structures is motivated by the symmetry of their capacitance vs. voltage characteristic which permits odd harmonic conversion without the added complexity of even harmonic idlers and bias circuitry .

The Single Barrier Varactor

One possible structure is the single barrier varactor, shown in Figure 1a. The corresponding energy band diagrams under thermal equilibrium and bias are shown in 1b and 1c. The analogue of the metal-semiconductor electron energy barrier found in the Schottky varactor diode is the conduction band offset between the GaAs region and the wider bandgap $Al_xGa_{1-x}As$ layer. This energy barrier acts to inhibit electron transport through the structure and ideally should be as large as possible for the device impedance to be purely reactive. When one side is biased relative to the other, the GaAs region on the anode side is depleted of electrons and becomes positively charged, similar to the semiconductor region of a Schottky varactor under reverse bias. Electrons accumulate on the cathode side of the structure, forming a charge separation across the $Al_xGa_{1-x}As$ region. The relationship between the stored charge and the applied voltage is non-linear, resulting in a non-constant device capacitance. Moreover, since the structure is symmetric, reversing the sign of the applied voltage merely interchanges the roles of depletion and accumulation regions and does not affect the device capacitance. Therefore the capacitance-voltage characteristic has even symmetry. Early attempts at implementing such varactors were limited in efficiency by high leakage current densities [1]. Details of the leakage current analysis are described elsewhere in these proceedings [2].

By replacing the single heterostructure by a superlattice barrier, we propose to reduce the carrier transport through the device by increasing the effective barrier height seen

[1] Anders Rydberg, Hans Gronqvist, and Erik Kollberg, *Millimeter and Sub-Millimeter Wave Multipliers Using Quantum Barrier Varactor (QBV) Diodes*, IEEE Electron Device Letters, Vol. 11, No. 9. Sept. 1990, pp. 373-375.

[2] H. Hjelmgren, J. East and E. Kollberg, "Thermionic Emission Current in a Single Barrier Varactor,", these proceedings.

by an electron. A doping profile modification can improve the capacitance vs. voltage characteristic; however, a trade-off is seen between maintaining a high barrier height and a good C-V profile.

The Superlattice Barrier Varactor

Although the SBV presents a symmetric C-V characteristic, its efficiency is degraded due to the high leakage current associated with the device because a purely reactive multiplier is more efficient than a resistive one. The true thermionic emission energy barrier seen by an electron in the GaAs regions is not the Γ to Γ energy level offset but the considerably lower Γ to X energy level difference, as seen in Figure 2a. By means of a scattering process an electron incident on the barrier can pass through the $Al_xGa_{1-x}As$ region into the X valley of the barrier material. Thermionic emission over this X level requires less kinetic energy than emission over the Γ level and consequently a smaller bias voltage is needed to turn on the current.

The X valley transport can be suppressed by replacing the single heterojunction by a series of barriers interspersed with quantum wells, i.e., a superlattice. Such a superlattice appears in Figure 2b. The well regions are thin, resulting in quantum mechanical confinement. The energy mini-bands are shifted upward considerably with respect to the Γ point in bulk GaAs. A simple calculation indicates that the energy increase can be on the order of an electron volt. Unlike the SBV, there is no longer a continuous X valley current path since the well energies are higher than the X levels. The superlattice structure achieves a larger effective barrier than that of the SBV and suppresses the leakage current.

A thin, highly doped layer between the superlattice and each adjacent N^- region can be used to modify the capacitance. The so-called δ-doped regions (see Figure 3) are thin and contain a large amount of charge so that at zero bias they remain mostly undepleted. Flat band effects are minimized and the zero bias capacitance is increased. Varying the bias slightly causes almost no change in the depletion width and the capacitance remains constant. However, beyond a threshold voltage, the entire δ region becomes depleted and the lightly doped N^- region begins to deplete rapidly, causing a sharp drop in the capacitance from its zero bias value.

Advantages and Disadvantages

In designing superlattice varactors, two material systems were considered: GaAs/AlAs and InGaAs/InAlAs lattice matched to InP. Structure I, seen in Figure 4, shows a 10 period, 20 Å / 20 Å GaAs/AlAs superlattice barrier varactor chosen for examination of the barrier properties. The MBE grown wafer was processed on the front side by photolithography. Contacts were made to the front and back by evaporating a Ni/Ge/Au/Ti/Au

sequence and annealing at 405 degrees Celsius. Mesa diameters of 5 to 90 μm were then chemically etched. The measured room temperature I-V curve in Figure 5 demonstrates the effectiveness of the superlattice in keeping the current to a minimum. At a bias of 1 volt the current density is about 1 A/cm^2, compared with about 150 A/cm^2 for the single barrier varactor. However, the ratio of maximum to minimum capacitance is insufficient for any significant harmonic conversion.

The second structure, a 40 Å / 40 Å InGaAs/InAlAs superlattice, was designed with doping spikes added, as outlined in Figure 6a. Figure 6b shows the C-V data, taken at 80 K to reduce the parallel conduction current [3]. A close agreement is observed with the capacitance characteristic predicted by a self-consistent quantum mechanical and Poisson solution for the charge and potential distribution throughout the superlattice varactor. When a voltage of approximately 0.2 volts is applied, the capacitance drops sharply to about one-fifth of its zero bias value, corroborating the theoretical expectation. Thus doping profile modifications allow good control of the capacitance-voltage characteristic.

The final structure utilized the low leakage properties of the GaAs/AlAs superlattice and incorporated the doping modifications that had been tested in the InGaAs/InAlAs system. In structure III the same superlattice as Structure I (with one well layer removed from the end for symmetry) was grown on a new varactor wafer which incorporated a doping spike of sheet density 1x10^{12} cm^{-2} and a more lightly doped N$^-$ region than the previous GaAs/AlAs wafer. Figures 7 and 8 present the room temperature I-V and C-V data from 90 micron diameter mesas fabricated on this wafer. Compared with structure I, the leakage current density has increased. This current degradation can be attributed to the following mechanism: the effective electron thermionic emission barrier is reduced by band bending at the barrier edge due to the high electron density in the doping spike. The capacitance and parallel device conductance were simultaneously measured on a HP4275A LCR meter, where the bias was varied until the conductance exceeded the measurement capability of the machine. As seen in Figure 8, the C-V profile exhibits a swing ratio of close to 4. However, the zero bias capacitance was larger than the value predicted by the quantum mechanical analysis by about a factor of 2. The reason for this is not clearly understood at the present time.

Despite the fact that the current levels in the final structure were higher than expected, the superlattice varactor represents improvement over the single barrier varactor. Figure 9 compares the current densities for the two devices at low and high voltages and temperatures. For operation at low temperature or for small voltages the superlattice barrier fares better than the SBV.

[3] J. P. Sun, W. L. Chen, J. East and G. Haddad, *C-V Characteristics of Quantum Well Varactors*, Proceedings of the 1991 International Semiconductor Devices Research Symposium.

Conclusions

We have demonstrated a superlattice barrier varactor in the GaAs/AlAs system which promises to be useful in odd harmonic generation due to its reduced leakage properties when compared with the SBV. Moreover, modification of the capacitance by means of an appropriate doping profile has been demonstrated in the InGaAs/InAlAs material system. A compromise appears, however, between minimizing leakage current levels in the device and achieving a large maximum to minimum capacitance swing ratio. We hope to begin RF testing of the superlattice barrier varactors in the near future.

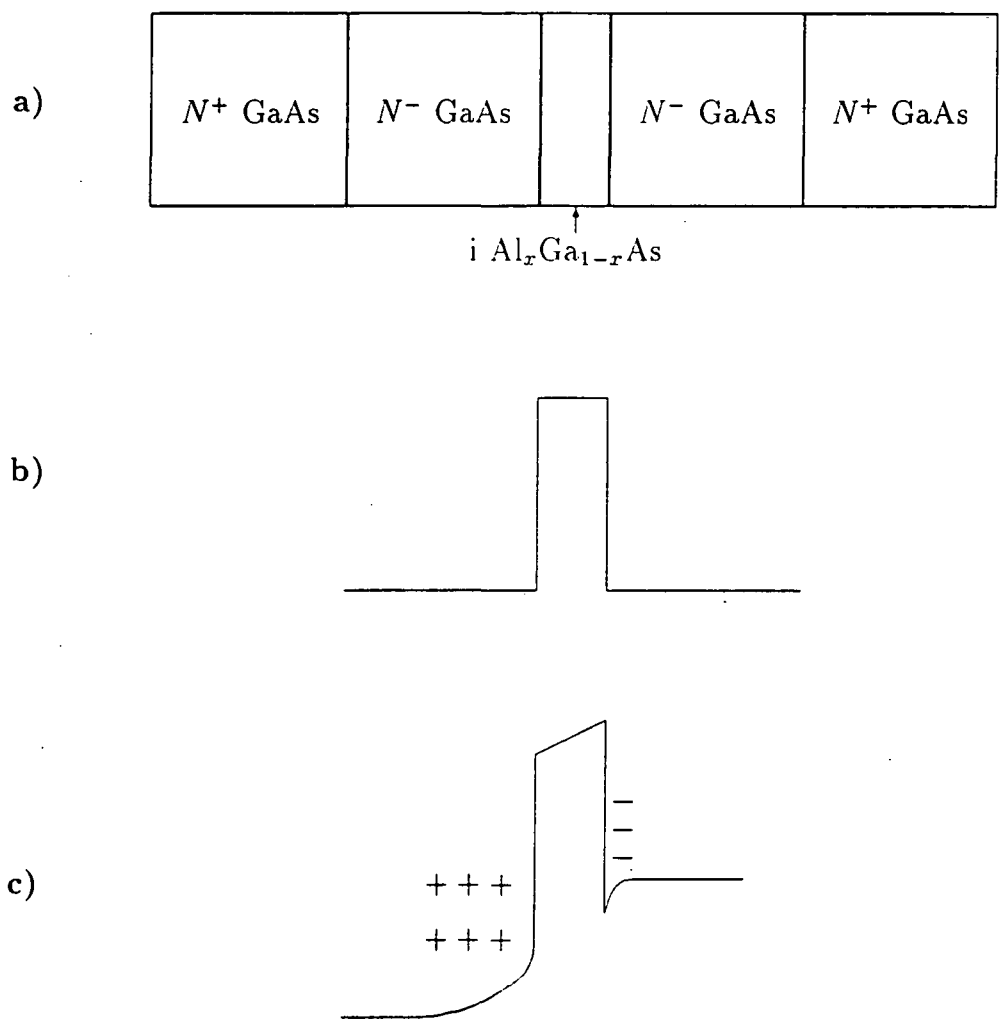

FIGURE (1): (a) Single Barrier Varactor , (b) band diagram under equilibrium, (c) band diagram under bias.

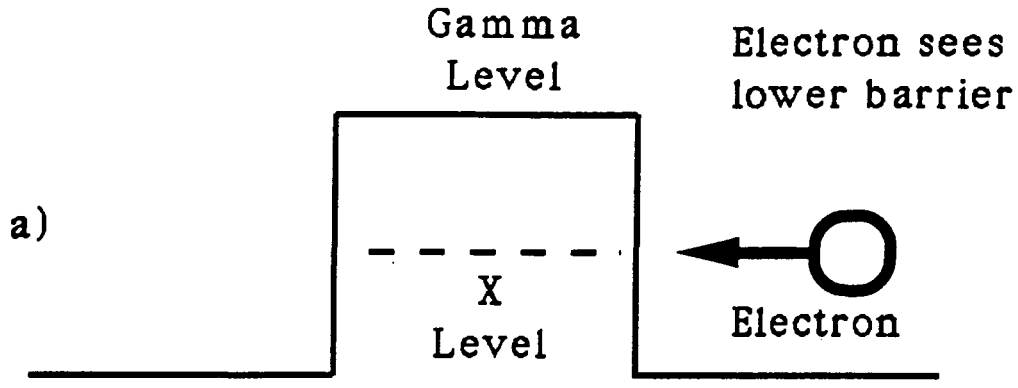

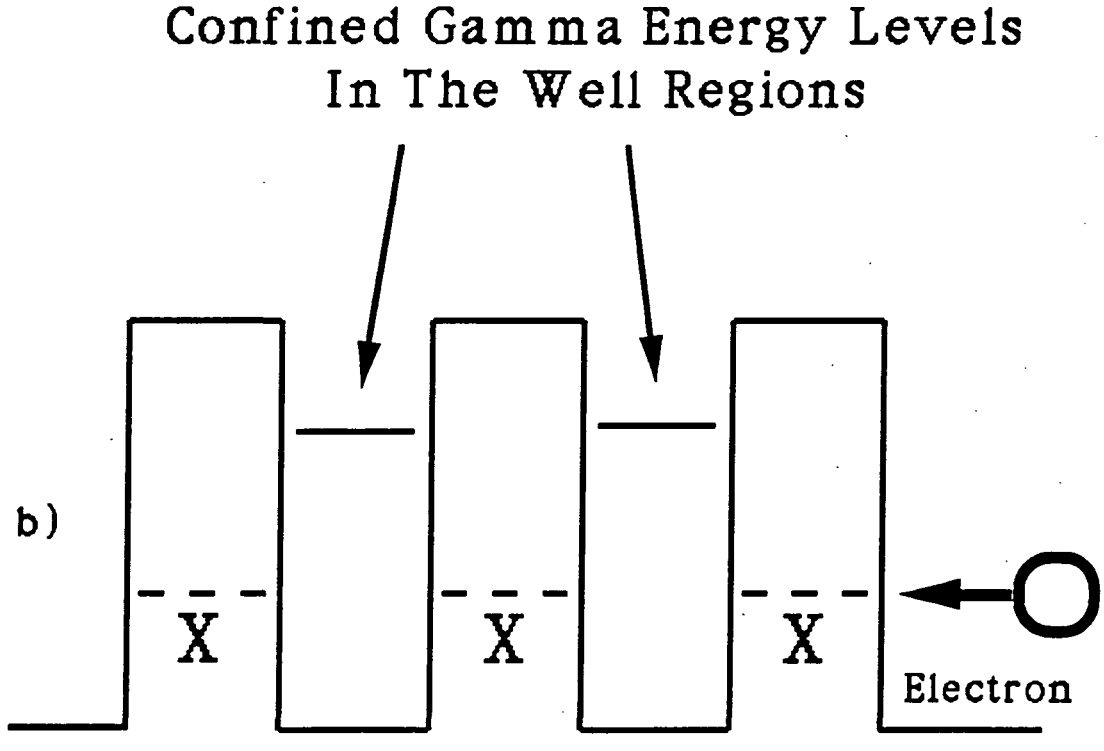

FIGURE (2): (a) X valley transport in Single Barrier Varactor, (b) Suppression of X transport by superlattice.

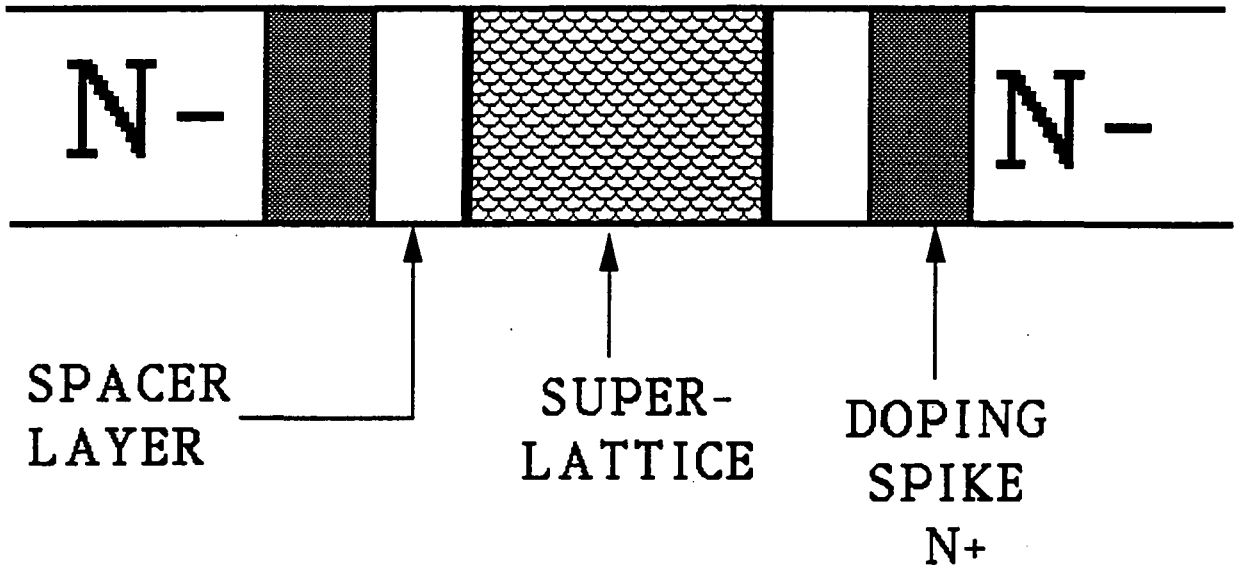

FIGURE (3): Superlattice with doping spikes

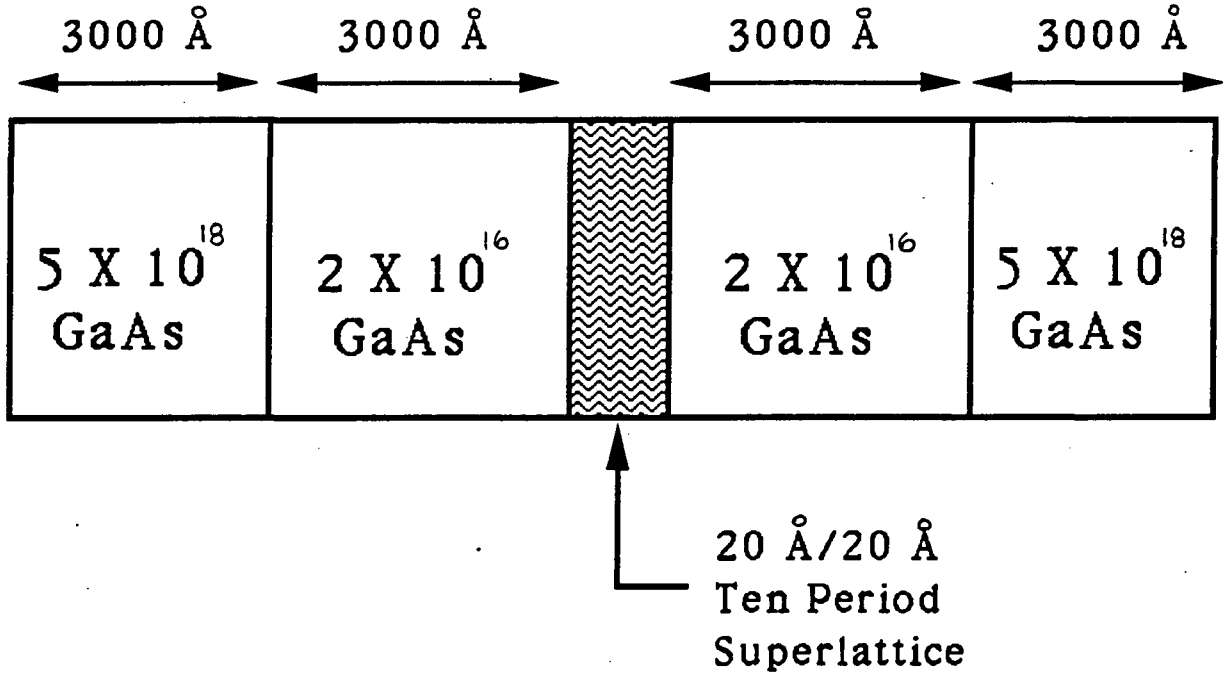

FIGURE (4): Structure I: GaAs/AlAs superlattice varactor

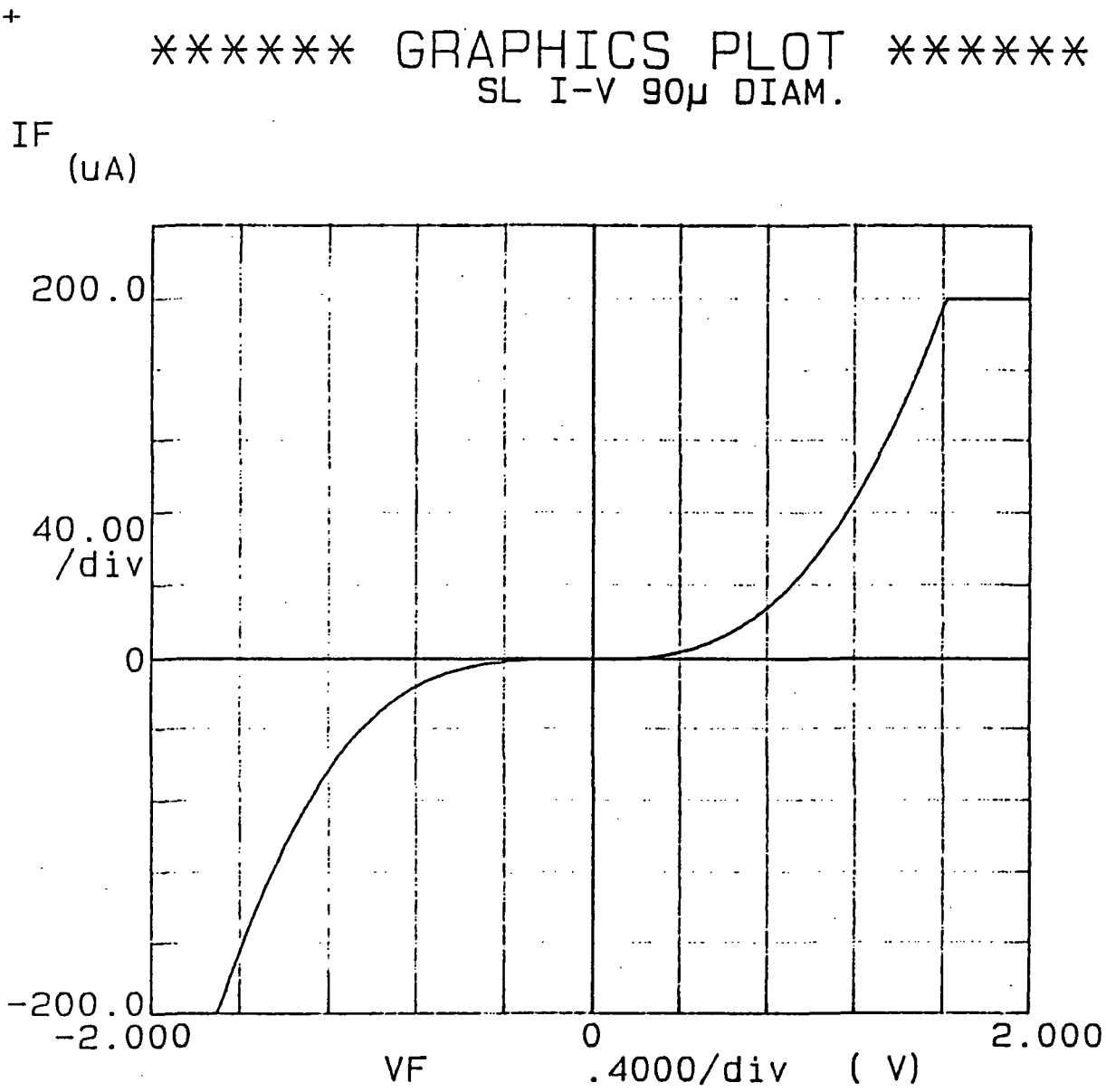

FIGURE (5): Structure I: I-V characteristic

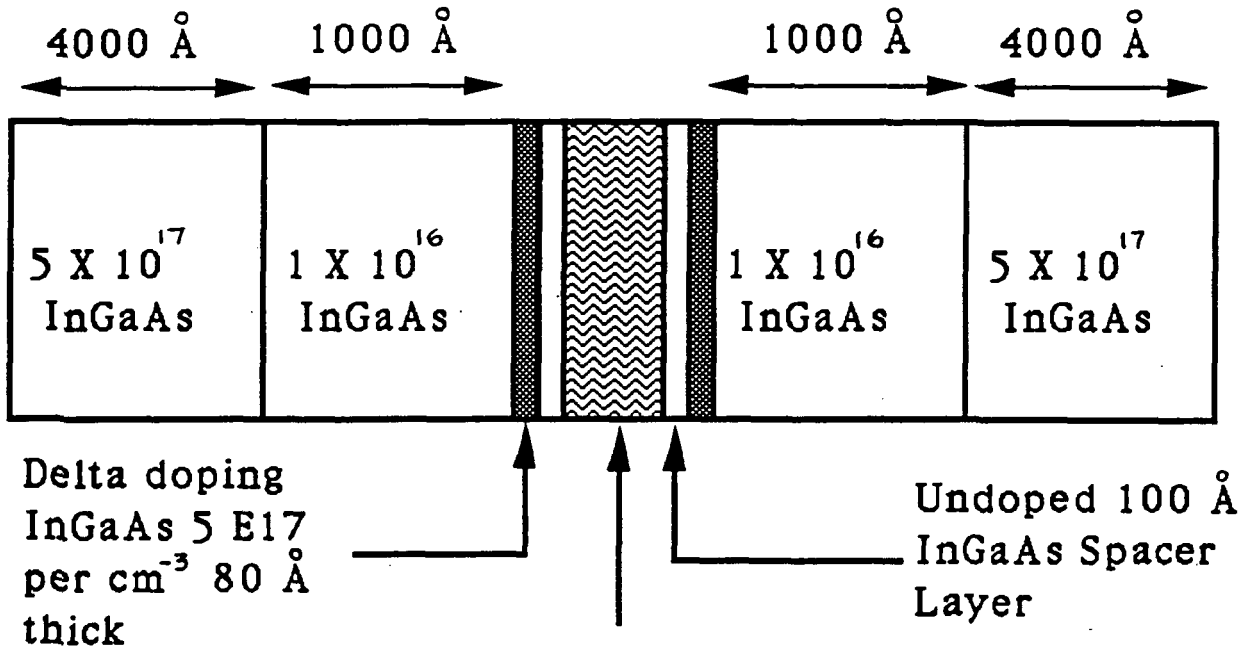

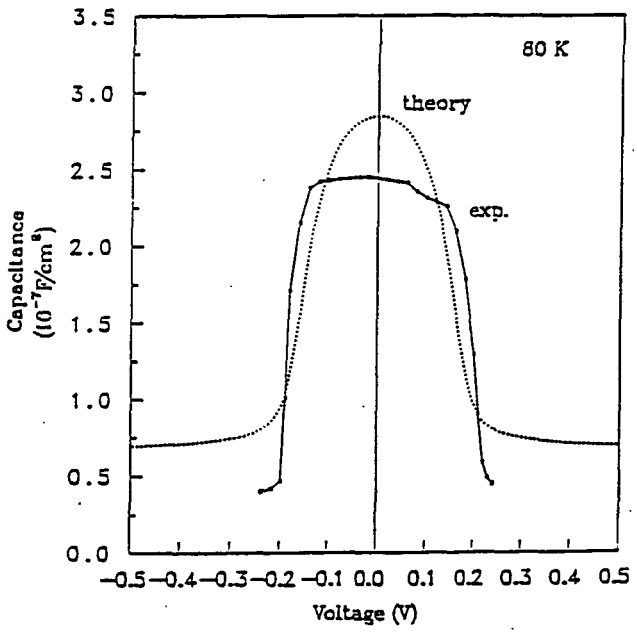

FIGURE (6): (a) Structure II: InGaAs/InAlAs superlattice varactor with doping spikes, (b) Structure II: C-V characteristic

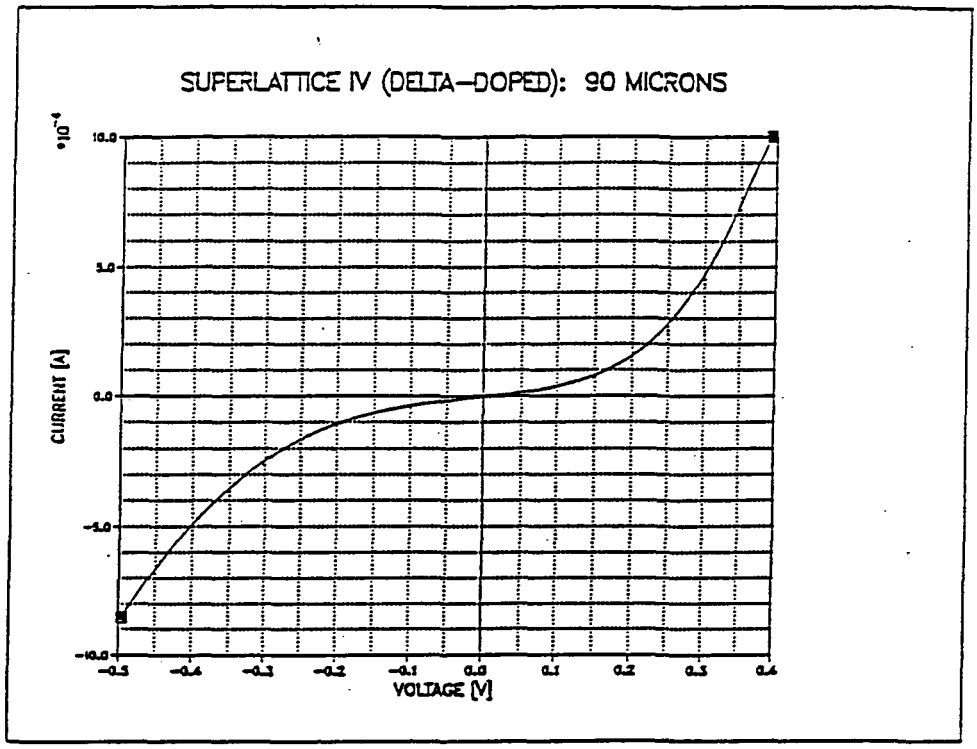

FIGURE (7): Structure III: I-V characteristic

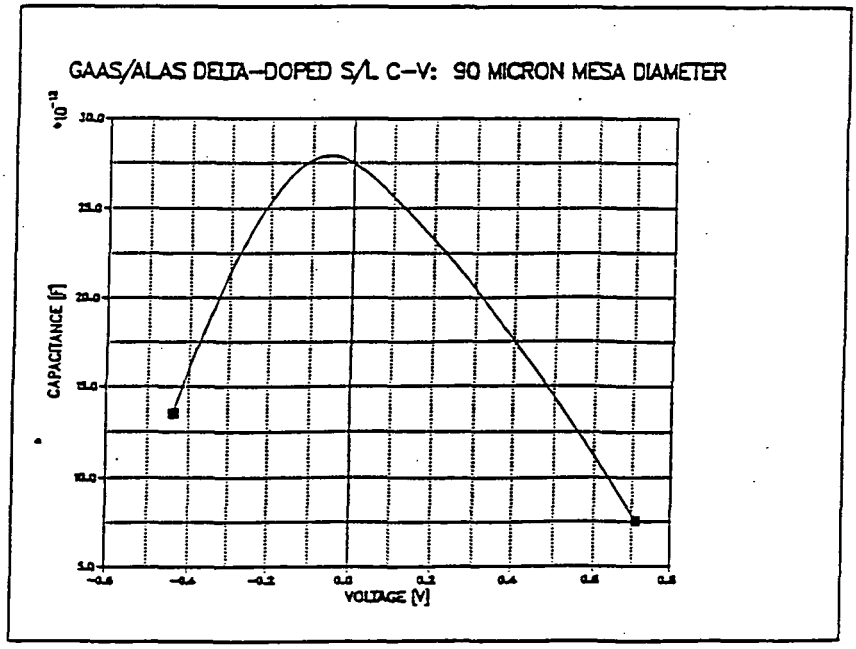

FIGURE (8): Structure III: C-V characteristic

J (Amps/sqcm)

	At V = 0.1 volts	At V = 0.4 volts
SBV	1.1 @ 300 K 0.2 @ 100 K	9.4 @ 300 K 1.8 @ 100 K
AlAs/ GaAs S/L	0.7 @ 294 K negligible @ 90 K	16.5 @ 294 K 0.2 @ 90 K

FIGURE (9): Comparison of improvements

A NEW FABRICATION TECHNIQUE FOR BACK-TO-BACK VARACTOR DIODES

R. Peter Smith, Debabani Choudhury, Suzanne Martin, and M.A. Frerking,
John K. Liu, and Frank A. Grunthaner

Center for Space Microelectronic Technology
Jet Propulsion Laboratory/California Institute of Technology
4800 Oak Grove Drive
Pasadena, CA 91109

Abstract: A new varactor diode process has been developed in which much of the processing is done from the back of an extremely thin semiconductor wafer laminated to a low-dielectric substrate. Back-to-back BNN diodes were fabricated with this technique; excellent DC and low-frequecy capacitance measurements were obtained. Advantages of the new technique relative to other techniques include greatly reduced frontside wafer damage from exposure to process chemicals, improved capability to integrate devices (e.g., for antenna patterns, transmission lines, or wafer-scale grids), and higher line yield. BNN diodes fabricated with this technique exhibit approximately the expected capacitance-voltage characteristics while showing leakage currents under 10 mA at voltages three times that needed to deplete the varactor. This leakage is many orders of magnitude better than comparable Schottky diodes.

Introduction:

Planar varactor diodes[1] are being developed in place of whisker-contacted devices in order to improve the performance and ruggedness of spaceborne submillimeter-wave heterodyne receivers; at the same time thin heterostructure layers are being used to improve diode performance, making processing more demanding. Such devices could be more useful if integrated into relatively large arrays that could potentially be used for communications systems. It is expected that such back-to-back multiplier diodes with Schottky contacts and heterostructure barriers can be made to operate reasonably efficiently at frequencies over one terahertz[2,3,4]. In this paper we present results from devices in which the isolation was performed from the back. This technique simplifies processing, greatly increasing yield and providing a much lower dielectric constant, and thus low loss, environment for antennas and other circuit patterns.

Conventional multiplier diode isolation techniques have a number of problem areas. Isolation implants are commonly used, but the removal of masking materials from the wafer often presents difficulties. An alternative technique for isolating the active devices is to perform a mesa etch, but connection of the contacts to the top of the mesa is problematic. One approach attempted here requires relatively difficult planarization processing that can potentially damage the thin barrier layer. Metal step coverage may be also a problem with this approach. Air bridging can also be used with mesa isolation, but this also exposes the top of the semiconductor material to a larger number of process steps. Some inactive semiconductor material, with its associated high dielectric constant, is generally left in place with all of these approaches.

We have developed an alternative processing technique that promises to be simpler and more robust. In this process, no inactive semiconductor material is left, and the front of the wafer is exposed to the absolute minimum of processing possible for a front-side back-to-

back diode process. In our work, the remaining process steps were completed with the devices laminated to a 3 mil quartz substrate. This quartz is the same as is typically used for the crossed-field waveguide multiplier filter structures for which the devices were intended. Clearly, there is a wide lattitude in substrate material, which adds a great deal of flexibility to the design of submillimeter-wave components. The total number of steps is relatively low, improving yield. Since thinned[1] or lifted off[5] devices never need to be handled off of the substrate material, relatively large scale integration can potentially be achieved with this process.

Initial fabrication runs have been successful. Back-to-back BNN diodes have been fabricated using the new technique and then measured for DC and low-frequency capacitance characteristics. Eight micron mesas with 1.5 and 3.75 micron wide Schottky metalization showed good C-V and outstanding I-V characteristics. While the C-V pulses were approximately two to three volts wide (full-width half-maximum), leakage currents were as low as 50 nA with 10 volts between pads. Mesas as small as 1 micron were successfully patterned.

Device Fabrication:

A. Semiconductor layer structure

Details regarding appropriate BNN layer structures have been addressed before[2,3,4]. The general approach for a GaAs-based BNN diode, from the top surface down, is to include: (1-optional) a thin GaAs cap layer, (2) an AlGaAs layer that is sufficiently thick to preclude tunneling but sufficiently thin to allow a large capacitance per unit area - 15 to 20 nm of $Al_{0.45}Ga_{0.55}As$ is typical, (3) near the AlGaAs, a highly doped region in order to ensure that the high capacitance mentioned above is achieved at zero voltage, (4) a moderately doped GaAs drift/varactor region in which all of the doping can be depleted with little parasitic conduction to the metal pads, and (5) a highly doped region that provides a low-resistance path between the two Schottky pads.

The structure used for these devices is as follows: (1) a 2 nm GaAs cap, (2) a 15 nm $Al_{0.45}Ga_{0.55}As$ barrier, (3) a 3 nm GaAs spacer followed by $5x10^{12}/cm^2$ silicon planar doping, (4) a $1x10^{17}/cm^3$ by 125 nm drift region, and (5) a $5x10^{18}/cm^3$ by 900 nm conducting base. A 600 nm undoped $Al_{0.45}Ga_{0.55}As$ layer for use as an etch stop layer was located just below the active device layers, although much thinner layers have also been successfully used. The layer structure is shown schematically in Figure 1. Capacitance-voltage measurements between large capacitance pads on another area of the same wafer gave the data shown in Figure 2.

The process is shown in Figure 3. We processed GaAs wafer pieces about 1.7 cm on a side that were laminated onto quartz pieces 76 microns (3 mils) thick by 2.5 cm in diameter. The GaAs wafers were initially 510 microns (20 mils) thick.

The Schottky contacts are defined by exposing AZ 5214 with a standard image reversal technique and then evaporating and lifting off Ti/Pt/Au. While we did not do a surface isolation, the devices should show less leakage current and particularly less parasitic capacitance if etching (or implanting) were done through (or into) the delta-doped layer. Etching by using the metal as a mask has been done successfully but not on the wafers processed in this work.

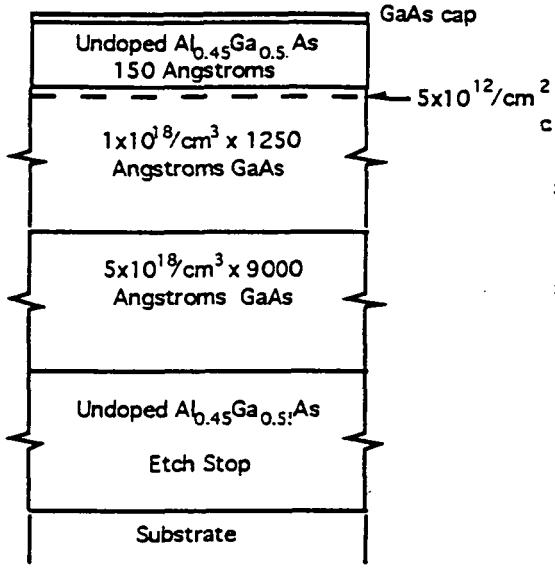

Figure 1: Epitaxially grown GaAs/AlGaAs layer for BNN diodes used in this study. Wafer layers were grown with molecular beam epitaxy. Doping is silicon.

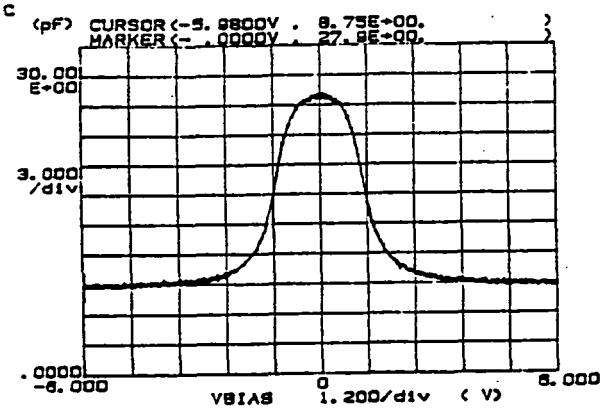

Figure 2: Capacitance-voltage characteristics measured at 1 MHz using large dots.

B. Device Processing

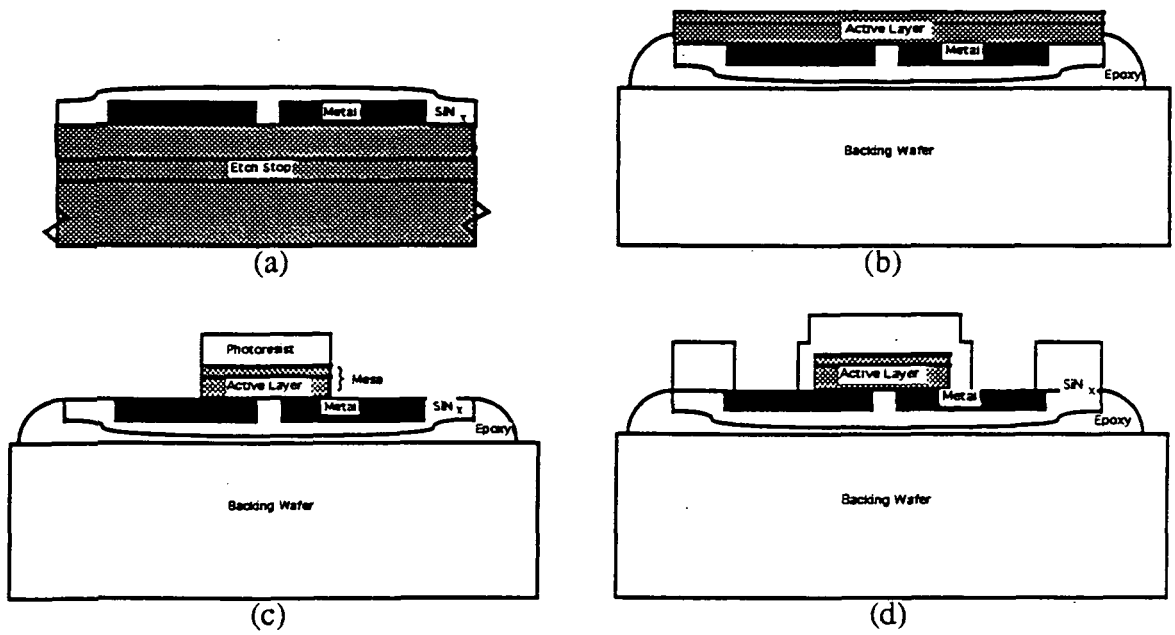

Figure 3: (1-a) The Schottky contacts are deposited, and a thin isolation through the delta-doped region is etched optionally, (2-a) front-side passivation is deposited, (3-b) the wafer is mounted face-down on a quartz wafer with wax for thinning (this wafer must be suitably thin to serve as the final substrate for the device and may be mounted in turn on a sturdier substrate), (4-b) conventional lapping and then selective thinning to an AlGaAs etch stop layer located just below the active layer, (5-c) lithography for mesa isolation is performed from the back of the wafer (at this point the wafer is sufficiently thin that the front-side metal can be viewed from the back through the substrate), and (6-c) the wafer is etched, (7-d) thin Si_3N_4 or SiO_2 is deposited in order to passivate the back and, if necessary, opened for bonding pads, and (8-d) the thin quartz wafer is diced.

The GaAs wafers were glued face down to a 75 micron thick quartz wafer, 2.5 cm in diameter, with UV-curing glue. The GaAs wafers were then lapped down to a 100 micron thickness using 5 micron, 1 micron, and finally 0.3 micron grit. Polishing was done with a silica colloidal suspension and pad. Selective thinning to the etch stop layer (5, above) was done using a 95/5 solution of ammonia and peroxide[1]. The peroxide/ammonia etch undercut the edges of the wafer two to three hundred microns, two to three times the vertical etch distance. Little damage of scale larger than pinholes of a micron or two in diameter could be seen over most of the wafers processed. A brief dip in HCl and water was used to remove the remaining oxide layer.

It should be noted that the wafers were remarkably rugged. The single cracked wafer observed so far occured during the lapping operation, which in our lab is performed using a relatively violent vibration table. The wafer that broke lost some small portions of the edge, but the area on which the GaAs was epoxied proved to be extremely tough despite cracks through the quartz. The wafer was processed to completion despite the cracks, with no allowances made to ease the normal rigors of microelectronic processing (spinning, contact lithography, etc.).

Mesas were defined by standard positive photolithography and dry etching. Wet etching was unsuccessful using either photoresist masks (excessive undercutting for the smaller, 1 micron mesas) or nitride masks (adhesion problems). The mesas were aligned to the frontside metal with IR backlighting, although the semiconductor is thin enough to permit aligning with optical backlighting if available.

Additional process steps have been done, including backside passivation with more ECR nitride and etching of contact holes with a CF4/O2 plasma. Clearly, the ability to deposit more metal in order to further reduce loss and to make MIM capacitors with the frontside metal and backside nitride is very attractive. Also, we have tried thinning the glue with acetone prior to spinning; this results in a much thinner layer (roughly 10 microns) between the GaAs wafer and the quartz substrate.

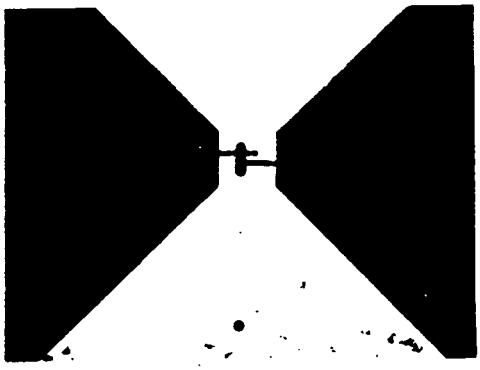

Figure 4: Backlit photograph of central portion of device. The small dark rectangle in the center is the approximately 4 x 16 micron micron mesa. The larger, dark portions with the thinner protrusions (2 micron fingers) are the Ti/Pt/Au pads. The remaining area is quartz.

The ECR nitride process is then repeated on the back, with windows opened with CF4/O2 RIE to the frontside metal for contacting. Other MMIC-style processing, including plating, MIM capacitor formation, etc. could be performed at this point.

Figure 4 shows a photograph of a completed device.

Electrical Measurements

Devices were checked for DC and capacitance characteristics after processing. Figure 5 shows the 1 MHz capacitance of a 3.75 x 8 micron device. While the peak capacitance is lower than expected from the capacitance data shown in Figure 2, it is thought that the difference is probably due to the fact that the processed wafer piece is from the edge of the MBE wafer. Figure 6 shows the DC current leakage before backside passivation. The measured current is many orders of magnitude lower than would be observed with comparable Schottky diodes, leading us to believe that the BNN is potentially superior as a multiplied power source.

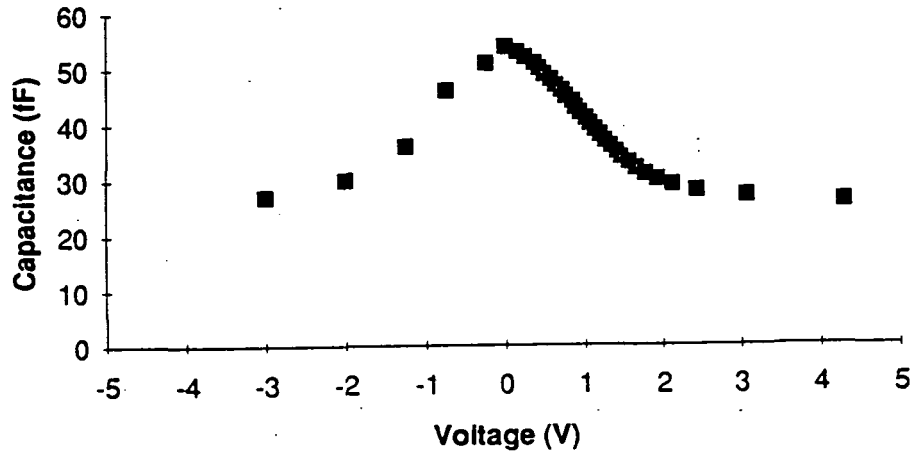

Figure 5: Measured C-V characteristics of a device with back-to-back 3.75 x 8 micron BNN diode.

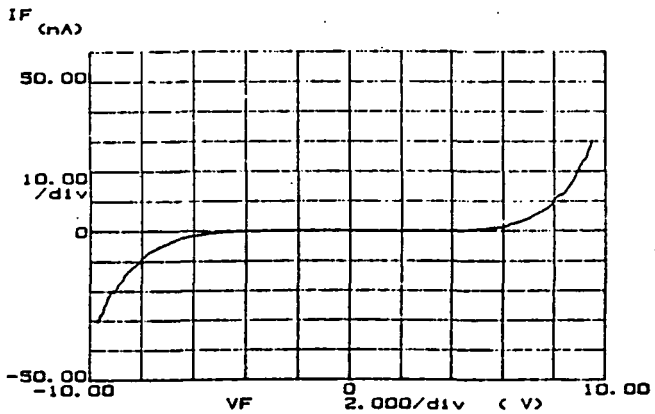

Figure 6: Measured DC leakage current for back-to-back 3.75 x 8 micron diode. Traces for positive and negative voltages were taken by sweeping away from zero volts. Higher leakage currents can be measured instantaneously if the voltage is not slowly swept; similar behavior commonly observed in MESFETs leads us to believe that the method used above is the most relevant.

Conclusions

We have demonstrated a new process for back-to-back diode fabrication using a BNN structure. The process should make integration of submillimeter-wave diodes much easier while simultaneously reducing RF losses through the elimination of all non-essential high-dielectric semiconductor. The BNN diodes constructed with this process show a strikingly low leakage current.

Acknowledgements

The research described in this paper was performed at the Center for Space Microelectronics Technology, Jet Propulsion Laboratory, California Institute of Technology and was sponsored by the National Aeronautics and Space Administration, Office of Aeronautics, Space, and Technology, and by the Army Research Office.

References

1 W.L. Bishop, E.R. Meiburg, R.J. Mattauch, and T.W. Crowe, "A Micron Thickness Planar Schottky Diode Chip for Terahertz Applications with Theoretical Minimum Capacitance," 1990 IEEE MTT-S International Microwave Symposium Digest, p. 1305.

2 U. Lieneweg and U. Maserjian, "Harmonic generation in the near-millimeter-wave range by thin-MOS structures," presented at Sixth International Conference on Infrared and Millimeter Waves, Miami, FL, 1981.

3 U. Lieneweg, T. Tomunen, M. Frerking, and J. Maserjian, "Design of Planar varactor Frequency Multiplier Devices with Blocking Barrier," submitted to IEEE MTT Special Issue on Terahertz Technology, 1991.

4 E. Kollberg, T. Tolmunen, M. Frerking, and J. East, "Current Saturation in Submillimeter Wave Varactors," submitted to thte IEEE MTT Special Issue on Terahertz Technology, 1991.

5 E. Yablonovich, T. Gmitter, J.P. Harbison, and R. Bhat, "Extreme Selectivity in the Lift-Off of Epitaxial GaAs Films," Appl. Phys. Lett. vol. 51, p. 2222 (1987).

6 Norland Optical Adhesive 61, Norland Products Inc., P.O. Box 145, New Brunswick, NJ 18902.

A 200 GHz TRIPLER USING SINGLE BARRIER VARACTOR

Debabani Choudhury, Margaret A. Frerking and Paul D. Batelaan

Jet Propulsion Laboratory
California Institute of Technology
Pasadena, California 91109, USA

ABSTRACT

The GaAs Schottky varactor diode is the non-linear device most commonly used for submillimeter wave harmonic generation. Output power adequate to serve as a local oscillator source for SIS tunnel junctions has been demonstrated with whisker-contacted GaAs Schottky varactor multipliers in waveguide mounts up to about 800 GHz. In this paper, we present results for a tripler to 200 GHz using a new multiplier device, the single barrier varactor (SBV). This new varactor has a potential advantages such as stronger non-linearities or special symmetry, which make it attractive for submillimeter wave frequency multiplication.

The performance of a tripler using a SBV over a output frequency range from 186 to 207 GHz has been measured in a crossed waveguide mount. The theoretical performance of the device has been calculated using large signal analysis. A comparison

of theoretical and measured results and a discussion of various losses in the mount and the varactor have also been presented.

INTRODUCTION

Heterodyne receivers are used for high spectral resolution shorter-millimeter and sub-millimeter wave astrophysics and earth remote sensing observations. Local oscillator, mixer and antenna are the critical components in a receiver. One approach to provide sub-millimeter power is to use the combination of a high-power millimeter-wave source with a harmonic multiplier for higher frequency generation. Frequency multipliers use a non-linear device to generate harmonics of the input frequency from a fundamental oscillator. Although the Manley-Rowe relations show that an ideal harmonic genarator with 100% efficiency is possible with a varactor, real multiplier circuits are limited by loss in the device and circuit and by impedance matching limitations at the input, output, idler and harmonic frequencies [1,2]. As the circuits become smaller with increase in frequency, impedances and losses become more difficult to control.

To achieve the full capability of the diode, appropriate embedding impedances must be provided by the multiplier mount. The impedances at the input and output frequencies must be set to maximize coupling power into or out of the device. In higher order multipliers, current flow at the intermediate harmonics (i.e. the idler frequencies) will enhance harmonic conversion. Therefore, the diode must be terminated with a lossless reactance at these frequencies. The embedding impedances are provided by the multiplier mount. Nonlinearities symmetric about zero bias will generate only odd

harmonics, greatly simplifying the multiplier mount design. For instance a tripler mount for a symmetric device will be equivalent to a doubler mount for a device without symmetry. Similarly, a quintupler mount will be equivalent to a tripler mount, both requiring one idler.

This paper presents the theoretical and experimental results of a 200 GHz tripler using a single barrier varactor (SBV) as the nonlinear device.

MULTIPLIER DEVICE

The single barrier varactor diode used as the multiplier device in our experiment, was developed at the Chalmers University of Technology [3,4]. These Chalmers devices were fabricated with the epitaxial GaAs/$Al_{0.7}Ga_{0.3}As$/GaAs material grown as indicated in Fig.1. It is inherently a symmetric device. The $Al_{0.7}Ga_{0.3}As$ barrier

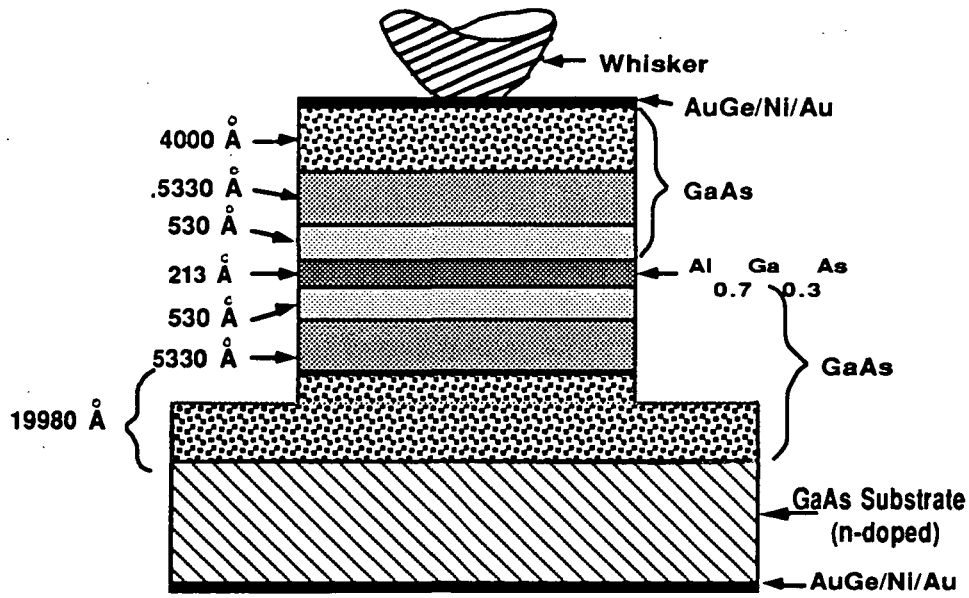

Fig.1: Schematic of the Chalmers Device

which blocks the current flow is in the center having a thickness of 213 Å. On either side of the barrier, there is an undoped GaAs spacer having a thickness of 53 Å. GaAs depletion region ($n=1x10^{17}$ cm^{-3}) on either side has a thickness of 5330 Å. Top and bottom contacts are formed on highly doped GaAs regions ($n=3.4x10^{18}$ cm^{-3}) using 1000 Å AuGe, 200 Å Ni and 1600 Å Au. The top contact is made with a whisker and the bottom is a large area ohmic contact. The $Al_{0.7}Ga_{0.3}As$ barrier will to a large extent prevent electrons from passing through the structure. Thus the conduction current through the device is very small. For moderate voltages, the conduction current is essentially caused by thermionic emission. The width of the depleted part of the moderately doped epitaxial layer will vary with bias voltage, thus forming a voltage dependent capacitance C(V). When the diode is biased in the forward direction, the depleted region will appear on one side of the barrier, and the depletion capacitance of the device will decrease with increasing voltage. Since the diode is symmetric, a reverse bias will in the same way cause a decrease in the capacitance value of the device. Hence, the maximum capacitance is obtained for zero voltage and is determined by the thickness of the $Al_{0.7}Ga_{0.3}As$ barrier. The minimum capacitance which occurs for maximum bias voltage, is determined by the doping concentration and the extension of the moderately doped drift region. For an appropriately designed device, similar capacitance swing with voltage as for the Schottky-varactor diode is expected [5].

The losses due to the series resistance may be larger in the SBV diode than in Schottky varactors, since the maximum current $i_{max}= CdV/dt$ will occur for V(t) = 0, i.e. when both dV/dt and C are maximum and n-doped drift regions on both sides of the barrier are undepleted and contribute to the series resistance. In addition, for small area device, the ohmic contacts exhibits higher resistance than Schottky contacts. However for a Schottky varactor tripler, the idler current at the second harmonic will degrade

the tripler performance, since any finite reactance termination will cause power losses in the series resistance. For the SBV tripler, this particular problem is virtually non-existent [4].

The Chalmers devices tested here, have a mesa height of about 2.5 microns and area of 5x5 micron^2. In order to evaluate the dc characteristics, the device has been mounted in a coaxial mount as shown in Fig.2. The S-parameters are measured using a HP 8510B Network Analyzer. The K-connector provides 50 ohms up to the whisker to allow accurate de-embedding of the mount [6]. The equivalent circuit of the diode mounted in a co-axial mount is shown in Fig.3. Chalmers device was measured to have a dc series resistance of 7 ohms. The measured C-V and I-V characteristics for the 5x5 micron^2 Chalmers device are shown in Fig.4. The measured maximum capacitance is

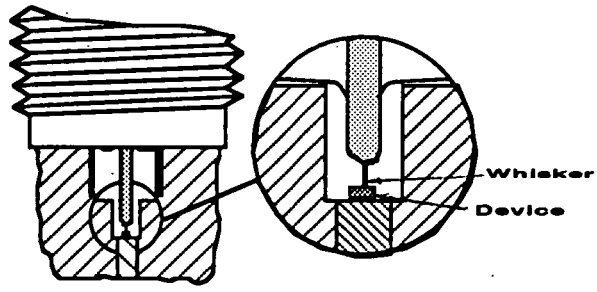

Fig.2 : Schematic diagram of the device mounted in a coaxial mount

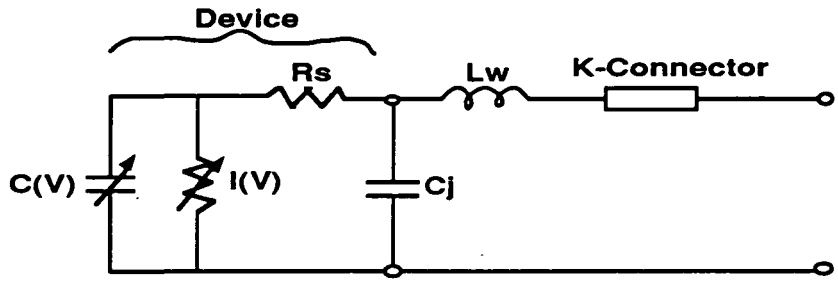

Fig. 3 : Equivalent circuit of a device in a coaxial mount

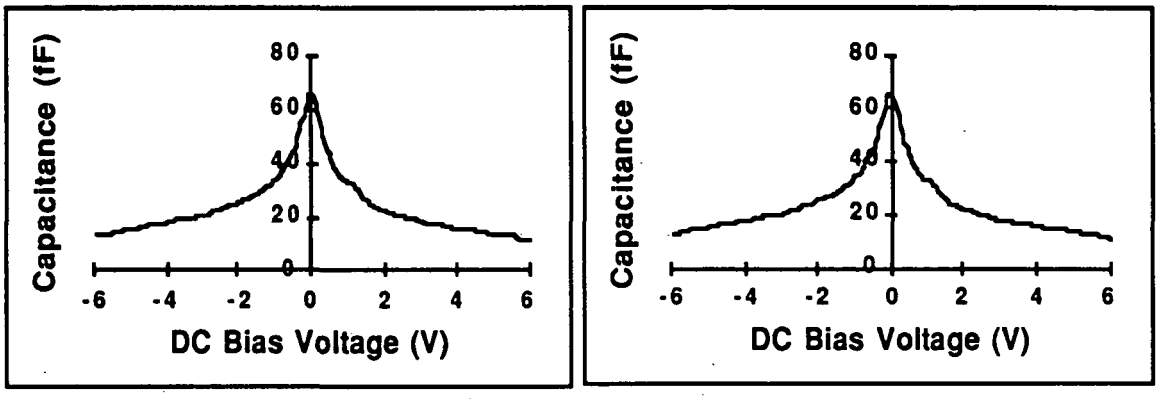

Fig.4 : Measured C-V and I-V characteristics of Chalmers device

65.6 fF and minimum capacitance is 12.4 fF. The figure of merit of the diode, which is its cut-off frequency, is given by,

$$f_c = \frac{1}{2\pi R_s}\left\{\frac{1}{C_{min}} - \frac{1}{C_{max}}\right\}$$

Chalmers device has a cut-off frequency of 1200 GHz. The diodes are found to be damaged when the dc voltage exceeded about 6V.

LARGE SIGNAL ANALYSIS

The critical step in the multiplier analysis is to solve the voltage and current waveforms of the nonlinear device which is pumped and biased in an arbitrary embedding network. A common solution of this nonlinear problem is to use a type of harmonic balance technique. Time-domain current and voltage solution are sought which

satisfy the diode conditions and frequency-domain solutions are sought which satisfy the external circuit equations. In this work, a modified nonlinear program based on Siegel, Kerr and Hwang [5] has been used in order to calculate the tripling efficiency of the Chalmers single barrier varactor diodes. Fig. 5 shows the equivalent circuit of a

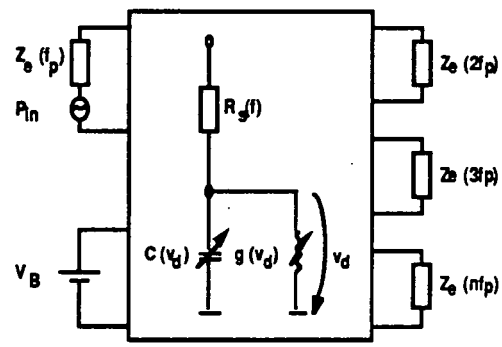

Fig.5 : Eduivalent circuit of a multiplier

multiplier. Harmonic triplers with 186 GHz,192 GHz, 200 GHz, 207 GHz output frequencies are calculated. We have optimized the impedance at the third harmonic frequency. The idler and the higher harmonics are set to open circuits. Impedance up to 12th harmonic are analyzed. In the analyses, the measured C-V and I-V characteristic shown in Fig.4 have been used. Since the series resistance is important in the device performance, the calculations are carried out for a range of resistances, 5 ohm, 10 ohm, 15 ohm and 20 ohm.

Fig.6 presents efficiency versus the input power for a SBV tripler to 192 GHz taking series resistance of the device as a parameter. In order to quantify the effect of current flow in the device on the multiplier performance, we have calculated the performance for a device with 5 ohm series resistance with no current. The theoretical efficiency is found to degrade from 45% to 20% when the measured current is included. Higher device series resistance degrades the tripler performance significantly as the

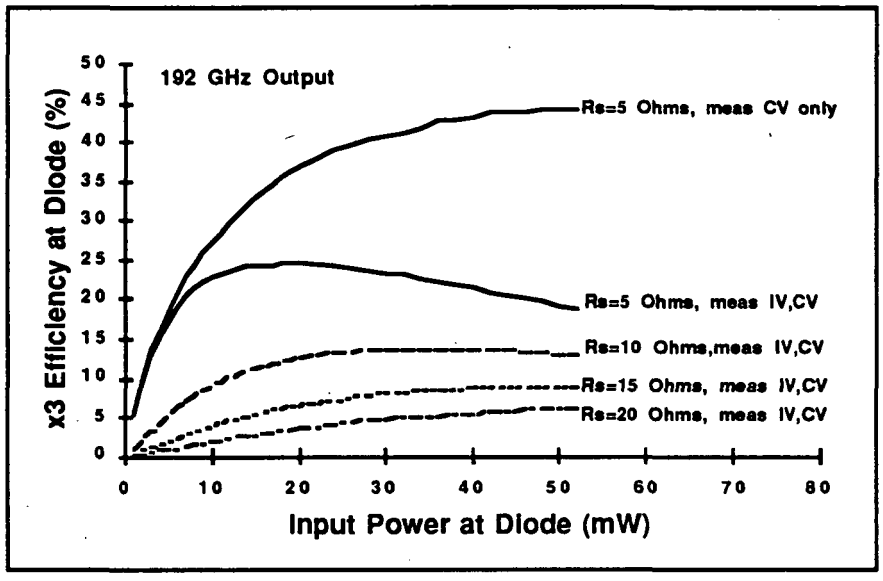

Fig.6 : Calculated tripling efficiency for Chalmers device

series resistance of 20 ohm results in about a factor of four worst performance than a series resistance of 5 ohm.

200 GHz WAVEGUIDE MOUNT

To achieve optimum performance of the device, it must be provided with the appropriate circuit embedding impedances. The impedances at the input and output frequencies must be set to maximize coupling power into or out of the device. In higher order multipliers, current flow at the intermediate harmonics i.e. the idler frequencies will enhance the harmonic conversion. Therefore, the diode must be terminated with a lossless reactance at these frequencies.

An output of the large signal analysis, used to optimize the device, is the

required embedding impedance. In fig.7, the real part of the optimum impedance is

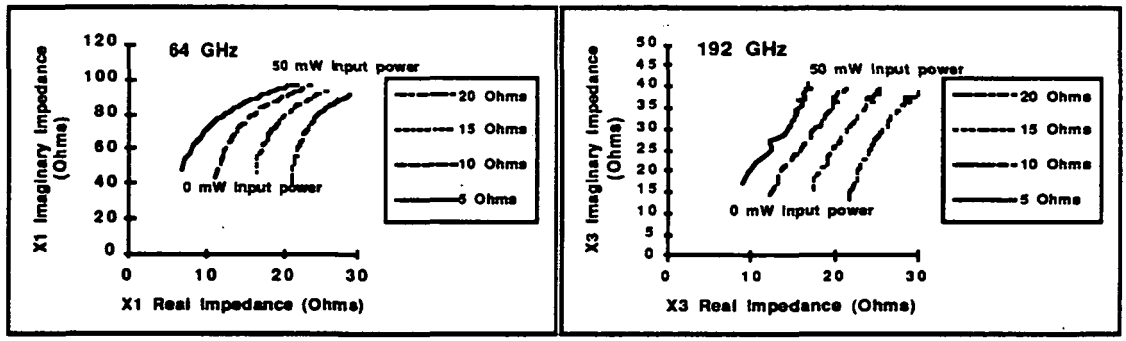

Fig. 7 : Input and output circuit optimum embedding impedances calculated by large signal analysis

shown on the horizontal axis and the imaginary part on the vertical axis, parameterized by the input power for both the input frequency (R_1, X_1) and the output frequency (R_3, X_3). Impedances are plotted for different series resistances of the device. Input power increases from 0 mW to 50 mW. At low input power the real part is same as the device series resistance. The input imaginary impedance is the impedance corresponding to the maximum capacitance at input frequency. As the input power increases, the device capacitance decreases increasing the impedance. The real impedances needed are in the range from 7-30 Ohms. The imaginary impedances range from 40-100 Ohms for the input circuit and from 15-42 Ohms for the output circuit respectively.

The embedding impedances are provided to the single barrier varactor (SBV) device by a crossed waveguide mount. In addition the mount distributes the power. A schematic drawing of the crossed waveguide mount is shown in Fig.8. The single barrier varactor device is mounted spanning the output waveguide. The output waveguide is actually oriented perpendicular to the plane of the paper. Power at the input frequency travels down the input waveguide. A low pass filter consisting of Au metallization on the

quartz substrate couples the input power from the waveguide to the whisker contacted

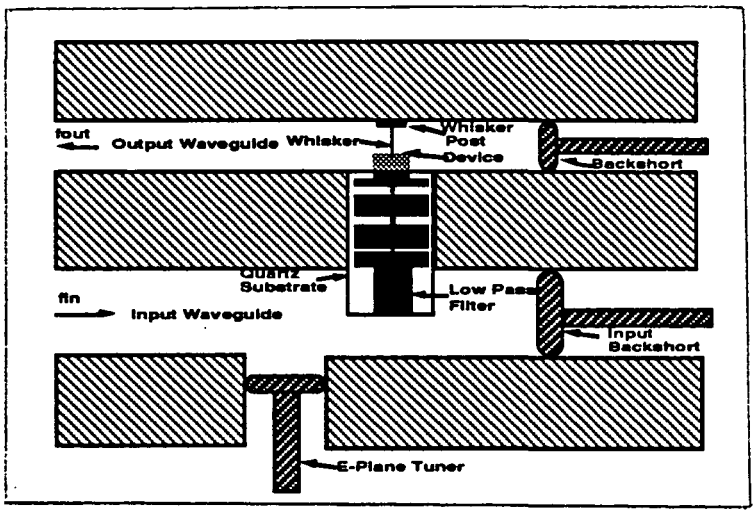

Fig.8 : Schematic diagram of the device in the mount

SBV device located at the output waveguide. An E-plane tuner and a backshort at the input waveguide provide adjustments to optimize the embedding impedance at the input frequency. The output waveguide is cutoff at the input frequency preventing propagation down it, thereby confining the input power to the vicinity of the SBV device. The tripled power is coupled out the output waveguide. The embedding impedance at the output frequency is adjusted by varying the whisker length and by a movable backshort. The low pass filter prevents the output frequency from traveling to the input waveguide. A scanning electron micrograph of the device in the mount is shown in Fig. 9.

EXPERIMENTAL RESULTS

The set-up for 200 GHz tripler measurements is shown schematically in Fig.10. A 60-70 GHz klystron is used as the pump source. The input power is monitored

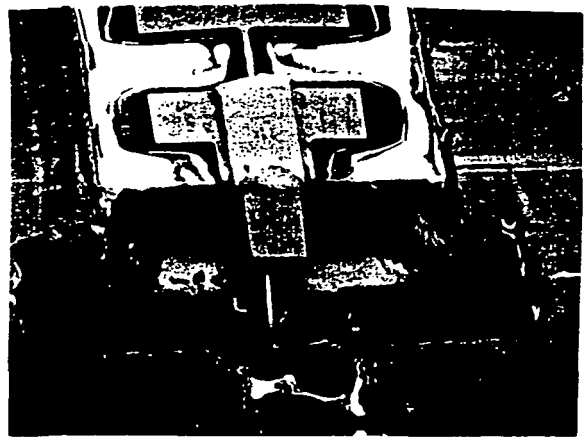

Fig. 9 : Scanning Electron Micrograph of the device in the mount

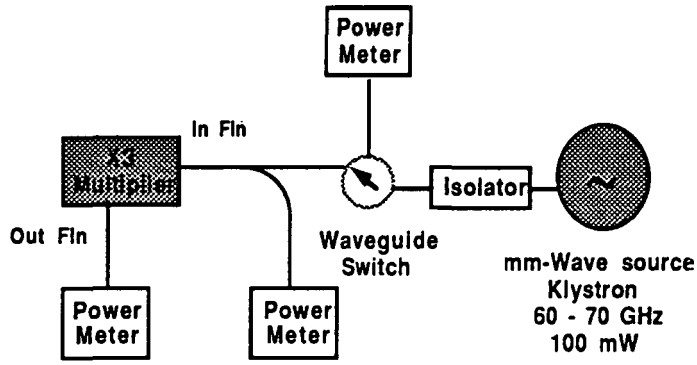

Fig.10 : Test setup for the 200 GHz tripler measurement

by a Anritsu power meter, calibrated to give the power at the input flange. The reflected power is measured using a directional coupler coupled to a second power meter. The third harmonic output power is measured by a third powermeter. We determine the loss at the third harmonic in the waveguide from the output flange to the powermeter by a substitution technique. The observed loss in the WR4 output waveguide is 0.032 dB/λ,

consistent with the resistive losses corresponding to the metal conductivity of $2x10^7$ mho/m. The flange-to-flange efficiency is defined as the ratio of the power at output flange to the power available at the input flange. Using various whisker lengths, the efficiency and output power were measured between 186-207 GHz. Measurements were taken with three different whisker lengths, 6 mil, 8.4 mil and 11 mil. It was seen that, the Chalmers 25 micron^2 device, contacted with a 8.4 mils long whisker gives best tripler performance. The measured efficiency versus input power for 186 GHz, 192 GHz, 196.5 GHz and 201 GHz output frequencies are shown in Fig.11 for a 8.4 mil long

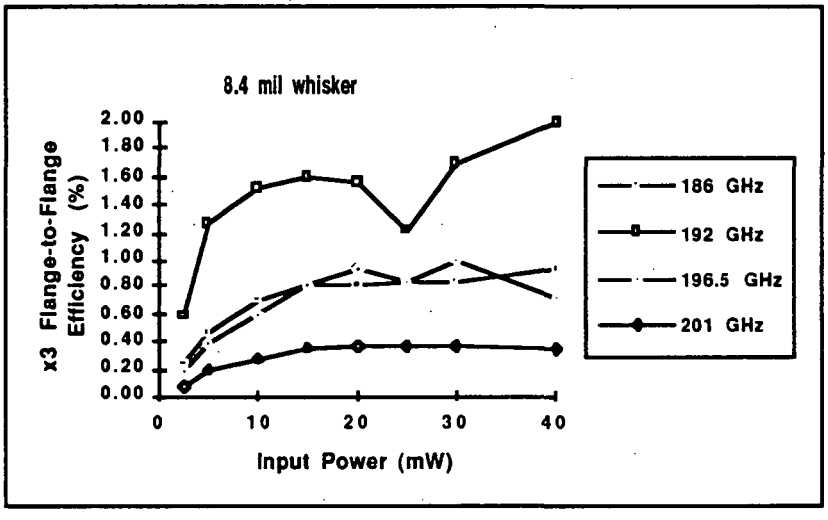

Fig.11 : Measured efficiency versus input power plot for the tripler

whisker contact. The best performance has been achieved at 192 GHz, giving an efficiency of more than 2% at 40 mW input power. This is similar to the results demonstrated by Rydberg et al. using the same device [3].

To compare the experimental results to the performance predicted by large signal analysis, the loss in the multiplier mount is assesed. Loss arises from several mechanisms. At the input frequency, the finite conductivity of the waveguide and

dielectric loss in the filter are very small. The primary loss mechanism is due to the impedance mismatch. By measuring reflected power at the input, less than 0.2 dB loss due to mismatch was observed, over the frequency range tested.

At the output frequency, the impact of finite conductivity is higher. In addition, losses due to imperfections in the backshort are critical. Other mechanisms include the impedance mismatch and higher harmonic generation.

Some of these loss mechanisms at the output frequency have been modeled using Hewlett Packard's Microwave Design System (MDS) package. Fig.12 shows the

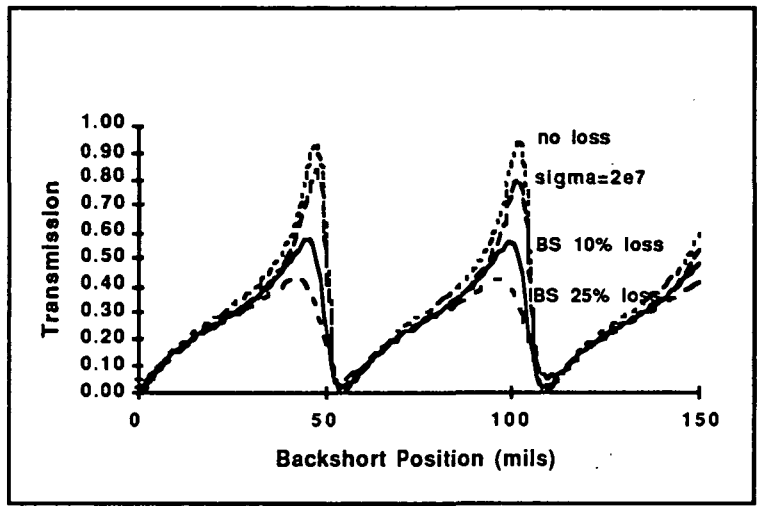

Fig.12 : Calculated transmission from the diode to the output flange of the tripler mount

calculated transmission from diode in the tripler mount to the output flange of the mount as a function of backshort position. When there is no loss, the transmission is 100% at resonant positions of backshort. If a finite conductivity of 2×10^7 mho/m, the measured conductivity of the WR4 output waveguide is included, the peak transmission reduces to about 90%. If in addition, the backshort has a 10% loss, the transmission reduces to

about 60%. For a backshort loss of 25%, the transmission goes down to 40%. The losses reduce the height of the peaks and the sharpness of the resonances out. In addition, the antiresonant backshort positions donot give zero percent transmission.

The measured results are plotted in Fig.13, which shows the relative

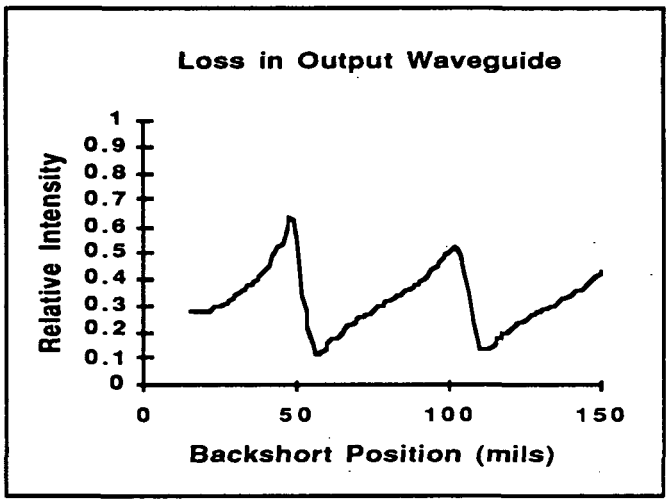

Fig.13 : Plot of measured output power as a fumction of output backshort position

output power as a function of output backshort position. This looks qualitatively similar to the theoretical results. The measured first peak match the theoretical results with 10% backshort loss, while the valley and second peak are closer to the 25% backshort loss.

Based on these observations, the multiplier mount loss budget is presented in Table-I. In the output circuit, the loss due to the finite conductivity is estimated as 1 dB. Loss due to backshort is 3 dB. Impedance mismatch loss and loss due to higher harmonics are not known. Therefore, the loss in the output circuit is estimated to be more than 4 dB. Input circuit loss is estimated to be less than 0.2 dB. Using these loss values, 0.2 dB at input and 4 dB at output, the measured flange-to-flange efficiency is

Table - I

	Loss
Output Circuit	
Finite Conductivity	**1 dB**
Backshort Loss	**3 dB**
Impedance mismatch	**?**
Higher harmonics	**?**
Total	**> 4 dB**
Input Circuit	
Impedance Mismatch (Reflected power)	**0.2 dB**

corrected to determine the efficiency at diode, which is plotted in Fig.14. Superimposed of diode efficiencies are the theoretical efficiency calculated from the measured CV and IV curves for series resistances 10 ohm, 15 ohm and 20 ohm. At low input power the measured efficiency follows the theoretical efficiency for a series resistance of about 12 ohm. The measured dc series resistance is 7 ohm. At 192 GHz, the series resistance is

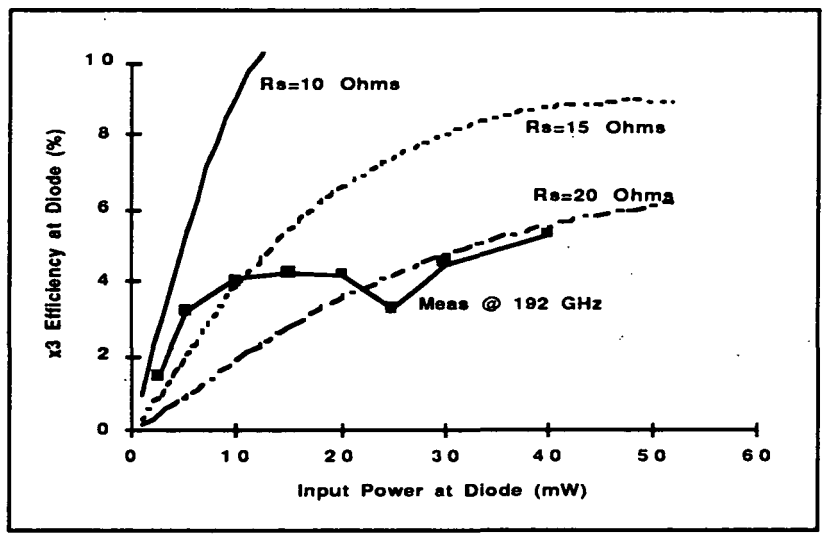

Fig.14 : Tripling efficiency at diode versus input power plot

expected to be somewhat higher due to skin effect. At higher power the efficiency falls off. This fall off corresponds to the power at which the device starts drawing significant current. This suggests that the impact of the current flow in the device on the multiplier performance is not well understood.

DISCUSSION AND CONCLUSION

The single barrier varactor diode has been shown to be able to provide more than 5% efficiency as a 200 GHz tripler. About 2% flange-to-flange tripling efficiency is obtained using the crossed-waveguide tripler mount for symmetric devices. The multiplier mount has a 0.2 dB input circuit loss due to the impedance mismatch, introduced by the reflected power. A total loss of more than 4 dB is estimated at the output circuit. This includes the 1 dB loss due to finite conductivity of the waveguide and 3 dB loss due to the backshort.

Development of devices with lower leakage current will significantly improve the tripler performance. Results can be further improved by reducing the output circuit 4 dB loss by improving the imperfect backshort.

ACKNOWLEDGEMENTS

The research described in this paper was performed by the Center for Space Microelectronics, Jet Propulsion Laboratory, California Institute of Technology and was sponsored by the National Aeronautics and Space Administration, Office of

Aeronautics, Space and Technology. Authors would like to thank Prof. E.Kollberg for kindly supplying the SBV devices and Mark Natzic for whisker contacting the devices into the multiplier mount. Authors also would wish to thank T.J.Tolmunen for various useful discussions and Hans Grönqvist for giving some valuable information about the device.

REFERENCES

[1] T.J.Tolmunen and M.A.Frerking,'Theoretical Efficiency of Multiplier Devices', Second International Symposium on Space Terahertz Technology, 197- 211, (1991).

[2] P.W.Penfield and R.P.Rafuse,'Varactor Applications', The MIT Press, Cambridge, MA, (1962).

[3] A.Rydberg, H.Grönqvist and E.Kollberg, 'Millimeter- and submillimeter-wave Multipliers using Quantum Barrier varactor (QBV) Diodes', IEEE Electron Device Letters, 373-375, vol.11, No.9, September, (1990).

[4] E.Kollberg and A.Rydberg,'Quantum-Barrier-varactor Diodes for High-Efficiency Millimeter-wave Multipliers', Electronics Letters, 1696-1698, Vol.25, No.25, (1989).

[5] O.Boric, T.J.Tolmunen, E.K.Kollberg and M.A.Frerking,'The Anamolous Capacitance of Quantum Well Double-Barrier Diodes', submitted to International Journal of Infrared and Millimeter Waves (1992).

[6] M.Frerking and J.East,'Novel Varactors', submitted to the Proceeding of the IEEE (1991).

[7] P.H.Siegel, A.R.Kerr and W.Hwang,'Topics in the Optimization of Millimeter-wave Mixers', NASA Tech. Paper 2287, (1984).

A Submillimeter Tripler Using a Quasi–Waveguide Structure

Neal R. Erickson and German Cortes–Medellin
Five College Radio Astronomy Observatory
Department of Physics and Astronomy
University of Massachusetts
Amherst, MA 01003

Abstract

A new type of frequency multiplier structure is being developed which is suitable for application at frequencies above 1 THz. This structure preserves some of the properties of waveguide for mode control, yet is not truly single mode. The device resembles a sectoral horn, with a varactor diode mounted near the throat. Input and output coupling are through the same aperture, requiring a quasi–optical diplexer. Initial tests are directed at building a tripler at 500 GHz, for comparison with waveguide structures. The diplexer is a blazed diffraction grating with appropriate focusing optics. Model studies show that the impedance match to a varactor should be good, and initial tests of the beam patterns of the prototype indicate that optical coupling efficiency should be very high. The structure also has the potential for use as a fundamental mixer, or as a third harmonic mixer.

Introduction

As the operating frequencies of receiver systems shift toward ever higher frequencies, it has become apparent that there is no clear upper limit to the application of single mode waveguide [1,2]. However, the machining and assembly problems increase rapidly above ~300 GHz, and it seems clear that by some frequency of ~1THz, the cost of waveguide components will be too high for use in most systems. This limitation is purely a practical one; the loss of waveguide does not seem to be a serious limit since submillimeter parts use very short waveguide runs. However, the loss is high enough to be of some concern. Cube corner mixers have been used in the higher frequency range, but suffer from a low beam efficiency and a rather high embedding impedance. This paper suggests a new type of mounting structure to replace waveguide at these frequencies, which combines some of the advantages of both waveguide and quasi–optical structures.

An ideal mounting structure for a >1THz multiplier should have the following characteristics:

1. Ease of fabrication, both in the machining and the assembly with the diode.
2. Good mode control at all frequencies involved.
3. Resistive losses should be low.
4. Impedance level should match varactors, which tend to have a low real part and require series inductance for matching.
5. The structure should be readily suited for whisker contacted diodes. Shape or size of the chip should not be critical, and whiskers should not be too short.
6. If the device is optically coupled, the ports should be linearly polarized.
7. Beamwidth should be reasonably narrow to ease the design of coupling optics.

The structure being studied appears capable of satisfying all of these points, although tests are still in progress. The relative ease of fabrication of the 500 GHz prototype indicates that a scaled device at well over 1 THz should be practical. Additionally the needed coupling optics have been developed, which appear capable of separating the input and output beams with low loss as well as coupling them to a source and load.

Quasi–waveguide Mount

The structure as shown in Fig. 1, is essentially a pair of parallel metal plates separated by less than $\lambda/2$ at the highest frequency of interest, with two intersecting sidewalls to guide the beam. The sidewalls intersect at 90° in the prototype, although other angles may be equally good or better. The varactor is mounted between the top and bottom plates, spaced from the vertex by less then 0.71λ at the highest frequency. With these constraints, the structure can couple only to a mode with the electric field uniform and perpendicular to the plates, and the mode pattern in the H plane has single maximum. To produce a convenient output beamwidth, the top and bottom plates are made nonparallel so that the separation becomes a few wavelengths at the opening. The best situation for ease of design would be to make the planes parallel at the diode, and then change the angle to begin the flare, as in a typical waveguide–horn interface. However, this makes the structure impractical to build at >1THz, so the approach taken was to maintain a continuous flare, which is slow enough to not greatly perturb the embedding conditions at the diode. If this flare becomes too fast, the embedding impedances may change and the evanescent higher modes at the diode are not sufficiently cut off before the separation becomes great enough for

them to propagate. The relatively large spacing of the plates (compared to reduced height waveguide) makes mounting a diode and whisker easier, and reduces the losses. The wide side wall spacing minimizes their contribution to the loss except near the vertex.

A model study was done to determine the embedding impedances in this structure. A coaxial probe was introduced up to the effective terminal where the diode would be contacted, and a "contact whisker" of various lengths and shapes extended to the opposite wall. Various vertex distances within the constraint of the maximum spacing were also tested. The general result is that any antenna within this structure acts as an inefficient radiator so that it maintains the character of a lossy transmission line, with the loss increasing with frequency. Thus it shows resonant behavior, which is pronounced when the plate spacing is as wide as used here. The diode terminal impedance circles the Smith chart, at a high value of ρ, with approximately periodic behavior dependent on the physical length of the whisker, rather than the plate spacing. The match initially appears quite poor at all but the highest frequencies, but it is found that through the choice of whisker length and shape, it is possible to achieve a considerable range of impedances at three harmonically related frequencies. By adding a short circuited transmission line in series with the contact whisker (with two adjustable parameters, length and impedance), it is possible to produce an even wider range of values. The net result is that a reasonable match may be made to the impedance of a varactor, over a bandwidth of 5%, at all three frequencies required for a tripler, including a low resistance at the idler. The best configuration occurs with the

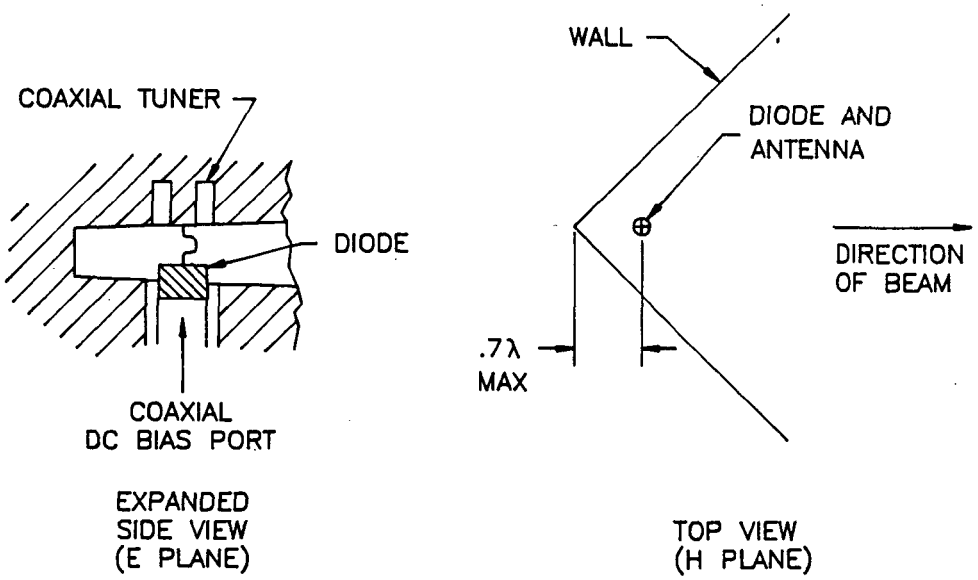

Fig. 1. Top view and side view cross section of the quasi–waveguide tripler.

maximum plate separation and vertex distance allowable, but there is still some freedom in the choice of whisker parameters (length, diameter and shape). No other flare angles were tested, so this remains as another possible adjustment. While the bandwidth of this particular choice of geometry is limited, it seems good enough to evaluate the potential of the device.

Based on this design, a prototype tripler has been fabricated for an output frequency of 500 GHz. Initial tests seemed best at a frequency where comparison with the results for waveguide mounted devices is possible, while this frequency is high enough to permit a realistic assessment of the fabrication difficulties. The structure is built as a split block, with the bottom plane and side walls in one part, and a flat plate forming the other half. The diode in this device is biased through a coaxial filter designed to present a short circuit at all three frequencies involved. As in typical mixers and multipliers, the diode chip is mounted on the end of the coaxial filter, forming much of the final section. The diode chosen is U.Va. type 2T2 with $C_j(0) = 6fF$, $R_s = 12\Omega$, and $V_b = 11V$. The flare angle of the plates is 9°, over a total length of 2.3 cm, so that the opening aperture is 3.6 mm. The whisker is mounted on the end of a short circuited coaxial section providing the needed reactances at the input and output.

While the bottom half of the mount was made by electroforming over the corner of a cube, it could also easily be machined, except for the vertex itself, where a small radius has little effect. Probably the most difficult machining area is in the coaxial bias filter, which would be impractical at substantially higher frequencies. An alternative is to use a very thin capacitor for rf bypass between the diode and the bottom plane; this would also require a thin diode. A bias wire can then connect to a feedthrough at the vertex.

Coupling Optics and Diplexer

A quasi–optical device is only of value if it can be coupled efficiently with optics. In this case the input power is likely to be derived from a waveguide mounted varactor multiplier with a feed horn on the output, which may be approximated by a Gaussian beam waist. The output load will almost certainly be an antenna coupled mixer but the details of the pattern of such a mixer are presently unknown. We can only assume that a Gaussian beam is suitable.

Beam patterns for this device are expected to be those of a uniformly illuminated aperture in the E plane and one sector of that due to a square array of four antennas in the H plane. The E plane pattern has a moderate sidelobe level reducing its coupling efficiency to about 85% to a Gaussian mode, while the H plane pattern is well tapered with no sidelobes, and thus couples with high efficiency. The beam is unusual in that the phase centers for the two planes are far apart. The H plane originates essentially at the vertex, while the E plane center is at the physical aperture. Thus the optics must be very astigmatic. In addition, the beams at the input and output are very different in size, particularly in the E plane.

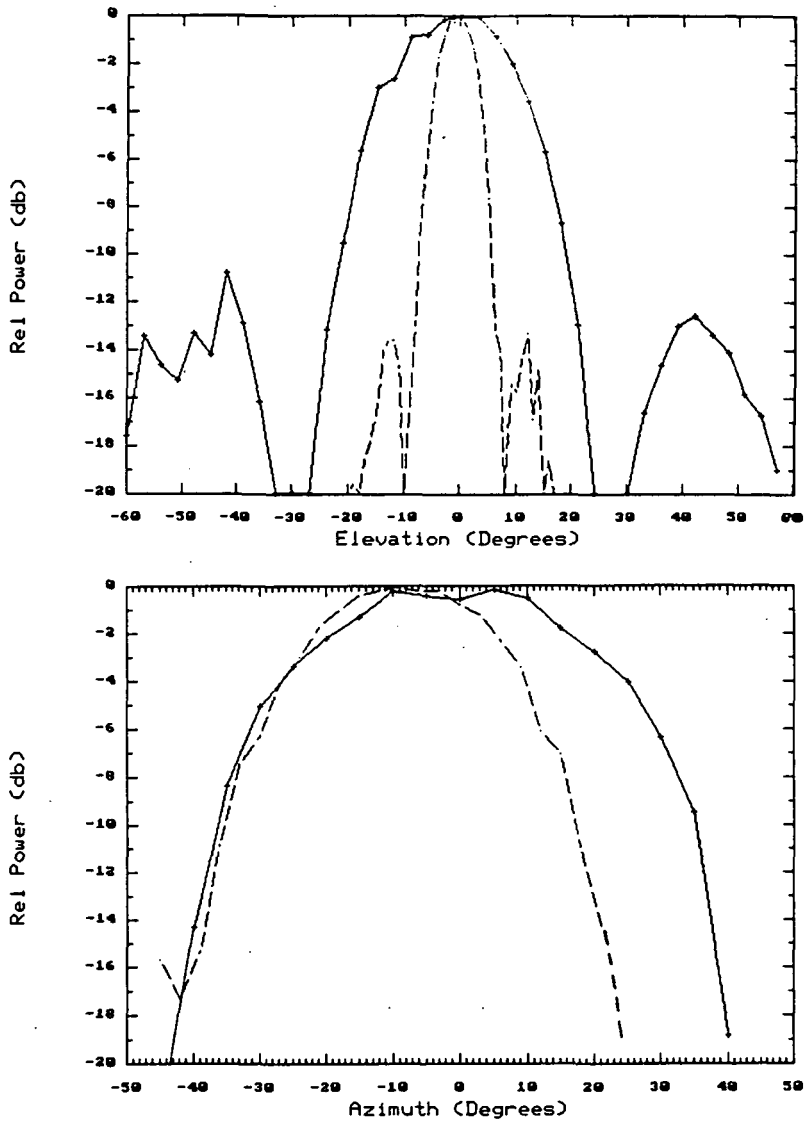

Fig. 2. Cuts through the principle planes of the beams in the E plane (azimuth) and the H plane (elevation). Solid line is at 164 GHz, dashed line is at 492 GHz. Beams are for the tripler without additional optics.

Tests have been performed using the varactor diode as a video detector at both frequencies, with sources at 164 GHz using a doubled Gunn oscillator, and at 492 GHz using the same oscillator multiplied by six. E and H plane cuts are shown for the prototype in Fig. 2, for both frequencies of interest. Full contour maps show no additional features out of the principle planes. These patterns confirm the theoretical predictions, but the H plane at the output frequency is off center by about 9°. This is due to a small asymmetry in the whisker location or shape, but otherwise the beam shape is as expected.

Frequency separation in the submillimeter may be done in several ways, but is particularly easy for a tripler because of the large frequency ratio. While a perforated plate high pass filter would work well [3], an easier device to fabricate is a diffraction grating. With the correct grating period, the input frequency can be below the onset of diffraction so that the grating behaves as a simple mirror, while the output can be scattered in a very different direction in the first order. A particular advantage of this mode of operation is that the input signal is well isolated from the output, which makes measurement of the output power easier since filters are not needed. The efficiency of this scattering can be made very high through the correct choice of reflection geometry and the blaze angle of the grooves. The electric field must be perpendicular to the ruling direction for high efficiency. A convenient configuration is with the grating tilted by 45° relative to the two beams, reflecting the input through 90° and the output by 45°. This requires a blaze angle to the grooves of 22.5° and a period of 0.86 mm. These optics are shown in Fig. 3. There is no

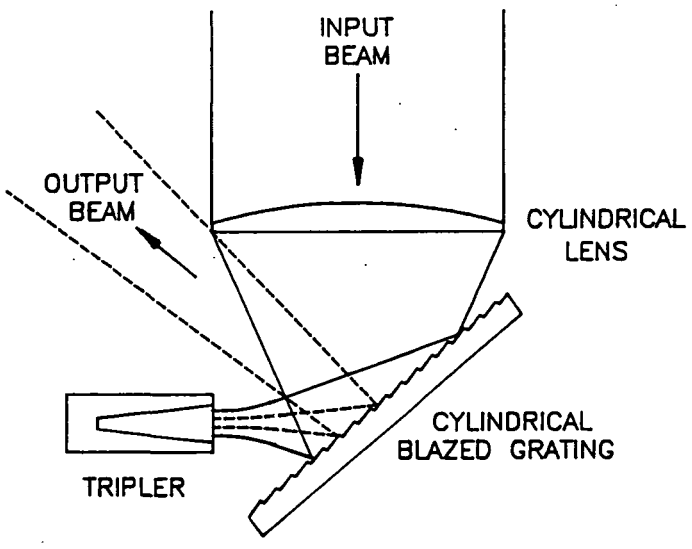

Fig. 3. Diplexer and optics to separate and focus the beams. The grating is cylindrical in the plane out of the figure.

scattering loss at the input, while the theoretical scattering into the two possible unwanted orders at the output totals about 5%. Gratings may be curved in one dimension without loss of function, so a cylindrical grating with a radius of curvature of 5.3 cm is used to eliminate the the very rapid divergence in the H plane. For a highly curved surface such as this one at an off–axis angle, there is higher loss at the edges due to the projected tilt of the grooves relative to the polarization vector.

These optics have been tested with the prototype and show essentially the intended function. The grating efficiency is in fact very high and a scan through two orders shows only 3% of the power in zeroth order relative to the desired first order. The spurious second order is exactly backscattered and is unmeasurable, but is predicted to be the same as the zeroth order. The focusing action is very good in the H plane, producing a beam at the input requiring only one further cylindrical focusing mirror or lens (in the other plane). At the output frequency the beam can be made fairly symmetric with just the one mirror. One additional complication is due to the off axis cylinder; the focal length of such a mirror

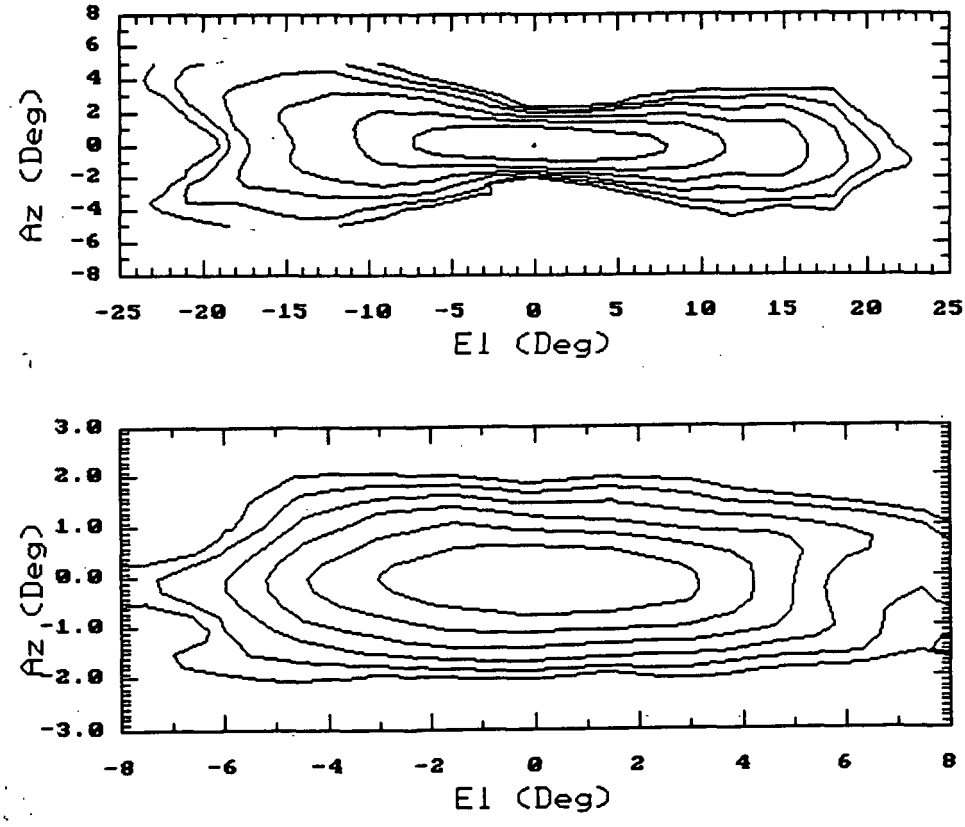

Fig. 4. Beam pattern measured at the line focus of the cylindrical grating at (a) 164 GHz and (b) 492 GHz. Contour interval is 3 dB. The focal distance is different for the two frequencies.

depends on the incidence angle (in the plane of Fig. 3). Because the beams are broad in this dimension, this is quite noticeable in the beam patterns, particularly for the input since this beam is the widest, and the most off–axis. This effect is apparent in the contour map of the input beam, shown in Fig. 4a, as measured near the refocusing point about 50 cm away. The problem is much less apparent in the output beam, shown in Fig. 4b. The easiest cure is to make the grating a different shape, but a periodic ruling can only be made on a few surfaces. It appears that a conical grating can satisfy the requirements, if it represents only a small distortion of a cylinder, but this solution remains to be tested. Optics beyond this point are still being designed, but appear to be straightforward mirrors or lenses.

Conclusions

A new type of mounting structure is proposed for use in a frequency tripler, which is relatively easily fabricated for frequencies above 1 THz. Beam patterns are suitable for efficient coupling to an input source, although the optimum optical system remains to be designed. The present use of a blazed diffraction grating appears to be an excellent means to separate frequencies, with high input–output isolation. The behavior of the device seems less suitable for use as a doubler, although this has not been explored in detail.

A second use might be as a mixer mount for a higher performance submillimeter mixer than cube corner mixers. The application would be much more narrow band, but offers more optimal impedances and a greatly reduced side lobe level. It might also be practical to use for a third harmonic mixer, extending the frequency range of mixers using multiplied sources. A recent analysis of a third harmonic mixer for 1 THz indicates that a properly designed mixer should be quite competitive [4], but this analysis has not been extended to the impedance environment presented by this structure.

References

1. B.L.A. Rydberg, B.N. Lyons, and U.S. Lidholm, "Multipliers for THz heterodyne systems," Proceedings of the Second Int'l. Conf. on Space THz Tech., pp. 212–217, 1991.

2. N.R. Erickson, "Low noise 500–700 GHz receivers using single–diode harmonic mixers," Proceedings of the First Int'l Symposium on Space THz Tech., pp. 339–408, 1990.

3. P.H. Siegel, R.J. Dengler, and J.C. Chen, "THz dichroic plates for use at high angles of incidence," IEEE Microwave and Guided Wave Lett., Vol. 1, pp. 8–9, 1991.

4. N.R. Erickson, "Low noise submillimeter receivers using single–diode harmonic mixers," to be published in Proceedings of the IEEE, Nov. 1992.

A 380 GHz SIS Receiver using $Nb/AlO_x/Nb$ Junctions for a RadioAstronomical Balloon-borne Experiment : PRONAOS

P. Febvre*+, P. Feautrier**,C.Robert*,J.C. Pernot**,
A. Germont*,M. Hanus**,R. Maoli*,M. Gheudin*,G. Beaudin*, P. Encrenaz**

**Observatoire de Paris-Meudon, DEMIRM - URA 336*
5, Place Jules Janssen 92195 Meudon - France
*** Ecole Normale Supérieure, Laboratoire de Radioastronomie,*
24 rue Lhomond 75005 Paris - France
+ Now at Jet Propulsion Laboratory
M.S. 168-314
4800 Oak Grove Drive
Pasadena, California 91109 USA

ABSTRACT

The superheterodyne detection technique used for the spectrometer instrument of the PRONAOS project will provide a very high spectral resolution ($\Delta\nu/\nu = 10^{-6}$). The most critical components are those located at the front-end of the receiver : their contribution dominates the total noise of the receiver. Therefore it is important to perform accurate studies for specific components, such as mixers and multipliers working in the submillimeter wave range.

Difficulties in generating enough local oscillator (L.O.) power at high frequencies make SIS mixers very desirable for operation above 300 GHz. The low L.O. power requirements and the low noise temperature of these mixers are the primary reason for buiding an SIS receiver.

This paper will report the successful fabrication of small ($\leq 1\ \mu m^2$) Nb/Al-Ox/Nb junctions and arrays with excellent I-V characteristics and very good reliability, resulting in a low noise receiver performance measured in the 368/380 GHz frequency range.

I - INTRODUCTION

Observations from a stratospheric balloon are unobstructed by the atmosphere which is opaque at submillimeter and far-infrared wavelengths from the ground. For this reason, a submillimeter balloon-borne observatory is being developed under the responsibility of the "Centre National d'Etudes Spatiales" (CNES), the French Space Agency.

It consists of a stabilized gondola supporting a 2 meter diameter telescope, associated alternately with an infrared multiband spectrometer or a submillimeter heterodyne spectrometer (SMH). This last instrument will be used to simultaneously detect the 368 GHz O_2 line and the 380 GHz H_2O line in the interstellar medium. It is scheduled to fly in fall 1994 using a 1,000,000 m^3 balloon at an altitude of 37 km.

Receivers using SIS tunnel junctions have shown better sensitivities than Schottky diode receivers operated at millimeter and submillimeter wavelengths. Theoretically, sensitivities approaching the quantum limit can be achieved [1].

Up to about 300 GHz the most sensitive receivers use waveguides and superconducting RF tuning circuits integrated with the SIS junctions [2,3,4,5,6,7,8]. Above this frequency, two options appear to be available. The first possibility is to design a waveguide mixer (with full-height or reduced-height waveguide) using two tuners (i.e. generally a backshort and an E-plane tuner) [9,10]. A DSB receiver noise temperature of 150 K at 345 GHz has been reported with this design [9]. Another possibility is to use a quasioptical SIS mixer, which is very promising above 500 GHz where very small waveguides are very difficult to machine [11,12,13,14]. This design is compatible with tuning elements.

Finally we have chosen for our first experiments a waveguide design because it is better understood than open-structure mixers.

II - RECEIVER DESCRIPTION

A block diagram of our submillimeter wave heterodyne spectrometer is shown in figure 1. Rotation of a flat mirror set allows the calibration of the receiver by commuting the incoming beam from the telescope between a hot and a cold load. Due to the short wavelengths, a quasioptical free space propagation is adopted [15]. A Mach-Zehnder type diplexer is used for the 374 GHz local oscillator signal injection into the SIS mixer. The L.O. source consists of a phase-locked 93.5 GHz Gunn diode oscillator combined with two varactor diode doublers connected in series. The intermediate frequency (I.F.) is chosen at 5.85 GHz to allow the simultaneous detection of the O_2 line in the lower band at 368 GHz and the H_2O line in the upper band at 380 GHz. The I.F. output feeds a specially designed cooled low-noise HEMT amplifier with a gain of 30 dB. A noise temperature of 18 K has been achieved at 5.85 GHz over a 700 MHz bandwidth at a temperature of

27 K [16]. The signal is then amplified at room-temperature and coupled to the acousto optical spectrometer (AOS) subsystem with a resolution of 800 kHz in a 800 MHz bandwidth.

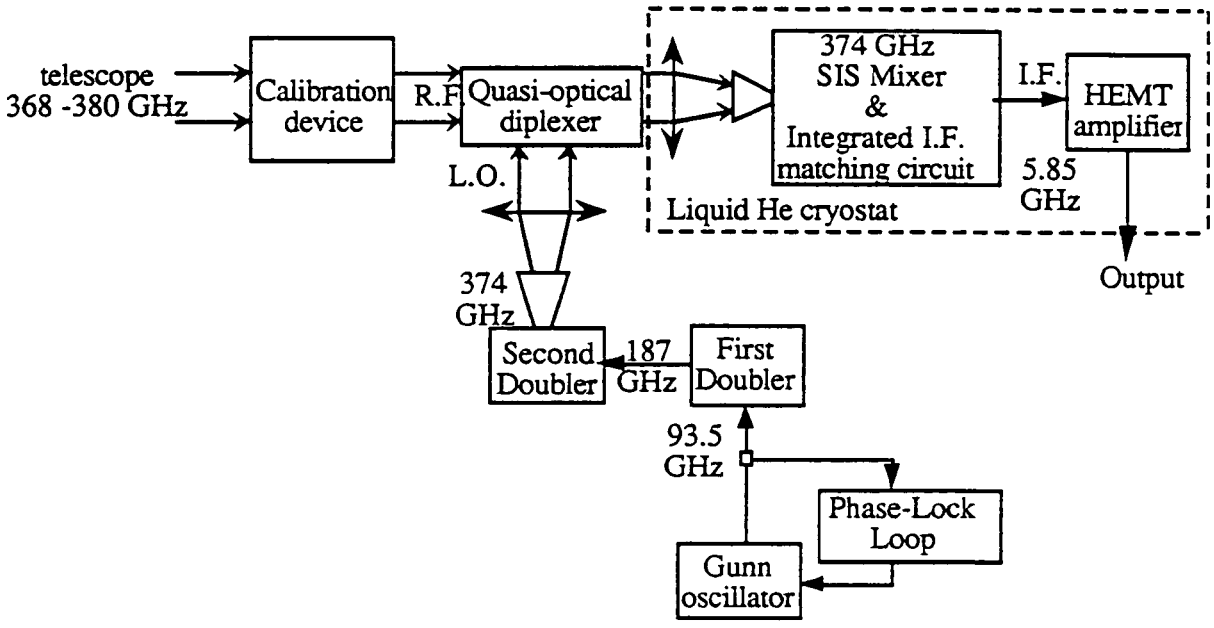

Figure 1: Block diagram of the receiver front-end used for PRONAOS

III - 380 GHz SUBMILLIMETER RECEIVER FRONT-END

III-1 - SIS junctions fabrication procedure

We report here the fabrication process of Nb/Al-AlOx/Nb junctions with very sharp I-V curves and a gap voltage for one junction about 2.9 mV at 4.2 K. A high gap voltage is known to be necessary for good results at high frequencies (above 300 GHz). It is the reason why NbN junctions are promising for very high frequencies (above 500 GHz). The smallest junction area achievable with our technology without deterioration of the I-V curve is 0.9 μm^2. Our process has already been described in a previous paper [17]. Some parameters have changed since this article to obtain the desired junction area for the 380 GHz mixer.

The fabrication process is described on figure 2 .The Nb/Al-AlOx/Nb trilayer is deposited on the whole substrate without breaking the vacuum in order to have a good barrier interface (see fig. 2-a). The diameter of this substrate is one inch, and the thickness is 95 ± 5 µm. It is made of fused quartz and is polished on one side. During the deposition the substrate is attached to a copper heat sink cooled by a closed water circuit at 20 °C. The vacuum is made by a cryopump with a background pressure typically under 5. 10^{-6} Pa. The Nb and Al films are sputter deposited by a DC magnetron at an argon pressure of 1.1 Pa. The Nb base electrode (170 nm thick) and

counterelectrode (100 nm thick) are evaporated at a rate of 1.9 nm/sec. The Al film (10 nm) is deposited with an oscillating substrate table at a rate of 0.2 nm/sec and is oxidized by introducing Ar + 10% 0_2 into the chamber for 20 to 30 min at 60 to 1000 Pa.

A positive photoresist is deposited and patterned to define the RF filter with an etching technique. Nb and Al films are etched by reactive ion etching in SF_6. Nb is etched with a 10 sccm SF_6 flow at 0.7 Pa using 60 W of power. The corresponding etching rate is 200 nm/min. Al is etched at lower pressure and higher power with an etching rate of 10 nm/min; the SF_6 flow is 5 sccm, the pressure is 0.3 Pa and the power is 80 W. Under these conditions, the etching is dominated by a mechanical action rather than a chemical effect like in the plasma etching method. We observed that a CF_4 gas does not etch Al even at low pressure. RIE with Ar has not been selected, because it produces too much damage on the resist (with Ar, it is only a mechanical etching process).

After removing the remaining photoresist in acetone (see fig. 2-b), a new resist layer is deposited to define the junction area (see fig.2-c). This is the critical point of the process which limits the smallest area achievable by this technology. Our mask aligner uses a 400 nm UV source and is limited to 0.8 µm resolution. In practice, it is impossible to define a diameter smaller than 1 µm (ie. an area smaller than 0.9 μm^2). This resist is used to protect the upper layer of Nb etched by RIE under the following conditions : 20 sccm of SF_6, 6 sccm of 0_2, a pressure of 0.7 Pa and a power of 60 W. If the etching rate (100 nm/min) is lower than for the trilayer etching (see fig. 2-a), these conditions provide sloped edges which are easier to insulate without microshorts in the next step. The etch stops at the Al_2O_3/Al barrier, because the etching rate of Al is very low with SF_6/O_2. We use laser end point detection to avoid overetching (it is necessary to have a sufficient thickness of resist for the SiO lift-off).

Once the upper Nb etched then a 300 nm layer of SiO is evaporated to insulate the junction perimeter (see fig.2-d). The excess SiO is removed in acetone (lift-off). Then, the junctions in series are connected together by a 300 nm layer of Nb sputter deposited with a rate of 1.3 nm/s through another resist stencil. The excess Nb is finally lifted-off in acetone. Different experimental investigations have been made to optimise each parameter. For example, the stresses in Nb films have been minimized by changing the Ar pressure during the sputtering step. The stresses are evaluated by optical interferometry. The Nb edge is another parameter we have studied. We succeeded in obtaining sloped edges with a reasonable selectivity by using a mixture of SF_6 and O_2 at low pressure for the RIE. Finally, anodisation spectroscopy was an useful method to investigate the quality of the interfaces Nb/Al and to understand the diffusion problem of Al into Nb; such a diffusion process gives poor quality junctions .

Then, the individual junctions (400 junctions per substrate of 1 inch diameter) are cut with a dicing saw and cooled in liquid helium at 4.2 K to test their I-V characteristics. It is possible to test 6 junctions in one run. The junctions are connected with spring contacts on gold pads evaporated at the ends of the R.F. filter. With this technique, we can contact the 6 junctions very quickly without problem of series resistance on Nb surface.

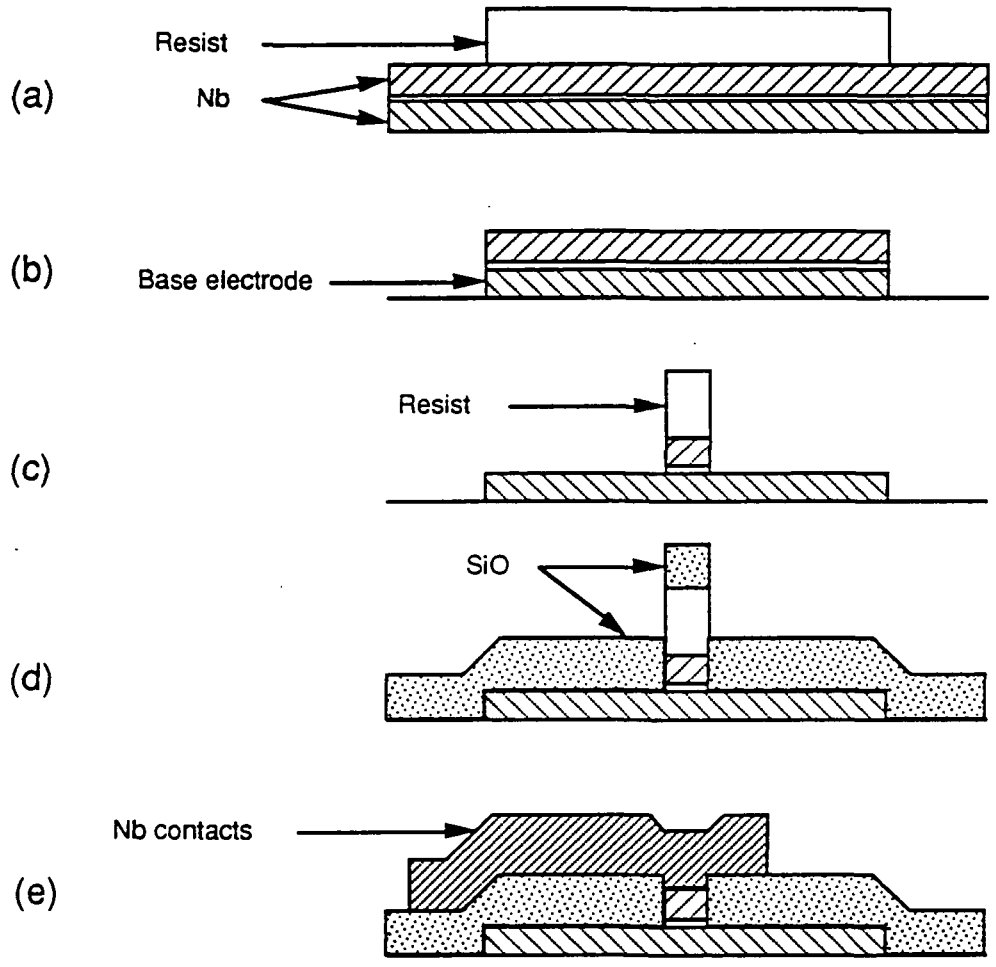

Figure 2: Fabrication process of Nb/Al-AlOx/Nb junctions

(a) Nb/Al-AlOx/Nb deposition.Definition of the base electrode by photolithography. (b) Etching of the trilayer. (c) Etching of the upper electrode. (d) Self-aligned deposition of a SiO insulating layer. (e) Nb interconnection layer.

Figure 3 gives an example of a typical I-V curve of an array of 2 junctions in series. The area of each junction is 0.9 μm^2, so the effective area of the array is about 0.45 μm^2.

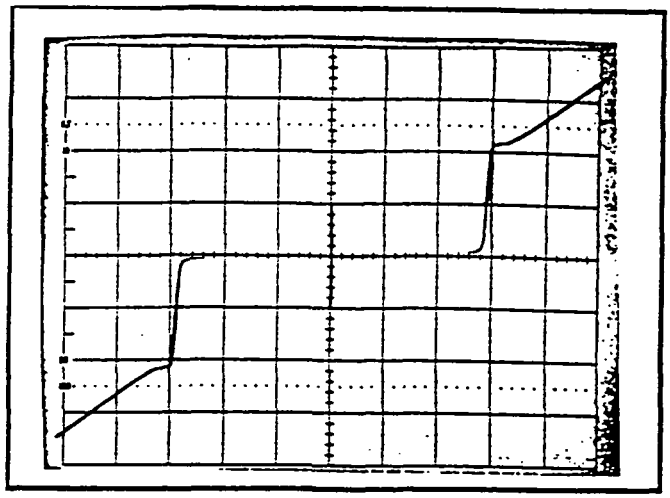

Figure 3

20 μA / div

2 mV / div

$A_{eff} = 0.47\ \mu m^2$

$R_N = 150\ \Omega$

$R_{300\ K} = 182\ \Omega$

III-2 - Mixer design

a) General features

The SIS mixer block is based on the Ellison design [9]. It includes an electroformed integrated dual-mode Potter horn [18] transformed by a circular to rectangular transition into a third-height reduced waveguide [19] to increase R.F. bandwidth and decrease the characteristic impedance at 150 Ω . Superconducting coils (to suppress the Josephson Current), an I.F. matching circuit and junction DC bias are integrated in the mixer block in order to facilitate the installation of the SIS mixer in the laboratory cryogenerator or in the flight cryostat . This also allows better reproducibility of mixer performance due to the optimization of the mixer mount for the SIS junctions. Dimensions of the waveguide are 700 μm x 120 μm and two contacting tuners (i.e. a backshort and an E-plane tuner placed at λg/2 towards the feedhorn in front of the junction) provide a large range of embedding impedances to the SIS junctions (see figure 4).

b) Mixer configuration

A low-pass microstrip filter designed on Touchtone [20] is fabricated by photolithography on a 0.1 mm thick fused quartz substrate; its rejection is about 20 dB at 374 GHz. The metallization is made of Nb like the SIS junction and this 1.8 mm long 0.2 mm wide substrate is only put down in the mixer block channel on a thin silicon grease film for a better thermal contact. Mechanical support is provided by this silicon grease film when cooled at 4 K and by the 25 μm gold wires contacting the filter to ground and the I.F. output. This assembly allows numerous tries of different junctions without breaking substrates. The I.F. output gold wire is fixed with silver glue on the low-pass filter at one end and directly on the I.F. matching circuit at the other end. This matching circuit formed on Duroïd ($\varepsilon_r = 10.2$) supports the junction DC bias too. This avoids the sudden impedance change of a SMA connector, increases the I.F. bandwith and decreases the I.F. losses. The DC bias includes two 10 kΩ chip resistors (to prevent junction from being destroyed by voltage spikes) followed by an insulated wire soldered at λ/4 of a λ/2 stub (see figure 5) to provide approximately an open circuit at the I.F. frequency of 5.85 GHz on a 700 MHz bandwidth. The

25 µm gold wire is the first part of the I.F. matching circuit, then a length of a microstrip line provides a real impedance transformed into 50 Ω by a λ/4 line (figure 5).

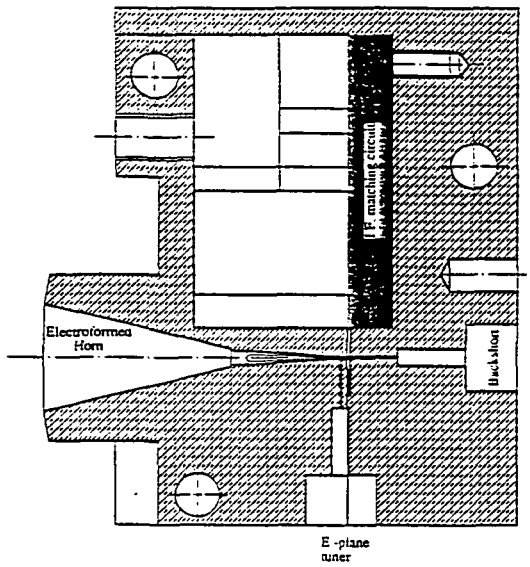

Figure 4

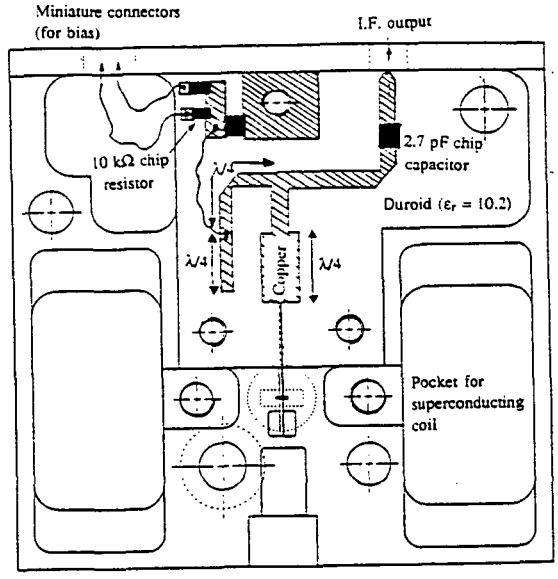

figure 5

The 1.8 cm diameter superconducting coils have been designed to produce 310 Gauss with a current of 1 A. Each one is made of about 1200 turns of Niobium-Titanium superconducting wire. Indeed, for circular junctions of surface S, the magnetic field suppressing the Josephson current is given by :

$$B(\text{Gauss}) = \frac{2{,}23 \cdot 10^{-11}}{d.\sqrt{S}} \quad \text{(for one flux quantum)}$$

with : $d = 2\lambda_L + w$ where:

λ_L = London penetration depth of Nb (m)

w = width of insulator between the two superconductors (m)

The area of the smallest junctions fabricated in the laboratory is about 1 μm^2. So, with a pessimistic value of the London penetration depth (400 Å), B = 255 Gauss ; the real value should be lower. The coils are small, because the flight cryostat was specified for a smaller Schottky mixer. Moreover, some constraints about the optical axis were already fixed in the flight cryostat. The mixer block is a Faraday cage for these coils against electromagnetic spikes even if any external magnetic field can penetrate into it .

IV - LABORATORY MEASUREMENT BENCH

Results shown further have been obtained on a laboratory bench with a 4 K cryogenerator including two closed circuits of helium. The first one is a classical CTI 1020 compressor including two stages at 50 K and 12 K. The second one is a Joule-Thomson expansion pumping on the 12 K stage to reach 3 to 4 K on the "4 K" stage. Temperature can be quickly changed and stabilized by varying the return helium pressure of the 4 K helium circuit [21]. A teflon corrugated window is used on the room temperature shield for the quasioptical RF input. The heat flux entering the cryogenerator is then reduced with an IR filter. It's a 80 µm thick (one wavelength at 374 GHz) 48 mm diameter crystalline quartz plate mounted on the 50 K stage shield. Then a 0.8 mm thick fluorogold window, 38 mm diameter, filters the far IR 50 K blackbody radiations. The SIS mixer is on the 4 K stage at the focus of a cold corrugated teflon lens cooled by the same stage.

Mechanical contacting tuners are operated by vacuum feedthroughs and are manually movable with micrometer drives when measuring receiver performance. Each electrical wire, I.F. cable or tuner drive is thermalized at 12 K and 50 K to exhaust heat flows. Some miniature connectors are used for the DC bias. A four points measurement of the I-V curve releases us from any series resistance.

The I.F. output of the SIS mixer is connected to a semi-rigid cable followed by a coupler, an isolator and the HEMT amplifier. This low-noise amplifier is installed on the 12 K stage, its output cable is thermalized at 50 K before going out of the cryogenerator (see figure 6). The coupler is

used to inject an additive noise at the I.F. mixer output to know its match relatively to 50 Ω. A preliminary calibration without mixer allows us to calculate approximatively the mixer temperature T_M and its conversion losses L_M.

The socket ot the superconductive coils is installed on the 12 K stage to have a better thermal contact between superconducting and copper wires and to prevent a heating of the 4 K stage. The L.O. and signal injections are achieved by a quasi-optical diplexer. The coupling ratio for the L.O. is higher than 90 %.

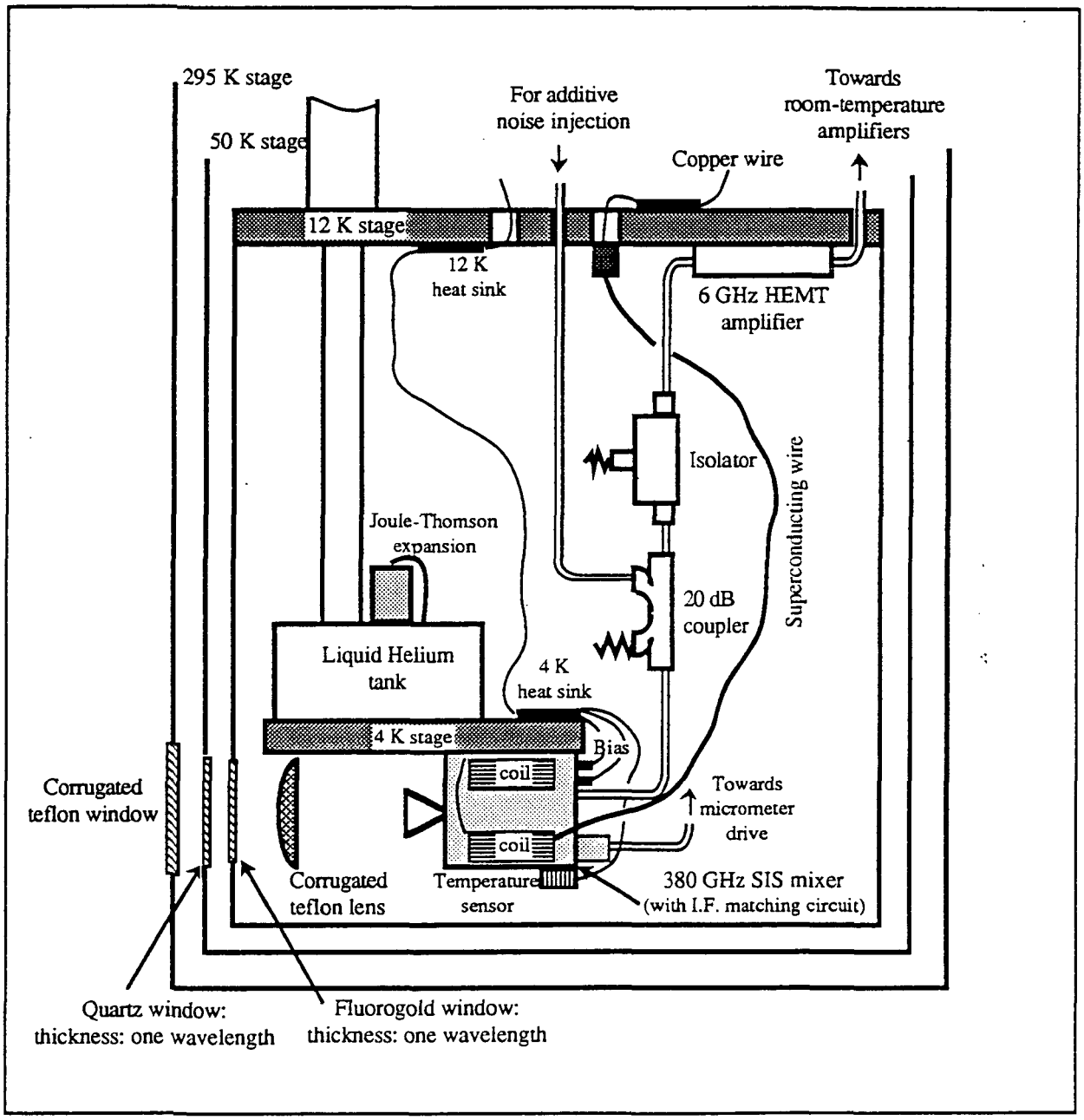

Figure 6

V - LOCAL OSCILLATOR VARACTOR DIODE DOUBLERS

The structure of each doubler has already been described in a previous paper [22]. The maximum efficiency found for the first doubler was about 18 % for an incident power of 15 mW with a 5P8 diode of the University of Virginia. The input frequency was 91.6 GHz and the output power was higher than 6 mW with a 50 mW input power. These results haven't been found again with the other doubler block at 93.5 GHz. They were due to a very good coupling between the diode and the waveguide by the whisker. More commonly, we can reach 3 to 4.5 mW with a good reproducibility and with an input power of 50 mW at 93.5 GHz. A typical curve of our last results is shown on figure 7.

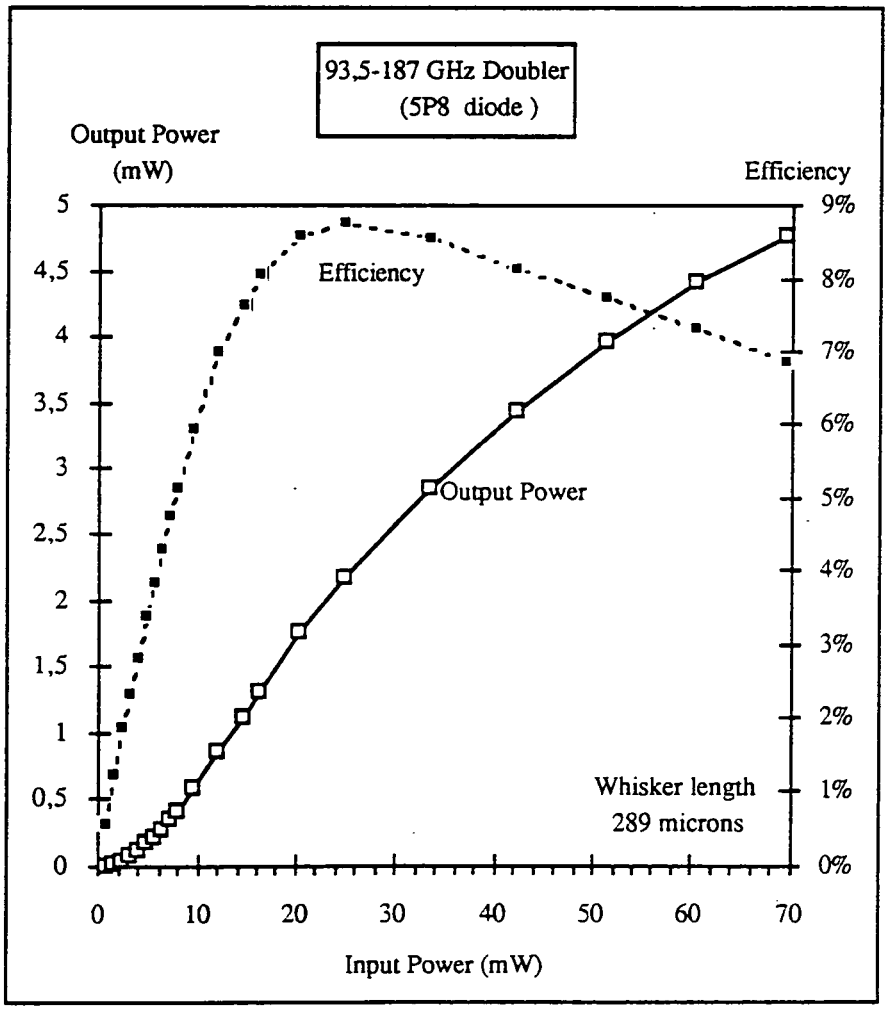

Figure 7

Concerning the second doubler, its input power (approximatively the output power of the first doubler) is low and consequently its efficiency is relatively low. Indeed, we can see on

figure 7 that the efficiency of the first doubler is lower than 4 % at 187 GHz for an input power of about 5 mW.

Partly due to the much higher frequency, we can foresee that the second doubler will not produce so much power. Such a local oscillator cannot be used for a Schottky mixer. Nevertheless, some diodes whose the maximum efficiency is obtained for a 3-4 mW input power like bbBNN diodes could provide sufficient power to pump a Schottky mixer [23]. The best output power obtained at 374 GHz is approximatively 30 μW with the bolometer horn put directly across from the second doubler horn, i.e. an efficiency lower than 1%. Two types of diodes have been tested, 2T8 and 2T9, they come from the University of Virginia and we can see on the following figure 8 that the 2T8 diode provides more power than the 2T9 diode. This is partly due to its smaller capacitance (4 fF versus 8 fF for the 2T9 diode).

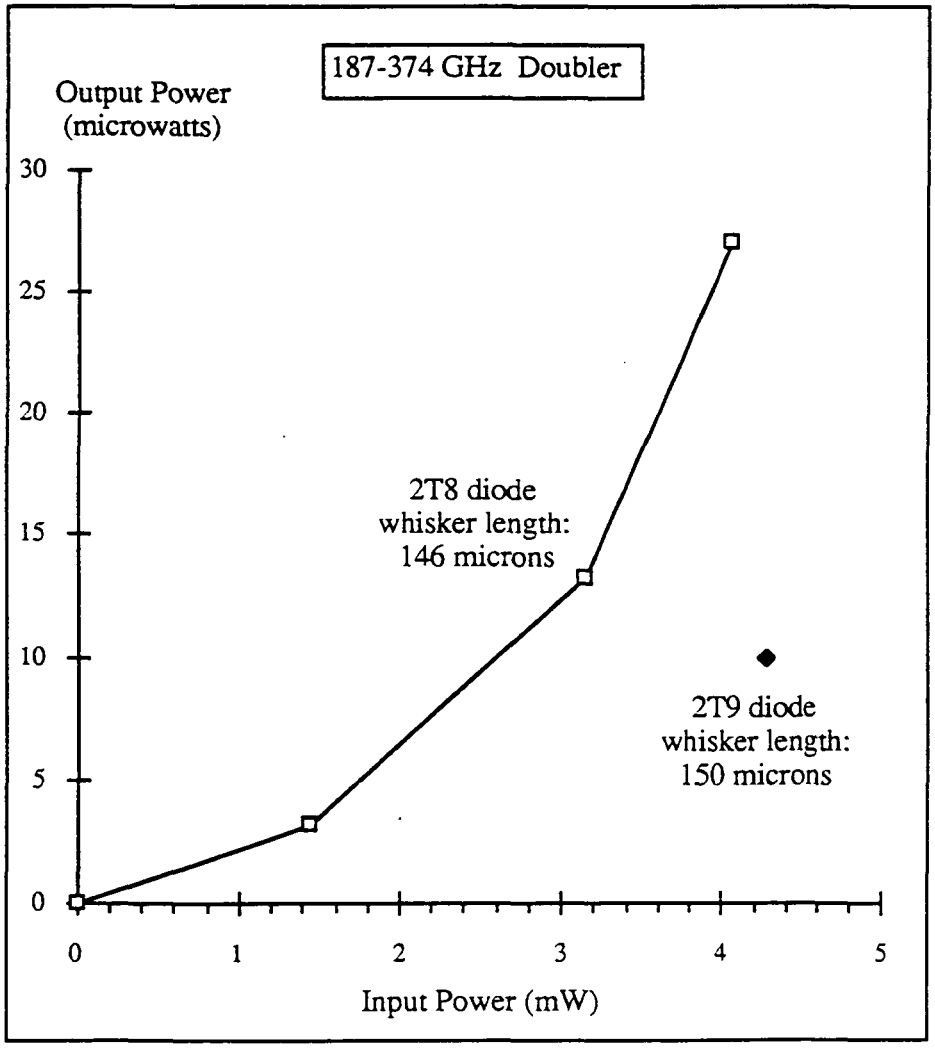

Figure 8

To prevent the second doubler diode from being destroyed by voltage spikes and due to the low input power, it has been short circuited in direct current instead of being reverse biased for an optimum efficiency, this diminishes the output power. Moreover, input and output backshorts of each doubler have been fixed or soldered which still damages performance. So the output power at 374 GHz is about 13 μW. Other measurements have been made with a quasi-optical bench composed of two corrugated lenses which is approximately the bench used for the measurements of the SIS mixer. The output power is then 10 μW. This local oscilltor signal is powerful enough, even to pump four SIS junctions in series.

VI - RESULTS

Different types of junctions have been tested with 2, 3 or 4 junctions in series coming from the same wafer. The best results obtained with each substrate are summarized in table I. The L.O. frequency is 374 GHz, the I.F. center frequency is 5.85 GHz. Measurements have been made with a 285 MHz I.F. bandwidth filter, we used the Y-factor method with 2 loads at 77 K and 295 K.

❑ We can firstly point out the good match between calculated and measured values of the magnetic field suppressing the Josephson current I_J. The product $B(I_J = 0) \times D$ is reported on the following table II (for one flux quantum), where $B(I_J = 0)$ is the magnetic field suppressing the Josephson current and D the diameter of one junction. This product should be constant for junctions fabricated on the same wafer according to the previous formula of III-2-b: d is a parameter depending only on the oxidation time of aluminium in Al_2O_3. We see that $B(I_J=0)x$ D is nearly constant to within about 10 %, this comes from the uncertainty of the junction areas. We can also deduce the London penetration depth of our niobium films which is about 600 Å.

❑ Nevertheless, the Josephson Current is not always completely suppressed with one flux quantum, because the areas of the junctions in series are slightly different. The Josephson current for each of the couple of junctions in series of one substrate is reported on figure 9.

The relative difference of the magnetic field suppressing the Josephson Current of each junction taken individually is about 5 to 10 %, that means a relative difference of area between the two junctions of 10 to 20 %. Such a difference is in good agreement with the accuracy of photolithography to define small junction areas. For this reason, the current densities and the $\omega R_N C$ products are not exactly the same for the different junctions of the table I. This corresponds to the uncertainty of the value of the junction area.

❑ The measurements of the required L.O. power are deduced from a preliminary calibration of the L.O. output power as a function of the first doubler self-biased voltage. The required power depends on the square of the number of junctions in series; four junctions in series should require

about four times as much power as two junctions in series. We observed a 3.7 dB difference between expected and measured values which corresponds mainly to the R.F. mismatch at the 374 GHz frequency since we measured the incoming L.O. power. And we can see that the difference of the conversion losses for these junctions is 3 dB, this point confirms the first one.

Junction	E380-1-8-2	E380-1-6-5	E380-1-8-4	E380-1-4-1	E380-1-8-6
Diameter (μm)	1.1	1.5	1.1	1.9	1.1
Number of junctions in series	2	3	2	4	2
Effective surface (μm^2)	0.47	0.59	0.47	0.71	0.47
$R_N(\Omega)$	143	137	150	113	143
$\omega R_N C$ at 374 GHz	9.5	11.4	10	11.3	9.5
j_c (A/cm^2)	4600	3600	4600	4200	4400
L.O. power (μW)	?	?	?	7.5	0.8
Magnetic field applied (Gauss)	175	255 (2 flux quanta)	175	192 (2 flux quanta)	185
DSB receiver temperature (K)	**1200**	**470**	**360**	**525**	**310**
Mixer noise temperature T_M (K)	?	200	195	225	155
Conversion losses (dB)	?	11	9,1	11,8	8,8
Transmitted I.F. power	between 10 and 40 %	≈ 90 %	≈ 90%	≈ 98 %	≈ 97 %
Contribution of amplifier to noise	> 70 %	57 %	46 %	57 %	50 %

table I

Junction	E380-1-8-2	E380-1-6-5	E380-1-8-4	E380-1-4-1	E380-1-8-6
$B(I_J = 0) \times D$ (Gauss x μm)	193	191	193	182	203

table II

❑ Relatively high conversion losses result in a contribution of 50 % for the HEMT amplifier in the receiver noise temperature. These conversion losses include intrinsic conversion losses increased by RF quasioptical injection, RF and I.F. mismatches, RF filter and I.F. matching circuit losses. Differences of receiver noise are mainly due to miscellaneous conversion losses. Indeed, some different effective areas of junction have been tested and the couple of tuners don't enable to completely tune out the junction capacitance because the $\omega R_N C$ product is high (>8). So the excess of conversion losses corresponds to a higher RF mismatch.

Some typical curves of different measured junctions are shown on figure 10.

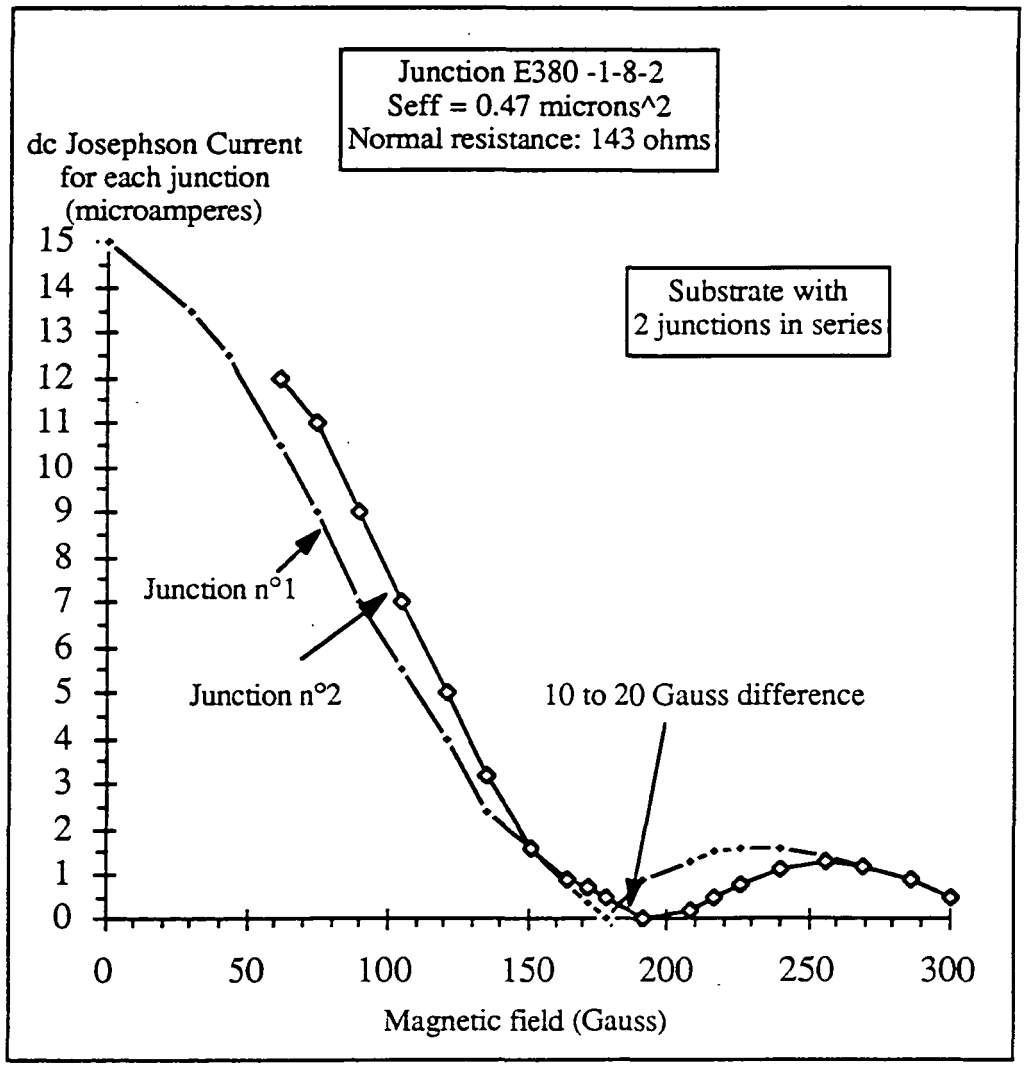

figure 9

Remark : Exact values of magnetic fields haven't been measured but calculated with current flowing through the coils. Error is around ±5 %.

The three curves shown below are some experimental curves digitalized by our data acquisition system of different arrays of SIS junctions in series fabricated on the same wafer with nearly the same normal resistances (about 150 Ω). Fot this reason, the current densities are of the same order of magnitude for each array.

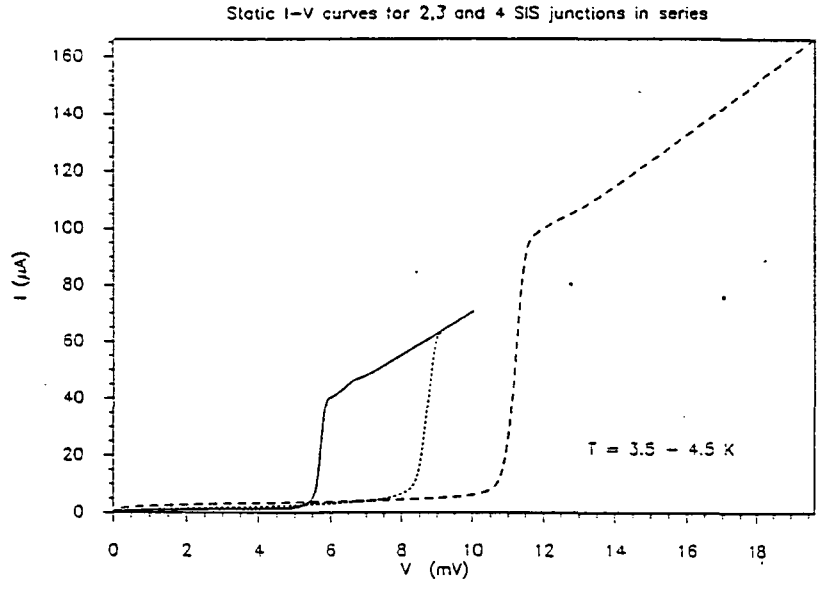

figure 10

We can see on figure 11 the dc characteristic of the junction E380-1-8-6 (a). Also shown on this figure is the I-V curve of the same junction pumped with the 374 GHz L.O.. The width of the photon assisted step is $2.h.\nu_{L.O}/e$ where h is the Planck constant , e is the electron charge and $\nu_{L.O}$ is the frequency of the local oscillator.

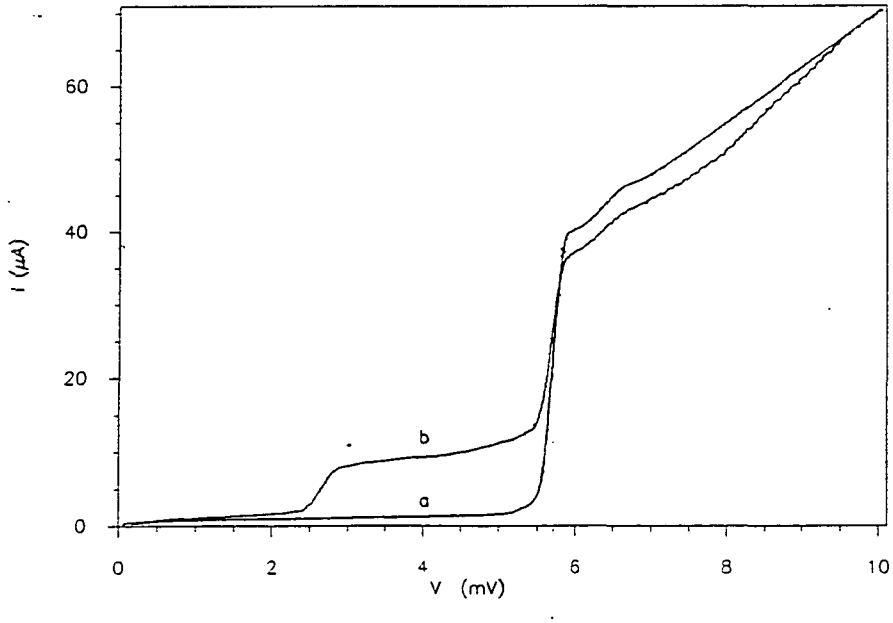

figure 11

The static impedance at the bias point (approximatively 4 mV:the middle of the first photon step) is about 500 Ω so the I.F. circuit has been designed to match this impedance, we assumed that it is close to the impedance at 5.85 GHz ($R_{I.F.}$). The normal resistance is 143 Ω and the range of the quotient $R_{I.F.}/R_N$ has been found to be contained between 3 and 4.5, the value of $R_{I.F.}$ being adjusted by varying the L.O. power. We can see in table I that the I.F. match for the last four junctions is good which validates our assumption.

On the contrary the high receiver noise temperature measured for the first junction was due to a poor I.F. match, the I.F. impedance being unknown at that time.

Some I-V curves with and without suppression of the Josephson current are plotted on the following figure 12. We can observe 3 Shapiro steps due to the coupling of the L.O. power with the Josephson current.when it is not suppressed. The width of these steps is exactly one half of the quasiparticle step due to the L.O. power. These sharp steps partly explain the instabilities observed when the Josephson current is not completely suppressed.

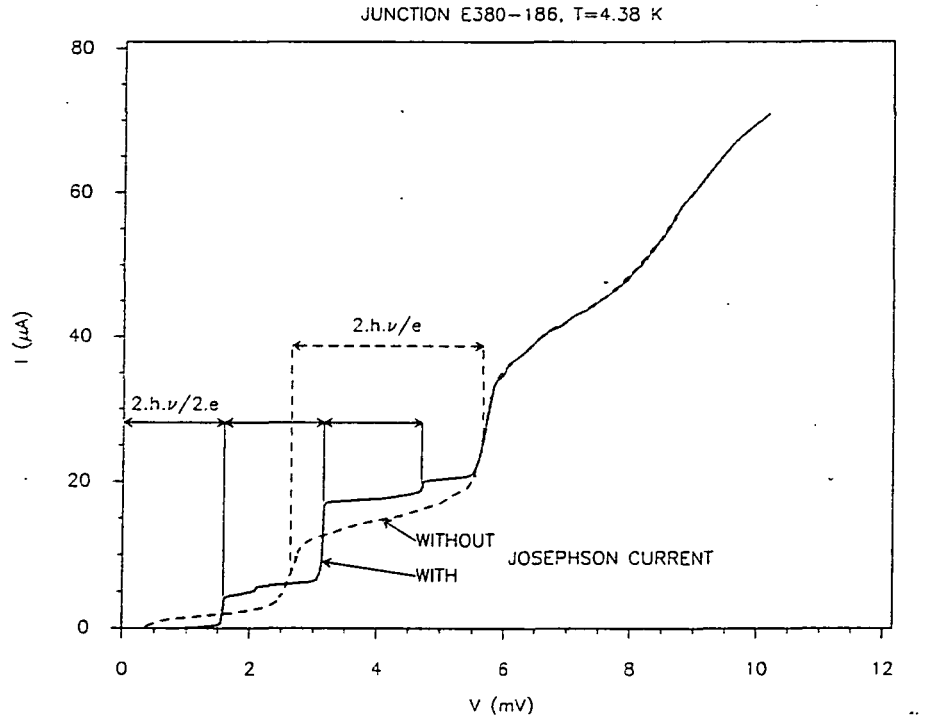

figure 12

Some dependances of different parameters are shown on the following figures. We can see on figure 13 the influence of the magnetic field to the noise receiver.

The noise temperature begins to increase for a magnetic field lower than 170 Gauss which corresponds to a residual Josephson Current of about 1 μA providing an additive Josephson noise coming with instabilities of the I.F. output power.

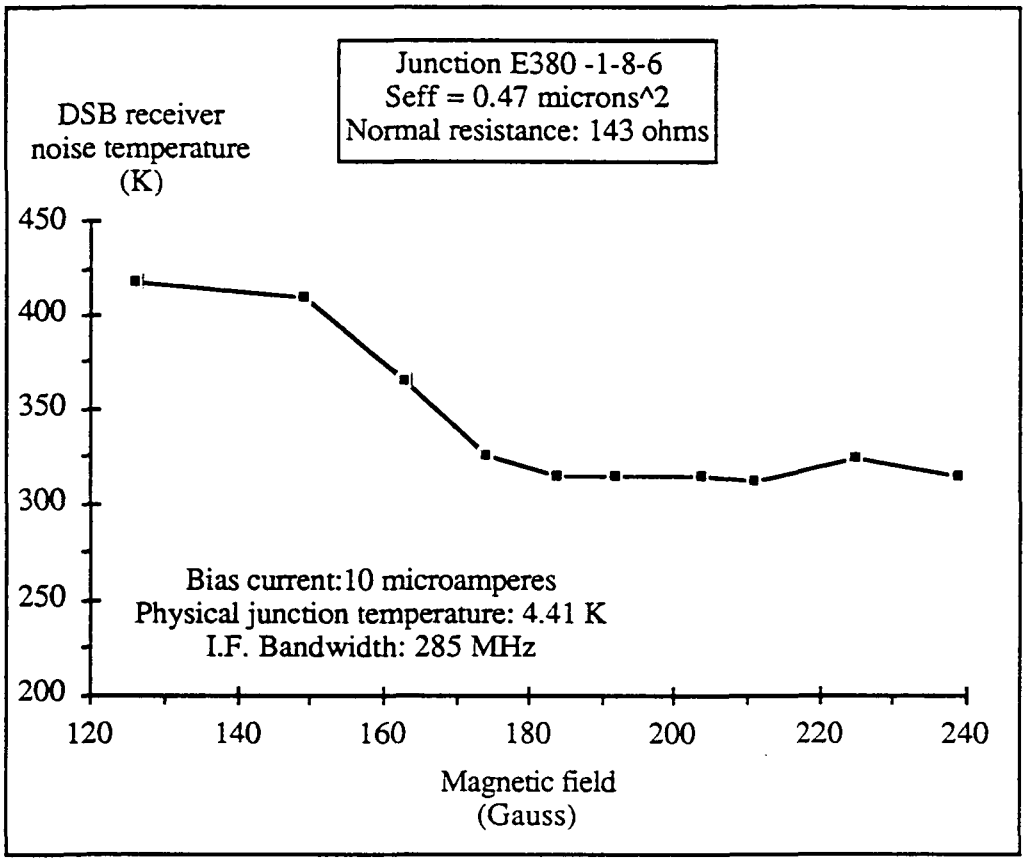

figure 13

The noise temperature is plotted as a function of bias current on figure 14. The receiver noise temperature remains lower than 330 K with a relative variation of bias current of 20 % which is adequate for our balloon-borne experiment where there is no remote control of the DC bias; all the other parameters remained unchanged.

At last, the L.O. frequency was varied from 345 to 385 GHz (see figure 15) the receiver noise temperature is higher at lower and higher frequencies than 374 GHz. This is partly due to the narrow RF bandwidth of the Potter horn. We can point out that the receiver temperature is below 380 K in the frequency range from 355 to 385 GHz.

Influence of temperature was only observed with the junction E380-1-6-5. With other junctions, the mixer noise temperature has not decreased by cooling more the junction; this is certainly due to a poor thermal contact with the silicon grease film.

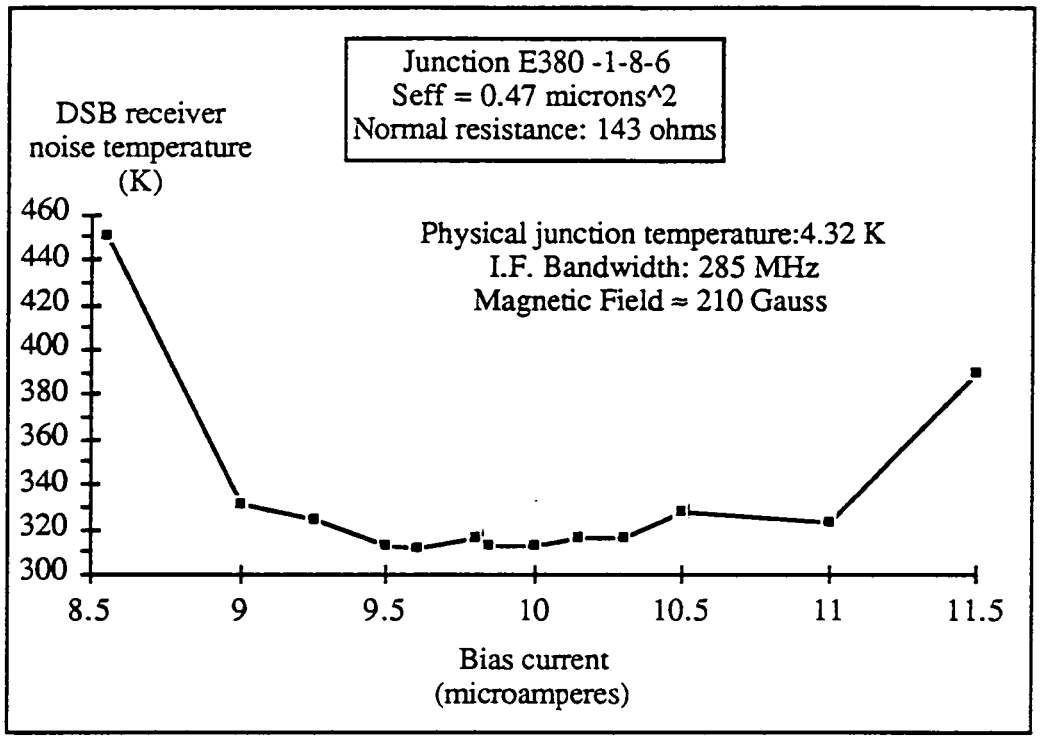

figure 14

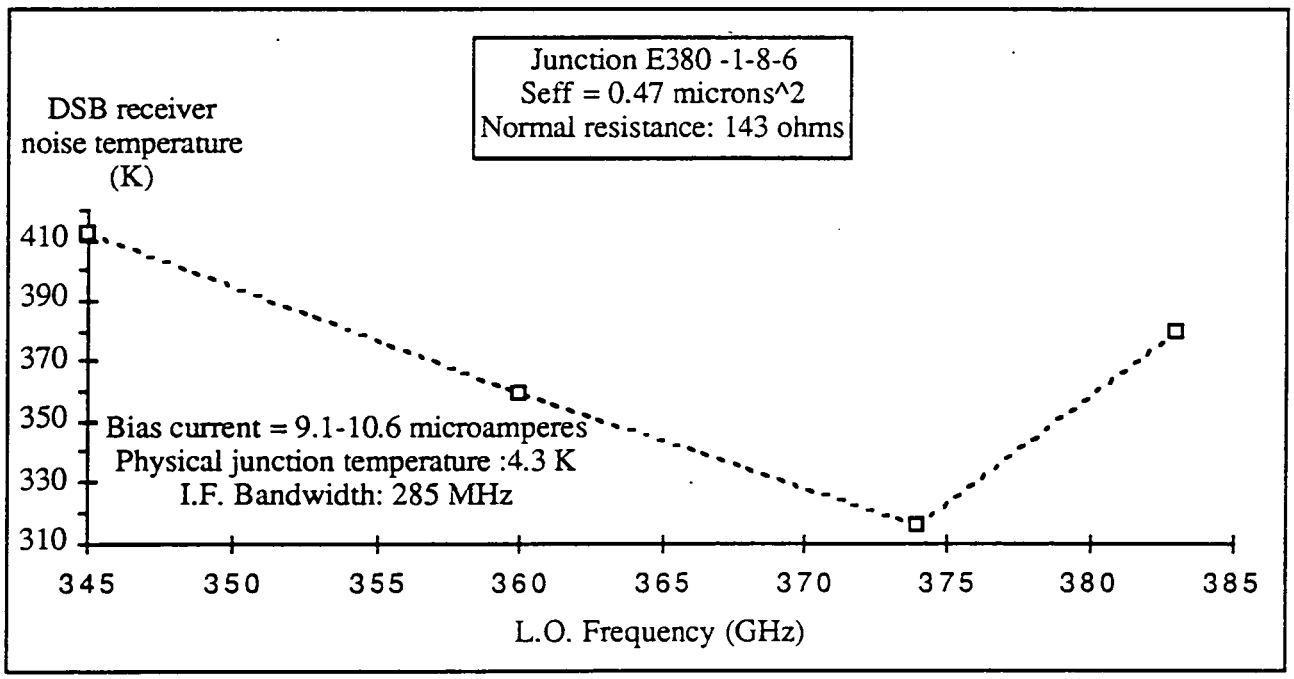

figure 15

V - CONCLUSION

Some Nb/Al-Al_2O_3/Al SIS junctions with small areas and sharp I-V curves have been successfully fabricated, dc measured and integrated in the mixer. The smallest area achievable with our process is about 0.9 μm^2. Arrays of two junctions with this area have been made, the effective area is then around 0.45 μm^2. They are very stable according to some repeated thermal cycles: more than 15 cycles have been completed between room temperature and 4 K temperature and no change has been detected. This reliability is essential for space applications.

The 380 GHz SIS mixer was designed with an integrated I.F. matching circuit and two integrated superconducting coils; it has been tested over a 40 GHz L.O. bandwidth. The best receiver noise temperature (310 K DSB) has been measured with an array of a couple of junctions in series having an effective surface of 0.47 μm^2 and a normal resistance of 143 Ω. The L.O. frequency was 374 GHz. The relatively high conversion losses (8.8 dB) reveal a R.F. mismatch. It could be decreased by using junctions with lower capacitances (i.e. areas) and lower normal resistances. Then the fabrication of SIS junctions with higher current densities is planned. The lowest **mixer** noise temperature is around **155** K and some new junctions with lower normal resistances should also reduce it. So we are optimistic for the following.

The 374 GHz L.O. source has been made with a fundamental InP Gunn Oscillator at 93.5 GHz followed by two GaAs varactor doublers in series. This subsystem provides enough power to drive the SIS mixer even with 4 junctions in series but a more powerful first multiplier will be necessary to produce more power at higher frequencies (above 500 GHz) for the future.

A 6 GHz low-noise H.E.M.T. amplifier has been specifically designed for cryogenic applications, it meets fully the specifications and will be used in connexion with the SIS mixer. The contribution of the amplifier to the system noise is about 50 % due to the high conversion losses. We hope that the new junctions will decrease this contribution.

Acknowledgments : We would like to thank Gilles Ruffié for his valuable aid and support, André Deschamps for the data acquisition system and Olivier Perrin for the design of the doubler blocks. We are especially grateful to Serge Lebourg and Jean Morin for their help on the mechanical realizations for the measurement bench. We also wish to thank Véronique Serpette (Observatoire de Paris) for the numerous photolithographies of the I.F. matching circuits. In addition we thank Marc David for his assistance and support on cryogeny. Thanks also to Albert Brel, Annick Gassais and Françoise Gadéa for their technical help. We would also like to thank Matthew Carter and Jacques Blondel of IRAM (Institut de Radioastronomie Millimétrique) for useful discussions.
Finally we are greatly indebted to William R. McGrath for his careful reading and numerous comments on this article.
This work is supported by the Centre National d'Etudes Spatiales (CNES) and the C.N.R.S. (URA 336)

REFERENCES

[1] J.R. Tucker: "Quantum limited detection in tunnel junction mixers", IEEE J. Quantum Electron, vol QE 15, pp 1234-1258,Nov.1979

[2] S.K. Pan, A.R. Kerr, M.J. Feldman, A.W. Kleinsasser, J.W. Stasiak, R.L. Sandstrom and W.J. Gallagher: "A 85-116 GHz SIS receiver using inductively shunted edge junctions", IEEE Trans. MTT, Vol.37,N° 3, March 1989

[3] A.R. Kerr, S.K. Pan: "Some recent developments in the design of SIS mixers",Int. J. of Infrared and Millimeter Waves, Vol.11,N° 10,1990

[4] R. Blundell, M. Carter and K.H. Gundlach:"A low-noise SIS receiver covering the frequency range 215-250 GHz, IntJ. of Infrared and Millimeter Waves, Vol 9,N°4,1988

[5] B.N. Ellison and R.E. Miller:"A low-noise 230 GHz SIS receiver", IntJ. of Infrared and Millimeter Waves, Vol.8,pp 609-625,June 1987

[6] H.H.S. Javadi, W.R. McGrath,S.R. Cypher, B. Bumble, B.D. Hunt and H.G. Leduc:"Performance of SIS mixers at 205 GHz employing submicron Nb and NbN tunnel junctions",Digest of the 15th International Conference on Infrared and Millimeter Waves,December 1990

[7] D. Winkler, W.G. Ugras, A.H. Worsham and D.E. Prober, N.R. Erickson and P.F. Goldsmith: "A full-band waveguide SIS receiver with integrated tuning", IEEE Trans. on Magnetics, vol.27,n°2, March 1991

[8] J.W. Kooi, M. Chan, T.G. Phillips, B. Bumble and H. G. Leduc:"A low-noise 230 GHz heterodyne receiver employing 0.25 μm^2 Area Nb/AlOx/Nb tunnel junctions", 2nd International Symposium on Space Terahertz Technology, Jet Propulsion Laboratory, California Institute of Technology, Pasadena, Feb. 1991

[9] B.N.Ellison, P.L.Schaffer, W.Schaal, D.Vail, R.E.Miller : "A 345 GHz SIS receiver for radio astronomy ", IntJ. of Infrared and Millimeter Waves, Vol. 10, N° 8, 1989

[10] C.E. Honingh, M.M.T.M. Dierichs, H.H.A. Schaeffer, T.M. Klapwijk and Th. de Graauw:"A 345 GHz waveguide mixer with two mechanical tuners using an array of four Nb-Al-Al_2O_3-Nb SIS junctions", 2nd International Symposium on Space Terahertz Technology, Jet Propulsion Laboratory, California Institute of Technology, Pasadena, Feb. 1991

[11] M. Wengler, D.P. Woody, R.E. Miller, T.G. Phillips:"A low noise receiver for millimeter and submillimeter wavelengths",Int. J. of Infrared and Millimeter Waves, Vol. 6, pp 697-706, 1985

[12] T.H. Büttgenbach, R.E. Miller, M.G. Wengler, D.M. Watson, T.G. Phillips:"A broad-band low-noise SIS receiver for submillimiter astronomy", IEEE Trans. MTT, Vol. MTT 36, pp 1720-1726, Dec. 1985

[13] X.Li, P.L. Richards, F.L. Lloyd, "SIS quasiparticle mixers with bow-tie antennas", Int. J. of Infrared and Millimeter Waves, Vol. 9, pp 101-103, 1988

[14] J. Zmuidzinas, H.G. Leduc, "Quasi-optical slot antenna SIS mixers", to be published in IEEE Trans. MTT, 1992 and 2nd International Symposium on Space Terahertz Technology, Jet Propulsion Laboratory, California Institute of Technology, Pasadena, Feb. 1991

[15] P.F.Goldsmith, " Quasi-optical techniques at millimeter and submillimeter wavelengths", Infrared and Millimeter Waves vol 6 :System and components, K.J.Button (editor), Academic Press, New York, p 277-343, 1982 .

[16] C.Robert, M.Gheudin: " A 6 GHz HEMT low-noise cooled amplifier for a radioastronomical submillimeter heterodyne receiver ", 15th International Conference on Infrared and Millimeter Waves, Conference digest, pp. 127-128, Orlando, dec. 1990.

[17] P.Feautrier, J.Blondel, M.Hanus, J.Y.Chenu, P.Encrenaz, M.Carter :"Low noise 80-115 GHz quasiparticle mixer with small Nb/Al-Oxyde/Nb tunnel junctions", Int. J. of Infrared and Millimeter Waves, Vol. 11, No. 2, 1990 .

[18] H.M. Pickett, J.C. Hardy and J. Farhoomand:"Characterization of a Dual-Mode Horn for Submillimeter Wavelengths", IEEE Trans. on MTT, vol. MTT-32,N°8,August 1984

[19] Mixer block constructed by Radiometer Physics, Meckenheim, Germany

[20] Touchtone CAD Software, Eesof

[21] J.C.Maréchal, J.C.Pernot, P.J.Encrenaz: "A 2K closed cycle cryogenerator", Conf. URSI, Granada, Sept. 1984.

[22] O.Perrin, C.Robert, P.Feautrier, P.Febvre, G.Beaudin, P.Encrenaz, M.Gheudin, J.Lacroix, G.Montignac : "380 GHz receiver front-end for the balloon-borne radioastronomical experiment PRONAOS", 2nd. International Symposium on Space Terahertz Technology, Jet Propulsion Laboratory, California Institute of Technology, Pasadena, feb. 1991 .

[23] T.J.Tolmunen, M.A. Frerking: "Theoretical performances of novel multipliers at millimeter and submillimeter wavelengths", Int. J. of Infrared and Millimeter Waves, Vol. 12, No. 10, 1991.

A low noise 410-495 heterodyne two tuner mixer, using submicron $Nb/Al_2O_3/Nb$ Tunneljunctions

G. DE LANGE#, C.E. HONINGH*, M.M.T.M. DIERICHS#, R.A. PANHUYZEN#, H.H.A. SCHAEFFER*, T.M. KLAPWIJK#, H. VAN DE STADT*, M.W.M DE GRAAUW*. #University of Groningen, Nijenborgh 4, 9747 AG Groningen; *Space Research Organisation of the Netherlands, Landleven 12, 9747 AD Groningen.

A 410-495 GHz Heterodyne receiver, with an array of two $Nb/Al_2O_3/Nb$ tunneljunctions as mixing element is described. The noise temperature of this receiver is below 230 K (DSB) over the whole frequency range, and has lowest values of 160 K in the 435-460 GHz range. The calculated DSB mixergain over the whole frequency range varies from -11.9 ± 0.6 dB to -12.6 ± 0.6 dB and the mixer noise is 90 ± 30 K.

Introduction

SIS-mixers are currently being used as heterodyne receivers up to submillimeter wavelengths [1][2]. Two different types of mixers are used to achieve low noise receivers: quasi-optical mixers, with a fixed tuned broadband planar antenna, and waveguide mixers, with one or two tuning elements.

In this paper a two tuner waveguide mixer designed for the 400-500 GHz range is described. The used mixing elements are two different arrays of two $Nb/Al_2O_3/Nb$ tunneljunctions. This mixer is the second frequency step towards our goal to make a THz receiver (350-490-750-1000 GHz). At these high frequencies the dimensions of a waveguide structure become very small (100-400 μm) and it is unclear how far losses due to surface irregularities deteriorate the mixer performance.

The laboratory tests of the mixer show that in the 400 to 500 GHz frequency range, waveguide mixers can still achieve low noise temperatures (as low as 160 K DSB), and the flat response over the band indicates that the current design can be scaled up to higher frequencies.

The behaviour of SIS-mixers is well described by theory [3][4]. An extensive comparison between theory and measurements has been performed at 345 GHz [5] and this comparison is started in the 410-490 GHz range. First results show a good agreement between calculated and measured IV-curves, from which the electromagnetic environment of the junction is deduced.

This paper describes the design of the mixer, the results from the two different arrays of junctions and some preliminary analysis of the mixer performance.

Receiver design

The mixer block design for 400-500 GHz is a scaled version of the 345 GHz mixer described by Honingh et al.[6].

The mixer system is placed inside an Infrared Laboratories HD 3 cryostat. The signal and LO-power enter the cryostat via a 1 mm thick HDP window of 3 cm diameter. On the 77 K radiation shield a 200 μm thick quartz plate serves as heat filter.

A diagonal horn with an aperture size of 4.5 mm, a length of 12 mm and a flare angle of 11 degrees is used. Laboratory tests of this horn showed a good gaussian beam-coupling (side lobes <-15db), equal beamwidth in E-,D- and H- planes and a low cross-polarisation (<-15 dB). In front of the horn a F=31.4 mm HDP lens is used. The lens is mounted in a holder which can be directly mounted on the mixerblock. The mixerblock is cut in OFHC. The full height waveguide with dimensions 0.44*0.22 mm, has a cut off frequency of 340 GHz. The waveguide system has two moving shorts as tuning elements, each with a quarter wave choke section to improve the quality of the short. In order to suppress the Josephson currents in the junction, a coil with 10.000 turns of 0.1 mm Nb wire is placed around the horn, in front of the mixerblock. The IF-chain consists of a Radiall R443533 T-bias, a Pamtech LTE 1290 isolator and a Berkshire Technologies L-1.4-30H IF-amplifier.

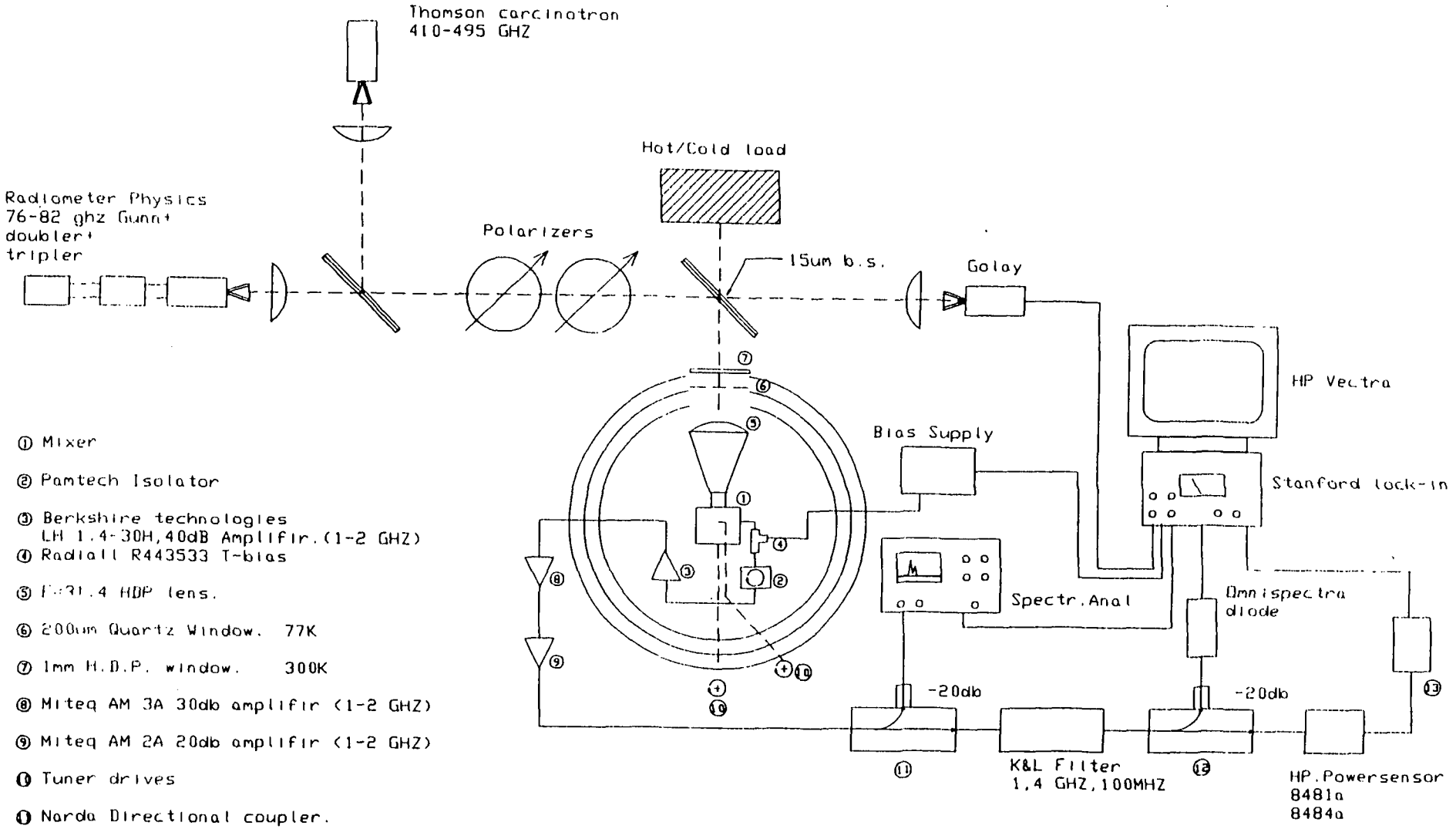
Thomson carcinotron
410-495 GHZ
Hot/Cold load
Radiometer Physics
76-82 ghz Gunn+
doubler+
tripler
Polarizers
15um b.s.
Golay
HP Vectra
Bias Supply
Stanford lock-in
Spectr.Anal
Omnispectra
diode
-20db
-20db
K&L Filter
1,4 GHZ,100MHZ
HP.Powersensor
8481a
8484a
① Mixer
② Pamtech Isolator
③ Berkshire technologies
LH 1.4-30H,40dB Amplifir.(1-2 GHZ)
④ Radiall R443533 T-bias
⑤ F=31.4 HDP lens.
⑥ 200um Quartz Window. 77K
⑦ 1mm H.D.P. window. 300K
⑧ Miteq AM 3A 30db amplifir (1-2 GHZ)
⑨ Miteq AM 2A 20db amplifir (1-2 GHZ)
⑩ Tuner drives
⑪ Narda Directional coupler.
⑫ Radiall Directional coupler
⑬ HP 436a Power meter

SIS-junctions

The fabrication of the used junction arrays, is described elsewhere [7]. Up to now two different types of arrays have been used. The arrays differ in junction area, current density, RF-filterstructure and gapvoltage. An overview is given in table 1.

Junction array	Q34	Q35
A (1 junction) (μm^2)	0.8	2
I_c (A/cm^2)	7000	12.000
R_n (Ω)	100	22
RF-filter	Chebychev	¼ λ
Gap-voltage (mV)	2.7	2.4

Table 1. Overview of the 2 different junction arrays.

The lower gapvoltage of junctions Q35 is caused by a higher oxygen background pressure during sputter deposition of the trilayer.

Measurement set-up

A schematic diagram of the measurement set-up is given in Fig. 1. The use of two coherent sources, in combination with a spectrum analyser allow to analyse the mixer performance at the LO and the upper and lower sideband frequencies. In the measurements the carcinotron acted as LO-source.

The noise temperature of the mixer was measured by using the well known "Y-factor" method. The measurements were corrected for the loss of the beamsplitter (15 μm mylar, 95% transmission).

Results

The DSB noise temperature of the receiver is shown in Fig. 2 for two different junction arrays. Array Q34 (Rn = 100 Ω, A = 0.8 μm^2, Chebychev RF-filter) has noise temperatures below 230 K over the whole 410-495 GHz range. The lowest value measured was 160 K at 445 GHz. Array Q35 (Rn = 22 Ω, 2 μm^2 ,1/4 λ RF-filter) has noise temperatures between 260 K to 220 K in the frequency range 445-495 GHz. The noise temperature increases sharply below 445 GHz, due to leakage of the RF-filter.

SRON 410-490 GHZ 2-tuner mixer

Q35 Rn=22 Ohms, 1/4 λfilter, 2 μm ^{2}
Q34 Rn=100 Ohms, Chebychev filter .8 μm ^{2}
2-junction array

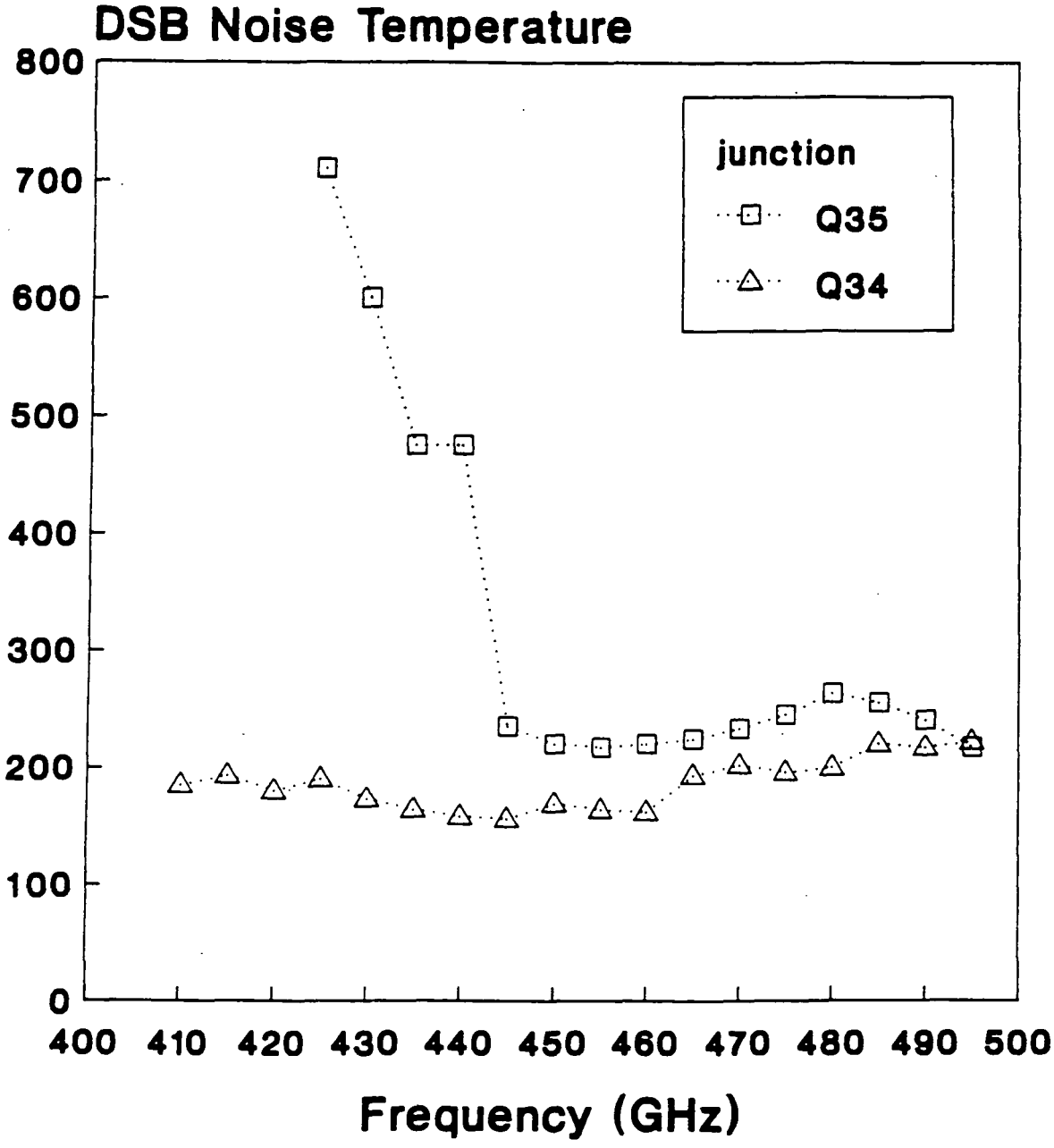

State University Groningen
SRON Groningen, The Netherlands

Fig. 2

SRON 490 GHZ 2-tuner mixer
Tuned and instantaneous bandwidth
Q34 Rn=100 Ohms ,Chebychev-filter

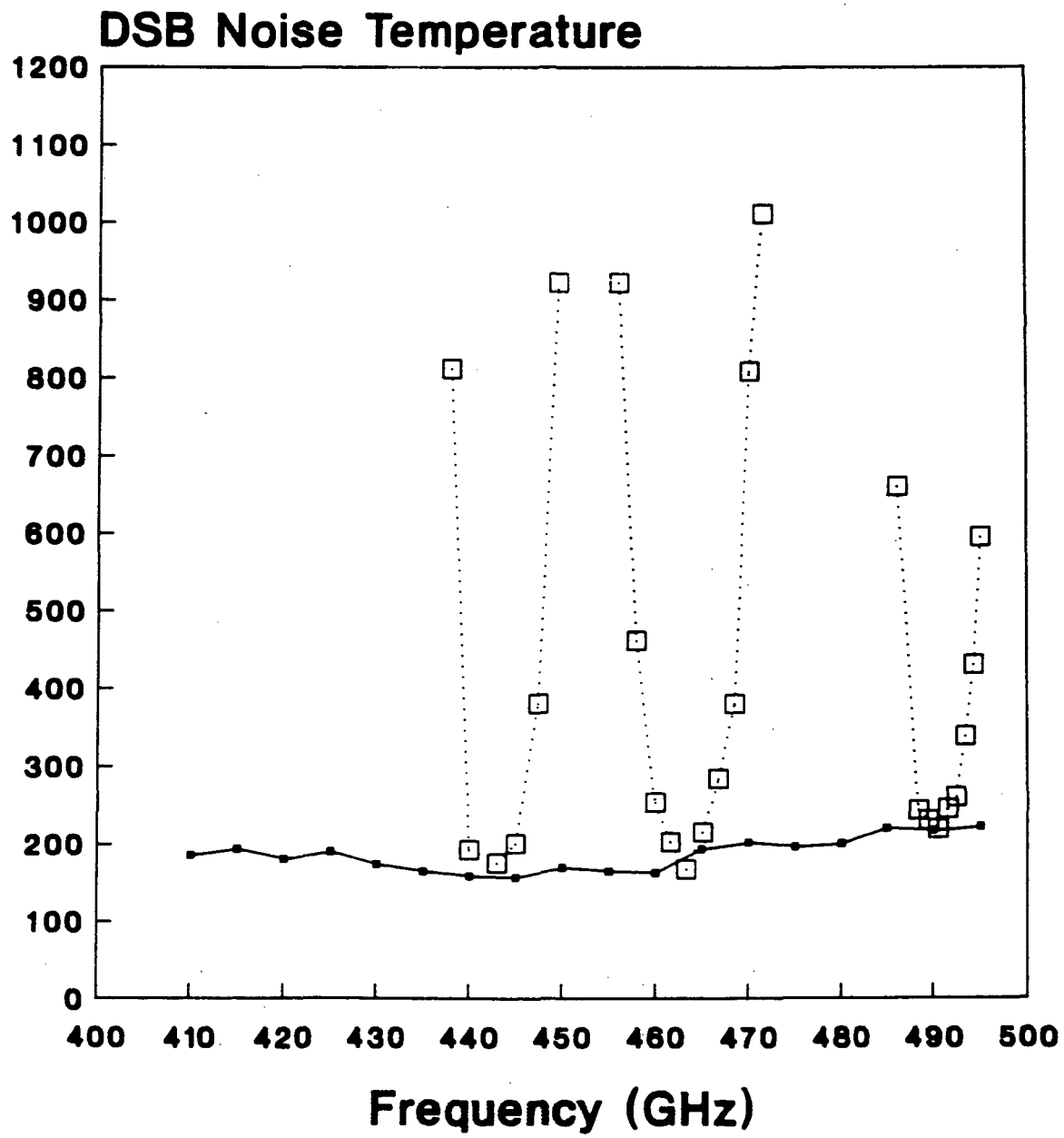

State University Groningen
SRON Groningen, The Netherlands

Fig. 3

The instantaneous bandwidth of junction Q34 is shown in Fig. 3. Here the frequency was changed without adjusting the tuners, only the pump power was adjusted for optimum H/C response.

The unpumped and pumped IV-curves of the two arrays at two different frequencies are shown in Fig. 4. Array Q34 has a low leakage current, a gap voltage of 2.7 mV (1 junction) and a well defined photon step above the gap. The gap voltage of array Q35 is 2.4 mV and it is clearly observed that if the LO-power is radiated on the junction the gap voltage decreases due to heating. The shape of the photon step above the gap also indicates heating effects occur in the junction.

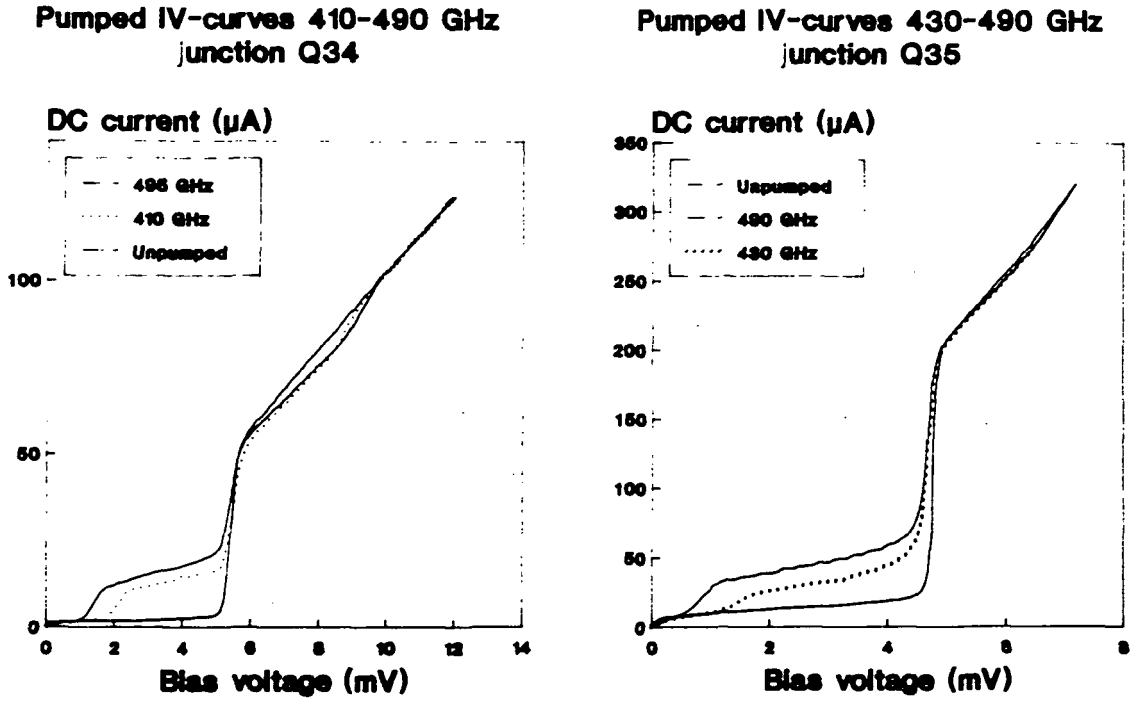

Fig. 4 Pumped and unpumped IV-curves of the two junction arrays

Fig. 5 shows the IF power output at two LO-frequencies, when a hot or cold load are placed in front of the junction. The smooth curves indicate that the Josephson current is suppressed sufficiently. The structure (at 3 mV) in the IF-output seen at 495 GHz is due to the fact that the second photonstep from the negative bias voltage range "creeps" into the first photonstep at the positive voltage range.

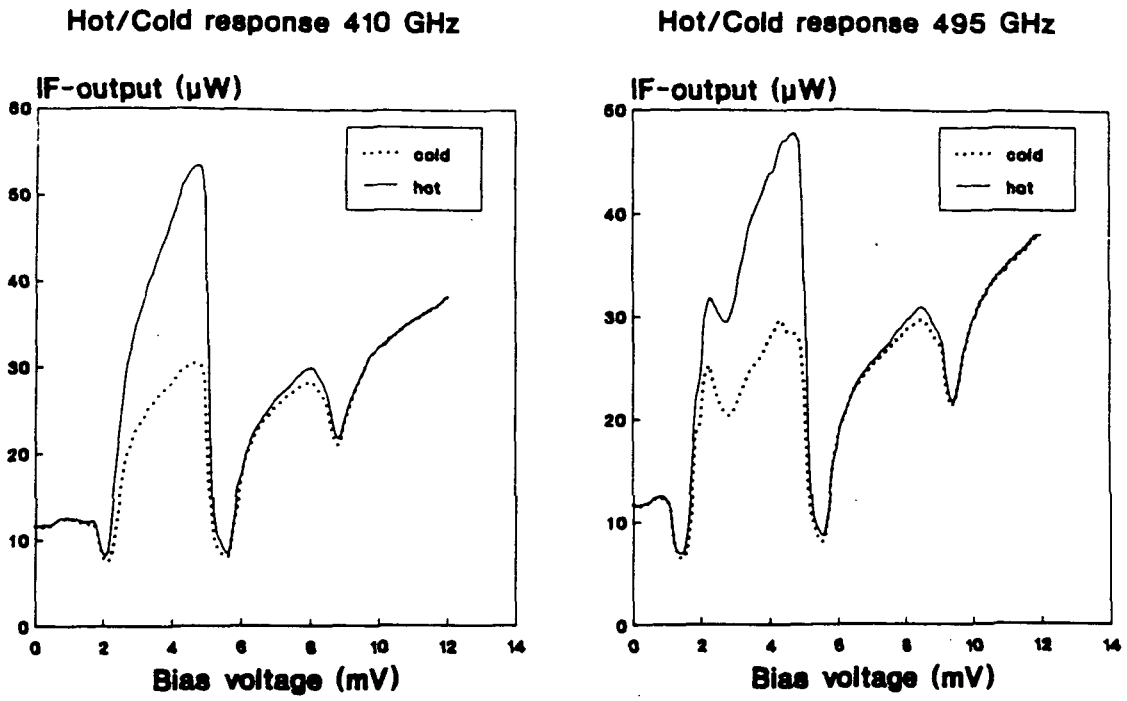

Fig. 5 IF-output with hot and cold signal

Analysis

In the analysis of the noise temperatures, the receiver is divided into three elements: the RF-input, the mixer and the IF-output. A schematic diagram of the whole receiver is given in Fig. 6. Each of these elements contributes to the total receiever noise and gain.

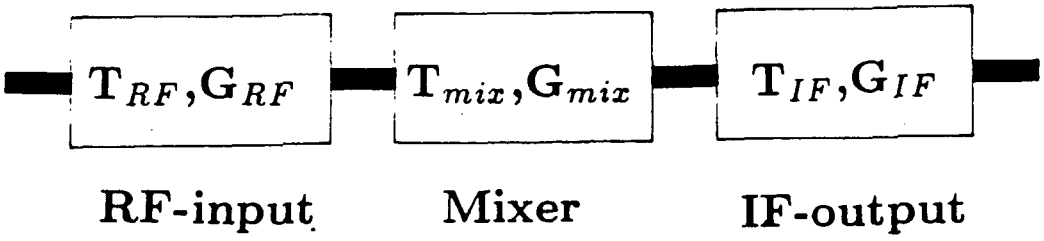

Fig. 6 Schematic representation of the noise and gain contributions in the receiver

For the analysis of the contribution of the IF chain (T-bias, isolator, IF-amplifiers), the shotnoise of an unpumped junction is used. With the known shotnoise of an unpumped junction a Y-factor measurement on the IF-chain is performed. The total power at the end of the IF-chain is given by (1). Here Γ is the reflection coefficient between the 50 Ω line and the junction. P_{junc},P_{isol} and P_{IF} are the noise powers

coming from the junction, the isolator load and the IF-amplifier. G_{IF},G_{isol} and $G_{T\text{-}bias}$ are the gains from the various components. The noisepower from an unpumped array of two junctions is given by (2), where B is the bandwidth, R_{dyn} is the dynamic resistance of the array and V is the voltage over the entire array.

$$P_{out} = (P_{junc}\Gamma + P_{isol}(1-\Gamma) + \frac{P_{IF}}{G_{isol}G_{T-bias}})G_{IF}G_{isol}G_{T-bias} \qquad (1)$$

$$P_{junc} = \frac{1}{8} < I_0^2 > R_{dyn} = \frac{1}{8} 2eB \coth(\frac{eV}{4k_BT}) I(V) R_{dyn} \qquad (2)$$

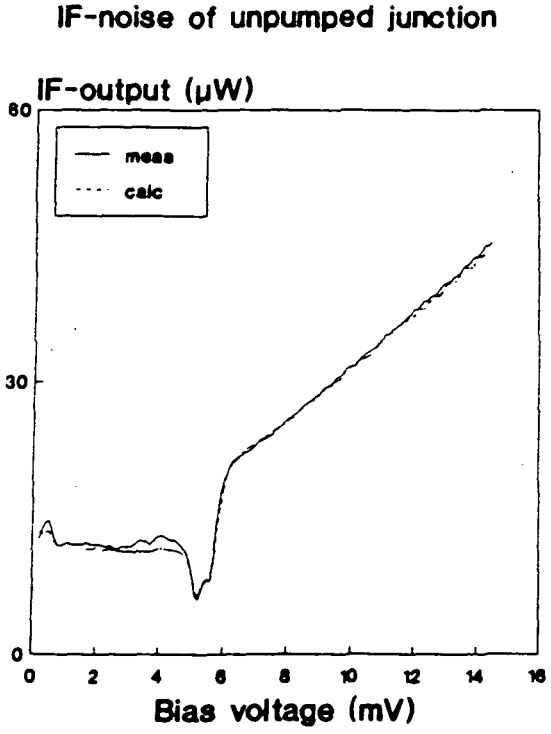

Fig. 7 Measured and calculated noisepower output of an unpumped array of two junctions

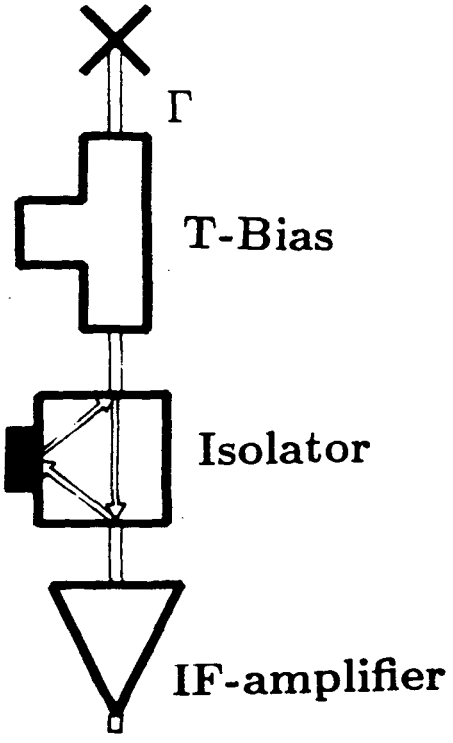

Schematic Diagram of junction and IF-chain

Fig. 7 shows the experimental and fitted curves. The values for the gain and noise contributions of the IF-chain are: G_{IF}=88.4 ± 0.1 dB, T_{IF}=4.8 ± 0.2 K.

The gain and noise contributions of the RF input (beamsplitter, HDP-window, quartz-filter, lens, horn, waveguide and tuners) are difficult to estimate. Several elements were measured seperately, but reflections at the horn waveguide transition and losses in the waveguide and the two tuners are difficult to find. The total gain and noise at the RF-input are: G_{RF}=0.77 ± 0.1 and T_{RF}=56 ± 20 K.

The mixer noise and gain are now calculated with (3) and (4), where δP_{out} is measured power difference at the IF-frequency and δP_{in} is the difference in input power from the hot and the cold load. T_{rec} is the measured total receiver noise temperature.

$$G_{mix} = \frac{\delta P_{out}}{G_{RF} G_{IF} \delta P_{in}} \tag{3}$$

$$T_{mix} = T_{rec} G_{RF} - T_{RF} G_{RF} - \frac{T_{IF}}{G_{mix}} \tag{4}$$

The gain and noise of the mixer are, just as the receiver noise temperature, nearly constant over the 400-500 GHz band. Typical values for the contributions in the receiver DSB gain and noise are: G_{mix} = -12.5 dB ± 0.6 dB and T_{mix} = 90 ± 30 K.

For a complete calculation of the mixer performance it is necessary to know the embedding admittances at the LO and the upper and lower sideband frequencies. These admittances are found by fitting a calculated pumped IV-curve to a measured pumped IV-curve. An example of the quality of this fit at two different frequencies is shown in Fig. 8.

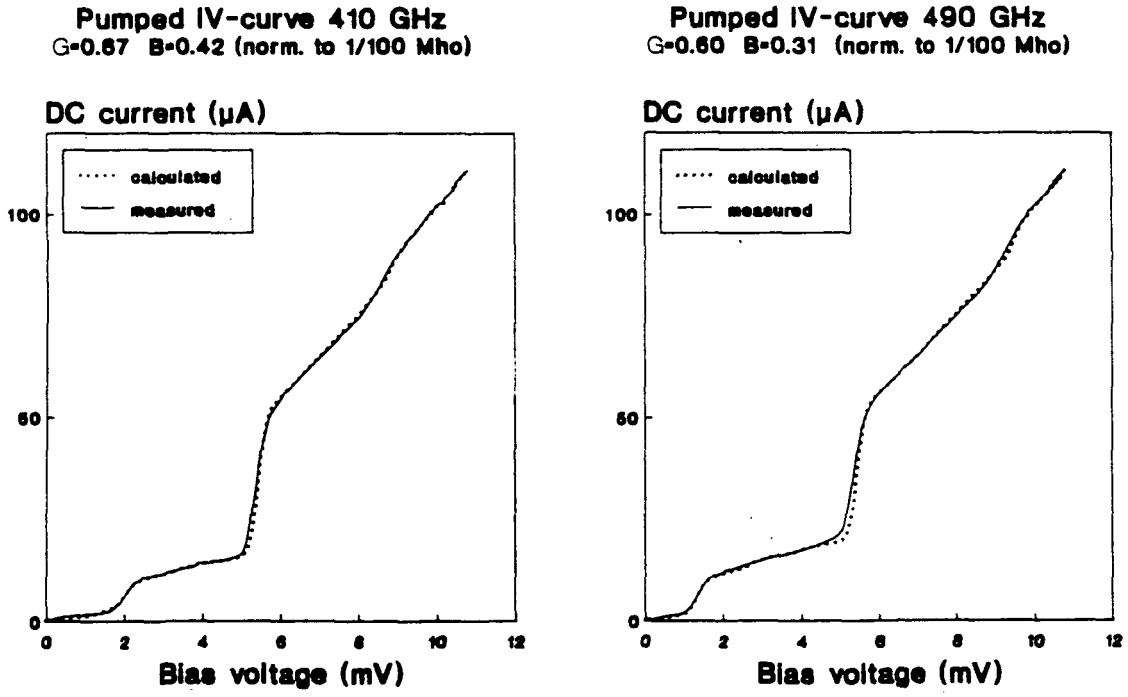

Fig. 8 Measured and calculated IV-curves. The embedding parameters are shown in the header

It is observed that the quality of the fit is good, except for the discrepancy near the gap, which is due to heating and difficult to model. The derived embedding admittances indicate that the tuning elements are able to compensate the junction capacitance. Unfortunately the sideband admittances are not yet calculated and a full analysis cannot be performed at the moment. The result of a calculation of the mixergain, under the assumption that the sideband admittances are equal to the LO-admitance, is shown in Fig. 10.

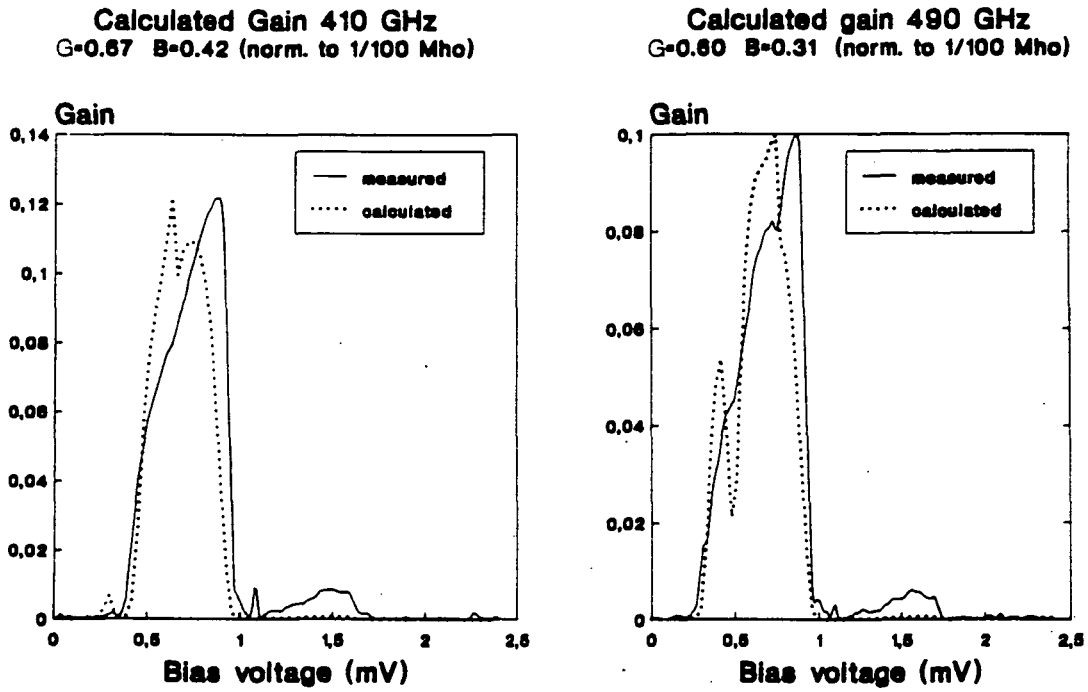

Fig. 10 Measured and calculated mixer gain

In this figure the calculated and measured gain are normalized to each other. One observes a big discrepancy between the measured and calculated gain, which indicates that the LO and sideband frequencies differ significantly.

In both the calculated and the measured gain, some fine structure on the first photonstep region is observed, indicating that the calculation method is working properly, but the input parameters are wrong.

Summary

Measurements were performed in the 400-500 GHz range with a two tuner waveguide mixer. The measured (receiver) noise temperatures are amongst the lowest values measured at these frequencies. The results show that an array of two

junctions is suitable in achieving a low noise receiver in the 400-500 GHz range. It is also found that a qualitatively "bad" junction with a low gap-voltage can still serve as a low noise mixer element. The preliminary comparisons between theory and measurement show a good agreement between calculated and measured pumped IV-curves. Gain calculations indicate that the measured noise temperatures are not fully DSB measurements. Further analysis is needed to determine the USB and LSB gain and noise contributions.

Acknowledgements:
This work was supported by ESA under contract No. 7898/88/NL/PB(SC), the Stichting Technische Wetenschappen and the Stichting voor Fundamenteel Onderzoek der Materie.

References

1 J.Zmuidzinas, H.G. LeDuc, "Quasi-Optical Slot Antenna SIS Mixer", *Proceedings of the Second International Symposium on THz Technology.*

2 C.K. Walker, M.Chen, P.L. Shafer, H.G. LeDuc, J.E. Carlstrom, T.G. Carlstrom, T.G. Phillips, "A 492 GHz SIS Waveguid Receiver for Submillimeter Astronomy", *Int J. of IR and Millimeter Waves 1992.*

3 J.R. Tucker, M.J. Feldman, "Quantum Detection at Millimeter Wavelengths" *Rev. Mod. Phys 57, 1055 (1985)*

4 C.A. Mears, Qing Hu, P.L. Richards, A.H. Worsham, D.E. Prober, A.V. Räisänen, "Quantum Limited Quasiparticles Mixers at 100 GHz", *IEEE Trans. Magn., vol 27, 2, 1991*

5 C.E. Honingh, G. de Lange, M.M.T.M Dierichs, H.H.A. Schaeffer, J. Wezelman, J. v.d. Kuur, Th. de Graauw, T.M. Klapwijk, "Comparison of Measured and Predicted Performance of a SIS Waveguide Mixer at 345 GHz", *these proceedings*

6 C.E. Honingh, unpublished results

7 M.M.T.M. Dierichs, unpublished results

Double Dipole Antenna SIS Receivers at 100 and 400 GHz

A. Skalare* **, H. van de Stadt**, Th. de Graauw**, R. A. Panhuyzen***, M. M. T. M. Dierichs***

* Dept. of Applied Electron Physics, Rännvagen 6, Chalmers University of Technology, Göteborg, Sweden.

** Space Research Organization of the Netherlands (SRON), Landleven 12, 9747 AD Groningen, the Netherlands.

*** Dept. of Applied Physics and Materials Science Center, University of Groningen, Nijenborgh 4, 9747 AG Groningen, the Netherlands

Abstract

Antenna patterns were measured between 95 and 120 GHz for a double dipole antenna / ellipsoidal lens combination. The structure produces a non-astigmatic beam with low side lobe levels over that whole band. A heterodyne SIS receiver based on this concept gave a best noise temperature of 145K DSB at 98 GHz. Measurements were also made with a 400 GHz heterodyne SIS receiver, using a double dipole antenna in conjunction with a hyperhemispherical lens. The best noise temperature was 220 K DSB at 402 GHz. On-chip stubs were used to tune out the SIS junction capacitance.

Introduction

We here describe two SIS heterodyne receivers, both using double dipole antennas [1,2,3,4] placed on the back plane of a thick dielectric lens. In both cases, the antenna consisted of two half wave dipoles, connected by a stripline with the SIS mixer at the mid point, Fig.1 . The quartz chip with the antenna was mounted on the back plane of a thick quartz lens, and was backed by a quarter wave thick quartz slab and a reflector, Fig.2 . Some early low frequency scale model measurements of this structure can be found in [4].

Both receivers were designed in similar but not identical ways, and will be described separately.

100 GHz Receiver Design

The size of the dipole antenna was chosen to give a center frequency of 100 GHz. The 11mm diameter quartz lens was polished to an ellipsoidal shape, designed to produce a

diffraction limited main lobe. The polishing tool was a brass rod with an ellipsoidal hole at one end, machined with a numerically controlled milling machine.

As shown in Fig.3 the mixer fixture pinched the lens between a copper back plate and two flanges, which fitted into two grooves in the quartz. With the help of a small amount of vacuum grease, this provided excellent 4K cooling of the lens and the mixer chip.

The mixer itself was a series array of two Nb-Al/AlOx-Nb SIS junctions with a normal state resistance of 34 ohms. The size of each junction was 2 square microns. No attempts were made to tune out the parasitic capacitance of the junctions.

The mixer chip was contacted by a flexible strip transmission line, Fig.4 , which was soldered to a 85 mil output co-ax. The strip was cut to high accuracy from a Kapton/copper laminated sheet, to give a characteristic impedance close to 50 ohms. As shown in Fig.5 , the strip line would work well even for intermediate frequencies of up to 8 GHz, where resonances in the lens fixture begin to appear.

100 GHz Measurements

The antenna pattern of the dipole/lens fixture was measured at room temperature with a bismuth bolometer in place of the SIS junctions, Fig.6 . Both the E- and H-plane beam profiles were of high quality over the whole 95-120 GHz band, in good agreement with earlier scale model measurements [4].

Y-factor measurements with the SIS mixer in a 4.2K helium cryostat gave a best receiver noise temperature of 145K DSB at 98 GHz, Fig.7 . The intermediate frequency amplifier was a 1.5 GHz cooled Berkshire HEMT, with a noise temperature of 4K (from the manufacturers data sheets). We believe that the noise performance can be improved considerably by the use of on-chip tuning structures, but have not yet implemented this in the 100 GHz receiver.

400 GHz Receiver Design

The 400 GHz receiver differed from the 100 GHz one in a few ways, namely :

1. We chose to use a hyperhemisperical lens, mainly because it can be manufactured to higher tolerances than an ellipsoidal one.

2. The antenna was a scaled down version of the 100 GHz structure. The center frequency was chosen to 310 GHz, which puts the upper frequency limit of the antenna itself somewhere around 430 GHz (one octave bandwidth).

3. The SIS parasitic capacitances were tuned by on-chip stubs, as can be seen in Figs.8 and 9 . A series array of two junctions, each of 3 square microns, was used.

4. We used two different IF amplifier chains, one with a 1.5 GHz FET with approximately 11K noise temperature, the other with a 4 GHz Berkshire Technology

HEMT with 4K noise temperature.

5. The Josephson effect was suppressed by a superconducting coil.

400 GHz Measurements

The video response of the receiver over the range 100-600 GHz was studied with a Fourier transform spectrometer, Fig.10 . Two peaks are visible in the diagram, one just above 200 GHz and one close to 400 GHz. The approximate positions of the peaks could be predicted from a simple circuit model, where each junction was represented by a capacitance of 165 fF in parallel with its normal state resistance.

Two initial Y-factor measurements with the same mixer chip are shown in Fig.11 . The best performance was at the lower end of the available local oscillator band, with a lowest noise temperature of 220K DSB.

Summary

The dipole / ellipsoidal lens configuration was investigated in terms both of antenna pattern and of matching to SIS junctions. The pattern measurements showed low side lobe levels, and a non-astigmatic beam over the whole band 95-120 GHz. The best receiver noise temperature was 145K DSB at 98 GHz, a value we believe will be improved with the use of integrated tuning structures.

The initial measurements with the other receiver, in which a double dipole antenna is combined with a hyperhemispherical lens, yielded a best noise temperature of 220K DSB at 402 GHz.

The Kapton laminate strip should function well up to 8 GHz as an intermediate frequency connection to the mixer chips.

Acknowledgements

The authors extend their gratitude to Prof Dr Ir T. M. Klapwijk for his advice and for useful discussions, to Mr. H. Schaeffer for his technical support, and to Mr. G. de Lange and Ms. C. E. Honingh for their assistance in the noise temperature measurements. The work presented here was supported financially by the European Space Agency (ESA), through contract 7898/88/NL/PB(SC).

References

[1] P. T. Parrish, T. C. L. G. Sollner, R. H. Mathews, H. R. Fetterman, C. D. Parker, P. E. Tannenwald, A. G. Cardiasmenos, "Printed Dipole-Schottky Diode Millimeter Wave Antenna Array", SPIE Millimeter Wave Technology, Vol. 337, 1982, pp.49-52

[2] W. Chew, H. R. Fetterman, "Printed Circuit Antennas with Integrated FET Detectors for mm-Wave Quasi-Optics", IEEE Trans. Microwave Theory Tech., Vol. MTT-37, No. 3, 1989.

[3] J. A. Taylor, T. C. L. G. Sollner, D. D. Parker, J. A. Calviello, "Planar Dipole-fed Mixer Arrays for Imaging at Millimeter and Sub-Millimeter Wavelenghts", Proc. of the 1985 Int. Conf. on IR and mm-Waves, 1985, pp.197-188.

[4] A. Skalare, Th. de Graauw, H. van de Stadt, "A Planar Dipole Array Antenna with an Elliptical Lens", Microwave and Optical Tech. Letters, Vol.4, No.1, Jan. 1991.

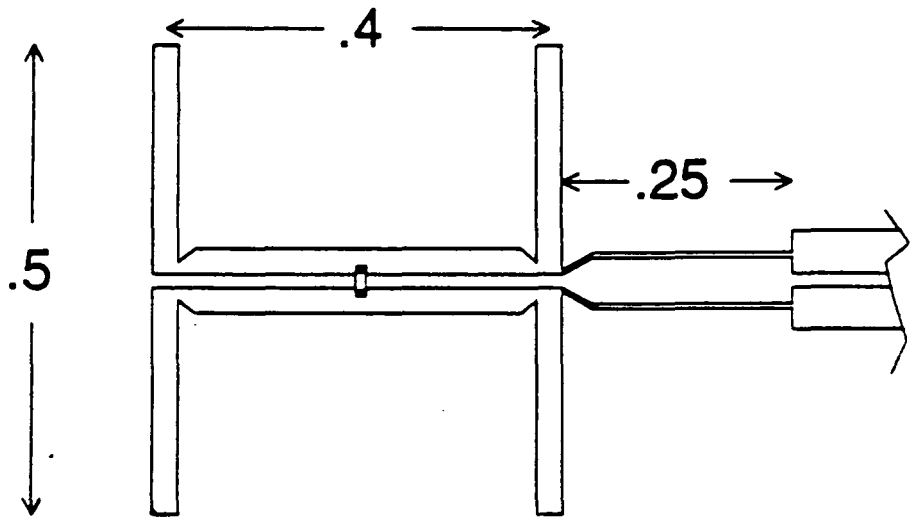

Fig.1 : The geometry of the 100 GHz double dipole antenna. The dimensions are in units of wavelength at the design frequency.

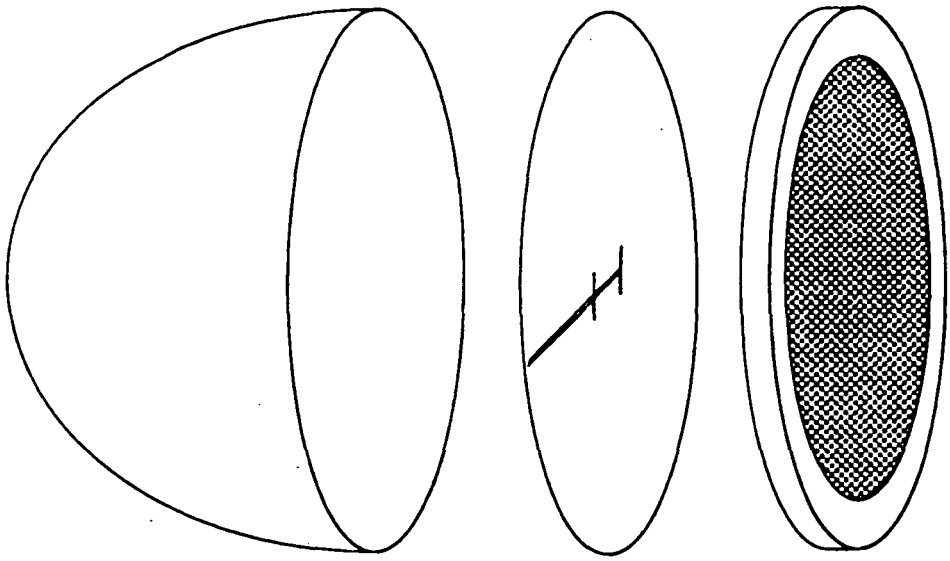

Fig. 2 : The antenna chip is placed between a quartz lens and a quarter wavelength thick quartz slab with a reflector.

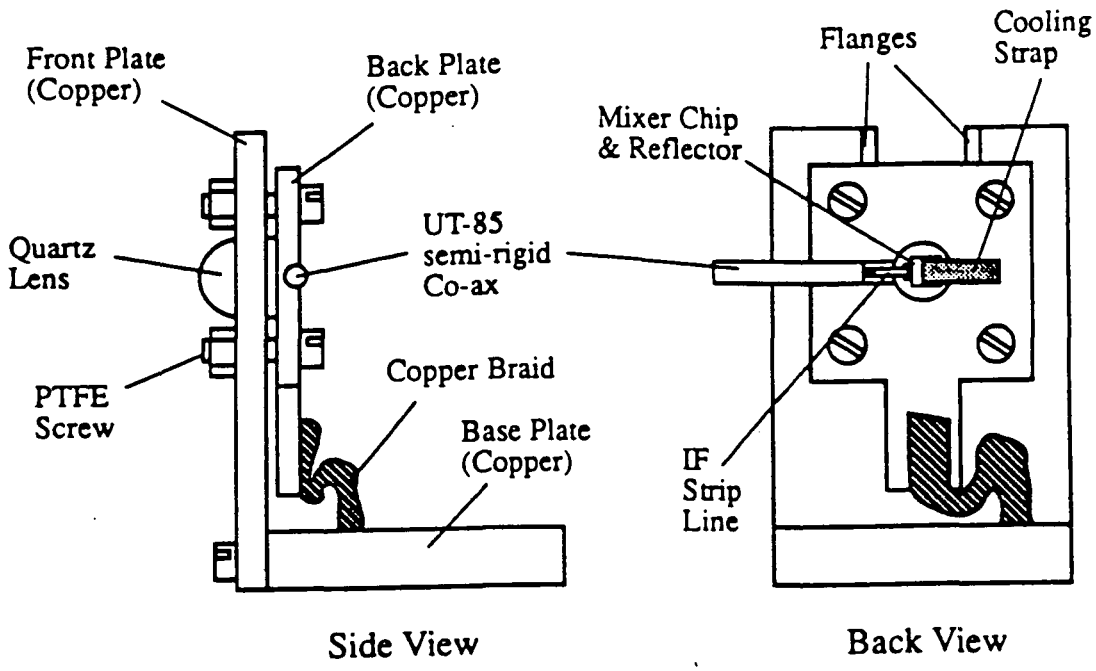

Fig.3 : The fixture that holds the lens and the mixer chip. The diameter of the lens in this figure is 11mm.

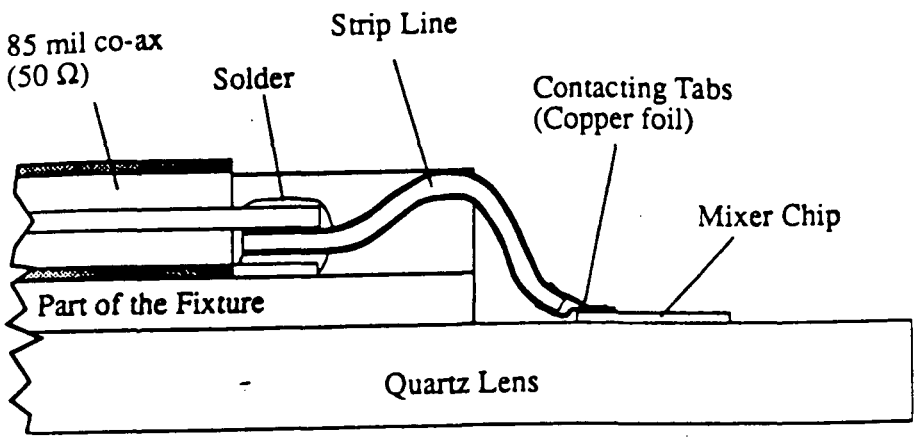

Fig.4 : The flexible Kapton laminate strip line used for the DC & IF connections. The tabs at the end of the strip are glued to the contact pads on the chip with silver paint.

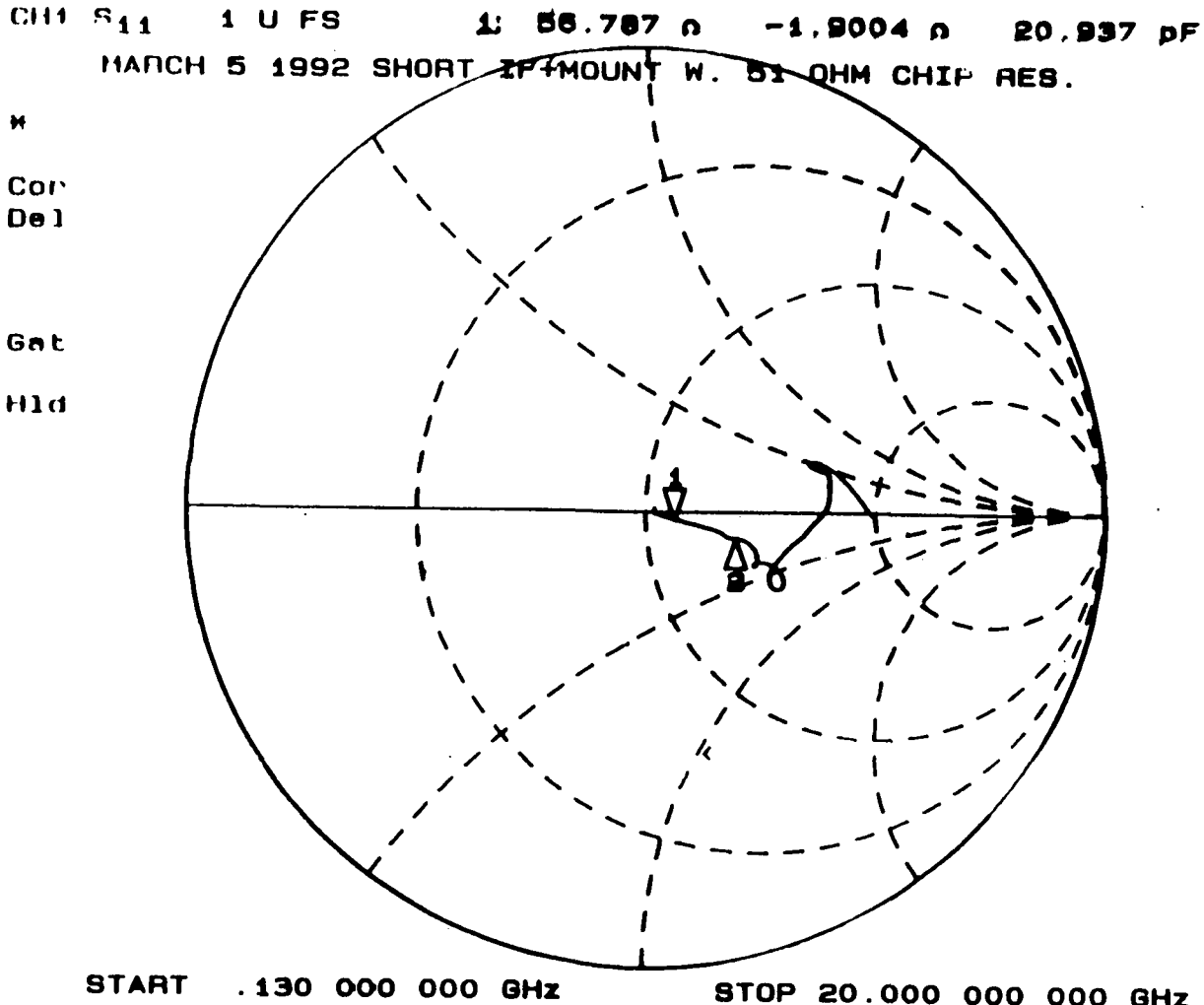

Fig.5 : The room temperature S11 reflection on the IF line in Figs. 3 & 4, with the mixer chip replaced with a chip resistor (51 ohms). A time gate was applied around the co-ax to strip transition, the strip itself and the resistor. Marker 1 is at 4 GHz and Marker 2 is at 8 GHz.

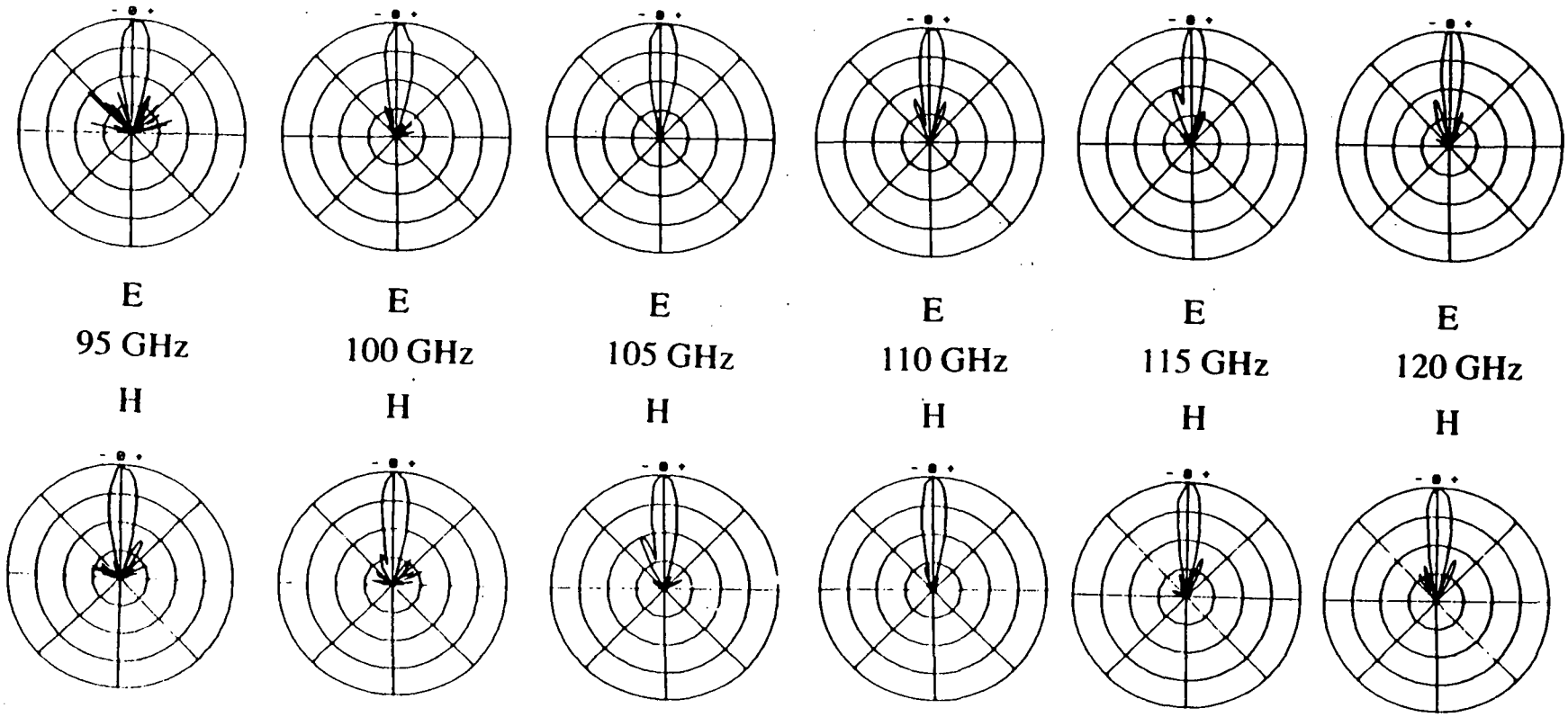

Fig.6 : Antenna patterns of the double dipole / ellipsoidal lens combination. The patterns were measured with a Bismuth bolometer, and the radial scale is 5 dB per division.

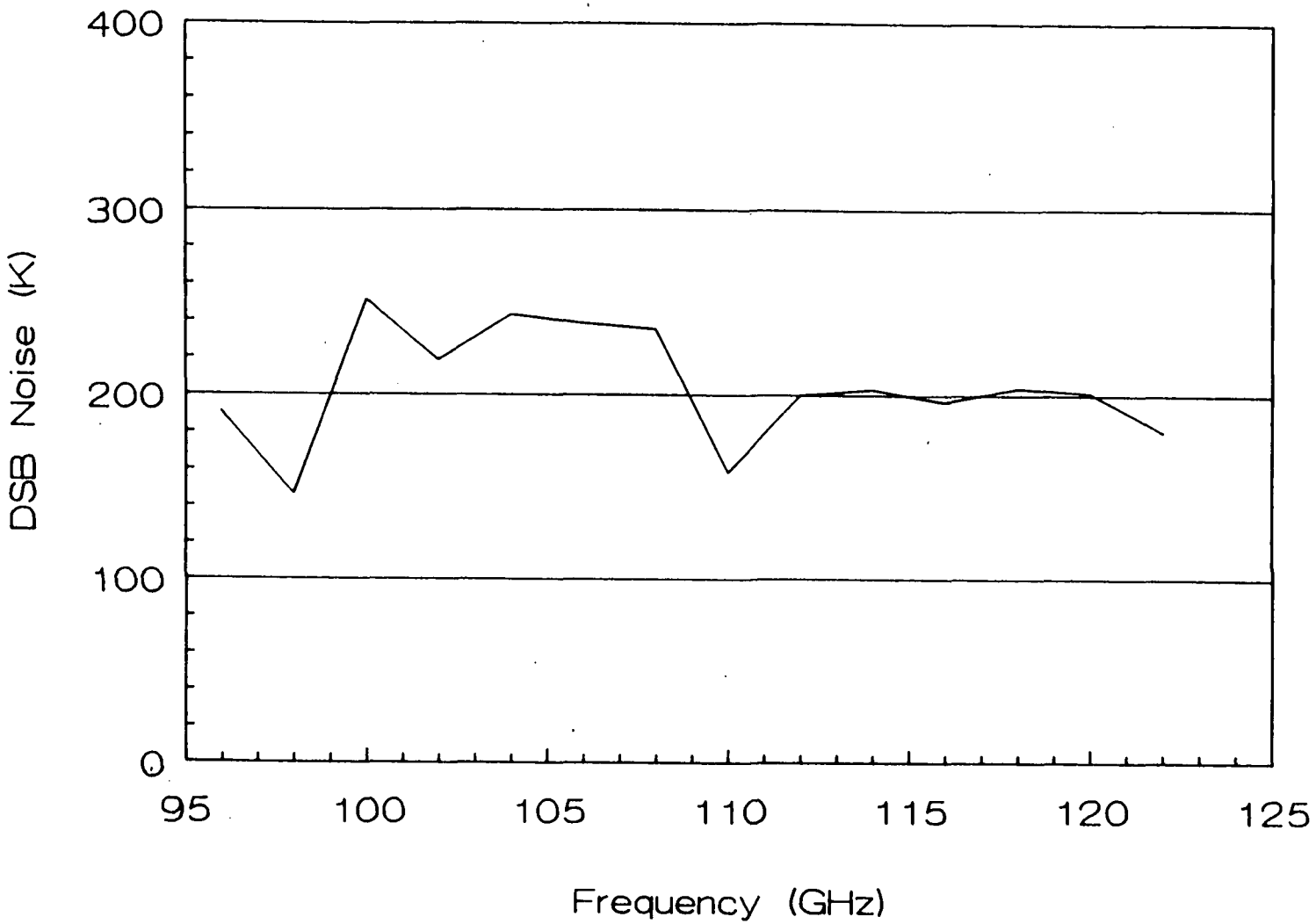

Fig.7 : The double sideband noise temperature of the 100 GHz receiver. The data was corrected for the transmission of the LO injection beam splitter (95%) .

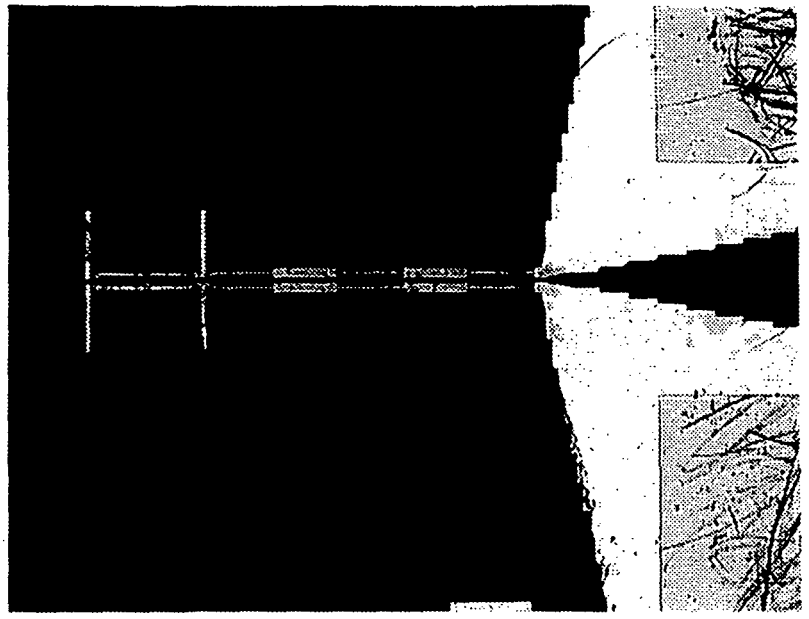

Fig.8 : The 400 GHz mixer chip.

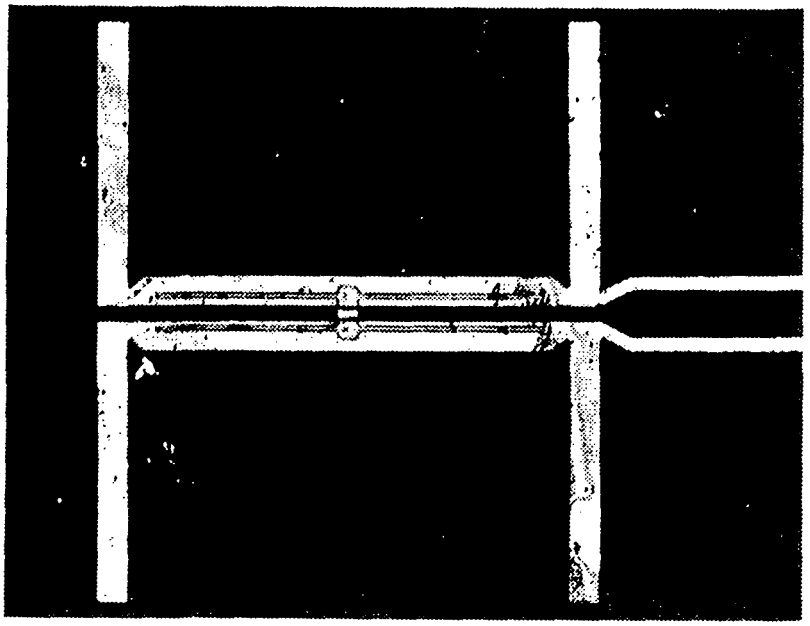

Fig.9 : The 400 GHz antenna chip, detail.

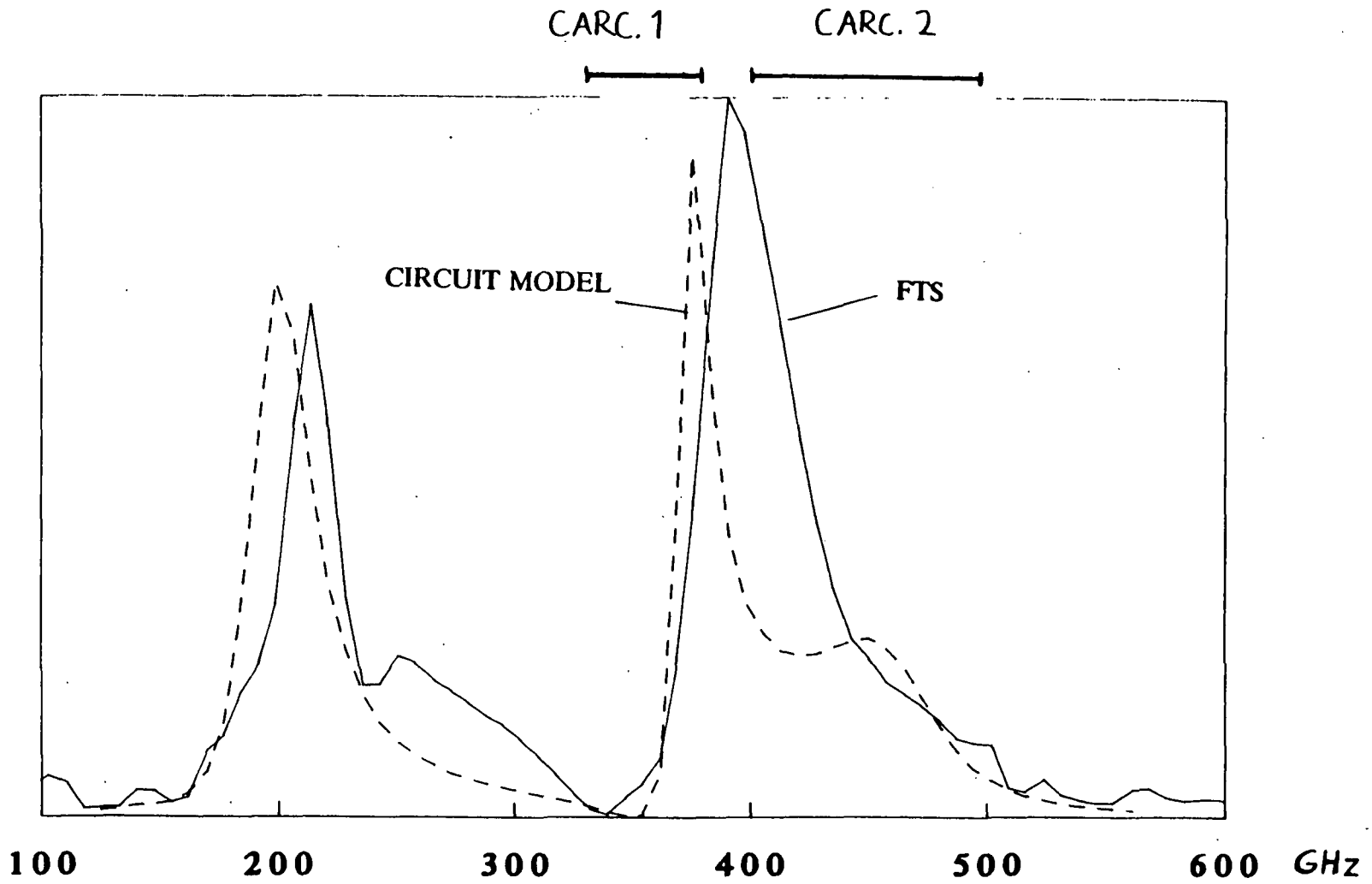

Fig.10 : The Fourier transform spectrogram (arbitrary units on the vertical scale). "CARC2" marks the frequency range where noise temperature measurements have been made.

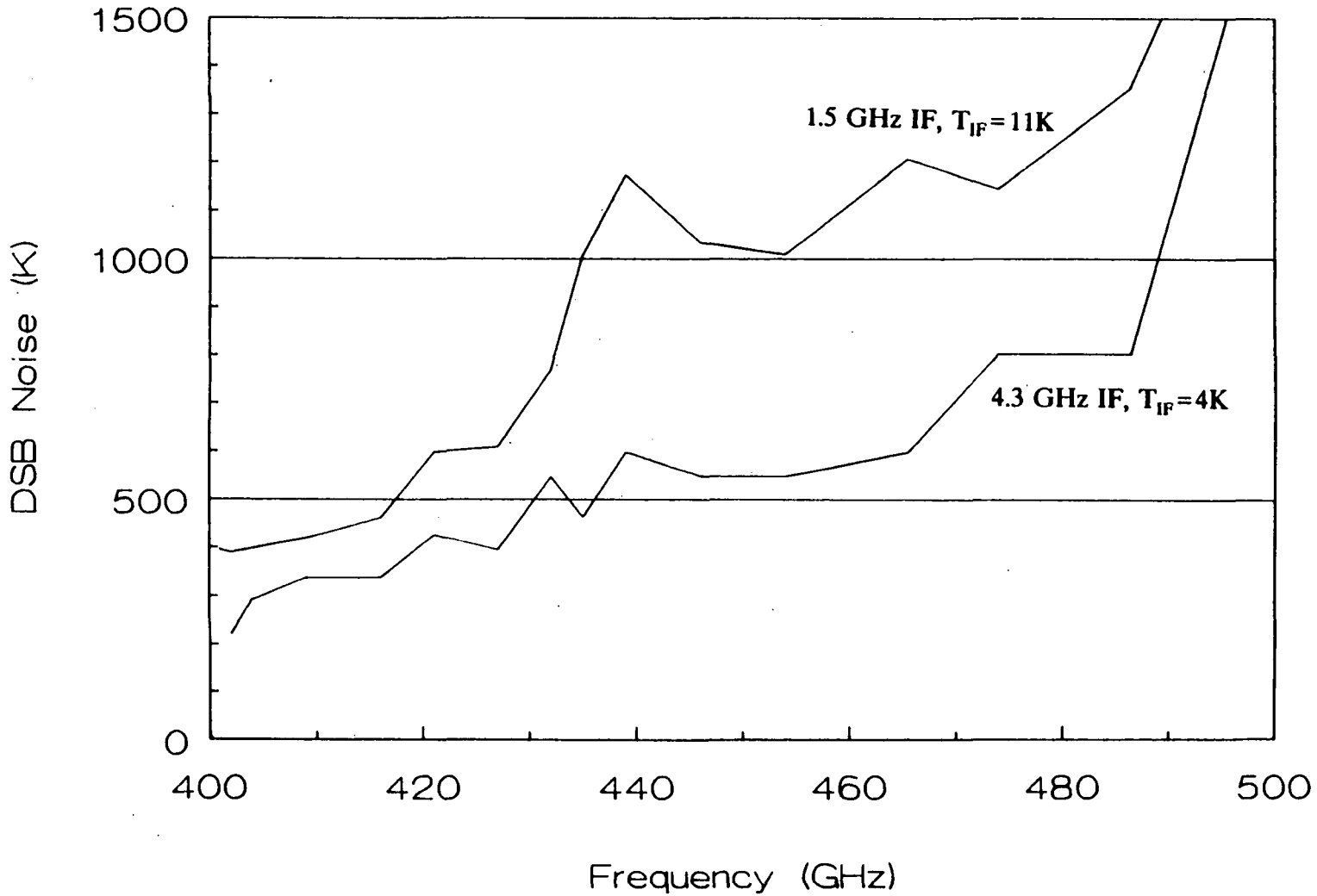

Fig.11 : DSB Noise measurement with the 400 GHz receiver. The data was corrected for the transmission of the LO injection beam splitter (65%) .

Slot Antenna SIS Mixers for Submillimeter Wavelengths

Jonas Zmuidzinas*, H. G. LeDuc**, and J. A. Stern

We are developing improved versions of a slot antenna SIS mixer which we have previously described [1]. The initial work demonstrated a double sideband noise temperature of 420 K for a 500 GHz quasi-optical SIS mixer employing a twin-slot antenna on a quartz dielectric substrate. A quartz hyperhemispherical lens is used to focus the incoming radiation onto the twin-slot antenna. The advantages of a twin-slot antenna include a low impedance (35 Ω) and a clean, symmetric beam pattern into the dielectric with a 70% efficiency. In our original mixer, the radiation was coupled from the two slot antennas onto superconducting microstrip lines which fed the SIS junction. By performing an impedance transformation using tapered lines and by feeding the radiation from the two slots to the junction in parallel, the effective (real) impedance seen by the junction was reduced to just 4 Ω. This very low impedance allowed a junction area of 2.3 μm^2 to be used at 500 GHz, which was manufactured using optical lithography. However, no attempt was made to tune out the junction capacitance. We estimate that this capacitance reduces the impedance coupling efficiency to $\eta_Z \approx 0.23$, for our junction with $\omega R_N C = 5.3$ at 500 GHz.

The recent development [2] of techniques using electron-beam lithography to manufacture junctions with very small areas ($\approx 0.1\ \mu m^2$) now allows considerably more flexibility in the design of SIS mixer circuits. We have redesigned the slot-antenna mixer to take advantage of this possibility. In particular, we have included a novel circuit which allows the junction capacitance to be tune out over a broad bandwidth. For instance, mixers designed for 800 GHz using NbN/MgO/NbN junctions with realistic parameters achieve a 3 dB impedance bandwidth of nearly 400 GHz. Furthermore, our circuit uses only short lengths of microstrip and should therefore be less sensitive to RF losses than other designs. The improved impedance match should give a large reduction in noise temperature as compared to our previous mixer. The new devices are currently under fabrication. Further details of the design and any available experimental results will be discussed.

---

*Jonas Zmuidzinas is with the Downs Laboratory of Physics, California Institute of Technology.

**H. G. LeDuc and J. A. Stern are with the Jet Propulsion Laboratory, California Institute of Technology.

[1]J. Zmuidzinas and H. G. LeDuc, "Quasi-optical Slot Antenna SIS Mixers," *IEEE Trans. Microwave Theory Tech.*, in press, 1992.

[2]H. G. Leduc, A. Judas, S. R. Cypher, B. Bumble, B. D. Hunt, and J. A. Stern, "Submicron Area NbN/MgO/NbN Tunnel Junctions for SIS mixer Applications," *IEEE Trans. Magn.*, MAG-27, 3192, 1991.

A PLANAR QUASI-OPTICAL SIS RECEIVER FOR ARRAY APPLICATIONS

Philip A. Stimson, Robert J. Dengler, Peter H. Siegel and Henry G. LeDuc

Jet Propulsion Laboratory, Pasadena, CA, 91109

***Abstract*—A novel planar, quasi-optical SIS receiver operating at 230 GHz is described. The receiver consists of a 2×5 array of half wave dipole antennas with ten niobium–aluminum oxide–niobium SIS junctions on a quartz dielectric-filled parabola. The 1.4 GHz intermediate frequency is coupled from the mixer via coplanar strip transmission lines and 4:1 balun transformers. The receiver is operated at 4.2 K in a liquid helium immersion cryostat. We report here accurate measurements of the performance of single receiver elements. A mixer noise temperature of 89 K DSB, receiver noise temperature of 156 K DSB and conversion loss of 8 dB into a matched load have been obtained.**

INTRODUCTION

The quasiparticle superconductor-insulator-superconductor (SIS) mixer is the most sensitive detector in the millimeter-wave region and forms the basis of most high quality receivers for millimeter-wave astronomy [1]. The quantum limit for noise temperature (in a SSB mixer) has essentially been reached at 100 GHz [2] [6], but at higher frequencies the available performance is poorer, with 10 times the quantum limit being a more realistic goal. This figure has recently been reported from the best waveguide mixers around 200 GHz [3] [4] [5]. The major cause of the performance reduction at high frequency is the SIS junction capacitance, which presents a smaller parallel reactance and shunts the quasiparticle response. Tuning structures can, in principle, alleviate this limitation but are not yet well understood at higher frequencies [8]. The approach most often used, and that used here, is to fabricate high current density junctions with exceedingly small areas ($< 1\ \mu m^2$) to reduce the capacitance. Another serious problem is control of Josephson currents in the junction. Noise temperatures obtained with broadband hot and cold loads may be highly inaccurate in the presence of Josephson currents. These effects become more important as the frequency and/or bandwidth is increased. Other

problems include losses in conductors and dielectrics, the fabrication difficulties of small waveguide components and difficulties in obtaining convenient local oscillators.

Quasi-optical receivers with planar circuit mixers are an attractive approach for systems at frequencies in the neighborhood of 1 THz [7] [8] [9]. They suffer the disadvantage of being fixed tuned but provide the advantage of convenient monolithic fabrication. Planar configurations are also a desirable approach to realizing array receivers.

In this paper, we report accurate measurements on a quasi-optical array-type receiver at 230 GHz. We have been able to suppress Josephson currents almost completely, and our intermediate frequency versus bias voltage curve exhibits the smooth oscillatory behavior of the best waveguide mixers [3]. Our configuration is designed to allow an array of mixers to be measured during one cool down cycle. We report here the performance of a single array element. We will report on complete array performance in a separate paper. The SIS junctions used for these experiments were nominally identical to those used in recent waveguide receivers [3] [4], with which our results may be compared.

SIS JUNCTION FABRICATION

The junction wafer used for this receiver carries a 2×5 array of resonant dipole antennas with 0.4×0.4 μm niobium–aluminum oxide–niobium SIS junctions at the terminals. The junctions were fabricated using a self aligned lift-off trilayer process. The niobium–aluminum oxide–niobium trilayer was sputtered onto the 0.25 mm thick, 17 mm diameter quartz substrate through a photoresist stencil. The trilayer remaining af-

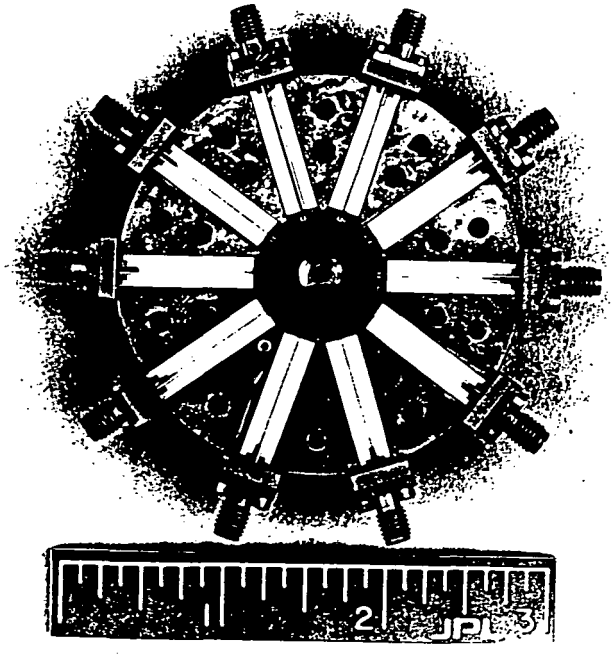

Fig. 1. The mixer block with the upper half removed. The central dielectric-filled parabola (dark), containing 10 antenna and mixer elements, is surrounded by 10 IF baluns (light) and SSMA connectors at the edge of the block.

ter lift-off formed half of each antenna and the ten coplanar strip transmission lines used for the IF. The junction mesa was patterned using electron beam lithography on 1200 Å thick PMMA over a 4000 Å thick polyimide layer, followed by evaporation of 500 Å of chromium metal and lift-off. The chromium stencil was transferred to the polyimide underlayer by reactive ion etching in an oxygen plasma. The contact regions of the trilayer were then protected with a resist stencil and the chromium/polyimide mask was used to etch the junction. Thermal SiO was deposited using the same stencil to provide electrical isolation of the base electrode and to provide dielectric for two RF blocking capacitors located one quarter and three quarter wavelengths away from the junction down the coplanar strips. The polyimide was then removed with dichloromethane. The second half of the antennas was made by deposition of niobium and reactive ion etching.

RECEIVER DESIGN

The mixer block, shown in Figure 1, consists of the junction/antenna wafer, a quartz reflector, and IF baluns and connectors mounted in a brass housing. The wafer is held on the flat face of a quartz parabolic lens, whose rear surface is metalized. Incoming radiation is reflected by the metal surface and focussed onto the antenna elements at the center of the wafer. The configuration, called a Dielectric-Filled Parabola (DFP), is analogous to a conventional parabolic dish antenna. The IF signals are coupled from the wafer via coplanar strip transmission lines. Monolithic IF baluns transform the 200 Ω characteristic impedance of the coplanar strips to that of 50 Ω coaxial transmission line. Details of this design, including extensive low frequency modeling, are described by Siegel et al. [10] [16]. A superconducting magnetic field coil is mounted on the block to suppress Josephson currents in the junctions.

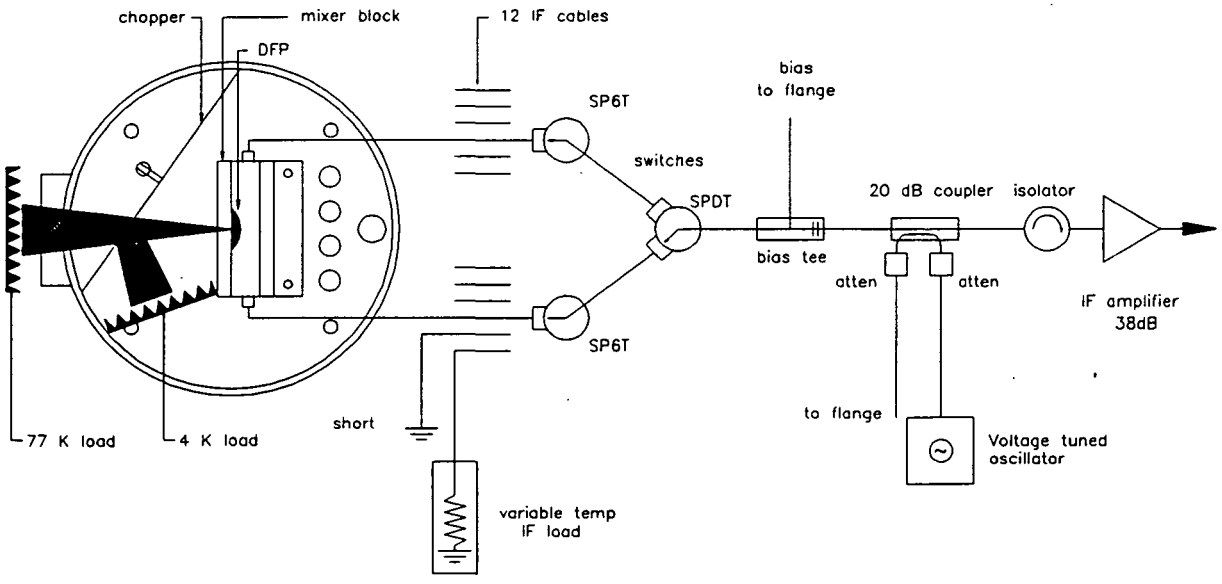

Fig. 2. Schematic diagram of the IF system of the array receiver. The entire system is immersed in liquid helium except for the 77 K load which is bolted to the liquid nitrogen shield of the cryostat.

The IF system shown in Figure 2, consists of ten IF cables routed through two 6-position coaxial switches and one 2-position switch to a single amplifier chain. The remaining two switch positions are used to connect a short and a variable temperature IF load to the amplifier input. The load consists of a resistor terminating a stainless steel coax cable on a thermally isolated plate which contains a heater resistor and diode thermometer. The structure is enclosed in an indium sealed can. This permits accurate calibration of the IF system and very accurate mixer measurements [11]. An isolator is used to reduce the SWR at the amplifier input and a directional coupler with cooled attenuators allows signals to be injected into the IF system to measure the mixer reflection coefficient. After removal from the cryostat the IF signal is further amplified and passed through a variable center frequency 50 MHz wide filter and fed to a power detector. The IF system noise temperature is approximately 7 K at 1.4 GHz.

The optical system consists of a chopper mounted directly in front of the mixer, and the hot and cold loads. When the chopper blade is closed the input beam is directed onto a 4 K (cold) load mounted on the receiver plate; when it is open the beam passes through a quartz window to a 77 K (hot) load mounted on the liquid nitrogen shield of the cryostat. The loads are pyramidal absorbers manufactured from Eccosorb CR-110, which is known to provide high absorption and low reflection at this frequency. Reflection from a flat plate of CR-110 has been measured at less than -10 dB in this frequency range [12]. The window is exactly five wavelengths thick and passes almost all the incident 230 GHz radiation. The theoretical transmittance is 0.999; we measured a transmittance of over 0.95. Local oscillator radiation is produced by a Gunn diode and Schottky diode doubler and is injected through the back of the mixer block. No diplexer is required.

The entire receiver is immersed in liquid helium which eliminates heat sinking problems. The dielectric constant of the helium is 1.048 [15]. The switches, thermometers,

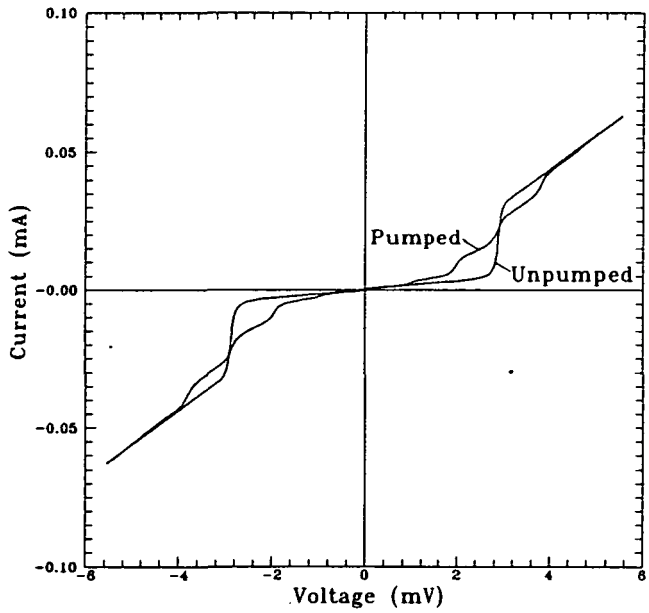

Fig. 3. Pumped and unpumped IV curves for a typical Nb-AlO_x-Nb SIS junction used in the planar receiver.

liquid level meter...etc., and all data aquisition is controlled by a computer.

MEASUREMENT TECHNIQUE

We use a variation of the technique of McGrath et al. [11], to obtain mixer gain and noise temperature. First, the IF system is calibrated by plotting the temperature of the IF load as a function of the IF output power. This measures the IF system noise temperature T_{IF}. The receiver noise temperature T_R is measured using the hot and cold loads (T_H and T_C), the ratio of the IF output powers $Y = P_{IFH}/P_{IFC}$ and Equation 1.

$$T_R = \frac{T_H - YT_C}{Y - 1} \tag{1}$$

$$T_M = T_R - \frac{(T_{IF} + T_S\Gamma^2)}{(1 - \Gamma^2)}L_M \tag{2}$$

$$\frac{1}{L_M} = \left(\frac{T_{IFH} - T_{IFC}}{T_H - T_C}\right)\left(\frac{1 - \gamma^2}{1 - \Gamma^2}\right) \tag{3}$$

Next, the temperatures of the IF load, T_{IFH} and T_{IFC}, which produce output powers P_{IFH} and P_{IFC} are calculated from the calibration, and the effective bath temperature T_S determined by measuring the power output from the IF system with a shorted input. The IF reflection coefficient of the mixer Γ (and of the load γ) is measured by injecting a signal from a voltage tuned oscillator through the coupler and recording the difference in reflection between the mixer and the short. The loss into a matched load and noise temperature are then calculated from Equations 2 and 3.

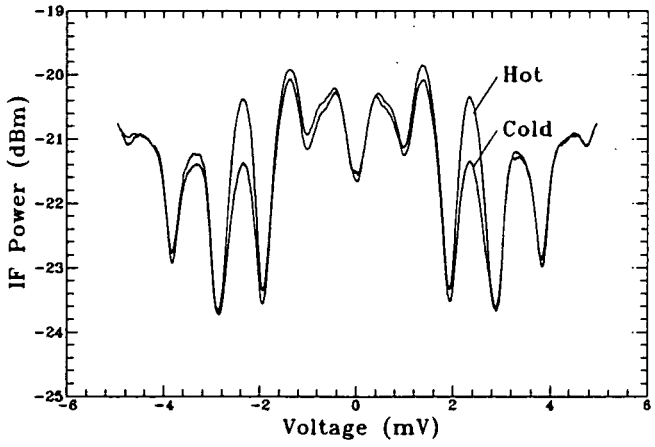

Fig. 4. IF output power as a function of bias voltage for hot and cold load inputs. The curve exhibits a smooth oscillatory behavior similar to that expected from theory with no sharp spikes or discontinuities indicating excellent control of Josephson currents.

RESULTS

Typical pumped and unpumped IV characteristics are shown in Figure 3, and IF output power as a function of bias voltage for hot and cold load inputs is shown in Figure 4. A superconducting magnet was used to suppress Josephson currents. The curve exhibits a smooth oscillatory behavior similar to that expected from theory [13] [14] with no sharp spikes or discontinuities. The IF output power is expected to decline towards zero bias; the fact that there is some power output at zero bias indicates some remaining Josephson currents which were not fully suppressed. These remain visible on the IF curve even though the IV curve appears smooth. Nevertheless, we believe that this is the best IF behaviour reported from a planar quasi-optical SIS receiver.

The most recent experiments performed with this receiver used junctions with an area of $0.2\,\mu m^2$. The normal state resistance was $56\,\Omega$, the critical current density was $15\,kAcm^{-2}$ and the ωRC product was approximately 1.3. The mixer and receiver noise temperatures and mixer conversion loss are plotted as a function of IF frequency in Figure 5. The LO frequency was 230 GHz. The best results are obtained at 1.35 GHz where a T_M of 89 K DSB, a T_R of 156 K DSB and conversion losses of 8 dB (into a matched load) were measured. The IF mismatch is approximately 1 dB across the IF band. Estimated uncertainties in the noise temperatures are ± 5 K, and in the loss, ± 0.5 dB. These values neglect any uncertainty due to RF load reflections or beam spillover. The largest Y-factor was obtained on the first quasiparticle step below the energy gap, at a bias voltage of approximately 2.3 mV. An inferior Y-factor was noted on the second step. The

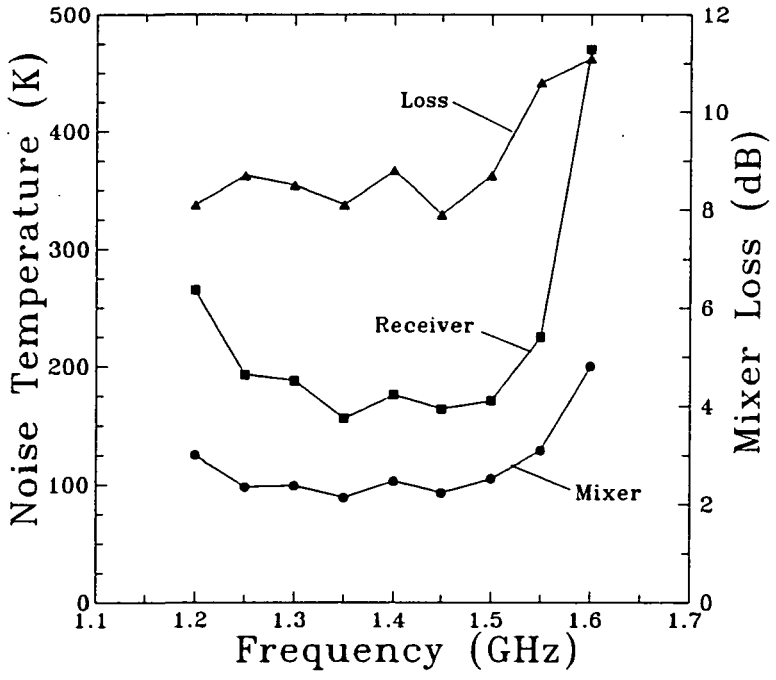

Fig. 5. Mixer and receiver noise temperatures and mixer loss as a function of IF frequency. The best results are obtained at 1.35 GHz where a T_M of 89 K DSB, a T_R of 156 K DSB and conversion losses of 8 dB were measured.

mixer noise temperature and conversion loss are seen to be essentially constant across the IF band. Mixer noise temperature is referred to the optically coupled loads at the system input and includes the effects of all components through to the IF connectors at the output of the balun transformers. The receiver noise temperature follows the noise behavior of the IF amplifier.

At each data point on the curves, the change in IF reflection coefficient, and the change in bias point, caused by switching between the hot and cold loads was measured. This is necessary to ensure that the observed Y-factor is not produced by different LO pumping conditions, or change in bias point when observing the hot and cold loads. Different pumping would be expected to change the junction output impedance and the IV curve shape. The reflection coefficient change was verified to be less than 1 %, and the change in bias voltage less than 0.02 mV. This indicates that the observed Y-factor has no appreciable component due to these factors.

Recent results from waveguide mixers at similar frequencies using junctions with similar specifications from the same fabrication process [3] [4] give mixer temperatures of 48 K DSB and 60 K SSB and conversion losses of 2 dB. Our noise temperature results, although a factor of two higher, are consistent with these values given the lack of tuning capability inherent in our planar circuit.

CONCLUSION

We have demonstrated a planar quasi-optical SIS mixer and low noise receiver which is suitable for array applications. Best performance of an individual element at 230 GHz was a mixer noise temperature of 89 K DSB, a receiver temperature of 156 K DSB and a conversion loss of 8 dB. The IF output shows a smooth variation with bias, indicating good control of Josephson currents. The noise results are consistent with recent measurements using similar junctions in waveguide receivers, and are only a factor of two higher. The conversion loss is rather large, but consistent with other planar mixer values. We will report on array performance in a future publication.

ACKNOWLEDGEMENT

We are extremely grateful for the constant assistance and encouragement of Dr. W.R. McGrath, without whom this work could not have been completed. We also thank Dr. H.H.S. Javadi and Dr. M.A. Frerking of JPL, and Dr. A.R. Kerr and Dr. S.K. Pan of NRAO for useful advice and discussions. We acknowledge the support of Mr. B. Bumble, Dr. J. Stern and Mr. S.R. Cypher on junction fabrication, Mr. H. Moham for fabricating the array mount, and Mr. R. McMillan for fabricating the quartz parabola. This work was carried out at the Jet Propulsion Laboratory, California Institute of Technology under contract with the National Aeronautics and Space Administration.

REFERENCES

[1] P.L. Richards and Q. Hu, *Proceedings of the IEEE*, vol. 77, 8, pp. 1233-1245 (1989).

[2] C.A. Mears, Q. Hu, P.L Richards, A.H. Worsham, D.E. Prober and A.V Räisänen, *IEEE Transactions on Magnetics*, vol. 27, 2, pp. 3363-3369 (1991).

[3] W.R. McGrath, H.H.S. Javadi, S.R. Cypher, B. Bumble, B.D. Hunt and H.G. LeDuc, *Second International Symposium on Space Terahertz Technology*, Pasadena, CA, Feb. 26-28 (1991), pp. 423-428.

[4] J.W. Kooi, M. Chan, T.G. Phillips, B. Bumble and H.G. LeDuc, *Second International Symposium on Space Terahertz Technology*, Pasadena, CA, Feb. 26-28 (1991), pp. 459-472.

[5] A.W. Lichtenberger, D.M. Lea, A.C. Hicks, J.D. Prince, R. Densing, D. Petersen and B.S. Deaver, *Second International Symposium on Space Terahertz Technology*, Pasadena, CA, Feb. 26-28 (1991), pp. 439-458.

[6] S.K. Pan, A.R. Kerr, M.J. Feldman, A.W. Kleinsasser, J.W. Stasiak, R.L. Sandstrom and W.J. Gallagher, *IEEE Transactions on Microwave Theory and Techniques*, vol. 37, 3, pp. 580-592, (1989).

[7] J. Zmuidzinas and H.G. LeDuc, *Second International Symposium on Space Terahertz Technology*, Pasadena, CA, Feb. 26-28 (1991), pp. 481-490.

[8] Q. Hu, C.A. Mears, P.L. Richards and F.L. Lloyd, *IEEE Transactions on Magnetics*, vol. 25, 2, pp. 1380-1383, (1989).

[9] T.H. Büttgenbach, R.E. Miller, M.J. Wengler, D.M. Watson and T.G. Philips, *IEEE Transactions on Microwave Theory and Techniques*, vol. 36, 12, pp. 1720-1725 (1988).

[10] P.H. Siegel and R.J. Dengler, *IEEE Transactions on Antennas and Propagation*, vol. 39, 1, pp. 40-47 (1991).

[11] W.R. McGrath, A.V. Räisänen and P.L. Richards, *International Journal of Infrared and Millimeter Waves*, vol. 7, 4, pp. 543-553 (1986).

[12] J.B. Peterson and P.L. Richards, *International Journal of Infrared and Millimeter Waves*, vol. 5, p. 1507, (1984).

[13] J.R. Tucker and M.J. Feldman, *Rev. Modern Physics*, vol. 57, pp. 1055-1113 (1985).

[14] J.R. Tucker, *IEEE Journal of Quantum Electronics*, vol. 15, 1234-1258 (1979).

[15] "Handbook of Chemistry and Physics", CRC Press, 56'th ed. (1976), p. E-55.

[16] P.H. Siegel, *First International Symposium on Space Terahertz Technology*, Ann Arbor, MI, Mar. 5-6, (1990) pp. 218-227.

A Fixed Tuned Broadband Matching Structure for Submillimeter SIS Receivers

Thomas H. Büttgenbach*, Henry G. LeDuc**,
Paul D. Maker**, and T. G. Phillips*

We have designed, fabricated and tested a quasi optical spiral antenna mixer with a $Nb/AlO_x/Nb$ tunnel junction. This design incorporates a hybrid antenna fed by a planar logarithmic spiral antenna to couple to the radiation field, as previously done with Pb based devices, as well as a newly designed matching circuit. This matching circuit is a relatively complex structure requiring several layers of photolithographic processing on top of the actual tunneling device. Computer modeling of the device predicted the measured bandwidth to within 8%, making scale model measurements unnecessary. We have obtained a good match from 210 GHz to 460 GHz between the antenna and a relatively large area (1.25 by 1.25 μm^2) tunnel junction with $\omega R_N C \approx 2 - 4.4$. This compares to simple inductive stubs that attain only a few percent of total bandwidth in the submillimeter band or inductively tuned SIS arrays with an upper limit of operating frequencies well below the submillimeter band. Noise temperatures were measured at 345 GHz, 426 GHz and 492 GHz yielding double sideband noise temperatures at 200 K, 220 K and 500 K, respectively.

---

*Thomas H. Büttgenbach and T. G. Phillips are with the Division of Physics, Mathematics and Astronomy, California Institute of Technology.

**Henry G. LeDuc and Paul D. Maker are with the Jet Propulsion Laboratory, California Institute of Technology.

Modelling and Performance of Nb SIS Mixers in the 1.3mm and 0.8mm Bands

Karpov, A., Carter, M., Lazareff, B., Billon-Pierron, D., Gundlach, K.H.
Institut de Radioastronomie Millimétrique (IRAM)
300, Rue de la Piscine
38406 ST MARTIN D'HERES Cedex (FRANCE)

Abstract

We describe the modelling and subsequent improvements of SIS waveguide mixers for the 200–270 and 330–370 GHz bands (Blundell, Carter, and Gundlach 1988, Carter *et al* 1991). These mixers are constructed for use in receivers on IRAM radiotelescopes on Pico Veleta (Spain, Sierra Nevada) and Plateau de Bure (French Alps), and must meet specific requirements.

The standard reduced height waveguide structure with suspended stripline is first analyzed and a model is validated through comparison with scale model and working scale measurements. In the first step, the intrinsic limitations of the standard mixer structure are identified, and the parameters are optimized bearing in mind the radioastronomical applications. In the second step, inductive tuning of the junctions is introduced and optimized for minimum noise and maximum bandwidth. In the 1.3mm band, a DSB receiver temperature of less than 110K (minimum 80K) is measured from 180 through 260 GHz. In the 0.8mm band, a DSB receiver temperature of less than 250K (minimum 175K) is obtained between 325 and 355 GHz. All these results are obtained with room-temperature optics and a 4 GHz IF chain having a 500 MHz bandwidth and a noise temperature of 14K.

Design goals

A receiver for radioastronomical use should meet specific design goals besides low noise at a particular frequency such as : reliability, ease of tuning, wide tuning range, capability for SSB tuning (increasingly important when the

atmospheric radiation is a significant contribution to the system noise), good coupling to the antenna, wide IF bandwidth (especially for extragalactic work).

Junctions

The mixers described in the this report use $Nb/Al_2O_3/Nb$ junctions fabricated in the IRAM facility (Lehnert *et al* 1991) Two junction series arrays are fabricated with an integrated IF filter. Trilayers are deposited into resist stencils, followed by lift-off. This technique is thought to reduce the mechanical sress in the trilayer (Yuda, Kuroda, and Nakano 1987). The substrate is fused quartz $100\mu m$ thick. The base electrode is 130nm, the counter electrode 30nm, and the wiring layer 240nm thick. The junctions are isolated by anodisation, up to 10V, and a sputtered SiO_2 layer 200nm thick.

Individual junction areas used in this work are about $2\mu m^2$, but progress in photolithography should allow use of smaller areas. The results presented here are obtained with 2-junction arrays having a total normal-state resistance R_N near 50Ω. Some 4-junction arrays were also fabricated.

The normal resistance of the junctions can be adjusted after fabrication by controlled thermal annealing (Lehnert *et al* 1992).

Mixers currently in use on IRAM telescopes

A simple equivalent circuit was used for the suspended-stripline, reduced-height waveguide mixer mount (Karpov *et al* 1992). The values of the circuit elements were derived from electromagnetic theory. They were then validated by measuring the embedding impedance of the pure SIS junction as measured via a coaxial probe on a scale model, and comparing the results with model predictions. Figure **1** shows the good agreement between modelled and measured values for the return loss.

Figure **2** shows the measured DSB receiver noise. The degradation of receiver noise at the band edges and in the vicinity of 220 GHz was caused by degradations of coupling efficiency at corresponding frequencies, which are intrinsic to the basic mixer structure. Because 220 GHz is an astronomically important frequency : $^{13}CO(2-1)$, it was decided to adjust one parameter of the mixer —the length of the last section of the suspended stripline filter— to shift this problem to a lower frequency; see fig. **3**.

Good agreement is found between predicted and measured values for several parameters : optimum backshort position (fig. **4**), upper sideband rejection

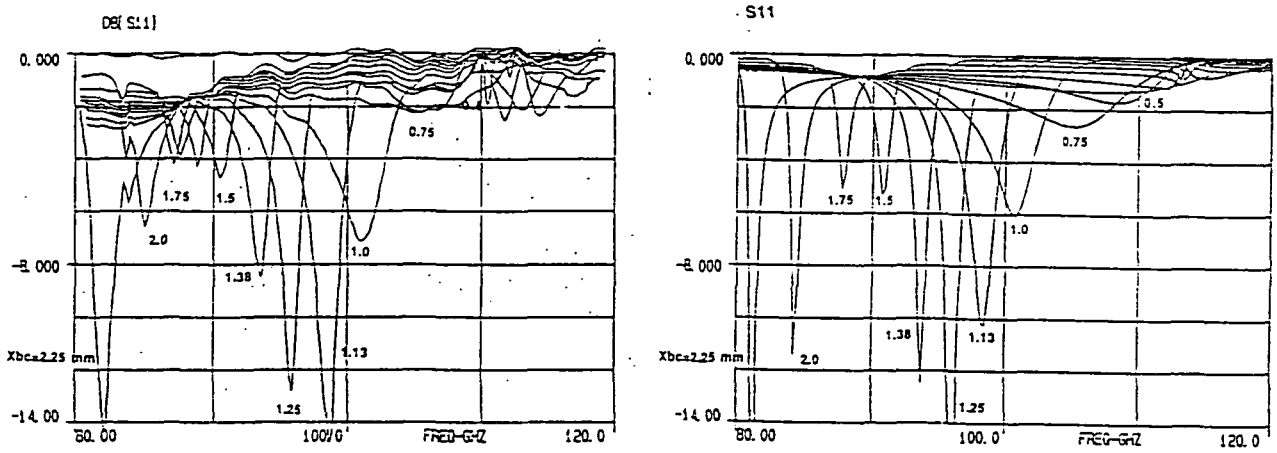

Figure 1. Comparison of measured and computed values for the return loss between the embedding circuit and a 50Ω junction. Frequencies have been scaled to the 3mm range.

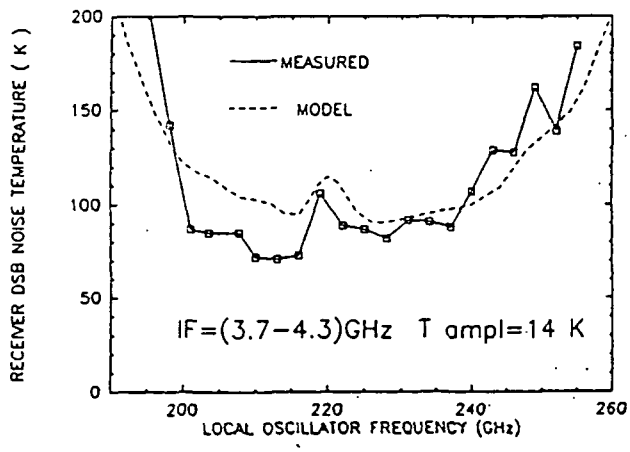

Figure 2. DSB receiver noise versus LO frequency for the original 1.3mm mixer.

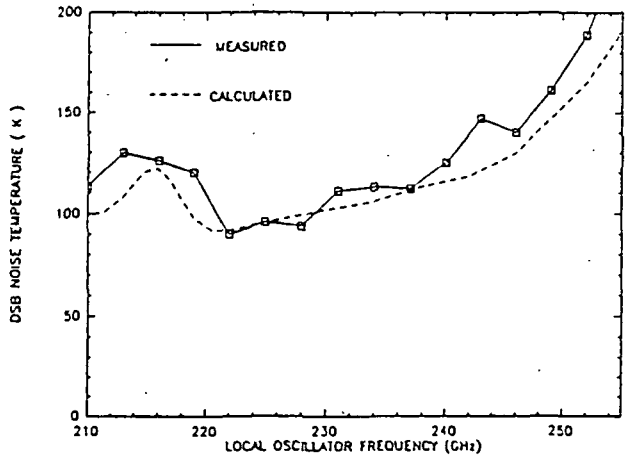

Figure 3. Same as Fig. 2 for modified mixer.

versus backshort position (fig. 5), DSB receiver noise versus backshort position for fixed LO frequency (fig. 6). Note that at 230GHz, an SSB receiver temperature of 135K results when the mixer is tuned for 10 dB rejection of the USB, versus 215K SSB when tuned DSB.

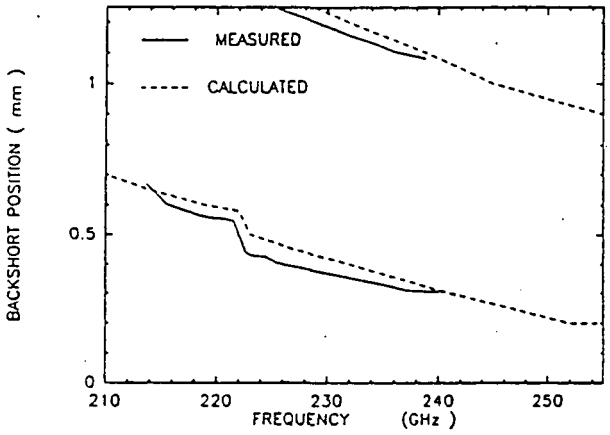

Figure 4. Backshort positions for optimum performance at each frequency. Comparison of predicted and measured values.

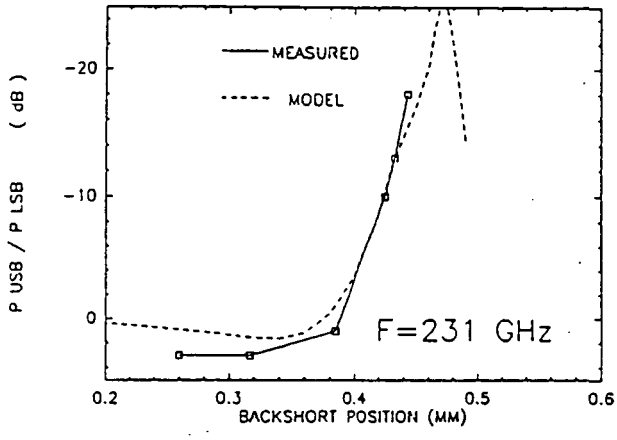

Figure 5. USB rejection versus backshort position. Comparison of predicted and measured values.

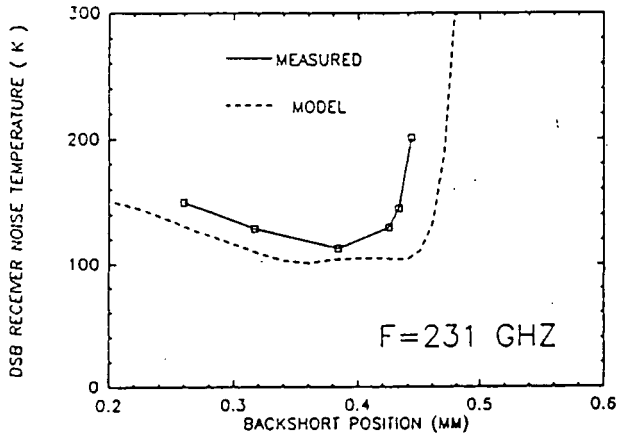

Figure 6. DSB receiver temperature versus backshort position. Comparison of predicted and measured values.

Next generation receivers in the laboratory.

The large capacitance of SIS junctions causes a large mismatch, especially at the higher frequencies. A reactive tuning structure with a high transformation ratio is needed. A backshort can in principle accomplish this, but only

over a limited frequency range (unless one is ready to accept the complication of a two-backshort structure), and the performance is critically sensitive to the backshort losses.

Local tuning with superconducting circuit elements overcomes these limitations. With the junction capacitance tuned out at least approximately over the frequency range, the demand on backshort reactive tuning is considerably diminished, and better performance can be obtained. We have designed optimized tuning structures for the 1.3mm and 0.8mm bands. Figure **7** shows the predicted mismatch loss and the measured laboratory performance for the 1.3mm receiver. Figure **8** shows the same quantities for the 0.8mm receiver. Both receivers were measured with a Mach-Zender diplexer for LO injection, a room-temperature lens producing a beam matched to the f/10 Nasmyth focus of the IRAM 30-M telescope, and a 4 GHz IF chain having a 14 K input noise temperature. We plan to improve these receivers by using cold optics.

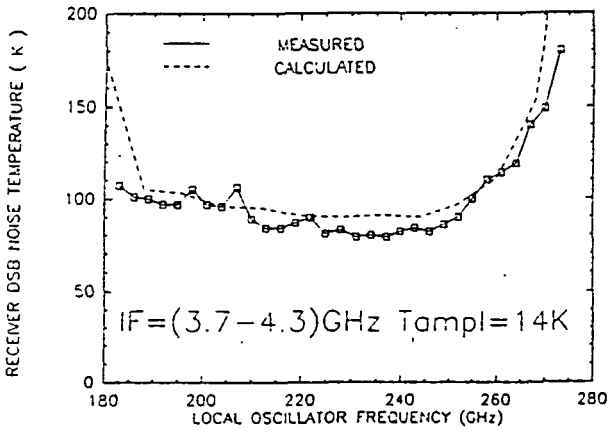

Figure 7. DSB receiver noise versus LO frequency for 1.3mm mixer with inductive compensation. Comparison of predicted and measured values.

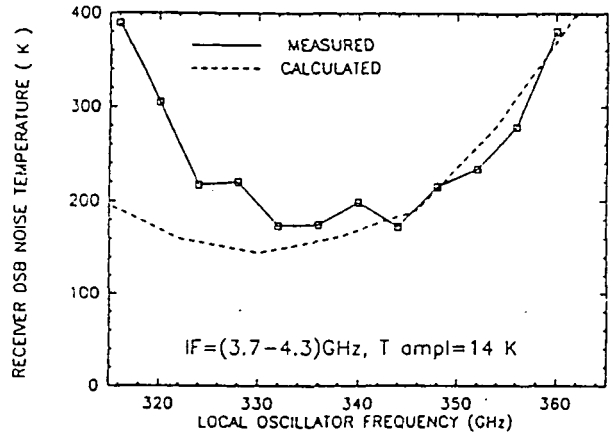

Figure 8. Same as Fig. 7, for the 0.8mm receiver.

Figure **9** summarizes the performance of receivers now operating on the IRAM telescopes, and of improved receivers being developed in the laboratory. Figure **10** illustrates the discovery of Aluminum fluoride in the evolved star IRC+10216, made at the IRAm 30-M telescope with one of the two 1.3mm SIS receivers.

Conclusion.

A relatively simple equivalent circuit can be used successfully to model and

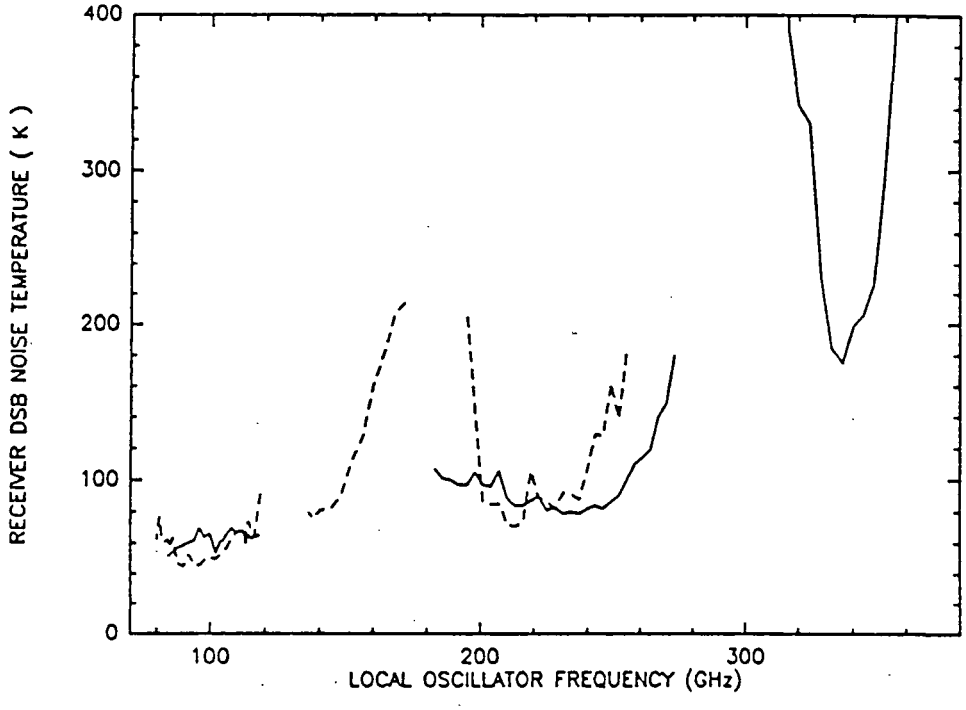

Figure 9. DSB noise versus frequency for IRAM SIS receivers. Dotted lines : receivers now on the telescopes; continuous lines : receivers in the laboratory.

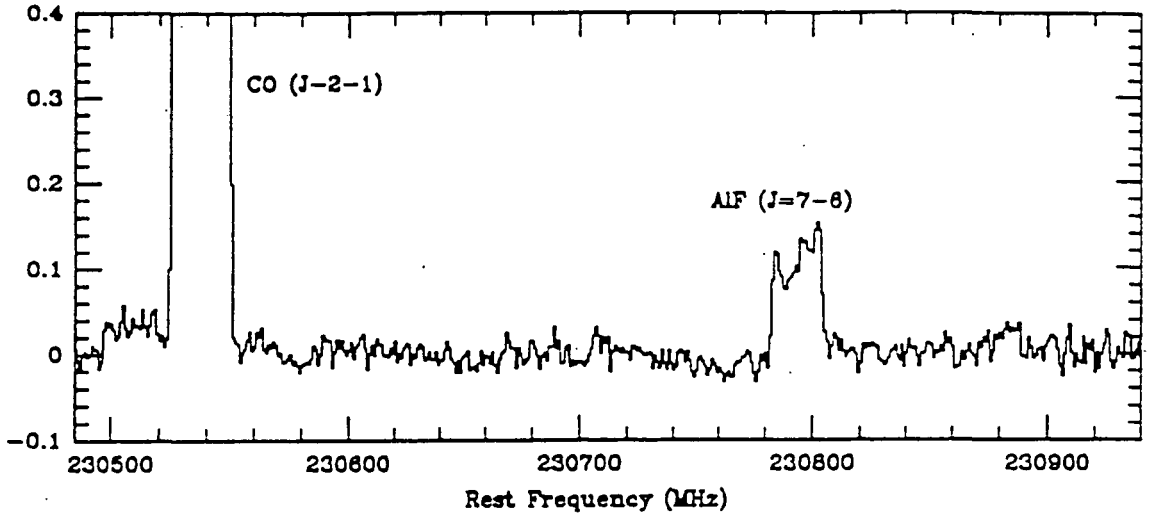

Figure 10. Detection of aluminum fluoride with one of the two 1.3mm SIS receivers at the IRAM Pico Veleta radiotelescope (Cernicharo and Guélin 1987).

improve the suspended stripline mixer mount. The performance of such a mixer using an SIS junction can be significantly improved by employing inductive tuning of the junction capacitance. It is also noteworthy that focusing the design effort on mismatch losses, and leaving aside intrinsic conversion loss, we can show good correlation between computed mismatch losses and measured receiver temperature, and that such modelling can serve as an effective guide to improving significantly the receiver performance.

References

Blundell, R. Carter, M., and Gundlach, K.H. 1988 *Int. J. of Infrared and Millimeter Waves*, **8**, 361

Carter, M.C., Navarro, S., Karpov, A., Billon-Pierron, D., Lehnert, T., Gundlach, K.H. 1991 *Proceedings 16th Int. Conf. Infrared and Millimeter Waves.*

Cernicharo, J., and Guélin, M., 1987 *Astronomy and Astrophysics* **183**, L10.

Karpov, A., Blondel, J., Mattiocco, F., and Lazareff, B., 1992 *Journées d'Études Micro-Ondes et Espace*, Toulouse CNES/CNET.

Lehnert, T., Grassl, C., Gundlach, K.H., and Blondel, J. 1991 *Supercond. Sci. Technol.* **4**, 419

Yuda, M., Kuroda, K., and Nakano, J. 1987 *Japan. J. Appl. Phys.* **26**, 166

Lehnert, T., Billon-Pierron, D., Grassl, C., and Gundlach, K.H. 1992 *Iram Working Report* **210**

Comparison of Measured and Predicted Performance of a SIS Waveguide Mixer at 345 GHz

C.E.Honingh#, G.de Lange*, M.M.T.M.Dierichs*, H.H.A. Schaeffer#, J.Wezelman#, J.v.d.Kuur*, Th.de Graauw#, and T.M.Klapwijk*

Space Research Organization of the Netherlands (S.R.O.N.), Landleven 12, 9747 AD Groningen, The Netherlands

* Dept. Applied Physics and Materials Science Centre, University of Groningen, Nijenborg 4, 9747 AG Groningen,
The Netherlands

Abstract

The measured gain and noise of a SIS waveguide mixer at 345 GHz have been compared with theoretical values, calculated from the quantum mixer theory using a three port model. As mixing element we use a series array of two Nb-Al_2O_3-Nb SIS junctions. The area of each junction is 0.8 μm^2 and the normal state resistance is 52 Ω. The embedding impedance of the mixer has been determined from the pumped DC-IV curves of the junction and is compared to results from scale model measurements (105 x). Good agreement was obtained. The measured mixer gain however is a factor of 0.45 ± 0.5 lower than the theoretical predicted gain. The measured mixer noise temperature is a factor of 4 - 5 higher than the calculated one. These discrepan-

cies are independent on pump power and are valid for a broad range of tuning conditions.

Introduction and measurement set up.

This study is done as part of an ESA research contract to investigate the feasibility of SIS-mixers as space qualified THz-mixers. Predictions of the mixer performance are mainly based on the quantum mixer theory, by Tucker, reviewed in [1]. At lower frequencies the validity of the theory has been investigated thoroughly [2], and quantum limited noise behaviour has been measured in very few cases [3].

Our main purpose for this study is to identify sources of noise in the receiver and to asses the quality of the tuning of the mixer. Receiver noise temperatures measured with the Y-factor method are shown in Fig.1. An overview of the route that we follow to obtain all information using only noise measurements is outlined in Fig.2.

Measurements were done with two different mixerblocks. One mixer block (TT) a backshort and an E-plane tuner[4] , and another similar mixerblock (ST), without the E-plane tuner. We use non-contacting backshorts with two quarter lambda high/low impedance sections covered with an insulating SiO_2 layer of 200 nm.

As mixing element we use an array of two Nb-Al_2O_3-Nb junctions in series, each with an area of .8 μm^2 and a normal state resistance of 52 Ω. The ωRC product of the array is approximately 5 at 350 GHz. All measurements have been done with a magnetic field of two fluxquanta in the junctions and over an IF bandwidth (B) of 80

MHz around 1.4 GHz.

Measured mixer data

The mixer gain (GMM) is calculated from the subtraction of the IF-output power in response to a 300 K and a 77 K input load. GMM={Pout(300)-Pout(77)}/{Gif.Gf.-ΔPin}, where Gif is the gain of the IF-chain, Gf is the gain of the IR-filter at 77 K, and ΔPin is the difference in input power between a 300K and a 77K load on the 77 K radiation screen in the dewar.

To achieve the highest accuracy Gif is determined in situ by using the unpumped mixer junctions as a calibrated noise source as a function of bias voltage[5]. The total IF output power as a function of bias voltage is given by

$$Pif_{up}(V) = G_{IF}\left[2eBG_1 I_{dc}(V)\coth\left(\frac{eV}{2kT}\right)\left(\frac{dI_{dc}}{dV}(V)+G_1\right)^{-2}+kB\left(T_{isol}|\Gamma_{IF}(V)|^2+T_{IF}\right)\right]$$

and is fitted to the measured power. V is the biasvoltage, and $I_{DC}(V)$ is the unpumped IV-curve. e is the electron charge, k is Boltzmanns' constant and T is the physical temperature of the junction, taken to be 4.5 K. G_1 is the input impedance of the IF-chain.

Gif is obtained with an accuracy of 5% from the slope of measured IF-power as a function of bias voltage above aprroximately two times the gap voltage. The noise temperature of the IF-stage is $T_{IF} + |\Gamma(V)|^2 T_{isol}$, where T_{IF} is the noise temperature of the HEMT-amplifier (Berkshire Technologies) and T_{isol} assembles the noise contri-

butions from the bath temperature, and possible contributions of imperfect isolation between amplifier and mixer. $\Gamma(V)$ is the reflection due to the impedance mismatch between the IF-chain and the junction. Since $T_{if} = 3 \pm 0.5$ K and $T_{isol} = 5.5 \pm 0.5$ K are obtained from the fitting, the second term, which is essentially depedend of the dynamical conductance of the junction array, can have a significant contribution.

ΔP_{in} is calculated from Plancks' law. The gain of the dewar window (G_w), the beamsplitter (G_{bs}) and the IR-filter (G_f) have been measured separately with a Michelson interferometer. $G_{bs} = 0.89 \pm 1\%$, $G_w = 95 \pm 2\%$ and $G_f = 95 \pm 1\%$ for the frequency of interest. In the calculation of the input power on the mixer it is assumed that the window is at 300 K.

GMM is given in Fig. 3 as a function of bias voltage for both mixers.

Determination of the embedding impedance

Knowledge of the embedding impedance is crucial to the theoretical calculation of the mixer performance of an SIS junction. For design purposes we used a 105 x scale model of the mixer mount. The impedance measured on the final structure as a function of backshort position and at optimum E-plane tuner position, is given by the larger circle in Fig. 4. The estimated geometrical capacitance of the junction array (22 fF) has been added in parallel to the impedance measured in the scale model.

The embedding impedance in the real mixer has been determined from the pumped IV-curves. We regard the series array of two junctions as one equivalent junction. The measured and calculated pumped curves are compared using the voltage match method[6], where both the embedding impedance and the pump power are adapted to

give a best fit. A typical example of a measured and a fitted curve is given in Fig. 5. The correspondence between the two curves was always very good execpt for a small region at the quasi particle step above the gap voltage.

The embedding impedance has been determined for various backshort positions at one (optimum) E-plane tuner position. The expected circle in the Smith chart is fitted through the points in Fig. 4. The given points are lying in a very small part of one half lambda cycle of the backhort. The pattern is repeated for the next half lamba cycle, without a measureable increase in loss. To make that more clear the data of two cycles are given as a function of backshort position in Fig 4. The data as predicted by the scale model and a direct measurement of the coupled power (the pump step height) are also given as a function of backshort position. The DC-current at a biaspoint on the quasiparticle step has been normalized to one.

Comparison between measured and calculated mixer performance

The embedding impedances determined from the pumped IV-curves (and checked by the scale model measurement) have been used to calculate the gain and the noise behaviour of the mixer. We used the three port model in the low IF approximation, justified by the ωRC-product of the junctions and the IF frequency of 1.4 GHz. The terminations on the LO-port and at both side band ports were each determined separately. They differed considerably as can be seen in Fig.6, giving the pumped IV-curves at a single tuner setting for three different frequencies.

1 GAIN

The calculated mixer gain (GMC)

$$GMC(V) = 4G_L(G_{usb}|Z_{01}(V)|^2 + G_{lsb}|Z_{0-1}(V)|^2)$$

is given as a function of bias voltage in Fig.3. Z_{01} and Z_{0_1} are the relevant elements of the 3x3 conversion matrix[1] and Gusb and Glsb are the real parts of the terminating impedances at both side band frequencies, as determined from the pumped IV-curve. This gain is directly compared to the gain (GMM) determined from the measurements in Fig.3.

The discrepancy between GMM and GMC is independent of LO-power and also within a 15% error independent of the tuning conditions. It must be noted this has only been checked for the points given in the Smith Chart of Fig. 4. Around those points the fitting of the embedding impedances is the most accurate. For the most inductive tuning points the discrepancy in the gain is larger. At those points the bias supply seems to skip over the regions with negative differential resistance, deteriating the DC-curve and IF-output. For points more to the edge of the Smith Chart the amount of pump power necessary to get a well developed pump step is larger and the gap of the superconductor decreases, making accurate fits more elaborate.

2 NOISE

To obtain a measure for the noise contribution of the mixer we compared the

measured and the calculated total noise output of the receiver in an IF-bandwidth of 80 MHz.

The noise contribution of the mixer is calculated from the DC-IV curve and the embedding impedances using the current correlation matrix[1]. As in the unpumped case the junctions array is regarded as one equivalent junction obtained by dividing both the measured current as the measured voltage by the number of junctions. The mixer gain used in the calculation is the gain determined from the measurements. This means that we attribute the discrepancy between GMC and GMM fully to the loss/coupling efficieny of the lens/horn/waveguide at 4K in front of the mixe. The calculated and the measured IF-output power as a function of bias voltage are given in Fig. 7a. However to get the correspondence at the first pump step as shown in Fig. 7a , an extra input noise power kBT_{ex}, with $T_{ex} = 80 \pm 20$ K, had to be added in the calculation at both side bands in addition to the shotnoise and temperature noise contribution. This value for T_{ex} is again independent of pump power and tuning conditions within the same restrictions to the tuning range as mentioned in the calculation of the gain. The calculated and measured noise contributions of the various parts of the receiver are given in terms of noise temperature in Fig. 7b.

The results in Fig. 7 are for the ST-mixerblock but a similar performance is found in the TT-block. Though still within the error margin the deviation in the gain has a tendency to be less in the ST-mixer compared to the TT-mixer, probably as a result of the improved fabrication and the use of an integrated horn.

We verified that the extra noise contribution was not a real extra input signal due to LO-signal at the side band frequencies by filtering the LO with a high Q Fabry-Pérot filter.

Discussion and Conclusions

We compared the performance of two types of waveguide SIS-mixers with the three port quantum mixer theory. We have obtained good agreement between the scale model measurements and impedances determined from pumped IV-curves. The quality of the fittings is very high in the sensitive tuning region of the mixer.

However we observed a reproducible difference between the measured and the calculated gain of both mixers. The difference can be explained partly by losses in the lens and horn.

The performance of the backshort seems to be quite lossless regarding the good agreement between the scale model measurements and the impedances fitted to the pumped IV-curves.

The noise values are more than a factor of four higher than expected from theory. This seems to be a general feature of mixers using a series array of junctions. Up to now we did not yet have single junction mixerrs available.

We acknowledge the financial support of the European Space Agency for this work under contract 7898/88/NL/PB(SC) and Herman v.d. Stadt for careful reading of this summary and Anders Skalare in general.

References

1 J.R.Tucker, and M.J.Feldman, Rev.Mod.Phys. 57, 1055 (1985)

2.W.R.McGrath, P.L.Richards, D.W.Face, D.E.Prober, and F.L.Lloyd, J.Appl.Phys. 63, 2479 (1988)

3.C.A.Mears, Qing Hu, P.L.Richards, A.H.Worsham, D.E.Prober, and A.V.Räisänen, IEEE Trans.Magn. MAG-27, 3363 (1991)

4. B.N.Ellison, P.L.Schaffer, W.Schaal, D.Vail, and R.E.Miller, Int.J. of IR and MM-waves 10, 937 (1989)

5. J.R. Tucker , IEEE J. Quantum Electron. QE-15, 1243 (1979)

6. A.Skalare, Int. J. of IR and MM waves 10, 1339 (1989)

C-4

Captions

Fig. 1 Receiver noise temperature for the two types of waveguide mixers measured with the Y-factor method, corrected for the beamsplitter loss.

Fig. 2 Overview of the different input an output parameters in the process of comparing the measured and calculated performance of the mixers.

The measurements yield Trec as result of a Y-factor (H/C) measurement. The gain and noise of the IF(Gif,Tif) and of the mixer(Gm,Tm) are obtained from the absolute IF-output power at different input loads, knowing the loss and the physical temperture of the input window(Gw,Tw).

The embedding impedance of the junctions is determined either with use of a scale model or by fitting the pumped IV-curves to the theory. When a scale model is used the geometrical (and parasitic) capacitance of the junction has to be estimated separately.

When the embedding impedance is known, the mixer performance is calculated as a function of bias supply at different LO-power levels.

Fig. 3 Measured (+) and calculated (•) coupled gain for both waveguide mixers. The TT-mixer has a 500-50 Ω transformer at the IF-port to enhance the gain.

Fig. 4 Embedding impedance as a function of backshort position, as calculated from the scale model (-+-) and as determined from the pumped IV-curves (■,●). As a direct measure of the coupled power the pumped step height at the optimum biaspoint (-o-) is also given as a function of backshort position

Fig. 5 Measured (-▪-) pumped IV-curve at 351 GHz and calculated(-) curve using the given fitting parameters for the embedding circuit. The admittances are normalized to the 104 Ω.

Fig. 6 Detailed view of DC-IV curve of the series array of junctions, pumped at three different frequencies. The tuning conditions and the pump power are identical at all frequencies.

Fig. 7A Total measured (+,o) and calculated (-) IF-output power in a bandwidth(B) of 80 MHz at two different input signals, as a function of bias voltage. For the calculated IF-power an extra noise power of 80kB has been added to the input of the mixer. The contributions of the shot noise and temperature noise of the junctions (dPjunctie) and of the IF-stage (dPif) are given also.

Fig. 7B The total measured (+) and calculated (•) reciever noise temperature as a function of bias voltage. For reference the contribution to the calculated reciever noise temperature of the IF-stage (dTif), the junctions (dTm) and of the input losses (dTw) are also given.

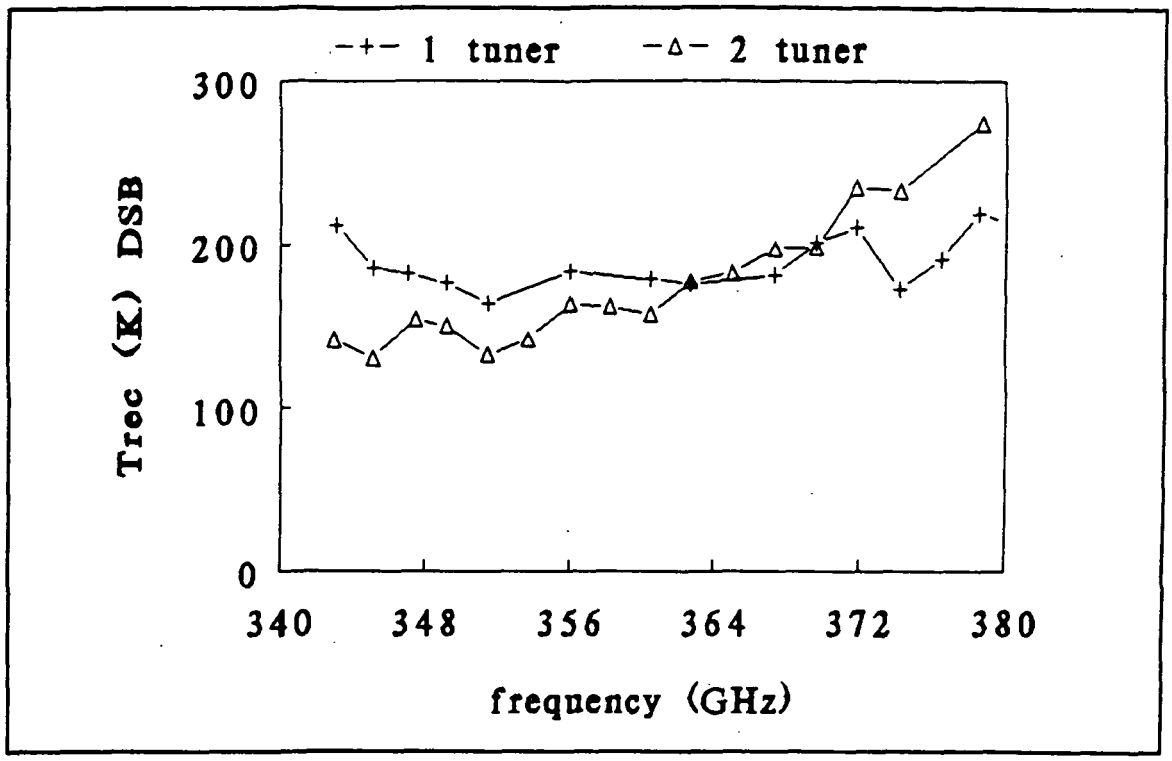
-+- 1 tuner
-Δ- 2 tuner
300
200
100
0
Trec (K) DSB
340
348
356
364
372
380
frequency (GHz)

Fig. 1

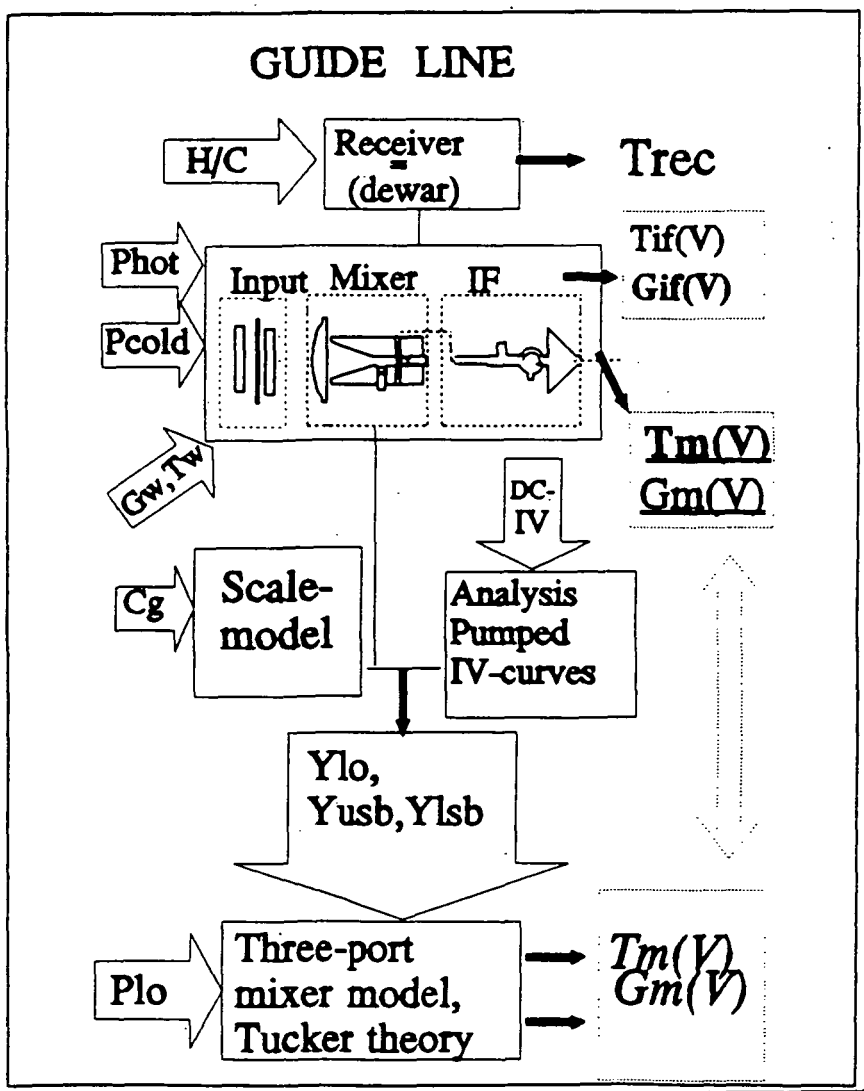
GUIDE LINE
H/C
Receiver (dewar)
Trec
Tif(V)
Gif(V)
Phot
Pcold
Input
Mixer
IF
Tm(V)
Gm(V)
Gw,Tw
DC-IV
Cg
Scale-model
Analysis Pumped IV-curves
Ylo, Yusb,Ylsb
Plo
Three-port mixer model, Tucker theory
Tm(V)
Gm(V)

Fig. 2

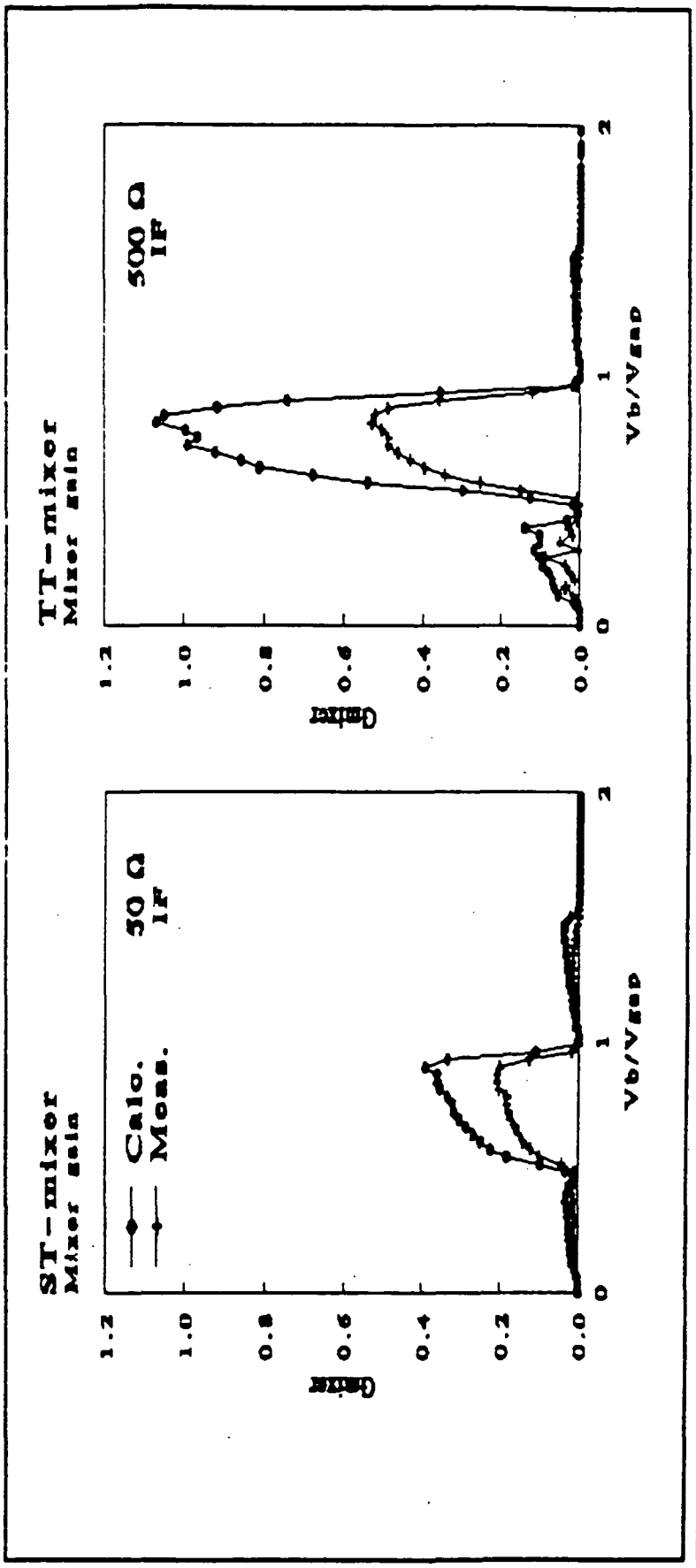
ST-mixer
Mixer #a1a
50 Ω
IF
Calc.
Meas.
Gain
Vb/Vsb
TT-mixer
Mixer #a1a
500 Ω
IF
Gain
Vb/Vsb

Fig. 3

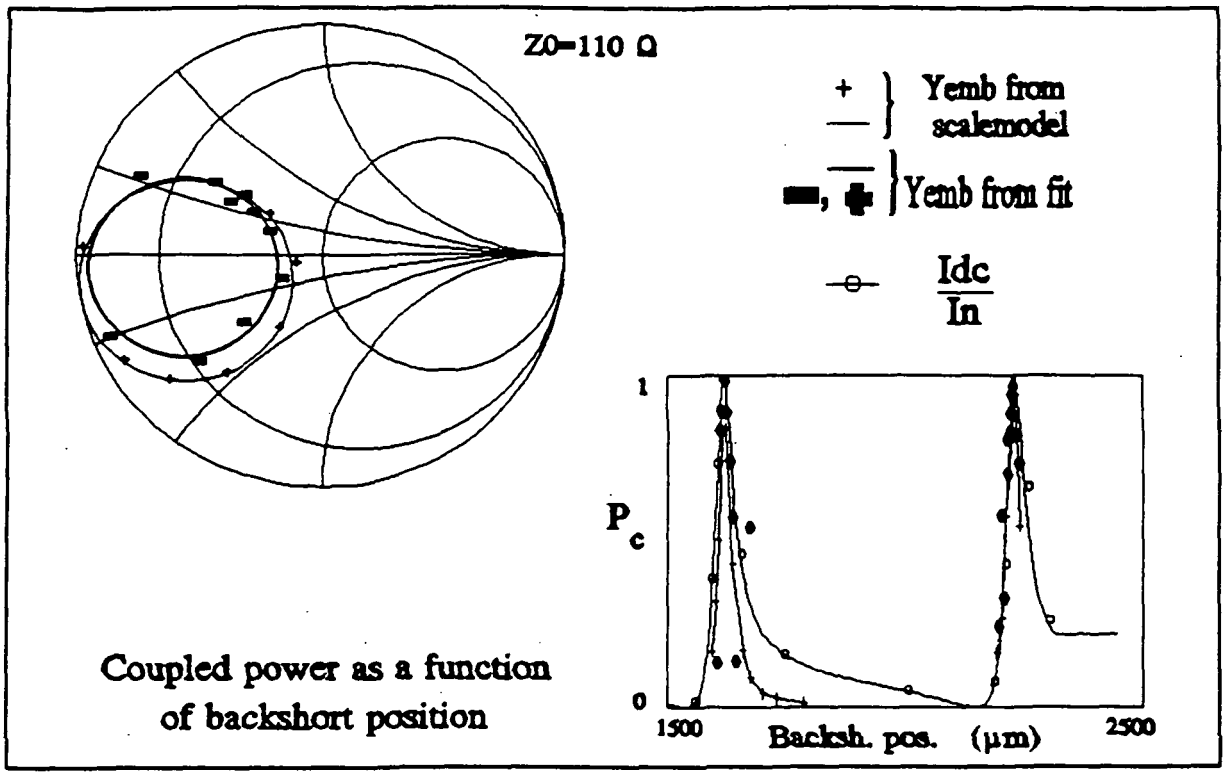
Z0=110 Ω
Yemb from scalemodel
Yemb from fit
Idc / In
1
Pc
0
1500
Backsh. pos. (μm)
2500
Coupled power as a function of backshort position

Fig. 4

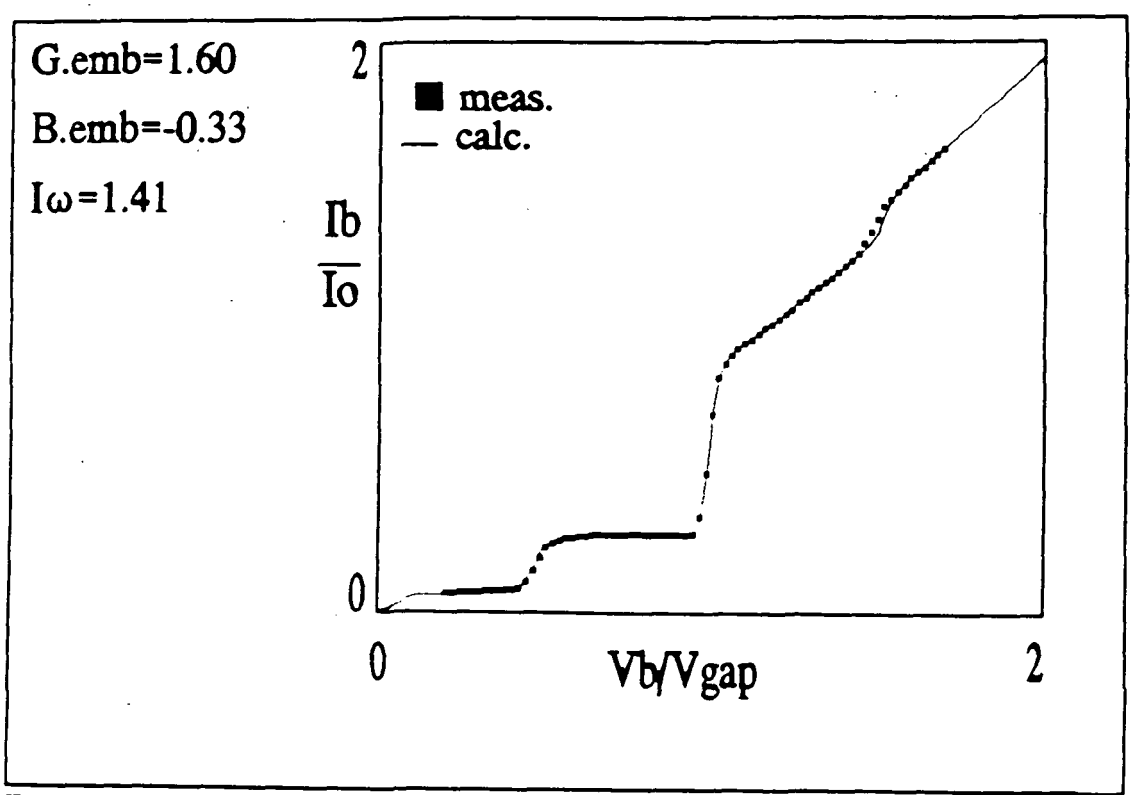
G.emb=1.60
B.emb=-0.33
Iω=1.41
2
meas.
calc.
Ib / Io
0
0
Vb/Vgap
2

Fig. 5

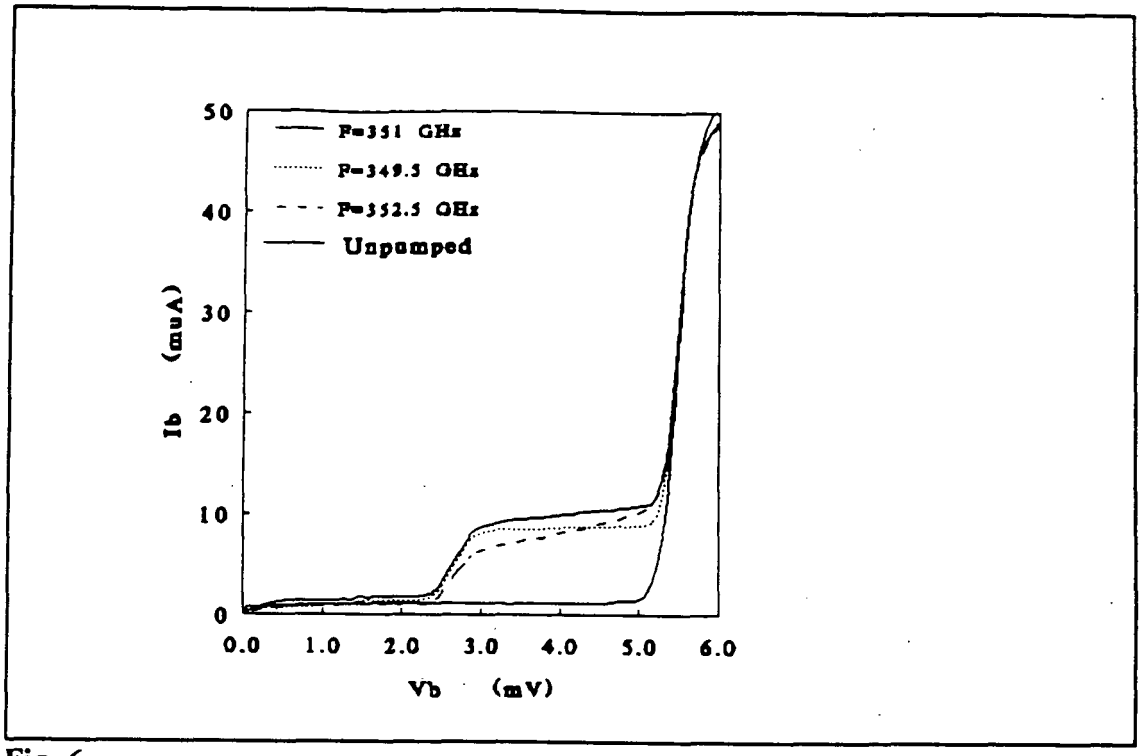
F=351 GHz
F=349.5 GHz
F=352.5 GHz
Unpumped
Ib (muA)
Vb (mV)
0
10
20
30
40
50
0.0
1.0
2.0
3.0
4.0
5.0
6.0

Fig. 6

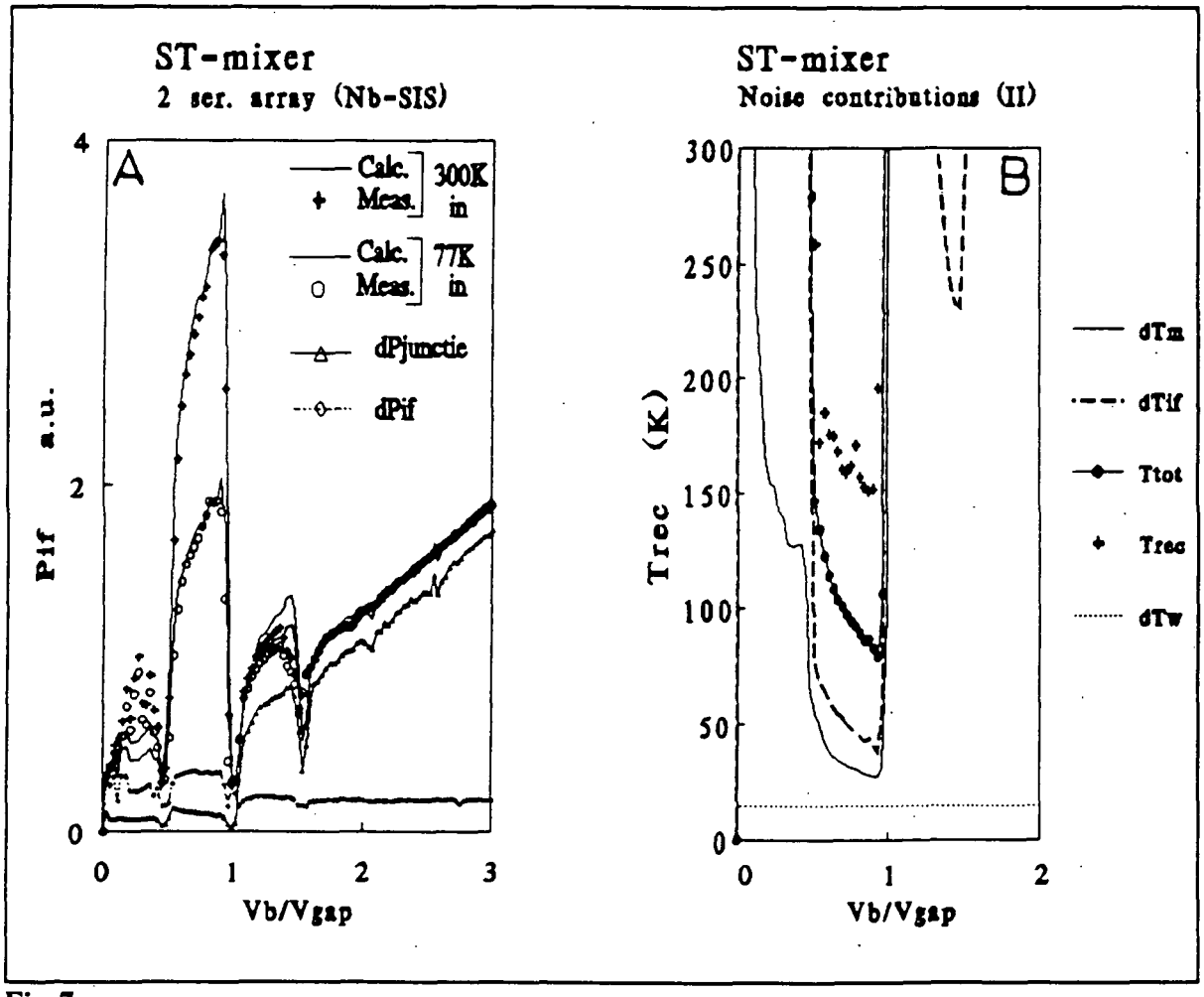
ST-mixer
2 ser. array (Nb-SIS)
A
Calc.
Meas.
300K in
Calc.
Meas.
77K in
dPjunctie
dPif
Pif a.u.
Vb/Vgap
ST-mixer
Noise contributions (II)
B
dTm
dTif
Ttot
Trec
dTw
Trec (K)
Vb/Vgap

Fig 7.

A Low-Noise 492 GHz SIS Waveguide Receiver

C. K. Walker[1,†], J. W. Kooi[1], M. Chan[1], H.G. LeDuc[2], P.L. Schaffer[1], J.E. Carlstrom[1], and T.G. Phillips[1]
[1] California Institute of Technology, Pasadena CA
[2] Jet Propulsion Laboratory, Pasadena CA
[†] Presently at the University of Arizona, Tucson AZ

Abstract

In this paper we discuss the design and performance of an SIS waveguide receiver which provides low noise performance from 375 to 510 GHz. At its design frequency of 492 GHz the receiver has a double sideband noise temperature of ~172 K. By using embedded magnetic field concentrators, we are able to effectively suppress Josephson pair tunneling. Techniques for improving receiver performance are discussed.

Introduction

Over the last decade SIS receivers have been replacing Schottky diode based systems at millimeter and submillimeter wavelengths. SIS junctions have a lower shot noise and a more pronounced D.C. nonlinearity than Schottky diodes, with the result being that mixers constructed with them are more sensitive and require less local oscillator power than their Schottky diode counterparts.

SIS mixers can be constructed using waveguide or an open structure geometry. To date, at all frequencies where they have been built, SIS waveguide mixers provide superior performance. The main advantage waveguide mixers have over open structure designs is that adjustable backshorts can be readily incorporated into the mixer block. Backshorts are usually needed to match the complex impedance, although recently structures employing lithographically produced matching networks for waveguide mounted junctions has proved highly successful (Kerr *et al.* 1987). Open structure mixers typically utilize a combination of lenses and planar antenna structures to couple the incoming radiation to the junction. With this combination of components it is not easy to incorporate an adjustable backshort. Fixed tuned reactive stubs can be fabricated along with the SIS device to tune out the junction's capacitance. A significant advantage of waveguide designs is that well characterized, efficient feedhorns can be used to couple waveguide modes to free space modes.

Until recently SIS waveguide receivers have been constructed with center frequencies only as high as 345 GHz. In this paper we discuss the construction and performance of an SIS waveguide receiver with a center frequency of 492 GHz. It is now permanently installed on the Caltech Submillimeter Observatory and has been used for astronomical observations since September 1991.

Receiver Construction

Optics

A block diagram of the 500 GHz receiver is shown in Figure 1. The receiver's optics are designed to provide a -10 db taper on the edge of the telescope's secondary mirror. The beam from the secondary is reflected from an offset parabola, a flat, and a final offset parabola before entering the cryostat. At the entrance to the cryostat a thin (~ 0.2 mil) mylar beamsplitter is mounted at 45° to the signal and local oscillator beams. With this thickness of mylar only 0.5% of the signal and local oscillator beam is reflected. Therefore only a tiny fraction of the signal is lost, while almost all the local oscillator power is terminated in an absorbing load.

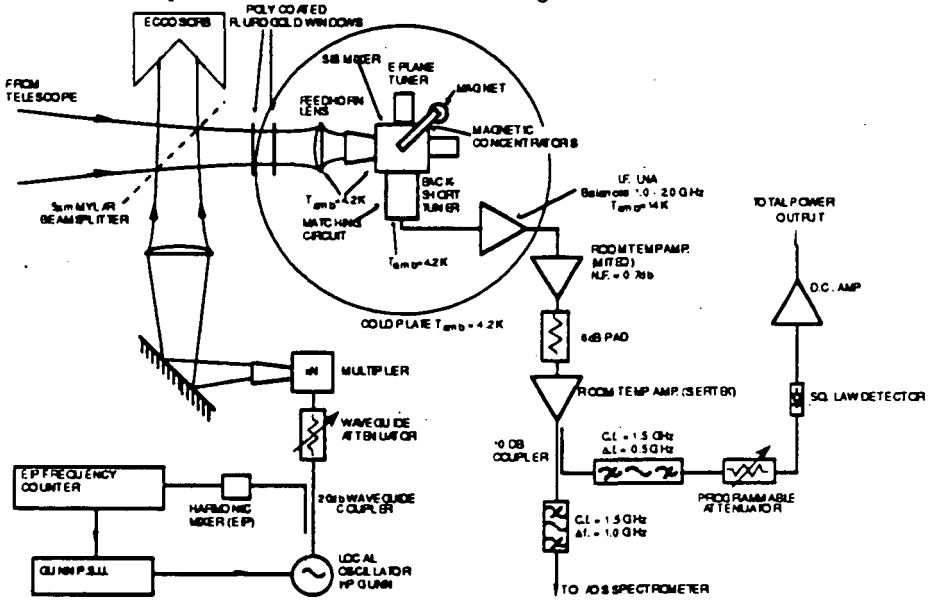

Figure 1

The cryostat vacuum window is a 1.0 mil mylar sheet. The windows on the 12 K and 77K shields are made from disks of fluorogold laminated to a quarter wavelength thickness of black polyethylene. The polyethylene reduces reflection losses. The overall thickness of the fluorogold and black polyethylene disks is 17 mils. The disks serve as near infrared blocking filters for the system.

The last optical component before the mixer block is a small, low density

polyethylene lens mounted in front of the feedhorn. The lens is designed using the equations of Silver (1966) and is located so that it provides frequency independent illumination of the secondary (Goldsmith 1982).

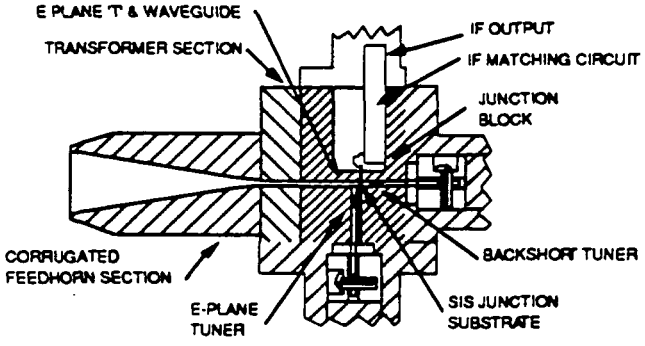

Diagram of Mixer Block

Figure 2

Mixer Block

A schematic representation of the mixer block is shown in Figure 2. An exploded view of the completed block is shown in Figure 3. The basic design of the waveguide portions of the block follows that of Ellison *et al.* (1987). The block is divided into five sections along the longitudinal axis of the block. The first section consists of a corrugated feedhorn (Thomas 1978) which terminates in circular waveguide. The beamwidth of the horn, at its -10 db points is 13.4°. In the second section, the signal passes through a three step, circular to full-height rectangular, quarterwave transformer. This section also contains the waveguide for the E-plane tuner. The center of the E-plane tuner is located ~ $\lambda g/2$ in front of the SIS junction. The third section contains the SIS device, the IF impedance matching circuit, magnetic field concentrators, and the waveguide for the backshort. A face-on view of this section is shown in Figure 4. The location of the main circuit elements are indicated. The SIS junction substrate resides in a long 4.5 by 4 mil channel milled across the center of the waveguide. When the junction substrate is placed in the channel, it is oriented so that the junction itself is in the center of the waveguide facing the oncoming radiation. A RF choke is fabricated on the substrate at the same time the junction is made. The choke, shown in Figure 5, is made from a series of high and low impedance sections of microstrip line. Each section is a $\lambda/4$ in length at the RF center frequency. The ground side of the junction is held in place with silver paint. The "hot" side of the junction is connected to the IF matching circuit via a short 1.0 mil gold wire. The wire is silver painted to the last section of the RF choke located on the junction substrate. To keep the silver paint from inadvertently shorting the hot side of the junction substrate to the block, the block is designed so that the last 8 mils of the junction substrate is suspended in free space.

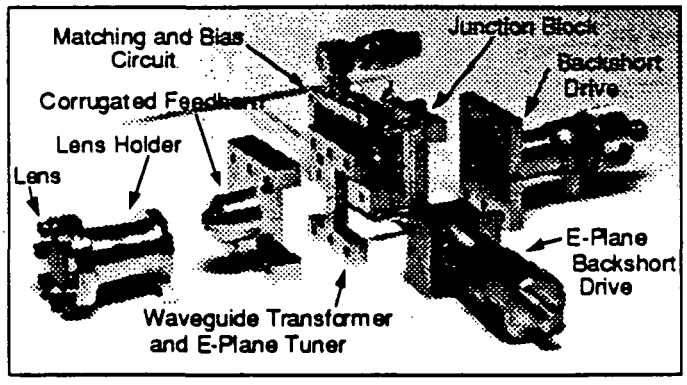

Exploded View of the 490 Block
Figure 3

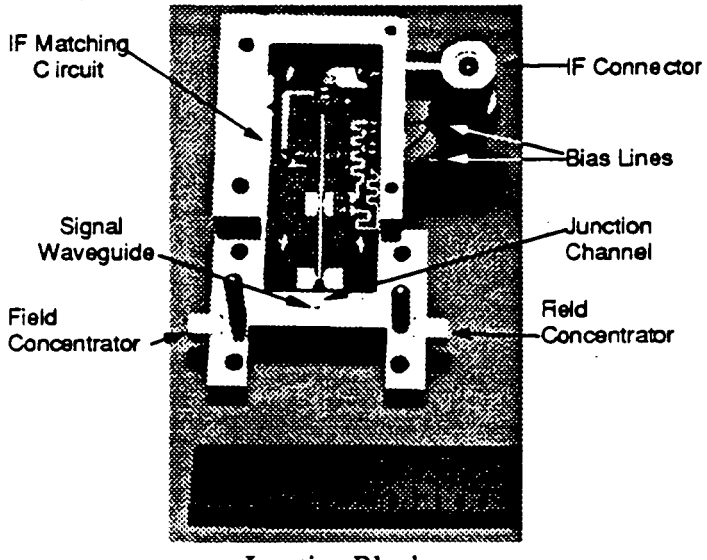

Junction Block
Figure 4

A detailed discussion of the integrated IF matching circuit has been given by Kooi *et al.* (1992). It utilizes a 5-pole Chebyshev low pass filter and transformer to match the IF impedance of the SIS junction to the input impedance of the IF amplifier (~ 50 Ω) over a 1 to 2 GHz frequency range. The IF impedance of the junction is roughly 2.5 times the junction's normal state resistance. The matching circuit is designed for an SIS IF impedance of ~ 160 Ω.

The magnetic field concentrators and the core of the external electromagnet to which they are connected are made out of Cryoperm, a material which retains a high magnetic permeability even at 4 K. To reduce heat loading on the 4 K cold plate, the magnet's coil is made from niobium wire. The backshorts are non-contacting and were designed using the techniques discussed by Brewer and Rasianen (1982). Non-

contacting backshorts were chosen over contacting backshorts because of their durability.

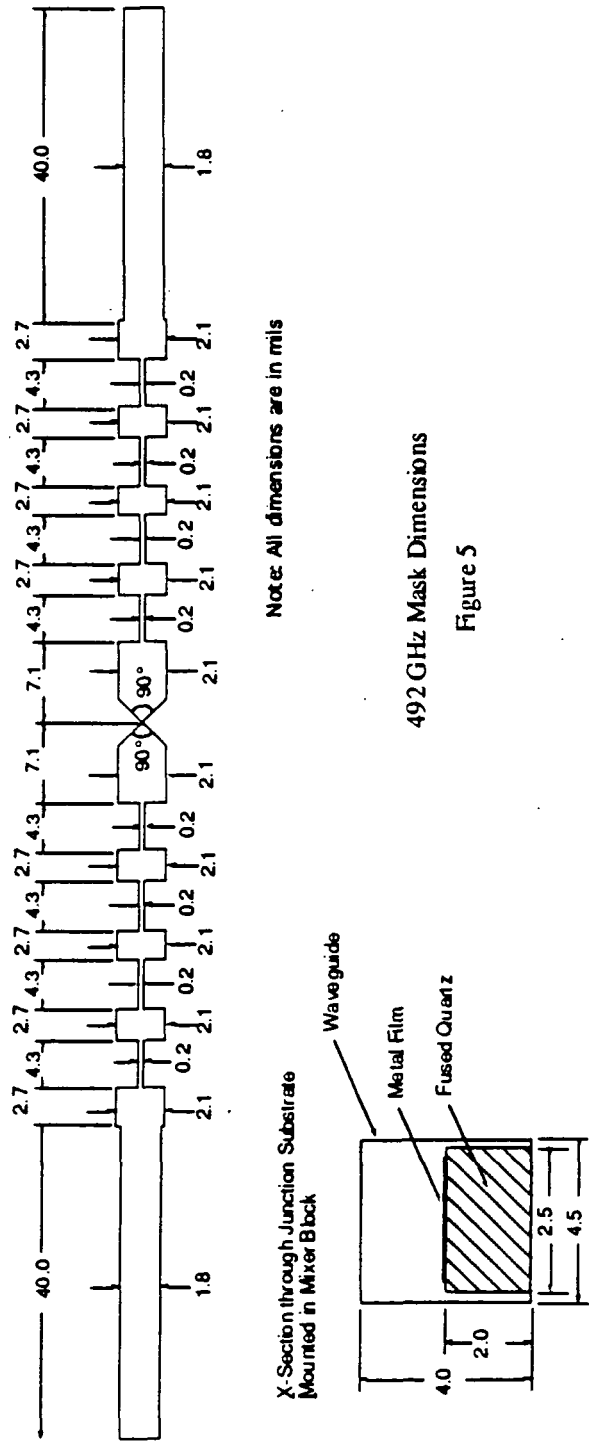

492 GHz Mask Dimensions

Figure 5

Junction Fabrication

The $Nb/ALO_x/Nb$ tunnel junctions used in this receiver are planar, submicron area devices defined by electron beam lithography. The junctions are fabricated using a variant of the self-aligned-liftoff trilayer process (Shoji *et al.* 1983) with modifications for electron beam lithographic patterning of junction area. The $Nb/ALO_x/Nb$ trilayer is deposited in a high vacuum sputter deposition system (base pressure 1.3×10^{-7} Torr). The Nb/Al layers are dc/rf-magnetron sputtered from 75 mm diameter targets. The AlO_x tunnel barrier on the trilayer is formed by an in situ oxidation in an oxygen/argon mixture. A gold layer (≈ 30 nm) is deposited on the trilayer to act as a contact layer. The junctions are patterned by forming submicron holes in PMMA by electron beam lithography (JEOL JBX5) followed by the deposition and lift-off of chromium metal. The chromium pattern is transferred to an underlying polyamide film using oxygen reactive ion etching (RIE). Junctions are formed by RIE using a gas mixture containing CCl_2F_2 (chosen for its highly anisotropic etch characteristics) and electrically isolated using thermally evaporated silicon monoxide. Contact wiring is deposited and patterned using RIE to complete the device. Tunnel junctions with areas of 0.25 μm^2 and 0.13 μm^2 were fabricated on on the same wafer

Receiver Performance

Figure 6a is a plot of the I-V (current versus voltage) curve of the SIS junction used in the receiver. The solid line is the I-V curve with no local oscillator power applied. The curve has a sharp knee at the voltage (~ 2.78 mV) corresponding to the band gap energy of the niobium junction. At the knee, the leakage current through the junction is about 5 μA. The normal state resistance of the junction is about 90 Ω. The dotted line is the I-V curve with local oscillator applied. With local oscillator power applied a single wide photon step is observed below the knee of the curve. A single wide photon step is observed below the knee of the curve. The width of this step corresponds to the voltage ($h\nu/e$) of a 492 GHz photon (~ 2 mV). Figure 6b is a plot of IF power versus SIS bias voltage. The top curve is the IF power obtained with the receiver looking into a room temperature load (T_H ~ 280 K). The lower curve is the IF power obtained with the receiver looking into a cold load (T_C ~ 80 K). As expected, the IF conversion peak occurs at a bias voltage corresponding to the middle of the first photon step below the gap voltage. The ratio of the IF power obtained with the receiver looking into the room temperature load to the IF power obtained with it looking into the cold load is a measure of the receiver's sensitivity and is often referred to as the Y-factor. The receiver noise temperature is derived from the Y-factor using the following relation.

$$T_R = \frac{T_H - YT_C}{Y - 1}$$

At 492 GHz the highest Y-factor obtained with this receiver was 1.84, which corresponds to a double sideband receiver noise temperature of ~ 172 K. This value is a true receiver noise temperature, no corrections have been made for signal losses in the beamsplitter or input optics, losses resulting from impedance mismatches, or from IF amplifier noise. The bias voltage and current used during this measurement were 2.3 mV and 12 μA. At this bias voltage the receiver noise temperature increased when the LO power was reduced to a level where the junction current became less than ~ 9 μA. Similarly, if the LO power was increased such that the junction current reached a value greater than 16 μm, the receiver sensitivity decreased.

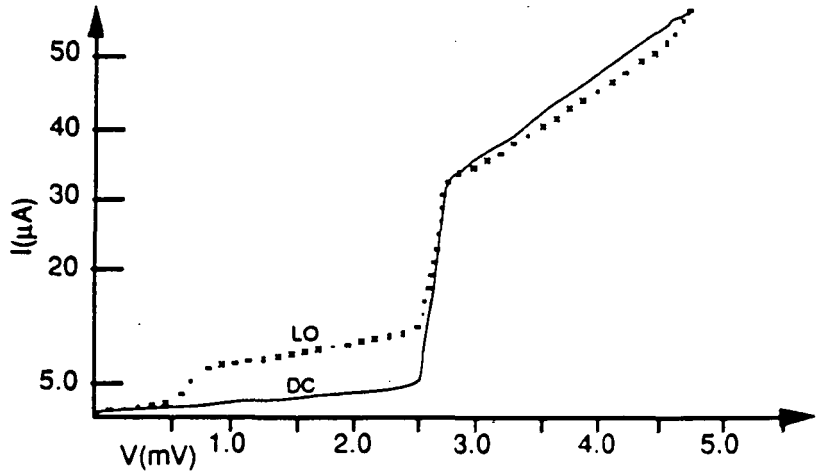

SIS RECEIVER I/V CURVE

FIGURE 6a

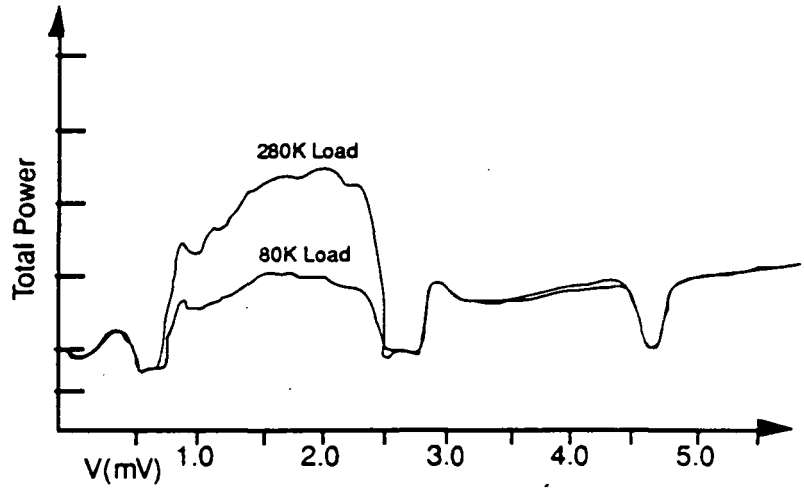

SIS RECEIVER IF POWER vs. BIAS VOLTAGE

FIGURE 6b

During these measurements the magnetic field strength was adjusted so as to minimize the manifestation on the I-V characteristics of the Josephson pair tunneling current. As the magnetic field strength was increased, the Josephson super-current went through several minima. A minimum in the super-current occurs when one or more magnetic flux quanta are present across the junction. Since more than one minimum was observed, we conclude the magnetic circuit used in this design is capable of placing several flux quanta across the junction. Without the magnetic field the smooth IF power curves of Figure 6b become jagged. In Figure 7 we present IF power curves made at 420 GHz. Figure 7a shows the smooth IF power curves that can be obtained with an optimized magnetic field. In Figure 7b the same IF power curves are plotted, but with the applied magnetic field less than optimum. In 7a and 7b we also plot the corresponding junction I-V curve. The small dips in the IF power curve of Figure 7a become more prominent in Figure 7b, and occur at voltages where Josephson steps are seen in the pumped I-V curve. The association between the dips and the Josephson steps indicates that these structures are the result of Josephson effect tunneling. These results show that, even at high frequencies, a magnetic field can be used to effectively suppress Josephson pair currents in small area junctions.

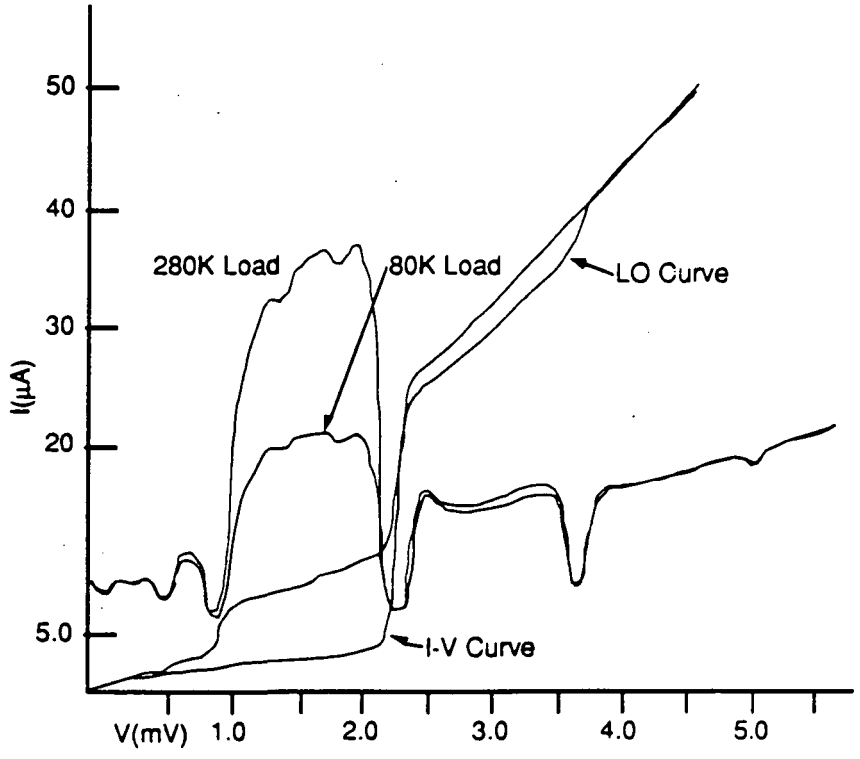

JUNCTION I/V & IF POWER CURVES WITH MAGNETIC FIELD
FIGURE 7a

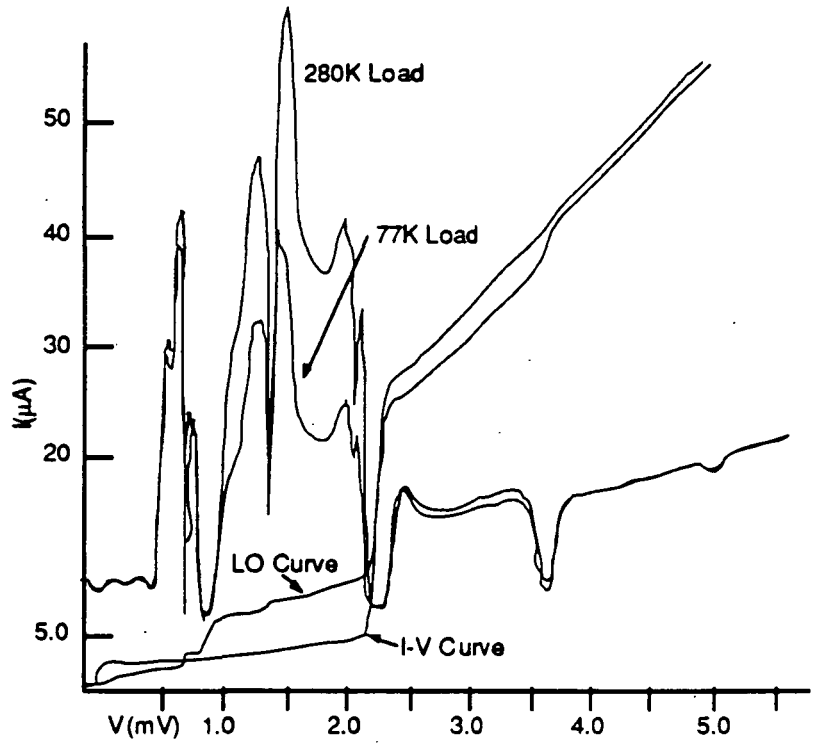

JUNCTION I/V & IF POWER CURVES WITH REDUCED MAGNETIC FIELD
FIGURE 7b

In Figure 8 we show spectrum analyzer measurements of the receiver bandpass from 0.9 GHz to 2.1 GHz. The lower curve in the figure is the bandpass with the receiver looking into a room temperature (280 K) load. The bandpass is fairly flat, with a total power variation of only ~ 3.5 db from 1 to 2 GHz. The upper curve is a plot of the receiver's Y-factor across the IF band. This curve is essentially flat, indicating the receiver's sensitivity is constant across the band.

In Figure 9 we present a double sideband, 500 MHz wide spectrum taken with the receiver on the Caltech Submillimeter Observatory toward the young stellar source Orion IRC2. The center frequency of the spectrum is 492.16 GHz. An acousto-optical spectrometer was used to produce the spectrum. An atomic line and several molecular lines were observed. They are identified in Figure 9. The ordinate is in units of antenna temperature (K) and the abscissa is in units of frequency (GHz). The total on source integration time was ~ 1.3 minutes. At this frequency, the system noise is dominated by the atmosphere. During the time this spectrum was taken the single sideband noise temperature on the sky, which includes the noise contributions of the atmosphere, telescope, and receiver, was ~ 5000 K.

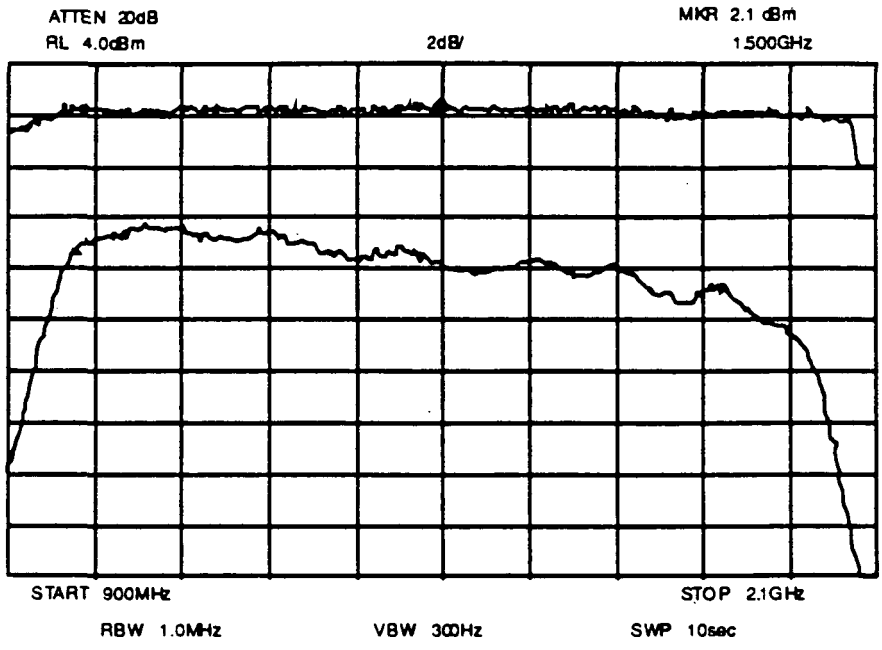

Receiver Bandpass Plot
Figure 8

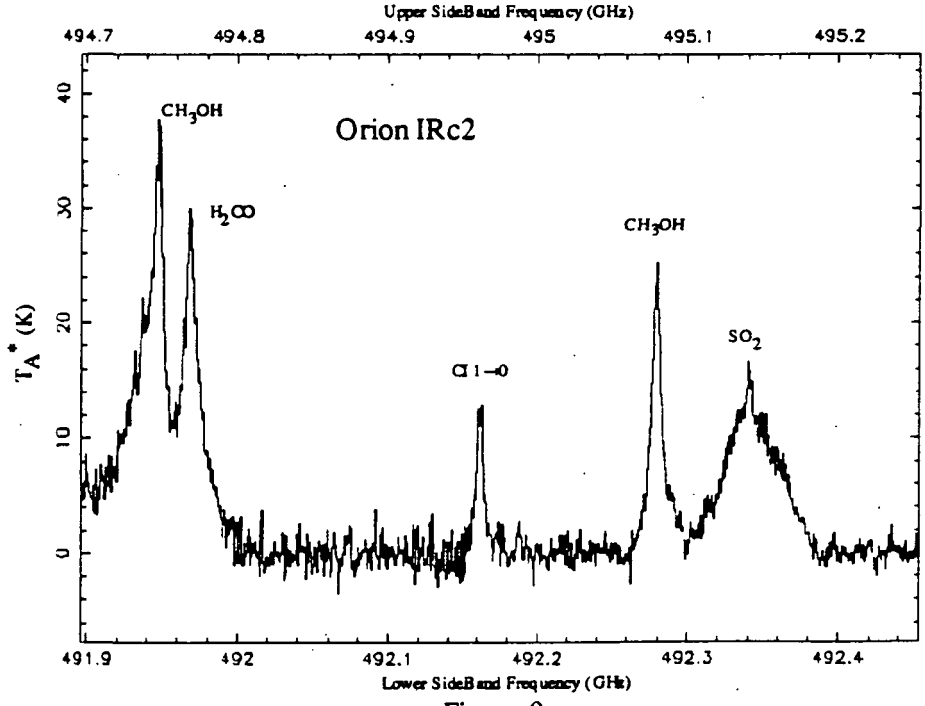

Figure 9

The receiver noise temperature, T_R, is determined by a number of factors. These include the mixer noise temperature, (T_M), the conversion loss in the mixer (C_{Loss}), the noise temperature of the first IF amplifier (T_{IF}), and the coupling efficiency between the IF port of the junction and the input port of the first IF amplifier (η_{IF}).

Receiver Performance Comparison

Parameter	230Nb	345Pb	492Nb
Rn(Ω)	82	54	85
TR (K)	48	159	176
Tmix (K)	34	129	123
C. Loss (db)	3.1	8.3	8.9
Tmix Cor	26	91	95
TIF (K)	7.0	4.2	6.8
IF Contrib.	14	30	53

Table 1

In Table1 we list the values of these parameters for the receiver described in this paper and for the two other SIS waveguide receivers presently in use at the Caltech Submillimeter Observatory. The values of T_M, T_{IF}, C_{Loss}, and η_{IF} were calculated using the shot noise technique described by Tucker and Feldman (1985). The other two receivers in the table were designed with center frequencies of 230 and 345 GHz. All three receivers use the same basic double stub tuner design. Like the 492 GHz receiver, the 230 GHz system employs a niobium junction and the IF matching circuit described by Kooi *et al.* (1992). The 345 GHz receiver uses a lead based SIS junction fabricated by Ron Miller at AT&T Bell Laboratories. This receiver uses an older, less efficient IF matching circuit. In the table R_N refers to the normal state resistance of the SIS junction used in each receiver. T_M^{cor} refers to the mixer temperature corrected for the different beam splitter thicknesses used in each receiver. The value of T_R for the 230 GHz system is a factor of 3 to 4 less than the T_R achieved with the 492 GHz system. The decrease in system performance at 492 GHz is due to a factor of ~ 3 increase in C_{Loss} and T_M. The performance of the 345 and 492 GHz receivers are comparable. This similarity in performance is most likely due to the niobium junction in the 492 GHz receiver having a better high frequency response than the lead junction used in the 345 GHz receiver.

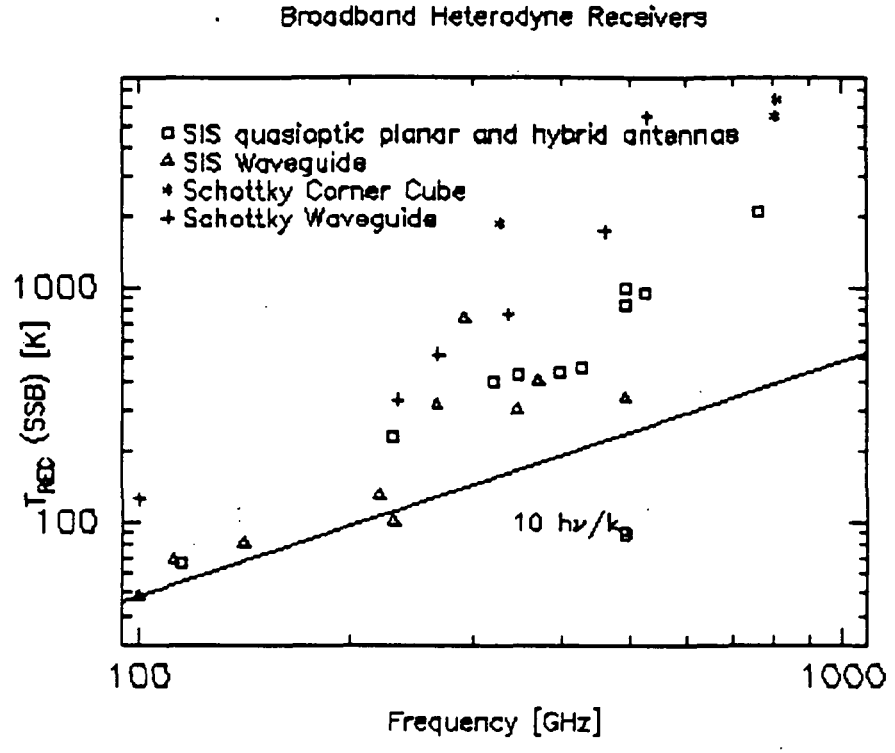

FIGURE 10

In Figure 10 we compare the performance of the 492 GHz receiver to other receivers operating at millimeter and submillimeter wavelengths. At each frequency where they have been built, SIS waveguide receivers have proven to be the most sensitive. These receivers typically operate with noise temperatures 10 to 14 times the quantum noise limit ($h\nu/k$). The receiver reported in this paper continues this trend. We have also tested the 492 GHz receiver at 376 GHz and 420 GHz. We obtained T_R values of 238 and 212 K respectively. (These measurements were taken at sea level where the physical temperature of the mixer was ~ 0.62 K higher than at the altitude where the 172 K, 492 GHz noise temperature measurements were made.) These noise temperatures include all the losses in the system. If we simply compensate for the difference in the thickness of beamsplitter used in the measurements, then we infer a noise temperature of 200 K at 376 GHz and 168 K at 420 GHz. These results suggest the receiver will have its optimum performance between 420 and 492 GHz.

Improving Receiver Performance

Lower values of T_R would be achieved if we could reduce T_{IF}, increase η_{IF}, or decrease either C_{Loss} and/or T_M. In a properly designed amplifier, the value of T_{IF} is a function of the quality of the HEMT devices used and the desired IF bandwidth. In the receiver described here the value of η_{IF} is almost unity, so there is not much to be gained in improving the design of the IF matching circuit. Significantly lower

noise temperatures could be achieved if the conversion loss of the mixer were reduced. Lower conversion losses can be obtained by improving the impedance match between the junction and waveguide embedding impedence. In the current design this match is achieved by adjusting the positions of the two backshorts. The ultimate quality of the impedance match depends on the performance of the backshorts. Since this receiver will be tuned several times a day, non-contacting backshorts were used to reduce wear. The backshorts are insulated from the block by a thin (~ 16 μm) layer of mylar tape. The performance of the backshorts could be improved (perhaps at the sacrifice of durability) by using a thinner insulating material. Ellison *et al.* (1991) have recently demonstrated that a 1 to 2 μm layer of silicon dioxide evaporated onto metallic backshorts serves as an effective insulating layer and improves backshort performance. An improvement in the rf match could also be achieved by reducing the capacitance of the SIS junction. The most direct way of doing this is by reducing the size of the junction. If the normal state resistance of the junction is to remain the same, the thickness of the insulating layer must be decreased simultaneously. These last two statements are equivalent to saying we need a high current density junction with a low ωRC. The limiting factor in obtaining small, high current density junctions is the junction fabrication process itself. However, over the past few years great strides have been made in improving processing techniques. There is every indication that this trend will continue. The effective capacitance that the backshorts need to tune out can also be reduced by fabricating broadband, inductive stubs on the SIS junction itself. This technique has worked well at frequencies below 300 GHz (Kerr *et al.* (1987)). However, as one goes up in frequency, the dimensional tolerances on these matching circuits becomes more severe, making fabrication difficult. Even so, recent work by Büttgenbach *et al.*. (1992), and Jacobs K. *et al.* (1992) suggests that if a broadband rf matching network is included, this technique can be used effectively even at submillimeter wavelengths. Indeed, we plan to test a mixer block like the one discussed here with a broadband, two section, RF transformer matched SIS junction in the near future. Another way to reduce the effective capacitance is to use a series array of junctions. Two difficulties with this technique are that the array elements must be similar (a fabrication challenge) and the required LO power increases as the square of the number of array elements. At submillimeter wavelengths, where it can be difficult to generate LO power, the extra power needed to drive a series array can become prohibitive.

If there were no Josephson pair tunneling, one might expect that an SIS bias voltage corresponding to the center of the first photon step below the gap would provide the best receiver noise temperatures. However, we find that even with an optimized magnetic field, the best receiver noise temperatures are found at bias voltages close to the gap voltage. To some degree this result is due to the matching requirements of the waveguide and IF matching network. However, this dependence of the receiver noise temperature on bias voltage suggests that, while significantly suppressed by the magnetic field, Josephson pair tunneling does add noise to the system. To avoid this problem, SIS junctions with larger bandgap energies are needed.

Summary

We have constructed an SIS waveguide receiver which provides low noise performance from 375 GHz to 510 GHz. The receiver is a facility instrument at the Caltech Submillimeter Observatory, where it has been in use since September 1991. The SIS junction used in the receiver is a 0.25 μm^2 niobium trilayer device with a current density of ~ $10^4 A\ cm^{-2}$. At its design frequency of 492 GHz, the receiver has a double sideband noise temperature of ~ 172 K. By embedding magnetic field concentrators in the mixer block, we are able to put several quanta of magnetic flux across the SIS junction. By adjusting the strength of the magnetic field we are able to effectively suppress Josephson pair tunneling. The success of this receiver suggests that SIS waveguide receivers can provide low noise performance at even shorter wavelengths.

This work was supported by NSF contract AST 9015755 to the CSO and a gift from AT&T to purchase the spectrum analyzer used to perform some of the measurements.

References

Brewer, M. K. and Raisanen, A. V. 1982, *EEE. Trans. Microwave Theory and Techniques*, 30, 708.

Büttgenbach, T. H. 1992, private communication.

Ellison, B. N., Little, L. T., Mann, C. M., and Matheson, D. N. 1991, *Electronics Letters*, 27, 139.

Ellison, B. N. and Miller, R. E. 1987, *Int. J. Infrared and Millimeter Waves*, 6, 697.

Goldsmith, P.F. 1982, in, *Infrared and Millimeter Waves*

Kerr, A. R., Pan, S. K., and Feldman M. J. 1987, *Int. J. Infrared and Millimeter Waves*, 9, 203.

Kooi, J. W., Chan, M., Phillips, T. G., Bumble, B., and LeDuc, H. G. 1992, preprint.

Shoji, A., Kosaka, F., Shinoki, M., Aoyagi, M. and Hayakawa, H. 1983, *IEEE Trans. Magnetism*, 19, 827.

Silver, S. 1966, *IEE Electromagnetic Waves Series*, 19, 95.

Thomas, B. M. 1978, IEEE Trans. *Antennas and Propagation*, 26, 367.

Jacobs K., Kotthaus U., andVowinkel B., *International Journal of Infrared and Millimeter Waves*, Vol. 13, No. 1, 1992

Slot-line end-fire antennas for THz frequencies

by

H. Ekström, S. Gearhart*, P. R. Acharya, H. Davé**,
G. Rebeiz*, S. Jacobsson, E. Kollberg, G. Chin**

Department of Applied Electron Physics
Chalmers University of Technology
S-412 96 Göteborg, Sweden

*NASA/Center for Space Terahertz Technology
Electrical Engineering and Computer Science Department
University of Michigan, Ann Arbor, MI 48109-2122, USA

**Planetary System Branch
NASA/Goddard Space Flight Center
Greenbelt, MD 20771, USA

ABSTRACT

Tapered slot-line endfire antennas, of BLTSA type, have been fabricated on 1.7 μm thin SiO_2/Si_3N_4 (ε_r = 4.5) dielectric membranes. The antenna patterns, in the E-, H-, D- and D-cross planes, were measured at 270, 348, 370 and 802 GHz using bismuth micro bolometer detectors. The antennas have approximately 12 dB directivity, and the −10 dB beam widths are 50° and 55° in the E- and H-planes at 348 GHz, respectively. The measurements at millimeter/submillimeter wavelengths compare well with scale measurements at 45 GHz as well as with theoretical predictions. The overall results are encouraging and show that slot-line antennas can be fabricated for use at THz frequencies. Furthermore, it is shown that the very thin SiO_2/Si_3N_4 membranes are strong enough to be used in practical applications.

INTRODUCTION

Tapered slot-line antennas are often considered for integration in planar millimeter/submillimeter wave circuits; *e.g.* in quasi optical mixers. These antennas can be operated over a wide bandwidth and radiate wide or narrow beams. Various types of endfire slot-line antennas can be found in the literature; *e.g.* the linearly tapered slot-line antenna (LTSA) [1], the exponentially tapered slot-line antenna "Vivaldi" [2] and the constant width slot-line antenna (CWSA) [3]. A review of antennas suitable for integration in circuits for millimeter and terahertz frequencies has been written by G. Rebeiz [4].

In this work we have studied yet another member belonging to the family of endfire slot line antennas; namely the BLTSA (Broken Linearly Tapered Slotline Antenna) [5], Fig. 1. The BLTSA has the advantage, among the slot-line antennas, to require the small substrate area. In addition, the BLTSA has been extensively studied by the Chalmers group.

Antennas of endfire slot-line type require a certain optimum substrate thickness $t = 0.03\,\lambda(\sqrt{\varepsilon_r}-1)^{-1}$ [3] to avoid pattern degradation and power loss due to surface modes. In the millimeter wave range the thickness should be only a couple of micrometers, hence the antenna must be fabricated on a thin dielectric membrane, a fact which introduces delicate manufacturing problems. A further complication is introduced by the fact that the membranes must be left unsupported in the endfire direction, Fig. 2.

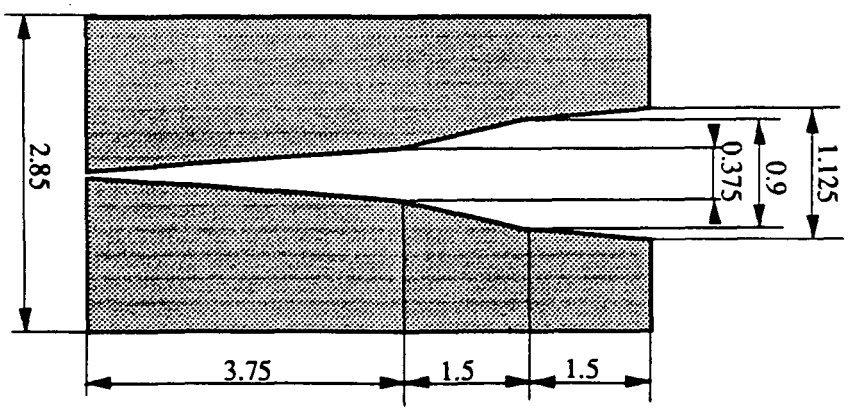

Fig. 1. Dimensions of the BLTSA. All dimensions are normalised to the vacuum wavelength.

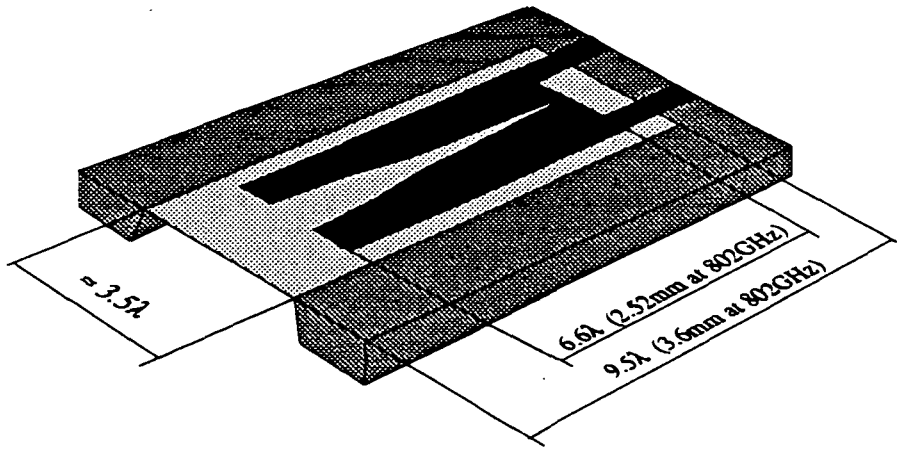

Fig. 2. The endfire slot line antenna deposited on BLTSA on 1.7 μm thin SiO_2/Si_3N_4 (ε_r = 4.5) membrane. The Si frame supporting the membrane has a thickness of 385 μm. Note that the membrane is unsupported in the end-fire direction.

FABRICATION

The 1.7 μm thin dielectric membrane supporting the antenna consists of three layers; thermally grown SiO_2, LPCVD deposited Si_3N_5 and SiO_2. With compressive oxide and tensile nitride, the relative thickness of the layers could be selected to form a slightly tensile, and consequently flat and rigid membrane. The membrane layers were deposited on both sides of 385 μm thick silicon wafers. To form the membrane region for the antennas, the silicon was etched in EDP from the backside of the wafer, with the backside nitride and oxide layers patterned with the membrane layout and used as etch mask. The nitride and oxide layers on the front side acted as etch stops for EDP. A considerably manufacturing problem is due to the fact that the antenna requires that the membrane is not supported by silicon in the endfire direction. In order to simplify the photo lithography were the antennas fabricated on fully supported membranes. After the antennas were fabricated was the silicon support in the endfire direction removed. The fragility of the membrane limits the area to roughly 3×9 mm^2. Thus, the maximum available membrane size limits this particular antenna design to frequencies above 300 GHz.

MEASUREMENTS

Several scaled versions of BLTSA's were fabricated on 25.4 μm thick Kapton foil and measured at 45 GHz. The best antenna design was then scaled to 348 and 802 GHz (dimensions normalized to vacuum wavelength are given in Fig. 1). These antennas were fabricated on the 1.7 μm thin dielectric membranes, Fig. 2.

Bismuth micro bolometers were used as detectors. A Gunn oscillator with a tripler/quadrupler was use as signal source at 270 and 348 GHz, whereas an optically pumped far infrared laser was used to generate the 802 GHz signal. The dynamic range in the antenna pattern measurements was approximately 20 dB.

The E-, H-, D- and Dx- planes of the 348 GHz antenna were measured at four frequencies: 270, 348, 370 and 802 GHz, respectively, whereas the 802 GHz design was only measured at 802 GHz. Measurements of the 348 GHz design at 270 and 802 GHz, Figs. 3a, b and c, show the wide bandwidth of this type of antenna. At the design frequency the –10 dB beam width varies between 43 and 55° in the measured planes. The D-plane crosspol level is as high as –6 dB, which is a typical value for endfire slot-line antennas. The directivity was calculated to approximately 12 dB. In the calculations the lobes outside the measured range and the back lobes were set to –14 dB and –20 dB respectively.

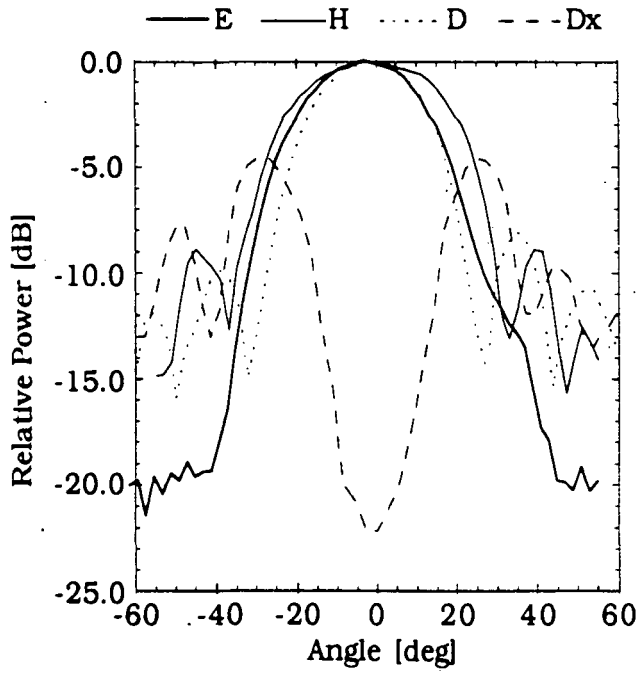

Fig. 3a. Antenna patterns for the BLTSA designed for 348 GHz but measured at 270 GHz

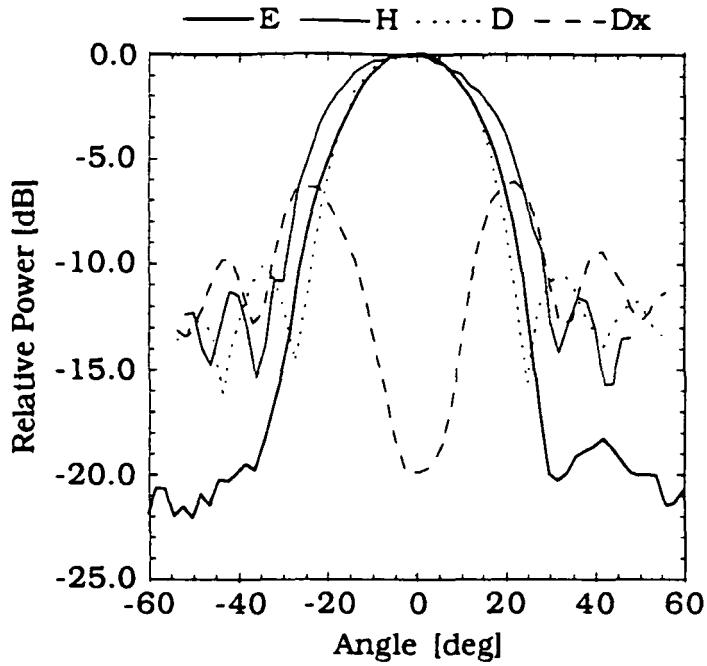

Fig. 3b. Antenna patterns for the BLTSA designed for the 348 GHz design measured at 348 GHz

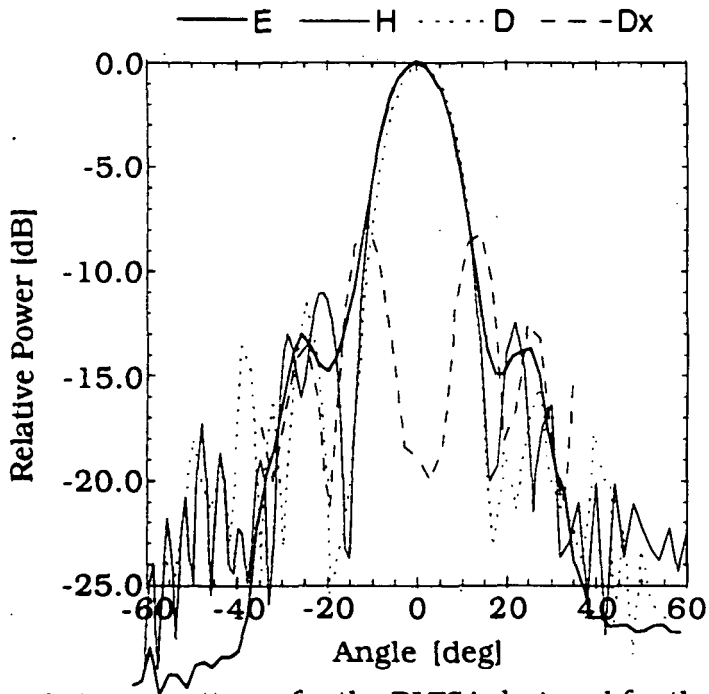

Fig. 3c. Antenna patterns for the BLTSA designed for the 348 GHz design measured at 802 GHz

At 802 GHz the antenna beam is narrower and more symmetric (39 °- 43° at –10 dB level and the directivity is approximately 13 dB) with slightly lower sidelobes than the pattern at 348 GHz, also the D-plane cross-pol level is lower (–8 dB), Fig. 4a, b. The improved pattern at 802 GHz was expected since the membrane is relatively thicker

(expressed in wavelengths) and closer to the optimum thickness. In fact, the optimum frequency for these membranes is approximately 4 THz Thus, at THz frequencies, it is expected that the antenna pattern would be even more symmetric and the D-plane crosspol level could be as low as -10 to -15 dB below the co-polarized level.

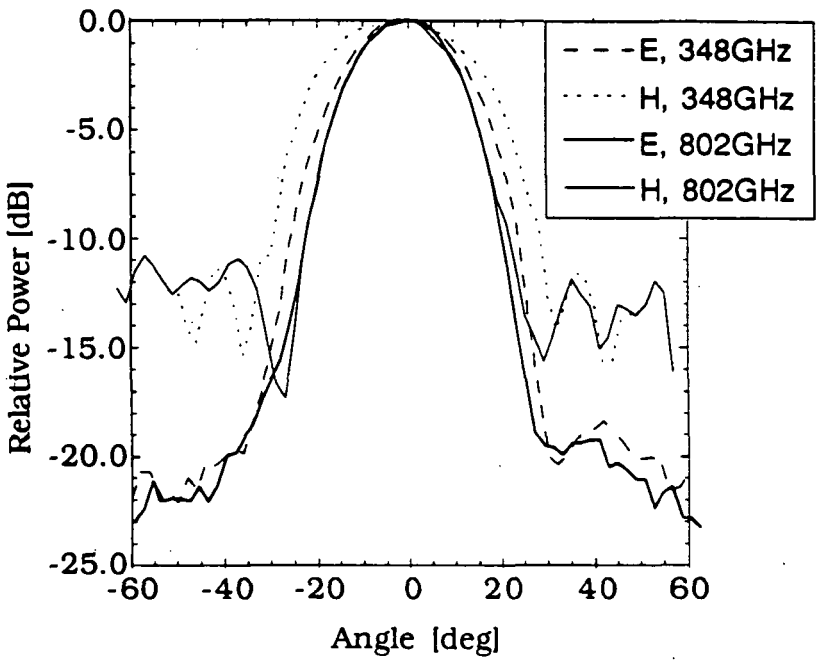

Fig. 4a. Measured E- and H plane of the 802 GHz design at 802 GHz, and the 348 GHz design at 348 GHz

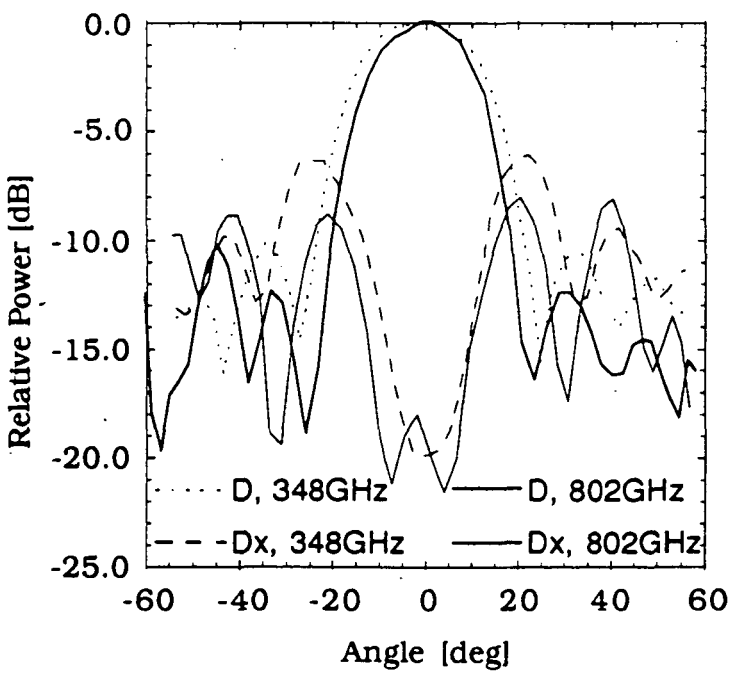

Fig. 4b. Measured D- and Dx plane of the 802 GHz design at 802 GHz, and the 348 GHz design at 348 GHz

The performance of the BLTSA end-fire antennas on 1.7 μm thin membranes is summarized in the table below.

Frequency		GHz	270	348	370	802
E-plane	-10 dB beam width		59°	50°	49°	43°
	side lobe level	dB	-12	-19	-19	-20
H-plane	-10 dB beam width		64°	55°	53	44°
	side lobe level	dB	-8	-11	-11	-11
D-plane	-10 dB beam width		50°	43°	42°	39°
	side lobe level	dB	-7	-10	-10	-12
D-cross	lobe level	dB	-4	-6	-6.5	-8
Directivity		dB	11	12	12	13

Table 1. Compiled measured antenna data. All antennas were fabricated on a 1.7 μm thick SiO_2/Si_3N_4 membrane. The thick frames around 348 and 802 GHz indicate the design frequencies. The 348 GHz antenna was also measured at 270, 370 and 802 GHz. The 802 GHz antenna was only measured at 802 GHz.

Scale measurements at 45 GHz show that the E and H-plane patterns agree reasonably well with the patterns at the higher frequencies, Fig. 5. These antennas were made on 25.4 μm thick Kapton™ foil (ε_r=3.5). Note that, this substrate thickness is comparatively thicker (measured in wavelengths) at the scale frequency than the thickness of the dielectric in the 270 - 802 GHz measurements.

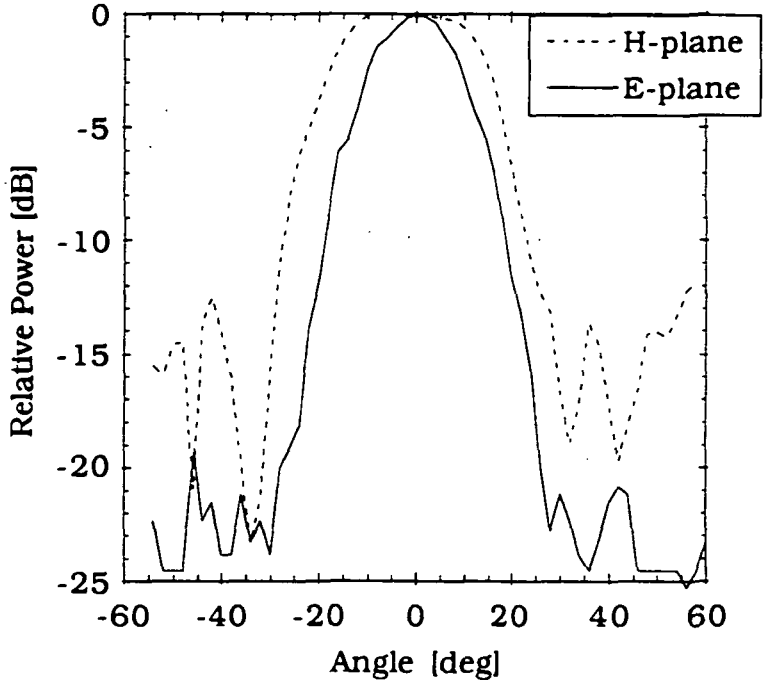

Fig. 5. E and H-plane patterns of a scale model of the BLTSA. The measurements are performed at 45 GHz.

THEORY

The end-fire slot-line antennas have been analyzed by using method previously described by *e.g.* Janasawamy [6]. In this method, the antenna tapering is approximated by a "staircase"-function in a number of steps of different widths but equal lengths, as shown in figure 6. Thus, the slot-line antenna can now be treated as a linear array of apertures each fed with different phases and amplitudes. Furthermore, power conversion is applied to relate the amplitudes and fields in neighbouring apertures. The characteristic impedance and the wavelength of each slot is calculated by using a spectral domain technique [7]. The far field pattern of the antenna is calculated by applying an appropriate Green's function and adding the field contributions from all apertures. In these calculations we ignore the reflections from the discontinuities in the antenna taper (which has been confirmed in computer simulations).

The theoretical patterns agree reasonably well with measured patterns, Fig. 7, 8, considering the approximations in the calculations. The calculated and measured beam width correspond very well, and it is possible to predict level and position of the sidelobes within 2 dB and 5°. The biggest difference between the calculated and measured patterns is in the crosspolarized D-plane, where the theory predicts a level 2-3 dB higher than the measured level.

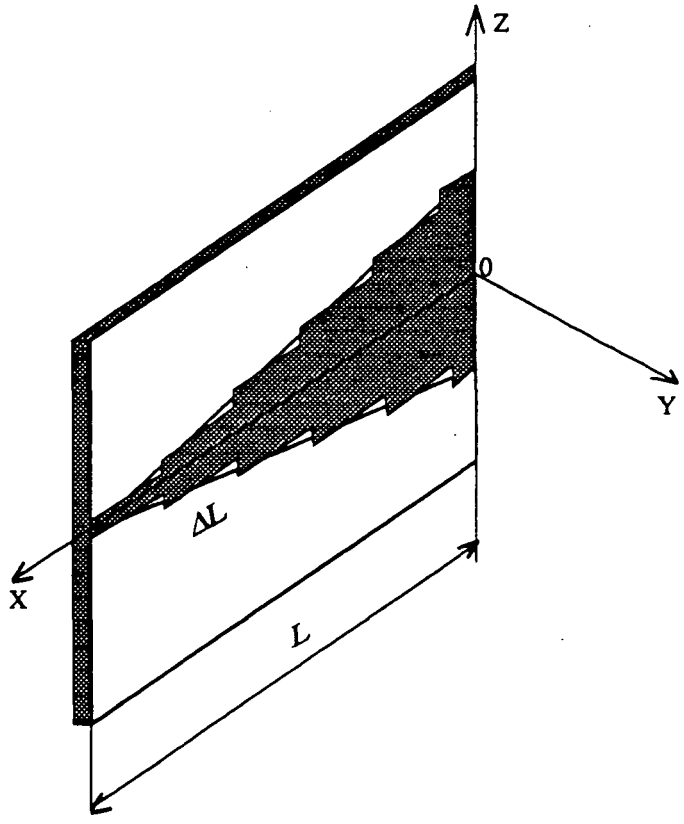

Fig. 6. Approximation of the slot-line antenna by an array of slots.

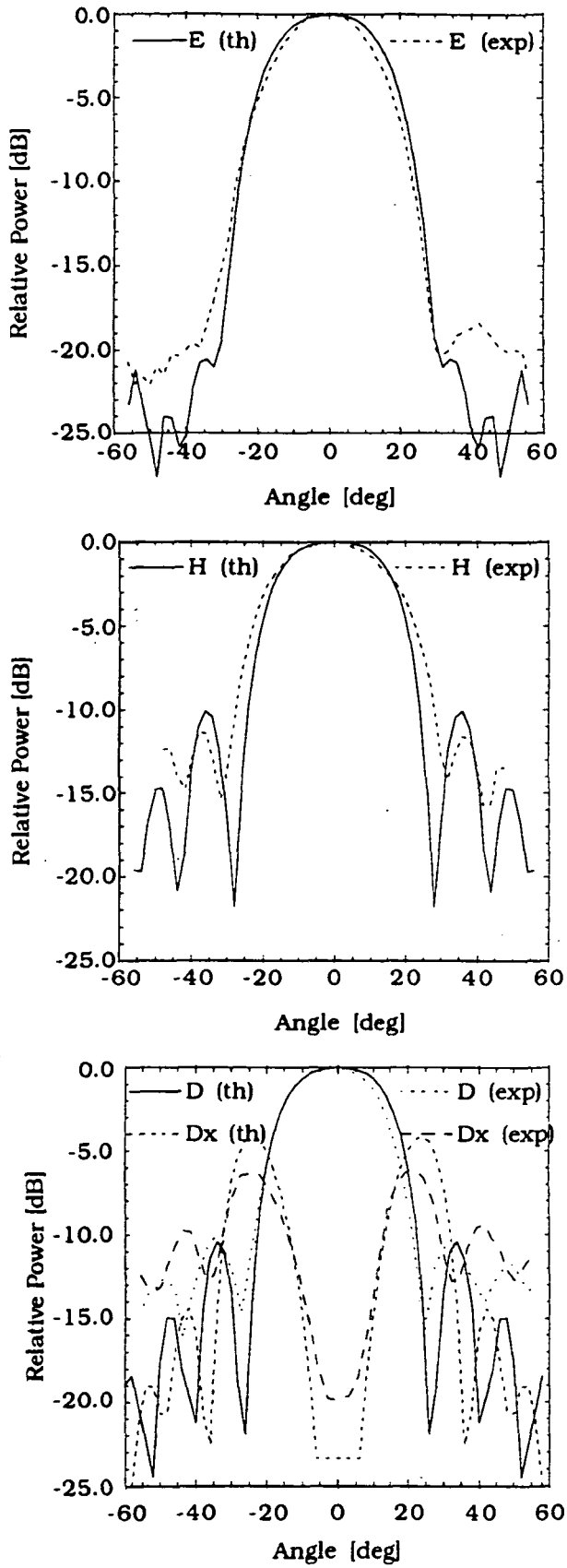

Fig. 7. Calculated (th) and measured (exp) antenna patterns at 348 GHz

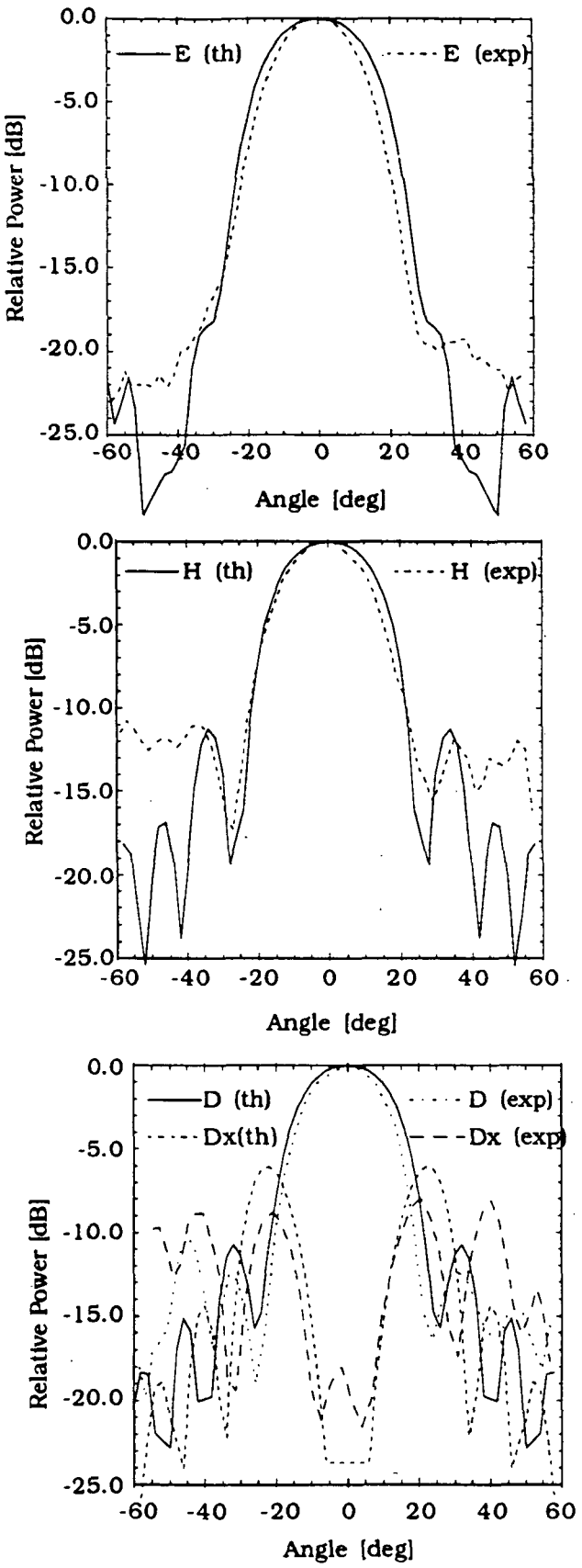

Fig. 8. Calculated (th) and measured (exp) patterns at 802 GHz

REFERENCES

[1] S.N. Prasad, and S. Mahapatra, *A novel MIC slot-line aerial*, Proc. 9th Eur. Microwave Conf., pp. 120-124, Brighton, UK, 1979.

[2] P.J. Gibson, *The Vivaldi aerial*, 9th Eur. Microwave Conf., pp. 101-105, Brighton, UK, 1979.

[3] K.S. Yngvesson, D.H. Schaubert, T.L. Korzeniowski, E.L. Kollberg, T. Thungren, and J. Johansson, *Endfire tapered slot-line antennas on dielectric substrates*, IEEE Trans. Antennas. Propagat., vol. AP-33, N.12, pp1392-1400, 1985.

[4] G. Rebeiz, *Millimeter-wave and terahertz integrated-circuit antennas*, preprint, to appear in the October issue on Space terahertz Technology in the IEEE-Proceedings.

[5] P.R. Acharya, J. Johansson, and E.L. Kollberg, *Slotline antennas for millimetre and sub millimetre wavelengths*, Proc. 20th Eur. Microwave Conf., pp. 353-358, Budapest, Hungary, Sept 1990.

[6] R. Janasawamy, D. Schaubert, *Analysis of Tapered Slotline Antenna*, IEEE Trans. Antennas Propgat., vol. AP-35, no.9, pp. 1058-1065, Sept. 1987.

[7] G. Johansson, P.R. Acharya, J. Johansson, *Determination of Slot Line Characteristics*, Technical Report No. 97L, 1991, Chalmers University of Technology.

QUASI-OPTICAL ANTENNA-MIXER-ARRAY DESIGN FOR TERAHERTZ FREQUENCIES

Yong Guo
Department of Electrical and Computer Engineering
College of Engineering, Clemson University
Clemson, SC 29634

Kent A. Potter, David B. Rutledge
Division of Engineering and Applied Science
California Institute of Technology
Pasadena, CA 91125

ABSTRACT

A new quasi-optical antenna-mixer-array design for terahertz frequencies is presented in this paper. In the design, antenna and mixer are combined into an entity, based on the technology in which millimeter-wave horn antenna arrays have been fabricated in silicon wafers. It consists of a set of forward- and backward-looking horns made with a set of silicon wafers. The front side is used to receive incoming signal, and the back side is used to feed local oscillator signal. Intermediate frequency is led out from the side of the array. Signal received by the horn array is picked up by antenna probes suspended on thin silicon-oxynitride membranes inside the horns. Mixer diodes will be located on the membranes inside the horns. Modeling of such an antenna-mixer-array design is done on a scaled model at microwave frequencies. The impedance matching, RF and LO isolation, and patterns of the array have been tested and analyzed.

I. INTRODUCTION

In submillimeter-wave and terahertz frequency systems, because of their much shorter wavelengths compared with microwave systems, waveguide circuits become much smaller, which makes them very difficult and expensive to build. However, quasi-optical components provide a solution to this problem. Quasi-optical antenna-mixer-array combines antennas and mixer circuits into a single entity. The design is based on an existing technology by which dipole excited integrated-circuit horn antennas are made in silicon [1]. The horn antennas consist of probes suspended on a thin oxynitride membrane inside pyramidal horns which are chemically etched in silicon. The antennas are free of dielectric losses and have plenty of space for electronic interconnections between the probes. The aperture efficiency of these etched horn antennas has been improved to 72 % [2]. Recent research shows that the experimental results agree well with the theoretical analysis, including radiation patterns and resonant dipole impedances [3]. Various antenna probes inside the pyramidal horns have also been studied [4].

This integration of antenna and mixer eliminates the need for RF and LO circuit-fashion connections. Such construction offers a device with potential of smaller size,

lighter weight, more ruggedness and less cost, as compared to conventional methods. Moreover, this kind of design potentially can be mass produced by standard integrated-circuit technology. The applications of the integrated-circuit antenna-mixer array include imaging systems, radars, and satellite communications.

II. Horn Structure and Mixer Circuitry Design

In order to avoid the difficulty to supply an LO power at a frequency close to RF, a subharmonically-pumped antenna-mixer array is designed which is pumped by an LO at only half of the RF frequency. Since the RF and the LO frequencies differ by approximately a factor of two, in principle, it is easier to realize the isolation between the RF and the LO. Furthermore, spurious responses associated with the odd harmonics of the LO can be rejected by using an antiparallel diode pair. The subharmonically-pumped horn-antenna-mixer array is shown in Figures 1 and 2. It consists of a set of forward- and backward-looking horns facing back to each other made silicon wafers. Every four RF horns are provided with one LO horn which is a rectangular-shaped horn. The spacing between RF horns is 1λ. By using the sub-array concept, every four RF horns can be taken as a sub-array. Four RF horns, together

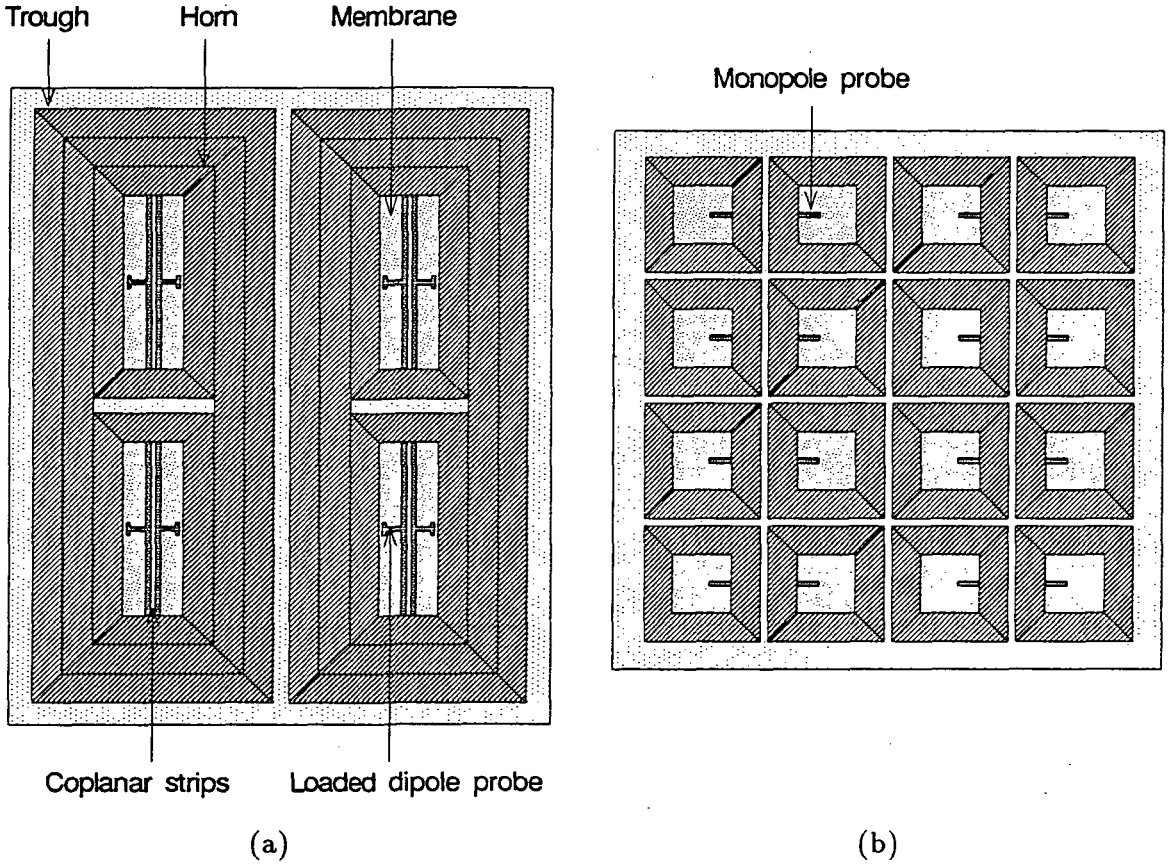

Figure 1 The horn structure of the subharmonically-pumped mixer design, one LO horn corresponding to four RF horns; (a) LO horns, the trough made of two silicon wafers is put on the top of the horns. (b) RF horns, monopoles are used for the RF reception.

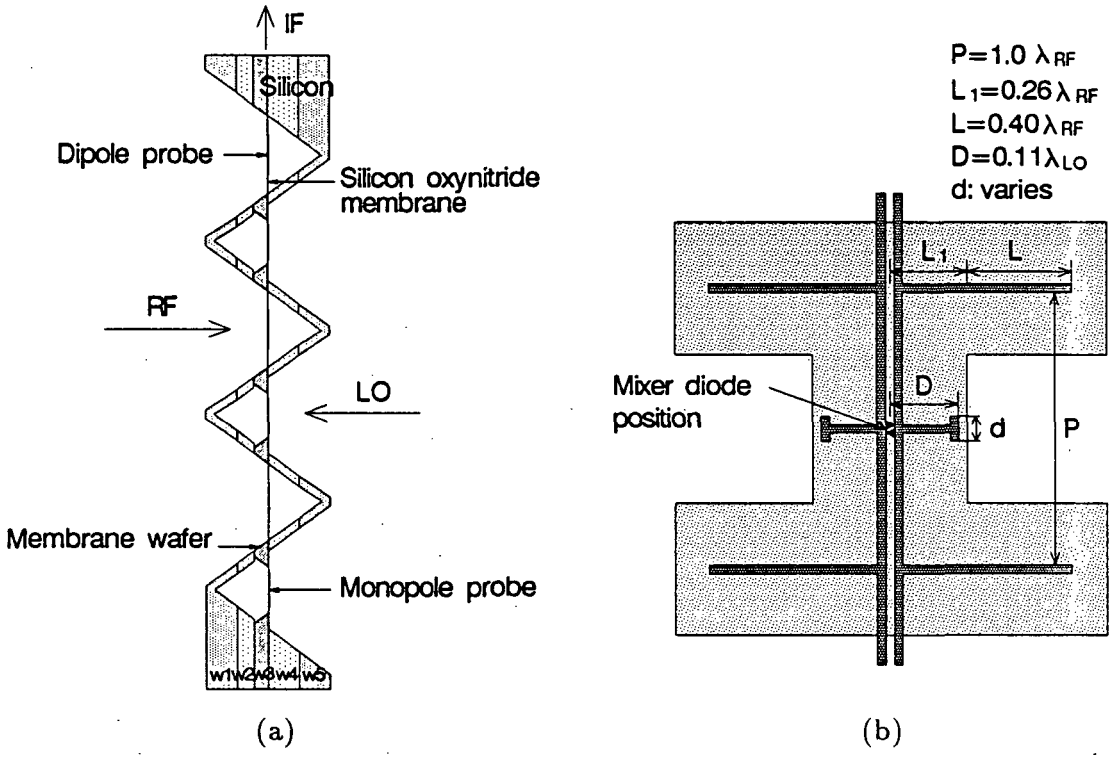

Figure 2 (a) Cross-sectional view of the antenna-mixer array. (b) The mixer circuit design for a unit cell; four monopoles for the RF reception and one dipole for the LO reception; both RF and LO are detected by the mixer diodes located in the center of the unit cell; IF is led out from the ends of the LO horn through a coplanar-strip transmission line.

with one LO horn, form a unit cell. This design will keep the best symmetry, and the beam patterns of the sub-array will be improved by a factor of 4 compared with that of the single RF horn. Since the size of the LO horns should be twice that of the RF horns, half of the area on the LO side in each unit cell would be left unused. This would cause strong reflection from the flat surface, namely, a 3 dB reflection loss. In order to eliminate this 3 dB reflection loss, a structure is designed to be placed on the top of the LO horns. The structure has a long trough on each row of the LO horns and will fill up the space between the LO horns to converge the incoming energy into the LO horns. Figure 1 shows the antenna-mixer array with 2×2 LO horns looking from the LO side and 4×4 RF horns looking from the RF side. The cross-sectional view is shown in Figure 2(a). The mixer circuit design is shown in Figure 2(b). Every monopole from each of the four RF horns will couple the RF signal down to the LO horn through a coplanar-strip transmission line. A dipole probe is employed to receive the LO. The mixer diodes are located in the center of the LO membrane, and the IF is led out from the ends of the LO horn. The dipole probe is loaded on the ends near the sidewalls with a short stub, which, as a result, could compensate for the capacitive characteristic impedance of the short dipole probe.

III. Modeling

The mixer array design has been tested on a scaled model sub-array, which has four RF horns and one LO horn. The gain of such a sub-array will be increased by a factor of 4 compared with a single horn. Based on this scaled model sub-array, antenna impedances and receiving patterns were measured. Antenna probes are required not only to couple the free-space wave energy to the mixer circuit but also to provide a suitable impedance, the embedding impedance, to the mixer diodes. This impedance over a wide frequency range is also important for mixer performance because various frequency components exist in the mixer circuits. In order to achieve good isolation between the RF and the LO, as well as to match the impedances of the RF and the LO to the diode impedance, various mixer circuits have been tested. Trade-off has been made among the impedance match and the isolation between the RF and the LO so as to minimize losses.

The actual model consists of two square RF horns and a half rectangular LO horn, a half of the designed unit-cell, sitting on a big copper-clad circuit board which was used as an image plane. The monopole built in each of the RF horns will couple the incoming signals to the loaded dipole in the LO horn through the coplanar-strip transmission line. A small channel in the middle of the horns will let the monopole probes go through between the LO and RF horns. The design frequency for the RF is 10 GHz and the LO is 5 GHz, corresponding to the wavelength of 3 cm and 6 cm, respectively. The opening of RF horns is $1\,\lambda_{RF}$ square, while the height of the LO horn is $\lambda_{LO}/2$, and the LO horn width is $1\,\lambda_{LO}$. Mixer diodes are to be placed in the center of the dipole probe in the LO horn. An SMA bulkhead feed-through connector is soldered from the back of the circuit board to the place where the diodes are supposed to be. The inner conductor of the connector is soldered to the dipole probe, and the outside conductor is soldered to the circuit board used as a ground plane.

Measurements were done on an HP 8510 Network Analyzer and data were collected by a PC. Full two-port calibration was made in order to measure not only the reflection coefficients but also the receiving properties and the isolation between the RF port and LO port by measuring the transmission coefficient S_{12}. For this purpose, a broad-band horn antenna is used as a transmitting horn which has a working frequency range from 2 GHz to 18 GHz. The measured impedances are marked on the Smith chart in Figure 3(a). Although the impedances were measured on only a half unit-cell, consisting of two RF horns and a half LO horn, the impedances in a full unit-cell can be easily obtained by doubling those measured impedances in the half unit-cell. The impedances in Figure 3(a) are plotted by using Puff, a software CAD program [5]. Both the RF and the LO impedance should be matched to 50 Ω because each beam-lead diode in the antiparallel diode pair has a resistance of about 100 Ω. In the graph, when the loading stub on the dipole decreases in length, the LO impedance at 5 GHz changes from the inductive to the capacitive impedance, passing the resonant resistance at about 50 Ω, which is a very good matching impedance for the diode pair. This LO impedance of the circuit can be regarded as the LO dipole-probe impedance

parallel with the impedance of the coplanar transmission line plus the RF probes. At 5 GHz, the impedance of the coplanar transmission line plus the RF probes is very high as is illustrated by the LO frequency mark "5" when the entire LO dipole probe is taken away. Hence, the resonant LO impedance is mainly determined by the loaded dipole probe and is relatively independent of rest of the circuits. On the other hand, the RF impedances at 10 GHz are pretty high and independent of the loading-stub length changes. The average value of those RF impedances at 10 GHz is about $84 + j82\,\Omega$.

The normal-incident power receptions by the RF and the LO horns were tested over a wide frequency range, from 2.0 GHz to 12.0 GHz. This was done by putting a wide-band transmitting horn in front side of the RF horns or the LO horn. Figure 3(b) shows the measured power received by the RF horns when the transmitting horn is on that side (solid line) and by the LO horn when the transmitting horn is that side (dashed line). At the LO frequency of 5 GHz, the difference between the LO and the RF power is defined as the LO-RF isolation. The higher isolation, the lower the coupling loss, under the condition that other parameters stay the same. Similarly, the RF-LO isolation is the power difference between RF and LO at the RF frequency

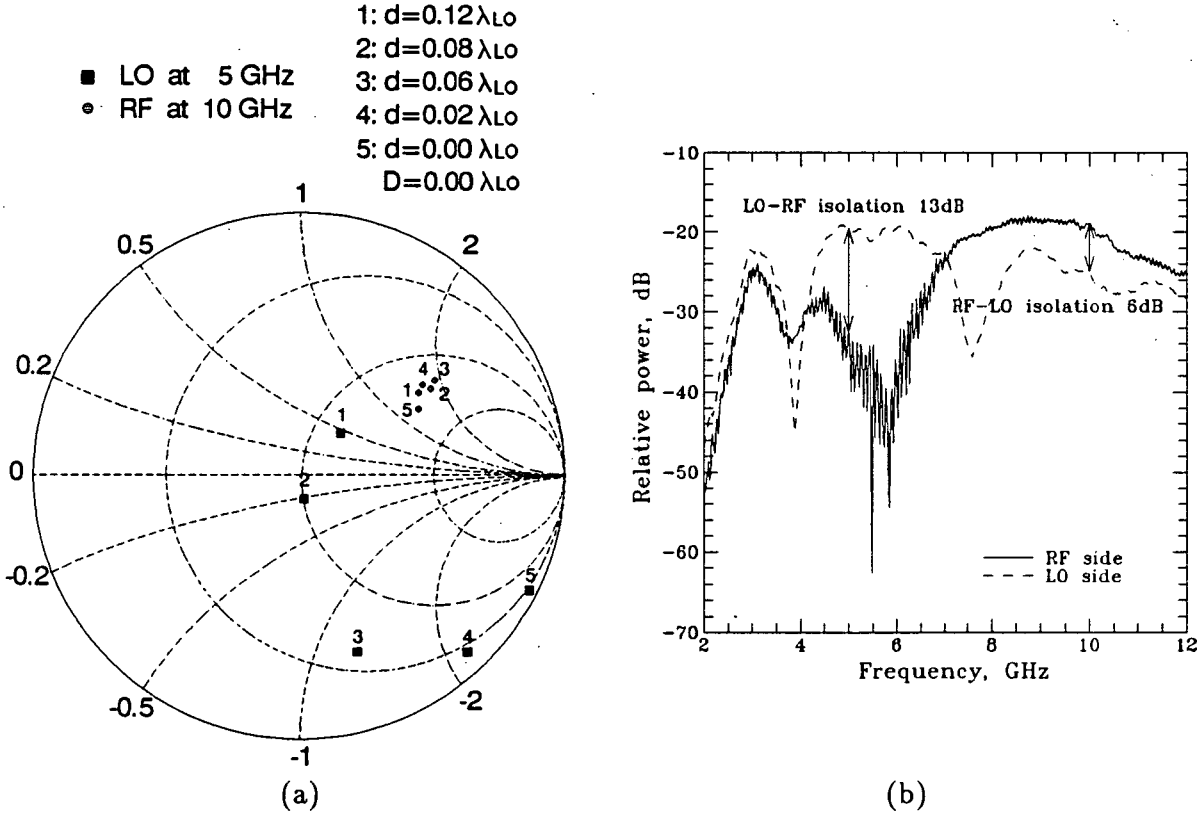

Figure 3 (a) The circuit impedances is indicated on the Smith chart with respect to the different loading-stub length d; measured at 10 GHz for the RF and 5 GHz for the LO. (b) Measured normal-incident power, received by the RF horns (solid line) and by the LO horn (dashed line) with equal distance.

Loss component	Simple-probe design	Split-LO-probe design
RF mismatch, dB	1.7	4.9
LO mismatch, dB	0.0	0.2
RF-LO coupling, dB	1.3	0.0
LO-RF coupling, dB	0.2	0.2

Figure 4 Comparison of the impedance-mismatch losses and the coupling losses between the two different mixer circuit designs.

of 10 GHz. The measured RF-LO isolation is 6 dB or a 25 % loss. If the LO probe is split into two, by tuning the spacing between two LO probes, minimum RF-LO isolation of 20 dB was achieved. As a comparison, of the simple-probe design and the split-LO-probe design, the impedance-mismatch losses and the coupling losses of the two designs are listed in the table in Figure 4. For both designs, the biggest loss comes from the RF-impedance mismatch, 1.7 dB for the simple probe and 4.9 dB for the split-LO-probe.

IV. Conclusion

A new antenna-mixer array design has been presented, which potentially can be made and used at submillimeter and terahertz frequencies. Modeling work shows that, for this design, compromises have to be made between the RF-impedance mismatch, the LO-impedance mismatch and the RF-LO coupling losses. In some applications, if certain LO loss is tolerable, then lower RF loss can be achieved (which means lower conversion loss) by sacrificing some LO impedance-mismatch losses and LO-RF coupling losses. The mixer elements could be either Schottky diodes [6] or superconducting SIS mixers [7].

V. Acknowledgements

We appreciate the support of Aerojet ElectroSystems Co., Azusa, CA. and the Army Research Office through the Jet Propulsion Laboratory.

VI. References

[1] G. M. Rebeiz, D. P. Kasilingam, Y. Guo, P. A. Stimson, D. B. Rutledge, "Monolithic Millimeter-Wave Two-Dimensional Horn Imaging Arrays," *IEEE Transactions on Antennas and Propagation*, September, 1990.

[2] Y. Guo, K. Lee, P. Stimson, K. Potter, and D. Rutledge, "Aperture Efficiency of Integrated-Circuit Horn Antennas," *Microwave and Optical Technology Letters*, January, 1991.

[3] G. V. Eleftheriades, W. Y. Ali-Ahmad, L. P. Katehi, G. M. Rebeiz, " Millimeter-Wave Integrated-Horn Antennas: Part I–Theory, Part II–Experiment " *IEEE Transactions on Antennas and Propagation*, November, 1991.

[4] Y. Guo, J.C. Chiao, K.A. Potter, D.B. Rutledge, "Probe Modeling for Millimeter-Wave Integrated-Circuit Horn Antennas," submitted to the *IEEE AP-S International Symposium*, July 18–25, 1992, Chicago, Illinois.

[5] R.C. Compton, S.W. Wedge, D.B. Rutledge, "*Puff*: Computer Aided Design for Microwave Integrated Circuits," Caltech Press, January, 1990.

[6] T.W. Crowe, W.C.B. Peatman, "GaAs Schottky Diodes for Mixing applications Beyond 1 THz," *Second International Symposium on Space Terahertz Technology*, JPL, Pasadena, CA, February 26–28, 1991.

[7] M.J. Wengler, N. Dubash, G Pance, R.E. Miller, "High Gain and Noise in SIS Mixers at the Submillimeter Wavelengths," *Second International Symposium on Space Terahertz Technology*, JPL, Pasadena, CA, February 26–28, 1991.

ANALYSIS OF A NOVEL NON-CONTACTING WAVEGUIDE BACKSHORT

T. M. Weller and L. P. B. Katehi,
University of Michigan NASA Center for Space Terahertz Technology
W. R. McGrath,
Jet Propulsion Laboratory Center for Space Microelectronics Technology

ABSTRACT A new non-contacting waveguide backshort has been developed for millimeter and submillimeter wave frequencies. The design consists of a metal bar with rectangular or circular holes cut into it, which is covered with a dielectric (mylar) layer to form a snug fit with the walls of a waveguide. Hole geometries are adjusted to obtain a periodic variation of the guide impedance on the correct length scale, in order to produce efficient reflection of rf power. It is a mechanically rugged design which can be easily fabricated for frequencies from 1 to 1000 GHz and is thus a sound alternative to the miniaturization of conventional non-contacting shorts. To aid in high-frequency design, a rigorous full-wave analysis has been completed which will allow variations of the size, number and spacing of the holes to be easily analyzed. This paper will review the backshort design and the method developed for theoretical characterization, followed by a comparison of the experimental and numerical results. Low frequency models operating from 4-6 GHz are shown to demonstrate return loss of $> -0.2\ dB$ over a 33% bandwidth. The theory is in good agreement with measured data.

INTRODUCTION

Waveguides are used in a wide variety of applications covering a frequency range from 1 GHz to over 600 GHz. These applications include radar, communications systems, microwave test equipment, and remote-sensing radiometers for atmospheric and astrophysical studies. Components made from waveguides include transmission lines, directional couplers, phase shifters, antennas, and heterodyne mixers, to name a few. In addition to the many commercial applications of waveguides, NASA needs such components in radiometers operating up to 1200 GHz for future space missions, and the Department of Defense is interested in submillimeter wave communications systems for frequencies near 1000 GHz.

One of the most frequent uses of waveguide is as a variable length transmission line. These lines are used as tuning elements in more complex circuits. Such a line is formed by a movable short circuit, or backshort, in the waveguide. A conventional approach is to use a contacting backshort where a springy metallic material, such as beryllium copper, makes DC contact with the broadwalls of the waveguide. The contacting area is critical, however, and must be maximized to produce an acceptable short circuit. These backshorts are excellent in that they provide a good short circuit over the entire waveguide band. The contacting areas can degrade, however, due to wear from sliding friction. It is also extremely difficult to get a uniform contact at frequencies above 300 GHz, where the waveguide dimensions become 0.5 mm x 0.25 mm for the 300-600 GHz band.

An alternative approach is the *non*-contacting backshort shown in Figure 1. A thin dielectric layer (such as mylar) prevents contact and allows the backshort to slide smoothly. In order to produce an rf short and, hence, a large reflection, this backshort has a series of high- and low-impedance sections which are approximately $\frac{\lambda_g}{4}$ in length, where λ_g is the guide wavelength. The rf impedance of this design is given approximately by [1]

$$Z_{rf} = \left(\frac{Z_{low}}{Z_{high}}\right)^n Z_{low} \qquad (1)$$

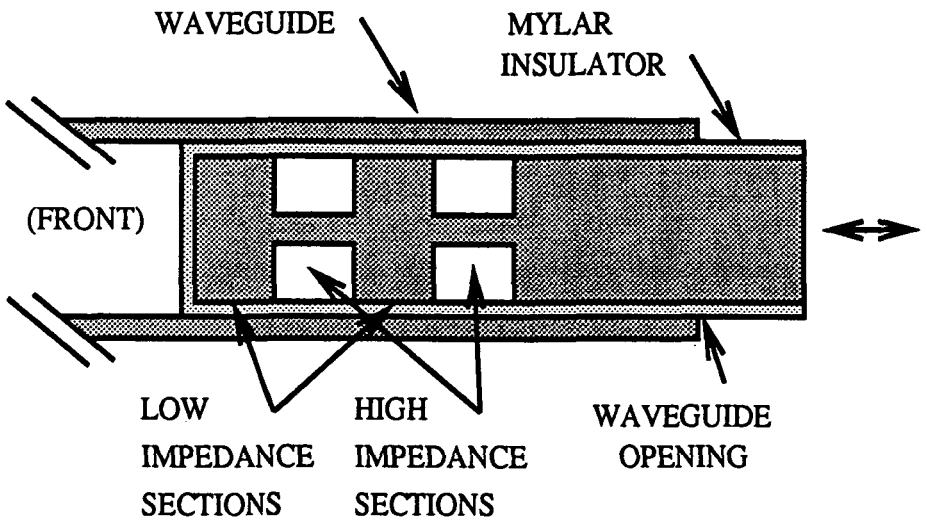

Figure 1: Cross sectional view of a conventional non-contacting backshort.

where Z_{low} is the impedance of the thick (low-impedance) sections, Z_{high} is the impedance of the thin (high-impedance) sections, and n is the number of sections. Beginning near 100 GHz, the thin high-impedance sections become difficult to fabricate, and fabrication may not even be feasible beyond 300 GHz. It would also be difficult to have the short slide snugly inside the waveguide at these high frequencies, as the thin sections would be very weak. To circumvent these problems, a novel non-contacting backshort design has recently been developed [2, 3] which is suitable for millimeter and submillimeter wave operation. It is a mechanically rugged design which can be easily fabricated for frequencies from 1 to 1000 GHz, and is thus a sound alternative to the miniaturization of conventional non-contacting shorts. Previously, however, the new backshort was optimized empirically using low-frequency models. This paper will discuss the new design and outline a new method developed for theoretical characterization. The formulation is a rigorous full-wave analysis which involves both mode-matching techniques and a coupled set of space domain integral equations. A description of the experimental setup is included, followed by a comparison of experimental and theoretical results. The new theoretical formulation fits these results well.

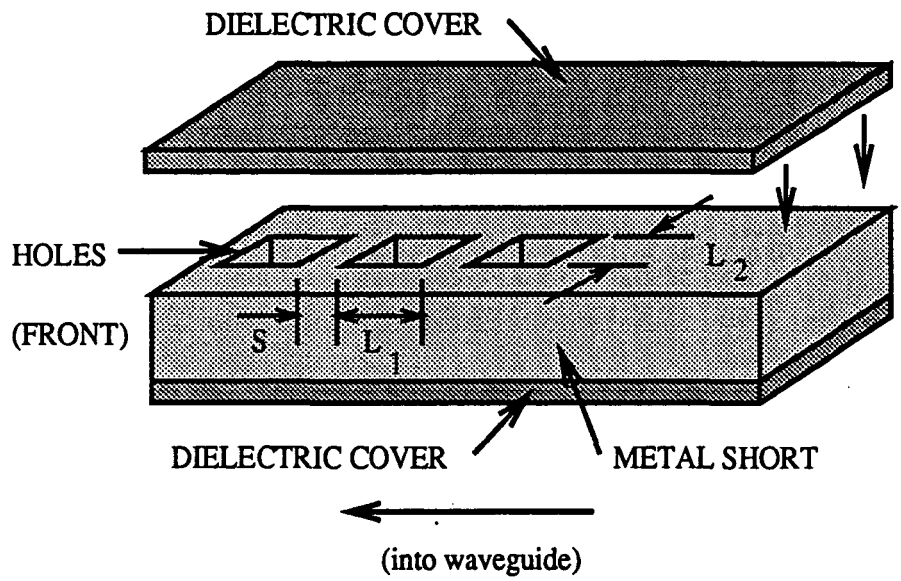

Figure 2: The new non-contacting backshort design, shown with three rectangular holes. The size, shape, and spacing of these holes are important in determining the rf properties of the short. S is the spacing, L_1 is the length, and L_2 is the width of each hole. The front of the backshort is inserted into the waveguide opening.

NOVEL NON-CONTACTING BACKSHORT DESIGN

The novel non-contacting backshort has the merits of easy fabrication up to Thz frequencies, flexibility of design, and very good performance over relatively broad bandwidths. The important features are briefly reviewed here. In order to obtain a large reflection, a non-contacting backshort must provide a periodic variation of guide impedance on the correct length scale. This is accomplished in the new design by either rectangular or circular holes, with the proper dimensions and spacing, cut into a metallic bar. A representative design is shown in Figure 2. This bar is sized to fill the waveguide cross-section and slide smoothly with a dielectric (mylar) insulator along the broadwalls. The holes replace the thin-metal, high-impedance sections in the conventional design shown in Figure 1. Since the holes extend completely through the bar, this yields a higher impedance than the corresponding sections in the conventional design. Thus, the high-to-low impedance ratio is larger in the new design. In addition, the electromagnetic fields are concentrated near the central axis of

calculated return loss for a backshort with no holes, inserted about 4.5 inches into the end of the waveguide, and covered with mylar ($\epsilon_r = 3.35$). The waveguide opening is assumed to present a 0 Ω impedance (i.e., it is covered with a metallic plate). Although the gap height is only 2.5% of the waveguide height, roughly 65% of the incident power is lost at resonance due to finite conductor and dielectric loss. The utility of the holes, then, is to minimize or eliminate these dropouts.

THEORETICAL CHARACTERIZATION

The theoretical characterization of the JPL backshort design is performed using a combination of two well known full-wave analysis methods, namely mode-matching and the application of equivalent magnetic currents in a space domain integral equation. In what follows, the approach will be outlined and the major governing equations presented. It is noted here that the symmetry of the backshort about the x-z plane (parallel to the plane of the waveguide broadwalls) has been utilized to reduce the number of unknown parameters. Furthermore, only rectangular holes (not round) have been considered in order to simplify the analysis. Neither of these points, however, are necessary restrictions in the formulation.

A discussion of the analysis is aided by the schematic in Figure 4, which represents the cross-sectional view of a backshort with two holes, inserted a distance d into the end of a rectangular waveguide. The structure is symmetric about the x-z plane, with equal dielectric regions (which are the dielectric covers shown in Figure 2) above and below the metal short. The problem of interest is to determine the reflection coefficient for the dominant waveguide mode, travelling in the $+z$ direction, at the front of the backshort ($z = 0$).

The formulation is based on the decomposition of the problem into two primary components. In the first part, we wish to compute the scattering matrix $[S]$ at $z = 0$, as depicted in Figure 4. As $[S]$ represents simply the scattering at a waveguide discontinuity, the presence of the holes may be neglected and thus becomes decoupled from the problem at hand. The

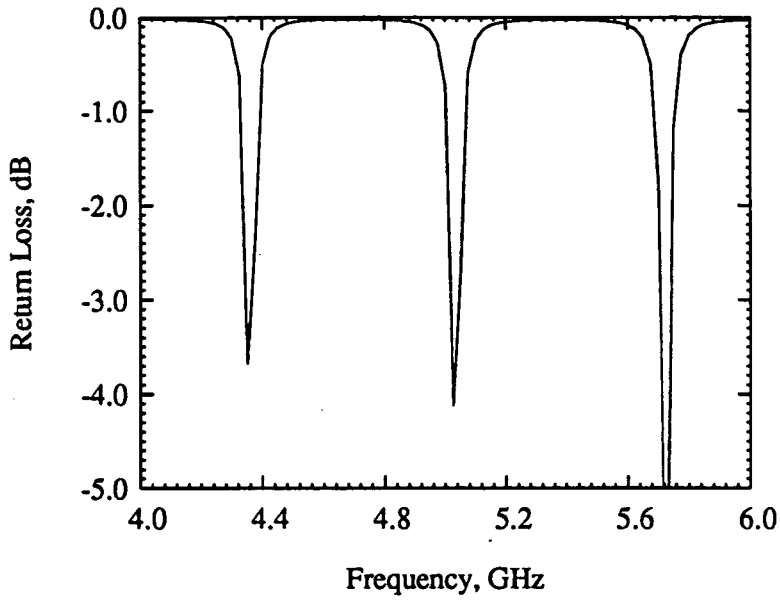

Figure 3: Calculated return loss versus frequency for a backshort with no holes, where the gap height is 2.5% of the total guide height.

the waveguide, such that the holes are effective in producing large correlated reflections, and thus acting as an efficient rf short. The new design is also easy to fabricate and can be used at any frequency between 1 GHz and 1000 GHz. For very high frequencies, above 300 GHz, the metallic bar is a piece of shim stock polished to the correct thickness. The holes can be formed by drilling, punching, or laser machining, or they can be etched using common lithography techniques.

It is important to note that the holes are a *critical* factor in obtaining efficient reflection from the non-contacting short. With the backshort inserted in the waveguide, a cavity forms between the metal bar and the broadwall of the waveguide, in the region occupied by the dielectric insulator. This cavity is terminated by the large discontinuities at the front of the short and at the waveguide opening. (This is more clearly illustrated in Figure 1 for the conventional design.) Deep dropouts in the return loss will occur at frequencies for which this cavity resonates, even though the height of each gap may be only a small fraction of the total waveguide height. The effect is well illustrated in Figure 3, which shows the

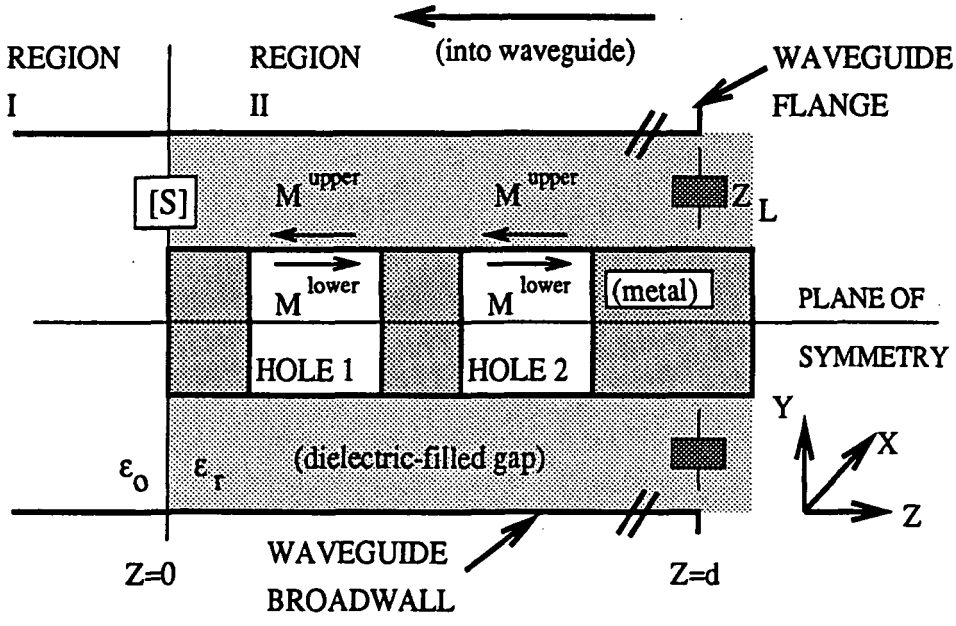

Figure 4: Cross-sectional schematic diagram (not to scale) of a two-hole non-contacting backshort, inserted a distance d into the end of a waveguide. The waveguide broadwalls are on the top and bottom in the figure.

well documented mode-matching method, which has been used to solve a variety of waveguide problems [4, 5, 6] is applied to determine $[S]$. With this method, the fields at each side of the reference plane ($z = 0$) are expanded in infinite series of orthogonal mode pairs (e.g. TE-to-z and TM-to-z), and continuity of the tangential electric and magnetic fields is enforced to determine the scattered field amplitudes. This results in the following set of generalized equations,

$$\sum_{n,m}^{\infty}(a_e^I + b_e^I)\vec{\Phi}_e^{E,I} + \sum_{n,m}^{\infty}(a_m^I + b_m^I)\vec{\Phi}_m^{E,I} = \sum_{n,m}^{\infty}(a_e^{II} + b_e^{II})\vec{\Phi}_e^{E,II} + \sum_{n,m}^{\infty}(a_m^{II} + b_m^{II})\vec{\Phi}_m^{E,II} \quad (2)$$

$$\sum_{n,m}^{\infty}(a_e^I - b_e^I)\vec{\Phi}_e^{H,I} + \sum_{n,m}^{\infty}(a_m^I - b_m^I)\vec{\Phi}_m^{H,I} = \sum_{n,m}^{\infty} -(a_e^{II} - b_e^{II})\vec{\Phi}_e^{H,II} + \sum_{n,m}^{\infty} -(a_m^{II} - b_m^{II})\vec{\Phi}_m^{H,II} \quad (3)$$

where (2) satisfies continuity of tangential $\vec{E}$ and (3) satisfies continuity of tangential $\vec{H}$. In the above, a and b represent the coefficients for waves travelling toward and away from the reference plane, respectively. The subscripts e and m are for TE-to-z and TM-to-z, while

the superscripts denote the field type (electric or magnetic) as well as the region to which they pertain (to the left or right of the reference plane). The vector functions Φ contain the appropriate constants and x- and y-dependencies for the transverse components of the respective fields. At this point inner-products are formed using $\vec{\Phi}_e^{E,I}$ and $\vec{\Phi}_m^{E,I}$ with (2), and $\vec{\Phi}_e^{H,II}$ and $\vec{\Phi}_m^{H,II}$ with (3). As these inner-products involve integration over the guide cross-section, a system is linear equations results due to the orthogonality of the modal components. This system is assembled into a matrix representation and, after inversion, the solution is expressed as

$$\{b\} = \{a\}^T [S] \tag{4}$$

With $[S]$ determined, the unknown scattered-field amplitudes $\{b\}$ are found from (4) given the known incident-field amplitudes, $\{a\}$. It is noted that the presence of a termination at $z = d$ (see Figure 4) is easily accounted for by assigning

$$b^I = a^I S_{11} + a^I S_{12}(I - \Gamma_L S_{22})^{-1}\Gamma_L S_{21}, \tag{5}$$

where I is the identity matrix and $[\Gamma_L]$ is a matrix which accounts for the reflection at $z = d$. As shown in the figure, we assume that the waveguide opening is terminated in a complex load Z_L for simplification. (This approximation is necessary because the conditions outside the short are difficult to control experimentally and, likewise, difficult to accurately characterize analytically. This will be discussed further in the section on results.) The matrix $[\Gamma_L]$ is thus a diagonal matrix of elements

$$(\Gamma_L)_{i,i} = \frac{Z_L - Z_g^i}{Z_L + Z_g^i} e^{-2\gamma_z^i d} \tag{6}$$

In (6), Z_g^i and γ_z^i are the guide impedance and propagation constant, respectively, for the i^{th} TE/TM mode. Conductor and dielectric loss may be included in the factor γ_z^i.

The second principle step in the formulation is to apply the space domain integral equation technique to solve the boundary value problem at the aperture of each of the holes. The

introduction of the equivalent magnetic currents, $\vec{M}^{upper}$ and $\vec{M}^{lower}$ (see Figure 4), allows the hole openings to be closed by an imaginary metallic surface, provided that no natural boundary conditions are violated. This is a crucial step in that it transforms the backshort structure into a combination of a simple rectangular waveguide, which is the dielectric-filled gap region, and a series of isolated metallic cavities, which are the holes. These unknown magnetic currents radiate electromagnetic fields in the dielectric region, and a modified form of (5) therefore results when treating a backshort with holes. The new expression is

$$\begin{aligned} b^I &= a^I S_{11} + a^I S_{12}(I - \Gamma_L S_{22})^{-1}\Gamma_L S_{21} + \\ &\quad \{(F^{>}\Gamma_L + F^{<})S_{22}(I - \Gamma_L S_{22})^{-1}\Gamma_L + F^{>}\Gamma_L + F^{<}\}S_{21}. \end{aligned} \tag{7}$$

Note that the only unknown variables in this equation are $F^{<}$ and $F^{>}$, as the components of the matrix $[S]$ and $[\Gamma_L]$ have previously been determined. These unknown components are functions of the imposed equivalent magnetic currents.

The solution for the unknown surface currents is uniquely determined by enforcing continuity of the total tangential fields across the hole apertures. This insures that the natural boundary conditions of the original problem are preserved. Continuity of the tangential electric field is satisfied immediately by setting $\vec{M}^{upper} = -\vec{M}^{lower} = \vec{M}$. Assuming a backshort with N holes, continuity of the magnetic field at the k^{th} hole leads to the following space domain integral equation (SDIE) in the unknown $\vec{M}$:

$$\begin{aligned} -\hat{n} \times \vec{H}^{inc} &= \hat{n} \times \{\vec{H}^{scat} + \\ &\quad \sum_{n=1}^{N} \left(\int\int_{S_n} ds' (\frac{j}{\omega\epsilon\mu}(k^2 \bar{\bar{I}} + \nabla\nabla) \cdot \bar{\bar{G}}_B) \cdot \vec{M}_n \right) + \\ &\quad \int\int_{S_k} ds' (\frac{j}{\omega\epsilon_o\mu}(k^2 \bar{\bar{I}} + \nabla\nabla) \cdot \bar{\bar{G}}_C) \cdot \vec{M}_k \} \end{aligned} \tag{8}$$

In the above, $\vec{H}^{inc}$ represents the known incident magnetic field, which results from scattering of the incoming wave at the waveguide step discontinuity (the reference plane). It is expressed

in terms of TE and TM modes, the coefficients being given by

$$\begin{aligned} a^{II} &= a^{I} S_{12}(I - \Gamma_L S_{22})^{-1}\Gamma_L \\ b^{II} &= a^{II} S_{22} \end{aligned} \tag{9}$$

for $+z$ and $-z$ travelling waves, respectively. $\bar{\bar{G}}_B$ and $\bar{\bar{G}}_C$ represent the dyadic Green's functions for an infinite rectangular waveguide and a metallic cavity, respectively. Closed-form expressions for these functions can be derived using well established boundary value formulations [7]. The use of an infinite-waveguide potential in the dielectric-filled gap region, which does not account for the actual finite length of uniform guide, is possible by considering the fields to be a superposition of *primary* and *scattered* components. The primary components satisfy boundary conditions at the source, and radiate away from $\vec{M}$ in the presence of matched conditions in either direction. These components are precisely those of the second term on the right hand side of (8). The scattered components are required to satisfy the boundary conditions away from the source, at the discontinuities at $z = 0, d$ and are also functions of $\vec{M}$. Expressions for these fields, which are represented by $\vec{H}^{scat}$ in (8), are similar in form to the primary components but also include factors from the scattering matrix $[S]$ and the matrix $[\Gamma_L]$.

The final step in the formulation is to solve the coupled set of integral equations which results from enforcing (8) over all N holes. This set may be reduced to a system of linear equations by applying the method of moments (Galerkin's method) [8]. This approach has been proven to yield excellent results and the convergence characteristics have been well documented [9, 10, 11]. Using this procedure, the aperture of each hole is first divided into discrete subsections using a rectangular grid. The unknown currents are then expanded in terms of overlapping subsectional rooftop basis functions of the form,

$$\vec{M} = \sum_{ij} \left(\hat{x} M^x_{ij} f_j(x') \phi_i(z') + \hat{z} M^z_{ij} \phi_j(x') f_i(z') \right) \tag{10}$$

$$f_n(w') = \begin{cases} \frac{sin[k\ (w'-w_{n-1})]}{sin(k\ l_n)} & \text{if } w_{n-1} < w' < w_n \\ \frac{sin[k\ (w_{n+1}-w')]}{sin(k\ l_n)} & \text{if } w_n < w' < w_{n+1} \end{cases}$$

$$\phi_n(w') = \begin{cases} 1 & \text{if } w_{n-1} < w' < w_{n+1} \\ 0 & \text{else} \end{cases}$$

where M_{ij}^x and M_{ij}^z are constant coefficients, l_n is the length of the n^{th} subsection in the w-direction, and k is the wave number in the medium. This expansion is inserted into the integral equation, and inner-products are then formed using weighting functions which are identical to the basis functions. The coupled equations are thereby reduced to the following matrix form:

$$\begin{pmatrix} \langle Y_{xx} \rangle & \langle Y_{xz} \rangle \\ \langle Y_{zx} \rangle & \langle Y_{zz} \rangle \end{pmatrix} \begin{pmatrix} \{M^x\} \\ \{M^z\} \end{pmatrix} = \begin{pmatrix} -\{\tilde{H}_x^{inc}\} \\ -\{\tilde{H}_z^{inc}\} \end{pmatrix} \tag{11}$$

where $\langle Y_{\zeta\xi}(\zeta, \xi = x, z) \rangle$ represents blocks of an admittance matrix. The unknown current coefficient vectors $\{M_{ij}^x\}$ and $\{M_{ij}^z\}$ are then determined by solving (11). With $\vec{M}$ determined, all elements of (7) may be computed and the solution is complete.

MEASUREMENT TECHNIQUES

The backshort design was optimized by testing the performance in WR-187 band waveguide (3.16 GHz - 6.32 GHz), for which the dimensions are 47.5 mm x 22.1 mm. The dielectric layer around the metal short was formed by stacking sheets of mylar tape. The magnitude and phase of the reflection coefficient were measured with an HP 8510B Vector Network Analyzer. A commercially available coaxial-to-waveguide transition connected the waveguide to the network analyzer. This measurement system was calibrated using two offset contacting shorts set at $\frac{\lambda_g}{8}$ and $\frac{3\lambda_g}{8}$, and a sliding waveguide load. Subsequent verification using a contacting short indicated a measurement error of about $\pm 0.2\ dB$ in the magnitude measurement.

RESULTS AND DISCUSSION

This section presents examples of measured data and analytical calculations. It will also address some conclusions drawn regarding the theoretical characterization and performance of the new design. Regarding the numerical aspects, the code developed to calculate the scattering matrix $[S]$ at the waveguide discontinuity agreed very well with results found in [12]. In particular, results were compared for the reflection coefficient from asymmetric (i.e., single-step) E-plane and H-plane waveguide junctions. The validation of the remainder of the theoretical formulation and the associated software was completed by comparison with measured data. Part of this validation included a study of convergence as a function of the hole (aperture) mesh size and the number of modes used in the dyadic Green's function expansions. It was found that using subsections which are approximately $\frac{\lambda_g}{16}$ on a side, where λ_g is the guide wavelength, yields a good compromise between accuracy and the requirements on storage and computation time. The number of modes for the Green's functions is kept ≥ 600.

The measurements performed to investigate the new design involved many variations on the size, shape, number, and spacing of the holes cut into the metal bar [2]. An additional test variable was the number of stacked mylar sheets used to form the dielectric layer. In many cases, the height of the backshort was such that a relatively large space was left between either side of the metal bar and the waveguide broadwalls. This large gap, combined with the variations in the mylar thickness, are used to help understand the effect that typical machining tolerances will have for operation at 200-300 GHz and above.

Results which are typical of the best performance to date are given in Figure 5b. This data is for a backshort with three rectangular holes, each with dimensions $L_1 = 19.3$ mm, $L_2 = 28.4$ mm and spacing $S = 8.7$ mm. The width and height of the bar are 47.5 mm and 19.7 mm, respectively, leaving a gap of 1.2 mm between the bar and the waveguide broadwalls. The measured results in Figure 5b were obtained using a total mylar thickness

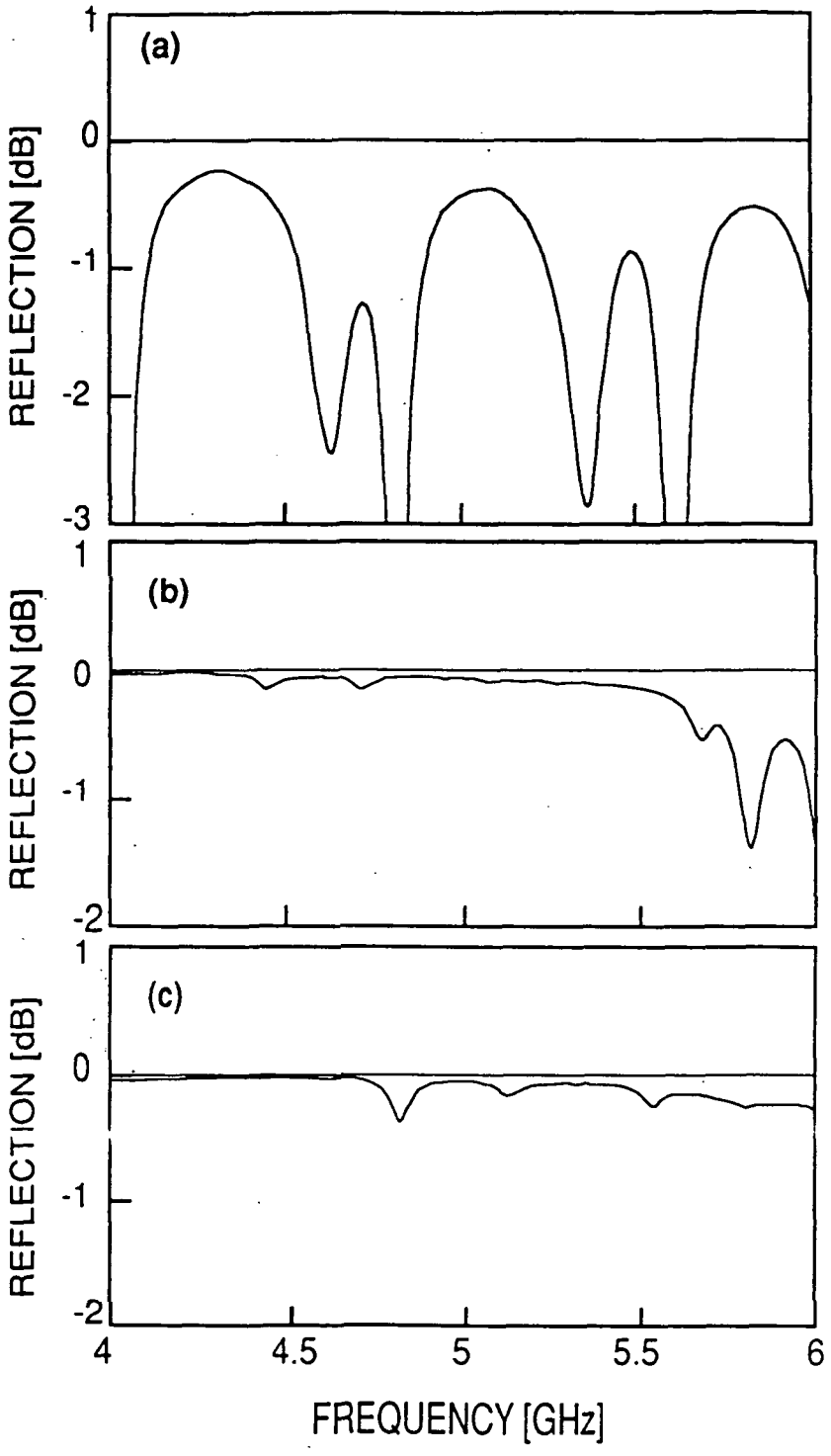

Figure 5: a) Reflected power measured from a solid bar without holes. This does not make a good backshort due to the several large dropouts across the frequency band. b) Reflected power measured from a backshort with three rectangular holes. The mylar is 0.89 mm thick. Excellent performance is obtained over a broad bandwidth. c) Same backshort as in (b), but mylar thickness has been reduced to 0.64 mm.

of 0.89 mm. The reflection coefficient in this case is greater than $-0.2\ dB$ (0.95 reflected power) over a 33% bandwidth centered around 4.8 GHz. For comparison, the measured results for the same backshort *without* holes are shown in Figure 5a. This data clearly illustrates the improvement from the holes. The complex structure of this response, relative to that shown in Figure 3, is caused by asymmetrical positioning of the bar inside the waveguide. Other measurements made with the gap completely filled by dielectric, which forced a near-symmetric positioning of the bar, agreed very well with our theory and were of the form shown in Figure 3. The effect of reducing the mylar thickness is seen in Figure 5c, which gives measured data using 0.64 mm of mylar. The large dropout near 5.8 GHz has been shifted out of band, due to the decrease in the effective dielectric constant. This response is comparable to that obtained for the conventional type of backshort shown in Figure 1. As expected, increasing the mylar thickness (and thus increasing the effective dielectric constant) moved the large dropouts lower in frequency.

Performance similar to that with rectangular holes could be obtained using circular holes. Results obtained with 3 circular holes and a mylar thickness of 0.89 mm demonstrated greater than 95% reflected power over a 32% bandwidth centered around 4.75 GHz. This is encouraging since round holes are easier to fabricate than rectangular holes for high frequencies.

Many other variations of the backshort parameters were tested. Also, the small dips around 4.5 GHz in Figure 5b, and those seen in Figure 5c, are currently being investigated. As noted for the plain metal bar, these dips may result from asymmetrical positioning of the backshort inside the waveguide [13]. A more extensive discussion of the systematic parameter variations, measurement observations, and comparisons with theory will be given at a later date. Some millimeter wave tests have also been performed and are discussed elsewhere [2].

In order to theoretically model the backshort performance, appropriate values were required for an effective dielectric constant, ϵ_r, and the terminating load impedance for the waveguide opening (Z_L in Figure 4). The problem of the dielectric constant arises because

the gap above and below the metal bar is only partially, and non-uniformly, filled by the mylar sheets. The transverse resonance technique [4] may be used to approximate ϵ_r by solving the exact inhomogeneous problem, and then assuming the entire guide is filled with some "average" material. (For the inhomogeneous case, a two-layer guide is assumed, where one layer is air-filled and the other is mylar-filled and of a thickness equal to the total mylar thickness.) A simpler approach, which yields higher values for the dielectric constant, is to merely compute ϵ_r based on the percentage of mylar relative to the total gap height. By numerical experimentation, it was found that the best approximation lies nearly midway between the two values. It is noted that obtaining an exact solution for a layered waveguide is not justified due to the unpredictable spacing of the various mylar sheets.

The other issue was determining the correct value for the load impedance, Z_L, to use in the calculations. Although an exact analysis is a formidable task, an approximate load impedance can be obtained to adequately model the waveguide discontinuity. This is done by first considering the exact impedance for a very thin aperture opening onto an infinite ground plane. For typical gap dimensions used here, this is a large, capacitive value, with real and imaginary parts which are both 3-5 times the dominant waveguide mode impedance. The extension of the backshort beyond the waveguide opening, however, will provide a better transition to free-space and effectively lower this impedance toward a better match. In many test cases, use of a normalized load impedance of $Z_L \approx 2.5 \pm .5 + j1$ in equation (6) yielded good agreement with the measured results. An important point, however, is that the predicted performance is nearly independent of Z_L in precisely the frequency bands where the backshort works well. This is as expected, as most of the incident power is reflected and never reaches the end of the guide. It follows that changes in Z_L do modify the dropout regions in the return loss, as these dropouts result from out-of-band power leaking past the backshort. (The performance of the bar without holes is likewise strongly dependent on Z_L. This fact can be used in determining an appropriate impedance for a given geometry, by

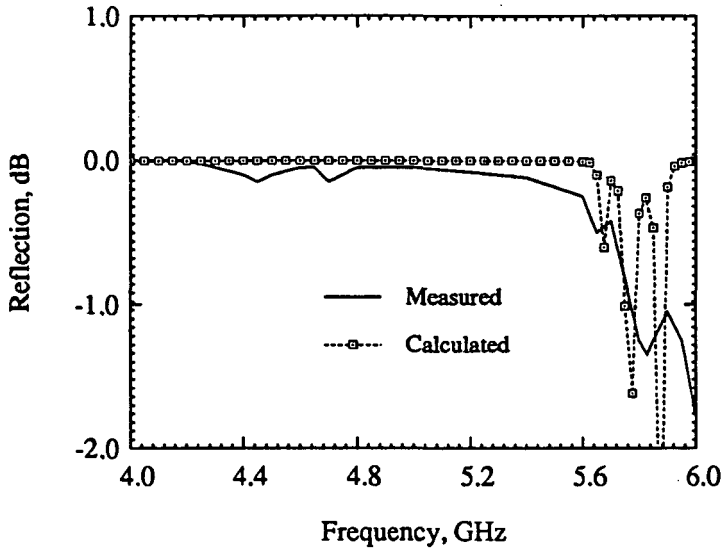

Figure 6: Measured data and calculated performance for the backshort with three rectangular holes. The mylar thickness is 0.89 mm.

comparing measured and theoretical results for various load values.)

A comparison between measured data and calculated performance is given in Figure 6. These results are for the backshort with three rectangular holes, using a mylar thickness of 0.89 mm. Very good agreement has been obtained. The broadening of the dropouts in the measured data, relative to the calculated results, is believed to be due Z_L and to loss in the measurement system which is not accounted for by the theory. The bandwidth is very accurately predicted, however, such that it should now be possible to design and analyze these backshorts for specific applications.

CONCLUSIONS

In summary, we have developed a theoretical analysis to predict the rf performance of a new non-contacting waveguide backshort. This backshort consists of a metallic bar with rectangular or circular holes which enhance the reflections of rf power. The simplicity of this design allows it to be easily scaled to millimeter wave and submillimeter wave frequencies. The new theoretical development is a rigorous full-wave analysis which employs a coupled set of space-domain integral equations and mode-matching techniques. Comparison between

theory and experiment on model backshorts optimized for best performance at 4-6 GHz show very good agreement.

ACKNOWLEDGEMENTS

This work was supported in part by the Jet Propulsion Laboratory, California Institute of Technology, under contract with the National Aeronautics and Space Administration, and the Innovative Science and Technology Office of the Strategic Defense Initiative Organization, and by the University of Michigan NASA Center for Space Terahertz Technology.

References

[1] Collin, R. E. *Foundations for Microwave Engineering*, New York: McGraw-Hill, 1966, pp. 259-262.

[2] McGrath, W. R. "A Novel Non-Contacting Waveguide Backshort for Millimeter and Submillimeter Wave Frequencies," *Conference Proceedings of the Second National Technology Transfer Conference*, NASA Conference Publication 3136, Vol. 1, pp. 161-168, December 1991.

[3] McGrath, W. R. "Non-contacting Waveguide Backshort," U.S. Patent pending.

[4] Itoh, Tatsuo (editor). *Numerical Techniques for Microwave and Millimeter-Wave Passive Structures*, John Wiley & Sons, 1989.

[5] Eleftheriades, G. V., Ali-Ahmad, W. Y., Katehi, P. B., and Rebeiz, G. M. "Millimeter-Wave Integrated-Horn Antennas: Part I - Theory", *IEEE Trans. A.P.* , vol. 39 , No. 11, November 1991, pp. 1575-1581.

[6] Masterman, P. H. and Clarricoats, P. J. B. "Computer field-matching solution of waveguide transverse discontinuities", *Proc. IEE*, vol. 118 , No. 1, January 1971, pp. 51-63.

[7] Collin, R. E. *Field Theory of Guided Waves*, Piscataway, NJ: IEEE Press, 1991, pp. 78-86.

[8] Harrington, R. F. *Field Computations by Moment Methods*, New York: Macmillan, 1968.

[9] Dib, N. I., Katehi, P. B., Ponchak, G. E., and Simons, R. N. "Theoretical and Experimental Characterization of Coplanar Waveguide Discontinuities for Filter Applications," *IEEE Trans. MTT* , vol. 39 , No. 5, May 1991, pp. 873-882.

[10] Dib, N. I., Katehi, P. B. "Modeling of Shielded CPW Discontinuities Using the Space Domain Integral Equation (SDIE)," *Journal of Electromagnetic Waves and Applications*, vol. 5 , No. 4/5, 1991, pp. 503-523.

[11] Dunleavy, L. P. "Discontinuity characterization in shielded microstrip: A theoretical and experimental study," Ph.D. Thesis, Radiation Laboratory, University of Michigan, Ann Arbor, 1988.

[12] Marcuvitz, N. *Waveguide Handbook*, vol. 10 of MIT Rad. Lab. Series, New York: McGraw-Hill, 1948.

[13] Kerr, A. R. "An Adjustable Short-Circuit for Millimeter Waveguides," *Electronics Division Internal Report No. 280*, National Radio Astronomy Observatory, Charlottesville, Virginia, July, 1988.

SILICON MICROMACHINED WAVEGUIDES FOR MILLIMETER AND SUBMILLIMETER WAVELENGTHS

Markus Yap,[1] Yu-Chong Tai,[1] William R. McGrath,[2] Christopher Walker [3]

1. Department of Electrical Engineering, California Institute of Technology, Pasadena, CA 91125
2. Center for Space Microelectronics Technology, Jet Propulsion Laboratory, California Institute of Technology, Pasadena, CA 91109
3. Department of Astronomy, University of Arizona, Tucson, AZ 85726

Abstract -- The majority of radio receivers, transmitters, and components operating at millimeter and submillimeter wavelengths utilize rectangular waveguides in some form. However, conventional machining techniques for waveguides operating above a few hundred GHz are complicated and costly. This paper reports on the development of silicon micromachining techniques to create silicon-based waveguide circuits which can operate at millimeter and submillimeter wavelengths. As a first step, rectangular WR-10 waveguide structures have been fabricated from (110) silicon wafers using micromachining techniques. The waveguide is split along the broad wall. Each half is formed by first etching a channel completely through a wafer. Potassium hydroxide is used to etch smooth mirror-like vertical walls and LPCVD silicon nitride is used as a masking layer. This wafer is then bonded to another flat wafer using a polyimide bonding technique and diced into the U-shaped half waveguides. Finally a gold layer is applied to the waveguide walls. Insertion loss measurements show losses comparable to those of standard metal waveguides. It is suggested that active devices and planar circuits can be integrated with the waveguides, solving the traditional mounting problems. Potential applications in Terahertz instrumentation technology are further discussed.

I. Introduction

Rectangular waveguide is a well characterized transmission medium which is used in a variety of complex rf components and circuits. Many sophisticated applications including radar, communications systems, test instruments, and heterodyne radiometers use waveguide components up to millimeter wave frequencies. The long history of development of waveguide components provides a broad base of knowledge to synthesize and evaluate new designs for higher frequencies.

Waveguide is typically fabricated from metals such as brass and copper using conventional machining techniques. However, at frequencies above a few hundred GHz, waveguide becomes so small (less than 0.3 mm x 0.15 mm for 500 GHz - 1000 GHz waveguide) that fabrication utilizing these conventional techniques is time consuming, costly and difficult. In addition, mounting active and passive devices such as mixer diodes, filters and planar probes on these waveguides is difficult.

A substantial research effort in recent years has been devoted to fabricating micromechanical structures in silicon using micromachining techniques. Moveable structures such as slider, gears, and spiral springs in the dimensional scale of 50-200 μm have been fabricated [1, 2]. We have taken a new approach in developing and adapting silicon micromachining techniques to create silicon-based waveguide circuits which can operate up to millimeter and submillimeter wavelengths.

As a first step we have started fabricating rectangular waveguides for frequencies between 100 GHz and 1000 GHz. Here we only emphasize WR-10 waveguides (operating at 75 GHz - 115 GHz) because it is compatible with our existing measurement equipment. Conventional WR-10 waveguide is a rectangular channel with inner wall dimensions of 0.1 x 0.05 inches. Our waveguide, however, is made of two half sections split along the broadwall as shown in Fig. 1. The reason for splitting the waveguide is to simplify the fabrication process and to facilitate integration of planar circuits and devices, which is further discussed in Section IV.

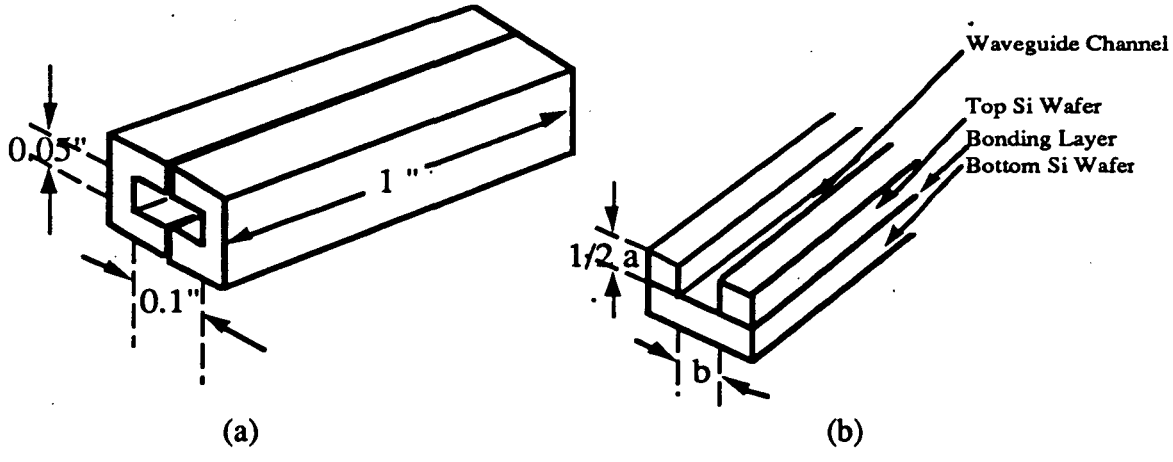

Fig. 1. a) The waveguide is split into 2 half sections.
b) One half section of a waveguide.

II. Fabrication Process

The fabrication process for the half sections with emphasis on the cross section is shown in Fig. 2. A thick (0.05 inches) double-side polished silicon wafer with (110) surface orientation is used. The major flat has a normal in the [111] direction within 0.4°. After a standard piranha-bath cleaning, a 1000 Å Low Pressure Chemical Vapor Deposited (LPCVD) silicon nitride layer is deposited on both sides of the wafer. Photolithographic techniques are then utilized to pattern the waveguide etching windows. Photoresist is used as a masking layer for etching the silicon nitride windows with an SF_6 plasma. The silicon nitride is used as an etching mask to define b, the waveguide height, shown in Fig. 1b. After removal of the photoresist using acetone solvent as shown in Fig. 2a, the wafer is put in a reflux system and etched in a water based solution of 40 % KOH at 80 °C. Figure 2b shows the wafer after it has been etched completely through to form half of the waveguide. The etching rate of (110) silicon in this KOH solution is 2 μm/min and the etching ratio of (110):(111) planes is 170:1. At this rate 0.05 inches (1270 μm) of silicon is etched thru in ~11 hours. Following removal of the nitride mask using hot hydrophosporic acid at 150 °C, a polyimide bonding technique is used to glue these etched grooves to a smooth silicon wafer with an identical thickness (0.05 inches) as shown in Fig. 2c. The wafer is then diced into pieces of half waveguides. Such a half waveguide is shown in Fig. 2d. Metalization is done by first depositing a thin (200 Å) chrome layer followed by a thicker (5000 Å) gold layer on the waveguide walls using vacuum evaporation. Further metalization is done by electroplating gold to a thickness of ~3 μm to reduce rf conduction losses.

III. Experimental Results

In order to perform insertion loss measurement, we designed a pair of brass mounting blocks. The two waveguide half-sections are put on the brass mounting blocks and mated together. This allows the silicon waveguide to be connected to microwave test equipment using conventional waveguide flanges. The silicon waveguides are rugged and can be firmly clamped to metallic flanges. The insertion loss of the WR-10 waveguide is measured over a frequency range of 75 GHz to 110 GHz. The measurement system is shown in Fig. 3. The source is a BWO which produces several milliwatts. A reference sweep is first taken without the waveguide. This is compared to a sweep with the waveguide inserted between the source and detector. The insertion loss for a 2.5 cm long section of waveguide is shown in Fig. 4 (the small wiggles in these curves are noise and do not reflect any resonances in the waveguide components). The measured loss is about 0.05 dB per wavelength (at 100 GHz) across most of the band. This is very good performance and is comparable to the result for commercially available waveguide which shows a loss of about 0.024 dB per wavelength. The small difference of 0.026 dB per wavelength is most probably due to differences in the quality of the gold plated surfaces. Our evaporated gold showed small pits which were still present in the plated layer. Also there was no gold on the ends of the silicon waveguide where contact was made to the metallic flanges of the test equipment. We expect improvements in the gold surface to be directly reflected in improvements in the rf losses.

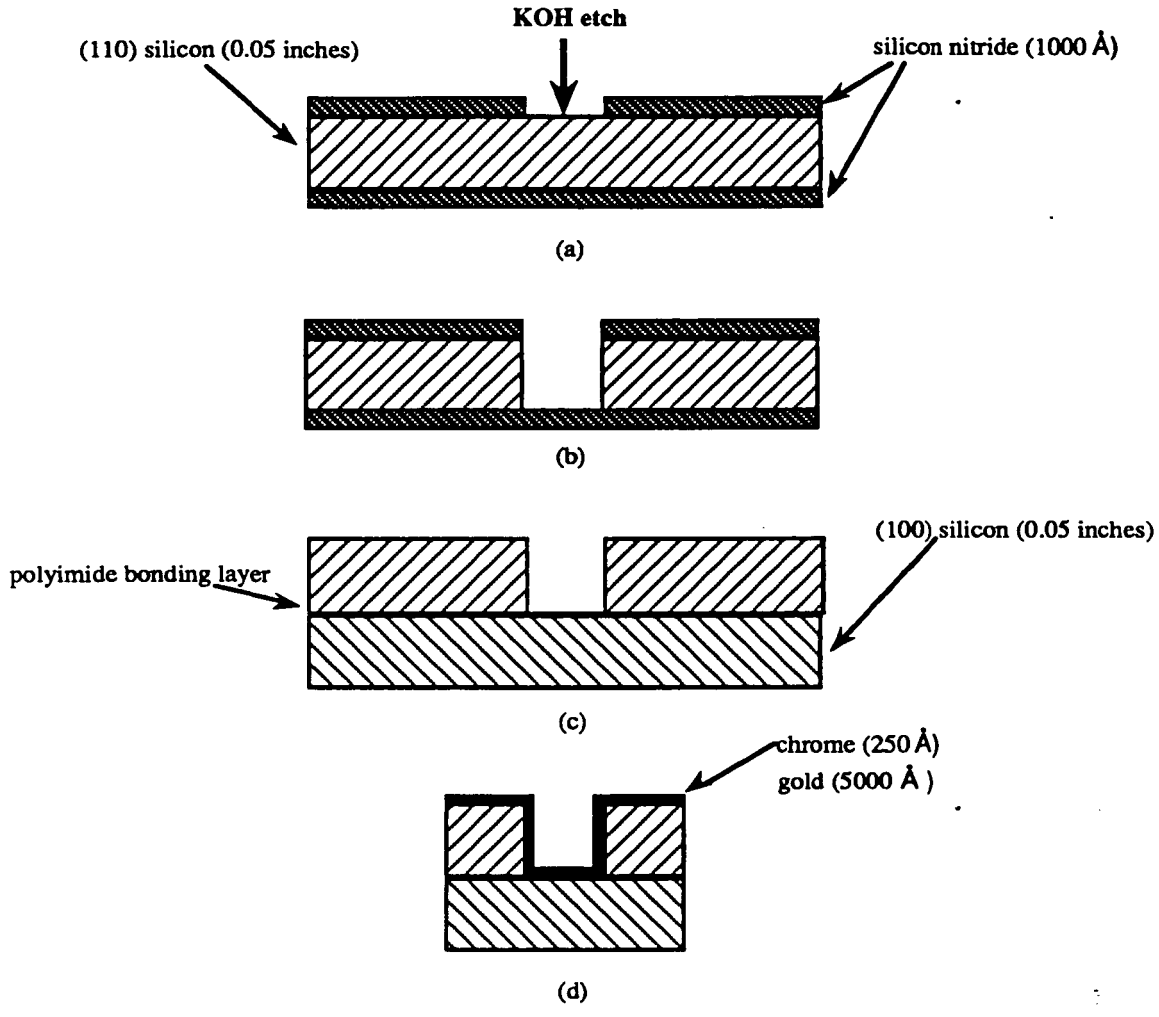

Fig. 2. A cross section view of the fabrication process.

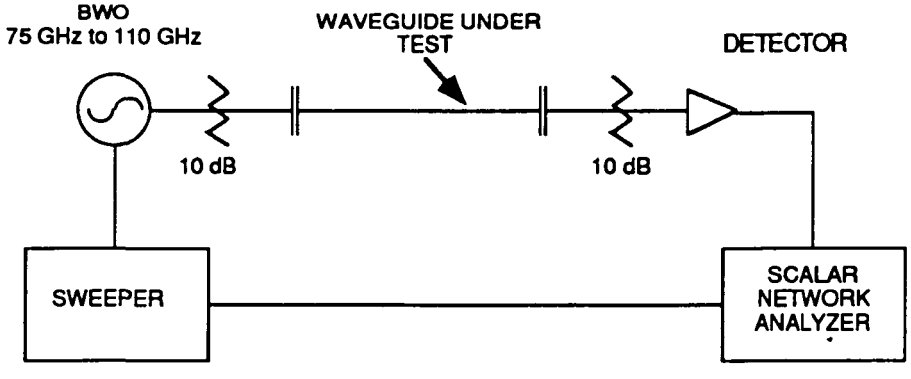

Fig. 3. Block diagram of millimeter wave insertion loss test system.

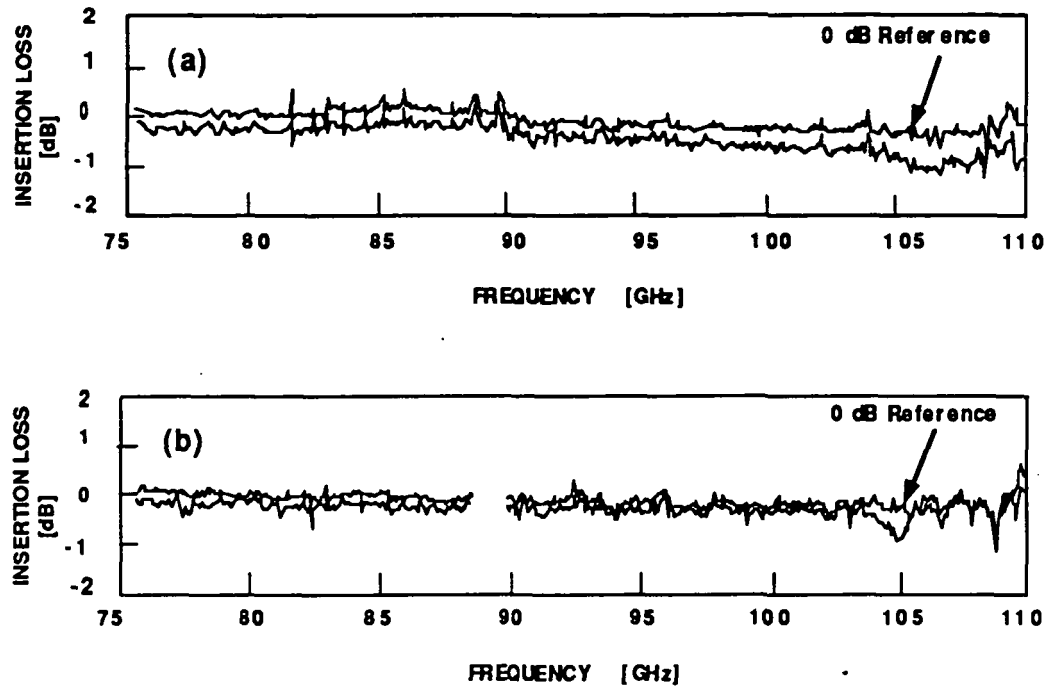

Fig. 4. (a) Measured loss of a 2.5 cm long section of Si-based WR-10 waveguide. The surface of the silicon was metallized with approximately 3 μm of gold to reduce rf losses. (b) Measured loss of a 2.5 cm long section of conventional metallic waveguide.

IV. Discussion

Waveguide circuits are preferable at frequencies above 100 GHz since waveguide has the advantage of adjustable rf tuning. This solves the difficulties of accurately designing fixed-tuned planar microwave integrated circuits. Unfortunately, millimeter and submillimeter waveguide components are hard to manufacture by conventional machining techniques. We have shown here the feasibility of making silicon waveguides. It is also possible to use silicon micromachining techniques to fabricate other components such as: directional couplers, waveguide transformers, waveguide-to-planar circuit transitions, low-loss filters, rectangular and conical feedhorns, and dichroic plates. This wide variety of waveguide components will become the building blocks for complicated circuits. For example, complex mixer and frequency multiplier embedding circuits can be built. These are important for ground-based and space-based radar, communications, and remote-sensing applications.

Silicon micromachined waveguide components have several important advantages: 1) These structures are produced by projecting the desired pattern onto silicon with photolithographic techniques. Therefore waveguides with dimensions suitable for use above 100 GHz can be easily fabricated. 2) Dimensional accuracy is in the order of a few microns, which is essential for the fabrication of high-Q components. 3) The waveguide walls would be atomically smooth, thereby minimizing rf losses [3]. 4) Several versions of a single component (with variations of a critical parameter) can be produced at the same time on a single wafer. This would allow for rapid optimization and reduced cost compared to conventional machining techniques where only one variation at a time is produced. 5) Most importantly, active and passive devices can be integrated with the waveguide. For example, a thin (~ 1μm) rf transparent silicon nitride membrane can be fabricated across the end of the waveguide or parallel to its length in the E-field direction. Active devices such as Schottky diodes and SIS tunnel junctions as well as micromechanical rf tuning elements[1, 4] can then be fabricated directly on the membrane as shown schematically in Fig. 5. This would eliminate the long-standing problem of mounting the devices and would represent a significant advance for waveguide technology.

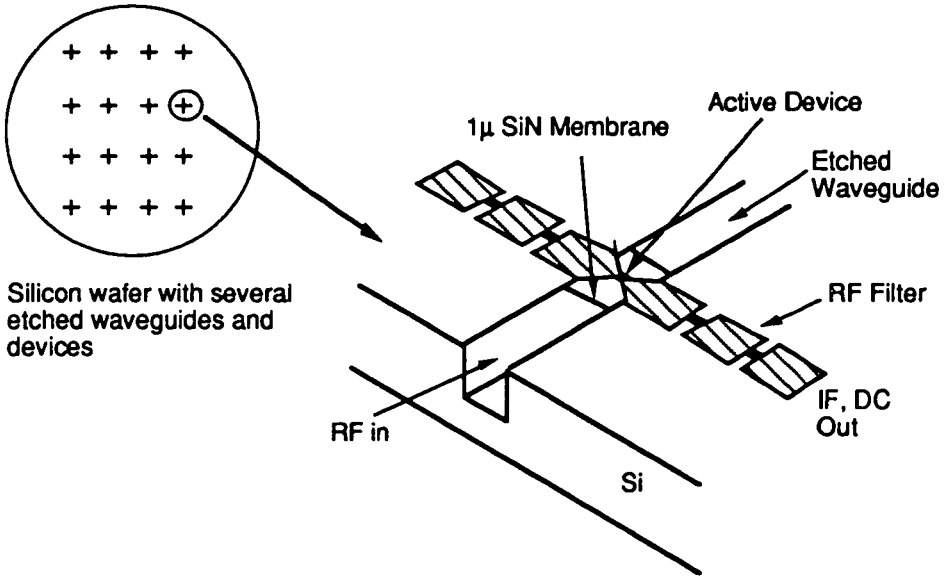

Fig.5 A schematic view of an integrated waveguide circuit. Several waveguide components can be produced on a single wafer. Active devices and planar circuits can be integrated directly on thin membranes spanning the waveguide. Micromechanical rf tuning elements can also be included in the waveguide.

Currently, we are fabricating WR-10 waveguides with SiN membranes in between the two half pieces of the waveguide. Metalization of the half sections of these waveguides will require selective plating of the silicon walls without plating the silicon nitride membranes. Tungsten substitution of silicon in an LPCVD environment [5] is proposed to meet this need. In this process, tungsten hexafluoride (WF_6) gas attacks silicon surface and a thin layer of tungsten atoms substitute for silicon atoms on the surface. Further metalization can be done by electroplating the tungsten surface with gold.

V . Summary

We have demonstrated a new approach in fabricating waveguide circuits using silicon micromachining technology. In particular, we have fabricated a 100 GHz silicon rectangular waveguide. The insertion loss of 0.05 dB/λ is comparable to a commercially available metal waveguide. As we improve our plated gold quality, we expect to improve the insertion loss. We have also proposed a new approach of integrating active/passive devices and micromechanical rf tuning elements with waveguide.

This work is supported in part by California Institute of Technology President's Fund under grant PF-347 and the Jet Propulsion Laboratory, California Institute of Technology, under contract with the National Aeronautics and Space Administration and the Innovative Science and Technology Office of the Strategic Defense Initiative Organization.

References

[1]. L.-S. Fan, Y.-C. Tai, and R. S. Muller, "Integrated Movable Micromechanical Structures for Sensors and Actuators," *IEEE Trans. on Electron Devices,* vol. 35, pp. 724-730, June 1988.

[2]. M. Mehregany, K. J. Gabriel, and W. S. N. Trimmer, "Integrated Fabrication of Polysilicon Mechanisms," *IEEE Trans. on Electron Devices,* vol. 35, pp. 719-730, June 1988.

[3]. F. J. Tischer, "Experimental Attenuation of Rectangular Waveguides at Millimeter Wavelengths," *IEEE Trans. Microwave Theory and Tech.,* vol. MTT-27, pp. 31-37, January 1979.

[4]. V. M. Lubecke, W. R. McGrath, and D. B. Rutledge, " Sliding Backshorts for Planar Circuits," *International Journal of Infrared and Millimeter Waves,* vol. 12, pp. 1387-1397, December 1991.

[5]. N. Kobayashi, M. Suzuki, and M. Saitou, "Tungsten Plug Technology Using Substitution of W for Si," *IEEE Trans. on Electron Devices*, vol. 37, pp. 577-582, March 1990.

This is intended as a review paper only and it summarizes work which has been submitted for publication in the *IEEE Transactions on MTT*.

PROGRESS IN INTEGRATED-CIRCUIT HORN ANTENNAS FOR RECEIVER APPLICATIONS

PART 1: Antenna Design

George V. Eleftheriades, Walid Y. Ali-Ahmad, and Gabriel M. Rebeiz

NASA/Center for Space Terahertz Technology
Electrical Engineering and Computer Science Department
University of Michigan
Ann Arbor, MI 48109-2122

ABSTRACT

The purpose of this work is to present a systematic method for the design of multimode quasi-integrated horn antennas. The design methodology is based on the Gaussian beam approach and the structures are optimized for achieving maximum fundamental Gaussian coupling efficiency. For this purpose, a hybrid technique is employed in which the integrated part of the antennas is treated using full-wave analysis, whereas the machined part is treated using an approximate method. This results in a simple and efficient design process. The developed design procedure has been applied for the design of a 20dB, a 23dB and a 25dB quasi-integrated horn antennas, all with a Gaussian coupling efficieny exceeding 97%. The designed antennas have been tested and characterized using both full-wave analysis and 90GHz/370GHz measurements.

I. QUASI-INTEGRATED HORN ANTENNA DESIGN : INTRODUCTION

The integrated-circuit horn antenna was introduced in [1] and analyzed using a full-wave analysis technique in [2]. It consists of a dipole (or monopole) feed evaporated on a thin dielectric membrane which is suspended in a pyramidal cavity etched in silicon or GaAs. Recently, this antenna has been used in several millimeter and submillimeter-wave applications including a double-polarized antenna design at 93GHz [4], a 256 element imaging array at 802GHz [5], and a monopulse tracking system at 94GHz [6]. However, the wide flare-angle of the integrated-circuit horn antenna, which is dictated by the anisotropic etching involved in its fabrication (70° in silicon), limits its useful aperture size to 1.6λ and its gain to 13dB. To this end the quasi-integrated horn antenna was introduced [3], which consists of a machined small flare-angle pyramidal section attached to the integrated portion (fig.1). The resulting structure is a simple multimode pyramidal horn with circularly symmetric patterns, high gain, and low cross-polarization, which is particularly attractive for submillimeter quasi-optical receiver applications. The minimum machined dimension involved in its fabrication is around 1.5λ which enables its fabrication to frequencies up to 2THz. The purpose of this paper is to describe a systematic approach towards the design of these horn antennas, and to provide a full range of practical quasi-integrated horn antenna designs along with their detailed radiation characteristics. Since a very desirable property of antennas intended for use in quasi-optical systems is the high Gaussian content of their radiated fields [7], the developed design methodology is based on the optimization of the quasi-integrated horns for achieving maximum fundamental Gaussian coupling efficiency. The Gaussian coupling efficiency is particularly important in quasi-optical receiver applications because it directly influences the total system performance with a pronounced effect on the receiver noise temperature [8].

II. MULTIMODE APERTURE ANALYSIS FOR MAXIMUM FUNDAMENTAL COUPLING EFFICIENCY

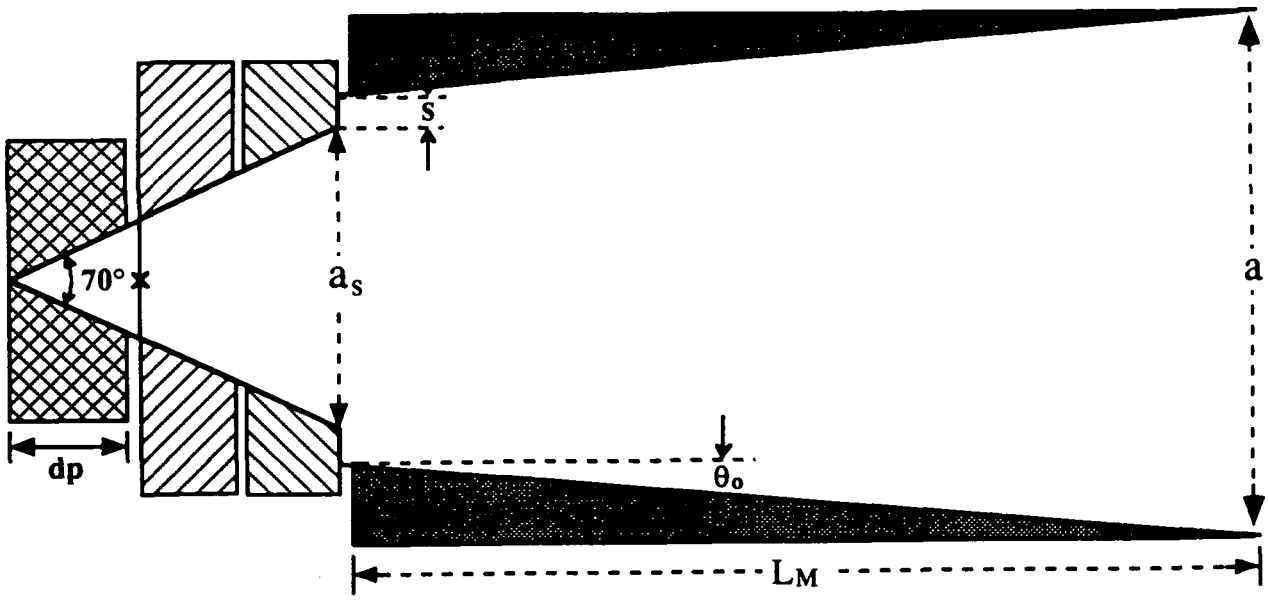

Fig.1 The general configuration of the quasi-integrated multimode horn antenna.

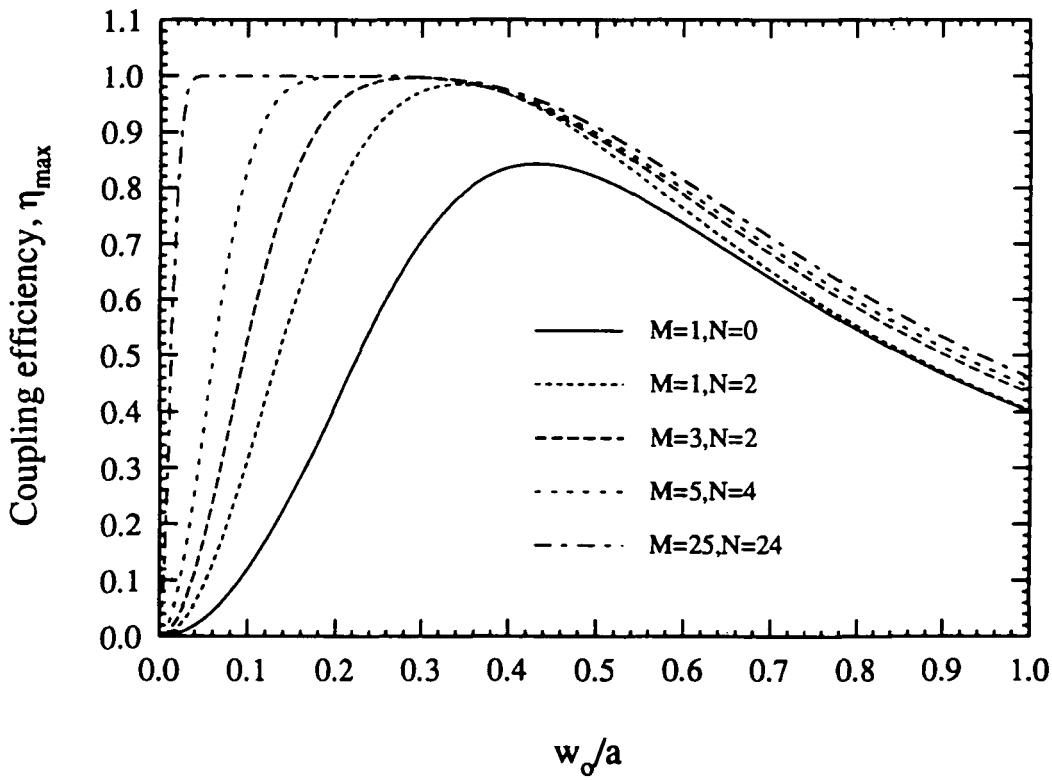

Fig.2 The maximum Gaussian coupling efficiency as a function of the w_o/a ratio for various aperture modes available for beamshaping (up to $TE_{M,N}/TM_{M,N}$, m = 1, 3 ... M, n = 0, 2 ... N) .

Consider a square aperture of side a in a ground-plane which is radiating in the half-space $z > 0$. The transverse electric field of the aperture at $z = 0$ can be expanded in terms of the eigenfunctions of a square waveguide of the same side a :

$$\bar{E}_{t,ap}(x,y) = \sum_{m,n}^{M,N} \{A_{mn}\bar{e}^{TE}_{mn}(x,y) + C_{mn}\bar{e}^{TM}_{mn}(x,y)\} \quad . \tag{1}$$

In (1) it is assumed that only modes with indices ($m = 1,3,5 \ldots M$ and $n = 0,2,4,6 \ldots N$) are present as is the case of a pyramidal horn which is either fed by a centered Hertzian dipole or by a waveguide which supports only the dominant TE_{10} mode [2]. We now proceed to determine the modal coefficients A_{mn}, B_{mn} so that the coupling between the aperture field and a fundamental beam is maximized. If the copolarized and cross-polarized components of the aperture field are defined to be the $\bar{E}_{x,ap}$ and the $\bar{E}_{y,ap}$ components respectively, then the transverse electric field can be rewritten in the form :

$$E_{y,ap}(x,y) = \sum_{m,n}^{M,N} d^{co}_{mn}\Psi^{co}_{mn}(x,y) \quad , E_{x,ap}(x,y) = \sum_{m,n}^{M,N} d^{xp}_{mn}\Psi^{xp}_{mn}(x,y) \tag{2}$$

where the orthonormalized copolarized and cross-polarized hybrid modes Ψ^{co}_{mn}, Ψ^{xp}_{mn} are:

$$\Psi^{co}_{mn}(x,y) = \frac{\sqrt{2\epsilon_n}}{a}(-1)^{\frac{m+n-1}{2}}\cos(\frac{m\pi x}{a})\cos(\frac{n\pi y}{a}) \quad , |x| \le a/2, |y| \le a/2 \tag{3}$$

$$\Psi^{xp}_{mn}(x,y) = \frac{\sqrt{2\epsilon_n}}{a}(-1)^{\frac{m+n+1}{2}}\sin(\frac{m\pi x}{a})\sin(\frac{n\pi y}{a}) \quad , |x| \le a/2, |y| \le a/2 \tag{4}$$

In (3) and (4) the origin of the Cartesian coordinates is located at the geometrical center of the aperture and $\epsilon_n = 2 - \delta_{n0}$ is the Neumann number. The corresponding copolarized and cross-polarized modal coefficients of (3-4) are related to the modal coefficients of (1) through:

$$d^{co}_{mn} = \frac{nC_{mn} - mA_{mn}}{\sqrt{m^2+n^2}} \quad , d^{xp}_{mn} = \frac{nA_{mn} + mC_{mn}}{\sqrt{m^2+n^2}}. \tag{5}$$

Now the coupling efficiency $\eta(w_o)$ of the aperture to a fundamental Gaussian beam of waist radius w_o, which has its waist on the aperture is given by [11] :

$$\eta(w_o) = \left|\sum_{m,n}^{M,N} d^{co}_{mn} I_{mn}(w_o)\right|^2 / \left(\frac{w_o^2\pi}{2}\sum_{m,n}^{M,N}(|d^{cp}_{mn}|^2 + |d^{xp}_{mn}|^2)\right) \tag{6}$$

$$\text{where,} \quad I_{mn}(w_o) = \iint_{apert.} \Psi^{co}_{mn}(x,y) exp(-(x^2+y^2)/w_o^2)\, dx\, dy. \tag{7}$$

We wish at this point to determine the modal coefficients d^{co}_{mn} and d^{xp}_{mn} so that the coupling efficiency $\eta(w_o)$ is maximized. For this purpose, the application of Schwarz's inequality to (6) immediately implies that the maximum coupling efficiency $\eta_{max}(w_o)$ occurs in the absence of cross-polarization and is obtained from :

$$\eta_{max}(w_o) = \frac{2}{w_o^2 \pi} \sum_{m,n}^{M,N} |I_{mn}(w_o)|^2 \tag{8}$$

with the corresponding co-polarization modal coefficients determined by :

$$d^{co}_{mn} \;/\; I_{mn}(w_o) = \text{constant}. \tag{9}$$

The condition for vanishing cross-polarization is (see 5) : $\quad nA_{mn} = -mC_{mn}$. (10)

Therefore, for maximum fundamental Gaussian coupling efficiency the aperture modes should add in phase and their relative magnitudes should satisfy conditions (9) and (10). The maximum coupling efficiency $\eta_{max}(w_o)$ of equation (9) still depends on the waist radius w_o and it is shown in figure 2 as a function of the ratio w_o/a for various indices (M,N). In table 1 we show the relative magnitudes between the modes at the optimum $w_{o,opt}/a$ ratio, for some practically encountered aperture sets of modes.

Available modes (M,N)	(1,0)	(1,2)	(1,2)+TE_{30}	(3,2)
$w_{o,opt}/a$	0.43	0.34	0.32	0.29
cpl. efficiency : η_{max}	84%	98.5%	99.2%	99.7%
d^{co}_{12}/d_{10}	-	0.51	0.56	0.64
d^{co}_{30}/d_{10}	-	-	0.11	0.17
d^{co}_{32}/d_{10}	-	-	-	-0.11

Table 1: Optimum parameters for maximum fundamental Gaussian coupling efficiency for certain practically encountered aperture modes available for beamshaping.

III. APPROXIMATE ANALYSIS OF THE MACHINED SECTION AND DESCRIPTION OF THE DESIGN PROCESS

Consider the gradually-flared pyramidal machined section of axial length L_M and of half flare-angle θ_o (see fig. 1) which is assumed excited at its throat by M × N locally propagating modes. Since the machined section is gradually flared and the incident modes propagating, reflections at the throat are considered negligible and the corresponding transverse electric field is given by :

$$\bar{E}_{t,thr}(x,y) = \sum_{m,n}^{M,N} \{A_{mn}^{th} \bar{e}_{mn}^{th,TE}(x,y) + C_{mn}^{th} \bar{e}_{mn}^{th,TM}(x,y)\} \quad . \tag{11}$$

To a first order approximation we can assume that each mode preserves its carried power upon propagating from the throat to the aperture. Also, each mode acquires a phase shift computed by :

$$\Phi_{mn} = \int_0^{L_M} \beta_{mn}(z)\, dz \tag{12}$$

where $\beta_{mn}(z)$ is the local propagation constant of the mn^{th}-mode. The above phase shift has been used extensively for the design of multimode horns [9-10] and it can be rigorously justified through a coupled-mode analysis of gradually flared tapers [13]. The aperture field is assumed to be modulated by a quadratic phase factor $Q_{L_T}(x,y)$ of curvature $L_T = a/(2\tan\theta_o)$ with L_T being the total virtual length of the taper. Under the above assumptions and neglecting reflections , the aperture field is simply given by :

$$\bar{E}_{t,ap}(x,y) = Q_{L_T}(x,y) \sum_{m,n}^{M,N} \{\acute{A}_{mn}^{ap} \bar{e}_{mn}^{ap,TE}(x,y) + \acute{C}_{mn}^{ap} \bar{e}_{mn}^{ap,TM}(x,y)\} \tag{13}$$

with the quadratically modulated aperture modal coefficients related to the throat modal coefficients through :

$$\acute{A}_{mn}^{ap} = A_{mn}^{th} \sqrt{Y_{mn}^{th,TE}/Y_o} \exp(-j\Phi_{mn}) \quad , \acute{C}_{mn}^{ap} = C_{mn}^{th} \sqrt{Y_{mn}^{th,TM}/Y_o} \exp(-j\Phi_{mn}) \tag{14}$$

where Y_{mn}^{th} is the throat admittance for the mn^{th} mode and Y_o is the free-space intrinsic admittance which has been assigned to the aperture modes. Based on the above simplified analysis for

the machined section and on a full-wave analysis of the integrated portion a three-stage design process has been established and is summarized below :

1. The integrated 70° flare-angle section of the antenna structure of figure 1 (including the step discontinuity) is selected and analyzed independently of the machined section. For this purpose, the dipole-fed integrated portion is assumed to be terminated by an infinite square waveguide of side $(a_s + 2s)$ and is analyzed using the full-wave analysis technique of [2] to obtain the throat modal coefficients A^{th}_{mn}, C^{th}_{mn}. The junction cross-section a_s and the step size s (see fig. 1) are selected so that the *magnitudes* of the radiating aperture modal coefficients, as predicted by equations 5 and 14, satisfy the optimal conditions (9) and (10) as closely as possible.

2. The infinite waveguide is now replaced by the gradually flared machined section and the assumption is made that the modal coefficients at the throat of the machined section retain their computed values of stage 1. This is a good approximation since the actual excited modal coefficients are determined by the difference between the integrated portion flare-angle and the machined section flare-angle and this difference is always dominated by the large 70° flare-angle of the integrated portion [10]. The length L_M and the flare-angle θ_o of the machined section are then selected iteratively (using 12) so that the modal coefficients $\acute{d}^{co}_{mn}$ appear in phase on the radiating aperture. The shortest possible length is chosen in order to achieve the maximum bandwidth.

3. Finally, the length and the flare-angle of the machined section are "fine-tuned" using the full-wave analysis of [2] for the entire quasi-integrated horn antenna and again for achieving maximum Gaussian coupling efficiency.

In table 2 we quantify several practical geometries of integrated portions which have resulted from the first stage of the design process.

IV. NUMERICAL AND EXPERIMENTAL RESULTS FOR SPECIFIC QUASI-INTEGRATED HORN ANTENNA DESIGNS.

The algorithm of section III has been employed for the design of a 20dB, a 23dB and a 25dB quasi-integrated horn antenna, all with a fundamental Gaussian coupling efficiency exceeding 97% and with a full-null beam efficiency around 99%. Although, in the design process the analysis of the machined section is performed using the approximate method of section III, the computation of the radiation characteristics of the finally designed horns is carried out using the full-wave analysis technique of [2]. Furthermore, using this full-wave analysis along with 6GHz scale-model measurements it was verified that the input impedance of the feeding strip-dipole in the integrated portion of the horn is not affected by the attachment of the machined section [3]. This is due to the fact that the input impedance of the feeding strip is mainly determined by its local geometrical environment which remains unaffected by the attachment of the machined section. The input impedance for the integrated-circuit horn antennas has already been analyzed theoretically and characterized experimentally in [2] where it was shown that by adjusting the dipole position inside the horn, the input impedance can be matched to either Schottky or SIS diodes. Therefore, the results of [2] are directly applicable to the case of the quasi-integrated horn antennas as well.

A. 20dB quasi-integrated horn antenna.

The geometrical parameters for the 20dB realization are calculated to be ($a_s = 1.35\lambda, s = 0.0, L_M = 7\lambda, \theta_o = 9°, dp = 0.39\lambda$) and the numerically computed patterns from the third stage of the design process along with the corresponding 90GHz measurements have been reported in [3]. In fig. 3 the principal patterns are compared to the patterns obtained by analyzing the machined section using the approximate method of section III. As shown, the approximate model agrees well with both the full-wave analysis and the measurements thus verifying the approximations used in the design process. The main radiation characteristics of this horn at

the design frequency and at the edges of the ±5% bandwidth are summarized in table 3. The indicated 10-dB beamwidth fluctuation corresponds to the variation of the beamwidth in an azimuthal far-field cut. The Gaussian-beam rolloff was calculated at the edges of the ±5% bandwidth using the Gaussian-beam parameters which were calculated at the design frequency f_o. The calculated phase center was found to be located at a distance of 1.5λ from the horn aperture for the E-plane and at 1.4λ for the H-plane.

B. 23dB quasi-integrated horn antenna.

The optimized design parameters for a 23dB quasi-integrated horn are found to be ($a_s = 1.52\lambda, s = 0.17\lambda, L_M = 13\lambda, \theta_o = 8.5^o$, $dp = 0.39\lambda$) and the computed principal patterns from both the full-wave analysis of the entire antenna and from the approximate model of section III are compared in figure 4 to corresponding 370GHz measurements. In figure 5 we include also the computed from the full-wave analysis and the measured patterns for the 45^o-plane. The radiation characteristics of this horn are being summarized in table 4. For the 23dB horn the phase center was calculated to be at 3.7λ inside the horn for the E-plane and at 3.5λ for the H-plane.

C. 25dB Quasi-integrated horn antenna.

In order to evaluate the efficiency of the design process and to provide a full range of practical designs, a 25dB quasi-integrated horn has also been designed and the computed geometrical parameters are found to be: ($a_s = 1.52\lambda, s = 0.0\lambda, L_M = 19.5\lambda, \theta_o = 10^o$, $dp = 0.39\lambda$). The radiation patterns, as calculated from the full-wave analysis and shown in figure 6 still exhibit excellent circular symmetry, low cross-polarization and suppressed sidelobes. The location of the phase center for this horn was computed to be at a distance of 13λ from the aperture for the E-plane and at 11λ for the H-plane. The rest of the main radiation characteristics of this horn antenna are being tabulated in table 5.

	Optimum	$a_s = 1.35\lambda$ $s = 0.0$	$a_s = 1.52\lambda$ $s = 0.0$	$a_s = 1.35\lambda$ $s = 0.17\lambda$	$a_s = 1.57\lambda$ $s = 0.0$
$\lvert\acute{d}_{12}^{co,ap}\rvert/\lvert\acute{d}_{10}^{ap}\rvert$	0.56*	0.52	0.50	0.55	0.51
$\lvert\acute{d}_{30}^{ap}\rvert/\lvert\acute{d}_{10}^{ap}\rvert$	0.114	-	0.11	0.117	0.146
$arg(\acute{C}_{12}^{ap}/\acute{A}_{12}^{ap})$	180°	200°	183°	182°	179°
$\lvert\acute{C}_{12}^{ap}\rvert/\lvert\acute{A}_{12}^{ap}\rvert$	2	4.5	4.4	5.1	4.3

Table 2: Comparison between the optimum aperture modal coefficients and the modal coefficients launched at the aperture by four practical integrated portion sections. The exciting dipole is positioned at a distance of 0.39λ from the apex of the horn. * The optimum ratio $\lvert\acute{d}_{12}^{co,ap}\rvert/\lvert\acute{d}_{10}^{ap}\rvert$ is 0.51 for the $a_s = 1.35\lambda$ geometry which only triggers the $TE_{10}, TE_{12}/TM_{12}$ modes.

	$0.95f_o$	f_o	$1.05f_o$
Gain	19.4dB	20dB	20.6dB
Aperture efficiency	60.6%	62.8%	65.4%
10dB Beamwidth	$37° \pm 1°$	$34° \pm 1.2°$	$32° \pm 1.8°$
Sidelobe-level (E-plane)	−23dB	−27dB	−26.3dB
Cross-pol.(45°)	−22.5dB	−22.7dB	−23dB
Beam-efficiency (to -10dB)	85%	86%	86.5%
Gaussian Coupling	96.4%	97.3%	96.9%
Gaussian Coupling rolloff	95.5%	97.3%	96.5%

Table 3: The main radiation characteristics of the 20dB quasi-integrated horn antenna (see text).

	$0.965f_o$	f_o	$1.035f_o$
Gain	22.2dB	22.8dB	23.6dB
Aperture efficiency	48.5%	52%	58.4%
10dB Beamwidth	$27.6 \pm 0.2°$	$25° \pm 1.1°$	$22.5° \pm 1.3°$
Sidelobe-level (E-plane)	−28dB	−33dB	−29.8dB
Cross-pol.(45°)	−20.5dB	−21dB	−22dB
Beam-efficiency (to -10dB)	86.6%	86%	86.6%
Gaussian Coupling	97.2%	97.3%	96.8%
Gaussian Coupling rolloff	96.3%	97.3%	96.0%

Table 4: The main radiation characteristics of the 23dB quasi-integrated horn antenna (see text).

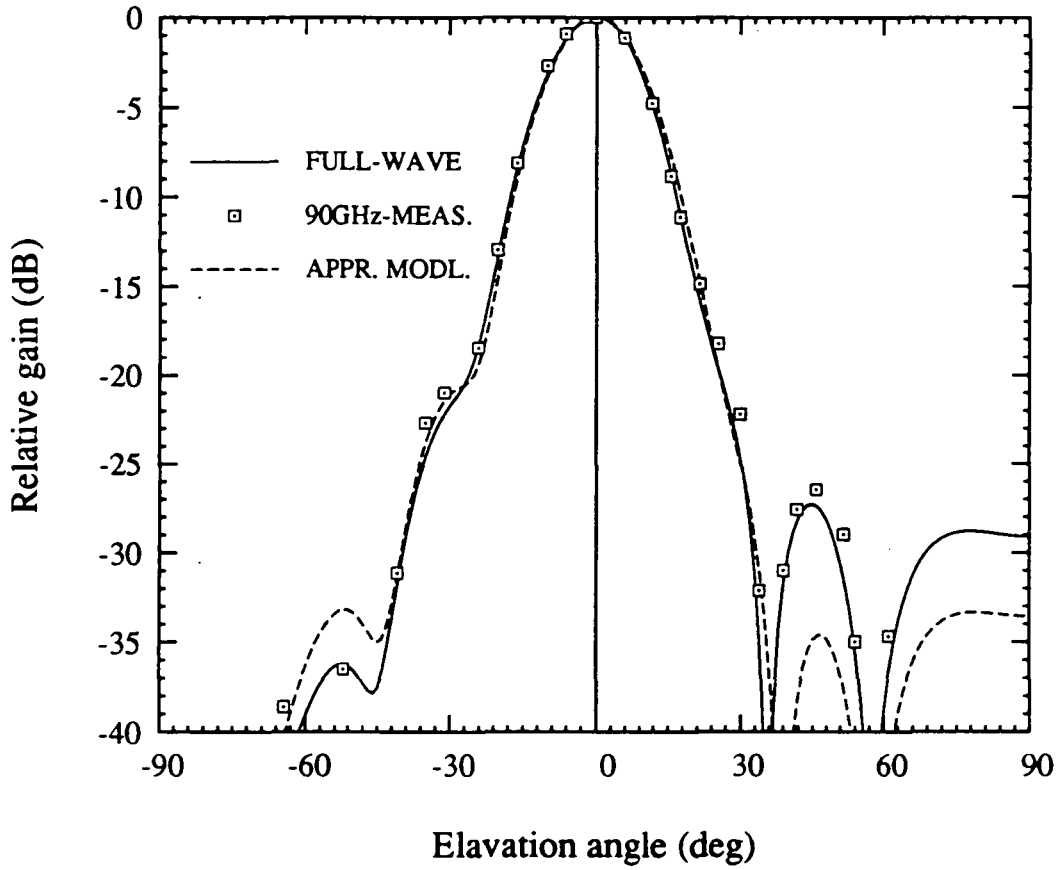

Fig.3 The E (right) and H-plane (left) patterns of the 20-dB quasi-integrated horn. The 90GHz measured patterns are compared to the full-wave analysis and the approximate analysis patterns. Detailed patterns including cross-polarization are shown in [3].

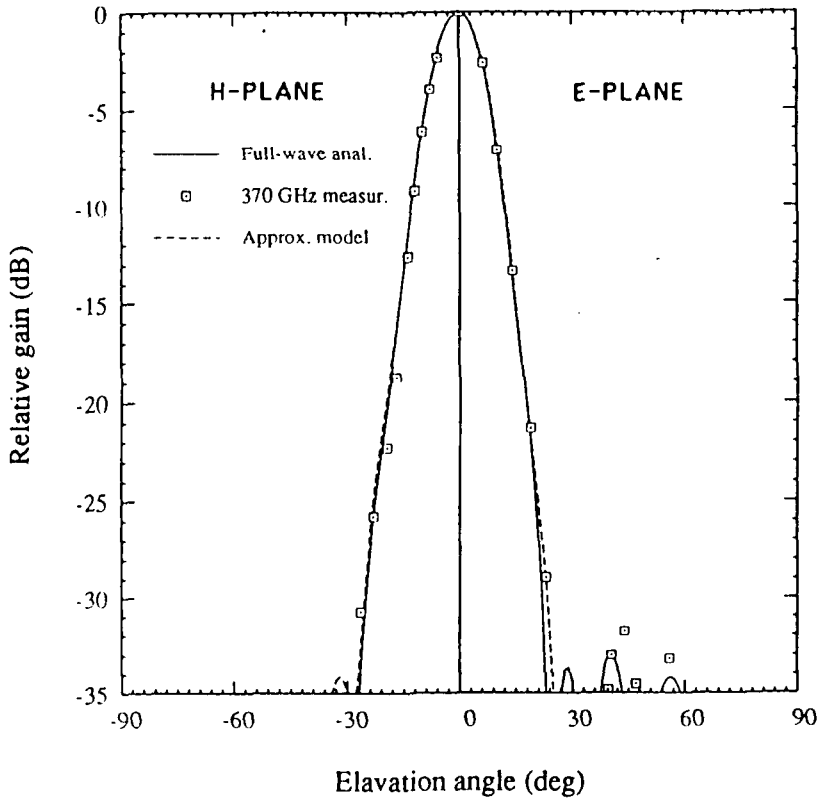

Fig.4 The E (right) and H-plane (left) patterns of the 23-dB quasi-integrated horn. The 370GHz measured patterns are compared to the full-wave analysis and the approximate analysis patterns.

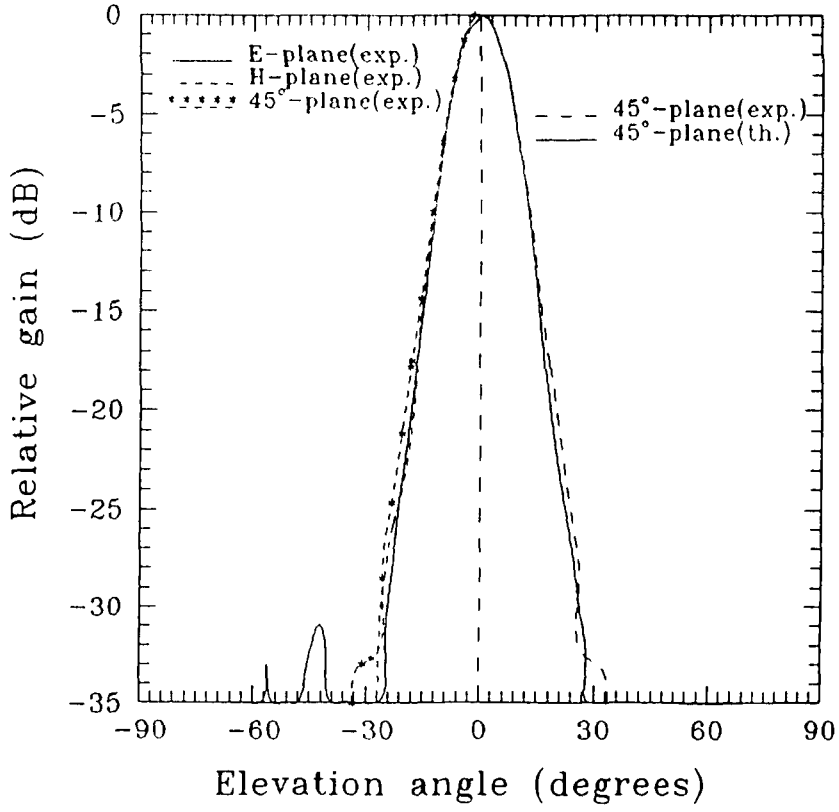

Fig.5 The measured at 370GHz E/H and 45°-plane patterns vs. the full-wave patterns of the 23-dB quasi-integrated horn.

	$0.965f_o$	f_o	$1.035f_o$
Gain	24.7dB	25.5dB	26.2dB
Aperture efficiency	36%	40%	44%
10dB Beamwidth	$21.6 \pm 0.8°$	$19.2° \pm 0.7°$	$17.5° \pm 0.5°$
Sidelobe-level (E-plane)	−28.7dB	−30.8dB	−30.8dB
Cross-pol.(45°)	−22.6dB	−24dB	−24.7dB
Beam-efficiency (to -10dB)	84.5%	85%	85%
Gaussian Coupling	97.1%	97.5%	97.4%
Gaussian Coupling rolloff	96.5%	97.5%	97.1%

Table 5: The main radiation characteristics of the 25dB quasi-integrated horn antenna (see text).

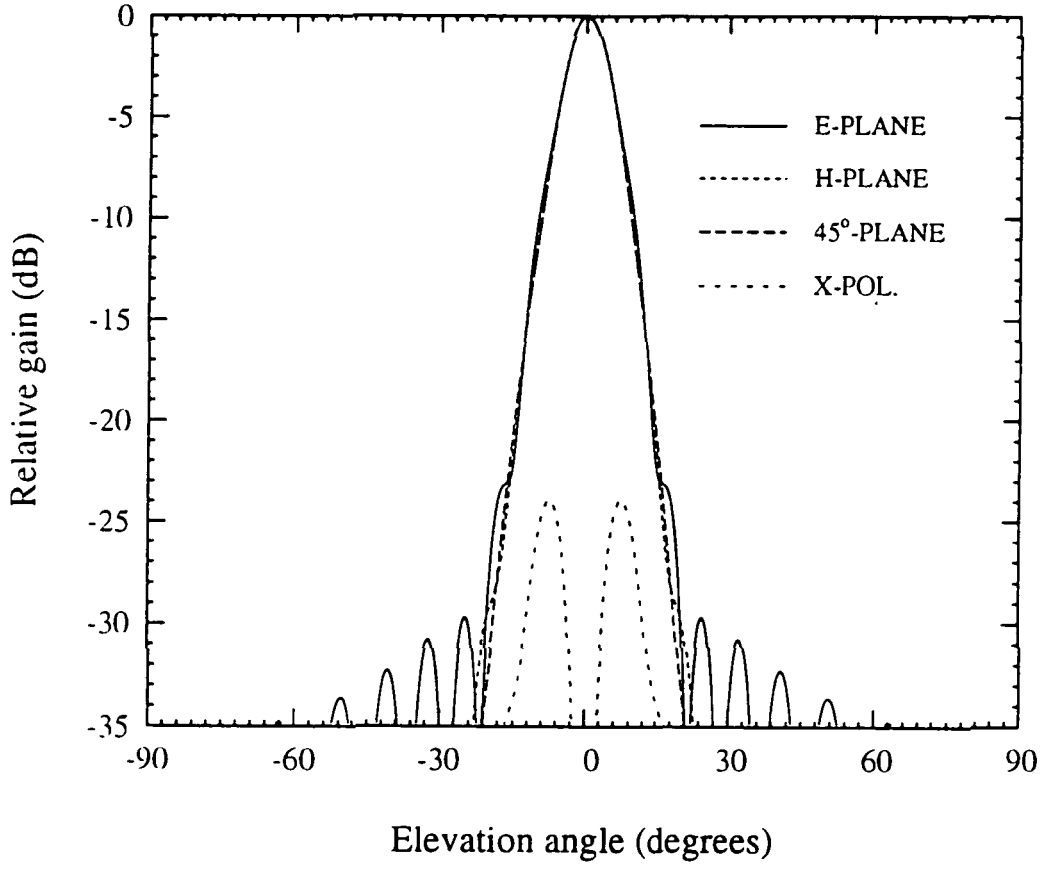

Figure 6: The calculated from the full-wave analysis patterns of the 25-dB quasi-integrated horn.

References

[1] G.M Rebeiz, D.P. Kasilingam, P.A. Stimson, Y. Guo and D.B. Rutledge, "Monolithic millimeter-wave two-dimensional horn imaging arrays," *IEEE Trans. Antennas Propagat.*, vol. AP-28, pp. 1473-1482, Sept 1990.

[2] G.V. Eleftheriades, W.Y. Ali-Ahmad, L.P.B. Katehi, and G.M. Rebeiz, "Millimeter-wave integrated-horn antennas Part I-Theory, and Part II-Experiment," *IEEE Trans. Antennas Propagat.*, vol. AP-39, pp. 1575-1586, Nov. 1991.

[3] G.V. Eleftheriades, W.Y. Ali-Ahmad, and G.M. Rebeiz, "A 20-dB Quasi-integrated horn antenna," *IEEE Microwave and Guided Wave Letters,* vol. 2,pp. 73-75, Feb. 1992.

[4] W.Y. Ali-Ahmad and G.M. Rebeiz, "92GHz dual-polarized integrated horn antennas," *IEEE Trans. Antennas Propagat.,* vol. AP-39, pp. 820-825, June 1991.

[5] W.Y. Ali-Ahmad, Gabriel M. Rebeiz, Hermant Dave, and Gordon Chin "802 GHz Integrated horn antennas imaging array," *International Journal of Infrared and Millimeter Waves,* vol. 12, No. 5.1991.

[6] C.C Ling and G.M Rebeiz, "94GHz Integrated monopulse antenna," IEEE AP-S International Symposium , Ontario, Canada, June 1991.

[7] P.F. Goldsmith, "Quasi-optical techniques at millimeter and submillimeter wavelengths," in *Infrared and Millimeter Waves,* vol. 6, New York : Academic, 1982, pp. 277-243.

[8] E. N. Grossman, "The coupling of submillimeter corner-cube antennas to Gaussian beams," *Infrared Phys.,* vol. 29, pp. 875-885, 1989.

[9] P.D. Potter, "A new horn antenna with suppressed sidelobes and equal beamwidths," *Microwave J.,* vol. VI, pp. 71-78, June 1963.

[10] S.B. Cohn, "Flare-angle changes in a horn as a means of pattern control," *Microwave Journal.,* vol. 13, pp. 41-46, Oct. 1970.

[11] G.V. Eleftheriades, and G.M. Rebeiz, "High-gain step-profiled integrated diagonal horn-antennas," To appear in *IEEE Trans. Microwave Theory Tech.,* mini special issue on Space Terahertz Technology, May 1992.

[12] C. E. Profera, "Complex radiation patterns of dual mode pyramidal horns," *IEEE Trans. Antennas Propagat.,* vol. AP-25, pp. 436-438, May 1977.

[13] L. Solymar, "Spurious mode generation in nonuniform waveguide," *IRE Trans. Microwave Theory Tech.,* vol. MTT-7, pp. 379-383, 1959.

PROGRESS IN INTEGRATED-CIRCUIT HORN ANTENNAS FOR RECEIVER APPLICATIONS

Part II: A 90 GHz Quasi-Integrated Horn Antenna Receiver

Walid Y. Ali-Ahmad, George V. Eleftheriades and Gabriel M. Rebeiz

NASA/Center for Space Terahertz Technology
Electrical Engineering and Computer Science Department
University of Michigan
Ann Arbor, MI 48109-2122

ABSTRACT

A receiver belonging to the family of integrated planar receivers has been developed at 90 GHz. It consists of a planar Schottky-diode placed at the feed of a dipole-probe suspended inside an integrated horn antenna. The measured planar mixer single-sideband conversion loss at 91.2 GHz (LO) with a 200 MHz IF frequency is 8.3dB±0.3dB. The low cost of fabrication and simplicity of this design makes it ideal for millimeter and submillimeter-wave receivers.

INTRODUCTION

Fundamental mixers are currently the front-ends components for all millimeter-wave receivers above 100 GHz. The mixers use a Schottky-diode suspended in a machined waveguide with an appropriate RF matching network. These components are expensive to manufacture especially above 200 GHz where waveguide tolerances become severe. A low noise planar receiver consisting of a planar Schottky diode integrated with an efficient planar antenna is a needed alternative at millimeter-wave frequencies. Recent advances in planar Schottky diodes resulted in excellence performance at 94 GHz with measured diode temperatures competitive with whisker-contacted diodes [1]. In this work, a planar diode is combined with an integrated horn antenna [2,3] to yield a 90 GHz receiver. The antenna feed-dipole impedance can be designed to conjugate match the RF diode impedance [4]. This eliminates the need for an RF matching network and thereby simplifies the mixer design. A machined section is attached to the front of the integrated horn antenna to yield a multi-mode horn [5]. The planar configuration results in an inexpensive quasi-monolithic receiver with an expected performance as good as the best waveguide receiver at 100 GHz.

MIXER DESIGN AND THEORETICAL PERFORMANCE

The length of the feed-dipole and its position inside the integrated horn antenna are designed so that its impedance conjugate matches the RF diode impedance [4]. As a result, the planar diode is epoxied right at the dipole apex. An RF choke is obtained by using two integrated lumped capacitors on a coplanar stripline. The first capacitor is $\lambda_o/4$ away from the dipole feed and the second capacitor is $\lambda_d/2$ away from the first one. These capacitors introduce an RF open circuit at the dipole feed and let the IF signal pass through the coplanar stripline (Fig.1). The circuit is integrated on highly resistive Silicon in order to minimize any losses of the IF signal on the surrounding dielectric substrate. A microstrip quarter-wave transformer over a Duroid 5870 substrate [7] is used to match the 1.4 GHz IF diode output impedance to 50Ω. Fig.2 shows the structure of the integrated horn antenna receiver. The machined section, not shown in this figure, is attached to the front aperture of the horn antenna. Gold

is evaporated on all the horn walls except on the membrane wafer walls, in order not to short-out the feed lines. The diode of choice to be used in this design is the UVa SC2R4 planar Schottky diode with 2.5μm anode diameter, a 5-6fF zero-bias junction capacitance, a 12-13fF parasitic capacitance and a 5-6Ω series resistance. A microwave model of the horn receiver structure shown in Fig.2 was built at 2.55 GHz in order to find the right feed-dipole impedance to conjugate match the UVa diode RF impedance. A feed-dipole, which is 0.392λ long and positioned 0.38λ from the apex of the horn, has an input impedance of 75+j55 Ω with the membrane walls uncoated and with no diode chip modeled at the dipole feeds. The input impedance dropped to 70+j10 Ω due to the capacitive effect of the diode block when it was modeled. A 1.1dB-1.3dB power loss was found in the microwave model by measuring the difference in powers detected by the feed- dipole for the case of coated and uncoated membrane walls respectively. Table I shows the mixer theoretical performance for the UVa diode at 91.2GHz(LO) and 91.4GHz(RF) for a bias of 0.65V and an available LO power of 2dBm. The analysis was done using the reflection algorithm [6]. the variation in conversion loss over 10% bandwidth is due to the variation in the feed dipole impedance.

Table I

f_{IF}(GHz)	0.2
f_{RF}(GHz)	91.4
$Z_{dipole,RF}(\Omega)$	70+j10
$Z_{dipole,2RF}(\Omega)$	14+j10
$Z^{in}_{diode,RF}(\Omega)$	62-j19
$Z^{in}_{diode,LO}(\Omega)$	55-j49
$Z^{out}_{diode,IF}(\Omega)$	86
Diode SC2R4 SSB Conversion loss(dB)	5.7
Diode SSB Conversion loss(dB) over 10% BW	5.7-6.2

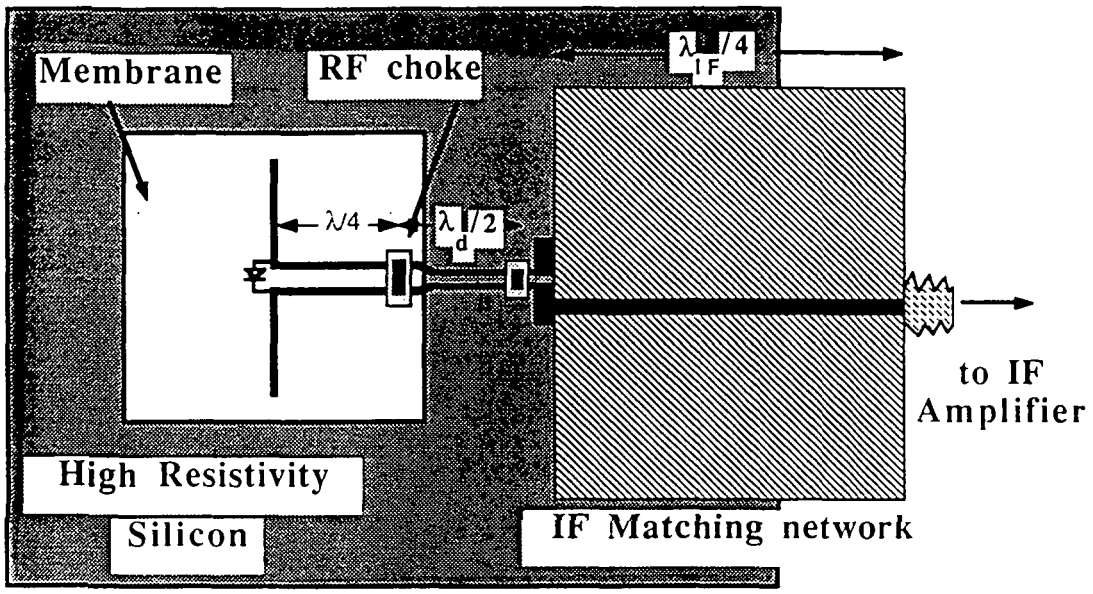

Figure 1: The mixer design consisting of the diode epoxied at the dipole feeds, the two lumped capacitors forming the RF choke, and the microstrip line IF matching network.

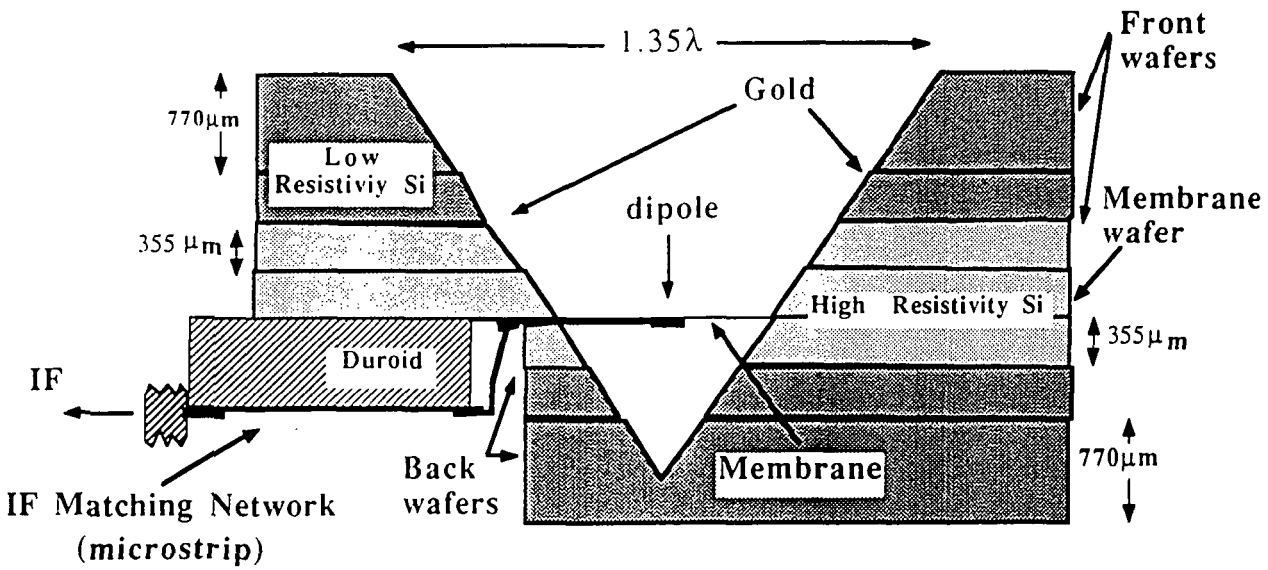

Figure 2: The integrated horn antenna receiver structure. The horn walls of the membrane wafer are not coated with gold.

RECEIVER MEASUREMENTS

A quasi-integrated horn antenna receiver was built at 91.4 GHz with a UVa SC2R4 diode epoxied at the dipole feeds. Video detection measurements were done at 91.4 GHz by shining a known plane wave power density onto the multi-mode antenna and measuring the output detected diode voltage using a lock-in amplifier. The diode theoretical video responsivity vs. bias current is fitted to the measured data by using the parameters shown in table II to model the receiver.

Table II

$\epsilon_{aperture}$	$\epsilon_{lossinwalls}$	Z_{dipole}	R_s	C_j	ϕ_{bi}	C_p	η
-2.0dB	-1.2dB	70+j10 Ω	6Ω	5.5 fF	0.88 V	12.5 fF	1.14

In fig.3, the measured video responsivity is equal to the ratio of the detected voltage across the diode over the plane wave power incident on the aperture of the quasi-integrated horn antenna. The diode parameters used in the model are those provided by University of Virginia. Although the receiver was designed for a 1.4 GHz IF frequency, we found that epoxy and solder at the junction between the duroid and the silicon substrate have added a parasitic IF capacitance. The measurements were therefore done at 200 MHz where this capacitance has negligeable effect. For the SSB conversion loss measurement, a calibrated 91.4 GHz RF plane wave and a 91.2 GHz LO were combined using a thin Mylar sheet and shined on the receiver. Figure 4 shows the measured planar mixer SSB conversion loss, defined as the received IF power divided by the RF power absorbed by the horn aperture (plane wave power density × horn area × horn aperture efficiency). The SSB conversion loss includes the 1.2dB loss in the uncoated membrane walls. An 8.3dB SSB conversion loss is measured at 91.4 GHz with 3.5dBm estimated LO power available at the feed-dipole terminals. The coupling efficiency of the horn aperture to a plane wave is normalized out of the measurement because in a receiver system the horn has a gaussian coupling efficiency of 97%. Also, the measured result can be directly compared to waveguide mixers performance which have no antennas attached. The 8.3 dB SSB conversion loss compares favorably with the best waveguide mixers performance (5.3±0.5dB) using the same diode [1].

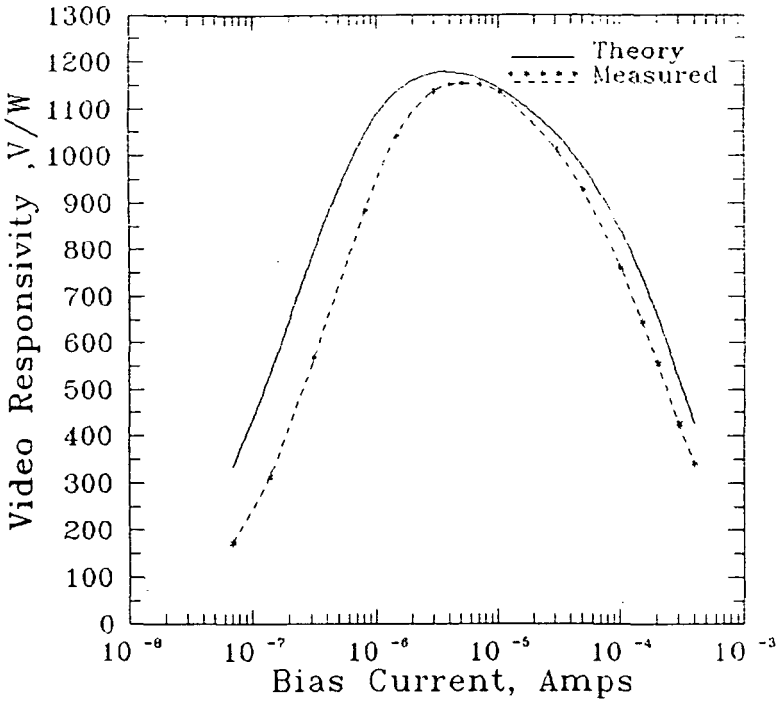

Figure 3: Measured and theoretical video responsivity at 91.4GHz.

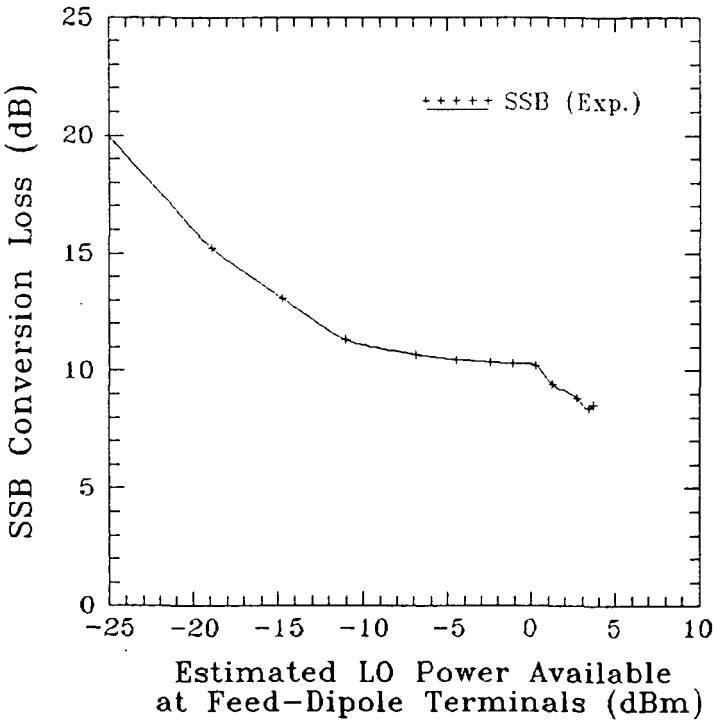

Figure 4: Measured planar mixer SSB conversion loss for the SC2R4 diode at 91.2 GHz (LO). The measured values include a 1.2dB loss attributed to power loss in the horn walls.

CONCLUSION

A 90GHz quasi-integrated horn antenna receiver has been designed and tested. The measurements show that this new receiver is a very good candidate for millimeter-wave applications. DSB measurements are being done on a new improved receiver design and using the UVa SC2T3 diode which has lower parasitic capacitance and series resistance than the UVa SC2R4 diode.

ACKNOWLEDGMENTS

This work was supported by the NASA/Center for Space Terahertz Technology at the University of Michigan, Ann Arbor. We thank G.V. Eleftheriades for the multi-mode horn design. We thank Dr. Thomas W. Crowe and William L. Bishop at the University of Virginia, for providing us with the diodes.

REFERENCES

[1] D.G. Garfield, R.J. Mattauch, and S. Weinreb,"RF Performance of a Novel Planar Millimeter-Wave Diode Incorporating an Etched Surface Channel," *Trans Microwave Theory Tech.*, vol MTT-39, pp. 1-5, Jan 1991.

[2] G.M. Rebeiz, D.P. Kasilingan, P.A. Stimson, Y. Guo, and D.B. Rutledge,"Monolithic millimeter-wave two-dimensional horn imaging arrays," *IEEE Trans. Antennas Propag.*, vol. AP-28, Sept. 1990.

[3] W.Y. Ali-Ahmad, and G.M. Rebeiz,"92 GHz dual-polarized integrated horn antennas," *IEEE Trans. Antennas Propag.*, vol. AP-39, June 1991.

[4] W.Y. Ali-Ahmad, G.V. Eleftheriades, L.P. Katehi, and G.M. Rebeiz,"Millimeter-Wave Integrated Horn Antennas, Part II: Experiment," *IEEE- Trans. Antennas Propagation*, vol. AP-39, pp. 1582-1587, Nov. 1991.

[5] G.V. Eleftheriades, W.Y. Ali-Ahmad, and G.M. Rebeiz,"A 20dB Quasi- Integrated Horn Antenna," *IEEE- Microwave Guided-Wave Lett.*, vol. 2, pp. 72-75, Feb. 1992.

[6] D.N. Held and A.R. Kerr,"Conversion loss and noise of microwave and millimeter-wave receivers: Part I-Theory; Part II-Experiment," *IEEE Trans. Microwave Theory Tech.*, vol. MTT-26, p.49-61, 1978.

[7] Duroid is a trademark of Rogers Corporation. We thank Rogers Co. for the donation of the substrate.

ZONE PLATE LENS ANTENNAS FOR MILLIMETER AND SUBMILLIMETER WAVELENGTHS

Paul F. Goldsmith

Five College Radio Astronomy Observatory
Department of Physics and Astronomy
University of Massachusetts, Amherst MA 01003

and

Millitech Corporation
P.O. Box 109
South Deerfield, Massachusetts 01373

Abstract

Zone plate lenses are a type of focusing element which function essentially as differential phase shifters, having a relatively few, coarsely quantized phase delays across the incident beam of radiation. The major advantages are ease of fabrication and much reduced thickness, compared to conventional refractive focusing elements. These considerations are both of particular importance for the submillimeter range, in which manufacturing tolerances for curved optical elements can pose significant problems, and where the absorption of readily available dielectric materials is quite large. In this presentation we briefly review the theory of zone plate lens operation, present a relatively simple method for calculating the aperture efficiency of zone plate lenses used as antennas, and show some theoretical and measured results in the 100 GHz range.

I. Lens Operation as a Phase Transformer

An ideal lens changes the radius of curvature of an incident beam of radiation without affecting its amplitude distribution. This situation is illustrated in Figure 1, which shows a phase transformer converting a diverging spherical wave (as might be produced by a feed horn) into a plane wave. In the paraxial limit, the phase variation of a spherical wave perpendicular to an axis from its focus is a quadratic function of the radius r from the axis:

$$\Delta\varphi(r) = \pi r^2/\lambda R \ , \tag{1}$$

where λ is the wavelength and R is the radius of curvature. The phase variation is defined in the sense that the phase delay increases with increasing distance from the axis of propagation.

A lens modifies the radius of curvature of the beam by making use of different propagation speeds in different media; these can be dielectrics for which the speed is less than that in free space by a factor n, and arrays of waveguides or metal plates for which the propagation speed is greater than c according to the general relationship

$$v = c/[1 - (\lambda/\lambda_{co})^2]^{0.5} \ . \tag{2}$$

Reduced to simplest terms, a dielectric lens modifies the phase distribution by providing a phase delay which decreases away from its axis according to

$$\Delta\varphi_l(r) = -\pi r^2/\lambda F \ , \tag{3}$$

where F is the focal length of the lens. The output phase variation is just the sum of that of the input beam given by (1) together with that of the lens given by (3), so that we obtain

$$\pi r^2/\lambda R_{out} = \pi r^2/\lambda R_{in} - \pi r^2/\lambda F \ , \tag{4a}$$

which leads immediately to the relationship

$$1/R_{out} = 1/R_{in} - 1/F \ . \tag{4b}$$

With the convention that $R_{in} = D_{in}$, the distance of the focal point of the input beam from the lens, and $R_{out} = -D_{out}$ (the distance to the focal point of the output beam), we recover the familiar expression

$$1/D_{in} + 1/D_{out} = 1/F \quad . \tag{4c}$$

Equation (4b) also applies to quasioptical Gaussian beams [1], while (4c), being dependent on the assumption that the radius of curvature is equal to the distance from the focal point, applies only to geometrical optics beams.

A converging dielectric lens of index of refraction n has a central thickness t_c determined by the maximum phase delay that is required:

$$\Delta\varphi_{max} = (2\pi/\lambda)\cdot t_c\cdot(n-1) \quad . \tag{5}$$

In the simplest approximation, we find that the central thickness of a lens of diameter D and focal length F is

$$t_c = D^2/8(n-1)F \quad . \tag{6}$$

II. LENS LOSS

A lens which operates perfectly as a phase transformer may still suffer loss as a result of reflections at free space – dielectric interfaces, and absorption within the lens itself. Reflection losses are typically a few percent per surface if no anti–reflection treatment is employed. The basic technique to reduce reflections is to include a matching layer, which may be a natural dielectric of the required index of refraction, or an artificial dielectric as formed by cutting grooves. Both approaches have limitations due to variations in incidence angle and polarization effects, but can reduce reflections significantly.

Absorption cannot be eliminated, and depends on the lens thickness, together with the material properties. We use the definition of the fractional power loss per unit distance to be α, so that the input and output power (or power density) after traversing a path through the dielectric of length L are related by

$$P_{out} = P_{in} \cdot \exp(-\alpha L) \ , \tag{7a}$$

where

$$\alpha = 2\pi \, n \tan \delta / \lambda \ . \tag{7b}$$

In the preceding equations, we have employed the usual definitions of the complex dielectric constant $\epsilon = \epsilon' + i\epsilon''$, the index of refraction $n = \sqrt{\epsilon'}$, and the loss tangent, $\tan \delta = \epsilon''/\epsilon'$.

At submillimeter wavelengths, information on dielectric properties is quite scarce and often not entirely consistent. Some of this may be a result of variations in sample properties, while measurement techniques and errors may also be playing a role. Teflon is a low–loss dielectric widely used for millimeter and submillimeter wavelength lenses. This material has an absorption coefficient which rises almost linearly with frequency, and is approximately 0.042 cm^{-1} at 300 GHz and 0.09 cm^{-1} at 600 GHz [2]. Other measurements give higher absorptions of 0.2 – 0.5 cm^{-1} at ≈ 900 GHz [3]. We adopt an absorption coefficient of 0.1 cm^{-1} at 600 GHz and a real part of the dielectric constant of 2.0. Rexolite^{tm} is often used at millimeter wavelengths due in part to its good mechanical properties. It is relatively lossy in the submillimeter range; different measurements give α = 0.70 – 1.0 cm^{-1} at 600 GHz [4].

Taking (6) as giving a representative lens thickness, we find $t_c = 0.31 \, D^2/F$. For a F = D = 5 cm lens at 600 GHz, we find t_c = 1.55 cm; a perfectly phase correcting plano–convex lens of the same focal length and diameter has t_c = 1.475 cm. The absorptive loss at the center of a F = D = 5 cm teflon lens (where most of the power is concentrated) will thus be about 15 %. A comparable rexolite^{tm} lens will have an absorption at its center of approximately 60 %! Clearly, these numbers are large enough to suggest the use of refractive optics. An alternative that merits serious consideration is the zone plate lens, which can be made far thinner and thus have negligible absorption loss.

III. Zone Plate Lens Operation

The monotonically decreasing phase delay as a function of distance from the axis of

symmetry characteristic of typical dielectric lenses (Figure 2a) can be interrupted by a step change in thickness. If at a particular frequency this produces an increase in the phase delay equal to 2π radians, it will nominally not have any effect on lens performance, except for possible shadowing by step boundaries. Such devices are generally called **zoned lenses**, or **Fresnel lenses** and are widely used to reduce the thickness of relatively large and thick lenses employed at microwave frequencies. As shown in Figure 2b, they still have at least one surface which has curved sections, so that manufacturing is, in fact, more difficult than conventional lenses since the steps are an added complication.

Zone plate lenses represent a more radical approach, in that, as illustrated in Figure 2c, they are designed using only surfaces perpendicular to the axis of propagation. This is not at all a new concept, deriving quite directly from concept of Fresnel zones in diffraction theory. A number of references which discuss theoretical and experimental aspects of zone plate lenses are given in [5]. The closely related zone plate reflector antenna is discussed in references [6].

Rather than attempting to achieve the desired phase error function (3), the zone plate lens allows the phase error to increase as a quadratic function of distance from the axis. When it has reached a certain point, the lens thickness is reduced to bring the phase error to zero. If we define the maximum allowed phase error to be $2\pi/p$, the axial size of the step is given by

$$t_1 = \lambda/(n-1)p \quad . \tag{8}$$

If this procedure were continued indefinitely, we would merely have a stepped approximation to a conventional lens, which would not be particularly thin. The zone plate lens is distinguished by the technique of ***increasing*** the phase delay by 2π radians at the design frequency, at points where the previously described procedure of reducing the phase delay would lead to an accumulated phase error of 2π radians. The maximum change in thickness of the zone plate lens is

$$\Delta t_{max} = [(p-1)/p]\cdot(\lambda/(n-1) \quad , \tag{9}$$

since at the next step the thickness returns to its original value rather than to $p\cdot t_1 = \lambda/(n-1)$. The total zone plate lens thickness is given by $\Delta t_{max} + t_{min}$, where the latter is the minimum thickness required for mechanical integrity. The total thickness is

thus on the order of a wavelength, far less than required for unzoned lenses. The absorption loss for a material with α proportional to frequency will thus be a constant, providing one of the most important advantages of zone plate lenses at submillimeter wavelengths.

The radii at which the zones occur are obtained by requiring that the total phase for rays representing a plane wave converged to focal point be constant for all initial radii from the axis of symmetry. We ignore any phase shift of constant thickness component of lens, and take the phase shift of the zone plate lens to be

$$\Delta\varphi_{zpl} = -2\pi k/p \quad , \tag{10}$$

where k is an index which increases by unity at each zone boundary. As illustrated in Figure 3, the radius of zone k is denoted r_k and the distance from the lens at this radius to the focal point R_k, so that the path phase difference between axial ray and an arbitrary ray is

$$\Delta\varphi = (2\pi/\lambda)[R_k - F] \quad . \tag{11}$$

The two previous equations can be combined with the constant total phase condition to determine R_k. With the additional approximation of ignoring effect of changes in the lens thickness on R_k, we obtain $R_k = [r_k^2 + F^2]^{0.5}$, which gives the relation

$$r_k = [2kF\lambda/p + (k\lambda/p)^2]^{0.5} \quad . \tag{12}$$

Some designs for zone plate lenses are shown in Figure 4, with p = 2, 4, 10, and 50. All are designed for 300 GHz and have F = D = 10 cm, with an index of refraction equal to 1.4. A minimum thickness of 0.1 cm has been arbitrarily chosen. In practice, it is effective to chose the minimum thickness to make the zone plate lens central thickness resonant at the design frequency.

If we restrict ourselves to the situation F/D >> 0.5, the first term in (12) dominates, and we obtain the nominal lens diameter

$$D_o = [8k_{max}f\lambda/p]^{0.5} \quad . \tag{13a}$$

Alternatively, we see that the number of zones in the lens is given by

$$k_{max} = pD_o^2/8f\lambda \quad . \tag{13b}$$

Although zone plate lens design concentrates on phase delays and ignores refraction, an important limitation must be borne in mind, which is that the zone width must be large enough that zones do not begin to act like waveguides, in the manner of matching layers on a conventional dielectric lens. For this reason it is useful to determine the minimum zone width, which is just the minimum value of $\Delta r = r_{k+1} - r_k$. This occurs at the outer radius of the lens where we find

$$\Delta r_{min} = (2/p)\cdot(f/D)\cdot\lambda \quad . \tag{14}$$

For a F/D = 1 zone plate lens with p = 4 we find $\Delta r_{min} = \lambda/2$, which is on the borderline of being a problem; it is apparent that the performance of the outer portion of fast zone plate lenses may be compromised by this effect. Detailed calculations remain to be carried out.

IV. Zone Plate Lens Efficiency

The major issue we wish to investigate is how the wave front errors which are a necessary consequence of the approximate nature of the zone plate lens design affect its efficiency as an antenna. We consider a lens being used to transform a spherical wave into a plane wave and start with a wave of radius of curvature R_{in}; the phase distribution as a function of distance from the axis is shown in Figure 5a; in the paraxial limit this is just that described by (1). To this we add the differential phase shift produced by the lens which has thickness t at radius r

$$\Delta\varphi_{zpl} = (2\pi/\lambda)\cdot(n-1)t(r) \quad . \tag{15}$$

The lens shown in cross section in Figure 5b has p = 4 and F/D = 1. The resulting output or aperture phase distribution is shown in Figure 5c; note that the phase delay increases essentially quadratically as a function of radius, except at the zone boundaries. The p = 4 lens has 3 successive zone boundaries at which the phase delay decreases by $2\pi/4$ radians, followed by a boundary at which the phase delay increases by 2π.

In order to calculate the aperture efficiency, we assume that we have a Gaussian feed distribution which yields an aperture field distribution with magnitude of the form

$$|E_{ap}(r)| = \exp[-(r/w)^2] \ , \tag{16a}$$

which defines the power edge taper

$$T_e(dB) = 8.69\,(R/w)^2 = 2.17\,(D/w)^2 \ . \tag{16b}$$

The taper efficiency is the efficiency with which the aperture is utilized, and is defined by

$$\epsilon_t = |\iint E_{ap}\cdot dS|^2 \,/\, \iint |E_{ap}|^2\cdot dS \cdot \iint dS \ , \tag{17a}$$

where all integrals extend over the aperture [7]. The spillover efficiency is the fraction of power in the feed pattern which is intercepted by the aperture, and is given by

$$\epsilon_s = \iint_{aperture} |E_{ap}|^2\cdot dS \ / \ \iint_{\substack{entire\\pattern}} |E_{ap}|^2\cdot dS \ . \tag{17b}$$

The aperture efficiency is the product of the two preceding contributions:

$$\epsilon_a = \epsilon_t \cdot \epsilon_s \ . \tag{17c}$$

The integral in the numerator of (17a) includes the effects of the phase errors; any deviation from a uniform phase distribution reduces the taper efficiency and thus the aperture efficiency.

The efficiencies can be calculated for different input beam characteristics for a given lens. An edge taper of approximately 10 dB yields the maximum efficiency for this type of illumination of an unblocked antenna [7]. The variation of taper efficiency as a function of input beam radius of curvature is shown in Figure 6a for a zone plate lens with p = 4 and F = D = 10 cm operating at a wavelength of 0.3 cm. As expected, the maximum efficiency occurs for $R_{in} = F$.

The behavior of the lens efficiency as a function of p is shown in Figure 6b, for the same lens conditions as above, fixing $R_{in} = F$. The values of the efficiencies for large p are

very close to those for a perfect phase transformer with the same 10 dB edge taper: $\epsilon_t = 0.9$, $\epsilon_s = 0.9$, and $\epsilon_a = 0.81$. The efficiencies for p = 2 and 3 are quite low, but for p = 4 we begin to approach the asymptotic behavior. Thus, the choice of p represents a compromise between obtaining the highest efficiency and ease of fabrication together with the requirement on minimum zone width given by (14).

V. Zone Plate Lens Measurements

We have fabricated and measured a zone plate lens designed for operation at 95 GHz, where test equipment is readily available. The lens was fabricated of Rexolite^{tm} (n = 1.59), with p = 4, f = 12.7 cm, D = 9.53 cm, and a central thickness of 0.59 cm. For comparison, we used a fused silica lens which was anti–reflection coated with layers of polyethylene. This lens had the same diameter, but a slightly different focal length of 14.5 cm. Both lenses were illuminated by a scalar feed horn giving a Gaussian illumination pattern with an edge taper of close to 10 dB. The measured patterns in one plane are shown in Figure 7. We see that the main lobe beamwidths are very similar. The sidelobe structure of the unzoned lens is essentially that predicted from the truncated Gaussian illumination. The zone plate lens shows more extended error pattern which is a consequence of the phase errors.

The gains of the two lens antennas were also measured using a compact range; their absolute values are compromised by uncertainty in the gain of the reference horn but are consistent with expectations. What is more reliable is the difference in gain between the unzoned lens and the zone plate lens, which indicate that the zone plate lens has 1.0 dB lower gain. The calculations for the p = 4 zone plate lens predict an efficiency 0.86 dB below that of an ideal phase transformer lens. The reflection loss of the n = 1.6 zone plate lens is 0.23 dB per surface at normal incidence. Given the possible imperfections in matching, phase transforming, and the absorption in the unzoned lens, the measurements and calculations are in satisfactory agreement.

VI. Conclusions

We have reviewed the theory of operation and design of zone plate lenses. Their very small thickness makes these devices attractive for use at submillimeter wavelengths where absorption loss of unzoned lenses can be appreciable. We have examined the

efficiency of zone plate lenses as a function of interzone phase shift, and find that for zone boundary phase shifts $< \pi/2$ the performance approaches that of an ideal phase transformer. Measurements and calculations of the efficiency of a 95 GHz lens agree quite well.

We thank John Kapitzky, Chris Koh and Ellen Moore for their contributions to this project.

References

[1] T.S. Chu, "Geometrical Representation of Gaussian Beam Propagation," ***Bell Syst. Tech. J.***, 45, pp. 287–299, 1966.

[2] M.N. Afsar, "Millimeter Wave Complex Refractive Index, Complex Dielectric Permittivity and Loss Tangent Measurements of Common Polar and Non–Polar Polymers," ***Proc. Tenth International Conference on Infrared and Millimeter Waves***, pp. 60–61, 1985.

[3] A.P. Sheppard, A. McSweeney, and K.H. Breeden, "Submillimeter Wave Material Properties and Techniques: Dielectric Constant, Loss Tangent, and Transmission Coefficients of Some Common Materials to 2000 GHz", ***Proc. Symposium Submillimeter Waves***, Vol. XX in Microwave Research Institute Symposia Series. Brooklyn: New York Polytechnic Institute Press, 1970, pp. 701–705. G.W. Chantry, ***Submillimetre Spectroscopy***. New York: Academic, 1971, p. 341.

[4] G.J. Simonis, J.P. Sattler, T.L. Worchesky, and R.P. Leavitt, "Characterization of Near–Millimeter Wave Materials by Means of Non–Dispersive Fourier Transform Spectroscopy," ***Int. J. Infrared and Millimeter Waves***, 5, pp. 57–72, 1984. R.H. Giles, A.J. Gatesman, and J. Waldman, "A Study of the Far–Infrared Optical Properties of Rexolite^{tm}," ***Int. J. Infrared and Millimeter Waves***, 11, pp. 1299–1302, 1990.

[5] M. Sussman, "Elementary Diffraction Theory of Zone Plates," ***Amer. J. Phys.***, 28, pp. 394–398, 1960. F. Sobel, F.L. Wentworth, and J.C. Wiltse, "Quasi–Optical Surface Waveguide and Other Components for the 100– to 300 Gc Region," ***IEEE Trans. Microwave Theory Tech.***, MTT–9, pp. 512–518, 1961. D. N. Black and J.C.

Wiltse, "Millimeter–Wave Characteristics of Phase–Correcting Fresnel Zone Plates," ***IEEE Trans. Microwave Theory Tech.***, MTT–35, pp. 1123–1129, 1987. J.E. Garrett and J.C. Wiltse, "Fresnel Zone Plate Antennas at Millimeter Wavelengths," ***Int. J. Infrared and Millimeter Waves***, 12, pp. 195–220, 1991. This includes a particularly complete of references on this topic.

[6] L.F. Van Buskirk and C.E. Hendrix, "The Zone Plate as a Radio–Frequency Focusing Element," ***IRE Trans. Antennas Propag.***, AP–9, pp. 319–320, 1961. Yu. N. Danilov and L.A. Fedorova, "Scattering Behavior in a Zoned Reflector Antenna," ***Izvestiya VUZ. Radioelektronika***, 32(2), pp. 61–65, 1989. R. Lambley, "Fresnel Antenna," ***Electronics & Wireless World***, 95, p. 1642, 1989. J.M. Franke and B.D. Leighty, "Reflection Zone Plate Antenna," ***NASA Tech. Brief LAR–13535***, 1989. M.A. Gouker and G.S. Smith, "A Millimeter–Wave Integrated Circuit Antenna Based on the Fresnel Zone Plate," ***1991 IEEE MTT–S Digest***, pp. 157–160.

[7] P.F. Goldsmith, "Radiation Patterns of Circular Aperture with Gaussian Illumination," ***Int. J. Infrared and Millimeter Waves***, 8, pp. 771–781, 1987.

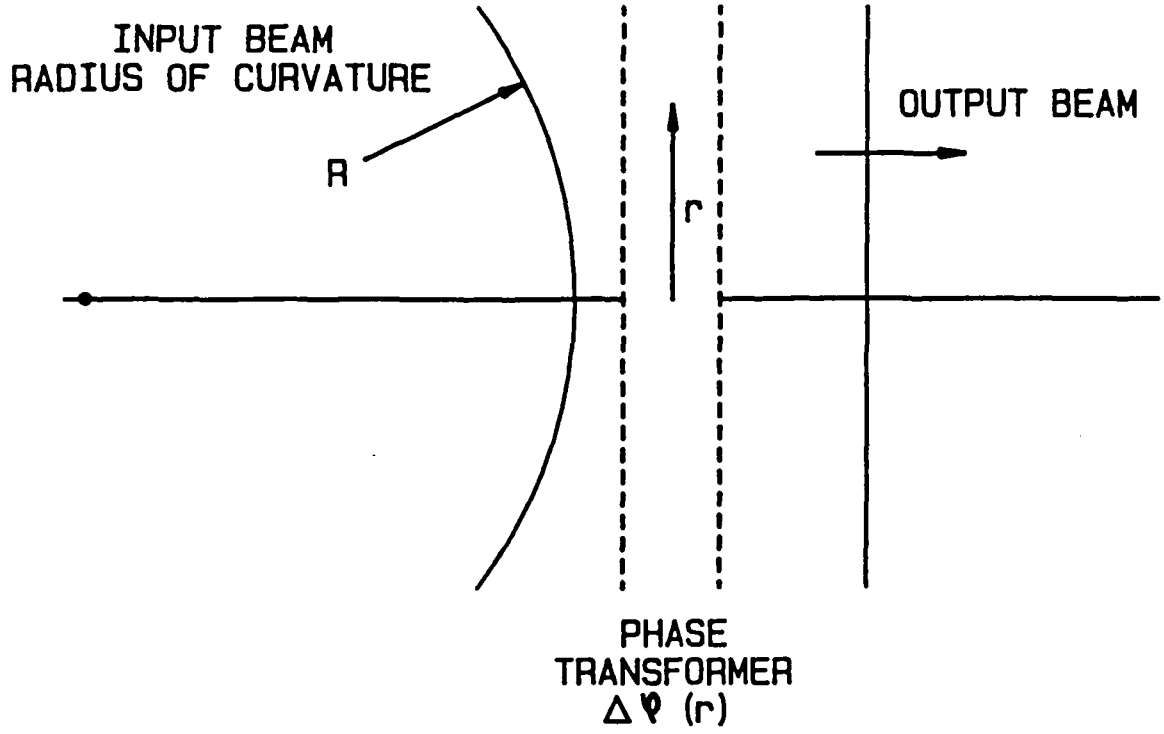

FIGURE 1 - OPERATION OF LENS AS PHASE TRANSFORMER

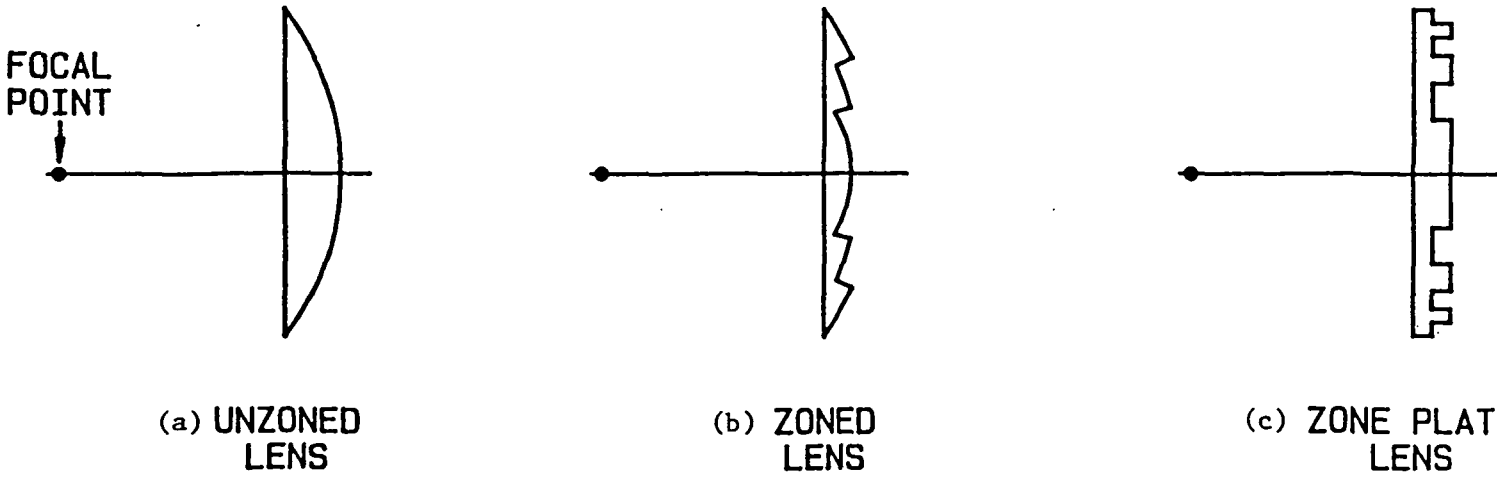

FIGURE 2 - DIFFERENT DESIGNS OF LENSES

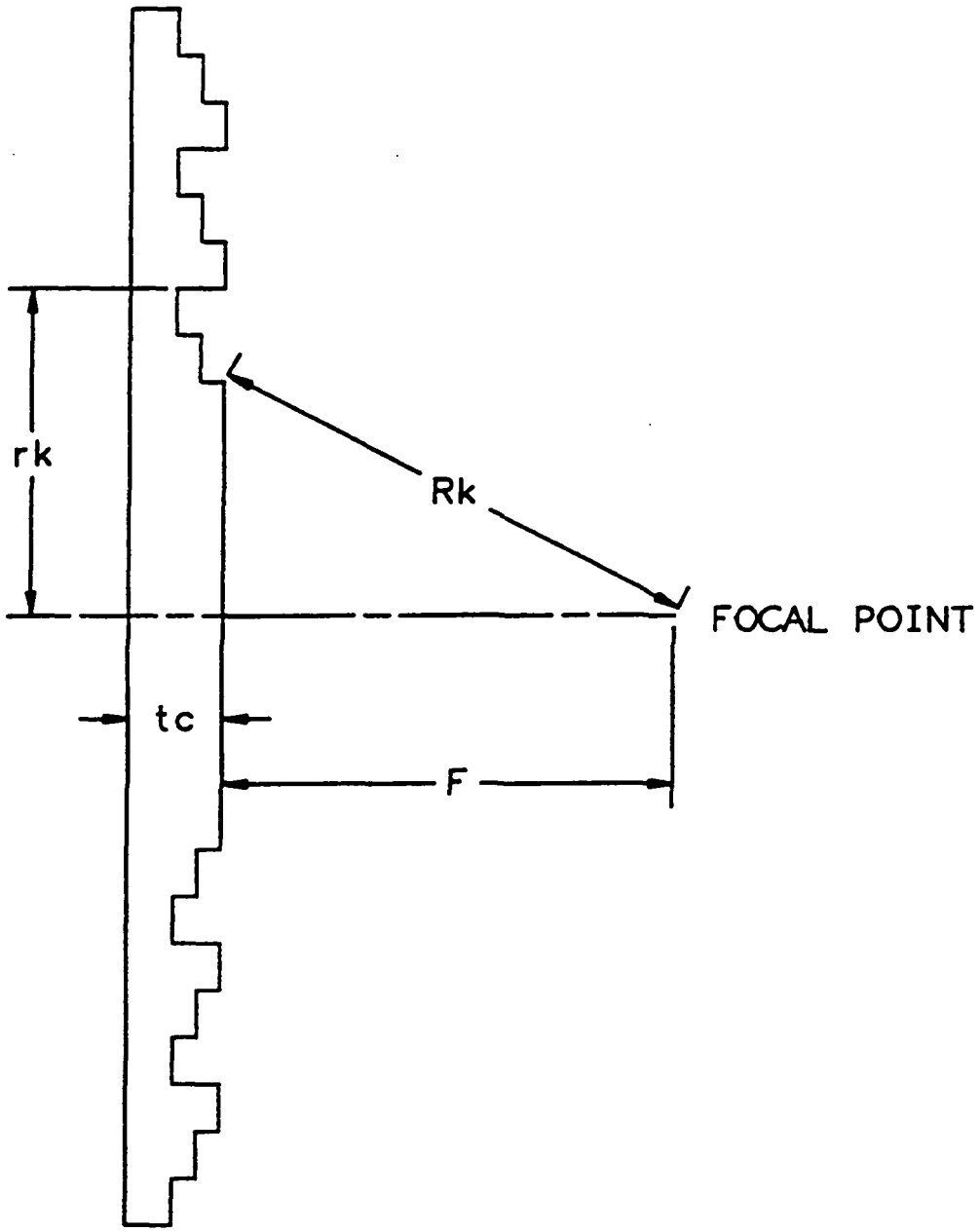

FIGURE 3 - ZONE PLATE LENS DESIGN PARAMETER DEFINITIONS

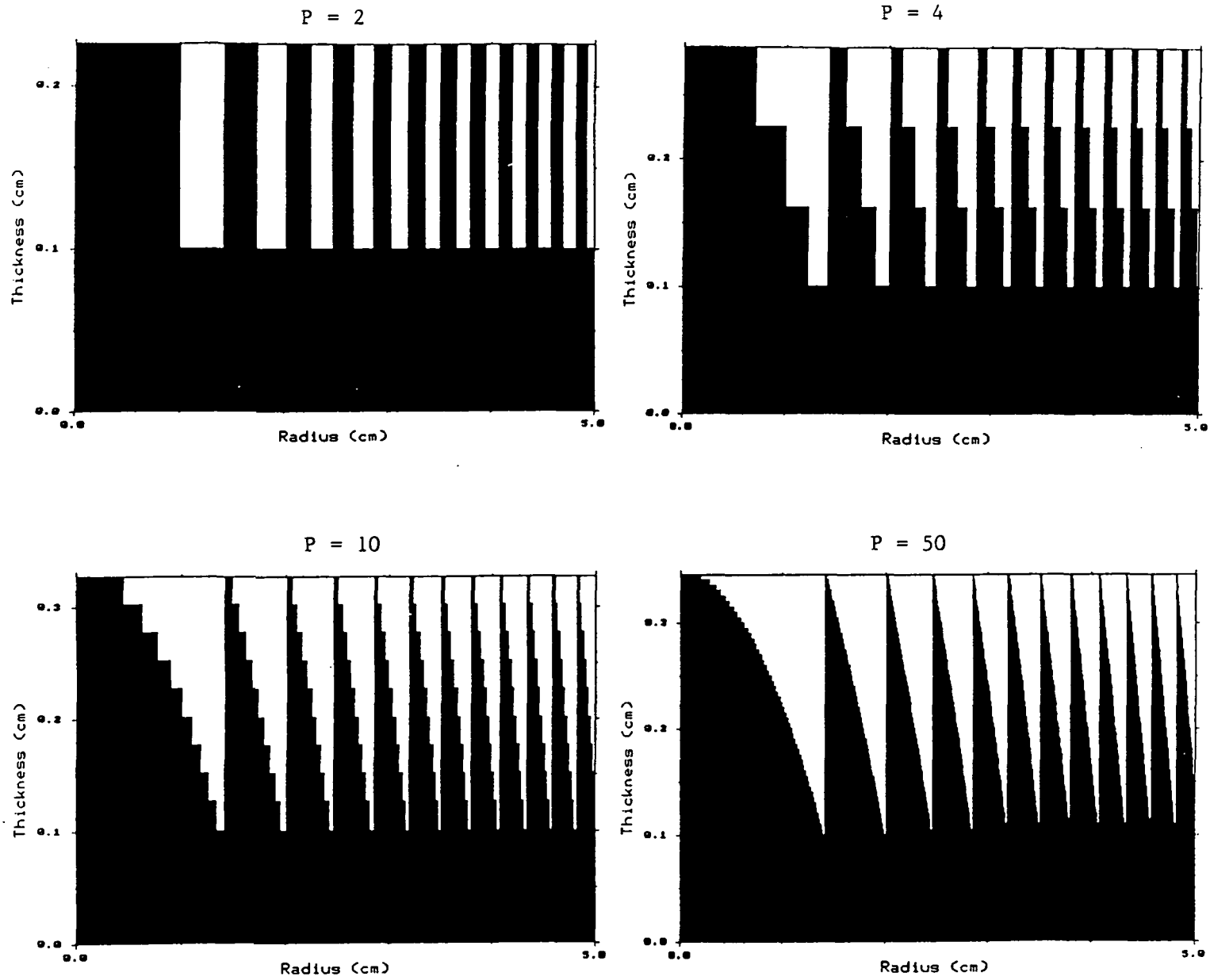

ZONE PLATE LENSES WITH F = D = 10 CM ; FREQUENCY = 300 GHz ; n = 1.4

FIGURE 4

FIGURE 5
100 GHZ ZONE PLATE LENS

FL = 10 cm DIA = 10 cm

n = 1.59 p = 4

INPUT PHASE DISTRIBUTION

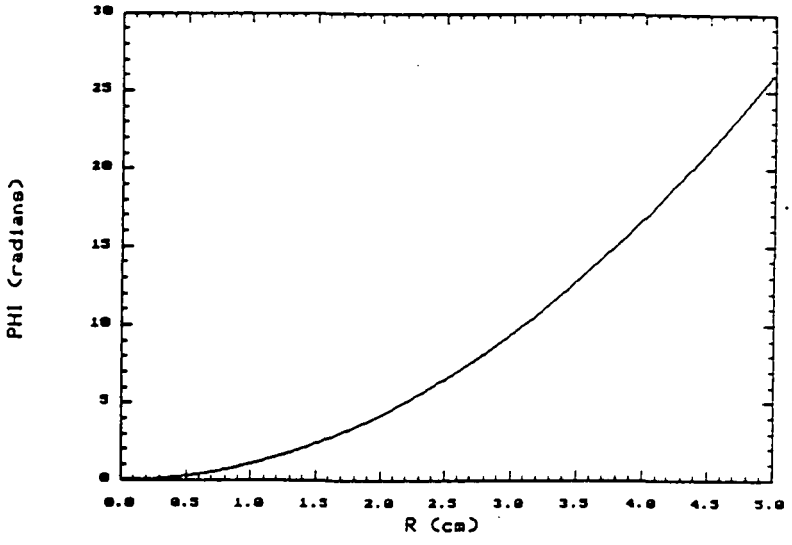

LENS CROSS SECTION

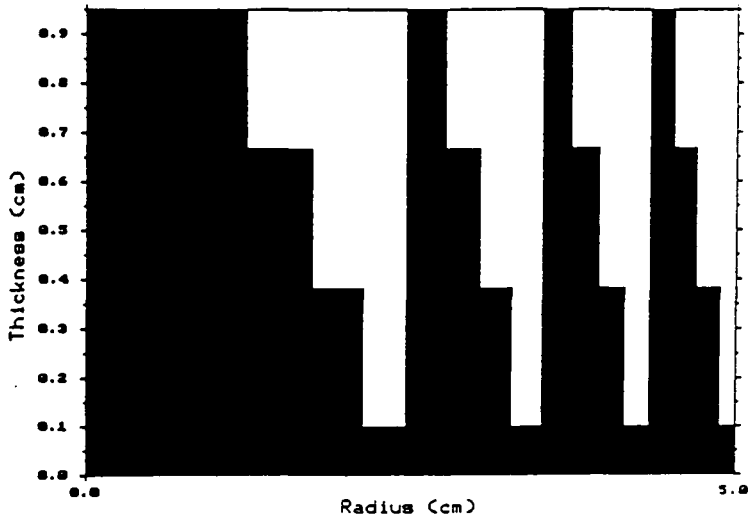

OUTPUT PHASE DISTRIBUTION

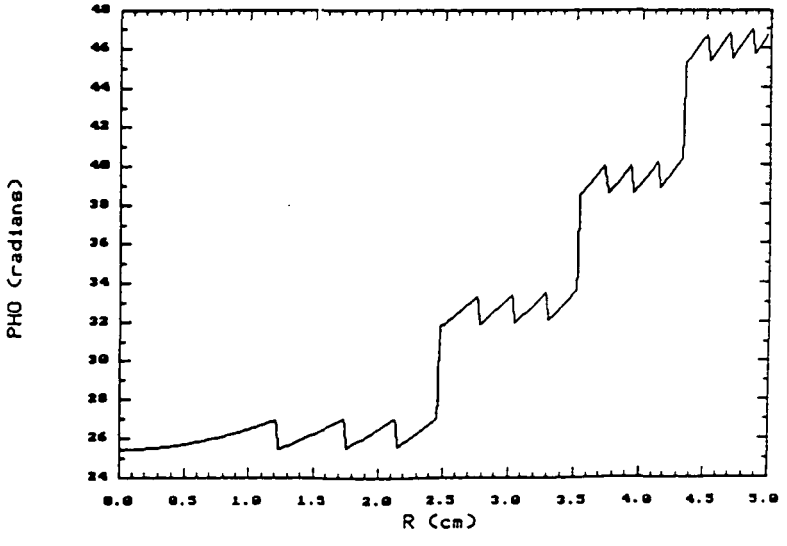

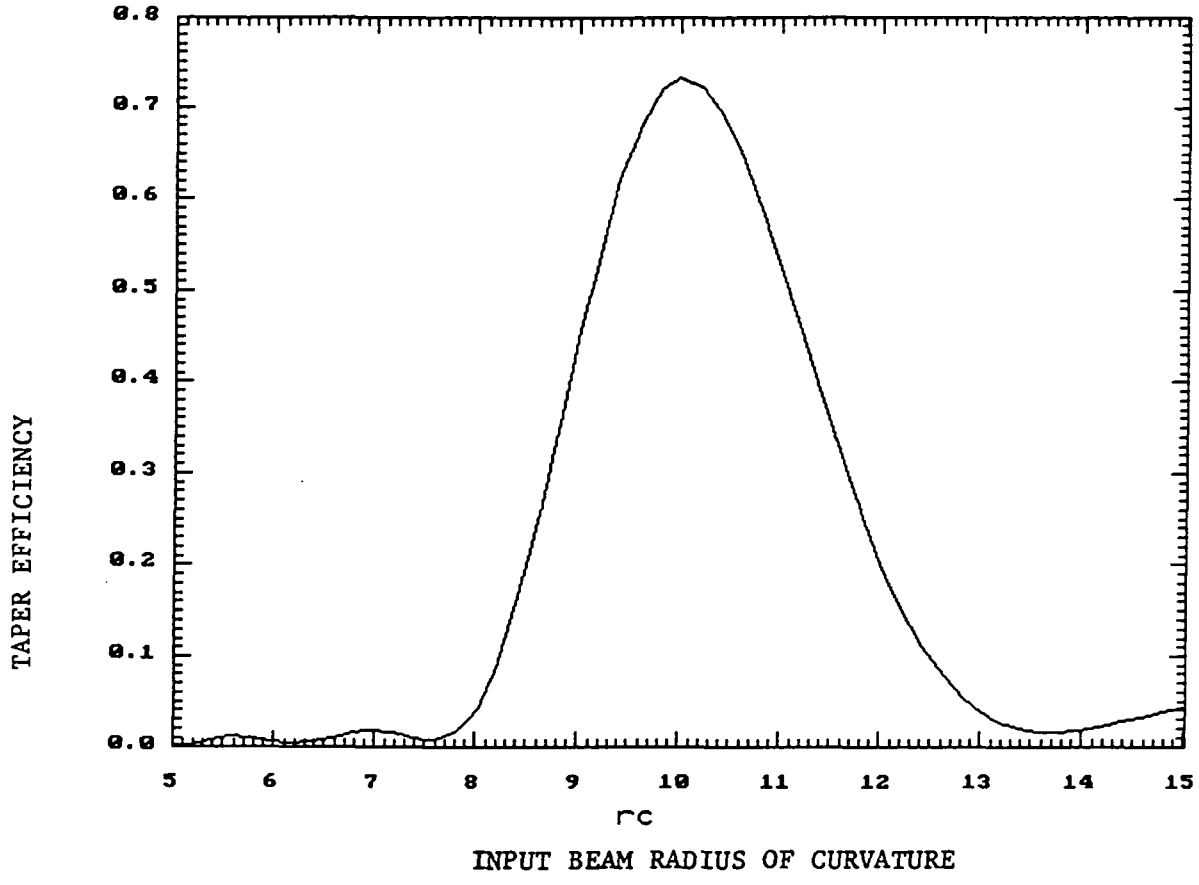

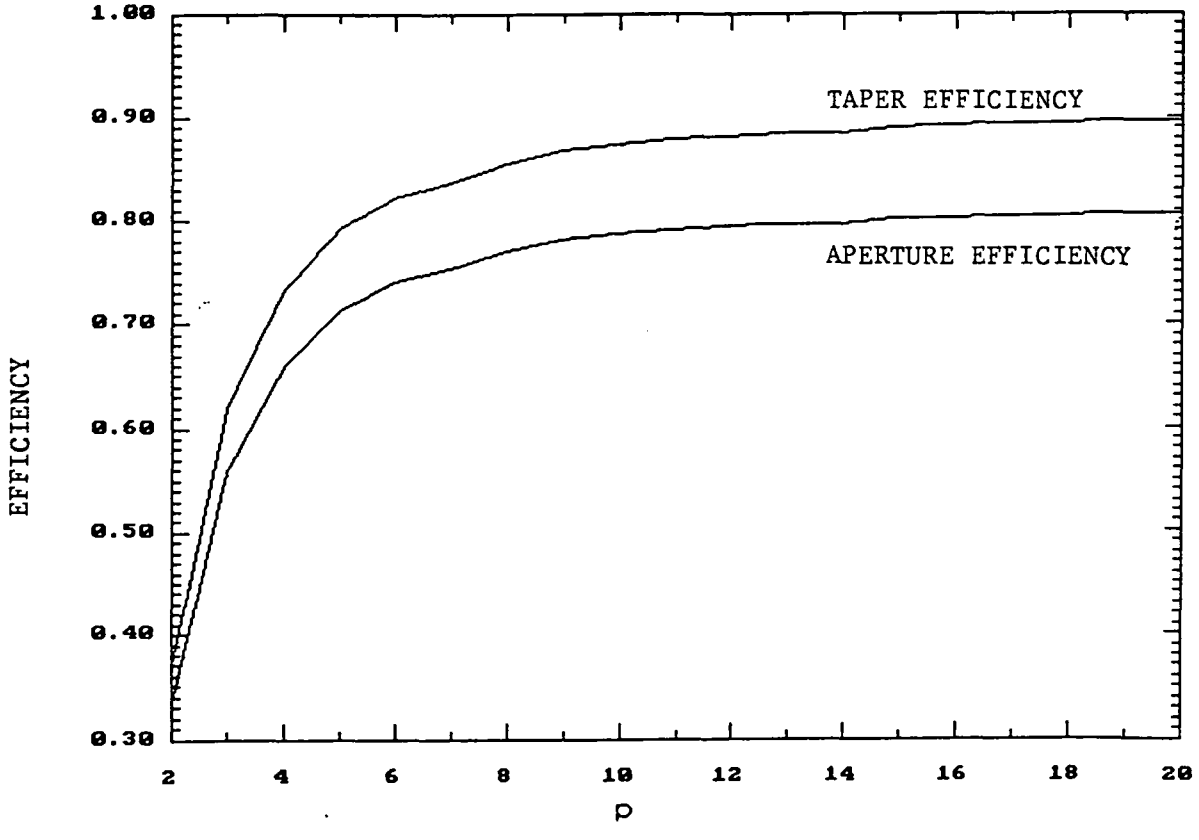

FIGURE 6 - (a) EFFICIENCY AS FUNCTION OF INPUT BEAM RADIUS OF CURVATURE
(b) EFFICIENCY VERSUS P

FIGURE 7

94GHz LENS COMPARISON

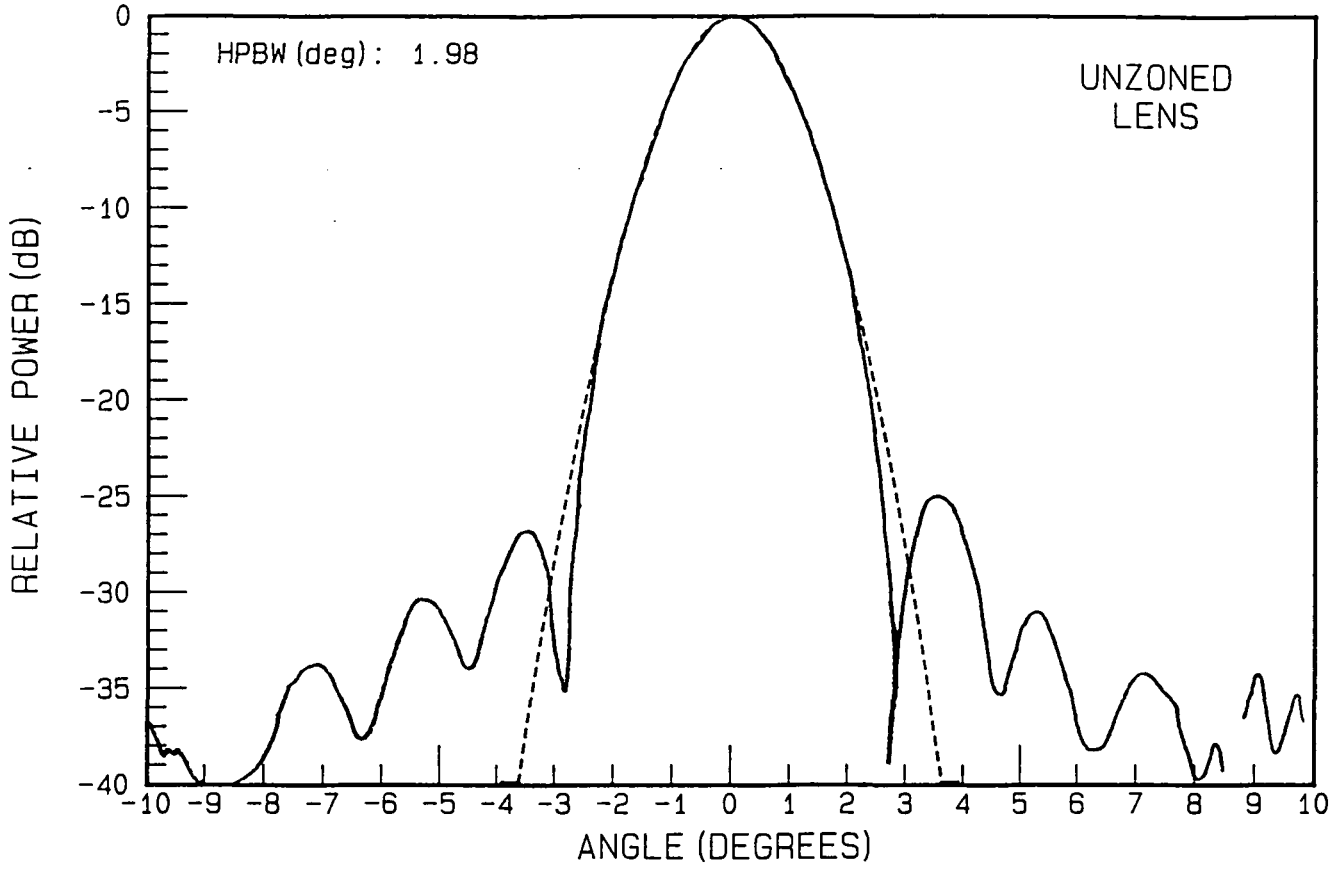

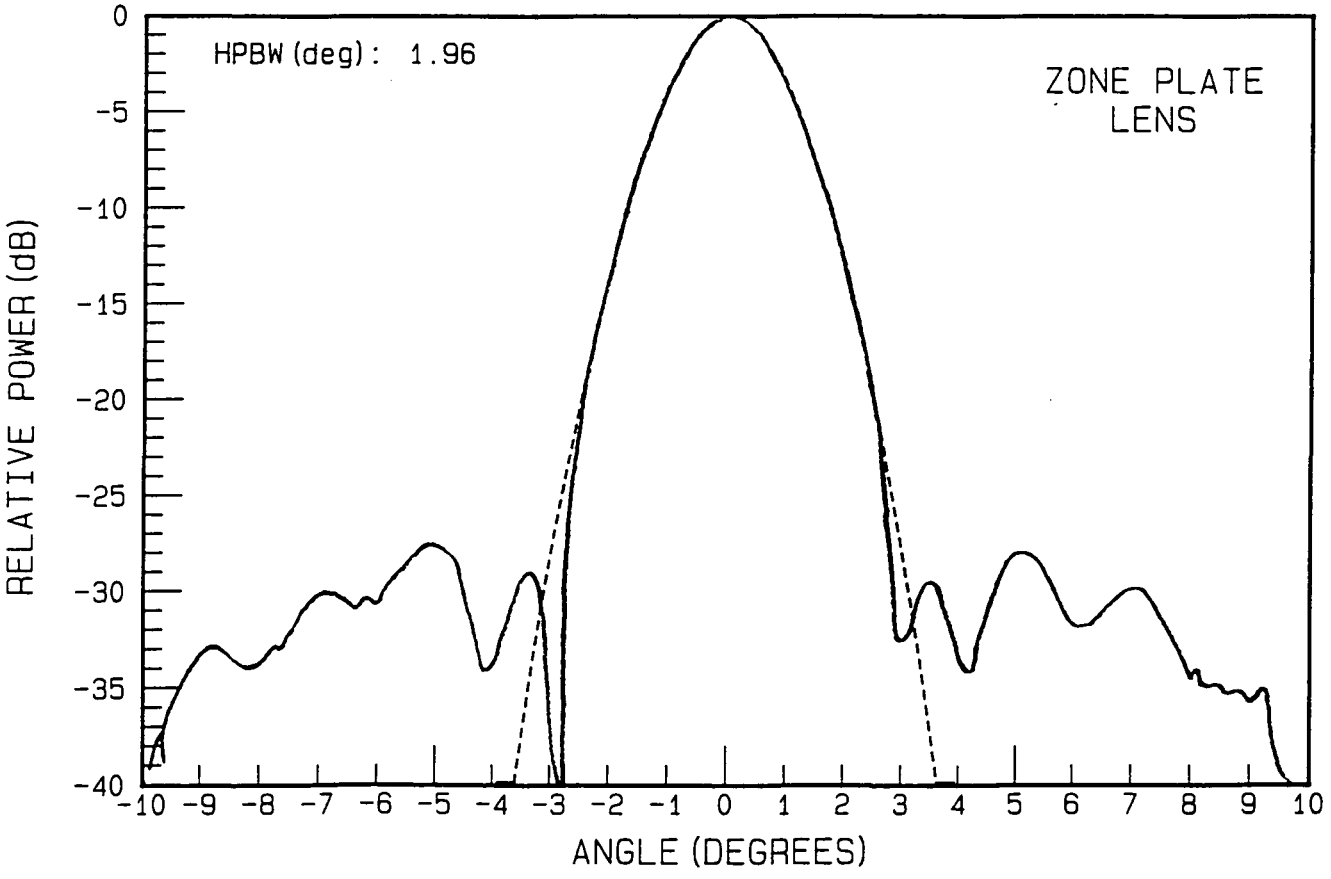

GS1179

ONSET OF DISPERSION IN Nb MICROSTRIP TRANSMISSION LINES AT SUBMILLIMETER WAVE FREQUENCIES

H. H. S. Javadi, W. R. McGrath, B. Bumble, H. G. LeDuc

Center for Space Microelectronics Technology
Jet Propulsion Laboratory
California Institute of Technology
Pasadena, CA 91109

ABSTRACT

We have measured the dispersion in phase velocity of a Nb-SiO_x-Nb microstrip transmission line resonator over a frequency range from 50 GHz to 800 GHz. A submicron Nb/Al-AlO_x/Nb Josephson junction was used as a voltage-controlled oscillator to excite the high order modes in the resonator. The same junction is used as a direct detector resulting in a series of step-like structures in the DC current-voltage characteristic at the position of each mode frequency. The transmission line is dispersionless up to about 500 GHz where the phase velocity begins to decrease. This is well below the gap frequency $f_g \approx 700$ GHz. Results agree qualitatively with the expected theoretical behavior near f_g. This onset of dispersion and loss in Nb transmission lines will have a significant impact on the design of submillimeter wave rf circuits.

Superconducting transmission lines have many important applications in high frequency analog circuits and high bit rate digital systems, to name a few. These transmission lines are expected to be nearly lossless and dispersion free up to frequencies near the superconducting energy gap frequency $f_g = 2\Delta / h$, where Δ is the superconductor energy gap parameter and h is Planck's constant. We are interested in superconductive microstrip transmission lines as integrated rf tuning elements for superconductor-insulator-superconductor (SIS) quasiparticle mixers at frequencies near 630 GHz. These SIS mixers provide near quantum-limited sensitivity throughout the millimeter wave band [1-3], provided they are optimized with an appropriate rf embedding circuit. The large geometrical capacitance C_J of the tunnel junction provides a susceptance which shunts the rf signal away from the nonlinear quasiparticle conductance channel. An open-circuited superconductive microstrip transmission line (stub) can provide a parallel inductance to resonate with the junction capacitance. This approach was first used successfully with an SIS mixer operating near 36 GHz [4] and since has been used at frequencies up to 360 GHz [5,6]. However, above 100 GHz, uncertainties in material, transmission line, and junction parameters generally lead to poor performance.

The phase velocity must be accurately known in order to correctly design the microstrip stub for a particular application. At high frequencies possible dispersion and loss are expected to degrade the performance. It is thus important to know the frequency range at which these effects become significant. Other groups [7,8] have measured short-pulse propagation on superconductive coplanar transmission lines using optical sampling techniques and indirectly determined loss and dispersion from a Fourier transform analysis of the pulse distortion.

We have taken a different approach, using a Josephson junction as both a sweep-oscillator and detector to sample the resonances of a microstrip stub. This stub is connected in parallel across the junction as shown in fig. 1. The ac Josephson effect provides a voltage-controlled oscillator. The frequency is $2eV_b/h \approx 0.485 \times V_b$ (μV) GHz where V_b is the junction bias voltage. This monochromatic signal sets up a standing wave in the stub. The junction detects this standing wave and a signature is developed in the DC current-voltage (I-V) curve of the junction by a frequency downconversion process. As the bias voltage, and thus frequency is swept, small current steps will appear in the DC I-V curve of the junction at frequencies corresponding to the modes of the stub. The

frequency spacing of the modes is given by $\Delta f = v_\phi/2l$ where v_ϕ is the phase velocity and l is the physical length of the stub. Thus by measuring the voltage interval between steps, the phase velocity can readily be obtained if it is constant over this interval. In general, this technique can be used at high frequencies well above the energy gap frequency f_g. A similar approach using microstrip resonators with a single resonance below f_g has recently been reported [9]. Values of surface resistance and phase velocity were determined up to about 400 GHz. We have used long microstrip resonators with many high order modes to determine the phase velocity as a function of frequency up to 800 GHz, which is above the gap frequency of niobium (Nb). The onset of dispersion has clearly been observed.

High quality Nb / Al-AlOx / Nb tunnel junctions are fabricated using a trilayer process [10]. The junction area, defined by electron-beam lithography, is between $0.3\mu^2$ and $1\mu^2$. The DC sputtered Nb films are 2000 - 3300 Å thick. The current density is as high as 10^4 A/cm^2 and the normal state resistance is 50Ω - 70Ω. SiO_x serves as both a planarization layer for the junction trilayer and the dielectric layer for the microstrip stub.

The thickness is $t_d \approx 1500$Å and the dielectric constant is taken to be $\varepsilon_r = 5.5$ [11]. The dielectric thickness is comparable to the magnetic penetration depth. In this case, the phase velocity is << c and hence is strongly affected by the field penetration into the Nb. This makes v_ϕ a sensitive probe of the superconductive properties of Nb.

Junctions fabricated for use as SIS mixers have stubs 2μ wide by 60μ - 70μ long to provide a fundamental broad band resonance near 630 GHz. However, to study the phase velocity, junctions were fabricated with stubs 2μ wide by 518μ or 1064μ long. A longer stub gives a smaller spacing between resonant modes, thus providing a better indication of the phase velocity in a given frequency range. Careful examination of these stubs however, indicated jagged edges and undercutting of the SiO_x. Additional junctions were fabricated with stubs 6μ and 12μ wide to reduce uncertainties due to these edge effects. These stubs were either 500μ, 750μ, or 1000μ long.

The fundamental resonance frequency of a 1000μ long stub is estimated to be about 50 GHz [4]. This leads to steps in the I-V curve which are ≈0.1 mV apart. The inset of fig. 2 shows one example. The

subgap conductance of this junction is very large with an almost point-contact type of appearance. While junctions with much lower subgap conductance also showed resonant peaks, the step structure was seen mostly in junctions similar to that shown in fig. 2. An external magnetic field was used to enhance the steps in different voltage ranges [12]. In order to accurately locate these small steps in current, a small amplitude, low frequency (~ 200 Hz) ac voltage was superimposed on V_b. The resulting ac signal was detected with a lock-in amplifier. The interval between two adjacent peaks is then measured to determine v_ϕ which is plotted as a function of the frequency of the higher step. Due to the discreteness of the data, the resolution for changes in velocity is the frequency spacing of the modes. Figure 2 shows the results for 4 different microstrip stubs. About 10 to 14 resonances were observed between 50 GHz and ~ 750 GHz. A smooth curve was drawn through the resulting velocity vs frequency data. The scatter in velocity values about this curve is typically 5%, with only a few points deviating by ~ 10%.

Curve 1 is an example of a junction with a 2μ wide stub. Resonances of these narrow stubs were usually not observable above about 500 GHz. This may be due to increased scattering or losses from the edge effects

mentioned earlier. Curves 2, 3, and 4 represent stubs 1000μ long with widths of 6μ or 12μ. At low frequencies, a slight curvature can been seen in the data as expected from the mode spacing (see discussion below). Otherwise the curves are horizontal up to about 500 GHz where they begin to bend down indicating the onset of dispersion. The gap frequency of a pristine Nb film is $f_g \approx 740$ GHz at 0K. Thus the dispersion begins at frequencies well below f_g. This agrees with previously reported results [8] using an optical sampling technique. While SIS mixers are predicted to operate well up to f_g [13], the resonant embedding circuit utilizing superconductive microstrip transmission lines is limited to lower frequencies.

Figure 3 shows the data for a 500μ long x 12μ wide stub. In this case, resonances, and hence the phase velocity, were obtained up to ≈ 800GHz which is above the gap frequency of Nb. At low frequencies, the velocity is dispersionless. Around 500 GHz, the velocity begins to decrease and reaches its lowest value near 730 GHz. For this data point, the frequency resolution for velocity change is about 50 GHz. This minimum is expected theoretically to occur near 770 GHz (see fig. 3) using a gap frequency of 660 GHz as determined from the I-V curve of this

junction at zero magnetic field (a more complete discussion of the theory will be given in the future [14]). In addition, we have observed a small suppression of the energy gap with external magnetic field in these junctions which may describe the lower frequency of the observed phase velocity minimum. Other loss mechanisms may also play a role. The velocity begins to increase above 730 GHz as is expected theoretically, since the superconductor begins to behave as a normal metal for frequencies well above f_g. The solid line in fig. 3 is the theoretical prediction for the velocity. We have used the approach followed by Kautz [15] which employs the Mattis-Bardeen [16] theory for the electrical conductivity. The magnetic penetration depth was adjusted to λ = 900Å to fit the theory to the low frequency asymptote of the velocity. As seen from fig. 3, theory and experiment show the same general trend. However, based on the Mattis-Bardeen conductivity, the theory predicts a 9% decrease in velocity at the dip whereas the experiment shows a 35% dip. Errors in velocity resulting from uncertainties in the mode spacings can result from end effects on the microstrip line and the possibility of a negative resistance loop in the I-V curve at the position of the resonance [17]. However for our geometry, the end-effect correction to the length is << 1%, and the worst-case negative resistance, predicted for a lightly-

damped resonance, could only cause a 5% shift in the apparant position of the resonance. Thus neither effect can account for the large change we observe. At low frequencies, superconductive microstrip is a slow-wave transmission line due to the penetration of the electromagnetic field into the superconductor over a length comparable to the thickness of the dielectric. For frequencies well above f_g, the phase velocity increases towards the value for a normal line. The onset of dispersion just below the gap frequency is due to the departure of the imaginary part of the pair conductivity from a 1/f frequency dependence [15].

Some additional insight may be gained by first considering a Josephson junction directly coupled to a lossless microstrip stub. Using the notation in reference [18], the resonant frequencies of the stub are solutions to the transcendental equation

$$-\pi \frac{C_J}{C_S} \frac{f}{f_S} = \tan\left(\frac{\pi f}{f_S}\right) \qquad (1)$$

where $C_s = \varepsilon_r \varepsilon_0 / w / t_d$ is the total capacitance of the stub and f_s is the fundamental mode of the stub. This mode occurs when the length of the

stub, l, equals one wavelength and is given by $f_s = v_\phi / 2l$.

In fig. 4 both sides of eqn. (1) are plotted vs (f/f_s) for an arbitrary value of C_J/C_s. At low frequencies, intersections between the straight line (left hand side of eqn. 1) and the tangent curves are between $(m-1/2)f_s$ and mf_s where m is an integer. These solutions move progressively toward $(m-1/2)f_s$ for $m >> 1$. Thus at high frequencies, the solutions of eqn. (1) (i.e.: the modes of the stub) are equidistant. If plotted in the spirit of fig. 2, they represent a horizontal line.

We have extended eqn. (1) to the case of a lossy transmission line, yielding

$$-\pi \frac{C_J}{C_S} \frac{f}{f_S} = \frac{2 \sin\left(\frac{2\pi f}{f_S}\right)}{\left(e^{2\alpha l} + e^{-2\alpha l}\right) + \cos\left(\frac{2\pi f}{f_S}\right)} \qquad (2)$$

where α is the attenuation constant. In fig. 4, the right hand side of eqn.

(2) is plotted for three arbitrary cases of loss: αl = 0.05, 0.10, and 0.15. As can be seen, the distance between the solutions first decreases and then increases as losses in the microstrip line increase. In light of this, our experimental observations can be interpreted as evidence for increased loss in either the superconductor or the dielectric layer. Losses due to radiation will be negligible given the cross sectional dimensions of the stub, 0.15μ x 12μ, compared to relevent free space wavelengths, λ_0 ~ 500μ [19]. It is expected that absorption of water in evaporated SiO_x films could contribute losses at microwave and millimeter wave frequencies. Losses due to absorbed water molecules constitute broad peaks in the frequency domain. The attenuation of a microstrip line is linearly proportional to frequency provided the loss in the dielectric is frequency independent. A linear dependence is much weaker than the sharp increase in attenuation expected near the gap frequency. Moreover, since we observe a strong dispersion near the Nb gap frequency, the superconductors are the most probable source for the losses. The superconducting electrodes of the microstrip line are not perfect, defect free, bulk crystalline materials, but are polycrystalline thin films with fine grains and possibly surface layers and interface defects. These

microstructural features of real films may be responsible, in part, for the large dispersion we observe.

In summary, we have presented evidence for the onset of dispersion and loss at submillimeter wave frequencies in Nb-SiO_x-Nb microstrip transmission lines. This behavior is expected at frequencies approaching the gap frequency, but the range over which Nb microstrip lines are dispersionless was previously not well known. These results will have a direct impact on the application of Nb microstrip lines in millimeter wave and submillimeter wave circuits. For operation near 1 THz, higher temperature superconductors such as NbN or NbCN will have to be investigated.

This work was supported in part by the Jet Propulsion Laboratory, California Institute Of Technology, under contract to the National Aeronautics and Space Administration and the Innovative Science and Technology Office of the Strategic Defense Initiative Organization.

REFERENCES

1. C.A. Mears, Q. Hu, P.L. Richards, A. H. Worsham, D.E. Prober, and A.V. Raisanen, Appl. Phys. Lett. **57**, 2487 (1990).
2. H.H.S. Javadi, W.R. McGrath, S.R. Cypher, B. Bumble, B.D. Hunt, and H.G. LeDuc, Digest, 15th. Int. Conf. on IR and Millimeter Waves, p.245, Orlando, FL (1990).
3. B.N. Ellison, P.L. Schaffer, W. Schaal, D. Vail, and R.E. Miller, Int. J. IR and mm Waves **10**, 937 (1989).
4. A.V. Raisanen, W.R. McGrath, P.L. Richards, F.L. Lloyd, IEEE Trans. Microwave Theory Techn. **MTT-33**, 1495 (1985).
5. Q. Hu, C.A. Mears, P.L. Richards, and F.L. Lloyd, IEEE Trans. Magn. **25**, 1380 (1989).
6. W.R. McGrath, J.A. Stern, H.H.S. Javadi, S.R. Cypher, B.D. Hunt, H.G. LeDuc, IEEE Trans. Magn. **27**, 2650 (1991).
7. M.C. Nuss and K.W. Goossen, IEEE J. Quantum Electronics **25**, 2596 (1989).
8. C.C. Chi, W.J. Gallagher, I.N. Duling III, D. Grischkowsky, N.J. Halas, M.B. Ketchen, and A.W. Kleinsasser, IEEE Trans. Magn. **MAG-23**, 1666 (1987).
9. B. Bi, K. Wan, W. Zhang, S. Han, J.E. Lukens, IEEE Trans. Appl. Superconductivity **1**, 145 (1991).

. H.G. LeDuc, B. Bumble, S.R. Cypher, and J.A. Stern, submitted to 3rd. International Symposium on Space Terahertz Technology, University of Michigan, Ann Arbor, March 1992.

. H.K. Olsson, IEEE Trans. Magn. **25**, 1115 (1989).

. I.O. Kulik, JETP Lett. **2**, 84, 1965.

. M.J. Feldman, Int. J. IR and mm Waves **8**, 1287 (1987).

. H.H.S. Javadi and W.R. McGrath, to be published.

. R.L. Kautz, J. Appl. Phys. **49**, 308 (1978).

. D.C. Mattis and J. Bardeen, Phys. Rev. **111**, 412 (1958).

. D.B. Tuckerman and J.H. Magerlein, Appl. Phys. Lett. **37**, 241 (1980).

. H.D. Jensen, A. Larsen, J. Mygind, IEEE Trans. Magn. **27**, 3355 (1991).

. T.C. Edwards, *Foundations for Microstrip Circuit Design* , John Wiley and Sons, New York (1981).

FIGURE CAPTIONS

Figure 1. (a) Geometry of open-circuited microstrip stub and Josephson junction. (b) Cross sectional view of stub and junction.

Figure 2. Phase velocity vs. frequency for four different Nb microstrip stubs at 4.2K. The stub dimensions are 1: 2μ x 1064μ; 2: 12μ X 1000μ; 3: 6μ X 1000μ; 4: 6μ X 1000μ. Inset shows current steps in DC IV curve associated with high order modes in the stub.

Figure 3. Phase velocity vs. frequency for a Nb stub 12μ wide X 500μ long. The different symbols refer to data taken with different applied external magnetic fields. The solid line is the theoretical prediction. The arrow indicates the gap frequency as determined for the Nb junction (at zero magnetic field) which is used in the calculation.

Figure 4. Graphical representation of both sides of the transcendental eqns (1) and (2). X-axis is frequency normalized to f_s (fundamental resonance of the stub). Straight line is a plot of the left hand side of eqns (1) and (2) with arbitrary slope. Right hand side of eqn (1) is represented by tangent

curves while right hand side of eqn (2) is plotted for values of αl = 0.05, 0.10, 0.15. Intersections of the straight line and the tangent curves represent the modes of the stub. When losses are significant ($\alpha l > 0$), the mode frequencies are determined by the closest approach of the two curves as indicated by the arrows.

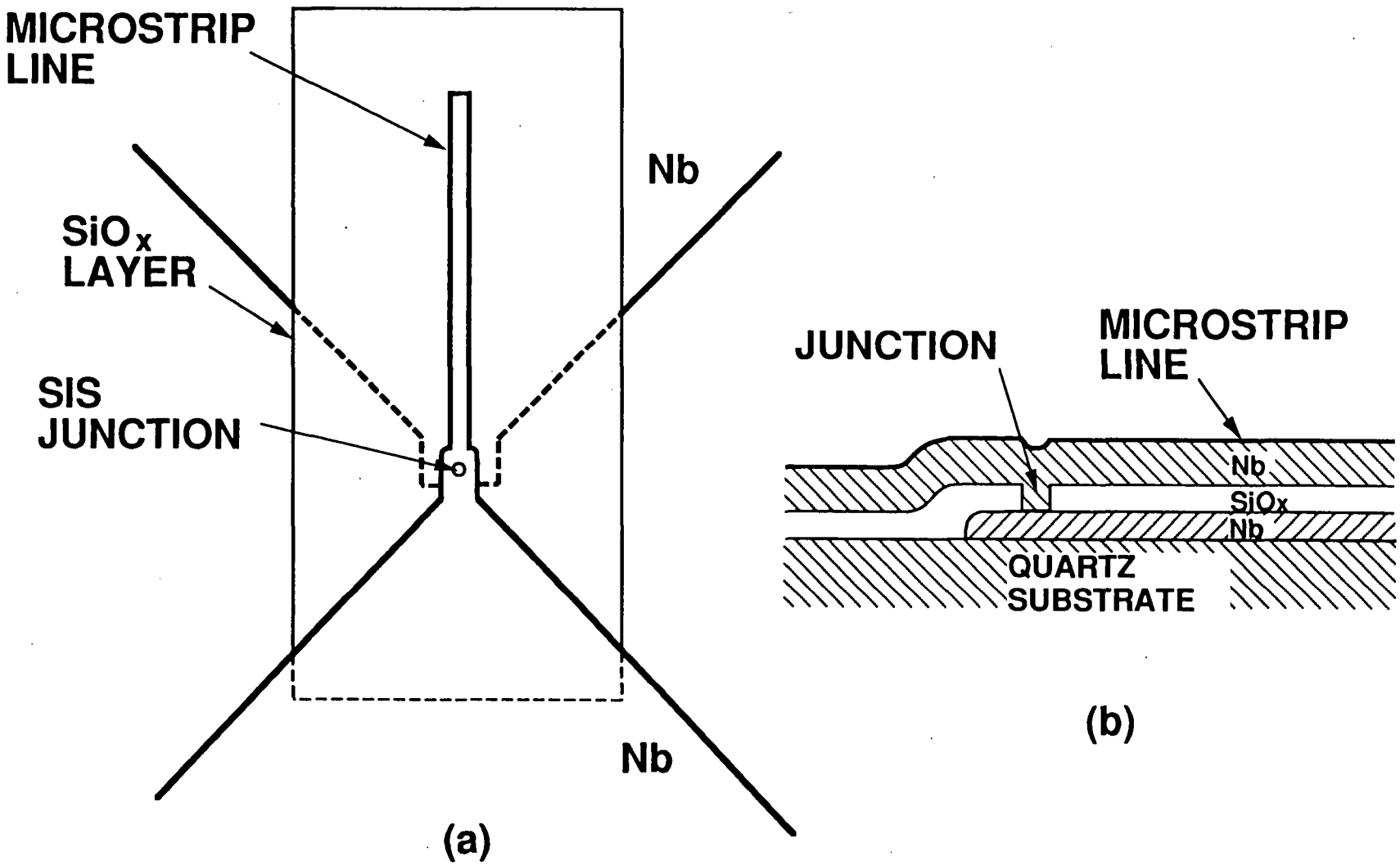
MICROSTRIP
LINE
Nb
SiOx
LAYER
SIS
JUNCTION
Nb
(a)
JUNCTION
MICROSTRIP
LINE
Nb
SiOx
Nb
QUARTZ
SUBSTRATE
(b)

Figure 1

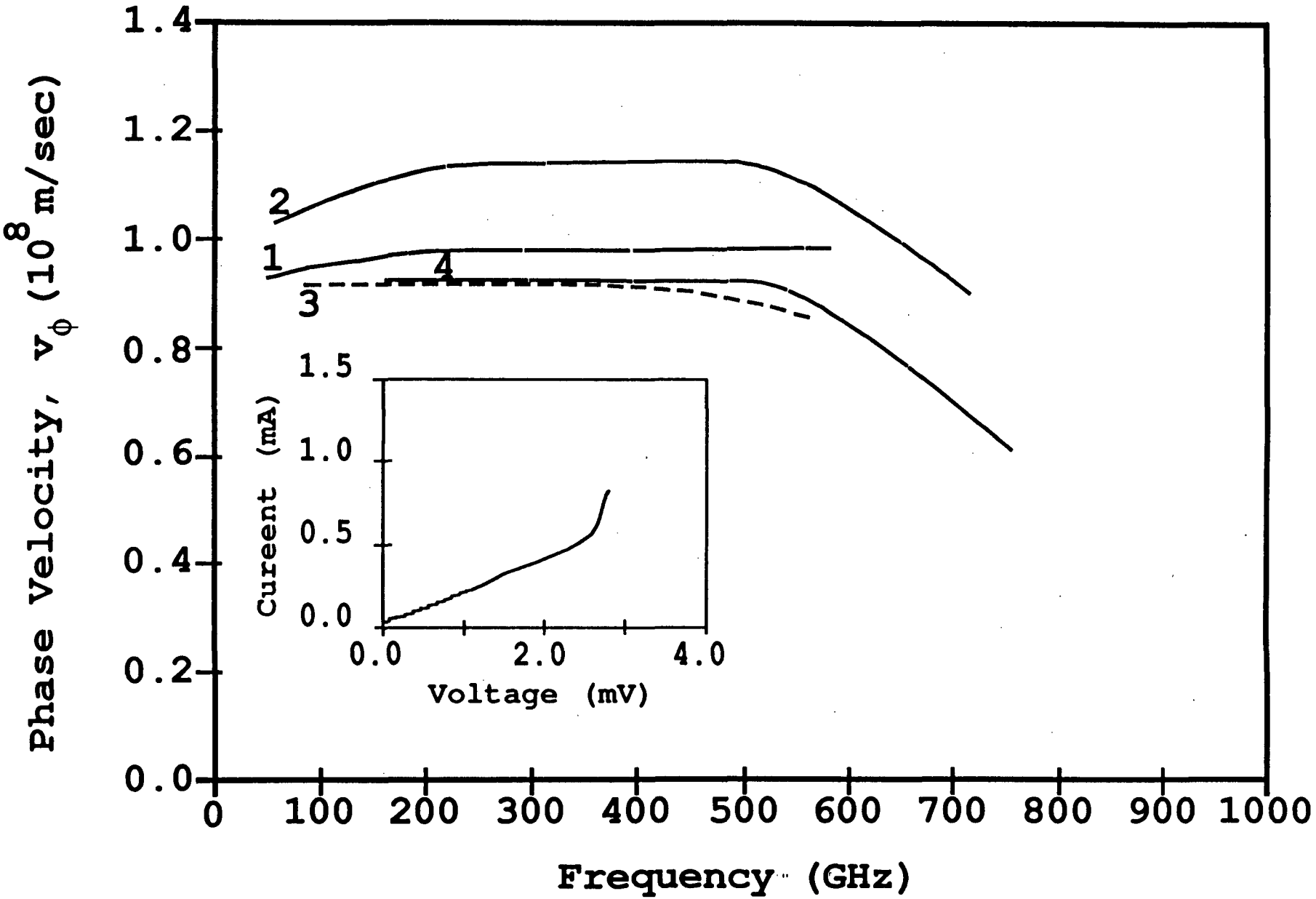
Phase Velocity, v_ϕ (10^8 m/sec)
1.4
1.2
1.0
0.8
0.6
0.4
0.2
0.0
0
100
200
300
400
500
600
700
800
900
1000
Frequency (GHz)
1
2
3
4
Cureent (mA)
1.5
1.0
0.5
0.0
0.0
2.0
4.0
Voltage (mV)

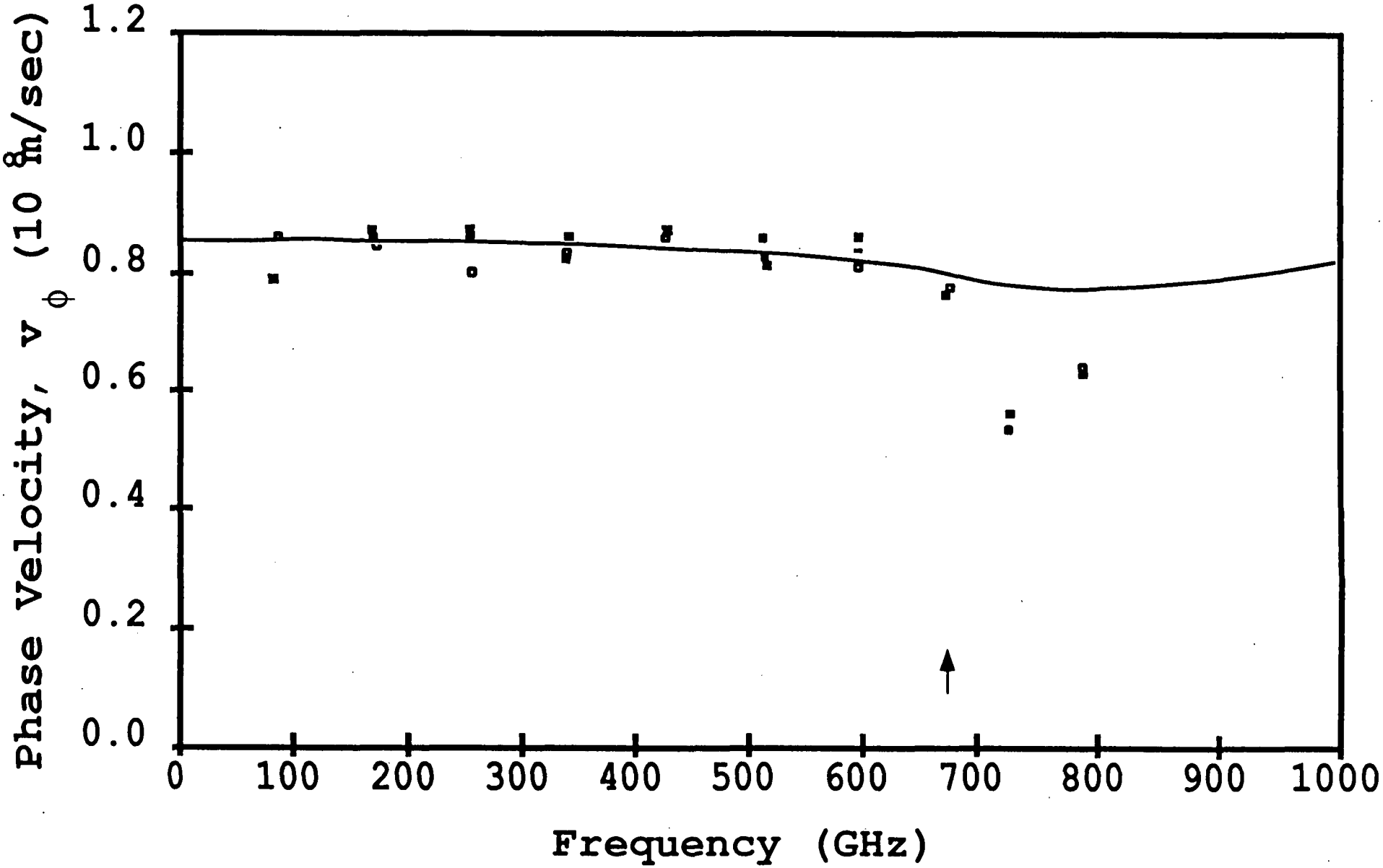

Javadi et al Fig. 3

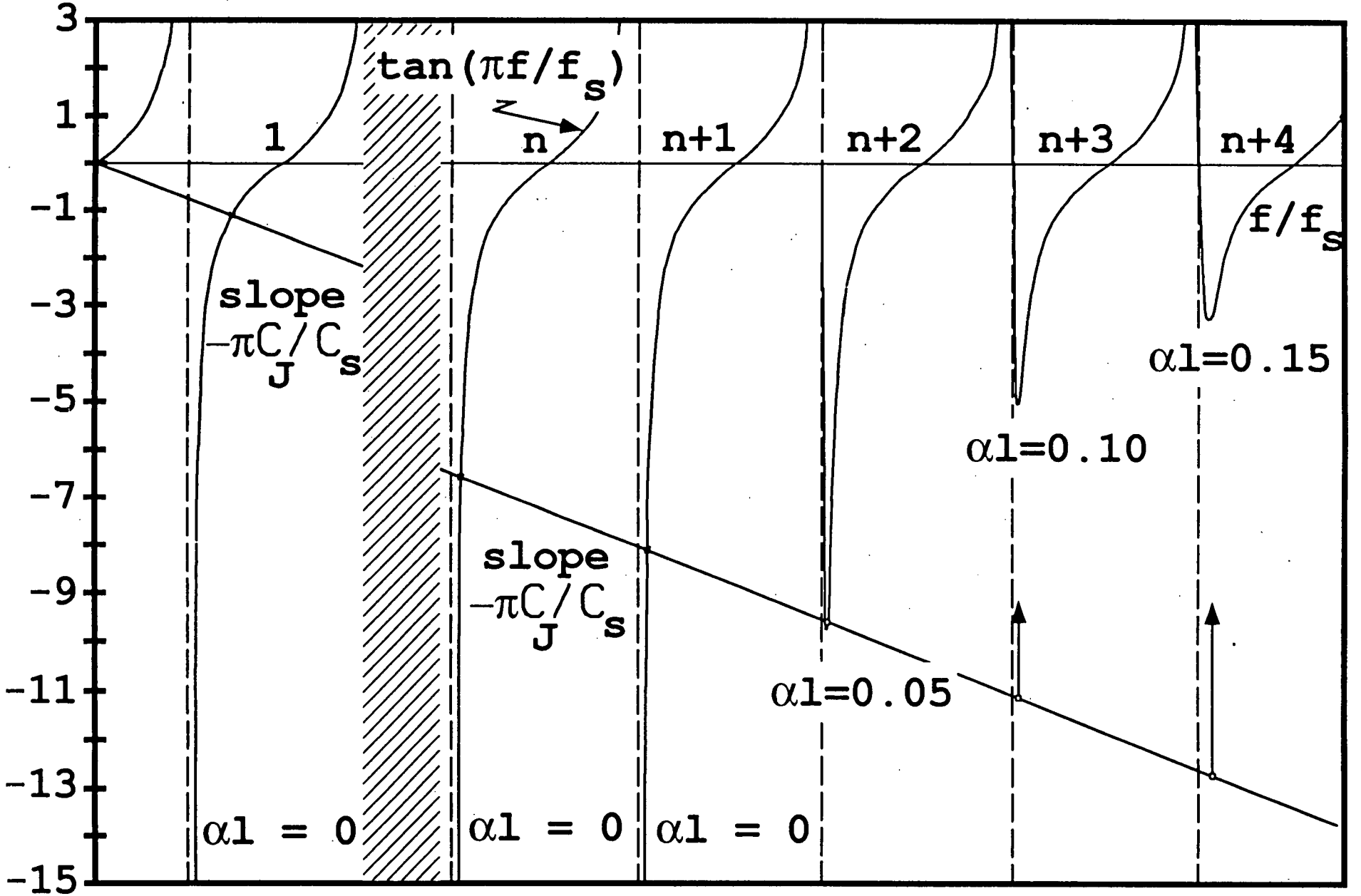
3
1
-1
-3
-5
-7
-9
-11
-13
-15
tan(πf/f_s)
z
1
n
n+1
n+2
n+3
n+4
f/f_s
slope
−πC_J/C_s
slope
−πC_J/C_s
αl=0.15
αl=0.10
αl=0.05
αl = 0
αl = 0
αl = 0

The material presented below is intended as a review only. A full length paper has been submitted for publication in IEEE/MTT (May 1992).

DOUBLE-SLOT ANTENNAS ON EXTENDED HEMISPHERICAL DIELECTRIC LENSES

Daniel F. Filipovic, Steve J. Gearhart, Brian K. Kormanyos and Gabriel M. Rebeiz

NASA/Center for Space Terahertz Technology
Electrical Engineering and Computer Science Department
University of Michigan
Ann Arbor, MI 48109-2122

ABSTRACT

An investigation of the coupling efficiencies to a gaussian-beam of a double-slot antenna on a hyperhemispherical lens is presented. It is shown that both lenses couple equally well to an appropriate gaussian beam (about 80%). The radiation patterns of both lenses with a double-slot antenna are computed using the ray-tracing method. The experimental radiation patterns are presented and show close agreement to the theoretically computed patterns.

I. INTRODUCTION

The use of a hemispherical lens with an attached extension length can greatly improve coupling to a gaussian-beam system. In optical theory, an extension length of r/n is used, and this extended lens is termed a hyperhemispherical lens. This extension length was chosen since it satisfies the sine condition, which is where first-order aberrations are removed [1]. The hyperhemispherical lens was borrowed into the millimeter-wave field [2,3,4], but it was found that radiation patterns from these lenses were very broad and even multi-lobed in some cases. The hyperhemispherical lens is capable of coupling well to a gaussian-beam system. However, it couples most efficiently to a converging beam and not to a plane wave. Recently, several researchers showed that a narrow, diffraction-limited beam could be achieved by putting the antennas on an elliptical lens [5,6]. The same effect was also found by taking a hyperhemispherical lens and adding a planar extension to it [7]. Figure 1 shows that the focus of this longer extension length lens superimposes exactly on the second focus of an elliptical lens. It is known from optical theory that a plane wave converges to the second focus of an ellipse, and therefore a lens with this extension length is simply a close geometrical approximation to an elliptical lens. The validity of this approximation depends on the maximum allowed phase tolerance. For high dielectric constants (see Fig. 1) and relatively low frequencies, the phase difference becomes small and the approximation is valid. Generally, for lens diameter of 12.5mm, ϵ larger than 4, and frequencies less than 300GHz, the approximation is very good.

II. THEORETICAL AND EXPERIMENTAL PATTERNS

The theoretical radiation patterns are computed using a ray-tracing technique [9]. First, the feed antenna pattern into the dielectric is calculated using standard far-field methods. Figure 2 shows the calculated radiation patterns for a double-slot antenna with $L = 0.28\lambda_{air}$ and $d = 0.16\lambda_{air}$. These parameters were chosen to result in a symmetric pattern inside the dielectric and a low cross-polarization in the 45°-plane. Ray-tracing is then used to calculate the electric field distribution across the aperture plane (Fig. 3). In this method, the fields are decomposed into TE/TM components at the lens/air interface, and the appropriate transmission formulas are used for each mode. The power reflected into the substrate is neglected in this analysis. A diffraction integral over the aperture then yields the far-field pattern from the lens. Experimental measurements were performed at 246GHz on a 13.7 mm diameter silicon lens (ϵ=11.7) with the double-slot antenna as a feed. Different values of extension length were achieved by adding high-resistivity silicon wafers, resulting in 3 extension lengths: hyperhemispherical, intermediate, and elliptical (Fig. 3). Measured patterns at the elliptical focus (Fig. 4) demonstrate a gain of 28.6dB±0.3dB with relatively low sidelobes (-16dB). From the measured patterns, the resulting aperture efficiency (coupling to a plane wave) is 73%. The theoretical patterns calculated for this position are a bit wider than the measured patterns (Fig. 5). This discrepancy arises from the fact that rays at a certain angle end up hitting the critical angle at the lens/air interface, resulting in no transmission of rays after this point. This limits the aperture size and results in a wider theoretical pattern. Note that this discrepancy is only significant at the elliptical focus for lenses with high dielectric constants. Measured patterns at the elliptical focus for ±10% of the

246GHz design frequency (Fig. 6) result in nearly the same gain, and therefore the double-slot antenna has good pattern bandwidth. The measured power at broadside is nearly the same from 222GHz-270GHz, also indicating good impedance bandwidth for the double-slot design. The measured patterns at the intermediate focus (Fig. 7) are similar to the elliptical focus, but with a gain of 24dB±0.3dB. In this case, the critical angle is not a problem, and there is close agreement between theory and experiment (Fig. 8). At the hyperhemispherical focus (Fig. 9), the pattern becomes very wide with a gain of 18.1dB±0.3dB and shows a multi-peak behaviour, as indicated by theory (Fig. 10). As will be seen later, this has no detrimental effect on the coupling efficiency to a converging beam. The ratio of the 246GHz measured received power at broadside for an elliptical lens and a hyperhemispherical lens was 10dB which is the same as the difference in the measured directivities. This indicates that no power is coupled to substrate modes that may arise in the flat wafers.

III. GAUSSIAN-BEAM COUPLING

In order to match the double-slot/extended hemisphere system to a gaussian beam, one could compute the electric field across the aperture and match this to a gaussian beam. Since we had already predicted the far-field amplitude and phase distributions, we chose to compute the coupling efficiency to a gaussian beam in the far-field (see Appendix). In this calculation, the power radiated by the slot antennas to the air-side (which is 11.5% of the total power) is taken into account, and no lens-air interface loss is considered. The power loss radiated to the air side could be reflected using an appropriately designed cavity at the expense of impedance bandwidth. Figure 11 gives the gaussian-beam parameters which

yield the highest coupling efficiency, and shows that all three focus positions are capable of coupling equally well to a gaussian beam. However, the non-elliptical foci require a converging wavefront, whereas the elliptical focus couples directly to a Gaussian beam with an equal phase wavefront. Note that equivalent gaussian-beam parameters in the near field may be found through a simple inverse Fourier transform. A gaussian beam experiment was performed at 246GHz, in which it was attempted to couple all the power coming out of a lens into the double-slot antenna. For the elliptical focus, the lens was placed at the minimum waist position, where the radius of curvature is infinite, indicating an equal phase wavefront. For the hyperhemispherical position, the lens was placed closer to the lens, at a position where there is a negative radius of curvature. The proper negative radius of curvature and position were computed knowing the gaussian-beam parameters from Figure 11. It was found that the ratio of powers with either focus is the same within experimental error ($\pm 4\%$), indicating that both the hyperhemispherical focus and the elliptical focus will match equally well to an appropriately designed gaussian-beam system. Similar measurements were done on a log-periodic antenna from 90-250GHz. The results are similar to those presented in this paper and have been submitted for publication in IRMMW (May 92).

IV. ACKNOWLEDGEMENTS

This work was supported by the NASA/Center for Space Terahertz Technology at the University of Michigan.

APPENDIX

The field representation of a Gaussian beam is of the form: $\mathbf{E}_{\mathrm{Gauss}}(\theta) = \hat{\epsilon}\ \exp^{-[\theta/\theta_0]^2} \exp^{j\pi[\theta/\theta_1]^2}$ The coupling efficiency between an antenna pattern and a gaussian beam is calculated using the formula [12,13]:

$$\eta_{Gauss} = \frac{|\iint[\hat{\epsilon}_{co} \cdot \mathbf{F}(\theta,\phi)^2]\ \exp^{-(\theta/\theta_0)^2} \exp^{j\pi(\theta/\theta_1)^2} \sin\theta \mathrm{d}\theta\mathrm{d}\phi|^2}{\iint |\mathbf{F}(\theta,\phi)|^2 \sin\theta\mathrm{d}\theta\mathrm{d}\phi \iint \exp^{-2(\theta/\theta_0)^2} \sin\theta\mathrm{d}\theta\mathrm{d}\phi}$$

where $\mathbf{F}(\theta,\phi)$ is the far-field pattern of the antenna, and $\hat{\epsilon}_{co}$ is the co-pol unit vector. The value Θ_0 controls the amplitude term and Θ_1 controls the phasing term. These values are varied to optimize the coupling efficiency.

REFERENCES

[1] Born and Wolf, *Principles of Optics* , Permagon Press, New York, 1959, pp. 252-252.

[2] D.B. Rutledge, D.P. Neikirk and D.P. Kasilingam, "Integrated Circuit Antennas," *Infrared and Millimeter-Waves*, Vol. 10, K.J. Button, Ed., Academic Press, New York, 1983, pp. 1-90.

[3] D.B. Rutledge and M. Muha, "Imaging antenna arrays," *IEEE Trans. Antennas Propagat.*, Vol. AP-30, 1982, pp.535-540.

[4] J. Zmuidzinas, "Quasi-optical slot antenna SIS mixers," *IEEE Trans. on Microwave Theory Tech.*, accepted for publication Jan. 1992. Also presented at the *2nd Int. Symp. on Space Terahertz Technology*, CA, March 1991.

[5] A. Skalare, Th. de Graauw, and H. van de Stadt,"A Planar Dipole Array Antenna with an Elliptical Lens," *Microwave and Optical Tech. Lett.*, Vol. 4, No. 1, 1991, pp. 9-12. Also, "Millimeter and Submillimeter Studies of Planar Antennas," *First Int. Symp. on Space Terahertz Technology*, Ann Arbor, MI, March 1990, pp. 235-255.

[6] C.J. Adler, C.R. Brewitt-Taylor, R.J. Davis, M. Dixon, R.D. Hodges, L.D. Irving, H.D. Rees, J. Warner, and A.R. Webb, "Microwave and Millimeter-Wave Staring Array Technology," *IEEE MTT-S Int. Microw. Symp. Digest*, June 1991, pp. 1249-1252.

[7] T.H. Büttgenbach, "A Fixed Tuned Broadband Matching Structure for Submillimeter SIS Receivers," presented at the *Third Int. Symp. on Space Terahertz Technology*, Ann Arbor, MI, March 1992.

[8] A.E. Siegman, *Lasers*, University Science Books, New York, 1986.

[9] R.E. Collin, *Antennas and Radiowave Propagation*, McGraw-Hill, New York, 1985, pp. 190-199.

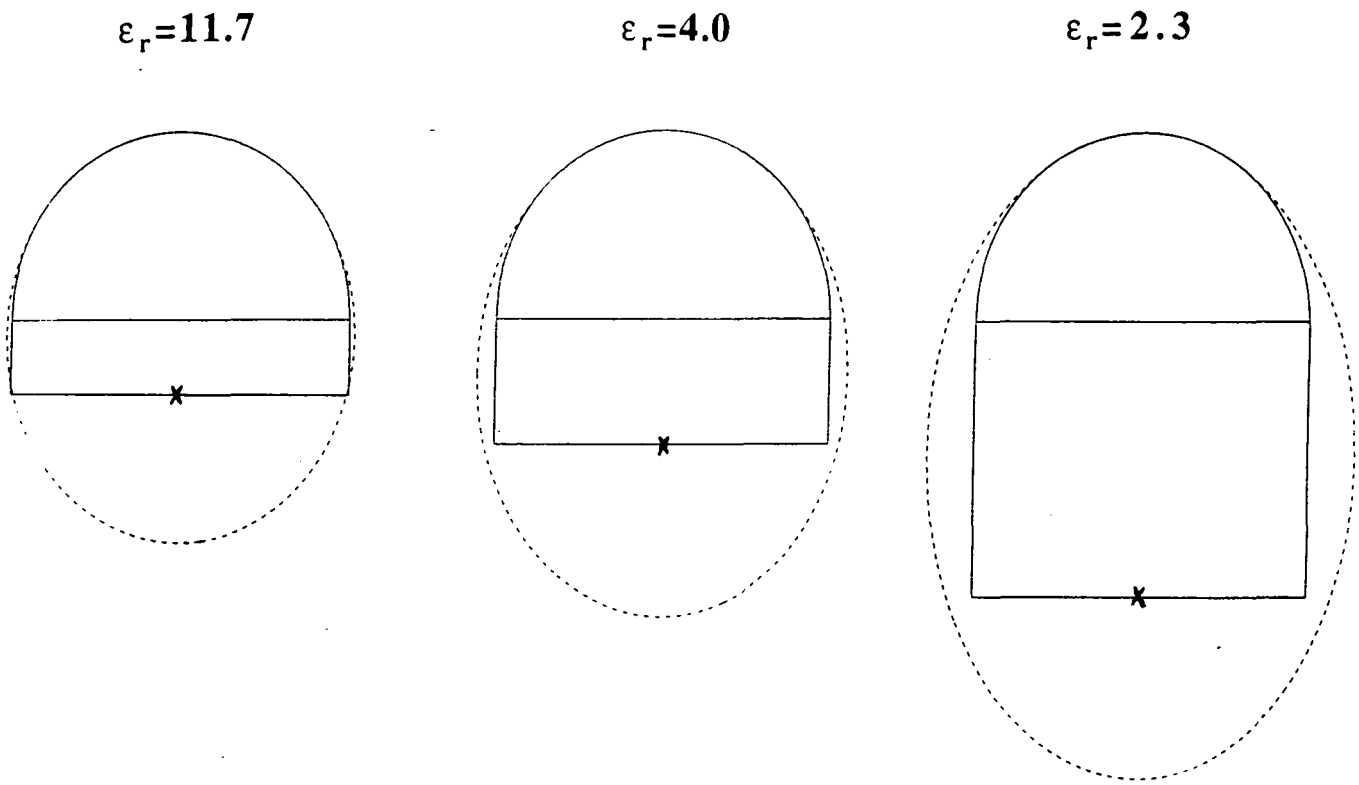

Figure 1: The synthesis of an elliptical lens from a hyperhemispherical lens and planar wafers. The extended hemisphere is a very good approximation to an elliptical lens at high dielectric constants.

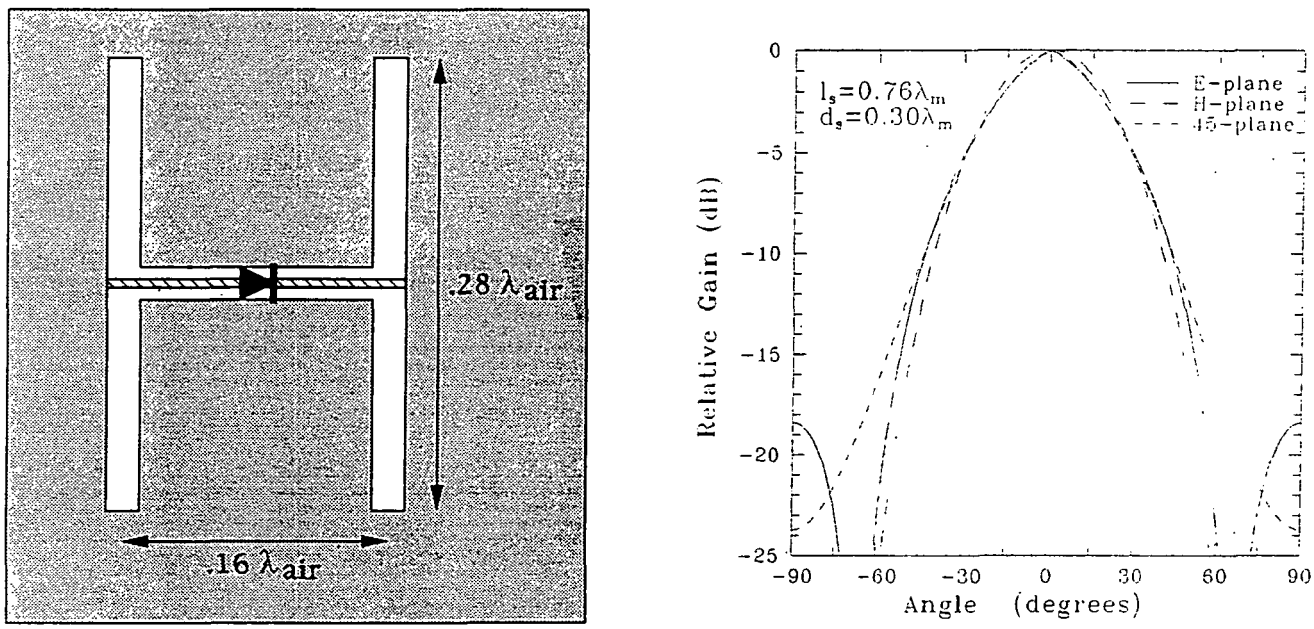

Figure 2: The double-slot antenna (left) and its radiation patterns into a silicon (ϵ=11.7) dielectric (right).

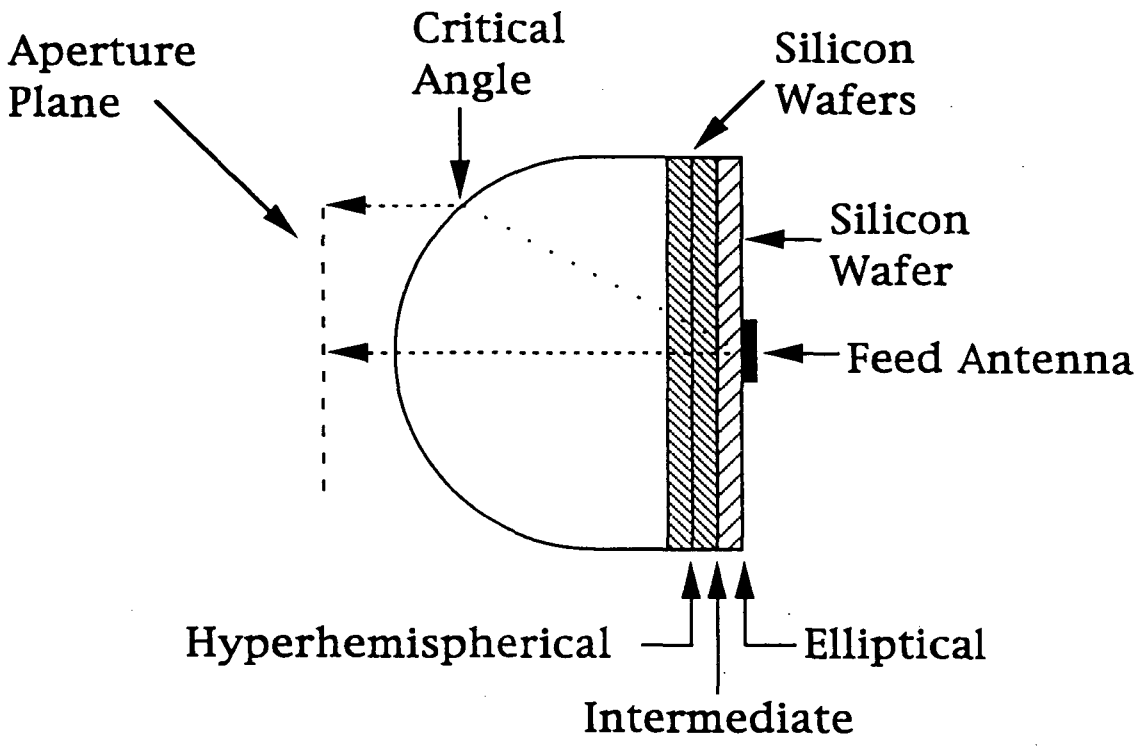

Figure 3: The ray-tracing method. Note the three focus positions that are achieved by adding high-resistivity silicon wafers.

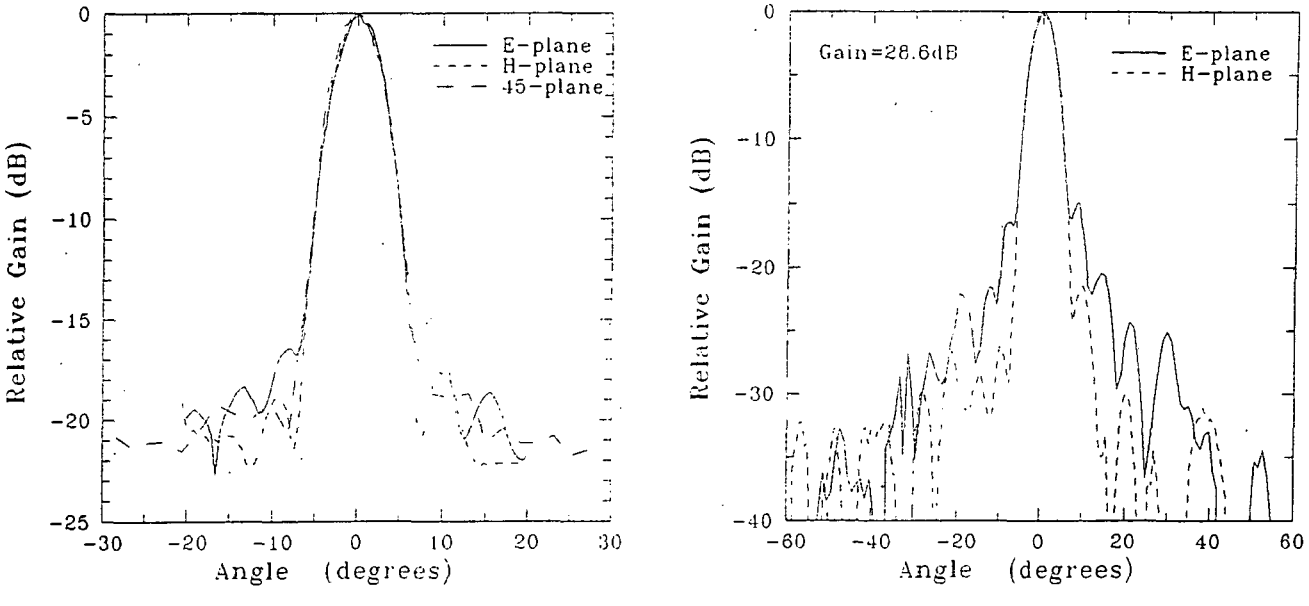

Figure 4: Measured patterns at the elliptical focus at 246GHz. The patterns are diffraction-limited by the size of the aperture

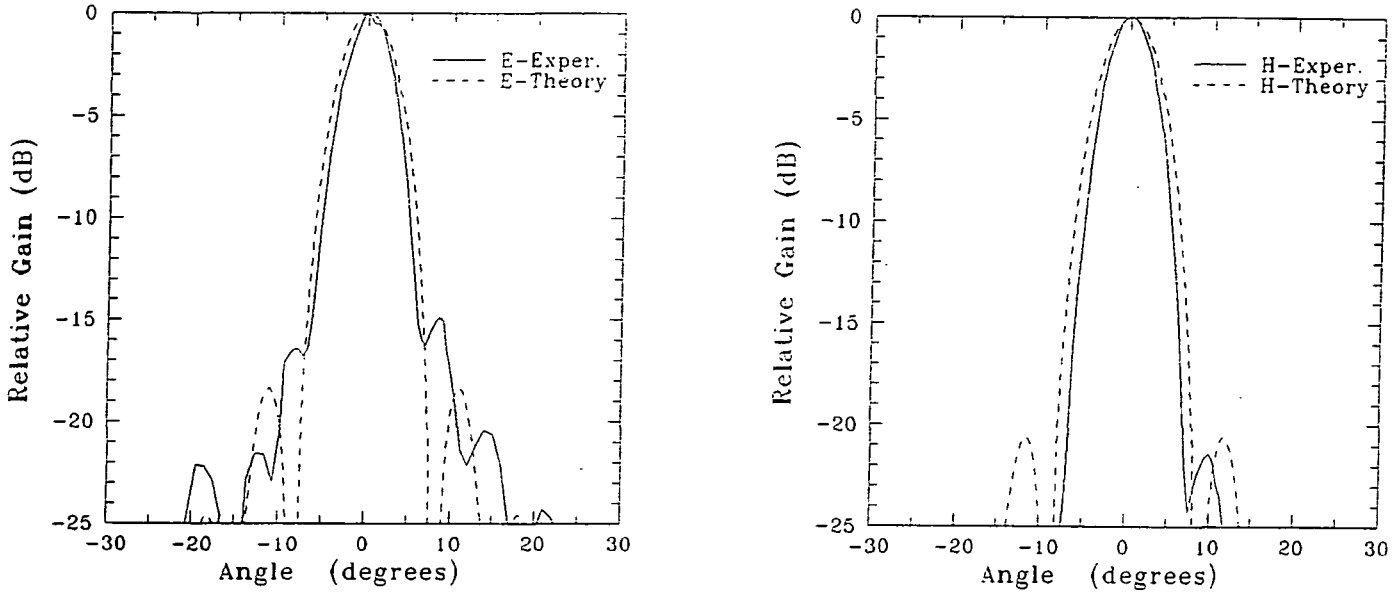

Figure 5: Comparison of theory vs. experiment for the elliptical focus. The critical angle limits the size of the aperture, resulting in wider theoretical patterns.

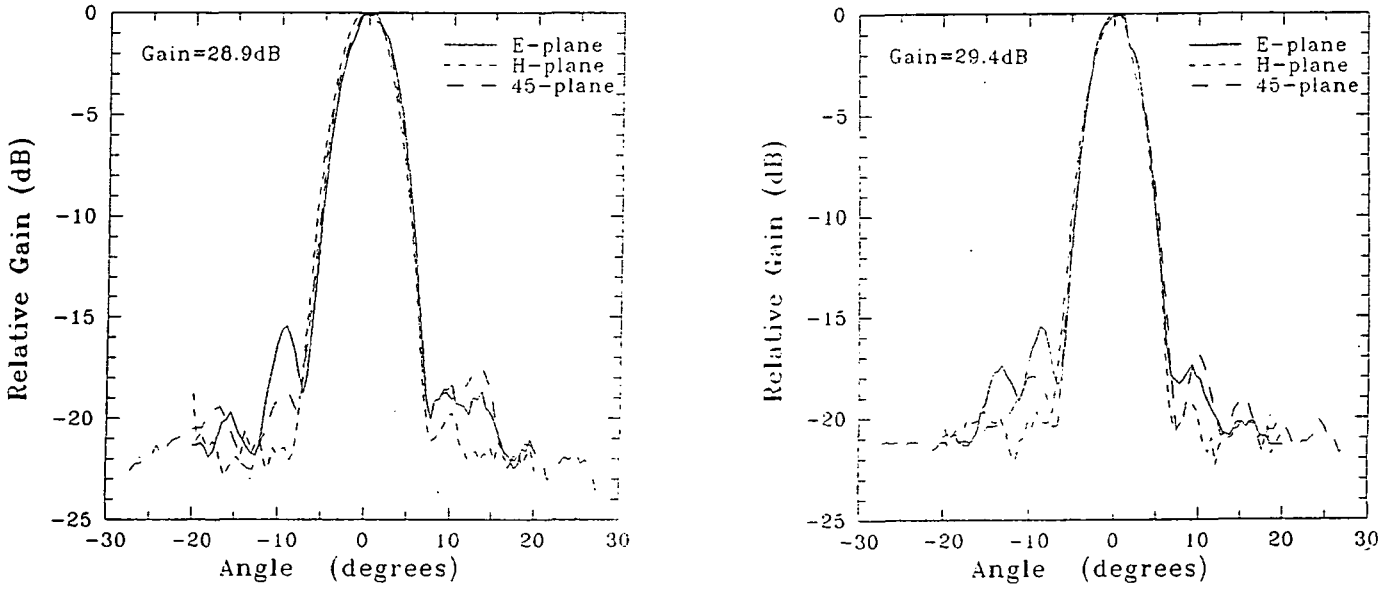

Figure 6: Measured patterns at the elliptical focus at 222GHz (left) and 270GHz (right).

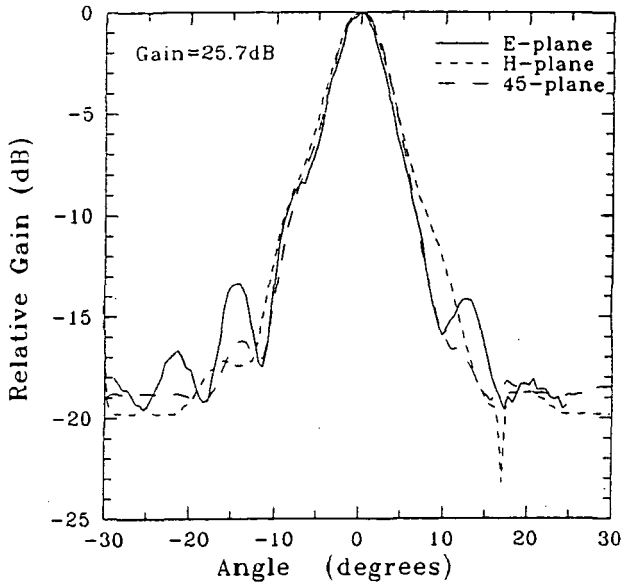

Figure 7: Measured patterns at the intermediate focus position at 246GHz.

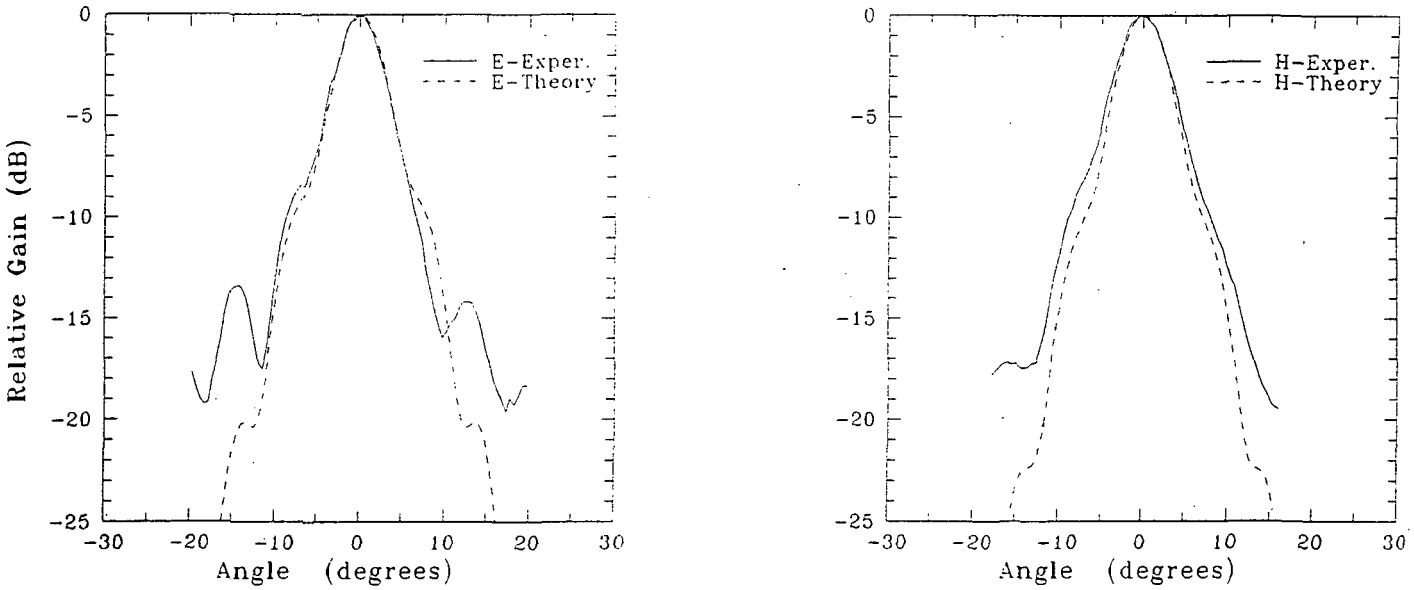

Figure 8: Comparison of theory vs. experiment for the intermediate focus.

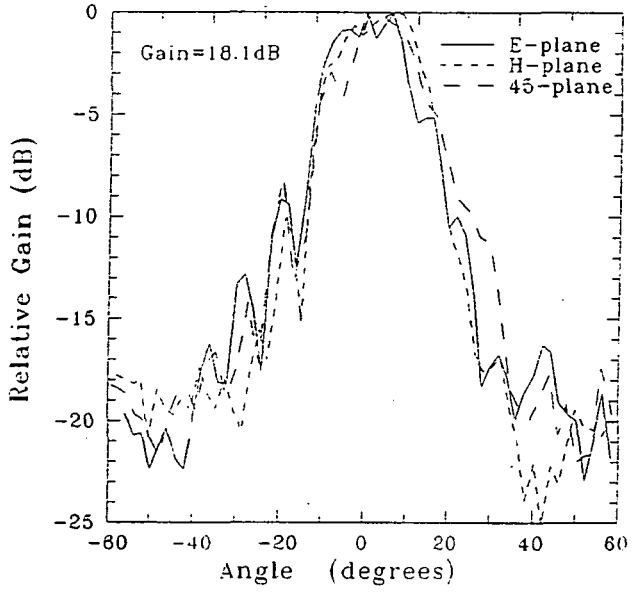

Figure 9: Measured patterns at the hyperhemispherical focus position at 246GHz.

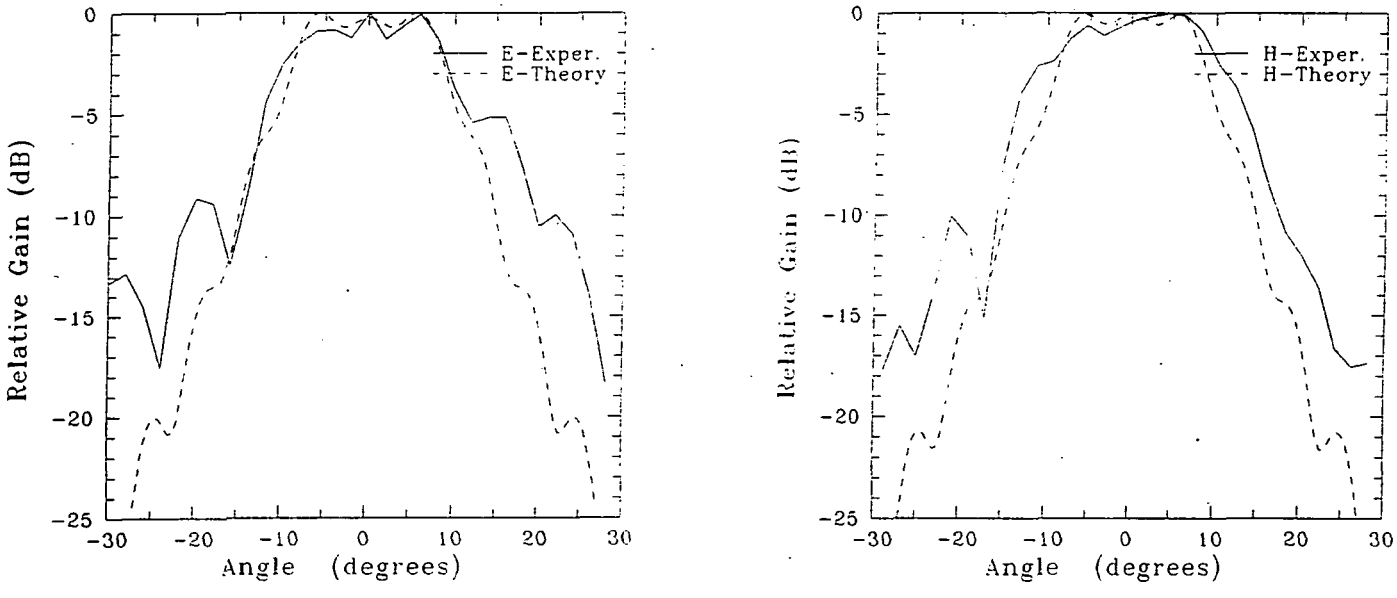

Figure 10: Comparison of theory vs. experiment for the hyperhemispherical focus. Notice the predicted multi-peak behaviour.

Coupling to Gaussian Beams

Focus Position (extension)	Gain	Gaussian Beam Parameters		Matching Efficiency
		Θ_0(amplitude)	Θ_1(phase)	
Elliptical (.39 radius)	28.6dB	5.0°	-	~ 79%
Intermediate (.32 radius)	25.7dB	8.2°	11.3°	~ 83%
Hyper-hemispherical (.25 radius)	18.1dB	13.3°	13.5°	~ 81%

Gaussian Beam Electric Field: $\exp[-(\Theta/\Theta_0)^2] \exp[j*\pi*(\Theta/\Theta_1)^2]$

$$\frac{\text{Max. Power Elliptical}}{\text{Max. Power Hyperhemispherical}} \cong 10\text{dB}$$

Figure 11: Table of Gaussian beam parameters.

EMBEDDING IMPEDANCE APPROXIMATIONS IN THE ANALYSIS OF SIS MIXERS

A. R. Kerr and S.-K. Pan
National Radio Astronomy Observatory*
Charlottesville, VA 22903

S. Withington
Cavendish Laboratory, University of Cambridge
Cambridge CB3 OHE, UK

ABSTRACT

Future millimeter-wave radio astronomy instruments will use arrays of many SIS receivers, either as focal plane arrays on individual radio telescopes, or as individual receivers on the many antennas of radio interferometers. Such applications will require broadband integrated mixers without mechanical tuners. To produce such mixers, it will be necessary to improve present mixer design techniques, most of which use the three-frequency approximation to Tucker's quantum mixer theory.

This paper examines the adequacy of three approximations to Tucker's theory: (i) the usual three-frequency approximation which assumes a sinusoidal LO voltage at the junction, and a short-circuit at all frequencies above the upper sideband, (ii) a five-frequency approximation which allows two LO voltage harmonics and five small-signal sidebands, and (iii) a quasi five-frequency approximation in which five small-signal sidebands are allowed, but the LO voltage is assumed sinusoidal. These are compared with a full harmonic-Newton solution of Tucker's equations, including eight LO harmonics and their corresponding sidebands, for realistic SIS mixer circuits.

It is shown that the accuracy of the three approximations depends strongly on the value of $\omega R_N C$ for the SIS junctions used. For large $\omega R_N C$, all three approximations approach the eight-harmonic solution. For $\omega R_N C$ values in the range 0.5 to 10, the range of most practical interest, the quasi five-frequency approximation is a considerable improvement over the three-frequency approximation, and should be suitable for much design work. For the realistic SIS mixers considered here, the five-frequency approximation gives results very close to those of the eight-harmonic solution.

Use of these approximations, where appropriate, considerably reduces the computational effort needed to analyze an SIS mixer, and allows the design and optimization of mixers using a personal computer.

---

*The National Radio Astronomy Observatory is operated by Associated Universities, Inc. under cooperative agreement with the National Science Foundation.

INTRODUCTION

The superior sensitivity of SIS mixer receivers at millimeter wavelengths has been clearly demonstrated in recent years [1], and SIS receivers are now used at almost all the world's major millimeter-wave radio astronomy observatories. SIS mixers appear for the most part to be well described by Tucker's quantum theory [2,3], which predicts strong non-classical behavior in a resistive mixer with an extremely sharp I-V nonlinearity. Tucker's theory is normally applied in its three-frequency approximation, in which form it is moderately tractable analytically and allows optimization of designs by small computer.

At present, the most sensitive SIS mixers have one or two mechanical waveguide tuners which allow the RF embedding impedance to be adjusted to suit the particular junction (or array of junctions). While mechanically tuned mixers are acceptable in applications requiring one or two receivers, plans for future radio astronomy instruments include arrays of many SIS receivers operating either all in the focal plane of a single radio telescope, or individually on the many antennas of a radio interferometer. For such applications, it is highly desirable to replace mechanically tuned mixers with broadband integrated mixers without mechanical tuners. To produce such mixers will require refinement of present mixer design techniques, most of which use Tucker's three-frequency approximation.

This paper examines the adequacy of three approximations to Tucker's theory: (i) the usual three-frequency approximation, (ii) a five-frequency approximation, and (iii) a quasi five-frequency approximation. These are compared with a full harmonic-Newton solution [4,5] of Tucker's equations up to the eighth LO harmonic for realistic SIS mixer circuits. Use of the approximations greatly reduces the computational effort needed to optimize a mixer design.

THE APPROXIMATIONS

In the so-called *three-frequency* approximation to Tucker's theory, it is assumed, as indicated in Fig. 1(a), that the embedding impedance seen by the junction is finite at the LO frequency ω_p, and at ω_u, ω_ℓ and ω_0, the upper and lower sideband and intermediate frequencies. At all higher frequencies the junction is short-circuited. This is likely to be a good approximation for junctions with large capacitance. The three-frequency approximation implies a sinusoidal LO voltage at the junction, for which case Tucker gives closed-form expressions for the coefficients $Y_{i,j}$ of the mixer's 3 x 3 small-signal conversion matrix as functions of the pumping parameter $\alpha = eV_p/\hbar\omega_p$ and DC bias voltage V_0.

The *quasi five-frequency* approximation assumes the same sinusoidal LO voltage waveform as above. However, while the second LO harmonic $2\omega_p$ is short-circuited at the junction, the second harmonic sidebands $2\omega_p \pm \omega_0$ are not. This is depicted in Fig. 1(b). Closed-form expressions for the elements of the 5 x 5 small-signal conversion matrix are given by Tucker. While this situation is not easy to implement practically, it is not physically unrealizable, and is expected to be a better approximation to a real mixer than the simple three-frequency approximation.

The *full five-frequency* approximation allows finite embedding impedances at all frequencies up to $2\omega_p + \omega_0$, but requires the junction to be short-circuited at all higher frequencies. This is depicted in Fig. 1(c). The LO voltage at the junction contains a second harmonic component, and an iterative algorithm must be used to determine the LO voltage waveform and thence the elements of the 5 x 5 small-signal conversion matrix.

SIMULATIONS

The three approximations are investigated using hypothetical double sideband SIS mixers at 115 and 345 GHz, with the desired embedding impedances at the LO harmonics and small-signal sideband frequencies. In all the examples, the junction capacitance is tuned out at frequencies ω_ℓ and ω_u by the source susceptance. The embedding impedance at frequencies $\omega > \omega_p + \omega_0$ is either zero or that of the junction capacitance alone, depending on the particular example. The RF source and IF load conductances are assumed equal. These assumptions are consistent with realistic low noise mixer designs [1] with low IF ($\omega_0 << \omega_p$).

The I-V curve used in the examples is that of the 4-junction array of Nb/Al-Al_2O_3/Nb junctions used in [1], and is shown in Fig. 2. The theoretical equivalence between a series array of junctions and a single junction is shown in [6].

Five values of $\omega_p R_N C$ are used: 0.5, 1, 2, 4, and 50. In all cases, the pumping parameter $\alpha = eV_1/\hbar\omega_p = 1.2$, where V_1 is the amplitude of the fundamental component of the LO voltage at the junction. The junction is voltage biased at the center of the first photon step below the gap voltage; *i.e.*, $V_0 = V_{gap} - \hbar\omega/2e$.

The mixer's (equivalent input) noise temperature, (transducer) conversion gain, input return loss, and output impedance are computed for each case as functions of R_{RF}/R_N, where R_{RF} is the reciprocal of the RF source conductance at the signal frequency and R_N is the normal resistance of the junction (or array of junctions). For comparison, the results of the full eight-harmonic analysis are shown on each graph.

RESULTS

Full five-frequency approximation

The results of the full five-frequency approximation are shown in Figs. 3(a)-(d) for 115 GHz and 345 GHz mixers. At 115 GHz it is clear that the only significant deviation from the eight-harmonic results is in the gain for the lowest value of $\omega R_N C$ (0.5), and that is only a small fraction of a decibel. At 345 GHz there is almost no difference between the full five-frequency approximation and the eight-harmonic results.

Quasi five-frequency approximation

Figures 4(a)-(d) show the results of the quasi five-frequency analysis of the same mixers as above. At both 115 and 345 GHz, the gain is within a decibel of that computed using eight harmonics. The mixer noise temperatures agree closely for $\omega R_N C = 50$ and are within about 10% for $\omega R_N C = 4$, but for $\omega R_N C = 0.5$ they differ by as much as 40%. The input return loss and output impedance show minor deviations from the eight-harmonic solution.

Three-frequency approximation

In the three-frequency case, the value of $\omega R_N C$ has no effect. This is because all relevant frequencies above the upper sideband are short-circuited, and we are assuming the junction capacitance is tuned out at the signal and image frequencies. The three-frequency case is thus equivalent to the high-$\omega R_N C$ limit of any of the other cases we have considered. The results of Figs. 3 or 4 with $\omega R_N C = 50$ are, in fact, indistinguishable from those of the three-frequency approximation.

DISCUSSION

In an earlier paper [1] we put forward design criteria for SIS mixers for millimeter-wave radio astronomy applications. They should have low noise, conversion gain near unity (to avoid saturation), and a reasonable RF input match. For wide frequency coverage, only double-sideband operation is considered. It was found that these conditions could be met if the mixer operated with equal RF source and IF load conductances, and that the output impedance of the mixer was then large (*i.e.*, the mixer operates as a current source).

The examples here likewise assume equal RF source and IF load conductances, and examine the mixer performance as a function of R_{RF}/R_N (R_{RF} is the reciprocal of the RF source conductance, and R_N is the normal resistance of the junction or array of junctions). As expected, the mixer noise temperature exhibits a broad minimum as R_{RF}/R_N is varied (Fig. 3). The (transducer) gain exhibits no minimum, but increases with R_{RF}/R_N.

At higher frequencies, the minimum noise temperature occurs at larger values of R_{RF}/R_N. This has an important implication for SIS mixer design: If the same mixer circuit is scaled for use at two different frequencies (*i.e.*, the embedding impedances are the same for the two designs), then the normal resistance of the junction (or array) should be smaller for the higher-frequency mixer. This is discussed in more detail in [1].

In designing a broadband tunerless SIS mixer, the choice of the value of $\omega R_N C$ is primarily a tradeoff between noise temperature and useable frequency range; large values of C will obviously limit frequency coverage, while too small an $\omega R_N C$ degrades the noise temperature as well as being more difficult to achieve without sacrificing junction quality. It is important, therefore, for the designer to have available a method of mixer analysis which reflects the effect of $\omega R_N C$ with sufficient accuracy. From the results in Figs. 3 and 4, it is clear that the quasi five-

frequency approximation describes the mixer performance quite well for $\omega R_N C \geq 4$. For $0.5 \leq \omega R_N C < 4$, the gain, input return loss, and output impedance are well enough predicted by the quasi five-frequency approximation for most mixer design work, but the mixer noise temperature can be too high by as much as 40%. Figure 5 shows the dependence of the minimum value of T_M (with respect to R_{RF}/R_N) on $\omega R_N C$ for each of the methods described here.

It may seem odd that the quasi five-frequency approximation should give quite accurate results for all the mixer parameters except the noise temperature. This is explained by considering the origin and nature of the noise at the output port of the mixer. This noise originates as shot noise from the current flowing in the SIS junction. The action of the local oscillator is, in effect, to amplitude modulate the shot noise produced by the DC current flowing in the junction, thereby generating correlated components at all the sideband frequencies $n\omega_p \pm \omega_0$, $n = 0, 1, \ldots$, etc. The mixing action of the time-varying junction conductance converts all these sideband components to the IF, preserving their correlation. The relative phase of each correlated IF component depends on the embedding impedance (including junction capacitance) at its sideband of origin, and on the phases of the harmonics in the LO waveform at the junction. The minimum noise occurs when these correlated IF noise components are phased so as to cancel to the greatest degree. (It is in this way that a classical diode mixer can, in principle, have zero noise temperature while operating with 3 dB conversion loss and many milliamps of rectified current.) The fact that, in low-noise operation, the SIS mixer has several quite large but strongly correlated output noise components which largely cancel one another, explains the sensitivity of the noise temperature results to the small changes in LO waveform between the quasi five-frequency and full five-frequency approximations. (A more detailed discussion of noise conversion in mixers, and additional references are given in [7].)

REFERENCES

[1] A. R. Kerr and S.-K. Pan, "Some recent developments in the design of SIS mixers," *Int. J. Infrared Millimeter Waves*, vol. 11, no. 10, Oct. 1990.

[2] J. R. Tucker, "Quantum limited detection in tunnel junction mixers," *IEEE J. of Quantum Electron.*, vol. QE-15, no. 11, pp. 1234-1258, Nov. 1979.

[3] J. R. Tucker and M. J. Feldman, "Quantum detection at millimeter wavelengths," *Rev. Mod. Phys.*, vol. 57, no. 4, pp. 1055-1113, Oct. 1985.

[4] C.-Y. E. Tong and R. Blundell, "Simulation of superconducting quasiparticle mixer using a five-port model," *IEEE Trans. Microwave Theory Tech.*, vol. MTT-38, no. 10, pp. 1391-1398, Oct. 1990.

[5] S. Withington and P. Kennedy, "Numerical procedure for simulating the large-signal quantum behavior of superconducting tunnel-junction circuits," *Proc. IEE*, part G, vol. 138, no. 1, pp. 70-76, Feb. 1991.

[6] M. J. Feldman and S. Rudner, "Mixing with SIS arrays," *Reviews of Infrared & Millimeter Waves*, (Plenum, New York), vol. 1, p. 47-75, 1983.

[7] D. N. Held and A. R. Kerr, "Conversion loss and noise of microwave and millimeter-wave mixers: Part 1 - Theory," *IEEE Trans. Microwave Theory Tech.*, vol. MTT-26, pp. 49-55, Feb. 1978.

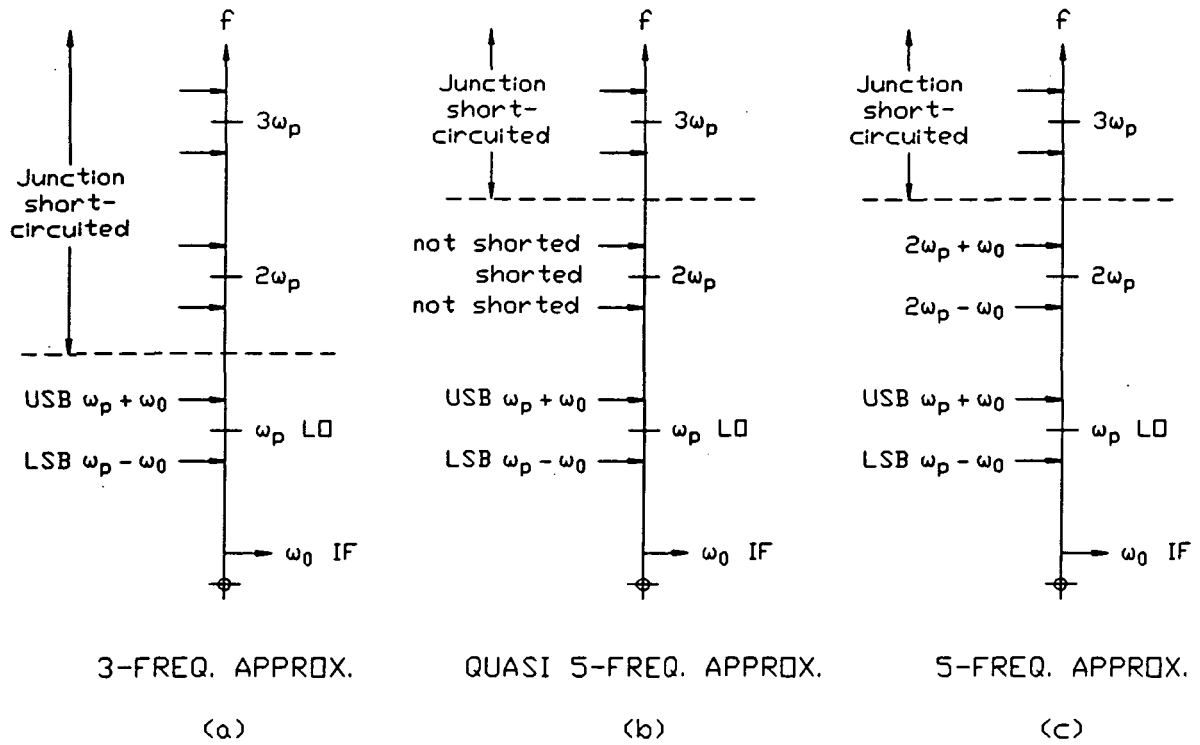

Fig. 1. Embedding impedance diagram indicating which frequencies are short-circuited for the three approximations: (a) three-frequency, (b) quasi five-frequency, and (c) full five-frequency.

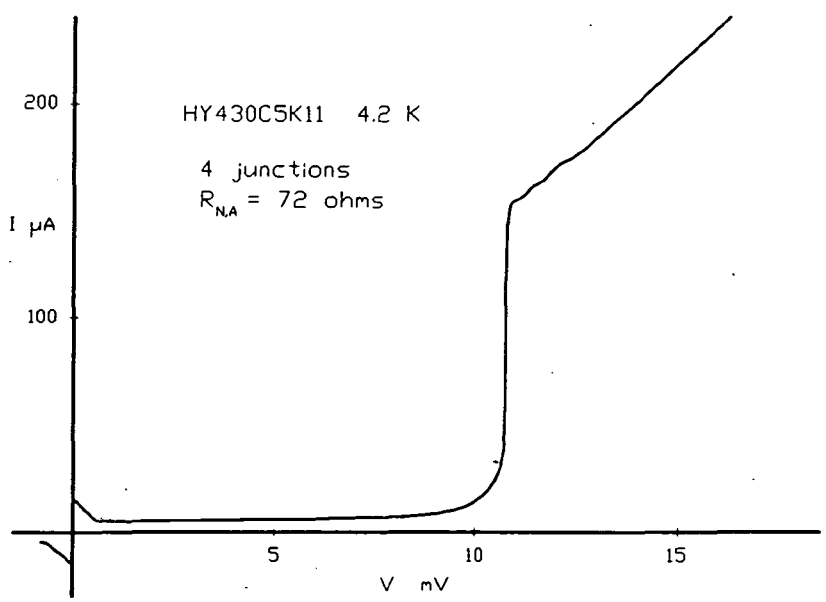

Fig. 2. I-V curve used in the simulations. This curve is for a four-junction array of Hypres Nb/Al-Al_2O_3/Nb junctions at 4.2K, as used in [1].

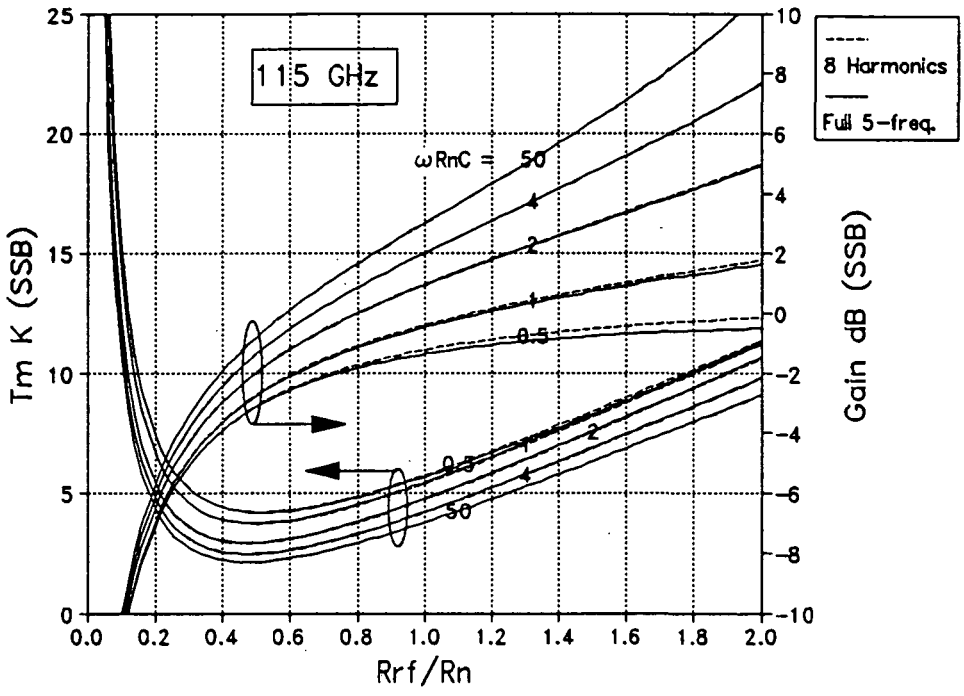

Fig. 3(a). Noise temperature and conversion gain as functions of R_{RF}/R_N for a 115 GHz SIS mixer, computed using the full five-frequency approximation (solid line) and with eight LO harmonics (broken line). Results are shown for $\omega R_N C$ = 0.5, 1, 2, 4, and 50.

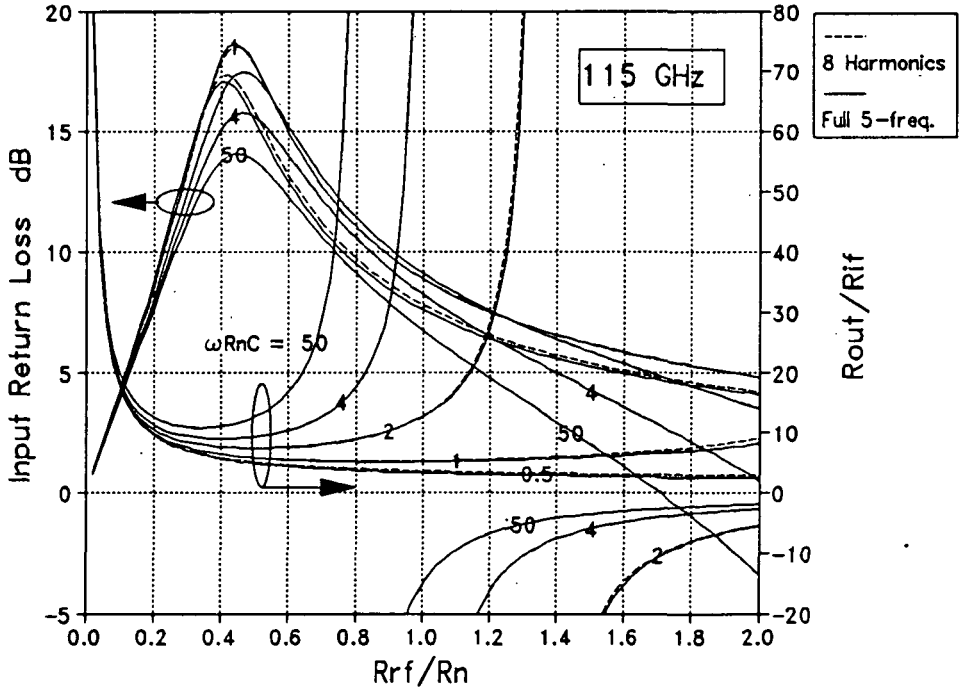

Fig. 3(b). Input return loss and output impedance as functions of R_{RF}/R_N for a 115 GHz SIS mixer, computed using the full five-frequency approximation (solid line) and with eight LO harmonics (broken line). The output resistance is normalized to the IF load resistance R_{IF}. Results are shown for $\omega R_N C$ = 0.5, 1, 2, 4, and 50.

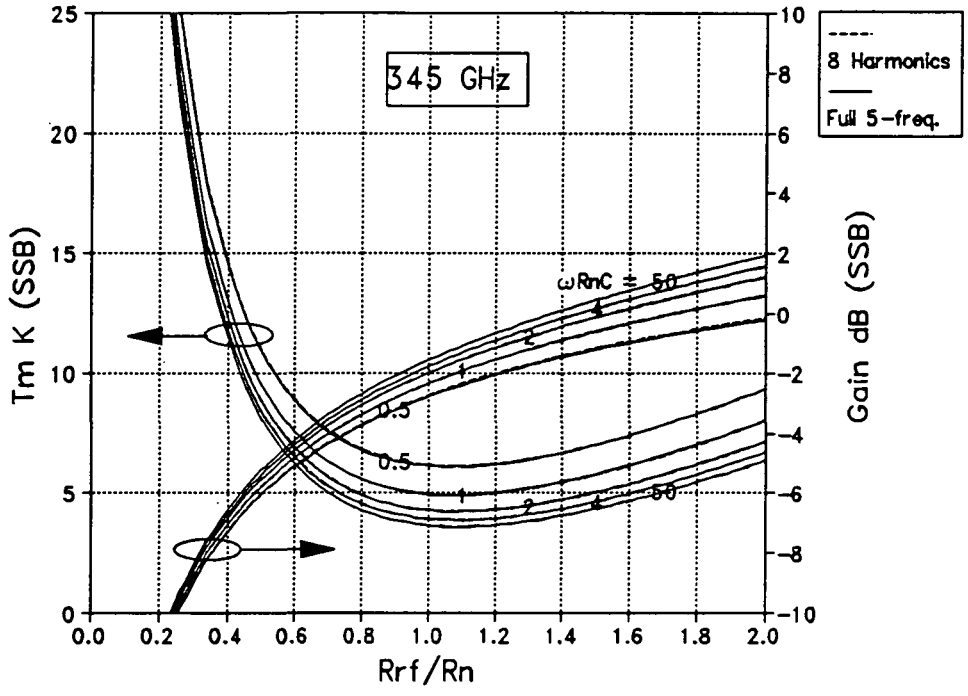

Fig. 3(c). Noise temperature and conversion gain as functions of R_{RF}/R_N for a 345 GHz SIS mixer, computed using the full five-frequency approximation (solid line) and with eight LO harmonics (broken lines -- almost obscured by the solid lines). Results are shown for $\omega R_N C$ = 0.5, 1, 2, 4, and 50.

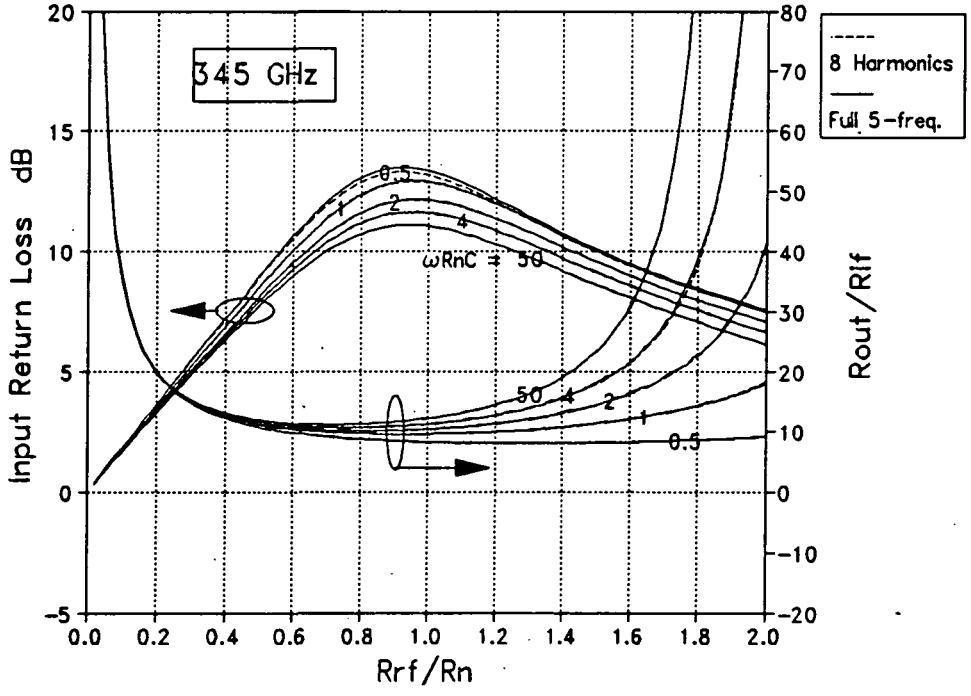

Fig. 3(d). Input return loss and output impedance as functions of R_{RF}/R_N for a 345 GHz SIS mixer, computed using the full five-frequency approximation (solid line) and with eight LO harmonics (broken lines -- almost obscured by the solid lines). The output resistance is normalized to the IF load resistance R_{IF}. Results are shown for $\omega R_N C$ = 0.5, 1, 2, 4, and 50.

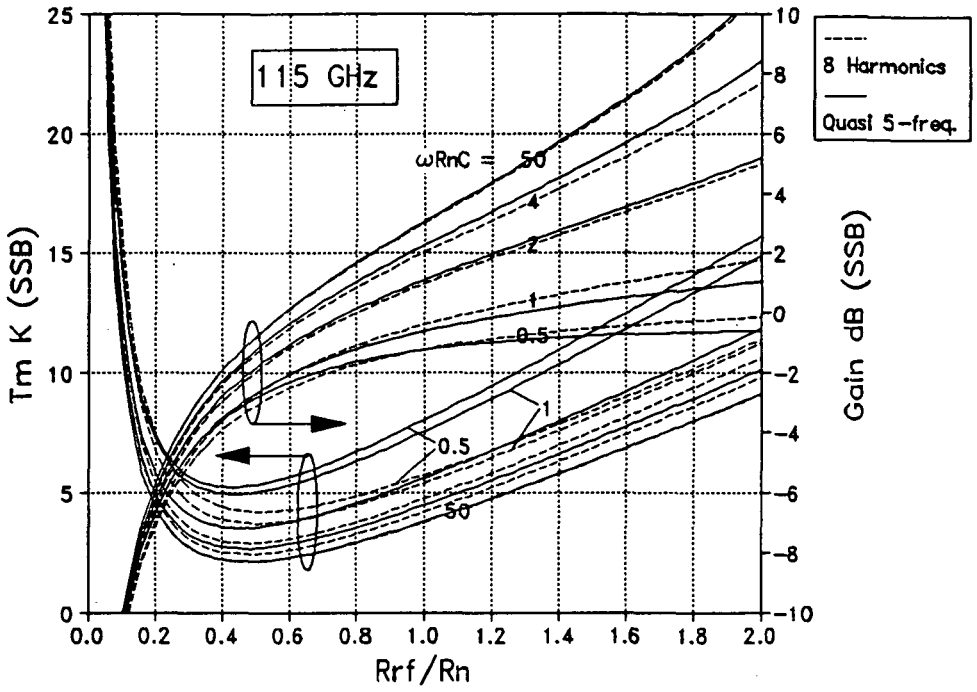

Fig. 4(a). Noise temperature and conversion gain as functions of R_{RF}/R_N for a 115 GHz SIS mixer, computed using the quasi five-frequency approximation (solid line) and with eight LO harmonics (broken line). Results are shown for $\omega R_N C$ = 0.5, 1, 2, 4, and 50.

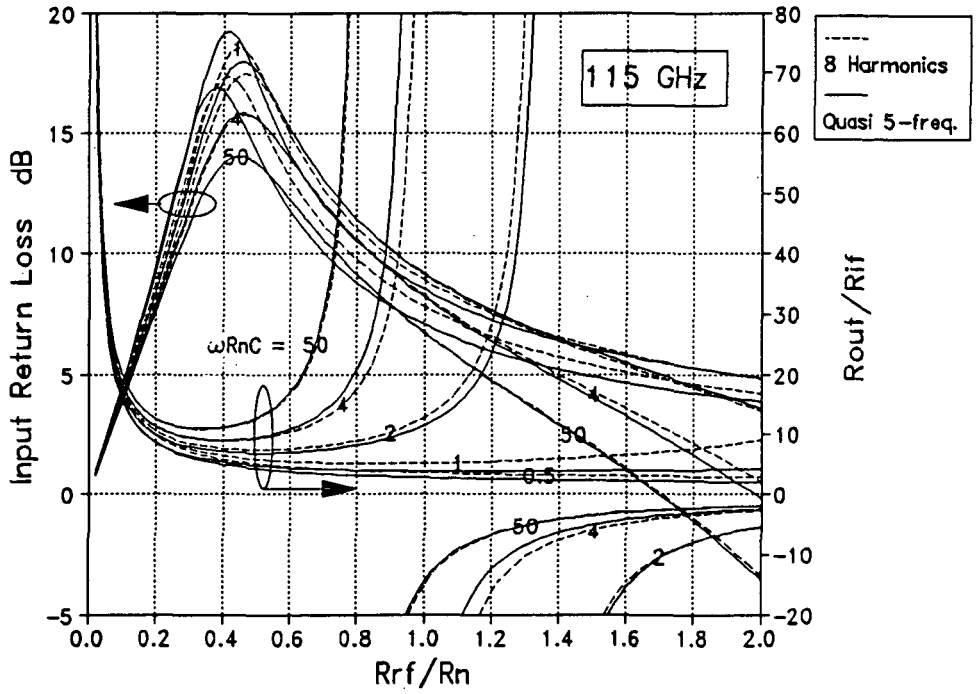

Fig. 4(b). Input return loss and output impedance as functions of R_{RF}/R_N for a 115 GHz SIS mixer, computed using the quasi five-frequency approximation (solid line) and with eight LO harmonics (broken line). The output resistance is normalized to the IF load resistance R_{IF}. Results are shown for $\omega R_N C$ = 0.5, 1, 2, 4, and 50.

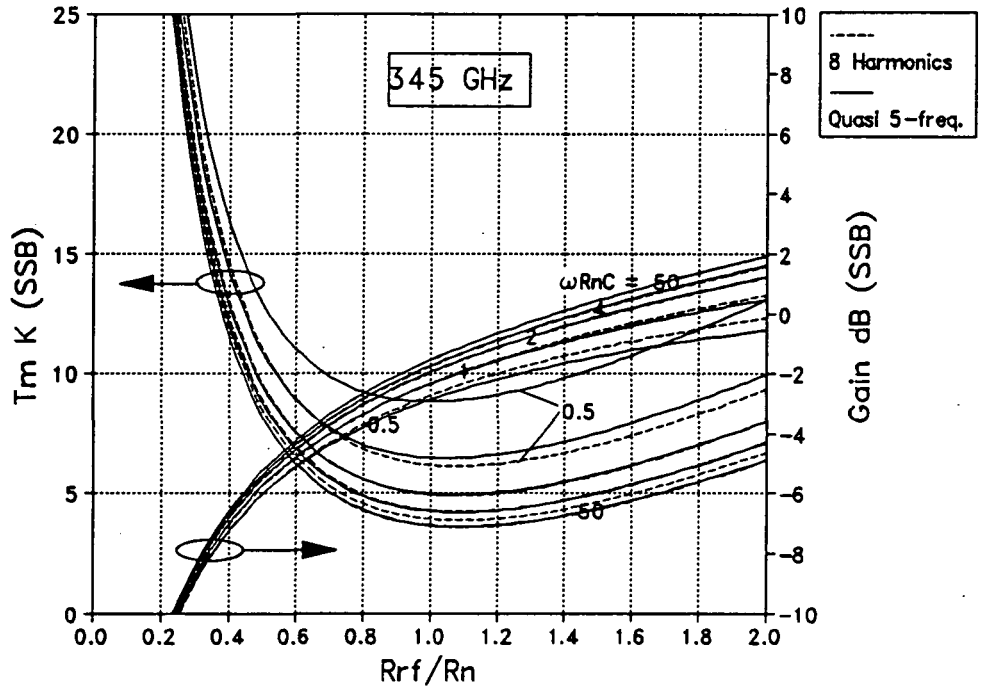

Fig. 4(c). Noise temperature and conversion gain as functions of R_{RF}/R_N for a 345 GHz SIS mixer, computed using the quasi five-frequency approximation (solid line) and with eight LO harmonics (broken line). Results are shown for $\omega R_N C$ = 0.5, 1, 2, 4, and 50.

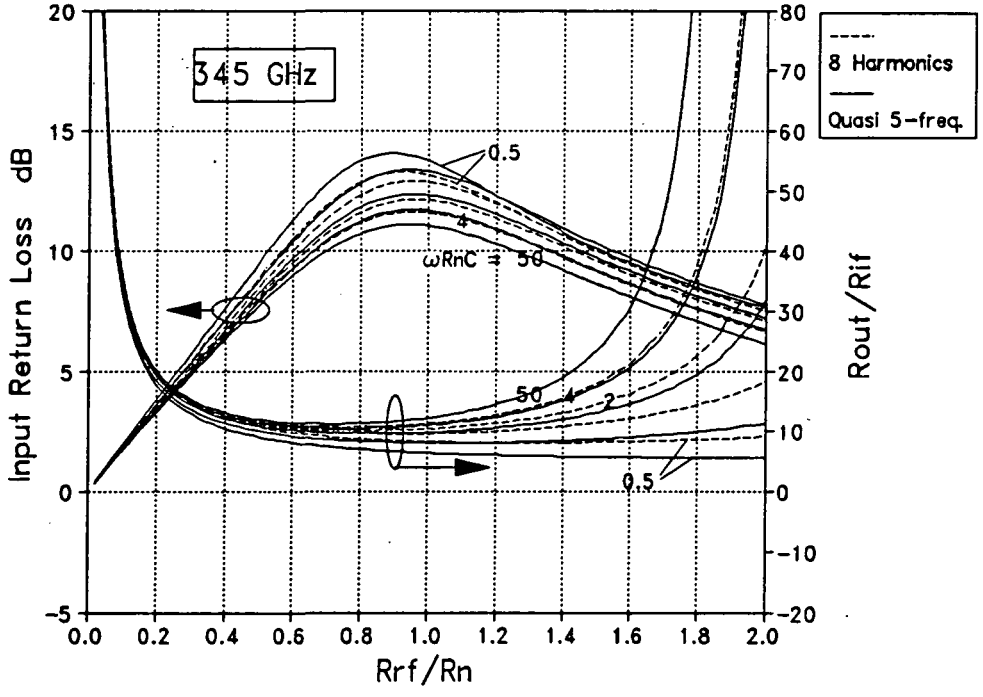

Fig. 4(d). Input return loss and output impedance as functions of R_{RF}/R_N for a 345 GHz SIS mixer, computed using the quasi five-frequency approximation (solid line) and with eight LO harmonics (broken line). The output resistance is normalized to the IF load resistance R_{IF}. Results are shown for $\omega R_N C$ = 0.5, 1, 2, 4, and 50.

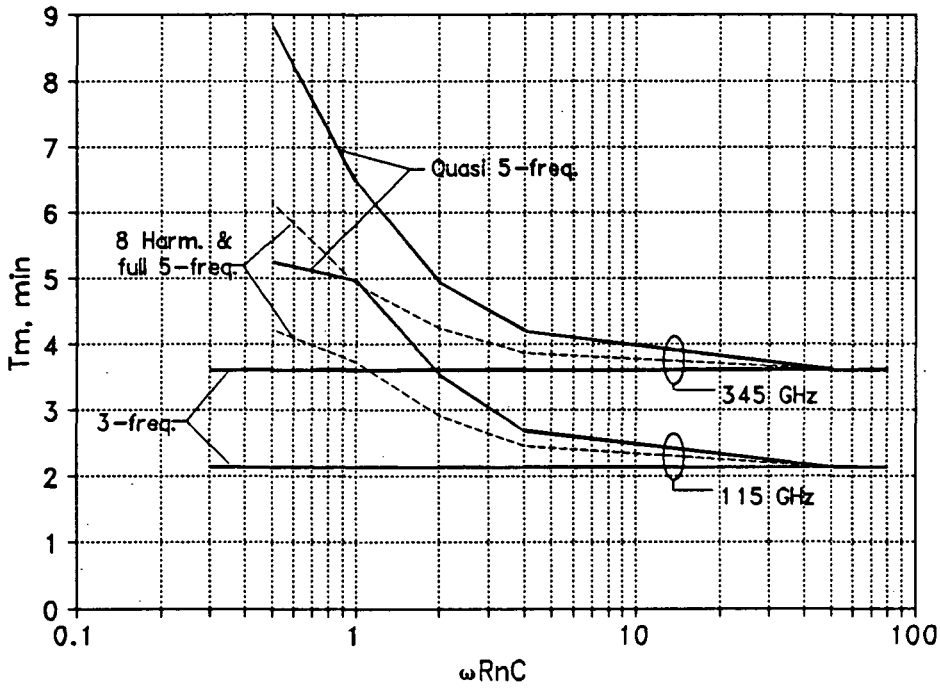

Fig. 5. Minimum mixer noise temperature as a function of $\omega R_N C$ for: (i) the full eight-harmonic and full 5-frequency solutions (broken line), (ii) the quasi 5-frequency approximation (solid line), and (iii) the 3-frequency approximation (horizontal lines).

SUB MICRON AREA Nb/AlO_x/Nb TUNNEL JUNCTIONS FOR SUBMM MIXER APPLICATIONS

H.G. LeDuc, B. Bumble, S.R. Cypher, A.J. Judas, and J.A. Stern*

Center for Space Microelectronics
Jet Propulsion Laboratory
California Institute of Technology
Pasadena, CA 91109

*Present Address: Stanford University
Palo Alto, CA

Abstract

In this paper, we report on a fabrication process developed for submicron area tunnel junctions. We have fabricated Nb/AlO_x/Nb tunnel junctions with areas down to 0.1 μm^2 using these techniques. The devices have shown excellent performance in receiver systems up to 500 GHz and are currently in use in radio astronomy observatories at 115, 230, and 500 GHz.

The junctions are fabricated using a variant of the self-aligned-liftoff trilayer process[1] with modifications for electron beam lithographic patterning of junction areas. In brief, the technique involves patterning submicron holes in PMMA using electron beam lithography. The negative of this pattern is formed by thermal deposition and liftoff of chromium metal using this PMMA stencil. The chromium pattern is transferred to an underlying polyimide film using oxygen RIE. Junctions are formed by RIE using a gas mixture containing CCl_2F_2 and electrically isolated with thermally evaporated silicon monoxide. Contact wiring and coupling/tuning structures are patterned by RIE.

Introduction

SIS tunnel junctions can be modeled as a nonlinear resistor in parallel with a shunt capacitor. A good figure-of-merit of the high frequency performance of these devices is

the ratio of the capacitive reactance to the real resistance (ωRC). The RC product, for SIS tunnel junctions, is determined by the tunnel barrier thickness and is independent of the device area. The junction area is chosen to provide the best impedance match to the mixer embedding circuit and is usually a compromise between minimizing the capacitance while maintaining a reasonable real impedance. In the best case, the embedding circuit can tune out the capacitance and the junction area is chosen to make the rf-resistance match the real part of the embedding circuit impedance (approximately 50 - 100 Ω). For small RC devices, the resistance-area product is small so that achieving the appropriate resistance using a single junction requires submicron areas. Series arrays or other novel coupling mechanisms may relieve the constraint on submicron areas, however, designing these elements may require a greater understanding of the high frequency characteristics of devices and materials than is currently available. We have chosen to use single junctions in the hope that the simplicity in understanding the high frequencies behavior of the mixers may outweigh the complexity associated with the fabrication of submicron devices. Since their development[2], high quality Nb/AlOx/Nb tunnel junctions represent the only all refractory SIS technology in use in radio astronomy receiver systems. This is primarily due to their nearly ideal tunneling characteristics and physical robustness. In this paper we describe techniques for fabricating submicron devices.

Tunnel Junction Fabrication

The tunnel junction fabrication process is similar to the self-aligned-liftoff process used to fabricate refractory tunnel junctions employing optical lithography[1,3]. The primary difference arises from the need to use higher resolution lithography in the tunnel junction patterning and to maintain this resolution throughout the fabrication process. The process steps are shown schematically in figure 1.

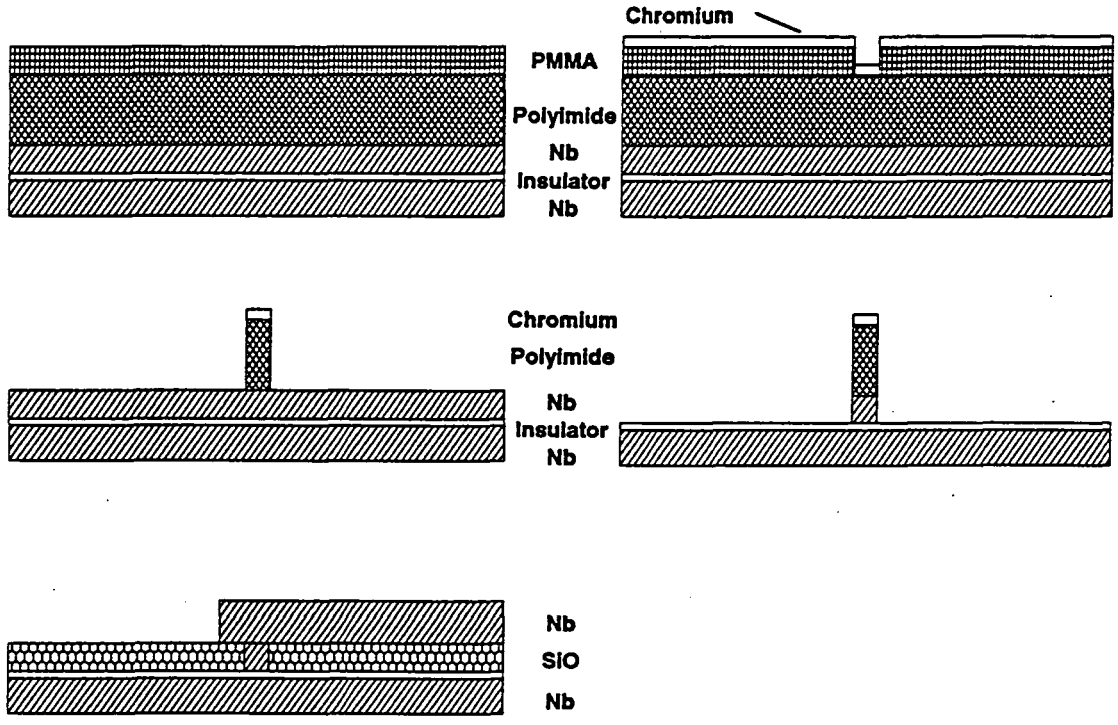

Figure 1. Submicron fabrication process schematic. (a) After trilayer deposition , wafers are spin coated with 400-600 nm of polyimide and 120 nm PMMA. (b) Chromium metal is thermally deposited. (c) Oxygen RIE of polyimide. (d) RIE of Nb counter electrode in $CCl_2F_2+CF_4+O_2$ gas mixture. (e) Deposition of SiO, lift-off, and wire electrode deposition and patterning.

a. $Nb/AlO_x/Nb$ Trilayer Deposition

The $Nb/AlO_x/Nb$ trilayer is deposited in-situ in a high vacuum system (base pressure 1.3 x 10^{-7} Pa) by magnetron sputtering. The substrates are oxidized silicon or quartz and are heat sunk to a thermal mass but not actively cooled during deposition. The large scale features of the trilayer are formed by lift-off using AZ5214 photoresist (AZ Hoechst) and image reversal. The Nb base and counter electrodes are approximately 160 nm and 120 nm respectively. The barrier is formed by depositing 6-10 nm of aluminum followed by an in-situ oxidation in an argon/oxygen gas mixture in a manner similar to that described by Morohashi et al.[3]. During this step the total process gas pressure is maintained constant by throttling the vacuum pump. A dc-plasma is formed during the oxidation process by applying approximately -500V to an aluminum ring placed in the system. This plasma has

been found to reduce oxidation times, but does not effect the quality of the barrier. After the Nb counter electrode deposition, 30 nm of gold is deposited on the trilayer to act as a contact layer.

b. Junction Patterning

The etch mask used to form the tunnel junction is patterned by electron beam (e-beam) lithography using a JEOL JBX-5 lithography system with a minimum spot size of 8 nm. The lithographic stencil must be robust enough to withstand Reactive Ion Etching (RIE) and provide a means to subsequently lift-off the SiO isolation layer. The high resolution e-beam resist, PMMA, is not suitable as the final RIE mask because it lacks the required etch resistance. Techniques have been developed which transfer the e-beam written pattern into polyimide while maintaining the required resolution[4]. The wafer is spin coated with a polyimide[5] film approximately 400 - 600 nm thick. Following a hot plate bake to drive the solvents from the polyimide, the wafer is spin coated with 120 nm of PMMA. It is then exposed in the e-beam lithography system to form holes in the PMMA film with the required junction dimensions. Chromium metal is thermally evaporated onto this stencil and the PMMA is removed in acetone, leaving metal where there were holes (polyimide is not soluble in acetone). The resulting pattern is etched in a parallel plate RIE system using oxygen gas to remove polyimide from areas of the wafer not protected by chromium. The RIE of polyimide is highly anisotropic, however, it is sensitive to surface contamination such as dust or material resputtered from the electrodes of the etcher and care must be taken to provide a clean environment for this process step. An SEM micrograph of an etch test pattern is shown in figure 2. The square etch stencils consisting of Cr(30nm) on Polyimide(550nm) have dimensions of 1.5, 1.0, 0.5, and 0.25 μm on a side. The minimum area is .06μm^2.

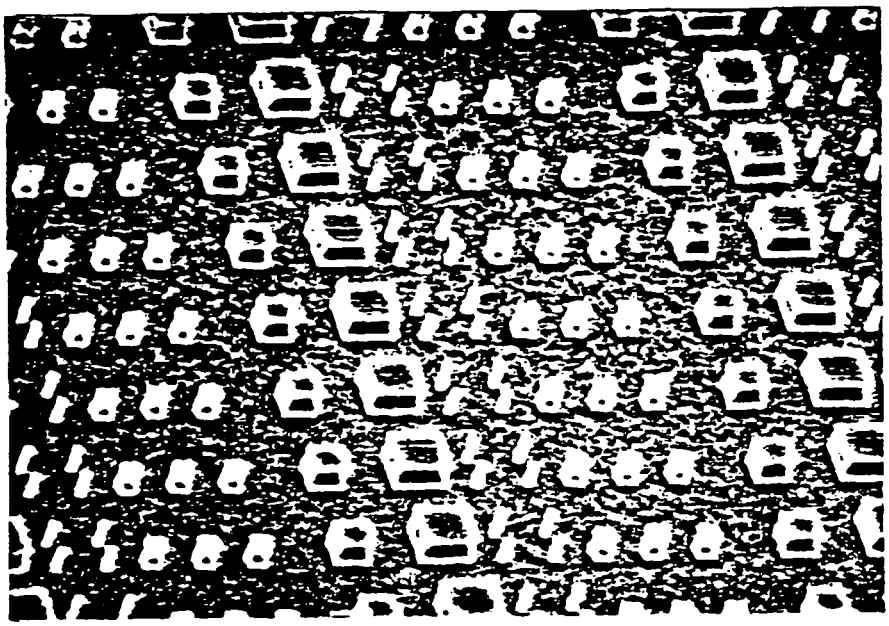

Figure 2. Test patterns etched in polyimide using oxygen RIE . The smallest features are $0.06\mu m^2$.

c. Junction Etch

The tunnel junction is formed using RIE by first etching the gold contact layer and then the Nb counter electrode. The gold is sputter etched using argon gas. Techniques for anisotropically etching Nb had to be developed. An etch profile for a submicron line patterned in an Nb film using a standard etch process (CF_4+20% O_2 ,4 Pa pressure, and 0.27 W/cm^2 power density) is shown in figure 3. The isotropic component of this etch mixture is clearly too large to be used in the fabrication of submicron devices. Anisotropy occurs in RIE when the etch mechanism requires predominantly normal incident ion impact energy to proceed[6]. Etching of Nb in CF_4/O_2 , however, occurs via a spontaneous rather than ion assisted reaction of fluorine and fluorine radicals with Nb. We have found a technique which achieves the required anisotropy. Etching with a gas mixture containing CCl_2F_2 produces very good etch anisotropy, which may be attributed to the a nonvolatile $NbCl_x$ product which forms on the sidewalls. Figure 4 shows the etch rate of Nb and NbN using mixtures of $CCl_2F_2+CF_4+O_2$. For these measurements, the total pressure was 4

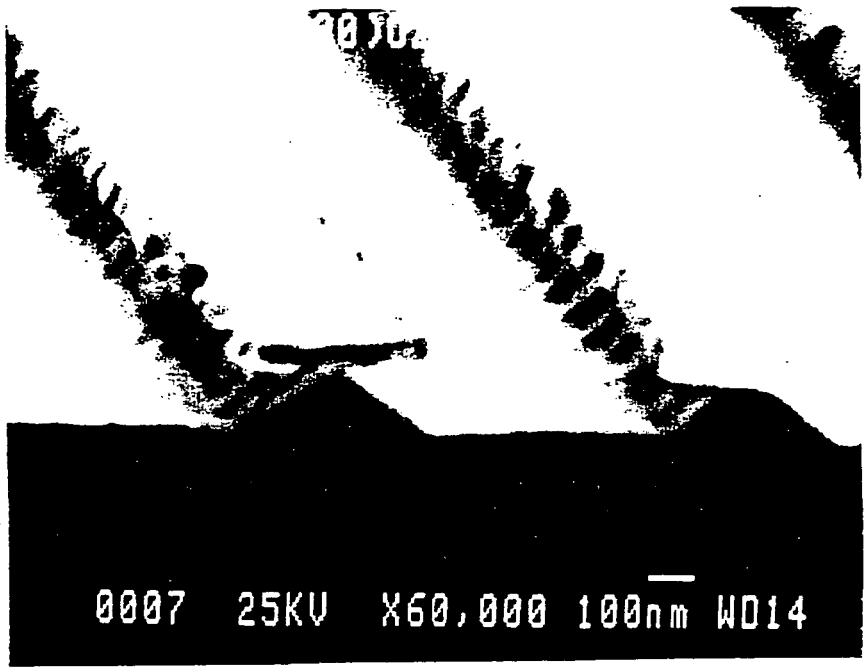

Figure 3. Submicron Nb lines etched by RIE using CF_4+O_2. The large undercut of the Nb line below the 0.4μm chromium etch stencil is evident.

Pa, the power density was 0.27 W/cm^2 and the oxygen flow was constant at 2 sccm, while the CCl_2F_2/CF_4 ratio was varied. The etch is highly anisotropic for mixtures containing greater than 60% CCl_2F_2 in $CCl_2F_2+CF_4$. Mixtures rich CF_4 exhibited isotropic etching. The region with approximately 20% to 50% CCl_2F_2 content was characterized by low etch rates and polymer formation. Shown in figure 5 is the etch profile of Nb achieved using 62% CCl_2F_2 in ($CCl_2F_2+CF_4$) and similar sample etched in CF_4+O_2. Structures etched in the CCl_2F_2 gas mixture show very little undercut while CF_4+O_2 produced a large undercut.

d. Electrical Isolation

Following the etch the counter electrode to form the junctions, a electrical isolation layer of SiO is deposited with the etch mask in place . The SiO is thermally deposited from a baffled source. To achieve good edge coverage, the samples are placed at a fixed angle

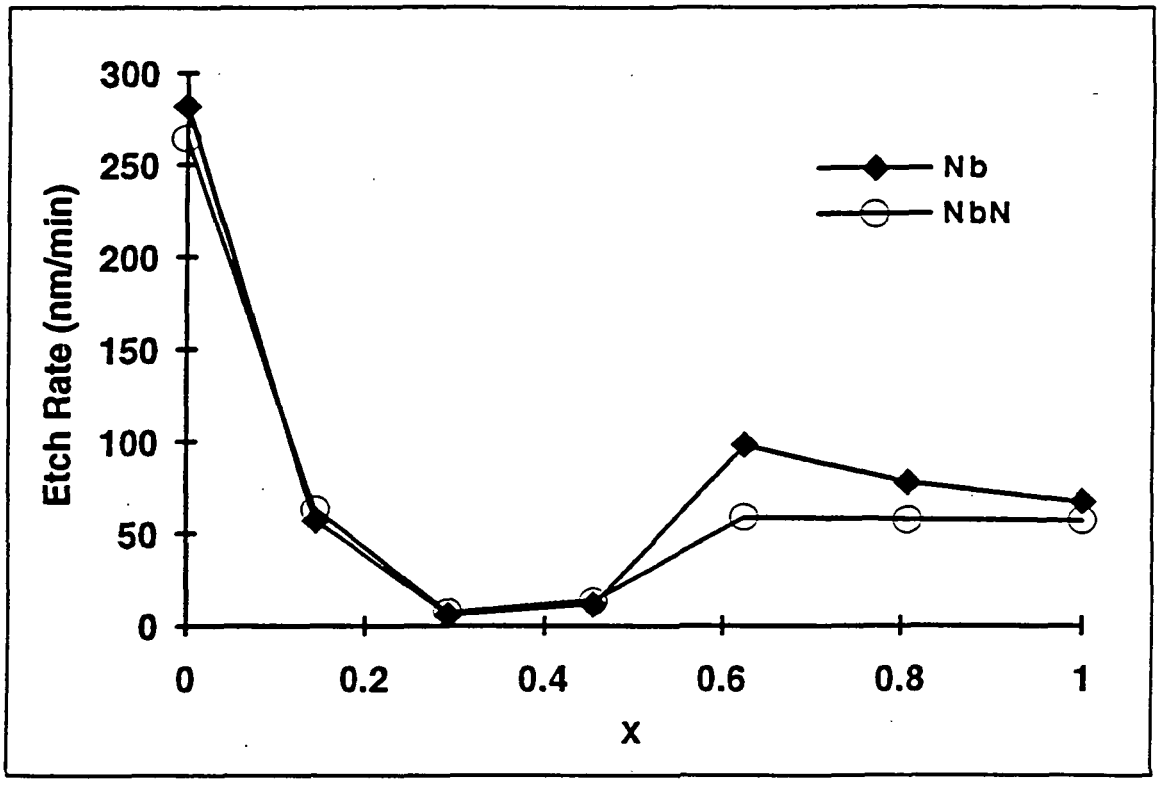

Figure 4. RIE etch rate for Nb and NbN as a function of gas composition. The etch gas consists of $85\%(x\ CCl_2F_2+(1-x)CF_4)+15\%O_2$.

relative to SiO flux and rotated during the deposition. Flux angles for normal incidence to approximately 60 degrees have been evaluated. Angles of 5-15 degrees have been found to provide a good compromise between side wall coverage and clean lift-off. SiO film thicknesses are typically 150-250 nanometers depending on the application. The polyimide and SiO are removed from the junction areas using dichloromethane solvent. A short RIE etch in oxygen is used to remove polyimide residues after the lift-off step.

e. Contact Wiring

Mixer elements are completed by depositing 250-350 nm of Nb by magnetron sputtering. The wire layer is patterned lithographically and etched using a RIE process similar to the one used for the junction etch. A typical current-voltage characteristic for a tunnel junction fabricated by this process is shown in figure 6. This device is 0.25 μm^2 in area and has a critical current density of 7.7 kA/cm^2.

Summary/Conclusions

In this paper, we have described techniques developed for the fabrication of submicron area tunnel junctions in refractory materials. The process described is applied specifically to the fabrication of $Nb/AlO_X/Nb$ tunnel junctions, however, much of the technology has also been used to fabricate NbN/MgO/NbN tunnel junctions[7] and is relevant to other submicron fabrication tasks. This process extends the self-aligned lift-off process used to fabricate refractory tunnel junctions using optical lithography. The primary new features are the use of electron beam lithography to form a submicron pattern in PMMA and the transfer of this pattern into chromium by lift-off. The chromium pattern is transferred into polyimide using oxygen RIE and the resulting Cr/polyimide is used to etch the trilayer counter electrode using a highly anisotropic RIE gas mixture containing CCl_2F_2. $Nb/AlO_X/Nb$ tunnel junctions with areas down to 0.1 μm^2 have been fabricated using these techniques. Mixer elements have been fabricated using this process for both wave guide[8,9,10] and quasi optically coupled[11,12,13] receiver systems. In wave guide receiver systems with operating frequencies up to 500 GHz, the capacitance associated with the submicron area $Nb/AlO_X/Nb$ devices is small enough so that the mixer block rf-embedding circuit provides enough tuning to achieve excellent performance (receiver noise temperatures, $T_R(DSB) = 180K$ at 485 GHz)[14] without integrated tuning structures. In principle junction areas can be scaled down further, however, in order to do so the junction relaxation times must also be scaled down so that the real part of the junction impedance in the correct range. The junction relaxation time (RC) is determined by the insulator barrier thickness, with thinner barriers producing smaller RCs. The limit for a given insulator barrier is determined by the thinnest barrier that can be achieved while maintaining suitable junction characteristics. It has been our experience with $Nb/AlO_X/Nb$ tunnel junctions, that the I-V characteristics degrade significantly for critical current densities of

greater than 15kA/cm^2 (RA≈ 12 Ω μm^2). For junctions with this current density, a 100 Ω junction has an area of ≈ 0.12 μm^2.

Acknowledgements

The research described in this paper was performed by the Center for Space Microelectronics Technology, Jet Propulsion Laboratory , California Institute of Technology, and was jointly sponsored by the Strategic Defense Initiative Organization / Innovative Science and Technology Office and the National Aeronautics and Space Administration / the Office of Aeronautics and Space Technology. We would also like to acknowledge P.D. Maker and R.E. Muller for the excellent electron beam lithography support and technical discussions.

References:

1 A. Shoji, F. Shinoki, S. Kosaka, M. Aoyagi, and H. Hayakawa, " *New Fabrication Process for Josephson Tunnel Junctions with (Nobium Nitride, Niobium) Double-Layered Electrodes*", Appl. Phys. Lett., 41,1097, (1982).

2 M. Gurvitch, M.A. Washington, and H.A. Huggins, "*High Quality Refractory Tunnel Junctions Utilizing Thin Aluminium Layers*", Appl. Phys. Lett., 42, 472 (1983).

3 S. Morohashi, F. Shinoki, A. Shoji, M. Aoyagi, and H. Hayakawa, "*High Quality Nb/Al-AlOx/Nb Josephson Junction*", Appl. Phys. Lett. **46**, 1179, (1985).

4 D.M. Byrne, A.J. Brouns, F.C. Case, R.C. Tiberio, B.L. Whitehead, and E.D. Wolf, "*Infrared Mesh Filters Fabricated by Electron-Beam Lithography*", J. Vac. Sci. Technol., B3, 268 (1985) and references within: M. Hatzakis, B.J. Canavello, and J.M. Shaw, IBM J. Res. Dev., **24**, 452 (1980).

5 Olin Ciba-Geigy, Probimide 200 series.

6 See for instance: J.W. Coburn, Plasma Etching and Reactive Ion Etching, AVS Monograph Series, Ed. N. Rey Whetten.

7 J.A. Stern, H.G. LeDuc, and A.J. Judas, "*Fabrication and Characterization of High Current-Density, Submicron, NbN/MgO/NbN Tunnel Junctions*", this conference.

8 H.H.S. Javadi, W.R. McGrath, S.R. Cypher, B.D. Hunt, and H.G. LeDuc, Digest 15th Int. Conf. on IR and Millimeter Waves, p245, Orlando, FL (1990).

9 J.W. Kooi, M. Chan, T.G. Phillips, B. Bumble, and H.G. LeDuc, "*A Low Noise 230 GHz Heterodyne*

Receiver Employing .25μm^2 Area Nb/AlO$_x$/Nb Tunnel Junctions", IEEE Microwave Theory and Techniques Journal, to be published.

10 C.K. Walker, M. Chen, P.L. Shafer, H.G. LeDuc, J.E. Carlstrom, and T.G. Phillips, "*A 492 GHz SIS Waveguide Receiver for Submillimeter Astronomy*", Int. J. of IR and Millimeter Waves, to be published.

11 T.H. Buttgenbach, H.G. LeDuc, P.D. Maker, and T.G. Phillips, "*A Fixed Tuned Broadband Matching Structure for Submillimeter SIS Receivers*", IEEE Trans. Appl. Superconductivity, to be published.

12 P.A. Stimson, R.J. Dengler, P.H. Siegel, and H.G. LeDuc, "*A Planar Quasi-Optical SIS Receiver for Array Applications*", this conference.

13 J. Zmuidzinas, H.G. LeDuc, and J.A. Stern, "*Slot Antenna SIS Mixers for Submillimeter Wavelengths*", this conference.

14 Private communication, C.K. Walker.

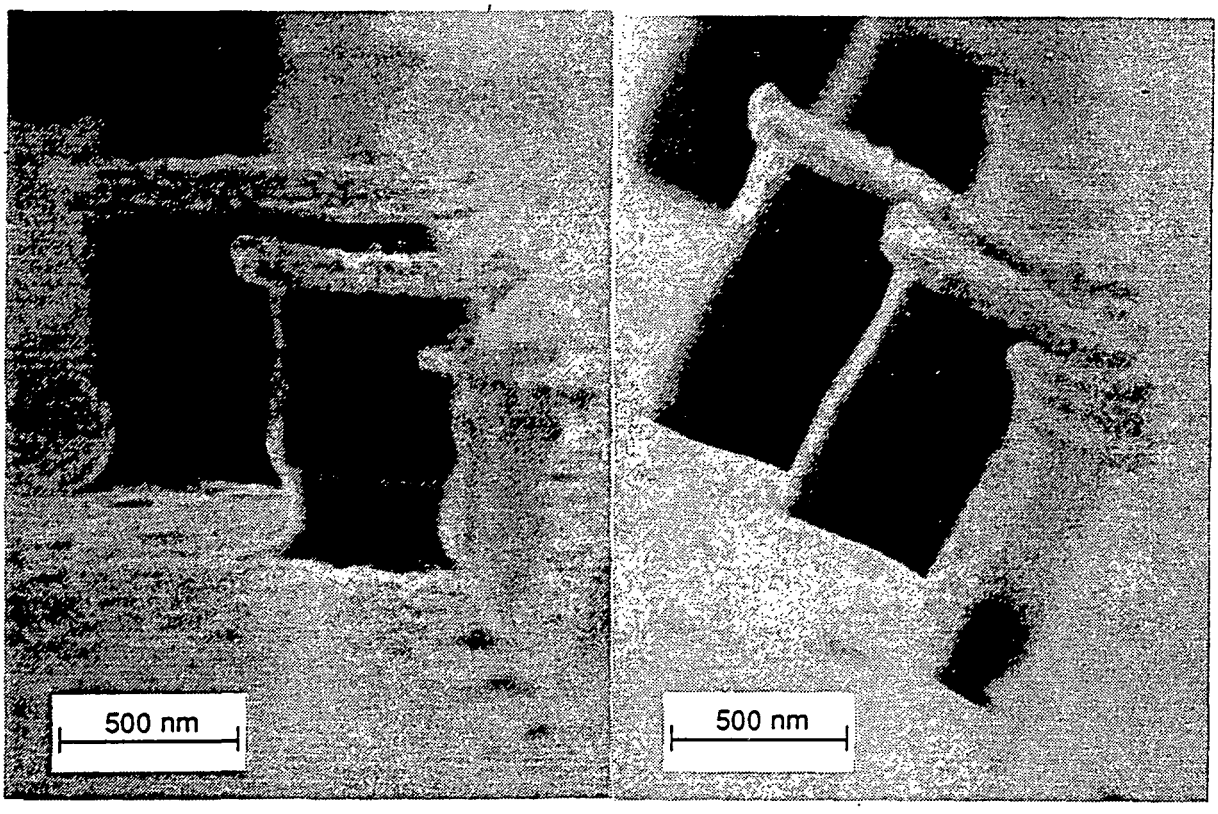

Figure 5. SEM micrographs showing etch comparrisons between CF_4+O2 (left) and CCl_2F_2+CF_4+O_2(right). The RIE mask is Cr(30 nm)/Polyimide(550 nm) patterned by e-beam lithography and oxygen RIE. The Nb film (400 nm thick) etchs anisotropically in the CCl_2F_2 containing etch gas.

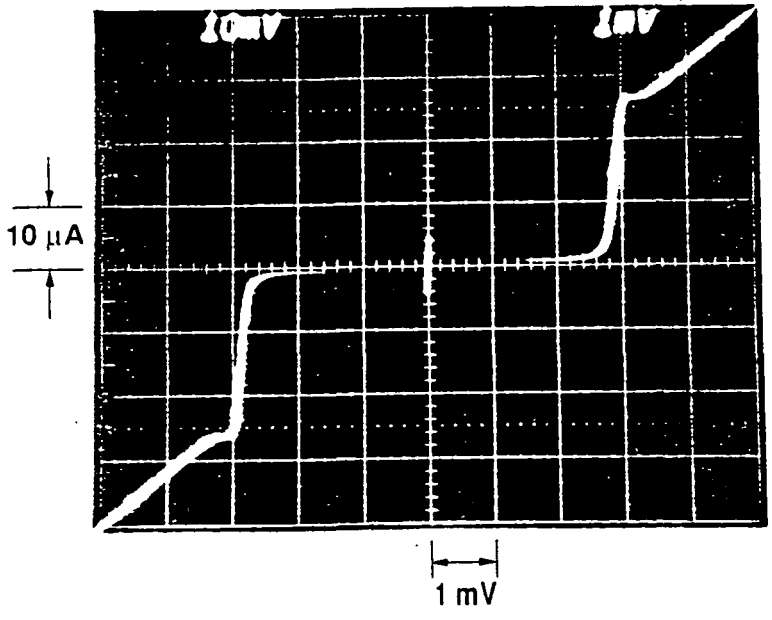

Figure 6. Typical tunneling current-voltage characteristic for a Nb/AlOx/Nb junction taken ar 4.2K. The junction area is 0.25 mm^2 and the critical current density is 7.7 kA/cm^2 .

Noise in Josephson Effect Mixers and the RSJ Model

R. Schoelkopf*, T. Phillips*, and J. Zmuidzinas*

Josephson effect mixers have previously been observed to display "excess" noise both in experiments with point contacts and in numerical simulations using the resistively shunted junction (RSJ) model. This excess noise causes the mixer noise temperature to be a factor of typically 20-100 times[1] the physical temperature of the device. Previously, this excess was ascribed to conversion from unwanted sidebands of the local oscillator and Josephson frequencies and their harmonics[2]. Our numerical modeling of the RSJ equations has led to a new understanding of the excess noise, which is simply due to the intrinsic Josephson oscillations of the device. In addition, we have extended the modeling to include the previously ignored case of finite device capacitance (i.e. RSJ capacitance parameter $\beta_c \neq 0$), which is more realistic for lithographically defined Josephson such as shunted tunnel junctions or SNS bridges. For some cases, this yields an improvement of a factor of two in noise temperature from the zero capacitance models. We will discuss the device parameters which optimize the mixer performance for frequencies approaching the characteristic frequency of the device, which is given by the Josephson frequency at the I_cR_n voltage ($\nu = 2eI_cR_n/h$). These modeling results predict good conversion efficiency and a noise temperature within a factor of a few of the physical temperature. Experiments are in progress to determine the accuracy of this modeling using a waveguide mixer at 100 GHz with optimized, resistively shunted Nb tunnel junctions. If the modeling results are valid, they are particularly encouraging for mixers in the submillimeter regime, given the possibility of obtaining non-hysteretic Josephson devices with I_cR_n products in excess of a millivolt, using, for instance, high-T_c SNS bridges. We discuss the modifications to the classical RSJ model which are necessary in the quantum regime ($h\nu > kT$), and conclude the Josephson mixers may attain noise temperatures less than ten times the quantum limit at high frequencies.

---

*R. Schoelkopf, T. Phillips, and J. Zmuidzinas are with California Institute of Technology.

[1]Y. Taur, *IEEE Transactions on Electron Devices*, ED-27, p. 1921, 1980.

[2]K.K. Likharev, *Dynamics of Josephson Junctions and Circuits*, New York: Gordon and Breach, p. 423, 1986.

FABRICATION AND CHARACTERIZATION OF HIGH CURRENT-DENSITY, SUBMICRON, NbN/MgO/NbN TUNNEL JUNCTIONS

J. A. Stern

H. G. LeDuc

*A. J. Judas**

Center for Space Microelectronics Technology
Jet Propulsion Laboratory
California Institute of Technology
Pasadena, California 91109
* Present Address: Stanford University
Palo Alto, California

Abstract

At near-millimeter wavelengths, heterodyne receivers based on SIS tunnel junctions are the most sensitive available. However, in order to scale these results to submillimeter wavelengths, certain device properties should be scaled. The tunnel-junction's current density should be increased to reduce the RC product. The device's area should be reduced to efficiently couple power from the antenna to the mixer. Finally, the superconductor used should have a large energy gap to minimize RF losses. Most SIS mixers use Nb or Pb-alloy tunnel junctions; the gap frequency for these materials is approximately 725 GHz. Above the gap frequency, these materials exhibit losses similar to those in a normal metal. The gap frequency in NbN films is as-large-as 1440 GHz. Therefore, we have developed a process to fabricate small area (down to 0.13 μ^2), high current density, NbN/MgO/NbN tunnel junctions.

In this paper, we describe a process used to fabricate submicron NbN junctions. Low-leakage current-voltage (I-V) characteristics are achieved for current densities up to 40 kA/cm^2. However, the quality of the I-V characteristics degrades significantly for higher current densities. Junction areas are patterned by lifting off a Cr stencil defined by electron beam lithography. This image is transferred to a polyimide stencil using reactive ion etching (RIE). The junctions are then etched and isolated using a self-aligned liftoff technique. The limitations of this technique and the quality of the resulting I-V characteristics will be discussed.

There are several device and materials parameters which must be known to properly design mixer circuits. The optimal imbedding impedance for the mixer is determined by the capacitance and I-V characteristic of the tunnel junction. If microstrip line circuits are used to achieve this impedance, the magnetic penetration depth of the NbN must be known to calculate the microstrip line impedance and propagation velocity. We have measured the junction capacitance versus current density and microstrip line inductance using superconducting quantum interference devices (SQUIDs). The propagation velocity was measured using long open-ended microstrip-lines connected to Josephson tunnel junctions. The magnetic penetration depth can be calculated from either the microstrip line inductance or the propagation velocity. The implications of these measurements will be discussed.

Introduction

There is a growing need for sensitive submillimeter (smm) wavelength detectors for both ground based and space based applications. Heterodyne receivers based on superconductor-insulator-superconductor (SIS) tunnel junctions are the most sensitive at millimeter and near-millimeter

wavelengths [1][2]. At wavelengths longer than 3 mm, the noise in these detectors has approached the quantum limit [3]. If these mixers designs could be redesigned for shorter wavelength operation, they would fill the need for smm wavelength mixers. For good performance to be achieved at smm wavelengths, a number of SIS tunnel junction properties must be adjusted. We have fabricated and characterized tunnel junctions which are suitable for smm use.

The junction capacitance is the property which has the largest impact on smm wave mixers. An SIS tunnel junction can be modeled as a nonlinear tunneling element in parallel with a shunt capacitance. The product of the shunt capacitance (C) and the RF resistance of the junction (approximately the normal state resistance, R_n) is one limit on the high frequency response of a tunnel junction, because the capacitance tends to shunt RF currents away from the nonlinear tunneling element. To reduce the R_nC time constant, the tunnel junction barrier is made thinner; this increases the junction capacitance

$$C=\epsilon_0\epsilon_r A/d,$$

where ϵ_0 is the dielectric constant of free space, ϵ_r is the relative dielectric constant of the barrier, A is the junction area and d is the barrier thickness, but it decreases the resistance more rapidly

$$R_n=\frac{h^2 d\cdot\exp\{4\pi d\sqrt{2m\phi}/h\}}{e^2 A\sqrt{2m\phi}}$$

where h is Plank's constant, m is the mass of the quasi-particle, ϕ is the barrier height and e the charge of the quasiparticle. Because the barrier cannot be made thinner than one monolayer, the R_nC product is ultimately limited by the barrier material properties (ϵ_r, ϕ and the lattice

constant). The R_nC product is independent of junction area, but the junction resistance must be roughly 100 Ω for it to couple efficiently to the antenna. Therefore, as the barrier is made thinner, the tunnel junction's area must also be reduced. At smm wavelengths, junctions with submicron areas are needed. Since the barrier thickness is difficult to measure, R_nA products can be used as an area-independent measure of junction relaxation time. The product of the critical current density (J_c) and R_nA is proportional to the energy gap, so the current density is also frequently used as a measure of the relaxation time.

The embedding circuit of a mixer can be designed to resonate out the junction capacitance over a frequency band. In waveguide mixer mounts, this can be accomplished using a back short and E-plane tuner; however, at high frequencies these tuners do not work as well as at lower frequencies. Additionally, quasi-optical mixers do not have these tuning elements. Monolithic embedding circuits can also be fabricated to resonate out the junction capacitance [4][5][6]. Many of these circuits use superconducting microstrip lines. To accurately design these circuits, the propagation velocity and impedance of the microstrip line must be known. Both of these parameters depend critically on the magnetic penetration depth of the superconductor [7].

The energy gap of the superconductor (2Δ) limits the use of SIS mixers at smm wavelengths. Above the gap frequency ($2\Delta/h$), the superconductor has losses similar to those in a normal metal; therefore, any embedding circuits will have losses[8]. Embedding circuits could be made of a larger gap superconductor or a low-loss normal metal (such as gold or copper).. In this case, the SIS mixer will perform well up to twice the gap frequency. Most mixers currently use

niobium based tunnel junctions. The gap frequency of niobium is 725 GHz. Above this frequency, other superconductors will probably be needed.

Based on the small gap in niobium, we have developed a process for fabricating junctions with NbN electrodes, which has a much larger gap frequency (up to 1440 GHz). The goal was to fabricate high current-density, submicron tunnel junctions with large energy gaps. The limitations of our process on both current density and junction area are discussed below. Additionally, we have measured several device properties necessary to design mixer circuits (NbN magnetic penetration depth, junction uniformity, yield and specific capacitance.)

Junction Fabrication

The tunnel junctions are fabricated by depositing the NbN/MgO/NbN trilayer over the entire substrate [9][10]. The NbN films are deposited by reactive DC-magnetron sputtering from a niobium target using a 5 cm diameter US inc. sputter gun in an argon and nitrogen atmosphere. The gas flow rates are 150 and 15 sccm respectively and the total pressure with the plasma off is 14.4 mTorr. The gun is typically biased at -232 Volts and 600 mAmps. The substrate is not heated and is approximately 6 cm from the sputter gun. Deposition rates are 45 nm/min. The thickness of the base and counter electrode are 315, 135 nm respectively. The superconducting transition temperature of the films is usually between 14.5 and 15.0 K.

The barrier layer is formed by depositing MgO and performing a pinhole cure in an oxygen plasma. MgO is deposited by RF sputtering from a US inc. 5 cm diameter source in a pure argon atmosphere. The Ar pressure is 10.0 mTorr and the power is 50 Watts. To promote

uniform growth of the barrier, deposition occurs intermittently as the substrate is rotated past the source in a circular orbit. After the barrier deposition, the sample is exposed to an oxygen-plasma glow discharge for 1 minute at 100 mTorr. The plasma is maintained with a high purity aluminum ring below the substrate; the ring is biased at -400 Volts and 2.0 mA. Barrier deposition times vary between 5.5 and 6.7 min. for current densities between 40 and 10 kA/cm^2.

The trilayer is completed by covering the entire NbN/MgO/NbN structure with 30 nm of gold. The gold prevents the top surface of the junction from oxidizing in air. In some cases, there is a thin (40 nm) layer of Nb between the counter electrode and the gold. The purpose of the Nb interlayer will be discussed below.

Tunnel junctions are fabricated using a submicron, self-aligned lift-off technique. This process is shown in figure 1. The trilayer is patterned using RIE and a photoresist stencil. The etcher used is a Semi Group System 1000, and the electrode area is 730 cm^2. The gold and MgO layers are etched using a straight argon sputter etch. The NbN layers are etched in a CF_4-O_2 mixture. The conditions for this and other reactive ion etches are given in table 1. After the etch, the photoresist is stripped in organic solvents.

The submicron tunnel junction stencil is formed in a polyimide layer [11]. The etched trilayer is coated in Ciba Geigy Probimide 286 and thinner 2:1 at 4000 rpm resulting in a 310 nm polyimide layer. The polyimide is cured at 150° C on a hot plate for 15 minutes and flood exposed with 315 nm radiation. A KTI Chemicals Inc. 950K 2% PMMA layer is spun on top of the polyimide at 4000 rpm and baked at 150° C. A thin aluminum layer is evaporated on top

of the PMMA to prevent charging during the exposure. The sample is exposed in a JEOL model JBX5 electron beam lithography system and subsequently developed to reveal square holes in the PMMA. A thin (35 nm) chromium layer is thermally evaporated and lifted off to define the junction area. Next an AZ 5214-E stencil is patterned using image reversal [12] to reveal an open area around the chromium dot. This stencil acts to protect the majority of the trilayer from the junction etch. The polyimide layer is etched using an oxygen plasma. During the etch, a polyimide (Kapton) sheet is about 3 cm above the sample to protect against particles falling on the sample during the etch. The oxygen etch is very anisotropic and an over etch is normally used to insure that the trilayer surface is completely clean.

The junction etch consists of an Ar sputter-etch of the gold and one of several NbN etches [13]. For micron size junctions, the CF_4-O_2 mixture can be used, however this etch is isotropic and it will undercut NbN mesa. A straight CF_4 etch can be used for submicron junctions. This etch is largely anisotropic, because a fluorinated carbon layer forms on the sidewall of the junction as it etches; however, there is about 50 nm of undercut. A mixture of CCl_2F_2-CF_4-O_2 produces an anisotropic etch, however it reacts at the Au-NbN interface and produces a superconductor-normal metal-superconductor type I-V characteristic in series with the SIS I-V characteristic. This series weak link can be avoided by inserting a niobium layer between the gold and NbN layers and by rinsing the sample in water after the etch. The niobium buffer removes the series weak link which seams to occur at the NbN-Au interface Regardless of the etch used, a monitor sample is used to detect the endpoint of the junction etch. After the junction etch, a 1 minute argon sputter etch is done to improve the adhesion of the dielectric isolation layer.

Table 1. Summary of Reactive Ion Etch Conditions

Material	Etch Gases	Flow Rates (sccm)	Pressure (mTorr)	Power (Watts)	Etch Rate (nm/min)
Polyimide	O_2	20	30	130	100
Gold	Ar	20	30	118	15
NbN	CF_4,O_2	20,2	30	118	65
NbN	CF_4	20	30	118	52
NbN	CCl_2F_2, CF_4,O_2	23,7,2	30	118	58

The junction is electrically isolated by thermally evaporating 150 nm of Silicon monoxide on the sample. The wafer is rotated at a 5 to 15° angle during the evaporation to improve SiO coverage. The photoresist protection layer is then lifted off in acetone, followed by the polyimide in dichloromethane. The polyimide liftoff is done in an ultrasonic cleaner followed by a mechanical scrub with a q-tip to remove the SiO flags that form on the side-walls of the polyimide pillar. The liftoff yield, even for the smallest junctions, is excellent. Following the polyimide liftoff, an oxygen etch is done to remove any polyimide residue which will lead to a contact resistance.

The NbN wiring layer is deposited on top of the electrically isolated junction. To avoid breaks at step edges, the wiring is typically 600 nm thick. The wiring is patterned and etched like the trilayer, although if small features are desired, one of the anisotropic etches is used.

Results

The quality of tunnel junction I-V characteristics depends strongly on the critical current density. As the current density increases, the ratio of the subgap resistance (measured at 3 mV) to the normal state resistance decreases. Figure 2 shows a plot of this ratio as a function of critical current density. Above 50 kA/cm^2, the ratio R_{sg}/R_n is reduced to two; however, for current densities up to 40 kA/cm^2 the I-V characteristics are still reasonable. An example of a 0.42x0.42 μ^2, 35 kA/cm^2 junction is shown in figure 3; this junction was fabricated for 626 GHz mixer tests.

A second form of I-V degradation occurs at high current densities. For a fixed area junction, the gap voltage decreases as the current density increases. This is caused by a non-thermal distribution of quasi-particles near the barrier. As the tunneling current increases, the number of quasi-particles injected into the superconducting electrode increases; this represents a local heating of the quasiparticle bath and leads to a reduction in the gap voltage. The quasi-particle heating can be minimized by reducing the junction area. Table 2 shows the gap for different area junction on the same wafer; the current density is 28 kA/cm^2.

Table 2. Energy Gap as a Function of Junction Size

size (microns)	Energy Gap (meV)
1.0	4.15
0.7	4.3
0.5	4.4
0.36	4.45

Junction uniformity and yield was measured by fabricating series arrays of 100 tunnel junctions. Typical I-V characteristics for arrays of 0.49, 0.25 and .13 μ^2 junctions are shown in figure 4. For these size junctions, the standard deviation of the critical currents is typically $\pm$5.4, 6.6 and 7.7% respectively. For comparison, the standard deviation for optically defined, 4 μ^2 junctions is 3.9%. Typical minimum-to-maximum uniformity is $\pm$17% for 0.25 μ^2 junctions. When the fabrication process was successful, junction yields were better than 99 %. The uniformity and yield for this process were high enough that a monolithic array of mixers could be fabricated.

SQUIDs have been fabricated to measure the magnetic penetration depth of NbN films and the specific capacitance of NbN/MgO/NbN junctions. The design of the SQUIDs is based on that of Magerlein [14] and is described in detail elsewhere [15]. Briefly, the SQUID design is a microstrip line over a ground plane with two tunnel junctions connecting the microstrip to the ground plane. The inductance of the microstrip line, and therefore the magnetic penetration depth, can be determined by observing the critical current of the two parallel-junctions versus control current passing along the microstrip line. The loop of the SQUID and the junction capacitance form an LC tank circuit. The Josephson oscillations will interact with this tank circuit to form a current step at a voltage proportional to this resonant frequency. The junction capacitance can be determined from the resonance voltage and the critical-current modulation curve.

The magnetic penetration depth can also be determined using an open-ended microstrip-line connected to a Josephson junction. The microstrip line has an impedance which is periodic with frequency. The Josephson oscillations interact with the microstrip line circuit to yield a series

of resonances whenever the microstrip line reflects an inductance that cancels out the junction capacitance. An example of these resonances is shown in figure 5. The propagation velocity of the microstrip line can be calculated to be

$$V_p = e \cdot \delta V / h \cdot 2L,$$

where δV is the spacing or the resonances and L is the length of the microstrip line stub. The penetration depth can be calculated from the propagation velocity. These microstrip line stubs are a good method of verifying the SQUID results and directly measuring the microstrip line propagation velocity.

The specific capacitance of our junctions as a function of J_c is shown in figure 6 for critical current densities ranging from 500 to 50,000 A/cm^2. Much of this data has been published previously[14]; however, we have extended the data to include the highest current densities shown here (10 to 40 kA/cm^2). Also shown in figure 6 is the R_nC frequency as a function of current density. At 40 kA/cm^2, the roll off frequency is only 140 GHz; therefore, at smm wavelengths, the capacitance must be tuned out to achieve optimal performance.

The magnetic penetration depth of our NbN films has also been measured using SQUIDs. The penetration depth varies significantly with film quality and is typically between 270 and 380 nm. The propagation velocity of microstrip lines with 150 nm SiO dielectric layers is typically 0.16 to 0.18 times the speed of light in a vacuum. The penetration depth calculated from these numbers is 300 to 365 nm, which agrees well with the SQUID results. Because the penetration depth depends critically on film quality, SQUID and microstrip line circuits are usually added to mixer mask-designs, so the penetration depth can be measured for each set of tunnel junctions

that are fabricated. These circuits are small (2.5 mm × 2.5 mm) and 12 test dies take up roughly one sixth of a 25 mm diameter quartz wafer.

Conclusions

We have developed a process for fabricating high critical current, submicron NbN/MgO/NbN tunnel junctions. The yield and uniformity of this process is good and should be sufficient for most mixer needs. However, the R_nC frequency can only be made 140 GHz without seriously degrading the I-V quality. Submillimeter wave mixers will either require high Q circuits to resonate out the junction capacitance or a new barrier material with a lower dielectric constant or barrier height. Although NbN films should have low RF losses even at smm wavelengths, the actual losses need to be measured in order to evaluate potential high Q tuning circuits. In addition, the effects, if any, of quasi-particle heating on mixer performance need to be investigated.

Work Supported by NASA and SDI/IST

References

[1] C. K. Walker, M. Chen, P. L. Shafer, H. G. LeDuc, J. E. Carlstrom and T. G. Phillips, "A 492 GHz SIS Waveguide Receiver for Submillimeter Astronomy," *Int. J. of IR and Millimeter Waves,* Submitted 1992.

[2] T. H. Buttgenbach, H. G. LeDuc, P. D. Maker and T. G. Phillips, "A Fixed Tuned Broadband Matching Structure for Submillimeter SIS Receivers," *IEEE Trans. Appl. Superconductivity,* Submitted Feb. 1992.

[3] C. A. Mears, Qing Hu, P. L. Richards, A. H. Worsham, D. E. Prober and A. V. Räisänen, "Quantum Limited Quasiparticle Mixers at 100 GHz," *IEEE Trans. on Magn.*, vol. 27, no. 2, 1991.

[4] L. R. D'Addario, "An SIS Mixer for 90-120 GHz with Gain and Wide Bandwidth," *Int. J. of IR and Millimeter Waves,* vol. 5, no. 11, 1419-1442, 1984.

[5] A. V. Räisänen, W. R. McGrath, P. L. Richards and F. L. Lloyd, "Broad-Band Match to a Millimeter-Wave SIS Quasi-Particle Mixer," *IEEE Trans. on Microwave Theory and Technique,* vol. 4, no. 12, December 1985.

[6] S. K. Pan, A. R. Kerr, M. J. Feldman, A. W. Kleinsasser, J. Stasiak, R. L. Sandstrom and W. J. Gallagher, "An 85-116 GHz SIS Receiver Using Inductively Shunted Edge-Junctions ," *IEEE Trans. on Microwave Theory and Technique,* vol. 37, no. 3, 580-592, March 1989.

[7] W. H. Chan, "The Inductance of a Superconducting Strip Transmission Line," *J. Appl. Phys.,* vol.50, no. 12, Dec. 1979.

[8] R. L. Kautz, "Picosecond Pulses on Superconducting Striplines," *J. Appl. Phys.,* vol. 49, 308-314, 1978.

[9] H. G. LeDuc, J. A. Stern, S. Thakoor and S. Khanna, "All Refractory NbN/MgO/NbN Tunnel Junctions," *IEEE Trans. Magn.* vol. 23, March 1987.

[10] J. A. Stern, B. D. Hunt, H. G. LeDuc, A. Judas, W. R. McGrath, S. R. Cypher and S. K. Khanna, "NbN/MgO/NbN SIS Tunnel Junctions for Submm Wave Mixers," *IEEE Trans. Magn.,* vol 25, 1989.

[11] A. W. Lichtenberger, D. M. Lea, C. Li, F. Lloyd, M. J. Feldman and R. J. Mattauch, "Fabrication of Micron Size Nb/Al-Al_2O_3/Nb Junctions with a Trilevel Resist Liftoff Process," *IEEE Trans on Magnetics,* vol. 27, no. 2, March 1991.

[12] M. Spak, D. Mammato, S. Jain and D. Durham, "Mechanism and Lithographic Evaluation of Image Reversal in AZ 5214 Photoresist," As Presented at: *Seventh International Technical Conference on Photopolymers, Ellenville, New York,* Reprints Available from American Hoechst Corporation, AZ Photoresist Products.

[13] H. G. LeDuc, A. Judas, S. R. Cypher, B. Bumble, B. D. Hunt and J. A. Stern, "Submicron Area NbN/MgO/NbN Tunnel Junctions For SIS Mixer Applications," *IEEE Trans. on Magnetics,* vol. 27, no. 2, March 1991.

[14] J. H. Magerlein, "Specific Capacitance of Josephson Tunnel Junctions," *IEEE Trans. Magn.,* vol. 17, no. 2, 286-289, 1981.

[15] J. A. Stern and H. G. LeDuc, "Characterization of NbN Films and Tunnel Junctions," *IEEE Trans. Magn.,* vol 27, no. 2, March 1991.

Figure Captions

Figure 1 *Submicron, self-aligned liftoff process.*

Figure 2 *Subgap resistance divided by the normal state resistance as a function of critical-current density*

Figure 3 *I-V characteristic of a .42x.42 μ^2, 35 kA/cm^2, tunnel junction. The current scale is 20 μA/div. and the voltage scale 1 mV/div.*

Figure 4 *I-V characteristics for series arrays of 100 tunnel junctions. The voltage scale is 50 mV/div. The area of the junctions is 0.13, 0.25, 0.49 μ^2, and the current scale is 10 20 and 50 μA/div for figures a, b and c respectively.*

Figure 5 *I-V characteristic of a 1 μ^2 tunnel junction connected to a 6 μ by 750 μ open-ended microstrip-line stub. The current scale is 5 μA/div, and the voltage scale is 100 μV/div. The resonance spacing is 65 μV leading to a propagation velocity of 0.16 times the speed of light.*

Figure 6 *Junction specific capacitance (a) and R_nC roll-off frequency ($1/2\pi R_nC$) (b) as a function of critical-current density.*

Figure 1.

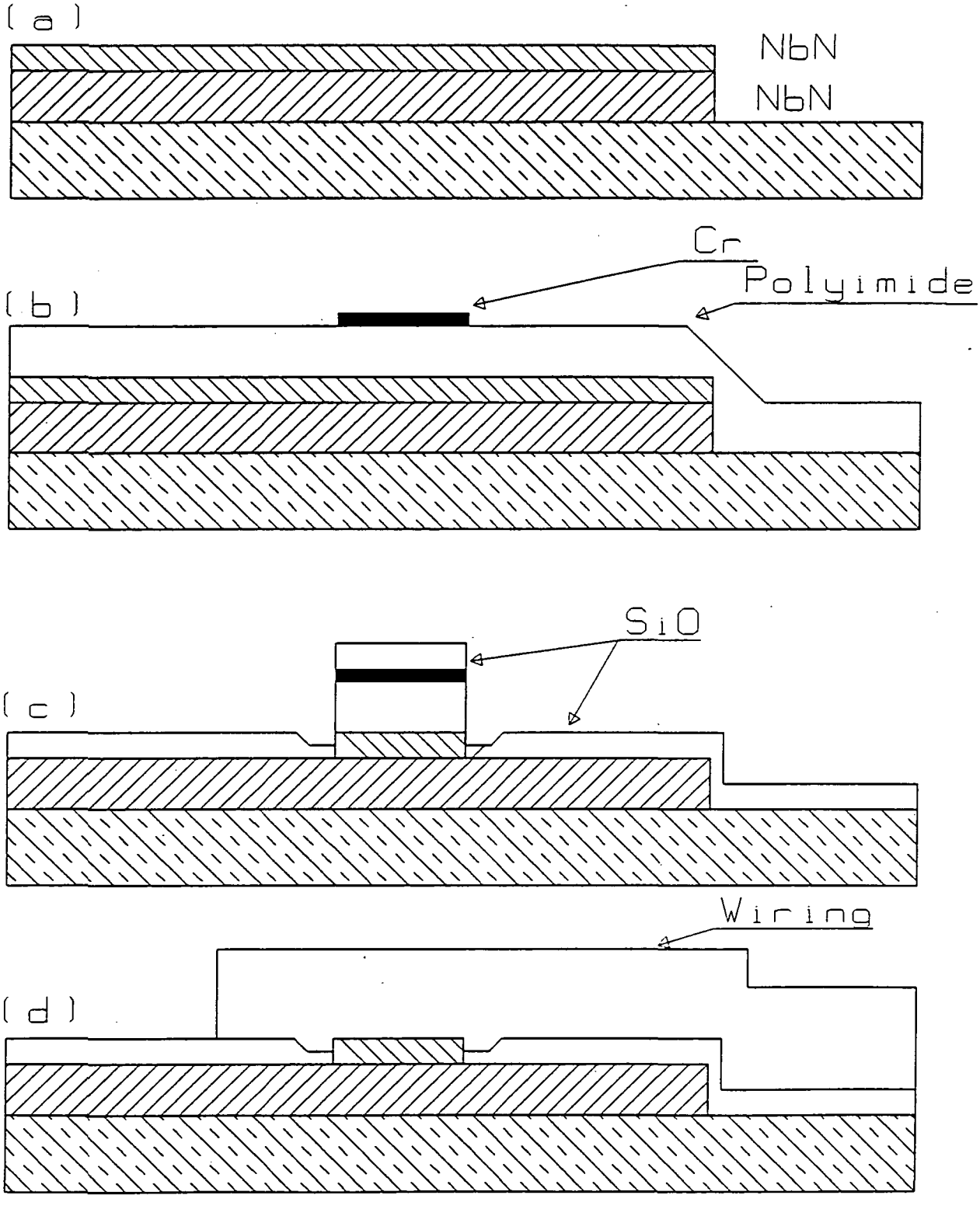

Figure 2.

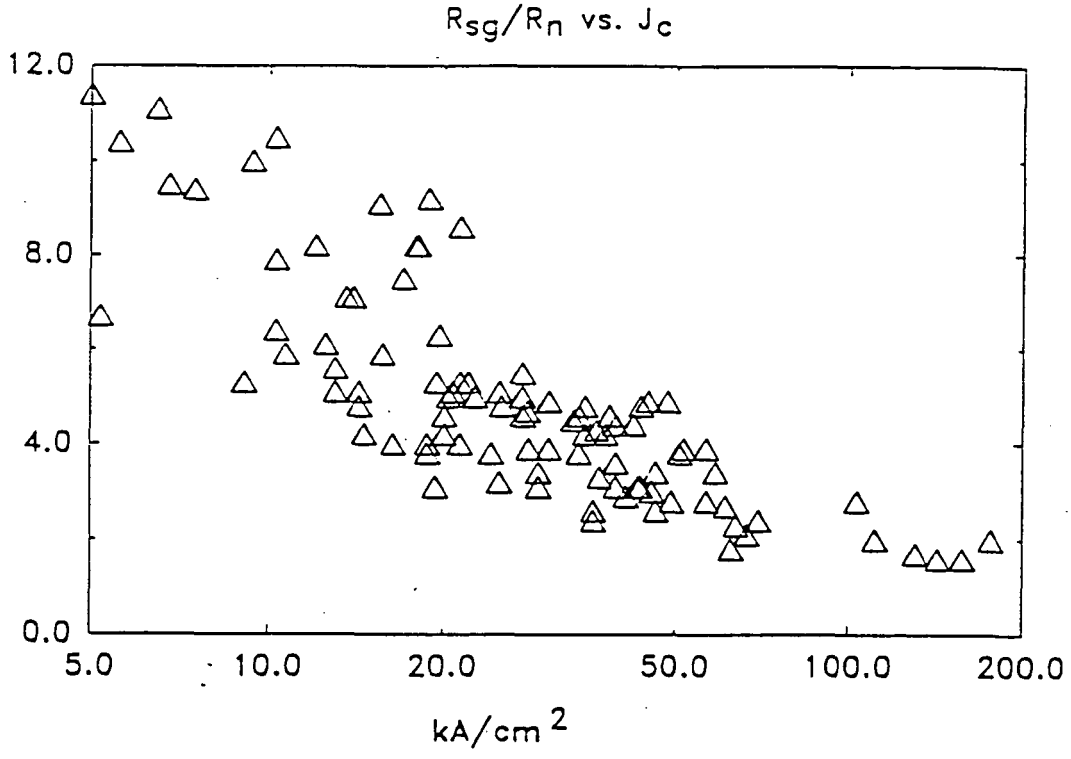

Figure 3.

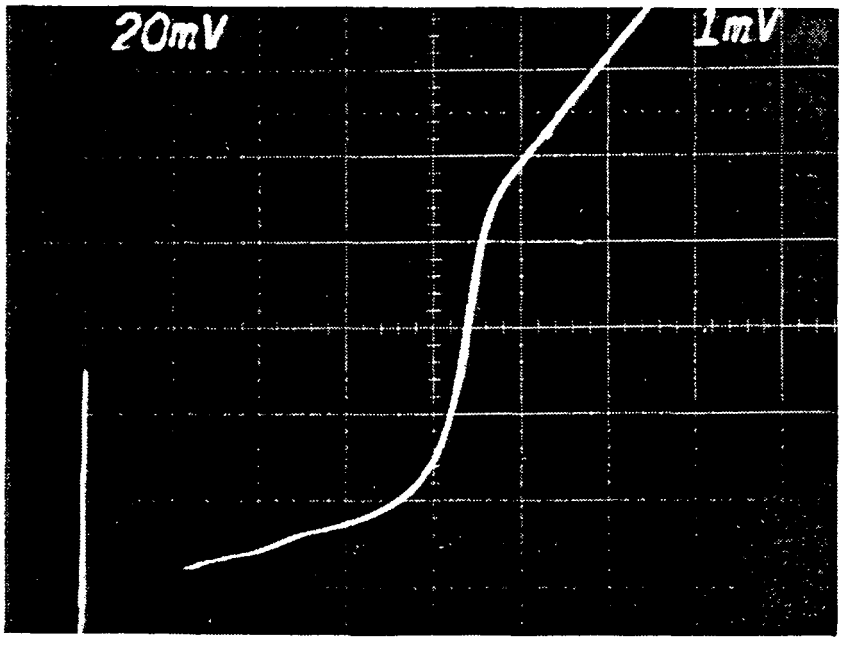

Figure 4.

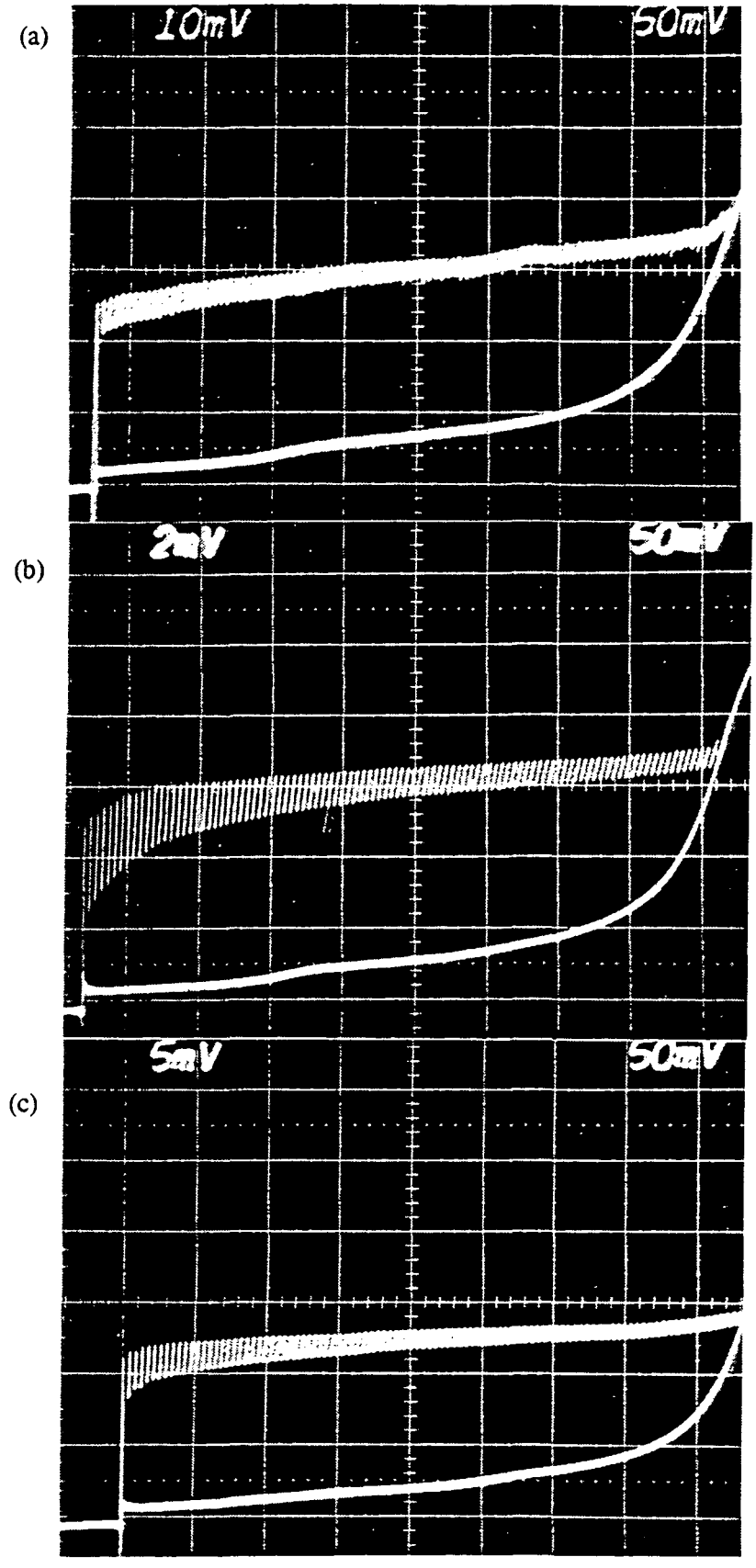

Figure 5.

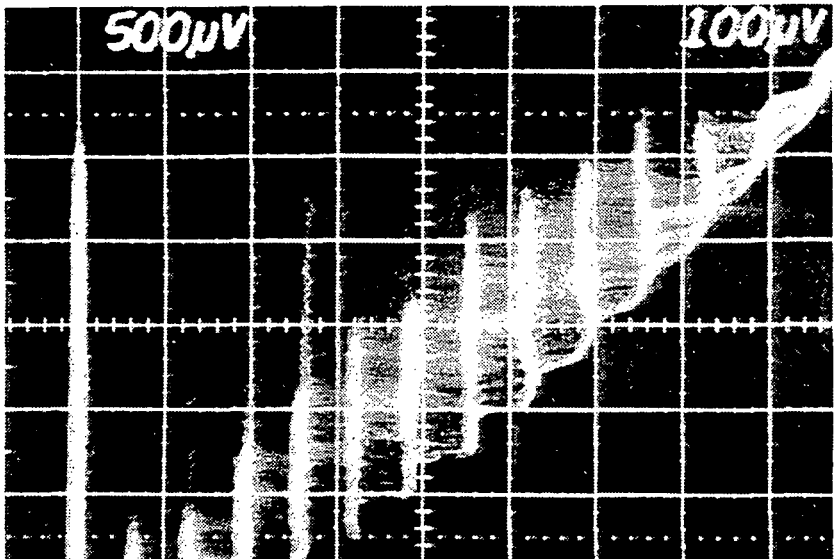

Figure 6.

(a)

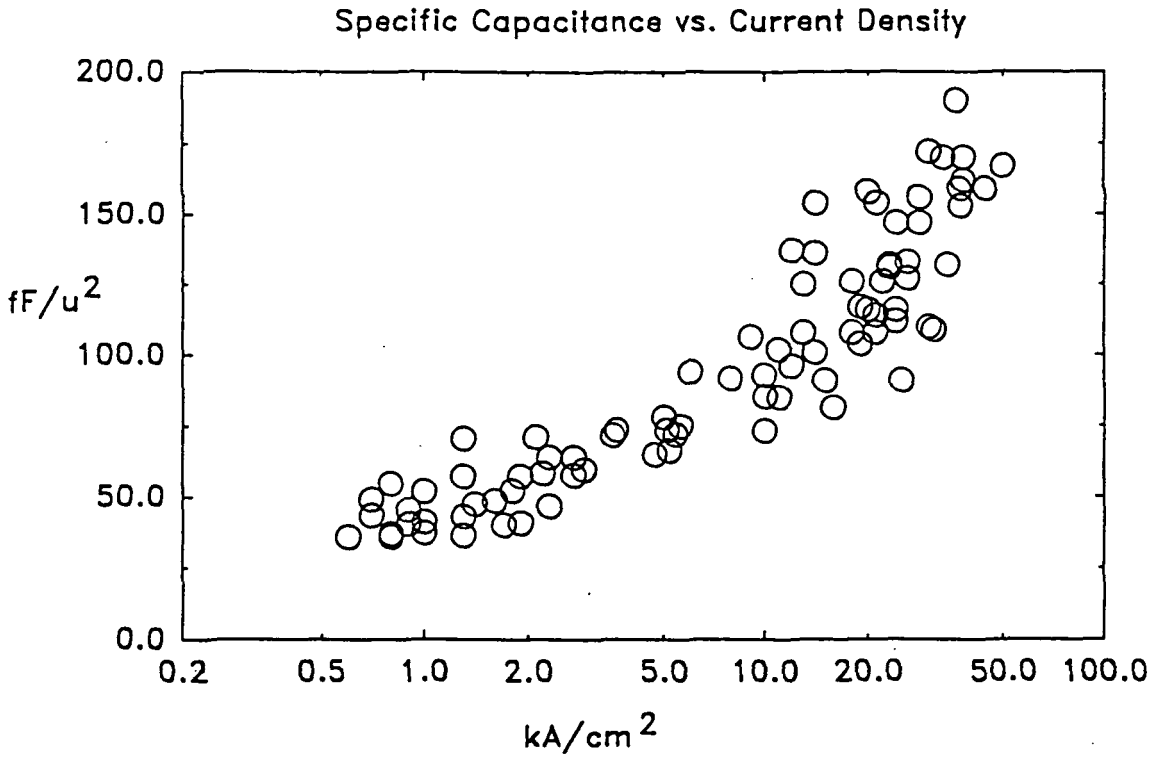
Specific Capacitance vs. Current Density
200.0
150.0
fF/u2
100.0
50.0
0.0
0.2
0.5
1.0
2.0
5.0
10.0
20.0
50.0
100.0
kA/cm 2

(b)

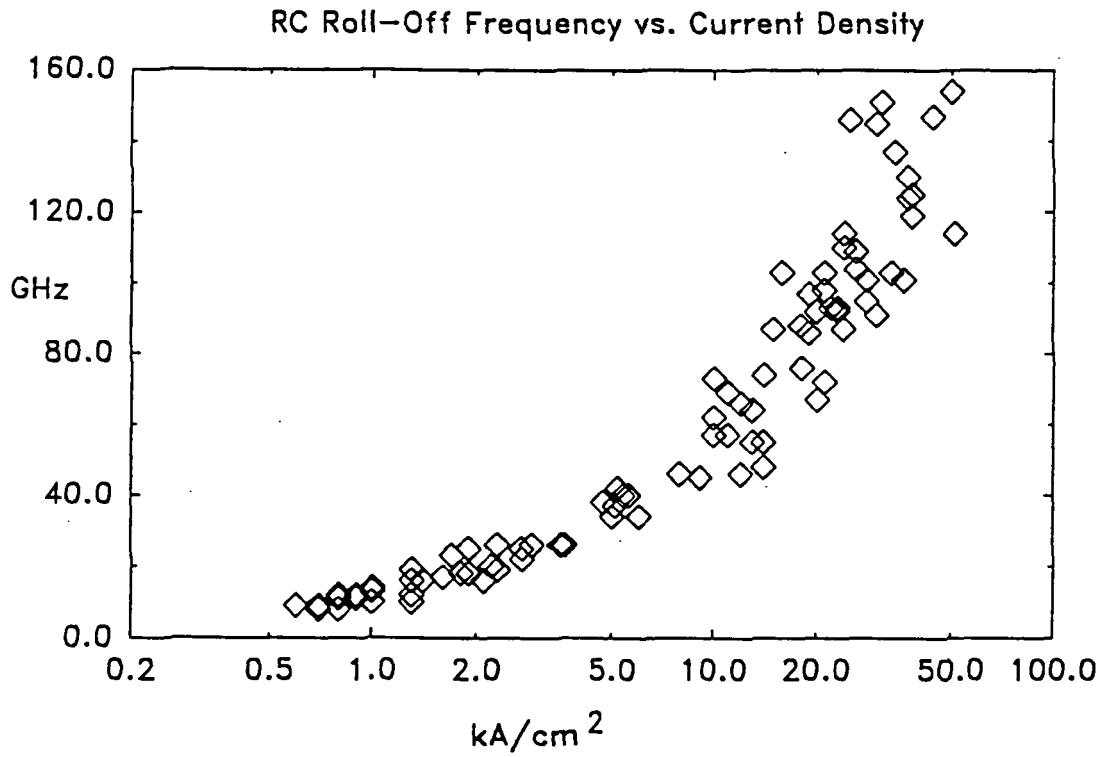
RC Roll-Off Frequency vs. Current Density
160.0
120.0
GHz
80.0
40.0
0.0
0.2
0.5
1.0
2.0
5.0
10.0
20.0
50.0
100.0
kA/cm 2

A Quasioptical Resonant-Tunneling-Diode Oscillator Operating Above 200 GHz

E. R. Brown*, C. D. Parker*, K. M. Molvar*, A. R. Calawa*, and M. J. Manfra*

We have fabricated and characterized a quasioptically stabilized resonant-tunneling-diode (RTD) oscillator having attractive performance characteristics for application as a radiometric local oscillator. The fundamental frequency of the oscillator is tunable from about 200 to 215 GHz, the instantaneous linewidth is between 10 and 20 kHz, and the output power across the tuning band is about 50 μW. The narrow linewidth and fine tuning of the frequency are made possible by a scanning semiconfocal open cavity which acts as the high-Q resonator for the oscillator. The cavity is compact, portable, and insensitive to vibration and temperature variation. The total dc power consumption (RTD plus bias supply) is only 10 mW.

The present oscillator provides the highest power obtained to date from an RTD above 200 GHz. We attribute this partly to the use of the quasioptical resonator, but primarily to the quality of the RTD. It is fabricated from the $In_{0.53}Ga_{0.47}As/AlAs$ materials system, which historically has yielded the best overall resonant-tunneling characteristics of any material system. The RTD active area is 4 μm^2, and the room-temperature peak current density and peak-to-valley current ratio are 2.5×10^5 A cm^{-2} and 9, respectively. The RTD is mounted in a WR-3 standard-height rectangular waveguide and is contacted across the waveguide by a fine wire that protrudes through a via hole in a Si_3N_4 "honeycomb" overlayer. We estimate that the theoretical maximum frequency of oscillation of this RTD is approximately 1.1 THz, and that scaled-down versions of the same quasioptical oscillator design should operate in a fundamental mode up to frequencies of at least 500 GHz.

This work was sponsored by NASA-OAST through the Jet Propulsion Laboratory and by the U.S. Army Research Office.

---

*E. R. Brown, C. D. Parker, K. M. Molvar, A. R. Calawa, and M. J. Manfra are with Lincoln Laboratory, Massachusetts Institute of Technology.

TRANSIT-TIME DEVICES AS LOCAL OSCILLATORS FOR FREQUENCIES ABOVE 100 GHz *)

H. Eisele, C. Kidner, G. I. Haddad

Center for Space Terahertz Technology
Department of Electrical Engineering & Computer Science
2231 EECS Building
The University of Michigan
Ann Arbor, Michigan 48109-2122

Abstract:

Very promising preliminary experimental results have been obtained from GaAs IMPATT diodes at F-band frequencies (75 mW, 3.5 % @ 111.1 GHz and 20 mW, 1.4 % @ 120.6 GHz) and from GaAs TUNNETT diodes at W-band frequencies (26 mW, 1.6 % @ 87.2 GHz and 32 mW, 2.6 % @ 93.5 GHz). These results indicate that IMPATT, MITATT and TUNNETT diodes have the highest potential of delivering significant amounts of power at Terahertz frequencies. As shown recently, the noise performance of GaAs W-band IMPATT diodes can compete with that of Gunn devices. Since TUNNETT diodes take advantage of the quieter tunnel injection, they are expected to be especially suited for low-noise local oscillators. This paper will focus on the two different design principles for IMPATT and TUNNETT diodes, the material parameters involved in the design and some aspects of the present device technology. Single-drift flat-profile GaAs D-band IMPATT diodes had oscillations up to 129 GHz with 9 mW, 0.9 % @ 128.4 GHz. Single-drift GaAs TUNNETT diodes had oscillations up to 112.5 GHz with 16 mW and output power levels up to 33 mW and efficiencies up to 3.4 % around 102 GHz. These results are the best reported so far from GaAs IMPATT and TUNNETT diodes.

---

*) This work was supported by NASA under contract No. NAGW 1334.

1. Introduction

GaAs IMPact ionization Avalanche Transit-Time (IMPATT) diodes have long been thought to be limited to frequencies below 60 GHz. Little has been reported regarding the operation of GaAs IMPATT or MITATT diodes above 100 GHz [1,2]. Experimental results of W-band IMPATT diodes (up to 320 mW, 6.0 % @ 95 GHz) [3] with excellent noise performance [4] clearly indicate that IMPATT diodes are one prime candidate to fulfill the growing need for local oscillators above 100 GHz. TUNNEl injection Transit-Time (TUNNETT) diodes were already proposed in 1958 and are considered another prime candidate for low-noise, medium power sources at millimeter and submillimeter frequencies. Although pulsed oscillations were demonstrated up to 338 GHz in 1979 [5], CW power has only recently been obtained from devices with low impact ionization carrier multiplication [6]. This significant progress is mainly due to the fact that refined epitaxial growth techniques have become widely available. Despite the impressive progress in oscillators with three-terminal devices at mm-wave frequencies [7] two-terminal devices hold the highest potential in delivering significant amounts of power with clean spectra above 100 GHz.

2. Design of single-drift flat-profile IMPATT diodes

In GaAs, the first derivative of the ionization rates of electrons and holes with respect to the electric field saturates around 500 $kVcm^{-1}$ [8-10]. Together with dead space effects in the avalanche zone [11] this saturation phenomenon favors a flat-profile structure for frequencies above V-band (50 - 75 GHz). The performance of a single-drift structure is the least sensitive to doping profile variations. The design of this structure is based on the assumption that the center of the avalanche region occurs where the electron concentration equals the hole concentration for the applied bias voltage [12] and that such a defined avalanche region is electrically equivalent to an avalanche region of the same width l_a but constant electric field and ionization rates [10]. The drift region - where ionization is to be neglected - is defined in its length l_d by the maximum in the well known transit-time function [13]

$$l_d = \frac{3\, v_s}{8 f_o} \quad , \tag{1}$$

where v_s is the average saturated drift velocity (4.5×10^6 cms^{-1} in GaAs for T_j = 500 K) [9,10] and f_o the operating frequency. Several structures for operating frequencies between 130 GHz and 160 GHz have been designed and the nominal doping profile of such a $p^{++}nn^{+}$ structure is given in Figure 1. A bias current density J_{DC} of 60 $kAcm^{-2}$ extrapolated from the experimental results in W-band [3] was taken into account.

3. Design of single-drift TUNNETT diodes

The design of the TUNNETT diode structure is based on a first order large signal theory [14] and experimental studies of highly doped MBE grown $p^{++}n^{+}$ structures. The carrier generation rate due to tunneling does not depend on the current density, but does strongly depend on the electric field. Therefore, a sharp pulse of electrons is injected at the $p^{++}n^{+}$ junction when the RF field reaches its maximum.

Under these assumptions for the $p^{++}n^{+}nn^{+}$ structure the first order large signal theory predicts a maximum in RF output power and DC to RF conversion efficiency [13,14] for

$$l_i + l_d = \frac{5\, v_s}{7 f_o} \quad , \tag{2}$$

where l_i is the length of the n^{+} region in the $p^{++}n^{+}$ junction, l_d is the length of the n region, v_s is the average saturated drift velocity (4.6×10^6 cms^{-1} for T_j = 500 K) [9,15] and f_o the operating frequency. Since the design is based on considerably lower electric fields in the drift region compared to the ones in the IMPATT diodes above, a slightly higher value for v_s is appropriate. Further details of the design procedure are given in References 16 and 17. The carrier concentration due to a current density J_{DC} of 25 kAcm^{-2} is taken into account in the doping profile. The nominal doping profile of this $p^{++}n^{+}nn^{+}$ TUNNETT diode structure is depicted in Figure 2.

4. Device technology

The operating current density of 60 kAcm^{-2} in a single-drift flat-profile GaAs D-band IMPATT diode requires a diamond heat sink to keep the operating junction temperature below 250 °C. Therefore all IMPATT diodes were fabricated using a well established selective etching technology for substrateless diodes on diamond heat sinks which gives up to 600 diodes per cm^2 wafer area with high uniformity [18]. This technology implements an $Al_{.55}Ga_{.45}As$ etch-stop layer between the substrate and the epitaxial layers for the device. In order to get the steep transitions for doping profiles in the submicron range, all wafers were grown by MBE. Figure 3 shows the flow chart of this technology process. The epitaxial side of the wafer is metallized with Ti/Pt/Au for a p^{+} ohmic contact, then selectively plated with gold to form a grating for mechanical support and glued on a ceramic carrier. In the next step the substrate is removed by selective wet chemical etch and subsequently the etch-stop layer in another selective wet chemical etch. A Ni/Ge/Au contact metallization is evaporated on top of the n^{+} layer and plated with gold to ease bonding. Contact patterns and diode mesas are defined by standard positive photoresist technology and wet chemical etching. The diodes outside the supporting grating are tested and selected for good DC characteristics

and thermocompression bonded on diamond heat sinks which are embedded in plated copper blocks. Electrical contact to the diode is provided by four metallized quartz stand-offs thermocompression bonded onto the heat sink and tapered gold ribbons bonded on the diode and the stand-offs.

The TUNNETT diodes were designed to operate at a maximum current density of 25 $kAcm^{-2}$ and a DC bias voltage comparable to the one of the IMPATT diodes. This allows fabrication of TUNNETT diodes with an integral heat sink. The wet chemical etching in the previously described technology limits the choice of materials and the minimum diameter for the n^+ ohmic contact. Therefore a different process has been developed, which likewise implements an $Al_{.55}Ga_{.45}As$ etch-stop layer between the substrate and the epitaxial layers for the device. Its flow chart is given in Figure 4 and further details are discussed in Reference 19.

Before the epitaxial side of the MBE-grown wafer is metallized with Ti/Pt/Au for a p^+ ohmic contact, grooves are selectively etched down to the AlGaAs etch-stop layer to divide the device layers into square shaped islands. This reduces the stress in the device layers during annealing. Furthermore, it shapes the Ti/Pt/Au layers and the plated gold layer of the integral heat sink thus providing additional mechanical strength for the subsequent processing steps after the substrate has been removed. The contacts are defined by standard lift-off technology and an additional metallization and photolithography step gives holes on top of the n^+ ohmic contact through which up to 3 µm of gold is electroplated. The mesas are formed by a wet chemical etch. After annealing the sample is diced into individual diodes and diodes with the desired size and DC characteristic are soldered or glued to a gold plated copper block. Electrical contact to the diode is provided by four metallized quartz stand-offs thermocompression bonded onto the plated block and tapered gold ribbons bonded on the diode and the stand-offs.

5. Experimental results

RF testing is performed in full height waveguide cavities with a resonant cap on top of the diode. IMPATT diodes are tested both in W-band (WR-10 waveguide) and D-band (WR-6 waveguide). TUNNETT diodes are only tested in W-band.

Figure 5 shows RF output power, DC to RF conversion efficiency and oscillation frequency of the best IMPATT diode in a W-band cavity as a function of the bias current. At each bias point the short plunger of the cavity and at some bias points also the E-H-tuner were adjusted for maximum output power. As can be seen from Figure 5, the efficiency reaches its maximum of 3.8 % at an output power of 72 mW.

An output power of 85 mW at 102.0 GHz with an efficiency of 2.5 % in WR-10 waveguide cavity and 20 mW at 120.6 GHz with an efficiency of 1.4 % in a WR-10 waveguide cavity were obtained from other

IMPATT diodes. The highest oscillation frequency of 128.4 GHz could be observed in a WR-6 waveguide cavity. At this frequency the output power was 9 mW and the efficiency 0.9 %. Table 1 summarizes the experimental results obtained from these diodes. The operating junction temperature was limited up to T_j = 550 K in order to ensure reliable long-term operation.

Frequency [GHz]	102.0	111.1	111.5	120.6	128.4
Output power [mW]	85	75	48	20	9
Efficiency [%]	2.5	3.5	2.3	1.4	0.9
Cavity (W/D)	W	W	W	D	D

Table 1: Experimental results of IMPATT diodes in W-band and D-band cavities.

To verify the mode of operation the DC I-V characteristics are measured at room temperature (T = 300 K) and an elevated temperature (T = 370 K). As shown in Figure 6a for low bias currents and Figure 6b for high bias currents, the breakdown of the D-band IMPATT diode is sharp and the bias voltage always increases with increasing temperature due to the decreasing ionization rates. The breakdown voltage at T = 300 K agrees well with breakdown voltages that were calculated from ionization rates evaluated in Reference 9, and which are plotted in Figure 7 together with the peak electric field strength. The sharp breakdown also proves that tunneling is significant only for electric field strengths above 1.0 $MVcm^{-1}$.

Figure 8 shows RF output power, DC to RF conversion efficiency and oscillation frequency of two TUNNETT diodes in W-band cavities as a function of the bias current. At each bias point the short plunger and the E-H-tuner were adjusted for maximum output power. As can be seen from Figure 8a and 8b, neither output power nor efficiency saturate up to the highest applied bias currents. The oscillation frequency varies only slightly and is mainly determined by the resonant cap. An output power of 33 mW at 93.5 GHz with an efficiency of 2.65 % and an output power 31.5 mW at 107.36 GHz with an efficiency of 3.35 % were obtained. The highest oscillation frequency of another diode was 112.5 GHz with an output power of 16 mW and the corresponding efficiency of 2.55 %. Table 2 summarizes the experimental results obtained from the so far best diodes. The operating junction temperature was well below T_j = 550 K in each case.

Frequency [GHz]	87.22	93.50	102.66	107.30	112.50
Output power [mW]	27	33	33	31.5	16
Efficiency [%]	1.75	2.65	3.35	3.35	2.55

Table 2: Experimental results of TUNNETT diodes in W-band cavities

A plot of the output power and efficiency of the W-band diodes that have been mounted and tested to date is given in Figure 9. There appears to be a broad peak in the RF output power and DC to RF conversion efficiency around the nominal design frequency of 100 GHz. This peak confirms that the first order design rules accurately predict the operating frequency of the TUNNETT diodes. It also indicates that the high field, high temperature electron average drift velocity in GaAs TUNNETT diodes is close to 4.6×10^6 cms^{-1}. The power levels and efficiencies above 100 GHz are comparable to the ones obtained from Gunn devices in this frequency range [20-22].

To verify the mode of operation the DC I-V characteristics are measured at room temperature (T = 300 K) and elevated temperatures (T = 470 K). The I-V curves of a 25 μm diameter W-band TUNNETT diode shown in Figure 10 clearly demonstrate that the injection mechanism is predominantly tunneling. For comparison the I-V curves of a 55 μm V-band MIxed Tunneling and Avalanche Transit-Time (MITATT) diode are also given in Figure 10. At room temperature the MITATT diode has a sharp increase in current at about 18 V due to the onset of impact ionization [16]. The TUNNETT diode I-V curve at room temperature exhibits no sign of this behavior. Tunneling as the dominant breakdown mechanism also explains the temperature dependence of the TUNNETT diode I-V curves. Increasing the junction temperature of the device enhances tunneling and suppresses impact ionization as can be seen in the temperature behavior of the MITATT diode. For low bias voltages the current increases, thus indicating tunneling. The voltage for the sharp increase in current has a positive temperature coefficient, characteristic of impact ionization as previously shown in Figure 6. For the range of applied bias voltages the current in the TUNNETT diode always increases as a function of temperature implying that impact ionization is not significant.

Figure 11 shows the measured spectra of a free running W-band IMPATT diode oscillator with 42.8 mW at 89.2 GHz (Figure 11a) and a free running W-band TUNNETT diode oscillator with 9.2 mW at 92.2 GHz (Figure 11b). and proves that the oscillations have clean spectra. The spectrum of another free running TUNNETT diode oscillator in Figure 12 was taken using the same settings (vertical scale, scan width and resolution bandwidth) of the spectrum analyzer as in Reference 23 for an free running InP Gunn device oscillator and it compares favorably to the spectrum of this Gunn device oscillator.

6. Device simulation

In order to determine the capabilities of GaAs IMPATT diodes at D-band frequencies and in order to find an explanation for the significant decrease in output power above 110 GHz, the device structures were simulated using two IMPATT diode simulation programs, a drift-diffusion (DD) model [24] and an energy-momentum (EM) model [25]. Table 3 shows calculated output power and efficiency at f = 95 GHz as preliminary results for both programs. The data for the device area A_D and current density J_{DC} are

taken from Reference 3. The energy-momentum program shows slightly higher breakdown voltages and higher efficiency and output power. If a series resistance $R_s = 0.18\ \Omega$ is taken into account for this diode, the calculated output power and efficiency are much closer to the measured values. This series resistance is comparable to the value obtained from small signal impedance measurements in forward direction at 32 MHz [9,10].

W-band IMPATT diode

Frequency: 95 GHz Area A_D: 8×10^{-6} cm^2 Current density: 50 kAcm^{-2}

Model	Voltage	Power ($R_s = 0\ \Omega$)	Efficiency	Power ($R_s = 0.18\ \Omega$)	Efficiency
	[V]	[mW]	[%]	[mW]	[%]
DD	12.2	550	11.3	320	6.5
EM	12.5	700	14.0	510	10.2

D-band IMPATT diode

Frequency: 140 GHz Area A_D: 5×10^{-6} cm^2 Current density: 60 kAcm^{-2}

Model	Voltage	Power ($R_s = 0\ \Omega$)	Efficiency	Power ($R_s = 0.20\ \Omega$)	Efficiency	Power ($R_s = 0.288\ \Omega$)	Efficiency
	[V]	[mW]	[%]	[mW]	[%]	[mW]	[%]
DD	10.4	120	3.8	35	1.1	12	0.4
EM	10.9	215	6.5	80	2.4	18	0.5

Table 3: Calculated results for GaAs single-drift flat-profile IMPATT diodes.

The results for the D-band structure in Table 3 were calculated for no series resistance and two different values of the series resistance. $R_s = 0.288\ \Omega$ assumes that the series resistance is mainly due to the contact resistances of the p^+ and n^+ layers and scales with reciprocal area, i.e. it is equivalent to $R_s = 0.18\ \Omega$ of the W-band diode. For this series resistance the output power is reduced to about one tenth of the output

power for the case of no series resistance taken into account. Since the calculated output power agrees with the experimental value of 9 mW at 128.4 GHz, the series resistance is believed to be the main reason for the significant rolloff in performance above 110 GHz. As can be seen also from Table 3, the output power reduction is only about one third and therefore much less pronounced, if a slightly smaller $R_s \times A_D$ (1×10^{-6} Ωcm^2) is assumed. This demands better technology for contacts on both p^+- and n^+-type GaAs.

Neither the drift-diffusion model nor the energy-momentum model consider any losses in the cavity. These losses are due to the large transformation ratio (up to 500) from the low impedance level between the contacts of the diode and the high impedance level of the waveguide.

The simplified large-signal model for TUNNETT diodes [14] which was employed in the design was also used to determine how strongly the series resistance influences output power and efficiency of these devices. The above mentioned drift velocity v_s and the actual device dimensions (mesa height and diameter, heat sink thickness, etc.) were used for the simulation. In Table 4 the specific contact resistance was assumed to be $\rho_c = 1 \times 10^{-7}$ Ωcm^2 for the p^+ ohmic as well as for the n^+ ohmic contact. In this case the predicted RF output power into a load of R_l = 1 Ω is 251 mW for experimentally investigated diameters around 25 μm.

Freq (GHz)	Drift Length (μm)	Drift Field (kV/cm)	V_{DC} (Volts)	V_{RF} (Volts)	V_{DC}/V_{RF}	J_{DC} kA/cm²
100.0	0.345	309.8	12.29	10.89	0.886	32.84

DIAM (μm)	AREA (μm²)	R_s (Ohm)	R_d (Ohm)	R_l (Ohm)	V_{RF} (Volt)	I_{DC} (mA)	P_{DC} (W)	P_{RF} (Gen) (mW)	P_{RF} (Load) (mW)
15	177	0.33	2.36	2.02	10.89	58	0.71	134	115
20	314	0.21	1.33	1.12	10.89	103	1.27	238	201
25	491	0.15	1.15	1.00	8.40	161	1.98	287	251
30	707	0.11	1.11	1.00	6.35	232	2.85	313	281

DIAM (μm)	P_{DC} (W)	P_{RF} (mW)	R_{th} (Cu) (°C/W)	R_{th} (Di) (°C/W)	ΔT (Cu) (°C)	ΔT (Di) (°C)
15	0.71	115	213	140	127	84
20	1.26	201	140	86	149	91
25	1.98	251	103	59	178	102
30	2.85	281	80	44	207	113

Table 4: Performance of TUNNETT diodes at 100 GHz for $\rho_c = 1 \times 10^{-7}$ Ωcm^2 and $V_{RF}/V_{DC} \leq 0.886$.

As described above for the IMPATT diodes, present GaAs technology, however, gives a specific contact resistance closer to $\rho_c = 7.5 \times 10^{-7}$ Ωcm^2. As a result, the RF output power into 1 Ω decreases to 171 mW. For the predicted results in Table 4 and 5 the maximum RF voltage was limited to 88.6 % of the applied DC bias voltage. Since IMPATT diodes at millimeter wave frequencies operate at an RF voltage around or less than 50 % of the DC bias voltage, this case was also investigated for the TUNNETT diodes. As can be seen from Table 6 the RF output power drops to 158 mW for experimentally investigated diameters around 25 µm.

Freq (GHz)	Drift Length (µm)	Drift Field (kV/cm)	V_{DC} (Volts)	V_{RF} (Volts)	V_{DC}/V_{RF}	J_{DC} kA/cm²
100.0	0.345	309.8	12.29	10.89	0.886	32.84

DIAM (µm)	AREA (µm²)	R_s (Ohm)	R_d (Ohm)	R_l (Ohm)	V_{RF} (Volt)	I_{DC} (mA)	P_{DC} (W)	P_{RF} (Gen) (mW)	P_{RF} (Load) (mW)
15	177	1.07	2.36	1.29	10.89	58	0.71	134	73
20	314	0.62	1.62	1.00	9.15	103	1.27	200	124
25	491	0.41	1.41	1.00	7.05	161	1.98	241	171
30	707	0.30	1.30	1.00	5.61	232	2.85	276	213

DIAM (µm)	P_{DC} (W)	P_{RF} (mW)	R_{th} (Cu) (°C/W)	R_{th} (Di) (°C/W)	ΔT (Cu) (°C)	ΔT (Di) (°C)
15	0.71	73	213	140	136	90
20	1.27	124	140	86	160	98
25	1.98	171	103	59	186	107
30	2.85	213	80	44	212	116

Table 5: Performance of TUNNETT diodes at 100 GHz for $\rho_c = 7.5 \times 10^{-7}$ Ωcm^2 and $V_{RF}/V_{DC} \leq 0.886$.

The calculated values of the thermal resistance R_{th} and temperature rise ΔT for a copper (Cu) or diamond (Di) heat sink are also included in Tables 4, 5 and 6. It should be noted that experimental values for the thermal resistance always are higher than calculated. Therefore, a diode with a diameter of 30 µm on a copper heat sink will be operated at a lower DC input power P_{DC} and therefore reduced RF output power P_{RF} to achieve an operating junction temperature below 250 °C.

Similar to the IMPATT diode simulation, the simplified large-signal TUNNETT diode simulation does not account for any losses due to the large transformation ratio from the low impedance level between the contacts of the diode and the high impedance level of the waveguide. Since the structure of the resonant cap full height waveguide cavity has been optimized for IMPATT diodes its impedance transformation losses are expected to be higher for the TUNNETT diodes.

Freq (GHz)	Drift Length (μm)	Drift Field (kV/cm)	V_{DC} (Volts)	V_{RF} (Volts)	V_{DC}/V_{RF}	J_{DC} kA/cm^2
100.0	0.345	309.8	12.29	10.89	0.500	32.84

DIAM (μm)	AREA (μm^2)	R_s (Ohm)	R_d (Ohm)	R_l (Ohm)	V_{RF} (Volt)	I_{DC} (mA)	P_{DC} (W)	P_{RF} (Gen) (mW)	P_{RF} (Load) (mW)
15	177	1.07	4.63	3.56	6.14	58	0.71	76	58
20	314	0.62	2.61	1.99	6.14	103	1.27	134	103
25	491	0.41	1.67	1.26	6.14	161	1.98	210	158
30	707	0.30	1.30	1.00	5.61	232	2.85	276	213

DIAM (μm)	P_{DC} (W)	P_{RF} (mW)	R_{th} (Cu) (°C/W)	R_{th} (Di) (°C/W)	ΔT (Cu) (°C)	ΔT (Di) (°C)
15	0.71	58	213	140	136	90
20	1.27	103	140	86	162	98
25	1.98	158	103	59	186	107
30	2.85	213	80	44	212	116

Table 6: Performance of TUNNETT diodes at 100 GHz for $\rho_c = 7.5 \times 10^{-7}$ Ωcm^2 and $V_{RF}/V_{DC} \leq 0.50$.

7. Conclusions

The experimental results clearly show that GaAs IMPATT diodes are powerful devices not only for frequencies below 60 GHz, but also above 100 GHz. The predicted results of two different simulation programs agree with the experiment. These simulations also reveal that the contact technology is very crucial for high output power and efficiency and must be improved considerably for GaAs D-band IMPATT diodes. The results from D-band GaAs IMPATT diodes and from W-band GaAs TUNNETT diodes are the best reported to date. Both IMPATT and TUNNETT diodes exhibit clean spectra for local oscillator applications. The TUNNETT diodes demonstrate useful power levels and efficiencies comparable to Gunn devices. Since RF output power and DC to RF conversion efficiency do not saturate up to the highest applied DC bias currents, still higher output power levels and efficiencies can be expected from TUNNETT diodes on diamond heat sinks in optimized cavities.

References

[1] Elta, M. E., Fettermann, H. R., Macropoulos, W. V., and Lambert, J.: "150 GHz GaAs MITATT source", *IEEE Electron Device Letters*, EDL-1, 1980, pp. 115-116.

[2] Chang, K., Kung, J. K., Asher, P. G., Hayashibara, G. M., and Ying, R. S.: "GaAs Read-type IMPATT diode for 130 GHz CW operation", *Electronics Letters*, 17, 1981, pp. 471-473.

[3] Eisele, H., and Grothe, H.: "GaAs W-band IMPATT diodes made by MBE", *Proc. MIOP '89*, Sindelfingen, FRG, Feb. 28th - March 3rd 1989, Session 3A.6.

[4] Eisele, H.: "GaAs W-band IMPATT diodes for very low-noise oscillators", *Electronics Letters*, **26**, 1990, pp. 109-110.

[5] Nishizawa, J., Motoya, K., and Okuno, Y.: "Submillimeter Wave Oscillation from GaAs TUNNETT Diode", *Proceedings of the 9th European Microwave Conference*, 1979, pp. 463-467.

[6] Pöbl, M., Freyer, J.: "Characterization of W-Band CW TUNNETT Diode", *Proceedings of the 21st European Microwave Conference*, Stuttgart, FRG, 1991, pp. 1496-1501.

[7] Kwon, Y., Pavlidis, D., Tutt, M., Ng, G. I., Lai, R., and Brock, T.: "W-Band Monolithic Oscillator Using InAlAs/InGaAs HEMT's", *Electronics Letters*, **26**(18), 1990, pp. 1425-1426.

[8] Rolland P. A., Friscourt M. R., Lippens D., Dalle C., and Nieruchalski, J. L.: "Millimeter Wave Solid-State Power Sources", *Proceedings of the International Workshop on Millimeter Waves*, Rome, Italy, April 2-4, 1986, pp. 125-177.

[9] Eisele, H.: "Electron properties in GaAs for the design of mm-wave IMPATTs", *International Journal of Infrared and Millimeter Waves*, **4**, 1991, pp. 345-354.

[10] Eisele, H.: "GaAs W-Band IMPATT diodes: The first step to higher frequencies", *Microwave Journal*, **34**, 1991, pp. 275-282.

[11] Okuto, Y., and Crowell, C. R., "Threshold energy effects on avalanche breakdown voltage in semiconductor junctions", *Solid-State Electronics*, **18**, 1975, pp. 161-168.

[12] Hulin, R.: "Großsignalmodell von Lawinenlaufzeitdioden", Ph.D. Thesis Techn. University Braunschweig, Braunschweig, 1973.

[13] Harth., W., Claassen, M.: "Aktive Mikrowellendioden", Springer-Verlag, Berlin, 1981.

[14] Haddad, G. I., East, J. R., and Kidner, C.: "Tunnel Transit-Time (TUNNETT) Devices for Terahertz Sources", *Microwave and Optical Technology Letters*, **4**, 1991, pp. 23-29.

[15] Allam, R., and Pribetich, J.: "Temperature Dependence of Electron Saturation Velocity in GaAs", *Electronics Letters*, **26**, 1990, pp. 688-689.

[16] Kidner, C., Eisele, H., and Haddad, G. I.: "Tunnel Injection Transit-Time Diodes for W-Band Power Generation", *Electronics Letters*, **28**, 1992, pp. 511-513.

[17] Kidner, C., Eisele, H., East, J., and Haddad, G. I.: "Design, Fabrication and Evaluation of Tunnel Transit-Time Diodes for V-Band and W-Band Power Generation", to be presented at the *1992 IEEE MTT-S International Microwave Symposium*, June 1 - June 5, 1992, Albuquerque, New Mexico.

[18] Eisele, H.: "Selective etching technology for 94 GHz GaAs IMPATT diodes on diamond heat sinks", *Solid-State Electronics*, **32**, 1989, pp. 253-257.

[19] Kamoua, R., Eisele, H., East, J. R., Haddad, G. I., Munns, G., Sherwin, M.: "Modeling, Design, Fabrication, and Testing of InP Gunn Devices in the D-Band (110 GHz - 170 GHz), these *Proceedings of the 3rd International Symposium on Space Terahertz Technology*, March 24-26, 1992, Ann Arbor, Michigan.

[20] Wandinger, L.: "mm-Wave InP Gunn Devices: Status and Trends", *Microwave Journal.*, **24**(3), 1981, pp. 71-78.

[21] Eddison, I. G., et al.: "Efficient fundamental frequency oscillation from mm-wave InP n^+-n-n^+ TEOs", *Electronics Letters*, **17**(20), 1981, pp. 758-760.

[22] Teng, S. J. J., Goldwasser, R. E.: "High Performance Second-Harmonic Operation W-Band GaAs Gunn Diodes", *IEEE Electron Device Letters*, **EDL-10**(9), 1989, pp. 412-414.

[23] Perrin, O., et al.: "380 GHz Receiver Front-End for the Balloon-Borne Radioastronomical Experiment", *Proceedings of the 2nd International Symposium on Space Terahertz Technology*, February 26-28, 1991, Pasadena, California, pp. 622-640.

[24] Bauhahn, P. E., and Haddad, G. I.: "IMPATT device simulation and properties", *IEEE Transactions on Electron Devices*, **ED-24**, 1977, pp. 634-642.

[25] Mains, R. K., Haddad, G. I., and Blakey, P. A.: "Simulation of GaAs IMPATT Diodes Including Energy and Velocity Transport Equations", *IEEE Transactions on Electron Devices*, **ED-30**, 1983, pp. 1327-1338.

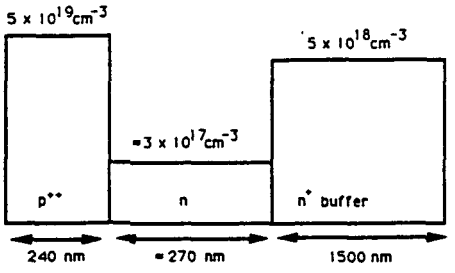

Fig. 1: Nominal device structure of a GaAs D-band single-drift flat-profile IMPATT diode.

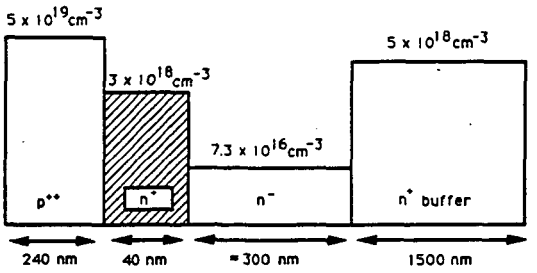

Fig. 2: Nominal device structure of a GaAs W-band single-drift TUNNETT diode.

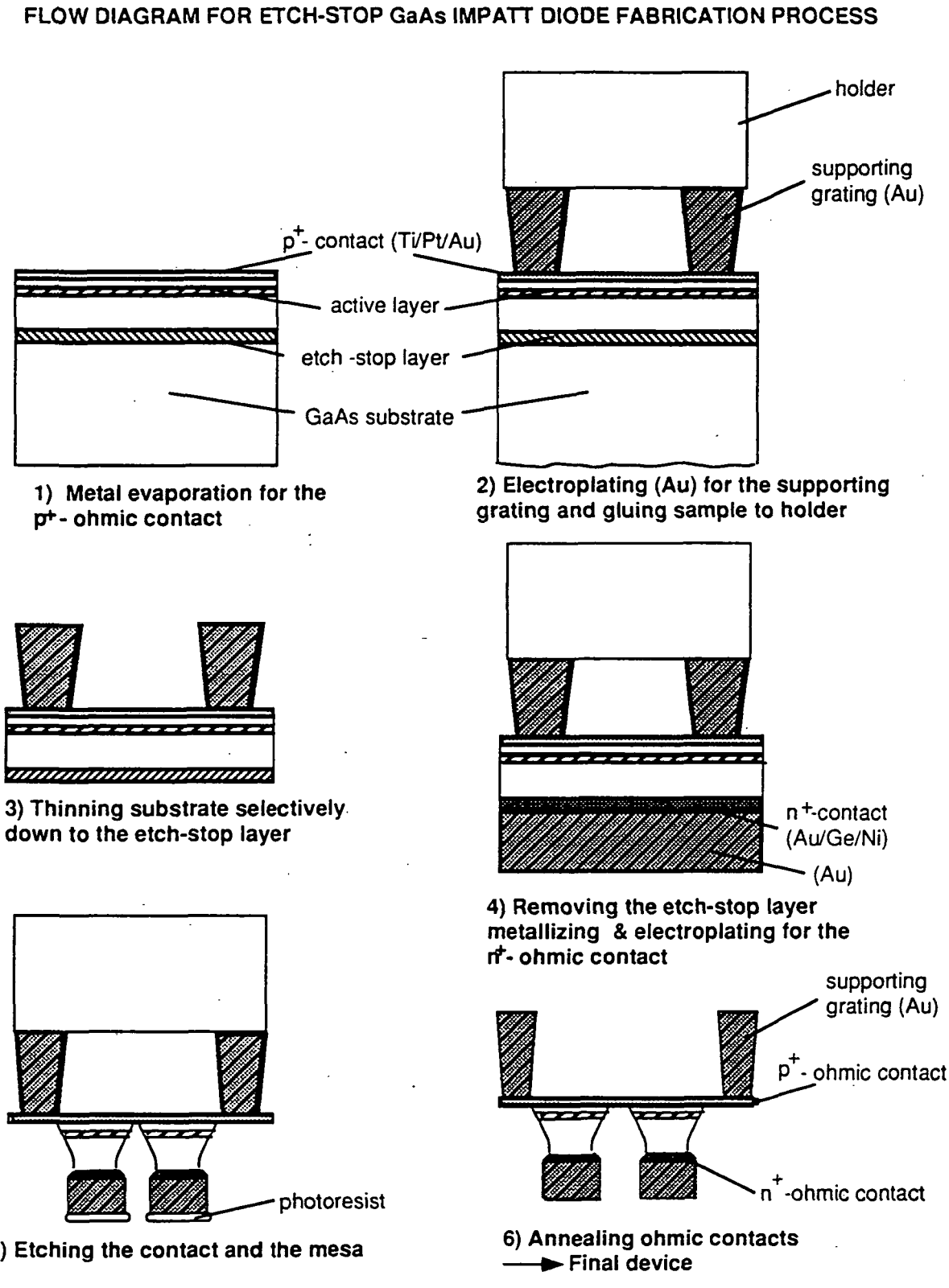

Fig. 3: Flow chart for IMPATT diodes device fabrication.

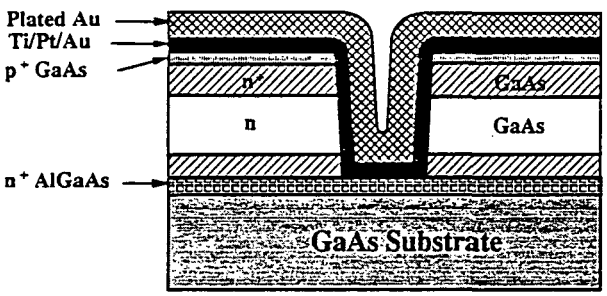

a) Island definition, p-ohmic evaporation, and gold plating (~ 15 μm)

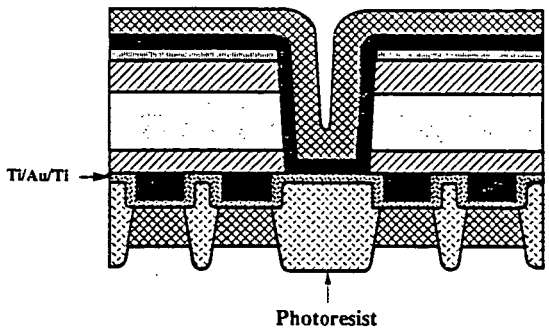

c) Gold plating of ohmic contacts

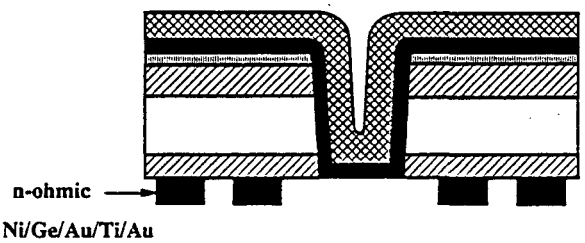

b) Substrate thinning, etch stop layer removal, and n-ohmic evaporation

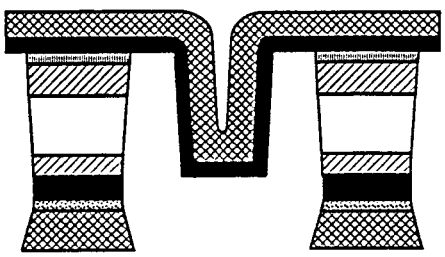

d) Final diodes after annealing and mesa etch

Fig. 4: Flow chart for TUNNETT diodes device fabrication.

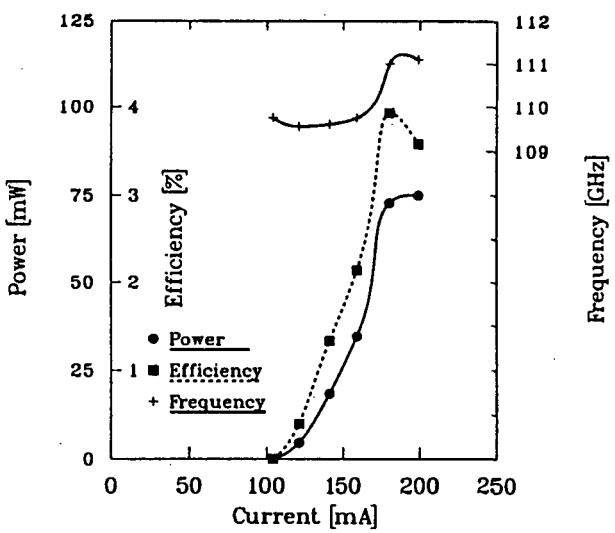

Fig. 5: Output power, efficiency and oscillation frequency as a function of bias current for a GaAs single-drift flat-profile IMPATT diode.

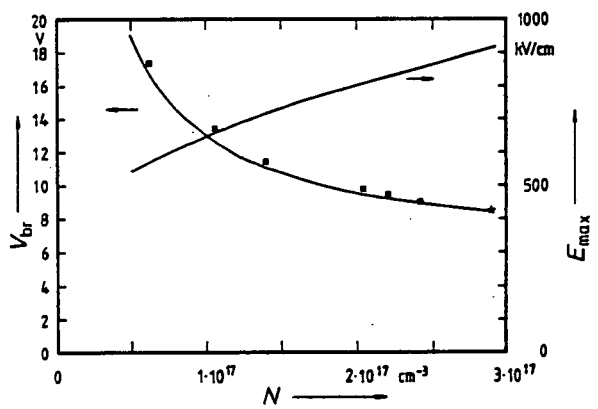

Fig. 7: Breakdown voltage V_{br} and peak electric field E_{max} of an abrupt p⁺n-junction.
■ ★ : measured
—— : calculated.

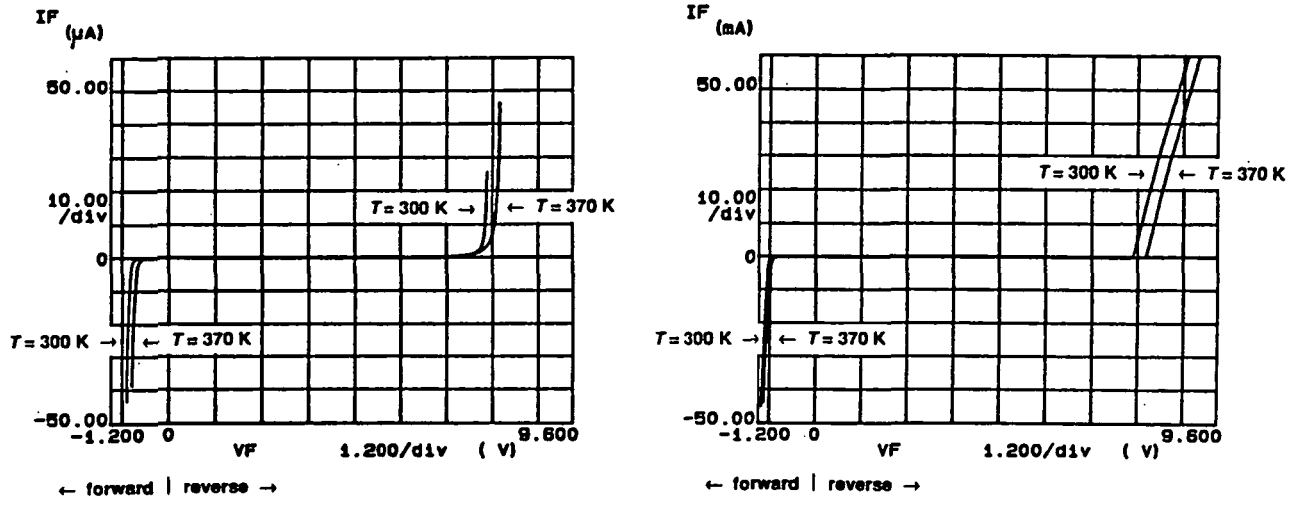

(a) (b)

Fig. 6: Current-voltage characteristics of a GaAs single-drift flat-profile IMPATT diode at room temperature (300 K) and an elevated temperature (370 K).

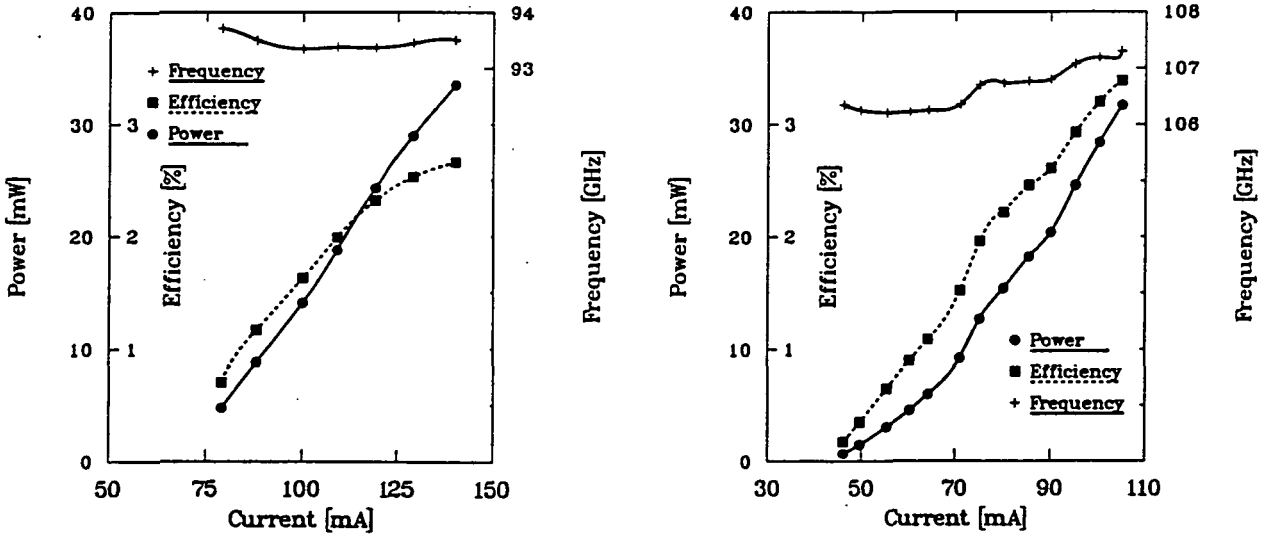

(a) (b)

Fig. 8: Output power, efficiency and oscillation frequency as a function of bias current for two W-band GaAs single-drift TUNNETT diodes.

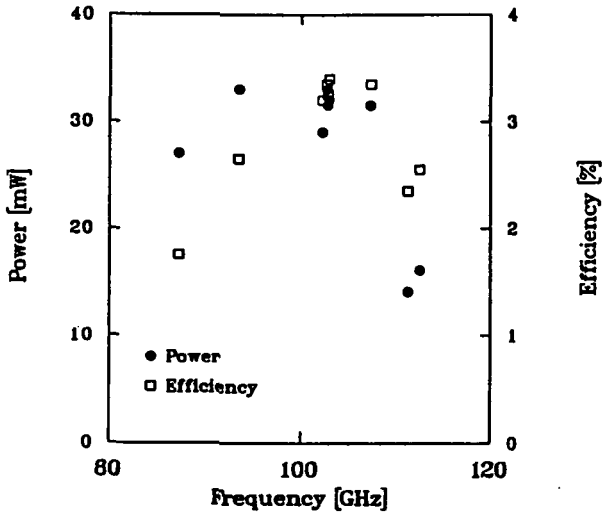

Fig. 9: Output power and efficiency of GaAs single-drift TUNNETT diodes in W-band.

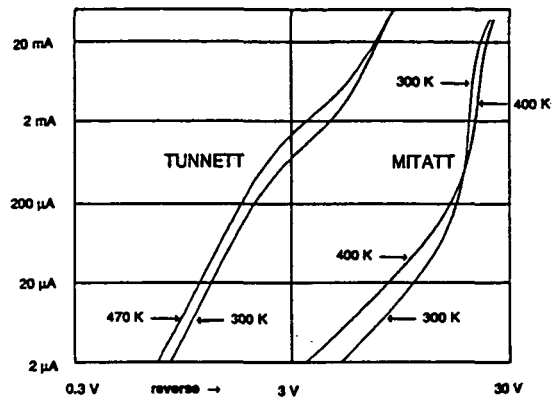

Fig. 10: Reverse bias current-voltage characteristics for pure tunnel injection (TUNNETT) and mixed tunnel injection and impact ionization (MITATT) at room temperature (300 K) and elevated temperatures (470 K and 400 K, respectively).

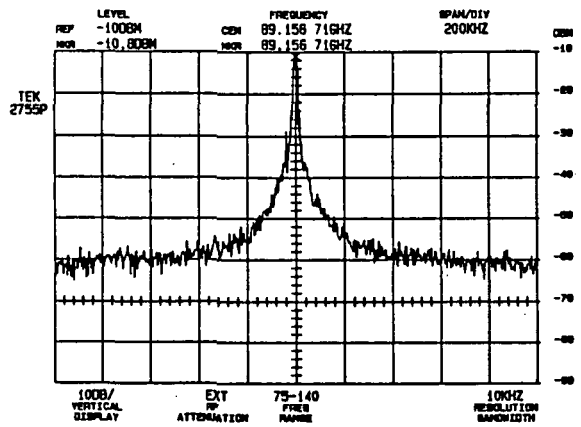

(a)

Fig. 11: Spectrum of a W-band IMPATT diode free running oscillator, power level 42.8 mW, center frequency 89.16 GHz, vertical scale 10 dB/div, horizontal scale 200 kHz/div, BW 10 kHz.

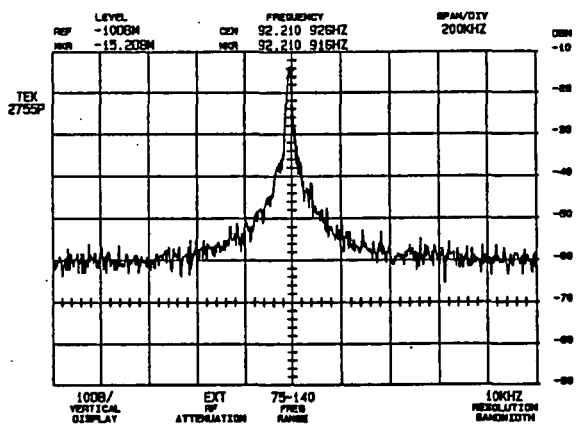

(b)

Fig. 11: Spectrum of a W-band TUNNETT diode free running oscillator, power level 9.2 mW, center frequency 92.21 GHz, vertical scale 10 dB/div, horizontal scale 200 kHz/div, BW 10 kHz.

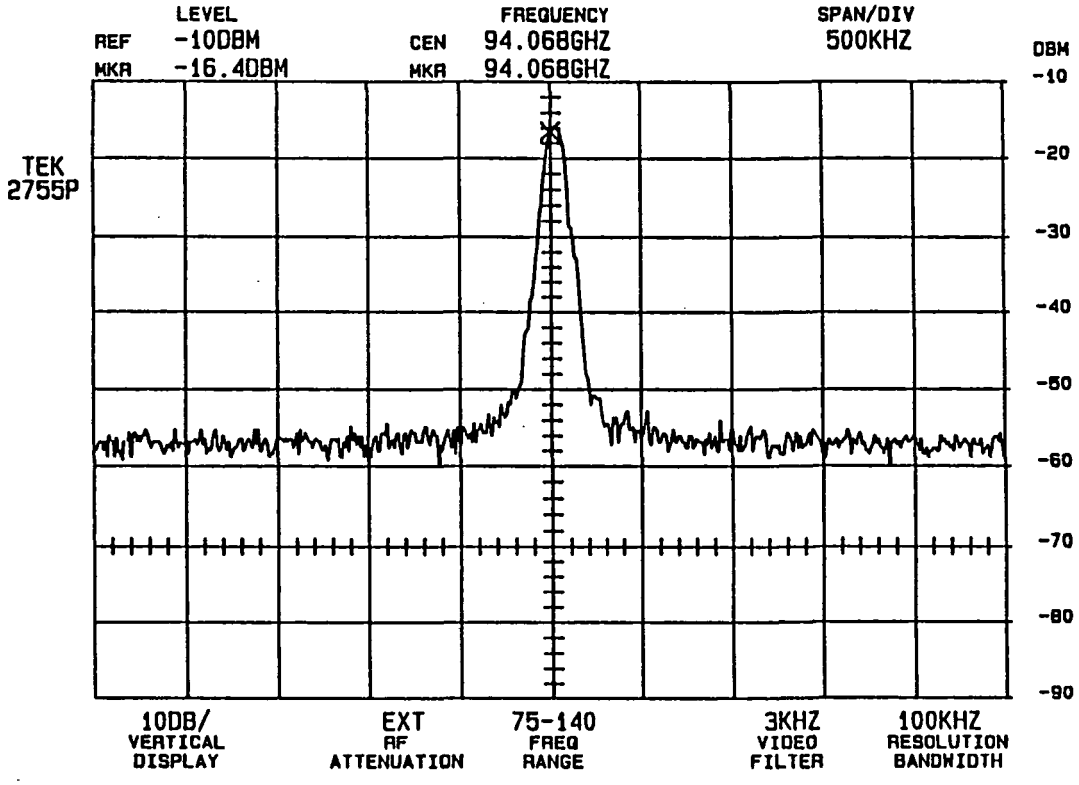

Fig. 12: Spectrum of a W-band TUNNETT diode free running oscillator, power level 8.8 mW, center frequency 94.07 GHz, vertical scale 10 dB/div, horizontal scale 500 kHz/div, BW 100 kHz.

Negative Differential Resistance (NDR) Frequency Conversion with Gain

R. J. Hwu, R. W. Alm, and S. C. Lee

Department of Electrical Engineering

University of Utah

Abstract--The dependence of the I-V characteristic of the negative differential resistance (NDR) devices on the power level and frequency of the rf input signal has been theoretically analyzed with a modified large- and small-signal nonlinear circuit analysis program [1,2]. The NDR devices we used in this work include both the tunnel diode (without the antisymmetry in the I-V characteristic) and resonant-tunneling devices (with the antisymmetry in the I-V characteristic). Absolute negative conductance can be found from a zero-biased resonant tunneling device when the applied pump power is within a small range. This study verifies the work of Sollner et al. [3]. Variable negative conductances at the fundamental and harmonic frequencies can also be obtained from both the unbiased and biased tunnel diodes. The magnitude of the negative conductances can be adjusted by varying the pump amplitude--a very useful circuit property. However, the voltage range over which the negative conductance occurs moves towards the more positive side of the voltage axis with increasing frequency. Furthermore, the range of the pumping amplitude to obtain negative conductance varies with the parasitics (resistance and capacitance) of the device. The theoretical observation of the dependence of the I-V characteristic of the NDR devices on the power and frequency of the applied pump signal is supported by the experimental results. In addition, novel functions of a NDR device such as self-oscillating frequency multiplier and mixer with gain have been experimentally demonstrated. The unbiased oscillator have also been successfully realized with a NDR

device with an antisymmetrical I-V characteristic. Finally, the applications of these device functions will be discussed.

INTRODUCTION

There have been increased interest in the study of resonant tunneling devices due to the fact that the characteristics of these devices can be engineered to have properties for very high-speed applications. In particular, their ability to exhibit negative differential resistance (NDR) regions lead to their potential use as gain elements in circuits and offers a new opportunity for circuit design. The presence of peaks and valleys in the I-V curve combined with the overall antisymmetry of the I-V curve about the origin [i.e., I(V) = -I(-V)], also offers the potential for efficient odd-harmonic generation with an unbiased resonant tunneling device [4,5]. The key lies in pumping the device so that the peak amplitude of the voltage across the device occurs above the resonant current peaks. This will produce more than three local maxima in the device current waveform over one cycle, corresponding to third or higher odd harmonic generation. The resonant tunneling frequency multiplier, therefore, has several distinct advantages over existing resistive multipliers, which are usually based on Schottky barrier diodes. The antisymmetrical response provides the potential for efficient odd harmonic frequency multiplication with an unbiased resonant tunneling device due to cancellation of the even harmonics, therefore greatly simplifying the circuit design. The maximum harmonic generation efficiency of a resonant tunneling device is significantly higher than the $1/n^2$ (n is the harmonic number) value that applies to standard resistive multipliers because of its negative resistance [4,5] (i.e., nonmonotonically increasing function I-V characteristic). The resonant tunneling device also has the ability to act as an efficient mixer due to the rapid variation of the dynamic conductance with voltage near the NDR region of the I-V curve. The resonant tunneling mixer has the potential to displace the Schottky diode in many microwave and millimeter-wave applications. The most intriguing aspect of the resonant tunneling

frequency multiplier and mixer is its intrinsic capability to achieve conversion gain (efficiency > 1).

LARGE- AND SMALL-SIGNAL NONLINEAR-CIRCUIT ANALYSIS

A large- and small-signal analysis program has been developed to analyze the behavior of dc and microwave negative conductance of a NDR device. The analysis technique was developed by T. Kerr [6] and the computer program was implemented for analyzing ideal Schottky barrier diodes by Siegel et. al. [1]. The analysis program has been modified to take into account the negative resistance of the NDR device [2]. The I-V characteristics measured from the NDR devices as can be seen in Fig. 1 have been used in the nonlinear-circuit analysis. Since the devices were mounted on a 50 Ω microstrip line for the measurements in this work, the embedding impedance of 50 Ω at every harmonic frequency has been used. A simple experiment has been carried out to verify that the embedding impedance at higher harmonic frequencies is equal to 50 Ω [7].

Tunnel Diode--Without Antisymmetry in the I-V Characteristic

The differential conductance of a tunnel diode biased at zero voltage and in the positive differential resistance (PDR) region (close to the current peak) under different rf pumping conditions has been studied in this work. No negative conductance has been observed at dc for a tunnel diode biased at zero voltage and in the PDR region. However, negative conductances at the fundamental and different harmonic frequencies have been observed from a tunnel diode biased at zero voltage and in the PDR region. The magnitude of the negative conductance varies with the pump amplitude (see Fig. 2). The pump amplitude region required to achieve the negative conductance moves toward the more positive side of the power axis with increasing pumping frequency (also see Fig. 2). This can be easily explained using the equivalent circuit model of a tunnel diode (see Fig. 1 (c)). Since the impedance of the parallel circuit section decreases with the increasing frequency, more voltage will be distributed on the series resistance and less voltage on the parallel circuit section for the higher pumping frequency. The negative conductance observed at the

fundamental and different harmonic frequencies can be used as the basis for harmonic oscillators. It should be pointed out that the magnitude of the negative conductance at the fundamental is much higher than those at other harmonic frequencies with a tunnel diode biased in the PDR region, close to the current peak (see Fig. 2 (b) and (c)). At this bias point, near the region of greatest curvature, the Fourier series of the conductance waveform has a predominant coefficient at the oscillation frequency. In addition, the negative conductances at the odd harmonic frequencies are higher than those at the even harmonic frequencies for the tunnel diode biased in the PDR region, close to the current peak due to the antisymmetrical conductance-voltage (G-V) characteristic at this bias point. The power levels at which the maximum negative conductances at the fundamental and second harmonic frequency occur are smaller than those for a unbiased tunnel diode.

The differential conductance of a tunnel diode biased at the center of the NDR region has also been studied. From the results shown in Fig. 3 (a), an absolute negative conductance to dc has been obtained from a tunnel diode biased in the NDR region when the applied pump amplitude is within a small range. That is, the conductance of the resonant tunneling device will be negative at any frequency when the pump amplitude is within this small range. The value of the absolute negative conductance is approximately the same as that found in the NDR region. The magnitude of the negative conductances changes with the pumping power level (see Fig. 3). That the absolute negative conductance occurs for the tunnel diode biased in the NDR region asserts that oscillation can occur at any frequency if the pumping power is within the region that the negative conductance occurs. The magnitude of the negative conductance at the second harmonic is higher than those at dc, the fundamental and third harmonic frequencies due to the symmetrical G-V characteristic at this bias point (see Fig. 3 (b)). The variable absolute negative conductance observed can be used as the basis for oscillators and harmonic oscillators up to the cut-off frequency of the diode. The self-oscillation capability of a tunnel diode biased in the NDR region can, therefore, finds applications as biased self-

oscillating mixers and frequency multipliers. The self-oscillating frequency multiplier and mixer discussed here do not require a large-signal rf pump.

It should be noted that the self-oscillation at the fundamental generates its own harmonics using the nonlinearity of the NDR device; this will be referred to as the self-oscillating frequency multiplier. While the harmonic oscillator refers to the case that the NDR device oscillates at a particular harmonic frequency using the negative conductance at that harmonic frequency. It should be pointed out that the conversion gain (efficiency > 1) can be achieved from the biased self-oscillating frequency multiplier and mixer.

Resonant Tunneling Device--With Antisymmetry in the I-V Characteristic

From the nonlinear-circuit analysis results, an absolute negative conductance to dc can be found from a resonant tunneling device at zero bias when the applied pump power is within a small range (see Figs. 4 (a) and (b)). The value of the negative conductance is approximately the same as that found in the NDR region. As can be seen from the results in Figs. 4 (a) and (b), the magnitude of the negative conductance can be adjusted by varying the pump amplitude. This study verifies the work of Sollner et al. [3]. However, the voltage range over which the negative conductance occurs is strongly dependent on the pumping frequency. This region moves towards the more positive side of the power axis when the pumping frequency increases (see Figs. 4 (a) and (b)). The reason for this can, again, be explained with a equivalent circuit model (discussed for the tunnel diode in previous section).

We found that the range of the applied pump power to obtain absolute negative conductance varies with the parasitics (series resistance and capacitance) of the device. As can be seen from Fig. 5, the pumping power region over which the negative conductance occurs move towards the more positive side of the power axis with increasing capacitance and series resistance of the device. This again can be seen from the equivalent circuit model of a NDR diode. When the series resistance and/or capacitance of the device increases, more voltage drops across the series resistance and, therefore, less power is

developed across the parallel circuit section of the equivalent circuit. It should be pointed out that the dependence of the conductance on the parasitics of the device is similar to that on the rf input frequency.

The conductance of the resonant tunneling diode will be negative at any frequency when the pump amplitude is within a small range. Figures 4 (c) and (d) show the differential conductance at the second harmonic frequency versus pumping power and pump amplitude, respectively. The magnitude of the negative conductance at the second harmonic frequency is larger than the negative conductances at dc and at fundamental frequency. This is due to the symmetrical G-V characteristic of the resonant tunneling device. The variable absolute negative conductance observed can be used for oscillators up to the cut-off frequency of the diode.

From these studies, one can expect to find absolute negative resistance whenever a material with negative differential conductance and an I-V curve that is antisymmetrical is driven with a pump of the right amplitude and frequency. The resonant tunneling device can also perform the same functions such as the self-oscillating frequency multiplier and mixer discussed for a tunnel diode if it is biased in the NDR region. It should be pointed out that the biased tunnel and resonant tunneling device (in the PDR region) requires less pumping power to achieve self-oscillation than the unbiased device. The biased self-oscillation tunnel diode and resonant tunneling frequency multipliers and mixers have the intrinsic capability of conversion gain. For the unbiased oscillator operations, it should be noted that little in the way of negative conductance or dynamic range has been sacrificed with this operation, and the advantage of operating with zero DC bias voltage has been gained. It should be further noted that the increase in negative conductance at a specific frequency (depending upon the operating point) could simplify frequency selection for oscillator designs.

EXPERIMENTAL RESULTS

During the experimental measurements, it was observed that the dc I-V characteristic of the NDR device is very strongly dependent on the power level of the rf input signal. The dc I-V characteristics of the NDR devices (with and without the antisymmetrical I-V characteristics) measured at different rf input power levels are shown in Figs. 6 and 7, respectively. The dc I-V characteristics of the tunnel diode measured at different rf input frequencies are shown in Fig. 8. Based on these results, the dc I-V characteristics of the NDR device changes dramatically with the increasing input power level and frequency. The dependence of the I-V characteristics of the NDR device on the frequency of the rf input signal can easily be seen from the equivalent circuit model of the NDR device. The frequency dependence of the impedance across the parallel circuit section of the equivalent circuit results in the power dependence of the I-V characteristics. The power dependence of the negative conductance complicates the dependence of the negative conductance on the frequency. The nonlinear circuit analysis was used to theoretically verify this observation. The I-V curves measured at different pumping power levels as shown in Figs. 6 and 7 and the I-V curves measured at different pumping frequencies as shown in Fig. 8 compare favorably to the simulation results.

Based upon this study, the design, operation, and performance of the NDR frequency multiplier, self-oscillating frequency multiplier and mixer and harmonic oscillator can be complicated. For a constant rf input frequency, the biasing and pumping conditions and output power of the self oscillation of the NDR device vary with the rf input power level. In addition, the onset of self oscillation of a NDR device biased in the NDR region also depends upon the rf input power level. For example, the self oscillation can be suppressed by changing the rf input power level (tuning the I-V characteristic) in the frequency multiplication operation of a NDR device. However, this will cause the conversion efficiency of the device to change as well since the nonlinearity is not the same. In addition, the self-oscillation with a constant rf input frequency may disappear for a given dc bias depending upon the rf input power level for the self-oscillating frequency

multiplier, mixer and harmonic oscillator applications. Determination of the biasing and operating conditions and performance of the NDR frequency multiplier, self-oscillating frequency multiplier and mixer, and harmonic oscillator, therefore, requires complete information of the I-V characteristics at different rf input frequencies and power levels. This can be accomplished by extensive simulations of the NDR device under different pumping conditions using the modified large- and small-signal nonlinear circuit analysis program as mentioned above.

A NDR biased in the NDR region can be used for the self-oscillating frequency multiplier and mixer. Both the self-oscillating frequency multiplier and mixer have been successfully demonstrated using a tunnel diode biased in the NDR region. The results from a self-oscillating frequency multiplier can be seen in Fig. 9. The highest tripling efficiency has been obtained at the center of the NDR region while the highest doubling efficiency has been obtained at the edges of the NDR region of the tunnel diode as expected. This is due to the I-V characteristic being antisymmetrical when biased at the center of the NDR region, and the I-V characteristic being almost symmetrical when biased close to the current peak. It should be pointed out that the circuit used does not allow independent tuning of the harmonics.

APPLICATIONS

The wide use of resonant tunnel devices is limited, to a considerable extent, by the low level of their output power. Power combining techniques are employed to increase the output power of the resonant tunneling devices. The device-grid array approach is a potentially attractive way to spatially combine the output power of large numbers of resonant tunneling devices. In this approach, a grid is monolithically integrated with thousands of devices thereby overcoming the power limitations of a single device since the power is distributed among the many devices making possible watt-level CW output power throughout the microwave and millimeter-wave region [8,9]. This kind of array can find applications as a high frequency, high power solid-state rf power source. All the

interconnections of the high- and low-frequency leads of each port of each device (especially, three-terminal devices) present an extremely difficult problem for the development of such arrays. The demonstration of novel unbiased oscillators is most useful for the development of monolithic planar wafer-scale device arrays since no dc bias lines are required, which greatly simplify the grid design.

In addition, the pumping power for a device grid is significantly higher than that for a single device (proportional to the number of the devices). Therefore, it is important to minimize the amount of input power required to pump each individual device. Based upon the theoretical and experimental work which have been performed in this study, the possibility of biasing a NDR diode to minimize the amount of power required to pump each individual diode into the desired operation point has been verified. The bias lines can be easily employed in the design of diode grid (two terminal device grid) to provide dc bias and minimize the required pumping power [9]. In addition, frequency multiplication and mixing with gain can be obtained from these biased NDR diodes as discussed in this paper.

CONCLUSION

This work employs a modified large- and small-signal nonlinear-circuit analysis [2] to verify the previous work of Sollner et al. using a simple mathematical model [3]. The absolute negative conductance can be obtained from an unbiased resonant tunneling device when the applied pump power is within a small region. The variable absolute negative conductance can be used as the basis for oscillators up to the cutoff frequency of the device. Furthermore, a NDR device biased in the NDR region can be used as the basis for the self-oscillating frequency multiplier and mixer. The biased self-oscillating frequency multiplier and mixer can achieve conversion gain (efficiency > 1). These functions have been experimentally demonstrated in this work. The advantage of a unbiased oscillator using a resonant tunneling device comes from the fact that the negative conductance can be adjusted by varying the pump amplitude--a very useful circuit property. In addition, the negative conductance is larger at even harmonic frequencies which could simplify

frequency selection of an oscillator design based upon this effect. The advantage of operating with zero dc bias voltage is also gained. Through this study, the power dependence of the negative conductance of a NDR device on the rf input signal has been observed. The biasing and pumping conditions and performance of the frequency multiplier, self-oscillating frequency multiplier and mixer, and harmonic oscillator requires complete information of the I-V characteristics of a NDR device at different input frequencies and power levels. This information can be obtained using the modified large- and small-signal nonlinear-circuit analysis as discussed in this paper.

References

[1] H. Siegel, A. R. Kerr, and W. Hwang, "Topics in the Optimization of MM Wave Mixers," NASA Technical Paper #2287, 1987.

[2] R. J. Hwu and N. C. Luhmann, Jr., "Quantum Well Diode Frequency Multiplier Study," Second International Symposium on Space Terahertz Technology, Proceedings, pp. 226-237, 1991.

[3] T. C. L. G. Sollner, E. R. Brown, and W. D. Goodhue, Picosecond Electronics and Optoelectronics II, Editors: F. J. Leonberger, C. H. Lee, F. Capasso, and H. Morkoc, Springer-Series in Electronics and Photonics, **Vol. 24**, pp. 102-108, 1987.

[4] P. D. Batelaan and M. A. Frerking, 13th Int'l Conf. on Infrared and Millimeter Waves, Proceedings, 1988.

[5] T. C. L. G. Sollner, E. R. Brown, W. D. Goodhue, and C. A. Correa, J. Appl. Phys., **Vol. 64**, P. 4248, 1988.

[6] D. N. Held and A. R. Kerr, "Conversion Loss and Noise of Microwave and Millimeter-Wave Mixers: Part 1 - Theory," IEEE Trans. on Microwave Theory and Tech., **MTT-26**, PP. 49-55, 1978.

[7] P. P. Huang, "I-V Characterization of Negative Resistance Device by Microwave Reflection Coefficients," M.S. thesis, UCLA, pp. 49-51, 1989.

[8] D. B. Rutledge and S. E. Schwarz, "Planar Multimode Detector Arrays for Infrared and Millimeter Waves Applications," IEEE J. Quantum Electronics, **QE-17**, pp. 407-414, 1981.

[9] R. J. Hwu, C. F. Jou, N. C. Luhmann, Jr., M. Kim, W. W. Lam, Z. B. Popovic, D. B. Rutledge, "Array Concepts for Solid-State and Vacuum Microelectronics

Millimeter-Wave Generation," IEEE Trans. on Electron Device, **ED-36**, No. 11, pp. 2645-2650, 1989.

Figure Captions

Fig. 1 The I-V curves of a (a). tunnel diode and a (b). resonant tunneling device used in the nonlinear circuit analysis. (c). The equivalent circuit of a NDR device.

Fig. 2 The differential conductance of a tunnel diode biased in the PDR region (close to the current peak) at the (a). dc, (b). fundamental, and (c). third harmonic frequency from the nonlinear circuit analysis.

Fig. 3 The differential conductance of a tunnel diode biased at the center of the NDR region at the (a). dc, and (b). second harmonic frequency from the nonlinear circuit analysis.

Fig. 4 The differential conductance at dc versus (a). pump power level, and (b). pump amplitude of a zero-biased resonant tunneling device. The differential conductance at the second harmonic frequency versus (c). pump power level and (d). pump amplitude of a zero-biased resonant tunneling device from the nonlinear circuit analysis.

Fig. 5 The differential conductance at dc of a zero-biased resonant tunneling device with different (a). capacitance values of 1 pF and 1 fF with three rf input frequencies of 0.7, 12, and 90 GHz, and (b). series resistance values of 12.5 Ω, 625 Ω, and 1.25 kΩ with an rf input frequency of 0.7 GHz from the nonlinear circuit analysis.

Fig. 6 The measured I-V curves of a tunnel diode with different rf input power levels at two rf input frequencies of (a). 0.7 GHz, and (b). 2.5 GHz.

Fig. 7 The measured I-V curves of a NDR device (with an antisymmetrical I-V characteristic) with two different rf input power levels at an rf input frequency of 10 MHz.

Fig. 8 The measured I-V curves of a tunnel diode with different rf input frequencies at an rf input power level of 2 mW.

Fig. 9 The ratio of the output power to the fundamental power of a self-oscillating frequency multiplier using the tunnel diode of Fig. 6 versus different bias points in the NDR region with a rf input frequency of 0.7 GHz.

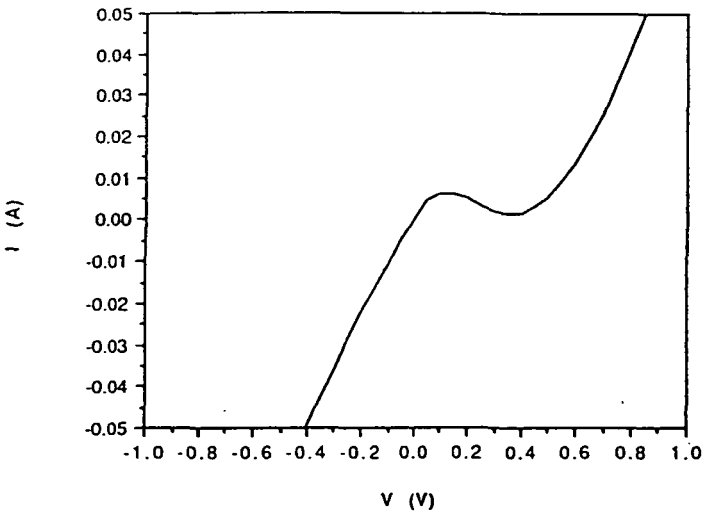

Fig. 1 (a)

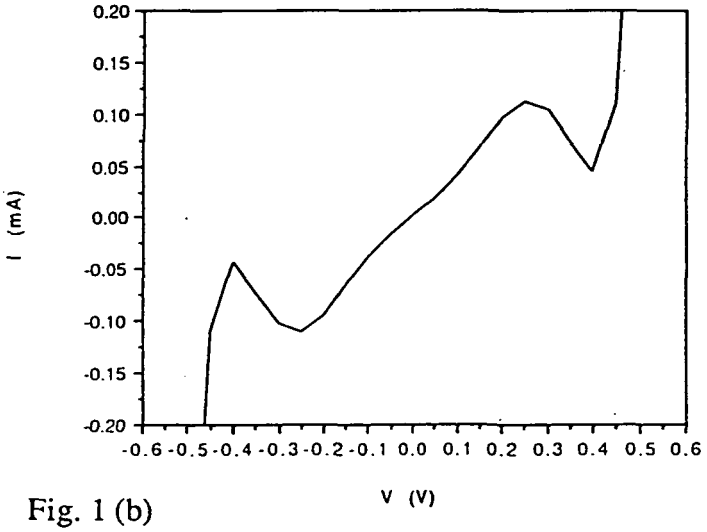

Fig. 1 (b)

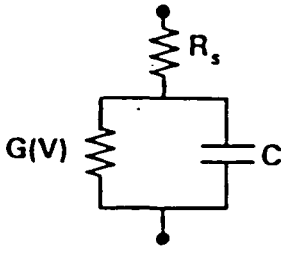

Fig. 1 (c)

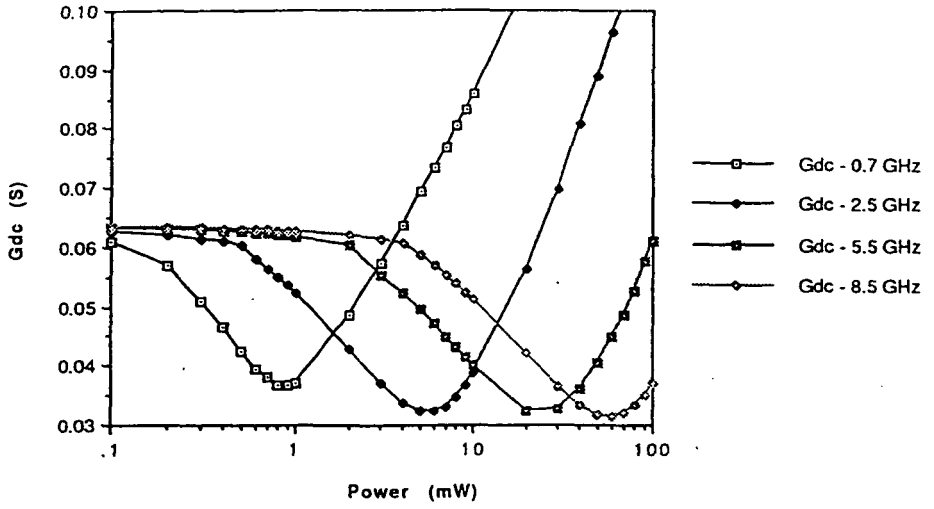

Fig. 2 (a)

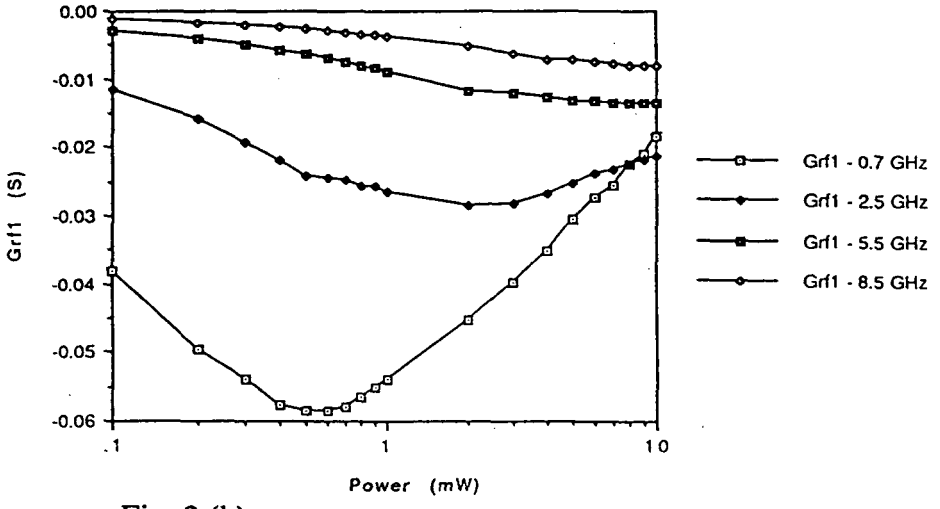

Fig. 2 (b)

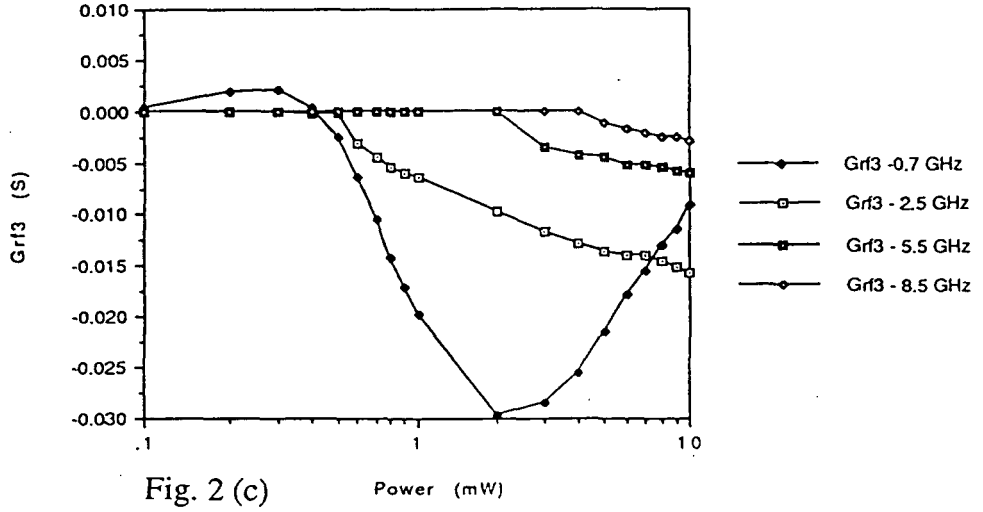

Fig. 2 (c)

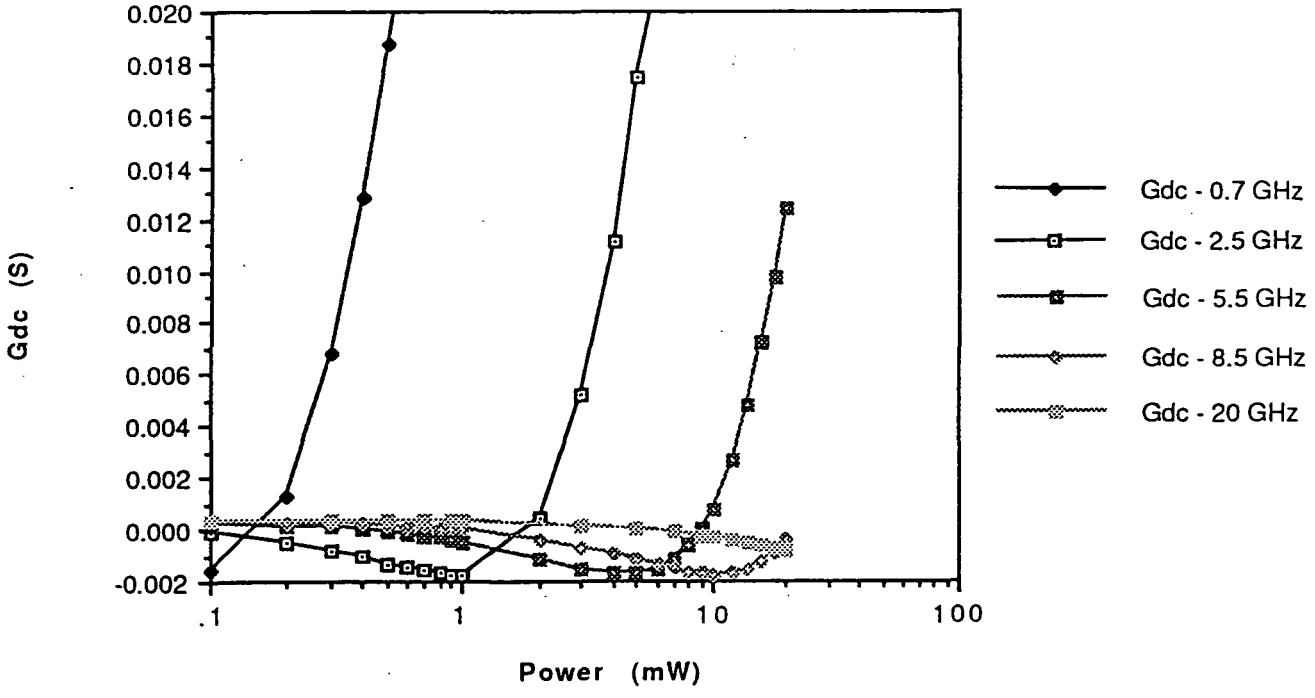
0.020
0.018
0.016
0.014
0.012
0.010
0.008
0.006
0.004
0.002
0.000
-0.002
Gdc (S)
.1
1
10
100
Power (mW)
Gdc - 0.7 GHz
Gdc - 2.5 GHz
Gdc - 5.5 GHz
Gdc - 8.5 GHz
Gdc - 20 GHz

Fig. 3 (a)

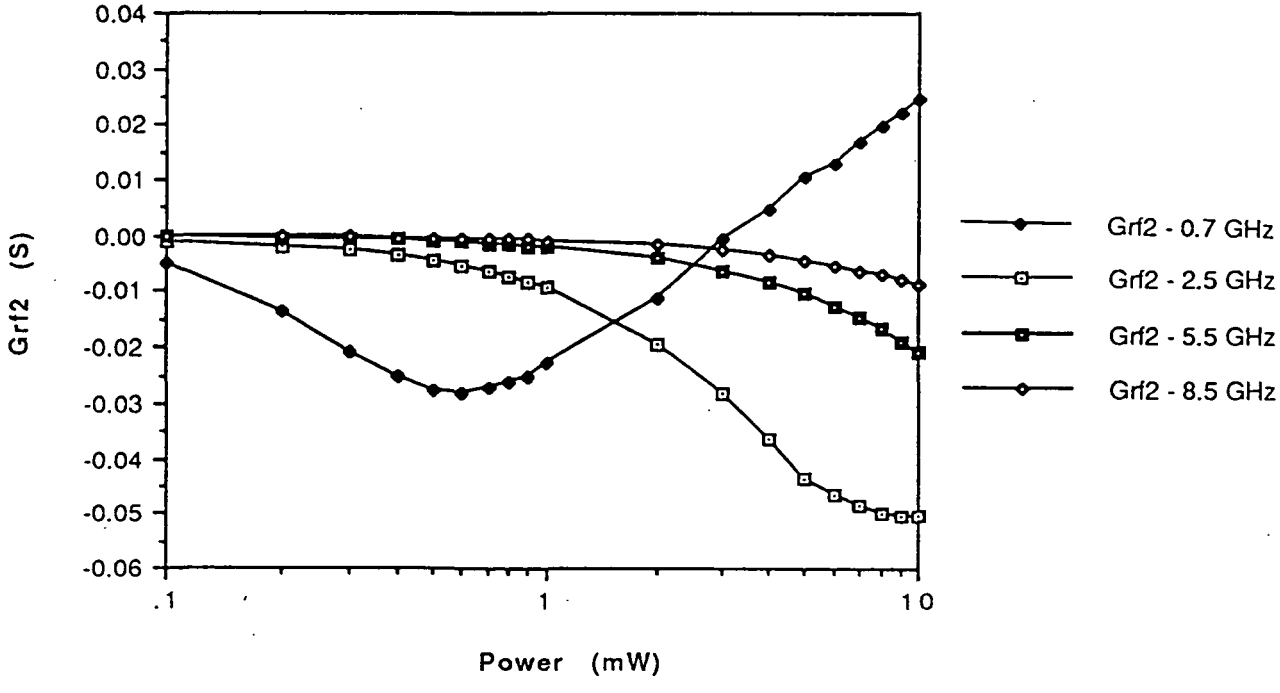
0.04
0.03
0.02
0.01
0.00
-0.01
-0.02
-0.03
-0.04
-0.05
-0.06
Grf2 (S)
.1
1
10
Power (mW)
Grf2 - 0.7 GHz
Grf2 - 2.5 GHz
Grf2 - 5.5 GHz
Grf2 - 8.5 GHz

Fig. 3 (b)

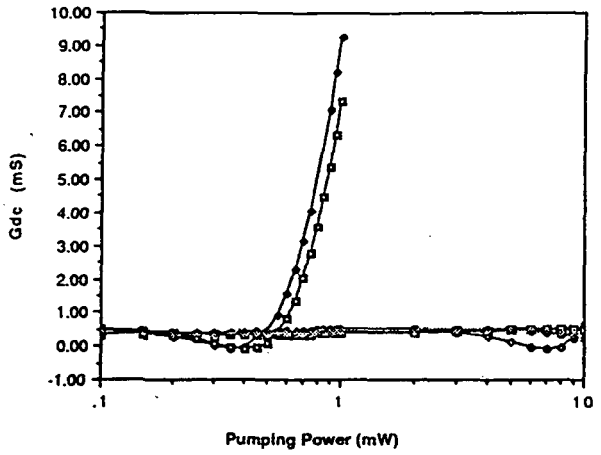

Fig. 4 (a)

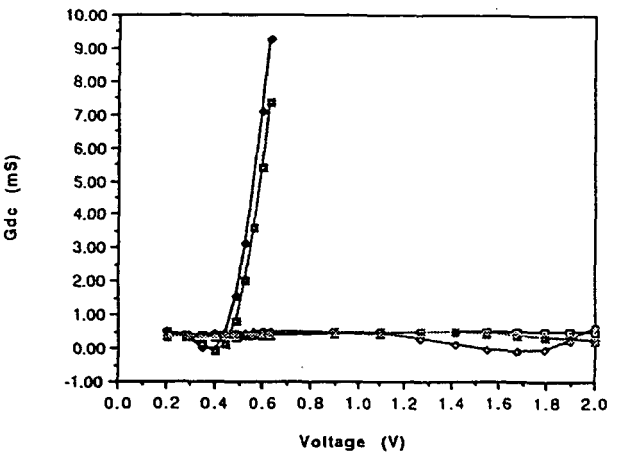

Fig. 4 (b)

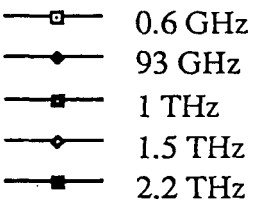

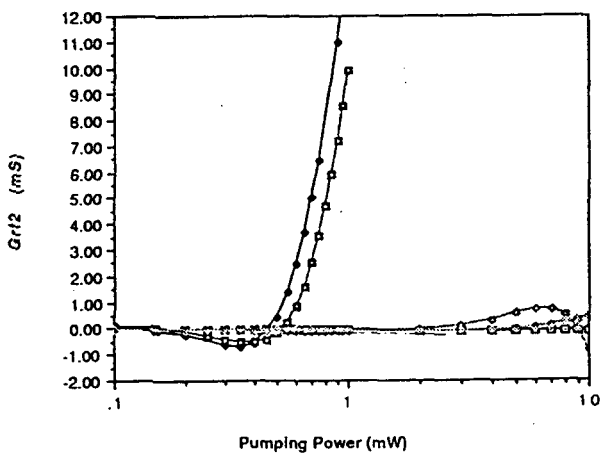

Fig. 4 (c)

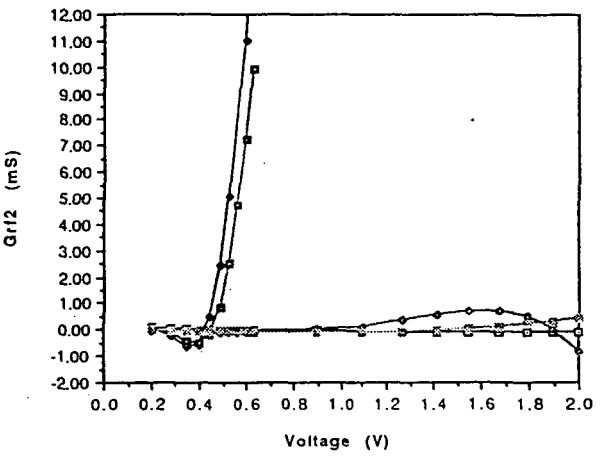

Fig. 4 (d)

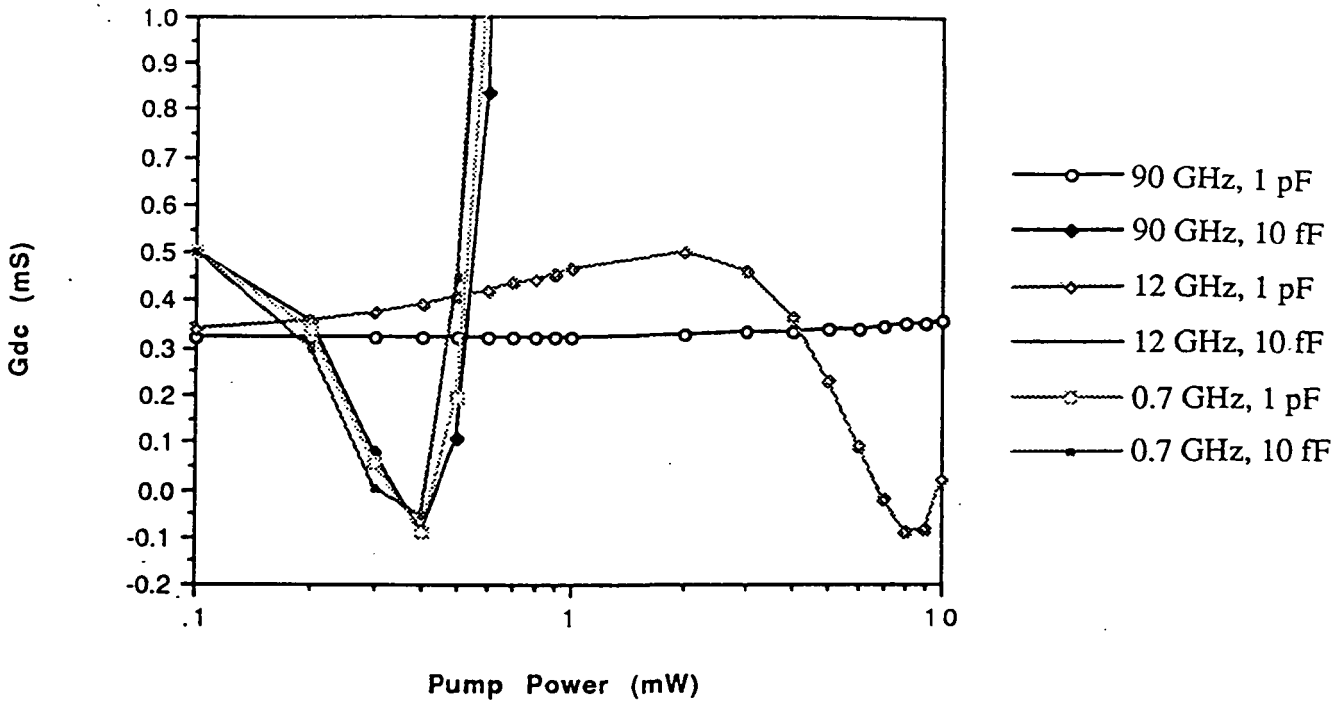
Gdc (mS)
1.0
0.9
0.8
0.7
0.6
0.5
0.4
0.3
0.2
0.1
0.0
-0.1
-0.2
.1
1
10
Pump Power (mW)
90 GHz, 1 pF
90 GHz, 10 fF
12 GHz, 1 pF
12 GHz, 10 fF
0.7 GHz, 1 pF
0.7 GHz, 10 fF

Fig. 5 (a)

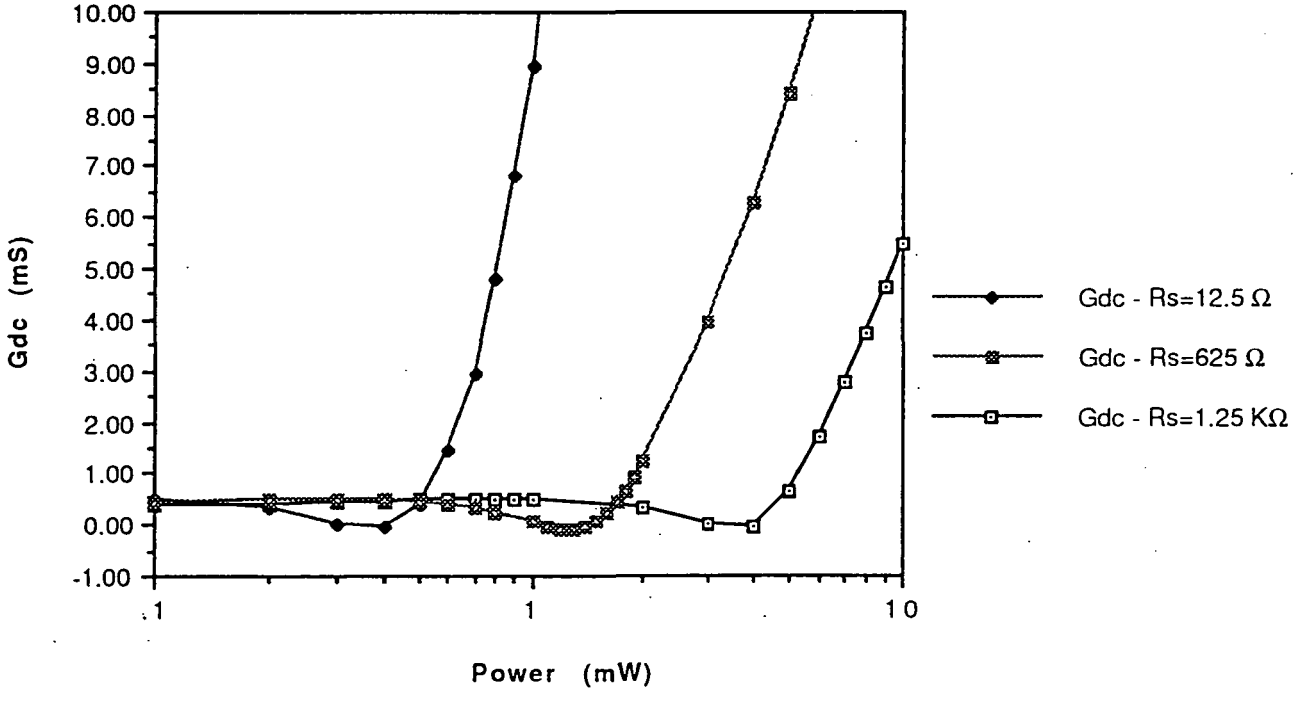
Gdc (mS)
10.00
9.00
8.00
7.00
6.00
5.00
4.00
3.00
2.00
1.00
0.00
-1.00
.1
1
10
Power (mW)
Gdc - Rs=12.5 Ω
Gdc - Rs=625 Ω
Gdc - Rs=1.25 KΩ

Fig. 5 (b)

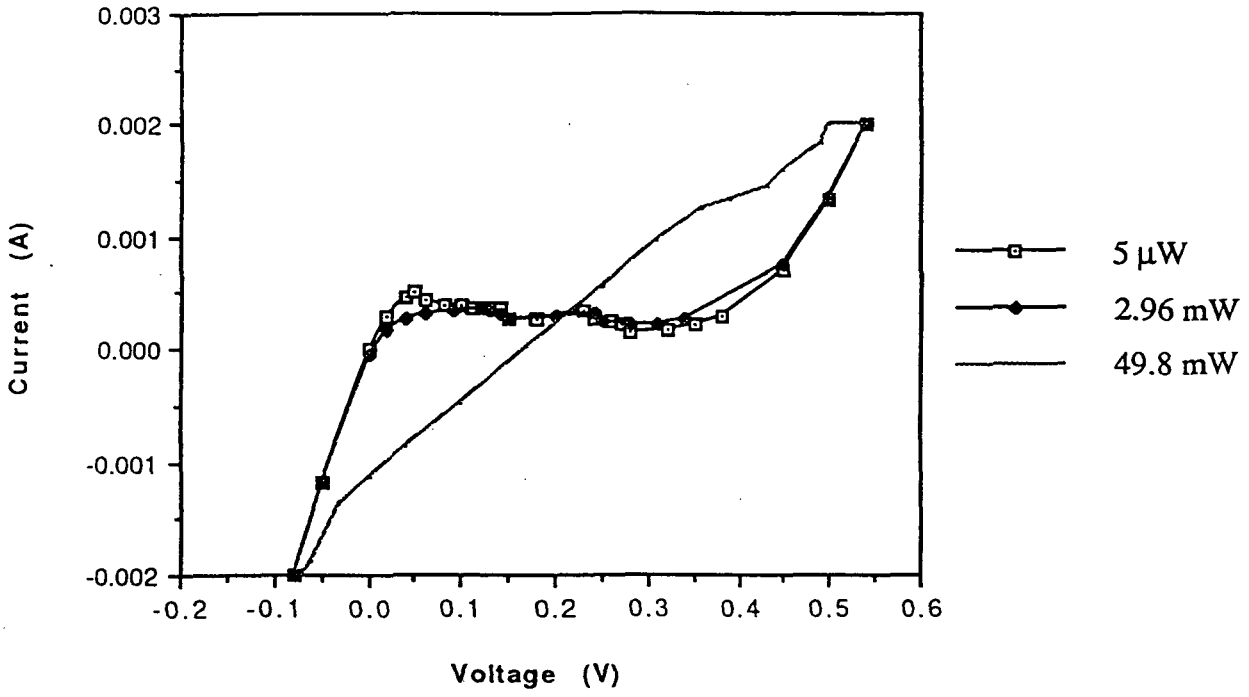
0.003
0.002
0.001
0.000
-0.001
-0.002
Current (A)
-0.2
-0.1
0.0
0.1
0.2
0.3
0.4
0.5
0.6
Voltage (V)
5 μW
2.96 mW
49.8 mW

Fig. 6 (a)

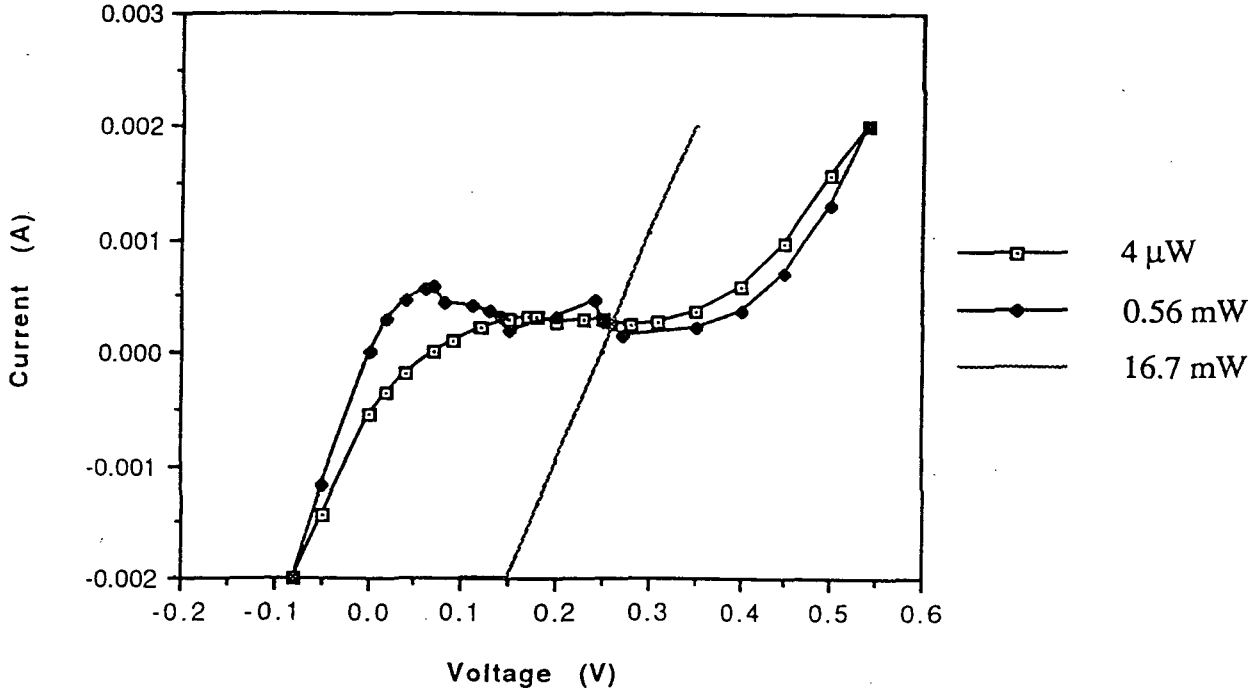
0.003
0.002
0.001
0.000
-0.001
-0.002
Current (A)
-0.2
-0.1
0.0
0.1
0.2
0.3
0.4
0.5
0.6
Voltage (V)
4 μW
0.56 mW
16.7 mW

Fig. 6 (b)

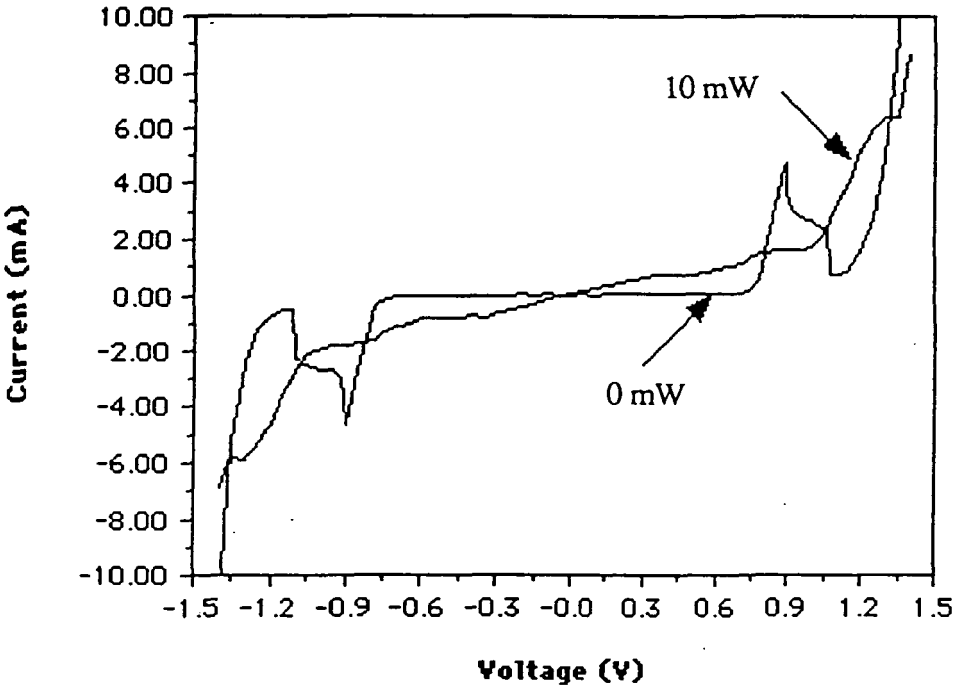
10.00
8.00
6.00
4.00
2.00
0.00
-2.00
-4.00
-6.00
-8.00
-10.00
Current (mA)
-1.5 -1.2 -0.9 -0.6 -0.3 -0.0 0.3 0.6 0.9 1.2 1.5
Voltage (V)
10 mW
0 mW

Fig. 7

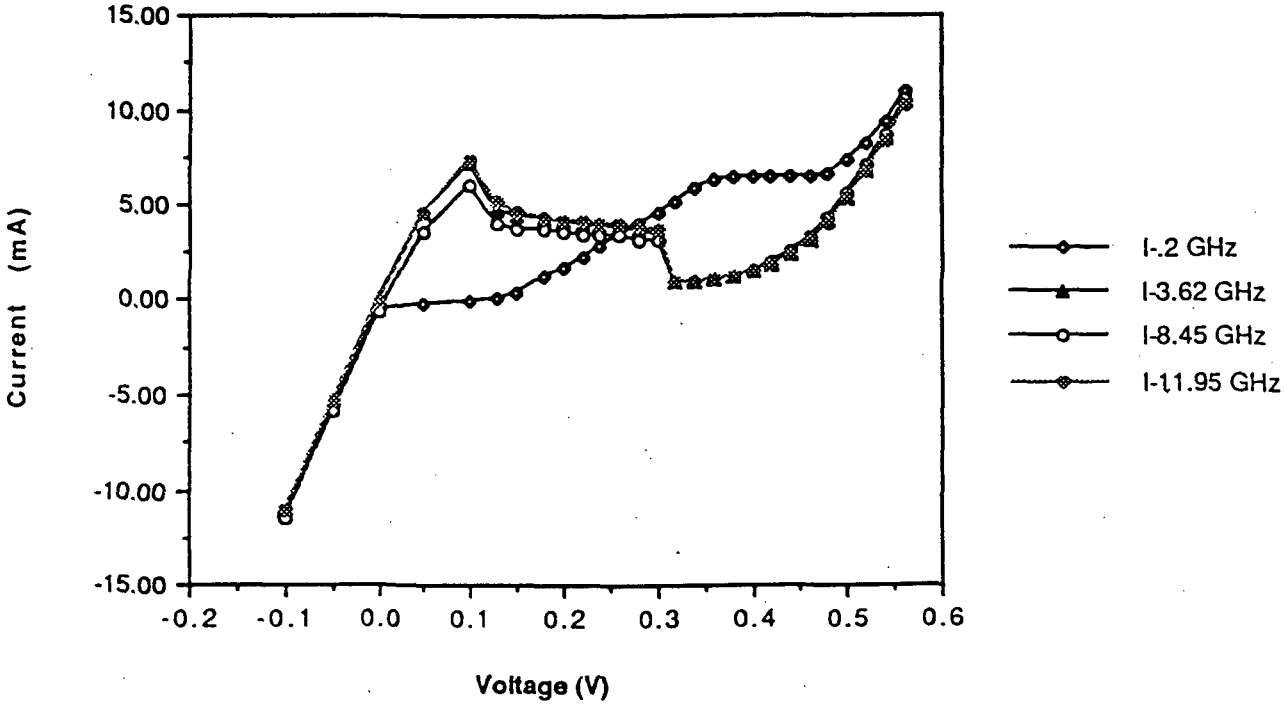
15.00
10.00
5.00
0.00
-5.00
-10.00
-15.00
Current (mA)
-0.2
-0.1
0.0
0.1
0.2
0.3
0.4
0.5
0.6
Voltage (V)
I-.2 GHz
I-3.62 GHz
I-8.45 GHz
I-11.95 GHz

Fig. 8

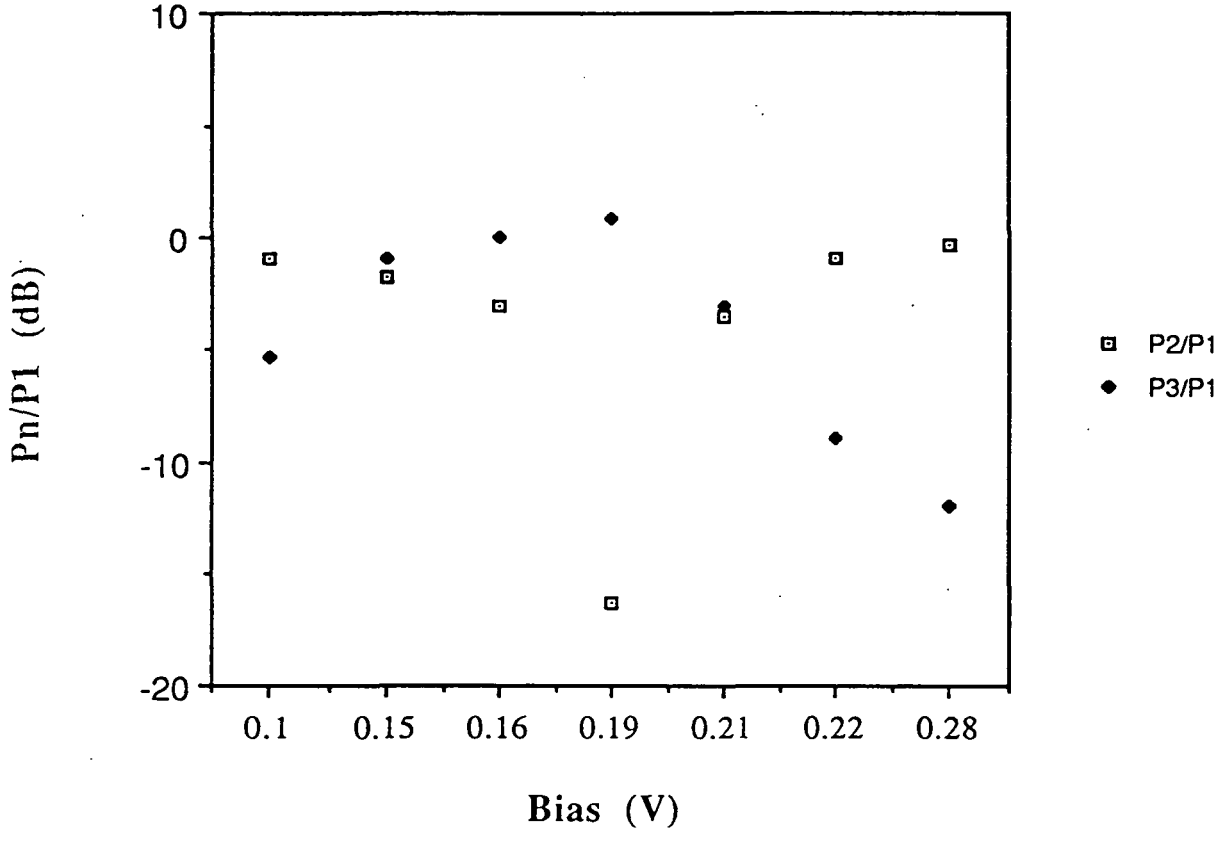

Fig. 9

Modeling, Design, Fabrication, and Testing of InP Gunn Devices in the D-band (110 GHz - 170 GHz) [1]

R. Kamoua [2], H. Eisele, J. R. East, G. I. Haddad,
G. Munns, and M. Sherwin

Solid-State Electronics Laboratory
Department of Electrical Engineering and Computer Science
The University of Michigan, Ann Arbor, MI 48109-2122

Abstract

The development of fundamental Gunn sources for D-band frequencies requires improvements of doping profiles, processing technology, and circuit design. We have developed a technology for fabricating InP Gunn diodes using an InGaAs etch-stop layer between the InP substrate and the device layers. The epitaxial layers were grown by CBE. During device processing, the substrate is completely removed. Substrateless devices with an n^+ InGaAs cap layer are expected to have reduced contact and series resistances, and skin effect losses. This technology gives better uniformity and control of the device geometry across the processed chip.

InP Gunn devices with a 1.7 μm long active region (doping : 9×10^{15} cm^{-3}) have been mounted on copper heat sinks. Two tapered leads were then bonded to the diode and to four quartz standoffs. As a preliminary result, an output power of 13 mW at 82 GHz was obtained. Based on these RF measurements, we determine appropriate material parameters to be used in the Ensemble Monte Carlo model. Subsequently, we use this model to design and evaluate the performance of InP Gunn Devices for D-band frequencies. Using the same technology, we are currently processing Gunn devices with a 1μm long active region for operation at higher frequencies.

[1]This work was supported by the Center for Space Terahertz Technology under Contract No. NAGW-1334

[2]R. Kamoua is currently with the Department of Electrical Engineering, State University of New York at Stony Brook, Stony Brook, NY 11794-2350

1 Introduction

Gunn devices are widely used as local pump oscillators in the W-band frequency region. At these frequencies, the technology is well developed. In particular at 94 GHz, GaAs and InP Gunn devices are available with very good performance. At frequencies above 100 GHz, the situation is quite different. Although there is a strong demand for sources at these frequencies, fundamental Gunn devices are generally not available. There are two reasons. First, most of the research effort has been focused at 94 GHz. Second, extending the fundamental oscillation frequency of Gunn devices into the submillimeter region is exceedingly difficult because the Gunn effect is being pushed to its high frequency limit.

This paper discusses a systematic approach toward the *modeling, design, fabrication*, and *testing* of InP Gunn devices in the D-band region. Compared with GaAs, InP material parameters are more favorable for operating Gunn devices in the D-band. The approach taken in this work is both experimental and theoretical. Experimentally, the conventional processing technology is improved by incorporating etch-stop layers in the wafer design. The RF results obtained from devices fabricated using this technology are then used to improve the accuracy of the theoretical model. Subsequently, the improved model is used to design the optimum Gunn structure for the desired frequency of operation.

2 Simulation Model

The self consistent Ensemble Monte Carlo model is used to estimate the performance of InP Gunn devices at high frequencies. This model is an extension of the one particle Monte Carlo technique [1]. In order to describe the transport process in a structure with nonuniform doping and with time varying fields, an ensemble of electrons needs to be simulated simultaneously. The electric field has to be updated regularly since it is evolving as the electrons redistribute in the structure. The analysis is carried out assuming the device behavior is mainly one dimensional which is justified for two terminal devices. A diode structure of length L is divided into cells of equal length ($\Delta x = 50$ Å). Any attributes of the electrons are averaged over each cell and assigned to the midway position of the cell. The cell size should be smaller than the smallest Debye length in the structure which occurs at the highly doped regions.

The simulation algorithm consists of monitoring the evolution in real space and momentum space of an ensemble of electrons. The simulation time is partitioned into time steps ($\Delta t = 5\times10^{-15}$ sec) each terminated by a call to a Poisson solver in order to update the field. In each time step every electron is submitted to successive free flights terminated by a scattering process which is selected using a random number generator. Electrons crossing cell boundaries are temporarily stopped at that boundary and then resumed with the electric field in the new cell. An analogous procedure is followed when it is time to update the electric field and the electron is in the middle of a free flight. In this case the remaining flight time is stored, and the flight is resumed when all other electrons are simulated for one time step, the carrier density is calculated, and the electric field is updated. The predicted performance of a particular Gunn structure is estimated by applying an RF voltage across the device and simulating the current response over many RF periods (about 10). The resulting particle current density is Fourier analyzed and the fundamental component is

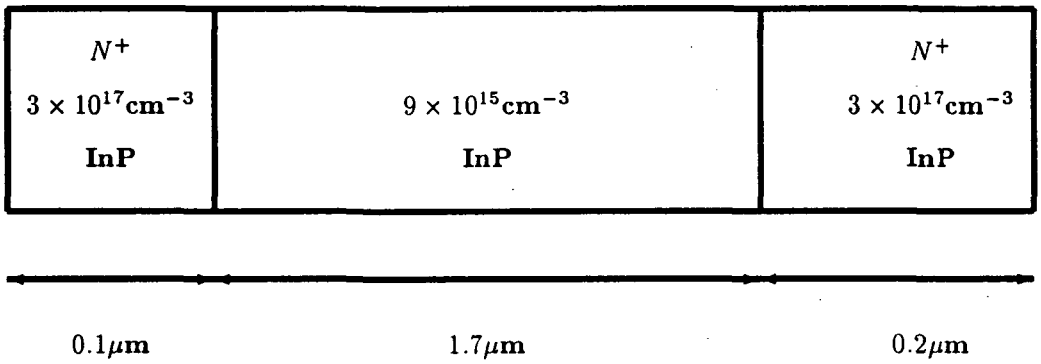

Figure 1: Dimensions and doping profile of Gunn structures.

used to determine the device admittance. The RF output power is estimated by considering the Gunn device in a resonant circuit represented by a load resistance and a resonating inductance. A series resistance is included in the equivalent circuit that takes into account effects of contact resistances, any substrate resistances, and skin effect losses.

The accuracy of the Monte Carlo model is strongly dependent on the accuracy of the material parameters used. Unfortunately, one finds a wide range of values that are being used in the literature. In particular, some of the material parameters that are important to the Gunn effect have the following range of values ([2, 3, 4, 5]):

$\Gamma - L$ valley separation (eV)	0.4	$\Longleftrightarrow$	0.832,
L valley effective mass ratio ($\frac{m}{m_0}$)	0.26	$\Longleftrightarrow$	0.4,
$\Gamma - L$ coupling constant ($\times 10^9$ eV.cm^{-1})	0.1	$\Longleftrightarrow$	2.5,
$\Gamma - X$ coupling constant ($\times 10^9$ eV.cm^{-1})	0.43	$\Longleftrightarrow$	1.0.

There is more than an order of magnitude uncertainty in the Γ to L intervally coupling constant. In the next section, the material parameters that yield the best agreement with the RF measured results will be identified.

3 Method for Extracting Accurate InP Material Parameters for a 3-Valley Nonparabolic EMC Model

The appropriate material parameters are determined by comparing measurements at high frequencies with results predicted by the model. The structure considered for comparison is shown in Figure 1. It has 1.7 μm long active region doped at 9×10^{15} cm^{-3}, a 0.1μm cathode region doped at 3×10^{17} cm^{-3} and a 0.2 μm anode region doped at 3×10^{17} cm^{-3}.

An InP wafer with this structure has been processed. The relevant fabrication technology will be described later. Diodes with various sizes have been mounted on copper heat sinks. Tapered ribbons were then used to bond a diode to four quartz standoffs. A 40 μm diode was tested in a W-band resonant cavity with the following results:

Bias voltage	4.0 V to 4.5 V,
Oscillation frequency	82 GHz,
output power	13 mW,
conversion efficiency	1 %,
DC current	350 mA.

The structure shown in Figure 1 is simulated using the model described above. The DC bias is 4.5 V, the RF voltage is 1.0 V, and the operating temperature is assumed to be 400 K. The material parameters are considered to be accurate if oscillations at 82 GHz are predicted with a performance comparable to experimental results. The starting combination of parameters is listed in Table 1 and is referred to as the *initial parameter set.* No oscillations occurred with this set of values for frequencies ranging from 75 GHz to 120 GHz. It appears that the $\Gamma - L$ intervalley energy separation of 0.832 eV is too large. As a result, the following modifications to the initial set are considered:

- Case 1. The same parameters as the initial set are used except $\Gamma - L$ valley separation = 0.6 eV. No oscillations occurred at 82 GHz.
- Case 2. The same parameters as the initial set are used except $\Gamma - L$ valley separation = 0.4 eV. No oscillations occurred at 82 GHz.
- Case 3. The same parameters as the initial set are used except $\Gamma - L$ energy separation = 0.4 eV and $\Gamma - X$ energy separation = 0.7 eV. No oscillations occurred at 82 GHz.
- Case 4. The same parameters as the initial set are used except L valley effective mass ratio = 0.4 and X valley effective mass ratio = 0.4. No oscillations occurred at 82 GHz.
- Case 5. The same parameters as the initial set are used except $\Gamma - L$ coupling constant = 1.0×10^9 eV.cm^{-1}. No oscillations occurred at 82 GHz.
- Case 6. The same material parameters as the initial set are used except $\Gamma - L$ energy separation = 0.5 eV, $\Gamma - X$ energy separation = 0.8 eV, $\Gamma - L$ coupling constant = 1.0×10^9 eV.cm^{-1} and $\Gamma - X$ coupling constant = 1.0×10^9 eV.cm^{-1}. Very weak oscillations were obtained. The efficiency was 0.032 % and the output power was 0.22 mW.
- Case 7. The same parameters as the initial set are used except $\Gamma - L$ energy separation = 0.45 eV, $\Gamma - X$ energy separation = 0.775 eV, L valley effective mass ratio = 0.4 eV, X valley effective mass ratio = 0.4 eV, $\Gamma - L$ coupling constant = 1.0×10^9 eV.cm^{-1}, $\Gamma - X$ coupling constant = 1.0×10^9 eV.cm^{-1} and acoustic deformation potential = 5 eV. Oscillations were obtained at 82 GHz even though the DC bias was 4.0 V instead of 4.5 V. With 1.0 V RF voltage, the predicted output power for a 40 μm diode was 7.2 mW with 0.52 % efficiency.

The last parameter set appears to be promising and was considered in more detail. At an RF voltage of 1.5 V, the predicted efficiency was 1.1 % and the predicted output power

Energy Separation (eV)	Γ-L	0.832
	Γ-X	1.5
Effective Mass ($\frac{m^*}{m_0}$)	Γ	0.082
	L	0.26
	X	0.325
Nonparabolicity factor ($[eV]^{-1}$)	Γ	0.83
	L	0.23
	X	0.38
Intervalley Coupling Constant (10^9 eV.cm^{-1})	Γ-L	0.506
	Γ-X	0.498
	L-X	0.468
	L-L	0.575
	X-X	0.28
Acoustic Deformation Potential (eV)	Γ	7
	L	7
	X	7
LO Phonon Energy (eV)	Γ	0.043
	L	0.0423
	X	0.0416
Static Dielectric Constant		12.61
Optical Dielectric Constant		9.61

Table 1: InP initial material parameter set.

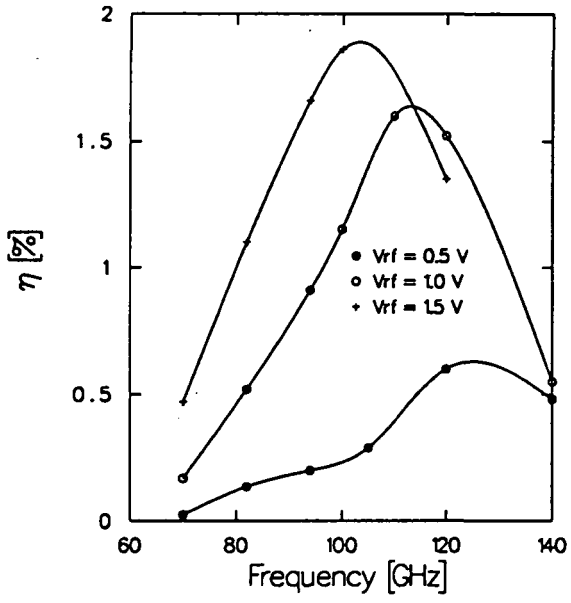

Figure 2: Efficiency vs. frequency for a 1.7 μm long InP Gunn device doped at 9×10^{15} cm^{-3}. Diameter = 40 μm, Vdc = 4.0 V, T = 450 K.

was 14.9 mW for a 40 μm diode. The necessary load resistance for matching the diode was 6.5 Ω. The simulated DC current density has a value of 2.7×10^4 $A.cm^{-2}$ which results in a current of 340 mA. The simulated device performance is in good agreement with the measured RF results. In summary, we found it necessary to decrease the intervalley energy separation and increase the electron effective mass in the upper valleys and the intervalley deformation potentials in order to obtain oscillations at 82 GHz. The actual device was operated at higher temperature than room temperature. This suggests that the lower values for the intervalley separation and the higher values for the deformation potentials might be caused by temperature effects on the band-structure. The last parameter set will be used to analyze various InP Gunn structures. In the next section, the 1.7 μm structure will be considered in more detail.

4 Simulation of 1.7 μm InP Gunn Devices

The results presented in this section correspond to a DC bias voltage of 4.0 V and an operating temperature of 450 K. For comparison purposes, the load resistance was adjusted so that the device area is 40 μm. Figure 2 shows a comparison of the conversion efficiency as a function of frequency for three RF voltage amplitudes: 0.5 V, 1.0 V and 1.5 V. The peak efficiency for a 1.5 V RF voltage is 1.86 % at 100 GHz. The corresponding comparison of the output power is shown in Figure 3. A peak power of 23 mW at 100 GHz was obtained for the case where the RF voltage is 1.5 V.

In general, the operating temperature is 80 K to 90 K above the room temperature. Therefore, it is possible to extract more power by either increasing the device area or the DC bias or a combination of both. Increasing the device area is limited by thermal effects

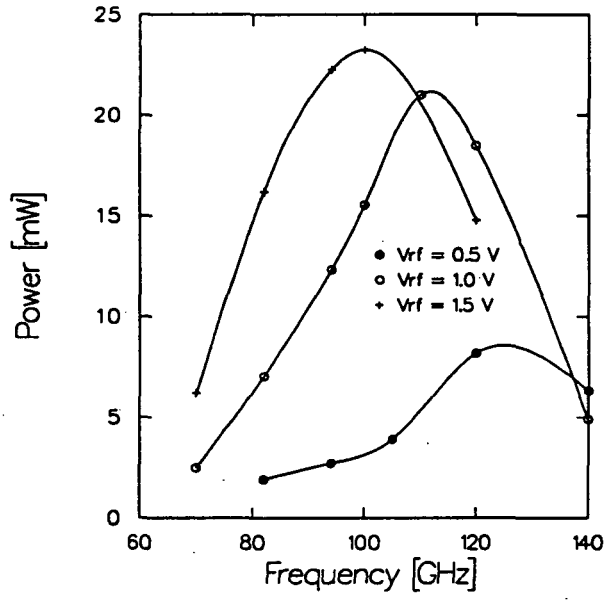

Figure 3: Power vs. frequency for a 1.7 μm long InP Gunn device doped at 9×10^{15} cm^{-3}. Diameter = 40 μm, Vdc = 4.0 V, T = 450 K.

and by the minimum load provided by the resonant circuit. On the other hand, increasing the DC bias voltage is limited by thermal effects and breakdown due to the large electric field at the anode. For example, increasing the diode diameter from 40 μm to 60 μm results in 50 mW output power at 100 GHz with an RF voltage of 1.5 V. The required matching load is 2 Ω compared to 3.75 Ω for the smaller device and the temperature increase is 120 K compared to 86 K.

5 Simulation of 1.0 μm InP Gunn Devices for Operation in D-band Frequency Region

The 1.7 μm device considered in the previous section had an optimum operating frequency around 100 GHz. For higher frequencies in D-band, structures with shorter active regions need to be considered. In this section, simulation results of a 1 μm long InP device are presented.

5.1 Flat Doping Profile

Two flat doping profiles in the active region 1×10^{16} cm^{-3} and 2×10^{16} cm^{-3} are considered. Figure 4 compares the corresponding efficiency as a function of frequency for a DC bias of 4.0 V, an RF voltage of 0.5 V, and an operating temperature of 450 K. The structure with 2×10^{16} cm^{-3} doping results in a higher efficiency at all frequencies. The output power into a 2 Ω load is shown in figure 5. Near 160 GHz, the predicted output power from the highly doped structure is more than 5 times higher than the output power from the low doped structure. However, for a meaningful comparison, thermal effects and current density levels

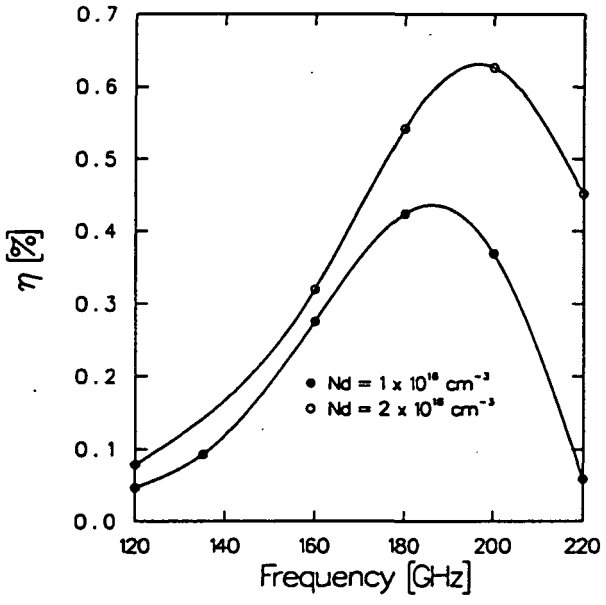

Figure 4: Efficiency versus frequency for a 1.0 μm long InP Gunn device. Vdc = 4.5 V, Vrf = 0.5 V, $R_L \approx 2\ \Omega$, T = 450 K.

need to be considered.

The DC current density in the structure with a lower doping is about 3.95×10^4 A.cm^{-2} at 160 GHz whereas it is about 6.7×10^4 A.cm^{-2} for the other structure. The device with the higher doping has a very large current density which results in an operating temperature approaching the limit for a 30 μm diameter device. For smaller diodes, bonding becomes very difficult. Therefore, there is a need for improving the efficiency while keeping the current density from increasing rapidly. It will be shown in the next section that a graded doping profile in the active region provides such an improvement.

5.2 Graded Doping Profile

This section examines methods of improving the efficiency of InP Gunn devices and optimizing the design for operation around 160 GHz. In addition to the structure with a flat doping of 1×10^{16} cm^{-3}, three linearly graded doping profiles are considered:

	N_1 ($\times 10^{16}$ cm^{-3})	N_2 ($\times 10^{16}$ cm^{-3})
Structure 1	1.0	1.0
Structure 2	0.8	1.5
Structure 3	0.8	3.0
Structure 4	0.8	4.0

In the above table, N_1 is the doping density in the active region at the cathode side and N_2 is the corresponding doping at the anode side. The results presented in this section correspond to a bias of 4.0 V, an RF voltage of 1.0 V, an operating temperature of 450 K,

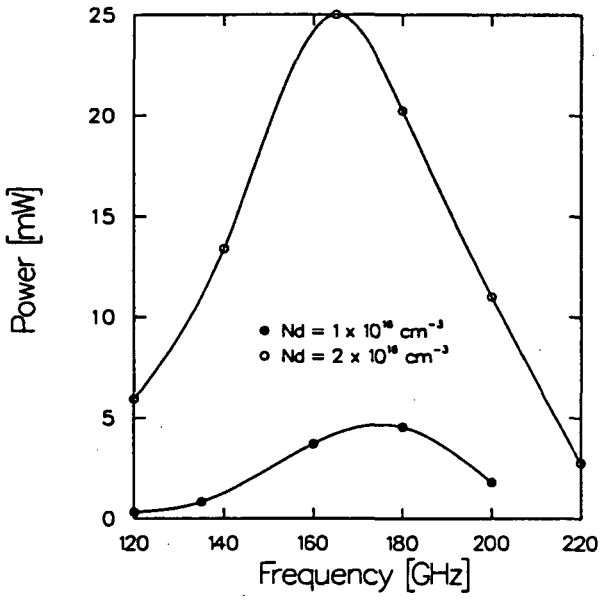

Figure 5: Power versus frequency for a 1.0 μm long InP Gunn device. Vdc = 4.5 V, Vrf = 0.5 V, R_L = 2 Ω, T = 450 K.

and a matching load of 2 Ω.

Figure 6 shows the efficiency versus frequency for the three structures. The efficiency is increasing as the doping profile becomes steeper. At 180 GHz, structure 3 results in 2 % efficiency which is twice the efficiency obtained from structure 1. A comparison of the output power is shown in Figure 7. The optimum frequency for power generation is 160 GHz where structure 3 resulted in 73.4 mW compared with 8.6 mW for structure 1. The DC current density in structure 3 is 5.18×10^4 A.cm^{-2} compared with 3.84×10^4 A.cm^{-2} in structure 1 at 160 GHz. This increase in the current density is much smaller than the corresponding increase in the 2×10^{16} cm^{-3} doped structure. Structure 4 has higher efficiencies than structure 3 but the current is also higher. For diodes with a mesa diameter of 30 μm or larger, structure 3 is likely to be the optimum design for operation at 160 GHz.

The graded doping profile results in a higher electric field near the cathode and a lower field near the anode due to electron diffusion toward the lower doped region. This change in the field has two consequences: first, a higher cathode field results in a larger fraction of the electrons transferring to the upper valleys, second, a lower anode field permits application of a larger DC bias without breakdown. The electric field in structure 1 peaks at 125 kV.cm^{-1} near the anode side whereas the field in structure 4 is less than 100 kV.cm^{-1} at the anode.

In addition to improving the efficiency and reducing the field at the anode, a graded doping profile provides a modest increase in the current density. The graded doping profile can provide the same performance as the flat doped profile with a smaller current density. The reason is that the higher fraction of the electron population transferring to the upper valleys in the graded structure results in a reduction of the average velocity. This is not the case for the structure with a flat doping where an increase in the carrier density does not alter the distribution of the field across the structure. Figure 8 compares the current

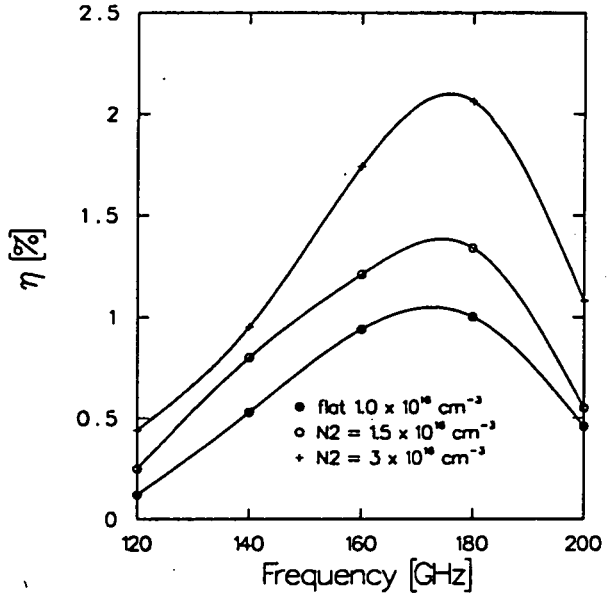

Figure 6: Efficiency versus frequency for a 1.0 μm InP Gunn device. Vdc = 4.0 V, Vrf = 1.0 V, RL = 2 Ω, T = 450 K.

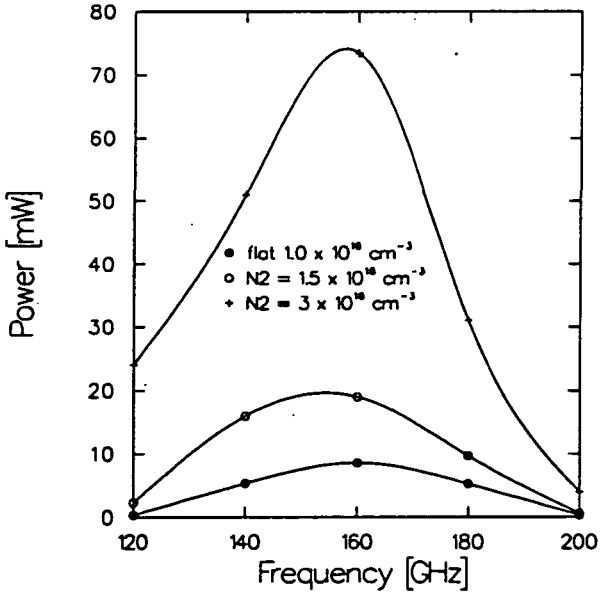

Figure 7: Power versus frequency for a 1.0 μm InP Gunn device. Vdc = 4.0 V, Vrf = 1.0 V, RL = 2 Ω, T = 450 K.

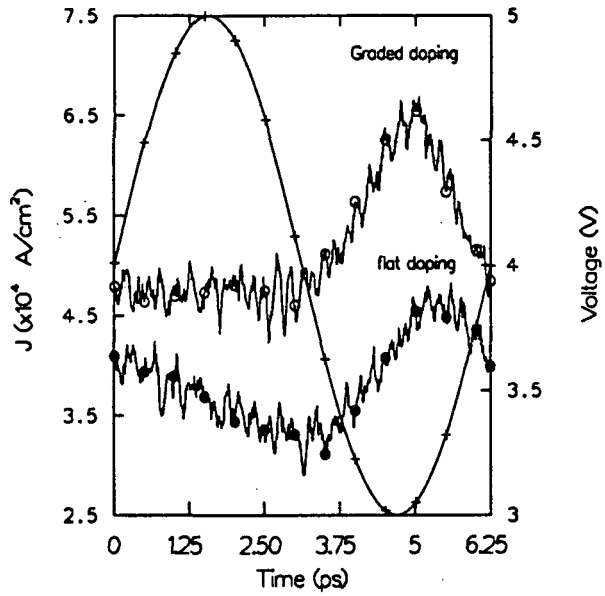

Figure 8: Comparison of the current density in structure 1 and structure 3 at 160 GHz. Vdc = 4.0 V, Vrf = 1.0 V, T = 450 K.

waveforms in one RF period as obtained from structure 1 and structure 3. The current density in structure 3 resembles a pulse 180 degrees out of phase with the RF voltage whereas in structure 1, it is more sinusoidal and is not perfectly out of phase. This shows that structure 3 is more efficient and the space charge layers are more developed.

To verify that the highly doped side of the active region should be at the anode side for best performance, structure 3 was considered with the opposite polarity. Figure 9 shows a comparison of the output power as a function of frequency. The structure with the doping decreasing toward the anode contribute to much smaller output power levels when compared with structure 3. An examination of the electric field revealed a peak electric field near the anode close to 200 kV.cm^{-1} compared with 100 kV.cm^{-1} in structure 3. In addition the current density is higher, at 160 GHz it has a average value of 6.9×10^4 A.cm^{-2} compared with 5.2×10^4 A.cm^{-2} in structure 3.

6 InP GUNN DEVICE TECHNOLOGY

Among the many techniques used for fabricating Gunn devices, the most common are based on the Integral Heat Sink process (IHS) [7, 8] or the flip-chip process [9]. In the IHS process, the heat sink is formed as an integral part of the diode. The wafer front side is metallized and plated with copper, silver, or gold to a thickness of several thousands of an inch. The substrate is chemically or mechanically thinned to a thickness of 10 μm to 15 μm . Next, ohmic contacts are metallized and standard photoresist techniques are used to define the mesas. Individual chips are then mounted in standard packages. In the flip-chip process the mesas are defined on the epitaxial side. The mesa chip is then flipped and mounted on a heat sink pedestal. Finally, the substrate is thinned to about 100 μm .

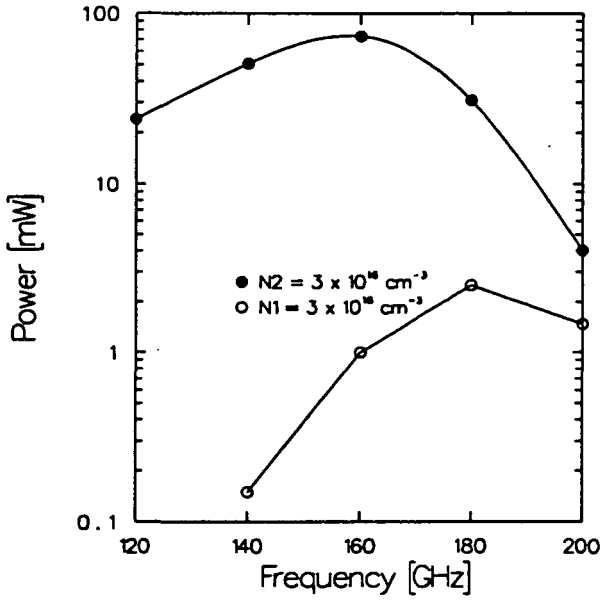

Figure 9: Comparison of the power versus frequency for structure 3 with different bias polarities . Vdc = 4.0 V, Vrf = 1.0 V, RL = 2 Ω, T = 450 K.

These two processing techniques have been used successfully for fabricating Gunn devices in the W-band. At higher frequencies, it is necessary to reduce further the substrate thickness to minimize the series resistance. In addition, the smaller size of the mesas presents new challenges to the bonding procedure. In this chapter a new fabrication technology allowing the complete removal of the substrate is developed. This process is an extension of the integral heat sink technique with the additional step of plating the top contact to facilitate bonding.

Figure 10 shows the epitaxial layers of an unprocessed InP wafer. The different layers, starting from the n^+ doped substrate consist of

- an n^+ InP substrate,
- a 0.5 μm n^+ InGaAs layer doped at 2.0×10^{18} cm^{-3},
- a 0.6 μm n^+ InP contact layer doped at 2.0×10^{18} cm^{-3},
- a 1.0 μm n InP active region doped doped at 1.0×10^{16} cm^{-3},
- a 0.2 μm n^+ InP contact layer doped at 2.0×10^{18} cm^{-3}, and
- a 0.1 μm n^+ InGaAs cap layer doped at 2.0×10^{18} cm^{-3}.

Prior to processing the wafer, the doping profile in the active region is characterized through C-V measurements. To perform these measurements, the top n^+ InGaAs and InP layers are chemically etched from a small sample so that Schottky contacts can be formed. The processing sequence for Gunn device fabrication is shown in figure 11 and described below.

6.1 Island Definition and Integral Heat Sink Formation

The first step consists of defining square islands approximately 400 μm $\times$ 400 μm in size separated on all sides by 100 μm wide trenches. These trenches are etched down to the InGaAs etch-stop layer. An n-ohmic contact (Ni/Ge/Au/Ti/Au) is evaporated over the whole surface and then gold is plated to a thickness of 25 μm to form the integral heat sink. The top InGaAs cap layer reduces the contact resistance [10] of the ohmic contact because InGaAs has a lower bandgap than GaAs. The isolation provided by the trenches is helpful in reducing the cracking of the semiconductor epilayers during the annealing process. Cracks occur because the gold heat sink and the InP semiconductor have different thermal expansion coefficients. Figure 11(a) shows a cross section of the sample at the end of the gold plating.

6.2 Substrate Thinning and Top Contact Definition

The InGaAs layer, referred to as an etch-stop layer, permits the complete removal of the substrate by chemical etching. The chemical solution HCl:H_2O (4:1) selectively etches InP and does not etch InGaAs. Once the substrate is removed, the InGaAs etch-stop layer is etched away using H_3PO_4:H_2O_2:H_2O (1:1:8) which does not attack the InP n^+ region. Standard lift-off techniques are used to define circular diodes with sizes varying from 30 to 65 μm in diameter which are then metallized to form n-ohmic contacts. Figure 11(b) shows a cross section of the sample after the substrate thinning and the heat sink formation.

6.3 Gold Plating of Top Contacts

In the standard IHS technique, the next step would be to etch the mesa. However problems in bonding have been encountered due to the thin ohmic contact. A thick ohmic contact is obtained by plating gold on top of the evaporated ohmic contacts. A conductive metal layer is needed to electroplate uniformly over all the contacts. A Ti/Au/Ti layer is evaporated over the whole surface, then an alignment over the ohmic contacts is used to open holes in a thick photoresist (3 μm). The photoresist is removed from a small region at the edge of the sample. The exposed Ti layer is also removed in Buffered HF and the sample is plated for a thickness of 2 μm - 3 μm. Figure 11(c) shows a cross section of the sample after the plating step.

6.4 Mesa Definition and Annealing

The final step before mounting individual chips consists of etching the mesas and annealing the ohmic contacts. The final structure is shown in figure 11(d).

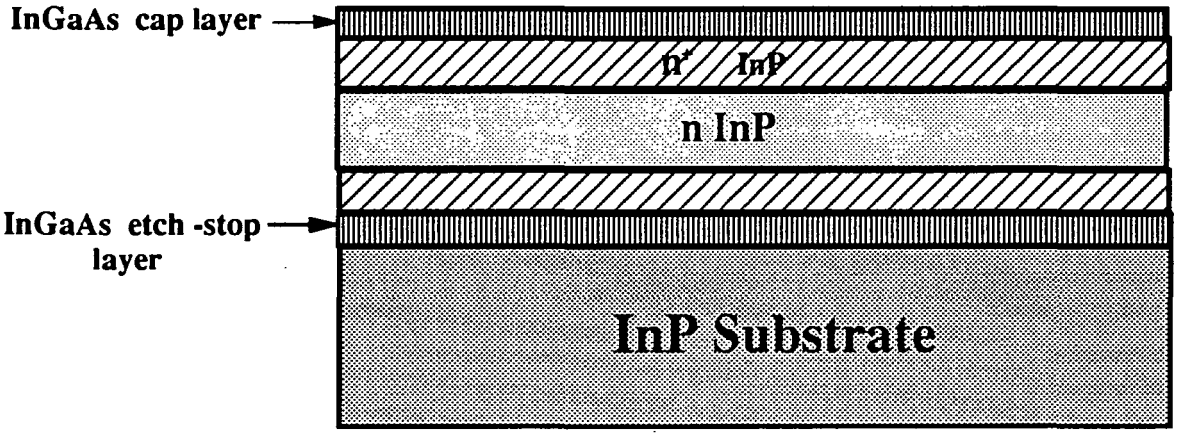

Figure 10: InP Gunn structure

7 Conclusions

A new method has been developed for estimating the material parameters used in the Monte Carlo model. By comparing simulation and experimental results in the W-band, we obtained more accurate material parameters. *Lower* values for the intervalley energy separation and *higher* values for the deformation potentials than stated in the literature were used. A possible explanation for these trends is the high operating temperature of the Gunn device which perturbs the band-structure.

Using these parameters, it was shown that it is possible to operate fundamental mode InP Gunn devices in the D-band. The performance of a flat doped structure can be considerably improved by employing a graded doping profile in the active region. Specifically, a linearly graded doping increasing from the cathode toward the anode improves the conversion efficiency, the output power, reduces the electric field at the anode, and results in a smaller current density compared with a flat profile. A structure with a doping decreasing toward the anode is not desirable because it increases the electric field at the anode and does not reduce the dead zone. As a result, the device breaks down at lower voltages and the performance is degraded.

A processing technology for GaAs and InP Gunn devices has been developed based on the integral heat sink processing technique. An Etch-stop layer between the substrate and the epilayers was included in the wafer design in order to completely remove the substrate and obtain better uniformity across the chip. InGaAs cap layers were used to reduce the contact resistance. A process was developed for plating the top contacts with gold to facilitate bonding.

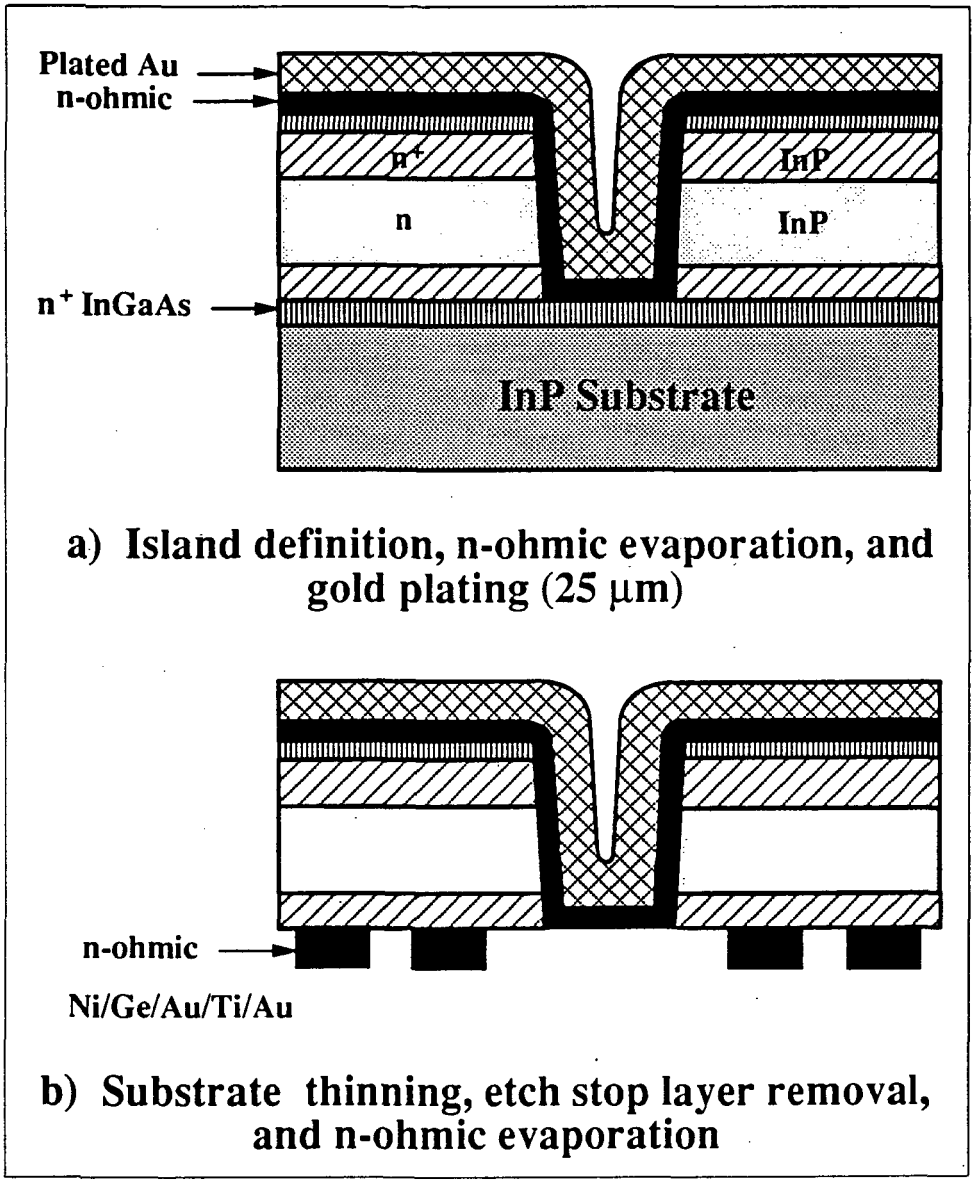

Figure 11: Processing sequence for InP Gunn fabrication

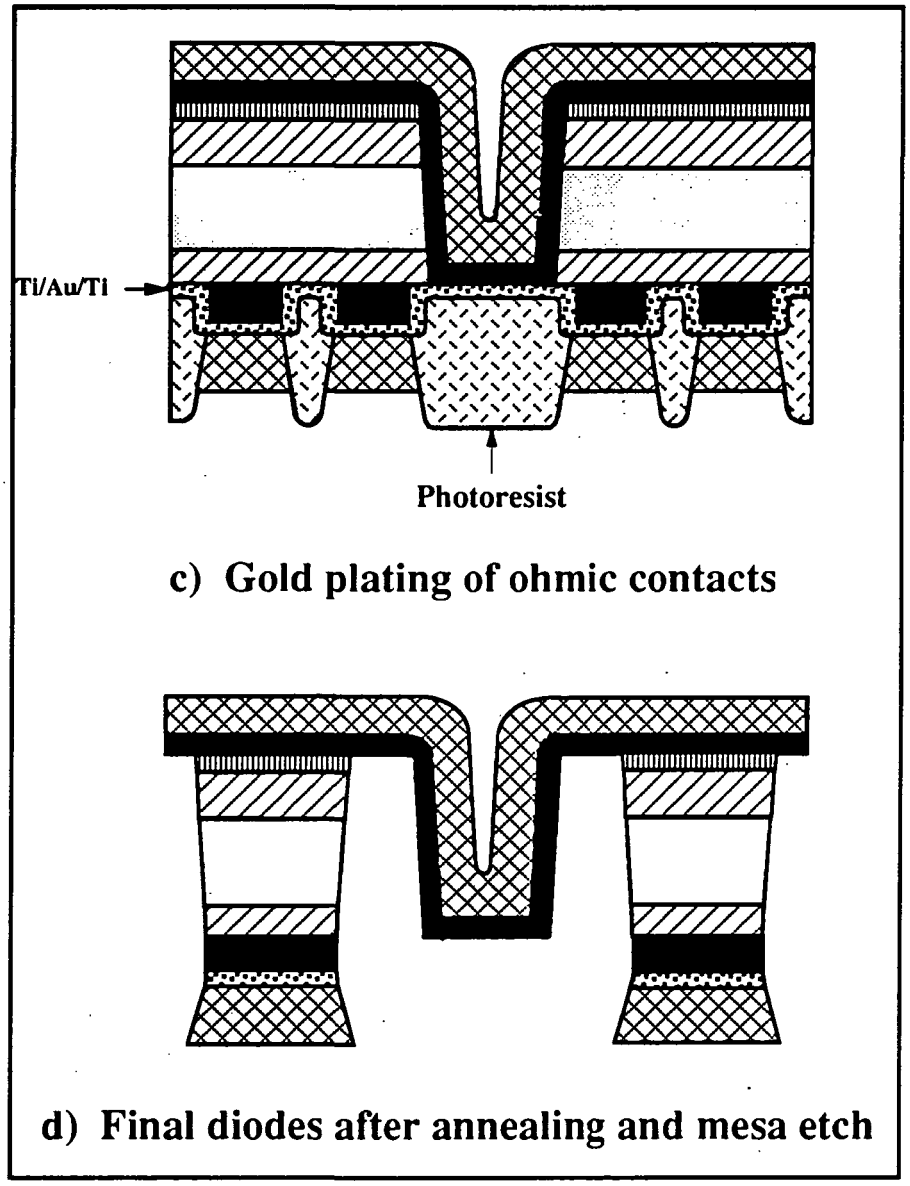

Figure 11: Cont. Processing sequence for InP Gunn fabrication

References

[1] W. Fawcett, A. D. Boardman and S. Swain,"Monte Carlo Determination of Electron Transport Properties in Gallium Arsenide," *J. Phys. Chem. Solids,* **30**, 1969, pp. 643.

[2] K. Brennan, K. Hess, J. Y. Tang, and G. J. Iafrate, "Transient Electronic Transport in InP Under the Condition of High-Energy Electron Injection," *IEEE Trans. on Electron Dev.,* **ED-30**, 12, pp. 1750-1753, Dec. 1983.

[3] D. C. Herbert, W. Fawcett, and C. Hilsum, "High Field Transport in Indium Phosphide," *J. Phys. C: Solid State Phys.,* Vol. 9, pp. 3969-3975, 1976.

[4] G. H. Glover, "Study of Electron energy Relaxation Times in GaAs and InP," *J. Appl. Phys.,* **44**, No. 3, pp. 1295-1301, March 1973.

[5] T. J. Maloney, and J. Frey, "Transient and Steady-State Electron Transport Properties of GaAs and InP," *J. Appl. Phys.,* **48**, No. 2, pp. 781-787, Feb. 1977.

[6] M. V. Fischetti, "Monte Carlo Simulation of Transport in Technologically Significant Semiconductors of the Diamond and Zinc-Blende Structures-Part I: Homogeneous Transport," *IEEE Trans. on Electron Dev.,* **ED-38**, No. 3, pp. 634-649, March 1991.

[7] R. A. Zettler, and A. M. Cowley, "Batch fabrication of Integral-Heat Sink IMPATT Diodes," *Electronics Letters*, Vol. 5, No. 26, pp. 693-694, Dec. 1969.

[8] S. Y. Narayan, J. P. Paczkowski, "Integral Heat Sink Transferred Electron Oscillators," *RCA Review*, Vol. 33, pp. 752-765, Dec. 1972.

[9] A. Paolella, R. L. Ross, and J. Ondria, "Advanced mm-Wave Sources by Automated MBE," *Microwave Journal*, p. 149, April 1986.

[10] J. M. Woodall, J. L. Freeouf, G. D. Pettit, T. Jackson, and P. Kirchner, "Ohmic Contacts to n-GaAs using Graded Band Gap Layers of $Ga_{1-x}In_xAs$ Grown by Molecular Beam Epitaxy," *J. Vac. Sci. Technol.,* **19**, No. 3, Sept./Oct. 1981, p. 626.

Recent Advances in Superconducting-Mixer Simulations

S. Withington and P.R. Kennedy
Cavendish Laboratory,
University of Cambridge,
England.

March 22, 1992

1 Introduction

Over the last few years, considerable progress has been made in the development of techniques for fabricating high-quality superconducting circuits, and this success, together with major advances in the theoretical understanding of quantum detection and mixing at millimetre and submillimetre wavelengths [1], has made the development of CAD techniques for superconducting nonlinear circuits an important new enterprise. For example, arrays of quasioptical mixers are now being manufactured, where the antennas, matching networks, filters and superconducting tunnel junctions are all fabricated by depositing niobium and a variety of oxides on a single quartz substrate. There are no adjustable tuning elements on these integrated circuits, and therefore, one must be able to predict their electrical behaviour precisely. This requirement, together with a general interest in the generic behaviour of devices such as direct detectors and harmonic mixers, has lead us to develop a range of CAD tools for simulating the large-signal, small-signal, and noise behaviour of superconducting tunnel junction circuits.

2 Large-signal analysis

To model the behaviour of a quasiparticle mixer, it is first necessary to simulate the large-signal steady-state dynamics of the local-oscillator circuit. Once the large-signal operating point is known, it is then possible to perturb, either numerically or analytically, the underlying system of equations to gain information about the linear relationships between signal and noise variables.

The main problem is how does one calculate the periodic current that flows through a tunnel junction when a periodic voltage is applied? For semiconductor devices this calculation is almost always carried out in the time domain, and fast Fourier transforms are used to interface the terminal waveforms to the frequency-domain description of the embedding circuit.

Classical resistive mixer diodes are relatively easy to simulate because the induced current is an instantaneous function of the terminal voltage. Quantum mixer diodes on the other hand are difficult to simulate because the tunnelling current depends on the voltage that was across the junction at very long times in the past. In the time domain

the current is calculated through an integral which is similar to the convolution integral of linear systems theory, and the tunnel junction is characterised by a response function which oscillates at the gap frequency with an envelope which decays inversely with time at large times. To evaluate the tunnelling current it is necessary to sample the terminal voltage at a rate greater than the gap frequency , and to integrate beyond a limit which is inversely related to the voltage width of the dc nonlinearity. Time-domain simulations are useful for studying the switching behaviour of tunnel junctions, but they are inappropriate for studying the steady-state behaviour of RF circuits.

When a sinusoidal potential is applied to a superconducting tunnel junction, the wave-functions associated with the quasiparticle states on one side of the barrier are coherently phase modulated. The spectrum of the phase factor is a comb of delta functions whose coefficients are the elements of a Bessel-function sequence. The Bessel functions have the same argument, determined by the voltage drive level, and consecutive orders ranging from some large positive integer to the same negative integer. The trick is to recognize that when a periodic potential is applied, the spectrum of the overall phase factor is the convolution of the spectra associated with the individual harmonic contributions. Once the spectrum of the overall phase factor is known, it is possible to calculate the harmonic phasors of the tunnelling current from the dc I-V curve and its Hilbert transform [2].

The above procedure describes a way of calculating the periodic current that flows in a tunnel junction when a periodic potential is applied. In a real circuit the tunnel junction is embedded in a linear network and the problem of determining the various voltages and currents is complex. Applying the method of harmonic balance [3] to a generic circuit comprising a tunnel junction and a Thévenin voltage source, leads to a system of coupled nonlinear algebraic equations. Mathematically, the problem then consists of finding the roots of these equations; electrically, the problem is equivalent to searching for a waveform that simultaneously satisfies the circuit equations at every harmonic frequency. In nonlinear CAD terminology, the scheme is a frequency-domain spectral-balance method, however, unlike other versions, the spectral decomposition is based on device physics, rather than on expanding the terminal behaviour in a set of basis functions.

The set of algebraic equations that results from applying the method of harmonic balance to a tunnel-junction circuit must, in general, be solved numerically. By repeatedly analyzing, in different ways, a large pseudo-random set of tunnel-junction circuits, we have investigated the speeds and stabilities of a range of iterative root-finding techniques. A comparison of the techniques is shown in Fig. 1, where we have plotted the percentage of circuits that converge, and the mean number of iterations taken, as a function of the damping factor. The damping factor is a coefficient between 0 and 1 which determines the degree to which the result of an iteration influences the next guess. A small value improves stability at the expense of reducing the rate of convergence. The solid and dashed lines in Fig. 1 correspond to two different quality characteristics. It should be appreciated that the plots represent a total of around 20,000 circuit simulations.

The tunnel junction is a nonlinear admittance in the sense that it is most easy to calculate the current in terms of the terminal voltage. However, fixed-point voltage-update methods [4] are inappropriate for analyzing tunnel-junction circuits, especially in a common-user environment, because they fail to converge when the large-signal harmonic admittances of the tunnel junction are much greater than those of the embedding circuit. This problem is clearly demonstrated in Fig. 1 where it is seen that the routine will only converge if the system is heavily damped. A slightly more sophisticated way of finding the roots is

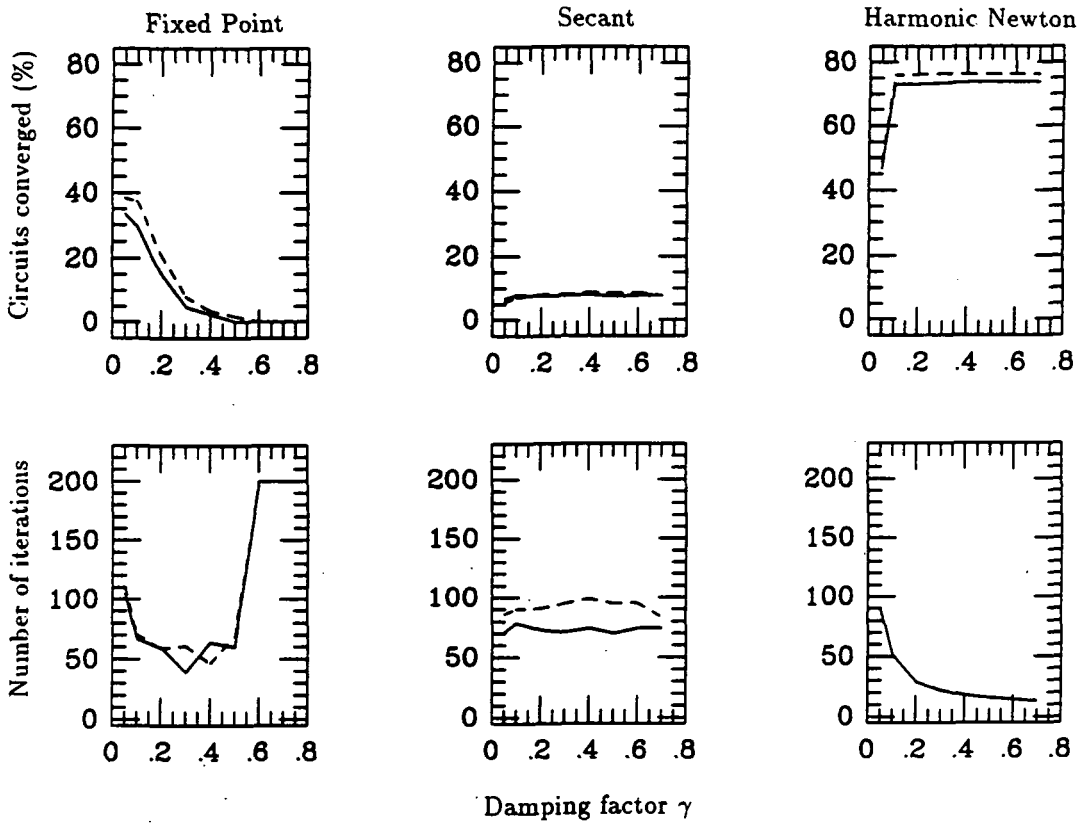

Figure 1: Comparison of various techniques for calculating the large-signal quantum behaviour of superconducting tunnel-junction circuits.

to use a multi-dimensional variant of the secant method [5]. This method is similar to the fixed-point method, in the sense that it is only necessary to calculate the tunnelling current once per iteration, however, because coarse derivative information is included one might expect the routine to behave more reasonably. Somewhat surprisingly, the routine is significantly worse despite the additional information. The problem is caused by the fact that, effectively, only the terms on the leading diagonal of the Jacobian matrix are included, and coupling between harmonics relies on the current calculations. As long as the current at a given harmonic is most strongly influenced by the voltage at the same harmonic then the routine will work well. In a highly nonlinear tunnel-junction circuit, however, there is strong coupling between harmonics and the routine is inadequate. Fig. 1 shows the behaviour of a harmonic-Newton [6] [7] scheme where the full Jacobian matrix is used. It is possible to calculate the Jacobian matrix analytically, however, we prefer to calculate the Jacobian matrix using finite differences. Harmonic Newton results in the least number of failures; in fact, it finds a solution for 75 % of the circuits studied, and to a large extent the stability of the method is independent of the quality of the junction being investigated. The fact that the convergence parameter has little effect on this fraction, together with the almost reciprocal dependence of the mean number of iterations, shows that if it is possible for the method to find a solution then it will eventually do so. Reducing the damping factor

simply reduces the size of the voltage steps taken at each iteration, however, these steps are usually in the correct direction.

We have now performed a very large number of real circuit simulations, and despite the fact that 25 % of the randomly generated circuits failed to converge, we have never come across a real circuit that has not converged. We have investigated this problem in some detail, and we have found that many of the circuits that do not converge are behaving in a non-periodic manner. This behaviour usually requires that the embedding circuit impedances are very much larger than the normal-state resistance.

An alternative approach to finding a root in many dimensions is to recast the problem into a multidimensional optimization. To do this change, the error function is used to construct a scalar quantity that has a global minimum at the required root. One of the attractions of optimization is that uninteresting variables, such as the local oscillator drive level, can be eliminated from the analysis by making the variable part of the objective function. In general, we have found that optimization methods are slow and should not be used unless there is a particular reason to do so. Unfortunately, there is insufficient time to discuss this more advanced topic in this short paper.

The results of a typical large-signal analysis are shown in Fig. 2. The sequence of plots shows how the pumped dc I-V curve of a typical Nb-AlOx-Nb tunnel junction evolves as the ωCR product is changed. As the capacitance decreases the subgap current increases, and non-classical negative differential resistance is induced on a number of photon steps. Notice that large capacitances are required before the characteristic relaxes to its constant sinusoidal-voltage-driven form. Also shown, for comparison, is an analysis where the harmonic feedback is turned off. Curiously, it seems as if internal harmonic pumping can enhance the negative differential resistance induced on high-order photon steps—for this reason it is possible, in certain circumstances, for the small-signal behaviour of a mixer to be very sensitive to harmonic impedance levels.

3 Small-signal analysis

Once the large-signal behaviour of a mixer has been established, it is possible to calculate the small-signal and noise performance. The admittance and noise-current correlation matrices are determined, in the usual way, through quantum-mechanical generalizations of commonly used classical concepts. We then use a selection of linear transforms to reduce the admittance parameters to two-port impedance and scattering parameters, and the current correlation matrix to a noise-temperature matrix from which the standard two-port noise parameters can be deduced [8] [9]. It transpires that the whole scheme, both signal and noise, can be very elegantly normalized to the gap voltage and gap current of the tunnel barrier. The advantages of our generalized approach are that one does not have to specify before hand which ports are to be used for the input and output, and one can easily calculate the two-port small-signal and noise parameters which can then be loaded into proprietary microwave circuit simulators for further analysis. For example, we are interested in designing mixers that have the first stage of low-noise IF amplification in the mixer block. A further advantage of our scheme is that the noise performance is described in terms of correlated travelling noise waves, and this approach is an elegant way of considering a mixer as an integral part of a quasioptical system along which noise waves propagate.

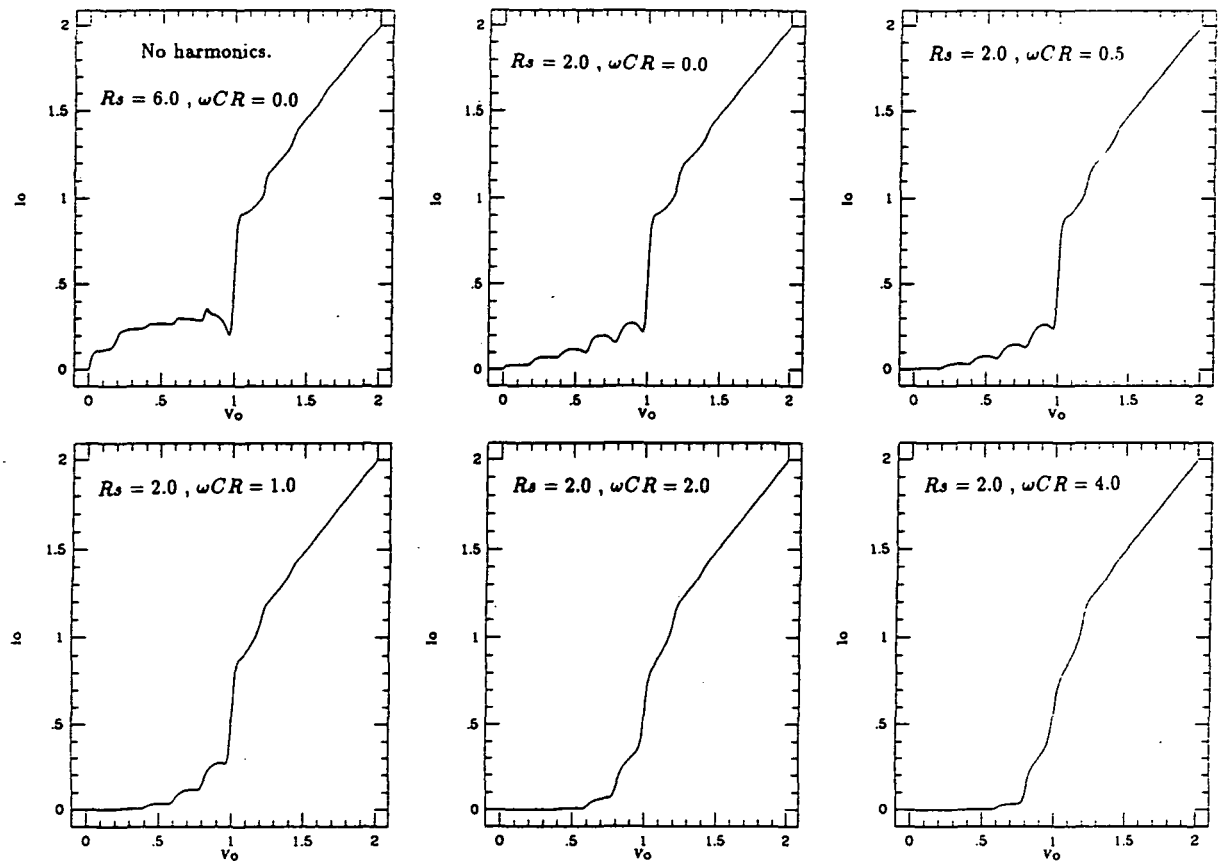

Figure 2: The dc I-V curve of a pumped Nb-AlOx-Nb tunnel junction for different values of ωCR product. The first plot does not include internal harmonic pumping.

4 Mixer simulations

To date we have studied the large-signal, small-signal, and noise behaviour of mixers by adopting the design procedure suggested by Kerr [10]. That is to say, the mixer is operated in a double-sideband mode, and the source and load impedances are assumed to be real. The ratio of the source and load impedances, which in practice is determined by the geometry of the mount, is set at some fixed value. In general, we use a value of unity as a higher value tends to degrade the input return loss of the mixer. It is interesting to note, however, that it may be possible to choose the ratio so as to minimize the sensitivity of the gain to variations in the source resistance. The free parameter, as far as the design process is concerned, is the normal-state resistance. Although we assume that the capacitance of the tunnel junction is tuned out at the fundamental, we assume that the impedance at the harmonics is given by the capacitance of the tunnel junction alone. The effects of junction capacitance are considered in companion paper [11], here we simply demonstrate the procedure by plotting, in Fig. 3, the transducer gain, noise temperature, input return loss, and normalized output impedance of a typical Nb-AlOx-Nb mixer as a function of the normalized source resistance; the various curves are for different normalized frequencies (normalized to the gap frequency). It is interesting to note that the overall performance is

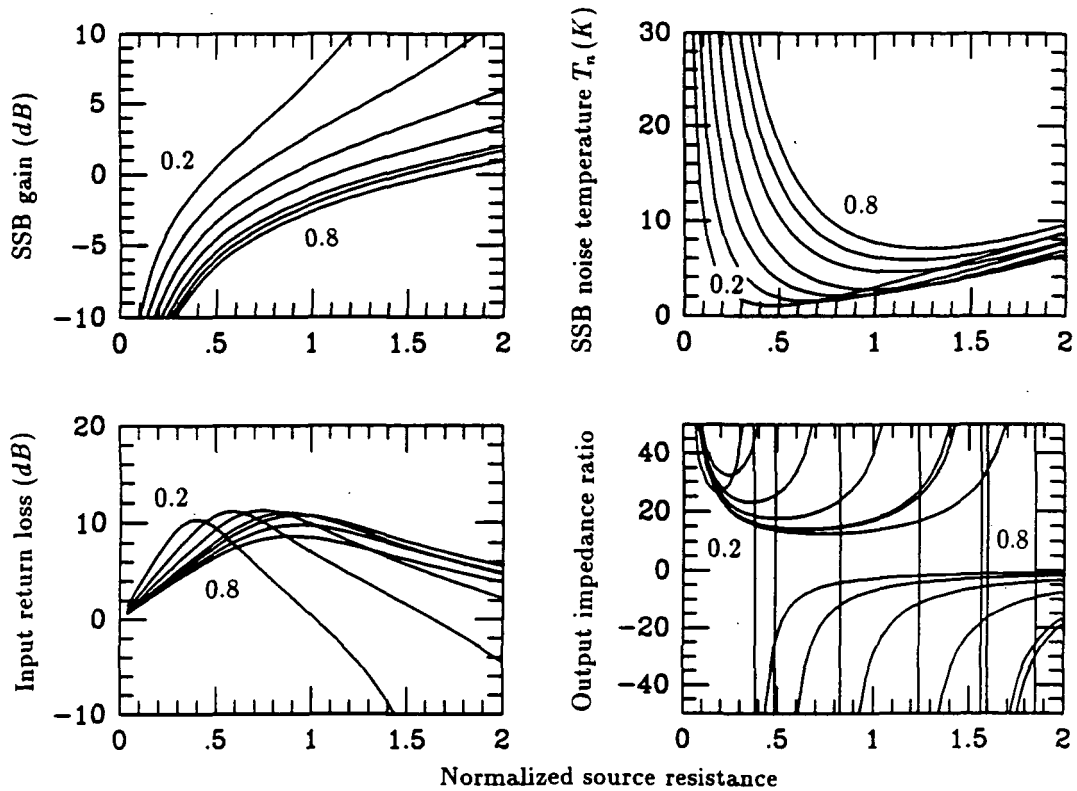

Figure 3: The transducer gain, noise temperature, input return loss, and normalized output impedance of a typical Nb-AlOx-Nb mixer as a function of the normalized source resistance.

very poor for low values of source resistance, and this is probably the single most important reason why mixer performances improve significantly when integrated tuning elements are used.

A useful normalized expression can easily be derived for the source resistance at which unity gain, good input match, and minimum noise temperature can be achieved. The expression is

$$\frac{R_n}{R_s} = 0.5V_{PH}^{-0.92} = 78\left[\frac{f(GHz)}{V_g(mV)}\right]^{-0.92} \quad (1)$$

and it applies for frequencies between 0.2 and 0.8 of the gap frequency. The exponent is slightly different from that given by Kerr and Pan, because we have taken into account the fact that the optimum bias point does not remain in the middle of the first photon step below the gap for frequencies greater than about 0.5 of the gap frequency.

It is well known that if one plots the conversion gain, at a given frequency, as a function of the ωCR product, at some point the conversion gain becomes depressed. This can be regarded as the frequency at which harmonic effects become significant; or equivalently, the frequency at which the five-port, rather than the three-port model should be used. Using the above value for the source resistance, we have investigated this behaviour and generated

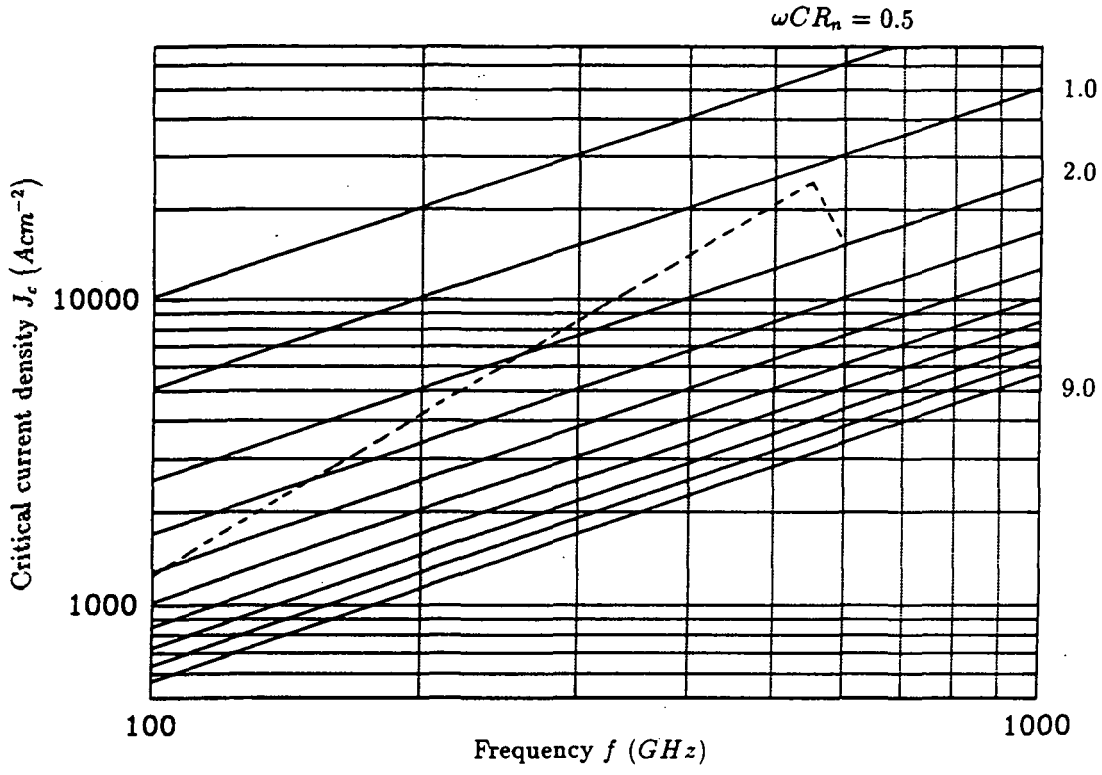

Figure 4: Critical current density against frequency for different values of ωCR product. The dotted line shows the optimum current density as a function of frequency.

the following expression for the optimum ωCR product

$$\omega CR\,|_{opt} = V_{PH}^{-0.75} = 61\left[\frac{V_g\,(mV)}{f\,(GHz)}\right]^{0.75}, \qquad (2)$$

and this in turn generates the following expression for the optimum value of the critical current density: $J_c\,(Acm^{-2}) = 0.4f\,(GHz)^{1.75}$. We have assumed $I_cR_n = 1.8mV$ and a specific capacitance of $45fF\mu m^{-2}$. Once again the above requirement is less severe than that published by Kerr. Finally, in Fig. 4 we plot the optimum critical current density as a function of frequency, and we show lines of constant ωCR product. Above the dotted line, harmonic effects are important, whereas below the dotted line harmonic effects can be ignored.

References

[1] J.R. Tucker and M.J. Feldman, "Quantum detection at millimetre wavelengths," Rev. Mod. Phys., vol. 57, pp.1055-1113, 1985.

[2] S. Withington and E.L. Kollberg, "Spectral-domain analysis of harmonic effects in superconducting quasi-particle mixers,"IEEE Trans. Microwave Theory Tech., vol. MTT-37, pp. 231-238, 1989.

[3] K.S. Kundert and A. Sangiovanni-Vincentelli, "Simulation of nonlinear circuits in the frequency domain,"IEEE Trans. Computer-Aided Design, vol. CAD-5, pp. 521-535, Oct. 1986.

[4] R.G. Hicks and P.Kahn, "Numerical analysis of nonlinear solid-state device excitation in microwave circuits," IEEE Trans. Microwave Theory Tech., vol. MTT-30, pp. 251-259, Mar. 1982.

[5] C. Camacho-Peñalosa, "Numerical steady-state analysis of nonlinear microwave circuits with periodic excitation,"IEEE Trans. Microwave Theory Tech., vol. MTT-31, pp. 724-730, Sep. 1983.

[6] C.-Y.E. Tong and R. Blundell, "Simulation of superconducting quasiparticle mixer using a five-port model," IEEE Trans. Microwave Theory Tech., vol. MTT-38, pp.1391-1398, Oct. 1990.

[7] S. Withington and P. Kennedy, "Numerical procedure for simulating the large-signal quantum behaviour of superconducting tunnel-junction circuits," Proc. IEE, part G, vol. 138, pp. 70-76, Feb. 1991.

[8] S. Withington, "Scattered noise waves in microwave and millimetre-wave networks,"Microwave Journal, vol. 32, pp. 169-178, 1989.

[9] L.R. D'Addario, "Noise parameters of SIS mixers," IEEE Trans. Microwave Theory Tech., vol. MTT-36, pp. 1196-1206, July 1988.

[10] A.R. Kerr and S.-K. Pan, "Some recent developments in the design of SIS mixers," Infrared and MIllimetre Waves, vol. 11, pp.1169-1187, 1990.

[11] A.R. Kerr, S.-K. Pan, and S. Withington, "Embedding impedance approximations in the analysis of SIS mixers," Proceedings Space Terahertz Conference, 1992.

SUBMILLIMETER WAVE DETECTION WITH SUPERCONDUCTING TUNNEL DIODES

Michael J. Wengler
University of Rochester

ABSTRACT

Superconductor-Insulator-Superconductor (SIS) diodes are the detector elements in the most sensitive heterodyne receivers available from 100 to 500 GHz. SIS mixers are the front end of radio astronomical systems around the world. SIS mixer technology is being extended to 1 THz and higher frequencies for eventual use on spaceborne astronomical experiments.

Here is a short review of submillimeter SIS mixers. The role of impedance matching in the proper design of an SIS mixer is described. A variety of methods for achieving good impedance match at submillimeter frequencies are presented. The experimental state of the submillimeter SIS mixer art is described and summarized.

1. INTRODUCTION

Twelve years ago, the first descriptions of mixing on a superconducting tunnel diode called a Superconductor-Insulator-Superconductor (SIS) were published [1, 2] . At about the same time, a comprehensive theoretical investigation of the SIS made clear that SIS's respond to photons at millimeter and submillimeter wavelengths [3]. The SIS has become the instrument of choice for millimeter spectroscopic radio astronomy, finding use on radio telescopes around the world [4-13]. Since the discovery of the SIS mixer, the technology for fabricating SIS circuits has improved immensely so that nearly ideal niobium devices with sub-micron feature sizes can be fabricated [14-20]. Recently, the high performance of SIS mixers has been extended to submillimeter wavelength radio astronomy [8, 21-23, 20, 24].

This paper is a shortened version of a review published elsewhere [25]. The full review includes an in-depth introduction to the field of SIS mixing. An excellent and comprehensive earlier review of both theory and experiment is that of Tucker and Feldman [26]. Reviews of the state of the art of SIS mixers have appeared regularly [27-30]. Other reviews include both SIS mixers and competing receiver technologies used in radio astronomy [31, 32].

2. RF ADMITTANCE OF THE SIS

The SIS mixer has two important rf input admittances. The first one is Y_{LO}, the admittance the SIS presents to the LO. The second is Y_{IN}, the admittance the SIS mixer presents at the signal frequency. Because the signal power must always be much less than the absorbed LO power for a mixer to avoid saturation, it is useful to think of Y_{LO} as the "large signal admittance" of the SIS, and Y_{IN} as the "small signal admittance."

For a submillimeter SIS mixer, Y_{LO} is generally quite close to G_N, the dc normal state admittance of the SIS. Y_{LO} is nearly constant over the range of useful dc and LO biasing conditions. Y_{LO} is completely independent of the signal, image, LO, and harmonic source admittances to which the SIS is coupled. In fact, Y_{LO} is the admittance presented by the SIS seen as a passive absorber of radiation.

Y_{IN}, on the other hand, is a highly variable quantity. It does change with all of the parameters mentioned above. It is possible for Y_{IN} to have a negative real part, while Y_{LO} must always have a positive real part. For this reason, Y_{IN} must be interpreted as the input admittance of the SIS viewed as an active device powered by the LO.

2.1. SIS Parasitic Capacitance

In submillimeter SIS mixers, a dominant part of the SIS's rf admittance is due to its parasitic capacitance. The capacitance per unit area of the SIS junctions used in submillimeter mixers is nearly a constant depending only on the materials from which the junctions are made. Numbers commonly used in design are 50 fF/$(\mu m)^2$ for lead alloy SIS's, and 50 to 70 fF/$(\mu m)^2$ for niobium SIS's with aluminum-oxide insulating layers.

Many mixer designers aim to minimize the SIS capacitance. In fact, many of the best SIS mixers have been built with low capacitance junctions. The lowest SIS receiver noise temperature at 230 GHz are achieved with 0.25 $(\mu m)^2$ Nb junctions with $C = 1.7 \times G_N/2\pi f$ [13]. Open-structure SIS mixers have work fairly well at their low frequency ends where $C < 1.0 \times G_N/2\pi f$ [8, 33].

However, there is some evidence that $C \approx 3 \times G_N/2\pi f$ provides more benefit than harm in a well designed SIS mixer. The reasons for this, and the value of the optimum capacitance are

discussed in these references [11, 34]. The larger capacitance seems especially important when series arrays of SIS's are used [35].

Whether or not a non-zero capacitance is helpful becomes a less important question as the operation frequency of SIS mixers is raised. All suggestions of a non-zero capacitance still have that optimum falling as f^{-1} or f^{-2}. As f is raised it becomes increasingly difficult to fabricate SIS's with C less than any of the proposed optimum values.

2.2. Optimum Signal Source Admittance: Match to Y_{LO}

The signal appears to come from a source admittance Y_S. The value of Y_S is one of the major design available to an SIS mixer designer. For submillimeter SIS mixers, the proper choice is $Y_S = Y^*_{LO}$. This choice of Y_S minimizes the SIS mixer noise temperature. This result is predicted from photodiode mixer theory [25], and also by detailed Tucker theory calculations [36].

It is paradoxical that it is not the actual small signal admittance Y_{IN} to which the mixer structure must supply a match, but the large signal LO admittance, Y_{LO}. In fact, a choice of $Y_S = Y^*_{IN}$ will maximize the SIS mixer's gain instead of its noise. Because IF amplifiers have very low noise levels, it is much more important to minimize mixer noise than to maximize mixer gain in submillimeter SIS mixers.

3. IMPEDANCE MATCHING TECHNIQUES

There are two tasks which must be accomplished to match the signal source admittance Y_S to the SIS's input admittance Y_{LO}. First, the values of Y_{LO} typical of SIS's are much larger than the source admittances presented by most antennas and waveguide structures. Second, the parasitic capacitance of the SIS must be tuned out. These two tasks can be accomplished in a few different ways. In some cases, a single tuning structure can do both of these things simultaneously.

3.1. Integrated tuning

It is a relatively simple matter to integrate tuning structures with the SIS diode in its photolithographic stage of fabrication. There are at least two layers of low loss superconductor required in SIS fabrication, which allows for various "two-wire" tuning elements. With the addition of a thick (around 2,000 Å) insulating layer, stripline tuning structures can be fabricated.

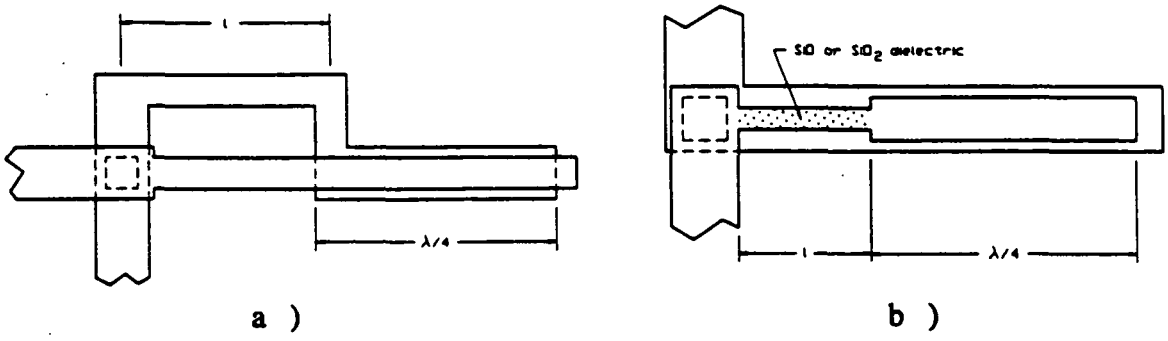

Figure 1 [38]. Two tuning structures integrated with SIS junctions. a) The sickle-shaped piece is the bottom layer of superconductor, the straight piece the top. Where the two layers overlap, they are actually separated by a thick (~2,000 Å) layer of insulator, except in the dashed square, where they come much closer to form the SIS. b) A tuning structure based entirely on microstrip.

Direct measurements of the efficacy of tuning elements in the 100-500 GHz range have been made using Fourier Transform Spectrometer (FTS) measurements [37].

The two tuning structures shown in fig. 1 are compact and simple designs proposed by Kerr, Pan, and Feldman [38]. Their primary role is to provide an inductance at the SIS which tunes out its parasitic capacitance. The structure shown in b) is particularly appropriate for higher rf frequencies. In both a) and b) structures are shown which are $\lambda/4$ in length. Here, λ refers to the wavelength associated with rf radiation propagating along the integrated tuning structure. The structures labeled with length $\lambda/4$ are designed to present a short circuit to the rf at their left ends, but are open circuited at dc and f_{IF}. In a), the tuning structure shown to be *l* long is essentially a single-turn inductor. In b), the tuning structure shown to be *l* long is a short length of high impedance microstrip. Since it is rf-shorted at one end, it presents an inductive susceptance across the SIS. The reactances associated with these structures are very small at the IF and so have no effect on the IF or dc properties of the mixer.

Using SIS circuits designed with integrated tuning, it is possible to build SIS mixers with no mechanical tuning which have excellent responsivity over an entire waveguide band at millimeter wavelengths [11, 39]. These two mixers are quite different in their design, both should be reviewed for a good appreciation of the range of integrated tuning circuitry which is possible.

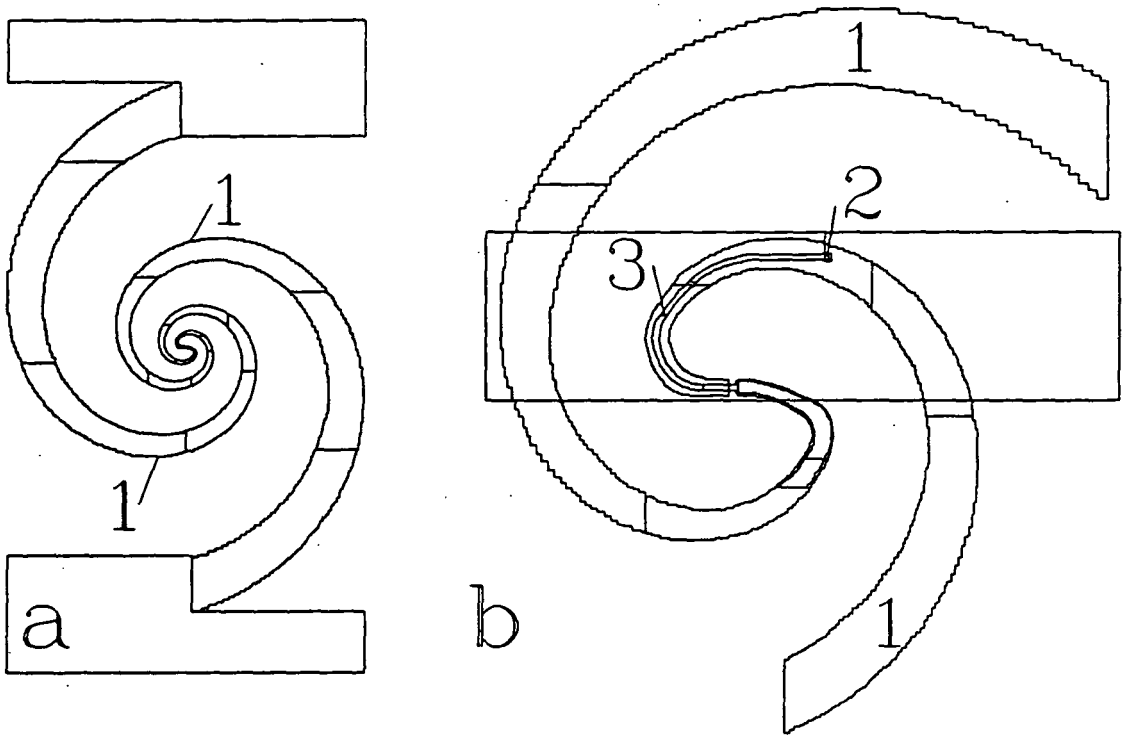

Figure 2 [40]. A spiral antenna SIS mixer with transmission line tuning. a) The radiation coupling structure is a 3.4 mm diameter spiral antenna. b) Instead of placing the SIS at the central leads of the spiral (1), a microstripline (3) is formed and the SIS (2) is placed at its end.

3.2. *Microstrip transmission line transformers*

The inductive structures shown above address only the problem of tuning out SIS parasitic capacitance. Using microstrip transmission lines, it is possible to tune out the SIS's capacitance and to lower Y_{LO} to a more convenient value.

The simplest circuit which does this is shown in fig. 2. The large-scale structure shown in a) is a spiral dipole antenna. Radiation coupled by this antenna to the antenna leads at its center has a source admittance of about $(114\ \Omega)^{-1}$. Rather than placing the SIS at the center of the antenna, the SIS is placed at the end of a microstrip transmission line as shown in b). One of the poles of the antenna is used as the ground plane for this transmission line. The transmission line has a fairly low impedance and a length chosen so that the SIS's high value of Y_{LO} is transformed down to about $(114\ \Omega)^{-1}$ where it is connected to the center of the antenna. In fact, the transmission line transformer is a little longer than a standard quarter-wave transformer so that it also tunes out the SIS's parasitic capacitance.

This simple technique can be extended in useful ways. The junction need not be placed at the end of the transmission line structure [41]. A symmetric structure with junctions and transmission lines on both antenna leads adds flexibility to design and will avoid mismatch due to the transition from a balanced mode on the antenna to an unbalanced mode on the microstrip [41]. A multi-step (Chebyshev) transformer can be used for excellent broadband performance [42]. The transformation to low impedance junctions improves the dynamic range of the mixer [41]. A tapered transmission line transformer can provide a broadband match [23].

4. SIS MIXER RESULTS

SIS mixers of some variety have been built. Niobium technology is the best current choice for submillimeter SIS's. Both waveguide and quasioptical coupling structures are useful at these high frequencies. Integrated tuning structures of increasing complexity are being used to improve mixer performance.

4.1. SIS Junction Fabrication

Many of the best SIS mixers use lead alloy SIS junctions. However, niobium and niobium alloy junctions have such great advantages that even the fabricators of lead alloy SIS's are developing niobium technology. Niobium junctions have been fabricated and used in high performance SIS mixers [15, 18, 19, 43, 13, 23]. Niobium-nitride alloy SIS's [17, 44] are interesting as they will operate at higher temperatures, and possibly higher frequencies than pure niobium SIS's.

4.2. Radiation coupling structures

A sensitive SIS mixer requires an SIS junction which is well coupled to its input radiation. The coupling structure chosen effects this in two important ways. 1) The coupling structure determines Y_S, the source admittance from which the radiation appears to come. 2) The coupling structure determines the beam pattern of the SIS mixer. A good beam pattern is essential for high efficiency coupling between the mixer and the radiation it is intended to detect. Table 1 shows the reported results of a variety of SIS mixers and receivers along with the coupling structure that each one uses.

Table 1. Summary of some of the best reported SIS receiver results. The bold lines separate the results into frequency ranges. Within a frequency range, the results are listed in order of increasing T_{RECDSB}.

Rf (GHz)	T_{REC} DSB (K)	T_{MIX} DSB (K)	Gain DSB (dB)	SIS material, size, configuration	Coupling (waveguide or antenna shape)	Reference
230	48	38	–2.6	0.25 sq. micron Nb	waveguide	[13]
230	48			Nb	waveguide	[11]
230	80	60	–2	PbBi alloy	waveguide	[7]
240	100			Nb	waveguide	[47]
228	114			PbInAu submicron	waveguide	[6]
230	116			PbInAu submicron	spiral	[8]
241	153	85	–7.5	PbInAu submicron	waveguide	[5]
228	163			PbInAu submicron	waveguide	[6]
230	200		–8	PbInAu submicron	waveguide	[10]
220	250	25	–9	SIN! (NOT an SIS)	waveguide	[48]
345	150			PbInAu submicron	waveguide	[21]
345	200			Nb	spiral	[42]
345	215			PbInAu submicron	spiral	[8]
342	214			3 PbBi in series	quasioptic	[24]
312	275		–9.5	Nb/PbInAu	waveguide	[22]
492	171	114	–9	0.25 sq. micron Nb	waveguide	[20]
426	220			Nb	spiral	[42]
490	420	240	–10	Nb	twin slot	[23]
525	470			PbInAu submicron	spiral	[8]
492	500			Nb	spiral	[42]
761	1100			PbInAu submicron	spiral	[8]

4.3. Waveguide SIS mixers

Until 1985, all SIS mixers used waveguide coupling structures. The rf input side of the mixer is almost always coupled to a scalar feedhorn [45, 46] which provides a very high quality Gaussian beam pattern. The waveguide behind the mixer usually contains a movable back short which can help tune out the parasitic reactances of the SIS and its mounting structure. In some designs, a second waveguide tuner can be included to increase the range of tuning which is possible. In other designs, no mechanical tuning is necessary.

A full height rectangular waveguide has dimensions a little smaller than $1/2 \times 1/4\ \lambda_0$ where λ_0 is the free-space wavelength at f_{rf}. At 500 GHz, this waveguide is quite small, $300 \times 150\ \mu m$. It is hard to say what the upper frequency limit is for a waveguide design. SIS's in waveguides

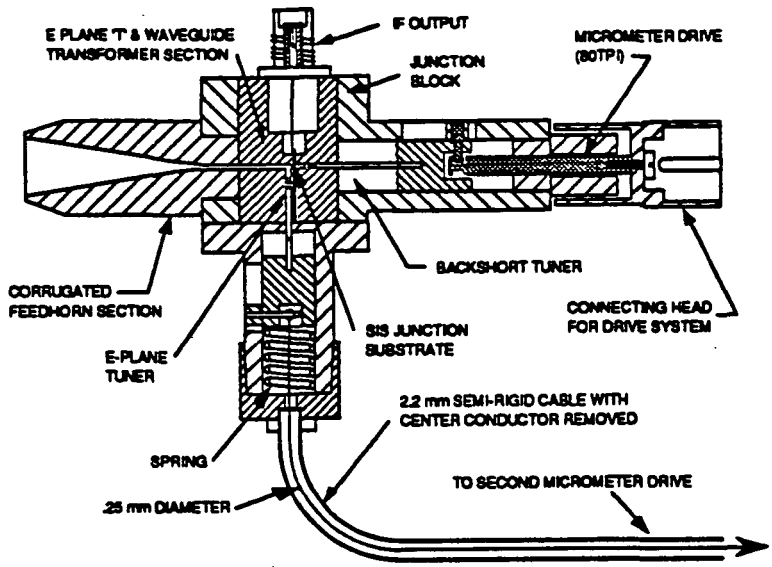

Figure 3 [6]. The two-tuner waveguide design which has been implemented for 230, 345, and 492 GHz band mixers.

are the most sensitive available mixer at 500 GHz Walker, 1991 #134]. It seems clear that waveguide designs will be attempted to at least 800 GHz.

The good features of waveguide designs are summarized. They provide excellent control over the rf source impedance seen by the SIS, either through fixed or mechanically tuned structures. They have excellent beam patterns capable of high efficiency coupling to radio telescopes and other signal sources.

4.3.1. Ellison's Waveguide Mixer

Some of the lowest noise SIS receivers for the 200 to 500 GHz frequency range [13, 21, 20] have been built at the California Institute of Technology using a mixer designed by Ellison [6]. This design, shown in fig. 3, includes two movable waveguide shorts, one behind the junction (back-short), and one in a waveguide tee in the E-plane wall of the waveguide near the junction (E-plane tuner). The SIS is mounted across the E-plane of the waveguide. One side of the SIS is shorted directly to the mixer block. The other side is coupled through an rf-choke structure to the IF and dc-bias circuits. In later designs, a symmetric mount is designed so that the ground connection is made at the end of an rf-choke.

This design has been verified and improved through the use of microwave scale modeling [49]. These models showed that the rf impedance seen by the SIS can be tuned over more than

half the area of a Smith chart at almost all frequencies in the waveguide band. This modeling also demonstrated the critical importance of the placement of the SIS in the waveguide. The SIS must be centered in the waveguide to avoid extra reactance due to coupling to a higher order waveguide mode.

In all of the mixers based on Ellison's design, a great amount of attention has been paid to the IF matching circuit. This circuit is designed for two criteria: 1) transform the 50 Ω IF amplifier to a higher impedance, 100 to 200 Ω, at the SIS and 2) provide a low impedance at the SIS at frequencies outside the desired IF band. The first criterion improves the coupled gain of the SIS mixer since its IF output impedance is very high. The second criterion protects the SIS from IF saturation [50, 51].

4.3.2. Round Waveguide Mixer

An early attempt at designs that would be appropriate for high frequency scaling is Woody's round waveguide mixer [4]. Mixers based on this design have been built for 115 GHz [4], 230 GHz [5], and 345 GHz [22]. This design is relatively easy to scale to high frequencies. The round waveguide is fabricated by drilling the proper sized hole in a block. The rf choke is built into the mixer block. The SIS junction has no rf choking or any other frequency dependent structures on it, so the chip can be made very small. While the sensitivity of the round waveguide mixers is good, the greater complexity of the other designs discussed here is clearly justified by their lower noise temperatures.

4.3.3. IRAM Mixer

SIS mixers are built at the *Institut de Radio Astronomie Millimétrique* (IRAM) for use on European radio telescopes. The IRAM mixer block uses a reduced height rectangular waveguide with the SIS junction mounted across its E-plane. The reduced height waveguide provides a lower rf input impedance than full height waveguide, and eliminates resonant coupling to higher order modes which trouble Ellison's design. There is a single mechanical tuner, a backshort in the waveguide behind the SIS. The rf choke is fabricated integrally with the SIS and is symmetric around the junction: it is the basis for the rf choke structure now used in Ellison designed mixers. IRAM mixers have been built for 100 GHz [19] and 230 GHz [7, 47]. An SIS mixer is now being

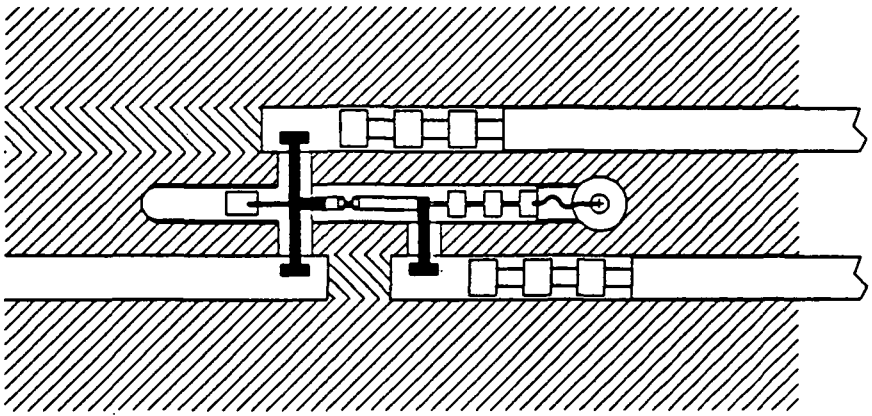

Figure 4 [11]. The NRAO-401 170-260 GHz mixer. The center channel contains microstrip circuitry including the SIS junctions with inductive tuning. The channel on the left is a waveguide carrying the signal and LO into the mixer. The top and bottom channels on the right are waveguides containing movable shorts for tuning. Stripline to waveguide coupling structures are shown in solid black.

developed for 345 GHz [47]. The simplicity and success of the IRAM design make it a good candidate for higher frequency operation.

4.4. Waveguide-Substrate Mixers

A number of mixer designs use a mechanically simple waveguide design to couple input radiation to a microstrip or coplanar transmission line built on a dielectric substrate. Critical rf circuit components in these mixers are fabricated photolithographically. It is easier to fabricate small components this way than to machine them into a waveguide block. Because of this, the approach is very promising for higher frequency mixers. These designs have been fabricated up to 230 GHz with excellent results. They should perform equally well at higher frequencies in the future. A few of these designs are presented below.

4.4.1. NRAO-401

The National Radio Astronomy Observatory makes a wide variety of receivers for radio astronomy in the US. Their NRAO-401 SIS mixer is shown in fig. 4 [11]. The rf is coupled from an input waveguide into stripline circuit through a broadband transition very similar to commercial waveguide to coaxial transitions available at much lower frequencies. Two adjustable waveguide tuning elements are also coupled to the circuit through similar probes to provide series and parallel reactances to the SIS. This mixer's sensitivity in a 230 GHz DSB receiver is the best currently

available. A similar mixer is part of a 40 K DSB receiver at 100 GHz [9]. Both of these mixers can be tuned for SSB operation with 20 dB image rejection.

4.4.2. NRAO Tunerless Mixer

Another NRAO SIS mixer achieves 40-80 K DSB receiver temperatures over the entire WR-10 waveguide band, 75-110 GHz, without any mechanical tuning [11]. As in the NRAO-401, the waveguide to stripline transition couples radiation from the input waveguide to the substrate circuit. The stripline radiation makes a second transition to coplanar waveguide before it reaches the SIS and its integrated tuners.

4.4.3. Yale Waveguide-Microstrip Mixer

In this design, the input waveguide is coupled to a microstrip circuit with a 4-section Chebyshev single ridge transformer [39]. Nearly full WR-10 band coverage is achieved with no mechanical tuning. Circuits with microstrip inductive compensation of the SIS capacitance were investigated, but the lowest noise temperatures for this mixer were achieved without inductive tuning. Because of its simple mechanical design, this mixer is a good candidate for scaling to higher frequencies.

4.5. Quasioptic SIS mixers

An interesting alternative to waveguide coupling is shown in fig. 5. The SIS is fabricated integrally with a planar antenna. The SIS-antenna is placed on a hyperhemispherical lens. The lens focuses the input radiation into the center of the SIS-antenna which earns this scheme the name "quasioptic." A comprehensive introduction to the properties of antennas on dielectrics is given by Rutledge *et al.* [52]. The superconducting films from which the SIS-antenna is made are very good conductors, so the fabricated antennas will have low resistive losses despite the submillimeter frequencies involved. This low-loss property may not hold for $f_{rf} > 2\Delta/h$, about 700 GHz for niobium technology.

The planar antenna designs have the following positive features. Many of these mixers can be used over a few octaves of f_{rf}. The spiral and bowtie planar antennas are frequency independent both in their beam pattern and in their antenna impedance. The SIS-antennas are fabricated photolithographically so no waveguide or feedhorn must be machined. Large substrates can be used. If an SIS is to be placed across a waveguide, the SIS and its substrate must be much smaller

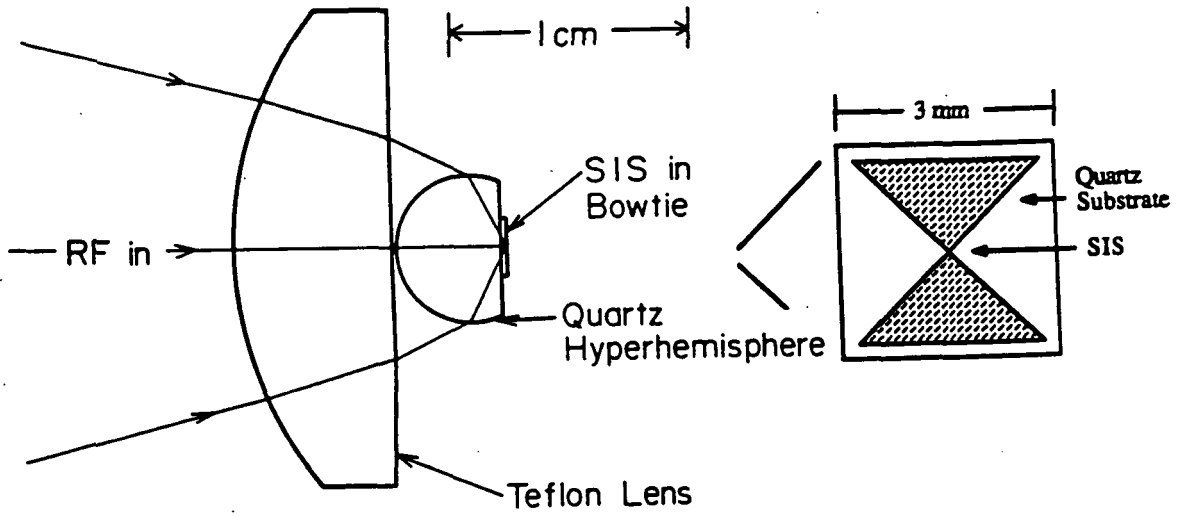

Figure 5 [33]. The bowtie dipole antenna is formed as an extension of the leads of the SIS diode. The radiation from this antenna is focussed into a fairly narrow beam by a hyperhemispherical lens placed up against the substrate. Further focussing is provided by a plastic lens

than an rf wavelength. An SIS-antenna, however, should actually be fabricated on a substrate which is bigger than a wavelength.

4.5.1. Spiral and Bowtie Antennas

The bowtie mixer in fig. 5 was improved on by using a spiral-shaped dipole antenna [8] like the one shown in fig. 2a. The mixer with spiral antenna had noise temperatures about half those of the bowtie mixer over the same large frequency range. This mixer has been used at the Caltech Submillimeter Observatory for radio astronomy at 115, 230, 345 and 492 GHz. Its beam couples to the telescope about as well as the beam from a waveguide receiver, resolving a difficulty with the bowtie design.

The spiral antenna has a much cleaner beam pattern than the bowtie, with sidelobe and pedestal structure at the -20 dB level. The cleaner beam is primarily due to the better radiation pattern of the spiral, but it is also helped by the use of a mirror less than 1 mm behind the SIS-antenna. The lower noise of the spiral SIS is attributable to its better beam pattern, as is its excellent coupling efficiency to the CSO radio telescope.

The submillimeter spiral SIS mixer has very recently been improved remarkably at the expense of its multi-octave bandwidth [42]. The design is similar to that shown in fig. 2b, but the

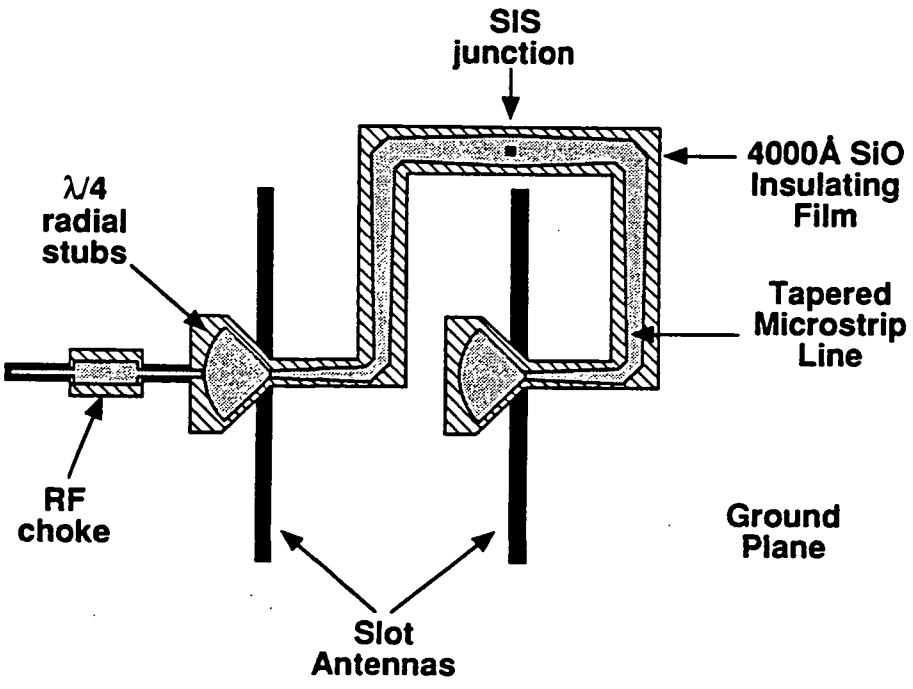

Figure 6. The planar antenna-SIS mixer of Zmuidzinas and LeDuc [23]. The entire structure is built on a niobium ground plane which is etched away to create the two slot antennas.

transformer is a more complicated two section Chebyshev design. The result is 75% or better coupling between the SIS and the spiral antenna in a one-octave rf band centered at 350 GHz. Receiver results using this mixer are included in Table 1. The fall-off in performance at 492 GHz is due to the low center frequency of this particular mixer. It should be a simple matter to adjust the design so that $T_{RECDSB} \leq 250$ K is achieved at 492 GHz.

4.5.2. Twin-slot antenna

Fig. 6 shows a different planar antenna design used in the mixer developed by Zmuidzinas and LeDuc [23]. This receiver is reported in further detail elsewhere in this conference publication. This design couples a single SIS junction to two planar slot dipole antennas as shown in fig. 6. Unlike the bowtie and spiral, the twin-slot is a resonant antenna, but it is reasonable to expect the rf bandwidth of this mixer to be similar to that of waveguide designs: about one-half octave.

The slot antennas have a low antenna impedance. They are coupled to the SIS through tapered transmission lines which reduce the impedance even further. Finally, the radiation impedance is reduced even further since the two slots appear in parallel across the SIS. The source admittance of radiation presented to the SIS at the design frequency is $Y_S \approx (4\ \Omega)^{-1}$. As a result, an SIS with a large junction area, 2.3 $(\mu m)^2$, can be used. The result is $T_{RECDSB} = 420$ K at

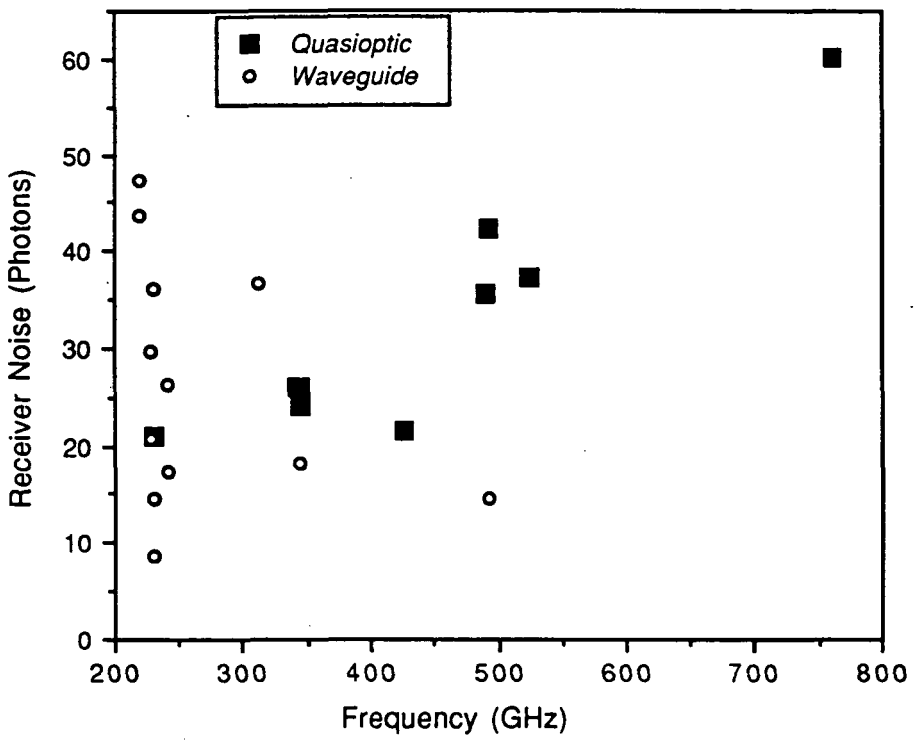

Figure 7. The noise of the receivers summarized in Table 1. Plotted is $T_{RECDSB}/(hf/2k_B)$. This normalizes the receiver noise to its quantum limit value.

492 GHz (the conference publication on this receiver should be reviewed for the most up to date information. It is reasonable to expect that the noise of this kind of receiver will drop quickly as more is learned about its design.

4.6. Overall performance summary

A summary of the best reported SIS receiver results is shown in fig. 7 and in Table 1. The most common results reported are T_{RECDSB}, so those are tabulated. DSB values of gain or mixer temperature are included in the table when they are quoted in the literature. Generally, SSB values can be estimated by doubling T_{RECDSB}, doubling T_{MIXDSB}, and subtracting 3 dB from the DSB Gain. The receiver noises in fig. 7 are normalized to the quantum limit of $N_{REC} = 1$ for an ideal photodiode mixer. The noise values achieved are many times this limiting value. However, these noise values represent a very great improvement over values available just a few years ago. It is reasonable to expect that they will continue to fall in the future.

4.7. *Unusual Mixers for Higher Frequencies*

This section is concluded with the mention of some unusual modes of superconducting mixer operation. None of these methods have been developed to the point that they are useful on a radio telescope. However, each method addresses problems with submillimeter SIS mixers in ways which may be useful in higher frequency superconducting mixers.

4.7.1. Harmonic mixing

A mixer can be designed so that it is sensitive to input signals at $f_S = n f_{LO} \pm f_{IF}$ where n is an integer. If $n \geq 2$, the mixer is said to be subharmonically pumped. Belitsky *et al.* investigated the gain of their spiral-transformer mixer with subharmonic pumps [53]. The mixer gain fell off slowly as n increased from 1 to 3. The advantages of subharmonic pumping include 1) it is easier to get powerful oscillators at lower LO frequencies and 2) the large separation between f_{LO} and f_S makes it easier to couple both of these to the SIS with high efficiency.

4.7.2. SIN junction mixer

If one of the superconducting sides of an SIS is replaced by a non-superconducting metal film, the resulting diode is a Superconductor-Insulator-Normal metal junction, or SIN. The SIN does not have as sharp a non-linearity in its IV as the SIS. But it also doesn't have any Josephson currents, which can be a problem in high frequency SIS mixers.

An SIN mixer at 230 GHz was built and tested by Blundell and Gundlach [48]. Compared to a similar SIS mixer, its gain was about 7 dB lower, but its mixer noise was quite low. Considering the very low noise IF amplifiers now available ($T_{IF} \approx 3$ K at 1.5 GHz), this is a very promising result. While it does not give any advantage over an SIS at 230 GHz, its lack of Josephson currents might make the SIN mixer useful at submillimeter wavelengths. Theoretical work on the SIN mixer operated both as a fundamental mixer [36, 54] and as a subharmonically pumped mixer [55] suggest it should be capable of $T_{RECDSB} < 100$ K up to 660 GHz.

4.7.3. Josephson effect mixing

While the Josephson effect is known to produce excess noise in submillimeter mixers, it is also capable of enhancing the gain of these mixers [33, 56]. While the current results for Josephson mixing show the noise increasing faster than the gain, the mixers tested are not

designed to take advantage of the Josephson currents. Much work remains to be done on this type of mixer before it is known if it will be useful.

5. SUMMARY AND CONCLUSIONS

SIS mixers are used extensively for 100 to 500 GHz radio astronomical receivers. Many useful techniques have been developed for using SIS's at submillimeter wavelengths. The waveguide-feedhorn and the planar-antenna-lens (quasioptical) techniques provide excellent radiation beam patterns for SIS mixers. Integrated tuning elements including inductive components and transmission-line-transformers allow impedance matching of the SIS to both of these radiation coupling structures. SIS mixers using these techniques have been reviewed here.

6. ACKNOWLEDGEMENTS

The author thanks the many researchers who sent letters and reprints which helped him to write this review. The development of this article was supported by National Science Foundation Grant ECS-8857868.

7. REFERENCES

[1] P. L. Richards, T. M. Shen, R. E. Harris and F. L. Lloyd, "Quasiparticle heterodyne mixing in SIS tunnel junctions," *Appl. Phys. Lett.*, vol. 34, 1 March, 1979, pp. 345-347.

[2] G. J. Dolan, T. G. Phillips and D. P. Woody, "Low-noise 115-GHz mixing in superconducting oxide-barrier tunnel junctions," *Appl. Phys. Lett.*, vol. 34, 1 March, 1979, pp. 347-349.

[3] J. R. Tucker, "Quantum limited detection in tunnel junction mixers," *IEEE J. Quantum Electron.*, vol. QE-15, November, 1979, pp. 1234-1258.

[4] D. P. Woody, R. E. Miller and M. J. Wengler, "85-115 GHz receivers for radio astronomy," *IEEE Trans. Microwaves Theory and Techniques*, vol. MTT-33, February, 1985, pp. 90-95.

[5] E. C. Sutton, "A superconducting tunnel junction receiver for 230 GHz," *IEEE Trans. Microwaves Theory and Techniques*, vol. MTT-31, July, 1983, pp. 589-592.

[6] B. N. Ellison and R. E. Miller, "A low noise 230 GHz receiver," *Int. J. of IR and MM Waves*, vol. 8, 1987, pp. 608-625.

[7] R. Blundell, M. Carter and K. H. Gundlach, "A low noise SIS receiver covering the frequency range 215-250 GHz," *Intl. J. of IR and MM Waves*, vol. 9, April, 1988, pp. 361-370.

[8] T. H. Büttgenbach, R. E. Miller, M. J. Wengler, D. M. Watson and T. G. Phillips, "A broad-band low-noise SIS receiver for submillimeter astronomy," *IEEE Transactions on Microwave Theory and Techniques*, vol. 36, December, 1988, pp. 1720-1726.

[9] S.-K. Pan, A. R. Kerr, M. J. Feldman, A. W. Kleinsasser, J. W. Stasiak, R. L. Sandstrom and W. J. Gallagher, "An 85-116 GHz SIS receiver using inductively shunted edge-junctions," *IEEE Trans. Microwaves Theory and Techniques*, vol. 37, March, 1989, pp. 580-592.

[10] D. P. Woody, C. J. Giovanine and R. E. Miller, "Dual channel 115 and 230 GHz SIS receivers in operation at the Owens Valley Radio Observatory," *IEEE Trans. Magn.*, vol. 25, March, 1989, pp. 1366-1370.

[11] A. R. Kerr and S.-K. Pan, "Some recent developments in the design of SIS mixers," *Int'l J. of IR and MM Waves*, vol. 11, October, 1990, pp. 1169-1187.

[12] H. Ogawa, A. Mizuno, H. Hoko, H. Ishikawa and Y. Fukui, "A 110 GHz SIS receiver for radio astronomy," *Intl. J. of IR and MM Waves*, vol. 11, June, 1990, pp. 717-726.

[13] J. W. Kooi, M. Chan, T. G. Phillips, B. Bumble and H. G. Leduc, "A low noise 230 GHz heterodyne receiver employing .25," vol. 1991,

[14] H. G. LeDuc, S. K. Khanna, J. A. Stern and S. Thakoor, "All refractory NbN/MgO/NbN tunnel-junctions," *IEEE Trans. Magn.*, vol. 23, March, 1987, pp. 863-865.

[15] A. W. Lichtenberger, C. P. McClay, R. J. Mattauch, M. J. Feldman, S.-K. Pan and A. R. Kerr, "Fabrication of Nb/Al-Al_2O_3/Nb junctions with extremely low leakage current," *IEEE Trans. Magn.*, vol. 25, March, 1989, pp. 1247-1250.

[16] W. C. Danchi, E. C. Sutton, P. A. Jaminet and R. H. Ono, "Nb edge junction process for submillimeter wave SIS mixers," *IEEE Trans. Magn.*, vol. 25, March, 1989, pp. 1064-1067.

[17] J. A. Stern, B. D. Hunt, H. G. LeDuc, A. Judas, W. R. McGrath, S. R. Cypher and S. K. Khanna, "NbN/MgO/NbN SIS tunnel junctions for submm wave mixers," *IEEE Trans. Magn.*, vol. 25, March, 1989, pp. 1054-1059.

[18] A. H. Worsham, D. E. Prober, J. H. Kang, J. X. Przybysz and M. J. Rooks, "High quality sub-micron Nb Trilayer tunnel junctions for a 100 GHz SIS receiver," *IEEE Trans. Magn.*, vol. 27, March, 1991, pp. 3165-3167.

[19] T. Lehnert, C. Grassl, K. H. Gundlach and J. Blondel, "Nb-Aloxide-Nb junctions for 3-mm SIS receivers," *ISEC*, vol. 1991,

[20] C. K. Walker, J. W. Kooi, M. Chan, H. G. LeDuc, J. E. Carlstrom and T. G. Phillips, "A 492 GHz SIS waveguide receiver for submillimeter astronomy," *Intl. J. of IR and MM Waves*, vol. submitted, 1991,

[21] B. N. Ellison, P. L. Schaffer, W. Schaal, D. Vail and R. E. Miller, "A 345 GHz receiver for radio astronomy," *Int. J. of IR and MM Waves*, vol. 10, 1989, pp. 937-947.

[22] E. C. Sutton, W. C. Danchi, P. A. Jaminet and R. H. Ono, "A superconducting tunnel junction receiver for 345 GHz," *Intl. J. of IR and MM Waves*, vol. 11, February, 1990, pp. 133-149.

[23] J. Zmuidzinas and H. G. LeDuc, "Quasi-optical slot antenna SIS mixers," *IEEE Trans. Microwaves Theory and Techniques*, vol. Submitted, 1991,

[24] H. Rothermel, D. Billon-Pierron and K. H. Gundlach, "An open structure SIS mixer for 350 GHz," *Digest of the16th Int. Conf. on Infrared and Millimeter Waves, Lausanne*, vol. August, 1991,

[25] M. J. Wengler, "Submillimeter wave detection with superconducting tunnel diodes," *Proc. IEEE*, vol. Accepted, 1992,

[26] J. R. Tucker and M. J. Feldman, "Quantum detection at millimeter wavelengths," *Rev. Mod. Phys.*, vol. 57, 1985, pp. 1055-1113.

[27] T. G. Phillips, "Submillimeter and far-infrared detectors," *Astro. Lett. and Communications*, vol. 26, 1988, pp. 293-304.

[28] P. L. Richards and Q. Hu, "Superconducting components for infrared and millimeter-wave receivers," *Proc. IEEE*, vol. 77, August, 1989, pp. 1233-1246.

[29] R. Blundell and D. Winkler, "The superconductor insulator superconductor mixer receiver - a review," in *NATO Applied Research Workshop on Superconducting Electronics and 2nd Workshop on Josephson Devices*. Capri, Italy: 1990.

[30] D. Winkler, Z. Ivanov and T. Claeson, "Superconducting detectors for mm and sub-mm waves," in *2nd Nordic Symposium on Superconductivity*. Røros, Norway: World Scientific, 1991.

[31] J. W. Archer, "Low-noise heterodyne receivers for near-millimeter wave radio astronomy," *Proc. IEEE*, vol. 73, 1985, pp. 109-130.

[32] J. M. Payne, "Millimeter and Submillimeter Wavelength Radio Astronomy," *Proc. IEEE*, vol. 77, 1989, pp. 993-1017.

[33] M. J. Wengler, D. P. Woody, R. E. Miller and T. G. Phillips, "A low noise receiver for millimeter and submillimeter wavelengths," *Intl. J. of IR and MM Waves*, vol. 6, August, 1985, pp. 697-706.

[34] S. Withington and E. L. Kollberg, "Spectral-domain analysis of harmonic effects in superconducting quasiparticle mixers," *IEEE Trans. Microwaves Theory and Techniques*, vol. 37, January, 1989, pp. 231-238.

[35] D.-G. Crété, W. R. McGrath, P. L. Richards and F. L. Lloyd, "Performance of arrays of SIS junctions in heterodyne mixers," *IEEE Trans. Microwaves Theory and Techniques*, vol. MTT-35, April, 1987, pp. 435-440.

[36] M. J. Wengler and D. P. Woody, "Quantum noise in heterodyne detection," *IEEE J. of Quantum Electron.*, vol. QE-23, May, 1987, pp. 613-622.

[37] Q. Hu, C. A. Mears, P. L. Richards and F. L. Lloyd, "Measurement of integrated tuning elements for SIS mixers with a Fourier transform spectrometer," *Intl. J. of IR and MM Waves*, vol. 9, April, 1988, pp. 303-320.

[38] A. R. Kerr, S.-K. Pan and M. J. Feldman, "Integrated tuning elements for SIS mixers," *Intl. J. of IR and MM Waves*, vol. 9, February, 1988, pp. 203-212.

[39] D. Winkler, N. G. Ugras, A. H. Worsham, D. E. Prober, N. R. Erickson and P. F. Goldsmith, "A full-band waveguide SIS receiver with integrated tuning for 75-110 GHz," *IEEE Trans. Magn.*, vol. 27, March, 1991, pp. 2634-2637.

[40] V. Y. Belitsky, M. A. Tarasov, S. A. Kovtonjuk, L. V. Filippenko and O. V. Kaplunenko, "Low noise completely quasioptical SIS receiver for radioastronomy at 115 GHz," *21st European Microwave Conference, Stuttgart*, vol. September, 1991,

[41] J. A. Carpenter, A. D. Smith, E. R. Arambula, L. P. S. Lee , T. Nelson and L. Yujiri, "100 GHz SIS mixer with improved rf matching," *IEEE Trans. Magn.*, vol. 1991,

[42] T. H. Büttgenbach, H. G. LeDuc, P. D. Maker and T. G. Phillips, "A Fixed Tuned Broadband Matching Structure For Submillimeter SIS Receivers," *IEEE Trans. Appl. Superconduct..*, vol. submitted, 1992,

[43] A. B. Ermakov, V. P. Koshelets, I. L. Serpuchenko, L. F. Filippenko, S. V. Shitov and A. N. Vystavkin, "SNAP structures with Nb-AlO-Nb junctions for mm wave receivers," *IEEE Trans. Magn.*, vol. 25, March, 1989, pp. 1060-1064.

[44] W. R. McGrath, J. A. Stern, H. H. S. Javadi, S. R. Cypher, B. D. Hunt and H. G. LeDuc, "Performance of NbN Superconductive tunnel junctions as SIS mixers at 205 GHz," *IEEE Trans. Magn.*, vol. 27, March, 1991, pp. 2650-2653.

[45] B. M. Thomas, "Design of corrugated conical horns," *IEEE Trans. Antennas Propagat.*, vol. AP-26, March, 1978, pp. 367-372.

[46] P. F. Goldsmith, "Quasi-optical techniques at millimeter and submillimeter wavelengths," in *Infrared and Millimeter Waves,* K. J. Button, Editor. 1982, Academic Press: New York. pp. 277-343.

[47] M. C. Carter, S. Navarro, A. Karpov, D. Billon-Pierron, T. Lehnert and K. H. Gundlach, "Receiver development with Nb/Al-Oxide/Nb SIS mixers in the frequency ranges of (201-270) and (320-370) GHz," *Intl. J. of IR and MM Waves*, vol. in press, 1991,

[48] R. Blundell and K. H. Gundlach, "A quasiparticle SIN mixer for the 230 GHz frequency range," *Intl. J. of IR and MM Waves*, vol. 8, December, 1987, pp. 1573-1579.

[49] T. H. Büttgenbach, T. D. Groesbeck and B. N. Ellison, "A scale mixer model for SIS waveguide receivers," *Intl. J. of IR and MM Waves*, vol. 11, January, 1990, pp. 1-20.

[50] M. J. Feldman and S. Rudner, "Mixing with SIS arrays," in *Reviews of Infrared and Millimeter Waves,* K. J. Button, Editor. 1983, Plenum: pp. 47-75.

[51] A. D. Smith and P. L. Richards, "Analytic solutions to superconductor insulator superconductor quantum mixer theory," *J. Appl. Phys.*, vol. 53, May, 1982, pp. 3806-3812.

[52] D. B. Rutledge, D. P. Neikirk and D. P. Kasilingam, "Integrated-circuit antennas," in *Infrared and Millimeter Waves,* K. J. Button, Editor. 1983, Academic Press: New York. pp. 1-90.

[53] V. Y. Belitsky, I. L. Serpuchenko, M. A. Tarasov and A. N. Vystavkin, "Subharmonically pumped SIS mixer," in *19th European microwave conference.* London, UK: 1989.

[54] C. E. Tong, L. M. Chernin and R. Blundell, "Harmonic mixing in a superconducting tunnel junction," *J. Appl. Phys.*, vol. 68, 15 October, 1990, pp. 4192-4198.

[55] L. M. Chernin and R. Blundell, "Harmonic mixing in a superconductor-insulator-normal metal tunnel junction receiver," *J. Appl. Phys.*, vol. 69, 15 February, 1991, pp. 2682-2684.

[56] M. J. Wengler, N. Dubash, G. Pance and R. E. Miller, "Josephson effect gain and noise in SIS mixers," *IEEE Trans. Microwaves Theory and Techniques*, vol. 40, in press, 1992,

Evaluation of integrated tuning elements with SIS devices.

M.M.T.M. Dierichs[1], C.E. Honingh[2], R.A. Panhuyzen[2], B.J. Feenstra[1], A. Skalare[2,3], J.J. Wijnbergen[2], H. v.d. Stadt[2], Th. de Graauw[2].

1: Dept. of Applied Physics and Materials Science Centre, University of Groningen, Nijenborgh 4, 9747 AG Groningen, The Netherlands.

2: Space Research Organization of the Netherlands, Groningen, Landleven 12, 9747 AD Groningen, The Netherlands.

3: Dept. of Applied Electron Physics, Chalmers University of Technology, Gõteborg, Sweden.

Abstract.

The resonance of integrated tuning stubs in combination with SIS detectors is measured and modeled. The predicted resonances are compared with measurements of stubs integrated with $Nb/Al_2O_3/Nb$ junctions in a log-periodic antenna using a Michelson interferometer. Different stub lengths were made on different substrates (on 200 μm thick quartz and on a 7 μm thick silicon membrane) and the results show a fairly good

agreement with the model calculations. Quartz substrates showed resonances up to 580 GHz, silicon membrane stub resonances reach as high as 480 GHz. An observed resonance at 560 GHz is probably a substrate effect from the membrane. The gap frequency for all the samples is 650 GHz and no resonances are detected above this frequency. Up to the maximum detected frequency dispersion is found to be negligible.

I Introduction.

SIS mixers with $Nb/Al_2O_3/Nb$ junctions are very sensitive submm detectors. Recent progress in SIS mixer development is due to the ability to manufacture smaller junctions down to sub-micron dimensions[1,2]. Instead of continuing to put more effort into the fabrication of smaller junctions and thus reducing the junction capacitance, it is also possible to implement integrated tuning elements, which are fairly easy to fabricate and result in a high sensitivity and broad bandwith. It has been shown that junctions with integrated tuning used in submm-wave mixers give good results[3,4].

The first published stub measurements used the self-pumped steps in the I-V characteristic to measure the resonance of the stub[5]. A more accurate and complete evaluation can be performed with a wide-band Michelson interferometer as first shown by Hu et. al.[6].

In this paper we first describe our design criteria for niobium stubs in combination with niobium junctions. Next, we describe how they can be analyzed on a log-periodic antenna with two 1 μm^2 junctions in series. Each junction has its own stub. Stubs for 100 GHz

and 350 GHz have been designed. The first type is expected to have multiple resonances from which the dispersion in niobium can be calculated. These antennas are made on 200 μm thick quartz substrates and on 7 μm silicon membranes. The results are used to separate stub and antenna resonances and to estimate the dispersion.

The organization of this paper is as follows: the theoretical background will be introduced in Sec.II, the fabrication results are presented in Sec.III, the experimental details are described in Sec.IV, the comparison between theory and experiment is discussed in Sec.V, and the conclusion will be drawn in Sec.VI.

II Model calculation.

To tune out the geometric capacitance an inductive tuning element was used. An example of the devices studied is shown in Fig.1. Two junctions in series, placed in the center of a log-periodic antenna, were used. To each junction a stripline type inductor is attached. The total arrangement can be modelled with the circuit shown in Fig.2. For completeness the connecting strip between the two junctions is included as an inductor L_{leads}. In practice this inductance is negligible in evaluating the frequency response.

Using integrated tuning, the junction impedance can not simply be described as a pure resistor with a parallel capacitor. Instead, it must be described as a capacitor in parallel with a complex admittance with a conductive part (G_Q) and a susceptive part (B_Q). Since the experiment works in the small signal limit and the Josephson effect is suppressed by a magnetic field, the junction admittance can be described as follows[7,8]:

$$G_Q = \frac{e}{2\hbar\cdot\omega}\cdot\left[I_{dc}\left(V_0+\frac{\hbar\cdot\omega}{e}\right) - I_{dc}\left(V_0-\frac{\hbar\cdot\omega}{e}\right)\right] \quad (1)$$

$$B_Q = \frac{e}{2\hbar\cdot\omega}\cdot\left[I_{kk}\left(V_0+\frac{\hbar\cdot\omega}{e}\right) - 2\cdot I_{kk}(V_0) + I_{kk}\left(V_0-\frac{\hbar\cdot\omega}{e}\right)\right] \quad (2)$$

These equations show that the resonant frequency depends on the bias voltage and the photon-energy. In these equations is $\hbar\omega/e$ the energy of the photon step, V_0 is the bias voltage, and

$$I_{kk} = P\int_{-\infty}^{\infty}\frac{dV'}{\Pi}\cdot\frac{I_{dc}(V') - \frac{V'}{R_n}}{V'-V} \quad (3)$$

where I_{kk} is the Kramers-Kronig transform, which can be calculated from the dc-IV curve.

The inductance per unit length of the stub can be calculated as follows[9]:

$$L_s = \frac{\mu_0}{k\cdot w}\cdot\left[t_d + \frac{\lambda}{\tanh\left(\frac{t_1}{\lambda}\right)} + \frac{\lambda}{\tanh\left(\frac{t_2}{\lambda}\right)}\right] \quad (4)$$

where w is the width of the stub, k is the fringing factor[10], t_1, t_2 and t_d are the thicknesses of the ground plane, the stub, and the dielectric layer respectivily, and λ is the penetration depth of the niobium layers. The capacitance per unit length of the stub is given by:

$$C_s = k\cdot\varepsilon_{eff}\cdot\varepsilon_0\cdot\frac{w}{t_d} \quad (5)$$

Knowing the capacitance and the inductance of the stub, the impedance Z_0 and the phase velocity v_0 follow from the definitions:

$$Z_0 = \sqrt{\frac{L_s}{C_s}} \tag{6}$$

$$v_0 = \frac{1}{\sqrt{L_s \cdot C_s}} \tag{7}$$

The impedance of a transmission line with small loss and dispersion follows from:

$$Z = \frac{Z_0 \cdot \alpha \cdot l}{\sin^2\left(\frac{\omega \cdot l}{v_0}\right)} + \frac{Z_0}{j \cdot \tan\left(\frac{\omega \cdot l}{v_0}\right)} \tag{8}$$

Where α is the loss per unit length and l is the length of the stub. The RF coupling coefficient C_{RF} defined as the fraction of the available power dissipated in the junction is given by:

$$C_{RF} = 1 - \left|\frac{Y_A - Y_J^*}{Y_A + Y_J}\right|^2 \tag{9}$$

where $Y_A = 1/R_A$ is the simplified admittance of the antenna (1/120 Ω), and Y_J is the admittance of the right hand side of Fig.2.

If both areas and stub lengths are equal then the resonant frequency can be approximated from:

$$\omega \cdot C_j + \frac{1}{\omega \cdot X_s} + \frac{1}{\omega \cdot X_q} = 0 \tag{10}$$

In our equations we do not take into account the behaviour of the log-periodic antenna, this is rather complex and not known in all detail. Therefore it will be very difficult to identify the loss from the observed resonances, because it could be loss in niobium, bad coupling to the antenna or a combination of both.

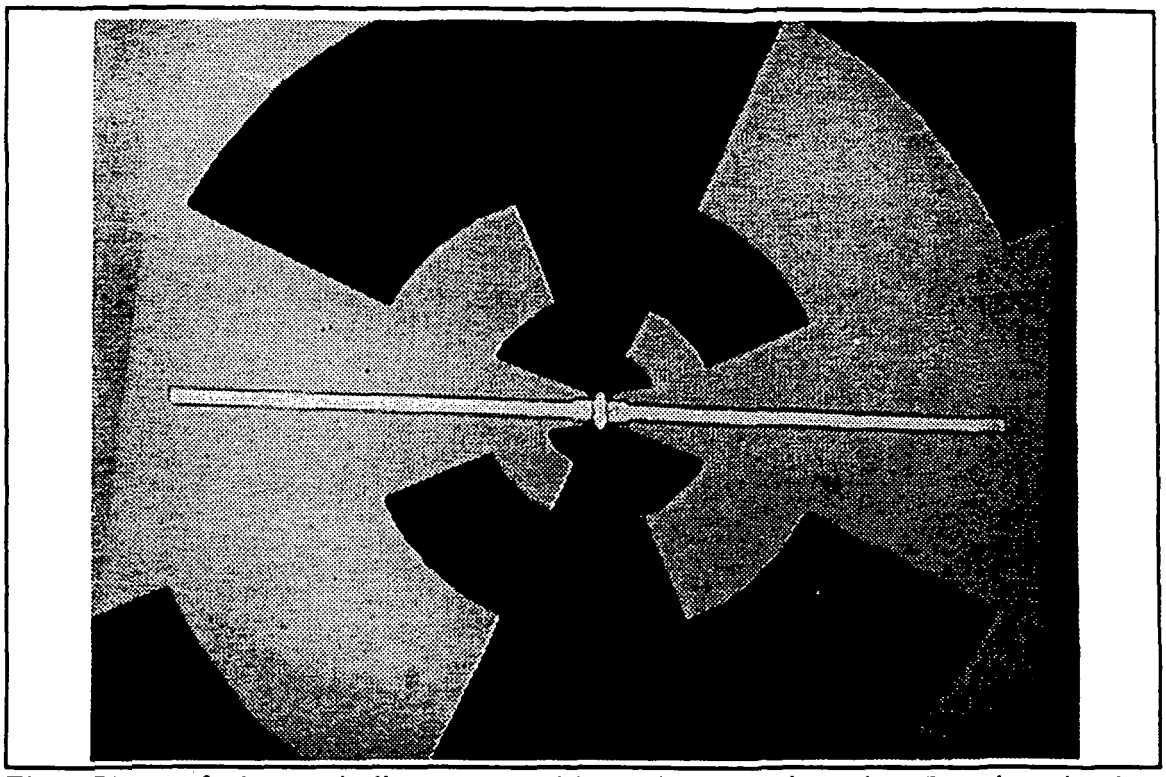

Fig.1. Photo of a log-periodic antenna with two junctions in series. Each junction has its own stub.

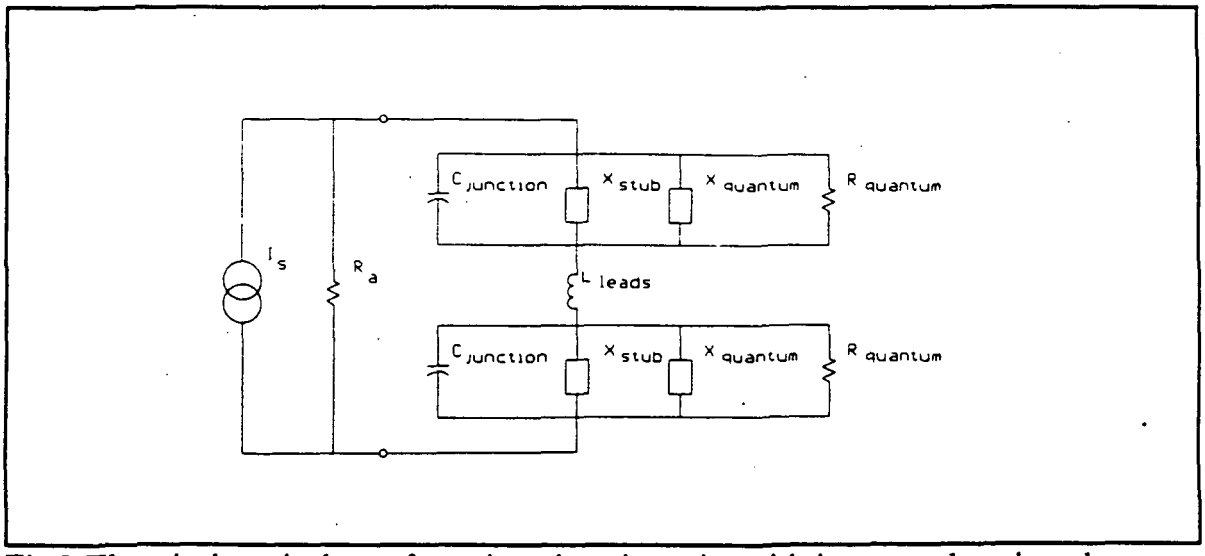

Fig.2 Electrical equivalent of two junctions in series with integrated tuning elements.

III Fabrication of devices.

The detector is positioned in the center of a broad-banded log-periodic antenna. We used 2 junctions in series of each 1 μm^2 and a current density of 12000 A/cm^2. On top of the junctions the wiring layer was defined with a stub for each junction (Fig.1.). The dielectric layer between the ground plane (antenna) and the stub was 250 nm thick sputtered SiO_2. The junctions have been fabricated with the Selective Niobium Over-Etch Process (SNOEP)[11].

Antennas have been fabricated on 200 μm thick quartz substrates and on 7 μm thick silicon membranes (Fig.3.). The membranes have been etched in ethylenediamine-pyrocatechol-water (EPW)[12]. The junctions on the membranes were fabricated after the etching of the membranes. With the obtained thickness, the membrane is transparent which simplifies the alignment of the antenna on the membrane.

Two different stub lengths were fabricated for different purposes. Firstly, short stubs (around 120 μm) were designed to resonate at 350 GHz. A single resonance simplifies the comparison with the model and it can easily be implemented in the waveguide mixer chip design. Secondly, long stubs (around 500 μm) were designed to have a fundamental resonance around 100 GHz and multiple resonances at higher frequencies. From the frequencies of the resonances in principle the dispersion and loss in niobium can be estimated.

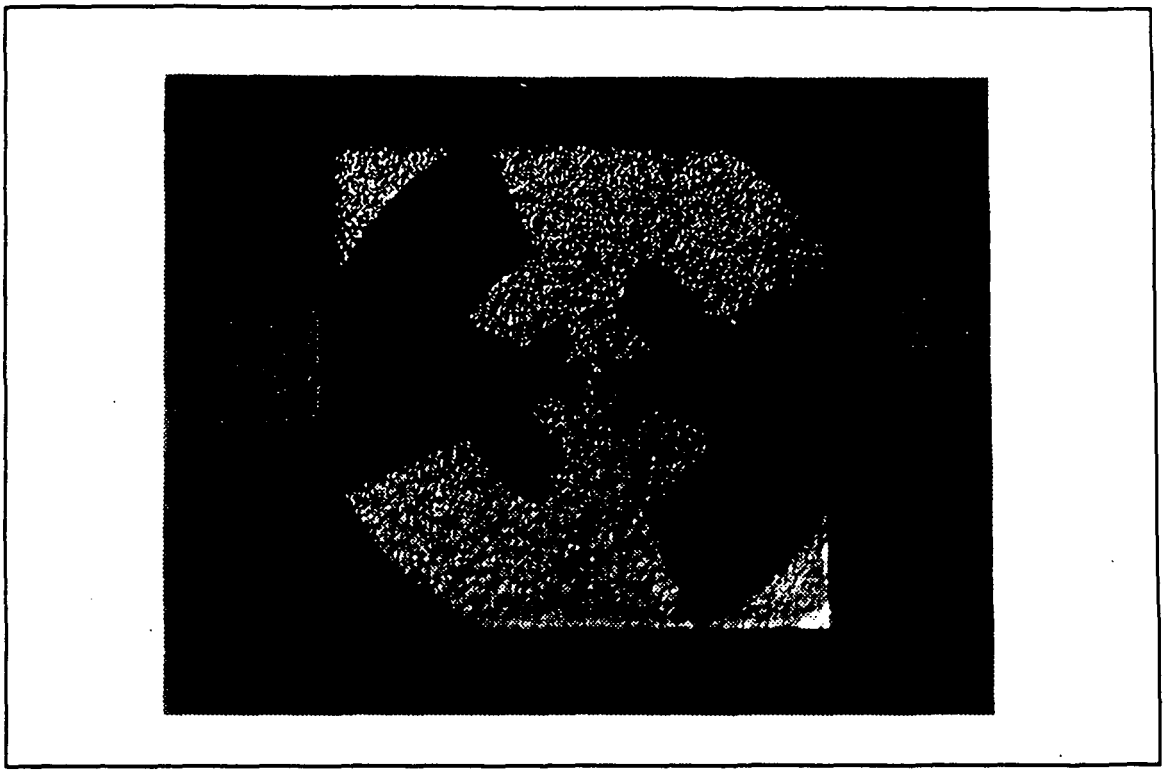

Fig.3. Photo of the antenna fabricated on a 7 μm thick silicon membrane.

IV Measurement set-up

For measuring the response of the detector, we used a Michelson interferometer with a Hg arc lamp as source[13] (Fig.4.). The operating frequency range was determined by a 50 μm thick kapton film beam-splitter. The mechanical traveling distance was 50 mm resulting in a resolution of 4 GHz. Both single sided and double sided interferograms were measured. An example of the resulting spectra with multiple resonances is plotted in Fig.5.

The antenna was mounted in a liquid helium dewar with dc-bias connections. Since the

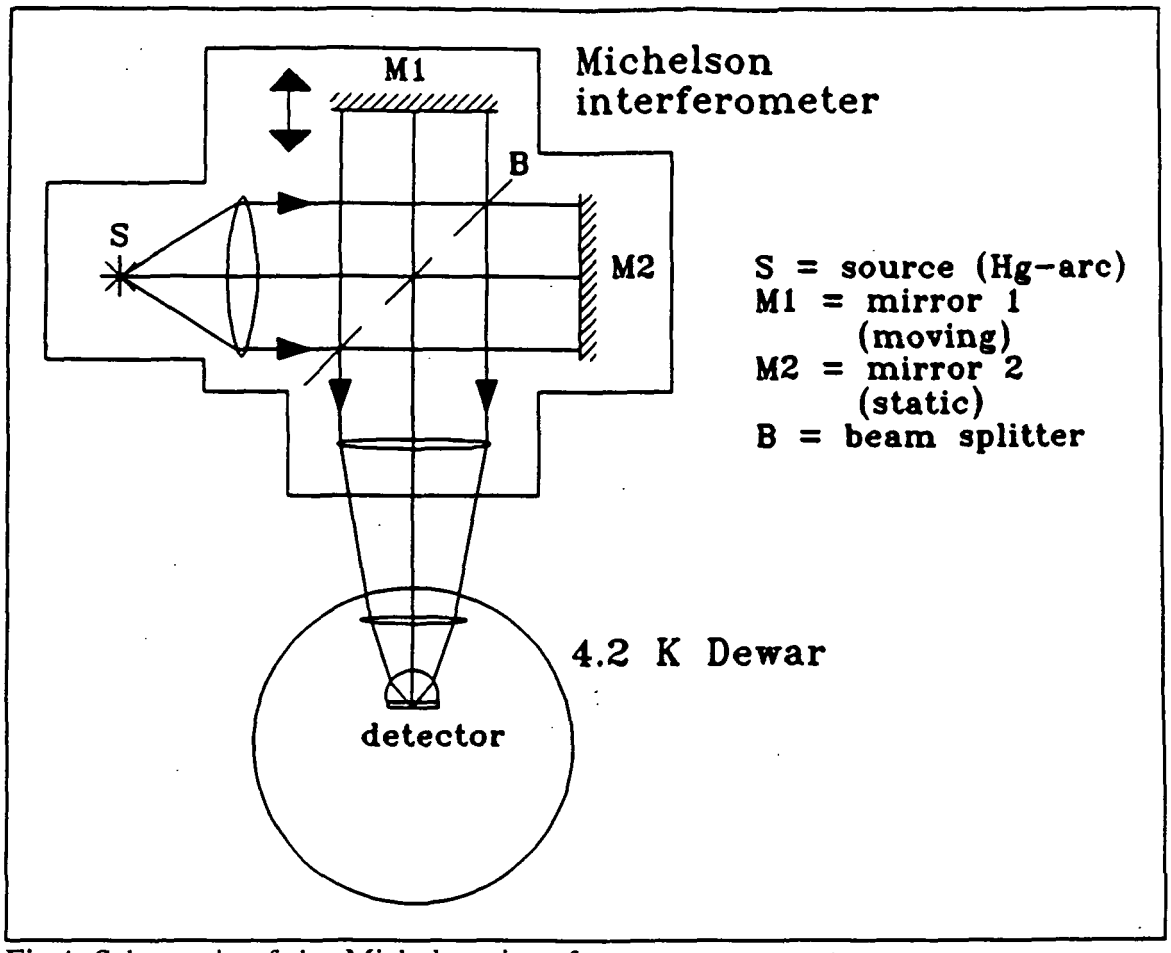

Fig.4. Schematic of the Michelson interferometer.

Michelson was not under vacuum during the measurement, the water absorption lines at 380 GHz, 448 GHz, 557 GHz and 752 GHz were visible when sufficient resolution was used. All antennas fabricated on a quartz substrate were glued to a quartz hyper-hemispherical lens. The lens optimizes the optical coupling and results in a better sensitivity. We have also performed measurements with the log-periodic antenna on a thin membrane. In that case no lens was used, resulting in a much lower signal. By using longer integration times we could improve the signal to noise ratio to an acceptable level.

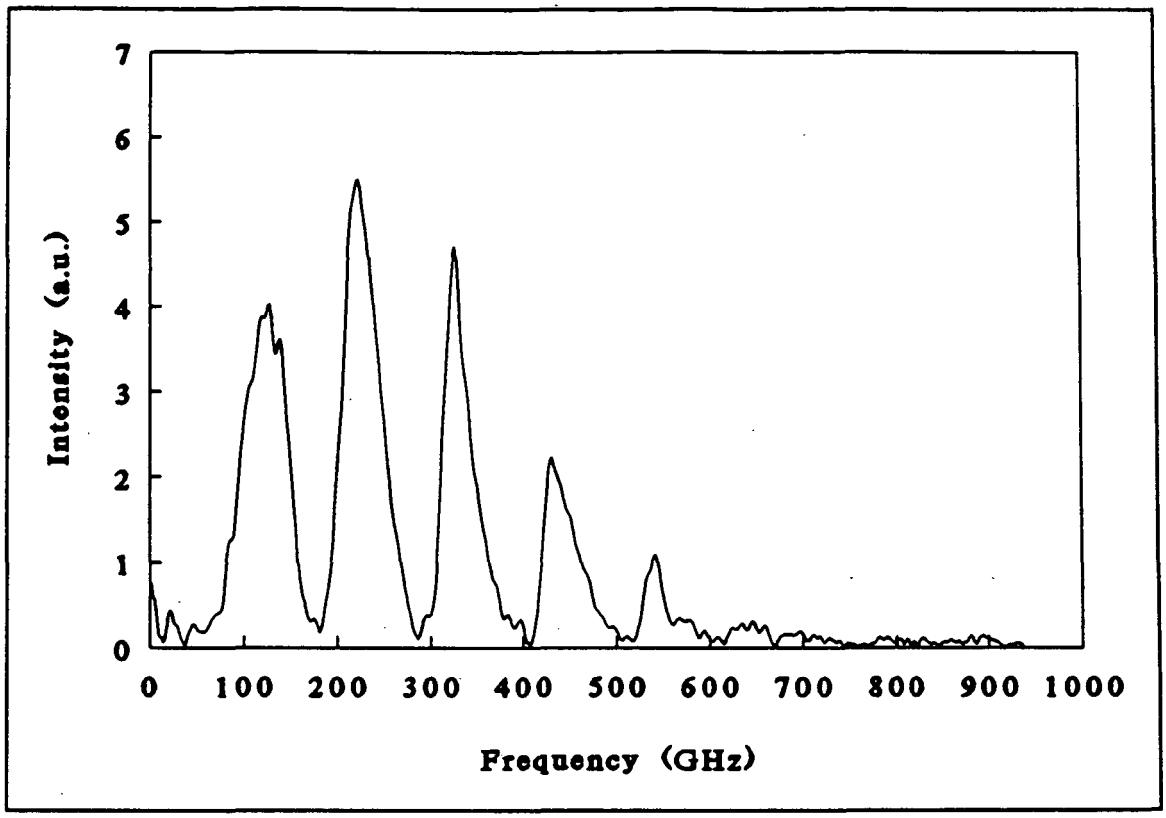

Fig.5 Spectrogram of a device with multiple resonances.

V Results

A: Short stubs on 200 μm quartz substrates.

Antennas with stub lenghts around 120 μm were investigated to determine the specific capacitance of the junction and the penetration depth of the niobium layers. Resonant frequencies were measured from two different batches. The resonant frequency is depending on the bias voltage due to the behaviour of the quantum impedance (eq.1 and eq.2). Calculated and measured results are shown in Fig.6. Best agreement between

theory and experiment was obtained with the assumption of a specific capacitance of 55 $fF/\mu m^2$ and a penetration depth of 100 nm. These values were further used in calculations of the long stubs. Differences between calculations and measurements are due to the noise in the spectrogram which complicates the determination of the resonant frequencies. No multiple resonance is observed.

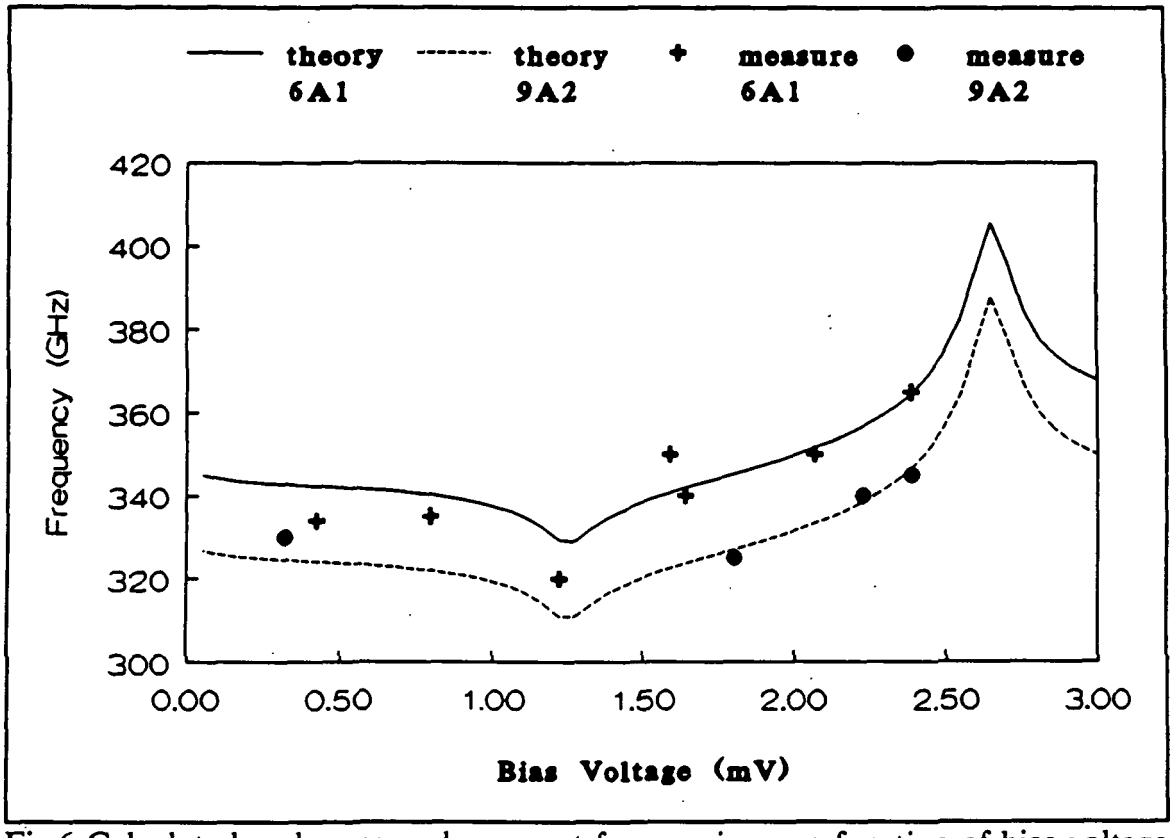

Fig.6 Calculated and measured resonant frequencies as a function of bias voltage for two different junction batches.

B: Long stubs on 200 μm quarz substrates.

Next, the resonances of a 527 μm long stub on a quartz substrate were measured. The results of the measurements at different bias voltages are plotted in Fig.7 and are

compared with model calculations. At the first two resonances the measurements agree fairly well with the model both below as well as above the gap voltage. The two higher resonances have a larger frequency shift close to the gap than the model predicts. More measurements with different lengths are planned for a more detailed evaluation. Stub resonances up to 580 GHz are observed, while no antenna resonances are visible. We do not see any dispersion in the resonances of the stubs (Fig.5).

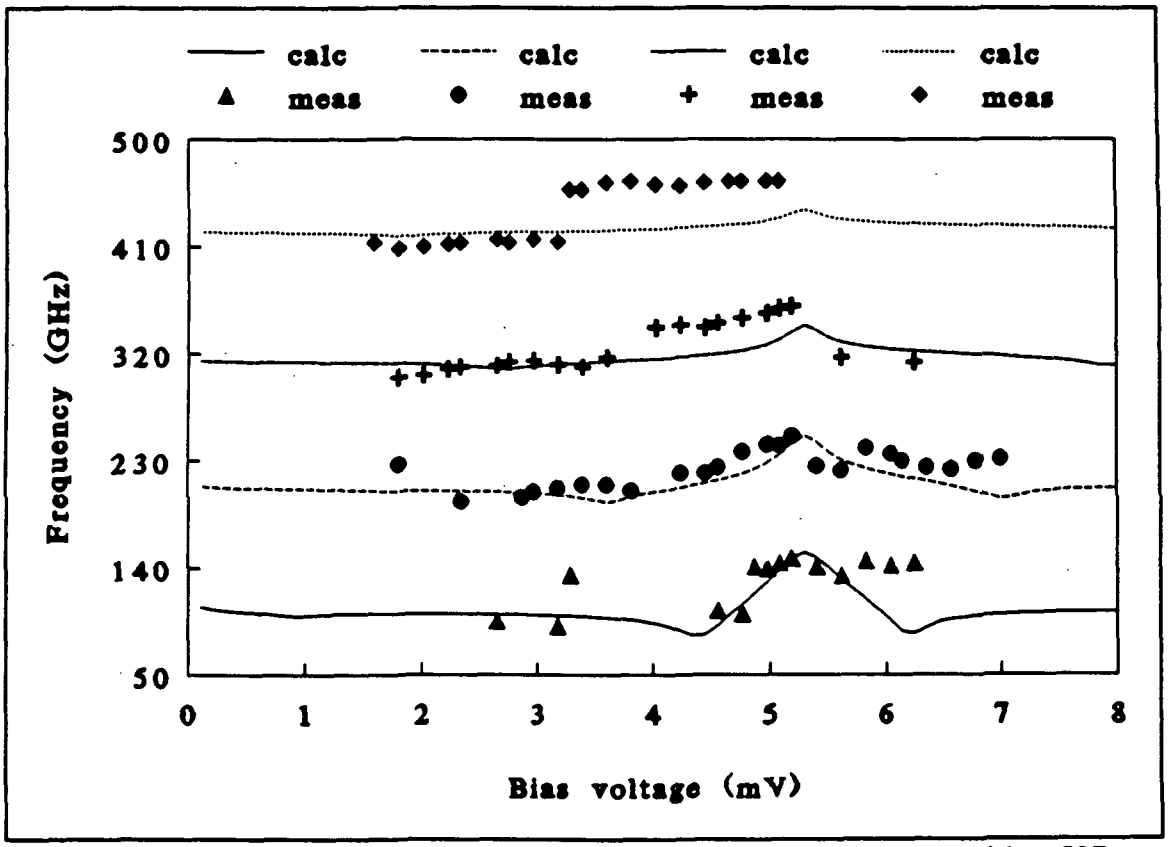

Fig.7 Calculated and measured resonant frequencies for an antenna with a 527 μm long stub on a quartz substrate as a function of bias voltage.

C: Long stubs on 7 μm silicon membranes.

The resonances of a 527 μm long stub on a 7 μm thick silicon membrane were measured. A double sided interferogram was used to decrease the noise in the spectrogram. The resolution (8 GHz) is lower because of the decreased scan length. The effect of the quantum susceptance is not clearly observed because of the loss in resolution and signal. We measured stub resonances at 110, 200 and 325 GHz. Incidentally resonances at 165, 310 and 540 GHz occur which are probably substrate resonances. The highest stub resonance appears to be at 450 GHz which is lower than the measurements on quartz. The lowest three resonances are compared with the model calculations in Fig.8. It is not clear why above 330 GHz no well defined resonances occur except for the substrate resonance at 540 GHz.

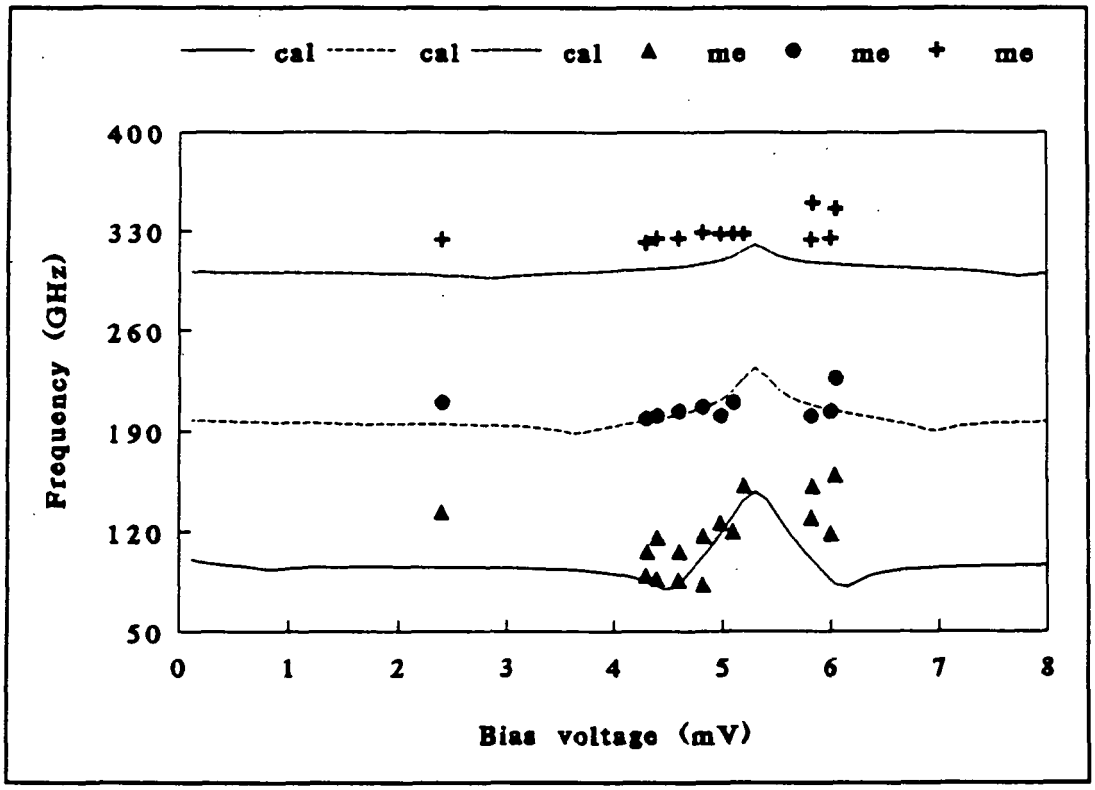

Fig.8 Calculated and measured resonance frequencies for a 527 μm long stub on a silicon membrane as a function of bias voltage.

VI Conclusions

The theoretical model and the experimental results for the short stubs lead to a penetration depth of 100 nm and a specific capacitance of 55 fF/μm^2. This is independent of the measured batch. For long stubs the model predicts a different behaviour at higher resonances than is measured. The measured frequency shift at the higher resonances is larger than the model predicts. Both below and above the gap voltage the resonances agree fairly well with the model. Resonances up to 580 GHz are observed. For antennas fabricated on 7 μm thick silicon membranes resonances up to 480 GHz are observed. Also possible substrate resonances are measured. No resonances above 600 GHz are observed, which is close to the gap frequency of niobium (650 GHz).

Acknowledgements

We thank T.M. Klapwijk for his stimulating discussions, H.G. Golstein and G. de Groot for their help with the Michelson interferometer, M.J. de Boer for etching the membranes, G. de Lange for his support with the model calculation and H.H.A. Schaeffer for the mechanical support. This work is supported by the Stichting Technische Wetenschappen (STW) and the Stichting voor Fundamenteel Onderzoek der Materie (FOM), which are part of the Nederlandse Organisatie voor Wetenschappelijk

Onderzoek (NWO). We also acknowledge the financial support of the European Space Research (ESA) through contract 7898/88/NL/PB(SC).

References

1. W.R. McGrath, H.H.S. Javadi, S.R. Cypher, B. Bumble, B.D. Hunt, and H.G. LeDuc, Proceedings of *Second International Symposium on Space TeraHertz Technology*, 423 (1991)

2. J.W. Kooi, M. Chan, T.G. Phillips, B. Bumble, and H.G. LeDuc, Proceedings of *Second International Symposium on Space TeraHertz Technology*, 459 (1991)

3. A.W. Lichtenberger, D.M. Lea, A.C. Hicks, J.D. Prince, R. Densing, D. Peterson, and B.S. Deaver, Proceedings of *Second International Symposium on Space TeraHertz Technology*, 439 (1991)

4: J. Zmuidzinas, and H.G. LeDuc, Proceedings of *Second International Symposium on Space TeraHertz Technology*, 481 (1991)

5. A.V. Räisänen, W.R. McGrath, P.L. Richards, and F.L. Lloyd, IEEE Trans Microwave Theory Tech. **33**, 1495 (1985)

6. Q. Hu, C.A. Mears, P.L. Richards, and F.L. Lloyd, Int. J. of Infrared and MM Waves, **9**, 303 (1988)

7. J.R. Tucker, and M.J. Feldman, Rev. Mod. Phys. **57**, 1055 (1985)

8. Q. Hu, C.A. Mears, P.L. Richards, and F.L. Lloyd, Phys. Rev. B, **42**,10250 (1990)

9. J.C. Swihart, J. Appl. Phys. **32**, 461 (1961)

10. W.H. Chang, J. Appl. Phys. **50**, 8129 (1979)

11. M.M.T.M. Dierichs, R.A. Panhuyzen, C.E. Honingh, M.J. de Boer, and T.M. Klapwijk (unpublished results)

12. K.E. Petersen, Proc. of the IEEE **70**, 420 (1982)

13. P.L. Richards, in *Spectroscopic Technique for Far Infrared Submillimeter and Milimeter Waves*, (North-Holland, Amsterdam, 1967)

SOURCE CONDUCTANCE SCALING FOR HIGH FREQUENCY SUPERCONDUCTING QUASIPARTICLE RECEIVERS

Qing Ke[1] and M. J. Feldman[2]

Physics Department[1] and Department of Electrical Engineering[2]
University of Rochester, Rochester, NY 14627

ABSTRACT

It has been suggested that the optimum source conductance G_S for the superconductor-insulator-superconductor (SIS) quasiparticle mixer should have a 1/f dependence. This would imply that the critical current density of SIS junctions used for mixing should increase as frequency *squared*, a stringent constraint on the design of submillimeter SIS mixers, rather than in simple proportion to frequency as previously believed. We have used Tucker's quantum theory of mixing for extensive numerical calculations to determine G_S for an optimized SIS receiver. We find that G_S is very roughly independent of frequency (except for the best junctions at low frequency), and discuss the implications of our results for the design of submillimeter SIS mixers.

INTRODUCTION

Superconductor-insulator-superconductor (SIS) quasiparticle mixers [1] are now firmly established as the most sensitive receiving devices in the vicinity of 100 to 200 GHz. Their behavior is well described by Tucker's quantum theory of mixing [2]. There are now many publications which show excellent agreement between the theory's predictions of a mixer's conversion properties and experimental results, especially at 100 GHz, and the theory also appears to be successful in predicting the noise temperature of the most sensitive SIS mixers.

Given the success of the Tucker theory at 100 GHz, it is desirable to know the predicted performance of SIS mixers at higher frequencies, where there are fewer experimental results but many experiments underway. A large step in this direction was taken by Kerr and Pan [3], who developed a "design procedure" for SIS mixers, really a

set of rules for scaling a successful and reasonably understood low-frequency SIS mixer design to higher frequency. Their argument was carried further and ratified in Ref. [4]. Kerr and Pan concluded that the critical current density of SIS junctions used for mixing should increase as frequency *squared*, rather than in simple proportion to frequency as previously believed. This result presents a stringent constraint on the design of submillimeter SIS mixers, implying that high frequency SIS mixers are much more difficult to realize than had previously been appreciated. This widely quoted conclusion certainly is influencing the design of the current generation of submillimeter SIS mixers.

Kerr and Pan based their analysis on the "$\omega R_N C = 4$ rule": the best SIS mixer performance appears to be obtained when the characteristic parameter $\omega R_N C$ is near 4, where ω is the LO frequency and R_N is the normal state resistance and C the capacitance of the SIS junction. As first advanced in Ref. [5] and more recently discussed in Ref. [6], all SIS mixer experiments exhibiting infinite available gain have $\omega R_N C \geq 4$, while $\omega R_N C < 1$ has always resulted in considerable conversion loss. (To our knowledge this correlation still holds to date.) Presumably, good mixer conversion requires the reduction of harmonic conversion effects by the relatively large capacitance. Indeed, computer simulations show that harmonic conversion becomes significant for $\omega R_N C < 4$ [7]. On the other hand, unnecessarily large capacitance entails greater difficulty in tuning and narrower bandwidth.

The damping time $R_N C$ of an SIS junction varies in inverse proportion to its critical current density, j_c. Therefore j_c must increase proportional to frequency to maintain a constant $\omega R_N C$, and this alone requires an inconveniently large j_c for submillimeter SIS mixers. However, Kerr and Pan rightly note that while the $\omega R_N C = 4$ rule may be valid for 100 GHz SIS mixers, there is no reason to expect that the optimum $\omega R_N C$ is independent of frequency. In particular, their calculations indicate that the quantity $G_s R_N$, the mixer source conductance normalized to R_N, "should have a 1/f dependence for mixers in the quantum-limited regime." This immediately implies that j_c should increase as frequency *squared*.

CALCULATIONS

It is not feasible to optimize an SIS mixer by maximizing the calculated conversion gain. There is no unique optimum bias point: the quantum theory of mixing predicts infinite gain for high quality SIS junctions over a wide range of parameter values. Such high gain is unrealistic and undesirable. Kerr and Pan avoid this difficulty by positing a set of requirements, including unity gain and moderately well matched input (VSWR $\leq$ 2), for optimum SIS design. We take a different approach.

We use the quantum mixer theory for extensive numerical calculations, to determine the minimum value of the SSB (single sideband) noise temperature T_R of an SIS receiver, subject to reasonable experimental constraints. Thus our calculation involves a trade-off between minimizing the mixer noise temperature and maximizing the mixer conversion gain, which is mediated by the noise temperature of the IF amplifier T_{IF}. Full details will appear elsewhere. For our current purpose we make the following approximations: We consider DSB (double sideband) operation in the three-frequency low-IF approximation, which should be a fairly good representation of most well-designed experimental mixers. We do not include any interference from the Josephson effect, although this is likely to be a problem for experiments at the higher frequencies. In addition, we ignore all reactances. Taken together, these approximations are equivalent to assuming 1) that the geometrical capacitance of the SIS junction is large enough to both short out the LO harmonics and their sidebands and to eliminate Josephson interference, 2) that the capacitance is itself resonated by a relatively broadband external tuning circuit, so that the intrinsic junction nonlinearity is presented with a resistive embedding impedance at all relevant frequencies, and 3) that the quantum susceptance has no significant effect. This third assumption is controversial. It has recently been argued that the quantum susceptance is a central element of the behavior of SIS mixers [8]. Nevertheless, we believe that this nonlinear reactance has little effect on the performance of an optimized SIS receiver, though it may affect the optimum bias point. This question will be addressed in further research.

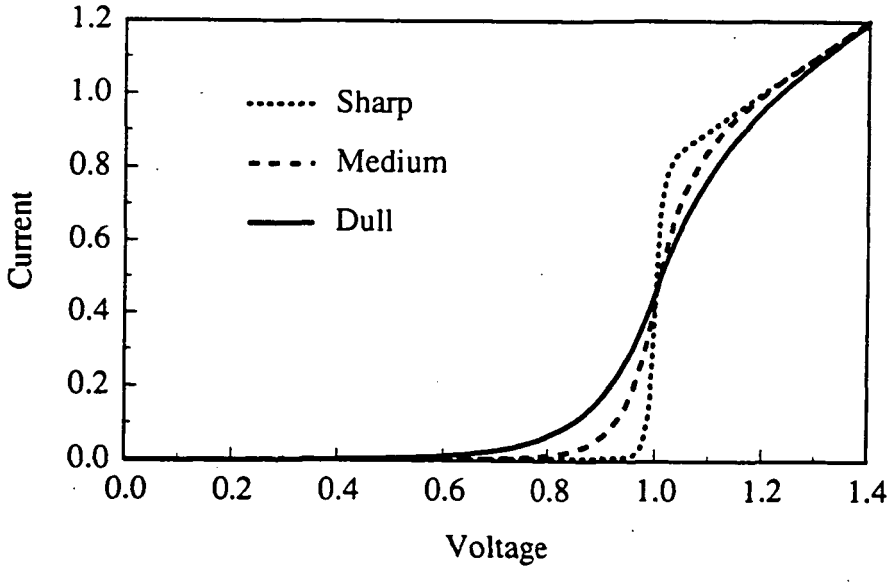

Fig. 1. Three synthetic normalized I-V characteristics used for these calculations.

The equations employed in the calculation of T_R are taken from Ref. [1] and will not be reproduced here. For convenience we assume zero physical temperature; the only serious effect of this is to ignore the thermal noise from the IF termination which is reflected from the mixer back into the IF amplifier. For real SIS receivers this can be an important contribution to the total noise. We require a reasonable input match: in particular we require that both the signal reflection gain *and also the signal-to-image conversion gain* be $\leq 1/4$ (which corresponds to VSWR ≤ 3). We find that this constraint completely eliminates every instance of high conversion gain. What remains is a distinct solution with stable moderate realistic conversion gain and low mixer noise. Moreover we find that our quantitative results are extremely insensitive to the level of returned signal or image power allowed. These topics are discussed at length in Ref. [9].

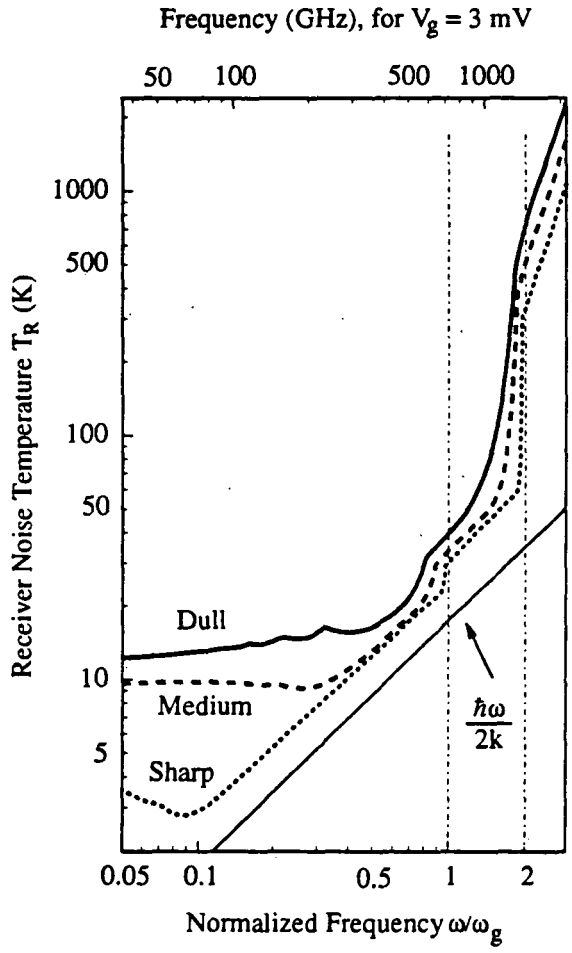

Fig. 2. The SSB noise temperature of a DSB SIS receiver optimized at each frequency, calculated for the three I-V curves of Fig. 1, $G_L = 0.3/R_N$, $T_{IF} = 3$ K, and $V_g = 3$ mV.

We have performed these calculations for each frequency for a wide range of parameters, but only a few of the results can be presented here. The illustrations given in this paper use the synthetic SIS junction I-V curves depicted in Fig. 1. The "sharp" curve corresponds to the best experimental SIS I-V curves, the "medium" curve corresponds to a good quality junction, and the "dull" curve corresponds to a moderate quality junction. We normalize voltages to the energy gap voltage V_g, conductances to the normal state resistance R_N, and frequencies to the energy gap frequency $\omega_g \equiv eV_g/\hbar$.

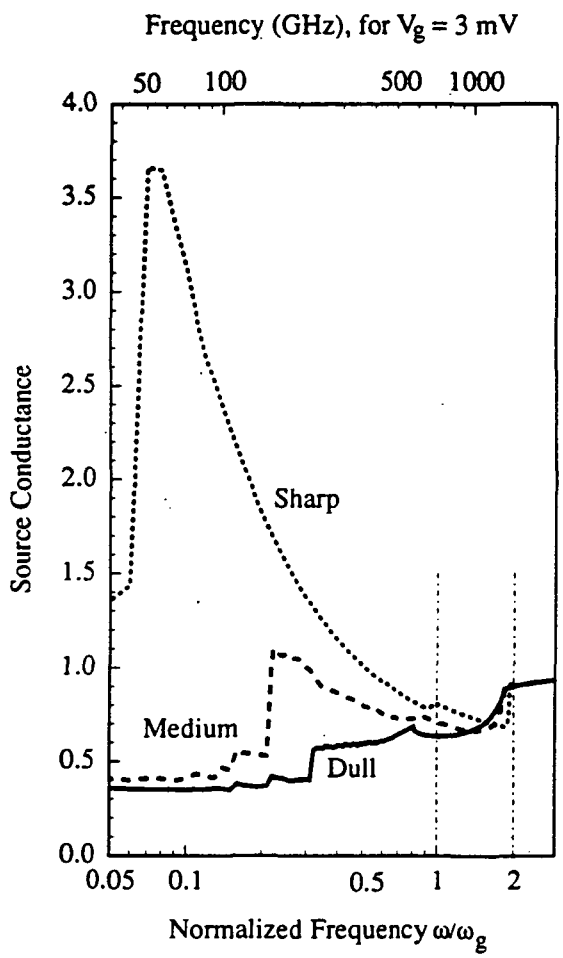

Fig. 3. The normalized source conductance G_SR_N required to optimize the receiver of Fig. 2, calculated for the three I-V curves of Fig. 1.

RESULTS

Figure 2 shows the minimum theoretical SSB noise temperature of a DSB SIS receiver with IF load conductance $G_L = 0.3/R_N$, $T_{IF} = 3$ K, and $V_g = 3$ mV, for the three I-V curves of Fig. 1. Figure 3 shows the optimum value of the normalized source conductance G_sR_N required to achieve the minimum T_R. At lower frequencies (below the vertical rise in each curve) the mixer is biased on higher number photon steps and G_S is relatively constant as expected for classical behavior. On the first photon step, however, the behavior of G_S is quite different. At the lowest frequencies on the first step G_S is strongly dependent on the I-V curve quality; for high quality junctions the optimum G_S is quite large. As the frequency increases, the optimum G_S gradually changes to approach a value ≈ 0.7, for all three I-V curves at frequencies near $2\omega_g$.

Figure 3 clearly shows that the optimum G_S does not have a 1/f dependence. To emphasize this point, in Fig. 4 we plot the quantity $G_S\omega$ vs. ω for the data of Fig. 3. The 1/f dependence predicted by Kerr and Pan [3] would give horizontal lines in Fig. 4, and horizontal lines are nowhere seen. Rather, the optimum G_S for the sharp curve is given by the empirical formula $G_S = 1/2 + 0.25/\omega$ for bias points on the first photon step. This behavior is quite widespread. For instance, Fig. 5 shows the the optimum G_S computed for SIS receivers with various values of T_{IF}, for the sharp I-V curve. The same empirical formula also works well when we consider different values of load conductance, I-V curves with considerable leakage current, etc.

In order to better understand the behavior of the optimum G_S, in Fig. 6 we compare it with all of the important "input" conductances in our calculations. It is seen that even though G_S is determined by a trade-off between the gain and the shot noise, the optimum G_S is quite close to that which minimizes the shot noise, G_{shot}, but far from that which maximizes the gain, G_S'. This surprising result can be explained by examination of the equations of the SIS mixer. On one hand, the dependence of the conversion gain upon G_S is given by a simple impedance matching formula which has its minimum at $G_S = |G_S'|$; a fairly large mismatch therefore results in only a small decrease in gain. On the other hand, the mixer noise is minimized by the exact cancellation of the correlated components of the shot noise at the IF and the signal and image frequencies, which occurs at $G_S = G_{shot}$. If G_S strays from this value the shot noise grows rapidly. The optimum G_S is also far from the signal input conductance, G_S°, but never more than a factor of three lest the signal reflection gain become too large.

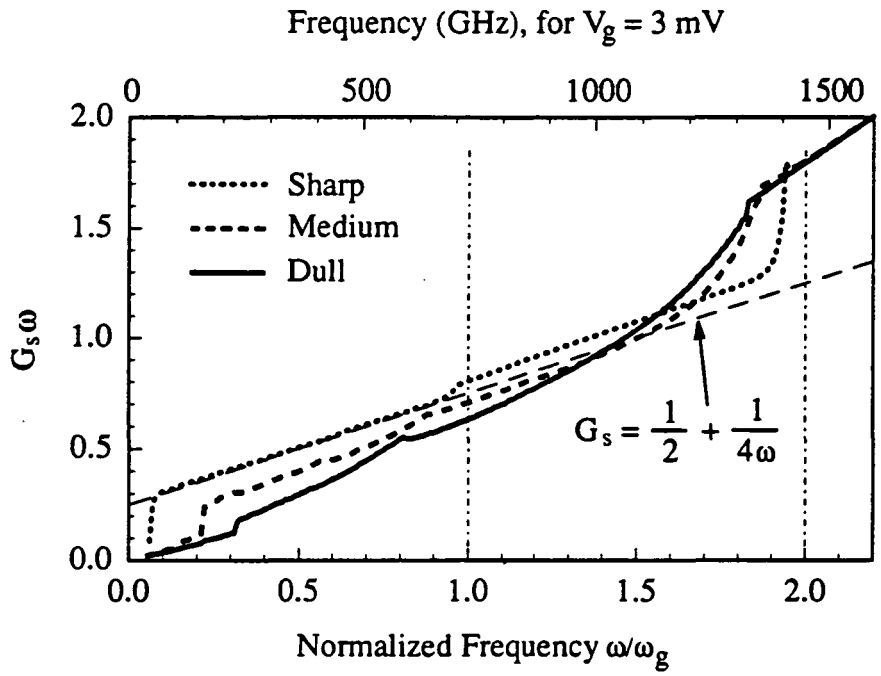

Fig. 4. The data of Fig. 3 are multiplied by ω and replotted (in normalized units), and are compared to an empirical formula.

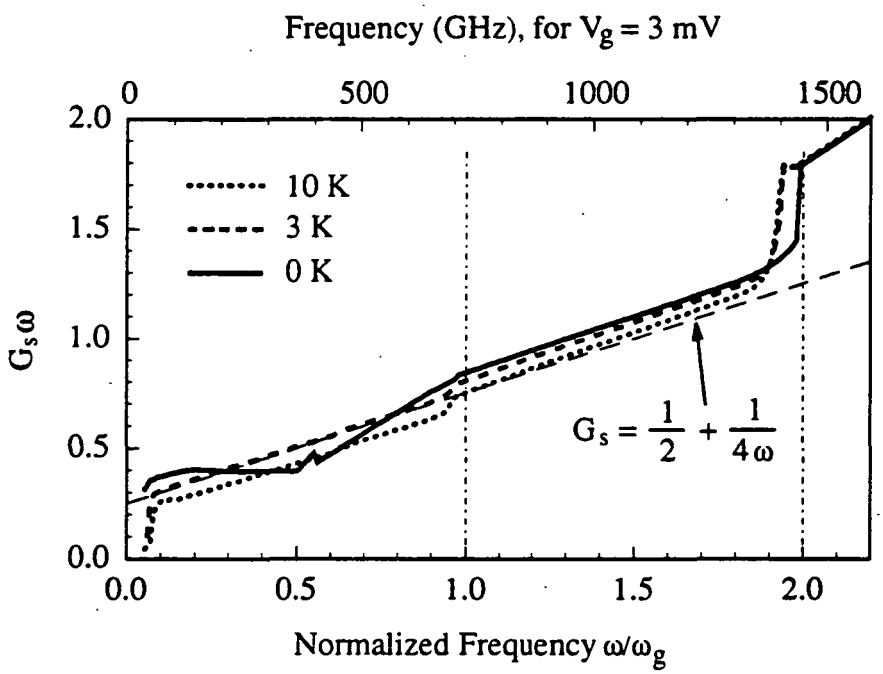

Fig. 5. The optimum source conductance G_S of an SIS receiver whose IF amplifier noise temperature T_{IF} = 10 K, 3 K, and 0 K, respectively, using the "sharp" I-V curve of Fig. 1, $G_L = 0.3/R_N$, and V_g = 3 mV.

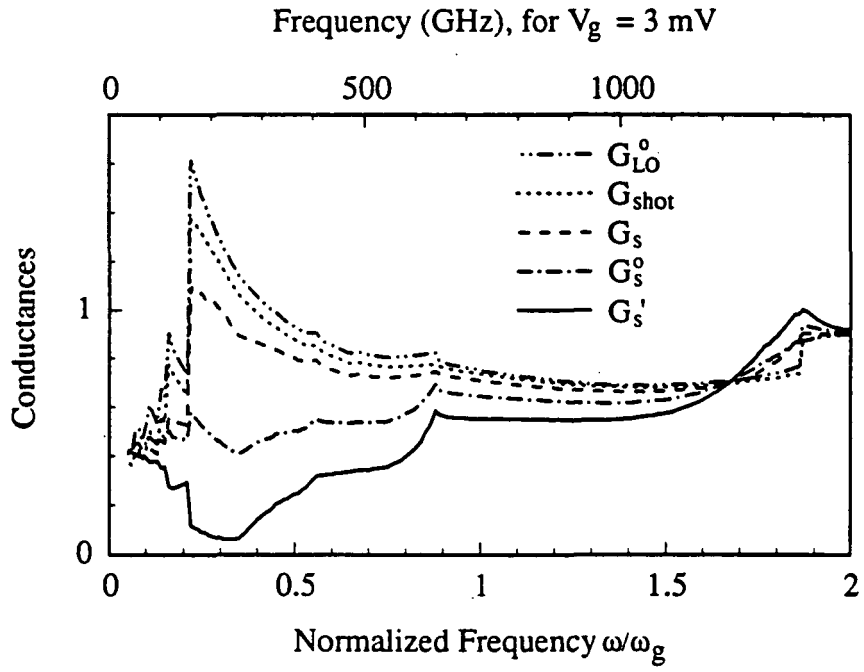

Fig. 6. The optimum source conductance G_S of an SIS receiver using the "medium" I-V curve of Fig. 1, $G_L = 0.3/R_N$, T_{IF} = 3 K, and V_g = 3 mV, compared to various "input" conductances: G^{o}_{LO} and G^{o}_{S} are the input conductances of the mixer at the LO and the signal frequencies, respectively, G_{shot} is the value of G_S which would minimize the shot noise of the mixer, and G'_S is the value of G_S which would maximize the gain of the mixer.

Note in Fig. 6 that G_{shot}, and thus the optimum G_S, follows closely the input conductance at the LO frequency, G^{o}_{LO}. This is exactly as predicted by the simple photodiode theory of SIS mixing [10], which reproduces the the equations of the quantum theory of mixing in the limit of small LO voltage amplitude (small α). It is surprising that G_{shot} follows G^{o}_{LO} so closely for the relatively large α of our simulations. In any case this enables us to explain the empirical formula $G_S = 1/2 + 0.25/\omega$. In the limit of small α, G^{o}_{LO} is the slope of the chord connecting the photon point $I_{dc}(V_0 - \hbar\omega/e)$ to the photon point $I_{dc}(V_0 + \hbar\omega/e)$ on the unpumped dc I-V curve. Therefore, using the preferred value for the optimum dc bias voltage $V_0 = 0.9$ for the sharp I-V curve, this gives $G^{o}_{LO} = 1/2 + 0.35/\omega$ in the small α limit. G_S follows but is slightly less than G^{o}_{LO} (Fig. 6) and so is very well approximated by the empirical formula.

DISCUSSION

The results presented here are for particular parameter values, but they are quite general and representative of our more extensive calculations. In disagreement with Ref. [3], we find that $G_S R_N$ is very roughly independent of frequency (except for the best junctions at low frequency). This means that there is no reason to suppose that it is advantageous to increase j_c as frequency squared in the design of high frequency SIS mixers.

Why do our results differ from Ref. [3]? It is likely that this disagreement arises because in Ref. [3] the gain was fixed to unity, whereas we find that the mixer gain of an optimized SIS receiver falls off roughly as $1/\omega$ for bias points on the first photon step (Fig. 7). Note in Fig. 7 that we find conversion gain as high as 8 dB in the vicinity of 100 GHz, but in our solution the mixer is operating far from instability [9] with low noise and quite low returned signal and image power.

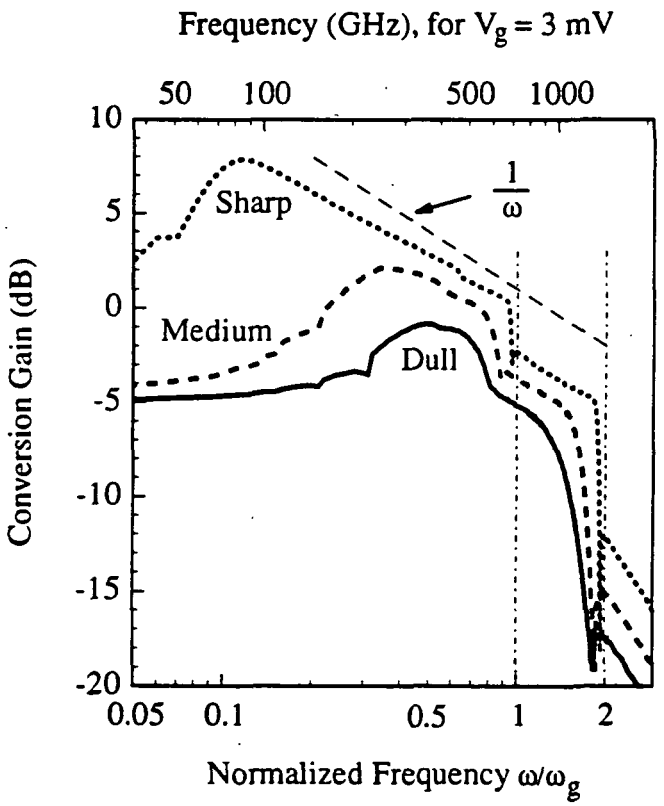

Fig. 7. The IF conversion gain corresponding to the three curves of Fig. 2.

Nevertheless, we agree with Ref. [3] that the "$\omega R_N C = 4$ rule" should be modified for submillimeter SIS mixers. Harmonic conversion effects should become much less important as the frequency is increased, because the SIS junction presents a much weaker nonlinearity for harmonic frequencies above ω_g, especially so for frequencies above $2\omega_g$. This implies that the beneficial effects of the capacitance are reduced as the frequency is increased, and smaller values of $\omega R_N C$ can be tolerated. Since it is more difficult to resonate the capacitance at high frequency, smaller values of $\omega R_N C$ are desirable. However, small area and high critical current SIS junctions are difficult to fabricate, and usually entail undesirable consequences such as inferior junction quality, poorer yield, etc. Therefore, the choice of $\omega R_N C$ for submillimeter SIS mixers will at best be an informed compromise.

Acknowledgment: Parts of this work were performed under funding from the Air Force Office of Scientific Research and from the National Science Foundation.

[1] J.R. Tucker and M.J. Feldman, "Quantum detection at millimeter wavelengths," *Rev. Mod. Phys.*, vol. 57, pp. 1055-1113, Oct. 1985.

[2] J.R. Tucker, "Quantum limited detection in tunnel junction mixers," *IEEE J. Quantum Electron.*, vol. QE-15, pp. 1234-58, Nov. 1979.

[3] A.R. Kerr and S.-K. Pan, "Some recent developments in the design of SIS mixers," in *Proceedings of the First International Symposium on Space Terahertz Technology*, 1990, pp. 363-376; published in *Int. J. Infrared Millimeter Waves*, vol. 11, 1169 (1990).

[4] R. Blundell and D. Winkler, "The superconductor-insulator-superconductor mixer receiver -- a review," in *NATO Applied Research Workshop on Superconducting Electronics and 2nd Workshop on Josephson Devices*, 1990, Capri, Italy.

[5] M.J. Feldman and S. Rudner, "Mixing with SIS arrays," *Reviews of Infrared & Millimeter Waves*, edited by K.J. Button (Plenum, New York), vol.1, pp.47-75, 1983.

[6] M.J. Feldman, "Theoretical considerations for THz SIS mixers," *Int. J. Infrared Millimeter Waves*, vol. 8, pp. 1287-1292, Oct. 1987.

[7] S. Withington and E.L. Kollberg, "Spectral-domain analysis of harmonic effects in superconducting quasiparticle mixers," *IEEE Trans. Microwave Theory Tech.*, vol. MTT-37, pp. 231-238, Jan. 1989.

[8] C.A. Mears, Qing Hu, and P.L. Richards, "The effect of the quantum susceptance on the gain of superconducting quasiparticle mixers," *IEEE Trans. Magnetics*, vol. MAG-27, pp. 3384-3387, March 1991.

[9] Qing Ke and M.J. Feldman, "Reflected power effects and high gain in the quantum theory of mixing," submitted to *IEEE Trans. Microwave Theory Tech.*

[10] M.J. Wengler, "Submillimeter wave detection with superconducting tunnel diodes," submitted to *Proc. IEEE*; see also M.J. Wengler and D.P. Woody, "Optimizing double-sideband SIS quasiparticle mixers," *IEEE Trans. Magnetics*, vol. MAG-27, pp. 3388-3390, March 1991.

RESONANT TUNNELING DIODES AS SOURCES FOR MILLIMETER AND SUBMILLIMETER WAVELENGTHS

O. Vanbésien, R. Bouregba, P. Mounaix and D. Lippens

Centre Hyperfréquences et Semiconducteurs U.A. CNRS N° 287
Université de Lille - 59655 Villeneuve d'Ascq Cédex - France

L. Palmateer[+], J.C. Pernot, G. Beaudin* and P. Encrenaz

Ecole Normale Supérieure 24, rue Lhomond 75231 PARIS
* Observatoire de Meudon 92195 Meudon Principal Cédex

E. Bockenhoff[++], J. Nagle, P. Bois, F. Chevoir and B. Vinter

Laboratoire Central de Recherche Thomson CSF
Domaine de Corbeville 91404 Orsay Cédex - France.

ABSTRACT

High-quality Resonant Tunneling Diodes have been fabricated and tested as sources for millimeter and submillimeter wavelengths. The devices have shown excellent I-V characteristics with peak-to-valley current ratios as high as 6:1 and current densities in the range of 50-150 kA/cm2 at 300 K. Used as local oscillators, the diodes are capable of state of the art output power delivered by AlGaAs-based tunneling devices. As harmonic multipliers, a frequency of 320 GHz has been achieved by quintupling the fundamental oscillation of a klystron source.

[+] Now at IBM, Yorktown Heights [++] at Mercedes Benz, Stuttgart

1. INTRODUCTION

Resonant Tunneling Diodes (RTD's) exhibit very strong non linearity with short time response which make them attractive in non linear applications for millimeter and submillimeter wavelengths [1]. RTD's have already demonstrated their potential for a variety of high speed/high frequency applications [2]-[5]. In this paper we report on the effort of a group of laboratories in France on these novel devices with special emphasis on local oscillators and harmonic multipliers. The fabrication procedures in a whisker contacted technology and in a microwave compatible technology suitable for monolithic integration are outlined in section 2. The DC and AC characterizations are reported in section 3 whereas the oscillator and multiplier results using the devices are described in section 4.

2. TECHNOLOGICAL PROCESS

The two types of epitaxial structures grown by molecular beam epitaxy are given in Figure 1(a) and (b). Both samples noted A and B had 17 Å - thick AlAs barriers and access regions with a stepped doping profile from 1-2x10^{17} cm^{-3} to 2-3x10^{18} cm^{-3}. They differ mainly owing to the strained $Ga_{0.9}In_{0.1}As$ layers so that structure B resembles a triple well resonant tunneling structure. By placing a GaInAs well just prior the growth of the double barrier heterostructure (DBH) it is expected that the peak-to-valley current ratio (PVCR's) should be enhanced because the negative differential resistance effect involves the anticrossing of two confined states [6] [7]. In addition by placing a GaInAs well rather than a GaAs one and by a proper choice of the well width (L_W = 40 Å), the ground state can be lowered in energy while keeping the excited state practically unchanged. The associated benefits are a reduction of the peak voltage and higher PVCR's [8]. Also note that structure A and B are grown on n^+ and S-I substrates respectively.

GaAs	$2\ 10^{18}cm^{-3}$	490 nm
GaAs	$2\ 10^{17}cm^{-3}$	50 nm
GaAs	undoped (UD)	5 nm
AlAs	UD	1.7 nm
GaAs	UD	4.5 nm
AlAs	UD	1.7 nm
GaAs	UD	5 nm
GaAs	$2\ 10^{17}cm^{-3}$	50 nm
GaAs	$2\ 10^{18}cm^{-3}$	500 nm
	n^+ substrate	

(a)

GaAs	$3\ 10^{18}cm^{-3}$	500 nm
GaAs	$10^{17}cm^{-3}$	10 nm
GaAs	undoped (UD)	5 nm
$In_{.1}Ga_{.9}As$	UD	5 nm
GaAs	UD	0.5 nm
AlAs	UD	1.7 nm
GaAs	UD	0.5 nm
$In_{.1}Ga_{.9}As$	UD	4 nm
	Symmetrical layers	

(b)

Figure 1 : Growth sequence for the epilayer on n^+ substrate (sample A). (a) Sample B grown on semi-insulating subtrate. (b)

The epilayers on n+ substrate were processed using a whisker contacted technology including patterning of Ni/GeAu layers into matrix of 3.5 μm diameter dots on the epitaxial side of the wafer and uniform deposition on the back side followed by alloying of these layers to make ohmic contacts. Mesa isolation was performed by chlorine ion beam assisted etching as shown in figure 2, using the patterned metal as a mask. As last stages some of the samples were thinned to a thickness of about 120 μm and polyimide was used to surround the diodes in order to aid whisker contact.

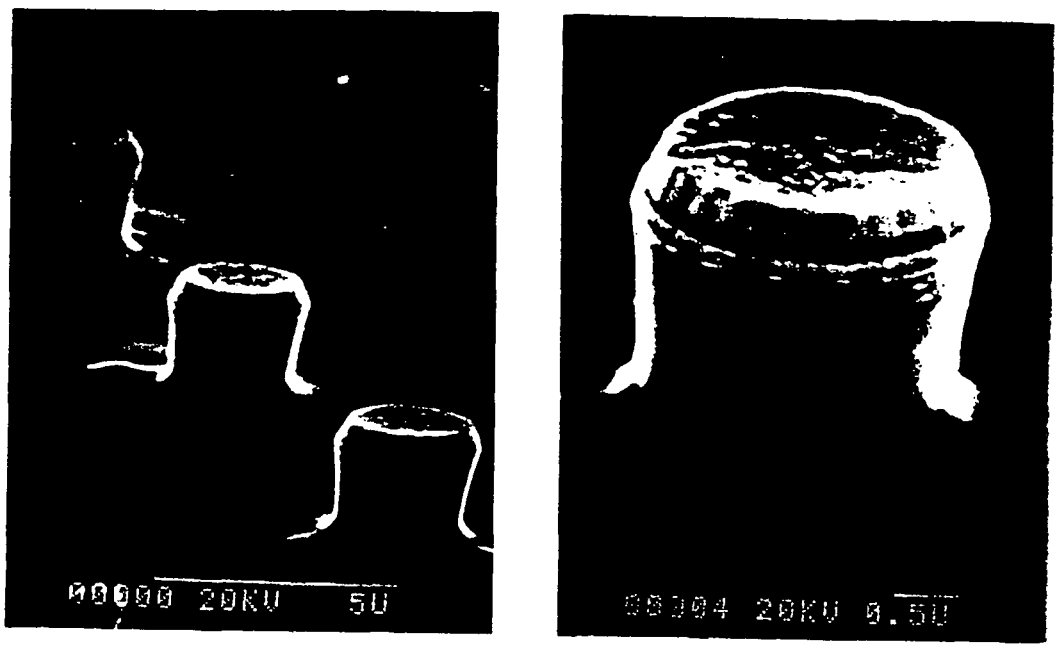

Figure 2 : SEM Photos of diodes formed by RIE.

For the epilayers on S-I substrate, the diodes were fabricated in a microwave-compatible two-step mesa technology [9]. In that case, the devices were connected to low-loss transmission lines in such a way that they can be characterized at the wafer level. Such vertically integrated devices require a means of connecting the contact on the top of the mesa to the pad of the transmission line. We thus developed two versions : (i) a dielectric assisted cross-over and (ii) an air bridge interconnection. A scanning electron micrograph of two representative devices are shown in figures 3 and 4. In figure 3 a coplanar probe configuration is apparent. Also clearly shown is the deposited strap which crosses over the mesa edges covered with $Si_3 N_4$ layer appearing in dark. In the second version, the dielectric cross-over is replaced by an air bridge yielding a reduced parasitic capacitance. Figure 4 illustrates the technology employed with the

mushroom shaped metallization which enables one to connect small anode fingers.

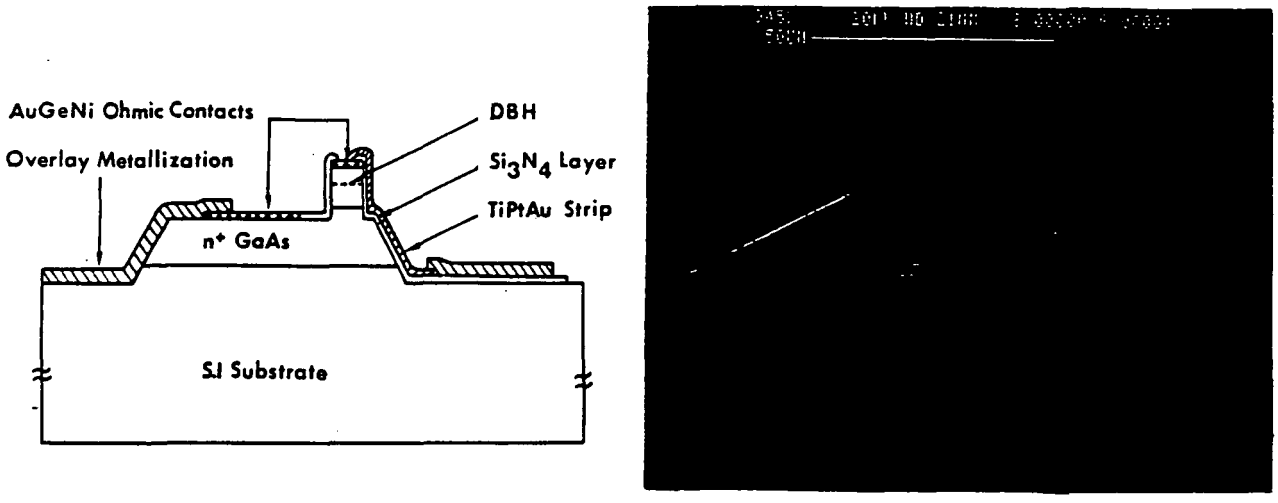

Figure 3 :Schematic cross section and SEM photo of the RTD fabricated in a planar technology.

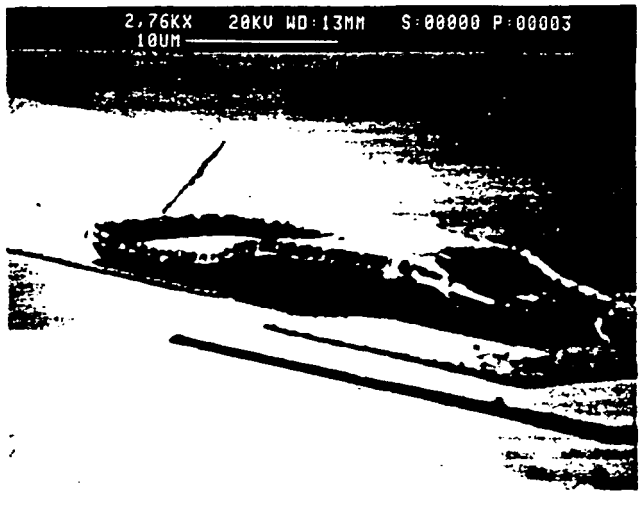

Figure 4 : SEM of a diode fabricated using air bridge techniques.

3. DC AND AC CHARACTERIZATION

Figure 5a shows a typical current voltage I-V characteristic for a GaAs/AlAs device on n+ substrate at 300K. The device exhibits a peak current of ~ 16 mA at ~ 1.8 V which corresponds to a peak current density of ~ 160 kA/cm2 for a 3,5 μm diameter diode. For larger size of the diodes, heating of the samples prevents us from achieving these densities. A typical DC characteristic for a device on SI substrate is displayed in Figure 5b. The device exhibits excellent characteristics with PVCR's as high as 6:1 along with simultaneously peak current density of 50 kA/cm^2 which compare favorably to the best published results [10] [11] Note also the high degree of symmetry in the I-V curve which is a good indicator of quality interfaces.

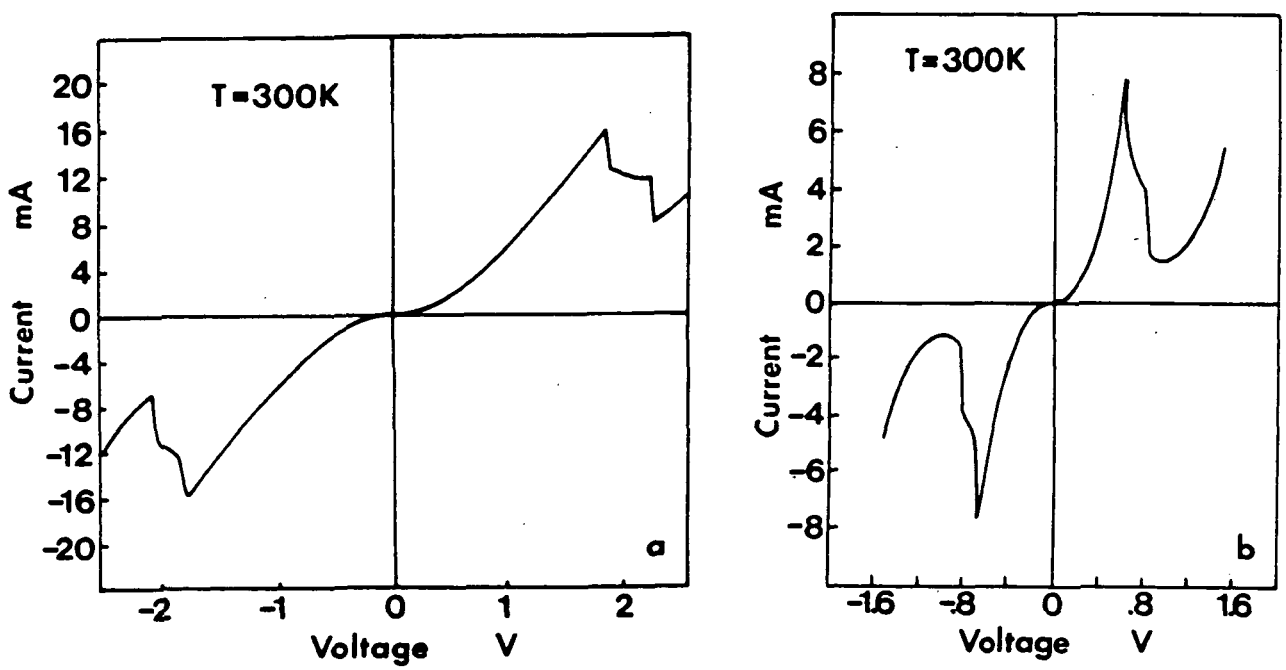

Figure 5 : Typical DC characteristics for a GaAs/AlAs device on n+ substrate (a) and for a GaInAs/GaAs/AlAs pseudomorphic device on SI substrate (b).

Following our previous work [12], on-wafer reflection gain measurements were performed between 50 MHz and 40 GHz using cascade RF probes and an 85107 A HP network analyser. Shown in Figure 6 is the one port measurement of a vertically integrated sample. The active area is 20 μm^2. The diode is biased in the NDR region. Note that no de-embedding was used at this stage to correct for parasitics. For frequency evaluation, we used the equivalent circuit which consists of a single capacitor C_d with a parallel negative resistance R_d. These intrinsic lumped elements are completed by the parasitic capacitance C_p, the inductance Lp attributable to the bonding and Rs the overall series resistance. A good fit was obtained for C_d = 36 fF, R_d = - 172 Ω, R_s = 9 Ω, L_p = 60 pH and C_p = 13 fF (air-bridge technology). With this set of data derived from experiment, the cut off frequency for NDR is in excess of 100 GHz. This frequency is limited by the high impedance level needed to satisfy the stability criteria.

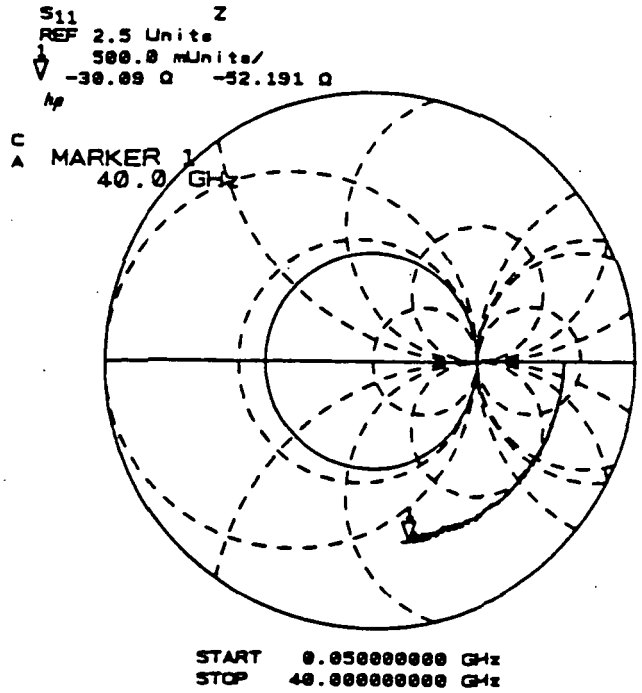

Figuer 6 : One port measurement of the impedance. The bias is adjusted in the NDR region to satisfy the stability criteria.

4. OSCILLATOR AND MULTIPLIER RESULTS

The wafers on n+ substrate were sawed into chips of 100x100 μm^2 and mounted in a test waveguide for measuring the oscillator power at 35 and 110 GHz. The power levels measured at 300 K with a bolometer were 36 µW at 38.6 GHz and 12 µW at 110 GHz. Referring to the oscillator results from the published literature on AlGaAs based RTD's [13] given in figure 7 the output power are state of the art results.

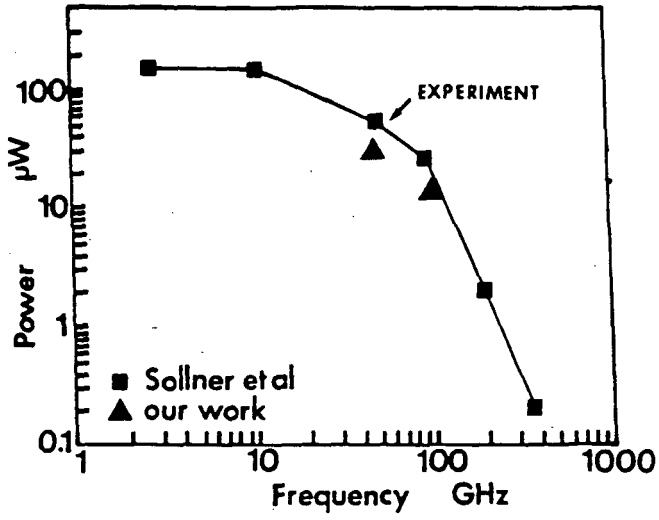

Figure 7 : Experimental powers for a 4 µm diameter diode from reference [13] and results from the present work for a 3.5 µm diameter diode.

For harmonic multiplication, the samples were mounted in a commercially available multiplier mount. The measurement set up has a quasi-optical scheme and was initially developed to study reactive species of astrophysical interest [14]. The diodes were driven by a klystron at 64 GHz and, in the output path, high filters enables one to spectrally analyze the power delivered by the diode. The receiver is a helium cooled InSb detector. Figure 8 shows the power response at 3rd harmonic (192 GHz) and 5th harmonic (320 GHz). For comparison in terms of available power commercial Schottky diodes were also tested under the same

experimental conditions. It is interesting to note that equivalent performances were obtained for both types of devices by increasing the multiplication order to frequency quintupling.

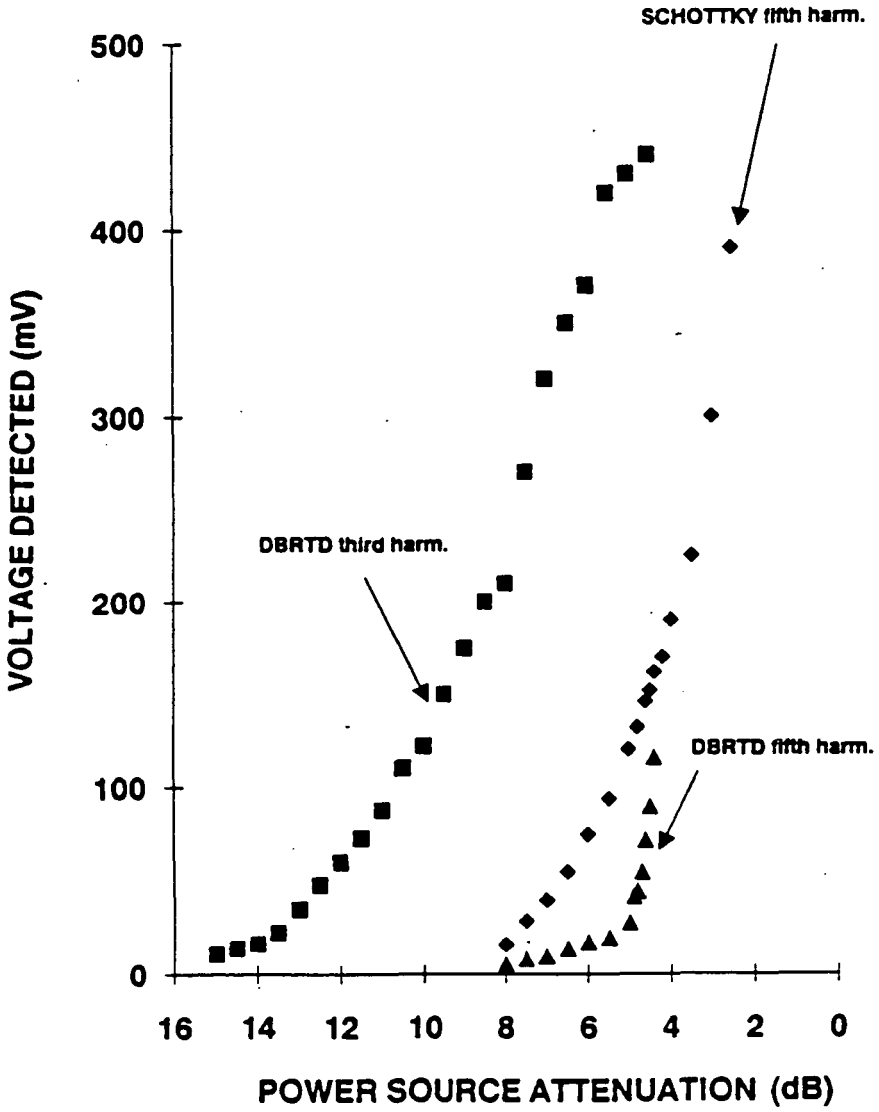

Figure 8 : Measured voltage of InSb detector against input power delivered by a klystron at 64 GHz.

In the multiplier experiment the devices were unbiased and driven in the NDR region to take advantage of multiple extrema in the current waveform. This requirement can be unfavorable especially for high threshold voltage devices when input power is limited [14]. From this viewpoint, it is clear that pseudomorphic structures with a buried well may overcome partly this difficulty. From Figure 3 it is apparent that a drastic decrease in the peak voltage 0.8 V instead of 1.8 V has been achieved by comparing structures A and B. In addition it can be noted that the PVCR's were enhanced. This suggests the superiority of these new tunneling devices for multiplication in view of the large harmonic content in the current and of the reduction of the amount of input power required to pump the diode.

5. CONCLUSION

High performance resonant tunneling diodes were sucessfully fabricated in a whisker contacted and in a planar technology. The RF capabilities of the diodes were demonstrated either by direct measurement of their small-signal impedance or by using them for oscillator and multiplier.

ACKNOWLEDGEMENTS

This work was supported by the Ministère de la Recherche et de la Technologie. Technical assistance of M. Bogey, J.L. Destombes and A. Lescluse with the Laboratoire de Spectroscopie Hertzienne of the Lille University is highly appreciated.

REFERENCES

[1] T.C.L.G. Sollner, E.R. Brown and H.Q. Le, "Microwave and Millemeter-wave Resonant Tunneling Devices". Physics of Quantum Electron Devices edited by F. Capasso Springer-Verlag.

[2] E.R. Brown, J.R. Söderstorm, CD. Parker, L.J. Mahoney, K.M. Kolvar and T.C. Mc Gill, "Oscillations up to 712 GHz in InAs/AlSb resonant tunneling diodes". Appl. Phys. Lett. 58, pp. 2291-2293, May 1991.

[3] A. Rydberg and H. Grönquist "Quantum well high efficiency millimeter-wave frequency tripler". Electronics Letters, Vol. 25, pp. 348-349, 1989.

[4] P.D. Batelaan and M.A. Frerking, "A quantum well frequency multiplier with millimeter wave output". Proc. 4th Conf. Infrared Physics Zurich, pp. 527-529, 1988.

[5] R. Bouregba, D. Lippens, L. Palmateer, E. Bockenhoff, M. Bogey, J.L. Destombes and A. Lecluse, "Frequency multiplication using resonant tunneling diode with output at submillimeter wavelengths". Electronics Lett. Vol.26, pp. 1804-1905, October 1990.

[6] D. Thomas, F. Chevoir, E. Barbier, Y. Guldner and J.P. Vieren, "Magneto tunneling of charge build up in double barrier diodes". Proc. of 4th International Conference on Superlattices Microstructures and Microdevices 5, pp. 219-224, 1989.

[7] P. Mounaix, O. Vanbesien and D. Lippens, "Effect of cathode spacer layer on the current-voltage characteristics of resonant tunneling diodes". Appl. Phys. Lett. 57, pp 1517-1519, October 1990.

[8] T.P.E. Broeckaert, W. Lee and C.G. Fonstad "Pseudomorphic $In_{0.53}Ga_{0.47}As$/AlAs/InAs resonant tunneling diodes with peak-to-valley current ratios of 30 at room temperature.

[9] D. Lippens, E. Barbier and P. Mounaix, "Fabrication of High-Performance $Al_xGa_{1-x}As/In_yGa_{1-y}As$/GaAs Resonant Tunneling Diodes using a Microwave-compatible Technology. IEEE Electron Dev. Lett. Vol. 12, pp. 114-116, March 1991.

[10] R.M. Kapre, A. Madhukar, and S. Guha "Highly strained GaAs/InGaAs/AlAs resonant tunneling diodes with simultaneously high peak current densities and peak-to-valley current ratios". Appl. Phys. Lett. 58, pp. 2255-2257, May 1991.

[11] H. Brugger, U. Meiners, C. Wölk, R. Deufel, A. Morten, M. Rossmanith, K.V. Klitzing and R. Sauer "Pseudomorphic Two Dimensional Electron-Gas-Emitter Resonant Tunneling Devices" Microelectronics Engineering Elsevier, 15, pp. 663-666, 1991.

[12] P. Mounaix, P. Bedu, D. Lippens and E. Barbier "Measurement of negative differential conductance up to 40 GHz for vertically integrated resonant tunneling diodes". Electronics Letters Vol. 27, pp. 1358-1359, July 1991.

[13] E.R. Brown, T.C.L.G. Sollner, C.D. Parker, W.D. Goodhue and C. Chen. "Oscillations up to 420 GHz in GaAs/AlAs resonant tunneling diodes" Appl. Phys. Lett. 55, pp. 1777-1779, October 1989.

[14] J.L. Destombes, C. Demuynck and M. Bogey "Millimeter-wave and submillimeter-wave spectroscopy of molecular ions". Phil. Trans. R. Soc. A 324, pp. 147-162, 1988.

Simulation of Electron Transport in Quantum Well Devices

D. R. Miller, K. K. Gullapalli, V. R. Reddy, and D. P. Neikirk

Department of Electrical and Computer Engineering
Microelectronics Research Center
The University of Texas at Austin

1.0 Introduction

Double barrier resonant tunneling diodes (DBRTD) have received much attention as possible terahertz devices. Experimentally, DBRTD's have shown detection capabilities at sub-millimeter wavelengths[1]. When used as oscillators, small amounts of power have also been measured in sub-millimeter range[2]. Despite these impressive experimental results, the specific of the device physics (i.e., how the electrons propagate through the structure) are only qualitatively understood. Therefore, better transport models are warranted if this technology is to mature.

Near the heterostructure double barrier region, it is generally accepted that quantum mechanical transport, via tunneling and reflections, dominate the electron dynamics. However, most DBRTDs in use today are designed with extended spacer regions. These spacer regions serve the function of increasing the real part of the overall device impedance while simultaneously reducing the imaginary part, thereby incorporating DBRTDs in millimeter wave circuits a far easier task. Since the spacer regions are sufficiently removed from the heterojunctions, electron propagation should be govern by semiclassical and not quantum mechanical considerations. Here, semiclassical refers to transport which is adequately describe using some form of the semiclassical Boltzmann equation.

Past simulation models of DBRTD structures have evolved from simple Schrödinger equation solutions of a free electron in a double barrier potential to more complicated methods involving multiband, multivalley Schrödinger solutions[3,4] or single valley kinetic equations that utilizes quantum Wigner functions[5,6,7]. These methods are expected to work reasonably well for ideal DBRTD structures with parabolic bands in which only quantum mechanical reflections and tunneling are important. However, because the Schrödinger or single valley Wigner models do not include realistic phonon scattering or band structure effects (i.e., multiple valleys, non-parabolicity, multiple bands, etc.) these models do not adequately address the transport through the semiclassical region. Alternatively, the semiclassical Boltzmann equation provides an adequate description of the semiclassical region, but fails completely near the DBRTD heterostructure region.

To model a DBRTD structure with two distinct transport regions, two options are available. The first option incorporates a composite scheme by which each region is modeled with an equation suitable for that region. The two solutions are then matched at a quantum / classical interface to obtain a self consistent solution throughout the device. We find combinations of a free particle Schrödinger equation for the quantum region coupled with either the drift/diffusion[8] or Monte Carlo[9] formalism for the semiclassical region quite useful. However, agreement between experiment and theory is still lacking since the simple Schrödinger equation is only an approximate solution of the electron transport within the heterostructure region.

The second option is to model the entire device with one self consistent formalism that, in principle, can account for all the important device physics for each region. The kinetic equation based upon the Lattice Wigner function is a promising candidate for such a task. In this paper, we will use the Lattice Wigner function to explain important transport issues associated with DBRTD device behavior.

2.0 The Lattice Wigner Function

The lattice Wigner function[10,11] we employ is based on the discrete spectrum composed of Wannier and Bloch crystal representations, making it different from other Wigner function methods. Because of the choice of representations, band structure effects are explicitly included in the kinetic equation. Thus, issues such as Γ to X tunneling, non-parabolicity of the conduction bands, or effective mass variations across the heterojunction,

can be examined in detail. Phonon scattering is also included through the standard semiclassical Boltzmann collision term.

In a multiple barrier heterostructure device with multiple non-parabolic conduction band valleys and no interband coupling, it is possible to write separate, but coupled, kinetic equations for each valley. The Wigner function for the i^{th} valley, f_i^W, is found from the solution of

$$0 = \frac{\partial f_i^W(\mathbf{R},\mathbf{k})}{\partial t} + \frac{1}{\hbar}\frac{\partial \varepsilon_n(\mathbf{k})}{\partial \mathbf{k}} \cdot \frac{\partial f_i^W(\mathbf{R},\mathbf{k})}{\partial \mathbf{R}} - \frac{e\mathbf{E}}{\hbar} \cdot \frac{\partial f_i^W(\mathbf{R},\mathbf{k})}{\partial \mathbf{k}} - \left(\frac{\partial f_i^W(\mathbf{R},\mathbf{k})}{\partial t}\right)_{Col} - \sum_{j=1}^{\#Valleys} \sum_{m=1}^{\#Barriers} B_0^{i,j,m} + B_1^{i,j,m} + B_2^{i,j,m} \quad (1)$$

where the barrier scattering matrices, B_0, B_1, and B_2 are given by

$$B_0^{i,j,m} = \frac{\Delta E_{c(m)}^i(\mathbf{k})}{i\hbar} \sum_{\mathbf{k}'} f_j^W(\mathbf{R},\mathbf{k}') \left(\frac{1}{N_L} \sum_{\mathbf{R}'} e^{i\mathbf{R}'(\mathbf{k}'-\mathbf{k})} \left(V_{Pulse(m)}^{nn}\left(\mathbf{R}+\frac{\mathbf{R}'}{2}\right) - V_{Pulse(m)}^{nn}\left(\mathbf{R}-\frac{\mathbf{R}'}{2}\right)\right)\right) \quad (2)$$

$$B_1^{i,j,m} = -\frac{\Delta v_\Delta^i}{2} \sum_{\mathbf{k}'} \frac{\partial f_j^W(\mathbf{R},\mathbf{k}')}{\partial \mathbf{R}} \left(\frac{1}{N_L} \sum_{\mathbf{R}'} e^{i\mathbf{R}'(\mathbf{k}'-\mathbf{k})} \left(V_{Pulse(m)}^{nn}\left(\mathbf{R}+\frac{\mathbf{R}'}{2}\right) + V_{Pulse(m)}^{nn}\left(\mathbf{R}-\frac{\mathbf{R}'}{2}\right)\right)\right) \quad (3)$$

$$B_2^{i,j,m} = -\frac{\hbar}{8im_\Delta^{i*}} \sum_{\mathbf{k}'} \frac{\partial^2 f_j^W(\mathbf{R},\mathbf{k}')}{\partial \mathbf{R}^2} \left(\frac{1}{N_L} \sum_{\mathbf{R}'} e^{i\mathbf{R}'(\mathbf{k}'-\mathbf{k})} \left(V_{Pulse(m)}^{nn}\left(\mathbf{R}+\frac{\mathbf{R}'}{2}\right) - V_{Pulse(m)}^{nn}\left(\mathbf{R}-\frac{\mathbf{R}'}{2}\right)\right)\right) \quad (4)$$

The indices, j and q, indicate the j^{th} conduction band valley and the q^{th} barrier. The coefficients, $B^{i,j,q}$, are the potential energy terms that account for one heterostructure barrier. In equations 1 through 4, n is the band index, $\mathbf{k}$ and $\mathbf{k}'$ are crystal momenta, $\mathbf{R}$ and $\mathbf{R}'$ are lattice vectors, N_L is the number of lattice sites, and $\mathbf{E}$ is the electric field. $V_{pulse}^{nn(q)}$ is the potential energy diagonal matrix element of the m^{th} pulse function that localizes the barrier. The change in the i^{th} valley effective mass (m_Δ^{*i}), velocity (v_Δ^{*i}), and the offset energy (ΔE^i) are given by

$$\frac{1}{m_\Delta^{*i}} = \frac{1}{m_{Barrier}^{*i}} - \frac{1}{m_{Bulk}^{*i}} \quad (5)$$

$$v_\Delta^i = \frac{1}{\hbar}\frac{\partial \varepsilon_n^{Barrier}(\mathbf{k})}{\partial \mathbf{k}} - \frac{1}{\hbar}\frac{\partial \varepsilon_n^{Bulk}(\mathbf{k})}{\partial \mathbf{k}} \quad (6)$$

$$\Delta E^i(\mathbf{k}) = \varepsilon_n^{Barrier}(\mathbf{k}) - \varepsilon_n^{Bulk}(\mathbf{k}) \quad (7)$$

where $\varepsilon_n^{barrier}(\mathbf{k}_i)$ and $\varepsilon_n^{bulk}(\mathbf{k}_i)$ are the minimum conduction band energies of the i^{th} valley for the barrier and bulk materials, respectively.

As noted earlier, equation 1 accounts for both effective mass variations across the heterostructure interface and intervalley coupling. The intervalley coupling is possible since the i^{th} valley distribution function f_i^W is coupled to the j^{th} valley distribution function f_j^W through the barrier terms. Effective mass variation effects are due to the crystal momentum dependence of the barrier, and result in the spatial derivatives of the distribution function in the $B_1^{j\,q}$ and $B_2^{j\,q}$ terms. Mass variations are also responsible for raising and/or lowering the barrier height, as seen in the expression for $B_0^{j\,q}$. This is because the energy band of the bulk material may rise at a different rate than the energy band of the barrier material for a given momentum change. For semiconductors with non-parabolic valleys, additional barrier scattering terms arise due to the higher derivatives associated with the Wigner-Moyal expansion. However, in this paper we will assume that the effective masses and the non-parabolicity factors are approximately the same for the bulk and barrier material. Therefore, B_1, B_2, and all other higher barrier scattering terms will be set to zero.

Including some sort of phonon collision processes into a Wigner function calculation of an DBRTD is not new. Most calculations have approximated the influence on carrier transport from phonon collisions using the relaxation time approximation[7,12,13]. In addition, these calculations have restricted phonon scattering events to one valley. However, because of the high electric fields within the DBRTD structure, intervalley scattering is required. Thus, we will assume that the total scattering matrix, S_{Total}, is given by

$$S_{Total}^{j,i}(\mathbf{k}',\mathbf{k}) = S_{pop}^{j,i}(\mathbf{k}',\mathbf{k}) + S_{Acoustic}^{j,i}(\mathbf{k}',\mathbf{k}) + S_{Intervalley}^{j,i}(\mathbf{k}',\mathbf{k}) \tag{9}$$

where S_{pop}, $S_{Acoustic}$, and $S_{Intervalley}$ refer to the polar optical, acoustical, and intervalley phonon scattering matrices, respectively. Assuming non-degenerate statistics, we can write the collision term in equation 1 for the i^{th} valley Wigner function as

$$\left(\frac{\partial f_i^W(\mathbf{R},\mathbf{k})}{\partial t}\right)_{Col} = \frac{1}{N_L}\sum_{j=1}^{N_V}\left\{\sum_{\mathbf{k}'}^{j^{th}Valley}\left(S_{Total}^{i,j}(\mathbf{k},\mathbf{k}')f_j^W(\mathbf{R},\mathbf{k}') - S_{Total}^{j,i}(\mathbf{k}',\mathbf{k})f_i^W(\mathbf{R},\mathbf{k})\right)\right\} \tag{8}$$

where N_V is the total number of valleys. The material parameters as well as the functional form for each scattering matrix are identical to those used in Monte Carlo device simulations and are given in reference 14.

The Wigner distribution function for each valley is defined in the three dimensional crystal momentum space. If the structure and the electric field are homogeneous in two of the spatial variables (independent of R_y and R_z), equation 1 reduces to a four dimensional integral/differential equation. Since solutions to the four dimensional problems are exceedingly difficult, further simplification is required. We do this by characterizing the distribution function that is transverse to the electric fields by a Maxwellian defined at some transverse temperature T_t. Furthermore T_t is assumed to vary with longitudinal position. Thus, for electric fields in the (100) direction with quantum well barriers grown in the (100) plane, the total distribution function is approximated by the product of a transverse and a longitudinal distribution functions

$$f_i^W(R_x,k_x,k_y,k_z) = f_i^{R_x}(R_x,k_x)\exp\left(-E_t^i / k_b T_t(R_x)\right) \tag{9}$$

where k_x, k_y, and k_z are defined with respect to the valley minimum. The transverse energy for non-parabolic valleys , E_t, is assumed to be of the form

$$E_t^i = \frac{\left(\frac{\hbar^2 k_y^2}{2m_y^{*i}} + \frac{\hbar^2 k_z^2}{2m_z^{*i}}\right)}{\left(1+\sqrt{1+4\alpha_i\left(\frac{\hbar^2 k_x^2}{2m_x^{*i}} + \frac{\hbar^2 k_y^2}{2m_y^{*i}} + \frac{\hbar^2 k_z^2}{2m_z^{*i}}\right)}\right)\Big/2} \tag{10}$$

where α_i is the non-parabolicity factor for the i^{th} valley. Note that although the longitudinal and transverse distribution functions are not coupled through the electric field or the barrier scattering matrix, they are coupled by the phonon scattering matrix. It is because of the this coupling that the transverse temperature significantly impacts the device physics, as discussed in the next section.

3.0 Simulation Results

The first obvious question that can be addressed with the lattice Wigner function is how close to the quantum well an electron is when quantum mechanical reflections and/or tunneling affect the electron's behavior. One measure of this distance is obtained by comparing the size of the barrier matrix (B_0) with the size of the phonon matrix (S_{Total}) at each lattice site. However, such a direct comparison may provide an overestimate of the extent of the quantum region. During one phonon scattering interval, an electron may

propagate through many lattice sites due to either a high electric field or a high initial velocity. Therefore, the effective barrier scattering strength is an average over all lattice sites occupied during the mean free flight time between collisions. In other words, the barriers' influence on the electrons is best determined by the matrix

$$B_{Total} = \frac{1}{t_1 - t_0} \sum_{j=1}^{\#Barriers} \int_{t_0}^{t_1} B_0^{i,j,m}(R_x(t), k_x(t))dt \qquad (11)$$

integrated over the classical trajectory. In equation 11, B_0 is the matrix defined by equation 2, and $R_x(t)$ and $k_x(t)$ are given by the semiclassical equations of motion.

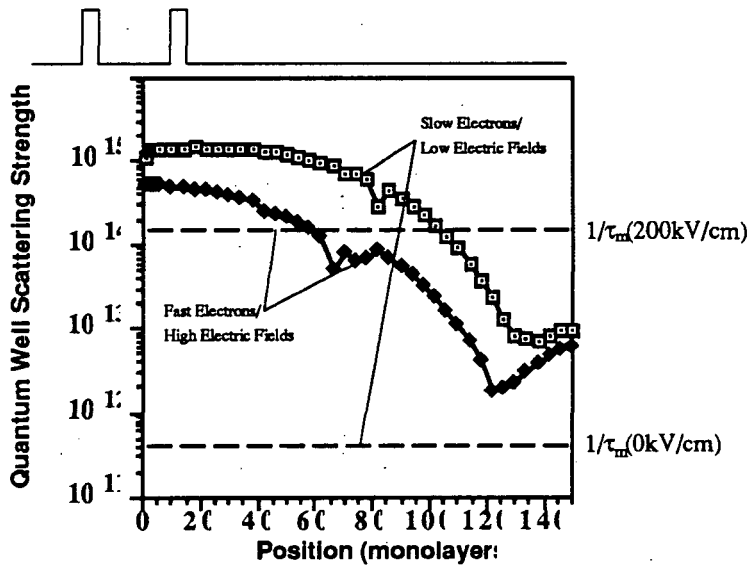

Figure 1. Effective quantum well scattering strength versus position from the center of a 6/19/6 GaAs/AlAs quantum well.

It is difficult to evaluate the above equation for the general case. However, Figure 1 shows the effective quantum well scattering strengths determined by taking the matrix norm of B_{Total} for two simplified conditions. The structure is a 6/19/6 GaAs/AlAs quantum well. The first solid line assumes the case of an extremely slow electron in which the electron transverses only one lattice site between phonon collisions. The second line assumes that the mean free path was 32 monolayers, corresponding to a distance of 90.6 Å. In both cases the electric field was set to zero, which significantly simplified the integration along the classical trajectory. Also plotted are the momentum relaxation times corresponding to different electric fields. These values represent the size of the phonon

scattering matrix (S_{Total}) determined using standard Monte Carlo simulations of homogeneous material[9]. Thus, when comparing the relative strengths of the quantum well and the phonon scattering matrices, one should compare the fast electron case with the high field momentum relaxation time since these two conditions usually exist together. Similarly, the slow electron case corresponds to the zero electric field relaxation time.

Two points are worth emphasizing from Figure 1. The first is that slow electrons are influenced by the quantum well with greater strength and at greater distances when compared to fast electrons. The second point, however, is the one which we want to emphasize. DBRTD structures are usually operated at extremely high electric fields (200 kV/cm) and under ballistic conditions. Therefore, as can be seen from the fast electron curve of Figure 1, the region where the barrier potential has the greatest impact on electron dynamics is within 65 monolayers of the center of the well. Beyond that region, phonon scattering is more important. This fact supports the hypothesis that much of the DBRTD is governed by semiclassical considerations for devices that extend 400 to 800 monolayers from the quantum well.

The Wigner function has been used extensively to account for the quantum transport within the heterostructure region of a DBRTD device. However, the question arises as too its ability to properly account for electron transport within the semiclassical region. To show that this is possible, we have used the Lattice Wigner Function to calculate the velocity versus electric field characteristics for homogeneous GaAs. For homogeneous samples, equation 1 reduces to

$$0 = -\frac{eE}{\hbar}\cdot\frac{\partial f_i^W(\mathbf{R},\mathbf{k})}{\partial \mathbf{k}} - \frac{1}{N_L}\sum_{j=1}^{N_v}\left\{\sum_{\mathbf{k}'}^{j^{th}\text{Valley}}\left(S_{Total}^{i,j}(\mathbf{k},\mathbf{k}')f_j^W(\mathbf{R},\mathbf{k}') - S_{Total}^{j,i}(\mathbf{k}',\mathbf{k})f_i^W(\mathbf{R},\mathbf{k})\right)\right\} \quad (12)$$

To solve this equation, the first step is to integrate over the transverse crystal momentum directions. The resulting one dimensional phonon scattering matrix is then combined with the matrix generated by the electric field term to yield the equation

$$0 = \mathbf{T}_{R'_x,j,k'_x}^{R_x,i,k_x}\cdot\mathbf{f}^{R'_x,j,k'_x} \quad (13)$$

where $\mathbf{T}$ is the combined phonon/electric field matrix and $\mathbf{f}_i^{Rx,j,kx}$ is the vectorized longitudinal distribution function. The valid solution exists when the minimum eigenvalue of $\mathbf{T}$ is equal to zero [15]. If the minimum eigenvalue is not zero, the electric field and the valley transverse temperatures, T_t, are adjusted so that homogeneous equation can be

satisfied. In affect, we are using the transverse valley temperatures as fitting parameters to achieve a reasonable velocity versus field curve. Once the zero eigenvalue is calculated, the eigenvector for that eigenvalue can be determined, from which the velocity is obtained. Note that pure state tunneling models using only the Schrödinger equation do not produce reasonable velocity-field curves for GaAs.

The above procedure yields good agreement with the Monte Carlo results, as indicated in Figure 2. Here, a velocity field curve generated by equations 12 and 13 is compared against a three valley model calculated using standard Monte Carlo techniques. Furthermore, the temperatures required to obtain this level of agreement are comparable to the transverse temperatures calculated from the homogeneous Monte Carlo simulations. However, at low electric fields there is a larger discrepancy between the two alternative approaches. This difference is probably due to the fact that the transverse distribution function is not precisely Maxwellian. However, this error is fairly small, demonstrating that the Lattice Wigner function is capable of simulating both the quantum transport region and the classical transport regions of a device.

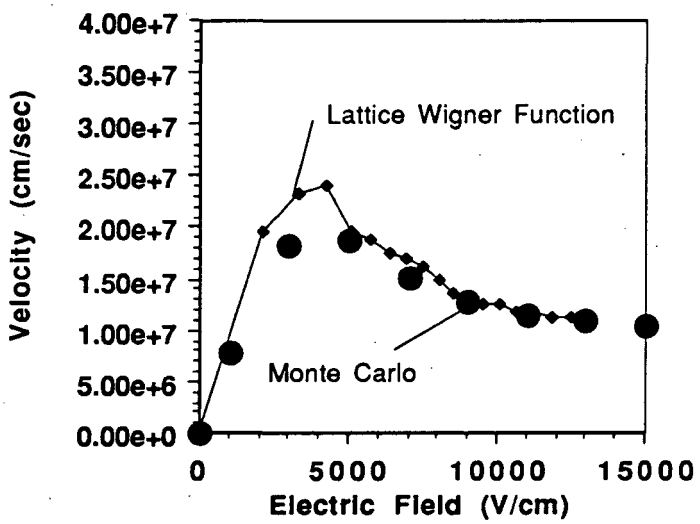

Figure 2. Velocity field calculation for a 3 valley spherical non-parabolic Wigner function model. Also shown is the corresponding result from a Monte Carlo simulation. The scattering parameters used for each calculation are identical, and are found in reference 14.

Thus far, we have applied the Lattice Wigner function to determine generic properties of bulk materials and of resonant tunneling transport. This formalism's real

usefulness can be demonstrated by applying it to an actual DBRTD device. Shown in Figure 3 is a typical GaAs/AlAs DBRTD. The quantum well consists of 6 monolayer AlAs barriers separated by 19 monolayer GaAs well. As can be seen in Figure 3, a moderately doped, extended spacer region is added to the right hand side of the quantum well. As will be shown latter, it is the semiclassical transport through the extended spacer layer that can have a serious impact on device behavior.

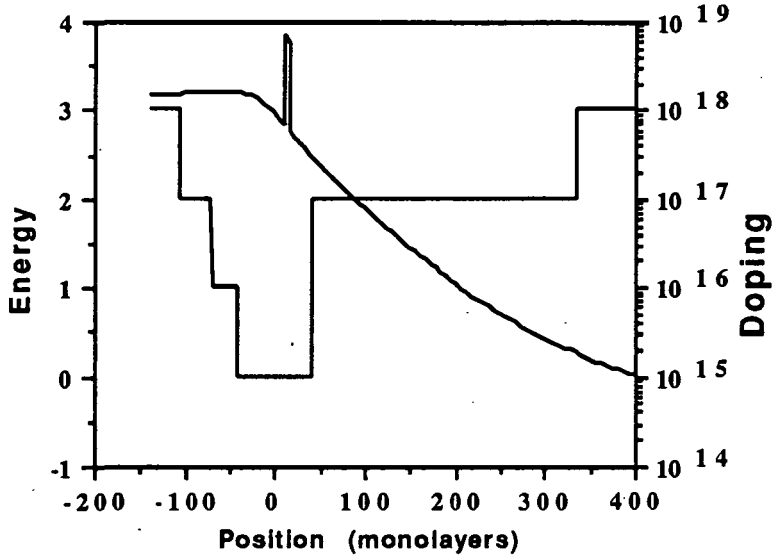

Figure 3. 6/19/6 GaAs/AlAs DBRTD used for the device simulations. The x axis origin is defined as the center of the quantum well.

The equilibrium electron concentration, found by integrating the Lattice Wigner function over momentum space, is shown in Figure 4. However, under bias conditions, obtaining the electron concentration via the Lattice Wigner function is much more complicated. The basic problem is in determining the transverse temperature profile of the spacer region. We have previously shown using a composite Schrödinger/Monte Carlo model [9], that for typical bias voltages, electrons are quickly scattered into the upper satellite values once they emerge from the quantum well. This intervalley scattering between equivalent and non-equivalent conduction band valleys quickly heats up the carrier distribution functions in the transverse direction. The effect of the carrier heating on the charge densities can be considerable.

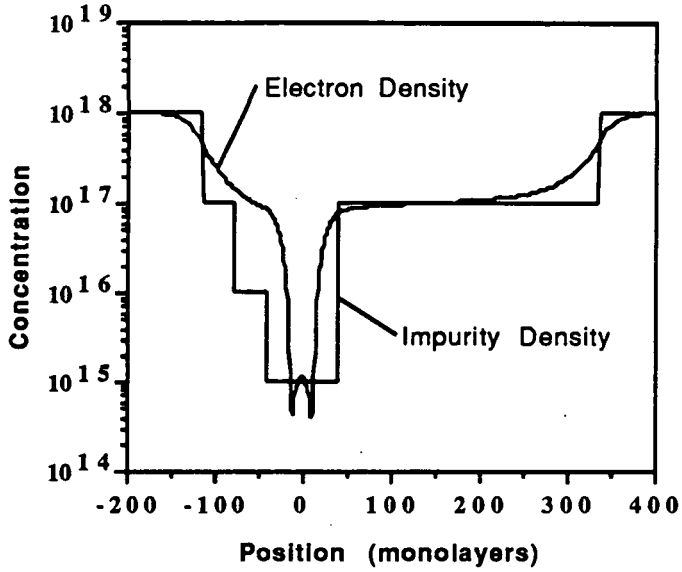

Figure 4. Equilibrium electron concentration for the device shown in Figure 3.

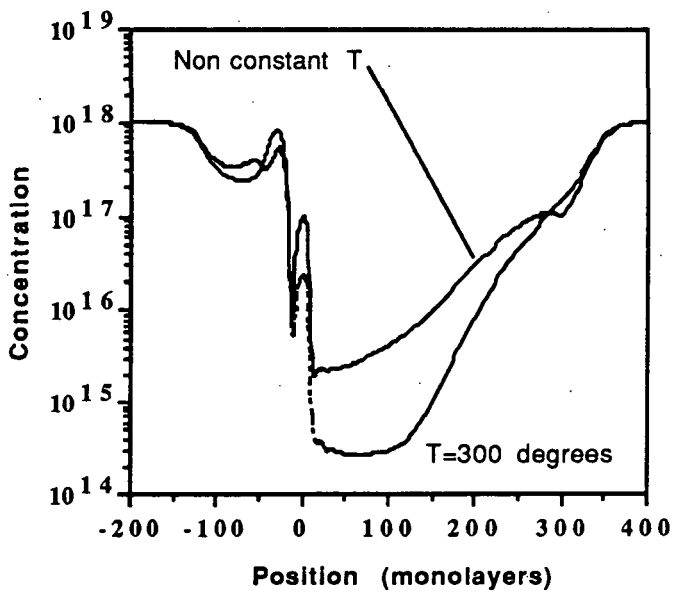

Figure 5. Electron concentrations obtained from the Lattice Wigner formalism for two different transverse temperature profiles. The dc bias is at 0.7 V.

Figure 5 illustrates the effect of transverse temperature on the simulated electron concentration for this device biased at 0.7 V. The dashed curve shown in this figure was generated under the assumption of constant transverse temperature within the spacer region. As seen from this curve, the electron density actually decreases past the quantum well region, indicating an increase in the overall electron velocities. The increase in the electron velocities is a result of a non-physical assumption. Because the transverse temperature in this space charge region is kept artificially low, the electron population is also artificially cooled, keeping all electrons in the fast Γ valley. Therefore, unrealistically high velocities would be predicted under this constant temperature assumption. This can lead to unrealistic high frequency performance predictions, since fast electrons generally result in improved frequency response.

Also shown in Figure 5 are the results of a Lattice Wigner function calculation using a transverse temperature profile obtained through the Schrödinger/Monte Carlo model. As seen from this figure, the electron concentration is increased significantly over the constant temperature model, indicating a slowing down of the electron population within the spacer region. The reduced velocity is a result of the increased phonon scattering within the Γ valley, as well as some Γ to L intervalley transfer. This slowing of the electrons can have an significant impact on the device performance, as discussed below.

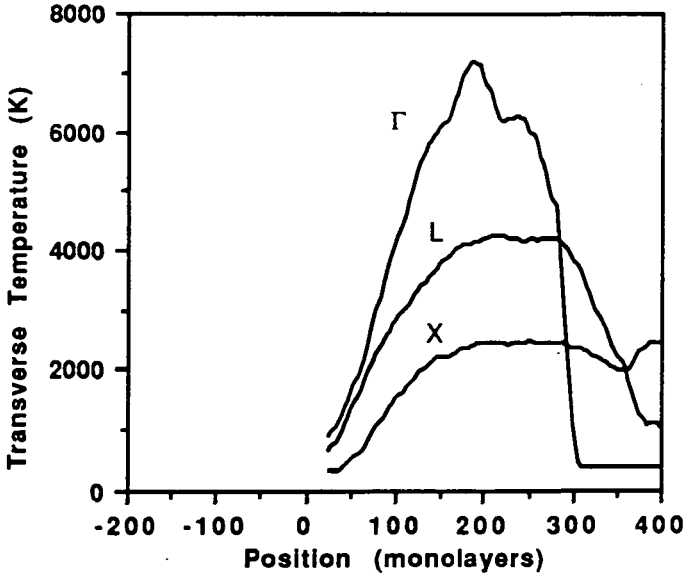

Figure 6. Transverse temperature profile for the device given in Figure 3. The dc bias is at 2.0 volts. The temperature was obtained from a Schrödinger/Monte Carlo transport model discussed in reference 9.

The bias of 0.7 V is well below the voltage at which peak current is expected in this device. However, even under these conditions, the Monte Carlo simulated Γ transverse temperature peaks at 2500 Kelvin. At even higher biases, the transverse temperature becomes extremely high. Figure 6 shows the transverse temperature profiles extracted through a three valley Schrödinger/Monte Carlo model for a device biased at 2.0 V . As seen from this figure, the Γ temperature can exceed 7000 degrees Kelvin. Even the upper satellite valleys are exceptionally hot. Thus, we would expect that most of the electrons for this bias voltage are in the upper satellite valley, which is indeed the case.

4.0 Impact on High Frequency Behavior

Much of the discussion concerning the ultimate frequency limitations of DBRTD devices has centered on the frequency limitations imposed by the quantum well itself. It has been projected that the quantum well is capable of operating at terahertz frequencies[16]. However, the preceding discussion illustrates that the semiclassical spacer regions can have a dramatic impact on the behavior of DBRTD devices. Because of the efficient phonon scattering processes, the actual number of free carriers within the spacer layer is much higher than predicted by either a pure state Schrödinger solution, a one valley Wigner solution, or a multiple valley constant temperature Lattice Wigner solution. This free charge contributes to a positive resistance which is equivalent in every way to the space charge resistance found in transit time diodes [17]. The magnitude of the space charge resistance is fundamentally determined by the total number of free carriers within the region. Therefore, any analysis which does not realistically describe electron densities cannot be used to project the high frequency performance of a real device.

Understanding space charge resistance is important because it is generally felt that in order to improve the output power of a DBRTD device, one must dramatically increase the current density. In reality, this procedure will be useful only up the point where deleterious space charge resistance effects become dominant. This can be seen even under static conditions. For example, considered the measured dc-*IV* curve of an InGaAs/AlAs DBRTD structure, shown in Figure 7. The total spacer region for this device was 1250Å. With available simulation tools, it is possible to model comparable structures with artificially increased current densities. Thus, five static simulations where performed using a composite quantum injector/drift/diffusion model, as described in reference 18. For each

simulation, the DBRTD spacer regions where kept constant. The only difference between each simulation is an assumed increase in the current density of the device, starting with the dc-*IV* curve given in Figure 7. The results of the simulations are shown in Figure 8. As the current density is magnified, the presence of the free carriers within the spacer regions can cause a major portion of the negative resistance regime to become positive. It is obvious that this positive resistance would prevent useful device operation, despite the fact that the difference between the peak and valley current is exceptionally high.

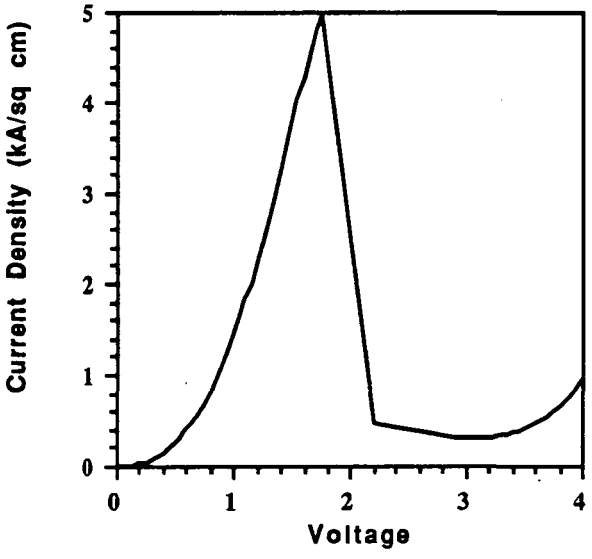

Figure 7. The experimentally measured dc-*IV* curve for an InGaAs/AlAs DBRTD. The structure is similar to Figure 3 except that the total spacer layer to the right of the quantum well is 1250Å.

The current density where space charge resistance becomes important depends on two factors. The first is the length of the spacer regions. As the length is decreased, the total number of carriers within the region is also reduced. The price paid for this reduction is a corresponding decrease in the overall device impedance. Furthermore, it is doubtful that the spacer region can be eliminated beyond a certain point, since there is always a depletion region formed due to the high electric fields near the quantum well. This is even true if the heavily doped contacts are immediately adjacent to the quantum well.

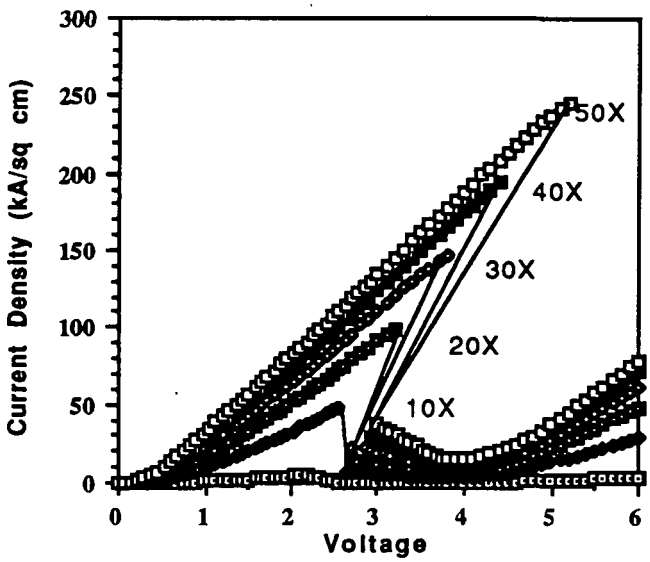

Figure 8. The simulated effect of the space charge resistance on the dc-*IV* curve. These curves were generated using the Schrödinger/Drift Diffusion composite model in which the current given by Figure 7 was scaled upward 10, 20, 30, 40, and 50 times.

The second factor dictating when the space charge resistance becomes important is determined by the velocity of the carriers. Higher velocities result in lower electron concentrations, since total current must be conserved. It is in predicting these concentrations and velocities that previous quantum mechanical models have failed, thus failing to predict the importance of the spacer regions in overall low and high frequency device behavior. Thus, in order to accurately project the ultimate performance of DBRTDs, it is critical to use a quantum kinetic formalism such as the Lattice Wigner function. Future results using this model should lead to a determination of the behavior of DBRTDs at terahertz frequencies.

This work has been supported by the Texas Advance Research Program.

5.0 References

1. T. C. L. G. Sollner, W. D. Goodhue, P. E. Tannenwald, C. D. Parker, and D. D. Peck, Applied Physics Letters, **43**, 588, (1983).

2. E. R. Brown, J. R. Söderström, C. D. Parker, L. J. Mahoney, K. M. Molvar, and T. C. McGill, Applied Physics Letters, **58**, 2291, (1991).

3. D. Z. Y. Ting, M. K. Jackson, D. H. Chow, J. R. Söderström, D. A. Collins, and T. C. McGill, Solid State Electronics, **32**, 1513, (1989).

4. E. T. Yu, M. K. Jackson, and T. C. McGill, Applied Physics Letters, **55**, 744, (1989).

5. W. R. Frensley, Physical Review B, **36**, 1570, (1987).

6. K. L. Jensen and F. A. Buot, Journal of Applied Physics, **65**, 5248, (1989).

7. N. C. Kluksdahl, A. M. Kriman, D. K. Ferry, Physical Review B, **39**, 7720, (1989).

8. D. R. Miller, V. K. Reddy, R. L. Rogers, and D. P. Neikirk, SPIE Proceedings on High-Speed Electronics and Device Scaling, **1288**, 167, March 18-19 1990.

9. K. K. Gullapalli, D. R. Miller, and D. P. Neikirk, 1991 International Electron Devices Meeting, Washington D. C., December 8-11, pg. 511, 1991.

10. F. A. Buot, Physical Review A, **33**, 2544 (1986).

11. D. R. Miller and D. P. Neikirk, Applied Physics Letters, **58**, 2803, (1991)

12. K. L. Jensen and F. A. Buot, Journal of Applied Physics, **67**, 7602, (1990)

13. W. Frensley, Proceedings of the International Symposium on Nanostructure Physics and Fabrication, College Station, March 13-15, pg. 231, 1989.

14. C. Jacoboni and P. Lugli, The Monte Carlo Method for Semiconductor Device Simulation, Springer-Verlag Wien, New York, 1989.

15. J. P. Aubert, J. C. Vaissiere, and J. P. Nougier, Journal of Applied Physics, **56**, 1128, (1984)

16. W. R. Frensley, Applied Physics Letters, **51**, 448, 1987.

17. S. M. Sze, Physics of Semiconductor Devices, 2nd Edition, Chapter 10, John Wiley, New York, 1981.

18. D. R. Miller, V. P. Kesan, R. L Rogers, C. M. Maziar, D. P. Neikirk, The 13th International Conference on Infrared and Millimeter Wave, 1988.

19 E. Wigner, Physical Review, **40**, 749, (1932)

Parallel Arrays of Josephson Junctions for Submillimeter Local Oscillators

Aleksandar Pance* and Michael J. Wengler

Department of Electrical Engineering
University of Rochester
Rochester, NY 14627

Abstract

In this paper we discuss the influence of the DC biasing circuit on operation of parallel biased quasioptical Josephson junction oscillator arrays. Because of nonuniform distribution of the DC biasing current along the length of the bias lines, there is a nonuniform distribution of magnetic flux in superconducting loops connecting every two junctions of the array. These DC self-field effects determine the states of the array. We present analysis and time-domain numerical simulations of these states for four biasing configurations. We find conditions for the in-phase states with maximum power output. We compare arrays with small and large inductances and determine the low inductance limit for nearly-in-phase array operation. We show how arrays can be steered in H-plane using the externally applied DC magnetic field.

Introduction

The Josephson junction is a natural choice for submillimeter local oscillator since it is a "voltage controlled oscillator" with typical voltage scales of mV and an oscillation frequency f_J = 483 GHz per mV of dc bias. The existence of Josephson radiation into the terahertz range has been demonstrated at Cornell [1]. A major disadvantage of the Josephson junction is its very low output power. With DC voltage bias of 1 mV at 483 GHz, a junction which could accept 100 μA will put out less than 100 nW of RF power. Therefore, practical local oscillators must use arrays of many junctions oscillating in phase. Submillimeter Josephson oscillator arrays with usable power levels have been made at Stony Brook [2] and NIST [3].

We have proposed to build a large 2-D active grid array of parallel biased Josephson junctions [4]. In our design, every junction drives a single antenna and the power from the whole array is quasioptically combined. By biasing all junctions in parallel, we assure that all of them

---

* 1991 Link Energy Foundation Fellow.

radiate at exactly the same frequency. For maximum radiated power, all junctions must also be in phase.

The DC biasing circuit of the 2-D quasioptical Josephson array plays a very important role in phase-locking of Josephson junctions. In a two-dimensional array the DC biasing current is supplied at the ends (Fig. 1). Because of that, the DC current is nonuniformly distributed along the length of the biasing line. This current induces the nonuniform DC magnetic flux in superconducting loops between every two neighboring junctions. Because of the superconducting quantum interference effects [5], these self-induced fluxes determine the phase differences between the neighboring junctions, and therefore the states of the array. These effects will be referred to as the DC self-field effects. It is clear that, depending on the particular bias circuit, the in-phase state can only be a special, rather than common state of the parallel 2-D Josephson junction array.

If the rows of the 2-D parallel Josephson array are biased independent from each other, the DC self-field effects are, to the first order, limited to each row, and the whole 2-D array can be looked at as a collection of 1-D parallel arrays. We will therefore investigate these DC self-field effects in linear parallel arrays.

N-junction linear parallel array

The most general biasing scheme for the linear parallel array is presented in Fig. 2. We use the RSJC model of the Josephson junction that consists of ideal Josephson junction, shunt resistance and parasitic capacitance (Fig. 2). The ideal Josephson junction is described by relationships between its current I, voltage V and phase difference ϕ of the superconducting quantum mechanical wave function between two sides of the junction

$$I = Ic \sin(\phi), \quad \frac{d\phi}{dt} = \frac{2e}{\hbar} V$$

where Ic is the junction critical current. Assuming that all junctions are identical, the circuit from Fig. 2 can be described with the following system of equations:

$$i_1(\tau) = \frac{1}{\lambda}(\phi_2(\tau) - \phi_1(\tau)) + \frac{\gamma_1}{2} - \frac{\gamma_R}{2} - \frac{2\pi}{\lambda}\varphi_{ex}$$

$$i_j(\tau) = \frac{1}{\lambda}(\phi_{j+1}(\tau) - 2\,\phi_j(\tau) + \phi_{j-1}(\tau)) + \frac{\gamma_j}{2}, \qquad j = (2, N-1)$$

$$i_N(\tau) = -\frac{1}{\lambda}(\phi_N(\tau) - \phi_{N-1}(\tau)) + \frac{\gamma_N}{2} + \frac{\gamma_L}{2} + \frac{2\pi}{\lambda}\varphi_{ex} \qquad (1.a)$$

where ϕ_j is the superconducting wave function phase difference across the j^{th} junction, i_j is the total current through the j^{th} junction, γ_j, γ_L and γ_R are biasing currents and φ_{ex} is the normalized externally applied DC magnetic flux,

$$i_j(\tau) = \beta\ddot{\phi}(\tau) + \dot{\phi}(\tau) + \sin(\phi(\tau))$$

$$\gamma_j = i_{Uj} + i_{Dj},$$

$$\gamma_L = i_{L\,in} + i_{L\,out}, \quad \gamma_R = i_{R\,in} + i_{R\,out}$$

$$\varphi_{ex} = \frac{\Phi_{ex}}{\Phi_0} \qquad (1.b)$$

with capacitance and inductance parameters β and λ, respectively, given by

$$\beta = \frac{R^2 C}{L_j}, \quad \lambda = \frac{L}{L_j}, \quad L_j = \frac{\Phi_0}{2\pi I_c}, \quad \Phi_0 = \frac{h}{2e} \qquad (1.c)$$

where L_j is the zero-bias Josephson junction inductance and $\Phi_0 = 2.07 \times 10^{-15}$ Wb is the flux quantum. In equations (1.a-c), time is given in units of $\frac{L_j}{R}$, all currents in units of I_c and normalized junction voltages, that are just time derivatives of junction phases ϕ_j, in units of I_cR.

In the case of 2-junction array, the in-phase solution has been reported by Ben-Jakob et al [6]. Here we present solutions for several N-junction arrays with different biasing configurations: the LL ("left"-"left"), LR ("left"-"right"), UD ("up"-"down") and CB ("central bias") biased array (Fig. 3). Although the LL and LR bias are directly applicable to parallel biased two-dimensional arrays, the other two configurations are used in other array architectures, such as series-parallel combinations, etc.

In-phase states

The general solution of eq. (1) for the junction phases ϕ_j is

$$\phi_j(\tau) = \omega\tau + f_j(\tau) + \phi_j(0)$$
$$\omega = \left\langle \dot{\phi}_j(\tau) \right\rangle$$
$$f_j(\tau+T) = f_j(\tau), \quad T = \frac{2\pi}{\omega}, \quad \left\langle \dot{f}_j(\tau) \right\rangle = 0 \qquad (2)$$

where "< >" denotes time average, ω is the normalized DC voltage across junctions, f_j's are some general, periodic functions with zero time-average and $\phi_j(0)$ are constants. For the in-phase solution, the following condition must hold for every two neighboring junctions

$$\phi_{j+1}(\tau) - \phi_j(\tau) = 2\pi m_j \qquad (3)$$

where m_j must be an integer. Note that m_j represents the number of fluxons in the j^{th} loop.

Condition (3) is fulfilled if

$$f_j(\tau) = f(\tau)$$
$$\phi_{j+1}(\tau) = \phi_j(\tau + \tau_j)$$
$$\tau_j = m_j T \qquad (4)$$

where τ_j is the time delay between the phases of the two neighboring junctions. Substituting (3) into the system (1.a) and equating all the currents i_j leads solutions

$$m_j = j\,a + \varphi_{ex} \qquad \text{(LL bias)} \qquad (5.a)$$

$$m_j = (j - \frac{N}{2})\,a + \varphi_{ex} \qquad \text{(LR bias)} \qquad (5.b)$$

$$m_j = \varphi_{ex} \qquad \text{(UD bias)} \qquad (5.c)$$

$$m_j = ([\frac{N}{2}] - j)\,a + \varphi_{ex} \qquad \text{(CB bias)} \qquad (5.d)$$

where "" in eq. 5.d denotes integer division, and parameter 'a' is given by

$$a = \frac{\lambda\, i_{DC}}{2\,\pi\, N} \tag{6}$$

where i_{DC} is the total DC biasing current. In order for m_j to be an integer, which is the precondition for the in-phase solution, it is necessary that both φ_{ex} and a be integers:

$$\varphi_{ex} = k_{\varphi}$$
$$a = \frac{\lambda\, i_{DC}}{2\,\pi\, N} = k \tag{7}$$

where k_{φ} and k are integers. The only exception is the LR array with odd number of junctions N, where "a" must be an even integer (2 k). The arrays will be in phase for all currents i_k that satisfy

$$i_k = k\,\frac{2\,\pi\, N}{\lambda} \tag{8}$$

Note that these in-phase states are achieved without external locking mechanisms.

Numerical simulations

System (1) is solved numerically using the 4th order Runge-Kutta method [7]. Figure 4 shows the I-V and dV/dI-I curves of the 4 junction LL biased array with λ=20 and β=0.5. According to eq. (8), the in-phase states appear for current bias i_k= 1.256 k (i_k'=0.314 k for bias current normalized to the number of junctions, N, as in the Figure 4). The in-phase states are visible as voltage maximums in the I-V curve and sharp and deep minimums in dV/dI-I curve, for k=4 to 7. Similar structure has been observed experimentally by Clarke et al [8].

Other states

The dV/dI-I curve of Figure 4 reveals considerable periodic structure between the in-phase states. Under certain conditions, that will be specified below, these "other" states, for current bias $i_{DC} \neq i_k$, correspond to the general solution of eq. (2) that satisfies the following:

$$f_{j+1}(\tau) - f_j(\tau) = \varepsilon_j(\tau)$$
$$\phi_{j+1}(\tau) \approx \phi_j(\tau + \tau_j)$$
$$\tau_j \approx \mu_j T \qquad \forall j \tag{9}$$

where $\varepsilon_j(\tau)$ is an error term and μ_j does not need to be an integer. Furthermore, μ_j is found from the same equations as m_j (5), except that a and φ_{ex} are no more restricted to integer numbers. In other words, all states of the parallel array are described with phases at neighboring junctions shifted in time by an amount determined by the DC biasing current and external magnetic field (eq. 5). It is convenient to define the relative normalized time shift θ_j between the waveforms of functions f_{j+1} and f_j

$$\theta_j = \tau_j \bmod T = \mu_j \bmod 1 \qquad (10)$$

where "mod" is the modulus function, so that $0 \le \theta_j \le 1$. It has been shown by perturbation analysis [6] that in the case of 2-junction array solution (9) holds in the neighborhood of the in-phase state ($i_{DC} = i_k + \Delta i_{DC}$) and it has been suggested that it will hold for any state between the in-phase states, for the case of weak coupling ($\lambda >> 1$).

Figure 5.a shows the circled part of the dV/dI-I curve of Fig. 4. Points labeled "1" and "4" correspond to the in-phase states with k=4 and k=5, respectively. The voltage waveforms on individual junctions for these two states are shown in Figures 6.a and 7.a, respectively. Point "2" of Fig. 5.a correspond to DC biasing current $i_{DC} = 5.65$, so eq. (5.a) gives μ_1=4.5, μ_2=5 and μ_3=5.5 for the number of fluxons in each loop. From eq. (10) we find that relative time shifts should be θ_1=0.5 between the voltages of the junctions 2 and 1, θ_2=0 for junctions 3 and 2 and θ_3=0.5 between junctions 4 and 3. Numerical simulations shown in Figure 6.b confirm this prediction.

Point "3" of Fig. 5.a correspond to $i_{DC} = 5.42$, and again from equations (5.a) and (10) we obtain θ_1=0.333, θ_2=0.666 and θ_3=0. The voltage (and phase) at junction 2 is time shifted by third of a period from that of junction 1, voltage at junction 3 is shifted by two-thirds from that of junction 2, so that it is in phase with junction 1. Finally, junction 4 is in phase with junctions 1 and 3. This situation is shown in Figure 6.c. All other states can be determined in a similar fashion.

Radiated power

As a measure of how good an array performs as an oscillator for a particular bias, we calculate the available radiation power. We are interested in power array would radiate broadside in the far-field. We define m^{th} harmonic power on unit (1 Ω) resistance as

$$P^{(m)} = (\Sigma V_j^{(m)})^2$$

where $V_j^{(m)}$ is m^{th} harmonic voltage on j^{th} junction. This power is given in units of $(Ic\ R)^2$. We assume that the resistance R of the RSJC model (Fig. 2) includes both the radiation resistance and losses. The actual radiated power will at best be the power $P^{(m)}$ on resistance $\frac{R}{2}$.

Figure 5.b shows the normalized first harmonic power radiated in the broadside direction for different states of the array. The maximum power is obtained only in the in-phase states (points "1" and "4"). Significant amount of power is also obtained in states where most of the array works in phase, as is the case with state "2".

Array properties

Several important properties of arrays of Fig. 3 can be derived from equations (5-10):

1) In the absence of external magnetic field:

- the UD array will be in phase for any DC bias; the in-phase state is a natural one for this array. Maximum power will be radiated at every operating frequency (Fig. 5.b).

- LR and CB arrays are symmetrical around the middle of the array; $m_{N-j} = -m_j$, which means that the junctions j and N-j are always in phase.

2) The LR array is equivalent to the LL array with equivalent external magnetic field $\varphi_{ex}' = \varphi_{ex} - \frac{N}{2} a$.

3) The larger the inductance parameter λ, the more in-phase states will be found in the given current bias span (eq. 8), and corresponding DC voltage and operating frequencies span. Similarly, the larger the array (N), the more identifiable "other" states will be found in the dV/dI-I curve (Fig. 5.a).

Magnetically steerable array

When an array is biased in the in-phase state ($i_{DC} = i_k$) the normalized relative time shift between every two neighboring junctions is the same and proportional to the external DC magnetic field:

$$\theta_j = \theta = \varphi_{ex} \bmod 1 , \quad \forall j \tag{11}$$

This situation is shown in Figure 7. In Fig. 7.a the LL array is biased at the in-phase state (point "4", Fig. 5.a) with no external magnetic field. When an external magnetic field equal to a quarter of the flux quantum is applied, the time shift between the voltages of every two neighbors is equal to a quarter of period.

The time shift θT translates into the linear phase shift in the frequency domain $2\pi\theta$. Assuming that every junction drives one antenna, the quasioptical Josephson array becomes a phased array [9]. The angular position α_0 of the main beam in the H-plane far-field radiation pattern of the linear Josephson phased array becomes

$$\cos(\alpha_0) = -\frac{2\pi\theta}{\frac{2\pi}{\lambda_0} d_X} = -\frac{\theta}{d_X}\lambda_0 \qquad (12)$$

where d_X is the spacing between the antennas and λ_0 is the free space wavelength . The broadside radiation corresponds to $\alpha_0 = 90^\circ$ ($\theta = 0$). Equations (11,12) suggest that by changing the externally applied DC magnetic field φ_{ex} it is possible to steer the Josephson array radiation pattern in the H-plane. As stated earlier, for the LL, LR and CB biased array, this is only true if the array is biased in the in-phase state. Since the UD array is always in the in-phase state, it can be steered using DC magnetic field at any bias.

Limitations

The expressions (9,10) derived for the "other" states will hold only in certain range of array parameters and bias conditions. We have derived expressions (5) for the in-phase states starting from (1) and assuming that all currents i_j are equal These expressions always hold for the in-phase states. The same expressions (5) are found for "other" states if we solve (1) with an assumption that DC currents $\langle i_j \rangle$ are approximately the same. The only part of the DC junction current that is different at every junction, due to DC self-field effects, is the supercurrent $\langle \sin(\phi_j) \rangle$. This part will be negligible if either the biasing current per junction is $\frac{i_{DC}}{N} >> 1$ or if there is non-vanishing capacitance ($\beta > 1$).

In our account of DC self-field effects we assumed the noiseless environment and the identical junctions. Therefore, the stability of in-phase and "other" states to noise and variations in junction and array parameters remains to be further investigated.

Strongly coupled arrays ($\lambda < 1$)

When the inductance parameter λ is small, it is evident from eq. (8) that the first in-phase state appears for very large DC biasing current, which translates into large DC voltage and operating frequency much above the critical frequency $\omega_c = (2e,\hbar)\, I_c\, R$. Depending on the capacitance parameter β and shunt resistance R, the operating frequency range is at best of the order of several ω_c. Therefore, the arrays with small inductances are operated in "other" states throughout the operating range. According to eq. (5), these states should be characterized with small time shifts between the junction phases/voltages. This is obvious, because in the limit of λ -> 0 the whole array operates as a single junction.

Figure 8.a presents simulations for 4 junction LL biased array with small inductance (λ = 0.628). The normalized harmonic radiated power is shown in the wide range of bias currents. The bias points a=0.25 and a=0.5 with no radiated first harmonic power correspond to the states where half of the junctions are in-phase and the other half out-of-phase, according to (5.a). As seen from the Figure 8.b, the maximum first harmonic power is below that of the UD array, with all junctions in-phase. Figure 9 compares the first harmonic power of 4- and 5-junction array with same parameters. The 5-junction array shows additional minimums in radiated power corresponding to states a=0.125 k. These minimums occur whenever there is one or more loops of array occupied by odd number of half-flux-quantums.

It is clear that in order for the array with small inductance to approach the performance of the UD array in the wide operating range, the condition for the inductance parameter must be $\lambda << \frac{1}{N}$. More precisely, if the total time shift across the array is required to be less than a quarter of a period, the condition is:

$$\lambda \; i_{DCmax} \leq \frac{\pi}{N+1} \qquad (13)$$

where i_{DCmax} is the DC bias at the end of the operating range. So, if we wanted a 4-junction LL biased array to approximately match the performance of UD array in Fig. 8.b, the inductance parameter should have been $\lambda = \frac{\pi}{120}$ instead of $\frac{\pi}{5}$. Such small inductances are rather unrealistic, specially because the λ parameter is proportional to the critical current I_c (eq. 1) which should be as large as possible for large output power.

As a final illustration, Figure 10 shows the influence of the Josephson junction capacitance.

The capacitance does not influence the occurrence or existence of in-phase and "other" states. However, it has a severe impact on radiated power. Even at not very big capacitance ($\beta = 3$) the first harmonic power is decreased at least an order of magnitude and the operating range is reduced below 2 ω_c.compared to the case of very small or no capacitance.

Conclusion

We have discussed how the DC biasing circuit determines the operation of linear parallel quasioptical Josephson junction arrays. We have shown that the maximum radiated power from the array can be achieved only at certain operating points, corresponding to the in-phase states. We have found that other states can be described by time-shifted phases and voltages of individual junctions, where the time-shift is determined from the DC biasing conditions. We have shown how the array can be steered from when in the in-phase state by application of DC magnetic field perpendicular to the array.

When the inductance parameter λ is large, there will be numerous in-phase bias points in the desired operating range. However, the stability of these states to noise and variations in junction parameters needs to be further investigated. When the inductance is relatively small, the radiated power will continuously change across the wide operating range, with several points where almost no power is radiated.

If one dimensional quasioptical arrays are designed, the UD biased array is a definite choice, because it is in the in-phase state at every bias point. The operation of this array need to be further analyzed when junction parameters are not identical. The extension of our considerations to 2-D arrays is straightforward, as long as rows of junctions are separately biased.

Acknowledgment

This work is supported by the Air Force Office of Scientific Research grant AFOSR-90-0233.

References

1. Robertazzi, R.P. and R.A. Buhrman, *Josephson terahertz local oscillator.* IEEE Trans. Magn., 1989. **25**: p. 1384-1387.

2. Wan, K., A.K. Jain and J.E. Lukens, *Submillimeter wave generation using Josephson junction arrays.* Appl. Phys. Lett., 1989. **54**: p. 1805-1807.

3. Benz, S.P. and C.J. Burroughs, *Coherent emission from two-dimensional Josephson junction arrays*. Appl. Phys. Lett., 1991. **58**(19): p. 2162-2164.

4. Wengler, M.J., A. Pance, B. Liu and R.E. Miller, *Quasioptical Josephson Oscillator*. IEEE Trans. Magn., 1991. **27**(2): p. 2708-2711.

5. Van Duzer, T. and C.W. Turner, *Principles of Supeconductive Devices and Circuits*. 1981, New York: Elsevier.

6. Ben-Jacob, E. and Y. Imry, *Dynamics of the DC-SQUID*. J. Appl. Phys., 1981. **52**(11): p. 6806-6815.

7. Press, W.H., B.P. Flannery, S.A. Teukolsky and W.T. Vetterling, *Numerical Recipes in C: The Art of Scientific Computing*. 1988, Cambridge, Mass.: Cambridge University Press.

8. Clarke, J. and T.A. Fulton, *Origin of Low-Voltage Structure and Asymmetry in the I-V Characteristics of Multiply-Connected Superconducting Junctions*. J. Appl. Phys., 1969. **40**(11): p. 4470-4476.

9. Steinberg, B.D., *Principles of Aperture and Array System Design*. 1976, New York: John Wiley & Sons, Inc.

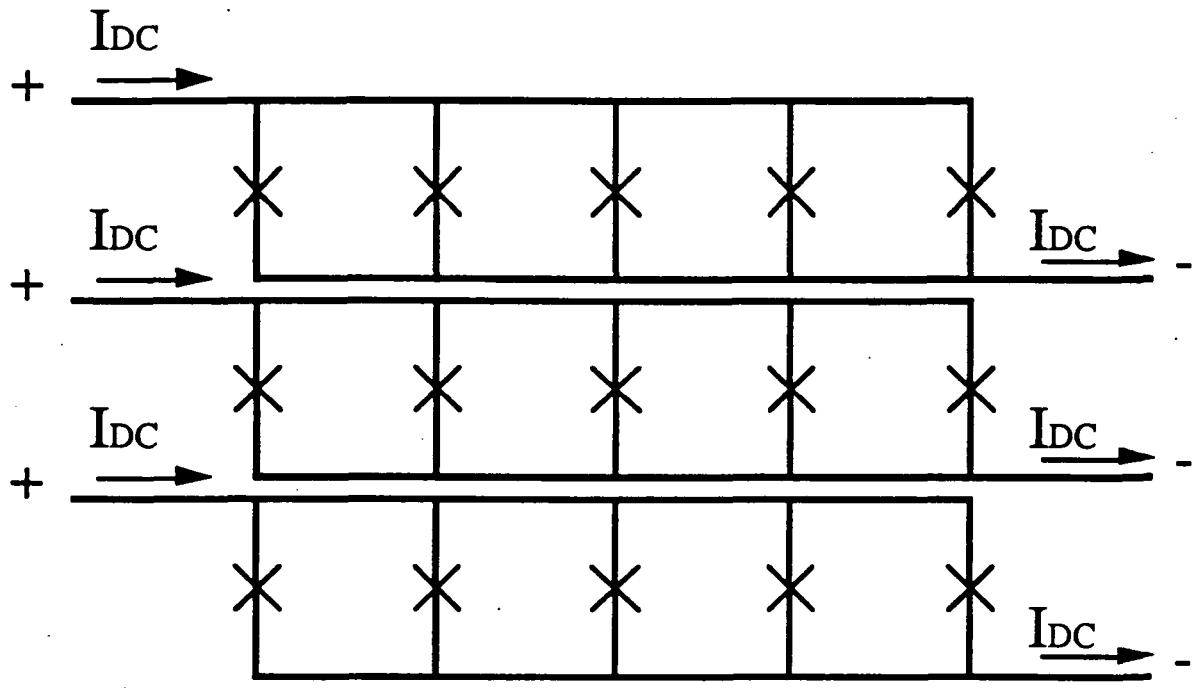

Figure 1. Separate row bias for parallel 2-D Josephson junction array.

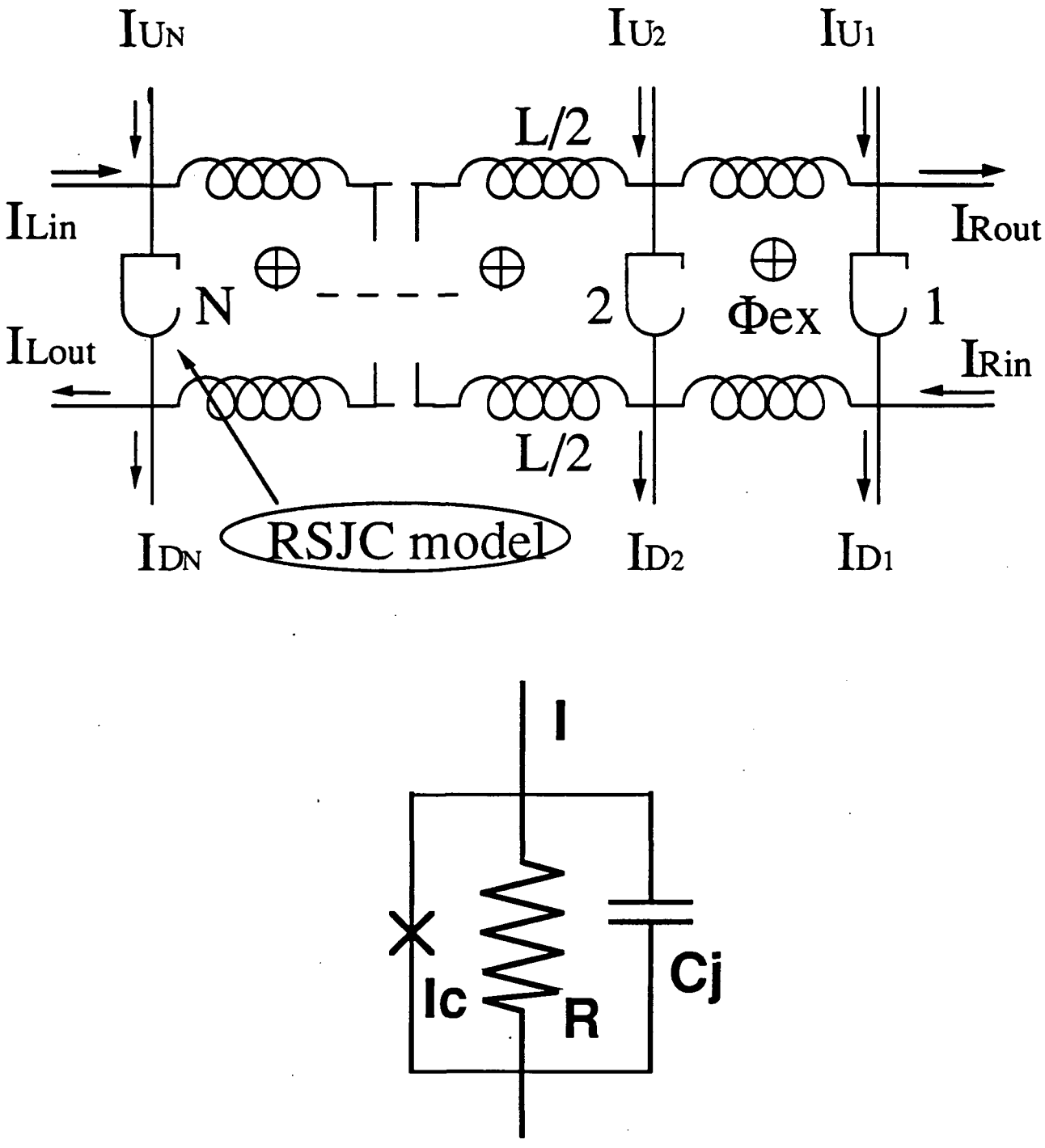

Figure 2. General biasing scheme for one-dimensional parallel Josephson junction array. The RSJC model used is shown below.

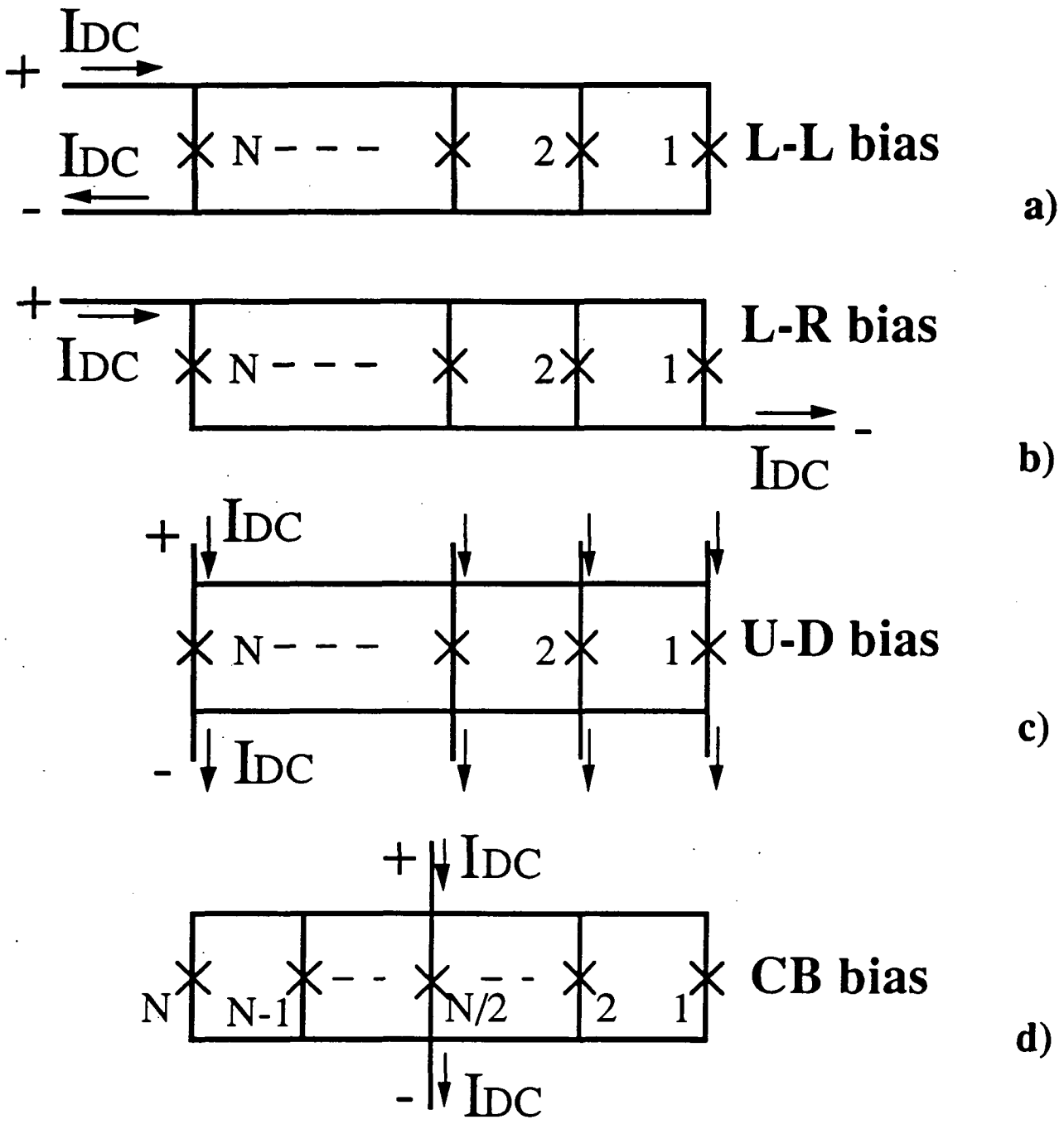

Figure 3. Four common biasing configurations of 1-D array.

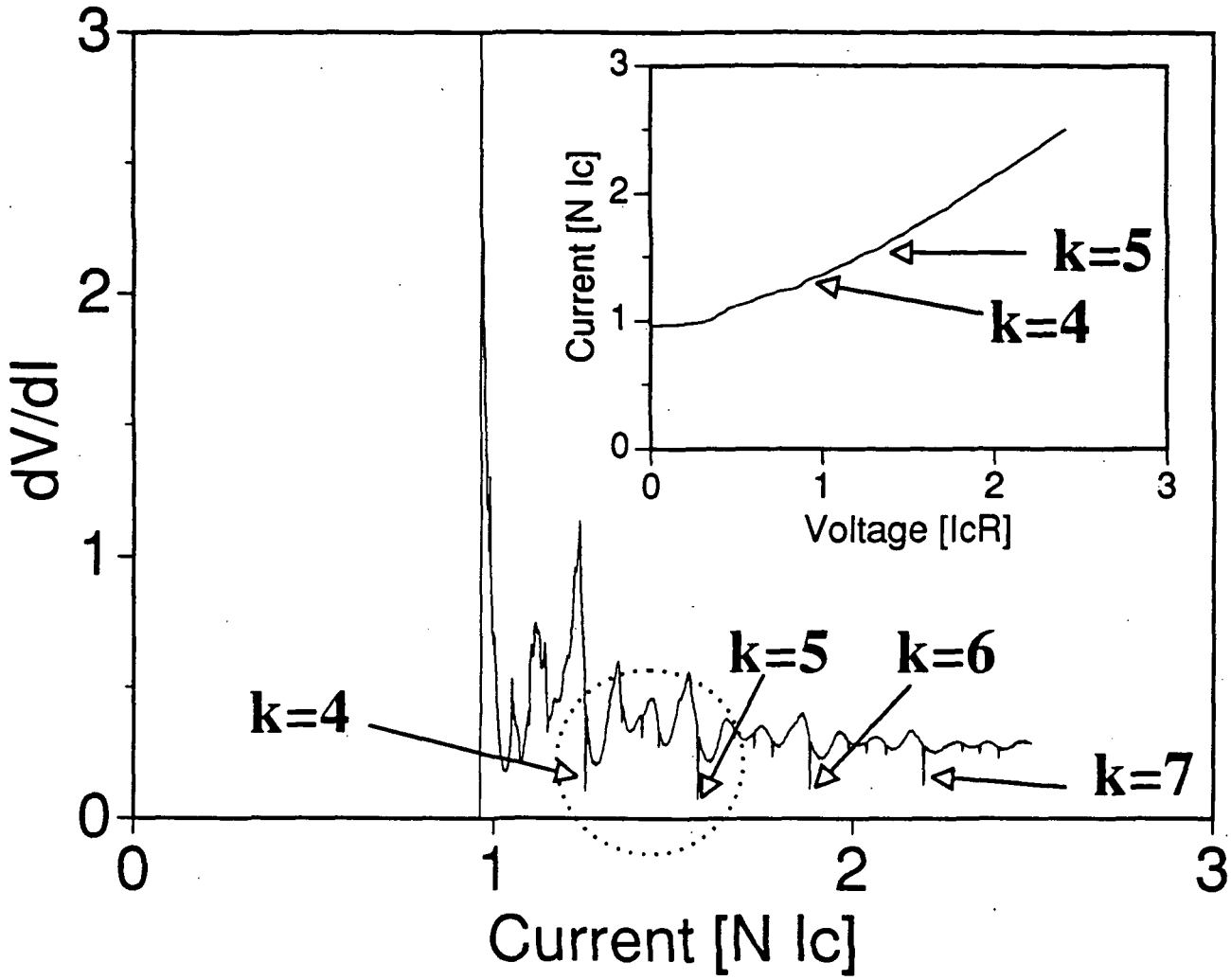

Figure 4. Dynamic resistance and I-V curve of 4 junction LL biased array with $\lambda = 20$ and $\beta = 0.5$. The in-phase states are seen as small steps in the I-V curve and sharp minimums in dV/dI-I curve , labeled k=4 to k=7. The area inside a circle is shown enlarged in Fig. 5.

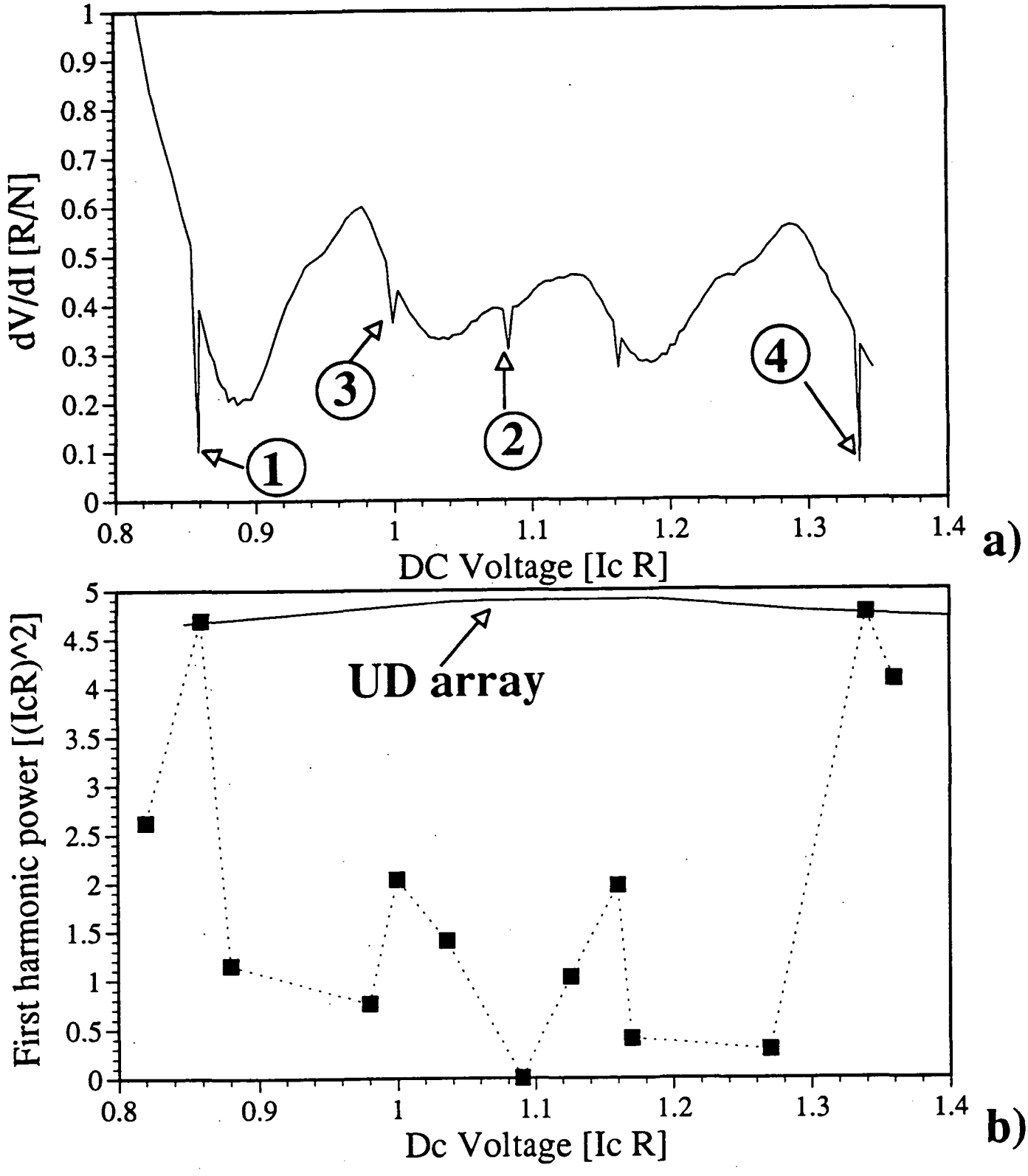

Figure 5. Four junction array, LL bias, $\lambda = 20$, $\beta = 0.5$. a) Enlarged portion of the dV/dI-I curve (Fig. 4) with in-phase states labeled "1" and "4" and two "other" states "2" and "3". The waveforms of individual junction voltages for these states are shown in Fig. 6 and 7. b) First harmonic power that correspond to states in a). The power is maximum in the in-phase states and equal to that of the equivalent UD array.

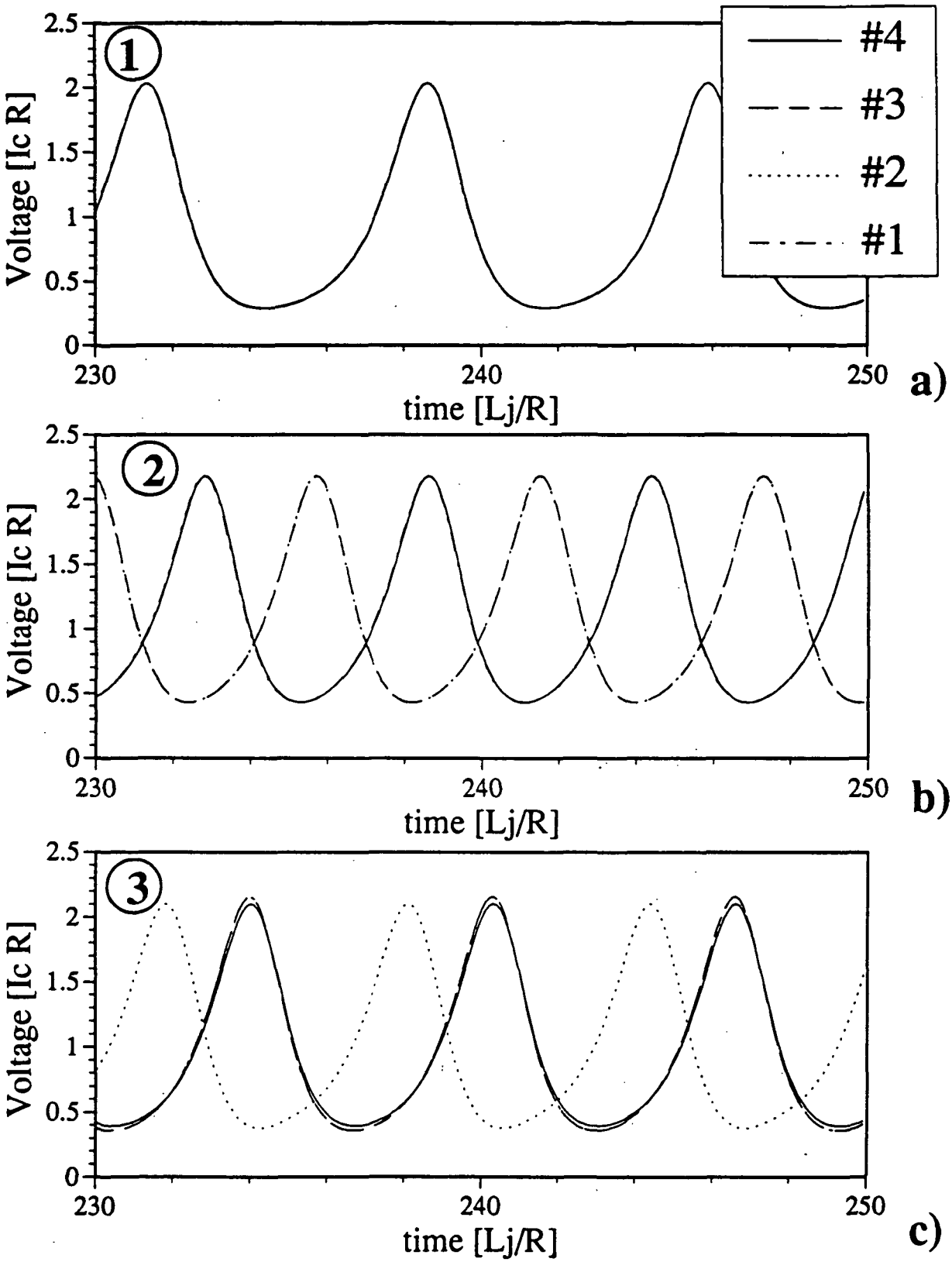

Figure 6. The waveforms of individual junction voltages for the states of Fig. 5. a) In-phase state. b) Junctions 1 &4 in phase, junctions 2 & 3 in phase , but out of phase with (1&4). No power radiated. c) Junctions 1,3 & 4 in phase, junction 2 "leads" a third of a period. Half the maximum power is radiated.

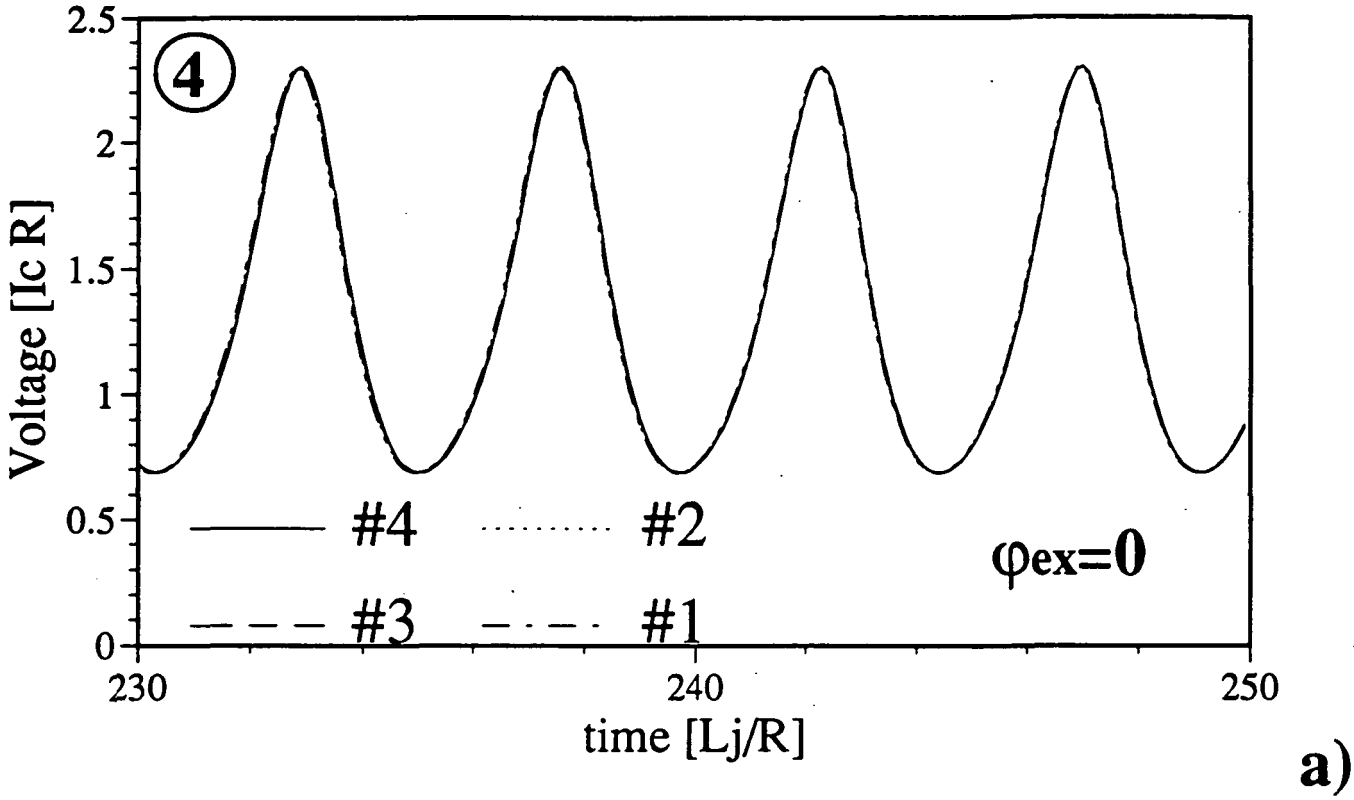

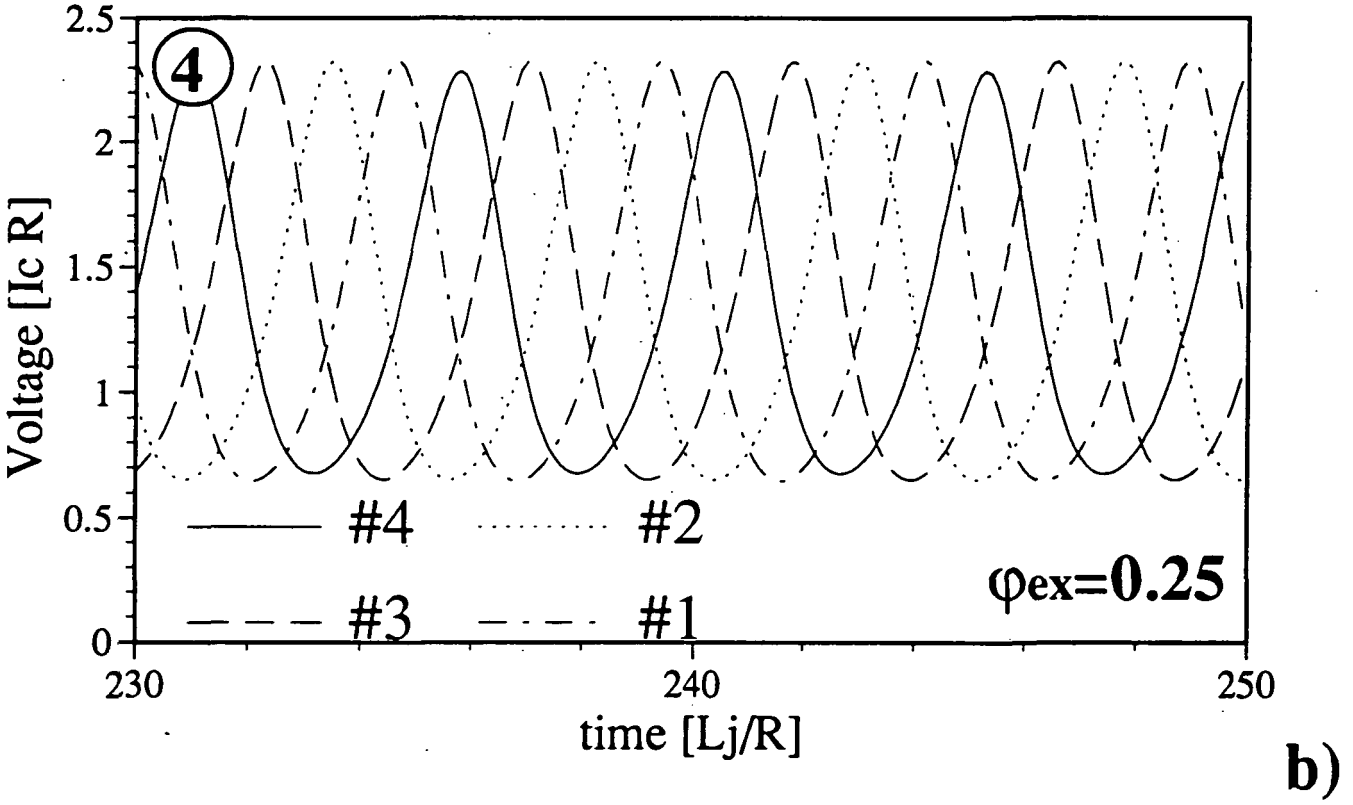

Figure 7. The waveforms of individual junction voltages for the in-phase state labeled "4" in Fig. 5. a) No DC magnetic field supplied. b) Quarter of the flux quantum in every loop supplied by the external magnetic field. Voltage waveforms uniformly shifted by quarter of a period. The main beam of the radiation is steered from the broadside direction.

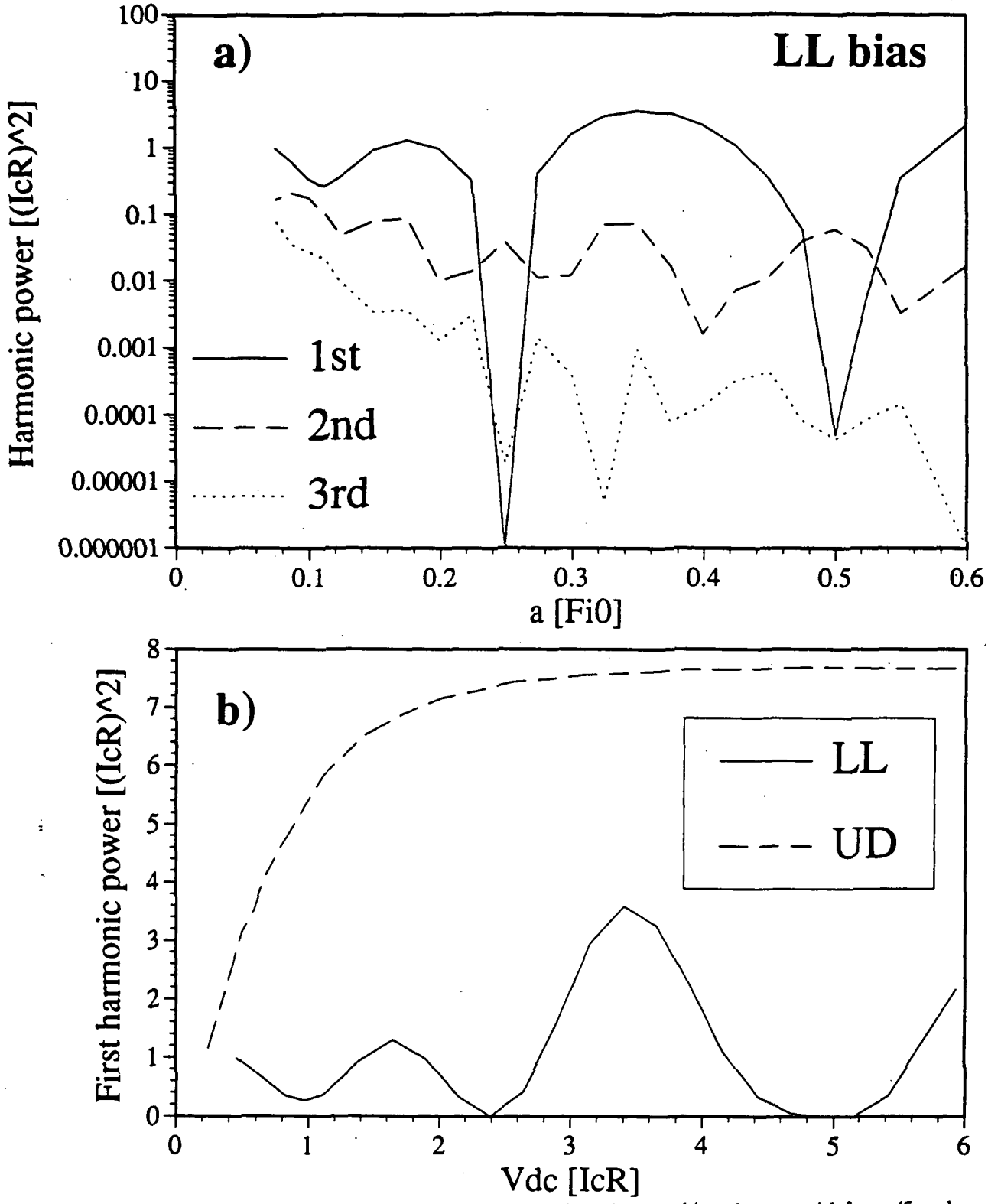

Figure 8. a) Harmonic power radiated by the 4-junction LL-biased array with $\lambda = \pi/5$ and $\beta = 0.03$. Minimums correspond to odd number of half-flux-quantums in some of the loops. b) Comparison between the LL and UD array with same parameters. Varying amount of power is radiated in the very broad operating range, but never a maximum possible power, as in the case of UD array.

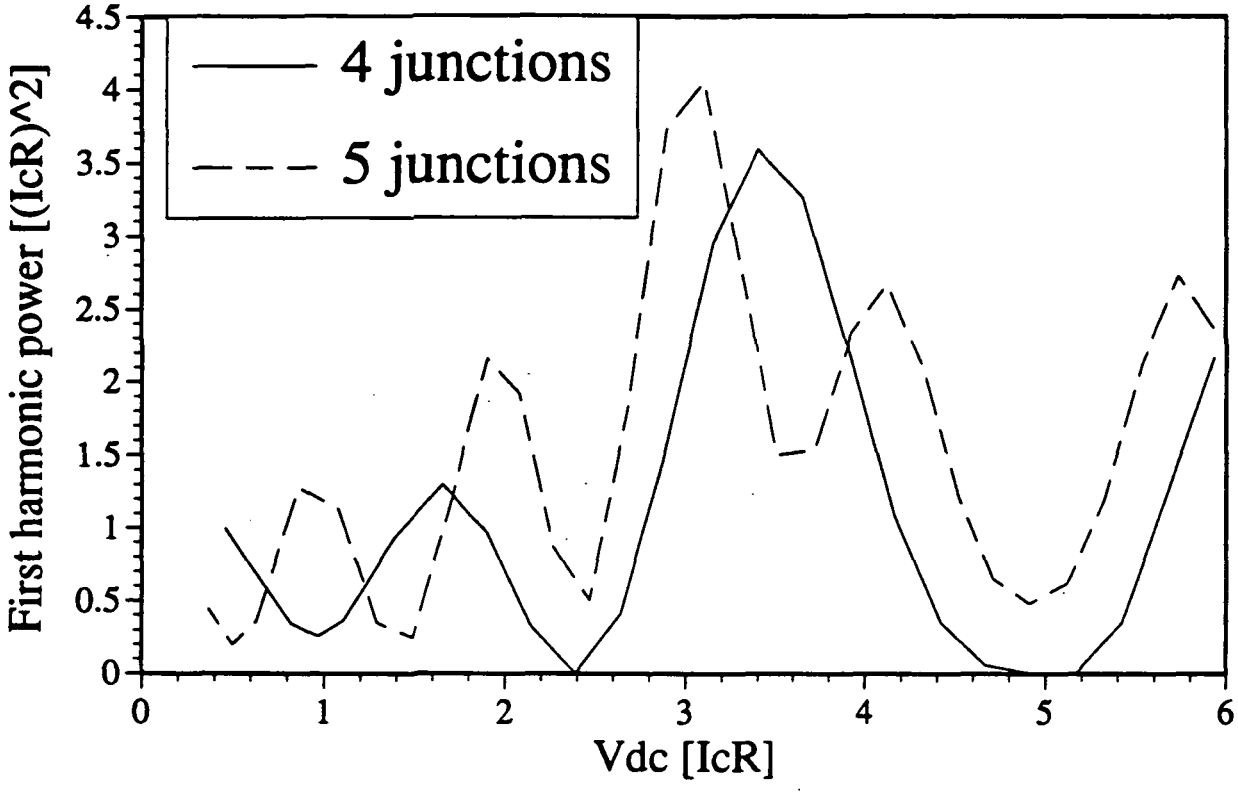

Figure 9. Comparison between the 4-junction and 5-junction small inductance arrays; $\lambda = \pi/5$, $\beta = 0.03$. As the number of junctions increase, more maximums and minimums appear throughout the operating range.

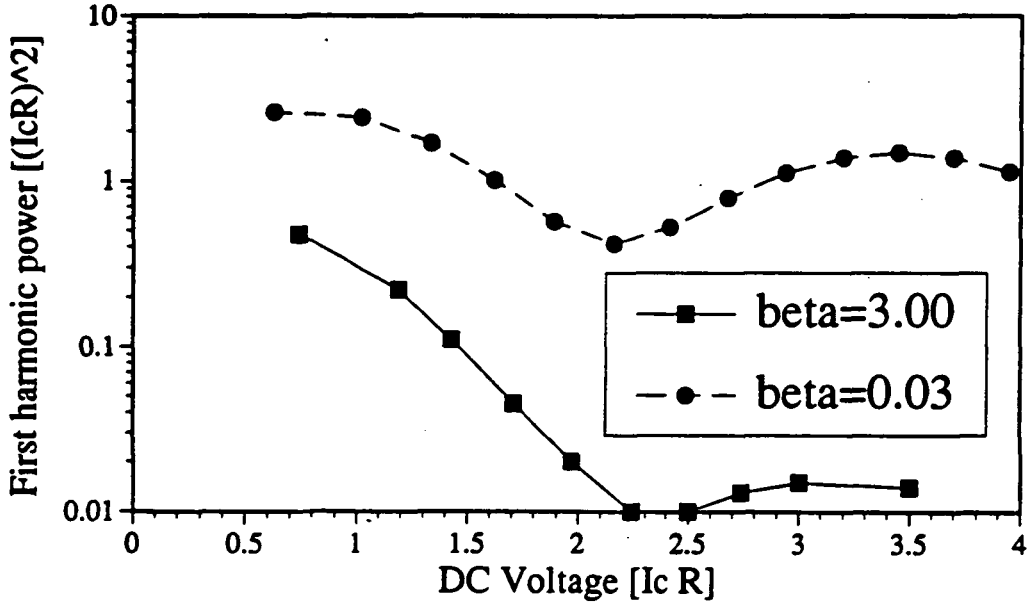

Figure 10. Four junction LL biased array, $\lambda = \pi/10$: Influence of the Josephson junction capacitance on power output. As the capacitance is increased, the maximum power and the operating range rapidly decreases.

MONOLITHIC MILLIMETER-WAVE DIODE GRID FREQUENCY MULTIPLIER ARRAYS

Hong-Xia L. Liu, X-H. Qin, L. B. Sjogren, W. Wu, E. Chung,
C. W. Domier, N. C. Luhmann, Jr.,
Center for High Frequency Electronics
Department of Electrical Engineering
University of California
Los Angeles, California 90024-1594

ABSTRACT

Monolithic diode frequency multiplier arrays, including barrier-N-N^+ (BNN) doubler, multi-quantum-barrier-varactor (MQBV) tripler, Schottky-quantum-barrier-varactor (SQBV) tripler, and resonant-tunneling-diode (RTD) tripler arrays, have been successfully fabricated with yields between 85% and 99%. Frequency doubling and/or tripling have been observed for all the arrays. Output powers of 2.4-2.6 W (η=10-18%) at 66 GHz with the BNN doubler and 3.8-10 W (η=1.7-4%) at 99 GHz with the SQBV tripler have been achieved.

INTRODUCTION

Quasi-optical spatial power combining techniques have, in recent years, been extensively investigated for millimeter and submillimeter power generation [1] [2] [3]. Our research efforts have been focused on monolithically integrating thousands of solid state devices to generate Watt level harmonics in the millimeter region. In addition to arrays of familiar devices such as the BNN and RTD, several new device concepts (MQBV and SQBV [4][5]) have been developed in the course of this work which promise to significantly improve the performance of frequency multipliers. Arrays of all of these devices have been successfully fabricated and tested. Several exciting results have been obtained. Improvements both in device design and in the matching system are underway to further optimize array performance.

FABRICATION AND RESULTS

(a) BNN frequency doubler array

A four-mask process based on the self-aligned aluminum Schottky diode process employed by C. Zah [6] is utilized to fabricate the BNN doubler array. Figure 1 shows an individual BNN device after fabrication. The array was then mounted on a quarter wavelength thick quartz plate. No bias is required due to the adjustment of the build-in voltage resulting from the δ doped layer (see Fig.2). The test system for the BNN frequency doubler is shown in Fig.3 except that the output filter was not used. Cutoff waveguides for the fundamental have been used to prevent contamination of the detected signal due to the pump signal. A variety of tests were employed to conclusively verify that the received signal was actually frequency doubled. All waveguide components including attenuators have been calibrated using at least two methods. The input and receiving horns have also been calibrated and compared with the theoretical values. Figure 4 displays the measured RF results. An output power of 2.4-2.6 W and a maximum efficiency of 10-18% have been achieved. The calculated cutoff frequency based on the measured low frequency parameters of this array is 280 GHz, which results in a maximum theoretical conversion efficiency of $\simeq$20%.

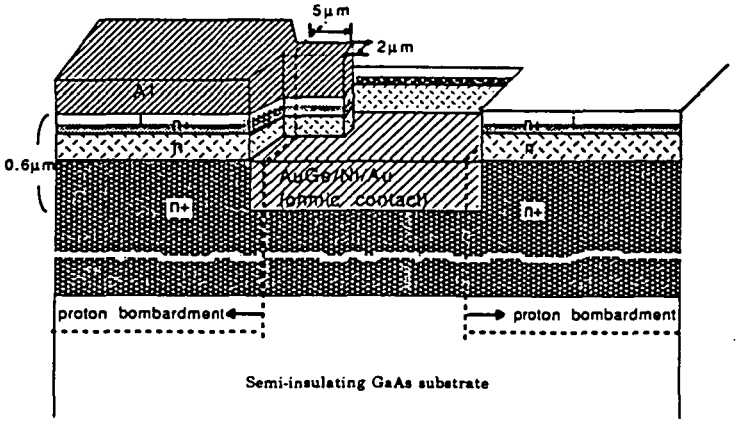

Figure 1. The fabricated individual BNN diode.

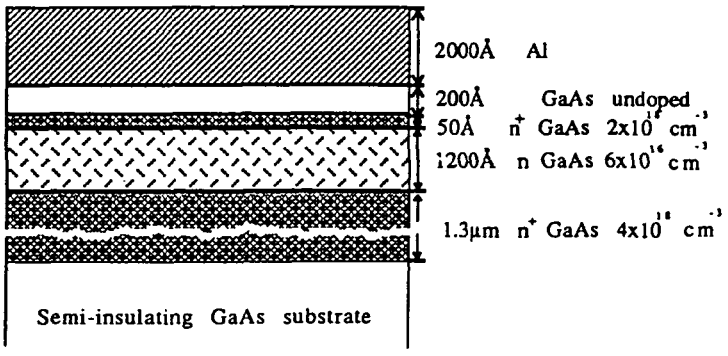

Figure 2. The profile of the BNN diode.

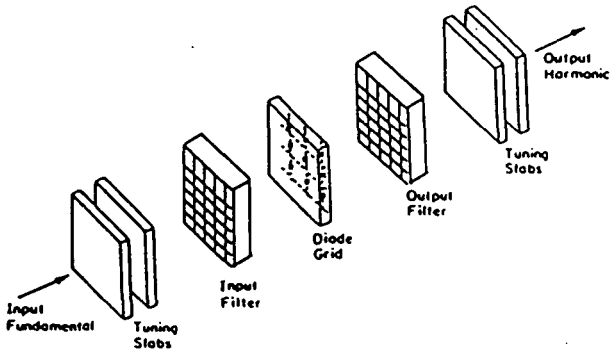

Figure 3. The frequency multiplier setup.

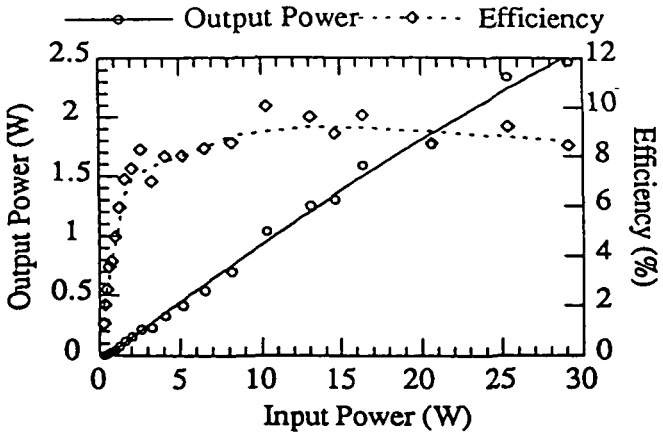

Figure 4. Measured frequency doubling output power and efficiency at 66 GHz as the function of the input power.

(b) Frequency tripler arrays

MQBV, SQBV and RTD arrays have been successfully fabricated using a back-to-back processing method [7]. As a result, all these arrays are suitable for odd harmonic generation due to the resulting symmetric C-V characteristics. Figure 5 displays the array layout. The period of each cell is 400 μm. There are 2250 devices on the MQBV array, 1300 devices on the SQBV array, and 500 devices on the RTD array, respectively. These arrays are tested using the system shown in Fig. 3. Since the input is identical for both the doubler and tripler arrays, the same input filter and tuning slabs have been used. The output filter for the frequency tripler is an inductive metal grid array [8], and quartz tuning slabs with a thickness of a quarter wavelength at the tripled output have been used for the output impedence matching. Figure 6 shows the measured output power and efficiency of the SQBV array at an output frequency of 99 GHz. An output power of 3.8-10 W and an efficiency of 1.7-4% have been achieved. Due to excessive pumping in the initial tests, the performance of the MQBV array was degraded significantly (f_c dropped from 550 GHz to 100 GHz). However, an output power of 0.1 W and an efficiency of 0.4% have been obtained for the degraded array which is in good agreement with the theoretical prediction (0.5%). Finally, a frequency tripling signal has also been observed with the RTD array. Tests are underway to measure the output power and efficiency as the function of the input power.

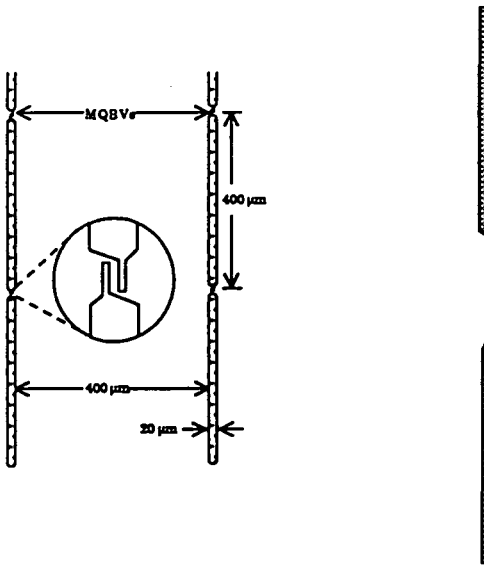

Figure 5. The MQBV and SQBV arrays layout.

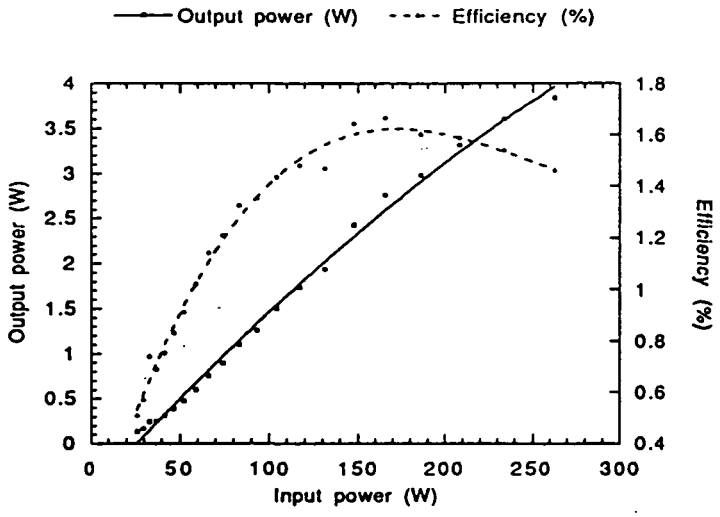

Figure 6. Measured frequency tripling output power and efficiency at 99 GHz as the function of the input power.

CONCLUSIONS

BNN, MQBV, SQBV, and RTD frequency multiplier arrays have been successfully fabricated with yields between 85 and 99%. All of these arrays have yielded frequency multiplication. An output power of 2.4-2.6 W with maximum efficiency of 10-18% has been achieved at 66 GHz with the BNN doubler array; an output power of 3.8-10 W with a maximum efficiency of 1.7-4% has been achieved at 99 GHz with the SQBV array.

ACKNOWLEDGEMENTS

This work was supported by the US Army Research Office and the US Department of Energy. The authors wish to thank Dr. J. Maserjian and P. Smith of Jet Proposion Lab. for providing the processing facilities and the MBE wafers. The authors also wish to acknowledge the generous assistance of Dr. R. Bhat and Dr. L. Florez of Bellcore, Professor M. Spencer of Howard University, and Dr. A. Miura of the Yokogawa Electric Corp. in providing MBE and MOCVD wafers for these studies.

REFERENCE

1. C.F. Jou, W.W. Lam, H.Z. Chen, K.S. Stolt, N.C. Luhmann,Jr., and D.B. Rutledge, "Millimeter Wave Diode-grid Frequency Doubler," *IEEE Trans. on Microwave Theory and Techniques*, 36, No. 11, 1 988.

2. W.W. Lam, C.F. Jou, N.C. Luhmann,Jr., and D.B. Rutledge, "Millimeter-W ave Diode-grid Phase Shifters," *IEEE Transactions on Microwave Theory and Techniques* 36, No. 5, pp. 902, 1988.

3. Z.B. Popovic, R.M. Weikle, M. Kim, K.A. Potter, and D.B. Rutledge, "Bar Grid Oscillators," *IEEE Transactions on Microwave Theory and Techniques* , 38 No. 3, pp. 225, 1990.

4. Hong-Xia L. King, L.B. Sjogren, and N.C. Luhmann,Jr., "New Concepts for High Frequency and High Power Frequency Multipliers and Their Impact on Quasi-Optical Monolithic Array Design", *International Journal of Infared and Millimeter Waves*, 13, pp.251, 1992.

5. Hong-Xia L. King, N.C. Luhmann,Jr., X-H. Qin, L.B. Sjogren, W. Wu, D.B. Rutledge, J. Maserjian, U. Lieneweg, C. Zah, and R. Bhat, "Millimeter Wave Quasi- optical Active Arrays", Proc. and Conference on Space Terahertz Technology, pp. 293-305, Feb. 1991.

6. C. Zah, D.P. Kasilingam, J.S. Smith, D.B. Rutledge, T. Wang, and S.E. Schwartz,"Millimeter-wave Monolithic Schottky Diode Imaging Arrays", *Int. J. of Infrared and Millimeter Waves*, 6, pp. 981-997, 1985.

7. R.J. Hwu, C.F. Jou, N.C. Luhmann, Jr., M. Kim, W.W. Lam, Z.B. Popovic, D.B. Rutledge, "Array Concepts for Solid-State and Vacuum Microelectronics Millimeter-Wave Generation," *IEEE Trans. on Elec. Dev.*, 36, No. 11, pp. 2645-2650, 1989.

8. Hong-Xia L. Liu, L.B. Sjogren, and N.C. Luhmann,Jr.,"Grid Bandpass Filters for Quasi-Optical Frequency Multiplier Array Application", submitted for publication in Microwave and Optical Technology Letters, 1992.

PLANAR GaAs DIODES FOR THz FREQUENCY MIXING APPLICATIONS

William L. Bishop, Thomas W. Crowe, Robert J. Mattauch, and Hasan Dossal
Semiconductor Device Laboratory
Department of Electrical Engineering
Thornton Hall
University of Virginia
Charlottesville, VA 22903-2442

I. Introduction

For many scientific applications in the terahertz frequency range, heterodyne reception is the only technique which exhibits the necessary combination of high spectral resolution, large instantaneous bandwidth and excellent sensitivity. A key component in these receivers is the non-linear resistive mixer element. In general, the mixer element should have high intrinsic speed, the sharpest possible non-linearity, low parasitic element values, low intrinsic noise and impedance levels which can be easily matched to the RF circuit. However, no single device exhibits all of these properties and some tradeoffs are necessary [1].

The GaAs Schottky barrier diode is the most widely used mixer element at submillimeter wavelengths. These diodes are commonly used in the temperature range from 300 K to 10 K and have demonstrated excellent performance from below 100 GHz to over 3 THz [2,3]. The closest competitor for Schottky diodes is the SIS element which has demonstrated record sensitivities at millimeter and long-submillimeter wavelengths [4,5,6]. However, SIS devices are not yet competitive at terahertz frequencies and present superconductor mixer elements require cryogenic cooling which increases the cost and size of the receiver system.

Schottky barrier diodes for terahertz applications are typically fabricated as a micron to sub-micron circular anode metallization on GaAs which is contacted with a sharp wire (whisker). This structure has the benefits of the simplicity of the fabrication of the diode chip, the minimal shunt capacitance of the whisker contact and the ability of the whisker wire to couple energy to the diode. However, whisker-contacted diodes are costly to assemble and difficult to qualify for space applications. Also, complex receiver systems which require many diodes are difficult to assemble [7,8].

The objective of this paper is to discuss the advantages of planar Schottky diodes for high frequency receiver applications and to summarize the problems of advancing the planar technology to the terahertz frequency range. Section II will discuss the structure, fabrication and performance of state-of-the-art planar Schottky diodes. In Section III the problems of designing and fabricating planar diodes for terahertz frequency operation are discussed along with a number of viable solutions. Section IV summarizes the need for futher research and cooperation between diode designers and RF engineers.

II. Planar Mixer Diodes

Planar Schottky barrier diodes have been developed by numerous laboratories over the past ten years [9,10,11,12]. This effort has resulted in many benefits. Not only has the troublesome and somewhat fragile whisker contact been eliminated, but receivers which require two or more individual diode chips, such as balanced mixers, are much easier to assemble. Single chips with two or more diodes in a fixed configuration, such as an antiparallel diode pair, are easy to fabricate and the extension of the diode contact pads to form a planar antenna has been demonstrated. Future work should allow additional receiver components such as filters, oscillators and amplifiers to be integrated with the diode.

The surface channel planar diode, shown in Figs. 1 and 2, has been developed for use at both millimeter and submillimeter wavelengths [9,13]. The chip substrate is semi-insulating GaAs. The epitaxial GaAs structure consists of a thin n-type layer on top of a thick, heavily doped n+ buffer layer. The anode is formed on the n-type GaAs with SiO_2 providing passivation and insulation. An ohmic cathode pad is formed on one end of the chip in close proximity to the anode. The anode is connected to a bonding pad by means of a narrow finger. A trench is formed beneath the finger and completely across the width of the chip to isolate the anode contact pad from the cathode. The isolation trench can be etched deeply into the semi-insulating substrate and the wall of this trench can be positioned very close to the anode. These two features combine with the inherent air-bridge to reduce the shunt capacitance between the contact pads and the shunt capacitance from the contact finger to the conductive GaAs of the cathode. This structure produces lower shunt capacitance than other designs which rely on mesa or proton isolation.

The major fabrication steps of the surface channel structure are illustrated in Fig. 3. Starting with the GaAs wafer (1), a layer of silicon dioxide is deposited using chemical vapor deposition from silane and oxygen (2). The ohmic contact region is patterned, the SiO_2 and n-GaAs are removed and the ohmic contact metallization is deposited and alloyed (3). An opening for the anode is patterned and etched into the SiO_2, leaving a thin layer of oxide to protect the GaAs until the anode metallization can be deposited. The remaining oxide in the anode well is removed with buffered hydrofluoric acid and platinum and gold are electroplated to form the diode and fill the oxide well (4). A thin layer of chromium and gold is deposited over the entire wafer by sputtering. Photoresist is applied and patterned and gold is plated into the opening to form the anode contact pad and finger. The resist is removed and the sputter deposited gold and chromium surrounding the anode contact pad and finger are

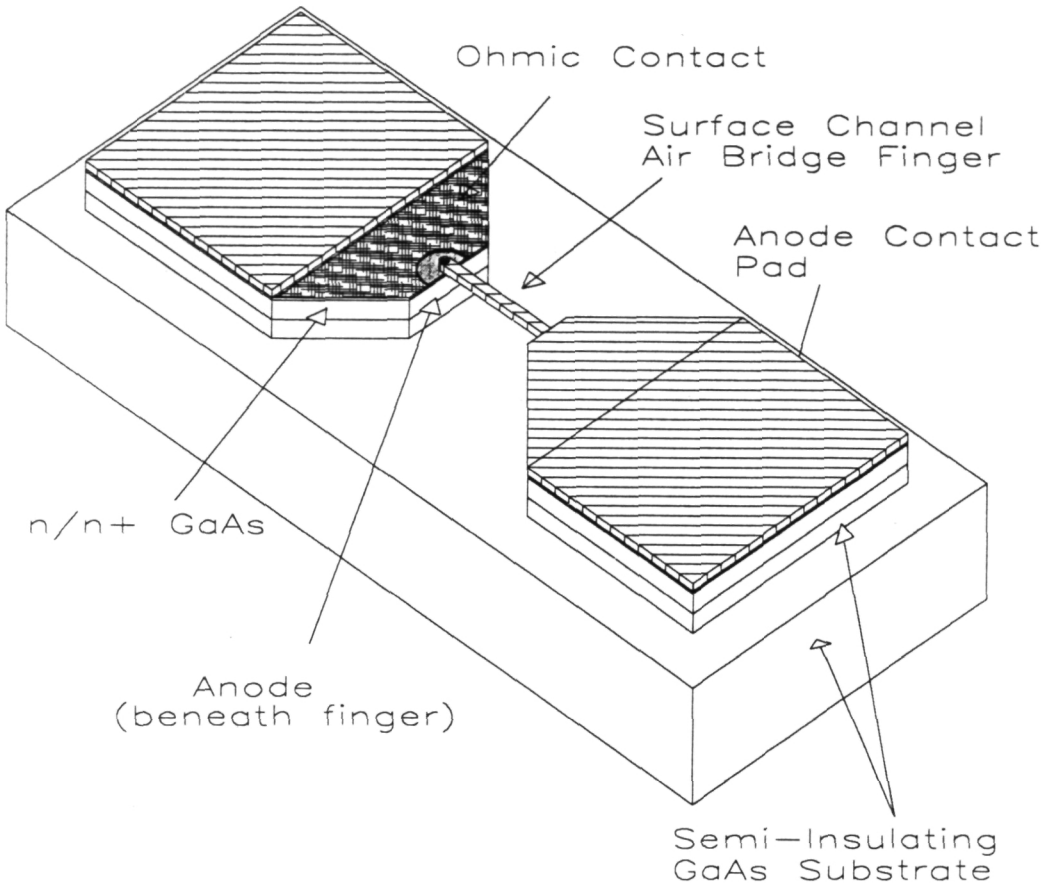

Figure 1. *Surface Channel Planar Diode Structure*

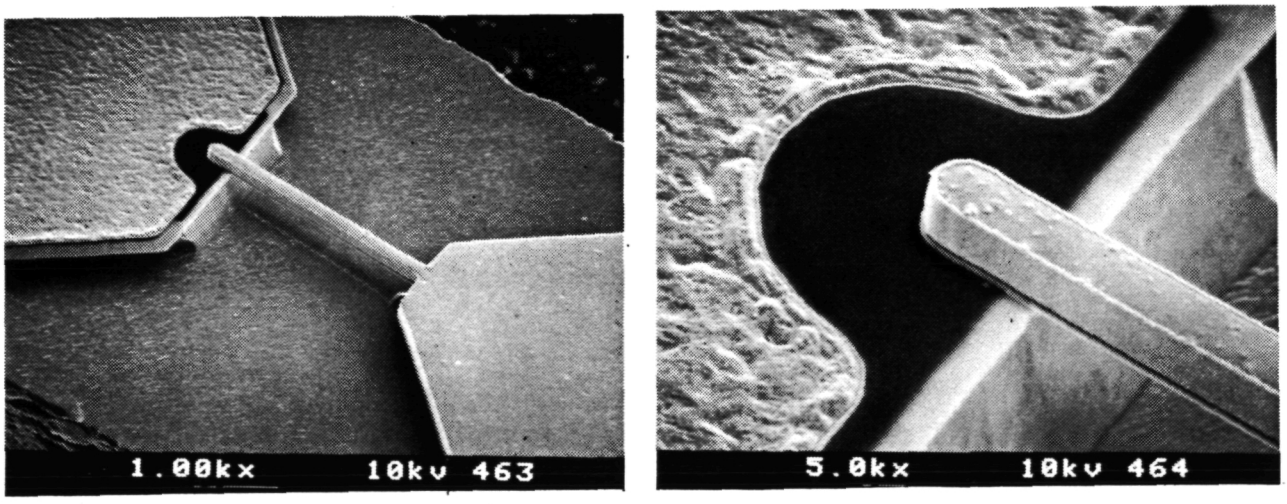

Figure 2. *SEM Photographs of a Surface Channel Planar Diode*

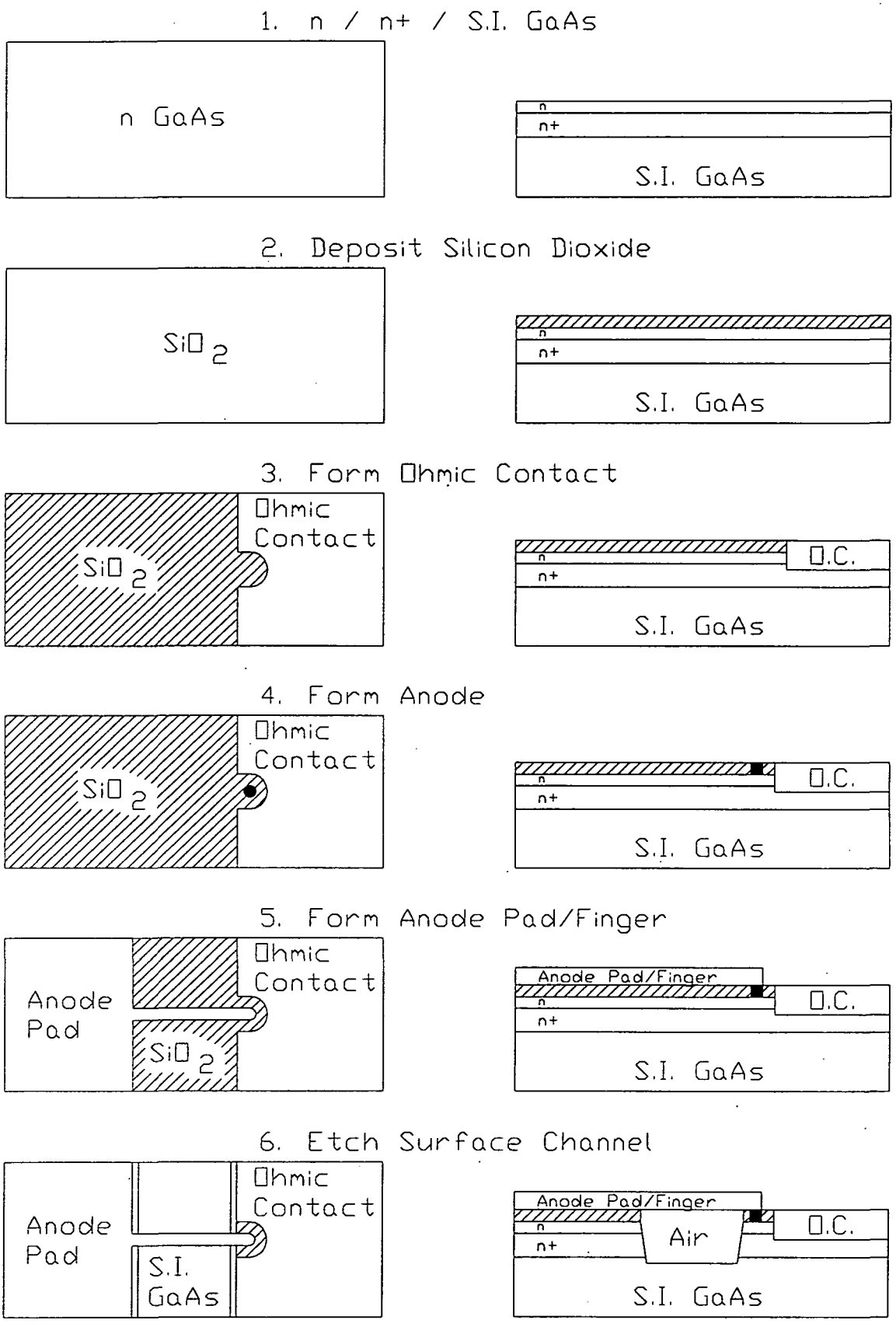

Figure 3. *Surface Channel Diode Fabrication Sequence*

etched away (5). Finally, the surface channel is patterned with photoresist and the SiO_2 and GaAs are etched to form the isolating trench (6).

This fabrication sequence offers several advantages compared to other configurations: (1) expensive and troublesome proton bombardment is not required, (2) planarization is unnecessary, and (3) the wafer surface is nearly flat for the critical steps of anode formation and anode-to-finger alignment.

SEM photographs of two surface channel diode chips are shown in Figs. 4 and 5. The SC2T1 single anode chip is about 125 x 375 x 75 microns. This device has a total capacitance of about 14 fF, zero-bias junction capacitance of 2.5 fF and series resistance of 12-15 Ω. This gives a figure-of-merit cutoff frequency of 4.2 THz for the junction. The SC2T1 has been tested in a room temperature mixer at 345 GHz with a mixer noise temperature of 1,370 K (DSB) and a conversion loss of 9.5 dB (SSB) [14]. This is comparable to the best whisker-contacted diode results. The SC1T4 chip is an antiparallel diode pair for subharmonic pumping. It is only 80 x 180 x 50 microns. These chips have a

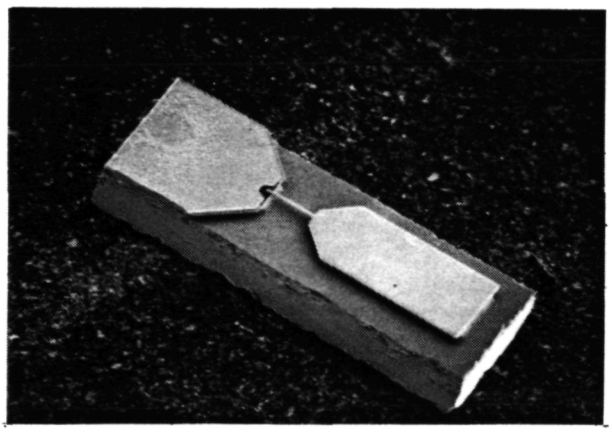

Figure 4. *SC2T1 Planar Diode Chip*

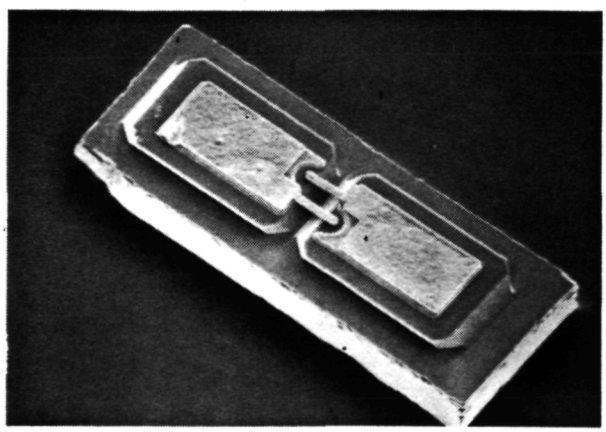

Figure 5. *SC1T4 Planar Antiparallel Diode Pair*

total capacitance of about 16 fF, zero-bias junction capacitance of 3 fF per anode and series resistance of 7-9 Ω. This diode has been successfully used in a room temperature mixer at 205 GHz with a mixer noise temperature of 800 K (DSB) and a conversion loss of 4.4 dB (DSB) using an LO of approximately 100 GHz [15]. This result is better than has been previously reported for antiparallel subharmonic mixers of either planar or whisker-contacted design.

A dual anode planar diode chip for balanced mixer operation is shown in Fig. 6. This chip was developed in collaboration with Aerojet General, Electronic Systems Division under the direction of Robert Haas. This configuration allows individual DC bias of each diode. This device has excellent DC electrical characteristics and is being evaluated in a 100 GHz mixer.

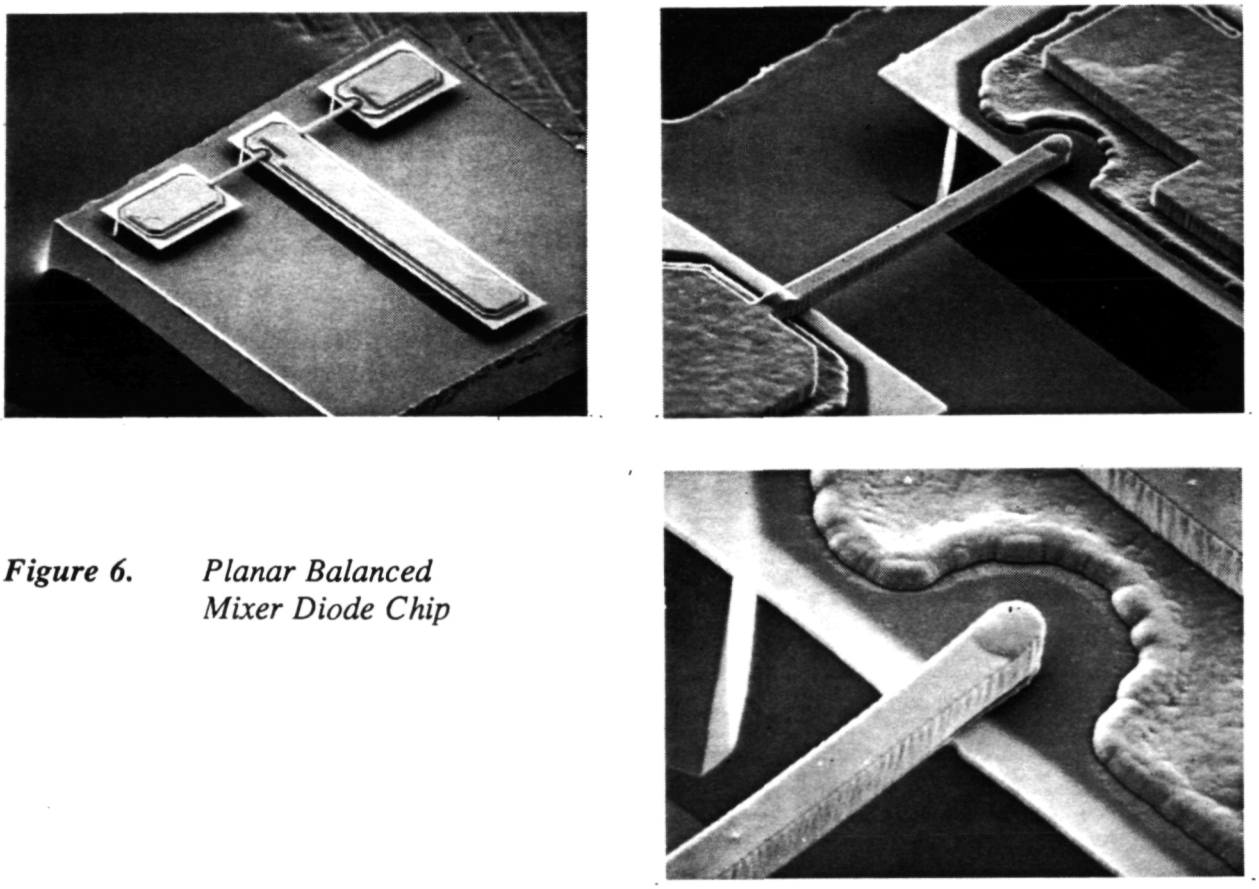

Figure 6. *Planar Balanced Mixer Diode Chip*

III. Planar Diodes for THz Frequency Applications

The surface channel diode structure must be optimized for terahertz operation. These improvements reflect the fundamental need to reduce the R_sC_{j0} product, minimize shunt capacitance, and to efficiently couple energy into the diode. These optimization issues are addressed in the following subsections:

A. Reduction of Anode Diameter

Theory and experimental results with whisker-contacted diodes have shown that very small anodes combined with higher active layer doping are necessary for good performance in the THz range [16]. Whisker-contacted diode chips have been fabricated at UVa with anodes as small as 0.25 microns using direct write electron beam lithography and reactive ion etching [17]. Planar diodes have been fabricated at UVa with 0.5 micron diameter anodes using optical lithography and reactive ion etching. We are also investigating a novel Electroplate Window Shrink (EWS) technique. In this method, circular openings are etched through a thin (0.1 micron) metal layer which overlies silicon dioxide, using UV lithography and wet or dry etch methods. Metal is then electroplated onto this thin conductive layer. Since the plating proceeds laterally as well as vertically, the diameter of the openings is reduced. These reduced-diameter windows are then used as a non-eroding mask to RIE etch the silicon dioxide. Etched wells less than 0.2 microns in diameter have been formed in this manner.

It should be realized that the main issue is not just the fundamental task of forming small anode wells, but also the problems of uniformity and control of anode size. The UVa anode formation process depends on leaving a thin layer of SiO_2 of known thickness in the bottom of the anode wells after RIE. This protective layer is removed by etching with

buffered hydofluoric acid just prior to anode formation. Underetching of this remaining oxide results in open circuits or high resistance. Overetching can result in high C_{j0} and in some cases, excessive diode noise [18]. Unlike whisker-contacted diode chips which can be etched and plated on a chip-by-chip basis, all planar diode anodes on a wafer are formed simultaneously. This obviously places very tight limits on dielectric thickness, thickness uniformity and etch rate calibration.

For these reasons, it would be most helpful to have a very thin RIE etch stop layer to protect the GaAs. This etch stop layer would relax the requirements for oxide thickness and uniformity and allow reasonable overetching during RIE without the risk of damage or contamination of the junction area. Schemes which utilize mutiple layers of different dielectrics could, in principle, satisfy this need. A very thin layer (100-500 Å) of silicon dioxide could first be deposited onto the GaAs. This would be followed with a thicker layer of another dielectric, such as silicon nitride, polyimide or boron-doped silicon dioxide. This thick layer could be patterned and selectively etched (possibly with a dielectric or metal mask) so that the underlying thin layer of oxide acts as an RIE etch stop. Research in this important fabrication area will provide improved control of anode diameter and the reliable production of sub-half micron planar diode anodes.

B. Optimization of Chip Geometry

The dimensions and layout of planar diode chips must be optimized for terahertz frequency applications. The volume of the chip must be reduced to minimize the field disturbing effect of high dielectric constant GaAs and to allow the devices to fit into the smaller waveguides which are required at higher frequencies. The geometry of the planar diode must be improved to minimize shunt capacitance.

Shunt capacitance in the planar diode structure can be separated into two primary components: capacitance from the anode contact finger and pad-to-pad capacitance through the high dielectric constant substrate. Finger capacitance will be reduced by several means. The width of the contact finger can be reduced from the current value of about 2.5 microns to 1 micron. Improved mask design, alignment and surface channel etch control will allow the surface channel wall to be etched as close as possible to the anode. A thick (1 micron) dielectric, perhaps a polyimide, would further reduce finger capacitance.

Pad-to-pad shunt capacitance can be reduced by decreasing pad area, increasing pad separation, increasing the surface channel depth and/or reducing substrate thickness. Our present technology produces chips which are 50 microns thick with pads which are 30 x 60 microns and a surface channel depth of 10 microns. For the lowest possible pad-to-pad capacitance, the GaAs substrate can be removed. This has been demonstrated in a procedure that replaces the GaAs with quartz, as shown in Fig. 7 [19]. The quartz substrate can be permanent or it can be removed once the chip is bonded to a circuit as shown in Fig. 8.

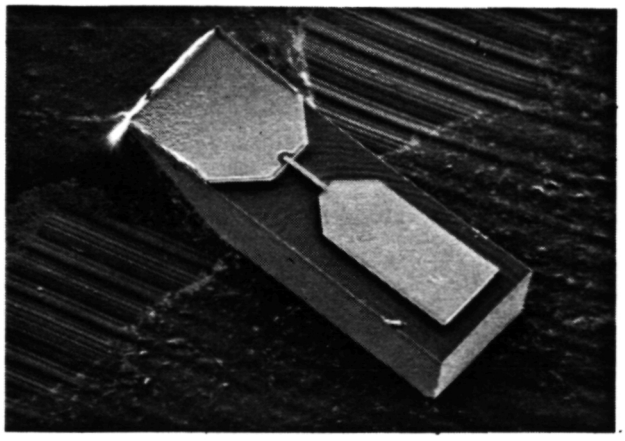

Figure 7. *Surface Channel Diode Chip with Quartz Substrate*

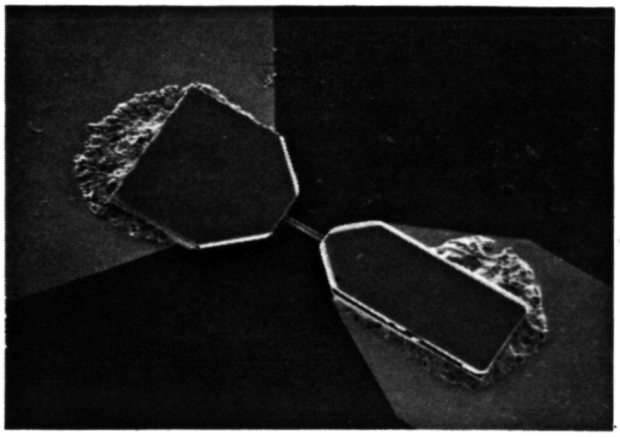

Figure 8. *Surface Channel Diode Chip with Quartz Substrate Removed After Bonding*

The effect of finger length on planar diode performance is an important issue, particularly for waveguide mixers. Longer fingers result in reduced pad-to-pad capacitance but increased finger inductance. A new mask set has been fabricated which will provide small area, antiparallel planar diodes with finger lengths from 10 microns to 50 microns in 10 micron steps on the same wafer. This mask was designed in collaboration with Peter Seigel of JPL and the devices will be RF tested at JPL in a waveguide mixer at frequencies as high as 600 GHz.

Very short contact fingers are required in integrated antenna designs. Surface channel formation is very difficult when the contact finger is under 10 microns in length. Research is underway to characterize a combination of chlorine-based reactive ion etching and wet chemical etching processes to form the surface channel isolation trench with these short contact fingers. The new mask sets for both the small area antiparallel chips and the log periodic antenna designs include levels for this new process.

C. Minimization of Ohmic Contact Resistance

Ohmic contact resistance contributes to diode series resistance and thus reduces cutoff frequency. As contact pad dimensions shrink, ohmic contact resistance increases. This is of particular importance in the case of integrated antenna devices where the pad geometry is dictated by the antenna design. Specific contact resistance can be improved by using a very highly doped buffer layer and through the use of a more advanced ohmic contact technology. For example, ohmic contacts to an n^{++} InGaAs layer are reported to have specific contact resistivity as low as 10^{-7} Ω-cm^2, a factor of 50 to 100 better than our present ohmic contacts.

This would be most beneficial for planar THz antenna structures which require small pad geometries near the anode.

D. Integration of Antenna Structures

The problem of efficient energy coupling to the planar diode is exacerbated at higher frequencies where the wavelength begins to approach the size of the chip. For whisker-contacted diodes, the whisker itself is used as the antenna element and mixers with a long whisker (4λ) positioned parallel to the axis of a corner cube have demonstrated excellent performance at frequencies as high as 4 THz [3].

Another approach for planar diodes is to integrate an antenna, in the form of a bow-tie or log periodic shape onto the chip [20]. The fabrication is straightforward, with the antenna being an extension of the anode and cathode pads and the radiation can be coupled to the antenna through the substrate (GaAs or quartz). An integrated bowtie antenna-diode is shown in Fig. 9. It is 700 x 1000 x 50 microns thick with a 0.5 micron anode and an 8 micron finger length. Preliminary RF testing with unoptimized coupling produced video response of 10 V/W.

Optimization of the integrated antenna will require close interaction between diode designers and RF engineers. As a first step towards this goal, a mask set for the fabrication of log periodic antenna-diodes has been designed in cooperation with Gabriel Rebeiz of the University of Michigan and devices will be fabricated in the near future. With proper diode design and good coupling of energy to the antenna and the diode, it is hoped that RF performance will exceed that of the best whisker-contacted diodes.

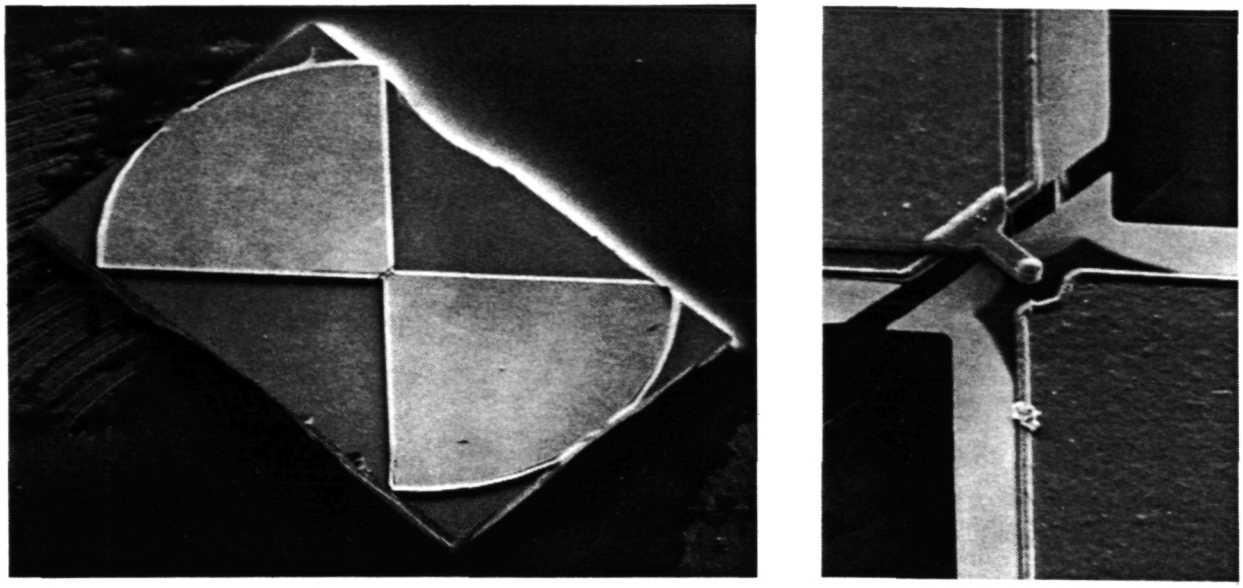

Figure 9. *Integrated Bowtie Antenna-Diode*

IV. Discussion

Development of the planar mixer diode was driven by the need for a rugged device which is inherently simple and easy to assemble in a mixer. However, the tradeoffs for this structural ruggedness and simplicity are a more complex and expensive fabrication procedure, and a more complex chip geometry with larger shunt capacitance. The RF circuit must be redesigned to efficiently couple energy to the diode. In spite of these changes, planar GaAs Schottky barrier diodes have demonstrated performance in the millimeter wavelength range equal to or better than that of the best whisker-contacted diodes.

Successful operation of planar diodes at THz frequencies will require several improvements in the diode chip including reduced anode diameter, improved control of anode diameter, smaller chip dimensions to reduce shunt capacitance, and reduced ohmic contact resistance. These concerns are being addressed through research of novel structures and fabrication methods. Successful application of planar diodes in the THz frequency range will also require optimization of the embedding circuitry and improved methods of coupling energy to the diode. Research is underway to apply novel antenna designs to this problem and to begin to test high performance planar diodes in waveguide assemblies and to test integrated

antennas in open structure mixers. The success of this effort will be hastened by very close interaction and cooperation between diode designers and RF engineers.

Acknowledgements

The authors wish to express their sincere appreciation to Peter Siegel of the Jet Propulsion Laboratory, Israel Galin and Robert Haas of Aerojet General and Gabriel Rebeiz of the University of Michigan for many helpful discussions regarding the design of planar diodes. This work was supported by the National Science Foundation (ECS-8720850), the U.S. Army and the Jet Propulsion Laboratory (958202).

References

[1] T.W. Crowe, R.J. Mattauch, H.P. Roeser, W.L. Bishop, W.C.B. Peatman, "GaAs Schottky Diodes for THz Mixing Application," Invited paper accepted for IEEE Proc., Special Issue on Terahertz Technology, to appear in 1992.

[2] C.R. Predmore, A.R. Raisanen, N.R. Erikson, P.F. Goldsmith, and J.L.R. Marrero, "A Broad-Band, Ultra-Low-Noise Schottky Diode Mixer Receiver for 80-115 GHz," IEEE Trans. Microwave Theory Tech., Vol. MTT-32, pp. 498-506, May 1984.

[3] H.P. Roser, R. Wattenbach, E.J. Durwen, and G.V. Schultz, "A High Resolution Spectrometer for 100 um to 1000 um and Detection of CO (J=7-6), CO (J=6-5) and ^{13}CO (J=3-2)," Astron. Astrophys., 165, 287-299, 1986.

[4] S.K. Pan, A.R. Kerr, M.J. Feldman, A. Kleinsasser, J. Stasiak, R.L. Sandstrom, and W.J. Gallagher," An 85-116 GHz SIS Receiver Using Inductively Shunted Edge-Junctions," IEEE Trans. Microwave Theory Tech., Vol. MTT-37, pp. 580-592, March 1989.

[5] A. W. Lichtenberger, D.M. Lea, and A.C. Hicks, "Nb-based SIS Mixer Elements for Millimeter and Submillimeter Wavelengths," 2nd Int'l. Symp. on Space Terahertz Tech., pp. 439-458, Feb. 1991.

[6] J. Zmuidzinas and H.G. LeDuc, "Quasi-Optical Slot Antenna SIS Mixers," 2nd Int'l. Symp. on Space Terehertz Tech., pp. 481-490, Feb, 1991.

[7] J.W. Waters, "A Proposal of the Earth Observing System, Microwave Limb Sounder," Jet Propulsion Laboratory, California Institute of Tech, July 1988.

[8] M.A. Frerking, "The Submillimeter Mission (SMMM) Heterodyne Instrument," 2nd Int'l. Symp. Space Terahertz Tech., pp.17-31, Feb. 1991.

[9] W.L. Bishop, K. Mckinney, R.J. Mattauch, T.W. Crowe, and G. Green, "A Novel Whiskerless Schottky Diode for Millimeter and Submillimeter Wave Applications," Proc. 1987 IEEE MTT-S Int'l Symp, pp.607-610, June 1987.

[10] J.W. Archer, R.A. Batchelor, and C.J. Smith, "Low-Parasitic, Planar Schottky Diodes for Millimeter-Wave Integrated Circuits," IEEE Trans. Microwave Theory Tech., Vol. MTT-38, No. 1, pp. 15-25, Jan. 1990.

[11] N.J. Cronin, and V.J. Law, "Planar Millimeter-Wave Diode Mixer," IEEE Trans. on Microwave Theory Tech., Vol. MTT-33, No. 9, pp. 827-830, Sept. 1985.

[12] J.A. Calviello, S. Nussbaum, and P.R. Bie, "High Performance GaAs Beam-Lead Mixer Diodes for Millimeter and Submillimeter Applications," Proc. of Intl. Electron Device Meeting, Dec. 7-9, 1981.

[13] W.L. Bishop, K.A. McLeod, R.J. Mattauch, "Whiskerless Schottky Diode," U.S. Patent 5,041,881, Aug. 20, 1991.

[14] T. Newman, W.L. Bishop, K.T. Ng, and S. Weinreb, "A Novel Planar Diode Mixer for Submillimeter-Wave Applications," IEEE Trans. Microwave Theory Tech., Vol. 39, No. 12, pp. 1964-1971, Dec. 1991.

[15] P.H. Seigel, R.J. Dengler, I. Mehdi, J.E. Oswald, W.L. Bishop, T.W. Crowe and R.J. Mattauch, "Measurements on a 215 GHz Subharmonically Pumped Waveguide Mixer Using Planar Back-to-Back Air Bridge Schottky Diodes," submitted for publication to IEEE Microwave and Guided Wave Letters, Oct. 1991.

[16] T.W. Crowe and R.J. Mattauch, "Analysis and Optimization of Millimeter-and-Submillimeter-Wavelength Mixer Diodes," IEEE Trans. Microwave Theory Tech., Vol. MTT-35, Vol. 2, pp. 159-168, Feb. 1987.

[17] W.C.B Peatman, P.A.D. Wood, D. Poterfield, T.W. Crowe and M.J. Rooks, "A Quarter-Micron GaAs Schottky Barrier Diode with High Video Responsivity at 118 Microns," submitted to the Appl. Physics Lett., Feb. 1992.

[18] E.M. Winkler, "A Study of the Effect of Reactive Ion Etching on the Noise Characteristics of Schottky Diodes," Master of Science Thesis, University of Virginia, Charlottesville, VA, August 1991.

[19] W.L. Bishop, E.R. Meiburg, R.J. Mattauch, T.W. Crowe, and L. Poli, "A Micron-Thickness, Planar Schottky Diode Chip For Terahertz Applications with Theoretical Minimum Parasitic Capacitance," Proc. 1990 IEEE MTT-S Int'l. Symp., pp. 1305-1308, May, 1990.

[20] P.H. Siegel, "A Planar Log-Periodic Mixtenna for Millimeter and Submillimeter Wavelengths," Proc. 1986 IEEE MTT-S Int'l. Symp., pp. 649-652, 1986.

Planar Doped Barrier Subharmonic Mixers*

T. H. Lee, J. R. East and G. I. Haddad

Center for Space Terahertz Technology
The University of Michigan
Ann Arbor, Michigan

Abstract

The PDB (Planar Doped Barrier) diode is a device consisting of a p^+ doping spike between two intrinsic layers and n^+ ohmic contacts. This device has the advantages of controllable barrier height, diode capacitance and forward to reverse current ratio. A symmetrically designed PDB has an anti-symmetric current vs. voltage characteristic and is ideal for use as millimeter wave subharmonic mixers. We have fabricated such devices with barrier heights of 0.3, 0.5 and 0.7 volts from GaAs and InGaAs using a multijunction honeycomb structure with junction diameters between one and ten microns. Initial RF measurements are encouraging. The 0.7 volt barrier height 4 micron GaAs devices were tested as subharmonic mixers at 202 Ghz with an IF frequency of 1 GHz and had 18 dB of conversion loss. The estimated mismatch loss was 7 dB and was due to higher diode capacitance. The LO frequency was 100.5 GHz and the pump power was 8 mW.

* This work was supported by NASA under Grant No. NAGW-1334

I. Introduction

Planar Doped Barrier devices were first proposed in 1980 by Malik *et al*[1]. The structure can be understood as a planar doped p^+ spike sandwiched between two lightly doped regions and heavily doped n-type ohmic contacts. Such an n^+-i-p^+-i-n^+ device has a triangular potential barrier which is adjustable by the parameters of epi-layer growth such as sheet charge doping density and intrinsic layer dimensions. The devices are unipolar and the charge transport over the potential barrier can be modeled by the thermionic emission theory. The current vs. voltage characteristic is similar to that of Schottky diodes. Accordingly PDB's can be used as a Schottky barrier diode replacement with the additional advantage of barrier height control.

The major applications of PDB devices are as mixers and detectors. If the device structure is designed symmetrically with the p^+ doping spike in the middle of the intrinsic region, the PDB diode has an anti-symmetrical I-V characteristics and is ideal for millimeter-wave subharmonic mixer applications. A summary of the theory and design techniques for symmetric PDB diodes as subharmonic mixers is given by Lee *et al*[2]. Several subharmonic PDB diodes operating at microwave frequencies have been reported[3,4,5]. Güttich *et al.* measured a D-band silicon PDB subharmonic mixer with a minimum conversion loss of 10.8 dB[6]. The structure can also be designed to have lightly doped regions of different thickness. This will provide a current vs. voltage characteristic that is useful in low barrier detectors applications. Dale *et al*[7,8]. reported a PDB single-ended mixer had a noise figure of approximately 6 dB at 9.4 GHz and required only 280 μW of local oscillator power. When used as video detectors, Anand *et al*[9]. showed zero bias PDBs for low level detection had a burnout limit comparable to high barrier Schottky diodes and were less sensitive to the electrostatic discharge.

PDB devices suffer from several problems. The space charge resistance is relatively high. By making the i-layer as short as possible we are able to reduce the space charge resistance. However, the i-layer width has to be larger than the Debye length of n^+ region to avoid the charge redistribution at i-n^+ interface. For a subharmonic PDB diode the ideality factor is at least

two. The conversion ability is thus degraded. A careful design is necessary to obtain an optimum performance.

In this paper we present a group of MBE grown GaAs wafers with a 250Å i-layer thickness and the p^+ spike doping densities of 1.5, 2.0 and 2.5×10^{12} cm^{-2} for mixer operation. The barrier height was designed for 0.3, 0.5 and 0.7 volts respectively. The impurity concentration of the intrinsic region is nominally less than 10^{14} cm^{-3}. Also presented are a group of InGaAs wafers grown via gas MBE at the University of Michigan. These wafers are of the same specifications as the GaAs ones except with longer n^+ layers. A preliminary RF result is reported.

II. Fabrication of Whisker-contact Subharmonic PDB Diodes

Two material systems have been chosen: GaAs and InGaAs. The use of GaAs has some advantages. GaAs is a more mature fabrication technology and tight parameter control of MBE grown GaAs is relatively easy. InGaAs, however, has a higher electron mobility and much lower contact resistivity than GaAs. For terahertz operation InGaAs might be a better material system. In this paper, we present diodes from both material systems.

A typical wafer structure for the subharmonic GaAs PDB is shown in Fig. 1. An optimum structure for small diameter whisker-contact PDB diodes with low series resistance and parasitic capacitance is achieved by completely removing the substrate and forming mesas. An etch stop layer of AlGaAs between the substrate and epi-layer was included for this substrate removal. A good selectivity between the substrate and etch stop layer is possible. In the InGaAs system hydrochloric acid was used to remove the InP substrate without affecting the InGaAs epi-layer.

The fabrication of whisker-contact PDB diodes consists of seven major steps as shown in Fig. 2:

(1) diode definition and metallization,

(2) mesa etch,

(3) SiO_2 passivation,

(4) opening contact holes,

(5) front side protection,

(6) backside thinning,

(7) final metallization and plating.

More details on the process steps are given in the next section.

The first step is diode definition and metallization. An image reversal photolithography process was characterized to attain desired diode patterns for ohmic metal lift-off. A positive photoresist was spun uniformly on the wafers, and then soft-baked at 105°C and UV exposed in the conventional way. Next a reversal bake and flood exposure altered the polarity of the solubility of photoresist in the images and fields, so that a negative image could be obtained after development. The exposure and bake parameters are optimized to obtain an undercut profile desirable for the lift-off.

Metallization was then performed by depositing layers of thin film metals on the photoresist patterned samples. Ni/Ge/Au/Ti/Au were evaporated in sequence. The metal covered wafers were soaked in the acetone for lift-off. The resulting dot-like patterns also served as a self-aligned mask for mesa etch.

The next step is the mesa etch. To avoid serious undercut we used a dry plasma etch instead of a wet chemical etch. Mesa etching was accomplished by a reactive-ion etching system. The GaAs wafers were etched in a low pressure chamber filled with BCl_3 and Ar gaseous plasmas of 11:9 ratio to obtain highly anisotropic sidewalls, while InGaAs wafers were etched by the mix of methane, hydrogen, and argon. The effective area of diodes was determined by the area of the p^+ doping spike. With plasma etching the precise control of device area is possible. The desired etch depth is into the first few hundred Å of the bottom n^+ layer. Sometimes a subsequent slow wet etch is used to remove a thin damaged layer.

The third step is SiO_2 deposition. After the wafers were mesa etched, a dielectric film was deposited for step coverage. A plasma-enhanced chemical vapor deposition system was used. A low temperature process was adopted to avoid heating the devices. A silane/oxygen plasma at 200°C for 90 minutes was used for optimum step coverage. This low temperature silicon dioxide layer was amorphous with low dielectric strength. A dielectric covered sample is shown in Fig. 3.

The fourth step is opening contact holes. At this stage, wafers were covered by PECVD SiO_2 everywhere. The mesa mask was used to open a hole where previously ohmic metals were deposited. The image reversal process as described in the first step with a careful alignment was required. The silicon dioxide on the top of ohmic metals was RIE-etched using gaseous plasmas of CHF_3 and CF_4. It was difficult to tell, under the microscope, whether ohmic metal has been reached. By probing the adjacent diodes and measuring the electrical properties, we made certain the dielectric had been removed completely and could move to next step. Fig. 4 shows the diode at this stage.

The fifth step is front side protection. The wafer prior to substrate removal has to be protected and supported on its front side. Wafers after backside thinning were less than one μm thick and simply too fragile to work on. A remedy is to spin a thin photoresist on the front side and then plate thick metal for support. The thin PR and plated metal could be striped off in the last step.

The sixth step is backside thinning. Selective etching was used for the substrate removal. In the GaAs/AlGaAs system, $NH_4OH:H_2O_2$ (1:24) was used. Hydrogen peroxide helps oxidizing GaAs whose oxide can be removed by ammonium hydroxide. The selectivity is a function of the percentage of Al composition in AlGaAs, and has to be high enough to stop etching. The subtle change of sample color implied the remaining thickness of the GaAs substrate. After the stop layer was reached, the thin AlGaAs film was then removed by hydrofluoric acid which would not attack GaAs. In the InGaAs system, hydrochloric acid quickly removed the InP substrate but

did not attack the InGaAs epi-layer. These thinned samples were ready for the final metallization.

The final step is the metallization and plating. Backside metallization was performed after substrate thinning. The same ohmic metals as for the front side contact were evaporated. If samples have been exposed in the air, the accumulated surface oxide should be removed before metallization. After metallization gold, for its good conductivity, was plated on the back for mechanical support. The process was done after we removed the front side protection by acetone. The samples were about 20 μm thick.

The finished device was a vertical diode with ohmic metal on the top and bottom. We have been successful in fabricating 1 μm, 2 μm, 4 μm and 10 μm diameter diodes. Fig. 5 shows the multijunction honeycomb structure for 4 μm diodes. All the diodes were evenly arranged in 125x125 μm squares, cut by diamond saws and bonded in a fixture. They are now ready for RF testing in a whisker mount.

III. Planar Doped Barrier Subharmonic Mixer Performance

The subharmonic mixer diodes were first characterized by their DC performance. Fig. 6 shows the I-V characteristics of a 4 μm diameter GaAs PDB diode of 0.7 volt barrier height. The low frequency capacitance was about 20 fF. The effective depletion length is approximately 700 Å. Fig. 7 shows the I-V curves for InGaAs 2 μm diameter devices with barrier heights of 0.3, 0.5 and 0.7 volts respectively. The capacitance of InGaAs 10 μm diodes was 170 fF, which scaled down to a value of 6.9 fF for 2 μm ones. The ideality factor was determined by the slope of I-V between 10 μA and 100 μA. The resulting value for PDB diodes with 0.7 volt barrier height was 2.34 for GaAs and 2.39 for InGaAs.

The RF measurement results for 4 μm GaAs diodes are shown in Table 1. The diode was tested as a subharmonic mixer with a pump frequency of 100.5 GHz, a signal frequency of 202 GHz and an IF frequency of 1 GHz. The mixer was a whisker-contact diode mount which was

designed to match a device of 5 fF capacitance at about 200 GHz. The tested 4 μm diode capacitance was 20 fF. With a pump power of 8 milliwatts, the mixer conversion loss was 18 dB. The mismatch was estimated at 7 dB, which implied a diode conversion loss of 11 dB. Measurements on the smaller devices and InGaAs devices are in progress.

V. Conclusion

The properties and fabrication techniques for planar doped barrier subharmonic mixer diodes have been described. The fabrication process produces mesa diodes for whisker contact mounts with diameters between one and ten microns. The diodes are based on the GaAs or InGaAs system and have barrier heights of 0.3, 0.5 and 0.7 volts. Initial subharmonic mixer results for a 4 μm diameter GaAs diode with 0.7 volt barrier height gave a conversion loss of 18 dB at 202 GHz with a local oscillator power of 8 milliwatts and an expected mismatch loss of 7 dB.

Reference

[1] Malik, R. J., T. R. Aucoin, R. L. Ross, K. Board, C. E. C. Wood and L. F. Eastman, "Planar-Doped Barriers in GaAs by Molecular Beam Epitaxy," *Electron. Lett.*, vol. 16, pp. 836-838, Oct. 1980.

[2] Lee, T. H., J. R. East and G. I. Haddad, "Planar Doped Barrier Devices for Subharmonic Mixers," *Microwave and Optical Technology Letters*, vol. 4, No. 1, pp.53-60, Jan. 1991.

[3] Malik, R. J., and S. Dixson, "A Subharmonic Mixer Using a Planar Doped Barrier Diode with Symmetric Conductance," *IEEE Electron Device Lett.*, vol. EDL-3, No. 7, pp. 205-207, Jul. 1982.

[4] Dixon, S., and R. J. Malik, "Subharmonic Planar Doped Barrier Mixer Conversion Loss Characteristics," *IEEE Trans. Microwave Theory Tech.*, vol. MTT-31, pp. 155-158, Feb. 1983.

[5] Chen, J., and D. Wong, "W-Band Beam Lead Planar Doped Barrier Subharmonic Mixer," *IEEE Microwave Symp Technical Digest*, pp. 178-180, 1985.

[6] Güttich, Ulrich, K. M. Strohm and F. Schäffler, "D-Band Subharmonic Mixer with Silicon Planar Doped Barrier Diodes," *IEEE Trans. Microwave Theory Tech.*, vol MTT-39, pp. 366-368, Feb. 1991.

[7] Dale, I., A. Condle, S. Neylon and M. Kearney, "Planar Doped Barrier Mixer and Detector Diodes as Alternatives to Schottky Diodes for Both Microwave and Millimeter Wave Applications," *IEEE Microwave Symp. Technical Digest*, pp. 467-470, 1989.

[8] Kearney, M. J., M. J. Kelly, R. A. Davies, T. M. Kerr, P. K. Rees, A. Condie and I. Dale, "Asymmetric Planar Doped Barrier Diodes for Mixer and Detector Applications," *Electron. Lett.*, vol. 25, pp. 1454-1456, Oct. 1989.

[9] Anand, Y., J. Hillson, A. Torabi and J. R. East, "Millimeter Wave Planar Doped Barrier Detector Diodes," Proceedings of 2nd Int. Symp. on Space Terahertz Technology, pp. 340-352, 1991.

Device profile of GaAs subharmonic PDB diodes

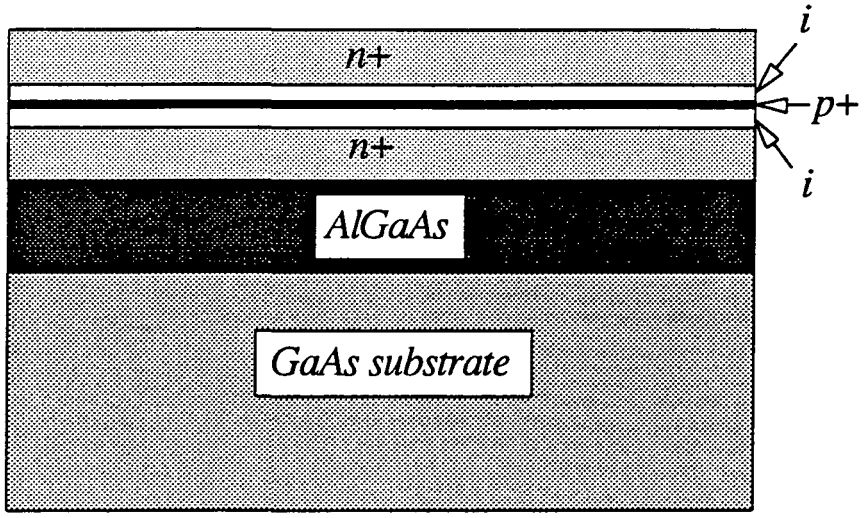

Figure (1) The device profile of GaAs subharmonic PDB diodes. The width of the intrinsic layer is 250 Å and that of the n^+ is 2500 Å on either side of the p^+ spike. The sheet charge doping density of the p^+ spike is 1.5, 2.0 and 2.5×10^{12} cm^{-2} for 0.3, 0.5 and 0.7 volt barrier height respectively.

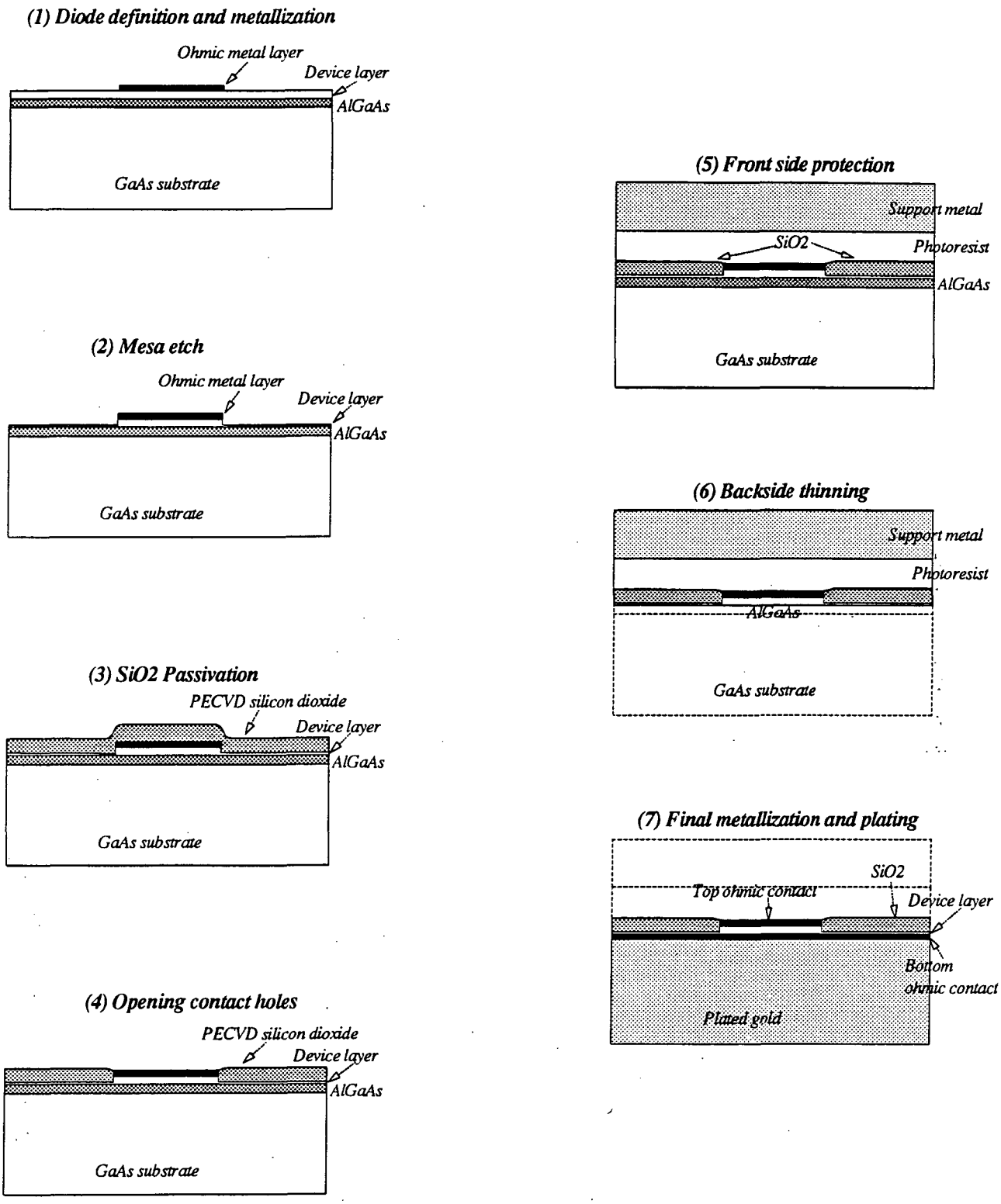

Figure (2) The fabrication sequence for GaAs subharmonic mixer diodes.

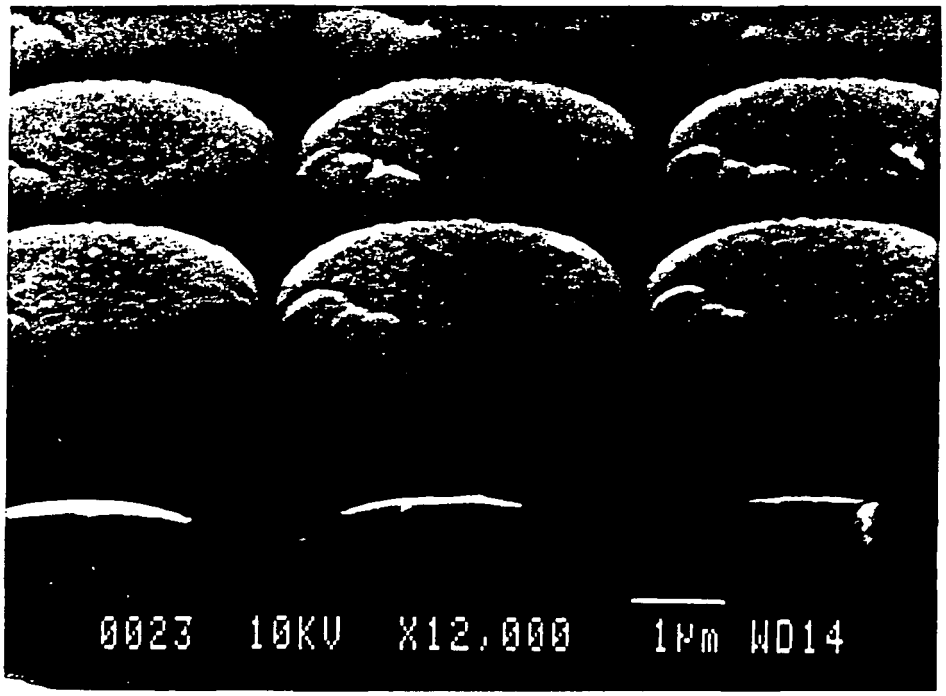

Figure (3) Diodes are covered by PECVD silicon dioxide everywhere. This picture was taken after fabrication step (3) as described in figure (2).

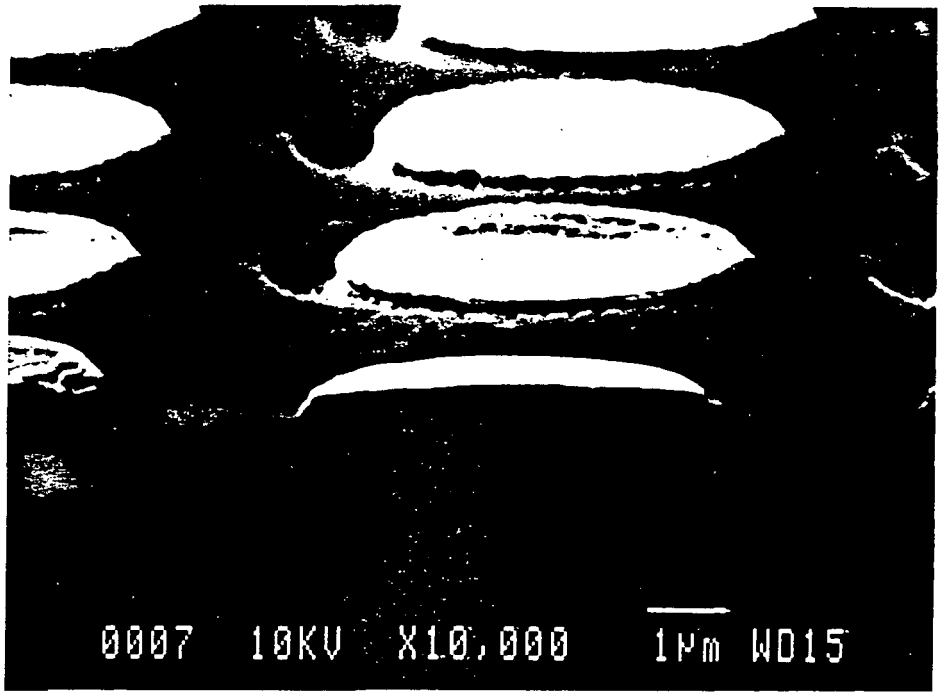

Figure (4) Contact holes are opened on the ohmic metals. This picture was taken after fabrication step (4) as described in figure (2).

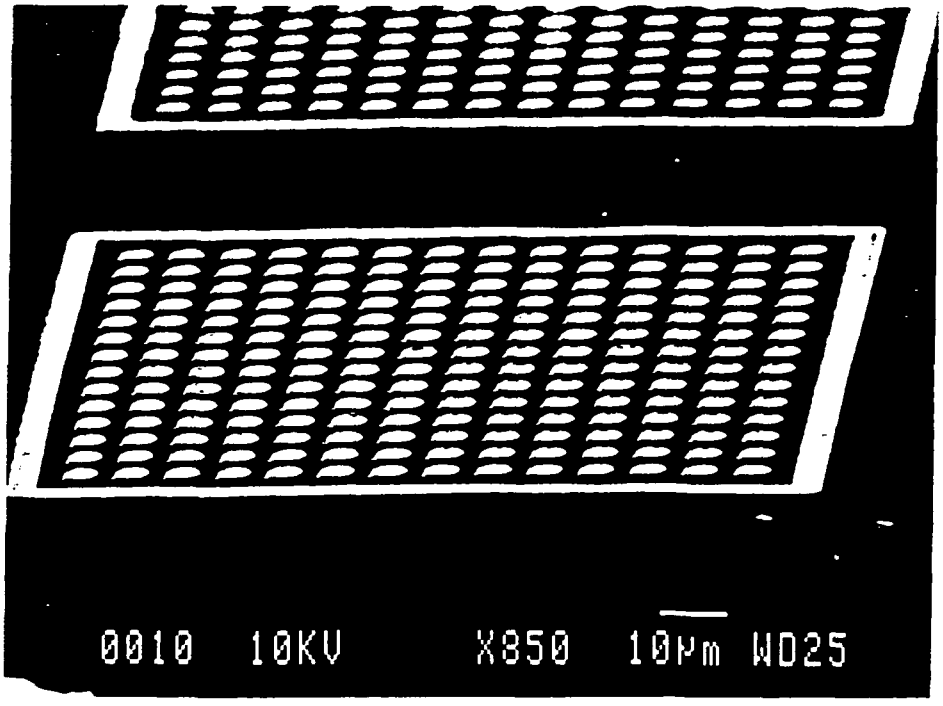

Figure (5) Finished diodes of honeycomb structure are in 125x125 µm squares. The dark area is covered by the dielectric layer.

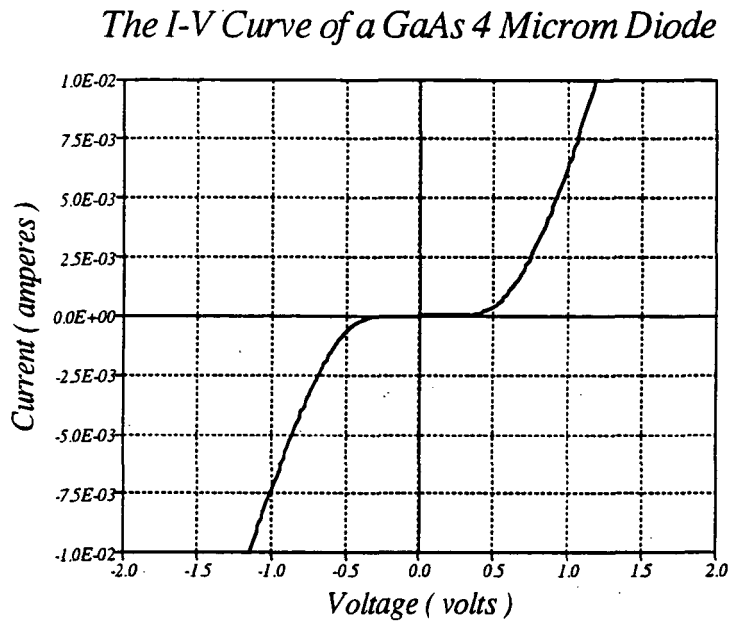

Figure (6) The I-V curve of a 4 μm GaAs subharmonic PDB diode.

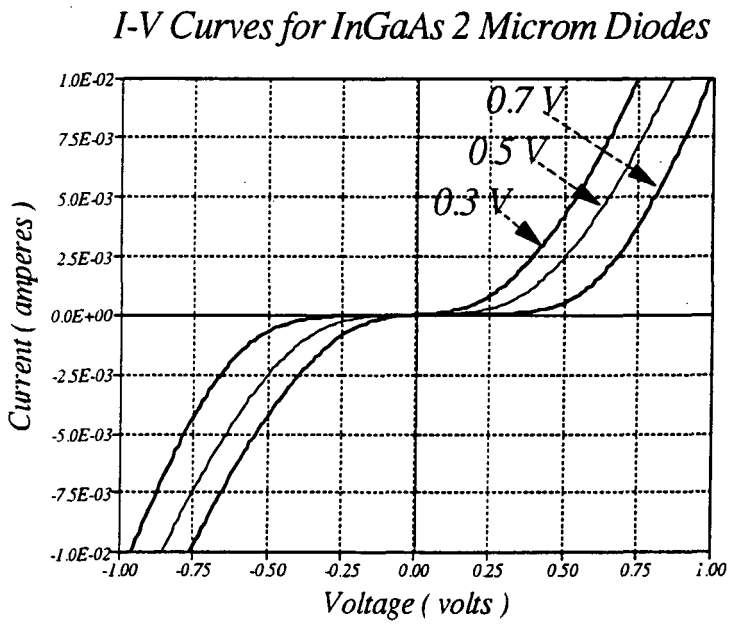

Figure (7) The I-V curves for 2 μm InGaAs diodes of 0.3, 0.5 and 0.7 volt barrier height, respectively.

Mixer Diode Performance (GaAs)	
Diode diameter	4 μm
p^+ spike doping	2.5×10^{12} cm^{-2}
Total *i* layer length	525 Å
Estimated barrier height	0.7 V
Ideality factor	2.39
Diode capacitance (measured)	20 fF
Contact resistance (by $\rho = 5 \times 10^{-7}$ Ω-cm^{-2})	3.9 Ω
RF	202 GHz
IF	1.0 GHz
LO	100.5 GHz, 8 mW
Mixer conversion loss	18 dB
Mixer waveguide impedence	150 Ω
Series inductance	0.01 nH
Mismatch loss	7 dB
Diode conversion loss	11 dB

Table (1) The performance of a 4 μm GaAs PDB diode as a subharmonic mixer.

New Approach to the Design of Schottky Barrier Diodes for THz Mixers

A. Jelenski [+], A. Grüb [*], V. Krozer [*], H.L. Hartnagel [*]

[*] *Institut für Hochfrequenztechnik, Technische Hochschule Darmstadt, Merckstr. 25, D-6100 Darmstadt, Germany, Phone: +49 6151 162162, Fax: +49 6151 164367*

[+] *Institut für Hochfrequenztechnik, Technische Universität Hannover, Appelstr. 9A, D-3000 Hannover, Germany, on leave from the Institute of Electronic Materials Technology, Warsaw, Poland Phone: +48 22 354416, Fax: +48 39120764*

Abstract

Near–ideal *GaAs* Schottky barrier diodes especially designed for mixing applications in the *THz* frequency range are presented.

A diode fabrication process for submicron diodes with near–ideal electrical and noise characteristics is described. This process is based on the electrolytic pulse etching of *GaAs* in combination with an in–situ platinum plating for the formation of the Schottky contacts. Schottky barrier diodes with a diameter of 1 μm fabricated by the process have already shown excellent results in a 650 *GHz* waveguide mixer at room temperature. A conversion loss of 7.5 *dB* and a mixer noise temperature of less than 2000 *K* have been obtained at an intermediate frequency of 4 *GHz*.

The optimization of the diode structure and the technology was possible due to the development of a generalized Schottky barrier diode model which is valid also at high current densities. The common diode design and optimization is discussed on the basis of the classical theory. However, the conventional formulas are valid only in a limited forward bias range corresponding to currents much smaller than the operating currents under submillimeter mixing conditions. The generalized new model takes into account not only the phenomena occurring at the junction such as current dependent recombination and drift/diffusion velocities, but also mobility and electron temperature variations in the undepleted epi–layer.

Calculated diode *I/V* and noise characteristics are in excellent agreement with the measured values. Thus, the model offers the possibility of optimizing the diode structure and predicting the diode performance under mixing conditions at *THz* frequencies.

Introduction

Schottky-barrier diodes have been recently applied for heterodyne receivers in the frequency range up to a few THz, the interesting point being how their realization and technology can be improved to obtain still better results at higher frequencies. Much effort has been done to reduce the feature sizes, but further reduction beyond approximately $0.5\mu m$ seems to be unpractical because of contacting difficulties. Since maximizing of the conversion efficiency requires a resistive mixing, the junction resistance at the operating point has to be much smaller than its capacitive reactance to avoid losses related with parametric downconversion.

Therefore, for the highest frequencies despite the decreasing diameter, the DC current at the operating point is always of the order of 0.5 mA, leading to an increased current density and therefore the bias approaches the so called flat-band voltage. The expressions for the I/V and the C/V characteristics of Schottky diodes are usually determined by the following well known formulas:

$$I = I_{sat} \exp\left(\frac{V_j}{nV_T}\right) \quad \text{giving} \quad R_j = \frac{nV_T}{I} \tag{1}$$

$$C_j = A\sqrt{\frac{q\epsilon N_d}{2(V_D - V_T - V)}} = \frac{C_{j0}}{\sqrt{1 - \frac{V_T}{V_D} - \frac{V}{V_D}}} \tag{2}$$

When the difference between the bias and the flat-band voltage is smaller than $3\,V_T = 3\,kT/q \sim 80\,mV$ at room temperature, eq. 1 and eq. 2 become invalid [1].

To avoid discrepancies between calculated and measured results some authors were forced to make unphysical assumptions like assuming that the flat-band voltage V_D equals the barrier height ϕ_b [2] and neglecting the V_T/V_D term in eq. 2 [3]. But these assumptions still do not solve the problem which results from the fact that under the so called flat-band condition, when the depleted layer disappears, the capacitance C_j becomes infinite, while the junction resistance R_j (eq. 1) is still finite and greater than zero. This phenomenon results from the approximations made in the derivation of eq. 1 and 2.

The examination of the I/V characteristics of the fabricated diodes shows that the dominating carrier transport mechanism is the thermionic field emission in the reverse bias and the thermionic emission and thermionic emission/diffusion for forward biases. In the frame of the diffusion theory, which determines the diode behavior near flat-band, eq. 1 is just an approximation of the solution given by the Dawson integral valid for $V \leq V_D - 4V_T$. A better approximation of this solution similar to that given already by

· Schottky [4] is

$$I = I_{fb}\frac{1}{2\sinh\left(\frac{V_D - V}{nV_T}\right)} \quad \text{giving} \quad R_j = \frac{nV_T}{I}\tanh\left(\frac{V_D - V}{nV_T}\right) \tag{3}$$

In this bias range the depletion approximation utilized in the derivation of eq. 2 is also not valid any more and the space charge must be taken into account. This leads to a novel expression for the junction capacitance:

$$C_j = \frac{1 - \exp\left(\frac{V_D - V}{V_T}\right)}{1 - \frac{V}{V_D} - \frac{V_T}{V_D}\left[1 - \exp\left(\frac{V_D - V}{V_T}\right)\right]} \tag{4}$$

These expressions should be used if one wants to calculate the mixer performance when the diode is operating near flat-band conditions. They can be easily inserted into the generalised program, results of which are presented in this contribution. The actual program takes into account the current dependent recombination velocity, the field dependent mobility and electron heating at high forward bias. This program can therefore be efficiently used to calculate mixer or frequency multiplier performances enabling a more realistic analysis and optimization similar to the analysis given in [5].

The noise generating mechanisms in Schottky-barrier diodes are also well understood and are indicated in fig.1. The basic noise generating mechanisms are: a) shot noise in the junction with $i_j^2 = 2qI\Delta f$ and b) thermal noise in the series resistance with $e_s^2 = 4kT_0R_s\Delta f$.

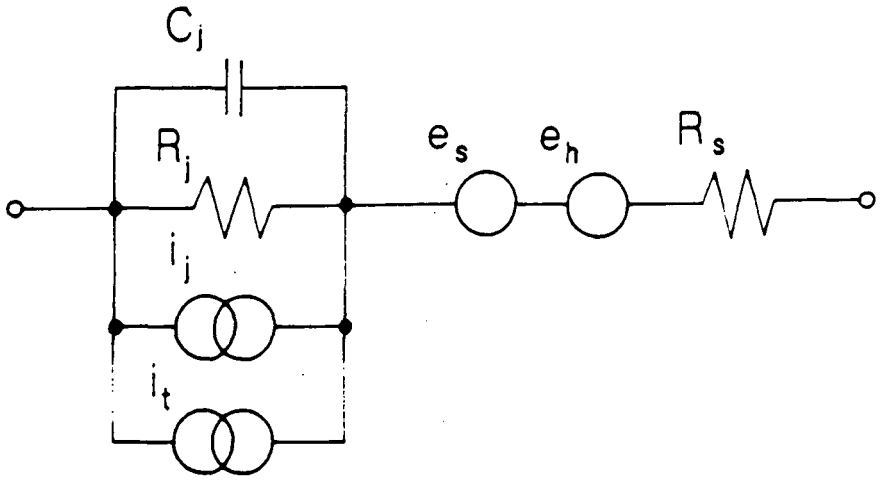

Figure 1: The equivalent circuit of the Schottky-barrier diode.

The well known expression first derived by Weisskopf in 1943 [6] gives the diode noise temperature for frequencies much lower than the junction cut-off frequency ω_j =

$1/(R_jC_j)$.

$$T_n = \frac{nT_0}{2}\frac{R_j}{R_s+R_j} + T_0\frac{R_s}{R_s+R_j} \tag{5}$$

For higher forward biases and diodes with low doped epi-layers, electrons are heated by the high electric field in the undepleted epi-layer and the excess noise temperature T_h due to the increased electron temperature has to be added to the thermal noise [7, 8].

$$e_h^2 = 4kT_0K_hI^2R_s\Delta f \tag{6}$$

In some diodes an excess noise can be observed probably due to some trapping effects at the interface. This phenomenon has been described by [8, 9] and the noise source i_t should be added to i_j.

$$i_t^2 = 2\,I^2\,\frac{N_T}{N_D}\,\frac{\tau}{1+(\omega\tau)^2} \tag{7}$$

where N_T is the concentration of presumed traps and τ is the time constant of this process.

The general expression to be compared with the experiment is then

$$T_n = \frac{nT_0}{2}\frac{R_j}{R_s+R_j} + \frac{C_T}{R_s+R_j} + T_0\frac{R_s}{R_s+R_j}\left(1+K_hI^2\right) \tag{8}$$

where C_T and K_h are constants. If a good fitting is obtained with these 2 constants it means that the above simple model well describes noise generation mechanisms in measured diodes.

Diode fabrication

The first major requirement for *GaAs* Schottky diodes for mixing applications in the submillimeter frequency range is a small Schottky contact area in order to achieve junction capacitances in the low fF or even subfF region. Secondly, a homogeneous metal/semiconductor contact free of interfacial layers is required in order to achieve near-ideal electrical and noise performance. Since practical submm Schottky diodes have a metal/semiconductor contact area of less than 1 μm^2, the *GaAs* surface treatment and Schottky metal deposition techniques are much more important than for other semiconductor devices. Therefore, the fabrication of low-noise Schottky diodes requires an especially optimized device technology in order to avoid any damage to the *GaAs* surface. The diodes presented in this paper have been fabricated by applying a novel *GaAs* etching technique which is called anodic pulse etching [10, 11]. Since the initial fabrication steps such as SiO_2-deposition, ohmic backside contact and SiO_2-structuring are the same as commonly used, the main subject of the fabrication section will be the description of the anodic pulse etching in combination with the electrolytic *Pt* deposition for the formation of near-ideal small-area Schottky contacts.

For the fabrication of the diodes high–quality MBE–grown layers have been used [12]. Besides the diode diameter, thickness and doping concentration of these layers are the important process parameters for optimum device performance. Epitaxial layers having doping concentrations of $2 \cdot 10^{16}\ cm^{-3}$, $8 \cdot 10^{16}\ cm^{-3}$ and $2 \cdot 10^{17}\ cm^{-3}$ with an original epi–layer thickness of 200 nm have been used. In addition, one epi–layer with a graded doping profile has been used. This layer has a surface doping concentration of $2 \cdot 10^{16}\ cm^{-3}$ which is increased exponentially to $6 \cdot 10^{18}\ cm^{-3}$ within 90 nm. By controlled etching of the $GaAs$ surface, hence any surface doping concentration can be achieved.

After thinning the n^+–substrate to a thickness of 50–70 μm by mechanical lapping and polishing in order to reduce the substrate resistance, a 500 nm thick SiO_2 layer is deposited onto the epitaxial side by e–beam evaporation. The SiO_2 is necessary in order to avoid As outdiffusion during the following formation of the ohmic backside contact and finally separates the single Schottky diodes and serves as a mechanical guide for the whisker contact. The ohmic backside contact is formed by evaporation of $Ni/AuGe/Ni$ followed by a rapid thermal annealing step in H_2–atmosphere. Subsequently, the honeycomb diode structure is transferred to a photoresist layer on the SiO_2 by conventional UV–lithography. The structured photoresist serves as an etch mask for the reactive ion etching of the SiO_2. The applied RIE–process with CHF_3/O_2 assures highly anisotropic etching of the SiO_2. Thus, honeycomb structures with smallest hole diameters of 0.8 μm have been defined. The RIE–process is followed by a short dip in buffered HF in order to remove any possible SiO_2 residues.

The next step is the formation of the small–area Schottky contacts which is of course most important since it defines the quality of the Schottky contact. Because of the introduced $GaAs$ surface damage due to the SiO_2 e–beam evaporation and the plasma etching, it is necessary to remove some ten nanometers of GaAs before the deposition of the Schottky metal.

The etching step usually is performed by wet chemical etching [13, 14] or anodic oxidation of the $GaAs$ surface with subsequent dissolution of the anodic oxide in a Pt electrolyte [15]. Since wet chemical etching is isotropic it leads to an enlargement of the contact area and thus to larger junction capacitances. Furthermore, the etched GaAs surface is in contact with air, leading to the formation of a thin interfacial oxide layer. The anodic oxidation process allows the in–situ Pt plating avoiding these interfacial layers. The drawbacks of this technique are the rather isotropic etching and, as well as for the wet chemical process, the poor control of the etched depth. Nevertheless, the anodic oxidation process has become the standard technique for the fabrication of $GaAs$ Schottky diodes for submm applications.

The anodic pulse etching technique avoids the above stated problems [10, 11]. The principle of this technique is outlined below. The $GaAs$ surface is brought into contact with a Pt electrolyte. The electrolyte/$GaAs$ junction which behaves like a Schottky junction is driven into an Avalanche breakdown by the application of short voltage pulses. During the impact ionization in the space charge region electron–hole pairs are generated. The holes drift to the electrolyte/$GaAs$ interface where they are essential for the anodic dissolution of $GaAs$. The short pulse width of 300 ns therefore enables an excellent control of the removed $GaAs$ thickness by the number of applied voltage pulses. The short pulses are also essential for the anisotropic etching since saturation effects due to diffusion limited transport of reaction species are avoided. Since the solution for the anodic pulse etching is the same which is used for the electrolytic Pt deposition, the in–situ metallization is possible. The most important aspects of this technique are summarized below.

1. anisotropic etching ⇒ suitable for fabrication of submicron structures
2. excellent control and reproducibility ⇒ suitable for process–oriented modelling
3. in–situ metallization ⇒ suitable for fabrication of near–ideal Schottky contacts because surface damage and interfacial layers are avoided

By application of the anodic pulse etching technique, 100 nm of epitaxial $GaAs$ have been removed, followed by the in–situ Pt deposition of 150 nm and a final electrolytic 150 nm thick Au deposition. After the formation of the Schottky junctions the samples are cut into single diode chips of $100 \cdot 100\ \mu m^2$.

$I/V-$, $C/V-$ and noise characteristics at 1.5 GHz were recorded by whisker contacting the diode chips soldered to a $BeCu$ whisker post. The whisker consists of a 15 μm $AuNi$ wire with an electrochemically etched tip. The whisker is soldered to another whisker post, which is mechanically advanced to the diode chip by a micromanipulator for contacting.

Experimental Results

Several Schottky diodes having different diameters, doping concentrations and doping profiles have been fabricated. All diodes show very good I/V characteristics in agreement with parameters predicted by the thermionic–field emission for reverse bias and ideality factors close to unity for forward bias. Fig.3 shows the measured and calculated values of the forward I/V characteristic of a Schottky diode with $1\mu m$ diameter and $2 \cdot 10^{17} cm^{-3}$ doping concentration. The higher value of the ideality factor are due to interfacial states and to thermionic–field emission for higher doping concentrations, as it can be inferred

from fig.4 in which ideality factors of several diodes manufactured at the Technical University of Darmstadt and at the University of Virginia are presented as a function of doping concentration.

In fig.5 and 6 diode noise temperatures are presented. The diode examined in fig.5 does not exhibit any trap noise, however due to the low doping concentration, hot electron noise becomes appreciable at a relatively low current density, its characteristic being fairly well described by eq. 8 with negligible trap noise. The opposite situation can be inferred from fig.6. Noise originating from a mechanism described by eq.7 makes a major contribution and again the agreement between the measured and calculated values is excellent.

Noise measurements performed at 3 distinct frequencies give an estimation for the value of τ ($\tau \simeq 0.2ns$) corresponding to very shallow traps at the interface.

Noise characteristics of a diode with a graded doping concentration (fig.7) in the epi–layer exhibits the noise temperature similar to the diodes with moderate doping in the region of the diode operation and lower than that for the $1\mu m$ diode, but the increase of the noise temperature at higher current densities as is the case for highly doped diodes.

The $1\mu m$ diode has already shown excellent results in a $650GHz$ waveguide mixer at room temperature. A noise temperature smaller than $2000K$ and a corresponding conversion loss of $7.5dB$ have been obtained at an intermediate frequency of $4GHz$ [16]. These results are comparable to others obtained with smaller diodes. It is expected that the lower noise temperature in the operating current region of the $0.8\mu m$ diode with a graded doping profile in the epi–layer will enable to even improve these results.

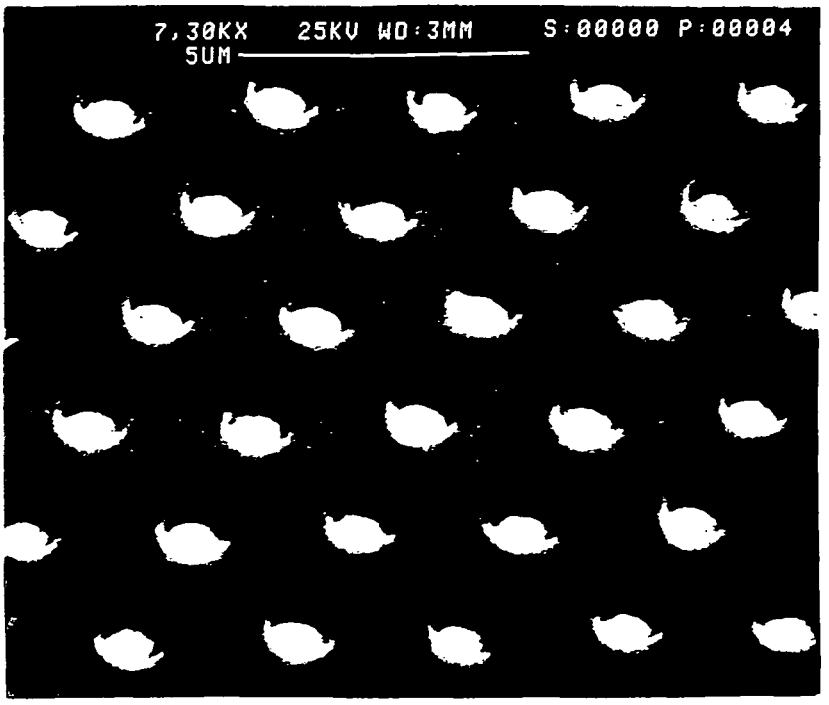

Figure 2: SEM photograph of the fabricated Schottky diode chip with $0.8\mu m$ diodes

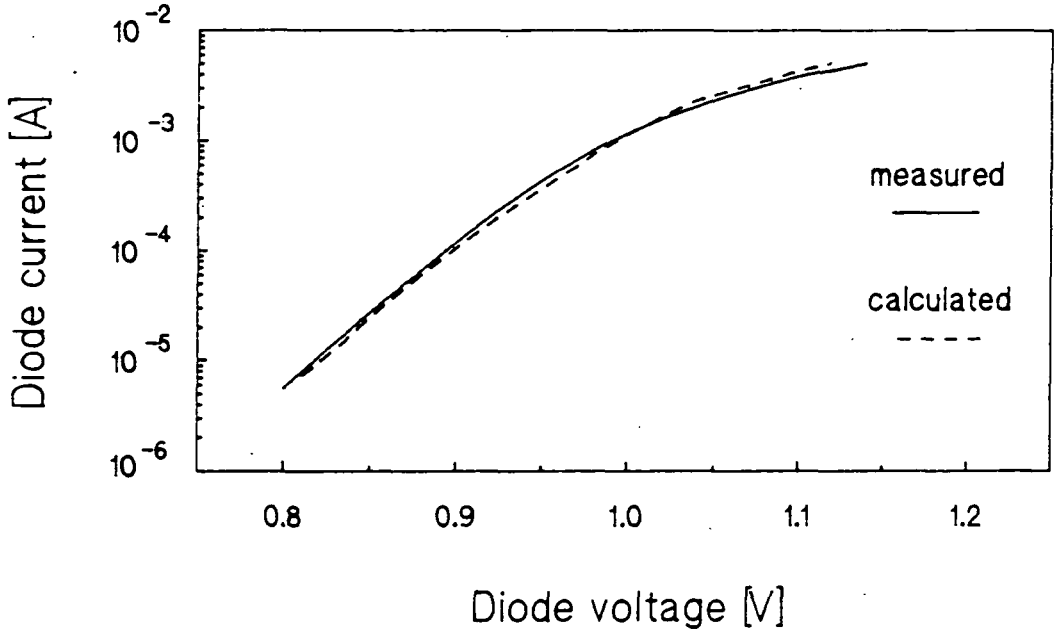

Figure 3: Measured and calculated values of the forward I/V characteristic for a diode with $1.0\mu m$ diode diameter and $2 \cdot 10^{17} cm^{-3}$ doping conctration.

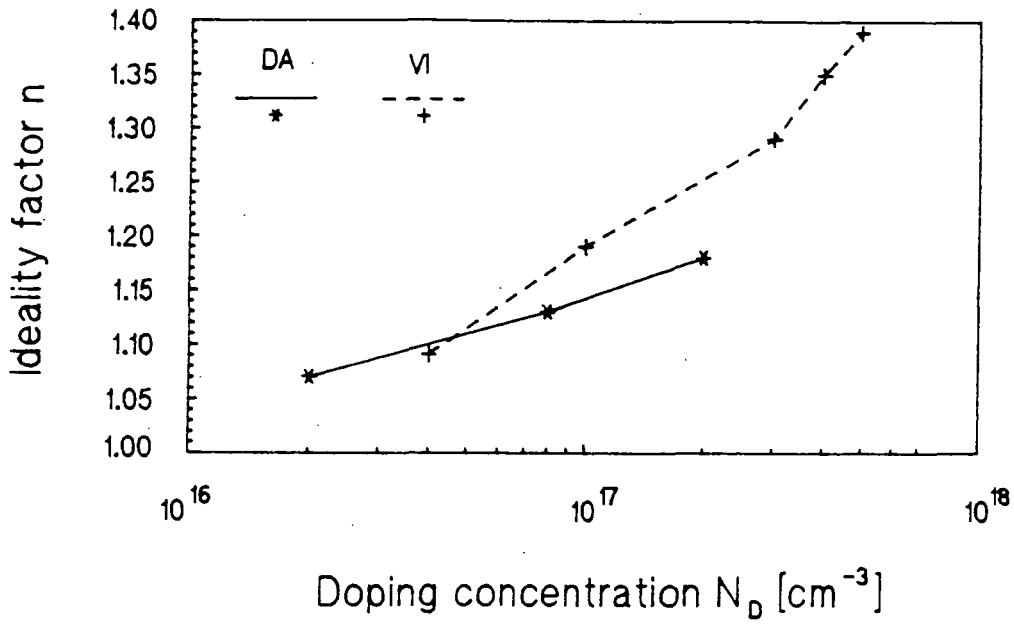

Figure 4: The ideality factor of Schottky-barrier diodes as a function of the doping concentration for diodes fabricated by the Technical University of Darmstadt (DA) and the University of Virginia (VI)

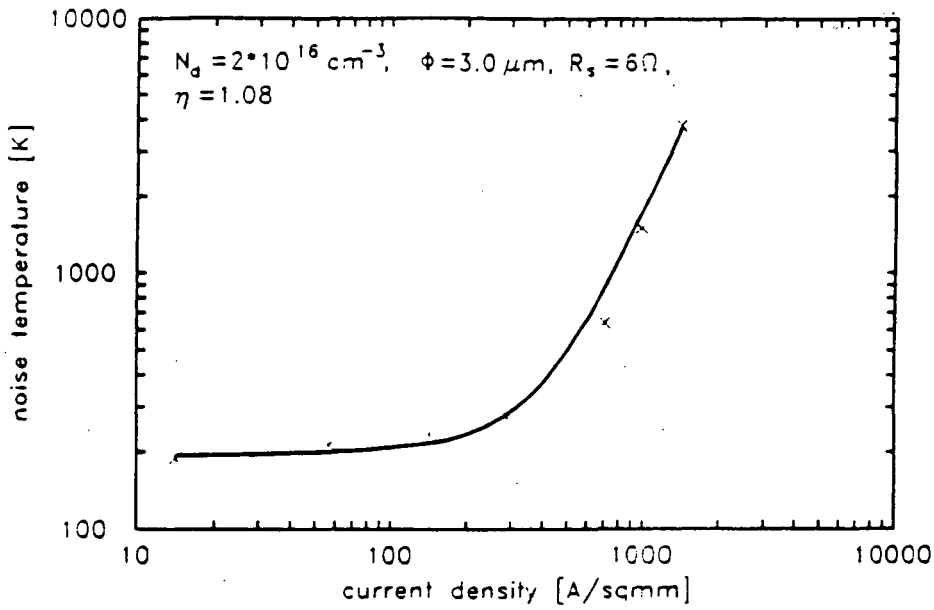

Figure 5: Comparison between measured and calculated (from eq. 8) noise characteristics of a low doped Schottky diode. The crosses indicated the measured data, the solid line stands for $T_n + T_h$ and the dotted line is $T_n + T_h + T_t$.

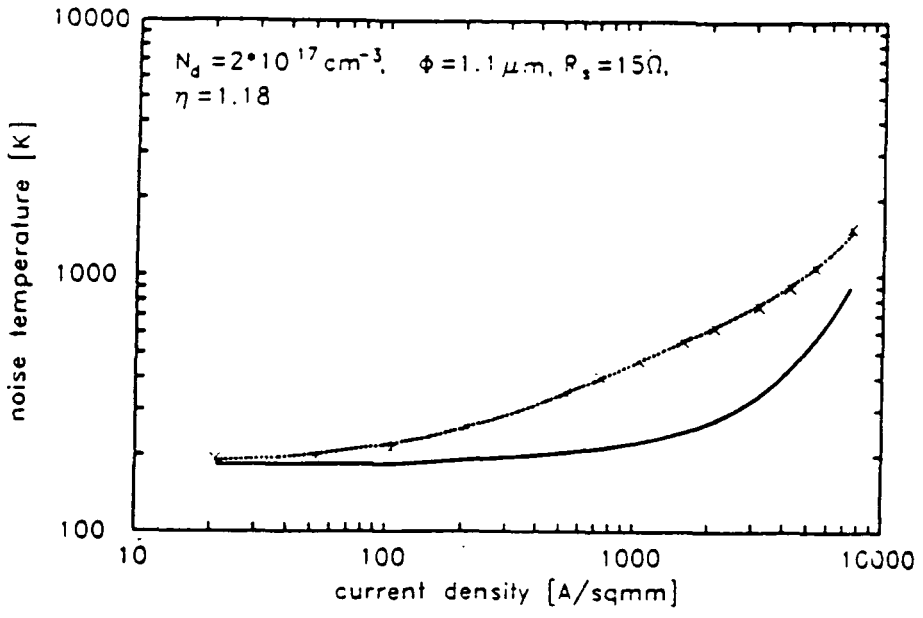

Figure 6: Comparison between measured and calculated (from eq. 8) noise characteristics of a highly doped Schottky diode. The crosses indicated the measured data, the solid line stands for $T_n + T_h$ and the dotted line is $T_n + T_h + T_t$.

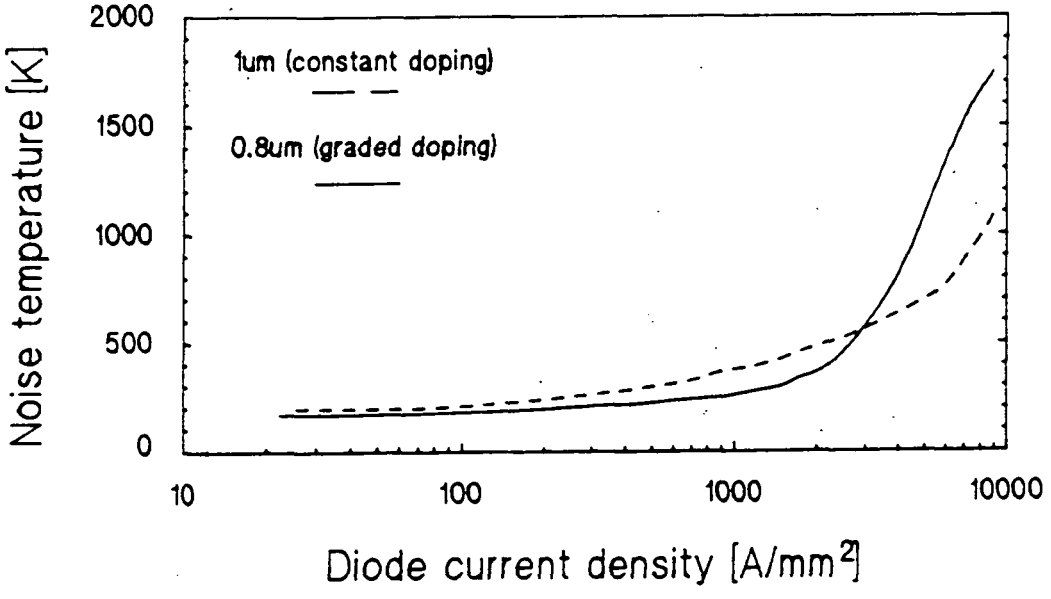

Figure 7: Noise characteristics of a $0.8\mu m$ diode with graded junction in comparison to the $1\mu m$ diode with constant $(2 \cdot 10^{17} cm^{-3})$ doping concentration

References

[1] E. Rhoderick and R. Williams, "Metal-Semiconductor Contacts,". *Monographs in Electrical and Electron. Eng., No. 19*, Oxford Science Publ., 2 ed., (1988).

[2] M. McColl, "Conversion loss limitations in Schottky barrier mixers," *IEEE Trans. Microwave Theory & Techniques*, Vol. MTT-25, (1977), S. 54-59.

[3] T. W. Crowe and R. J. Mattauch, "Conversion loss in GaAs Schottky-barrier mixer diodes," *IEEE Trans. Microwave Theory & Techniques*, Vol. MTT-34, (1986), Nr. 7, S. 753-759.

[4] W. Schottky and E. Spenke, "Zur quanitativen Durchführung der Raumladungs- und Randschichttheorie der Kristallgleichrichter," *Mitt. Zentralabt. Fernmeldetech. Siemens & Halske AG*, Vol. 18, (1939), Nr. 3, S. 225-291.

[5] G. Hegazi, A. Jelenski and S. Yngvesson, "Limitations of microwave and millimeter-wave mixers due to excess noise," in *Proc. of 1985 IEEE MTT-S Int. Microwave Symp. Dig.*, (St. Louis, USA), S. 431-434, (june 4th-6th 1985).

[6] Lawson, "Thereshold Signals," *MIT Rad. Lab. Series*, Vol. 24, (1946), S. 111.

[7] N. Keen and H. Zirath, "Hot-electron noise generation in Gallium Arsenide Schottky -barrier diodes," *Electronics Letters*, Vol. 19, (1983), Nr. 20, S. 853-854.

[8] A. Jelenski, E. Kollberg and H. Zirath, "Broad-band noise mechanisms and noise measurements of metal-semiconductor junctions," *IEEE Trans. Microwave Theory & Techniques*, Vol. MTT-34, (1986), Nr. 11, S. 1193-1201.

[9] M. VanVliet and J. R. Fawcett, "Fluctuations due to electronic transitions and transport in solids,". New York Academic Press, (1965).

[10] A. Grüb, K. Fricke and H. Hartnagel, "Highly controllable etching of epitaxial *GaAs* layers by the pulse etching method," *J. of Electrochemical Society*, Vol. 138, (1991), Nr. 3, S. 856-857.

[11] A. Grüb, R. Richter and H. Hartnagel, "Electrolytic processes for etching and metal deposition towards nanometre quantum structures," *Electronics Letters*, Vol. 27, (1991), Nr. 4, S. 306-307.

[12] H. Grothe and J. Freyer, "*Ga(Al)As* Molekularstrahlepitaxie für Submikronbauelemente," in *Proc. of MIOP 87*, (Wiesbaden, Germany), S. 6B/5, (1987).

[13] P. Verlangieri and M. Schneider, "Microfabrication of *GaAs* Schottky diodes for multipliers, mixers, and modulators," *Int. J. of Infrared and Millimeter Waves*, Vol. 6, (1985), Nr. 12, S. 1191–1201.

[14] W. Peatman and T. Crowe, "Design and fabrication of $0.5\mu m$ *GaAs* Schottky barrier diodes for low–noise Terahertz receiver applications," *Int. J. Infrared and Millimeter Waves*, Vol. 11, (1990), Nr. 3, S. 355–365.

[15] M. Schneider and R. Linke, "Low–noise millimeter-wave mixer diodes prepared by molecular beam epitaxy (MBE)," *Applied Physics Letters*, Vol. 31, (1977), Nr. 3, S. 219–221.

[16] N. Keen, A. Grüb, H. Hartnagel, J. Freyer, H. Grothe and R. Zimmermann, "New submillimeter–wave Schottky–barrier mixer diodes: First results," in *Proc. of* 16^{th} *Int. Conference on Infrared & Millimeter–Waves*, (Lausanne, Schweiz), (1991).

Electrical and Infrared Properties of Thin Niobium Microbolometers near T_c

E.N. Grossman, J.E. Sauvageau, and D.G. McDonald

Electromagnetic Technology Division
National Institute of Standards and Technology
Boulder, CO

Abstract

Niobium microbolometers approximately 1 μm wide × 2 μm long × 10 nm thick have been integrated at the feeds of equiangular spiral antennas made of 200 nm thick Nb. The device's current-voltage characteristic and infrared responsivity as a function of DC bias voltage were measured over a range of temperature spanning approximately ± 2 % around T_c. The greatest voltage responsivity occurs well below T_c, in a regime where the I-V curve is significantly hysteretic due to self-heating and resembles the I-V curve of a superconducting microbridge.

The idea of constructing sensitive terahertz-frequency bolometers by combining the principle of antenna-coupling with that of superconducting transition-edge thermometry has recently received much attention[1,2]. The idea is to use a lithographic antenna to concentrate the infrared power into an area much smaller than a square wavelength. At the feed of the antenna are integrated both an absorbing load (simply a film that is conjugately matched to the antenna impedance at the IR frequency), and a superconducting transition-edge thermometer, used to monitor the changes in the absorber's temperature as varying IR powers are applied to it. The absorber and the thermometer can physically be the same thin-film device, since at IR frequencies, well above the superconductor's gap frequency, its impedance is just that of the normal metal. The device is temperature-biased at the midpoint of the thermometer's resistive transition. A small bias current is applied to it and its resistance changes monitored by measuring the voltage developed across it. Previous analyses of these devices have electrically modelled the thermometer in a very simple way, namely as a lumped (i.e. spatially homogeneous) temperature-dependent ohmic resistance. That is, it has been assumed that near T_c the temperature and current dependent voltage may be separated as $V(I,T) = IR(T)$. This method of analysis naturally grew out of earlier, quite successful, work[3] on large area, surface-absorbing bolometers. However, there is some reason to expect that very small bolometers may behave differently from large ones. In particular, as the superconducting transition

temperature is approached from below, $(1 - t \rightarrow 0$, where $t = T/T_c)$, both the London penetration depth and the Ginzburg-Landau coherence length diverge, as $(1-t)^{-1/2}$. At quite realistic values of $(1-t)$, one or both length scales may become comparable to or larger than the lateral dimensions of a small bolometer at the feed of a lithographic microantenna. This can create qualitatively new physical effects. For example, if the bolometer is comparable in width to the penetration depth, flux flow conduction is strongly affected because the current distribution due to a single magnetic vortex is highly perturbed by the bolometer edges. If the the bolometer is comparable in size to the coherence length, a weak link, or localized region of depressed superconductivity, is created. Such finite-size effects have been recognized for a long time[4] as important to the the electrical properties of small microbridges near T_c.

Another method of creating a superconducting microbolometer is to monitor the temperature-induced change in the thermometer's inductance[5,6]. The inductance change is due to the variation in the pentration depth with temperature discussed above, and is not confined to a very narrow range of temperature near T_c. Such an inductive thermometer can be formed from exactly the same physical device as the resistive thermometer, namely a thin superconducting film patterned so as to contact and span the two antenna terminals. Aside from not requiring such precise temperature control as a transition-edge bolometer, operating well below T_c with an inductive thermometer allows the existence of a large population of unbroken Cooper pairs, which provides a separate, non-thermal mechanism for far-infrared detection, namely direct pair-breaking. Previous work[7] has indicated that this mechanism can be much faster than bolometric detection, at least in hard superconductors, such as niobium. Our research on such photoinductive detectors relies on the use of an integrated DC SQUID (superconducting quantum interference device) to convert changes in the device's inductance to measurable voltage changes. Unfortunately, we have not yet succeeded in reliably fabricating a DC SQUID integrated with a photoinductive film and a lithographic antenna. We have therefore investigated some of the properties of the thin detectors near T_c, where the resistive mode of operation obviates the need for a SQUID.

The devices consist of pure niobium films 10 nm thick, patterned by conventional optical lithography into bolometers nominally 1 μm wide by 2 μm long. The bolometer lies at the feed of a self-complementary spiral antenna with a 65° opening angle, formed from 200 nm thick niobium. (See figure 1.) Reliable, low resistance electrical contact between the antenna feed and the thin bolometer is accomplished by DC magnetron sputtering the two films successively, with an Al etch-stop layer between them, in a single deposition run, without breaking vacuum. The antenna, etch-stop layer, and bolometer are then patterned by a sequence of plasma and wet etches. At low

temperatures, the thin (10 nm) Al etch stop layer is rendered superconducting by the proximity effect from the much thicker Nb antenna lying on top of it, and can therefore be neglected electrically. The DC normal-state resistance of the bolometers is approximately 20 Ω. At frequencies well above the Nb energy gap frequency $2\Delta/h \approx 700$ GHz, but well below the normal electron relaxation frequency $v_F/l_e = 48$ THz[8], the impedance of the bolometer, both above and below T_c, should approximate the DC normal-state resistance. (v_F is the Fermi velocity and l_e the electronic mean free path.) This implies a loss of about 1.8 dB due to impedance mismatch with the antenna, if the antenna impedance can be approximated by the quasi-static value of about 75 Ω appropriate to a self-complementary design on a silicon substrate.

Figure 1. Photograph of the antenna-coupled microbolometer

The diced chips, 1 cm square, were placed circuit-side up against a Si hemisphere, and the infrared radiation coupled in through the hemisphere and substrate, in the conventional "reverse microscope" configuration[9]. Mechanical pressure was applied from the circuit side to hold the chip in place against the hemisphere and to maintain an optical quality contact between the polished Si surfaces of the substrate and hemisphere. The very wide antenna beam[10] was refocussed by an off-axis elliptical mirror operating at an angular magnification of 6.3 to a point inside the cryostat where a cold field stop was placed to reduce to a manageable level the total background power incident on the chip (i.e. the power in spatial modes other than the one coupled to the antenna).

This is necessary because the hemisphere/chip assembly is mounted on a thermal platform whose thermal resistance to the heat bath is fairly high in order to allow convenient temperature regulation and control. Any substantial optical background power would therefore raise the platform's (and chip's) temperature excessively. The refocussed beam from the elliptical mirror is then collimated by a cold lens before emerging through the cryostat window. (See figure 2.) The material of the collimating lens may be chosen to define a broad spectral bandpass and optical power level that is desired. In the optical measurements described here, a ZnSe lens was used to define a broad, short wavelength ($\lambda < 20$ μm) bandpass. The optical input was mechanically chopped between simple blackbody sources at 300 K and 77 K. Using handbook values[11] for the transmission of Si and ZnSe, the power coupled into the single spatial mode of the antenna is calculated from $P = \frac{(kT)^2}{h} \int_0^\infty \frac{xT(x)dx}{e^x - 1}$, where $x = h\nu/kT$ is the dimensionless frequency, h is Planck's constant, k Boltzmann's constant, $T(x)$ the transmittance of the combination of Si and ZnSe lenses, and T the absolute temperature. This yields a power difference $P(300K) - P(77K) = 1.86$ nW. When the reflection losses at the surfaces of the ZnSe and Si lenses and the KRS-5 cryostat window are included, a total incident optical signal power of 0.65 nW is obtained. The power-weighted mean frequency of the optical input is 28 THz (wavelength 11 μm).

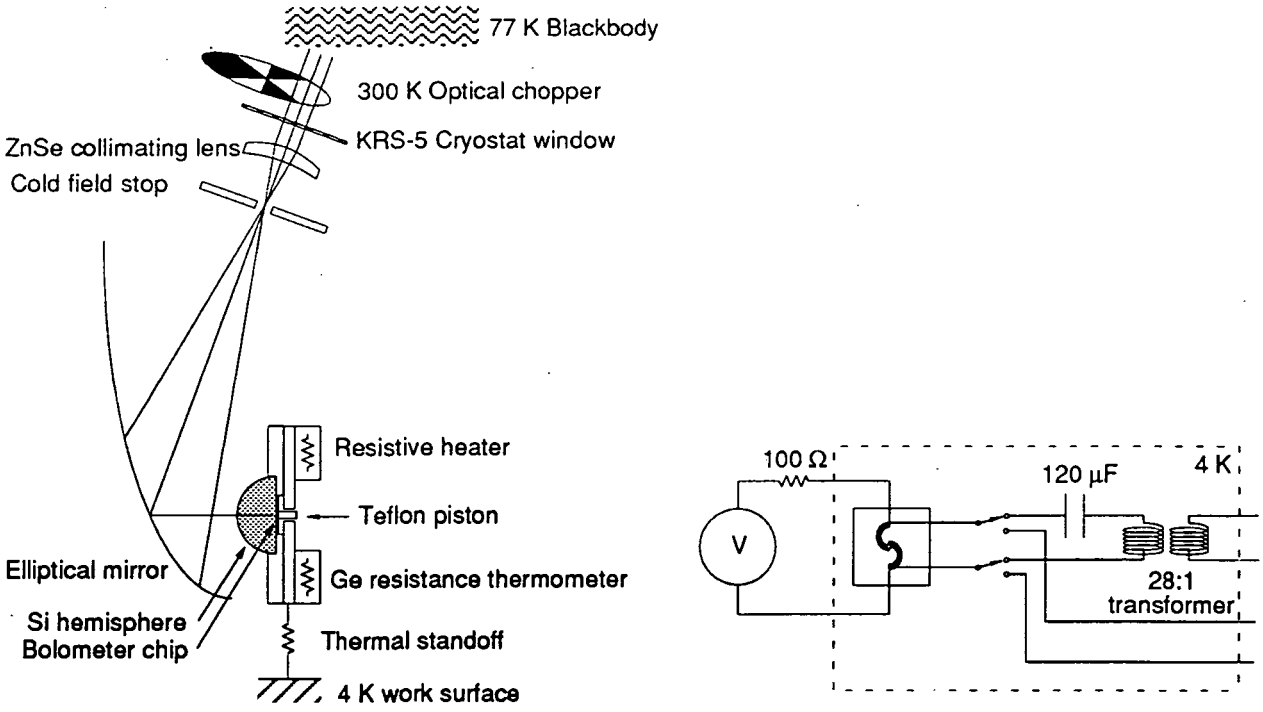

Figure 2. Experimental setup for the infrared responsivity measurements

The device was electrically biased through the antenna arms by a 100 Ω output impedance

source. The voltage was monitored (in a 4-terminal configuration) at the outer periphery of the antenna arms. Since the antenna is formed of much thicker Nb than the bolometer, the critical temperature of the antenna arms is some 0.8 K higher than that of the bolometer. Therefore, over the entire temperature range investigated, the antenna arms formed (at DC and audio frequencies) a superconducting short circuit, and the measured voltage was just that across the bolometer element itself. As shown in figure 2, a cold transformer, separately calibrated at 4 K, could be switched into the circuit to raise the signal voltage level and improve the match to the high impedance room temperature amplifier which followed. To obtain high sensitivity from a small superconducting detector (i.e. one which is not a long meander line), it is essential to provide such an impedance transformation. In many cases, however, we did not use the transformer in order to avoid certain ambiguities in interpretation of the data. For example, it turned out that the bias-dependent dynamic impedance of the device varied over a huge range; at its highest values, the RC rolloff frequency created between the post-transformer device impedance and the filter capacitance on the signal lines became comparable with the optical chopping frequencies (10 - 400 Hz). Obviously, this would cause spurious systematic structure in the curve of optical response versus bias, which was avoided by measuring the voltage before the transformer, where the signal impedance is much lower.

The basic data consist of curves of demodulated optical signal voltage and DC current versus DC bias voltage, obtained at various temperatures above and below the superconducting transition. (Since the dynamic impedance of the device is frequently comparable to the 100 Ω bias source impedance, the choice between DC voltage and current as the independent variable is more or less arbitrary.) The set of data with the most complete temperature coverage is shown in figure 3. It was taken with the cold transformer switched out of the circuit. As the DC voltage was slowly swept, the DC current and demodulated optical signal were recorded simultaneously. During all the measurements, the temperature of the platform was monitored with a Ge resistance thermometer and actively stabilized, with a precision of about 0.2 mK, by a commercial temperature controller driving a simple resistive heater. The critical temperature of the bolometer as defined by the onset of a supercurrent (i.e. vanishing zero-voltage resistance) was 7.978 $\pm$ .006 K. The critical temperature as defined by a zero-voltage resistance that is half the normal state resistance was 7.992 $\pm$ .010 K. The data cover a range in reduced temperature from about 2.4 % below to +2.2 % above the critical temperature, a much wider range than envisaged for "transition-edge" bolometers in the previous analyses[1,2].

The most obvious feature of the data is the huge increase in infrared responsivity at low voltage

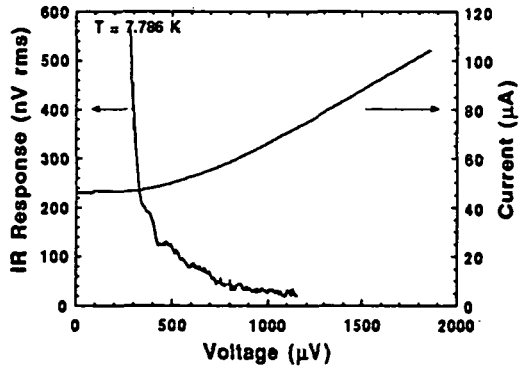
T = 7.786 K
IR Response (nV rms)
Current (μA)
Voltage (μV)

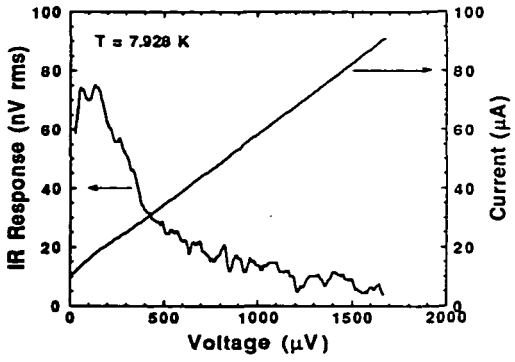
T = 7.928 K
IR Response (nV rms)
Current (μA)
Voltage (μV)

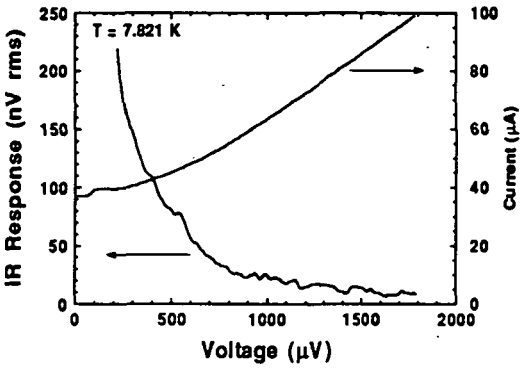
T = 7.821 K
IR Response (nV rms)
Current (μA)
Voltage (μV)

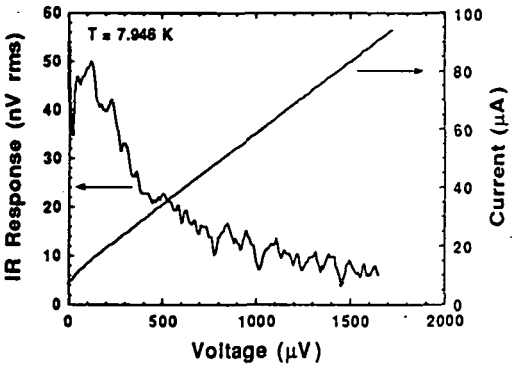
T = 7.948 K
IR Response (nV rms)
Current (μA)
Voltage (μV)

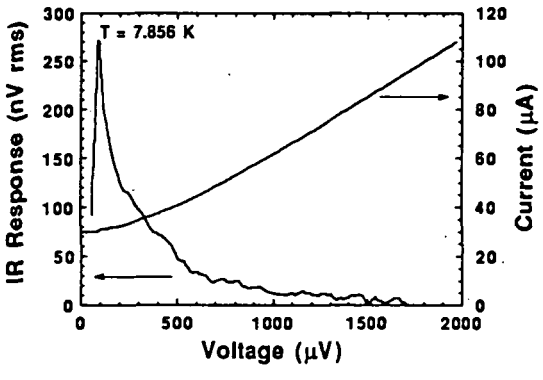
T = 7.856 K
IR Response (nV rms)
Current (μA)
Voltage (μV)

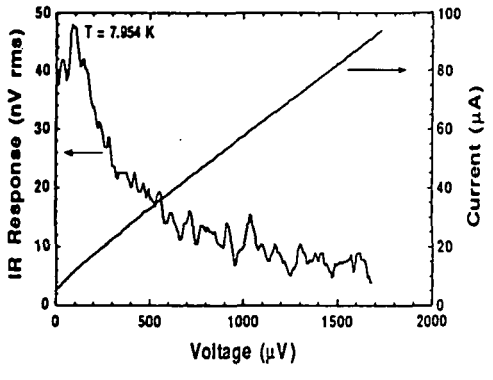
T = 7.954 K
IR Response (nV rms)
Current (μA)
Voltage (μV)

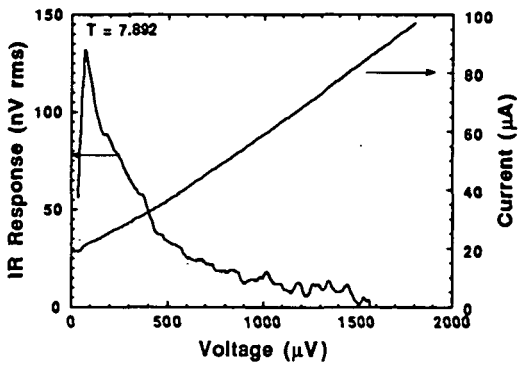
T = 7.892
IR Response (nV rms)
Current (μA)
Voltage (μV)

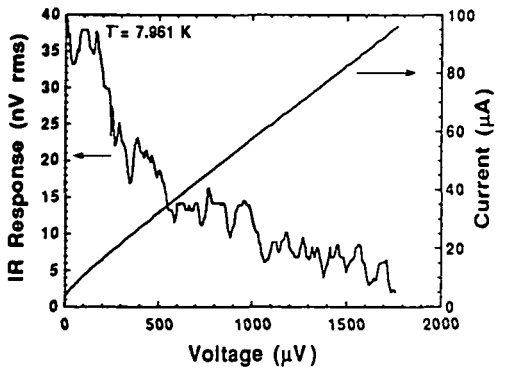
T = 7.961 K
IR Response (nV rms)
Current (μA)
Voltage (μV)

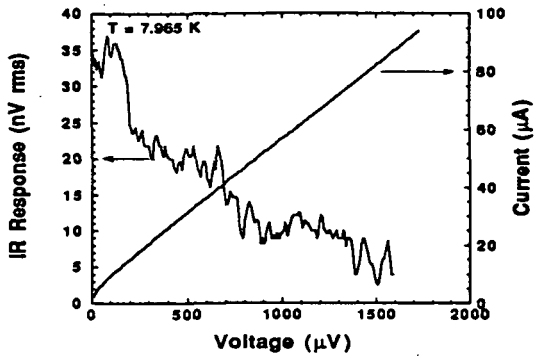
T = 7.965 K
IR Response (nV rms)
Current (μA)
Voltage (μV)

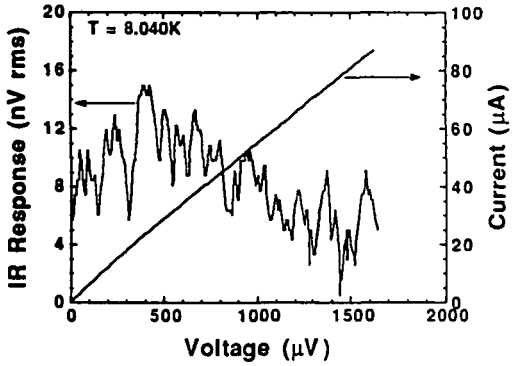
T = 8.040K
IR Response (nV rms)
Current (μA)
Voltage (μV)

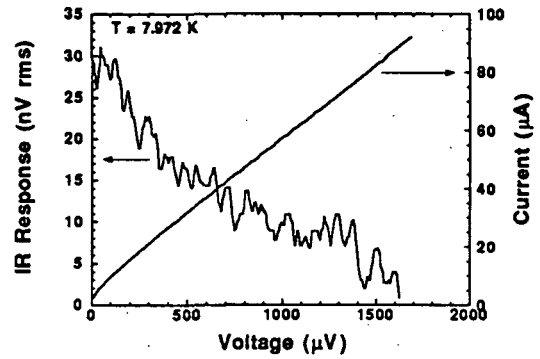
T = 7.972 K
IR Response (nV rms)
Current (μA)
Voltage (μV)

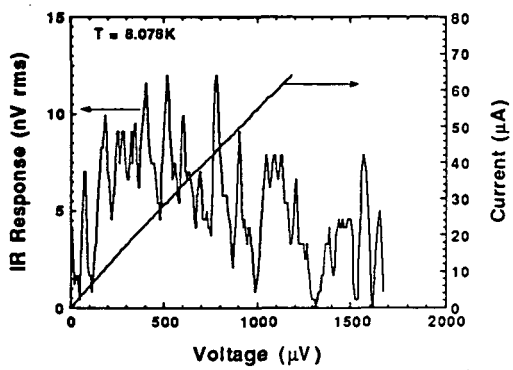
T = 8.078K
IR Response (nV rms)
Current (μA)
Voltage (μV)

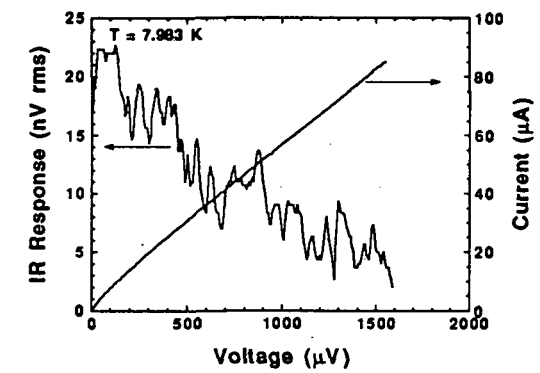
T = 7.983 K
IR Response (nV rms)
Current (μA)
Voltage (μV)

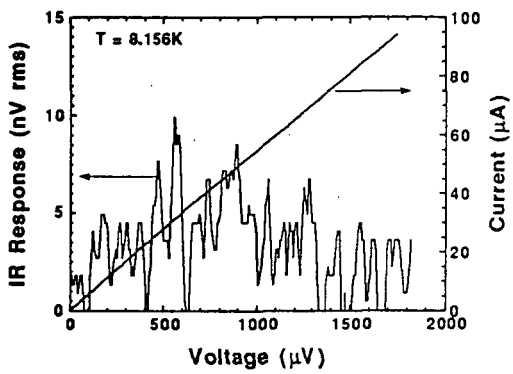
T = 8.156K
IR Response (nV rms)
Current (μA)
Voltage (μV)

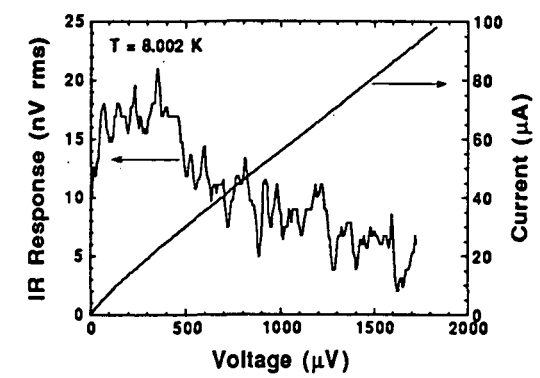
T = 8.002 K
IR Response (nV rms)
Current (μA)
Voltage (μV)

and low temperature. (Note the changes in scale of the IR response from graph to graph in figure 3.) This is partly due to the fact that, with a 100 Ω load line (nearly a current source on the scale of the figure) and voltage detection, the largest infrared signals will be obtained where the device's dynamic impedance is the greatest. Thus, for the graphs at $T \leq 7.856\ K$, the large increase in infrared responsivity corresponds with a large increase in dV/dI at $V \leq 1000\ \mu$V. Indeed, at these low temperatures, both the dynamic impedance and the IR responsivity apparently diverge as the bias approaches the point of instantaneous "dropback" to the zero-voltage branch. As this point is approached, it becomes increasingly difficult to bias the device stably. In these measurements, bias stability appears to be the practical limitation on increasing the responsivity by this means. At temperatures T ≤ 7.892 K, the I-V curve is hysteretic, undoubtedly due to ohmic self-heating (see below). Only the descending branch is plotted in fig. 3. For T = 7.892 K and 7.856 K, the hysteresis loop encloses only the small horizontal "step" visible at $V \leq 100\mu$V in the I-V curve, while at lower temperatures, the difference between the critical current (on the ascending branch) and the "dropback" current increases.

The data of figure 3 broadly describes the behavior of the IR responsivity over a large area in parameter space, the "big picture", but it does not give a very accurate idea of the responsivity in the region of optimum device performance. Other data we have taken exhibit much higher responsivities than those of figure 3; values as high as 4.8×10^4 V/W after the transformer and 7800 V/W before the transformer have been measured. Even these figures do not really reflect the device's capabilities, however, since the test conditions were not optimum for the unexpectedly high device impedances in this operating range. Firstly, the capacitance values for the cold blocking capacitor and the cryostat feedthru capacitors turned out to be inappropriate for attaining the full advantage of the transformer, and secondly, the operating temperature was not varied over a fine enough grid to find the optimum operating point of the bare bolometer. Nonetheless, these responsivity figures in themselves demonstrate technologically interesting levels of sensitivity for the bolometer.

The device's dynamic impedance cannot provide the entire explanation for the observed dependence of IR responsivity on bias visible in figure 3. This is clear from the data at $T \geq 7.928\ K$, where the dynamic impedance increases at *higher* bias voltages, yet the strong increase in IR responsivity at low voltage persists. An effect which certainly must be important in understanding this data is local ohmic heating. This creates temperature gradients on the chip, in the immediate vicinity of the bolometer, which of course are not probed or regulated by the Ge thermometer and temperature control unit mounted on the thermal platform. At the biases typical in figure 3, this is

the dominant effect, since the ohmic heating powers are in the range of tens of nW, which translates into hundreds of mK temperature rise, for typical thermal conductances of 1-5 $\times 10^{-7}$ W/K[12].

In the previous treatments of superconducting microbolometer performance[1,2], ohmic heating is incorporated by assuming the bolometer itself remains isothermal, (i.e. by ignoring any spatial temperature gradients across the bolometer) and by imposing a condition on the DC bias, that $\frac{dR}{dT}\frac{I_{bias}^2}{G} < 1$, where G is the thermal conductance of the bolometer to the heat bath. As long as this condition for avoiding thermal runaway is met, the device is treated as ohmic, with a temperature dependent resistance, implying that $dV/dT = V\frac{d(ln(R))}{dT}$ and the infrared responsivity should be linearly proportional to DC voltage. The regime in which this treatment is valid covers a small region near the origin of the graphs for $T \geq 7.98$ K.

For the regime at lower temperature, where the measured infrared responsivity is higher, an apparently more appropriate treatment is that developed by Skocpol, Beasley, and Tinkham[13,14] to describe self-heating effects and phase-slip centers in microbridges (see figure 7 in ref. 13 for example). This model explicitly includes spatial temperature gradients. In fact, it assumes that in general, part of the bridge can be normal and part superconducting. The voltage across the bridge at any particular substrate temperature and bias current is determined by the length of the region where $T > T_c$, which is in turn determined by a self-consistent balance between the ohmic heat generated in that region and the power conducted away from it, which depends on the geometry. Well below T_c, there is strong non-linearity in the I-V curve above the critical current due to the rapidly changing size of the normal region of the bridge. Presumably, the large infrared response we see in our devices well below T_c is due to the IR power, dissipated approximately uniformly across the bolometer's surface area, changing the thermal balance in such way as to move the boundary between the bolometer's normal and superconducting regions. Very small changes in IR power apparently move this boundary very far. In some sense, the ohmic heating due to the bias current adds some positive feedback to the process of driving the bridge normal with infrared heating.

Unfortunately, the theoretical results described in reference 13 cannot be directly applied to our devices because of a difference in length scales. The microbridges discussed there, which were fabricated mechanically rather than lithographically, were in general substantially larger than our devices. On the other hand, the characteristic length scale which figures into their model is the quasiparticle diffusion length. The devices in that study were formed of tin, a soft superconductor with a much larger diffusion length than niobium. Therefore, it is very likely on theoretical grounds that our devices can in fact be treated by that model, appropriately rescaled. More specific statements, however, including any theoretical estimate of the optimal infrared responsivity available

from this mechanism, must await the results of quantitative modeling.

In conclusion, we have measured the infrared responsivity of antenna-coupled, superconducting microbolometers as a function of DC bias and temperature, over a wider range than has been envisaged in previous theoretical treatments. We find the highest responsivity occurs in a regime well below T_c, where the effects of ohmic heating due to the bias current are of dominant importance. A model developed to describe self-heating and phase slip centers in tin microbridges may provide the most appropriate framework for analyzing the device's infrared response and electrical properties in this regime.

We are grateful to Ron Ono for bringing the microbridge self-heating model to our attention. This work was supported by the Innovative Science and Technology Agency of SDIO, and by NASA, through the Office of Space Science and Applications.

References

1. J. Mees, M. Nahum, and P.L. Richards, *Appl. Phys. Lett.*, **59**, p. 2329 (1991)

2. M. Nahum and P.L. Richards, *IEEE Trans. Magn.*, **MAG-27**, p. 2484 (1991)

3. J. Clarke, G.I. Hoffer, P.L. Richards, and N.H. Yeh, *J. Appl. Phys.*, **48**, p.4865 (1978)

4. R.D. Parks, J.M. Mochel, and L.V. Surgent, *Phys. Rev. Lett.*, **13**, p. 331a (1964)

5. D.G. McDonald, *Appl. Phys. Lett.*, **50**, p. 775 (1987)

6. E.N. Grossman, D.G. McDonald, and J.E. Sauvageau, *IEEE Trans. Magn.*, **27**, p. 2677 (1991)

7. M. Johnson, *Phys. Rev. Lett.*, **67**, p.374 (1991)

8. The electron relaxation frequency is obtained from the free-electron expression $\omega_\tau^2 = \frac{3\pi^2\hbar^3\sigma_0}{e^2m^2l_e^3}$, using a DC conductivity $\sigma_0(10\,K) = 1.58 \times 10^7\ \mathrm{m}^{-1}\Omega^{-1}$, W.H. Henkels and C.J. Kircher, *IEEE Trans. Magn.*, **MAG-13**, p. 63 (1977), and an electron mean free path $l_e = 6.3$ nm, S. Wolf, J.J Kennedy, and M. Nisenoff, *J. Vac. Sci. and Tech.*, **13**, p. 145 (1975)

9. D.B. Rutledge, D.P. Neikirk, and D. Kasilingham, chap. 1 in *Infrared and Millimeter Waves*, vol. 10, Academic Press, New York, (1983)

10. E.N. Grossman, J.E. Sauvageau, and D.G. McDonald, *Appl. Phys. Lett.*, **59**, p. 3225 (1991)

11. E.D. Palik (ed.) *Handbook of Optical Constants of Solids*, Academic Press, Orlando (1985), and
E.D. Palik (ed.) *Handbook of Optical Constants of Solids II*, Academic Press, San Diego (1991)

12. E.N. Grossman, D.G. McDonald, and J.E. Sauvageau, *Proceedings of the Second International Symposium on Space Terahertz Technology*, p. 407, JPL, Pasadena, CA (1991)

13. W.J. Skocpol, M.R. Beasley, and M. Tinkham, *J. Appl. Phys.*, **45**, p.4054 (1974)

14. W.J. Skocpol, M.R. Beasley, and M. Tinkham, *J. Low Temp. Phys.*, **16**, p. 145 (1974)

MEASUREMENTS OF THE SINGLE SIDEBAND SUPPRESSION FOR A 650 GHZ HETERODYNE RECEIVER

S. Crewell & H. Nett

Institute of Remote Sensing
University of Bremen, FB 1
P.O. Box 330440
D-2800 Bremen 33, FRG

ABSTRACT

A large number of atmospheric trace gases, involved in the process of stratospheric ozone depletion, show emission features in the submillimeter wavelength range (λ=0.1-1mm). High-resolution heterodyne techniques are a particularly useful tool in this spectral region as vertical distribution of these species can be deduced. Here the receiver has to be operated in the single sideband (ssb) mode preferably to avoid any interferences between the contributions in both receiver sidebands. In the 625-655 GHz heterodyne receiver developed at the University of Bremen a Martin-Puplett interferometer is used as a ssb-filter. A laboratory set-up has been built up to measure the performance of this interferometer.

INTRODUCTION

Since the detection of stratospheric ozone depletion research activities have been focused on the study of upper atmospheric chemistry. In the catalytic reactions destroying the ozone the chlorine monoxide molecule is a key substance. Its influence in the chlorine and the nitrogen cycle leading to the "Antarctic ozone hole" is described in [1]. ClO and also many other chemically important molecules, for example HCl, N_2O, OClO, BrO.. , have emission lines in the submillimeter region [2].

To detect the weak thermal emission of these molecules low-noise heterodyne receivers can be used. They provide the possibility to observe the line shape of the molecules with a high spectral resolution allowing to derive the vertical VMR (volume-mixing-ratio) profiles from the pressure broadening of the line.

Due to the strong water vapor absorption in the troposphere submillimeter measurements of atmospheric trace gases have to be performed from high flying aircraft.

A 625-655 GHz heterodyne receiver for airborne operation, **SUMAS** (**Sub**millimeter **A**tmospheric **S**ounder), has been developed at the University of Bremen in order to measure ClO, HCl, O_3, N_2O.... which all have transitions in this narrow frequency range.

Atmospheric measurements have been performed successfully on the research aircraft Falcon. The receiver has been further improved in a second project, **SMS**, with international participation funded by the ESA/ESTEC (*). The goal of this project was to develop spaceborne techniques for a submillimeter limb sounder and built up a demonstration model for airborne operation.

For atmospheric measurements it is desirable to operate the receiver in a ssb mode because emission lines, quite numerous in this frequency range, in the image band may interfere with the lines in the signal band. Due to the high ratio of radio frequency (r.f.) to intermediate frequency (i.f.) an external ssb-filter is preferable. In both radiometers a quasi-optical Martin-Puplett interferometer is used and the performance of this has to be verified over the bandwidth of interest.

In the following chapter the ssb transmission measurements for the HCl-frequency using the **SUMAS** radiometer will be discussed as an example .

Receiver Design

The **SUMAS** radiometer as illustrated in *Fig.1* consists of a quasi-optical section (r.f.) and a two-stage i.f. secton. In the r.f. part all elements are realized with a quasi-optical design.

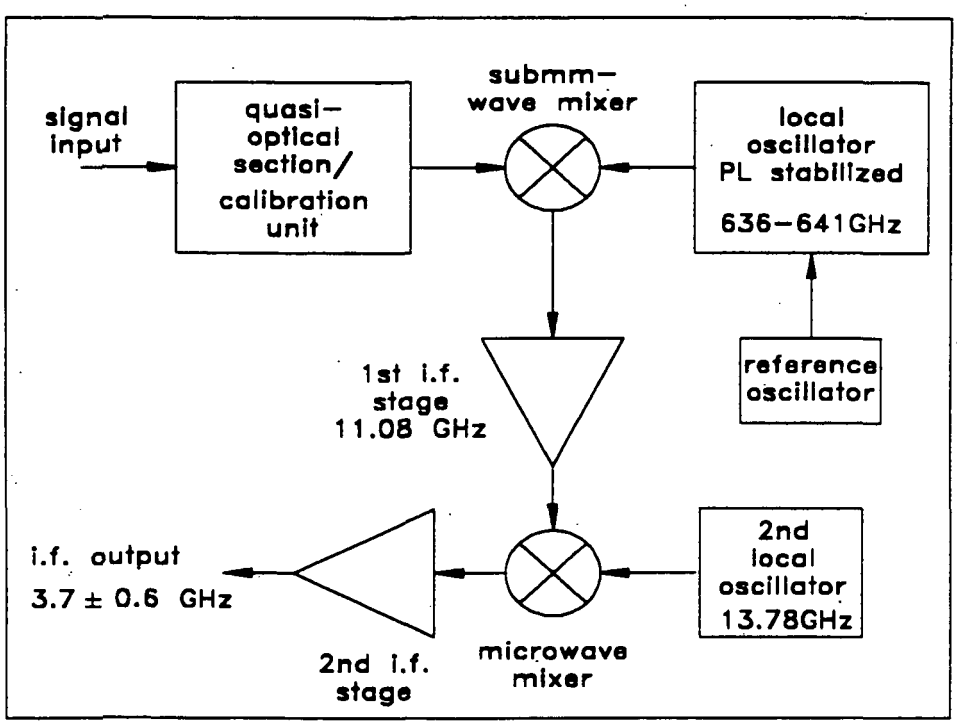

Fig.1 : Block diagramm of the SUMAS radiometer

(*) Estec Contract 8742/90/NL/PB "Limb Sounder Critical Technologies" This contract involves several industrial companies (MBB-GmbH-Deutsche Aerospace,Germany; Radiometer Physics, Germany) and several scientific institutes (University of Bern,Switzerland; , University of Bremen, Germany; Chalmers University, Sweden; University of Florence, Italy; Space Research organisation, The Netherlands).

Total power calibration is performed; a phase wobbler is used to avoid standing waves; two cascaded Martin-Puplett interferometer serve for ssb-filtering and for diplexing of the local oscillator (L.O.) and signal radiation, respectively. The L.O. is tunable between 636-641 GHz and is phase-locked to a highly stable reference. The quasi-optical Schottky diode mixer operating at room temperature has a 3 λ whisker forming an approximately gaussian beam. In the 1st i.f. section at 11.08 GHz a low-noise **HEMT** cooled by liquid nitrogen acts as a preamplifier. After additional amplifing the signal is down converted by a microwave mixer to the second i.f. stage centered at 3.7 GHz. Here a post-amplifier and filter are used to provide an i.f. output with a power level of 0-5 dbm and a bandwidth of 1.2 GHz. A detailed description of the radiometer can be found in [3] and [4].

Single Sideband Filter

For a quasi-optical ssb-filter two main principles, dual-beam and multi-beam interferometer, exist. The Mach-Zehnder, an amplitude dividing interferometer, and the Martin-Puplett interferometer, a polarisation rotating device, are examples for a two-beam interferometer while the Fabry-Perot is the most common multi-beam interferometer (for additional informations see [5]). The Martin-Puplett interferometer was found well suited to meet our frequency requirements since it is easy to tune and to adjust. It consists basically of two rooftop mirrors and a 45° grid. In our radiometer design an aditionally first grid (90°) serves to define the vertical polarisation for our interferometer input and later to direct the unwanted sideband to an absorbing load. An incoming vertical polarized signal is splitted by the 45° grid in two beams with orthogonal polarisations, 45° and 135° respectively. Then the beams are reflected at the rooftop mirrors in a way that the polarisation rotates by 90°. Now the beam initially reflected by the 45° grid will be transmitted and the other beam vice versa. The superposition of both beams is given by their phase difference and therefore the power transmission is a function of the beams pathlength difference Δ an the wavelength λ :

$$P_{V->V} = 0.5\,(\,1 + \cos(2\pi\Delta/\lambda)) \qquad (1)$$

In order to measure HCl (f_{HCL}=625.912 GHz) the L.O. is adjusted to 636.992 GHz and the upper sideband frequency (f_{usb}=648.072 GHz) should be suppressed. If the interferometer should act as a ssb-filter P in (1) is required to be a maximum for the signal wavelength ($\Delta=m\lambda_{HCL}$) and a minimum for the unwanted sideband ($\Delta=\lambda_{usb}\,(2n+1)/2$). The pathlength difference can easy be tuned by a micrometer screw that translates one rooftop mirror while the other is fixed. Although the relative accuracy of the micrometer is good ($\Delta x=2\mu m$) an absolute calibration has to be performed for each wavelength. For this a signal corresponding to the frequency of interest is generated with the help of the experimental set-up described in the next chapter and coupled to the radiometer input. The

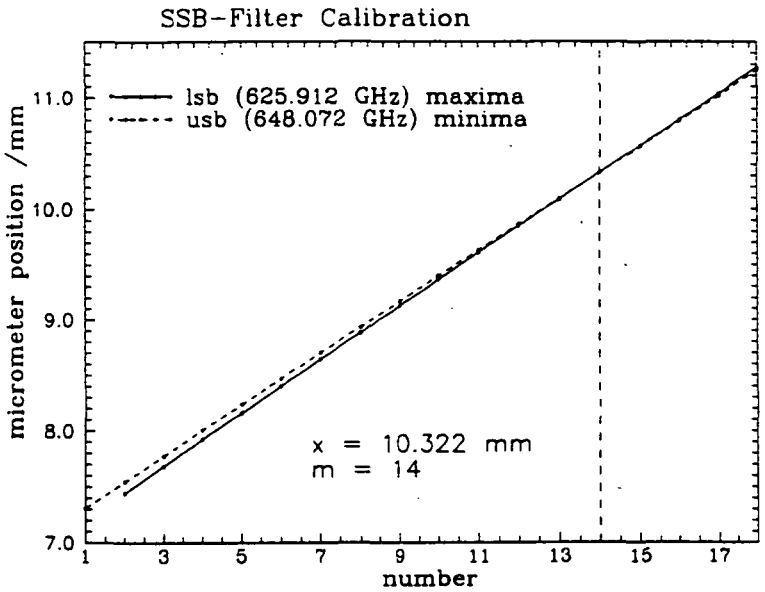

Fig. 2: Calibration curves for the ssb-filter

r.f. signal is detected by the radiometers submillimeter mixer and can be observed at the i.f. output with a spectrum analyzer or a powermeter. With this set-up the micrometer position for maximum and minimum transmission can be determined for each sideband. The results (*Fig.2*) show two straight lines, one for the maxima of f_{HCl} and the other for the minima of f_{usb}. Now the intersection of both curves give $m=14$ and $\Delta=6.706$ mm, the micrometer position for the ssb mode. The theoretical transmission curves given by (1) with this micrometer settings yield a suppression of higher then 20 dB over the whole radiometer bandwidth for the upper sideband and negligible losses for the atmospheric signal (see *Fig.3*).

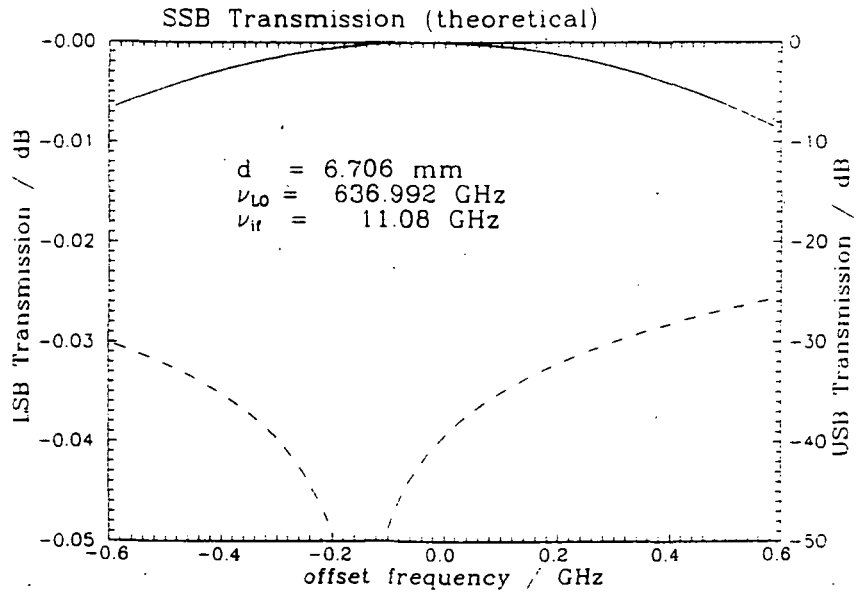

Fig. 3: Theoretical power transmission of the Martin-Puplett interferometer
solid curve : lower sideband (HCl) ; dashed curve : upper sideband

Experimental Setup

The experimental set-up (*Fig. 4*) used to measure the ssb-filter characteristic consists of three parts : a source generating the coherent submillimeter signal, the whole radiometer

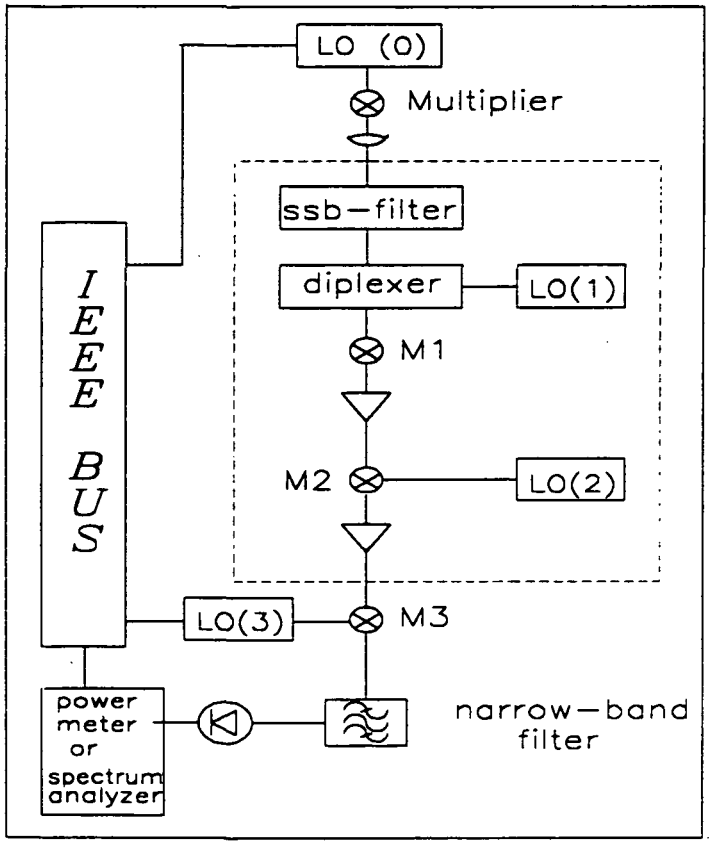

Fig.4 : Experimental set-up for measurements of the ssb-characteristics; dashed lines indicate the radiometer

with the integrated ssb-filter and a microwave output stage where the signal is analysed. A microwave synthesizer(HP 82620) operating in the range 11..13 GHz is used as a local oscillator LO(0). This signal is then multiplied by a quasi-optical schottky diode mixer mounted on a linear translation stage .This allows to move the block orthogonal to the axis of the radiometers antenna main lobe with a resolution of 0.5 μm in x and z direction. Additionally the multiplier signal can be matched to the receiver by a focusing (f=90mm) Teflon lens and it is possible to optimize the lens distance by a further linear translator. A coupling efficiency of more than 75 % can be attained theoretically by this set-up between both beams. In the quasi-optical part of the receiver the beam propagates through the ssb-filter and through the LO(1) diplexer and mixed down by the submillimeter mixer M1 of the radiometer. The signal is converted down to the second i.f. inside the radiometer by a microwave mixer M2 to the receiver output. In the analysing microwave stage a constant i.f. signal of 150 MHz is generated by a further microwave mixer that is driven by another tuneable microwave synthesizer LO(3). After narrowband-filtering the signal can be detected by a spectrum analyzer or a powermeter.

For a defined setting of the ssb-filter the incoupled signal can be tuned to any frequency in the lower or upper sideband including the whole bandwidth via the LO(0) . An experiment computer with a IEEE-bus system controlling the LO(0) provides a simultaneous tuning of the LO(3) that drives the Mixer 3 . The generated signal i.f. signal at 150 MHz is now monitored on a spectrum analyzer and recorded also via IEEE.

Measurement Results

If the generated signal corresponds to the HCl frequency largest power is obtained using the 49th harmonic of the LO(0) signal. Then a dynamic range of about 23 dB can be achieved for the measurements of the single sideband characteristics. The relative transmission curves for both sidebands with a given setting of the ssb-filter are obtained by normalyzing the measurement curves to the data measured for a pathlength difference $\Delta=0$. In addition, the output signal without the generated submillimeter radiation was recorded at the beginning and the end of the measurements in order to eliminate baseline and drift effects of the radiometer. The results shown in *Fig.5*, here with a resolution of 50 MHz, indicate that the lower sideband is not affected by the setting of the ssb-filter corresponding to the theoretical calculations (*Fig.3*) while the upper sideband is suppressed more than 20 dB over the whole bandwidth. This measurement gives a minimum value for the suppression of the unwanted sideband because it is limited by the strength of the generated signal. An improvement of this is expected by a further optimization of the multipliers antenna properties. In order to reduce the noise in the curves (*Fig.5*) a new measurement procedure with a sampling of data points will be applied during future measurements.

To improve the dynamic range a measurement has been performed using the high-resolution chirp Transform Spectrometer (CTS) on loan from the Max-Planck Institute for Aeronomy

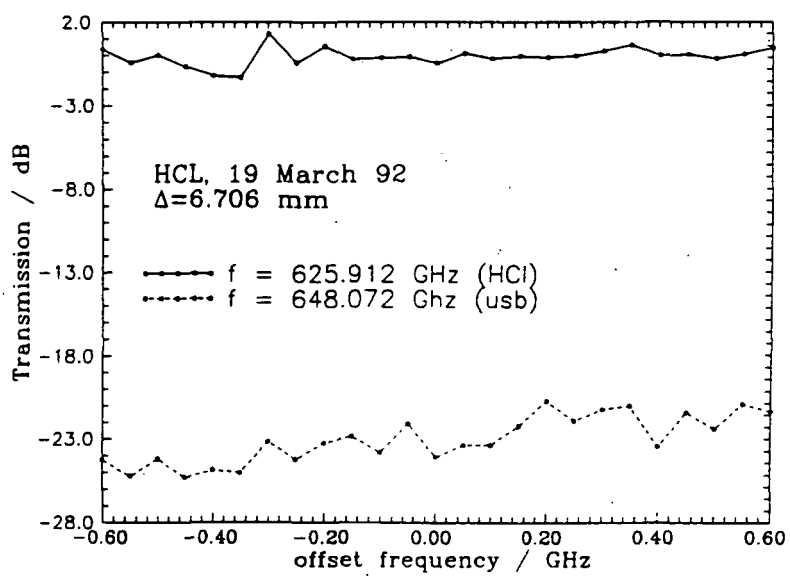

Fig.5: Measured power transmission of the Martin-Puplett interferometer
solid curve : lower sideband (HCl) ; dashed curve : upper sideband

to analyze the i.f. output. The receiver, here the SMS, was operated in a radiometric mode using the quasi-optical calibration unit (*Fig.1*) and adjusted in order to measure ClO. A submillimeter signal corresponding at the center frequency of the image sideband was generated and observed with a CTS resolution of 400 KHz resulting in a side suppression of about 32 dB. This measurement required an integration of 40 s.

Conclusions

For the performance of atmospheric measurements it is desirable to operate the receiver in a ssb mode. The characteristics of a Martin-Puplett interferometer used as a ssb-filter in a 625-655 GHz heterodyne receiver has been measured by a laboratory setup. When the ssb-filter is adjusted to measure at the HCl frequency, for example, a suppression of more than 20 dB was obtained over a bandwidth of 1.2 GHz. Up to now the measurement is limited by the strength of the generated submillimeter signal which is expected to be improved by optimizing the antenna. A measurement using a narrow band filter shows that the performance of the Martin-Puplett interferometer at the center frequency gives a suppression of about 32 dB.

References

[1] J.C.Farman, B.G.Gardiner, J.D.Shanklin, "Large Losses of Total Ozone in Antarctica reveal seasonal ClO_x /NO_x interaction", *Nature*, Vol. 315, 16 May 1985

[2] J.W.Waters, "Microwave Limb-Sounder of Earth's Upper Atmosphere", *Atm.Res.*, Vol. 23, pp 391-410, 1989

[3] H.Nett, S.Crewell, K.Künzi, "Heterodyne detection of stratosperic trace gases at sub-mm frequencies", *IGARSS 91,Digest*, Helsinki 91

[4] H.Nett, S.Crewell, K.Künzi, "A 625-650 GHz Heterodyne Receiver for Airborne Operation", *16th Int. conf. on Infrared and Millimeter Waves Symposium*,Digest, Vol. 1576, pp 460-461, 1991

[5] P.F.Goldsmith, *Infrared and Millimeter Waves. Vol.6,Ed.Button.K.S..Academic Press.* New York, pp 277-342, 1982

InGaAs/InP HETEROEPITAXIAL SCHOTTKY BARRIER DIODES FOR TERAHERTZ APPLICATIONS

Udayan V. Bhapkar, Yongjun Li, and Robert J. Mattauch

Semiconductor Device Laboratory
Department of Electrical Engineering
The University of Virginia
Charlottesville, VA 22903-2442

ABSTRACT

This paper explores the feasibility of planar, sub-harmonically pumped, anti-parallel InGaAs/InP heteroepitaxial Schottky diodes for terahertz applications. We present calculations of the (I-V) characteristics of such diodes using a numerical model that considers tunneling. We also present noise and conversion loss predictions of diode mixers operated at 500 GHz, and obtained from a multi-port mixer analysis, using the I-V characteristics predicted by our model.

Our calculations indicate that InGaAs/InP heteroepitaxial Schottky barrier diodes are expected to have an I-V characteristic with an ideality factor comparable to that of GaAs Schottky diodes. However, the reverse saturation current of InGaAs/InP diodes is expected to be much greater than that of GaAs diodes. These predictions are confirmed by experiment. The mixer analyses predict that sub-harmonically pumped anti-parallel InGaAs/InP diode mixers are expected to offer a 2 dB greater conversion loss and a somewhat higher single sideband noise temperature than their GaAs counterparts. More importantly, the InGaAs/InP devices are predicted to require only one-tenth of the local oscillator power required by similar GaAs diodes.

This work has been supported by the National Science Foundation under Grant ECS-9113123 and by NASA through the University of Michigan under Grant Z-25251.

I. Introduction

GaAs Schottky diodes are frequently used as mixer elements in heterodyne receivers for the few hundred gigahertz to few terahertz frequency range [1]. At present a major limitation on these devices for space-based applications is the difficulty in obtaining sufficient local oscillator (LO) power from solid state sources; the maximum available LO power decreases sharply with increasing LO frequency. One approach to overcoming this limitation is to use sub-harmonically pumped, anti-parallel diode pairs, which halves the frequency at which the LO power is needed to a range where obtaining sufficient LO power is less of an obstacle. Standard GaAs Schottky diodes have a large turn-on voltage, and consequently require a substantial applied bias to minimize LO power requirements and conversion loss. Unfortunately, it is not feasible for each diode to be biased individually in an anti-parallel configuration. To reduce the LO power requirement, InGaAs has been proposed as a material for use in sub-harmonically pumped, anti-parallel diode structures [2]. Schottky barriers formed from InGaAs have a height that decreases with increasing indium mole fraction. The resulting lower turn-on voltage of these diodes suggests that they will require smaller LO voltages, and therefore power, for optimum performance. An added benefit of using InGaAs instead of GaAs is its superior mobility, which will lead to a lower series resistance, which in turn will reduce the conversion loss.

Of crucial importance to both the conversion loss and noise of the mixer is the diode I-V characteristic. We have previously reported on a Schottky diode current-voltage analysis that considers electron tunneling and image force lowering [2]. In diodes with epitaxial layers doped to greater than about 5.0×10^{16} cm^{-3}, electron tunneling significantly affects the diode ideality factor.

We present the results of conversion loss and mixer noise calculations using the I-V characteristics obtained from our diode model. A single diode equivalent circuit was used to model diode mixers in the sub-harmonically pumped, anti-parallel configuration. We have used a computer program by P. Seigel to perform the analysis [3], which we have modified to use the current-voltage model discussed in this paper, rather than the standard thermionic-emission model.

We also discuss fabrication technology currently being developed for a planar, anti-parallel InGaAs/InP diode.

II. Diode Model

A. Anti-Parallel Planar Diodes

An electron micrograph of a GaAs anti-parallel planar diode is shown in Figure 1 [1]. The $In_{0.5}Ga_{0.5}As$/InP anti-parallel planar diodes being designed in this study will have an identical geometry. A cross-section of such a diode is shown in Figure 2. A circuit model of a planar diode showing the major parasitics is shown in Figure 3. The junction capacitance, C_j, and the series resistance, R_s, are the dominant parasitics at high frequencies, and should be minimized for optimum conversion performance. The effects of the pad-to-pad capacitance, C_{pp}, and the finger inductance, L_s, are smaller, and have not been considered in the mixer calculations presented in this paper. Furthermore, the junction conductance itself may deviate from ideal exponential behavior, particularly at high forward or reverse bias, and this can also affect the conversion performance. This effect is considered in the Schottky I-V analysis presented in this paper.

The series resistance of a Schottky diode can be reduced by increasing the conductivity of the epitaxial layer and/or the substrate, or by reducing the thickness of the undepleted epitaxial layer. The epilayer conductivity can be increased by increasing its doping concentration, however, this involves a trade-off: the diode ideality is also decreased. The use of InGaAs, which has a greater electron mobility than GaAs, allows for a high conductivity epilayer, and avoids this trade-off, as we shall show later. In addition, the epilayer in InGaAs diodes can be made much thinner than in GaAs diodes. This is because the epilayer is generally made slightly thicker than the zero-biased depletion depth, which is proportional to the square root of the Schottky barrier height. Therefore, in equally doped material, the zero-biased depletion depth in $In_{0.53}Ga_{0.47}As$ is about half that in GaAs.

The zero-biased junction capacitance of InGaAs diodes is greater than that of comparable GaAs diodes because the junction capacitance is, to first order, inversely proportional to the depletion depth. However, at the current densities reached in normal operation, the typical junction capacitances of the diodes are expected to be comparable. This is because the depletion depth depends on the remaining barrier, that is, the Schottky barrier height minus the applied voltage, and the current density is roughly proportional to the exponential of the remaining barrier.

B. Schottky I-V Model

We shall briefly outline the quantum-mechanical transmission current-voltage model, which is described in greater detail elsewhere [4], and is largely based on the work of Chang, Crowell, and Sze [5,6].

The current density is calculated through a numerical evaluation of the equation

$$J(V) = \frac{RT}{k} \int_{E_{min}}^{\infty} dE_n \left[\tau(E_n, V) \left[F_s(E_n, V) - F_m(E_n) \right] \right] \quad (1)$$

where R is the Richardson constant in the semiconductor, T is the temperature, k is Boltzmann's constant, τ is the electron transmission coefficient, F_s and F_m are the semiconductor and metal distribution functions respectively, V is the applied bias, E_n is the component of the incident electron energy normal to the metal, and E_{min} is the minimum allowed electron energy. E_{min} corresponds to the conduction band minimum in the metal or the semiconductor, depending on the applied bias.

The electron transmission coefficient is obtained through a one dimensional solution of Schrodinger's equation covering the region of the Schottky barrier, including the effects of image force lowering. The transmission coefficient has been shown to vary sharply with the electron energy, and ranges from near zero for electrons with energies much below the barrier maximum, to near unity for electrons with energies a few kT greater than the barrier maximum [4].

We have used a drifted-Maxwellian to model the electron energy distribution, which is given by [7]

$$F = \frac{m^{*1/2}}{(2\pi kT)^{1/2}} \exp\left[\frac{-m^*(v_n - v_d)^2}{2kT} \right], \quad (2)$$

where v_n is the normal component of electron velocity, and v_d is the drift velocity, defined as

$$v_d = \frac{J}{qN_d^+}, \quad (3)$$

where N_d^+ is the concentration of the ionized donors in the epitaxial layer outside the depletion region. The current density and drift velocity are calculated iteratively using (1-3) until they

converge to the desired level of accuracy.

C. I-V Predictions

Figures 4 and 5a-b show the I-V characteristics of the metal-semiconductor junctions (denoted by V_j) of GaAs and $In_{0.5}Ga_{0.5}As$ diodes respectively, as predicted by the algorithm discussed in Section B. V_j. Table 1 shows the diode parameters used. The reverse current in a $In_{0.5}Ga_{0.5}As$ diode is predicted to be several orders of magnitude greater than in a GaAs diode. However, it is still nearly two orders of magnitude smaller than the maximum forward current. Thus, while the reverse current is not negligible, it is not expected to degrade mixer performance drastically, as we shall demonstrate in the next section of this paper. It is also noteworthy that the voltage-dependent ideality factors of the two diodes at a forward current density of 10^4 A/cm^2 (which corresponds to a current of 0.08 mA in a 1 μm diameter diode) are nearly identical.

Figures 5a-b also show the overall I-V characteristic of a whisker-contacted $In_{0.5}Ga_{0.5}As$/InP diode fabricated in our laboratory, and includes the effects of the series resistance. These whisker-contacted diodes are research devices only, and will be superseded by planar devices. The data agree well with our model, in which the only adjustable parameter is the Schottky barrier height.

III. Mixer Analysis

The conversion loss and noise calculations presented in this paper have used the multiple reflection algorithm developed by Held and Kerr [8]. A FORTRAN language computer program by P. Seigel, known as GISSMIX [3], (with a few modifications) was used to perform the

calculations. The modifications to the program include the use of the I-V model described above, instead of the thermionic emission model, as well as changes to permit the calculation of subharmonically pumped mixer performance using the single diode equivalent circuit.

A. Held and Kerr Mixer Analysis

The Held and Kerr mixer analysis is based on the assumption of a large signal LO source, upon which is superimposed a small signal RF. The time-dependent conductance of the diode is determined through a non-linear analysis. The diode waveform is then resolved into the small signal admittance, and is represented in the frequency domain through its Fourier coefficients. These coefficients are then used to calculate the noise and conversion performance of the diode mixer circuit. The analysis assumes a knowledge of the diode parameters as well as the embedding impedances at the mixing frequencies. The analysis is amply described elsewhere, and therefore we shall not outline the details of the analysis [8].

The mixer performance is in general affected by the embedding impedances presented to the diode by the mixer block at several sideband and LO harmonic frequencies. These parameters can be obtained through a characterization of the diode mount; however, our investigation has not yet progressed to that point. Due to the absence of information on the embedding impedances, we have chosen to simplify and standardize our analysis by representing all higher order mixing frequencies as short circuits. In general, the use of such an approximation will slightly underestimate the conversion loss and noise temperature. The embedding impedances we have assumed are given in Table 2.

The performance of sub-harmonically pumped, anti-parallel diodes was estimated through use of the single diode equivalent circuit [9]. In this circuit model, the odd-harmonic embedding impedance is equal to twice that presented to a single diode, and the even-harmonic embedding

impedances are set to zero.

B. Calculations

Figure 6 shows the predicted upper-sideband (USB) conversion loss of GaAs and $In_{0.5}Ga_{0.5}As$ single diode mixers at 505 GHz, as a function of the available LO power. Zero applied bias is assumed. The diode parameters used in the mixer analysis are given in Table 1. The $In_{0.5}Ga_{0.5}As$ diode will offer a minimum conversion loss of about 7 dB with P_{LO} equal to 0.2 mW, in comparison to the GaAs diode, which will offer about 8 dB conversion loss with P_{LO} equal to nearly 2 mW. The superior predicted conversion loss of the $In_{0.5}Ga_{0.5}As$ diode is due primarily to its lower series resistance, and its lower LO power requirement with zero bias is due to its lower barrier height.

Figures 7 and 8 show the predicted upper-sideband (USB) conversion loss and noise temperature respectively, of sub-harmonically pumped, anti-parallel GaAs and $In_{0.5}Ga_{0.5}As$ diodes, as a function of the available LO power per diode. The total LO power required by the diode pair is therefore twice the amount shown. An LO frequency of 250 GHz and a signal frequency of 505 GHz were assumed. The minimum conversion loss of the $In_{0.5}Ga_{0.5}As$ diode pair is predicted to be about 11 dB with 0.2 mW of total available LO power, compared to about 9 dB with about 2 mW of available LO power for the GaAs diode pair. The minimum USB noise temperatures of the $In_{0.5}Ga_{0.5}As$ and GaAs diode pairs are predicted to be about 2000 K and 1300 K respectively. Thus, $In_{0.5}Ga_{0.5}As$/InP diode anti-parallel mixers are expected to reduce the LO power requirement by at least an order of magnitude compared to that of similar GaAs diode mixers, while increasing the conversion loss and noise by no more than 2 dB and 50 percent respectively. The RF performance of $In_{0.5}Ga_{0.5}As$/InP diodes in an anti-parallel configuration is expected to be somewhat degraded from that of single diodes of the same

material and with similar parameters. We believe this is due to the relatively high reverse saturation current of these diodes. However, this drawback is small in comparison to their primary advantage: they will require LO sources at frequencies half of the signal frequency.

IV. Diode Fabrication

The objective of this facet of our work was to develop a device fabrication technology which will enable us to produce predictable planar, anti-parallel $In_{0.53}Ga_{0.47}As$ mixer diodes with reliable electrical characteristics. The fabrication procedure for planar, anti-parallel diodes on $In_{0.53}Ga_{0.47}As$ is very similar to that on GaAs. A highly abbreviated outline follows.

1. Active Layer Thinning: The active layer of $In_{0.53}Ga_{0.47}As$ was intentionally grown thicker than the theoretical zero-bias depletion thickness. This allowed us to adjust the actual epitaxial layer thickness by using an electrochemical thinning technique. The actual epilayer thickness was measured using a standard C(V) profiling technique but with a 10 MHz frequency to allow the component of current through the space-charge capacitance to be dominant. This provided us a way to optimize the I-V characteristic by changing the actual active layer thickness.

2. Oxide Deposition. A thin (6000 A) layer of SiO_2 was pyrolytically deposited on the active layer.

3. Ohmic Contact Formation. An ohmic contact was formed by electroplating Sn-Ni/Ni/Au on n^{++} $In_{0.53}Ga_{0.47}As$ and subsequently alloying at 400°C. The TLM pattern test has shown that the Sn-Ni/Ni/Au ohmic contact on $In_{0.53}Ga_{0.47}As$ is about $2–3 \times 10^{-6}$ Ωcm^2, which is one order of magnitude better than that on GaAs.

4. Anode Definition. Standard photolithography and reactive ion etching were employed to define anode windows in the SiO_2 layer. The anode metals (Pt and Au) were DC electroplated through these windows onto the underlying active $In_{0.53}Ga_{0.47}As$ layer to form the Schottky diodes.

5. Anode Contact Finger. Conductive thin films of chromium and gold were first deposited over the entire wafer through use of a sputtering system. Next, the fingers were electroplated over a photolithographically defined region. Both dry and wet etching were used to remove the thin chromium/gold film covering the wafer, leaving the contact fingers in place.

6. Surface Channel Etching. A final photolithography step defines the surface channel. Buffered hydrofluoric acid was first used to remove the SiO_2 in the surface channel. Then, the conducting $In_{0.53}Ga_{0.47}As$ between the pads was removed by using H_3PO_4 : H_2O_2 : H_2O, which provides the desired etch profile for different InGaAs crystal directions, thus allowing the finger to be undercut.

Early results of ohmic contact formation have shown a problem associated with alloying: the oxide near the anode region was damaged after alloying. This problem was solved by changing the plating parameters and the alloying temperature without changing the quality of the contact. The most crucial step in device fabrication is anode formation. Early attempts at anode formation on planar, anti-parallel $In_{0.53}Ga_{0.47}As$ resulted in a low breakdown voltage, as well as instability and nonuniformity of the I-V. These problems were overcome by optimization of the plating parameters. Profiles resulting from several chemical etchants have been investigated with respect to the desired profile in forming the surface channel, which undercuts the anode fingers and protects the anode region. The H_3PO_4 : H_2O_2 : H_2O family has been found to provide the desired results.

V. Conclusion

In this paper we have presented I-V calculations of $In_{0.5}Ga_{0.5}As$/InP Shottky barrier diodes. The model we have used considers electron tunneling, image force barrier lowering, and the effect of a drifted Maxwellian electron distribution. The model has been shown to agree well with experimental data on whisker-contacted $In_{0.5}Ga_{0.5}As$/InP and GaAs diodes fabricated in our laboratory. The I-V characteristics of $In_{0.5}Ga_{0.5}As$/InP diodes have been shown to be similar to those of GaAs diodes, but are displaced in voltage and have a higher reverse saturation current.

The I-V characteristics obtained from our model were used to predict the mixer performance of both single and sub-harmonically pumped, anti-parallel diodes. A modified form of Seigel and Kerr's analysis was used. The calculations show that in unbiased operation, $In_{0.5}Ga_{0.5}As$/InP single diode mixers will offer conversion performance equal to that of comparable GaAs diode mixers, and require only one-tenth the LO power. Furthermore, sub-harmonically pumped, anti-parallel $In_{0.5}Ga_{0.5}As$/InP diode mixers are expected to offer performance nearly as good as that of the best GaAs diode mixers, but will require one-tenth as much LO power to achieve their optimum performance.

The fabrication techniques for anti-parallel, $In_{0.5}Ga_{0.5}As$/InP planar diodes with surface channels have been extensively investigated. Difficulties in anode plating and ohmic contact formation have been resolved, and suitable chemical etchants necessary for the fabrication sequence have been found.

REFERENCES

[1] T.W. Crowe and W.C.B. Peatman, "GaAs Schottky Diodes for Mixing Applications Beyond 1 THz," *Proc. Second Int. Symp. on Space Terahertz Tech.*, Feb. 1991, pp. 323-339.

[2] U.V. Bhapkar, T.A. Brennan, and R.J. Mattauch, "InGaAs Schottky Barrier Mixer Diodes for Minimum Conversion Loss and Low LO Power Requirements at Terahertz Frequencies," *Proc. Second Int. Symp. on Space Terahertz Tech.*, Feb. 1991, pp. 371-388.

[3] P.H. Seigel and A.R. Kerr, "The Measured and Computed Performance of a 140-220 GHz Schottky Diode Mixer," *IEEE Transactions*, Vol. MTT-32, Feb. 1984, pp. 1579-1590.

[4] U.V. Bhapkar and R.J. Mattauch, "The Numerical Simulation of the Current-Voltage Characteristics of Heteroepitaxial Schottky Barrier Diodes," not yet published.

[5] C.R. Crowell and S.M. Sze, "Quantum-Mechanical Reflection of Electrons at Metal-Semiconductors Barriers: Electron Transport in Semiconductor-Metal-Semiconductor Structures," *Journal of Applied Physics*, Vol. 37, No. 7, June 1966, pp. 2683-2689.

[6] C.Y. Chang and S.M. Sze, "Carrier Transport Across Metal-Semiconductor Barriers," *Solid-State Electronics*, Vol. 13, pp. 727-740.

[7] T. Vogelsang and W. Hansch, "The Electron High-Energy Distribution Function: A Comparison of Analytical Models with Monte Carlo Calculations," *J. Appl. Phys.*, Vol. 69, No. 6, 1991, pp. 3592-3595.

[8] D.N. Held and A.R. Kerr, "Conversion Loss and Noise of Microwave and Millimeter-Wave Mixers: Part I -- Theory," *IEEE Transactions*, Vol. MTT-26, Feb. 1978, pp. 49-55.

[9] S.A. Maas, *Nonlinear Microwave Circuits*, Artech House, 1988, pp. 232-237.

Table 1. Diode parameters.

diode materials	GaAs	$In_{0.5}Ga_{0.5}As/InP$
anode diameter	0.5 μm	0.5 μm
ohmic contact width	50 μm	50 μm
ohmic contact length	50 μm	50 μm
chip thickness	125 μm	125 μm
active layer thickness	0.110 μm	0.065 μm
ϕ_B	0.950 eV	0.277 eV
active layer doping	1.5×10^{17} cm^{-3}	1.5×10^{17} cm^{-3}
buffer layer doping	2.0×10^{18} cm^{-3}	2.0×10^{18} cm^{-3}
C_{jo}	1.22 fF	2.10 fF
C_{jmax}	10.0 fF	10.0 fF
I_{sat}	7.85×10^{-17} A	8.25×10^{-7} A
I_{max}	5.0×10^{-3} A	5.0×10^{-3} A
η	1.12	1.09
R_s	15.0 Ω	9.0 Ω

Table 2. Mixer embedding impedances.

ω_{RF}	75 Ω
ω_{image}	75 Ω
ω_{LO}	50 Ω
ω_{IF}	matched

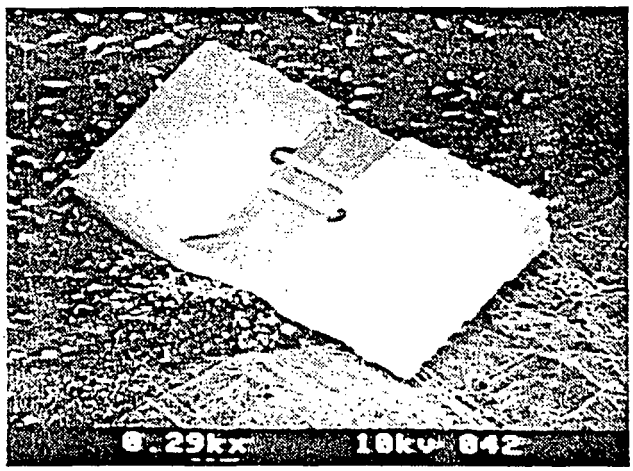

Figure 1. Electron micrograph of GaAs anti-parallel planar diode.

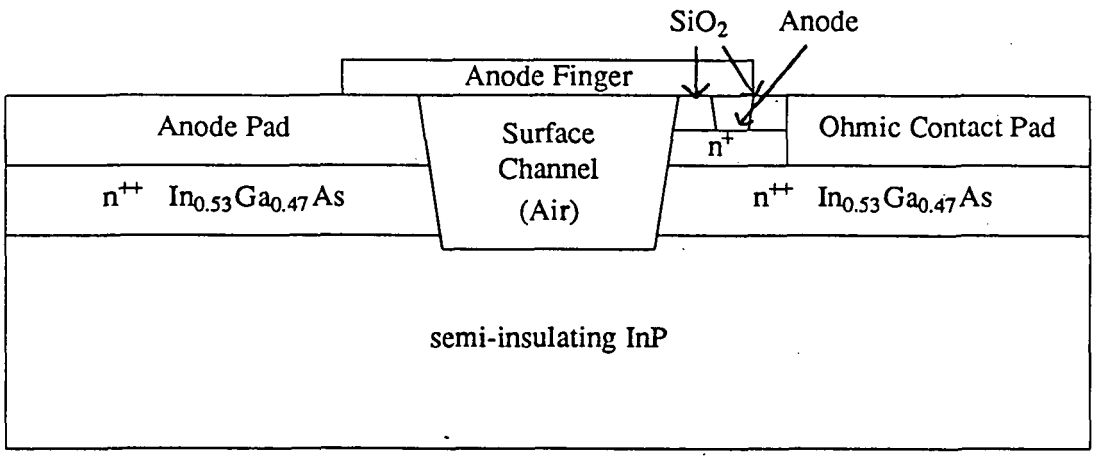

Figure 2. Cross-section of anti-parallel, planar InGaAs/InP diode (not to scale).

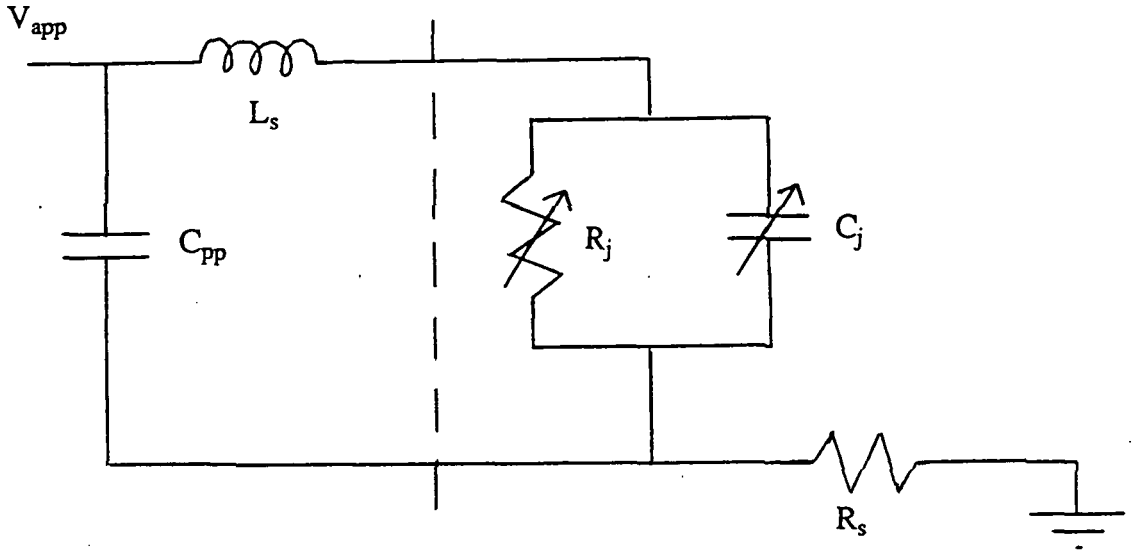

Figure 3. Circuit model of planar diode.

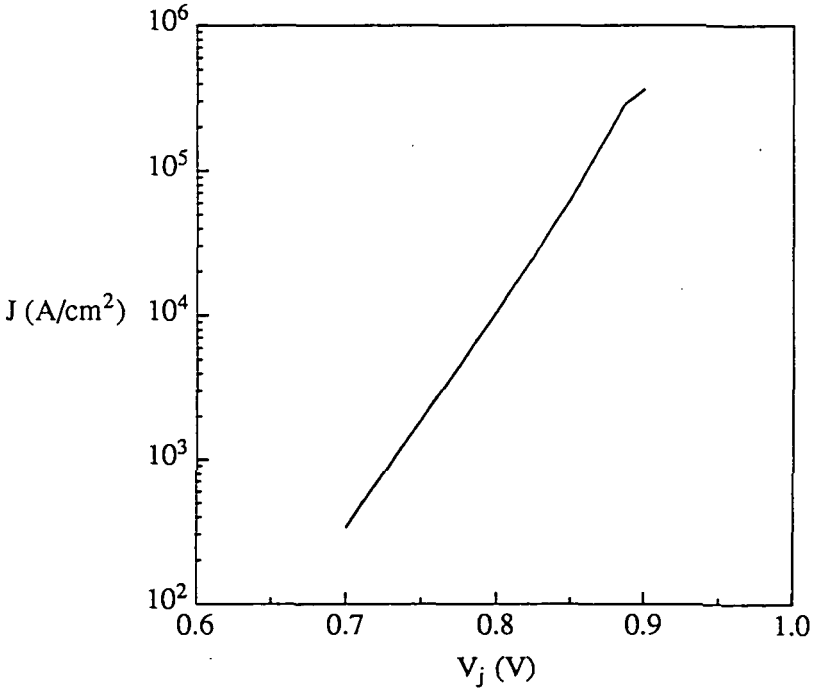

Figure 4. Forward current-voltage characteristic of GaAs Schottky diode.

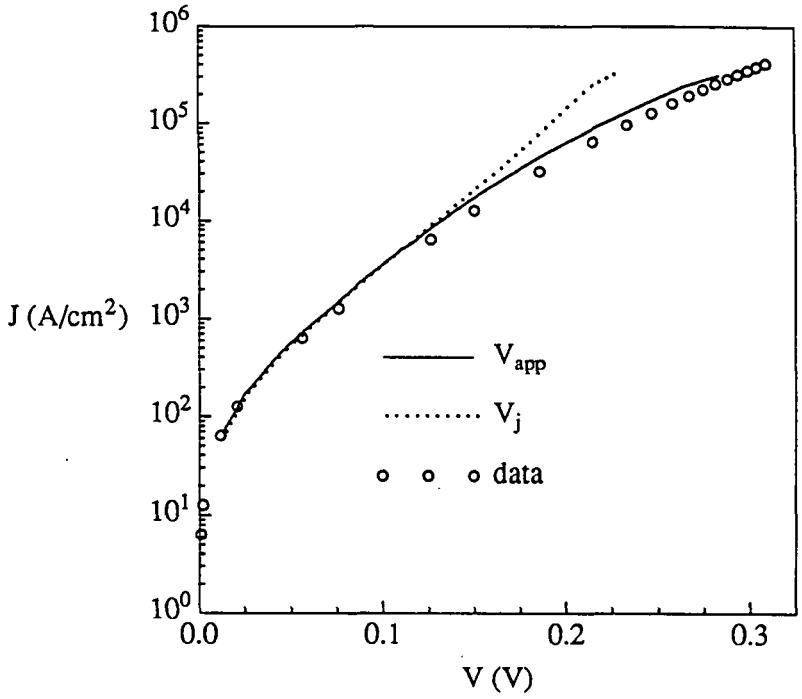

Figure 5a. Forward current-voltage characteristic of $In_{0.5}Ga_{0.5}As$/InP Schottky diode.

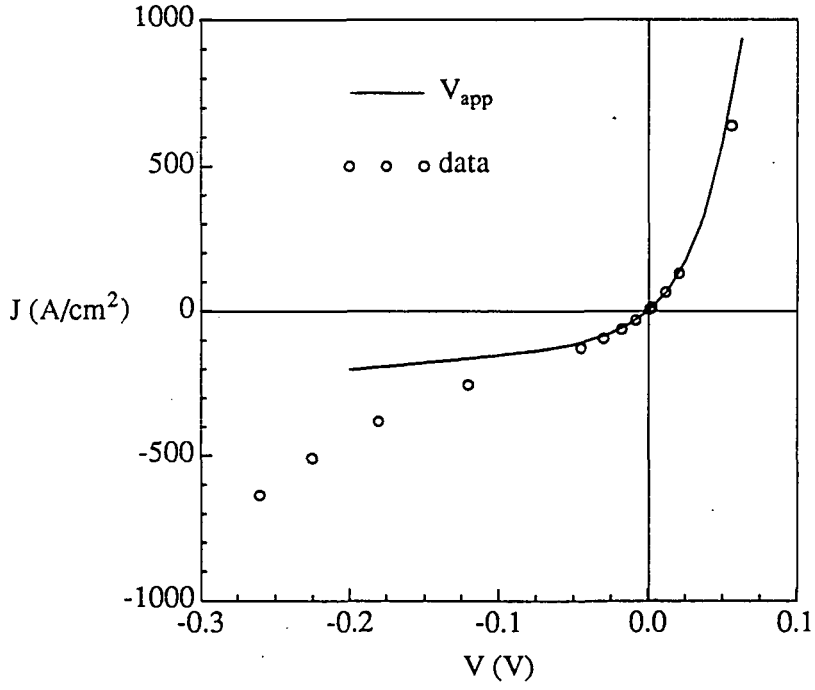

Figure 5b. Reverse current-voltage characteristic of $In_{0.5}Ga_{0.5}As$/InP Schottky diode.

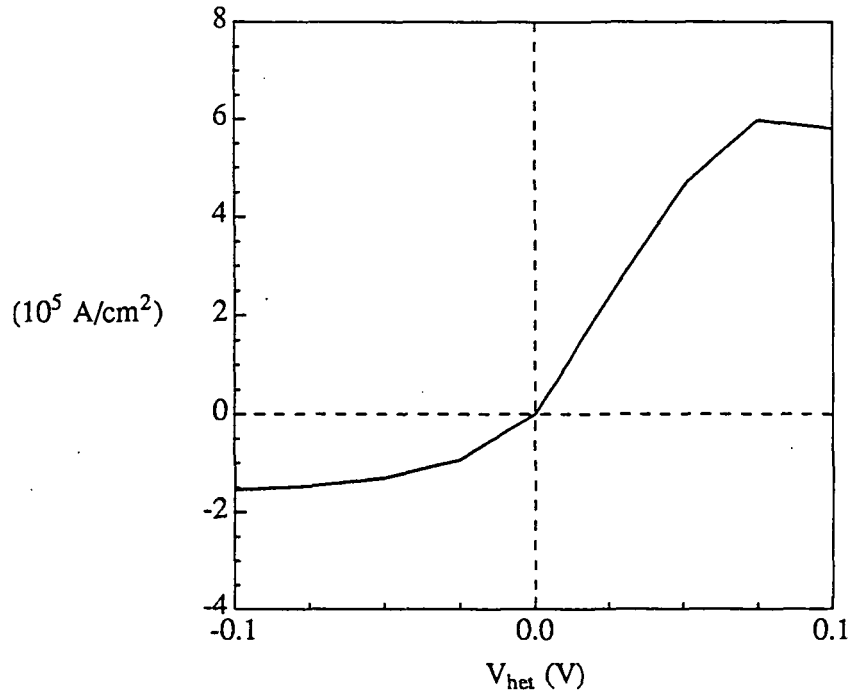

Figure 5c. Current-voltage characteristic of the heterojunction in an $In_{0.5}Ga_{0.5}As$/InP Schottky diode.

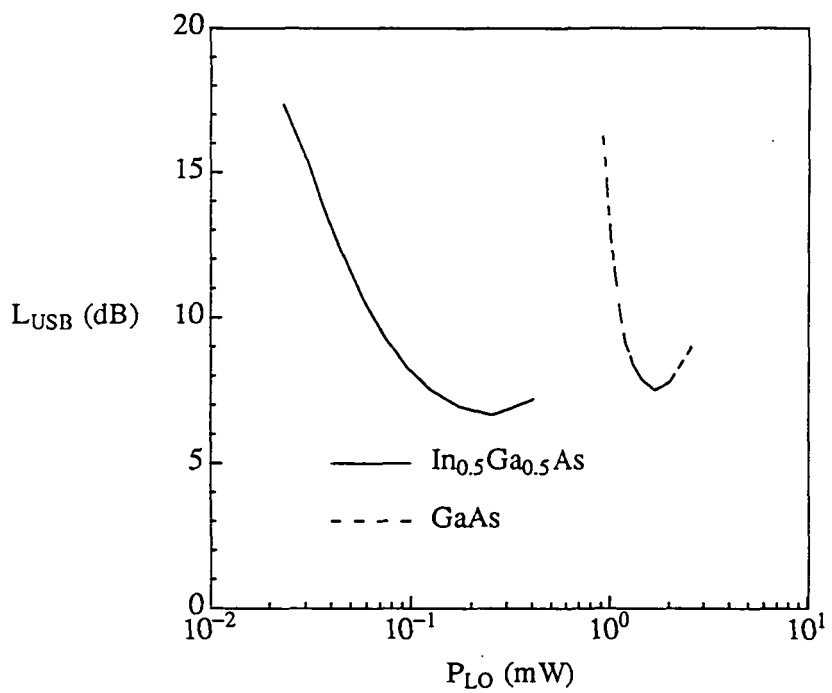

Figure 6. Conversion loss (USB) versus LO power of single Schottky diodes at 505 GHz.

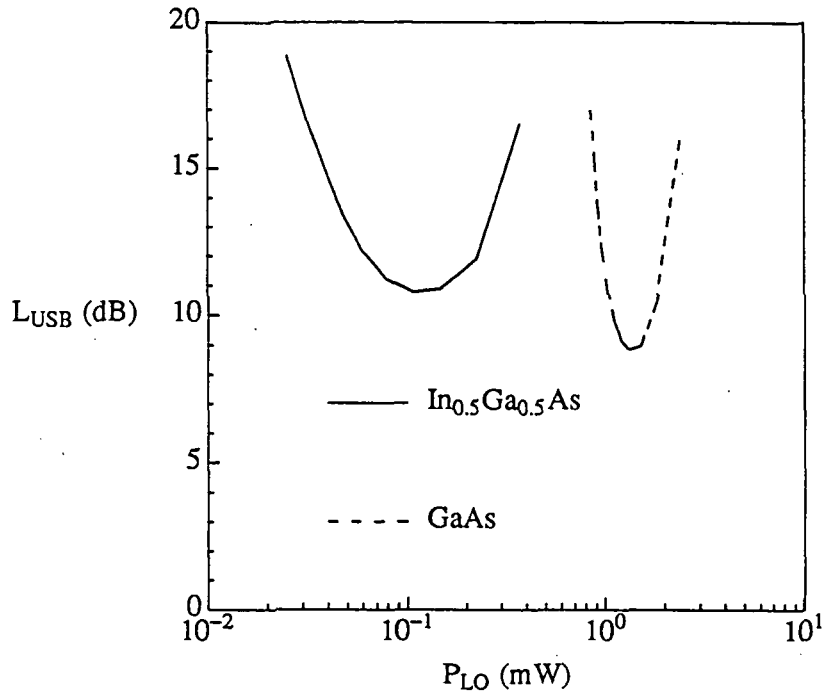

Figure 7. Conversion loss (USB) versus LO power per diode of sub-harmonically pumped, anti-parallel Schottky diodes at 505 GHz.

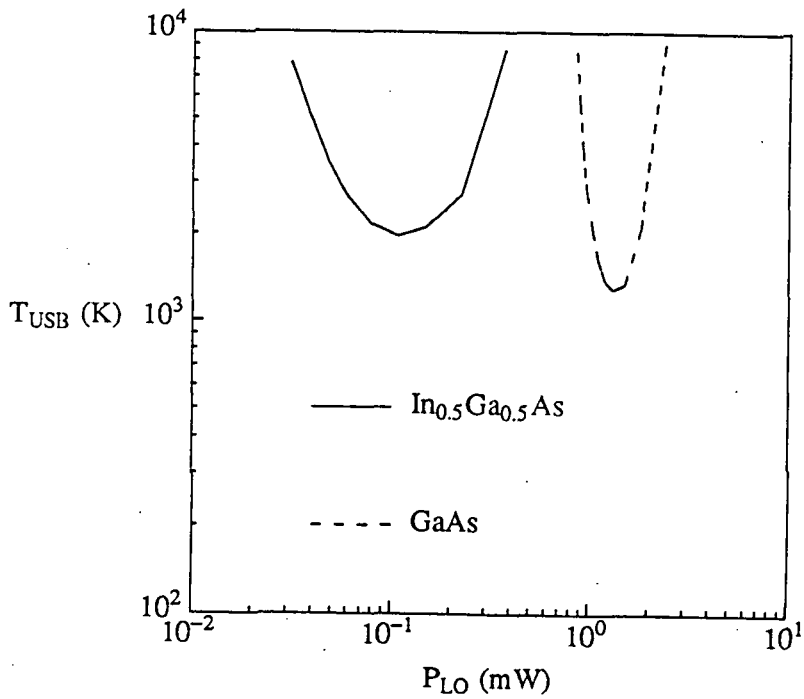

Figure 8. Noise temperature (USB) versus LO power per diode of sub-harmonically pumped, anti-parallel Schottky diodes at 505 GHz.

A BROADBAND THz RECEIVER FOR LOW BACKGROUND SPACE APPLICATIONS

C. Hagmann, D. J. Benford, A. C. Clapp, P. L. Richards, and P. Timbie†
Department of Physics, University of California, Berkeley CA 94720

ABSTRACT

We have developed a sensitive bolometric receiver for low background space applications. In a 10 % bandwidth at 1 THz, this receiver is approximately 100 times more sensitive than a quantum limited heterodyne receiver with a 1 GHz IF bandwidth. This receiver is designed to be used for the long wavelength band (200-700 μm) in the MIPS instrument on NASA's SIRTF satellite. The bolometers are cooled to 100 mK by an adiabatic demagnetization refrigerator. Roughly 60 g of cesium chrome alum salt is partially demagnetized to 100 mK, followed by a slow regulated downramp to compensate for the heat leak. The hold time of the ADR system is about 18 hours with a temperature stability of $\Delta T_{rms} \approx 10$ μK. The composite bolometers have electrical reponsivities of 10^9 V/W and electrical NEP's of about 3×10^{-17} W/√Hz. The bolometer signals are read out by JFET preamplifiers located on the helium plate and operated at 120 K. We have addressed a number of space qualification issues, such as the development of an analog magnet controller, construction of a cryogenic shake-table for bolometers and selection of the paramagnetic salt CCA which can survive a bakeout at 50 °C. The receiver is scheduled to be flown in the spring of 1992 on a balloon telescope. This flight has a dual purpose. One is to provide a realistic test of the capabilities of the new receiver. The other is to search for anisotropies in the cosmic microwave background on scales of a few degrees.

† Present address: Dept. of Physics, Brown University, Providence RI 02912

INTRODUCTION

Since the highly sucessful flight of the Infrared Astronomical Satellite (IRAS) in 1982, much work has been devoted towards the development of a new generation of low background receivers. NASA's Space Infrared Telescope Facility (SIRTF) is a LHe cooled long-life instrument, which will allow background or confusion limited observations for wavelengths ranging from 2-700 μm. The long wavelength band covers the spectral range of 200-700 μm, which is 0.4-1.5 THz. Scientific targets for the long wavelength capability of SIRTF include quasars, brown dwarfs, protogalaxies and the cosmic microwave background.

In principle either direct detectors or heterodyne receivers could be used at this wavelength. For broadband photometry, direct detectors are more sensitive than heterodyne receivers due to their wider bandwidth and lack of quantum noise. The baseline instrument for long wavelength photometry on SIRTF is a bolometric receiver operating at 0.1 K and cooled by an adiabatic demagnetization refrigerator (ADR). A prototype of this receiver has been constructed and will be flown on a balloon borne telescope as a realistic test of its flight worthiness.

REFRIGERATOR

The 100 mK refrigerator [1], shown in Figure 1, operates by adiabatically demagnetizing a paramagnetic salt. The ADR cycle starts by thermally shorting the 100 mK stage to the helium bath cold plate at T≈1.5 K. This is accomplished with a mechanical heat switch actuated by a superconducting solenoid located on the helium plate. In the 'ON' position, a current of 100 mA actuates the solenoid. which forces two jaws to clamp a cold finger

attached to the 100 mK stage. The resulting pressure contact has a thermal conductance of about 10 mW/K at T=1.5 K. In the 'OFF' position, a spring pushes the jaws apart.

The field for magnetizing the paramagnetic salt is produced by a conduction cooled superconducting solenoid with a rated central field of 2.5 T for 6 A of current. The magnet is surrounded by a ferromagnetic shield made of vanadium permendur to reduce the stray field to insignificant levels and to increase the field homogeneity within the coil. This shielding material was chosen because of its high saturation flux density and small remanence.

Our ADR uses the hydrated paramagnetic salt cesium chrome alum $CsCr(SO_4)_2 \cdot 12\,H_2O$ (CCA) as its working substance. The magnetic ions Cr^{3+} (J=3/2) in this salt have a density of 2.1×10^{21} cm^{-3} and order at around T= 20 mK due to their weak magnetic interaction. To make good thermal contact between the salt and the rest of the 100 mK stage, the salt is grown directly on a skeleton of 200 gold wires. The 60 g of salt in the pill is approximately 0.1 mole. The salt is corrosive and has a tendency to dehydrate in air. To prevent any degradation, the salt pill is sealed in a stainless steel can; the gold wires are brought outside through a hardsoldered seal and are hardsoldered to a copper cold stage.

The salt pill is suspended from the surrounding 1.5 K cold plate with two sets of six Kevlar ropes on each end. The suspension can be made very stiff because of the high tensile strength of Kevlar; the fundamental resonant frequency is about 200 Hz. The heat leak through the Kevlar suspension is measured to be 0.25 μW.

During isothermal magnetization, the magnetic field is ramped up to 2.5 Tesla and then held constant while the cold stage is allowed to equilibrate for about 30 minutes. The chromium spins align in the external field and the entropy is reduced by about 70 %. The heat switch is then opened and the magnetic field is ramped down, cooling the stage adiabatically. When the stage temperature reaches T= 100 mK, the fast downramp is stopped and a PC based temperature controller [2] maintains T=100 mK by slowly reducing the field, thereby compensating for the heat leak through suspension and wiring. The hold time has been measured to be 18 hours with a temperature stability of

$\Delta T_{rms} \approx 3\ \mu K$. For SIRTF and balloon use, a compact analog PID controller has been developed which has achieved temperature stabilities of about 10 μK.

After the magnetic field has been reduced to zero, the heat switch is closed and the refrigerator is cycled again. The duty cycle of the refrigerator is more than 95 %.

BOLOMETERS

We are currently testing and optimizing composite bolometers constructed in similar ways to the devices used at and above temperatures of 300 mK [3,4]. A schematic picture of a bolometer [4] is shown in Figure 2. The main elements of the bolometer are a radiation absorber, a thermistor to sense the deposited power and a weak thermal link to the 100 mK plate.

The absorber consists of a ≈ 600 Å thick film of Bi evaporated on a 2mm× 2mm× 35μm diamond substrate. The absorptivity of this structure has been measured to be about 50 % for frequencies from 15-250 cm^{-1} and normal incidence [5]. The bolometer is enclosed in an optical cavity to maximize the optical efficiency. The substrate is supported by two strands of ≈ 10 μm thick Nylon fiber under tension.

For the temperature sensing element we use a neutron transmutation doped chip of germanium (200μm× 200μm× 200μm) [6]. Ohmic contacts are provided on two faces by boron implantation and metallization with layers of Pd and Au. At helium temperatures, the doped germanium is in the hopping conduction regime with a resistance which varies as

$$R = R_0 \exp\left((A/T)^{0.5} \right). \qquad (1)$$

The constants R_0 and A depend on geometry and doping. Electrical connections are made by attaching two 6 μm thick graphite fibers to the contact pads with silver epoxy. The thermal conductance of the bolometer is

dominated by the Nylon with $G \approx 4\times10^{-11}$ W/K at T= 100 mK for 12 strands. The time constant of the bolometer is given by $\tau = C/G$ (C is the bolometer heat capacity) and measured to be about 30 ms. Our measured τ's turned out to be an order of magnitude larger than is extrapolated from values of C and G measured at 300 mK. Sources of this discrepancy are being investigated.

The bolometer sensitivity is typically expressed as a noise equivalent power which has the contributions

$$NEP^2 = NEP^2_{photon} + 4kT^2G + 4kT^2R/|S|^2 + e^2_n/|S|^2 \qquad (2)$$

where e_n is the voltage noise of the JFET preamp and S is the voltage responsivity given by

$$S(\omega) = I \cdot (dR/dT) \cdot |G + i\omega C|^{-1} \qquad (3)$$

and I is the bias current and $\omega/2\pi$ is the chopping frequency.

We have measured electrical NEP's of 3×10^{-17} W/$\sqrt{\text{Hz}}$ for a chopping frequency of 6 Hz. We are planning to measure the absorbed power NEP by replacing the Bi film absorber with a meander line bismuth heater. Other groups have seen indications of an electric field dependent thermistor resistance and an increasing thermal resistance between phonons and electrons in the NTD germanium at our operating temperatures. Either effect would give an absorbed power NEP which is larger than the electrically measured NEP.

The bolometer voltage is read out by a JFET pair (Interfet NJ132L) packaged in a light-tight can and heated to the optimum temperature of about 120 K. Typical noise voltages are 5-6 nV/$\sqrt{\text{Hz}}$ at 6 Hz. The JFET current noise is not significant for bolometer resistances of about 10MΩ. We use a Kapton stripline with Constantan conductors for the high impedance leads between the bolometer and the JFETs to avoid microphonic noise, crosstalk, and excessive thermal conductance.

SPACE FLIGHT ISSUES

In order to make our receiver space qualifiable, a number of issues need to be addressed. Since the SIRTF cryostat is likely to be baked during pump out, all ADR components have to survive a simulated bake out test. Commonly used paramagnetic salts such as FAA (ferric ammonium alum) and CPA (chrome potassium alum) dehydrate in sealed containers at temperatures as low as 35 °C. Bake out tests with CCA indicate allowed temperatures of at least 50 °C. The large size of the cesium ion leads to a tighter binding of the waters of hydration in the crystal. An undesirable side effect is the very low solubility of CCA in water, which complicates crystal growth.

Another important topic is survivability of the instrument during launch. We have already carried out a shake test of the suspension system at room temperature and at T= 77K. The tests show a fundamental resonance at 200 Hz with a Q of about 100. Since the flat vibration spectrum of the rocket is amplified at that frequency, it should not coincide with any bolometer resonances. To investigate the bolometer vibration spectrum of the bolometer, we developed a cryogenic shake table based on an electromagnetic vibrator immersed in liquid helium. The force is transmitted into a vacuum can through a bellows. We can subject small mass objects such as bolometers to accelerations of up to 60 g (rms).

We have run a reliability test on the mechanical heat switch by cycling it for 4000 times which corresponds to 8 years in orbit. No degradation in switch performance was detected.

An overall test of the system will be carried out during an upcoming flight of a balloon borne telescope [7,8] for measuring the anisotropy of the cosmic microwave background. In previous flights we used ^{3}He cooled bolometers with NEP's of about 1×10^{-16} W/$\sqrt{\text{Hz}}$. The 100 mK bolometers are expected to provide significantly lower noise. The balloon photometer has a multimode broadband feedhorn, and dichroic filters which split the beam into four bands at 3, 6, 9, and 12 cm^{-1} (90, 180, 270, and 360 GHz). In addition, we use quartz and glass bead filters to attenuate high frequency power. The overall

optical efficiency of the balloon photometer from cryostat window to detector is approximatey 20 %.

CONCLUSIONS

We have developed a bolometric THz receiver for space applications which operates at 100 mK and achieves an NEP of about 5×10^{-17} W/$\sqrt{\text{Hz}}$. To compare this with the potential sensitivity of heterodyne receivers, we can calculate the noise equivalent temperature (NET) for both types of receiver. Assuming a 10 % bandwidth at 1 THz, the diffraction limited Rayleigh-Jeans power is $P_s \cong 2kTB$ and NET $\cong$ NEP/2kB $\cong 1.8\times10^{-5}$ K/$\sqrt{\text{Hz}}$. For a quantum noise limited heterodyne receiver with an IF frequency of 1 GHz we calculate an NET = $h\nu/k\sqrt{B_{IF}} = 1.5\times10^{-3}$ K/$\sqrt{\text{Hz}}$. This particular example gives a 100 times greater sensitivity for the bolometric receiver.

At present the status of the bolometer channels on SIRTF is uncertain due to budgetary limitations. A great opportunity would be missed and much valuable science lost for the SIRTF mission if the bolometer channels were to be removed.

ACKNOWLEDGEMENTS

This work was supported by NASA grants NSG-7205, FD-NAGW-2121 and JPL contract 958764, and by the Center for Particle Astrophysics through NSF cooperative agreement AST 8809616.

REFERENCES

[1] P.T. Timbie, G.M. Bernstein, and P.L. Richards, *Cryogenics* **30**, 271, (1990).

[2] G. Bernstein, S. Labov, D. Landis, N. Madden, I. Millet, E. Silver, and P. Richards, *Cryogenics* **31**, 99, (1991).

[3] A.E. Lange, E. Kreysa, S.E. McBride, P.L. Richards, and E.E. Haller, *Intl. J. Infraared and Millimeter Waves*, 4(6), 689, (1983).

[4] D.C. Alsop, C. Inman, A.E. Lange, and T. Wilbanks (in preparation).

[5] J. Clarke, G.I. Hoffer, P.L. Richards, and N.H. Yeh, *J. Appl. Phys.*, **48**(12), 4865, (1977).

[6] E.E. Haller, *Infrared Phys.*, **25**, 257, (1985).

[7] M.L. Fischer, D.C. Alsop, E.S. Cheng, A.C. Clapp, D.A. Cottingham, J.O. Gunderson, T.C. Koch, E. Kreysa, P.R. Meinhold, A.E. Lange, P.M. Lubin, P.L. Richards, and G.F. Smoot, *Ap.J.* (in press).

[8] D.C. Alsop, E.S. Cheng, A.C. Clapp, D.A. Cottingham, M.L. Fischer, J.O. Gunderson, E. Kreysa, A.E. Lange, P.M. Lubin, P.R. Meinhold, P.L. Richards, and G.F. Smoot, *Ap.J.* (submitted).

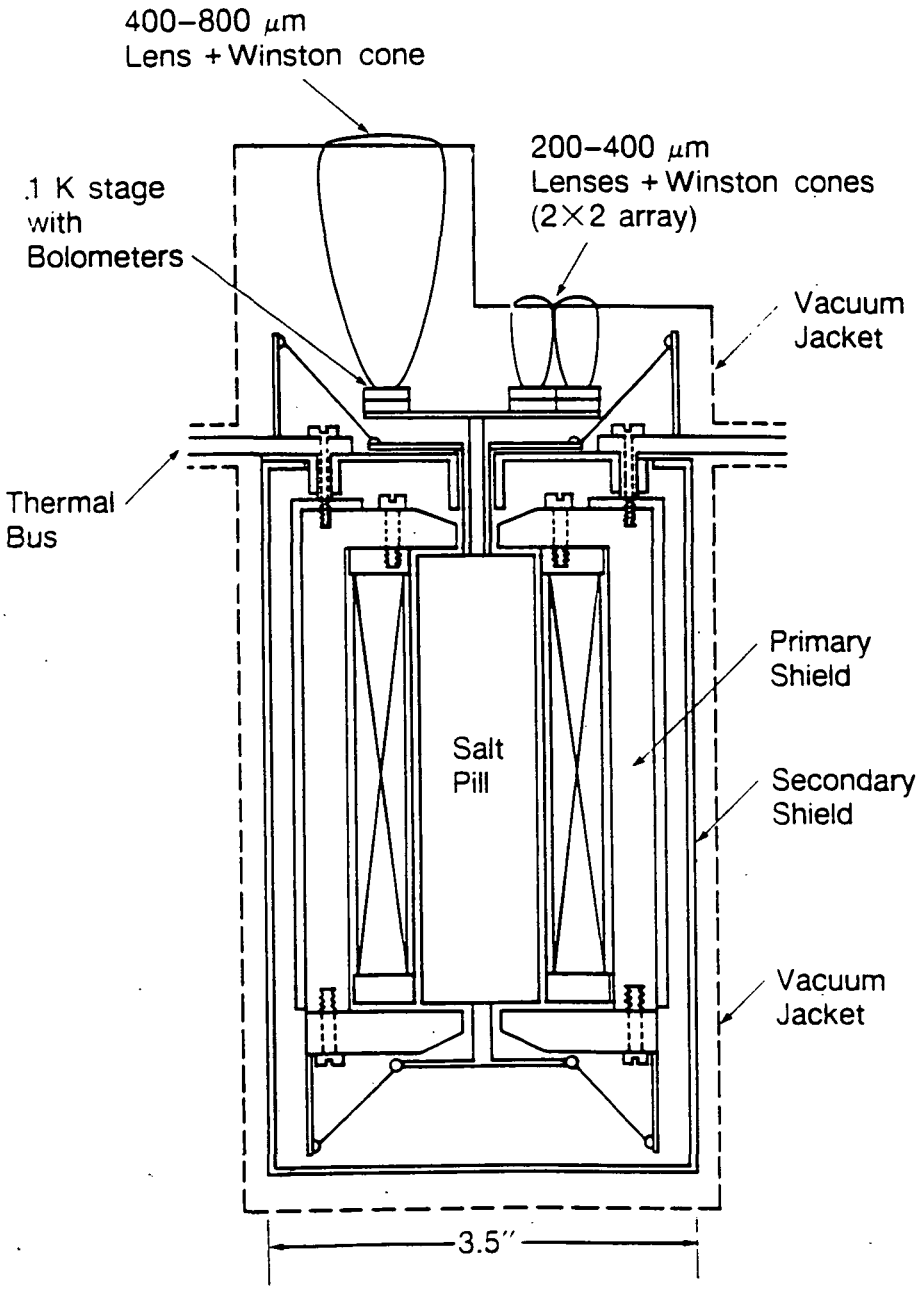

Figure 1: Adiabatic demagnetization refrigerator

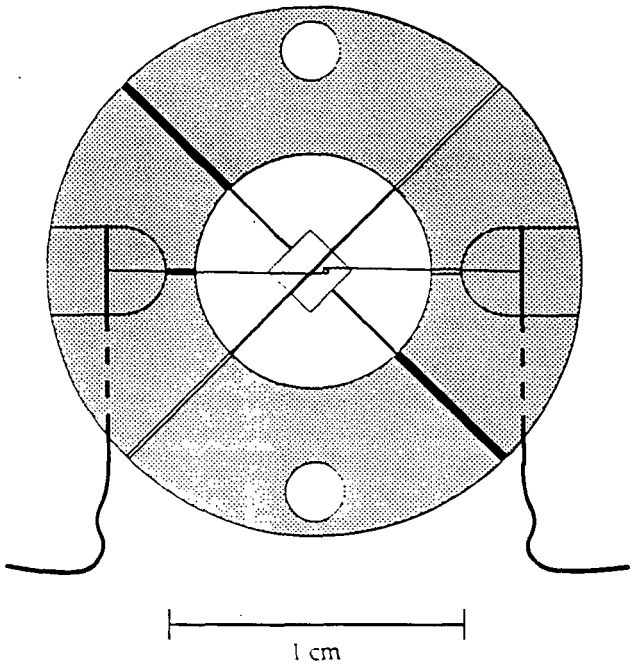

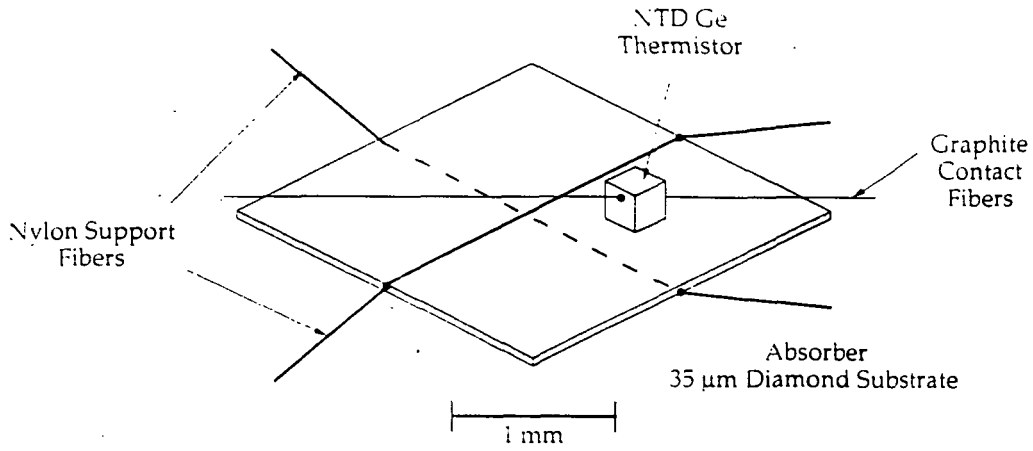

Figure 2: Sketch of a composite bolometer

S57-33
160571
P-14

AlGaAs/GaAs Quasi-Bulk Effect Mixers: Analysis and Experiments

N93-27783

K. S.Yngvesson, J.-X. Yang, F. Agahi, D. Dai, C. Musante, W. Grammer, and K.M. Lau

ABSTRACT

The lowest noise temperature for any receiver in the 0.5 to 1 THz range has been achieved with the bulk InSb hot electron mixer, which unfortunately suffers from the problem of having a very narrow bandwidth (1-2 MHz) We have demonstrated a three order of magnitude improvement in the bandwidth of hot electron mixers, by using the two-dimensional electron gas (2DEG) medium at the hetero-interface between AlGaAs and GaAs. We have tested both in-house MOCVD-grown material, and MBE material, with similar results. The conversion loss (L_c) at 94 GHz is presently 18 dB for a mixer operating at 20K, and calculations indicate that L_c can be decreased to about 10 dB in future devices. Calculated and measured curves of Lc versus PLO, and IDC, respectively, agree well. We argue that there are several different configurations of hot electron mixers, which will also show wide bandwidth, and that these devices are likely to become important as low-noise THz receivers in the future.

I. INTRODUCTION

In our contribution to the Second International Symposium on Space Terahertz Technology [1], we discussed the potential advantages of bulk and "quasi-bulk" (surface-oriented, or quasi-two-dimensional) mixer devices for the THz frequency range. A review of the receiver noise temperatures achieved in this range is given in Figure 1. This graph has been updated compared with the one in [1], using data given in presentations at the 1992 symposium. In the frequency range above 500 GHz, the lowest noise temperatures are still the ones reported for the InSb hot electron mixer [2]. Also, the frequency dependence of the receiver noise temperature of this mixer is much less steep than that for either the SIS or the Schottky diode mixers. We attribute these advantageous features to the bulk nature of the InSb mixer, which leads to a very small parasitic reactance. , In contrast, severe requirements have to be imposed on the size of SIS or Schottky devices for use at these frequencies.

This work has been supported by the National Aeronautics and Space Administration, under grant NAGW-1659
The authors are with the Department of Electrical and Computer Engineering, University of Massachusetts, Amherst, MA 01003

The InSb mixer has one major draw-back, i.e. its very narrow bandwidth (about 1 MHz), which has limited its use in practical systems. A similar narrow bandwidth was obtained for a bulk GaAs mixer [3]. As originally pointed out by Smith et al.[4], it does not appear that this limitation should apply to all hot electron mixers, however, and our earlier paper [1] gave preliminary results which supported this idea. We demonstrated conversion with at least 1 GHz bandwidth in a mixer which employs a nonlinear element based on the two-dimensional electron gas (2DEG) medium at a heterojunction interface formed between AlGaAs and GaAs. Our continued investigation of this mixer at 94 GHz, reported in the present paper, has yielded a 1.7 GHz bandwidth, while the conversion loss has been improved from 30 dB to 18 dB. We have also obtained good agreement between measured and calculated conversion loss.

In this paper, we review the properties of hot electron mixers, especially those employing the 2DEG medium, and present our measured and calculated data. Two different modes of operation have been attempted: (1) Type I: This is the type of mixer which we have demonstrated. It operates at temperatures up to about 100K, and requires LO power of the order of a milliwatt. (2) Type II: The Type II mixer was proposed by Smith et al. [4], operates at about 4K, and requires the use of a moderately large magnetic field There are two distinct magnetically biased hot electron mixers: Type IIa is tuned to cyclotron resonance with the help of a fairly low magnetic field (< 1T). So far, this type of device has been demonstrated as a detector, but not as a mixer. The LO power is predicted to be in the microwatt range, or lower. We have also proposed a mixer (Type IIb), which uses a somewhat larger magnetic field, 1-4 Tesla, i.e. in the region in which Shubnikov-DeHaas oscillations are seen for the DC resistance. Again, only detection has so far been demonstrated.

We briefly compare the 2DEG mixers with other potentially interesting hot electron mixers using thin film superconductors, which also employ a quasi-two dimensional geometry. We argue that there is a large class of different hot electron media, which can be used for mixing with bandwidths of about 1 GHz. The potential extension of two-dimensional hot electron mixers to THz frequencies is finally assessed.

II. FREQUENCY CONVERSION IN HOT ELECTRON MIXERS

Basic Mechanism

Hot electron mixers employ a nonlinear (electron) bolometer device of the type shown in Figure 2. In electron bolometers, the electron gas is heated by the applied power (DC and/or RF) to a temperature, T_e, above the lattice temperature, T_0. The advantage of an electron bolometer, compared with a standard bolometer, which relies on heating of the lattice, is that the specific heat of the

electrons is much smaller than that of the lattice As discussed in greater detail in [1], the basic nonlinearity which gives rise to mixing in hot electron mixers is associated with the fact that the resistance (R_B) of the device is a function of the electron temperature, and therefore also a function of the total power applied (P). A typical curve of $R_B = R_B(P)$ for a 2DEG device is shown in Figure 3.

Response Time and Bandwidth

The maximum rate at which the resistance of a hot electron bolometer can vary is determined by the response time of the electron gas. This response time is in turn given by the effective time for energy transfer from the electron gas to the lattice, which is basically the same as the energy relaxation time, τ_e. The bandwidth of the mixer extends up to a frequency given by [1]:

$$B \approx 1/2\pi\tau_e \qquad (1)$$

Values of τ_e are wellknown for a number of different media. In bulk semiconductors, τ_e is typically in the range 10^{-12} to 10^{-10} seconds, and both measurements and theory have been reviewed in standard reference works [5,6]. The much longer τ_e (10^{-7} to 10^{-6} s), which is found in bulk InSb and GaAs hot electron mixer devices, is due to a bottle neck for the energy relaxation process in these devices from the conduction band to the donor levels [2]. It is worthwhile to explore in some further depth why bulk semiconductors are limited to such a narrow bandwidth when used as hot electron mixers, and why no wider bandwidth devices have been developed during the last thirty years. The energy relaxation time which is typically calculated refers to energy transfer to the lattice from a hot electron distribution within the conduction band, as shown in Figure 4. At temperatures higher than what corresponds to the splitting between the donor levels and the conduction band (roughly 50-100K), almost all donors become ionized, and the only energy relaxation processes which are relevant are those within the condcution band, which thus are quite fast. At the much lower temperatures, which are used in bulk InSb or GaAs mixers, the donor states are occupied, and the much slower relaxation to these states dominates, as also shown in Figure 4. A wide band mixer employing bulk GaAs may be designed at the higher temperatures, but does not appear to have been attempted. One reason may be that too much heating of the lattice occurs, see the discussion below which compares "three-dimensional" and "two-dimensional" devices.

For the 2DEG medium at an AlGaAs/GaAs interface, Sakaki et al measured τ_e-values of 10^{-10} to 10^{-9} s for temperatures below 10 K [7]. The shorter energy relaxation time compared with bulk GaAs at these temperatures apparently occurs because the donors and the electrons are well separated due to the modulation-doped structure of the material, hence energy relaxation within the band (actually sub-band(s)) dominates. There is thus a very real advantage to using the heterostructure configuration in this case, in that a much wider

bandwidth should be feasible, as compared with bulk GaAs. At somewhat higher temperatures, 50 to 150 K, Shah found energy relaxation times of about 10^{-11} to 10^{-10} s [8]. At these temperatures, Shah found evidence for some lengthening of τ_e due to accumulation of optical phonons at the specific energy of about 36 meV (a so-called "hot phonon" effect). Due to this phenomenon, τ_e is shorter in material with a lower surface density of electrons, n_s , while at the lower temperatures the opposite dependence on n_s is obtained [7]. In both temperature ranges, the 2DEG medium should achieve bandwidths of the order of 1 GHz or greater, providing the solution for the longstanding problem of the narrow bandwidth of bulk semiconductor mixers. The 2DEG material systems have the further advantage that many different combinations of materials are feasible. They are the subject of an intensive research effort at present, so that considerable information is available on most aspects of physics and fabrication.

Recently, hot electrons have also been studied in thin films of superconductors [9,10]. These studies have shown that the energy relaxation time for Nb is such that bandwidths of the order of 100 MHz are feasible, while wider bandwidths should be possible in NbN, as well as in YBCO. Intrinsic mixer conversion loss of close to 0 dB and bandwidth of 40 MHz were deduced from measurements at about 140 GHz.

A distinct mode of operation of a superconducting film mixers is being pursued by Grossman et al., see another paper at this conference. A range of materials and modes of operation for hot electron mixers with much improved bandwidth capability thus is now available. Only detailed future studies will show which of these materials that is optimum for a THz hot electron mixer.

Two-Dimensional versus Three-Dimensional Geometry

The original bulk hot electron mixer device consisted of a bar of InSb across a waveguide. The device impedance needs to be matched to the microwave circuit, and this can be accomplished by adjusting the length to cross-sectional area ratio, once the carrier concentration and and mobility are given. The minimum size is determined by fabrication considerations, as well as the need to fit the device into the waveguide. Devices used in practise [2] contain close to 10^{10} electrons. In the 2DEG case, the device resistance (R_B) is

$$R_B = (L/W) * (1/en_s\mu) \qquad (2)$$

Here, L and W are the length and width of the active region, n_s is the density in carriers per cm^2, and μ the mobility in cm^2/Vs. It is easy to adjust L/W by using photolithography, and a number of devices with the same resistance which matches the microwave circuit are possible. Specifically, the total number of electrons in a

typical device is smaller ($\approx 10^6$). Less power is then required to drive the device nonlinear by heating the electrons, since the power loss per electron at a given temperature is basically a materials constant. This fact probably explains why a bulk GaAs hot electron device at 50-100 K may be difficult to realize.

Conversion Loss

The conversion loss for bulk semiconductor mixers was derived by Arams et al. [11]. We have extended their treatment to include some further effects, such as the finite reflection loss of a practical mixer ($T_0 = 1 - |\Gamma_0|^2$) [12]. The equivalent circuit of the device is shown in Figure 5. When the conversion loss, L_c, is optimized with respect to the ratio P_{DC}/P_{LO}, as well as the IF load impedance, R_L, one finds [12] :

$$L_c = 8\left(\frac{R_{Bo}}{T_o C P_o}\right)^2 \left[\frac{(R_L+R_{Bo})^2}{4R_L R_{Bo}}\right]\left[1 - \frac{CP_o}{R_{Bo}}\left(\frac{R_L - R_{Bo}}{R_L + R_{Bo}}\right)\right]\left\{1 + (\omega_{IF}\,\tau_e)^2\right\} \qquad (3)$$

We have introduced R_{Bo}, which is the device resistance at an equivalent operating point for which the DC power is equal to the total dissipated power (P_o) at the mixer operating point, i.e. $P_o = P_{LO} + P_{DC}$. Also, the factor C is defined as (compare Figure 2):

$$C = dR/dP \qquad (4)$$

The microwave circuit impedance Z_o, typically 100 ohms, is used to calculate T_o. The optimum value for L_c is 6 dB, which should be compared with 3 dB for a double-sideband Schottky-barrier diode mixer. SIS-mixers can have some conversion gain.

In order to compare calculated and measured conversion loss, one needs to perform a slightly different calculation than the one in (3), which assumes that the mixer has been optimized at all points of a curve of, say, L_c versus P_{LO}. An actual measured curve would represent L_c as a function of either P_{LO} or I_{DC}, with the other variable held constant. To perform this calculation, one finds it necessary to iteratively search for the correct operating point [12]. Data calculated using this method will be presented in the experimental section.

III. MATERIALS GROWTH AND DEVICE FABRICATION

2DEG Device Structure

A simple two-terminal device structure has been developed, which is shown in Figure 6. The sequence of epitaxial layers is the

same as is used for AlGaAs/GaAs HFET devices. Mesas are etched with a height of about 1.5 micrometers. The 2DEG sheet is then located within the mesa, which is surrounded by semi-insulating GaAs for isolation of the devices. The metalization of the devices consists of a standard sequence of evaporated layers for forming AuGe ohmic contacts, and the device pattern is then defined by a lift-off process. Typically, gold plating was used for building up the metalization to sufficient thickness. There is a thin top layer of highly doped GaAs which facilitates the formation of good ohmic contacts. This layer has to be etched off after the devices have been defined. The wafer was finally thinned to about 125 micrometers, and a small chip cut out by first scribing the wafer. The IV-characteristic was measured by probing the individual devices, which have sufficiently large contacts pads.

Materials Growth

The epitaxial layers are grown with low pressure MOCVD on undoped semi-insulating GaAs (100) substrates oriented 2 degrees off towards the (110) planes to achieve better morpology of the epi layers. The sources used were trimethylaluminum, trimethylgallium, 100% arsine, and silane as the n-type dopant. Further details of the process can be found in our paper at the previous conference. We have also utilized material grown by MBE, courtesy of Dr. D. Masse', Raytheon Company, Lexington, MA. The maximum mobility for both types of materials is quite similar, as shown in Figure 7.

IV-Characteristics

The Type I mixers were biased to the region indicated in Figure 7, where it may be noted that the mobility is a strong function of lattice temperature in this region. It may be assumed that the mobility as a function of *electron* temperature follows essentially the same curve [8]. We may then conclude that the IV-characteristic will tend to "saturate", as the electrons heat up when the voltage is increased. We show measured curves att low temperatures for three different devices in Figure 8. Dimensions and other data for the devices are given in the caption of this figure. The curves can be modeled with an analytical expression, which is useful in calculating data such as conversion loss:

$$I = \left(\frac{2I_o}{\pi}\right) \tan^{-1}(\alpha V) \qquad (5)$$

IV. EXPERIMENTS

Experimental setup

Two different experimental setups were used: (1) A liquid helium dewar with built-in superconducting magnet. (2) A

mechanical refrigerator which could provide temperatures to about 20 K. In both cases, the devices were mounted as flip-chips on a circuit etched on a Duroid 5880 substrate, which was inserted into a split-block mixer mount. The Duroid substrate is not ideal for low-temperature experiments, but was used for ease of fabrication and assembly. Improved mixer circuits on silicon substrates are under development [13], and will be used in the future. RF and LO power were fed to the mixer through a stain-less steel waveguide, which was connected to the mixer block. The circuit inside the mixer block was essentially a finline transition, with the device soldered across the narrow part of the finline. One side of the finline had to be insulated, to allow the device to be biased. The IF was extracted from the device through a simple transition to a coaxial cable.

Measurements on the Type I mixer

The Type I mixer was typically measured at about 20 K. The conversion loss is essentially independent of the lattice temperature over a wide range, up to about 100K, so the exact temperature of operation is not important. The RF power (from a GUNN source) at the mixer block input was carefully calibrated with a power meter. The IF power was measured with a spectrum analyzer, which was also calibrated with a power meter. The measured numbers represent the conversion loss from the input of the block to the IF output connector near the block. As the LO, we either made use of another GUNN source, or (for higher power) a BWO.

The first measurement of the Type I mixer was performed in the 4.2 K setup. It should be realized that the electron temperature is about the same, independent of the lattice temperature: we estimate a value of $T_e \approx 85$ - 90K at the operating point. The conversion loss in the first measurement was 30 dB. The normalized response versus IF frequency is displayed in Figure 9, which also shows the normalized response of InSb and GaAs bulk mixers as measured by others [2,3]. It is clear that the 2DEG mixer provides a roughly three orders of magnitude increase in bandwidth compared with previous hot electron mixers. The 3 dB bandwidth is 1.7 GHz. Subsequent measurements at about 20 K have consistently shown the same bandwidth, but the minimum conversion loss has been improved to 18 dB.

The conversion loss has been calculated for two devices, with IV-curves as shown in Figures 8(a) ("4.2K mixer") and 8(b) (19K mixer"), respectively. Figure 10 shows the calculated conversion loss as a function of LO power (curves), compared with the measured data (points). The agreement is good, and indicates the validity of using our theoretical approach. In Figure 11, calculated and experimental data for L_c versus I_{DC} are compared. Again, the agreement is good, with a small shift of the current scale at low currents. The minimum conversion loss is well predicted. The increased conversion loss for the 19K mixer at high bias currents may be due to lattice heating: the dissipated DC power at the highest current (10 mA) is about 200 mW! One general trend in comparing

different devices, is that a device with low maximum (saturated) current requires less LO power to drive to optimum conversion loss. It is clearly also advantageous to have a high initial slope for the IV-curve. The latter requirement can be satisfied by making the device wide, but this will lead to a larger saturation current. It si preferable to use a narrower device, and to maximize the initial slope by choosing material with high mobility, as well as by keeping the contact resistance as low as possible In the devices tested so far, the contact resistance appears to limit the value of the initial slope, and future devices are expected to yield considerably lower conversion loss. Another effect, which we have noticed, is that the initial resistance increases after the device has been soldered into the circuit. It is thus reasonable use the calculated conversion loss for the best device which we believe is feasible to fabricate, as an indication of the performance which should be feasible. The optimum conversion loss for such a "next generation" device is given in Figure 12. Note that both the conversion loss and the optimum LO power have been improved considerably.

Measured Results for the Type II Device

As mentioned earlier, the Type II device is expected to operate at about 4.2K, and be biased by a magnetic field. We have demonstrated a Type IIa detector at 94 GHz, similar to the one described by Smith, Cronin et al. [4], as shown in Figure 13. The peak response occurs at about the expected magnetic field for cyclotron resonance.The measured responsivity is about 1V/W, which is much lower than obtained by Cronin's group (about 250 V/W)[14]. The reason for the lower responsivity is very much an open question at this stage; it may, for example, be due to differences in the materials used. We have measured a larger responsivity (5-10 V/W), at both 94 and 238 GHz, in a newly discovered mode (Type IIb) at higher magnetic field, see Figure 14. The device in this case was severely mismatched to the microwave circuit due to its very high resistance at high magnetic fields ($\approx 2k\Omega$). We can therefore estimate that the responsivity in this mode may be increased to at least 50-100 V/W. The frequency independence of the responsivity up to 238 GHz is also noteworthy. The detection mechanism is again not yet known [12], but it is likely to involve transitions between (spatially) extended and confined states, which have been studied extensively in other work on the Shubnikov-deHaas and Quantum Hall effects.

We attempted to demonstrate mixing in both of the above Type II devices, but were not successful in doing this. One indication that this negative result is not unexpected can be obtained by using the following expression for the optimum conversion loss, derived in [11]:

$$L_{min} = 4\left[\frac{R_{Bo}}{CP_o}\right]^2\left[1 + \sqrt{1 - \left(\frac{CP_o}{R_{Bo}}\right)^2}\right] \qquad (6)$$

where the quantity in square brackets can also be written:

$$\left(\frac{R_{Bo}}{CP_o}\right) = 1 + \frac{1}{I_o \Re_o} \qquad (7)$$

Here, $\Re_o$ is the responsivity of the device as a detector at an equivalent bias current $I_o = \sqrt{\frac{P_o}{R_{Bo}}}$. For a responsivity of 10 V/W at a bias current of 10 μA, we predict $L_c \approx 86$ dB, which would not have been measurable. Further work on Type II mixers then needs to emphasize attaining an increased responsivity in the detector mode.

V. POTENTIAL OF HOT ELECTRON MIXERS FOR THZ FREQUENCIES

General Discussion

We have seen in the previous section that it is reasonable to assume that the conversion loss of the Type I mixer may be decreased toward the 10 dB level. In order to estimate how these results at 94 GHz will scale with frequency, we must investigate how the absorption of the 2DEG varies with frequency. As discussed at the previous conference, high mobility (i.e. long momentum relaxation time, τ_m) media, such as the 2DEG, will show evidence of charge carrier inertia at lower frequencies than one expects for typical semiconductors. At the electron temperature of 90 K, representative of the operating points for 2DEG Type I mixers, one may expect the $\omega\tau_m = 1$ point to occur at about 100 GHz. The equivalent circuit of the device (see Figure 15) then incorporates an inductance with a reactance of close to 100 ohms. At higher frequencies, it will become necessary to resonate out this reactance by inserting a monolithic capacitor in series, as also shown in this figure. Of course, other circuits may be used to match to the 2DEG device, such as a back-short in a waveguide, etc, but monolithic circuit should yield the widest bandwidth. A different approach may be to find other material combinations which show the required nonlinearity, but with a lower maximum mobility, so that the reactance is minimized. We are pursuing microprobe measurements of 2DEG devices at frequencies up to 40 GHz in order to build up a base of information for designing matching circuits for 2DEG mixers at the higher frequencies [13].

Estimated Noise Temperature of Hot Electron Mixers

We may roughly estimate the expected noise temperature of a hot electron mixer by assuming that a conversion loss of 10 dB is

achievable, and that the effective temperature of the device is equal to its electron temperature. A cooled IF amplifier with a noise temperature of 10K is also assumed. We then obtain:

$$T_R \approx L_c * T_e + (L_c-1) * T_{IF} \approx 1000K \quad (8)$$

This receiver noise temperature would be competitive at frequencies in the 500GHz to 1THz range. Hot electron mixers which operate at lower electron temperatures would have a potential for even lower noise temperatures. This is one of the reasons for continuing to pursue the development of the Type II mixers. It may be noted, though, that even a mixer with T_R = 1000K at close to 1THz, developed from the present 94 GHz prototype, may be a very good choice, since it may only require cooling to 50-80K.

VI. CONCLUSION

For many years, hot electron mixers have been known to be capable of achieving very low noise temperatures, even up to frequencies close to 1THz, but with only about 1 MHz bandwidth. In our work with a 94 GHz 2DEG hot electron mixer, operating at 20K, we have for the first time demonstrated a hot electron mixer with a bandwidth, which is sufficient for all typical applications in the THz range. This type of hot electron mixer has the same advantages of low parasitics as the InSb version, but with added features such as potential for monolithic integration with the IF amplifier and antennas, etc. Further development should demonstrate the eprformance of this type of mixers at higher frequencies, and with lower conversion loss. Noise temperature measurements will be performed in the near future, which will enable us to make a firmer estimate of the noise temperatures which can be achieved at higher frequencies. Finally, we note that wide bandwidth hot electron mixers may be the general rule, not the exception, as one may have been tempted to think based on the earlier results achieved by InSb and GaAs bulk mixers. Many different 2DEG media exist, which could potentially be more optimum than the one we have started with. Further striking evidence is provided by the results with superconducting film hot electron mixers [9,10]. A final tabulation compares different hot electron mixers, see Table 1. The evidence from these efforts supports the notion that the hot electron mixers will find a niche of applications in the THz range.

VII. REFERENCES

[1] Yang, J.-X., Grammer,W., Agahi,F., Lau,K.-M., and Yngvesson, K.S. "Two-Dimensional Electron Gas ("2DEG") Hot-Electron Mixers for Millimeter Waves and Submillimeter Waves," Second International Symposium on Space THz Technology, JPL, 1991, p.353.

[2] Brown, E.R., Keene, J., and Phillips, T.G., "A Heterodyne Receiver for the Submillimeter Wavelength Region Based on Cyclotron Resonance in *InSb* at Low Temperature," Intern.J.Infrared and Millimeter Waves, 6,1121, (1985).

[3] Fetterman, H., Tannenwald, P.E., and Parker, C.D., "Millimeter and Far Infrared Mixing in GaAs," Proc.Symp.SMM Waves, PIB, New York (1970).

[4] Smith, S.M., Cronin, N.J., Nicholas,R.J., Brummel, M.A., Harris, J.J., and Foxon, C.T.,"Millimeter and Submillimeter Detection Using $Ga_{1-x}Al_xAs$/GaAs Heterostructures," Intern.J.Infrared and Millimeter Waves, 8,793(1987).

[5] Seeger, K.,"Semiconductor Physics", Fourth Ed.,Springer Verlag, Berlin (1989), see for example p.102 and p.198.

[6] Conwell, E.M.,"High-Field Transport in Semiconductors," in Solid-State Physics, Suppl.,Vol.9, Academic Press ,New York (1967).

[7] Sakaki, H., Hirakawa, K., Yoshino, J., Svensson, S.P., Sekiguchi, Y., Hotta, T., and Nishii, S. "Effects of Electron Heating on the Two-Dimensional Magnetotransport in AlGaAs/GaAs Heterostructures," Surface Science,142,306 (1984).

[8] Shah, J., "Hot Carriers in Quasi-2D Polar Semiconductors," IEEE J.Qu. Electronics, QE-22, 1728 (1986).

[9] Gershenzon, E.M., Gol'tsman, G.N., Gousev, Y.P., Elant'ev, A.I., and Semenov, A.D., "Electromagnetic Radiation Mixer Based on Electron Heating in Resistive State of Superconductive Nb and YbaCuO Films," IEEE Trans. Magnetics, MAG-27, 1317 (1991).

[10] Kozyrev, A.B., Samoilova, T.B., Soldatenkov, O.I., and Vendik, O.G., "Destruction of Superconducting State in Thin Film by Microwave Pulse," Solid State Communications, 77,441 (1991).

[11] Arams, F., Allen, C., Peyton, B., and Sard, E.," Millimeter Mixing and Detection in Bulk InSb," Proc. IEEE,54,612 (1966).

[12] Yang, J.-X., "AlGaAs/GaAs Two Dimensional Electron Gas Devices: Applications in Millimeter and Submillimeter Waves, " Ph.D. Thesis, University of Massachusetts (to be publ.).

[13] Grammer, W., M.Sc. Thesis, University of Massachusetts (to be publ.).

[14] Cronin, N.J., University of Bath, Priv. Comm.

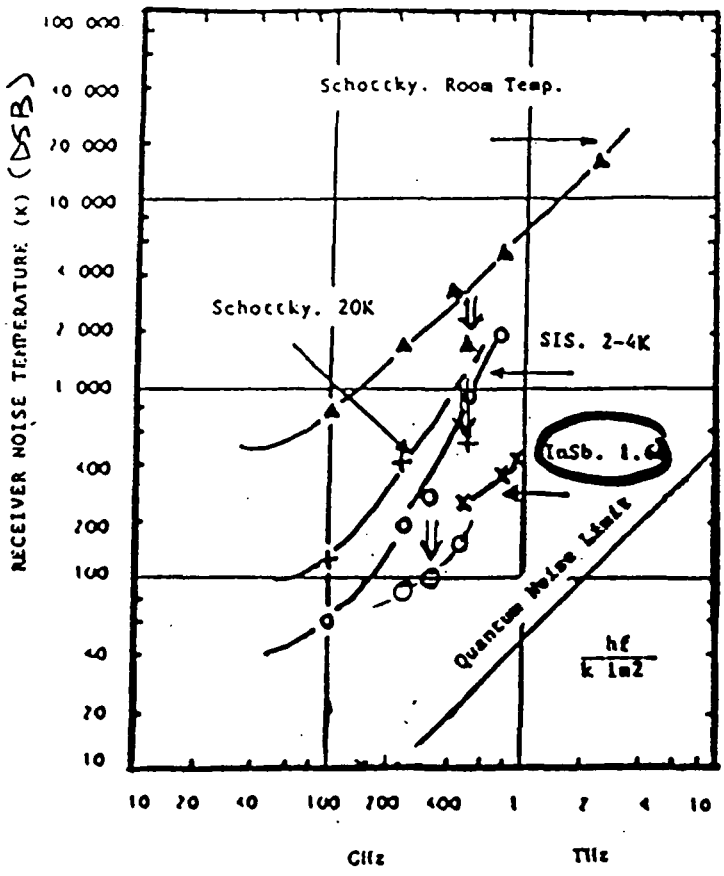

Figure 1. Receiver noise temperatures in the MM and Sub-MM range, versus frequency. The data for Schottky barrier diodes were originally compiled by E.L. Kollberg, and the SIS data by P.L. Richards. The InSb noise temperatures are from Brown et al. [2] .Some more recent data from this conference have been added (see arrows).

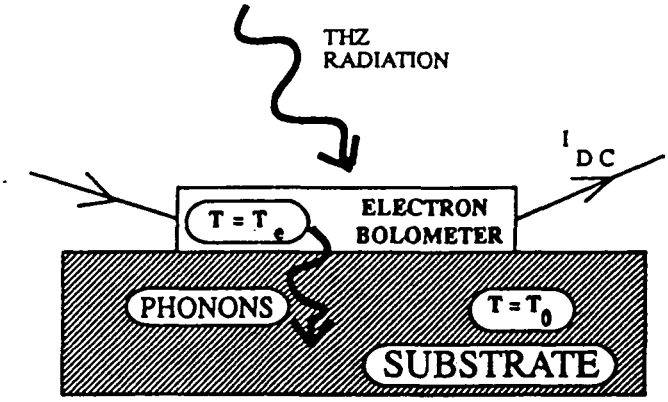

Figure 2. Schematic drawing of a generic electron bolometer device.

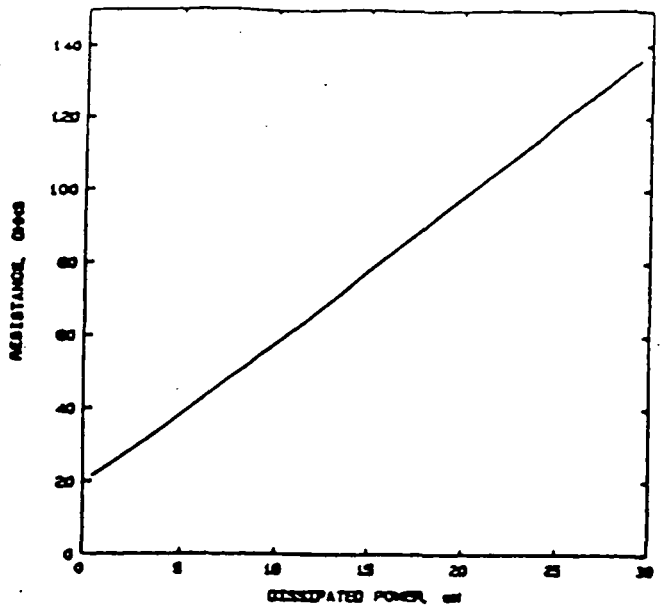

Figure 3. Typical curve of $R_B = R_B(P)$ for a 2DEG device.

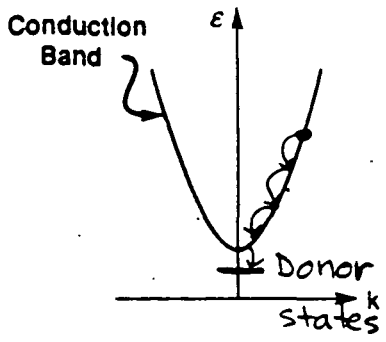

Figure 4. Energy relaxation proce in a semiconductor.

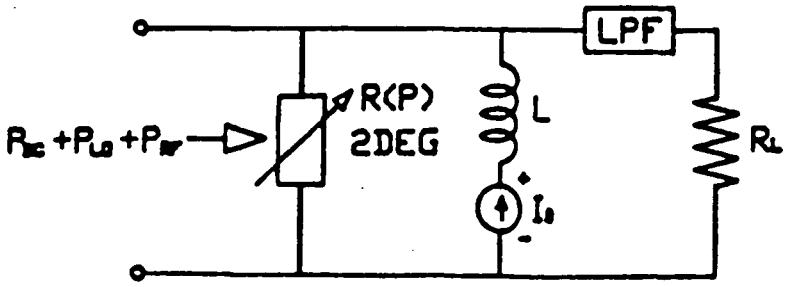

Figure 5. Equivalent circuit a hot electron mixer device.

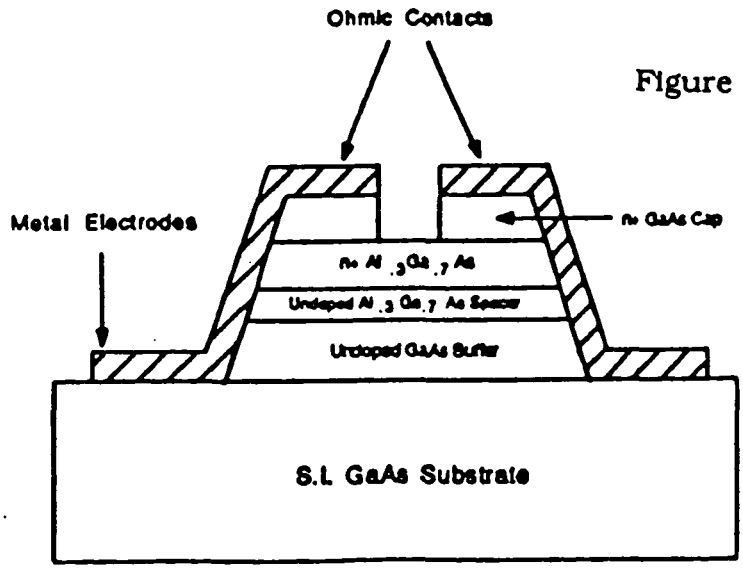

Figure 6. Structure of the 2DEG device.

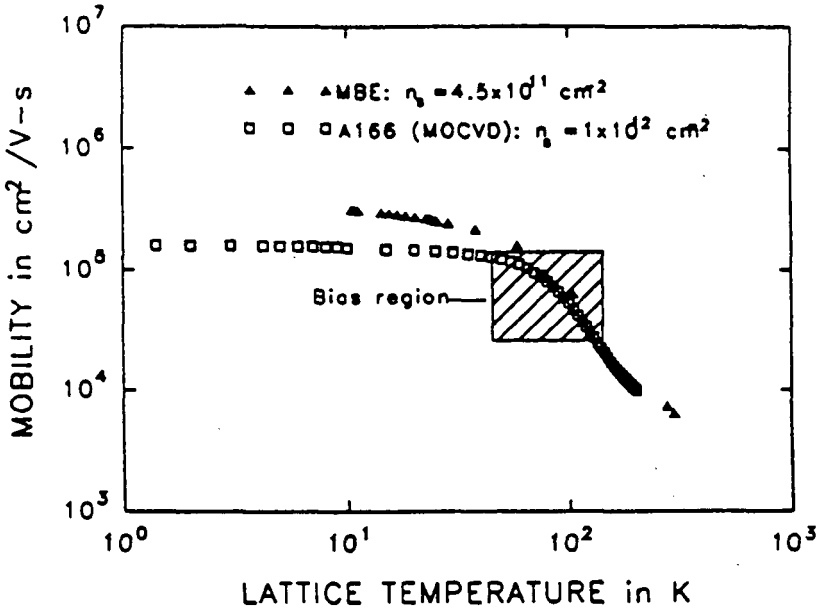

Figure 7. Mobility versus lattice temperature for two 2DEG devices.

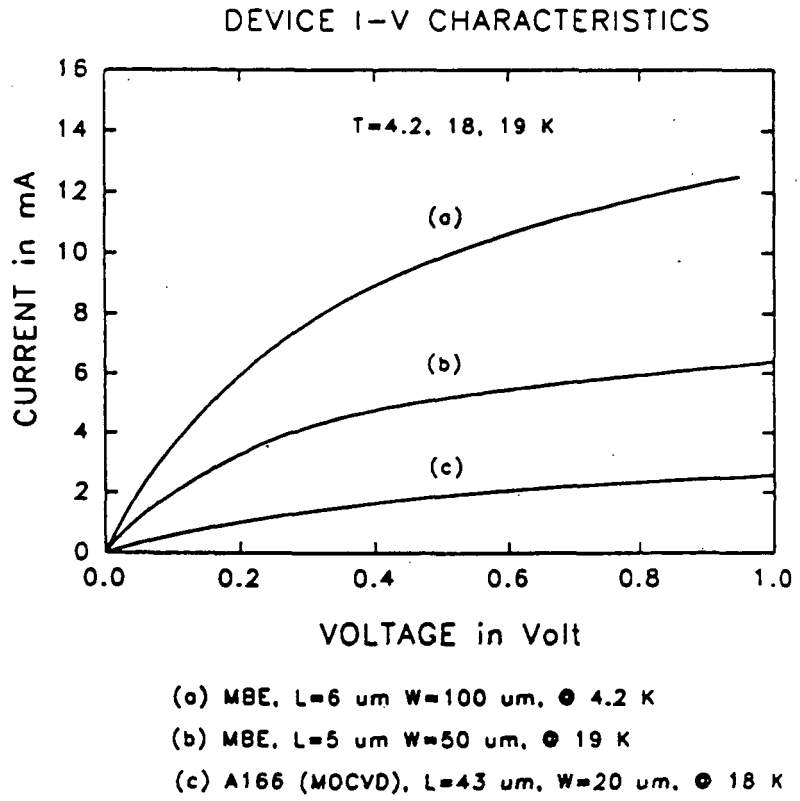

Figure 8. Measured IV-curves for three 2DEG devices.

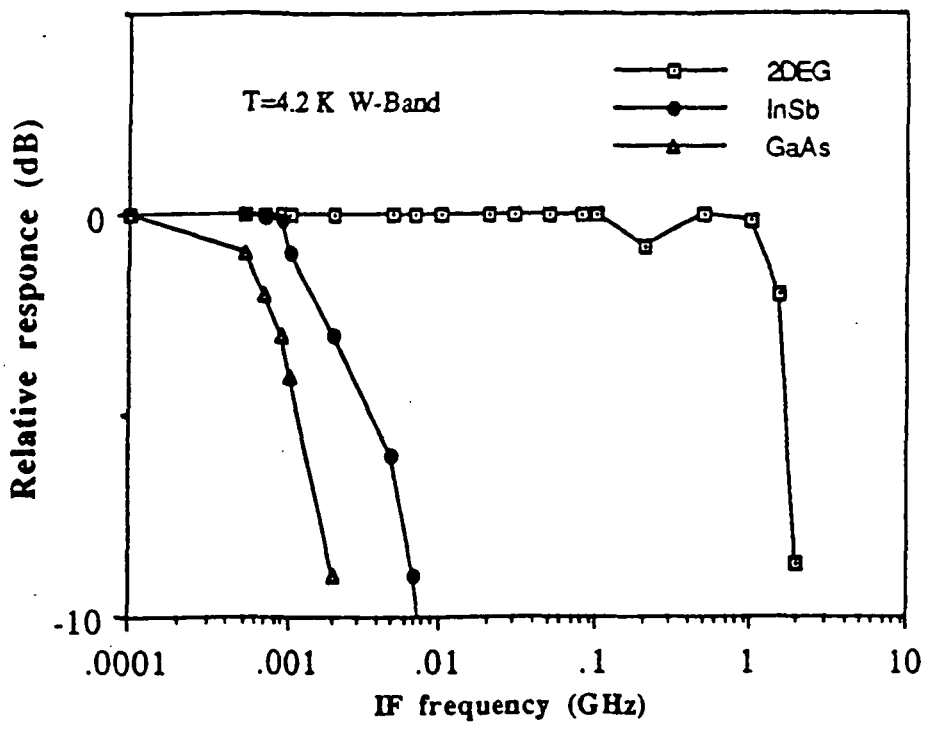

Figure 9. Normalized IF response for the 2DEG mixer, compared with InSb and GaAs bulk mixers.

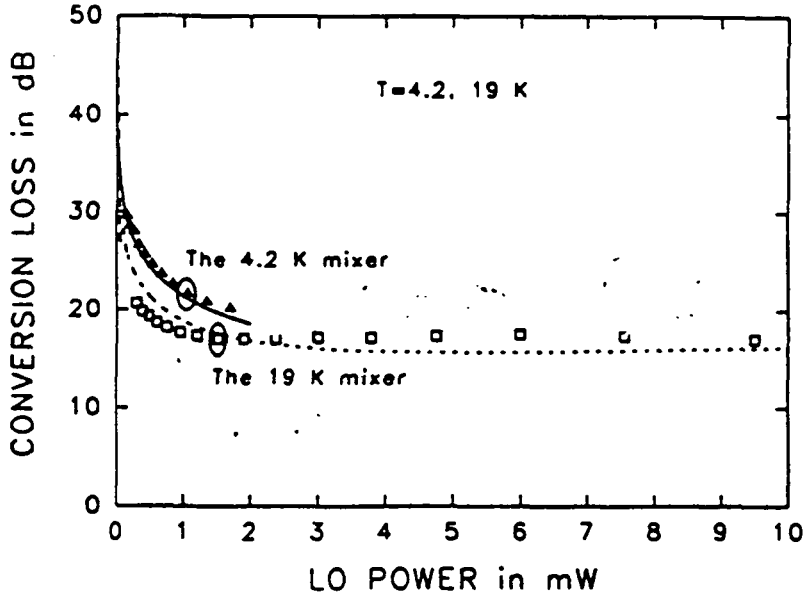

Figure 10. Calculated and measured conversion loss for two 2DEG devices, versus LO power.

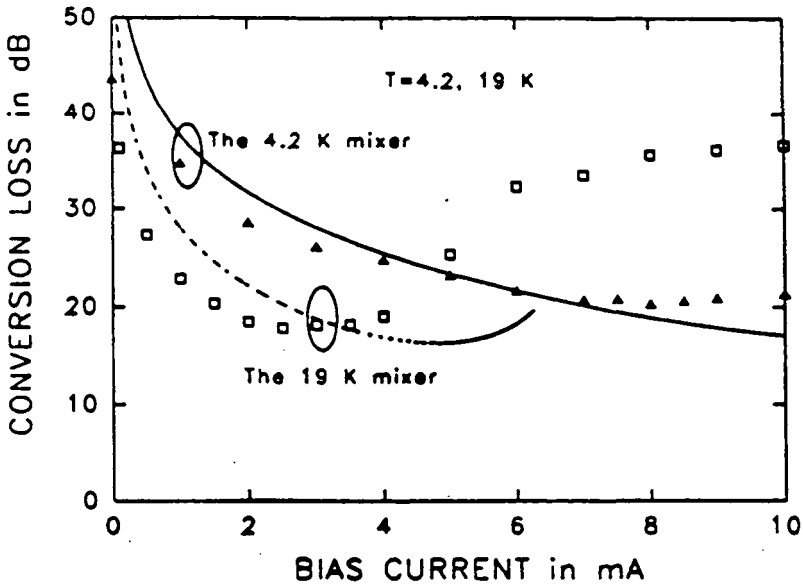

Figure 11. Calculated and measured conversion loss for two 2DEG devices, versus DC bias current.

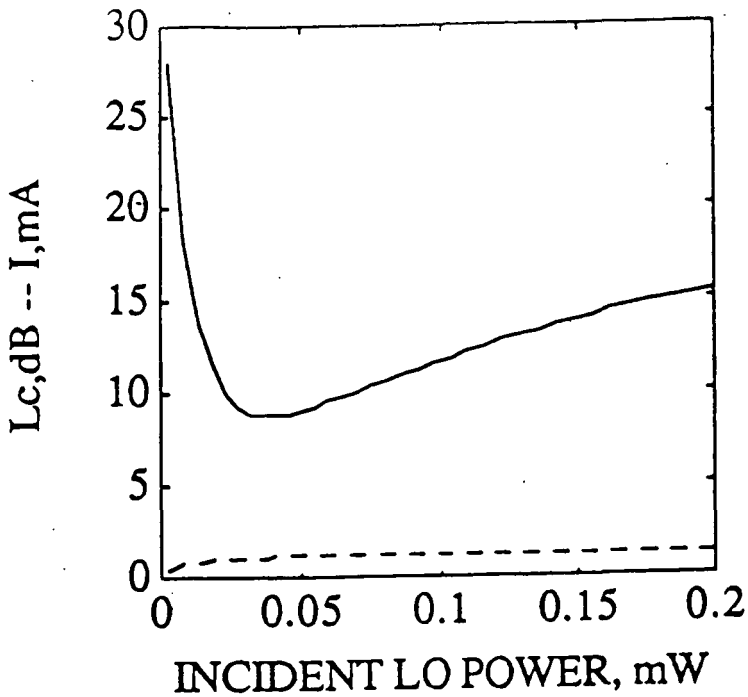

Figure 12. Calculated conversion loss for an "optimum" next generation 2DEG device.

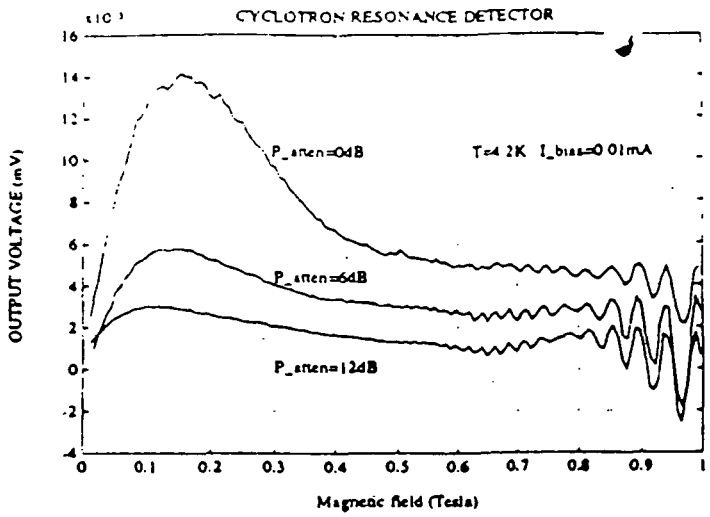

Figure 13. Detected voltage versus magnetic field for a Type IIa 2DEG device operating as a straight detector at 94 GHz.

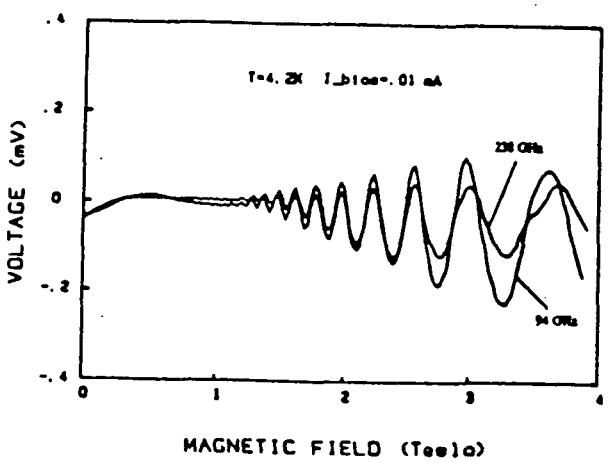

Figure 14. Measured detected voltage output versus magnetic field from a TypeIIb 2DEG device, operating as a straight detector at 94 and 238 GHz, respectively.

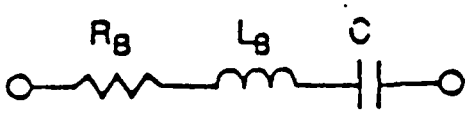

Figure 15. Equivalent circuit of a 2DEG device, including a matching capacitor in series.

COMPARISON OF DIFFERENT HOT ELECTRON MIXERS

MIXER TYPE		BAND-WIDTH	CONVERSION LOSS	T_R . KELVIN
SEMI COND.	InSb	1 MHz	≈ 12 dB	300-500
SEMI COND.	2DEG 20/50 K	2 GHZ	18 dB (meas.) 10 dB (proj.)	1000 ?
SEMI COND.	2DEG 4.2K, MAGN. FIELD	1-2 GHZ (proj.)	10-13 dB (proj.)	300-500?
SUPER COND.	Nb (meas.)	100 MHZ	7.5 dB *	?
SUPER COND.	NbN (proj.)	Several GHz	? MIXING MEAS. AT 1.5 GHz **	?
SUPER COND.	YBCO (proj.)	Several GHz	12 dB (meas. at 2 GHz) ***	?
SUPER COND.	Nb, Nonl. Ind.**** (proj.)	200MHz -1GHz		70,000 @3THz Alloys lower

*) Gershenzon et al., IEEE Trans.Magnetics, MAG-27,1317 (1991) [9]

**) O. Vendik, Priv. Comm.

***) Kolesov, Chaloupka, et al., to be published, 1992

****) Grossman et al, this conf.

ALL-SOLID-STATE RADIOMETERS FOR ENVIRONMENTAL STUDIES TO 700 GHZ

Ralph, Rüdiger and Peter Zimmermann
RPG Radiometer-physics GmbH
5309 Meckenheim, Germany

ABSTRACT

We report results with an all-solid-state radiometer for measurements of the ClO molecule at 649 GHz. The project is part of a program to provide low-noise, low-weight, low-power radiometers for space operation, and special effort has been expended on the development of high-efficiency solid-state frequency multipliers and Schottky-barrier mixers with low local oscillator power requirements.

The best measured system noise temperature was 1750 K with the mixer and preamplifier cooled to 77 K. The mixer diode was easily pumped into saturation, indicating that the design has excellent prospects of operating at higher frequencies - our present design goal being 1 THz. We comment on the principal design features of such systems and will report on stratospheric measurements performed with this system.

INTRODUCTION

All solid-state radiometers in the frequency range 60-560 GHz have been reported [1], [2], [3], [4], and the measured parameters for the highest frequency receivers are tabulated in Figure 1. The ever-increasing

importance of atmospheric investigations in the higher sub-millimeter wavelength-range has led to a consolidated program to reach 1 THz with such instruments. To this end a radiometer (s. Fig.2) has been constructed for the detection of the ClO molecule at 649 GHz; this is the subject of this paper.

The three principal sections of the system are the optics, the all solid-state local oscillator and the low-noise mixer-preamplifier.

QUASI-OPTICS

At frequencies above 200 GHz the losses of waveguide components are too high for sensitive radiometers, and quasi-optical systems become increasingly compact. The prime component requirements for coupling the antenna and local oscillator into the mixer are high efficiency feed-horns, precisely machined ofset-mirrors and low-loss wire grids for polarising couplers and filters. All mirrors are ellipsoids, whilst grids comprise 20 µm diameter tungsten wire with 50 µm spacings (between centres). For IF bandwidths $\Delta f/f \leq 0.5$ the Martin-Puplett coupler is preferred.

Figure 2 shows the total front-end schematic, including a single-sideband filter and path-length modulator (from University of Bremen, to be reported at this conference). The quasi-optical beams, beam-waist locations and sizes are also shown. The feedhorns in this receiver are dual-mode horns as shown schematically in Figure 3 [5] . These horns have been measured at lower frequencies and have in all cases symmetrical near gaussian beam-patterns, to at least -15 dB. The losses of the optics plus feedhorns were measured by connecting the output of the frequency multiplier

directly to the mixer, and then feeding the l.o. to the mixer via the two horns and the quasi-optics: the loss was around 1 dB.

LOCAL OSCILLATOR

The local oscillator power requirement for a mixer depends strongly on the diode quality and on the mixer mount- and coupling-losses between source and mixer. Particularly in the submillimeter-range these parameters are not easy to determine. By extrapolating from lower submillimeter-wavelength, we estimate the l.o. power requirement to be in the range 100 µW to 1 mW for a cooled mixer. The requirement was to build an all solid-state source for later space application.

In this paper the source comprises a Gunn oscillator, a waveguide cross-coupler plus harmonic mixer, a waveguide frequency doubler and tripler. All components are directly connected together, to reduce losses (Figure 4).

(a) Gunn-Oscillator

A Varian InP Gunn diode is mounted into a WR-8 waveguide (Figure 5). Bias is supplied to the diode via a coaxial low-pass filter held by teflon spacers.

The frequency is pretuned by a cap-resonator, fine adjustment over several GHz being provided by a dielectric tuning rod sliding under the cap. A waveguide back-short allows adjusting for maximum power. The power output is shown in Figure 6.

(b) Frequency Multiplier

There are several possibilities of attaining power at 650 GHz from a solid source followed by a multiplier. Gunn oscillators deliver output power up to 50 mW at frequencies up to 115 GHz. For this reason a sixtupler seems a natural choice. Though we build one with ~100 µW output power, it was very difficult to tune, as several idlers had to be optimised simultaneously. The better choice is a doubler-tripler or tripler-doubler combination, where each stage can be developed separately. Calculations using the program by Siegel et al. [6] showed that the doubler-tripler combination should result in higher efficiency; hence this combination was chosen.

To facilitate easy system construction and testing, especially for the case of cascaded multiplication stages, Radiometer-physics developed in 1987 "in-line" waveguide frequency multipliers (Figure 7). This means, that input- and output-waveguide are in-line, compared to the standard crossguide-type structure.

A schematic for both multipliers is shown in Figure 8. Input power is coupled from the input waveguide via a probe and coaxial filter to the diode which is part of the last section of this filter. The filter is of the low-pass Tchebycheff-type and has been modelled a lower frequencies. Probe and diode are located in the bend of input- and output-waveguides respectively.

The DOUBLER input waveguide dimensions are 2.0x1.0 mm, which are tapered to 2.0x0.5 mm at the probe. The dimensions of the output waveguide are 0.6x0.3 mm Backshorts are provided for tuning. The diode is a 6P4 from University of Virginia, with the following DC-parameters R_S = 12 ohm , C_j = 18 fF, V_{br} = 20 V. It is contacted by a whisker of length 0.3 mm and diameter 25 µm.

With 50 mW input signal an efficiency of 20% was achieved, compared with a theoretical efficiency of 37%. Power was measured with a Hughes Thermistor mount at the input. Output power was measured with an Anritsu power head 140-220 GHz with a tapered transition to match the input waveguide of the multiplier

The TRIPLER input and output waveguide dimensions are 0.6x0.3 mm and 0.4x0.2 mm respectively. It operates with a diode 2T2 again from University of Virginia. Its DC-characteristics are C_j = 6.0 fF, R_S = 12 ohm, V_{br} = -11V. The whisker is 0.2 mm long, with 12 µm diameter. An important feature of the tripler is the idler tuning circuit in form of a stub waveguide with a moving short. The output waveguide contains a short section of reduced-width waveguide to prevent idler propagation to the output. Low frequency modelling was important in attaining optimum waveguide dimensions. The output power achieved was 300 µW, which means an efficiency of 3% compared to 17% theoretical.

The measurement of output power in the range 600-700 GHz is not trivial, and caution should be taken in specifying power at such high frequencies - in particular the power standards should be quoted. In our case relative measurements were performed using the same Anritsu thermistor power-head as for the doubler, with appropiate waveguide transitions. The absolute power output was then measured with the Queen Mary College acoustic calorimeter at 624 GHz, where an absolute calibration exists: this showed that the absolute power from the l.o. input is about three times greater than the Anritsu reading. Hence to a first approximation we can multiply all Anritsu readings by factor 3. Absolute measurements were also performed at 690 GHz with a similar frequency multiplier chain, whereby 30 µW were measured with the Anritsu head and 90 µW with the QMC instrument - once again a factor 3.

It is relevant to draw attention to the problems arising due to using different lower frequency thermistor heads, this is illustrated in Figure 10 for three measurements from a 345 GHz frequency multiplier. -

To show the possibilities of achieving l.o. power from solid-state sources in the submm-range we have included Figure 10.

MIXER

The mixer is shown schematically in Figure 11. The dual-mode horn is identical to that used for the l.o. output. The waveguide dimensions are 0.6x0.2 mm and the contacting back-short is gold-plated beryllium-copper. The diode chip (type 1T6 from the University of Virginia) is mounted on the coaxial choke structure, as shown in Figure 12. The chip is turned down to a cylindrical form and gold plated on the cylindrical surface, so that the chip is also the first choke-section. It is seen that the choke is supported by a Macor disc: the dimensions of this disc are important for obtaining a broad i.f. bandwidth. The calculated impedance of the choke is shown in Figure 14 from d.c. to 1100 GHz. Figure 15 shows the measured output impedance of the mixer across the i.f. band 9-11 GHz, without and with an i.f. matching transformer

The 1T6 diode has the following d.c.-characteristics: R_s = 30 ohm C_{jo} = 0.35 fF, V_{br} = -6 V. The whisker is of gold-plated phosphorbronze, diameter 7 µm; the total whisker length is 0.2 mm, and includes a loop to take up slight changes in waveguide and choke dimensions on cooling the mixer to 77 K. To test that there was adequate l.o. power the diode was biased at room-temperature to 0.86 V, whereby the diode drew a current of

10 μA without l.o. and >600 μA with l.o.: hence there was adequate l.o.-power for optimum mixer operation.

SYSTEM RESULTS

The system was tested using standard hot-cold foam absorbers from Emerson and Cuming at the input to the diplexer for DSB- and at the input to the SSB-filter for SSB-measurements. In the final configuration the cold image termination was replaced by an absorber for constructional reasons, without any appreciable sacrifice of performance.

The cryogenic i.f. preamplifier was developed at Chalmers Technical University and had a noise temperature of 35 K at 77 K ambient. All other i.f. components preceding the spectrometer were commercially available.

Double-sideband system tests with a 2 GHz i.f. bandwidth yield the following results:

Tamb	Tsys	Tm	Lo
300 K	3800 K	1900 K	8.0 dB
77 K	1750 K	(1500 K)	(8.0 dB)

Tsys-values are measured directly, whilst T_M and L_M are corrected for residual power mismatch of 0.15, and we assume the same conversion loss at 77 K ambient.

For single-sideband system tests the SSB-filter was adjusted by using a tunable Gunn-oscillator and multiplier chain, identical to the l.o. chain and a spectrum analyzer. The sideband rejection was at least 25 dB.

The result was:

T_{usb} = 3800 K at 77 K

More than adequate l.o. power was available to reach minimum Tsys. It was noted that the noise temperature was fairly insensitive to changes in diode current in the range 400-800 μA.

The system has been flown on an aircraft contracted by the University of Bremen. A first uncorrected result shows the ClO line in Fig. 15.

PROSPECTS

It appears reasonable to expect spaceborne all-solid-state radiometer system to be feasible at least to 1 THz, using only waveguide techniques. Calculations using the computer model of Siegel and Kerr yield l.o. output powers of 360 μW at 1 THz; taking into account losses this still implies that sufficient l.o. power will be available at 1 THz to pump a Schottky-barrier mixer diode; such a development program has commenced at Radiometer-physics. Since completing the 650 GHz system new Schottky-barrier mixer diodes have been reported [7], [8]. Hence, with improvements in multiplier- and mixer-technology it should be possible to operate such systems at even higher frequencies.

ACKNOWLEDGEMENT

The authors express their thanks to:

Dr. Nett from University of Bremen and Dr. Albinson from Chalmers Institute of Technology, Sweden for their helpful collaboration

Dr. Th. Crowe from University of Virginia for providing the excellent Schottky barrier diodes

Dr. E. Armandillo for support under ESA contract: "Limb Sounder critical Receiver Technologies for Remote Sensing of the Atmosphere".

Mr. F. Leipold of Radiometer-physics for his indefatigable support

REFERENCES

1 P. Hartogh, G.K. Hartmann, P. Zimmermann
"Simultaneous Water Vapour and Ozone Measurements with MIllimeterwaves in the Stratosphere and Mesophere". IGRASS 3.-6. Juni Helsinki, 1991

2 F. Lewen, University of Cologne, private Communication

3 J. Hernichel, R. Schieder, J. Stutzki, B. Vowinkel, G. Winnewisser, P. Zimmermann
"A 492 GHz Cooled Schottky Receiver for Radio-Astronomy"
Proceeding of Third Intern. Symposium on Space Terahertz Technology, March 24-26, 1992, Michigan

4 R. Zimmermann, Ra. Zimmermann, P. Zimmermann
"All Solid-State Radiometer at 557 GHz", 21st European Microwave Conference Stuttgart 1991

5 M.H. Picket, J.C. Hardy, J. Farhoomand
"Characterisation of a Dual Mode Horn for Submillimeter Wavelengths", IEEE, MTT-32, 1984 (936-937)

6 P.H. Siegel, A. R. Kerr, W. Hwang
"Topics in the optimisation of millimeter-wave mixers"
NASA Techn. Paper 2287, March 1984

7 N. Keen, A. Grüb, H. Hartnagel, J. Freyer, H. Grote, Rü. Zimmermann
"New Submillimeter-Wave Schottky-Barrier Mixer, Diodes: First Results"
Revised late Paper, Stuttgart

8 T.W. Crowe, W.C.B. Peatmann
"GaAs Schottky Diodes for Mixing Applications byond 1 THz"
Proc. 2nd International Symposium on Space Terahertz Technology, Jet Propulsion Lab., Febr. 1991 (323-339)

	345 GHz [2] cooled 20 K	490 GHz [3] cooled 20 K	557 GHz [4] uncooled	650 GHz cooled 77 K
IF:	1.5 ± 0.25 GHz	1.5 ± 0.3 GHz	1.4 ± 0.3 GHz	10 ± 1 GHz
T_{IF}:	10 - 20 K	10 K	60 K	35 K
$T_{MIX,DSB}$	n.m. -	n.m. -	1200 K	2000 K *
$L_{C,DSB}$	n.m. -	n.m. -	8 dB	8.5 dB*
$T_{sys,DSB}$	350 K	550 K	1600 K	1750 K (3800 K SSB)

* only uncooled results; n.m. not measured

Fig. 1: RESULTS OF SYSTEMS WITH MIXERS AND MULTIPLIERS FROM RADIOMETER-PHYSICS

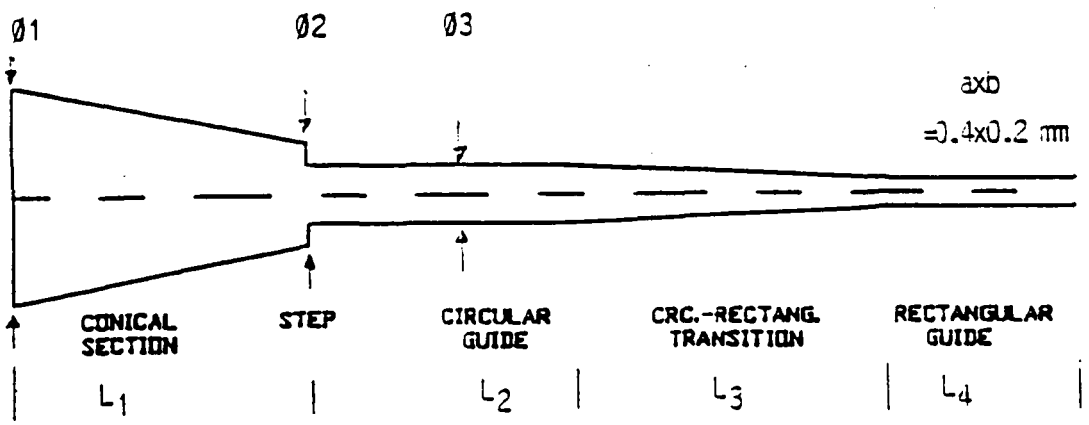

$Ø_1$ = 2.96 mm
$Ø_2$ = 0.60 mm
$Ø_3$ = 0.47 mm

L_1 = 4.9 mm
L_2 = 3.0 mm
L_3 = 2.3 mm
L_4 = 3.0 mm

Fig. 3: DUAL - MODE HORN (SCHEMATIC)

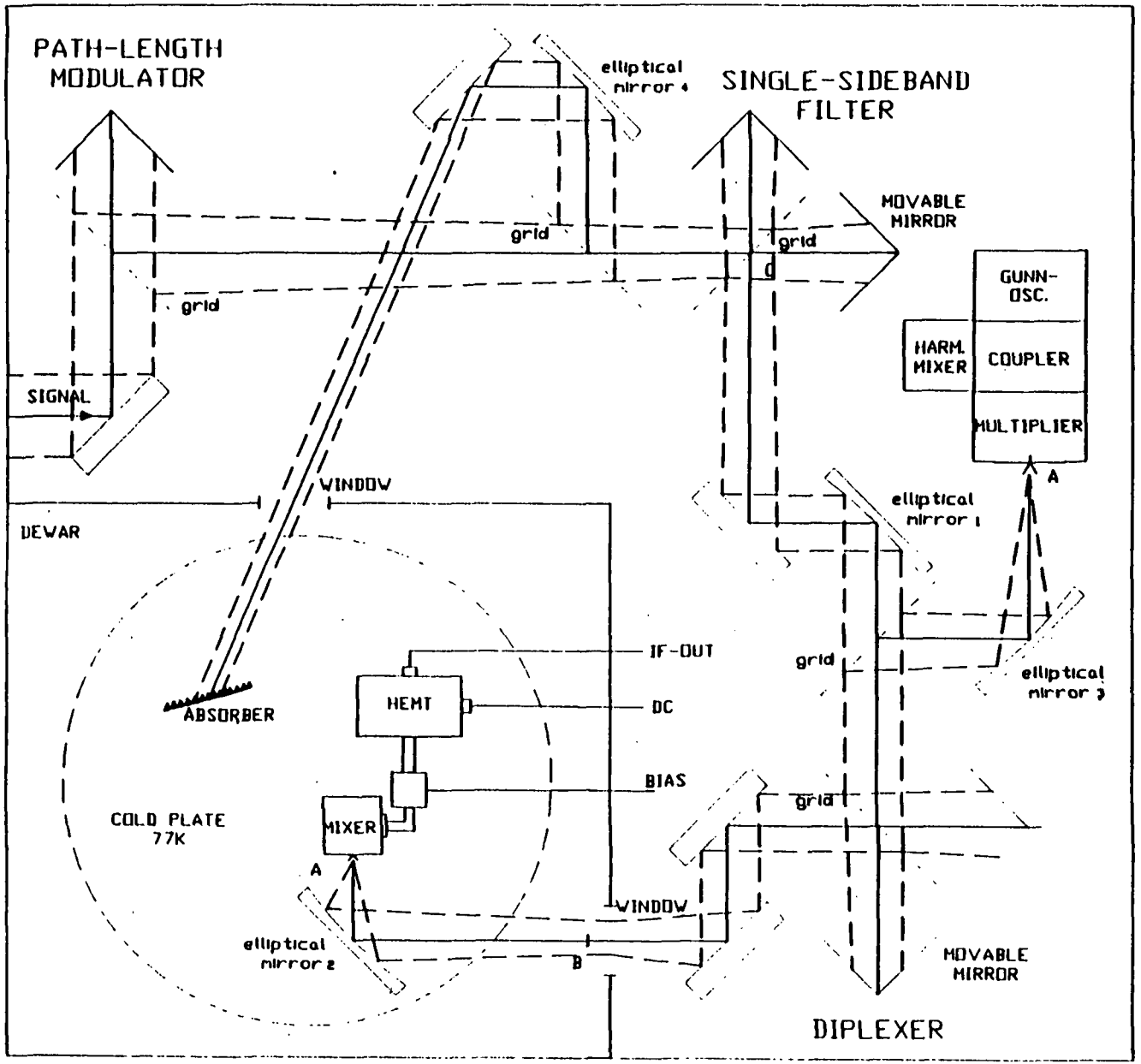

650 GHz COOLED SCHOTTKY RECEIVER BLOCK DIAGRAM

DIMENSIONS IN MM

BEAM WAISTS:

A: 0.82 mm
B: 6.0 mm
C: 4.65 mm
E: 4.0 mm

FIG. 2:
RECEIVER BLOCK DIAGRAM

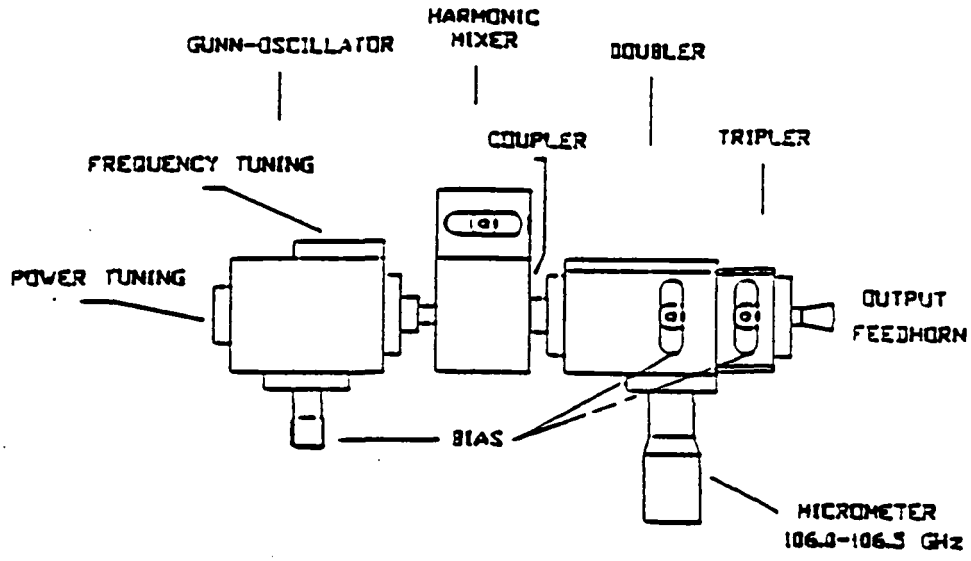

Fig. 4: LOCAL OSCILLATOR

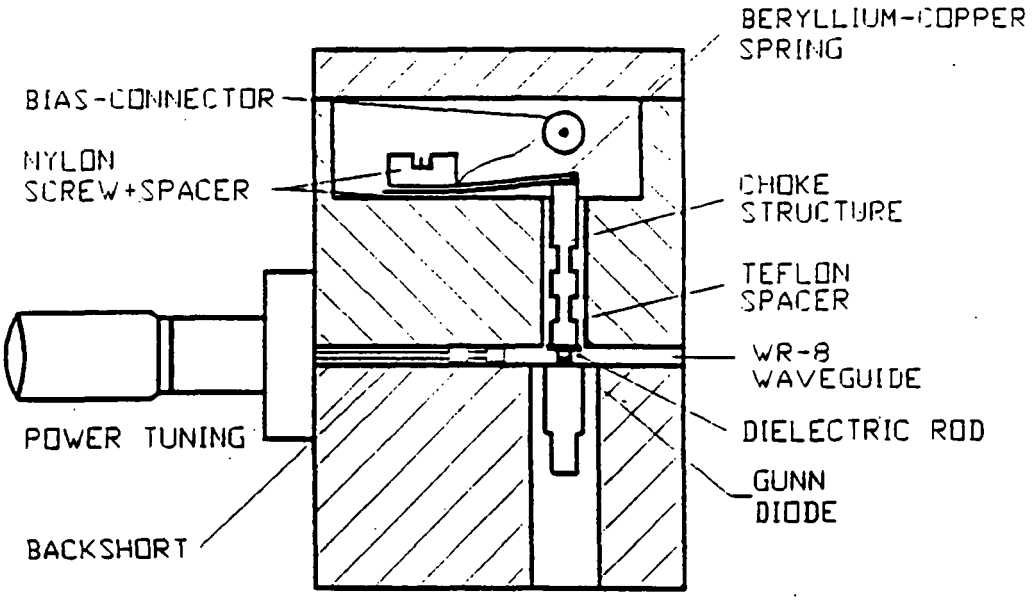

Fig. 5: GUNN-OSCILLATOR

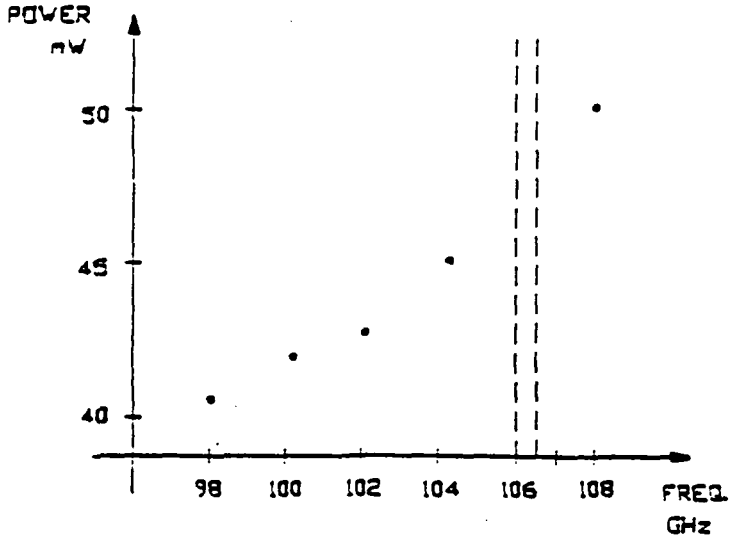

Fig. 6: GUNN OSCILLATOR OUTPUT POWER

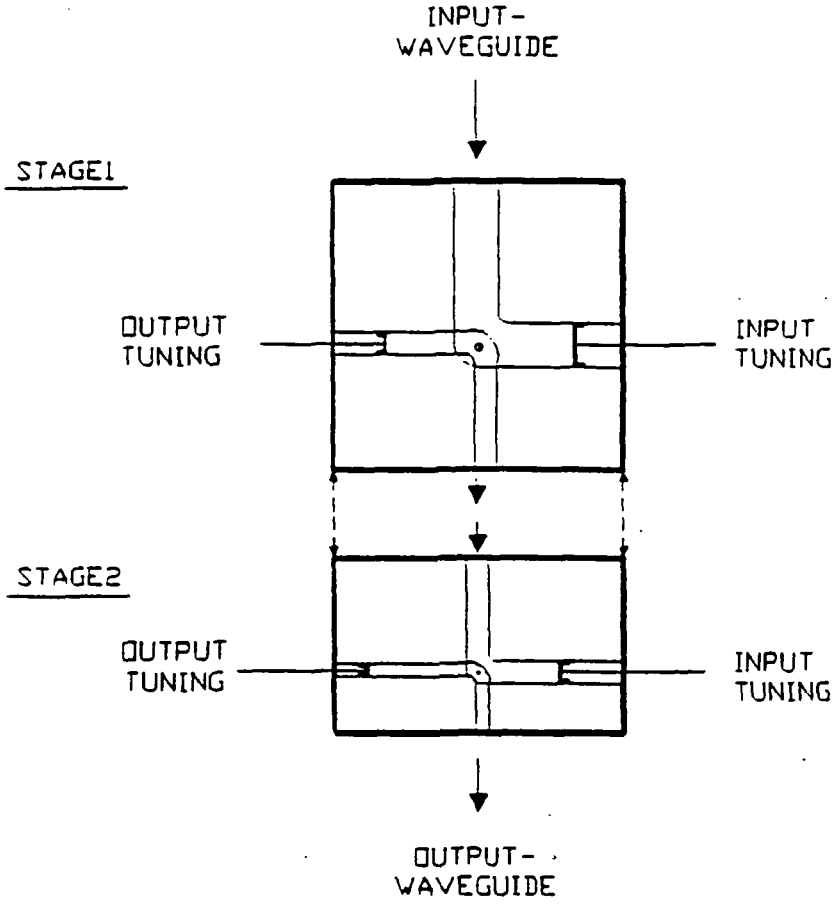

Fig. 7: ARRANGEMENT OF WAVEGUIDES FOR IN-LINE MULTIPLIERS

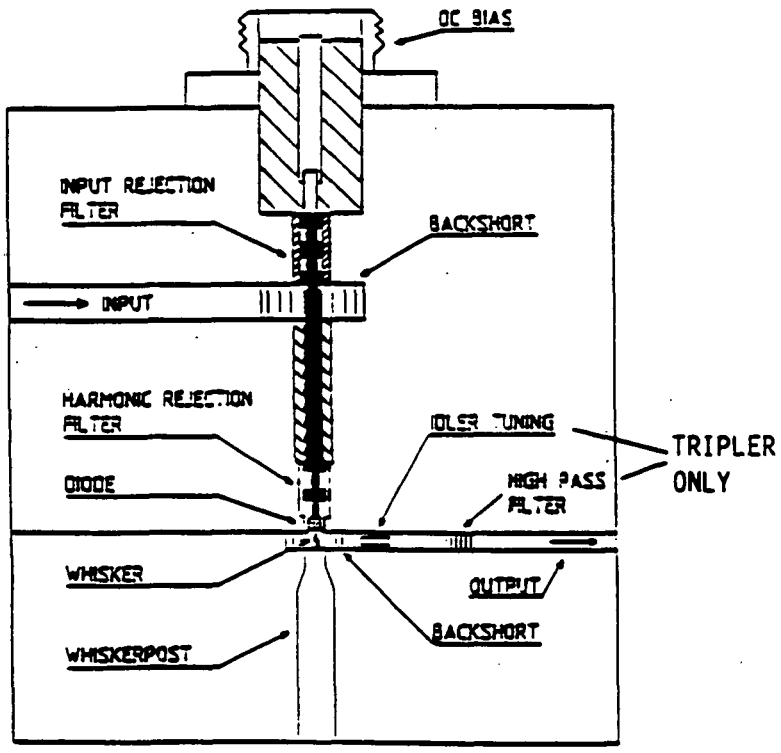

Fig. 8: MULTIPLIER (SCHEMATIC)

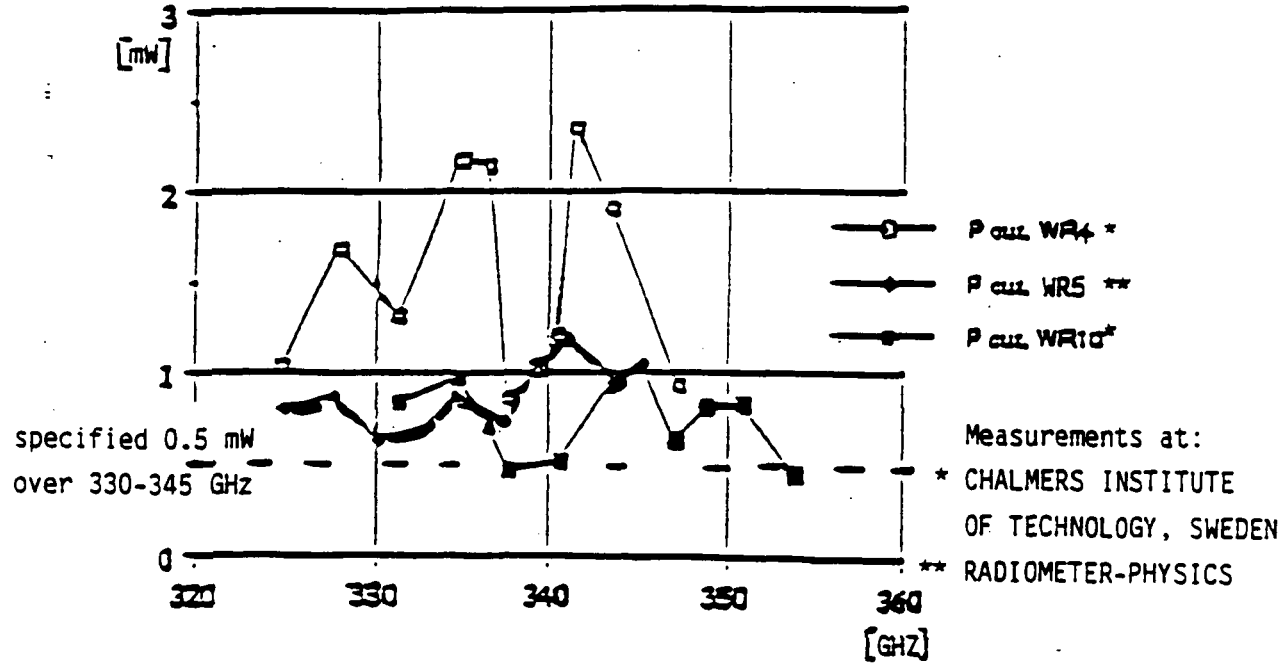

Fig. 9: MEASUREMENTS OF OUTPUT POWER WITH VARIOUS POWER METERS

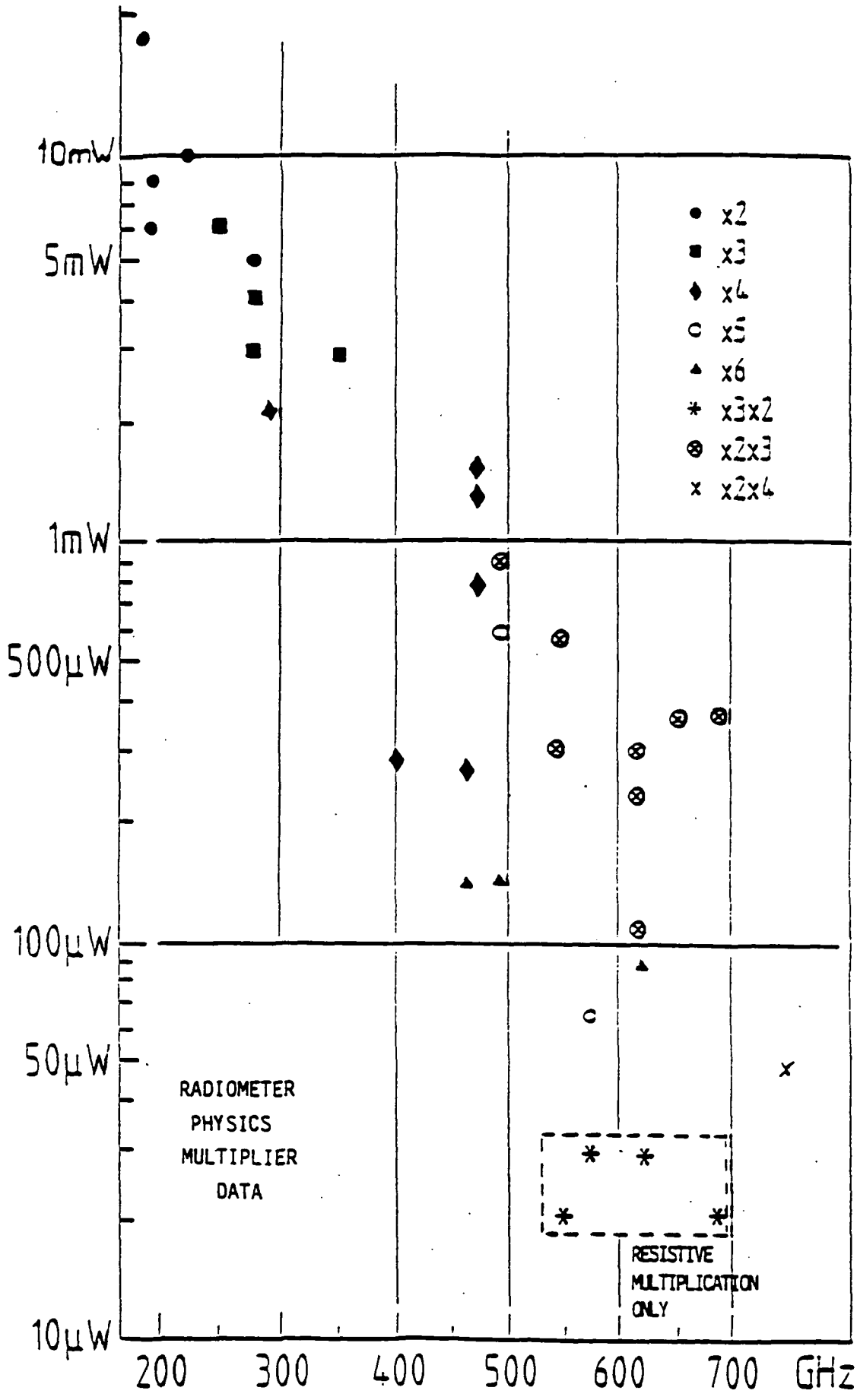

Fig. 10 POWER OUTPUTS FROM VARIOUS MULTIPLIERS

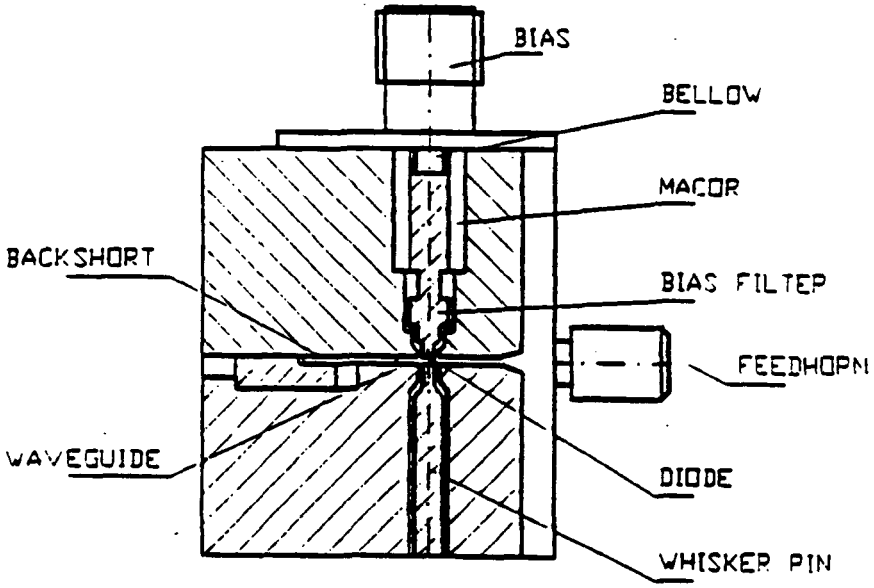

Fig. 11: MIXER (SCHEMATIC)

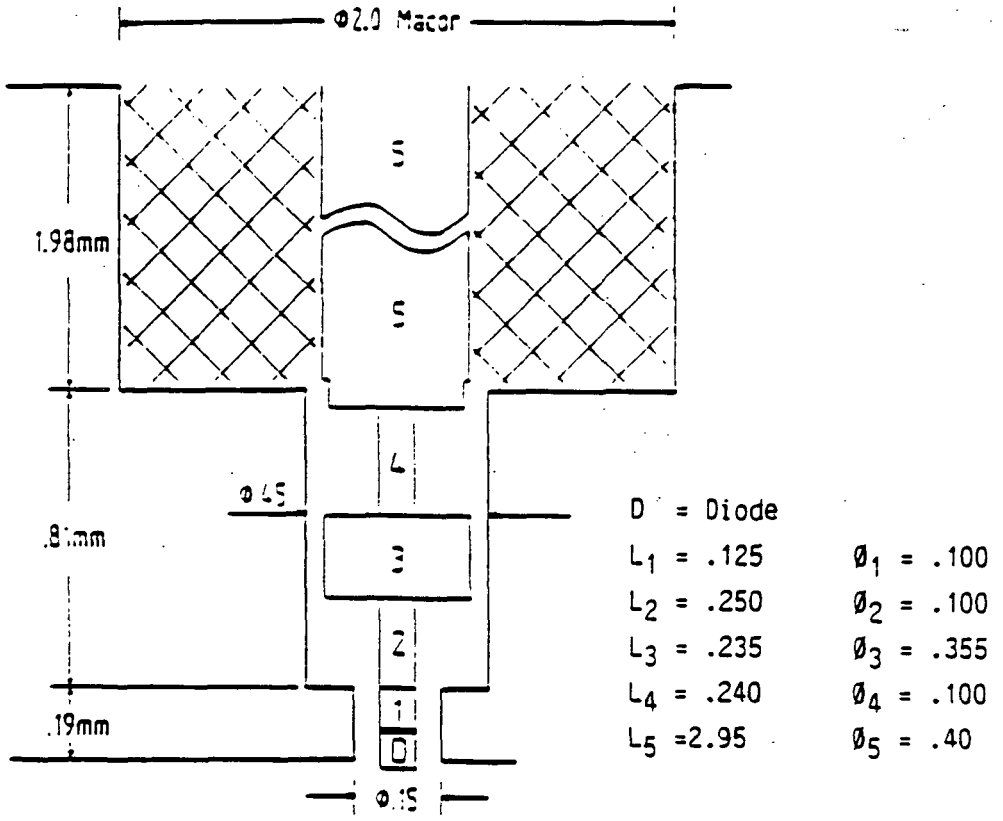

Fig. 12: MIXER CHOKE STUCTURE

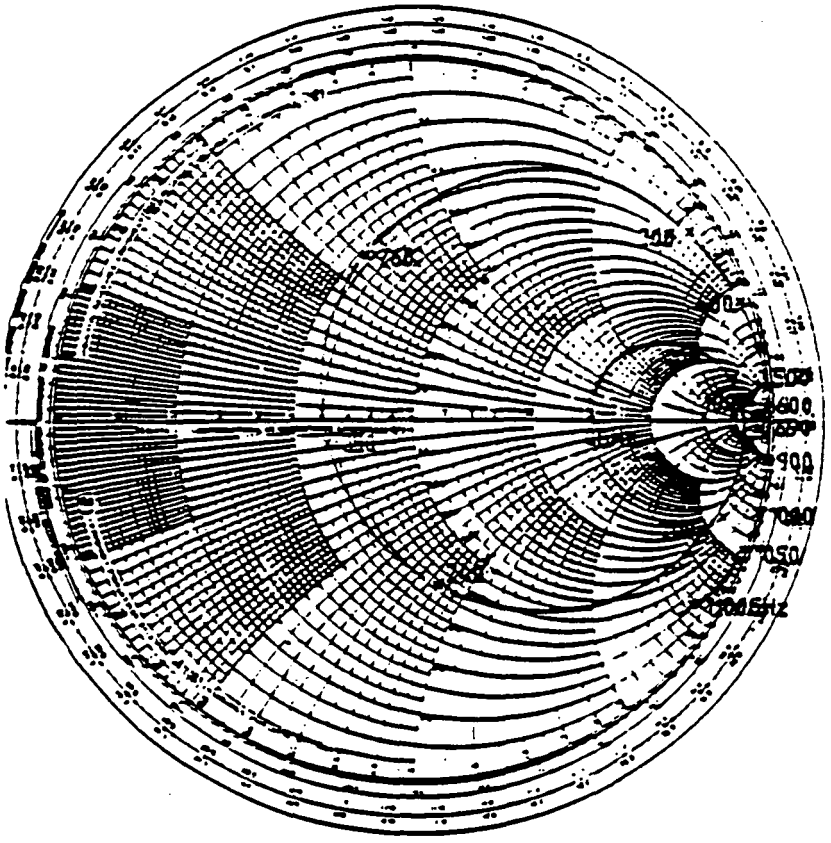

Fig. 13: MIXER CHOKE RF-IMPEDANCE

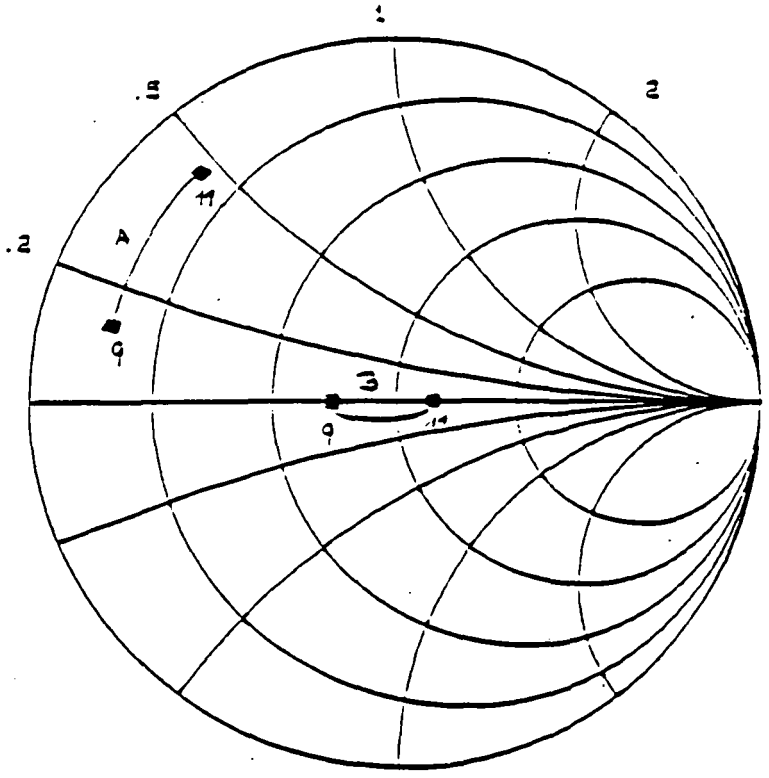

Fig. 14: MIXER IF-IMPEDANCE 9-11 GHZ
A: before B: after matching

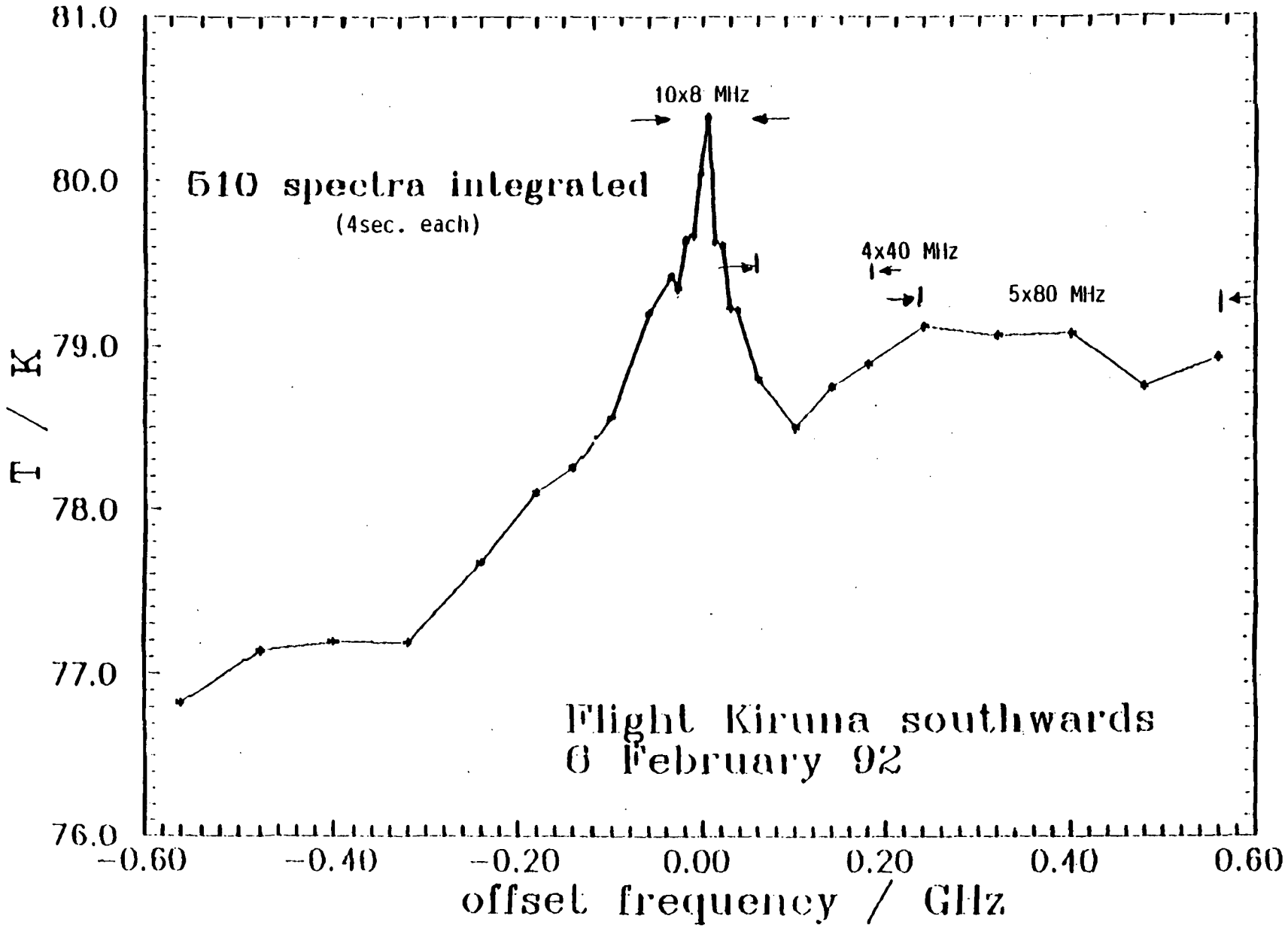

Fig. 15: ClO-LINE SPECTRUM

A 492 GHz Cooled Schottky Receiver for Radio-Astronomy

J. Hernichel, R. Schieder, J. Stutzki, B. Vowinkel,
G. Winnewisser, P. Zimmermann [1)]

I. Physikalisches Institut
Universität zu Köln
Zülpicher Straße 77
D-5000 Köln 41
Germany

Abstract

We developed a 492 GHz cooled GaAs Schottky receiver driven by a solid state local oscillator with a DSB noise temperature of 550 K measured at the telescope. The receiver-bandwidth is ≈1.0 GHz. Quasi-optical mirrors focus the sky and local oscillator radiation into the mixer. Stability analysis via the Allan variance method shows that the total system including a 1 GHz bandwidth acousto optical spectrometer built in Cologne allows integration times up to 100 sec per half switching cycle. We succesfully used the receiver at the KOSMA 3 m telescope on Gornergrat (3150m) located in the central Swiss Alps near Zermatt during January-February 1992 for observations of the 492 GHz, [CI] $^3P_1 \rightarrow {}^3P_0$ fine structure linie in several galactic sources. These observations confirm that Gornergrat is an excellent winter submillimeter site in accordance with previous predictions based on the atmospheric opacity from KOSMA 345 GHz measurements.

Introduction

After the first 345 GHz observing run in winter 1988/89 [7] followed by three succesfull runs in the subsequent winter periods, the 492 GHz receiver described here and the observations carried out in January-February 1992 are the second step in our development toward solid state LO Schottky receivers at 650 GHz and 800 GHz. The experience we made during the total observing time of 120 days for 345 GHz and 35 days for the 492 GHz receiver is that Gornergrat is an excellent ground based site for submillimeter radioastronomy during the winter period. Together with Mauna Kea, Hawaii, Gornergrat is the only site where 492 GHz observations have been carried out.

Receiver Description

Based on the experience of the 345 GHz receiver [2] we designed and built the receiver described here. The front end section is shown schematically in Fig. 1. The diplexer is a folded Fabry-Perot resonator using a mo vable elliptical mirror; the semi transparent plates ar wire grids with 125 lpi and 35 μm diameter wire; the yield 83 % reflection. A quasi-optical mirror arran gement focuses the sky and local oscillator radiatio through a Potter horn into the mixer. The mirror are corrected for phase errors [5] and were produce on a NC-milling machine at our Institute. Mixer an IF-amplifier are cooled to 20 K. The bandwidth of th HEMT amplifier is ≈1.0 GHz at 1.4 GHz center fre quency; its noise temperature is ≈8 K. Local oscilla tor power is delivered by a 98.2 GHz Gunn oscillato (60 mW) followed by a varactor quintupler, using a di ode type 2T2 (R_s=12 Ω, C_j=5 fF) from the SDL, Uni versity of Virginia. For an overview of typical multiplie performance see [8]. The local oscillator is PLL stabi lized. The Schottky- mixer is fundamentally pumped has a coaxial IF-section and uses a 1T6 diode from University of Virginia (R_s=20 Ω, C_j=0.35 fF). The mi xer is matched to the 50 Ω preamplifier impedance by a simple coaxial transformer, without using a circula tor. The receiver optics include two absorbing loads at ambient (295 K) and cold head (35 K) temperatures The receiver design is very compact; it consists of two packages: a) the optic front plate and dewar, b) the electronics, which fits in a 19" rack. A personal com puter is used to controle a) and b) fully remote. Fig. 2 shows the optics and dewar part; the optic-plate diame ter is 32 cm and the weight is less than 45 kg, including the cold head.

Receiver Characterization

The DSB receiver noise temperature was measured to be 500 K for a 600 MHz HEMT amplifier and 550 K for the 1 GHz broadband HEMT amplifier, installed at the telescope. Fig. 3 shows the receiver noise tempera ture versus mixer current for ambient and 20 K; coo ling thus reduces the noise temperature by a factor of 2.8. The receiver noise temperature measured over the

1 GHz bandwidth at the telescope, using the Y-factor method, is shown in Fig. 4: Receiver beam pattern measurements were made in the laboratory; the 1/e opening angle was measured to be 8.9° compared to the calculated value of 8.8°. Fig. 5 shows the two receiver beampattern (horizontal and vertical scan) the Gauss-fit and the 1/e-level which is the 13% power level. Similar to earlier publications [3] we used receiver stability tests, to verify the overall system performance. The Allan variance method [6] adopted in Cologne, using a 1 GHz bandwidth acousto optical spectrometer (AOS) yields an integration time in the total power mode of 100 sec per duty cycle (Fig. 6), without significant increase in baseline structure.

Observing Run on Gornergart

We observed several galactic sources during the observing run in January- February 1992 at the KOSMA telescope. Fig. 7 shows two highlights of the [C I] $^3P_1 \rightarrow {}^3P_0$ 492 GHz lines from the galactic sources S 140 and NGC 1977. The observations confirm that the KOSMA location is an excellent winter submillimeter site in accordance with previous predictions based on the atmospheric opacity from KOSMA 345 GHz measurements [4]. The precipitable water vapor is below 1 mm for about 20% of the time in the winter period. Surprisingly the site does not show a significant variation of transmission between day and night time. A Jupiter map (Fig. 8) shows a clean beam. The half power diameter of 54" results after deconvolution of Jupiter size at the time of observation in a beam FWHM of 48", consistent with the 47" predicted from the 12 dB edge taper measured at the telescope. The telescope surface was measured and adjusted by a holographic method [1] to an rms of $\approx 38\mu m$

Conclusion

We have designed and built a compact, cooled 492 GHz Schottky mixer receiver with solid state LO. The receiver was installed on the KOSMA 3 m telescope on Gornergrat during January-February 1992 and used to observe several galactic sources. It is shown that the telescope surface and the KOSMA site are well suited for 492 GHz observations. The receiver is build modular, compact and lightweight and thus is usable for observations on other telescopes. The receiver noise temperature is 550 K DSB at the telescope over a simultaneous bandwidth of ≈1.0 GHz.

Acknowledgements

We gratefully acknowledge the unconventional and efficient technical support during the observing run by Ralf and Rüdiger Zimmermann. The receiver development was funded by the Bundesminister für Forschung und Technology (BMFT). The KOSMA 3 m-telescope is operated by the University of Cologne and supported by the Deutsche Forschungsgemeinschaft (DFG) through grant SFB 301, as well as special funding from the Land Nordrhein-Westfalen.

References

[1] FUHR, W. ET AL: *Holographic alignment of the KOSMA 3 m reflector*, Univ. Cologne, in preparation.

[2] HERNICHEL, J.: *Aufbau und Inbetriebnahme des 345 GHz Empfängers für das Kölner 3 m-Radioteleskop*, Diplom Thesis, Univ. Cologne, (1989).

[3] HERNICHEL, J., LEWEN, F., MATTHES, K., KLUMB, M., ROSE, T., WINNEWISSER, G., ZIMMERMANN, P.: *Submillimeter Receiver Development at the University of Cologne*, Proc. of Second Intern. Symposium on Space Terahertz Technology, JPL, Pasadena, 641-647 (1991).

[4] KRAMER, C., STUTZKI, J.: *Atmospheric Transparency at Gornergrat*, Technical Memorandum, Univ. Cologne, (1990).

[5] ROSE, T.: *Aufbau eines SIS-Empfangssystem mit quasioptischem Mischer*, Diplom Thesis, Univ. Cologne, (1989).

[6] SCHIEDER, R., TOLLS, V., WINNEWISSER, G.: *The Cologne Acousto-Optical Spectrometers*, Experimental Astronomy **1**, 101 (1989).

[7] WINNEWISSER, G., ZIMMERMANN, P., HERNICHEL, J., MILLER, M., SCHIEDER, R., UNGERECHTS, H.: *CO submillimeter observations from Gornergrat*, Astron. Astrophys. **230**, 248-251 (1990).

[8] ZIMMERMANN, R., ZIMMERMANN, R., ZIMMERMANN, P.: *All Solid State Radiometers for Environmental Studies to 700 GHz*, this Conference.

[1)]present address: Radiometer Physics, Bergerwiesenstr.15, D-5309 Meckenheim, Germany

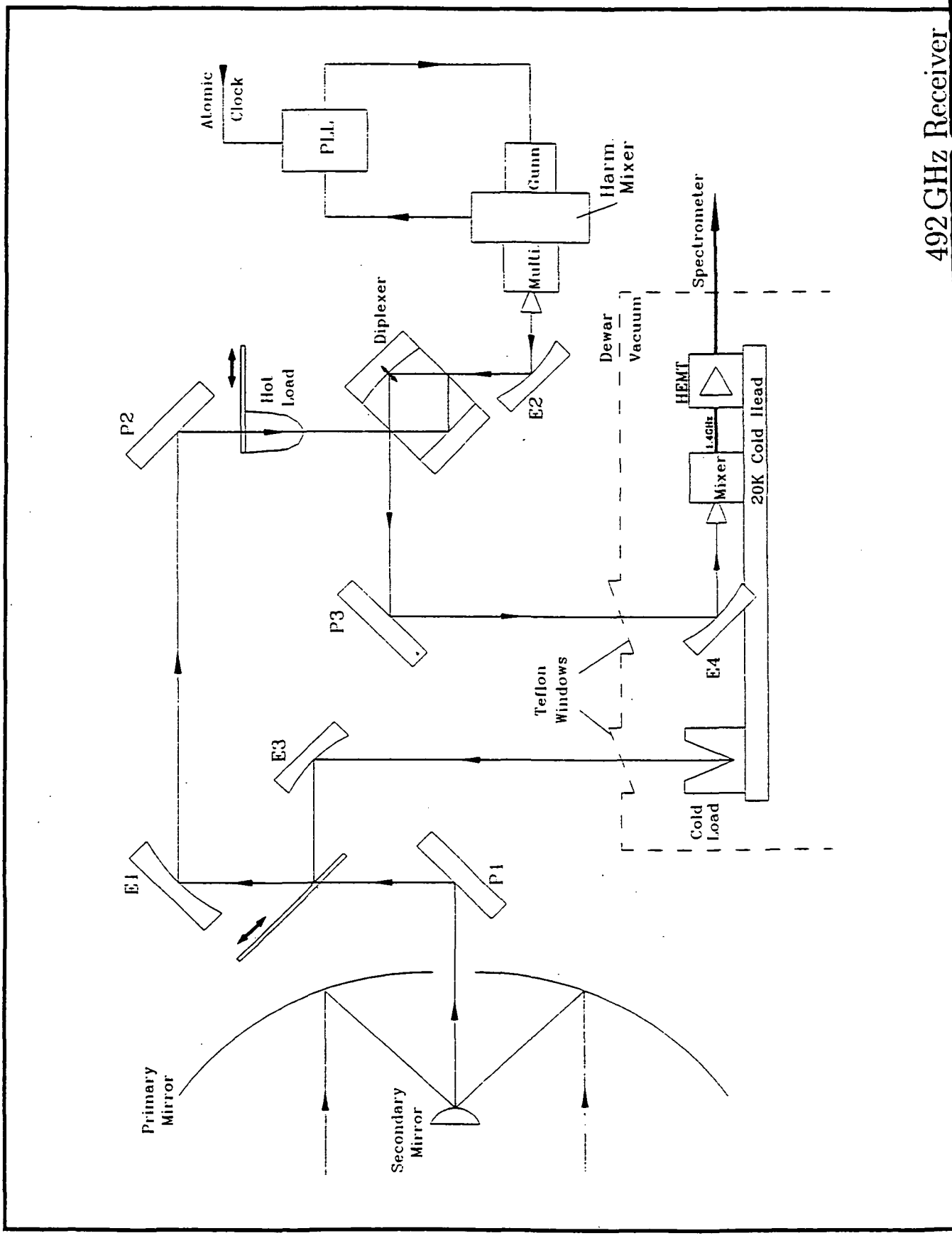
492 GHz Receiver
Atomic Clock
PLL
Gunn
Harm. Mixer
Multi.
Spectrometer
Diplexer
Dewar
Vacuum
HEMT
1.4GHz
Mixer
20K Cold Head
Hot Load
P2
E2
P3
E4
Teflon Windows
E3
Cold Load
E1
P1
Primary Mirror
Secondary Mirror

figure 1

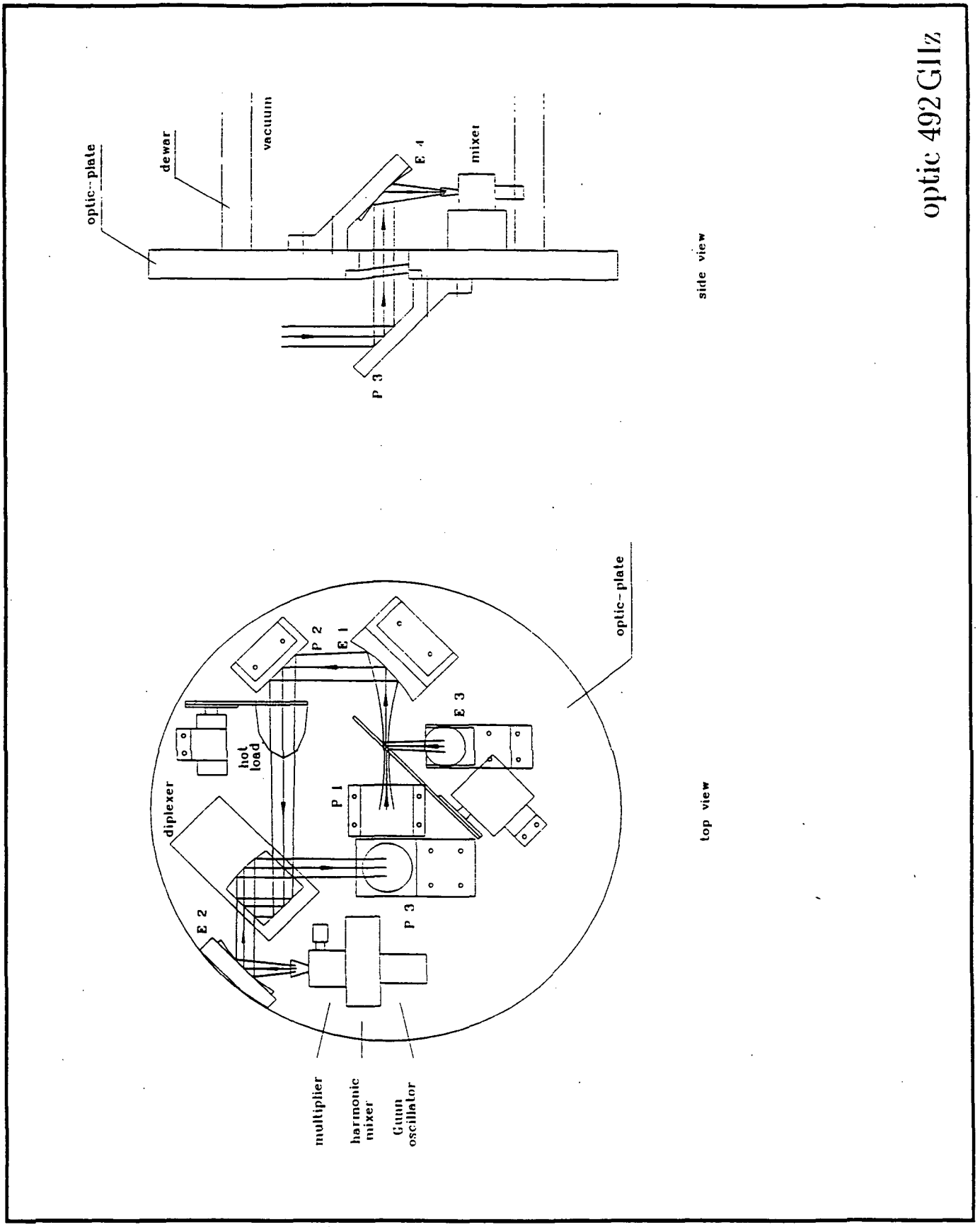
optic 492 GHz
optic-plate
dewar
vacuum
E 4
mixer
P 3
side view
optic-plate
P 2
E 1
E 3
hot load
diplexer
P 1
E 2
P 3
top view
multiplier
harmonic mixer
Gunn oscillator

figure 2

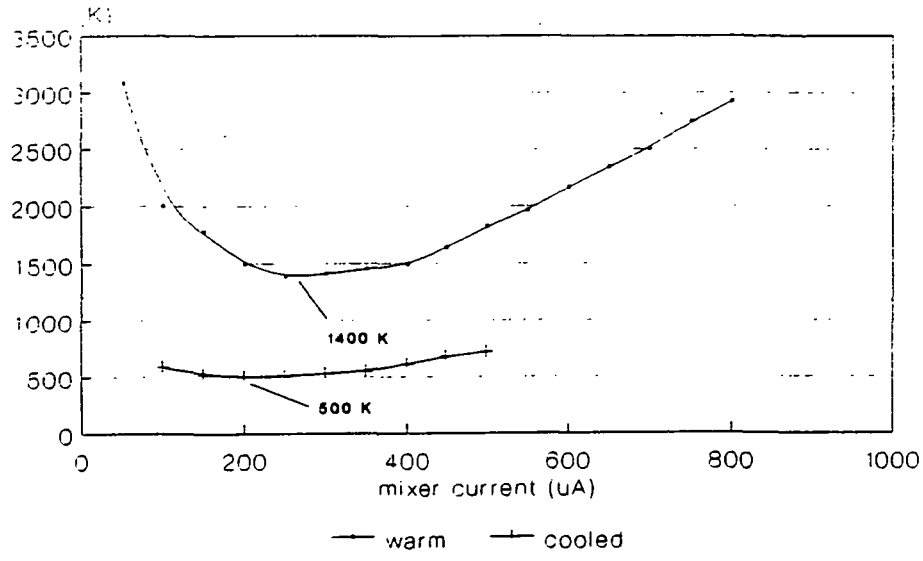

receiver noise temperature versus mixer current figure 3

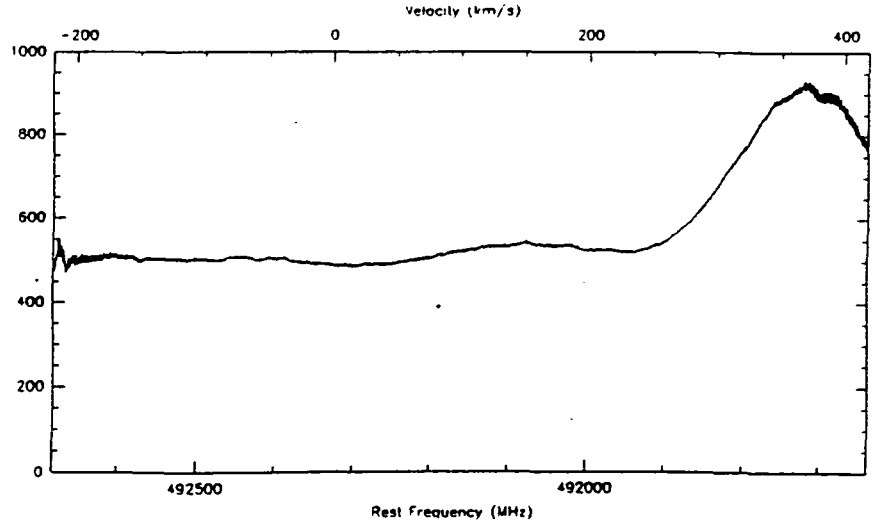

receiver noise temperature versus frequency figure 4

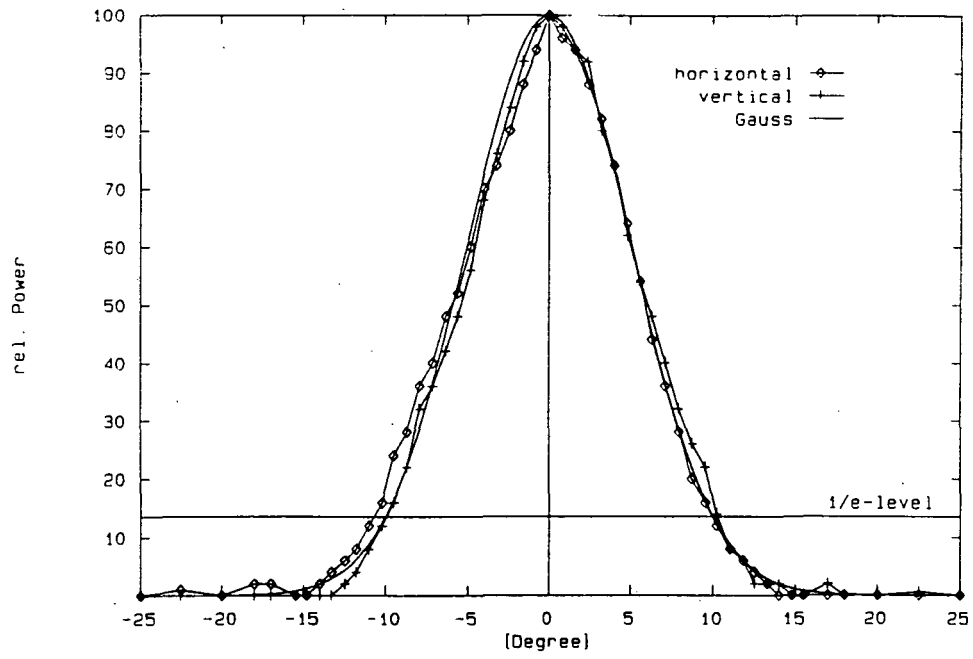

receiver beam pattern 492 GHz

figure 5

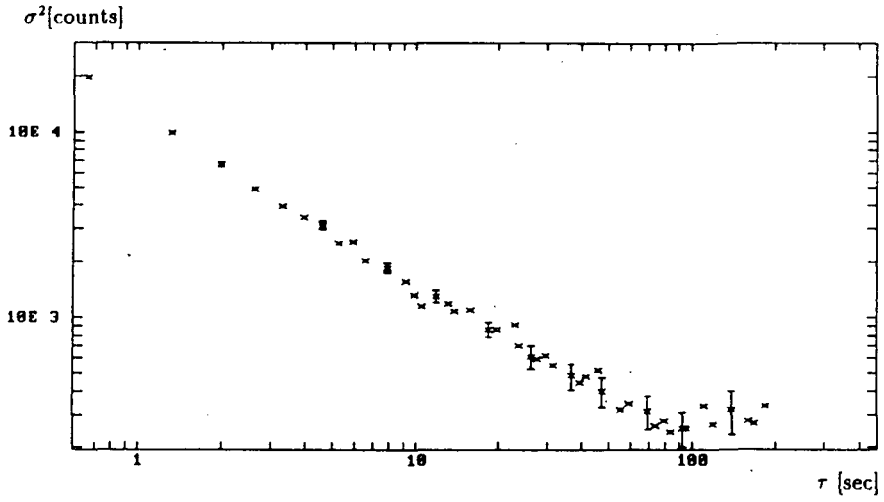

Allan plot

figure 6

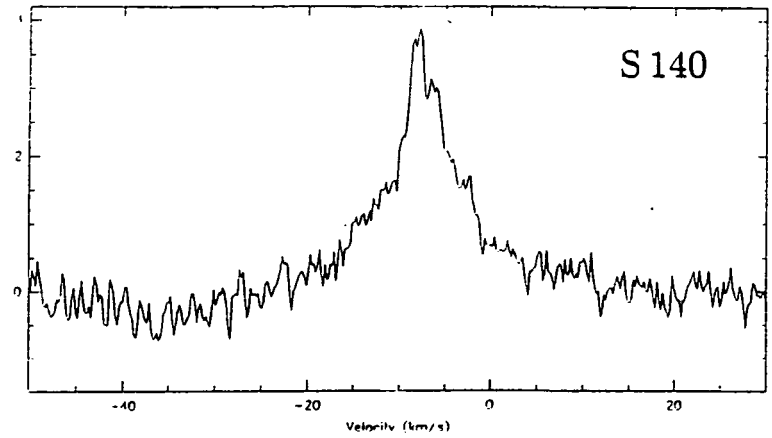

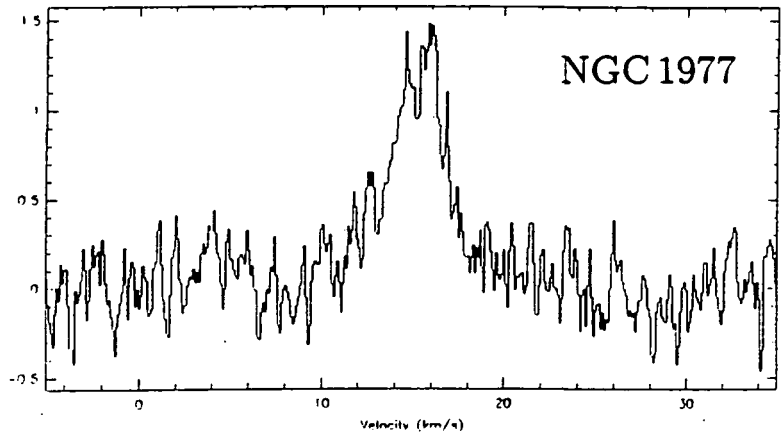

figure 7

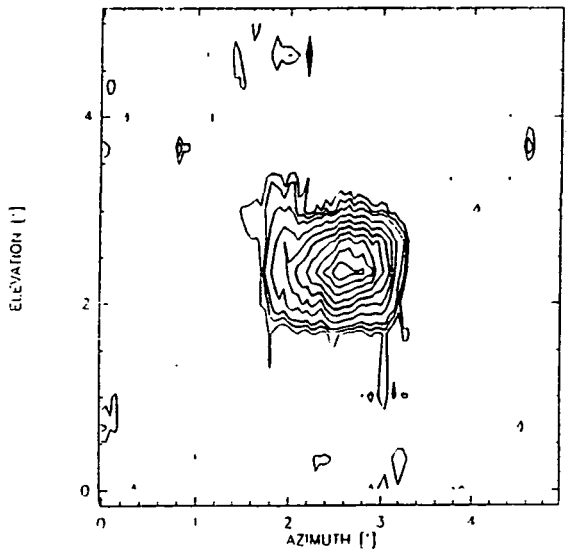

Jupiter beam map 492 GHz

10 15 20 (10)·90 % of peak

figure 8